UNITED STATES DEPARTMENT OF THE INTERIOR

GEOLOGICAL SURVEY

PROCEEDINGS OF

WORKSHOP XIX

ACTIVE TECTONIC AND MAGMATIC PROCESSES BENEATH LONG VALLEY CALDERA, EASTERN CALIFORNIA
VOLUME I

24 - 27 January 1984

Sponsored by

U.S. GEOLOGICAL SURVEY

VOLCANO HAZARDS PROGRAM

Editors and Convenors

David P. Hill
U.S. Geological Survey
Menlo Park, California 94025

Roy A. Bailey
U.S. Geological Survey
Menlo Park, California 94025

Allan S. Ryall
University of Nevada
Reno, Nevada 89557-0018

OPEN-FILE REPORT 84-939

Compiled by
Muriel Jacobson

MENLO PARK, CALIFORNIA
1984

1A

CONFERENCES TO DATE

Conference I	Abnormal Animal Behavior Prior to Earthquakes, I Not Open-Filed
Conference II	Experimental Studies of Rock Friction with Application to Earthquake Prediction Not Open-Filed
Conference III	Fault Mechanics and Its Relation to Earthquake Prediction Open-File No. 78-380
Conference IV	Use of Volunteers in the Earthquake Hazards Reduction Program Open-File No. 78-336
Conference V	Communicating Earthquake Hazard Reduction Information Open-File No. 78-933
Conference VI	Methodology for Identifying Seismic Gaps and Soon-to-Break Gaps Open-File No. 78-943
Conference VII	Stress and Strain Measurements Related to Earthquake Prediction Open-File No. 79-370
Conference VIII	Analysis of Actual Fault Zones in Bedrock Open-File No. 79-1239
Conference IX	Magnitude of Deviatoric Stresses in the Earth's Crust and Upper Mantle Open-File No. 80-625
Conference X	Earthquake Hazards Along the Wasatch and Sierra-Nevada Frontal Fault Zones Open-File No. 80-801
Conference XI	Abnormal Animal Behavior Prior to Earthquakes, II Open-File No. 80-453
Conference XII	Earthquake Prediction Information Open-File No. 80-843
Conference XIII	Evaluation of Regional Seismic Hazards and Risk Open-File No. 81-437

Open-File Service Section
Branch of Distribution
U.S. Geological Survey
Box 25425, Federal Center
Denver, Colorado 80225

CONFERENCES TO DATE

Workshop XV	Preparing for and Responding to a Damaging Earthquake in the Eastern United States Open-File No. 82-220
Workshop XVI	The Dynamic Characteristics of Faulting Inferred from Recordings of Strong Ground Motion Open-File No. 82-591
Workshop XVII	Hydraulic Fracturing Stress Measurements Open-File No. 82-1075
Workshop XVIII	Continuing Actions to Reduce Losses from Earthquakes in the Mississippi Valley Area Open-File No. 83-157
Workshop XIX	Active Tectonic and Magmatic Processes Beneath Long Valley Caldera, Eastern California Open-File No. 84-939
Workshop XX	The 1886 Charleston, South Carolina, Earthquake and its Implications for Today Open-File No. 83-843
Workshop XXI	A Workshop on "Continuing Actions To Reduce Potential Losses from Future Earthquakes in the Northeastern United States" Open-File No. 83-844
Workshop XXII	A Workshop on "Site-Specific Effects of Soil and Rock on Ground Motion and the Implications for Earthquake-Resistant Design" Open-File No. 83-845
Workshop XXIII	A Workshop on "Continuing Actions to Reduce Potential Losses from Future Earthquakes in Arkansas and Nearby States" Open-File No. 83-846
Workshop XXIV	A Workshop on "Geologic Hazards in Puerto Rico" Open-File No. 84-761
Workshop XXV	A Workshop on "Earthquakes Hazards in the Virgin Island Region" Open-File No. 84-762
Workshop XXVI	A Workshop on "Evaluating the Regional and Urban Earthquakes Hazards in Utah" Open-File No. 84-763

Open-File Service Section
Branch of Distribution
U.S. Geological Survey
Box 25425, Federal Center
Denver, Colorado 80225

TABLE OF CONTENTS

VOLUME I

GEOLOGY

GEOPHYSICS

RECENT ACTIVITY

VOLUME II

THE GEOTHERMAL SYSTEM

RELATED MAGMATIC SYSTEMS

ACKNOWLEDGEMENTS

This conference was sponsored by the U.S. Geological Survey under the Volcano Hazards Program. The initial suggestion for holding a "Redbook" conference on current activity in Long Valley caldera came from Bill Ellsworth. Both he and Patrick Muffler provided unfailing encouragement and support for this endeavor from start to finish.

Wanda Seiders arranged the transportation and accomodations for the conference as well as the many logistical details that permitted the participants to concentrate on the scientific issues at hand. Sherry Johnson and Janice Ellefson typed and dispatched the pre and post - conference notices and correspondence with accuracy and efficiency. Muriel Jacobson assembled the manuscripts contributed by the participants following the conference and applied the many finishing touches that have resulted in this final product. Their expert handeling of each of these critical details underlies the success of the conference and its proceedings.

David P. Hill
Roy A. Bailey
Alan S. Ryall

LIST OF PARTICIPANTS

Charles R. Bacon
U.S. Geological Survey
Branch of Igneous and
Geothermal Processes
345 Middlefield Road - MS 910
Menlo Park, California 94025

Roy A. Bailey
U.S. Geological Survey
Branch of Igneous and
Geothermal Processes
National Center - MS 951
Reston, Virginia 22092

David D. Blackwell
Department of Geological Sciences
Southern Methodist University
Dallas, Texas 75275

Bernard Chouet
U.S. Geological Survey
Branch of Seismology
345 Middlefield Road - MS 977
Menlo Park, California 94025

Robert L. Christiansen
U.S. Geological Survey
Branch of Igneous and
Geothermal Processes
345 Middlefield Road - MS 910
Menlo Park, California 94025

Robert S. Cockerham
345 Middlefield Road - MS 977
U.S. Geological Survey
Branch of Seismology
345 Middlefield Road - MS 977
Menlo Park, California 94025

G. Corrado
Vesuvius Observatony
University of Naples
Naples, Italy

Chris Cramer
California Division of
Mines and Geology
2815 O Street
Sacramento, California 95816

James F. Davis
California Division of
Mines and Geology
2815 O Street
Sacramento, California 95816

Daniel Dzurisin
U.S. Geological Survey
David A. Johnston
Cascades Volcano Observatory
5400 MacArthur Boulevard
Vancouver, Washington 98661

John C. Eichelberger
Sandia National Laboratories
Geochemistry Division, 1543
Albuquerque, New Mexico 87185

William L. Ellsworth
U.S. Geological Survey
Branch of Seismology
345 Middlefield Road - MS 977
Menlo Park, California 94025

John F. Hermance
Geophysical/Electromagnetic Laboratory
Department of Geological Sciences
Brown University
Providence, Rhode Island 02912

David P. Hill
U.S. Geological Survey
Branch of Seismology
345 Middlefield Road - MS 977
Menlo Park, California 94025

Robert C. Jackens
U.S. Geological Survey
Branch of Geophysics
345 Middlefield Road - MS 989
Menlo Park, California 94025

Bruce R. Julian
U.S. Geological Survey
Branch of Seismology
345 Middlefield Road - MS 977
Menlo Park, California 94025

Edy Kissling
Institut furr Geophysik
ETH - Hoenggerborg
CH8093 Zurich
Switzerland

Peter Lipman
U.S. Geological Survey
Central Environmental Geology Branch
Mail Stop 913
Denver, Colorado 80225

Jenny Metz
Department of Applied Sciences
Stanford University
Stanford, Californi 94305

Steve McNutt
California Division of
Mines and Geology
2815 O Street
Sacramento, California 95816

C. Dan Miller
U.S. Geological Survey
Branch of Igneous and
Geothermal Processes
Denver Federal Center - MS 903
Denver, Colorado 80225

Patrick Muffler
U.S. Geological Survey
Branch of Igneous and
Geothermal Processes
345 Middlefield Road - MS 910
Menlo Park, California 94025

Kazuaki Nakamura
Earthquake Research Institute
University of Tokyo
Tokyo, Japan

Chris G. Newhall
U.S. Geological Survey
David A. Johnston
Cascades Volcano Observatory
5400 MacArthur Boulevard
Vancouver, Washington 98661

David D. Pollard
Department of Applied Earth
Sciences
Stanford University
Stanford, California 94305

Keith Priestly
Seismological Laboratory
University of Nevada
Reno, Nevada 89557

John B. Rundle
Geophysics Division - 1541
Sandia National Laboratories
Albuquerque, New Mexico 87185

Alan Ryall
Seismological Laboratory
University of Nevada
Reno, Nevada 89557

Chris O. Sanders
Division of Geological
and Planetary Science
California Institute of Technology
Pasadena, California 91125

James C. Savage
U.S. Geological Survey
Branch of Tectonophysics
345 Middlefield Road - MS 977
Menlo Park, California 94025

Herbert R. Shaw
U.S. Geological Survey
Branch of Igneous and
Geothermal Processes
345 Middlefield Road - MS 910
Menlo Park, California 94025

Kerry Sieh
Division of Geological and
Planetary Science
California Institute of Technology
Pasadena, California 91125

Michael L. Sorey
U.S. Geological Survey
Office of the Regional Hydrologist
345 Middlefield Road - MS 939
Menlo Park, California 94025

Ute Vetter
Seismological Laboratory
University of Nevada
Reno, Nevada 89557

Terry C. Wallace
Department of Geosciences
University of Arizona
Tucson, Arizona 85721

James H. Whitcomb
Cooperative Institute for Research
in Environmental Sciences
University of Colorado/NOAA
Boulder, Colorado 80309

Stanley N. Williams
Department of Earth Sciences
Dartmouth College
Hanover, New Hampshire 03755

Mark D. Zoback
U.S. Geological Survey
Branch of Tectonophysics
345 Middlefield Road - MS 977
Menlo Park, California 94025

ACTIVE TECTONIC AND MAGMATIC PROCESSES BENEATH LONG VALLEY CALDERA, EASTERN CALIFORNIA: A SUMMARY

by

David P. Hill[1], Alan S. Ryall[2], and Roy A. Bailey[1]

[1]U.S. Geological Survey
345 Milldlfield Road
Menlo Park, CA 94025

[2]Seismological Laboratory
University of Nevada
Reno, NV 89557

INTRODUCTION

The Long Valley caldera - Mono Craters region of eastern California provides a rich field for the study of active tectonic and magmatic processes. For most of its recorded history (the last 150 years) the Long Valley region has maintained one of the highest rates of earthquake activity at the magnitude (M) 5 to 6 level in California. Moreover, the presence of large, well-exposed, Holocene fault scarps leave little doubt that the region experienced a number of major earthquakes (M > 6.5) over the last 10,000 to 20,000 years. The last volcanic eruptions in the area occurred just 500 to 600 years ago along the Inyo-Mono Craters chain. These are the most recent eruptions within the band of Quaternary volcanic centers that extends northward from the Salton Trough in southern California, through the central Mojave Desert, along the eastern escarpment of the Sierra Nevada range, and beyond into north-central Nevada. In fact, active volcanoes of the Cascade range aside, these are the most recent eruptions in the conterminous United States. Long Valley caldera, together with the Yellowstone caldera in Wyoming and the Valles caldera in New Mexico are the only three silicic volcanic systems in the conterminous United States to produce major, caldera-forming, ash-flow eruptions in the last 1 million years. This history of tectonic and volcanic activity together with a location at the base of the eastern escarpment of the Sierra Nevada range and the western margin of the Basin and Range province make the Long Valley region a particularly important example of the contemporary encroachment of Basin-and-Range extensional tectonics into a thick, stable crust of the Sierra Nevada block.

Scientific interest in the Long Valley region was heightened starting in October 1978 with the occurrence of a M-5.7 earthquake midway between Bishop and Mammoth Lakes followed a year and a half later by the swarm-like sequence of four, M-6 earthquakes that occured on May 25-27, 1980 (Cramer and Toppazada, 1980; Ryall and Ryall, 1981a,b). Interest was further fueled by the recurring sequence of moderate earthquake swarms, which included rapid-fire sequences of many small earthquakes having the appearence of spasmodic tremor, in the south moat of the caldera over the next three years (Ryall and Ryall, 1981b, 1983) and by evidence for inflation of the resurgent dome in the west-central part of the caldera that began in mid-1979 (Savage and Clark, 1982; Castle and others, 1984). The character of this activity together with recognition of the seismic and volcanic history of the region raised concerns over the possibility of a major earthquake (M > 6.5) somewhere in the Long Valley - Mono Lake - White Mountain region in the near future (VanWormer and Ryall, 1980; Wallace, 1978, 1984; Ryall and Ryall, 1983) and of renewed volcanic activity in the Long Valley - Mono Craters area (Miller and others, 1982). These concerns were officially expressed by the U.S. Geological Survey through release of a Hazard Watch on May 27, 1980, for potentially damaging earthquakes and release of a Hazard Notice on May 25, 1982, for potential volcanic activity. (On September 30, 1983, the three-level set of criteria used by the U.S. Geological Survey to formally express the relative urgency of geologic hazards was changed to a single-level criteria. Hazard Notice and Hazard Watch were the lowest and middle levels, respectively, under the old system. In a letter dated July 11, 1984, the Director of the U.S. Geological Sruvey advised officials of the State of California that the current level of activity in the Long Valley region does not satisfy the "imminent threat" criteria for a formal Hazard Warning under the single-level system.)

The series of papers in this volume are the product of a conference on the tectonic and magmatic processes behind these recent signs of unrest in the

Long Valley - Mono Craters area. The conference was held in Napa, California, on January 24-27, 1984, and attended by thirty eight earth scientists from a variety of government and academic institutions in the United States plus particiants from the Earthquake Research Institute, University of Tokyo, Japan, and the Vesuvius Observatory, University of Naples, Italy. Presentations and discussions during the conference centered around constraints and resolution of models provided by available data for the physical processes driving the recent activity. Because of the localized nature of this recent activity in the Long Valley area, we specifically focused on local magmatic processes and their relation to tectonic processes along the eastern Sierra Nevada escarpment at the expense of more regional seismogenic processes and the potential of a major earthquake in the White Mountains seismic gap.

In organizing the conference, we were motivated by recognition that the scientific insights on geologic processes resulting from the discussions would improve the basis for a reliable assessment of the nature of possible hazards posed by processes driving the current activity. In addition we felt that, although little time was devoted to discussions of monitoring techniques or a review of monitoring results, the insights gained from the conference would improve data collection and geophysical monitoring strategies for defining future patterns of activity and for providing adequate warning should the activity lead to an eruption.

Discussions during the conference and the papers in this volume fall under five general catagories: 1)Geological evidence on the history of volcanic activity and the chemical evolution of the associated magma chambers, 2) Geophysical evidence for subsurface structure and magma chamber geometry, 3) Recent seismicity and ground deformation as immediate symptoms of currently active processes, 4) The geothermal system and evidence for contemporary heat sources, and 5) Evidence on processes and structure from other active magmatic systems in the world and from erosional remnants of older magmatic systems.

CONSTRAINTS FROM THE GEOLOGIC RECORD

Knowledge of the eruptive history of a volcanic system based on field mapping and age-dating techniques and the chemical and thermal evolution of the underlying magma chambers based on petrological/geochemical studies of derived lava flows is critical to understanding the current state of the magmatic system and to assessing likely evolution of the system in the near future. Bailey (this volume) emphasizes that three closely-related volcanic systems currently exist in the Long Valley region, each in a different stage of development. Most of our attention in this conference focused on the large, mature system beneath Long Valley caldera and the adjacent, smaller, more youthful Inyo-Mono Craters system. The incipient Mono Lake system received but passing attention.

The Long Valley system is a fully developed resurgent caldron (Smith and Bailey, 1968) that produced a catastrophic caldera-forming, ash-flow eruption about 0.7 m.y. ago (Bailey and others, 1976). Bailey (this volume) presents evidence here that gradual cooling and crystallization of the residual magma chamber following the caldera-forming eruption was interupted 0.28 m.y. ago by a renewed episode of crustal heating presumably associated with the intrusion of mantle-derived, mafic magma into the lower crust. He points out that the last eruptions from the Long Valley magma chamber, which produced the Mammoth Knolls in the west moat 0.1 m.y. ago, are somewhat more crystal-rich than the 0.28-m.y.-old Hot Creek flow indicating a resumption of the cooling trend, but he goes on to suggest that the unrest shown by the caldera over the last few

years may be symptomatic of yet another episode of crustal heating and further recharge of the Long Valley magma chamber.

Clues to the state of the Long Valley magma chamber prior to the caldera-forming eruption are contained in the lava flows of Glass Mountain. This complex of high-silica rhyolite lavas began leaking from a growing Long Valley magma chamber along an incipient ring-fracture system as early as 2.1 m.y. ago. Metz and Mahood (this volume) find in their study of the Glass Mountain lava flows that, in contrast with many other major silicic systems, lavas of early eruptions from the pre-caldera magma chamber (between 2.1 and 1.3 m.y. ago) were not only more highly evolved than those of the later eruptions (between 1.1 and 0.8 m.y ago) but also more evolved than the caldera-forming Bishop Tuff erupted 0.7 m.y.ago. They also find evidence that the early Glass Mountain flows were cooler and less fluid than later flows. They think that the Long Valley magma chamber was probably in an unstable, potentially explosive state during most of the later-phase, pre-caldera eruptions 1.1 to 0.8 m.y ago and that eruption of the Bishop Tuff 0.7 m.y. ago was possibly triggered by a major tectonic event (earthquake) in the area. Although the texture of the 0.1-m.y-old Mammoth Knolls flows make it unlikley that the Long Valley caldera has returned to this unstable, pre-caldera state, the recent unrest may indicate resumption of a long-term trend in that direction.

The most recent eruptions in the Long Valley region occurred at the northern and southern end of the Inyo-Mono Craters chain 500 to 600 years ago. These eruptions were not fed by the Long Valley magma chamber but the smaller, more youthful system beneath the Mono Craters. Whether the lavas erupted from the southern end of the Inyo Craters have partially mixed with magma from the immediatly adjacent Long Valley system remains a matter of debate. In their independent studies of the products of these recent eruptions, Miller (this volume) and Sieh (this volume) find many similarities between the 500 to 550 year-old Inyo Craters eruptions and the 600-year-old Mono Craters eruptions. Both resulted from the injection of 6-to 8-km-long, silicic dikes into the shallow crust, and both breached the surface at several points to produce linear trends of eruptive vents. The successive eruptions from vents over each of these dikes occurred within a relatively short time (certainly within a matter of years and probably within months or less). The progression of events in both cases began with ground cracking and the formation of a graben over the long axis of the dike (presumably associated with intense earthquake swarm activity), followed in succession by phreatic explosions as shallow extensions of the dike interacted with the local ground water, plinian to sub-plinian, explosive eruptions producing ash-falls and pyroclastic flows, and concluding with the slow extrusion of viscous, dome-building, rhyolite flows. Eichelberger and Westrich (this volume) describe the relation of volatiles in the magma to this progression of eruption styles based on their study of obsidians from the recent Inyo and Mono vents.

As Miller (this volume) points out, these two most recent examples of eruptive activity in the Long Valley region indicate a likley progression of events should the current unrest lead to renewed eruptive activity from either the Inyo-Mono Craters system or from the Long Valley magma chamber. In particular, as a dike works its way toward the surface, we should see increasing deformation developing over the dike followed by the onset of ground cracking and the formation of a medial graben as described by Pollard, Fink, and Delaney (this volume). We should also expect the initial eruption to be followed by several subsequent eruptions over the ensuing weeks to perhaps months from vents that may be separated by several km from each other along the axis of the localized deformation and medial graben. We also recognize the

possibility that this sequence could be triggered by a major earthquake in the area and that, under this situation, events could evolve much more rapidly than might normally be anticipated.

STRUCTURE AND MAGMA CHAMBER GEOMETRY

The most direct evidence on the contemporary configuration of the magma chambers underlying the Long Valley region comes from a variety of geophysical measurements, and of these, seismic measurements provide the greatest resolution on location and geometry. Results summarized during this conference indicate that the upper surface of the Long Valley magma chamber is more irregular than previously thought (Steeples and Iyer, 1976; Ryall and Ryall, 1981a), and that, if a substantial magma chamber exists beneath the Mono Craters complex, it must be at least 10 km deep.

The recent seismic-refraction described by Hill, Kissling, Leutgert and Kradolfer (this volume) support earlier evidence (Hill, 1976) for reflections from the roof of the Long Valley magma chamber at a depth of 6 to 7 km beneath the northwestern margin of the resurgent dome. Evidence for the geometry of magma bodies in the Long Valley region is based on Sanders' (this volume) analysis of P and S wave attenuaton patterns for ray paths from almost 300 local earthquakes recorded at some 30 regional seismic stations (Sanders and Ryall, 1983; Sanders, 1984). The results of his study support the 6- to 7-km depth to the top of a magma body beneath the northwest section of the resurgent dome suggested by the seismic-refraction data, but they also suggest that a cupola-shaped protrusion of the magma body extends to within 4.5 km of the surface beneath the Casa Diablo area along the southeastern part of the resurgent dome. Subsequent work by Ryall and Ryall (1984) indicates the existence of smaller magma bodies or dike swarms along the Hilton Creek fault south of the caldera at depths of 5 to 6 km. We summarize some of these relations in a northwest-southeast cross-section through Long Valley caldera in Figure 1.

The absence of a substantial, shallow magma chamber beneath the Mono craters system is indicated by both the recent seismic-refraction measurements and by the magnetotelluric measurements described by Hermance, Slocum, and Neuwman (this volume). This geophysical evidence is consistent with Bacon's (this volume) reasoning that the linear, north-south trend of the Inyo-Mono vents is controlled by the regional tectonic stress field in an upper crust that is still too thick and brittle to reflect the perturbing effects of the underlying magma chamber.

The tomographic inversion of several thousand P-wave travel-times between local earthquakes and as many as 90 seismic stations described by Kissling, Ellsworth, and Cockerham (this volume) indicates that the deeper portions of the magma chambers in the Long valley region are aligned to form an elongate zone subparallel with the major range-front faults. Their result is consistant with the distribution of attenuating bodies found by Sanders (this volume) and Sanders and Ryall (1983) and it adds credence to Bailey's picture (Figure 2 in Bailey, this volume) showing a common mid-crustal root to the magma chambers underlying Mono Lake, the Mono-Inyo Craters system, and Long Valley caldera. The north-northwest trend of the mid-crustal, low-velocity body defined by the tomographic study suggests that injection of mafic magmas into the lower-to-mid crust is controlled by the same extensional tectonic stress field that produces the adjacent range-front, normal faults.

Although the telluric field patterns described by Hermance, Slocum, and Newman (this volume) are ambigious with respect to depths of anomalous bodies, the spatial pattern of low-resistivity anomalies they obtain is consistent

with the distribution of both surficial, fault-controlled basin structures and at least the upper portions of conductive, magma bodies suggested by the seismic studies.

RECENT ACTIVITY

The major earthquake sequence that began in the Long Valley region in the fall of 1978 includes a M-5.7 earthquake in October 1978, four M-6 events in May 1980, a M-5.9 event in September 1981, an intense swarm including two M-5 earthquakes in January 1983 within a background of thousands of smaller earthquakes. The associated inflation of the resurgent dome that began in mid-1979 has resulted in a cumulative uplift that now amounts to about 50 cm over the south-central section of the resurgent dome. We have summarized the temporal relation between the earthquake activity and uplift in Figure 2. Most of the discussion during the conference concentrated on specific aspects of this activity.

One of the more noteworthy aspects of this earthquake sequence is the fact that it does not seem to be related in any simple way to the major, range-front, normal faults that form the eastern escarpment of the Sierran Nevada range. Rather, it appears that the earthquakes are associated with complex brecciation of a large volume of the crust that includes the south moat of Long Valley caldera and an extensive, triangular-shaped region of the Sierran block to the south. With improved resolution of earthquake hypocentral locations afforded by better definition of crustal structure in the area, some systematic patterns begin to emerge from what initially appeared to be a diffuse distribution of earthquakes. Results described by Lide and Ryall (this volume) and Kissling, Ellsworth, and Cockerham and Pitt (this volume) show several subparallel lineations of epicenters with a north-northeast trend within the triangular-shaped aftershock zone. These lineations are parallel with the left-lateral, strike-slip plane in focal mechanisms obtained from many of the larger earthquakes in the sequence suggesting that left-lateral slip on subparallel north-northeast striking planes is a significant component of the seismogenic deformation within the Sierra Nevada block associated with this earthquake sequence. Based on their interpretation of three-dimensional plots of hypocenters for 2,200 well-located earthquakes of M>1 that occurred beneath the Sierra block south of the caldera between June 1, 1982 and July 31, 1984, however, Cockerham and Pitt (this volume) argue that some of the north-northeast lineations apparent in map view are actually two-dimensional projections of hypocenters distributed along north-northwest striking planes that dip to the northeast.

The increasing number of focal mechanisms obtained for earthquakes in the sequence provides further evidence that the least compressive stress in the southern part of the caldera and in the Sierran block to the south has an anomalous, northeast-southwest orientation with respect to the east-west to northwest-southeast orientation common throughout the rest of the western Great Basin (Vetter and Ryall, 1983). Vetter's (this volume) analysis of over 100 focal mechanisms in the sequence supports the results of the earlier study of Vetter and Ryall (1983) showing a tendency for the shallower events (depths less than 6 to 9 km) to have predominantly strike-slip mechanisms and for the deeper events to have normal mechanisms. She finds only weak evidence, however, for a systematic variation in focal mechanisms with depth for earthquakes inside the caldera where most earthquakes are less than 8 km deep. Savage and Cockerham (this volume) see no evidence for a systematic variation in focal mechanisms with depth in their sample of 60 earthquakes from the January 1983 swarm. Instead, they find that earthquakes occuring in the east

limb of the swarm have almost exclusively strike-slip mechanisms showing right-lateral slip on planes sub-parallel with the east-limb axis and that earthquakes in the west limb, which is largely coincident with the "epicentral area", include both strike-slip and normal mechanisms with the T-axes clustering about a north-northeast orientation.

An interesting seismological controversy has developed over the focal mechanisms for the M-5.8 earthquake of October 1978 and two of the M-6 earthquakes in the May 1980 sequence. This controversy is pursued in the papers by Julian and Sipkin, Wallace, and Chouet and Julian (all this volume). The seismic waves radiated by the October 1978 event and the first and last of the four M-6 events of May 1980 (the northern- and southern-most events in the north-trending linear trend) do not fit the standard double-couple radiation pattern found for most earthquakes. Julian and Sipkin expand on an earlier argument (Julian, 1983) that the anomalous radiation patterns are best explained by a compensated linear vector dipole (CLVD) mechanism, which they interpret as the abrupt injection of magma from a nearby reservoir into a north-northwest trending dike (a CLVD mechanism requires no volume change over the source dimension of the earthquake).

Wallace (this volume) and Lide and Ryall (this volume) argue the opposite viewpoint that the anomalous radiation patterns are due to complex shear failure on fault planes of differing orientation and that fluid (magma) injection is not required to explain these earthquakes. Chouet and Julian pursue a point made by Aki (1984) that the rapid opening of a crack by fluid injection would produce compressional P-wave first motions everywhere in contrast to that predicted by a pure CLVD mechanism. They go on to argue that, in the plane of the crack, a weak, compressional pulse would be followed by a much stronger dilatational pulse and that observed discrepancies between short- and long- period P waves may in fact be consistent with a fluid injection mechanism. At this stage, it seems that the available data are not adaquate for an unambigious decision between these competing possibilities.

Another remarkable aspect of the Long Valley earthquake sequence is the repeated occurrence of earthquake swarms in a small volume of the crust centered 2 to 3 km east-southeast of Mammoth Lakes (Ryall and Ryall, 1981a, 1983). Cockerham and Pitt (this volume) point out that, while numerous swarms and flurries of small earthquakes have occurred throughout the south moat of the caldera following the May 1980 earthquakes, all of the largest earthquake swarms (swarms that include at least one M>4 earthquake, at least 200 smaller events, and that persist for at least two days) within the caldera have occurred in this epicentral area. Moreover, it appears that the three largest earthquakes within the caldera also originated within this same, limited volume. Best estimates for the epicenter of the second M-6 event of May 25, 1980, place it at the northern end of this swarm area, and the two M-5 earthquakes that occurred during the first hour of the January 1983 swarm were located here as well. In addition, several of the swarms that occurred in this swarm area between May 1980 and May 1982 included rapid-fire sequences of small earthquakes that Ryall and Ryall (1981a; 1983) identified as spasmodic tremor, which is commonly but not exclusively associated with the injection of magmatic fluids. The small cluster of earthquakes that Smith (this volume) interprets as being due to a localized intrusion of magma or volatiles is also located in this swarm area.

The recharge of a small volume of the crust with strain energy to produce recurring earthquakes swarms is symptomatic of localized dike intrusions as suggested in a model for earthquake swarms by Hill (1977). The interpretation of the deformation associated with the January 1983 earthquake swarm by Savage

and Cockerham (this volume) weakly supports local intrusion to depths as shallow as 4 km within the volume of the western part of the January swarm as does the evidence for a small gravity high over the swarm area described by Jachens and Roberts (this volume). Rather than the mathematically idealized representation of the intrusion as a single, thin dike coincident with the long axis of the January swarm modeled by Savage and Cockerham, the intrusion may be in the form of diffuse distribution of smaller dikes throughout the highly brecciated crust of the swarm volume. Individual dikes may be oriented with their long axis in a west-northwest direction perpendicular to the local direction of the least compressive stress (earthquake T-axes) with shear failure (earthquakes) occurring on planes oblique to the dikes (see Hill, 1977; Vetter and Ryall, 1983). Pollard, Fink, and Delaney (this volume) demonstrate, however, that in an extensional stress regime, dikes can form in pre-existing fractures aligned with their long axis at a significant angle to the local, greatest principal stress direction. In any case, the magma intruded to form such a distribution of relatively small dikes in a volume of the crust sufficiently cool to sustain brittle failure (earthquakes) would solidify within a few days after emplacement.

Nakamura (this volume) describes three mechanisms for the elongate distribution of earthquakes. As Savage and Cockerham (this volume) point out, the elongated distribution of earthquakes in the January 1983 swarm actually consists of two segments differing in orientation by 20° separated by an aseismic zone. It appears that the eastern segment corresponds to Nakamura's first mechanism in which the earthquakes are aligned along a near-vertical strike-slip fault. The western segment, which is largely coincident with the area of earlier swarms, apparently corresponds more closely to his third mechanism. In this case, the elongate trend of earthquakes is sub-parallel with the local orientation of the greatest horizontal principal stress (P-axis) as is typical of many earthquake swarms in volcanic areas.

Deformation of the earth's surface during the January 1983 earthquake sequence is dominated by inflation of the Long Valley magma chamber. Although details differ between the models proposed by Savage and Cockerham (this volume), Savage and Clark (1982), and by Rundle and Whitcomb (this volume) to explain the measured vertical and horizontal deformation fields, both sets of models require a volume increase of from 0.1 to 0.2 km^3 in a magma chamber at depths between 5 and 10 km beneath the resurgent dome over the period from mid-1979 to the present, and both require about 15 cm of right-lateral slip along a vertical, west-northwest striking fault in the south moat during the January 1983 earthquake swarm. These results are clearly resolved by the available deformation data for 1975 through 1983.

Because all of these models provide acceptable fits to the deformation data, the differences in details such as the shape of the magma chamber, and the exact location and number of dislocation surfaces (faults) are not well resolved by the available data. Thus, for example, the Savage-Cockerham model weakly favors dike intrusion in the west limb of the January 1983 swarm; the Rundle-Whitcomb model does not include dike intrusion but places a magma chamber at a depth of only 5 km beneath the Casa Diablo area. Rundle and Whitcomb explain the aseismic gap in the central section of the swarm distribution as resulting from high normal stress acting across the fault due to increasing pressure in the shallow magma chamber beneath Casa Diablo; Savage and Cockerham see inflation resulting in the a trap-door-like uplift of a north-dipping roof to the magma chamber decreasing the normal stress across the fault, which permits dike injection within the west section of the swarm distribution. Whitcomb (this volume) suggests dike injection beneath the Inyo-

Mono Craters sometime between July 1982 and July 1983 based on repeated gravity measurements and his interpretation of the leveling data. Rundle and Whitcomb incorporate normal slip on a vertical representation of the Hilton Creek fault in their model; Savage and his colleagues do not include slip on the Hilton Creek fault in their models.

Another important aspect of the deformation field not adaquately resolved by the available deformation data is the temporal relation between episodes of inflation and earthquake activity (see Figure 2). The relatively infrequent measurements of the level lines and the trilateration networks through mid-1983 do not reveal whether inflation proceeded in a more or less steady manner, whether it occurred co-seismically with the larger earthquake sequences, or whether it occurred episodically with accelerating deformation prior to the the major earthquake swarms. In the case of the January 1983 swarm, the repeated high-precision gravity measurements made by Jachens and Roberts (this volume) provide evidence that most of the 7 cm uplift associated with this swarm occurred within a day or so following the largest earthquakes in the swarm. The enhanced deformation-monitoring program initiated in the spring of 1983 should enable us to clearly define the temporal relation of any future deformation to the associated earthquake activity.

EVIDENCE FROM THE GEOTHERMAL SYSTEM

The geothermal system in the Long Valley caldera offers some tantalizing but still enigmatic clues on the size and location of heat sources at depth and on the thermal evolution of these sources over the last several ten-thousand years. Blackwell (this volume) and Sorey (this volume) review what is currently known about the Long Valley geothermal system based on publicly available data and they explore some of the implications and remaining uncertanties attendant on these data.

The present-day thermal flux from Long Valley caldera is intermediate between the giant Yellowstone system and the smaller Valles caldera. A shallow, convective hydrothermal system circulating within the caldera fill and the Bishop tuff mask the conductive heat flux from deeper magmatic sources. The active thermal springs and fumaroles that breach the surface in the vicinity of Casa Diablo and Hot Creek, for example, are fed by a hot (100° to 170°C), westward-flowing aquifer at depths generally less than 100 to 150 m. Blackwell reviews three possible models to explain the contemporary hydrothermal system: 1) the heat is supplied entirely by the recent intrusive activity along the Inyo Craters system over the last 1000 years, and the deep system beneath the resurgent dome is either dead or effectively sealed from the shallow system by impermeable deposits above a waning magma chamber, 2) the shallow system is fed by a large system deep beneath the central section of the caldera by upwelling flow along fractures associated with the Hilton Creek fault system along the eastern side of the resurgent dome, or 3) the shallow system is fed by a deep source somewhere beneath the west or southwest part of the caldera. He argues that the second model is effectively eliminated from consideration by recent evidence from additional wells indicating the heat source for this shallow hydrothermal system lies somewhere west of Casa Diablo. Sorey points out, however, that hydraulic-head differences and stable isotope relations indicate a separate convective system in the east moat of the caldera with at least minor injection of thermal fluids along the Hilton Creek fault.

Sorey (this volume) reviews some remarkable geochemical evidence from the saline deposits of Searles Lake 200 km south-southeast of Long Valley first documented by G. I. Smith and his colleagues (see Smith and others, 1983)

indicating that these deposits were derived from the Long Valley geothermal system and that this system must have been active at its current level for the last 30,000 to 40,000 years. This evidence, together with the geophysical evidence for a contemporary magma chamber beneath the west-central section of the caldera favor a long-lived, deep source beneath the west or southwest part of the caldera for the Long Valley hydrothermal system (the third model in Blackwell's list and the model preferred by Sorey). Confirmation, however, will have to await the results of additional drill holes, some of which need to be deep enough to penetrate the convective hydrothermal system and directly sample the conductive geothermal gradients above the magma chamber roof. Sorey also points out that, because Sanders' cupola-like protrusion of the magma chamber to within 4.5 to 5 km of the surface beneath the Casa Diablo area has yet not significantly perturbed the thermal regime in the upper 2 km of the overlying crust, it has probably been in place for less than 60,000 years.

Williams and Hudnut (this volume) describe anomalous concentrations of soil mercury (Hg) and radon (Rn) that show some correlation with recent earthquake activity within the caldera. They suggest that these geochemical patterns are dominated by the Long Valley geothermal system, but that the changes in patterns may reflect recent magmatic resurgence within the caldera.

EVIDENCE FROM RELATED VOLCANIC SYSTEMS

Because the well-documented history of unrest in any single silicic volcanic system such as Long Valley covers but a small fraction of the evolutionary cycle of such a system, we must try to fill in the gaps with the study of similar systems elsewhere in the world showing different evolutionary stages and exhibiting different levels of activity. Newhall, Dzurisin, and Mullineaux (this volume) review the available literature on historical unrest of large Quaternary calderas throughout the world. They find that some 200 calderas have shown some signs of historic unrest and that roughly half of these are silicic in composition. They suggest, for example, that during a "typical" year, 14 systems show some signs of unrest; this unrest includes both seismic activity and ground deformation in three of the systems; and six or seven of the systems have some form of eruption. They find that eruptions from silicic systems are preceded by reports of seismic activity 50% of the time, reports of ground uplift 75% of the time, and harmonic tremor 100% of the time. Newhall and his coauthors caution, however, that historical reports are woefully incomplete and that early reports, in particular, are probably biased toward descriptions of unrest that eventually lead to an eruption. To minimize uneven reporting practices they have restricted most of their attention to unrest described in the last 100 years

Long Valley caldera is included with four major caldera systems in the world currently showing relatively intense seismic activity and ground uplift. In order of decreasing levels of unrest, these systems are Rabaul caldera (Papua, New Guinea), the Phlegrean Fields caldera (Pozzuoli, Italy), Long Valley caldera (California), and Yellowstone caldera (Wyoming). Dzurisin and Newhall (this volume) review and compare the nature and relative rates of activity at each of these systems. Christiansen (this volume) provides a detailed discussion of the post-caldera evolution of the Yellowstone system, and, during the conference, G. Corrado of the Vesuvius Observatory, Naples, presented a detailed description of recent Phlegrean Fields activity.

The activity at Rabaul and the Phlegrean Fields is remarkably similar; both are about the same size and both began the recent episode of activity in the early 1970s. Although both have experienced numerous earthquake swarms, the largest earthquakes are of modest size (M-4 in the Phlegrean Fields and M-

5.2 in Rabaul). The cumulative uplift in both cases since the early 1970s is measured in meters (3 m for the Phlegrean Fields and over 2 m in Rabaul); the uplift rate in the Phlegrean Fields since mid-1982 has averaged a remarkable 2- to 4-mm per day (about 1 m per year). In contrast, the cumulative uplift in the larger and older Long Valley and Yellowstone calderas is less than one meter (0.5 m in Long Valley since 1979 and 0.7 m in Yellowstone since 1923) but the earthquakes have been relatively large (four M-6 earthquakes in Long Valley and seven M-6 earthquakes in the Yellowstone region plus a M-7.1 event at Hebgen Lake).

One of the most important insights on the long-term behavior of these major calderas comes from the unique 2,000-year record of uplift and subsidence of the Phlegrean Fields caldera afforded by the Serapeo columns in Pozzuoli (Caputo, 1979, and Figure 14 in Dzurisin and Newhall, this volume). This record shows that nearly 10 centuries of gradual subsidence was terminated by the onset of inflation beginning in the 11th century, and that this inflation culminated in an episode of rapid, locally large uplift (6 m) followed within a week by the September 29, 1538, eruption of Monte Nuovo volcano some 3 km west of Pozzuoli. The eruption was followed by another period of gradual subsidence only to be interupted by the onset of renewed inflation in 1970. This latest episode of inflation resumed in 1982 following a ten year period of relative stability from 1972 to mid-1982. The uplift continues at a rate of several mm per day as we write this summary.

Lipman's (this volume) description of the late Oligocene Cuesta caldera in central New Mexico provides a rare chance to directly view the internal structure of a silicic caldera that is similar in many ways to the Long Valley caldera. The Questa caldera was formed in an extensional tectonic regime along the eastern margin of the Rio Grande rift some 26 million years ago. Its magma chamber has long since crystallized and erosion has cut deeply into the system exposing the roof of the magma chamber (now a granitic pluton) and its relation to the overlying caldera floor. Particularly striking are the many dikes intruded along the ring-fracture system of the caldera, the irregular shape of the roof structure, and the string of plutons (coeval magma chambers and dikes) south of the caldera. All of these features are analogous to the structures in our emerging image of the Long Valley caldera and the adjacent Inyo-Mono Craters system. Lipman points out that in the case of the Cuesta caldera, activity associated with the addition of new magma to the high-level parts of the system persisted for 3 to 4 my following caldera collapse. He also notes that only a small fraction of the many dikes intruded during this period reached the surface to produce eruptions.

CONCLUSIONS

Progress in understanding the physical processes driving the current unrest in a geologically complex region such as the Long Valley region comes, not from unambigous answers to each of the many outstanding questions, but through a process of limiting the range of plausible answers and providing the basis for more incisive questions to be addressed with future research. We feel the conference was very successful in this respect.

The weight of evidence indicates the existence of a large, long-lived,silicic magma chamber beneath the Long Valley caldera and a smaller, deeper, and probably younger, silicic magma chamber beneath the Mono Craters system. Although the Long Valley magma chamber may not have returned to the potentially explosive state that persisted for over 400,000 years prior to the caldera-forming Bishop tuff eruption, it, together with the Inyo-Mono Craters system, is certainly capable of producing small to moderate eruptions with

ejected magma volumes on the order of from 0.1 to 10 km^3. By way of comparison, the total volume of magma erupted from the Inyo-Mono Craters system 500 to 600 years ago was on the order of 2 km^3 with each of the vents ejecting approximatly 0.2 km^3 of magma. (As described by both Miller and Sieh, even these relatively small eruptions produced locally thick ash falls and pyroclastic flows that extended up to 6 km from the eruptive vents.) Some of the earlier eruptions from the Mono Craters system ejected on the order of 0.3 km^3 of magma, a volume comparable to that ejected in the May 1980 eruption of Mount St. Helens. (The total volume of material involved in the May 18, 1980, explosive eruption of Mount St. Helens including debris-avalanche deposits was about 1 km^3,and, by comparison, the caldera-forming eruption in Long Valley 700,000 years ago produced 600 km^3 of magma.)

Based on inflation of the resurgent dome since 1979, 0.1 to 0.2 km^3 of magma has been injected into the Long Valley magma chamber at an average rate of 0.02 to 0.04 km^3/y over the last 5 years. Exactly how much magma can be added to the chamber before it approaches a critical state capable of producing an eruption depends on both the effective strength of the overlying rocks and the initial stress state in these rocks. At this stage, we know little about either of these factors. Rundle and Whitcomb (this volume) use some simple assumptions to estimate that a critical state would be reached if another 0.07 km^3 of magma were added to the shallow (5 km deep) chamber beneath Casa Diablo, which would correspond to an additional 0.5 to 1.0 m of uplift of the southern part of the resurgent dome. In the case of the Phlegrean Fields caldera, however, injection of roughly 0.01 km^3/y of magma into an even shallower (3 to 4 km deep) magma chamber has resulted in over 2 m of uplift in the last two years and a total uplift of over 3 m since 1970 without yet producing an eruption. Nevertheless, it is quite clear that inflation cannot continue indefinitely at such rates without resulting in an eruption, and that, in general, the potential for an eruption increases with increasing inflation.

An additional element of uncertaintity is introduced in the Long Valley region by the possibility that a major tectonic earthquake in the area could trigger an eruption from a partially charged magma chamber. Newhall and others (this volume) point out that unrest in large calderas following a large tectonic earthquake in the region is relatively common and that in 13 out of 25 documented cases, the unrest culminated in a eruption. Some of these eruptions followed the "triggering" earthquake by only a few days, and Bacon (this volume) cites the example of Puyehue volcano in Chile, which erupted 48 hours following the great Chilean earthquake of 1960.

On a broad scale, research discussed at this conference supports the view that the activity in the Long Valley region is a result of lithospheric extension along the western margin of the Basin and Range province, which as suggested by Lachenbruch and Sass (1978), involves a combination of normal faulting in the upper, brittle crust and magmatic intrusion in the lower crust. According to Lachenbruch and Sass (1978), silicic volcanic centers such as those in the Long Valley region are localized within zones where the lithosphere is rapidly pulling apart and "drawing up basaltic magma from below to fill the void". According to Shaw (this volume), conditions for caldera-forming, ignimbrite eruptions result when the intrusion of basaltic magma from the mantle into the lower continental crust is sustained at rates averaging 0.01 km^3/y for periods of tens of thousands to several million years. The injection of 0.01 km^3/y into the lower half (20 km) of the crust coincident with the 40-km-long zone of low crustal velocities defined by Kissling and his co-workers would require a local lithospheric extension rate of about 1 cm/y.

This is close to the average extension rate across the Basin and Range province during late Cenozoic time (Minster and Jordan, 1984). Based on patterns of Quaternary faults, it appears that a large fraction of this extension over the last 2 to 3 million years has been concentrated in two belts: one along the Wasatch front at the eastern margin of the Basin and Range province and the other in eastern California (along the eastern escarpment of the Sierra Nevada range including the Long Valley region) extending into north-central Nevada (Wallace, 1983). The contemporary pattern of earthquake activity in the western United States indicates that this same pattern of activity persists today but with the eastern California-central Nevada belt showing a greater level of activity than the belt along the Wasatch front (see Smith, 1978).

Thus the regional tectonic picture is consistant with continued supply of heat into the crust beneath the Long Valley region in the form of basaltic magmas drawn into the lower crust from the upper mantle at rates sufficient to replenish the upper-level silicic magma chambers. We have no reason to believe that this closley coupled pattern of tectonic and magmatic activity will cease in the foreseeable future. The question in human terms becomes one of what sort of short-term fluctuations (years to tens of years) can we expect in this long-term trend in activity? While most would probably agree that short-term fluctuations in activity are related to minor variations in the motion between the major lithospheric plates, we have no basis for reliably predicting the course of these variations years to decades in advance. Accordingly, we must rely on careful monitoring of current activity looking in particular at the deformation field and seismicity patterns as evidence for changes in the supply of magma to shallow chambers and incipient failure of the confining rocks.

REFERENCES

Aki, K., Evidence for magma intrusion during the Mammoth Lakes earthquakes of May 1980 and implications of the absence of volcanic (harmonic) tremor, J. Geophys. Res., in press, 1984.

Bacon, C.R., Implications of silicic vent patterns for the presence of large crustal magma chambers, this volume, 1984

Bailey, R.A., Chemical evolution and current state of the Long Valley magma chamber, this volume, 1984.

Bailey, R.A., G.B. Dalrymple, and M.A. Lanphere, Volcanism, structure, and geochronology of Long Valley caldera, Mono County, California, J. Geophys. Res., 81, 725-744, 1976.

Blackwell, D.D., A transient model of the geothermal system of the Long Valley caldera, California, this volume, 1984.

Caputo, M., Two thousand years of geodetic and geophysical observations in the Phlegrean Fields near Naples, Geophys. J. R. Astr. Soc., 56, 319-328, 1979.

Castle, R.O., J.E. Estrem, and J.C. Savage, Uplift across Long Valley caldera, California, J. Geophys. Res., in press, 1984.

Cramer, C.H. and T.R. Toppozada, A seismological study of the May 1980 and earlier earthquake activity near Mammoth Lakes, California, Calif. Div. of Mines and Geology Special Report 150, 91-130, 1980.

Chouet, B., and B.R. Julian, Dynamics of an expanding fluid filled crack, this volume, 1984.

Christiansen, R.L., Postcaldera evolution and current activity of the Yellowstone caldera, this volume, 1984.

Cockerham, R.S., A.M. Pitt, Seismic activity in Long Valley caldera area, California: June 1982 through July 1984, this volume, 1984.

Dzurisin, D., and C.G. Newhall, Recent ground deformation and seismicity at Long Valley (California), Yellowstone (Wyoming), the Phlegrean Fields (Italy), and Rabaul (Papua New Guinea), this volume, 1984.

Hermance, J.F., W. Slocum, and G.A. Neumann, The Long Valley / Mono Craters volcanic complex; a preliminary interpretation based on telluric field patterns, this volume, 1984.

Hill, D.P., Structure of Long Valley caldera, California, from a seismic refraction experiment, J. Geoph. Res., 81, 745-753, 1976.

Hill, D.P., A model for earthquake swarms, J. Geoph. Res., 82, 1347-1352, 1977.

Hill, D.P., E. Kissling, J.H. Luetgert, and U. Kradolfer, Constraints on the

upper crustal structure of the Long Valley - Mono Craters volcanic complex, eastern California, from seismic-refraction measurements, this volume, 1984.

Jachens, R.C. and C.W. Roberts, Gravity investigations at Long Valley caldera, California, this volume, 1984.

Julian, B.R.,Evidence for dyke intrusion earthquake mechanisms near Long Valley, California, Nature, 303, 323-325, 1983.

Julian, B.R., and S. Sipkin, Earthquake processes in the Long Valley area, California, this volume, 1984

Kissling, E., W.L. Ellsworth, and R.S. Cockerham, Three-dimensionalstructure of the Long Valley caldera, California, region by geotomography, this volume, 1984.

Lachenbruch, A.H., and J.H. Sass, Models of an extending lithosphere and heat flow in the Basin and Range province, in Cenozoic tectonics and regional tectonics of the western Cordillera, R.B. Smith and G.P. Eaton, eds. Geol. Soc. America Memoir 152, 209-250, 1978.

Lide, C.S. and A.S. Ryall, Relationship between aftershock locations and mechanisms of the May, 1980, Mammoth Lakes earthquakes, this volume, 1984.

Lipman, P.W., Structure of the Tertiary Questa caldera, New Mexico — an eroded analog for current activity at Long Valley, this volume, 1984.

Luetgert, J.H., and W.D. Mooney, Earthquake profiles form the Mammoth Lakes, California, earthquake swarm, January, 1983: implications for deep crustal structure, Bull. Seismol. Soc. America, in press, 1984.

Metz, J., and G. Mahood, Eruptive history of Glass Mountain, Long Valley California: precursors to a large explosive eruption, this volume, 1984.

Miller, C.D., Holocene eruptions at the Inyo Volcanic cahin, California -- implications for possible eruptions in Long Valley caldera, this volume, 1984.

Miller, C.D., D.R. Mullineaux, D.R. Crandell, and R.A. Bailey, Potential hazards from future volcanic eruptions in the Long Valley-Mono Lake area, east-central California and southwestern Nevada — a preliminary assessment, U.S. Geological Survey Circular 77, 1-10, 1982.

Minster, J.B., and T.H. Jordan, Vector constraints on Quaternary deformation of the western United States east and west of the San Andreas fault, in Tectonics and sedimentation along the California margin, J.K. Crouch and S.B. Bachman eds., Pacific Section of the Soc.of Econ. Paleontologists and Mineralogists, Los Angeles, 1-16, 1984.

Nakamura, K., Three different mechanisms for elongate distribution of shallow earthquake epicenters, this volume, 1984.

Newhall, C.G., D. Dzurisin, and L.S. Mullineaux, Historical unrest at large

Quaternary calderas of the world, this volume, 1984.

Pollard, D.D., J.H. Fink, and P.T. Delaney, Igneous dikes at Long Valley, CA: emplacement mechanisms and associated geologic structures, this volume, 1984.

Rundle, J.B. and J.H. Whitcomb, A model for deformation in Long Valley, California, 1980 - 1983, this volume, 1984.

Ryall, A., and F. Ryall, Attenuation of P and S waves in a magma chamber in Long Valley caldera, California, Geoph. Res. Letters, 8, 557-560, 1981a.

Ryall, A. and F. Ryall, Spatial-temporal variations in seismicity preceding the May 1980 Mammoth Lakes earthquakes, California, Seis. Soc. America Bull., 71, 747-760, 1981b.

Ryall, A. and F. Ryall, Spasmodic tremor and possible magma injection in Long Valley caldera, eastern California, Science, 219, 1432-1433, 1983.

Ryall, A.S., and F.D. Ryall, Shallow magma bodies related to lithospheric extension in the western Great Basin, western Nevada and eastern California [abs.], Earthquake Notes, 55, 11-12, 1984.

Sanders, C.O., Location and configuration of magma bodies beneath Long Valley, California, determined from anomalous earthquake signals, this volume, 1984.

Sanders, C.O., and F. Ryall, Geometry of magma bodies beneath Long Valley, California, determined from anomalous earthquake signals, Geop. Res. Letters, 10, 690-692, 1983.

Savage, J.C. and M.M. Clark, Magmatic resurgence in Long VAlley caldera, Callifornia: possible cause of the 1980 Mammoth Lakes earthquakes, Science, 217, 531-533, 1982.

Savage, J.C., and R.S. Cockerham, Earthquake swarm in Long Valley caldera, California, January 1983: evidence for dike inflation, this volume, 1984.

Shaw, H.R., A note on links between magma-tectonic rate balances, plutonism and volcanism, this volume, 1984.

Sieh, K., Most recent eruptions of the Mono Craters, eastern central California, this volume, 1984.

Smith, A.T., High-resolution microseismicity study of possible magmatic intrusion in the Long Valley caldera, this volume, 1984.

Smith, G.I., V.J. Barczak, G.F. Moulton, and J.C. Liddicoat, Core KM-3, A surface-to-bedrock record of late Cenozoic sedimentation in Searles Valley, California, U.S. Geological Survey Prof. Paper 1256, 24 p., 1983.

Smith, R.B., Seismicity, crustal structure, and intraplate tectonics of the interior of the western Cordillera, in Cenozoic tectonics and regional tectonics of the western Cordillera, R.B. Smith and G.P. Eaton, eds.,

Geol. Soc. America Memoir 152, 111-144, 1978.

Smith, R.L., and R.A. Bailey, Resurgent cauldrons, Geol. Soc. America Memoir 116, 613-662, 1968.

Sorey, M.L., Evolution and present state of the hydrothermal system in Long Valley caldera, this volume, 1984.

Steeples, D.W., and H.M. Iyer, Low-velocity zone under Long Valley as determined from teleseismic events, J. Geophys. Res., 81, 849-860, 1976.

VanWormer, J.D., and A.S. Ryall, Sierra Nevada - Great Basin boundry zone: earthquake hazards related to structure,active tectonic processes, and anomalous patterns of earthquake occurrence, Bull. Seismol. Soc. America Bull., 70, 1557-1572, 1980.

Vetter, U.R., and A.S. Ryall, Systematic change of focal mechanisms with depth in the western Great Basin, J. Geophys. Res., 88, 8237-8250, 1983.

Vetter, U.R., Focal mechanisms and crustal stress patterns in the Mammoth Lakes area, this volume, 1984.

Wallace, R.E., Patterns of faulting and seismic gaps in the Great Basin province,in J. Everenten, ed., Proceedings of Conference VI, Methodology for Identifying Seismic Gaps and Soon-to-break Gaps, U.S. Geological Survey Open-File report 78-943, 858-868, 1978.

Wallace, R.E., Patterns and timing of late Quaternary faulting in the Great Basin province and relation to some regional tectonic features, J. Geophys. Res., 89, 5763-5769, 1984.

Wallace, T.C., A re-examination of the moment tensor solution of the 1980 Mammoth Lakes earthquakes, this volume, 1984.

FIGURE CAPTIONS

Figure 1: Schematic northwest-southeast cross-section through Long Valley caldera illustrating magma chamber geometry in relation to caldera structure and activity of the January 1983 earthquake swarm. Magma chamber geometry based on results of Sanders (this volume), Kissling and others (this volume). Heavy lines indicate approximate positions of reflecting boundaries identified by Hill and others (this volume) and Luetgert and Mooney (1984). Caldera structure generalized from results of Bailey and others (1976) and Hill and others (this volume). Hypocentral zone for January 1983 swarm and position of possible dike intrusion from Savage and Cockerham (this volume).

Figure 2: Summary of seismic activity and inflation of the resurgent dome in terms of cumulative seismic moment for earthquakes in the Long Valley region from 1978 through mid-1984 and elevation history of bench mark CASA AZ near Casa Diablo Hot Springs (Castle and others, 1984). Point of maximum uplift is approximatly 4 km north-northeast of CASA AZ (see Figure 7 of Savage and Cockerham, this volume). Seismicity data compiled by R.S. Cockerham using data from University of Nevada, Reno; University of California, Berkeley; and U.S. Geological Survey in Menlo Park, California.

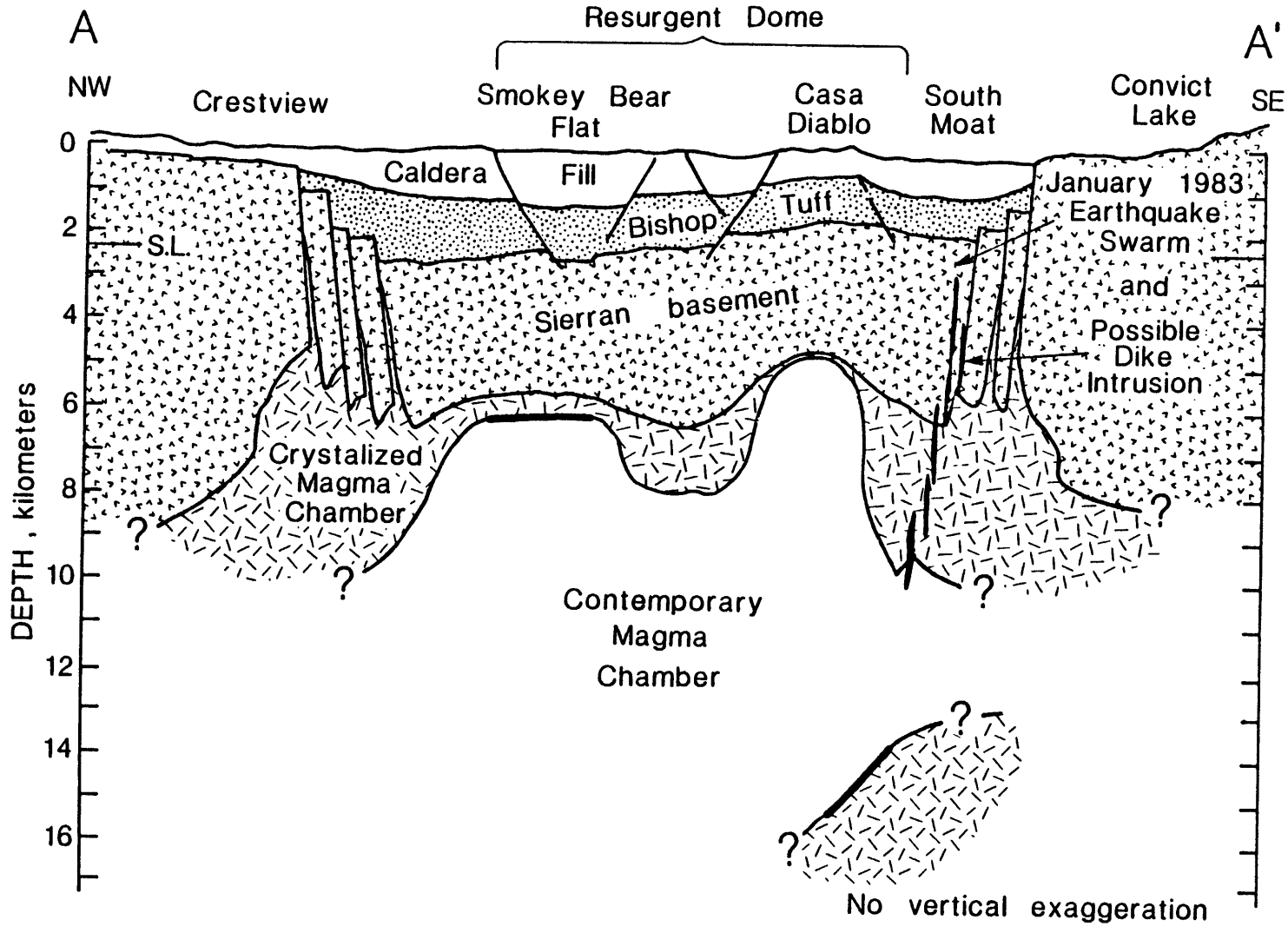
A
A'
NW
SE
Resurgent Dome
Crestview
Smokey Bear Flat
Casa Diablo
South Moat
Convict Lake
Caldera
Fill
Bishop Tuff
S.L.
Sierran basement
January 1983 Earthquake Swarm and Possible Dike Intrusion
Crystalized Magma Chamber
Contemporary Magma Chamber
DEPTH, kilometers
0
2
4
6
8
10
12
14
16
No vertical exaggeration

Figure 1

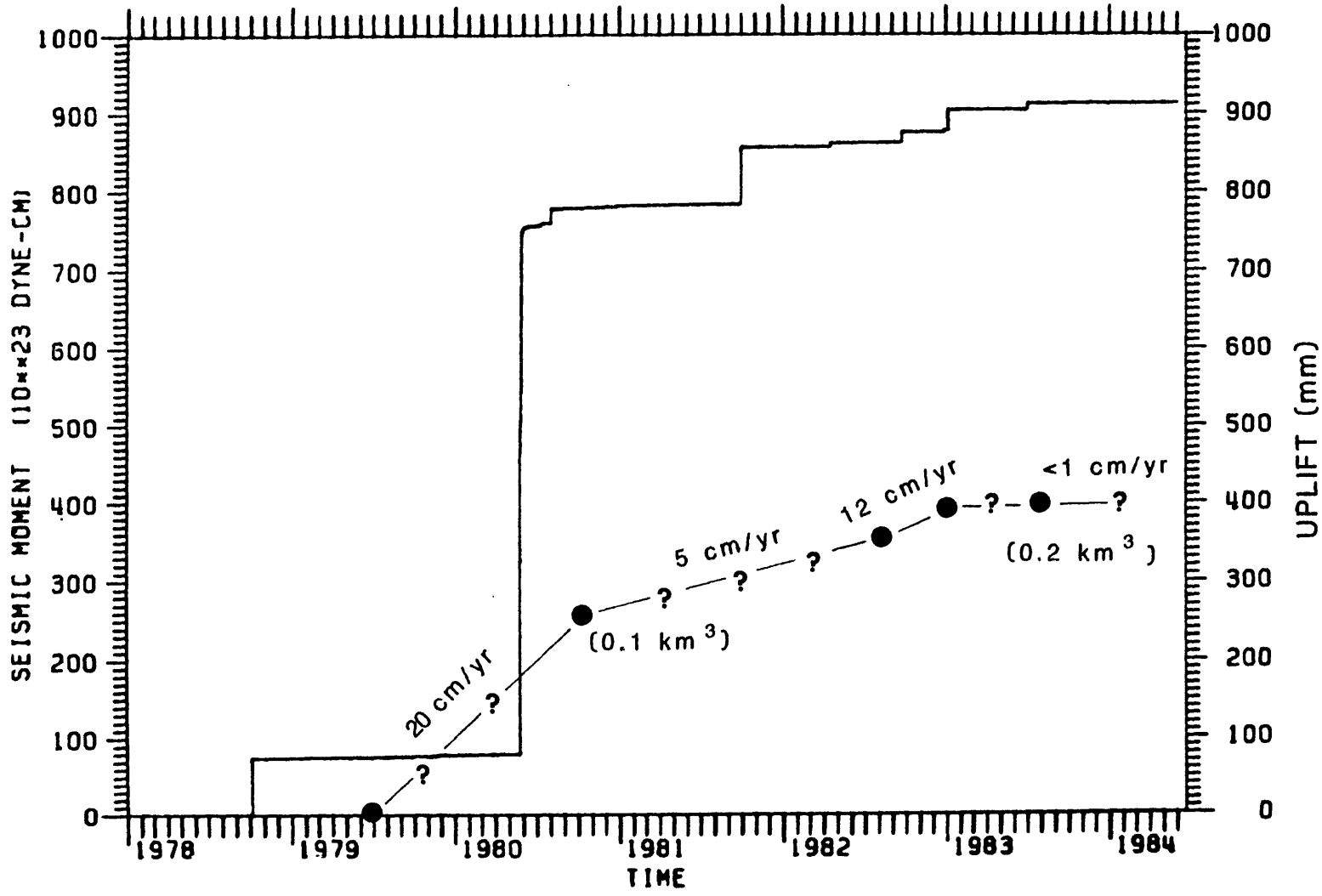
SEISMIC MOMENT (10**23 DYNE-CM)
UPLIFT (mm)
TIME
1000
900
800
700
600
500
400
300
200
100
0
1978
1979
1980
1981
1982
1983
1984
20 cm/yr
5 cm/yr
12 cm/yr
<1 cm/yr
(0.1 km 3)
(0.2 km 3)
?

Figure 2

Chemical Evolution and Current State of the Long Valley Magma Chamber

by

Roy A. Bailey

Chemical Evolution and Current State of the Long Valley Magma Chamber

by

Roy A. Bailey

ABSTRACT

Current knowledge of the postcaldera volcanic history of Long Valley caldera and of the postcaldera petrologic and geochemical evolution of the residual rhyolitic magma chamber provides a general magmatic model that is relevant to the recent seismicity and ground deformation in the area. Intracaldera volcanism between 0.28 and 0.06 m.y. ago suggests that injection of mafic magma into the roots of the Long Valley magmatic system 0.28 m.y. ago resulted in thermal and physicochemical rejuvenation of the shallow residual rhyolite magma chamber. The current seismicity and uplift of the resurgent dome may represent the onset of another such episode.

INTRODUCTION

In the several months following the Mammoth Lakes magnitude-6 earthquake sequence of May 25-27, 1980, available scientific evidence (Sherburne, 1980) suggested that the quakes probably were tectonic in origin and that, although an unusually intense sequence, they were basically similar to other quakes that had shaken the Eastern Sierra region every decade or so in the past. However, the discovery during the following year that the quakes were apparently accompanied by uplift of the resurgent dome within Long Valley caldera raised questions regarding the possible involvement of magma as a causative source (Savage and Clark, 1982). The likelihood of magmatic involvement was further strengthened by the localization and intensification of seismicity in the south moat of Long Valley caldera during 1981, 1982, and 1983 and by the recognition of the occurrence of spasmodic tremor, a seismic

phenomena commonly associated with active volcanoes (Ryall and Ryall, 1981; 1983). Moreover, recent seismic studies (Sanders, 1983, and this volume) have confirmed evidence from earlier studies (Hill, 1976; Steeples and Iyer, 1976) that the resurgent dome in Long Valley caldera is indeed underlain by a substantial volume of partially molten rock at depths below 7 km and possibly at depths as shallow as 4.5 km.

This mounting evidence that magma--more specifically the residual Long Valley magma chamber--is in part responsible for the current seismic and deformational activity within the caldera prompts a need to know more about the current chemical and physical state of that chamber and its potential to produce eruptions. This paper briefly outlines the postcaldera chemical evolution of the Long Valley magma chamber and discusses its possible bearing on understanding the current processes. This summary is based on in-progress petrologic and geochemical studies which are far from complete, and the conclusions are tentative.

REGIONAL VOLCANISM AND MAGMATISM

Assessment of the current state of the Long Valley magma chamber is complicated by the fact that within the region are, not one, but three centers of volcanism and that all three are intimately related both spatially and temporally (Bailey, 1980, 1982). The three are: (1) Long Valley caldera, (2) the Mono-Inyo Craters, and (3) the Mono Lake volcanoes (Figs. 1 and 2). Long Valley, the oldest and most evolved of the three, includes rocks that erupted between 3.2 and 0.1 m.y. ago; the Mono-Inyo Craters, centered about 20 km to the northwest but extending southward into the west moat of Long Valley caldera, includes rocks erupted between 0.2 m.y. and about 500 years ago; and the Mono Lake volcanoes, still further to the north, include rocks erupted 13,500 to <500 years ago. In this paper, only the volcanism centered about Long Valley is discussed.

VOLCANIC EVOLUTION OF THE LONG VALLEY CALDERA

The volcanic rocks directly associated with Long Valley caldera include: (1) a precaldera suite of trachybasaltic/andesitic and quartz latitic lavas 3.2 to 2.6 m.y. old, (2) the 1.9- to 0.8-m.y.-old rhyolites of Glass Mountain, (3) the 0.73-m.y.-old caldera-forming Bishop Tuff, and (4) a postcaldera suite of rhyolites 0.7 to 0.1 m.y. old (Bailey and others, 1976). Erosional remnants of the precaldera trachybasaltic/andesitic lavas and their vent complexes are scattered around the periphery of Long Valley caldera and extend northeastward to the Adobe Hills and southwestward into the High Sierra, encompassing an area in excess of 4000 km^2. These mafic lavas represent the tapping of an extensive mantle magma source during the late episode of Basin-and-Range faulting that initiated development of the present Sierran frontal fault escarpment. Somewhat younger (3.0- to 2.6-m.y.-old) quartz-latite lavas associated with these mafic lavas are exposed along San Joaquin Ridge and on the north rim of Long Valley caldera; they probably represent the onset of magmatic differentiation that culminated in formation of a large, shallow, rhyolitic magma chamber beneath the present site of Long Valley caldera. Early leakage from this rhyolitic chamber resulted in the formation of Glass Mountain Ridge, a 1.9- to 0.8-m.y..-old complex of rhyolite domes, flows, and tephras exposed on the north, northeast, and east rim of the caldera (Metz and Mahood, 1983, and this volume).

Long Valley caldera, a 20-by-30-km elliptical depression enclosing a 450 km^2 area, formed 0.73 m.y. ago during a brief episode of catastrophic, pyroclastic eruptions that ruptured and caused collapsed of the roof of the subjacent magma chamber. During these eruptions, 600 km^3 of rhyolite magma was expelled as ash fall and ash flows, the deposits of which now constitute the Bishop Tuff. Bishop ash flows inundated 1500 km^2 in upper Owens Valley, Adobe Valley, and Mono Basin. They also overflowed the crest of the Sierra

westward through the gorge of the Middle Fork San Joaquin River and possibly reached the eastern edge of the Great Valley. Thick deposits of Bishop Tuff also accumulated within the depression of Long Valley caldera itself.

Soon after eruption of the Bishop Tuff and collapse of Long Valley caldera, eruptions resumed on the caldera floor, first producing thick aphyric rhyolite tuffs and finally hot fluidal obsidian flows, collectively referred to as the early rhyolite (Bailey and others, 1976). Simultaneous with these eruptions, the caldera floor was uplifted and arched into a 10-km-diameter resurgent dome (Smith and Bailey, 1968), transected by a 4-km-wide, northwest-trending, medial graben (see Fig. 1). This episode of early postcaldera volcanism and simultaneous resurgent doming persisted for less than 100,000 years after caldera collapse.

After resurgent doming, intracaldera volcanism related to the residual Long Valley magma chamber was confined to the caldera moat and was probably guided by caldera ring-fractures. This moat rhyolite consists predominantly of coarsely porphyritic hornblende-biotite rhyolite, which forms steep-sided domes and flows that contrast strikingly with the thinner, apparently hotter and more fluid, early rhyolite obsidian flows exposed on the resurgent dome. Eruptions of moat rhyolite occurred at 0.2-m.y. intervals, about 0.5, 0.3, and 0.1 m.y. ago in the north, southeast, and west sectors of the moat, respectively.

CHEMICAL EVOLUTION OF THE POSTCALDERA RHYOLITES

The chemical evolution of the postcaldera moat rhyolite bears most directly on the current state and possible future course of eruptive activity of the Long Valley magma chamber. In the following discussion, the rhyolitic lavas erupted at the surface are assumed to represent leakage from the topmost part of the evolving source magma chamber.

Comparison of compositional trends and chemical fractionation patterns of the successive postcaldera eruptive units shows that the porphyritic moat rhyolites changed only slightly in composition and exhibited no marked or distinctive fractionation pattern between 0.5 and 0.3 m.y. ago (Figs. 3 and 4b). However, beginning with eruption of the 0.28-m.y.-old Hot Creek obsidian flow in the southeast moat (Figs. 1 and 5), distinct changes in composition and fractionation began to occur relative to earlier moat rhyolites. Nb and Ta (as well as most other trace elements) in the Hot Creek flow show marked changes in concentration (Fig. 3), and distinct changes in the fractionation of certain elements (Fig. 4c) began to occur, notably the depletion of most transition metals and enrichment of most rare-earth and incompatible elements. With eruption of the 0.1-m.y.-old rhyolites of the west moat, these concentration and fractionation trends became further enhanced (Figs. 3 and 4d) and more clearly began to resemble the patterns of the Bishop Tuff magma (Fig. 4a) just prior to its eruption 0.73 m.y. ago. These trends imply that between 0.5 and 0.3 the upper part of Long Valley magma chamber attained a state of chemical stagnation and probably began cooling and crystallizing from the margins inward, but that beginning 0.28 m.y. ago, the chamber was thermally rejuvenated, and convection, diffusion, and other physiochemical processes akin to those that led to evolution of Bishop Tuff compositions (Hildreth, 1977, 1979) dominated the chamber (Fig. 5). Whether these processes have continued unabetted since then is difficult to assess, but the fact that the 0.1-m.y.-old west-moat rhyolites are more crystal-rich than the 0.28-m.y.-old Hot Creek flow suggests that the processes may have slowed due to cooling, perhaps until just recently (see below).

The heat for this thermal and physicochemical rejuvenation of the Long Valley magma chamber 0.28 m.y. ago was most likely derived from renewed injection of mafic magma from the mantle into the roots of the Long Valley

magmatic system. Lachenbruch and others (1976) have pointed out that the upper-crustal Long Valley magma chamber could not have remained molten to produce the rhyolitic eruptions evident during the past 1 m.y. unless it were repeatedly resupplied with heat from deep crustal or subcrustal magmatic sources. Trachybasalt lavas associated with the Mono-Inyo Craters, which erupted in part from numerous vents in the west moat of Long Valley caldera between 0.20 and 0.06 m.y. ago, provide evidence for at least one such episode of resupply. Although these mafic lavas reached the surface after the initiation of changes observed in the moat rhyolites, the onset of mafic magma injection at depth and its effects on the rhyolitic chamber must have preceded eruption of trachybasalt at the surface.

Implications regarding the current activity

These chemical changes in the Long Valley magma chamber and the basaltic and rhyolitic eruptive events that occurred between 0.28 and 0.06 m.y. ago in the southeast and west moat provide a model for interpretation of the current seismicity and ground deformation in and near the caldera.

Evidence from reanalysis of focal mechanisms of the May 1980 Mammoth Lakes earthquake sequence (Julian, 1983) suggests that fluid injection occurred along faults in the Sierran block outside the caldera at the very onset of the current seismic episode. Whether these fluids were aqueous solutions migrating from the Long Valley hydrothermal system or were mafic magma from a deeper source is not known, but in either case the addition of thermal energy to the magmatic system would seem to be required. Evidence gained from monitoring and other recent research studies in Long Valley leaves little question that the continuing seismicity and ground deformation localized within the caldera are in some way related to the residual rhyolitic magma chamber beneath the resurgent dome.

In this context, the current activity may be interpreted as having been initiated by the injection of mafic magma into the roots of the Long Valley magmatic system, possibly with magma injecting fissures outside, as well as inside, the caldera. Alternatively, intracaldera mafic magma injection may have affected the associated intracaldera hydrothermal system forcing aqueous solutions laterally into fissures outside the caldera. Concomitant thermal perturbation of the subcaldera rhyolitic chamber caused its expansion and consequent uplift of the resurgent dome. The time response between deep injection and thermal perturbation of the shallower chamber would appear to be extremely short, in the order of a few years or less. The likelihood of eruptions occurring as a consequence of these processes very likely depends on the volume and frequency of mafic injections. If the 1980-83 episode represents an isolated short-lived event, the potential for eruptions would seem low, but if it is the first of many similar, closely spaced events yet to come, the potential for eruptions is likely to increase. Only continued long-term monitoring can distinguish between these alternatives.

Past eruptive history suggests that future eruptions in the currently active south-moat seismic epicentral zone would most likely be rhyolitic, but the possibility of basaltic eruptions should not be entirely ruled out. Both basaltic and rhyolitic eruptions occurred in the earlier 0.28- to 0.06-m.y. episode. Furthermore, although the present seismic epicentral zone coincides with the caldera ring-fracture system, which is most likely to tap the shallow rhyolitic chamber beneath the resurgent dome, it also lies on the projection of the Silver Lake fault, a major Sierran frontal fault, along which at least eight basaltic vents erupted during the above-mentioned earlier episode.

Thus, in summary, the present seismic and deformational activity in Long Valley caldera may be the result of injection of mafic magma from depth into the roots of the shallower rhyolitic magma chamber, which, together with its

associated hydrothermal system, may be in the initial stages of another episode of thermal and physicochemical rejuvenation. Whether the current activity will ultimately culminate in eruptions will depend on the magnitude and frequency of future such disturbances of the magmatic system. Should eruptions eventually occur, they could be either rhyolitic or basalitc. Although the relationship between volcanism and tectonism in the region is not well understood, the probable fundamental cause of such intermittent magmatic disturbances at Long Valley is regional extension in the Basin and Range province, as expounded by Lachenbruch and Sass (1978) and Lachenbruch (1979).

REFERENCES

Bailey, R. A., 1980, Structural and petrologic evolution of the Long Valley Mono Craters, and Mono Lake volcanic complexes, eastern California, (abs.): EOS. Transactions, American Geophysical Union, v. 61, no. 46, p. 1149.

Bailey, R. A., 1982, Other potential eruption centers in California; Long Valley-Mono lake, Coso, and Clear lake volcanic fields, in Martin, R. C., and Davis, J. F., Status of volcanic prediction and emergency response capabilities in volcanic hazard zones of California: California Division of Mines and Geology Special Publication 63, p. 17-28.

Bailey, R. A., Dalrymple, G. B., and Lanphere, M. A., 1976, Volcanism, structure, and geochronology of Long Valley caldera, Mono County, California: Journal of Geophysical Research, v. 81, no. 5, p. 725-744.

Hildreth, E. W., 1977, The magma chamber of the Bishop Tuff: gradients in temperature, pressure, and composition [Ph.D. thesis]: Berkeley, University of California, 328 p.

Hildreth, W., 1979, The Bishop Tuff: Evidence for the origin of compositional zoning in silicic magma chambers: Geological Society of America Special Paper 180, p. 43-75.

Hill, D. P., 1976, Structure of Long Valley caldera, California, from a seismic refraction experiment: Journal of Geophysical Research, v. 81, no. 5, p. 745-753.

Julian, B. R., 1983, Evidence for dyke intrusion earthquake mechanisms near Long Valley caldera, California: Nature, v. 303, p. 323-325.

Lachenbruch, A. R., Sass, J. H., Monroe, R. J., and Moses, T. H., Jr., 1976, Geothermal setting and simple heat conduction models for the Long Valley caldera: Jour. Geophys. Res., v. 81, n. 5, p. 769-784.

Lachenbruch, A. H., and Sass, J. H., 1978, Models of an extending lithosphere and heatflow in the Basin and Range Province: Geol. Soc. America Memoir 152, p. 209-250.

Lachenbruch, A. H., 1979, Heatflow in the Basin and Range Province and thermal effects of tectonic extension: PAGEOPH, v. 117, p. 34-50.

Metz, J. E., and Mahood, G., 1983, Chemistry and eruptive history of Glass Mountain, CA: Precursors to a major caldera-forming eruption, Amer. Geophys. Union Trans. (EOS), V. 64, n. 45, p. 883.

Ryall, Floriana, and Ryall, Alan, 1981, Attenuation of P and S waves in a magma chamber in Long Valley caldera, California: Geophys. Res. Letters, v. 1, n. 6, p. 557-560.

Ryall, Alan, and Ryall, Floriana, 1983, Spasmodic tremor and possible magma injection in Long Valley caldera, Eastern California: Science, v. 219, p. 1432-1433.

Sanders, C. O., 1983, Location and configuration of magma bodies beneath Long Valley, California, determined from anomalous earthquake signals (abs): Amer. Geophys. Union Trans. (EOS), v. 64, n. 45, p. 890.

Savage, J. C., and Clark, M. M., 1982, Magmatic resurgence in Long Valley caldera, California: Possible cause of the 1980 Mammoth Lakes earthquakes: , Science, v. 217, p. 531-532.

Smith, R. L., and Bailey, R. A., 1968, Resurgent cauldrons: Geol. Soc. Amer. Memoir 116, p. 613-662.

Sherburne, R. W., editor, 1980, Mammoth Lakes, California, Earthquakes of May 1980, California Div. of Mines and Geology Special Rept. 150, 141 p.

Steeples, D. W., and Iyer, H. M., 1976, Low-velocity zone under Long Valley as determined from teleseismic events: Jour. Geophys. Research, v. 81, n. 5, p. 849-860.

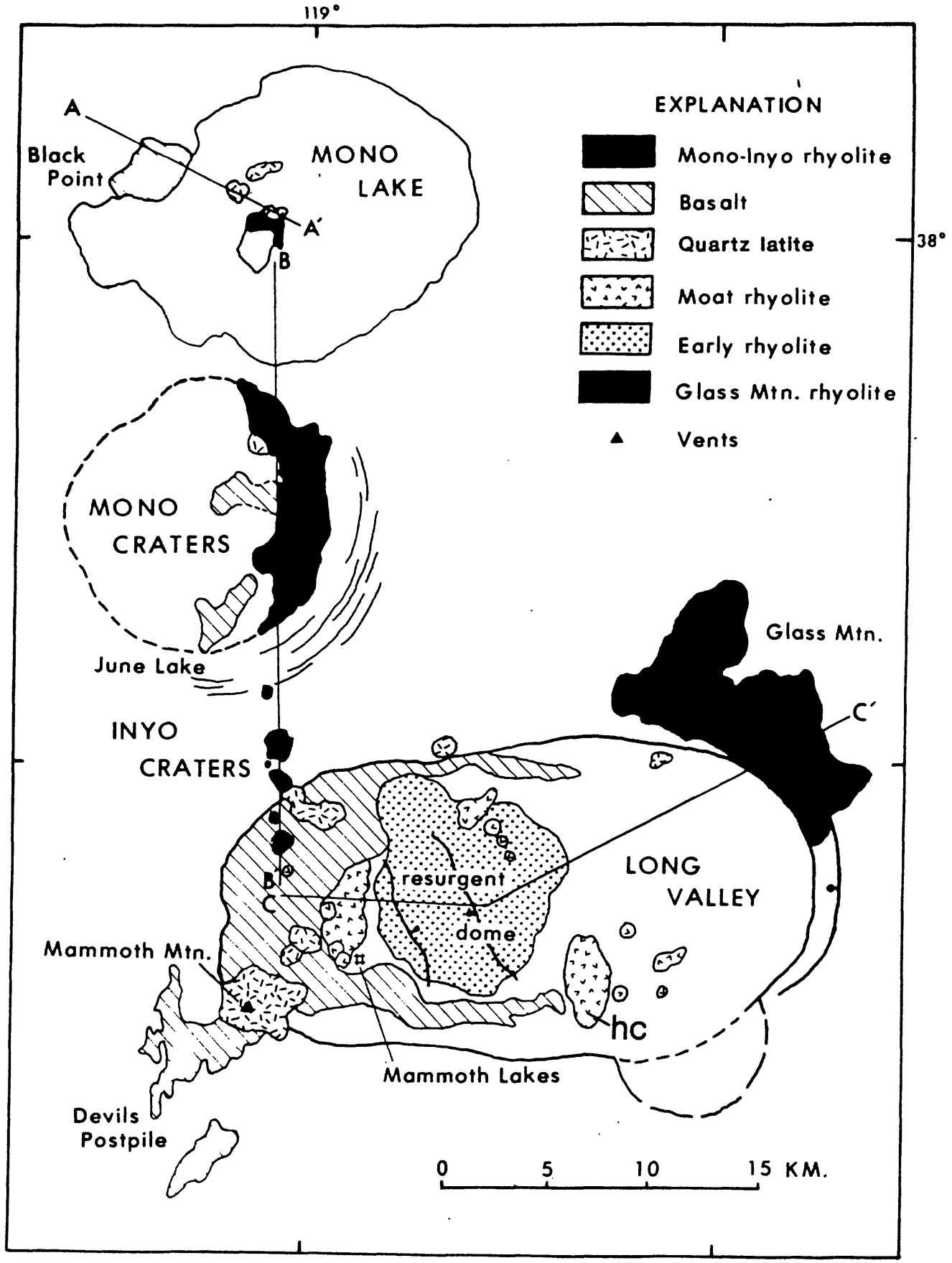

Figure 1. Geologic map of the Long Valley, Mono-Inyo Craters, and Mono Lake complexes. Lines A-A', B-B', and C-C' show location of composite cross section of Figure 2. hc: Hot Creek flow (from Bailey, 1982).

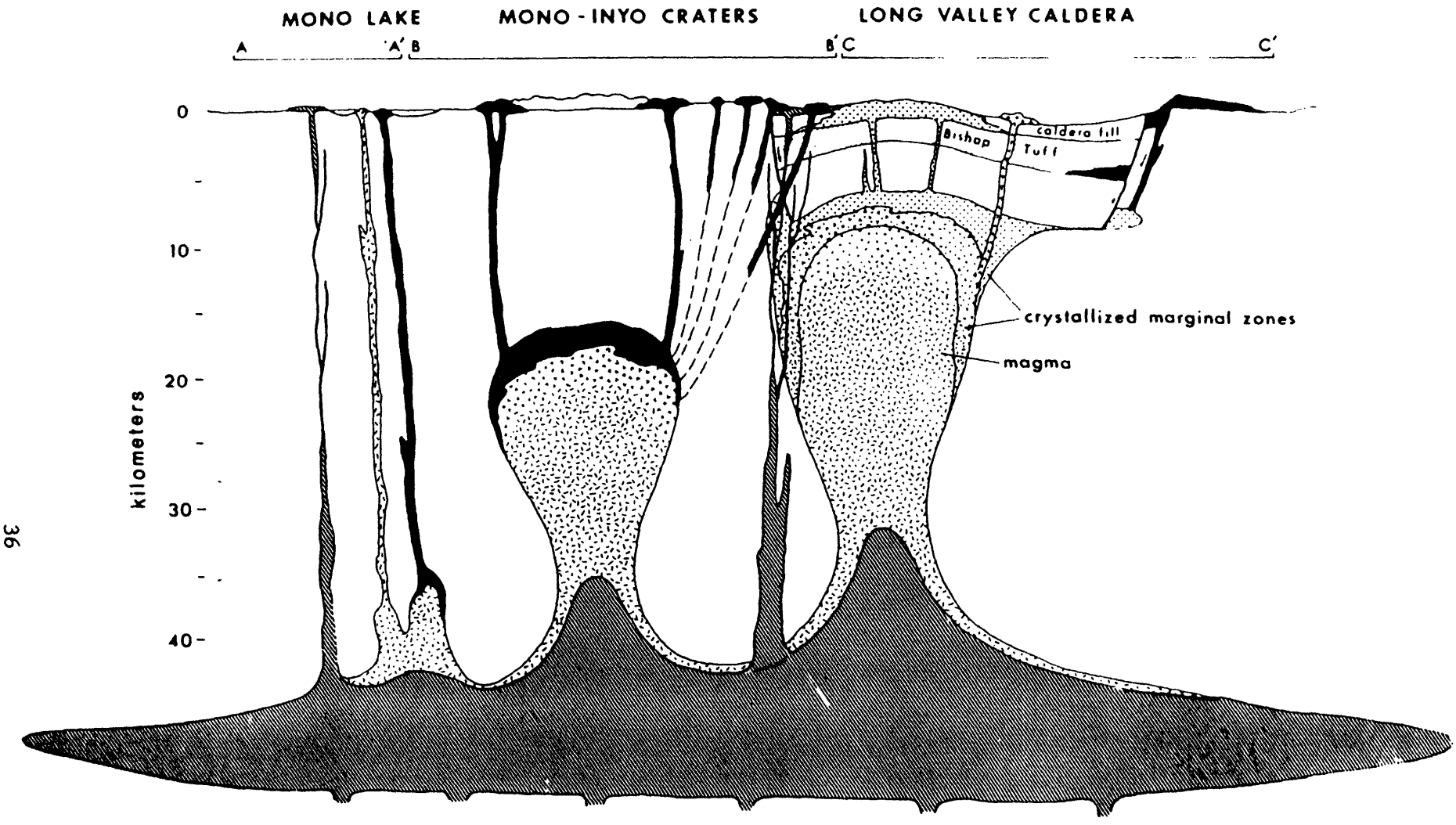

Figure 2. Composite schematic cross section of the Long Valley, Mono-Inyo Craters, and Mono Lake complexes showing inferred magma chambers. Segments A-A', B-B', and C-C' are located in Figure 1. Ornamentation same as Figure 1. Vertical and horizontal scale about equal (from Bailey, 1982).

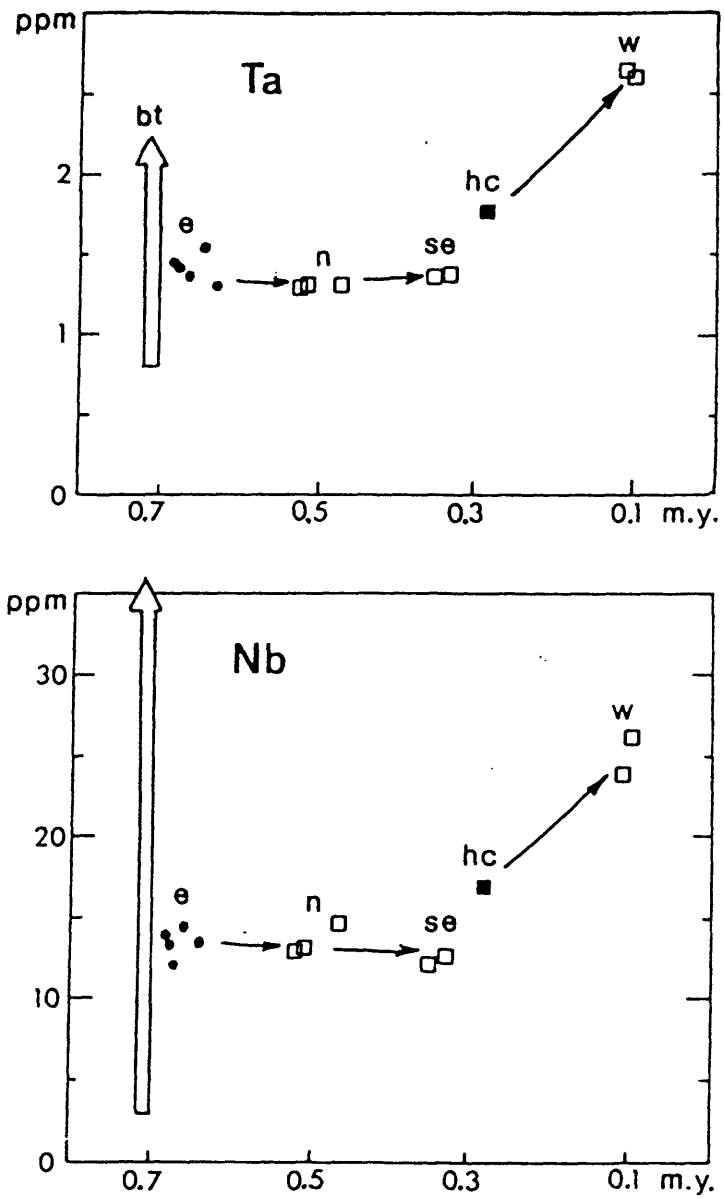

Figure 3. Change of elemental concentration of Nb and Ta in postcaldera rhyolites vs. age of lavas in millions of years. bt (open arrow): range of elemental content from bottom to top of precaldera magma chamber (foot to head of arrow) based on Bishop Tuff compositions (data from Hildreth, 1977); e: early rhyolite; n: north-moat rhyolite; se: southeast-moat rhyolite; hc: Hot Creek flow; w: west-moat rhyolite. Note little change from early rhyolite through southeast-moat rhyolite (0.7-0.3 m.y.), then marked increase from Hot Creek flow through west-moat rhyolite (0.28-0.1 m.y.) toward values approaching those at top of precaldera caldera chamber (bt).

Figure 4. Comparison of elemental fractionation diagrams for the Bishop Tuff and subsequent postcaldera moat rhyolites, showing change in the concentration of elements near the roof of the Long Valley magma chamber at successively younger times.

a. fractionation factors for the Bishop Tuff (early-erupted/late-erupted) showing characteristic enrichment of heavy rare-earth elements (HREE) and incompatible elements and depletion of Ca, Sr, Ba, Eu, most transition metals, and light rare-earth elements (LREE) toward the roof of the chambers (after Hildreth, 1977).

b. fractionation factors for 0.3-m.y.-old, southeast moat rhyolite, relative to 0.5-m.y.-old, north moat rhyolite, showing only minor enrichments and depletions accompanying probable cooling and crystallization of the chamber.

c. fractionation factors for 0.28-m.y.-old, Hot Creek flow relative to 0.3-m.y.-old southeast moat rhyolite, showing moderate enrichment of rare earth and incompatible elements and depletion of transition metals, marking the onset of thermal rejuvenation.

d. fractionation factors for 0.1-m.y.-old west moat rhyolite relative to 0.3-m.y.-old southeast moat rhyolite. Note the general resemblance to the enrichment and depletion of elements for the Bishop Tuff.

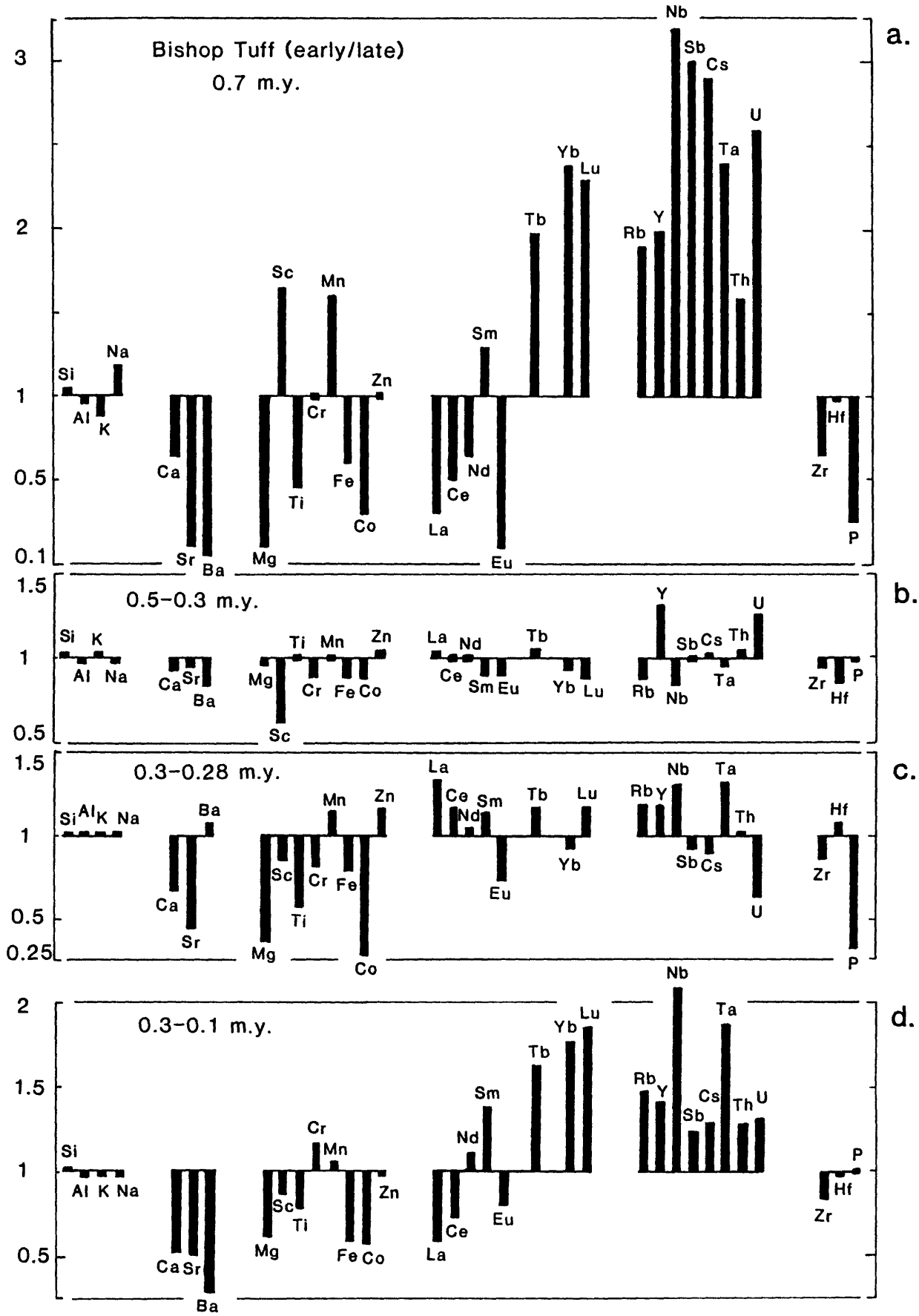
a.
Bishop Tuff (early/late)
0.7 m.y.
3
2
1
0.5
0.1
Si
Al
Na
K
Ca
Sr
Ba
Sc
Mn
Ti
Cr
Fe
Co
Mg
Zn
Sm
Tb
Yb
Lu
La
Ce
Nd
Eu
Nb
Sb
Cs
Ta
U
Rb
Y
Th
Zr
Hf
P
b.
0.5-0.3 m.y.
1.5
1
0.5
c.
0.3-0.28 m.y.
0.25
d.
0.3-0.1 m.y.

Figure 4

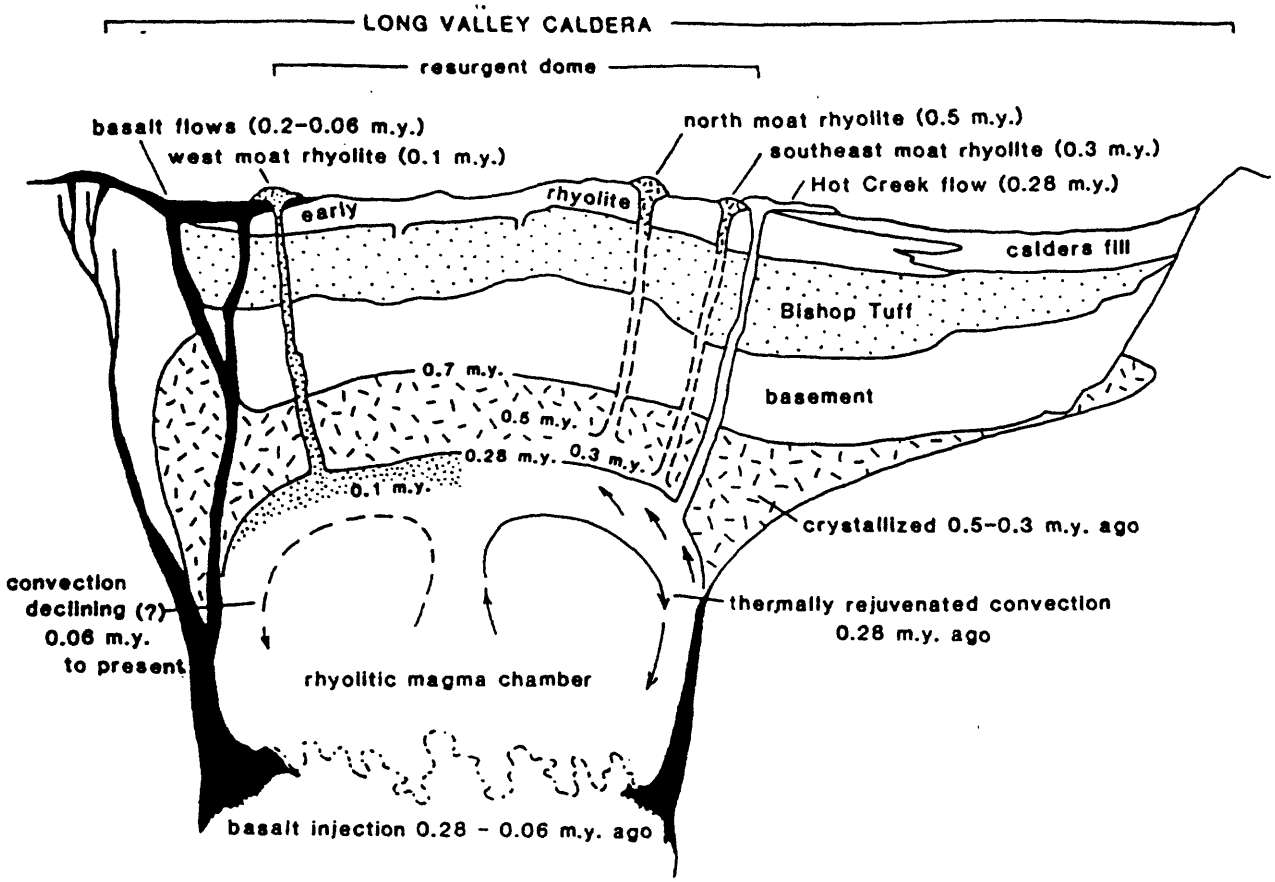

Figure 5. Schematic east-west cross section of Long Valley caldera and its inferred subjacent magma chamber. Right half of magma chamber shows evolution from 0.7 m.y. to 0.28 m.y. Left half of chamber shows evolution from 0.28 m.y. to present. Small numbers (i.e., 0.7 m.y., etc.) indicate positions of top of molten chamber at respective times.

Eruptive History of Glass Mountain, Long Valley, California: Precursors to a Large Explosive Eruption

JENNY METZ and GAIL MAHOOD

Department of Geology, Stanford University, Stanford CA 94305

ABSTRACT

Glass Mountain represents precaldera lavas of the Long Valley magma system. It consists of more than 40 high-silica rhyolite lavas extruded in two episodes, 2.1 to 1.3 and 1.1 to 0.8 Ma ago. The voluminous Bishop Tuff erupted from the same magma system ~0.1 Ma later; resultant caldera collapse truncated the Glass Mountain complex. Early Glass Mountain lavas are more evolved than later ones, as indicated by incompatible element contents, and most are more evolved than the Bishop Tuff. Early lavas apparently were cooler and less fluid than later ones; they contain ubiquitous biotite, whereas some later ones contain pyroxene.

Small amounts of tuff are intercalated with the lavas. Pumice-fall deposits, some of which have been found as far away as Ventura, California and Beaver, Utah, can be correlated with specific lavas. Explosive activity occurred throughout the eruptive history of Glass Mountain. There is no apparent correlation of explosive activity with magma composition.

The Glass Mountain sequence suggests that a potentially explosive magma chamber may not have been present during the older eruptive episode. The younger episode is thought to represent eruption from a large, integrated, magma chamber, as evidenced by the smaller composition range displayed by lavas of larger average volume that erupted at a greater volumetric rate per unit time. Although eruption rates were higher during the younger episode, apparently the eruptions were not large enough to depressurize the magma chamber and initiate a major explosive eruption. Long Valley is a tectonically active area, so depressurization of the magma chamber due to fault rupture is proposed as a possible mechanism for triggering the catastrophic eruption of the Bishop Tuff.

INTRODUCTION

The triggering mechanism for large-volume, silicic, explosive eruptions is as yet unknown. Build-up of volatile concentrations in a chemically evolving magma chamber seems to be a necessary but not sufficient condition. Pressure release caused by ring fractures penetrating the magma chamber (Christiansen, 1984a; 1984b), unloading caused by voluminous eruptions (Bacon, 1983a), and vapor saturation from crystallization-induced "second boiling" (Burnham and Ohmoto, 1980) have been postulated as possible triggering mechanisms. The current state of unrest at Long Valley has focussed attention on a possible repetition of the violent explosive eruption that produced the Bishop Tuff and formed the Long Valley caldera 0.73 Ma ago (Dalrymple et al., 1965). The lavas and pyroclastic material erupted from the Long Valley magma chamber prior to eruption of the Bishop Tuff are being studied to see if they could have been used to predict the timing, violence, and/or volume of the caldera-forming eruption. The only exposed material vented from the mature Long Valley magma chamber prior to the Bishop Tuff is the high-silica rhyolite complex of Glass Mountain (Fig. 1). In this paper we describe the physical evolution of Glass Mountain. Data on the timing, size, mineralogy, and explosivity of the different eruptive units are integrated to characterize development of the magmatic system for the more than 1 Ma prior to catastrophic eruption of the Bishop Tuff.

GEOLOGIC SETTING

Glass Mountain can be viewed as part of a continuum of volcanic activity that began in the Long Valley area ~3.2 Ma ago (Bailey et al., 1976) and continues today. Early eruptions consisted of widespread basalts and andesites that are exposed north, west, and south of the caldera. Quartz

latites erupted ~3 to 2.6 Ma ago on the southern margin of the caldera (R.A. Bailey, personal communication), at Bald Mountain near the north margin of the future caldera, and in the San Joaquin--Two Teats area to the west (Curry, 1971; Bailey et al., 1976). High-silica rhyolite lavas erupted in the area that is now northeast of the caldera (Fig. 2) to form Glass Mountain between 2.12 and 0.80 Ma b.p. Evacuation of >600 km^3 of magma to form the Bishop Tuff 0.73 Ma ago caused collapse of the Long Valley caldera and was followed immediately by resurgent doming and postcaldera rhyolite eruptions which continued until ~0.1 Ma ago (Bailey et al., 1976). Studies of the chemistry of these postcaldera rhyolites suggest that the 0.5 Ma and 0.3 Ma eruptions were part of the Bishop Tuff cycle, whereas the youngest ones may represent a new cycle of magma chamber differentiation (Bailey, 1983a; 1983b). Volcanic activity in the Long Valley area has continued with eruption of basalts in the eastern part of the caldera and in Mono Lake (Gilbert et al., 1968; Bailey et al., 1976; Bailey, 1980), the arc of rhyolitic Mono Craters (Kistler, 1966; Wood, 1977; Sieh et al., 1983), and the Inyo Dome eruptions (Miller, 1983; 1984). While these younger eruptions are unlikely to be products of the Long Valley magma chamber, they probably share the same heat source that localized the Long Valley system.

PREVIOUS WORK ON GLASS MOUNTAIN

Glass Mountain was first described by Gilbert (1941) who recognized it as a complex of interbedded rhyolitic lavas and tuffs truncated by faulting along its south side. The total volume of Glass Mountain was estimated as $\geq$15 km^3 by Rinehart and Ross (1957). Sanidine separated from a lava on the northeast shoulder of Glass Mountain yielded a K-Ar age of 0.9 $\pm$ 0.1 Ma, or 0.92 Ma recalculated with new constants (Gilbert et al., 1968), and one from

a sample at the base of Glass Mountain gave an age of 1.92 ± 0.05 Ma, or 1.97 Ma recalculated with new constants (Bailey et al., 1976), defining a long time span of preserved Glass Mountain eruptions.

Bailey et al. (1976) and Bailey and Koeppen (1977) mapped Glass Mountain as part of a comprehensive study of the Long Valley caldera, but did not differentiate separate eruptive units. Bailey et al. (1976) were the first to state explicitly that the southern part of Glass Mountain was downfaulted along ring faults, and therefore part of it is buried beneath caldera fill.

Rhyolite tuff from Glass Mountain overlies basalt and granite southeast of the mountain and is in turn covered to the south by the Bishop Tuff (Gilbert, 1941). The pumice-fall deposit on the east slope of the Benton Range and the apron of Glass Mountain pyroclastic material that extends northward into Adobe Valley were designated the Tuff of Taylor Canyon by Krauskopf and Bateman (1977).

GEOLOGY OF GLASS MOUNTAIN

General Description and Morphology

Glass Mountain is a complex of lava domes and flows with intercalated pyroclastic material (Fig. 1) that covers ~130 km^2 and has a volume of >50 km^3, not including pyroclastic deposits. At 3390 m, the top of Glass Mountain is 1200 m above the floor of Long Valley caldera (Fig. 2). Caldera collapse following eruption of the Bishop Tuff truncated Glass Mountain, leaving a steep scarp on the south side. An unknown volume of Glass Mountain lavas is buried beneath caldera fill.

It seems likely that Glass Mountain developed on a preexisting topographic high; basement rock crops out at high elevations on all sides (Fig. 2). Southeast of Glass Mountain the basement topography apparently was

relatively flat Mesozoic granitic rock at elevations of 2438 to 2743 m. Tertiary basalt with more variable topography is exposed on all sides of Glass Mountain.

Glass Mountain does not appear to have been glaciated during the Pleistocene. Although the north side of Glass Mountain peak is cirque-like, preservation of pumiceous carapace on top of the peak (Fig. 3) suggests that it was not glaciated. The Sierra Nevada had reached nearly its present elevation before onset of Pleistocene glaciation (Christiansen, 1966; Bateman and Wahrhaftig, 1966; Huber, 1981) and would have created a rain shadow, causing higher glacier levels in the White Mountains and Glass Mountain than in the Sierra Nevada. Glacier levels in the White Mountains were at $\geq$~3300 m (Krauskopf and Bateman, 1977), making it unlikely that there would be much glacier formation at Glass Mountain, which has a maximum elevation of 3390 m.

Physical Character of Lavas

Lavas generally are well preserved, but even the youngest units at Glass Mountain have lost some of the youthful features, such as steep margins, lobate morphology, and arcuate pressure ridges, that can be used as mapping criteria. Criteria for identifying individual lavas include physical continuity of exposures, degree of erosion, and phenocryst species and abundance (although some variation in phenocryst content with position in flows is seen). Vents (stars in Figs. 3 and 4) can be identified by attitudes of flow banding, by alteration of the rock, and by coarse vesicles lined with vapor-phase tridymite that commonly developed in vent areas.

The cooling zonation reflected in textural differences in the rocks also was used as a criterion for mapping individual lava flows (Fig. 3). There is a predictable progression from surface to interior of a flow or dome from

pumiceous carapace, to perlitic obsidian, to dense black glass, to lithophysal obsidian with cavities up to 1 m across, and finally to devitrified rhyolite. For some units a lower obsidian layer is exposed. Devitrified rhyolite and dense black glass are interlayered on a scale of meters to millimeters. Devitrified rhyolite commonly is macroscopically flow banded, and dense black glass may be. This cooling zonation differs from that documented by Fink (1980) for the <1100-year-old Little Glass Mountain flow of Medicine Lake Highland, California, in which the vertical zonation is surficial autobreccia, finely vesicular pumice, obsidian, coarsely vesicular pumice, and basal breccia (Fink, 1980; 1983). Little Glass Mountain is 15-60 m thick (Fink, 1983), whereas the lavas of Long Valley Glass Mountain commonly are $\geq$100 m thick. The Little Glass Mountain lava may not have been thick enough to develop a devitrified interior on cooling; alternatively, a devitrified core may be present but not yet exposed. The Southern Coulee of Mono Craters, California, is a 3.6-by-1.2-km rhyolite flow ~75 m thick. The internal structure was interpreted from drill cores: pumice becomes less vesicular and obsidian becomes more abundant downward, and at a depth of ~40 m the obsidian layers become spherulitic (Loney, 1968). This resembles the sequence found at Long Valley Glass Mountain in that obsidian becomes more abundant downward, and spherulitic obsidian is found near the center of units.

Older units are best exposed in the steep caldera scarp on the southwest side. In other areas, they appear as eroded remnants consisting of devitrified rhyolite, locally in conjunction with small amounts of hydrated glass. The younger units form recognizable domes on the northwest side of the mountain, but near the caldera margin to the southeast even younger units

are deeply eroded and exposures are fragmentary (Fig. 3).

K-Ar Dating of Lavas

K-Ar dating of glass, devitrified rhyolite matrix, and sanidine has been used to calibrate the stratigraphy developed from field mapping. Because most sample yield large proportions of radiogenic argon, estimated 1σ precisions for these dates are typically 0.03 Ma (Table 1). The 35 dates demonstrate that all the lavas erupted in two discrete episodes, 2.12 to 1.35 and 1.10 to 0.80 Ma ago (Table 1; Fig. 6). Twelve eruptive units are undated and at least half of these cannot be dated, apparently because of incorporation of atmospheric argon at the time of eruption. These 12 units are assigned to eruptive groups on the basis of stratigraphic position and/or degree of erosion with respect to adjacent dated units. The more than 40 identified eruptive units are shown schematically in Figure 4. Others must lie beneath the surface of Glass Mountain (Fig. 5) and buried within the caldera. Although each lettered unit in Figure 4 is a separate mappable lava, several may comprise a single eruptive pulse. Eruptions appear to have occurred along an incipient ring fracture zone, but there is no correlation of vent location with age of eruptive units (Fig. 4).

Sizes and Volumes of Lavas

Two well-exposed domes on the western part of Glass Mountain (A and B in Figs. 4 and 5) have been used to calculate the relative proportions of devitrified rhyolite (40%), dense black glass (~30%), and pumiceous carapace (~30%) for Glass Mountain units. Using these figures, magma equivalent volumes of Glass Mountain lavas range from <0.01 km^3 to ~2 km^3. These are minimum estimates as pre-erosion volumes were greater; the eroded material would have been highly inflated pumiceous carapace with porosity $\geq$40%.

Identified eruptive units range in rock volume from <0.01 to >3 km^3. The southeast end of Glass Mountain seems to be made up of a large number of smaller units; flow units cannot be traced as far as in the northeast. Even when allowances are made for disruption by faulting and increased erosion in the faulted areas, this difference seems to be real. The smallest exposed flow unit at Glass Mountain (R in Fig. 4) is a plug of obsidian that utilized the same conduit as an earlier, larger dome. The pumiceous carapace has been eroded away, but the total volume probably never was much more than the currently exposed <0.01 km^3. In contrast, the largest unit (C in Fig. 4) has a rock volume of ~3 km^3, and an estimated magma volume of ~2 km^3. It is the youngest and most fluid of the Glass Mountain eruptions, and covers an area 1.9 X 2.6 km, with a thickness of ~120 m.

TEMPORAL CHEMICAL AND PHYSICAL TRENDS IN GLASS MOUNTAIN LAVAS

All of the Glass Mountain lavas are high-silica rhyolites containing 76.9 to 77.4 wt. % SiO_2 (calculated on an anhydrous basis). Al_2O_3, MgO, and TiO_2 show a small range, and variations in Na_2O can largely be attributed to mobility during devitrification and hydration. There are, however, pronounced differences in abundances of K_2O, FeO, CaO, MnO, and trace elements such as Rb, Y, and Nb, which make it possible to chemically distinguish different lava units. Plots of any two of the elements Fe, Ca, K, Na, Rb, Mn, Nb, Y, and Zr separate units of the older and younger eruptive episodes with reasonable accuracy (Fig. 7). When the undated units are plotted in the same way, most of them fall within the same groups as indicated by field evidence. The earliest Glass Mountain lavas are the most evolved, and most of them are more evolved than the Bishop Tuff (Fig. 8). Both a long-term trend toward less-evolved compositions and short-term

fluctuations are present. The younger eruptive group shows a smaller range of abundances.

Older eruptive units tend to contain more phenocrysts than younger ones. A few of the oldest units contain up to 15-20% phenocrysts of quartz, sanidine, plagioclase, biotite, and titanomagnetite ± ilmenite; most contain ≤10%. Apatite and zircon are found mainly as inclusions in biotite. A 1.35-Ma-old dome on the westernmost edge of Glass Mountain contains ~30% phenocrysts, including strongly-zoned plagioclase. Eruption of this unit was followed by a period of quiescence before eruption of the younger lavas. Younger units contain 0-5% phenocrysts. Salic species are the same as in the older units, but mafic assemblages are more variable and consist of biotite, pyroxene, both, or neither (Fig. 6).

Flow and dome morphologies record a change to more fluid magmas with time. At least five units formed areally extensive flows rather than steep-sided domes. They are shown by arrows indicating flow direction in Figure 4. Flow G is 1.6 X 0.8 km and has a maximum exposed thickness of ~125 m. The flow that forms the top of Glass Mountain peak (H in Fig. 4; Fig. 5) is ~60 m thick and flowed about 1 km to the north, banking against an older unit (O in Fig. 4; Fig. 5). Four of these flows belong to the younger eruptive episode, and include the most voluminous, youngest, eruptive unit. The fifth is one of the youngest units of the older eruptive episode. The change in morphology can be attributed at least in part to hotter magma; Fe-Ti oxide analyses suggest that early Glass Mountain lavas were cooler than later ones.

The older eruptive episode lasted for 0.77 Ma and produced 18 eruptions, whereas the 0.3-Ma-long younger episode produced 25 eruptions. Calculated

total volumes for the episodes are ~3.5 and ~10.5 km^3, respectively. Because the older units are both more poorly exposed and more deeply eroded, the real magnitude of this difference may be less.

EXPLOSIVE ACTIVITY

Pyroclastic deposits associated with Glass Mountain lavas include tuffs intercalated with lavas, poorly exposed ash-flow tuffs peripheral to the mountain, and pumice-fall deposits found as far as 400 km from the mountain. Exposures of pyroclastic rocks within the main mass of Glass Mountain are rare. Their presence is inferred from the distribution of an ashy, light-colored soil with restricted occurrence and the presence of exotic cobbles of granitic rock or basalt in areas that lack outcrop. The southeastern end of Glass Mountain has the greatest abundance of these features. Tuff deposits are inferred to comprise ~10% of the mountain (Fig. 3).

Southeast of Glass Mountain is an area of low, rolling hills which largely consist of reworked material, possibly debris flows, from Glass Mountain. Subangular to subrounded cobbles of all textural varieties of Glass Mountain rhyolite are present throughout. A few small hills appear to be devitrified rhyolite extrusions, as noted by Gilbert (1941). They are badly preserved; pumiceous carapace and dense black glass are lacking. In the northwestern part of this area, which is nearest Glass Mountain, there are two small outcrops of ash-flow tuff as well as ashy soils that probably are derived from ash-flow tuffs.

Thick pumice-fall deposits are exposed in quarries along the west side of Benton Valley, approximately 12-20 km northeast of Glass Mountain. Individual pumice falls commonly are 1-2 m in thickness, and may be up to 5 m

thick. Maximum pumice clasts in these deposits range from 2-19 cm. Lithics consist of felsite, obsidian, basalt, and granitic clasts <0.5 to 5 cm in size. The total volume of tephra deposits in the Benton Valley exposures is estimated to be ~20 km^3, or ~10 km^3 of magma.

Pumice deposits attributed to a Glass Mountain source on the basis of trace element abundances include ashes from as far away as Ventura, California (Sarna-Wojcicki et al., 1980; Izett, 1981; 1982), and Beaver County, Utah (Izett, 1981; 1982). Sarna-Wojcicki et al. (1980) ascribe six ashes, ranging in age from 0.90 to >2.0 Ma, to a Glass Mountain source. The K-Ar age of the oldest is 2.3 Ma, but this age is believed by them to be too old as an underlying ash is correlated with the 2.0 Ma-old Pearlette B ash. Sarna-Wojcicki et al. noted temporal compositional trends in the Glass Mountain ashes, with younger ashes having lower Mn and higher Ca and Fe concentrations. Sarna-Wojcicki and Izett used different names for the same ashes in some cases; the correspondence of their samples is shown in Table 2, along with our tentative correlations of these ashes with Glass Mountain lavas. An important result of the tephra-lava correlations is documentation that explosive activity occurred throughout the eruptive history of Glass Mountain, implying that it was not restricted to association with lavas of a particular time period or degree of chemical evolution.

Correlative distal ashes are lacking, or have not yet been identified, for some of the pumice-fall deposits in Benton Valley that we have correlated with lavas at Glass Mountain. Izett (1981; 1982) correlated several ashes $\geq$2.1 Ma old with a Glass Mountain source, but preliminary correlations with Glass Mountain lavas suggest that these ages may be too old (Table 2). The Bailey ash (Table 2), dated at 1.2 Ma, is tentatively correlated with an

unsuccessfully dated lava, unit JJ (Fig. 4). If this correlation and the age of the ash are both correct, there was at least one eruption during the supposed hiatus between the older and younger eruptive groups.

GLASS MOUNTAIN COMPARED WITH PRECALDERA ERUPTIONS IN OTHER SYSTEMS

Glass Mountain appears to be unusual among precaldera complexes in that it erupted over a long period of time, is voluminous, and is chemically more evolved than the succeeding ash-flow tuff, although the small amount of data available on other precaldera lavas makes this conclusion tentative. A number of caldera-forming systems are now well-studied, but there is little documentation in the literature of the physical or chemical evolution of precaldera lavas.

Precaldera volcanism associated with voluminous silicic systems generally begins with widespread andesitic ± basaltic eruptions that span millions of years (e.g., Valles, Sierra la Primavera, Los Humeros, and the San Juan volcanic center in Table 3). This mafic to intermediate volcanism apparently provides the heat necessary for development of a high-level silicic magma chamber. In the classic model of resurgent cauldron formation (Smith and Bailey, 1968a), broad doming of an area over a magma chamber may be accompanied by eruptions from incipient ring fractures. Preservation of these early lavas during an explosive climactic eruption clearly is a matter of chance. The early lavas that leak from the ring fractures commonly are rhyodacite and/or quartz latite in composition (e.g., Valles and Twin Peaks in Table 3). Rhyolite or high-silica rhyolite eruptions that commonly are of small volume and short duration may occur after or instead of the rhyodacite/quartz latite lavas (e.g., Sierra la Primavera, Los Humeros, Mount Belknap, Yellowstone, and Timber Mountain-Oasis Valley). Precaldera lavas

commonly are more mafic than the first erupted portion of the caldera-forming tuff, and may show a progression toward more silicic compositions (e.g., Emory, Valles, and Questa). The less silicic precaldera eruptions may represent a base-level magma composition from which a more differentiated cap may evolve (Smith, 1979).

Magmatic systems such as those at Mono Craters and Coso, California (Table 3) have not produced caldera-forming eruptions, but it has been proposed that they may do so in the future (Bailey, 1980; Bacon et al., 1981). The Mono Craters chain is slightly arcuate in plan, giving rise to the speculation that it may lie on a developing ring fracture zone (Bailey, 1980), although geophysical evidence for high-level magma chambers is lacking for both these fields (Hermance, 1983; Bacon et al., 1981). The Coso rhyolites are evolved high-silica rhyolites (Bacon et al., 1981), making them compositionally analogous to Glass Mountain. Mono Craters is chemically virtually identical to the lavas of Glass Mountain (Jack and Carmichael, 1968). These systems may be good analogues for the older eruptive episode at Glass Mountain.

SUMMARY AND DISCUSSION

The high-silica rhyolite lava domes and flows preserved at Glass Mountain erupted in two episodes, 2.12 to 1.35 and 1.10 to 0.80 Ma ago. The volumetric eruptive rate and total volume erupted were smaller for the older eruptive episode. Despite this, the older episode shows a much wider range of compositions and greater fluctuations with time (Fig. 8). Phenocryst contents also vary irregularly with time, with the youngest of the lavas of the older eruptive group having the highest proportion of phenocrysts at Glass Mountain. Taken together, these observations suggest that an

integrated, high-level magma chamber was not present during the older eruptive episode. A case in point are two lavas from opposite ends of Glass Mountain dated at 1.92 Ma that have strikingly different compositions (Fig. 8). This indicates that either there was not a single magma chamber, or that the volume of the reservoir was so small that the eruptive rate exceeded the rate at which highly evolved magmas were formed. Silicic magma chambers do not arrive at high levels in the crust full-blown; they must form incrementally through addition of partial melts of the crust and of crystal fractionation products of hybridized intermediate rocks. The older eruptive episode at Glass Mountain may record this period of construction of the mature Long Valley magma chamber.

The lavas of the younger eruptive episode seem to record higher magma temperatures near the roof of the reservoir: they flowed farther, have fewer phenocrysts, and contain pyroxene at the expense of biotite. The few analyses of coexisting Fe-Ti oxides support this, with temperatures of 690-715^{0} for the older period and 710-780^{0} for the younger episode. One plausible explanation for the higher temperatures of the younger eruptive group is a higher heat input into the chamber, in the form of crustal partial melts or mantle-derived mafic magmas. An increasing supply of heat may be responsible for the overall trend toward less evolved compositions from the first Glass Mountain lavas to the Bishop Tuff, by the addition and incorporation of higher temperature partial melts into the chamber.

By chemically correlating pumice falls with lava domes we have shown that pyroclastic activity occurred throughout the eruptive history of Glass Mountain and that there is no obvious correlation with magma chemistry or phenocryst assemblage. Thus we do not have any positive evidence for a

secular increase in volatile abundances that might have eventually led to the explosive Bishop Tuff eruption. Long Valley caldera is in a tectonically active area so it is possible that the triggering mechanism for the Bishop Tuff eruption was earthquake-induced pressure release of a volatile-rich but not volatile-saturated magma.

ACKNOWLEDGEMENTS

R. A. Bailey of the U. S. Geological Survey very kindly suggested study of Glass Mountain as a worthwhile project. J. Chatoian and Mark Smith of the U. S. Forest Service rendered invaluable aid in the early phases of the field work. The assistance of R. H. Husk, Jr., A. Davis, and J. Miley in the field is appreciated. Material support was provided by NSF Grant No. EAR-836860 to Mahood, and Stanford Shell Fund grants to Metz.

REFERENCES

Bacon, C. R., Eruptive history of Mount Mazama and Crater Lake caldera, Cascade Range, U.S.A., J. Volc. Geoth. Res. 18, 57-115, 1983a.

Bacon, C. R., R. Macdonald, R. L. Smith, and P. A. Baedecker, Pleistocene high-silica rhyolites of the Coso volcanic field, Inyo County, California, J. Geophys. Res. 86, 10223-10241, 1981.

Bailey, R. A., Structural and petrologic evolution of the Long Valley, Mono Craters, and Mono Lake volcanic complexes, eastern California, Eos Trans. AGU 61, 1149, 1980.

Bailey, R. A., Geologic and petrologic data bearing on potential volcanic hazards in Long Valley caldera, eastern California, Seismological Society Abstracts 54, 72, 1983a.

Bailey, R. A., Postcaldera evolution of the Long Valley magma chamber, eastern California, Eos Trans. AGU 64, 889, 1983b.

Bailey, R. A., G. B. Dalrymple, and M. A. Lanphere, Volcanism, structure, and geochronology of Long Valley caldera, Mono County, California, J. Geophys. Res. 81, 725-744, 1976.

Bailey, R. A., and R. P. Koeppen, Preliminary geologic map of Long Valley caldera, Mono County, California, U. S. Geol. Surv.. Open File Map 77-468, 1977.

Bateman, P. C. and C. Wahrhaftig, Geology of the Sierra Nevada in Geology of Northern California, Calif. Div. Mines Geol. Bull. 190, 107-172, 1966.

Budding, K. E., Eruptive history, petrology, and petrogenesis of the Joe Lott Tuff member of the Mount Belknap volcanics, Marysvale volcanic field, west-central Utah, U. S. Geol. Surv. Open File Report 82-891, 1982.

Burnham, C. W., and H. Ohmoto, Late-stage processes of felsic magmatism, Soc. Mining Geol. Japan Special Issue 8, 1-11, 1980.

Christiansen, M. N., Late Cenozoic crustal movements in the Sierra Nevada of California, Geol. Soc. Amer. Bull. 77, 163-182, 1966.

Christiansen, R. L., Cooling units and composite sheets in relation to caldera structure in Chapin, C. E. and W. E. Elston, eds., Ash-flow Tuffs, Geol. Soc. Amer. Spec. Paper 180, 29-42, 1979.

Christiansen, R. L., The Quaternary and Pliocene Yellowstone Plateau volcanic field of Wyoming, Idaho, and Montana, U. S. Geol. Surv. Prof. Paper 729- , in press, 1984a.

Christiansen, R. L., Yellowstone magmatic evolution: its bearing on understanding large-scale explosive volcanism in Explosive Volcanism: inception, evolution, and hazards, National Academy Press Studies in Geophysics, 84-89, 1984b.

Christiansen, R. L., and H. R. Blank, Volcanic stratigraphy of the Quaternary rhyolite plateau in Yellowstone National Park, U. S. Geol. Surv.Prof. Paper 729-B, 18p, 1972.

Christiansen, R. L., P. W. Lipman, W. J. Carr, F. M. Byers, Jr., P. P. Orkild, and K. A. Sargent, Timber Mountain-Oasis Valley caldera complex of southern Nevada, Geol. Soc. Amer. Bull. 88, 943-959, 1977.

Crecraft, H. R., W. P. Nash, and S. H. Evans, Jr., Late Cenozoic volcanism at Twin Peaks Utah: geology and petrology, J. Geophys. Res. 86, 10303-10320, 1981.

Cunningham, C. G., and T. A. Steven, Mount Belknap and Red Hills calderas and associated rocks, Marysvale volcanic field, Utan, U. S. Geol. Surv. Bull. 1468, 34 p., 1979.

Curry, R. R., Glacial and Pleistocene history of the Mammoth Lakes Sierra: a geologic guidebook, University of Montana Geol. Series Pub. II, 49 p, 1971.

Dalrymple, G. B., A. Cox, and R. R. Doell, Potassium-argon age and paleomagnetism of the Bishop Tuff, California. Geol. Soc. Amer. Bull. 76, 665-674, 1965.

Duffield, W. A., C. R. Bacon, and G. B. Dalrymple, Late Cenozoic volcanism, geochronology, and structure of the Coso Range, Inyo County, California, Jour. Geophys. Res. 85, 2381-2404, 1980.

Elston, W. E., W. R. Seager, and R. E. Clemons, Emory cauldron, Black Range, New Mexico, source of the Kneeling Nun Tuff, New Mexico Geol. Soc. Guidebook, 26th Field Conf., 283-292, 1975.

Ferriz, H., and G. A. Mahood, Eruption rates and compositional trends at Los Humeros volcanic center, Puebla, Mexico, J. Geophys. Res., in press, 1984.

Fink, J., Surface folding and viscosity of lava flows, Geology 8, 250-254, 1980.

Fink, J. H., Structure and emplacement of a rhyolitic obsidian flow: Little Glass Mountain, Medicine Lake Highland, northern California, Geol. Soc. Amer. Bull. 94, 362-380, 1983.

Gilbert, C. M., Late Tertiary geology southeast of Mono Lake, California, Geol. Soc. Amer. Bull. 52, 781-816, 1941.

Gilbert, C. M., M. N. Christensen, Y. Al Rawi, and K. R. Lajoie, Structure and volcanic history of the Mono Basin, California-Nevada, Geol. Soc. Amer. Mem. 116, 275-329, 1968.

Guilbeau, K. P., and A. M. Kudo, Petrogenesis of the high-silica Bearhead

rhyolite and related calc-alkaline volcanics of the Jemez Mountains, Geol. Soc. Amer. Abstr. Programs 14, 504, 1982.

Hermance, J. F., The Long Valley/Mono Basin volcanic complex in eastern California: status of present knowledge and future research needs, Rev. Geophys. and Space Physics 21, 1545-1564, 1983.

Huber, N. K., Amount and timing of late Cenozoic uplift and tilt of the central Sierra Nevada, California-evidence from the upper San Joaquin River basin, U. S. Geol. Surv. Prof. Paper 1197, 28 p., 1981.

Izett, G. A., Volcanic ash beds: recorders of upper Cenozoic silcic pyroclastic volcanism in the western United States, J. Geophys. Res. 86, 10200-10222, 1981.

Izett, G. A., J. D. Obradovich, and H. H. Mehnert, The Bishop ash bed and some older compositionally similar ash beds in California, Nevada, and Utah, U.S. Geol. Surv. Open File Report 82-582, 1982.

Jack, R. N., and I. S. E. Carmichael, The chemical 'fingerprinting' of acid volcanic rocks, Calif. Div. Mines Geol. Spec. Rep. 100, 17-32, 1968.

Krauskopf, K. B., and P. C. Bateman, Geologic map of the Glass Mountain quadrangle, Mono County, California, and Mineral County, Nevada, U. S. Geol. Surv.. Map GQ-1099, 1977.

Kistler, R. W., Geologic map of the Mono Craters quadrangle, Mono and Tuolumne counties, California, U. S. Geol. Surv. Map GQ-462.

Lipman, P. W., The Miocene Questa caldera, northern New Mexico: relation to batholith emplacement and associated molybdenum mineralization, Proceedings of the Denver Region Exploration Geologists Symposium, 133-148, 1983.

Lipman, P. W., B. R. Doe, C. E. Hedge, and T. A. Steven, Petrologic evolution

of the San Juan volcanic field, southwestern Colorado: Pb and Sr isotope evidence, Geol. Soc. Amer. Bull. 89, 59-82, 1978.

Loney, R. A., Flow structure and composition of the Southern Coulee, Mono Craters, California-a pumiceous rhyolite flow, Geol. Soc. Amer. Mem. 116, 415-440, 1968.

Mahood, G. A., Summary of the geology and petrology of the Sierra la Primavera, Jalisco, Mexico, J. Geophys. Res. 86, 10137-10152, 1981.

Mahood, G. A., Discussion of "The Rio Caliente Ignimbrite: analysis of a compound intraplinian ignimbrite from a major late Quaternary Mexican eruption: by J. V. Wright, Bull. Volcanol. 46-2, 103-106, 1983.

Mahood, G. A., and R. E. Drake, K-Ar dating young rhyolitic rocks: a case study of the Sierra la Primavera, Jalisco, Mexico, Geol. Soc. Amer. Bull. 93, 1232-1241, 1982.

Miller, C. D., Chronology of Holocene eruptions at the Inyo-Mono eolcanic chain, California, Eos Trans. AGU 64, 900, 1983.

Miller, C. D., Chronology of Holocene eruptions at the Inyo volcanic chain, central eastern California: implications for possible eruptions in Long Valley, this volume, 1984.

Nielson, D. L., and J. B. Hulen, Internal geology and evolution of the Redondo dome, Valles caldera, New Mexico, J. Geophys. Res., in press, 1984.

Rinehart, C. D., and D. C. Ross, Geology of the Casa Diablo Mountain quadrangle, California, U. S. Geol. Surv. Map GQ-99, 1957.

Sarna-Wojcicki, A. M., H. R. Bowman, C. E. Meyer, P. C. Russell, F. Asaro, H. Michael, J. J. Rowe, P. A. Baedecker, and G. McCoy, Chemical analyses, correlations, and ages of late Cenozoic tephra units of east-central and

southern California, U. S. Geol. Surv. Open File Report 80-231, 1980.

Sieh, K., S. H. Wood, and S. Stine, Most recent eruption of the Mono Craters, eastern central California, Eos Trans. AGU 64, 889, 1983.

Smith, R. L., Ash-flow magmatism, Geol. Soc. Amer. Spec. Paper 180, 5-27, 1979.

Smith, R. L., and R. A. Bailey, Resurgent Cauldrons in Coats, R. R., R. L. Hay, and C. A. Anderson, eds., Studies in Volcanology, Geol. Soc. Amer. Mem. 116, 613-662, 1968a.

Smith, R. L., and R. A. Bailey, Stratigraphy, structure, and volcanic evolution of the Jemez Mountains, New Mexico, Colo. School Mines Quarterly 63, 259-260, 1968b.

Smith, R. L., R. A. Bailey, and C. S. Ross, Geologic Map of the Jemez Mountains, New Mexico, U. S. Geol. Surv. Map I-571, 1970.

Wood, S. H., Distribution, correlation, and radiocarbon dating of late Holocene tephra, Mono and Inyo Craters, eastern California, Geol. Soc. Amer. Bull. 88, 89-95, 1977.

Table 3. Summary of Precaldera Eruptions for Several Systems.

System	Precaldera Units: Andesite/basalt	Precaldera Units: Rhyodacite/qtz. latite	Rhyolite/high silica rhyolite: Age (Ma)	Rhyolite/high silica rhyolite: Preserved Volume[1]	Caldera-forming Eruption: Age (Ma)	Caldera-forming Eruption: Composition[2]	References
Long Valley	3.2 Ma	3-2.6 Ma	2.1-0.8	>50	0.7	hsr-rhy	Bailey et al., 1976
Valles	12-1 Ma	6.5-3.2 Ma	2.0-1.4	?	1.4	hsr-rhy	Smith and Bailey, 1968b; Smith et al., 1970; Smith, 1979; Guilbeau and Kudo, 1982; Nielson and Hulen, 1984.
Sierra la Primavera	yes	yes	.12-.10	∿1	0.095	hsr	Mahood, 1981; Mahood, 1983.
Los Humeros	3.5-1.9 Ma	no	.51	0.1	0.50	hsr-and	Ferriz and Mahood, 1984.
San Juan	35-30 Ma	?	?	-	30-26 (many)	hsr or rhy-qtz lat	Lipman et al., 1978.
Twin Peaks, Utah	?	2.7 Ma	?	-	2.6-2.4	hsr	Crecraft et al., 1981.
Joe Lott (Mt. Belknap)	30-29 Ma	?	?	lithics in tuff	19	hsr	Cunningham et al., 1979; Budding, 1982.
Yellowstone	Snake	no?	2.2-2.1	∿10	2.0	hsr-rhy	Christiansen and Blank, 1972; Christiansen 1979; 1984a,b.
	River	no?	yes	∿50	1.3	hsr-rhy	
	Plain	no?	1.3-0.8	>200	0.63	hsr-rhy	
Timber Mtn.-Oasis Valley	?	no?	13.4	?	13.2	hsr-rhy	Christiansen et al., 1977.
Emory	>37 Ma	?	?	-	33.4	rhy-lat	Elston et al., 1975.
Questa	27-26 Ma	?	?	?	26	hsr	Lipman, 1983.
Coso	6-2.5 Ma	3 Ma	1.04-.06	∿1.5	none	-	Bacon et al., 1981; Duffield et al., 1980.
Mono Craters	?	?	.04-.0005	∿10	none	-	Bailey, 1980; Wood, 1977

[1] km^3 magma volume

[2] hsr = high-silica rhyolite; rhy = rhyolite; lat = latite; and = andesite

Table 1. K-Ar Ages for Glass Mountain Lavas.

Sample	Unit[1]	Material	Sample Wt. (g)	K (%)	$^{40}Ar^*$ (10^{-12} mol/g)	$^{40}Ar^*$ (%)	Age (Ma)	1σ(Ma)[3]
Older Eruptive Group								
217	I	felsite[2]	4.23908	3.84	14.1	44.7	2.12	.04
036	K	glass	7.37628	3.70	12.2	23.7	1.92	.06
219	LL	felsite	4.04460	3.64	12.1	47.7	1.92	.04
146	V	glass	4.41499	3.97	13.0	63.8	1.89	.03
051	DD	glass	6.42040	3.93	12.4	88.5	1.82	.03
145	EE	glass	5.49481	3.93	12.1	71.4	1.77	.03
142	D	glass	5.27795	3.77	11.4	25.9	1.75	.05
144	CC	glass	4.72674	3.84	10.8	7.8	1.62	.15
155	Q	glass	4.17098	4.03	11.2	71.5	1.60	.02
227	Q	glass	3.18592	3.95	10.9	10.9	1.59	.10
143	BB	glass	5.06166	3.89	10.6	41.3	1.58	.03
153	P	glass	4.14852	3.85	9.56	18.4	1.43	.05
233	M	felsite	3.74568	3.62	8.85	13.7	1.41	.07
158	L	sanidine	1.83808	4.83	11.4	9.7	1.36	.10
263	L	felsite	3.38553	3.79	8.71	9.6	1.33	.10
Younger Eruptive Group								
229	II	felsite	4.16420	3.89	7.39	11.0	1.10	.04
138	B	glass	5.95793	4.13	7.84	3.0	1.09	.06
049	G	glass	5.76003	4.03	7.45	11.4	1.07	.07
226	NN	felsite	4.33375	4.18	7.67	26.7	1.06	.03
218	F	glass	3.92299	3.82	6.84	4.0	1.03	.19
225	FF	felsite	4.06289	3.98	6.89	16.2	1.00	.05
231	N	glass	3.57727	3.94	6.82	26.9	1.00	.03
220	GG	felsite	4.19131	3.79	6.44	32.7	0.98	.03
026	PP	glass	5.88680	4.08	6.83	54.1	0.97	.02
033	X	glass	6.98126	4.06	6.83	65.7	0.97	.02
141	R	glass	4.56715	4.02	6.72	51.5	0.96	.02
031	H	glass	7.89304	4.01	6.44	62.9	0.93	.02
162	A	glass	4.18348	4.10	6.25	24.0	0.88	.03
140	A	glass	4.45201	4.10	6.52	21.2	0.92	.03
148	Y	glass	4.82050	4.01	6.31	20.5	0.90	.03
037	Z	glass	5.59147	4.00	5.68	10.3	0.82	.06
187	S	glass	4.45757	4.05	5.79	35.5	0.82	.02
154	S	glass	4.9104	4.05	5.67	40.4	0.81	.02
139	U	felsite	5.75112	3.96	5.56	36.8	0.81	.02
038	C	glass	5.54192	4.15	5.66	41.7	0.80	.02

[1] Unit on Figure 4

[2] Felsite = devitrified matrix separates

[3] Calculated from Equation 2 of Mahood and Drake (1982)

Table 2. Comparison of Ash Deposits and Glass Mountain Lavas.

Location[1]	Sarna-Wojcicki et al. (1980) Ash Name	Age (Ma)	Izett (1981; 1982) Ash Name	Age (Ma)	Correlations with Glass Mountain lavas Unit (Fig. 4)	Age (Table 1)
Bishop, Mono, Ventura, Inyo	Ash of Mono Glass Mountain	<0.9[2]	Glass Mountain D	1.06[3]	Y	0.90
Bishop, Inyo, Ventura	Ash below Ash of Mono Glass Mtn.	0.96-1.2[4]	Glass Mountain G	--	W[5]	1.10
Ventura	Bailey Ash	1.2[6]	Bailey Ash	1.2[7]	JJ[5]	older group
Ventura	Ash below the Bailey Ash	1.3-1.6[8]	South Mountain	--	M	1.41
Beaver (UT)	--	--	Last Chance Bench	∿1.8[9]	none	--
San Bernardino	Upper White Ash, Manix Basin	--	Manix 3	--	none	--
San Bernardino	Middle White Ash, Manix Basin	<2.3[10]	Manix 2	--	K[5]	1.92

1 County; California except as noted

2 K-Ar on obsidian lithics in ash

3 K-Ar on sanidine

4 Younger limit constrained by paleomagnetism; older limit by age of underlying ash

5 Lavas that have been correlated with tephra deposits in Benton Valley

6 Fission track on glass

7 Fission track on zircon

8 Constrained by stratigraphy and sedimentation rates

9 Constrained by stratigraphy

10 K-Ar on sanidine, but believed by Sarna-Wojcicki et al. to be too old because underlying ash is 2.0 Ma

FIGURE CAPTIONS

Figure 1. Glass Mountain as seen from the north.

Figure 2. Distribution of Glass Mountain lavas and pyroclastic deposits. Top of Glass Mountain peak = filled triangle; lavas = light stipple; pyroclastic deposits = heavy stipple; basement rocks = diagonal ruling; Holocene cover = unpatterned; caldera margin = heavy dashed line. Contours are shown for 2438 m (8000′) and 2804 m (9200′). Inset shows location of Glass Mountain on the margin of Long Valley caldera and location of pyroclastic deposits attributed to a Glass Mountain source by Sarna-Wojcicki et al. (1980) and Izett (1981; 1982).

Figure 3. Geologic map of Glass Mountain. Unpatterned = Holocene cover; light stipple = pumiceous carapace; heavy stipple = dense glass; horizontal ruling = devitrified rhyolite; vertical ruling = intercalated tuff; heavy dashed line = caldera margin.

Figure 4. Schematic diagram of lavas and vent locations. Vent = star; heavy dashed line = caldera margin; units of the older eruptive episode = stippled pattern; units of the younger episode = unpatterned. Units T, GG, and FF may be multiple lobes of a single eruptive pulse; AA and BB may be the same unit. A-A′is line of section shown in Figure 5.

Figure 5. Schematic cross section through Glass Mountain. No vertical exaggeration. Units of older eruptive episode = dark stippled pattern; units of younger episode = unpatterned; tuff = light stippled pattern.

Figure 6. Histogram of dated lavas versus age. Patterns indicate presence of mafic phenocrysts; stipple = biotite; horizontal ruling = pyroxene; unpatterned = neither.

Figure 7. Variation diagrams. Lavas of older eruptive group = filled

circles; younger lavas = filled squares. Undated lavas assigned to older group on basis of field evidence = open circles; assigned to younger group on field evidence = open squares.

Figure 8. Element abundances versus age for dated Glass Mountain lavas.

FIGURE 1

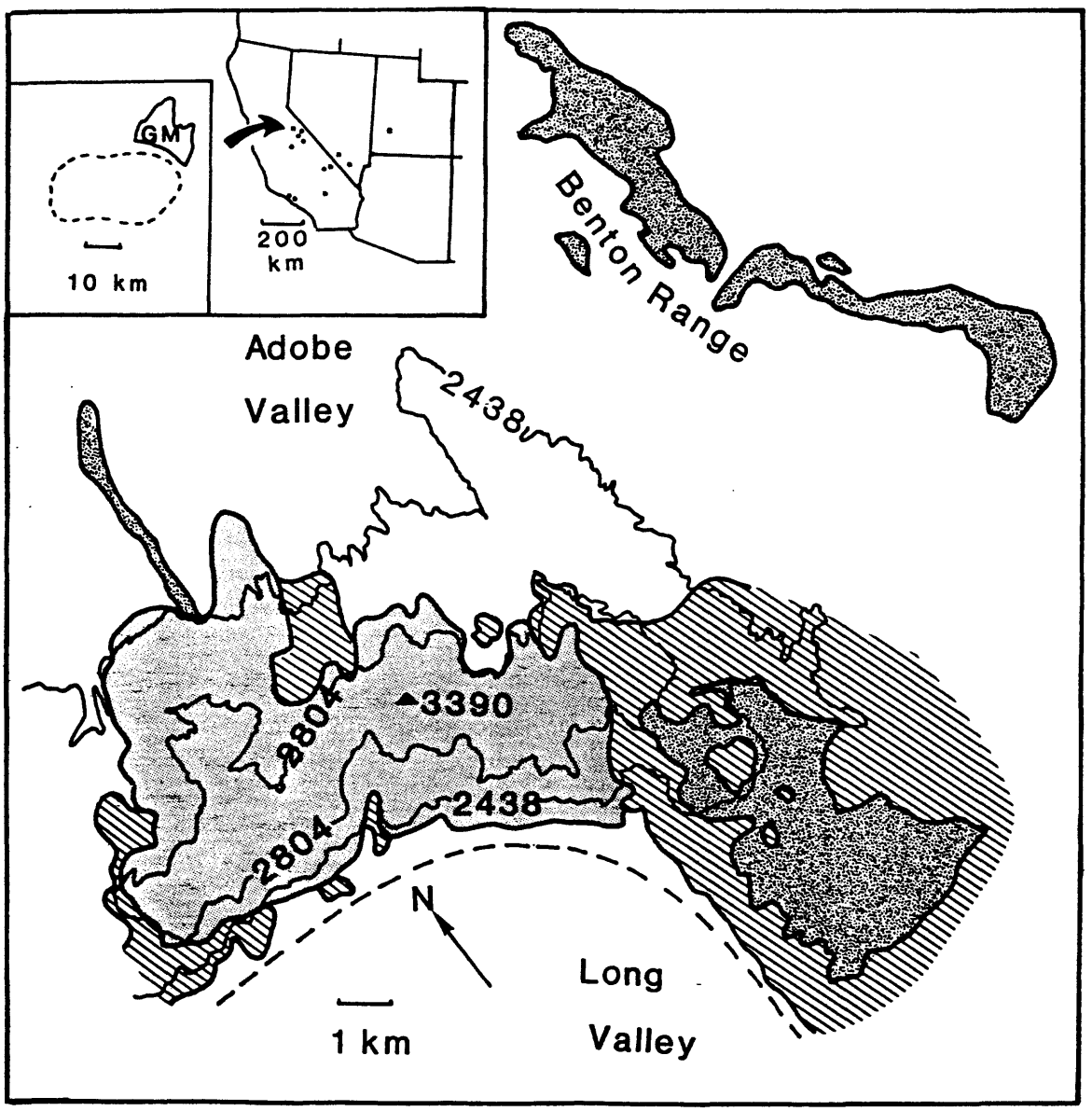
GM
10 km
200 km
Benton Range
Adobe Valley
2438
2804
3390
2438
2804
N
1 km
Long Valley

Figure 2

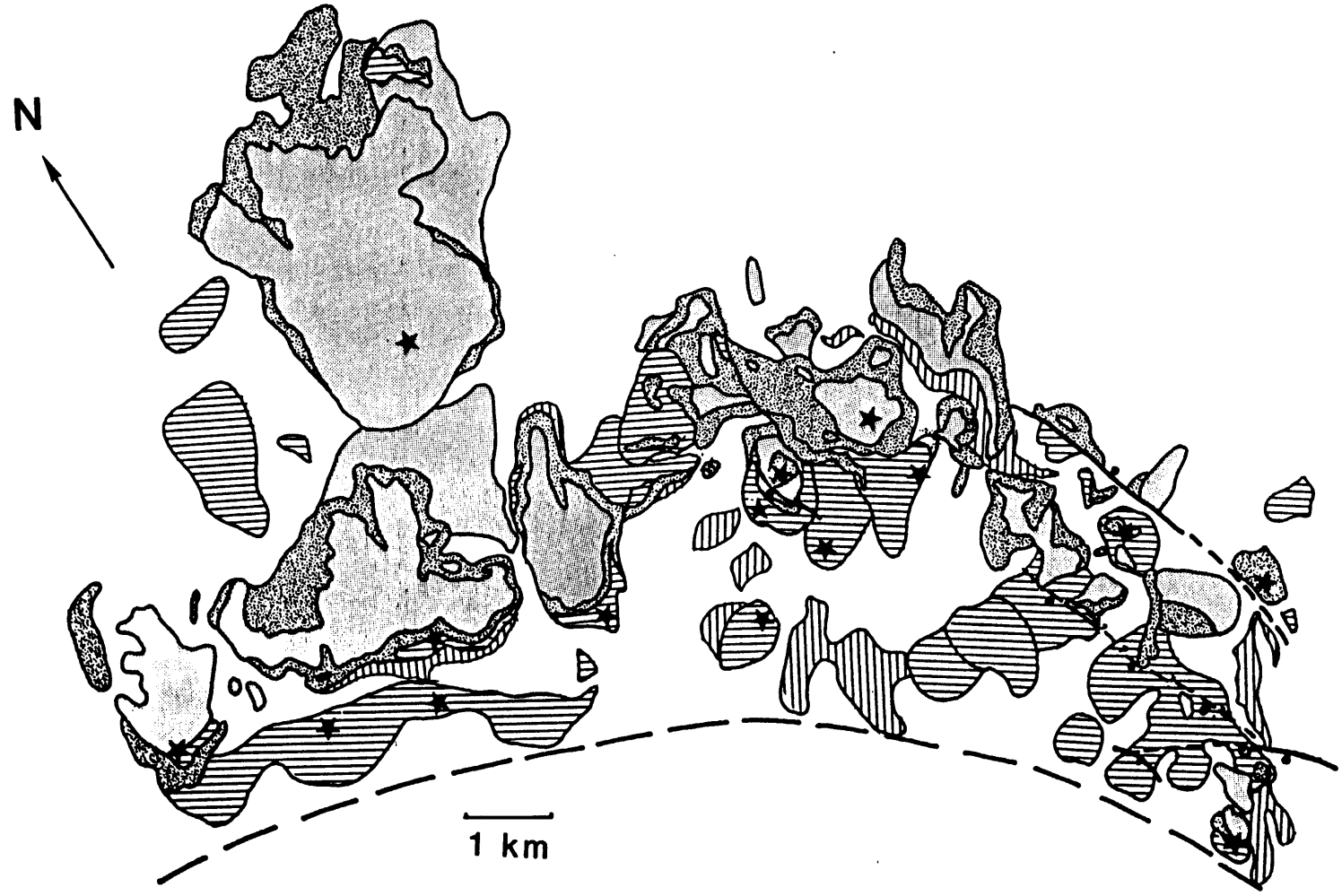

Figure 3

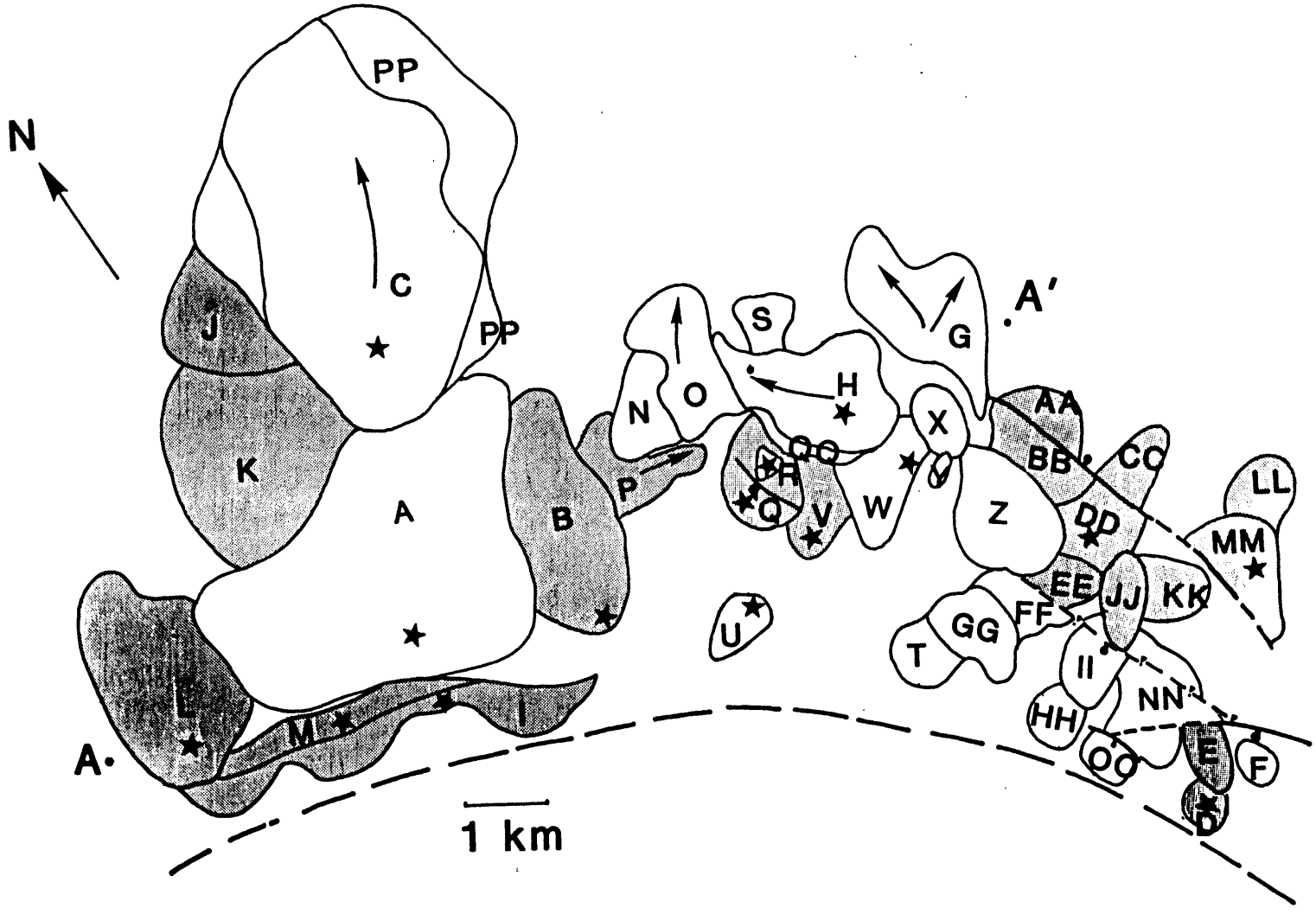
N
PP
C
J
PP
K
A
B
P
N
O
S
H
G
A'
X
AA
BB
CC
LL
MM
Q
R
QQ
V
W
Z
DD
EE
JJ
KK
FF
GG
T
U
II
NN
HH
OO
E
F
D
L
M
I
A
1 km

Figure 4

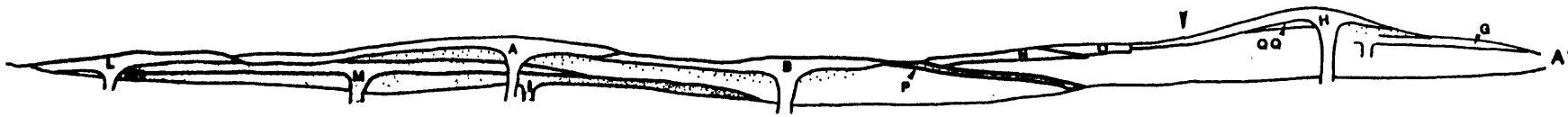

Figure 5

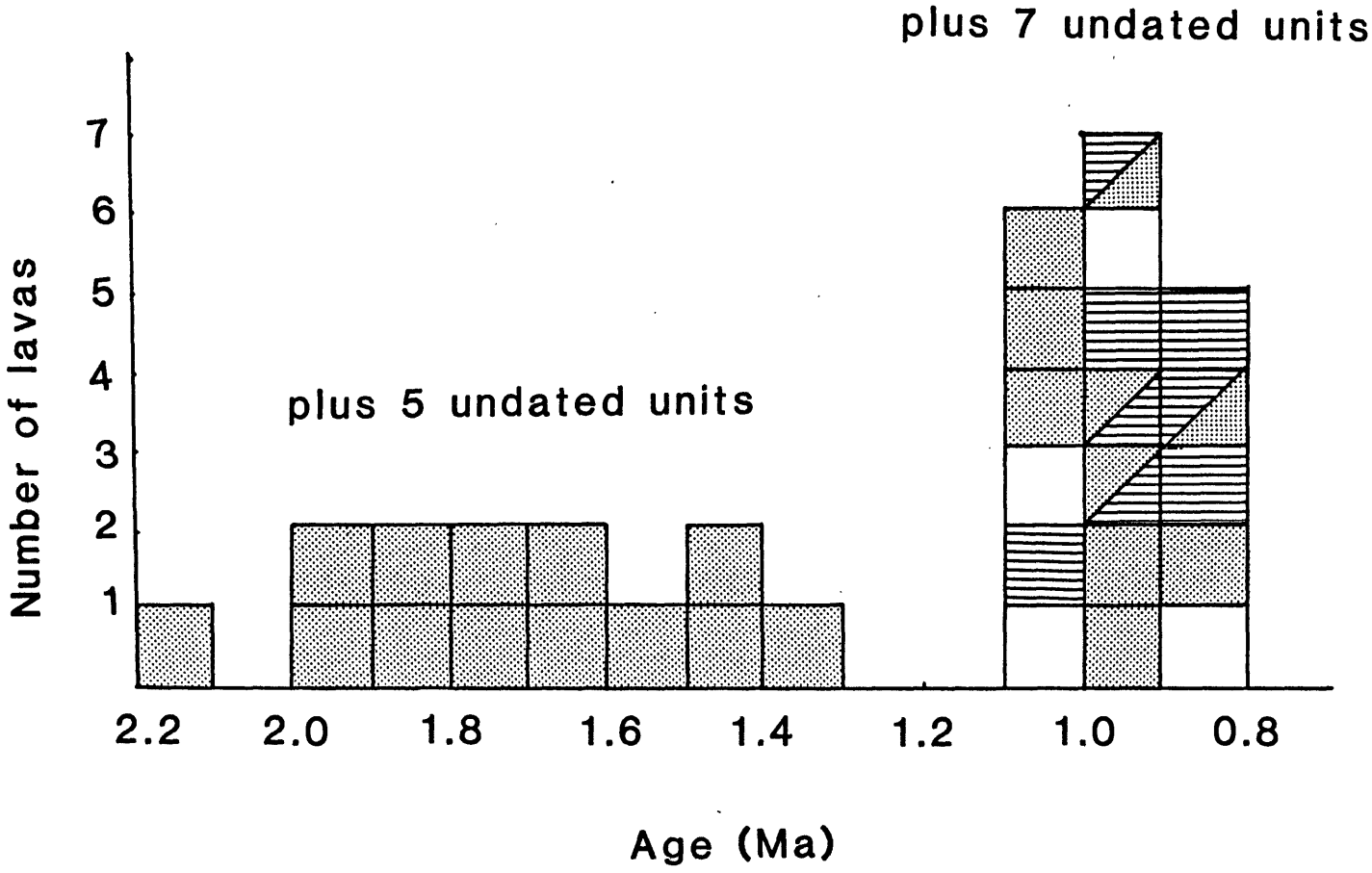
plus 7 undated units
plus 5 undated units
Number of lavas
7
6
5
4
3
2
1
2.2
2.0
1.8
1.6
1.4
1.2
1.0
0.8
Age (Ma)

Figure 6

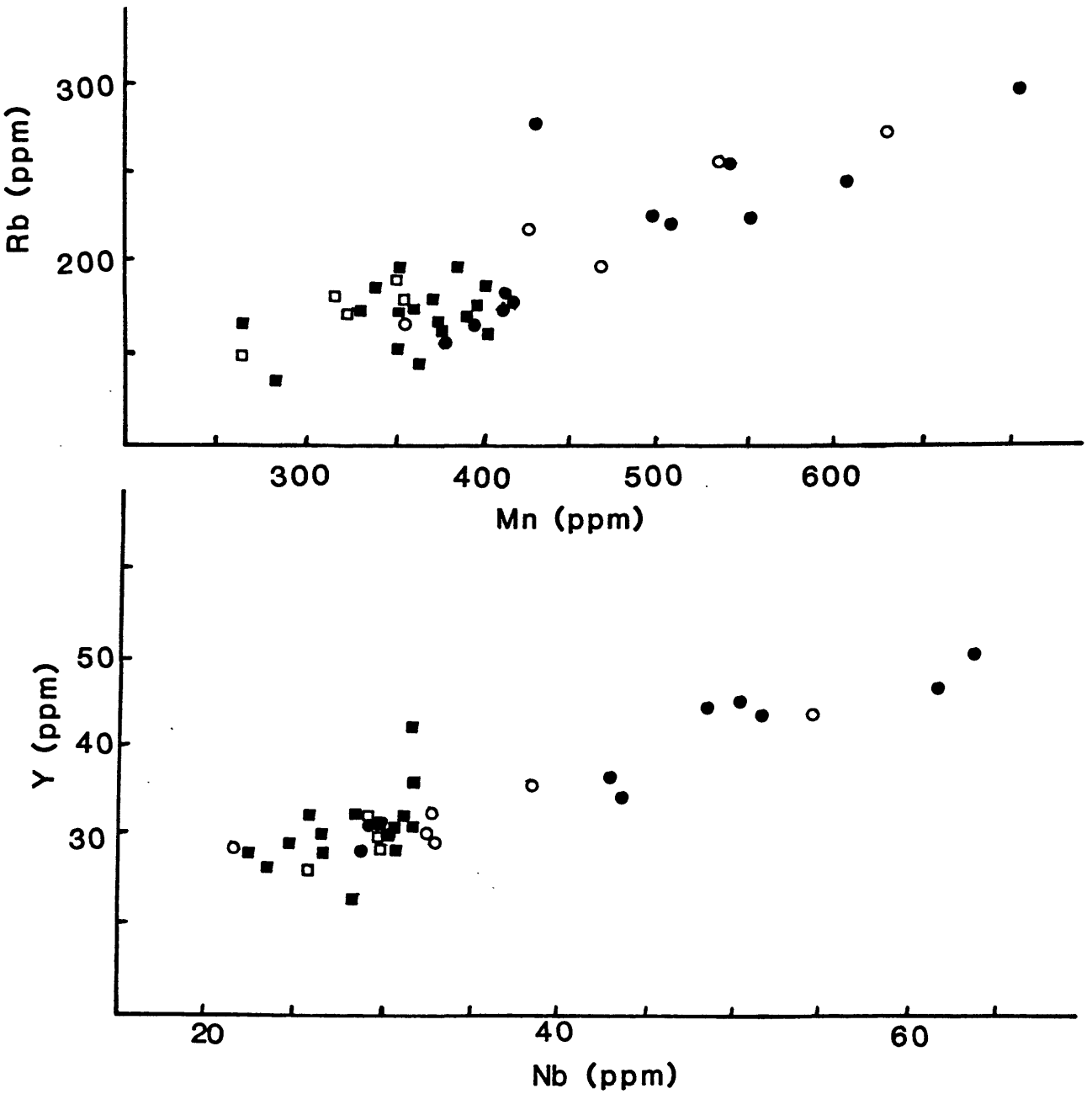

Figure 7

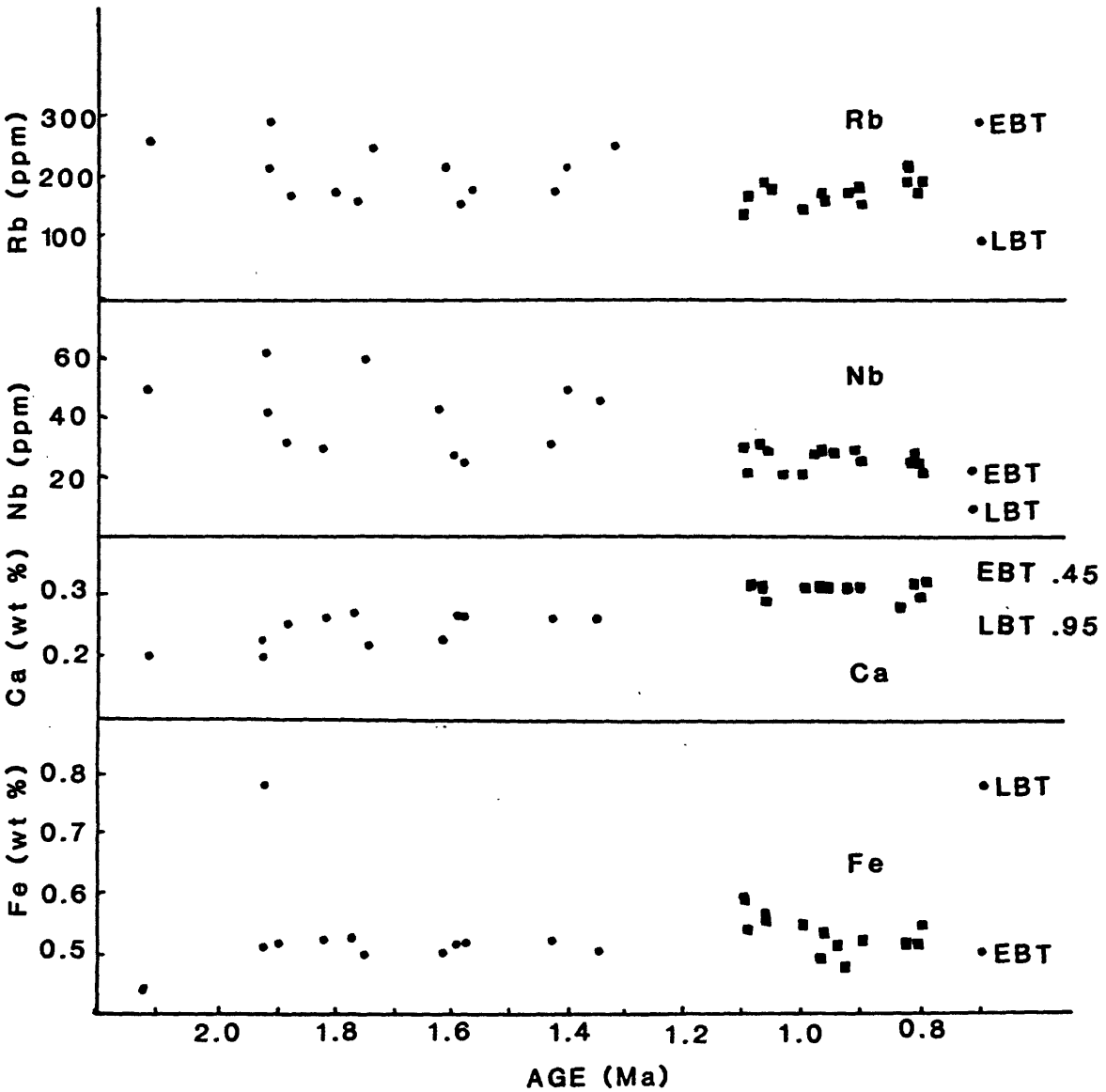
Rb (ppm)
300
200
100
Rb
•EBT
•LBT
Nb (ppm)
60
40
20
Nb
•EBT
•LBT
Ca (wt %)
0.3
0.2
EBT .45
LBT .95
Ca
Fe (wt %)
0.8
0.7
0.6
0.5
•LBT
Fe
•EBT
2.0
1.8
1.6
1.4
1.2
1.0
0.8
AGE (Ma)

Figure 8

Holocene eruptions at the Inyo Volcanic chain, California--Implications for possible eruptions in Long Valley Caldera

C. Dan Miller U.S. Geological Survey, Denver, Colorado 80225

ABSTRACT

The 11-km-long Inyo volcanic chain consists of 6 magmatic and more than 15 phreatic eruptive centers alined along a north-trending fracture. About 0.8 km^3 of rhyolitic magma erupted along the chain during at least three eruptive episodes. Pyroclastic deposits comprise about 40 percent of this volume. The earliest eruptive episode produced rhyolitic lava domes at Glass Creek and north of Deadman Creek. Although ages of the domes are poorly known, weathering characteristics suggest the dome north of Deadman Creek is more than several thousand years old. The second episode began with explosive eruptions of rhyolite at Wilson Butte about 1,350 ^{14}C yrs ago; these eruptions produced air-fall and pyroclastic-surge deposits near the vent and a 9-km long pyroclastic flow deposit. Subsequent emplacement of the Wilson Butte dome occurred prior to about 1,200 ^{14}C yrs ago. Rhyolite again erupted explosively during a third episode 600-500 yrs ago. Eruptions at South Deadman, Obsidian Flow, and Glass Creek vents produced lobes of pumiceous air fall that range in length from 20 to 190 km and cover areas of 100-9,000 km^2. Pumiceous pyroclastic flows from each vent covered areas of a few square kilometers to more than 15 km^2. Rhyolitic lava flows with volumes of about 0.1-0.2 km^3 erupted at the vents soon after explosive activity ended. Tephra erupted from the South Deadman and Glass Creek vents are overlain by phreatic deposits erupted at the nearby Inyo Craters about 550 ^{14}C yrs ago.

The chemical similarities, timing of eruptions, and alinement of magmatic and phreatic vents suggest that the third eruptive episode occurred when a vertical, tabular, silicic magma body was emplaced at a shallow depth. Other manifestations of this body include a north-trending graben and extensional fissures associated with some vents. A similar dikelike intrusion has recently been suggested to explain an increase in seismicity and deformation in the south moat of Long Valley Caldera. Events about 600-500 yrs ago at the Inyo chain provide a model for possible events during future eruptions in the south moat of the caldera.

INTRODUCTION

The Inyo volcanic chain consists of 6 magmatic and more than 15 phreatic eruptive centers alined along a north-trending 16-km-long fracture located east of the Sierra Nevada in central eastern California (Fig. 1). The Inyo vents extend from the south end of the Mono Craters (Fig. 1) into the northwest corner of the Long Valley Caldera (Fig. 2), a large elliptical depression formed by eruption of the Bishop Tuff about 700,000 yrs ago (Bailey et al., 1976). The Mono Craters are an arcuate chain of late Pleistocene and Holocene rhyolitic domes and lava flows that extends from the Inyo volcanic chain north about 17 km to the south shore of Mono Lake. During Holocene time, about 0.8 km^3 (dense-rock equivalent) of rhyolitic to rhyodacitic magma erupted along the Inyo chain in at least three eruptive episodes; pyroclastic deposits comprise about 40 percent of this volume. This paper describes the age, nature, and sequence of Holocene magmatic and phreatic eruptions at the Inyo volcanic chain and discusses the implications

of these data with regard to possible future eruptions in the south moat of Long Valley Caldera, where seismicity and deformation increased in 1980-83.

FIGURES 1 and 2 NEAR HERE

HOLOCENE ERUPTIONS

The location and alinement of vents in the Inyo volcanic chain is apparently due to repeated injection of magma into north-trending fractures at the base of the Sierra Nevada escarpment. The Inyo vents form an 11-km-long north-south line that coincides with a 16-km-long north-trending zone of faults and cracks (Fig. 2) resulting from east-west crustal extension. Many Inyo vents are within small grabens a few hundred meters wide; the chain as a whole is within a broad, shallow, poorly defined graben 2-3 km wide. North-trending fissures near several vents, and others west of Mammoth Lakes (Fig. 2), are tens to hundreds of meters long and vary in width from less than one to several meters wide. Many fissures are draped with thick pyroclastic debris in which elongate sags and sinkholes have developed. Field relations between deposits of the last eruptive episode and ground cracks suggest that crustal extension preceded and probably accompanied the rise of magma and resulting eruptions.

At least three episodes of Holocene eruptions have been identified at the Inyo volcanoes. Eruptions more than several thousand years ago produced rhyolite domes at Glass Creek and north of Deadman Creek. A second eruptive episode began about 1,350 ^{14}C yrs ago with pyroclastic eruptions and culminated prior to about 1,200 ^{14}C yrs ago with extrusion of a rhyolite dome at Wilson Butte. Most recently, between about 600 and 500 yrs ago, rhyolitic pyroclastics erupted at three vents, followed by phreatic explosions at

several locations along the Inyo chain; eruptive activity culminated in extrusion of rhyolite flows at three vents.

Early Eruptions

The earliest eruptions at the Inyo chain occurred when rhyolite domes were emplaced at two vents about 3 km apart. The dome at Glass Creek is about 700 m across, has an explosion crater at the top, and a volume of about 0.002 km^3; the dome north of Deadman Creek has a volume of about 0.04 km^3. No explosive magmatic activity has been correlated with these eruptions.

The ages of the domes are poorly known, but both domes are morphologically more subdued than 1,200- to 1,350-yr-old Wilson Butte, have thick mantles of younger tephras, and are thought to be at least several thousand years old. The dome north of Deadman Creek is overlain by tephra erupted from a vent in the Mono Craters chain that has been dated at 1,190±80 ^{14}C yrs (tephra 2: Wood, 1977). Comparison of obsidian-hydration data of Wood (1983) for the dome north of Deadman Creek with other volcanic deposits dated during this study suggests that this dome is about 6,000 yrs old.

Wilson Butte Eruptions

The Wilson Butte vent (Fig. 2) erupted rhyolite at the north end of the Inyo chain about 1,350-1,200 ^{14}C yrs ago. Initial explosive eruptions produced near-vent pyroclastic-fall and -surge deposits several meters thick and a thin widespread pyroclastic-flow deposit. The pyroclastic-flow deposit can be traced 9 km to the northeast and covers an area of at least 60 km^2. Assuming their average total thickness is 1 m and porosity is 35 percent, the pyroclastic-flow and near-vent deposits represent a combined magma volume of about 0.04 km^3. Charcoal samples collected from the pyroclastic-flow deposit

at two localities have radiocarbon ages of 1,380±70 (W-4598) and 1,330±50 (W-4600) yrs B.P. Wilson Butte, a rhyolite dome with a volume of about 0.05 km^3, was emplaced after the explosive activity. Wilson Butte and the Wilson Butte pyroclastic-flow deposit are overlain by the 1,190±80 ^{14}C-yr-old tephra 2 of Wood (1977). No weathering or erosion are apparent at the contact of the tephra and pyroclastic flow. The dome was thus erupted after about 1350 ^{14}C yrs ago and prior to 1,190±80 ^{14}C yrs ago. Wilson Butte lies within a broad young graben and is adjacent to at least one north-trending fissure (Fig. 2); these relations suggest that the Wilson Butte eruptions were associated with active east-west extension.

Most Recent Eruptions

Explosive eruptions of rhyolite, phreatic eruptions, and extrusion of rhyolite flows occurred along the Inyo chain about 600-500 yrs ago. Explosive magmatic eruptions at the South Deadman, Obsidian Flow, and Glass Creek vents (Fig. 2) produced thick blankets of near-vent pyroclastic-fall, -flow, and -surge deposits (Table 1). One or more lobes of air-fall tephra, deposited downwind from each vent, consist of varying proportions of juvenile pumice, crystals, glass, denser microvesicular rhyolite, and accidental lithic fragments. All explosive products from the most recent Inyo eruptions overlie the 1,190±80 ^{14}C-yr-old tephra 2 of Wood (1977).

TABLE 1 NEAR HERE

Explosive magmatic activity at these vents occurred during a short time interval and was followed closely by multiple phreatic explosions at sites along Glass Creek, south and west of Deer Mountain, and on the north and northeast flanks of Mammoth Mountain (Fig. 2). After explosive

magmatic and phreatic activity stopped, rhyolite flows were extruded at the South Deadman, Glass Creek, and Obsidian Flow vents.

South Deadman Eruptions

Eruptions of the most recent episode began at the South Deadman vent (Fig. 2) and deposited a lobe of rhyolitic tephra more than 20 km long toward the northeast (Fig. 3A). The tephra is more than 2 m thick near the vent, covers an area of more than 80 km^2, and assuming a porosity of 35 percent, represents a magma volume of about 0.01 km^3. Pumiceous pyroclastic-flow deposits immediately overlie the tephra deposit near the source (Fig. 3A). The pyroclastic-flow deposits are more than 10 m thick along Deadman Creek, where they consist of multiple flow units with interbedded surge deposits. The deposits extend 6 km to the northeast and several km to the west, cover an area of about 15 km^2, and represent a magma volume of about 0.05 km^3.

FIGURE 3 NEAR HERE

The second tephra lobe produced by the South Deadman vent trends south-southwest (Fig. 3B). This tephra is more than 4 m thick near the vent and extends more than 25 km to the south into the High Sierra. The minimum area covered by the deposit is 140 km^2, and the volume of magma represented is about 0.04 km^3. Lack of erosion between strata and results of dating suggest that the south-southwest lobe was emplaced soon after the northeast lobe.

Radiocarbon dates on charcoal collected from fragmental deposits erupted at the South Deadman vent during the two eruptive pulses range from <200 (W-4595) to 750±60 (W-4604) yrs B.P. Jeffrey Pine stumps rooted in pyroclastic flows of this episode have as many as 604 rings (David Yamaguchi, written commun., 1983), which indicates a minimum calendar age of A.D. 1380 for these eruptions. These tree-ring counts are thought to approximate the age of the

deposits, because their fine-grained matrix should have allowed rapid establishment of seedlings.

Obsidian-Flow Eruptions

Eruptions soon after those at South Deadman, at the Obsidian-Flow vent about 5 km to the north (Fig. 2), began with an explosive eruption that deposited a lobe of rhyolitic tephra to the northeast (Fig. 3C). The lobe can be traced more than 25 km, covers an area of more than 140 km^2, and represents a magma volume of about 0.02 km^3. Thin, small-volume pyroclastic-flow and -surge deposits overlie the tephra near the vent.

No radiocarbon dates have been obtained on these fragmental deposits. They overlie the north-northeast-trending tephra lobe from the South Deadman vent, and Jeffrey Pines growing on them have as many as 525 rings (David Yamaguchi, written commun., 1983).

Glass Creek Eruptions

The next vent to erupt, south of Glass Creek and about 1.5 km south of the Obsidian-Flow vent, produced a rhyolitic tephra that is more than 10 m thick near the vent (Fig. 3D). This deposit can be traced for more than 190 km to the south, covers an area of more than 9,000 km^2, and represents a magma volume of about 0.1 km^3 (Wood, 1977).

Poorly sorted pumiceous flowage deposits, at least one unit of which is incipiently welded, are exposed along Glass Creek. These deposits have an aggregate thickness of as much as 25 m near the source vent, and can be traced for several kilometers downvalley. Although they resemble deposits of pumiceous pyroclastic flows, these strata were probably generated from thick,

near-vent accumulations of Glass Creek tephra that avalanched down steep slopes west of the vent.

The Glass Creek tephra was first described by Wood (1977) who named it tephra 1; he determined its age to be 720±60 ^{14}C yrs B.P. and suggested that it was erupted from the South Deadman vent, based on its trace-element composition. Its distribution, and a detailed isopach map (fig. 3D) indicates that the tephra erupted from the Glass Creek vent, and it is here renamed the Glass Creek tephra, after its source; new ^{14}C dates obtained during this study suggest it is somewhat younger than thought by Wood.

The Glass Creek tephra overlies fragmental deposits erupted from both the South Deadman and Obsidian-Flow vents and killed a forest west of its source vent. A wood sample from the forest yields a date of 530±50 ^{14}C yrs B.P. (W-4603), and Jeffrey Pines growing on Glass Creek tephra have as many as 468 rings (David Yamaguchi, written commun., 1983). Thus, the calender age of the Glass Creek tephra is somewhat older than 468 yrs and may be several tens of years older, because the coarse, matrix-poor deposit at the site of the oldest dated tree would be expected to be colonized by seedlings only after a period of decades or longer.

Phreatic Eruptions

Soon after explosive magmatic activity ceased at the Inyo volcanoes, phreatic eruptions occurred along the north-south alinement of vents (Fig. 2). Three phreatic craters along Glass Creek, between the Glass Creek and Obsidian-Flow vents, formed in tephras erupted at nearby vents and thus postdate the youngest explosive Inyo magmatic activity; at least one crater predates extrusion of Obsidian Flow.

Following explosive magmatic activity at the South Deadman and Glass Creek vents, at least three phreatic eruptions occurred south of South Deadman Flow to form the Inyo craters; three additional phreatic craters that appear to be similar in age formed west of the Inyo craters (Fig. 2). The explosion craters lie within two small, complex grabens, one of which is alined north-south and lies directly on the trend of the magmatic vents (Fig. 2).

Deposits from the phreatic eruptions overlie tephras from South Deadman and Glass Creek vents. Radiocarbon dates on uncharred wood in phreatic debris from south Inyo crater suggest that at least one eruption occurred about 550±60 ^{14}C yrs ago (Wood, 1977). Huber and Rinehart (1967) noted that Jeffrey Pines and firs growing within the Inyo craters have as many as 400 rings.

Phreatic explosion craters on the north and northeast flank of Mammoth Mountain (Fig. 2) were recognized by Huber and Rinehart (1967). Debris from one of these was dated (Bailey and Koeppen, 1977; R. A. Bailey, written commun., 1983) at 500±200 ^{14}C yrs B.P. (W-3686).

Effusive Eruptions

After all explosive magmatic activity and all or most phreatic activity stopped, extensive rhyolite flows issued from the South Deadman, Glass Creek, and Obsidian Flow vents and covered areas of 1-2 km^2 with volumes of 0.1-0.2 km^3 (Table 1). No magmatic or phreatic tephra have been found on any of the rhyolite flows; all explosive activity along the chain had apparently ceased before eruption of any of the flows. This suggests that the entire eruptive episode occurred within a short time because effusive eruptions often begin soon after explosive activity stops.

No radiocarbon or closely limiting tree-ring dates have been obtained for the Inyo rhyolite flows. Previous attempts to date the flow rocks by K/Ar-

dating techniques (Dalrymple, 1968) have yielded ages that greatly exceed the radiocarbon ages of fragmental deposits that preceded eruption of the flows. Attempts to use paleomagmatic secular-variation techniques to date the flows are underway, but so far have yielded poor results because of post-cooling rotation of surface blocks of the flows.

Timing of the Most Recent Eruptive Episode

Several types of evidence suggest that the most recent eruptive episode occurred between about 600 and 500 yrs ago. Although radiocarbon dates for the episode range from <200 to 750±60 ^{14}C yrs B.P., several radiocarbon dates cluster between about 650 and 500 yrs B.P. Minimum ages derived from tree-ring counts range from about 600 yrs for the earliest eruption, to about 470 yrs for the youngest explosive magmatic activity. Extrusion of the three lava flows after all explosive activity had ceased suggests a short time interval for the entire eruptive episode. Finally, there is no evidence for erosion, or weathering between any of the strata deposited in this episode.

GEOMETRY OF FEEDER CONDUIT

Characteristics of the most recent eruptions suggest that events about 600-500 yrs ago resulted when a vertical dikelike body was emplaced into a zone of crustal extension. Evidence includes (1) alinement of vents, (2) "simultaneous" eruptions along a chain of vents, (3) chemical similarities of alined-vent magmas (Bailey et al., 1983), (4) paired zones of tensional cracks (Fink and Pollard, 1983), and (5) graben structures (Fink and Pollard, 1983).

Magmatic and phreatic vents active during the most recent episode form a north-south line 8-km long from Obsidian Flow south to the Inyo Craters; a 13-km-long line exists if phreatic vents on the northeast side of Mammoth

Mountain are included.

Radiocarbon and tree-ring dating, absence of tephra on rhyolite flows, and lack of weathering and erosion of successive deposits suggest that numerous vents along the chain were active during a "short" time interval, perhaps no more than a few years or a few decades.

Studies of the petrology and chemistry of the Inyo flows and domes by Bailey et al. (1983) suggest that magmas erupted during the last eruptive episode, and probably earlier episodes as well, came from a single chemically zoned magma chamber. They noted that rhyolite magmas erupted at the Obsidian Flow, Glass Creek, and South Deadman vents are chemically and petrographically heterogeneous; each flow typically includes a silicic, aphyric marginal facies and a more mafic, coarsely porphyritic core. From Obsidian Flow vent southward to the South Deadman flow, the proportion of the coarsely porphyritic facies increases. These data suggest that magma erupted during the last series of Inyo eruptions was supplied by a single elongate conduit system, and that two magmatic phases were supplied in different proportions within the dikelike feeder.

Paired zones of tensional cracks and fissures and graben structures, (Fig. 2), are similar to surface deformation related to dikelike feeder conduits and alined-vent eruptions elsewhere (e.g., Medicine Lake Highland, Fink and Pollard, 1983; South Sister, Scott, 1983).

Nearly "simultaneous" eruption of Inyo volcanic vents and their association with parallel-trending grabens and extensional features implies the existence of a dike or a set of subparallel dikes that acted as feeders for the last series of magmatic eruptions and as a heat source for associated phreatic explosions. Surface extensional cracks that continue south of the Inyo craters along the so-called "Earthquake Fault" (Fig. 2) suggest that

subsurface dike(s) extend south of the South Deadman vent to an area just west of the town of Mammoth Lakes; thus, the Inyo volcanoes may be underlain by a dikelike feeder system as long as 13 km.

IMPLICATIONS FOR CURRENT ACTIVITY IN LONG VALLEY CALDERA

Events about 600-500 yrs ago in the Inyo volcanic chain provide a model for possible future eruptions in the south moat of Long Valley Caldera. Ground-surface extension, uplift of a resurgent dome, and increased seismicity in Long Valley Caldera during 1980-83 (Ryall and Ryall, 1982; Miller et al., 1982; Miller and Newhall, 1983; Cockerham and Savage, 1983) have increased the concern about possible future eruptions in that area.

Cockerham and Savage (1983) recently interpreted the seismicity and ground-surface deformation southeast of Mammoth Lakes during 1983 as due to intrusion of a dike into the south ring fracture of the caldera. They proposed that magma may be intruding along a near-vertical plane that is 8.5 km long in a northwest-southeast direction and extends from the ground surface to a depth of 8 km. The geometry of a northeast-southwest extension across the area of earthquake hypocenters suggests (Cockerham and Savage, 1983) that a dike may have intruded to within 3 km of the surface.

If a dike is intruding under the south moat of Long Valley Caldera, events 600-500 yrs ago at the Inyo volcanoes provide insights into tectonic and eruptive events that might occur if a dike moves toward the surface. Past events at the Inyo chain suggest that dikelike conduits, such as the one postulated under the south moat, could produce extensive surface faulting and both explosive magmatic and phreatic eruptions closely spaced in time at many vents. The sequence of activities expected would be (1) surface deformation above a rising dike, (2) phreatic eruptions as a dike approaches the surface,

(3) a series of magmatic and phreatic eruptions at several to many points along the trend of a dike, and (4) extrusion of lava at magmatic vents.

The analogy between past volcanic events in the Inyo chain and recent changes in the south moat of Long Valley Caldera is discussed here mainly because, at both locations, injection of magma is postulated to take place into elongate zones undergoing crustal extension or deformation. It must be emphasized, however, that the size and nature of future eruption(s) in the Long Valley epicentral zone will depend on such factors as the nature of magma being injected, including its volume, composition, volatile content, and other physical characteristics. These are all unknown, and thus, a wide range of activity--eruptive and noneruptive--is possible within the epicentral area at Long Valley Caldera.

REFERENCES CITED

Bailey, R. A., Dalrymple, G. B., and Lamphere, M. A., 1976, Volcanism, structure, and geochronology of Long Valley Caldera, Mono County, California: Journal of Geophysical Research, v. 81, no. 5, p. 725-744.

Bailey, R. A., and Koeppen, 1977, Preliminary geologic map of Long Valley Caldera, Mono County, California: U.S. Geological Survey Open-File Map 77-468.

Bailey, R. A., MacDonald, R. A., and Thomas, J. E., 1983, The Inyo-Mono Craters: Products of an actively differentiating rhyolite magma chamber, eastern California [abs.]: EOS (American Geophysical Union), v. 64, no. 18, p. 336.

Cockerham, R. S., and Savage, J. C., 1983, Earthquake swarm in Long Valley, California, January 1983 [abs.]: EOS (American Geophysical Union), v. 64, no. 45, p. 890.

Dalrymple, G. B., 1967, Potassium-argon ages of recent rhyolites of the Mono and Inyo Craters, California: Earth and Planetary Science Letters, v. 3, p. 289-298.

Fink, J. H., and Pollard, D. D., 1983, Structural evidence for dikes beneath silicic domes, Medicine Lake Highland volcano, California: Geology, v. 11, no. 8, p. 458-461.

Huber, N. K., and Rinehart, C. D., 1967, Cenozoic volcanic rocks of the Devils Postpile quadrangle, eastern Sierra Nevada, California: U.S. Geological Survey Professional Paper 554-D, p. D1-D21.

Miller, C. D., Mullineaux, D. R., Crandell, D. R., and Bailey, R. A., 1982, Potential hazards from future volcanic eruptions in the Long Valley-Mono Lake area, east-central California and southwest Nevada--A preliminary assessment: U.S. Geological Survey Circular 877, 10 p.

Miller, C. D., and Newhall, C. G., 1983, Volcanic-hazards implications of recent seismicity, deformation, and hydrothermal activity, Long Valley Caldera, California, USA [abs.]: 1983 International Union of Geodesy and Geophysics, Program and Abstracts, p. 363.

Ryall, F., and Ryall, A., 1982, Propagation of effects and seismicity associated with magma in the Long Valley Caldera, eastern California: Earthquake Notes, v. 53, no. 1, p. 46-47.

Savage, J. C., and Cockerham, R. S., in press, Earthquake swarm in Long Valley caldera, California, January 1983: Evidence for dike intrusion: Journal of Geophysical Research.

Scott, W. E., 1983, Character and age of Holocene rhyodacite eruptions at South Sister volcano, Oregon: EOS (American Geophysical Union), v. 64, no. 45, p. 899-900.

Wood, S. H., 1977, Distribution, correlation, and radiocarbon dating of late Holocene tephra, Mono and Inyo Craters, eastern California: Geological Society of America Bulletin, v. 88, p. 89-95.

_____in press, Chronology of late Pleistocene volcanics, Long Valley and Mono Basin geothermal areas, eastern California: U.S. Geological Survey Open-File Report, 55 p.

ACKNOWLEDGMENTS

Reviewed by P. W. Lipman, R. P. Hoblitt, and M. K. Reagan who made valuable comments that led to improvement of the paper. I thank M. K. Reagan, W. E. Scott, and R. P. Hoblitt for assistance and valuable discussions in the field.

LIST OF ILLUSTRATIONS

LIST OF TABLES

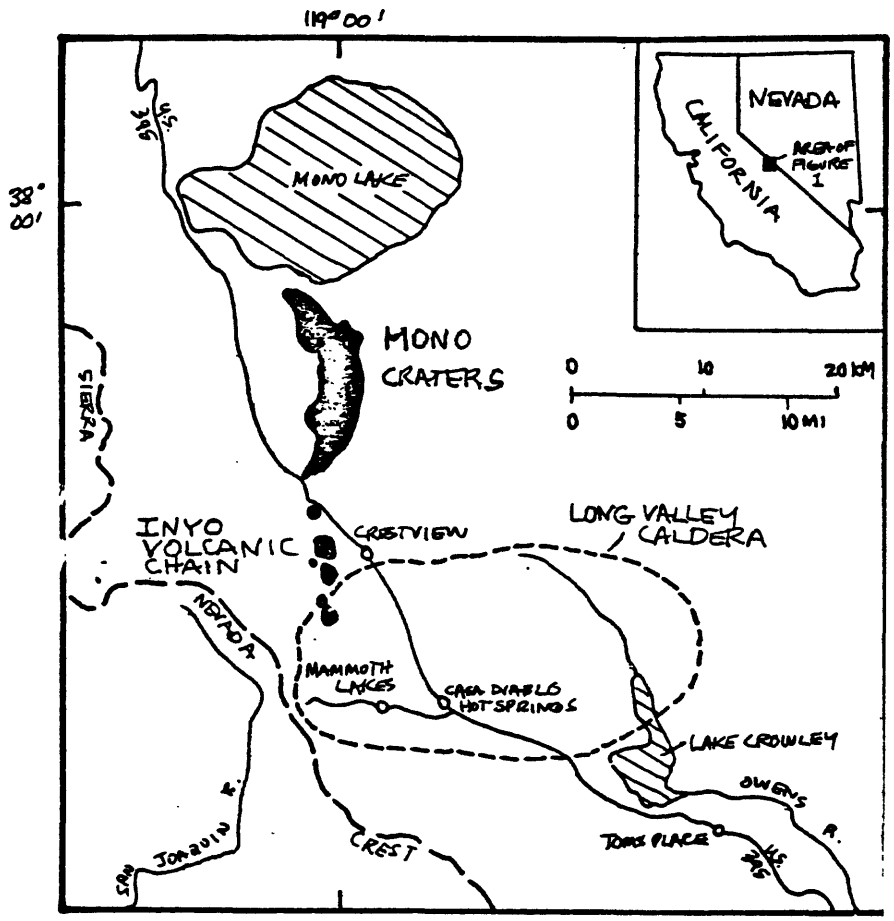
119° 00'
38° 00'
395
MONO LAKE
MONO CRATERS
SIERRA
INYO VOLCANIC CHAIN
CRESTVIEW
LONG VALLEY CALDERA
NORTH
MAMMOTH LAKES
CASA DIABLO HOT SPRINGS
LAKE CROWLEY
OWENS R.
JOAQUIN R.
SAN
CREST
TOMS PLACE
US 395
NEVADA
CALIFORNIA
AREA OF FIGURE 1
0 10 20 KM
0 5 10 MI

FIGURE 1.

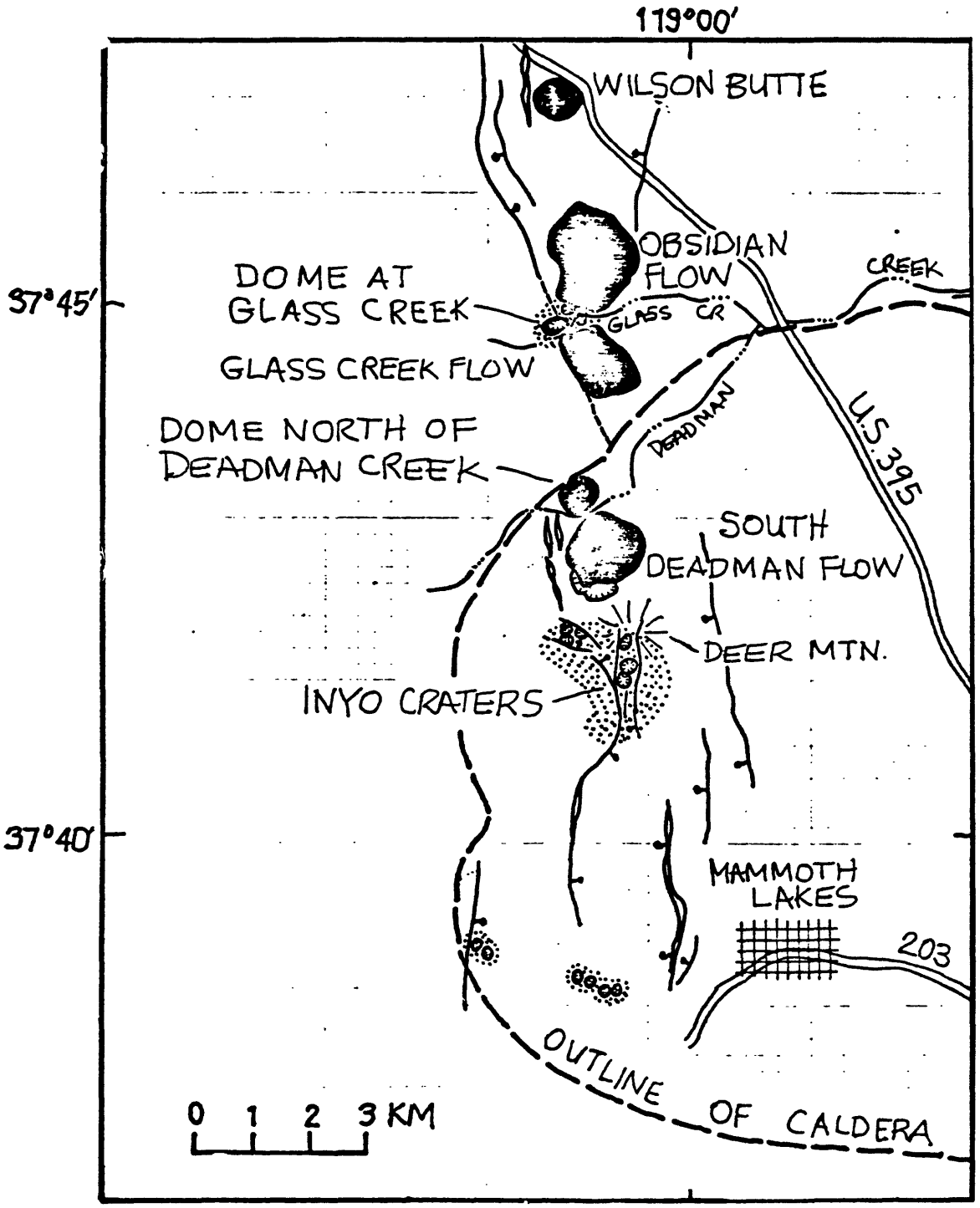
119°00'
WILSON BUTTE
OBSIDIAN FLOW
CREEK
37°45'
DOME AT GLASS CREEK
GLASS CR
GLASS CREEK FLOW
DEADMAN
U.S. 395
DOME NORTH OF DEADMAN CREEK
SOUTH DEADMAN FLOW
DEER MTN.
INYO CRATERS
37°40'
MAMMOTH LAKES
203
OUTLINE OF CALDERA
0 1 2 3 KM

FIGURE 2.

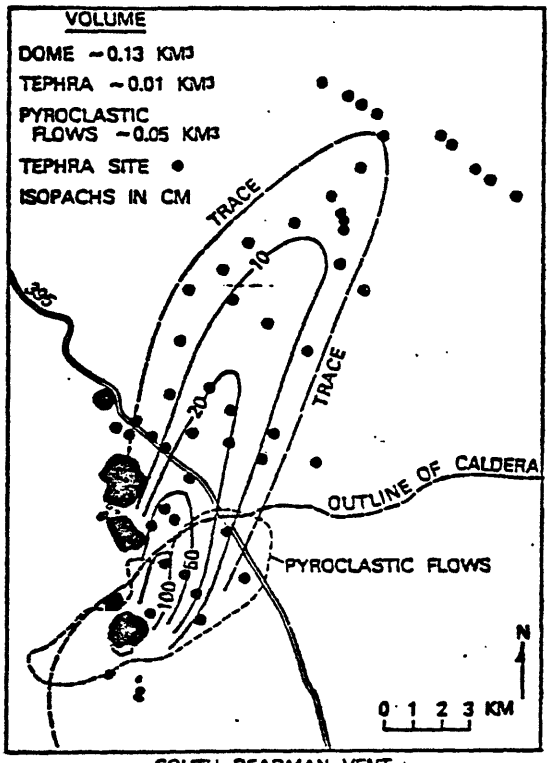

SOUTH DEADMAN VENT

(A)

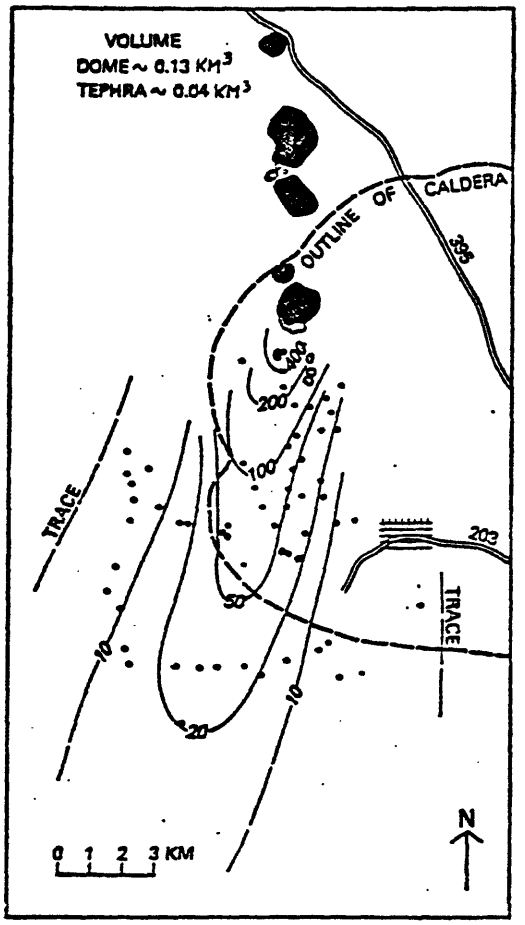

SOUTH DEADMAN VENT

(B)

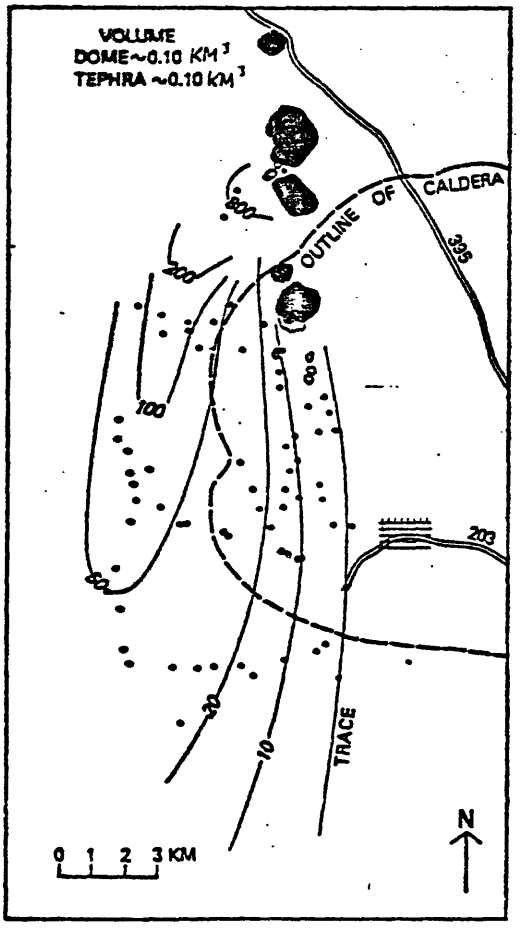

GLASS CREEK VENT

(D)

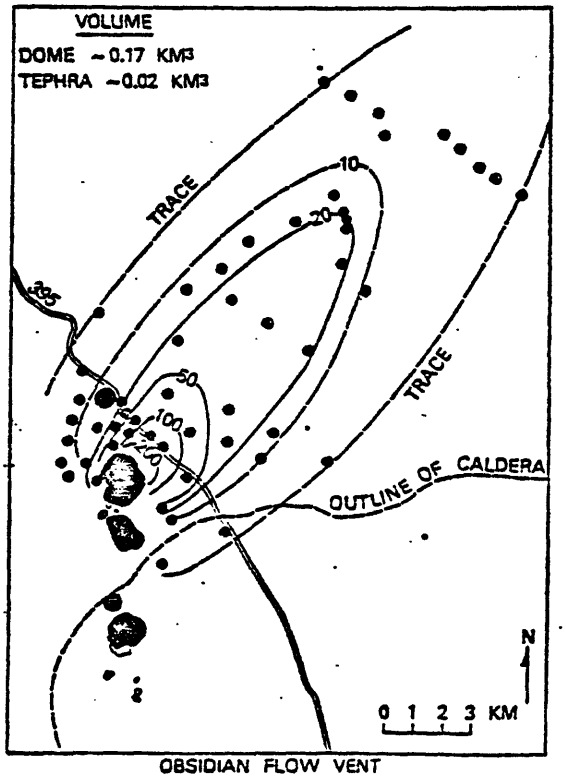

OBSIDIAN FLOW VENT

(C)

FIGURE 3

TABLE 1. CHARACTERISTICS OF DEPOSITS FROM ERUPTIONS ABOUT 600-500 YRS AGO AT THE GLASS CREEK, OBSIDIAN FLOW, AND SOUTH DEADMAN VENTS

Vent	Tephra			Pyroclastic flows			Domes	
	Length (km)	Area (km2)	Volume (km3)	Length (km)	Area (km2)	Volume (km3)	Area (km2)	Volume (km3)
Glass Creek vent	>190	>9,000	0.10	--	---	----	1.0	0.10
Obsidian Flow vent	>25	>140	0.02	<2	---	----	1.8	0.17
South Deadman vent								
SSW lobe	>25	>140	0.04					
NE lobe	>20	>80	0.01	6	>15	0.05	1.1	0.13

MOST RECENT ERUPTIONS OF THE MONO CRATERS, EASTERN CENTRAL CALIFORNIA

by

Kerry Sieh

Division of Geological & Planetary Sciences
California Institute of Technology
Pasadena, California 91125

ABSTRACT

The Mono Craters in eastern central California constitute an arcuate 17-km-long edifice of late Pleistocene and Holocene rhyolitic domes and flows. Radiocarbon analyses indicate that the latest subplinian to plinian eruptive episodes within this chain of volcanoes occurred in about 705 + 55 A.D. and 1395 + 50 A.D. Stratigraphic and sedimentologic studies reveal that the products of the most recent episode emanated from several aligned vents along the crest of the northernmost 5 km of the chain. The oldest products of this eruption are several subplinian tephras. These are overlain locally by pyroclastic flow and surge deposits. Tephra rings, domes and coulees were constructed near the vents during the waning stages of the eruption.

The eruption was preceded by formation of a 1-2 km-long graben along the range crest. Isopach and other data demonstrate that the basal tephra layer was erupted from aligned vents within this graben. This white pumiceous layer has a maximum measured thickness of 56 cm and a dispersal index >200 km^2. The dispersal axis trends NNE from the vents and across Mono Lake. Stratigraphy of the tephra near the lake margin suggest that lake level was about 29 feet higher at the time of the eruption than its present (1983) elevation of 6377 feet. Subsequent pyroclastic fall deposits are similar to the basal layer in extent and thickness and have dispersal axes trending NNW to NE. At least one of the these beds originated from a vent about 1 km north of the initial vents and graben. Pyroclastic flow deposits rest upon the fall deposits at distances up to about 4 km from the vents. One blocky pyroclastic flow emanated from the site of Panum Dome and flowed NW into Rush Creek and Mono Lake, causing spectacular liquefaction and decollement within the substrate. The final stages of the eruption involved relatively passive but complex construction of several tephra rings and the extrusion of Panum dome, Cratered dome, North Coulee, and two other unnamed intervening domes.

INTRODUCTION

The Mono and Inyo craters and the volcanoes of Mono Lake (all shown in black in Fig. 1) constitute a chain of late Quaternary silicic volcanic edifices that extends 40 km northward from the Long Valley Caldera to Mono Lake, along the eastern frontal faults of the Sierra Nevada (Russell, 1889, Putnam, 1949; Mayo et al., 1936; Kistler, 1966; Huber and Rinehart, 1967; Bailey et al., 1976). Most of all of these volcanic domes, flows and craters appear to be less than about 40,000 years old (LaJoie, 1968; Wood, 1977, as modified by Wood and Brooks, 1979). These and associated pyroclastic flow and fall deposits that blanket the region represent more than two dozen major silicic eruptive episodes. Hence, the chain is one of the most active volcanic sources in the western U.S.

I am interested in helping to characterize that hazard, and have begun by studying the nature and distribution of the products of the most recent eruptive episode of the Mono Craters.

The abutting and overlapping domes, flows and craters of the Mono Craters (Fig. 2) constitute the largest part of the volcanic chain and appear to plug the vents of most of the latest Quaternary (<40,000 years B.P.) eruptions (LaJoie, 1968). All of these rocks are high-silica rhyolites with markedly similar bulk chemistry and trace-element chemistry (Carmichael, 1967, Table 5; LaJoie, 1968, Fig. 23, Table 4; Loney, 1968). Texturally, the rocks are much more variable. Those domes, flows and pyroclastic deposits erupted prior to about 2,000 years ago are porphyritic glassy rhyolites, whereas younger erupted products are aphyric or very sparsely porphyritic.

Most of the aphyric ryolitic domes and flows (that is, Panum Dome, Cratered Dome, Upper Dome, North Coulee and South Coulee) are not mantled by

pyroclastic flow or fall deposits. The other domes and flows are thickly mantled with pyroclastic debris.

In the region surrounding these unmantled edifices, the youngest volcanic deposit consists of the pyroclastic fall and flow beds illustrated and discussed below. This series of beds rests upon various older beds of lacustrine, marsh, aeolian and volcanic origin. In most cases, the older, underlying units exhibit bioturbation and higher organic content in their upper portions (see for example, the bed indicated by an arrow in the photo of site "BB" Fig. 3). This indicates that the pyroclastic deposits blanketed a ground surface which had undergone mild pedogenic processes and bioturbation between the two most recent eruptions.

The basal part of the youngest pyroclastic blanket consists of several well-sorted, widespread, distinctive beds which are illustrated in the seven photographs of Figure 3. The basal beds are composed of white lineated pumice (W), light gray non-vitreous glass (G), and black obsidian (B), in percentages that differ from bed-to-bed.

The basal bed (1) at all localities is about 80 to 95% white lineated pumice (W). In all exposures, the bed is normally graded in its upper portion. This indicates a gradual diminishing of the energy of this initial phase of the eruption. At sites where the bed is very thick (for example, see photo of site "BB" Fig. 3), the lower part of the bed is rich in gray non-vitreous glassy clasts and accessory and accidental clasts that are commonly much larger than the white pumice clasts. This suggests that the initially erupted juvenile material (W) entrained materials from the walls of the volcanic conduit.

Figures 4a and 4b show the distribution and thickness of bed "1" in the area. Figure 4b is a blow-up of the near-source portion of 4a. Sites at which

data were collected are shown as black dots. Those localities illustrated by the photos of Fig. 3 are also labelled. Bed "1" is the most broadly distributed of the products of this latest eruption. It covers more than 500 square km and its dispersal index is at least 200 km^2, which puts it in the subplinian or plinian category of Walker. The thickest (and coarsest) portions of bed "1" are near North Coulee; this indicates a source or sources under and immediately northwest of the southwest portion of North Coulee. The next bed in the series is labelled bed "2" and is composed of W, G and B clasts typically in the ratio of about 4:3:3. The black obsidian clasts (B) are concentrated in the lower 40% of the bed (for example, see the photos of sites "AX" and "Z" Fig. 3). The NNW trend of the dispersal axis (Figs. 5a and 5b) indicates that the plume from which the pyroclasts of this bed fell was blown NNW, over Mono Lake. The thickest and coarsest part of this bed is immediately NW of Upper Dome. This indicates that the pyroclasts composing this bed were ejected from a vent under Upper Dome, not from the same vent or vents of bed "1".

The third eruptive pulse of the latest eruption is represented by bed "3" (Fig. 3). It is also composed of nearly equal amounts of W, G, and B pyroclasts. Concentrations of W occur at the base of the bed at near-source sites. The dispersal axis of bed "3" trends NNW near the source (Figs. 6a and 6b) but bends to the NNE about 10 km from the vents. This probably indicates that low level winds were blowing NNW at the time of the eruption and higher level winds are blowing NNE.

The source of bed "3" is not as well-defined as for "1" and "2", but at least one vent had to lie to the south of Upper Dome, judging from the trend of the isopach contours southwest of Upper Dome.

Younger pyroclastic fall beds composed principally of W, G, and B clasts overlie beds 1, 2 and 3, but these are not yet well correlated between sites. In general, however, it is clear that the dispersal axes of most of these beds trend northerly to easterly and originated from vents in the vicinity of Upper Dome and North Coulee.

Following the initial outbursts that resulted in deposition of the W, G and B-rich pyroclastic fall deposits, a series of pyroclastic flows emanated from vents in the vicinity of Upper Dome and North Coulee. We have been able to map only three of the several individual flows (A, B, and C in Fig. 7). Figure 7 gives a crude picture of distribution of these and the remaining undistributed pyroclastic flow deposits. Fig. 8 is a photo of site "X", 1 km southeast of Panum Dome, where a flow deposit overlies the airfall deposits. This flow probably emanated from the Panum vent, but is compositionally quite similar to flow deposits that emanated from Upper Dome and North Dome.

The region labelled "A" on Fig. 7 encompassed a geomorphologically well-defined flow deposit that originated from vents now buried by North Coulee. The deposit extends about 4-1/2 km westward from its source. It is characterized by an abrupt, lobate flow front and distinct ridges and troughs aligned parallel to the direction of the flow.

The region labelled "D" includes a broad area extending up to 9 km from the North Coulee vents. Most excavated exposures within this region reveal one or more massive poorly sorted pale pink to pale orange pumiceous beds ranging in thickness from 70 mm at distal sites to more than 3 m at a site immediately south of North Coulee and 1.5 m at a site northeast of Upper Dome. In the region between North Coulee, Upper Dome and Cratered Dome and the 300-year-old shoreline of Mono Lake, these deposits exhibit ridges and swales that trend perpendicularly to topographic contour. The extent of the

flow deposits north of the 300-year shoreline of the lake is unknown.

In the vicinity of Panum Dome, this unit consists of undifferentiated flow deposits from the vent underlying Panum Dome. These and the flows labelled "C" and "B" post-date the flows that emanated from the region of North Coulee and Upper Dome and are discussed below.

Vents for the various erupted products of the latest eruption of the Mono Craters are shown in Figure 9. Dots outline the several domes and coulees. Vents labelled "1" are based upon geomorphologic interpretation of the surface of North Coulee. Vents 2 and 4 are currently exposed craters. Vent 5 is based upon geomorphologic interpretation of the surface of Upper Dome and the existence of a small satellite dome and a tephra ring on its south flank. Vent 6 is Cratered Dome and vent 7 is the axial fissure through which Panum Dome was extruded.

The heavy hachured lines are normal faults with tens of meters of slip. These are cut by craters 2, 4 and 5 and appear to be draped by the basal pyroclastic fall deposits. These faults probably indicate that a 1 to 2 km-long "keystone" dropped down over the rising magma body prior to its initial eruption.

Exposures in the vicinity of Panum Dome are particularly good, due to quarrying of the Pumice Pit Dome and erosion by Rush Creek. Hence, the sequence of events has been studied more completely there than elsewhere. Figure 10 is a generalized, composite columnar section which displays the pyroclastic products emanating from the Panum vent in about 1400 A.D.

The basal airfall deposits of the 1400 A.D. eruption that emanated from vents near Upper Dome and North Coulee underlie all of the Panum deposits. There exists no evidence of a bioturbated or organic-accumulation layer between these airfall deposits and the deposits from Panum. Thus, the opening

of the Panum vent must have followed the airfall deposition by no more than a few years or decades.

Within a half-kilometer radius of Panum, a "throat clearing breccia" overlies the airfall tephra and ranges up to several meters in thickness. Overlying the breccia near the vent is a white to pale pink pumiceous pyroclastic flow bed of quite variable thickness. In excavations 1.1 and 1.7 km southwest of Panum, this pebbly, cobbly bed forms 500-mm-high pebbly dunes aligned northwest-southeast. On figure 11, the light lines in the quadrant southwest of Panum represent the crests of those dunes apparent on aerial photographs. In Figure 7, the dune field is labelled "B". Although white, pumiceous pyroclastic flow deposits are present in excavations in all quadrants from Panum, for some reason dunes are apparent only in the southwestern quadrant. Amplitude of the dunes ranges up to about 1 m and wavelength varies from about 10 to about 100 m. Slope angles of 20-25° are common. The dunes appear to be concentric about a point about 1000 m south of the center of Panum Dome, but the Panum vent, beneath Panum Dome , is the only plausible source for the dunes, because Pumice Pit Dome is blanketed by the basal airfall beds, throat-clearing breccia and the flow deposit. The pyroclasts of the dune bed must have been "bed load" at the base of a very hot radially expanding, southwesterly moving cloud.

Charred twigs of chapparal are common within the dune bed and yield a reservoir-corrected ^{14}C age of 530 ± 60 years B.P. (± 2σ). This is indistinguishable from an age of 550 ± 80 years B.P. on charred twigs within and just below the basal airfall tephra at another locality and an age of 580 ± 60 years b.p. on charred twigs within a pyroclastic flow in Rush Creek,

northwest of Panum. The averaged and dendrochronologically corrected age of these samples is 555 ± 50 years B.P. (or 1395 ± 50 A.D.).

Excavations within 1-1/2 km of the Panum vent expose cross-laminated silty beds overlying the white pyroclastic flow bed. These pyroclastic surge beds are about a meter thick and display several sets of planar- and cross-laminated beds in the Pumice Pit Dome Quarry (Fig. 12). Ripples that climb away from the source are dominant and erosional contacts are rare. Bomb-sags are common at several horizons. In Fig. 12 a local airfall bed and coarse cross-bedded layers overlie the principal surge deposit.

In the quadrant northwest of Panum a very coarse block breccia (labelled "C" in Fig. 7) overlies the surge and flow beds described above. At site "t" (Fig. 7), it is more than 6-1/2 m thick. Angular light-colored aphyric blocks up to several meters in diameter are common. These and smaller blocks show abundant white percussion marks that resulted from collisions with other blocks as the breccia was being emplaced. About 10% of the blocks are black, banded obsidian and pumice. Breadcrust texture is common and numerous light-colored clasts are pressed into the surface of the black obsidian and pumice. Apparently the light-colored clasts were cool and brittle when the breccia was emplaced, but the black clasts were hot and ductile. The breccia may well represent a collapsed dome.

In Figure 7, the block breccia is shown in a paler pattern where it underlies younger lacustrine deposits of Mono Lake. Fluvial deposits of Rush Creek that post-date the emplacement of the breccia are labelled "E" in Fig. 7. In the walls of Rush Creek Gorge, one can see spectacular evidence that sudden emplacement of the breccia resulted in liquefaction of and decollement within the lacustrine substrate and basal airfall beds onto which it flowed. Space, however, does not allow illustration of this chaotic folded and faulted assemblage.

Panum Dome, itself, and its associated tephra ring are very late and relatively passively erupted products of the latest eruption of the Mono Craters. The tephra ring, which rises as much as 60 m above the surrounding plain, rests upon the latest pyroclastic flow deposits that emanated from the Panum vent. Panum Dome is composed of four structurally and texturally distinct domes, the largest and youngest of which is called North Dome (Fig. 13). It consists of a light gray banded rhyolite surrounded by a collar of breadcrusted light gray pumiceous rhyolite and bisected by a north-south fissure. A slightly older and much smaller feature, South Dome, lies south of and is intruded by North Dome. This dome is cored by banded rhyolite and has a 10 m thick carapace of concentrically foliated pumice topped by a discontinuous shell of black structureless obsidian.

Southwest and east domes are remnants of domes older than South and North Dome. East Dome rocks bear the closest resemblance to rocks of the block breccia.

The latest eruption of the Mono Craters appears to have resulted from the intrusion of a rhyolite dike along at least a 6-km length of the chain. Figure 14 depicts an eruptive sequence consistent with the data outlined above.

Bailey, R., Dalrymple, G., and Lanphere, M. (1976) Volcanism, structure, and geochronology of Long Valley caldera, Mono County, California: J. Geophys. Res., 81, 725-744.

Carmichael, I. (1967) The Iron-Titanium oxides of salic volcanic rocks and their associated ferromagnesian silicates: Contr. Mineral. and Petrol., 14, 36-64.

Huber, N., and Rinehart, C. (1967) Cenozoic volcanic rocks of the Devil's Postpile quadrangle, eastern Sierra Nevada, California: U.S. Geol. Survey Prof. Paper 554-D, 21 p.

Kistler, R. (1966) Structure and metamorphism in the Mono Craters quadrangle, Sierra Nevada, California: U.S. Geol. Survey Bull. 1221-E, 53 p.

Lajoie, K. (1968) Late Quaternary stratigraphy and geologic history of Mono Basin, eastern California: Ph.D. thesis, Univ. Cal., Berkeley, 271 p.

Loney, R. (1968) Flow structure and composition and the southern Coulee, Mono Craters, California — a pumiceous rhyolite flow: Geol. Soc. America Memoir,116, 415-440.

Mayo, E., Conant, L., Chelikowsky, J. (1936) Southern extension of the Mono Craters, California: Amer. Jour. Sci., ser. 5, 32, 89-91.

Putnam, W. (1949) Quaternary geology of the June Lake District, California: Geol. Soc. America Bull., 60, 1281-1302.

Russell, I.C. (1889) Quaternary history at Mono Valley, California: U.S. Geol. Survey, Eighth Annual Report, 303-355.

Walker, G.P.L. (1973) Explosive volcanic eruptions -- a new classification scheme, Geologische Rundschau, 62, 431-446.

Wood, S. (1977) Chronology of late Pleistocene and Holocene and volcanics, Long Valley and Mono Basin geothermal areas, eastern California: Final Technical Report to U.S. Geol. Survey, Geothermal Research, Extramural Program, Contract No. 14-08-0001-15166.

Wood, S. and Brooks, R. (1979) Panum Crater dated 640 ± 40 years B.P., Mono Craters, California: in Abstracts with Programs, Geol. Soc. America, 11, no. 7, 543.

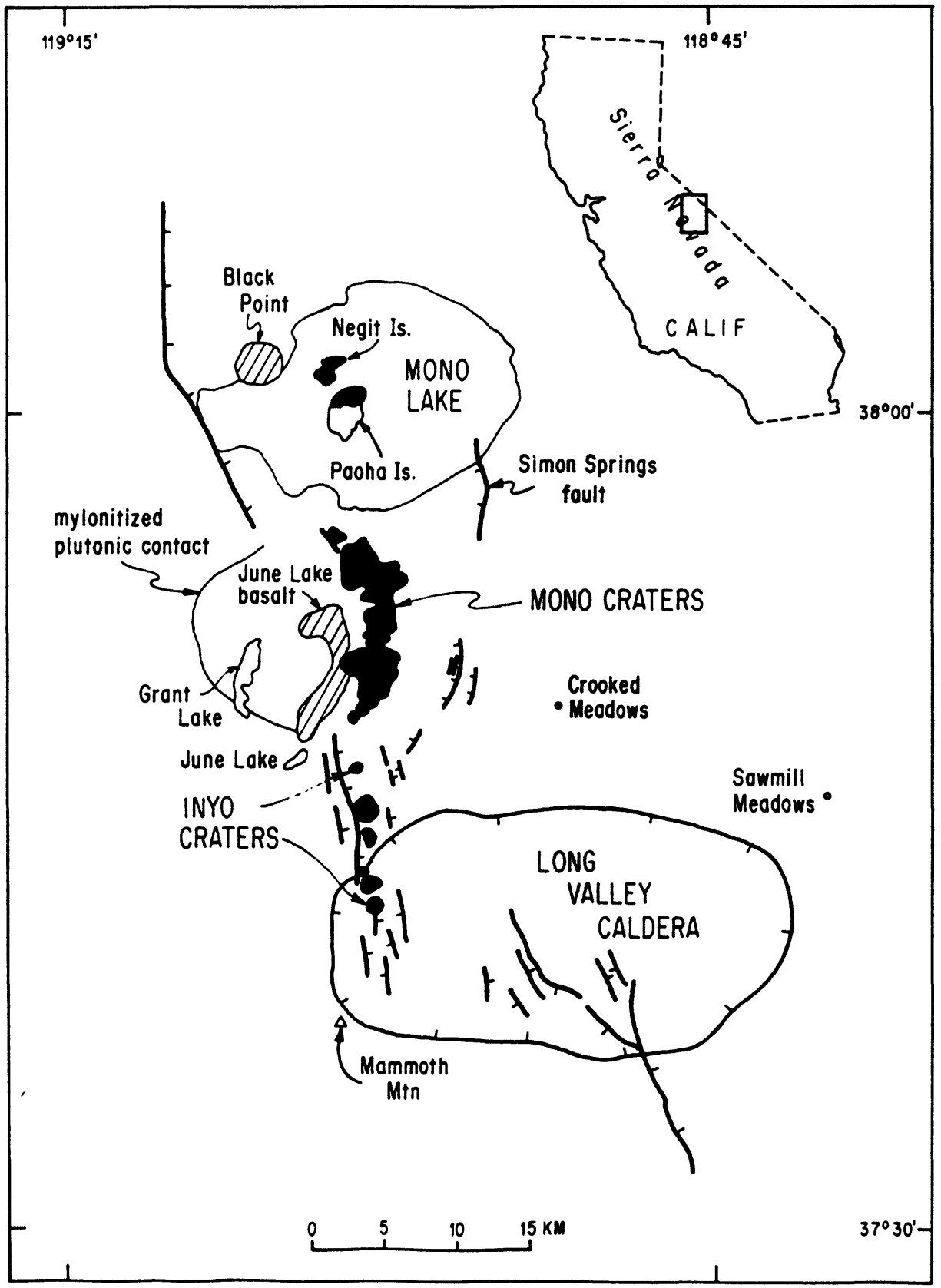

Figure 1. Index map of Mammoth/Mono Lake region. Mono Craters, Inyo Craters and volcanics of Mono Lake shown in solid black. Most of these are believed to be Holocene in age.

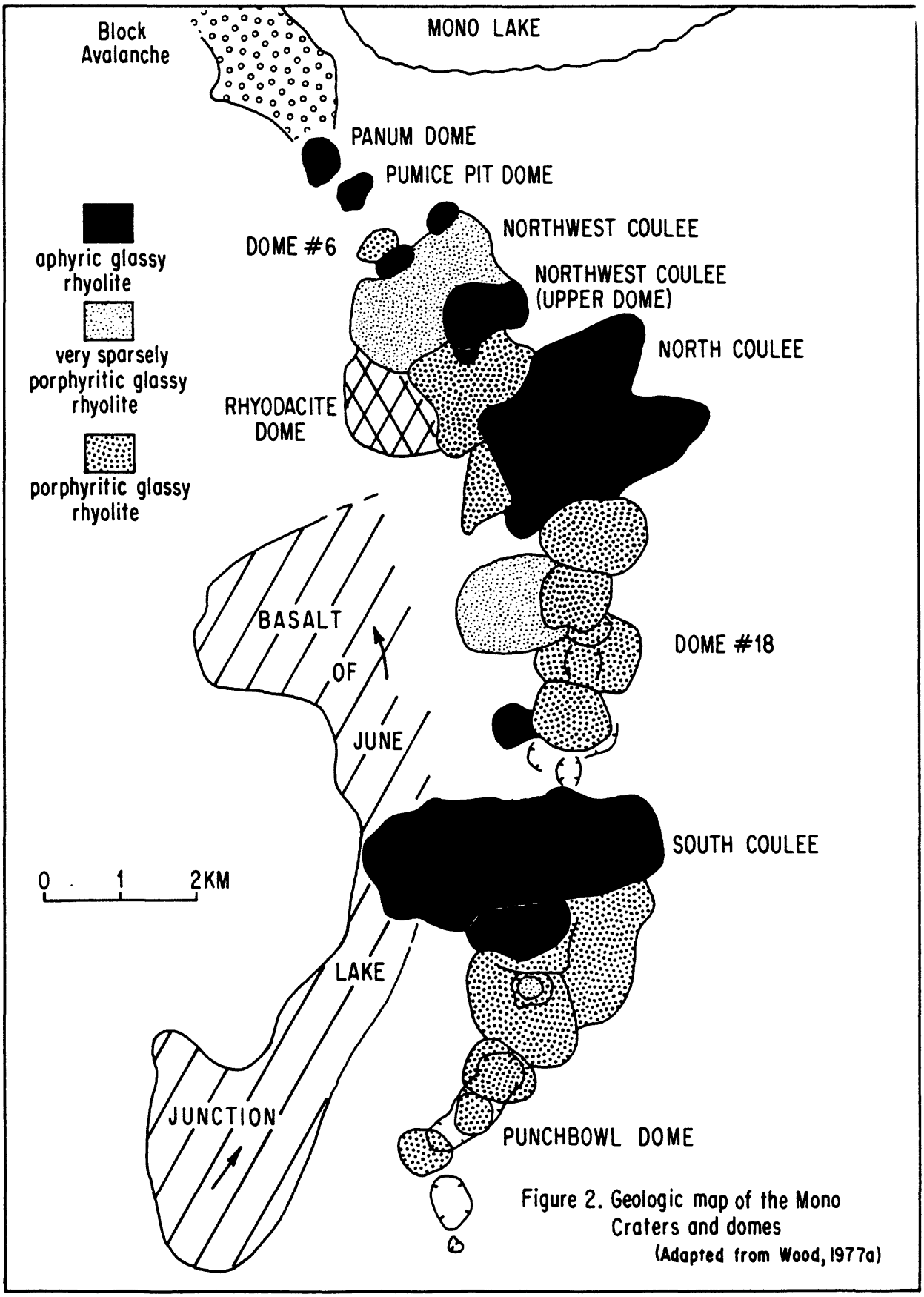

Figure 2. Geologic map of the Mono Craters and domes. Adapted from Wood, 1977a.

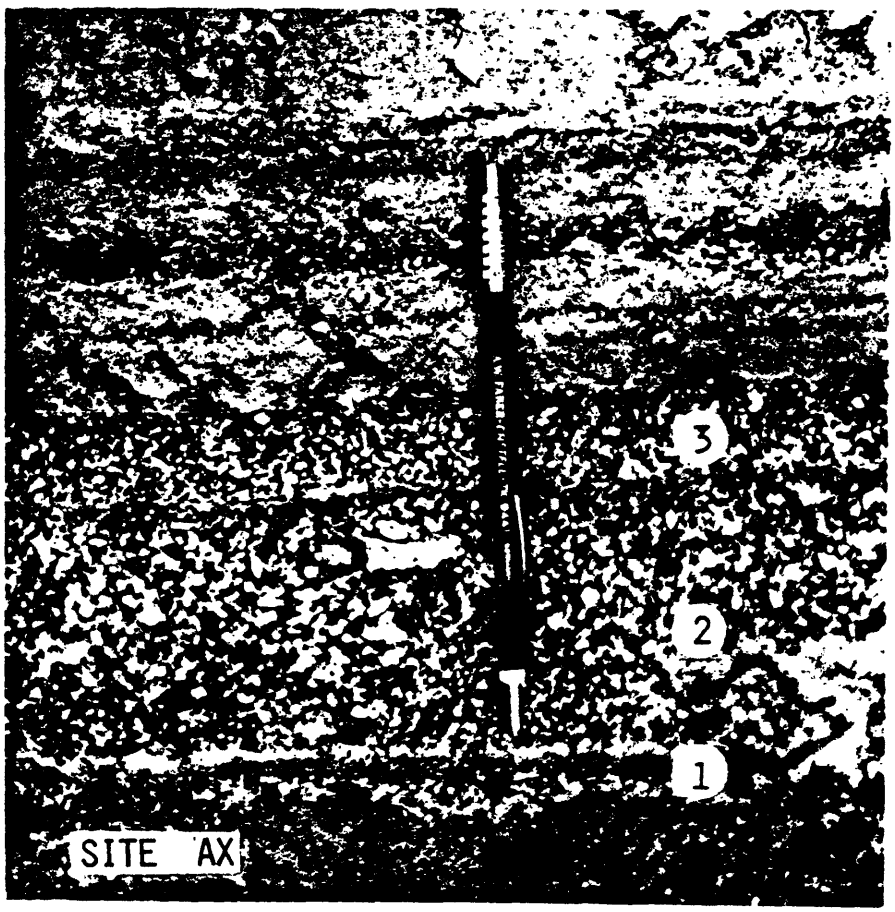

Figure 3a. Exposure of tephra from latest eruption of the Mono Craters. This exposure is near Rush Creek, west of Panum Crater and shows beds 1, 2 and 3 referred to in text. Pencil for scale.

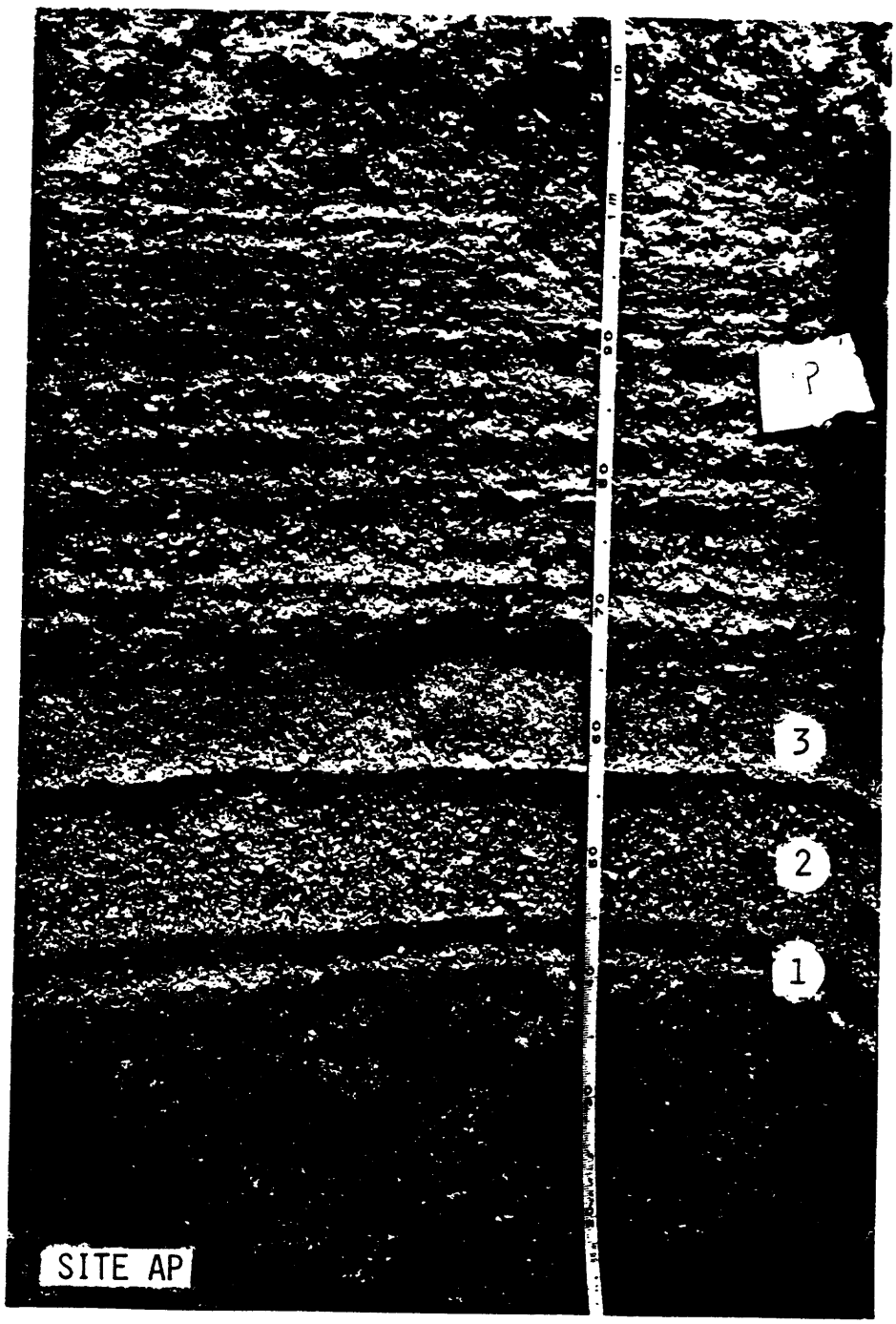

Figure 3b. Exposure of airfall beds from latest eruption. Beds 1, 2 and 3 are labelled. This site is on the south shore of Mono Lake near Panum Crater.

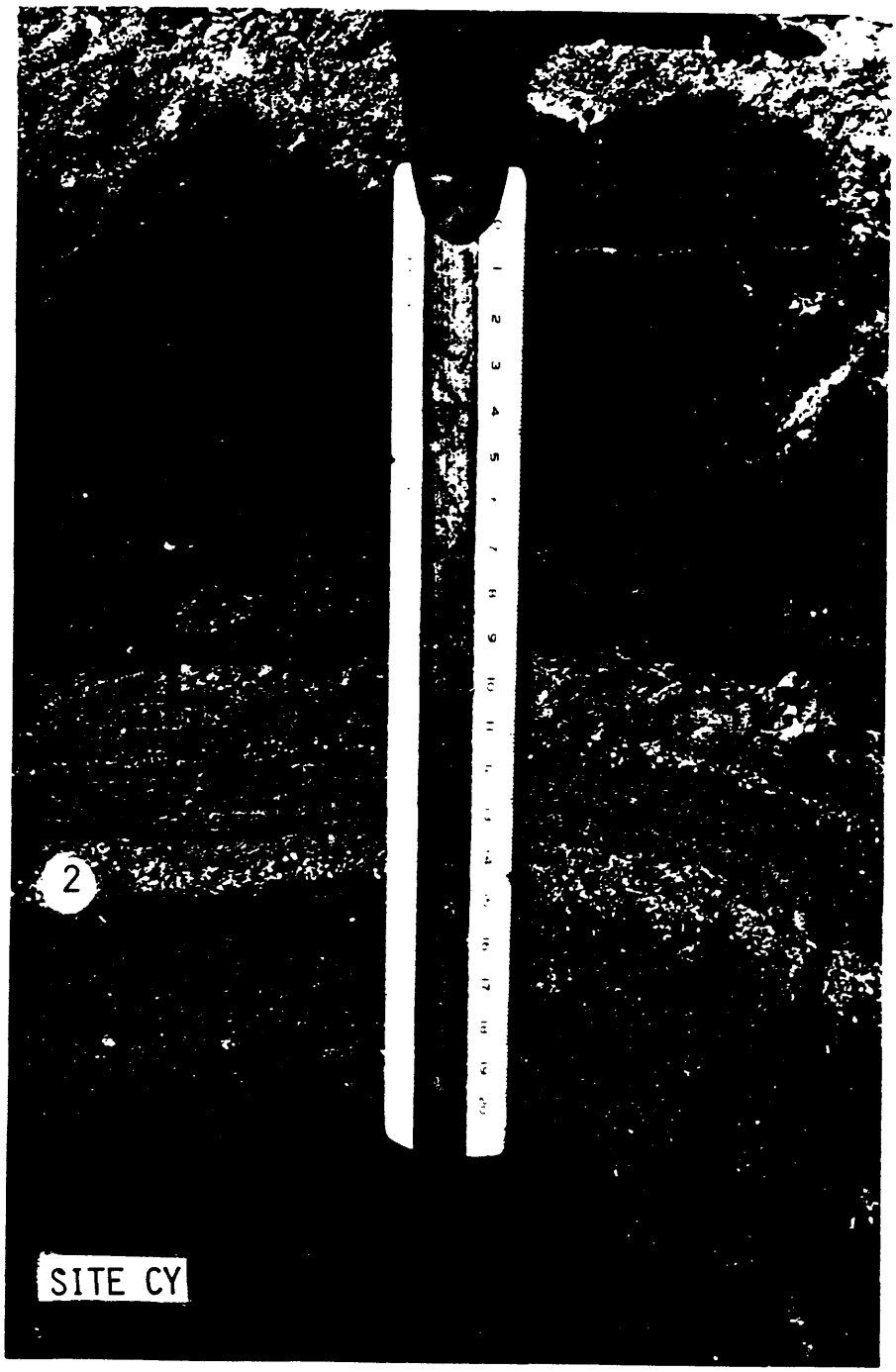

Figure 3c. Exposure in lake beds of Mono Lake at County Boat Launch on west side of lake, north of Lee Vining. Only bed 2 of the basal three beds was deposited at this site on the western margin of the airfall blanket. Scale is in centimeters. See Figure 4a for location of site.

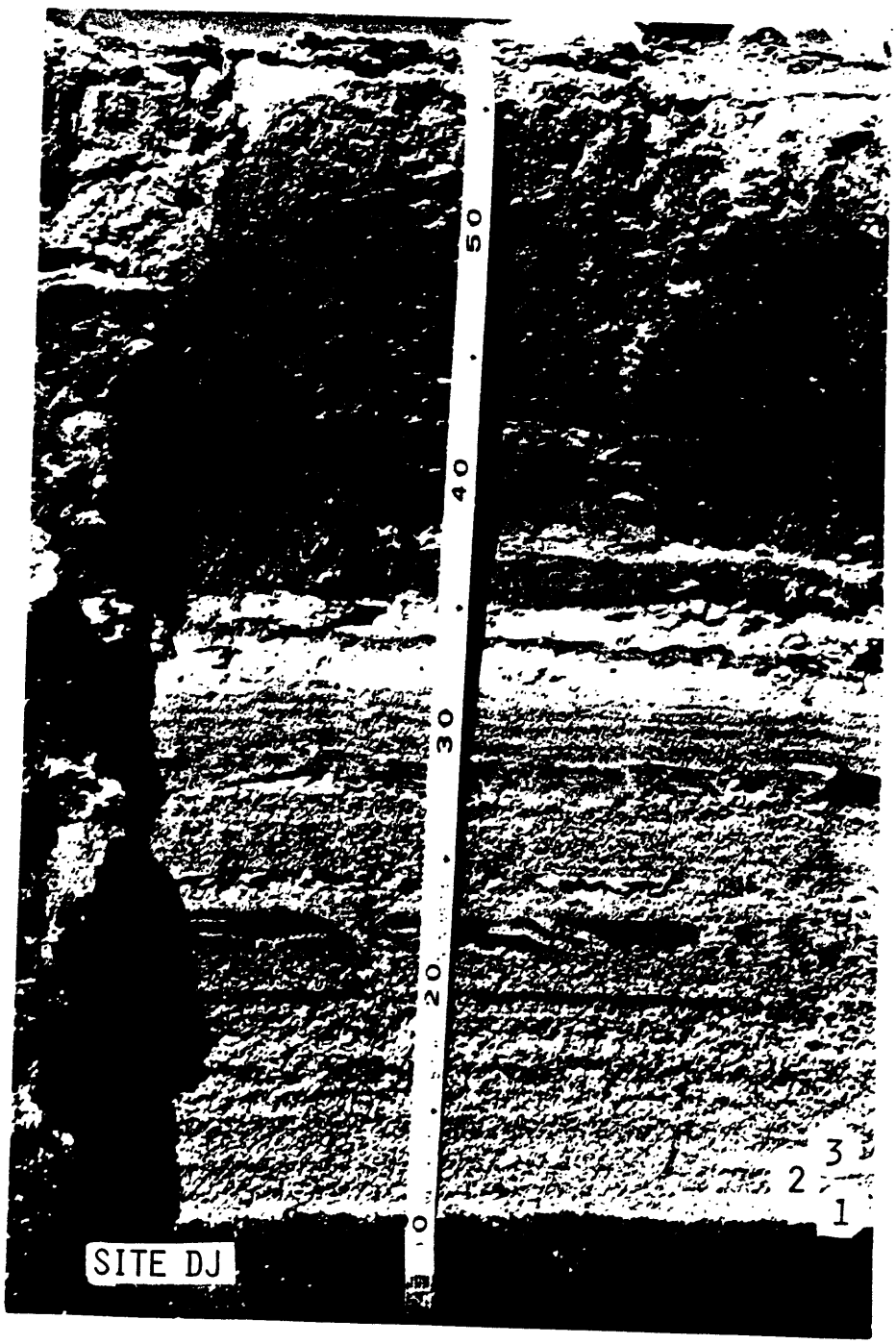

Figure 3d. Exposure of airfall products of latest eruption on north side of Mono Lake. These airfall beds are sandwiched between sediments of Mono Lake. Airfall beds 1, 2 and 3 are labelled. Scale is in centimeters. See Figure 4a for location of site.

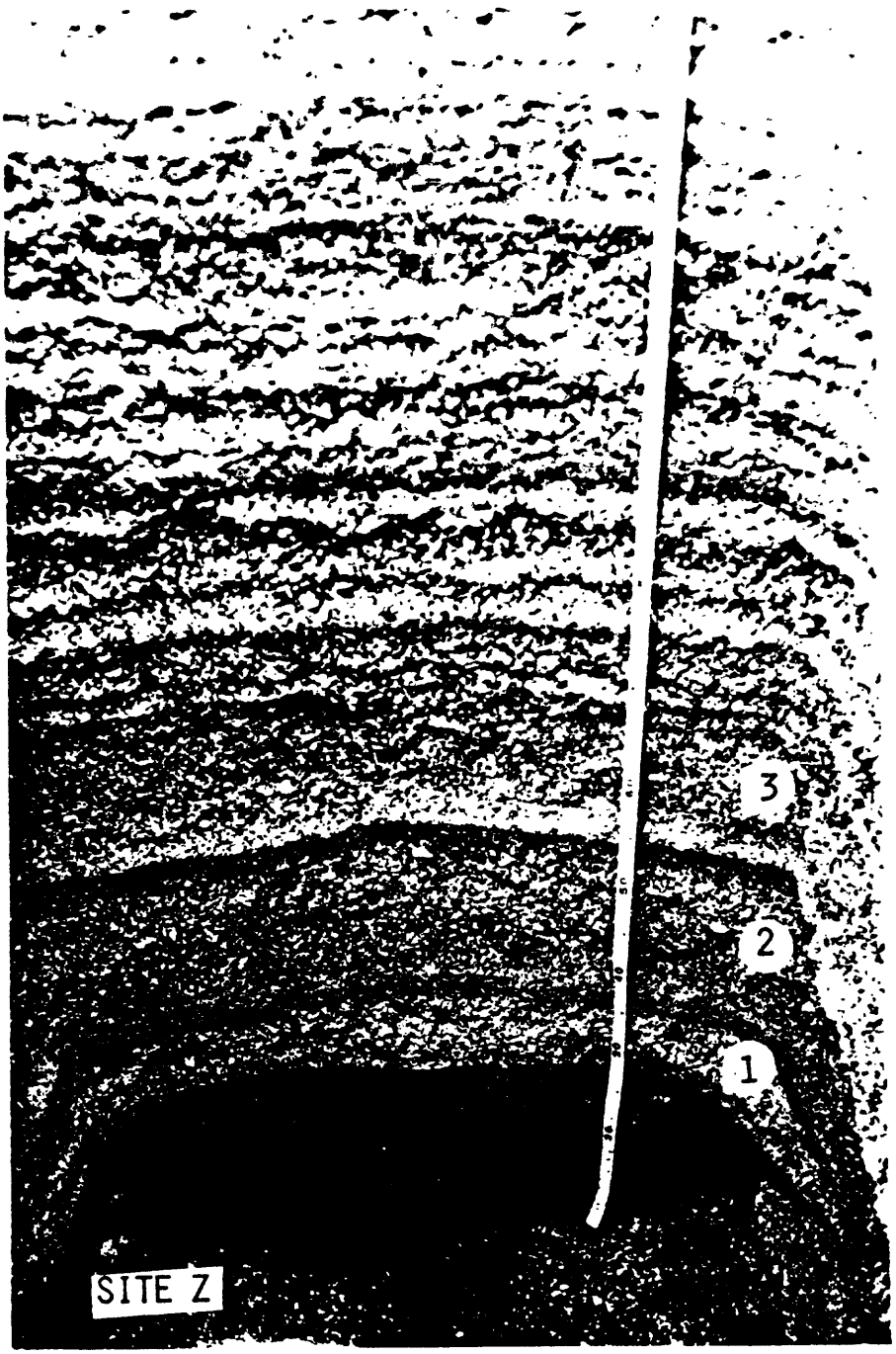

Figure 3e. Exposure of airfall beds east of Panum Crater. Beds 1, 2 and 3 are labelled. Scale is in centimeters.

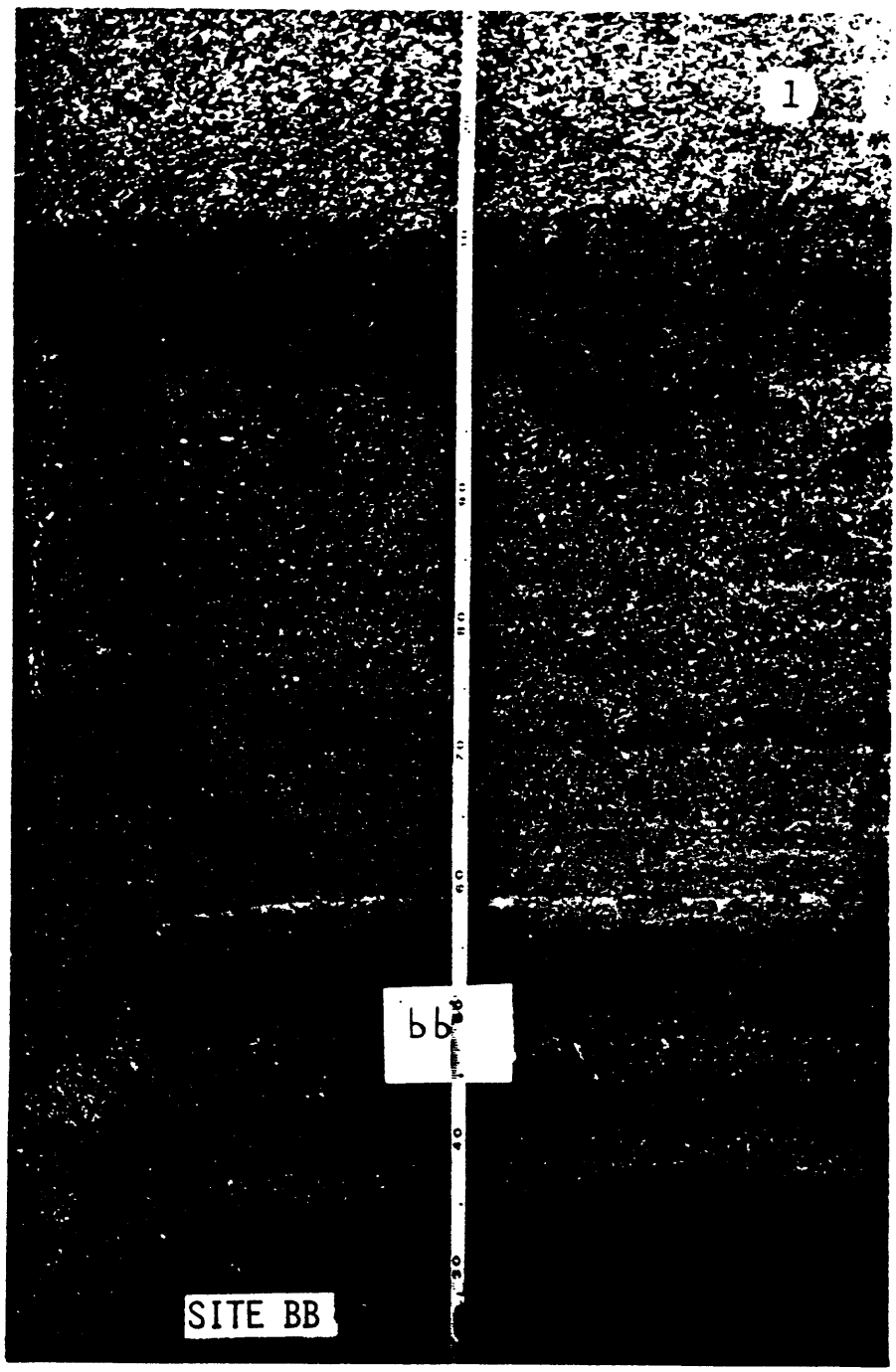

Figure 3f. Lower portion of exposure in gravel quarry north of Highway 120 and and about 2 km east of Panum Crater. This exposure reveals airfall series of penultimate eruption from Mono Craters. Note bed 1 of latest eruption at top of photograph. Scale is in centimeters. Source of this penultimate eruption is in the area of South Coulee.

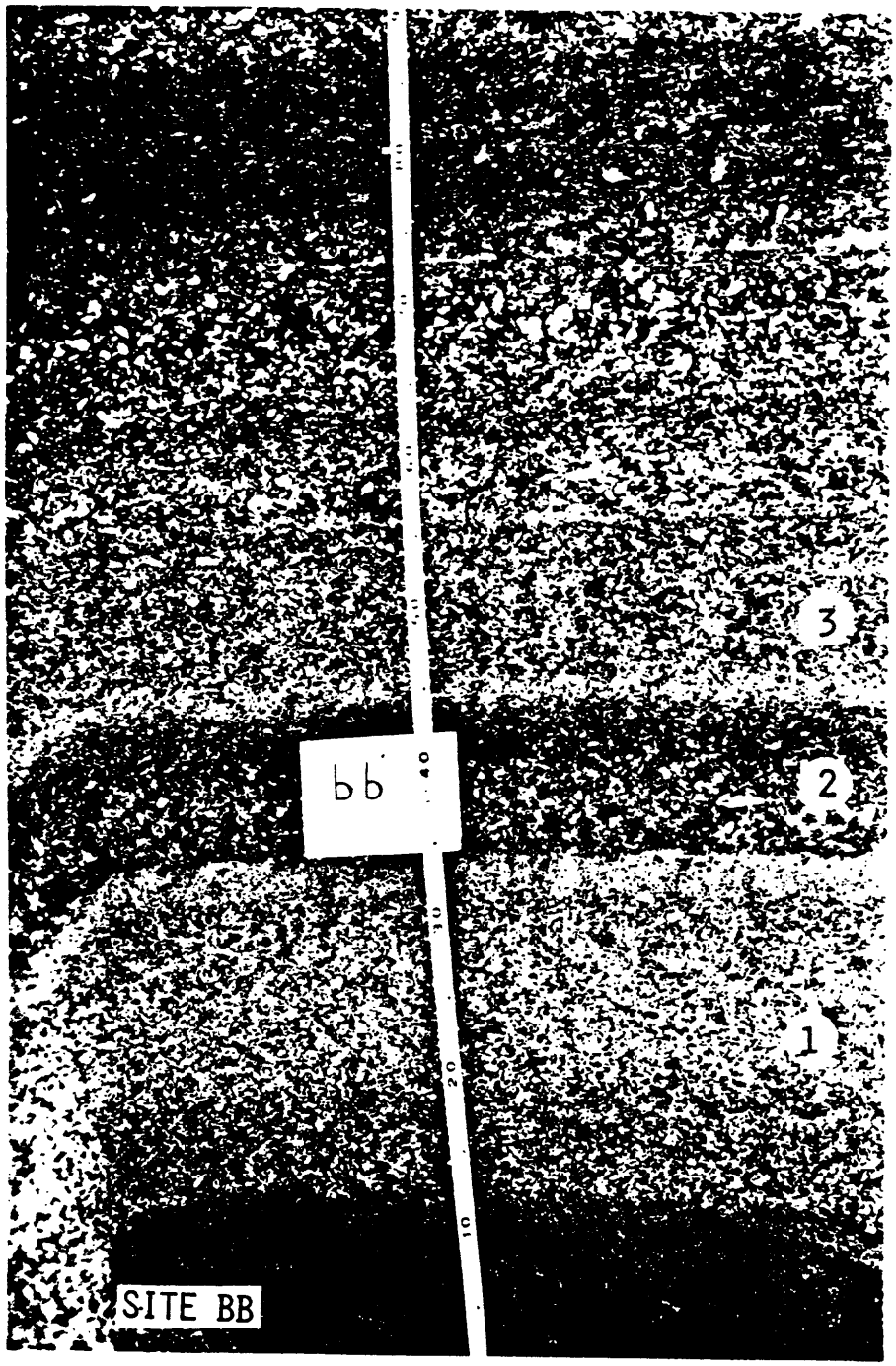

Figure 3g. Same locality as that shown in 3f. This photograph shows airfall beds of the latest eruption. Beds 1, 2 and 3 are labelled.

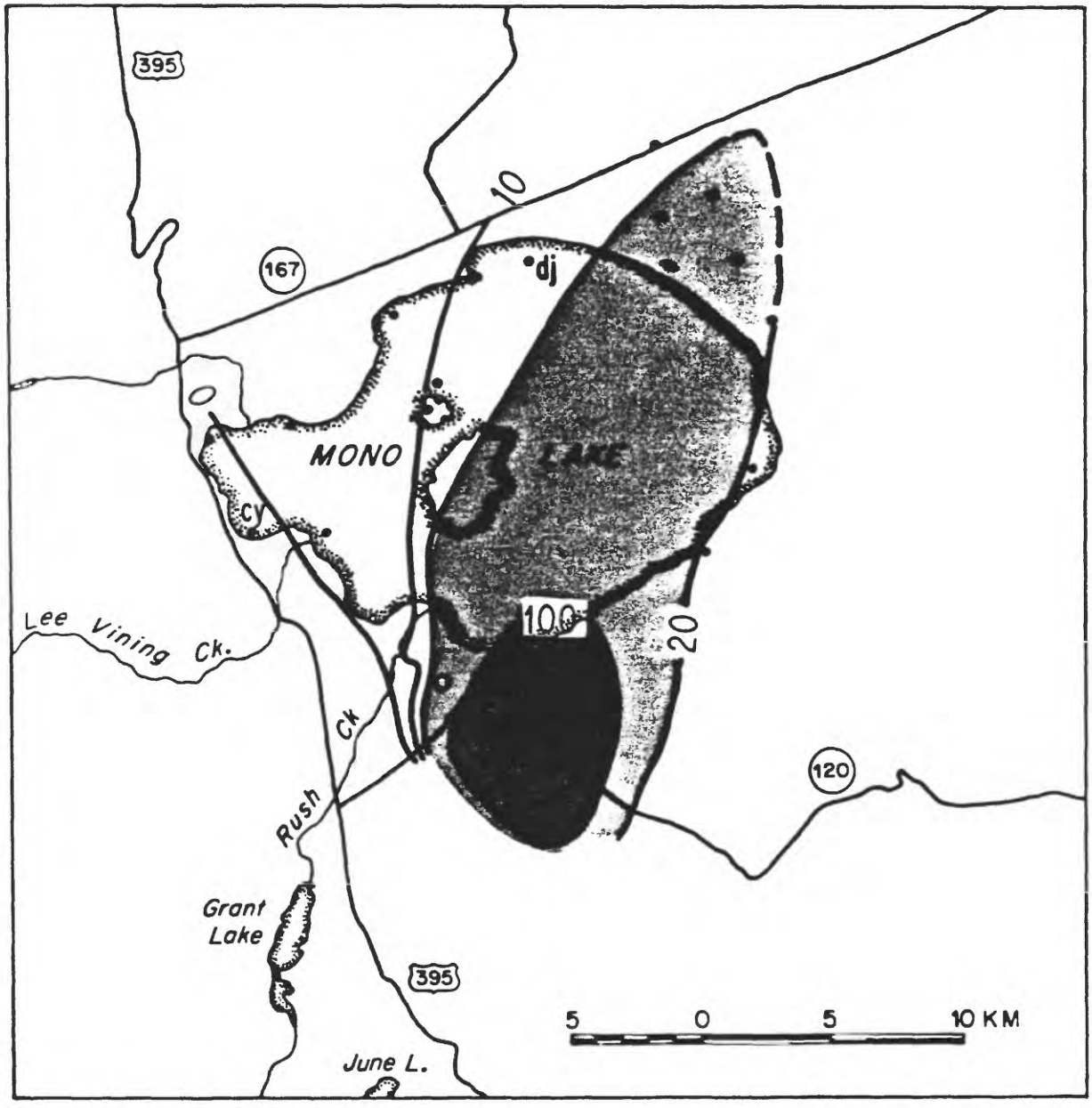

Figure 4a. Isopach map of bed 1 of latest eruption from the Mono Craters. Contours are in millimeters.

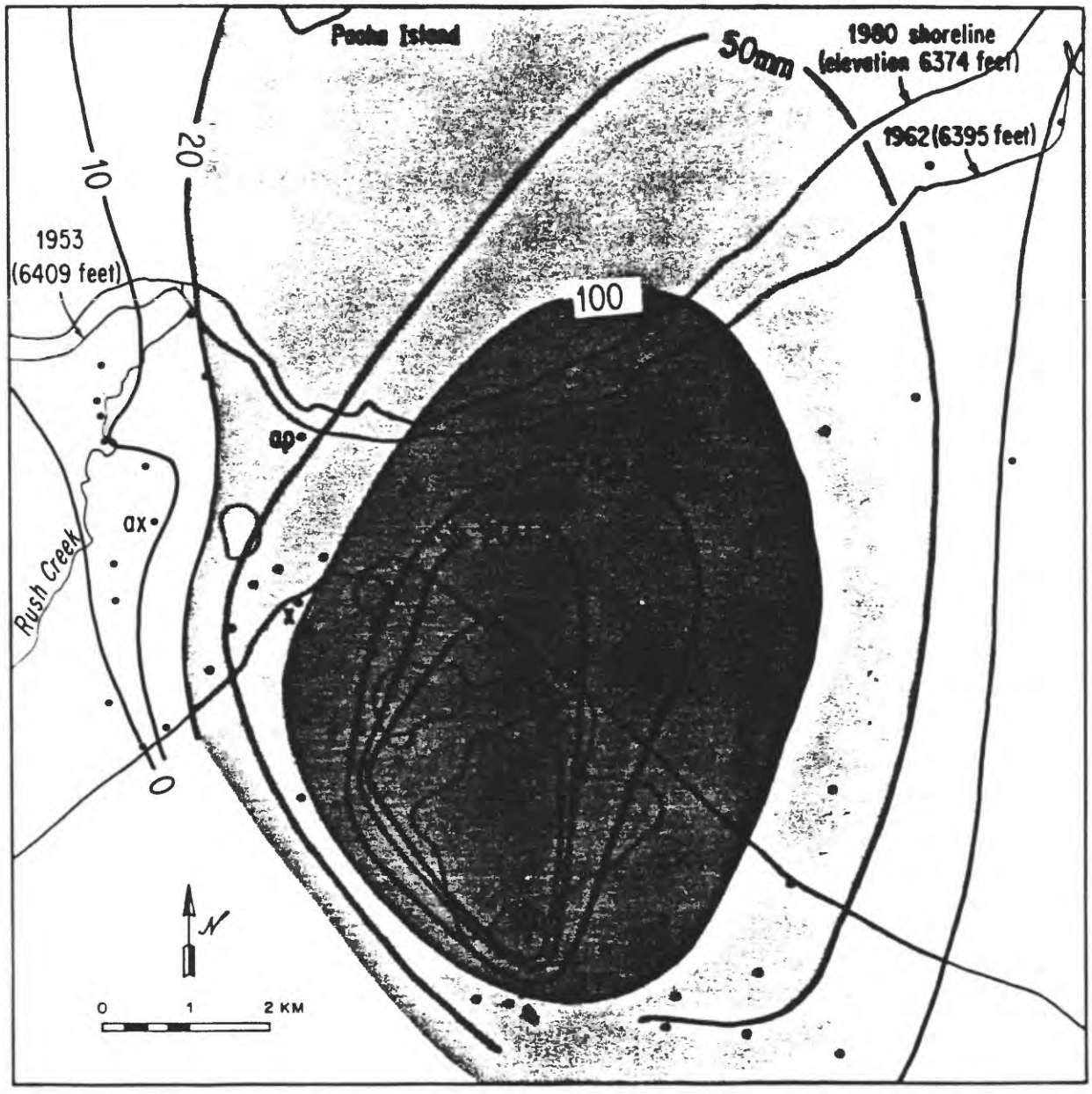

Figure 4b. Detail of isopach map of bed 1 in the source region, at the north end of the Mono Craters chain. Isopachs are in millimeters.

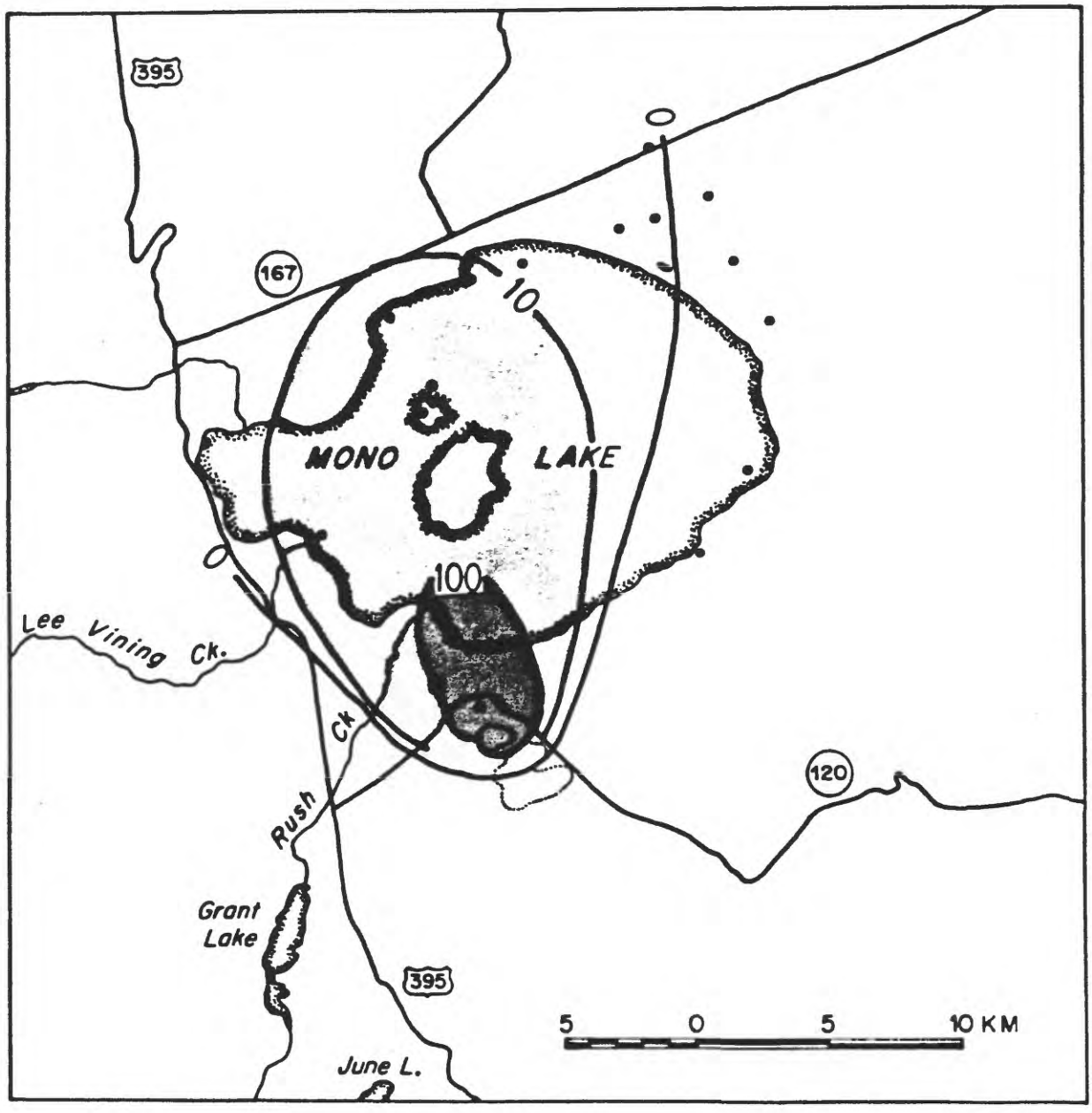

Figure 5a. Isopach map of bed 2 of latest eruption. Thicknesses are in millimeters.

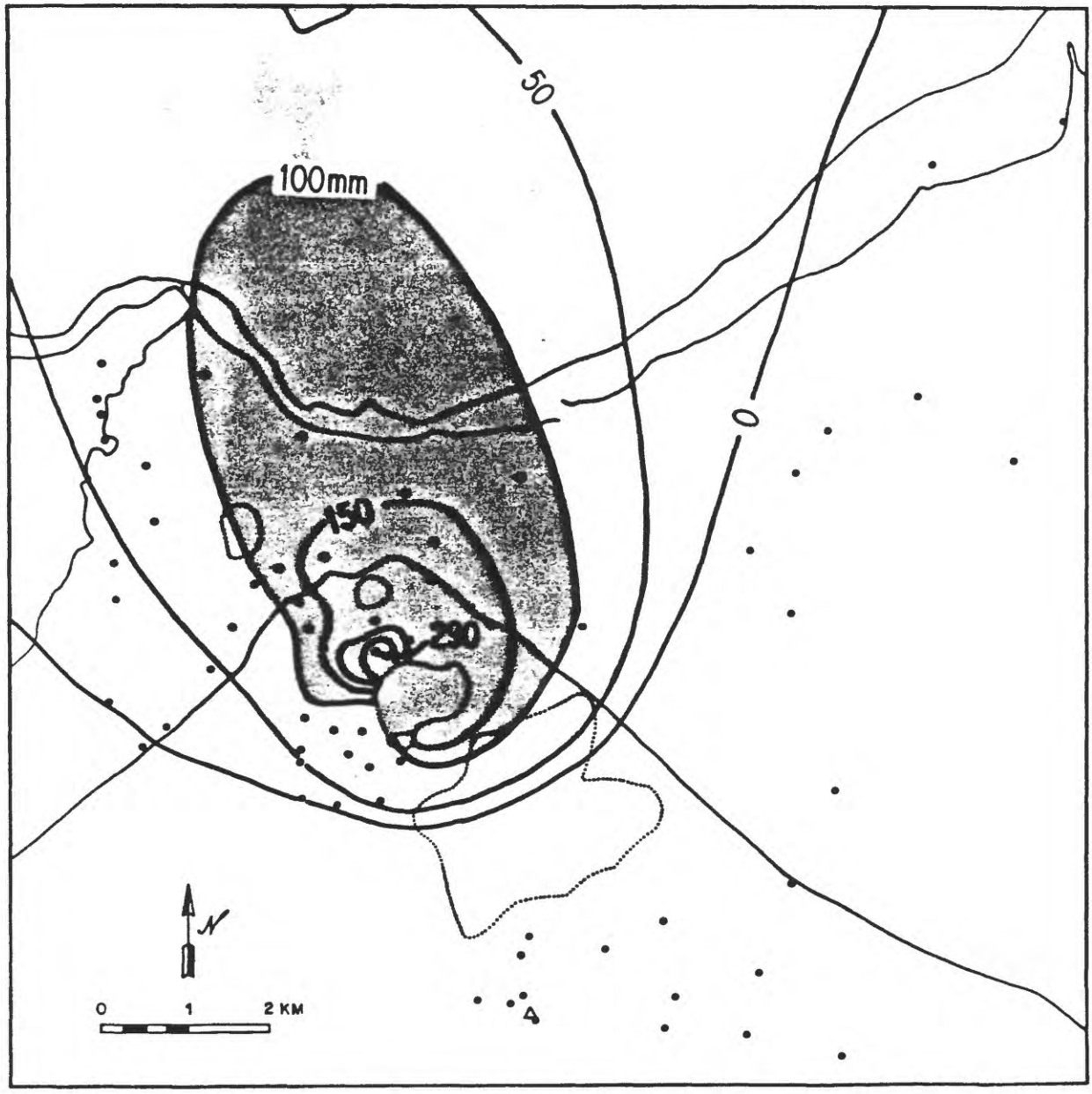

Figure 5b. Detail of isopach map of bed 2 in source region. Source of bed 2 is Upper Dome of Northwest Coulee.

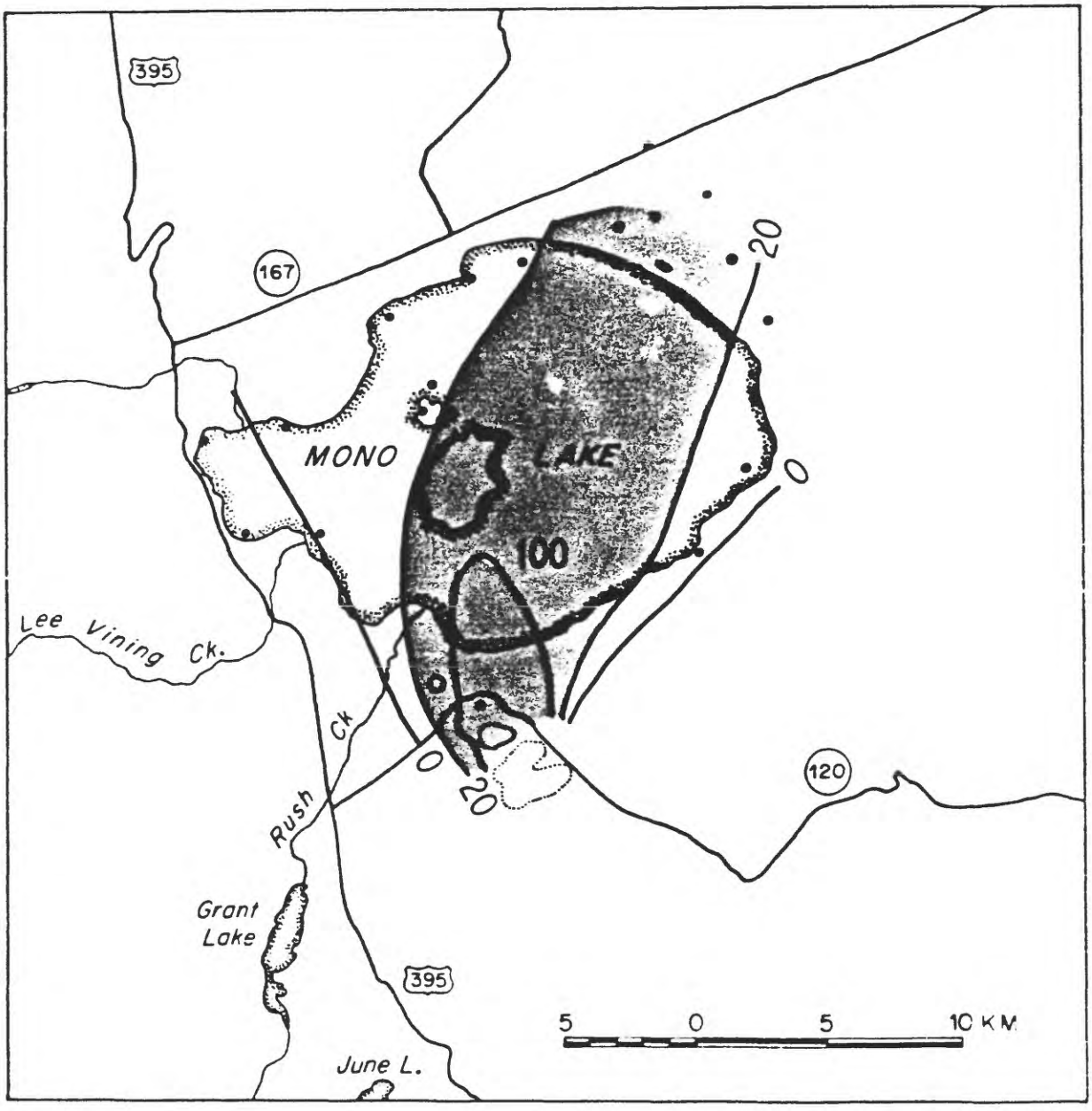

Figure 6a. Isopach map of bed 3. Note change in direction of dispersal axis, which probably indicates variable wind directions aloft at time of eruption.

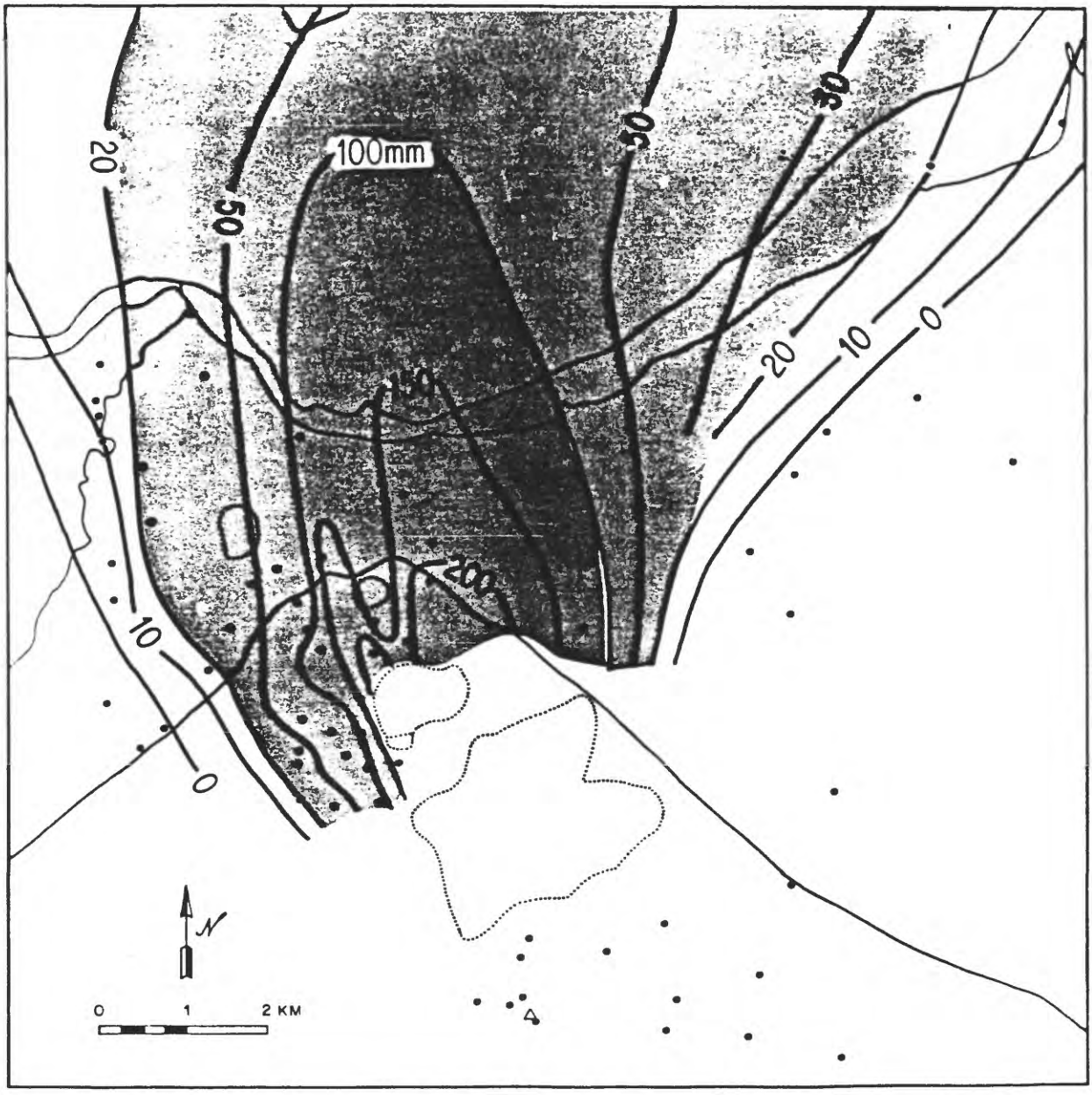

Figure 6b. Detail of isopach map of bed 3 near source which suggests bed 3 was erupted from more than one source.

Figure 7. Various pyroclastic flow deposits in the vicinity of the vents active at the time of the latest eruption. See text for discussion.

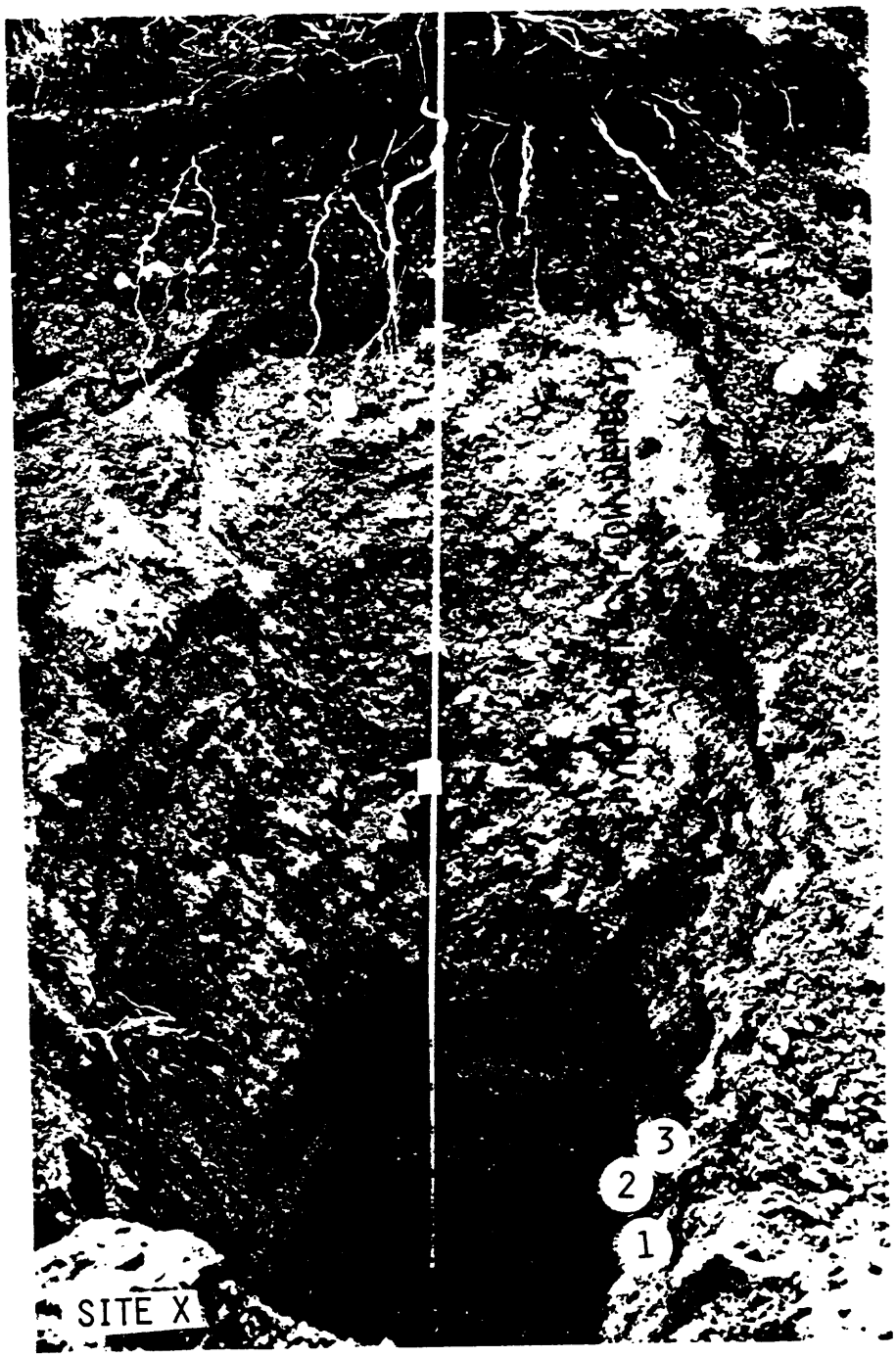

Figure 8. Exposure south of Highway 120 and southeast of Panum Crater, which reveals beds 1, 2 and 3 overlain by poorly sorted pyroclastic flow deposits.

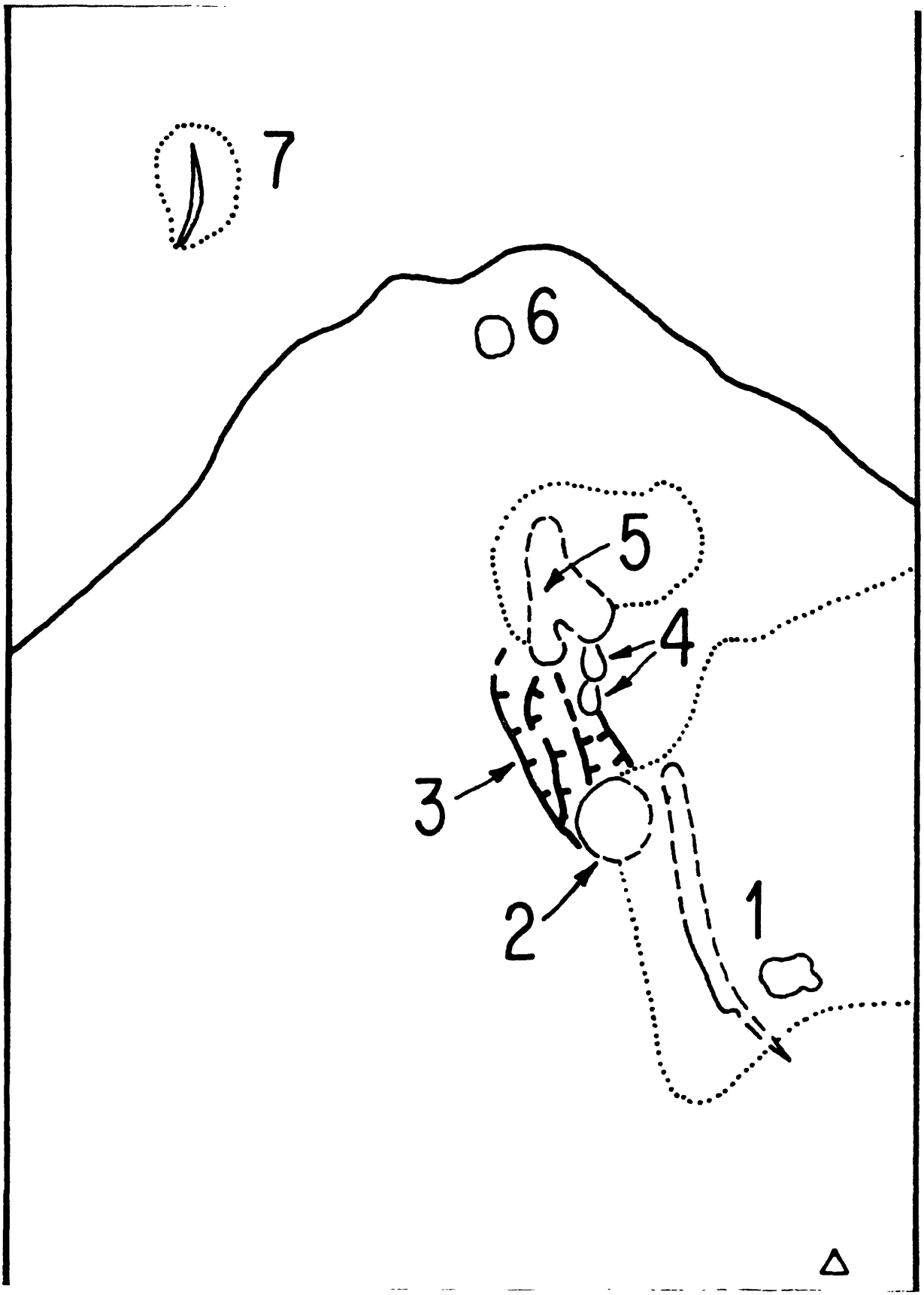

Figure 9. Sources of the various eruptive products of the latest eruption of the Mono Craters. Domes outlined by dotted lines; vents shown by solid and dashed lines. The numbers 1, 2, 4, 5, 6 and 7 refer to vents discussed in text. Numeral 3 refers to axial graben developed over the rising dike, just prior to eruption. The triangle in lower right is the summit of Crater Mountain.

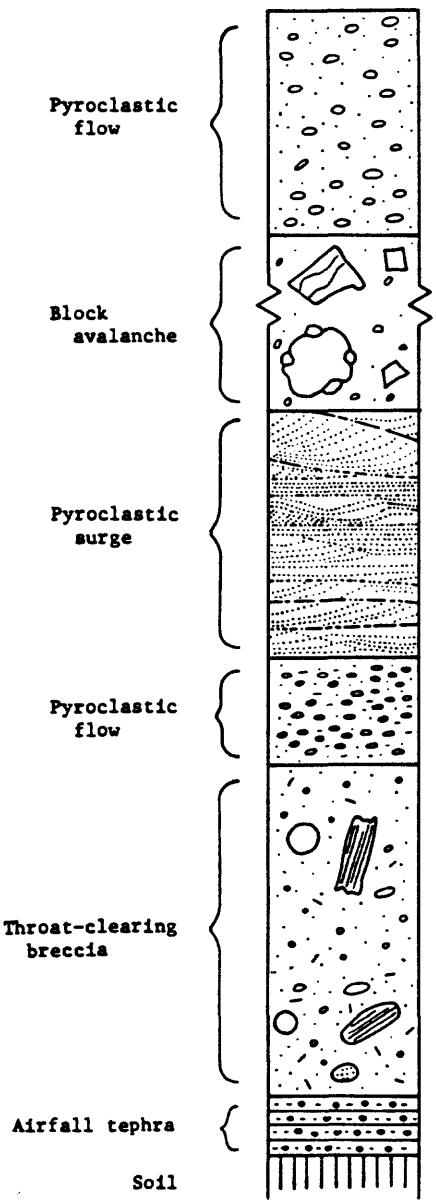

Massive, poorly sorted silty, sandy pebble gravel.

Massive, unsorted block breccia. Largest blocks several meters. Mostly angular rhyolite glassy blocks. Small % breadcrusted pumice with indentations holding adjacent pebbles. More than 10 m thick near Panum tephra ring.

Well-bedded cross- and planar-bedded silty sandy, mostly very fine and fine. Climbing crests of festooned antidunes migrate away from source.

Massive silty, sandy lapilli gravel. Mostly white lineated pumice. Forms 50 cm high dunes southwest of Panum. Abundant charcoal in lower parts of unit at greater distance from Panum.

Massive, unsorted heterogeneous breccia. Pebbles and cobbles are accidentals of lacustrine silt and rounded Sierran clasts. Loamy matrix contains juvenal pumice. More pumiceous toward top.

Well-sorted, well-bedded white lineated pumice, black obsidian and grey glass.

Figure 10. Generalized columnar section of beds deposited during latest eruption in the vicinity of Panum Crater.

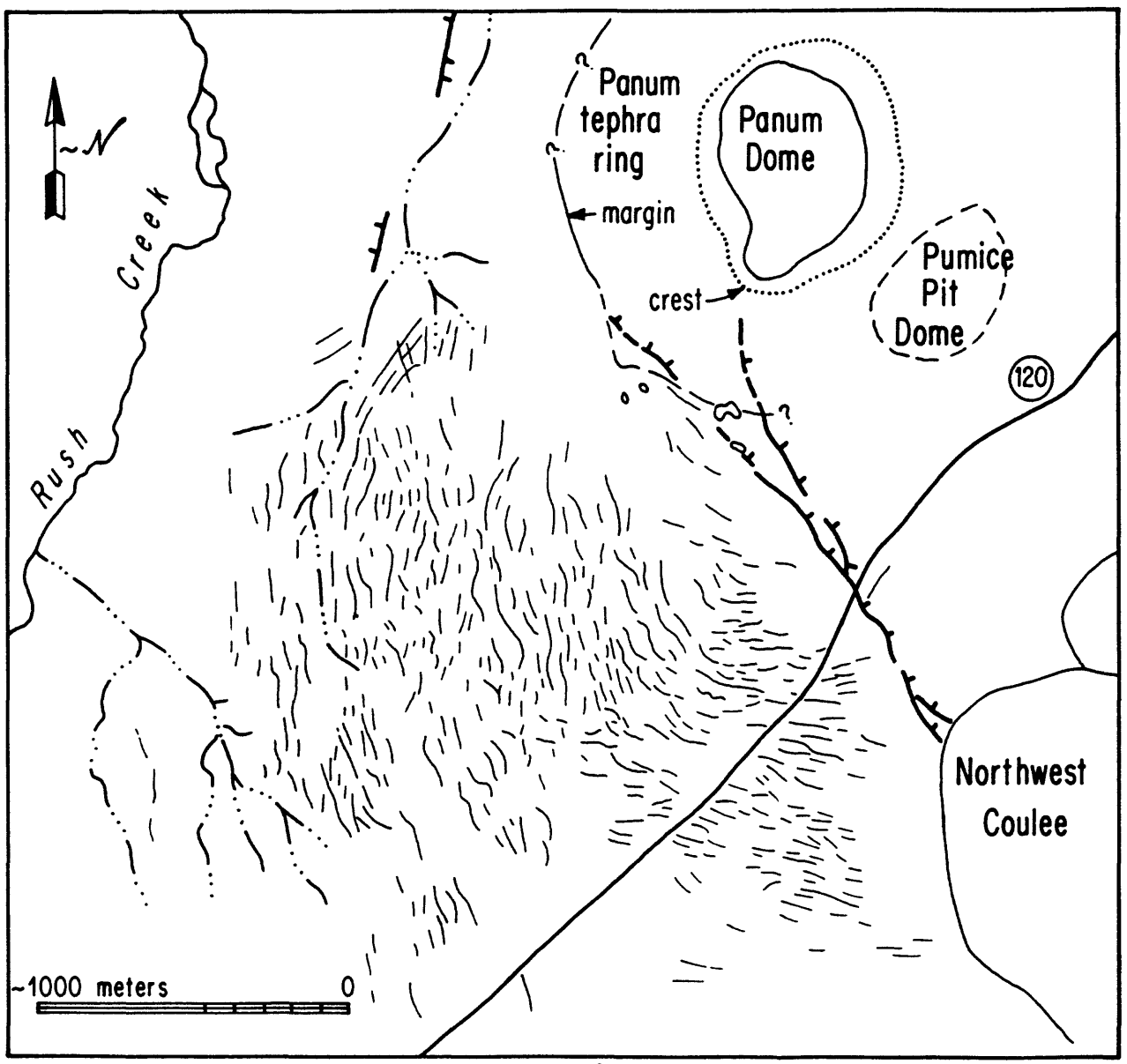

Figure 11. Dune field in quadrant southeast of Panum Dome. Discontinuous lines indicate dune crests.

Figure 12. Exposure of cross-stratified pyroclastic surge deposits overlying Pumice Pit Dome southeast of Panum Crater.

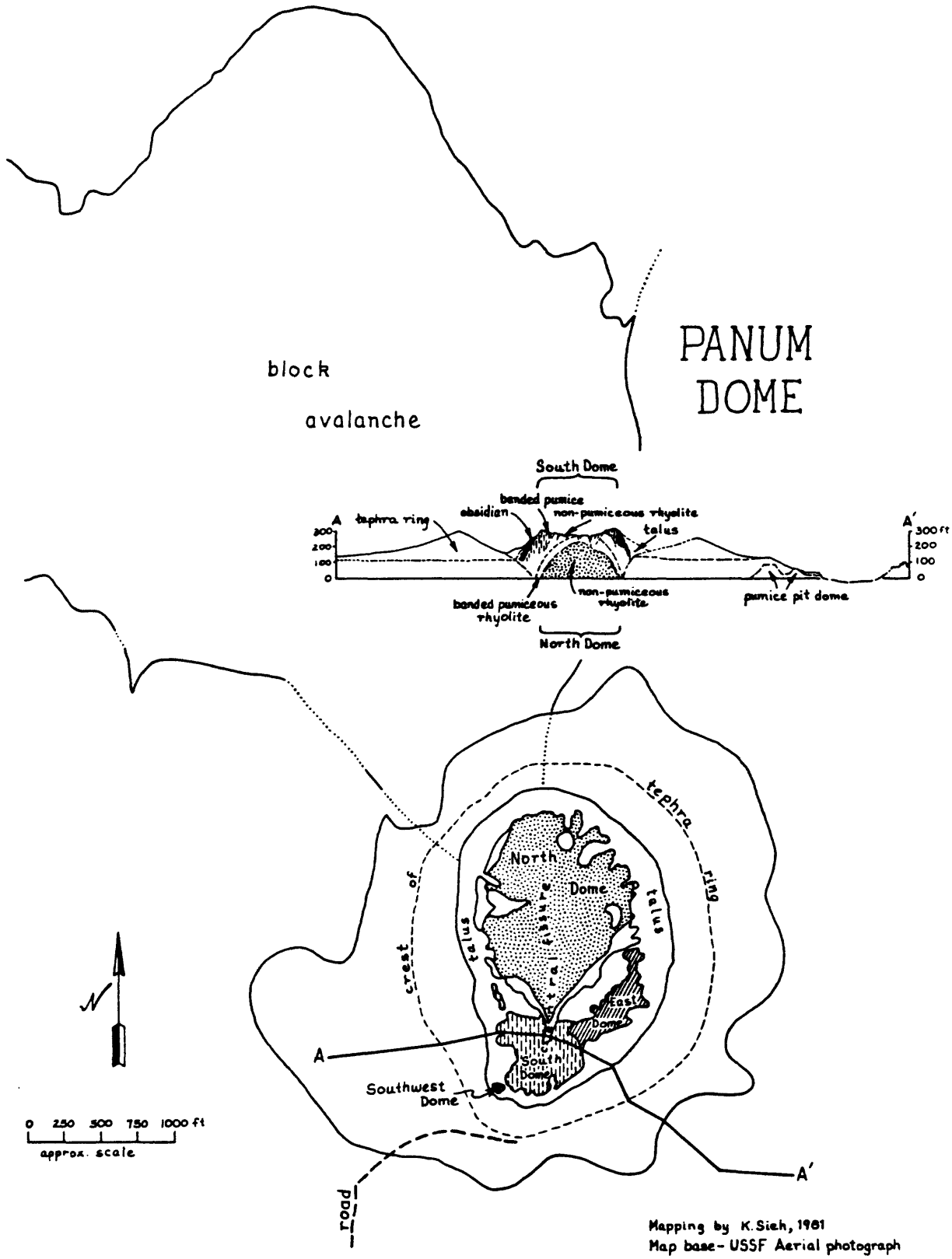

Figure 13. Simplified geologic map and cross-section of Panum Dome.

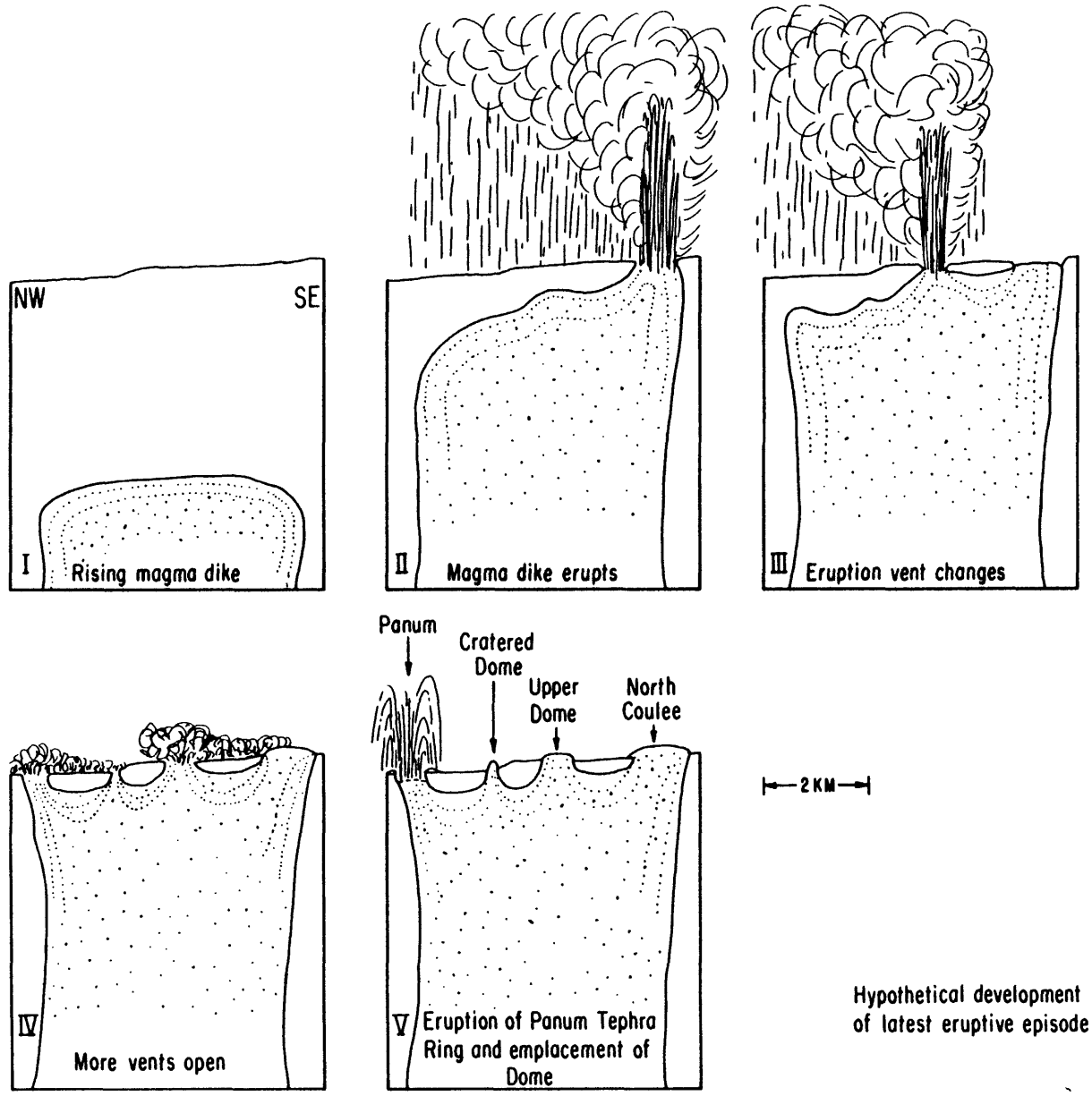

Figure 14. Hypothetical development of latest eruptive episode of the Mono Craters.

IGNEOUS DIKES AT LONG VALLEY, CA: EMPLACEMENT MECHANISMS AND ASSOCIATED GEOLOGIC STRUCTURES

David D. Pollard
Dept. of Applied Earth Sciences
Stanford University
Stanford, CA 94305

Jonathan H. Fink
Dept. of Geology
Arizona State University
Tempe, AZ 85287

Paul T. Delaney
U.S. Geological Survey
2255 N. Gemini Drive
Flagstaff, AZ 86001

Abstract

Two hypotheses for dike emplacement are: (1) magma flows into and dilates pre-existing fractures; or (2) magma flows into and dilates self-generated fractures. In the first case dikes should be parallel to an element of the rock fabric; in the second, they should be perpendicular to the least compressive stress. The two hypotheses suggest different dike intrusion and fissure eruption mechanisms and therefore different strategies for monitoring igneous events at Long Valley. We derive a method to distinguish the two mechanisms, a priori, from in-situ stress measurements and estimates of magma pressure. Estimates of relative dilation and slip across a dike plane from models constrained by surface displacement data provide a method to distinguish the two mechanisms, a posteriori. Joints cluster near dike contacts just as microcracks cluster near laboratory fractures. Such clusters define a process zone of secondary cracking that forms at the tip of a primary crack. For basaltic dikes in sedimentary host rocks of the Colorado Plateaus, the process zone size is about 10 m and the number of joints is in the range 10 to 100. The mechanical energy release rate for propagation of these dikes is estimated to be 10 to 100 times that for a single laboratory fracture. Data from proposed drill holes through rhyolite dikes under the Inyo Domes will elucidate propagation mechanisms and process zone characteristics. As a dike nears the Earth's surface, two sets of ground cracks open parallel to the dike trend. A "rule of thumb" is that the depth to the dike top is one-third to one-half the spacing between the innermost surface cracks of each set. Surface structures on and near the Inyo Domes suggest a NNE trend for shallow (< several hundred meters) dike segments, but dome alignment suggests a NNW trend for the feeder dikes at depth.

Introduction

Recent geophysical surveys (Steeples and Iyer, 1976; Hill, 1976; Sanders and Ryall, 1983) provide evidence for a magma reservoir beneath Long Valley Caldera. Geodetic measurements between 1975 and 1980 can be interpreted as an inflation of this reservoir under the resurgent dome of the caldera (Savage and Clark, 1982). Knowledge that the crust beneath Long Valley is pervaded by steeply-dipping faults, joints, and other planes of weakness (Bailey and Koeppen, 1977; Bailey et al., 1976) invites the hypothesis that magma from an inflating reservoir could flow into some of these pre-existing fractures, dilate them to form an igneous dike, and thereby establish a conduit that could transport magma to the surface. In this case, dike orientation is controlled by the pre-existing fractures, a relationship that has been advocated for numerous geologic settings (e.g. Wilson, 1970).

A contrasting emplacement hypothesis is that dike dilation generates sufficient tension in the host rock ahead of the dike tip to create new fractures, into which the magma may flow (Anderson, 1938). These fractures and the subsequent dike will be oriented perpendicular to the direction of least compressive stress. This obviates the need for pre-existing fractures and generates a dike orientation that is controlled by the state of stress. If the least compressive stress is subhorizontal, such dikes will be steeply-dipping and capable of transporting magma to the surface.

The two hypotheses for dike propagation admit different deductions about the relations among dike attitude, rock fabric, and tectonic stress orientation and suggest different fissure eruption mechanisms. If propagation along pre-existing fractures is the appropriate mechanism, then geological mapping and geophysical surveying of the rock fabric (fractures, faults, joint sets, etc.) will provide valuable data for forecasting likely locations of dikes and fissures. Three criteria must be

satisfied for this mechanism to be viable: the magma must find access to the fracture; it must be able to dilate the fracture; and it must flow a significant distance along the fracture. For dilation to occur magma pressure must exceed the compressive stress acting across the plane of the fracture. However, this compressive stress need not be a principal stress, so the directions of the principal stresses acting at the time of intrusion need bear no unique relation to the pre-existing fracture or the dike.

In contrast, if dike propagation along self-generated fractures is the appropriate fissure eruption mechanism, then measurement of the stress (or strain) field is crucial for monitoring and forecasting because of the unique relationship between orientations of dikes and principal stresses. This relationship has been exploited successfully to estimate paleostress directions from ancient dikes (e.g. Nakamura, 1977; Zoback and Zoback, 1980; Bacon et al., 1980; Delaney and Pollard, 1981). The inverse procedure could be used to interpret in situ stress measurements and geodetic (strain) data from Long Valley in order to forecast likely orientations of dikes and eruptive fissures.

Geophysical and structural geologic criteria are needed to distinguish between the two hypotheses and to establish which might be appropriate at Long Valley. In this paper we discuss several aspects of the rise of magma from a reservoir through dikes to the surface, including deformation and structures likely to develop at each stage of emplacement. We indicate which of these features might be detected at Long Valley, and which might be used to interpret data obtained from a drilling program such as that currently underway at the nearby Inyo Domes.

Relations Among Dike Attitude, Rock Fabric, and Tectonic Stress

In order for a dike to be emplaced along a steeply dipping plane of weakness (fracture), the magma pressure P_m must exceed the subhorizontal compressive

stress acting across that plane. Delaney et al. (in prep.) have used this necessary condition for dike dilation to relate the state of stress to dike attitude. The remote least compressive stress σ_1^r is subhorizontal, but of arbitrary orientation α relative to the normal to the fracture plane (Fig. 1, inset). The other subhorizontal principal stress σ_2^r may be the intermediate or maximum compressive stress. Tensile stress is taken as positive, and a ratio of stresses $\underline{R}$ is defined as

$$\underline{R} = (\sigma_1^r + \sigma_2^r + 2\underline{P}_m)/(\sigma_1^r - \sigma_2^r)$$

The condition defines two regions on Figure 1, a graph of stress ratio $\underline{R}$ versus angle α. For combinations of $\underline{R}$ and α falling in the lower area, dilation is impossible and therefore magma cannot invade the fracture. In the upper area dilation is possible, so a dike may form *if* the magma finds access to the fracture and *if* it can flow a significant distance before stagnating (Delaney and Pollard, 1982).

To apply this condition we must estimate the stress ratio $\underline{R}$. The magnitude of the magma pressure is estimated as $\underline{P}_m = \gamma_m \underline{d}$ where γ_m is the unit weight of the magma and $\underline{d}$ is depth. The principal regional stresses are estimated as $\sigma_1^r = -\underline{m}\gamma_r \underline{d}$ and $\sigma_2^r = -\underline{n}\gamma_r \underline{d}$ where $\underline{m} < \underline{n}$ are constants determined by the tectonic regime, γ_r is the unit weight of the rock, and we set $\gamma_m \simeq \gamma_r$. Based on in situ measurements described by McGarr (1982), the ratio $\underline{R}$ may be about +1 in some extensional tectonic regimes because $\underline{m} \simeq .5$ and $\underline{n} \simeq 1$. $\underline{R}$ may be about -1 in some contractional tectonic regimes because $\underline{m} \simeq 1$ and $\underline{n} \simeq 1.5$.

If Long Valley were considered to be in a contractional regime, Figure 1 suggests that magma could not easily invade planes of weakness, even those at small angles α, so dike orientation and principal stress planes should coincide. In contrast, if Long Valley is representative of an extensional regime, the stress directions may not be indicative of potential dike orientations. Rather, the rock

fabric may control dike orientation because planes of weakness at large angles α can be dilated. Additional data on the state of stress and magma pressure in the Long Valley region are needed to refine this analysis and to ascertain whether knowledge of the stress ratio R can be used to distinguish the two emplacement hypotheses.

Relations Among Dike Attitude, Dilation, and Slip

Shear stresses act across all planes of weakness not oriented in a principal stress plane. These shear stresses will not generate slip (faulting) if there is sufficient frictional resistance along the plane. However, if magma invades a plane of weakness, frictional resistance is removed and the shear stress will be relaxed by a shear displacement u_2, that accompanies the dilational displacement u_1 (Fig. 2, inset). Thus, detection of slip across eroded dikes by geologic mapping is an indication that the dike may not have been emplaced along a principal stress plane. Of course it must be demonstrated that the slip and dilation were contemporaneous.

To quantify relations among dike attitude, dilation, and slip, the ratio of these displacements at the center of a dilating plane of weakness is plotted versus angle α in Figure 2 using the stress ratio R as a parameter. For $R > 10$ (a condition produced by relatively great magma pressure and/or a small difference between the remote principal stresses), the displacement ratio is less than 0.1 for all α. That is, slip will be insignificant (and perhaps not measureable) relative to dilation no matter what the dike attitude was relative to the principal stresses. Clearly, the displacement ratio will not be a good criterion for distinguishing the emplacement hypotheses under these conditions. However, for smaller values of R the displacement ratio can be large, approaching unity for small angles α. Thus, where magma pressure is not great relative to the regional stresses and/or the

regional stress difference is large, the two hypotheses should be distinguishable.

For modern dike emplacement events, displacement usually cannot be measured at the buried dike contact. On the other hand, geodetic measurements record surface displacements that, in some instances, are known to have been caused by dike emplacement (Pollard et al., 1983). Such surface displacements can be used to constrain models from which one infers the displacement ratio at the dike contact. Model results of geodetic measurements at Long Valley indicate combinations of slip and dilation on planes at depth (Savage and Cockerham, 1984). This is consistent with dike emplacement along pre-existing planes of weakness that are not symmetric to the principal stresses. An alternate model (Rundle and Whitcomb, 1984) provides an adequate fit to the geodetic data using point sources of dilation (magma reservoirs) rather than slipping and dilating surfaces (faults and dikes). Apparently, the two subsurface configurations cannot be distinguished unambiguously using these geodetic data. However, additional data and model studies are indicated because the technique is sound in principle, and it provides one of the most direct measures of subsurface deformation.

Fractures Formed in the Process Zone of a Dike

Dike emplacement and propagation involves several complex processes, some of which are illustrated in Figure 3. Here we focus on the possible development of fractures near the dike tip. In so far as dikes act like pressurized cracks (Pollard, 1973), we may employ the methods of linear elastic fracture mechanics (Lawn and Wilshaw, 1975), to show that the stress field near the dike tip involves a concentration of tensile stress that could promote the formation of vertical joints (Delaney et al., in prep.). The region of jointing at the dike tip is analogous to the process zone of microcracking at the tip of a small fracture in rock (Hoagland et al., 1973). These joints, if present, will affect the cooling history of the intrusion

and local hydrothermal circulation. They will weaken the host rock and provide a pathway for flow of the magma, thus satisfying the second emplacement hypothesis. Surface exposures of igneous dikes are rare in the Long Valley area. However, slant drill holes are planned to penetrate the inferred dike below the vent area of one of the Inyo Domes during Autumn of 1984. Observations of joints and other fractures near this dike will elucidate the propagation mechanism.

Stresses near the dike tip are proportional to the square root of dike half-height divided by radial distance from the tip, $(a/r)^{1/2}$ (Lawn and Wilshaw, 1975). It is also proportional to the difference between the magma pressure and regional compressive stress acting across the dike plane, $(P_m - S)$. This driving pressure is a quantity about which we know very little. Nonetheless, we use an estimate of 1 to 10 MPa for the driving pressure and employ the criterion that the induced tensile stress must nullify the ambient compression ($S > 50$ MPa for depths > 2 km) and then exceed the tensile strength (1 to 10 MPa) of the host rock. This criterion leads to an estimate of the distance from the tip over which joints might form that ranges up to 0.01 times the dike height. For a dike from 1 to 10 km high the analysis suggests that joints might form at distances as great as 10 to 100 m from the tip. Drill hole observations will provide a direct measure of this distance.

The concentrated horizontal tensile stress σ_{11} (Fig. 4, inset) does not reach a maximum on the extension of the dike plane. Instead, two maxima exist on either side of the dike plane. This is illustrated in Figure 4, a graph of the horizontal stress induced by dike dilation normalized by driving pressure and plotted versus distance perpendicular to the dike plane. Distance above the dike tip is used as a parameter and all distances are normalized by dike half-height a. We suggest that vertical joints (Fig. 4, inset) form in response to these tensile maxima. This stress distribution provides an explanation for the formation of joints on either side of the

plane of a dike. As dike propagation continues, the joint set formed in this manner is bisected and the joints become adjacent to the dike contact.

Sedimentary rocks outcropping near mafic dikes of the Colorado Plateaus province commonly display a systematic joint set parallel to those dikes (Delaney, et al., in prep.). At some localities a distinctive set of dike-parallel joints is spatially restricted to distances from the contact that are a small fraction of dike length or height. Spacing of these joints increases with distance from the contact. A map (Fig. 5) of an outcrop of Jurassic Summerville Formation west of the San Rafael Monocline in south-central Utah shows a set of joints adjacent to a northerly-striking diabase dike. The dike-parallel set truncates a younger, northeasterly-striking set of joints that is unrelated to the igneous event. The dike-parallel set is not found more than 10 m from the contact. Outcrops like that in Figure 5 and the analysis mentioned above have persuaded us that joint formation near a dike tip is common and important.

The formation of numerous microcracks in the process zone of a small fracture in laboratory specimens of rock increases the amount of energy required for the fracture to propagate by one to two orders of magnitude over that required for a single microcrack in a mineral grain (Friedman et al., 1972). We suggest that each joint of a dike-parallel, adjacent set is similar to the laboratory fracture. Therefore, the formation of multiple joints in the process zone of a dike would increase the energy required for dike propagation over that for the single fracture. Because there typically are 10 to 100 dike-parallel joints, we would expect the mechanical energy release rate to be one to two orders of magnitude greater for dike propagation than for laboratory fracture propagation under similar conditions.

Surface Cracking and Faulting Over a Dike

As a propagating dike nears the Earth's surface, the tensile stress concentra-

tion above its tip spreads outward and upward, intersecting the surface at two points to form secondary stress maxima (Fig. 6). The direction of maximum tension at the surface is horizontal and perpendicular to the strike of the dike. Patterns of open ground cracks and steeply-dipping normal faults can be related to this stress distribution above dikes (Pollard, et al., 1983; Fink and Pollard, 1983a). In general the secondary maxima will produce these extensional structures in two linear clusters that align with the strike of the dike and straddle the ground through which a fissure eruption may occur. The middle ground is subject to smaller tensile stresses and therefore may not crack or fault. However, this ground may be dropped down along flanking normal faults to form a graben. Beyond the two tensile maxima the stress decreases and small compressive stresses are induced at a distance somewhat greater than the depth to the dike center.

A "rule of thumb" for estimating the depth to a dike top has been derived and is illustrated in Figure 7. The spacing $\underline{w}$ between positions of maximum tension is plotted on this graph versus the depth to the dike top ($\underline{d}$ - $\underline{a}$). Both lengths are normalized by the depth-to-center of the dike $\underline{d}$. As the dike tip propagates upward from a fixed central depth the spacing decreases. We suggest that surface cracks form near the position of the maximum tensile stress if it is of sufficient magnitude to overcome the tensile strength of the surficial material. The "rule" indicates that the depth to the dike top falls in the range between one third and one half of the spacing between the innermost set of surface cracks.

Preliminary mapping (Fig. 8) of cracks and faults along the trend of the Inyo Domes suggests the presence of a dike underlying and parallel to the domes. Two series of prominent earth cracks (Benioff and Gutenburg, 1939) define a graben approximately 1.5 km wide which extends north from Mammoth Mountain towards the Inyo Craters and Domes. These cracks are parallel to the general alignment of

the domes (≃ N 07° W). However, structures in the immediate vicinity of the domes and on the surfaces of the domes indicate that the extrusions emerged from elongate conduits oriented approximately N 05° E to N 15° E. This relationship may indicate that the domes were fed by a single dike trending NNW that separated into NNE-trending segments as it approached the surface (Fig. 8). Segmentation and change in orientation is a common response of dikes to a systematic change in orientation of the horizontal principal stresses (Delaney and Pollard, 1981). This suggests that dike orientation beneath the Inyo Domes was influenced by local stresses, thus favoring the hypothesis that the dike propagated independently of pre-existing faults and joints.

References Cited

Anderson, E.M., 1938, Proc. Roy. Soc. Edinburgh, 58, 242.

Bacon, C.R., Duffield, W.A., and Nakamura, K., 1980, J. Geophys. Res., 85, 2425.

Bailey, R.A. and Koeppen, 1977, U.S. Geol. Survey Open File Map, 77-468.

Bailey, R.A., Dalrymple, G.B., and Lanphere, M.A., 1976, J. Geophys. Res., 81, 725.

Benioff, H. and Gutenburg, B., 1939, Bull. Seism. Soc. Amer., 29, 333.

Delaney, P.T. and Pollard, D.D., 1981, U.S.G.S. Prof. Paper 1202, 61 p.

Delaney, P.T. and Pollard, D.D., 1982, Amer. J. Sci., 282, 856.

Delaney, P.T., Pollard, D.D., Ziony, J.I., and McKee, E.H., 1985, (in prep.)

Fink, J.H., and Pollard, D.D., 1983a, Geology, 11, 458.

Fink, J.H., and Pollard, D.D., 1983b, EOS, 64, 898.

Friedman, M., Handin, J., and Alani, G., 1972, Int. J. Rock Mech. Min. Sci., 9, 757.

Hill, D.P., 1976, J. Geophys. Res., 81, 745.

Hoagland, R.G., Hahn, A.R., and Rosenfield, A.R., 1973, Rock Mech., 5, 77.

Lawn, B.R., and Wilshaw, T.R., 1975, Fracture of Brittle Solids, 204 p.

McGarr, A.M., 1982, J. Geophys. Res., 87, 9279.

Nakamura, K., 1977, J. Volc. Geotherm. Res., 2, 1.

Pollard, D.D., 1973, Tectonophysics, 19, 233.

Pollard, D.D., Delaney, P.T., Duffield, W.A., Endo, E.T., and Okamura, A.T., 1983, Tectonophysics, 94, 541.

Rundle, J.B. and Whitcomb, J.H., 1984, (in prep.)

Sanders, C.O. and Ryall, F., 1983, Geophys. Res. Letters, 10, 2597.

Savage, J.C. and Cockerham, R.S., 1984, J. Geophys. Res., (in press)

Savage, J.C. and Clark, M.M., 1982, Science, 217, 531.

Steeples, D.W. and Iyer, H.M., 1976, J. Geophys. Res., 81, 849.

Wilson, G., 1970, Geol. Assoc. London Proc., 81, 595.

Zoback, M.L. and Zoback, M., 1980, J. Geophys. Res., 85, 6113.

Figure Captions

Figure 1. Plot of stress ratio $\underline{R}$ versus angle α between $\underline{x}_1$ axis and direction of remote principal stress σ^r_1. Curve separates region where dilation of plane of weakness is possible from region where dilation is not possible by magma at pressure $\underline{P}_m$.

Figure 2. Plot of shear to dilational displacement ratio $\underline{u}_2/\underline{u}_1$ versus angle α with stress ratio $\underline{R}$ as parameter. Displacements are calculated at center of dilating plane of weakness.

Figure 3. Schematic illustration of region near the tip of a vertical dike. Dotted curves outline process zone in which joints form. With continued propagation these joints become adjacent to dike contact.

Figure 4. Plot of change in horizontal stress σ_{11} from the ambient value $\sigma_1{}^r_1$ versus distance perpendicular to dike $\underline{x}_1$ with distance above dike $\underline{x}_2 - \underline{a}$ as a parameter. Stress is normalized by driving stress $\sigma_1{}^r_1 - \sigma_1{}^c_1$ and distance by dike half-height $\underline{a}$.

Figure 5. Map of sandstone outcrop with vertical dike-parallel joint set and diabase dike. Sandstone is member of Jurrassic Summerville Formation in south central Utah.

Figure 6. Contour map of maximum tensile stress near dike tip at shallow depth. Magma driving pressure is 1 MPa, gravitational gradient is 0.025 MPa/m, and dike is 100 m high. Short dashed lines are perpendicular to contoured stress in region of tension and indicate orientation of possible secondary cracks.

Figure 7. Plot of spacing between ground cracks $\underline{w}$ versus depth-to-dike-top ($\underline{d} - \underline{a}$), with both distances normalized by depth to dike center $\underline{d}$. Spacing of the two tensile maxima computed from the elastic model is compared to "rule-of-thumb" estimates.

Figure 8. Schematic illustration of segmented dike. Arrows indicate rotation of least compressive stress with depth about the dike propagation direction.

Figure 9. Sketch map of Inyo Domes area showing NNE trend of surfacial structures (paired dashed lines) and NNW trend of domes.

Figure 1

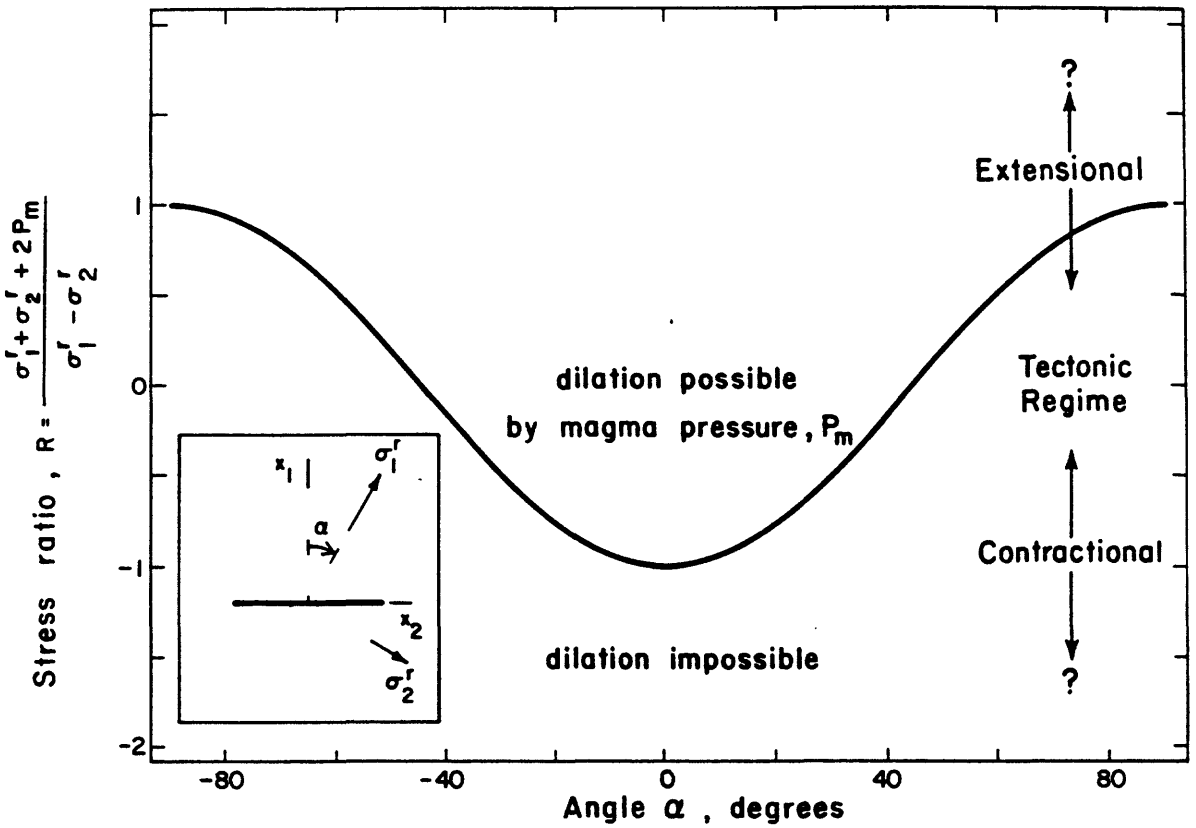

Figure 2

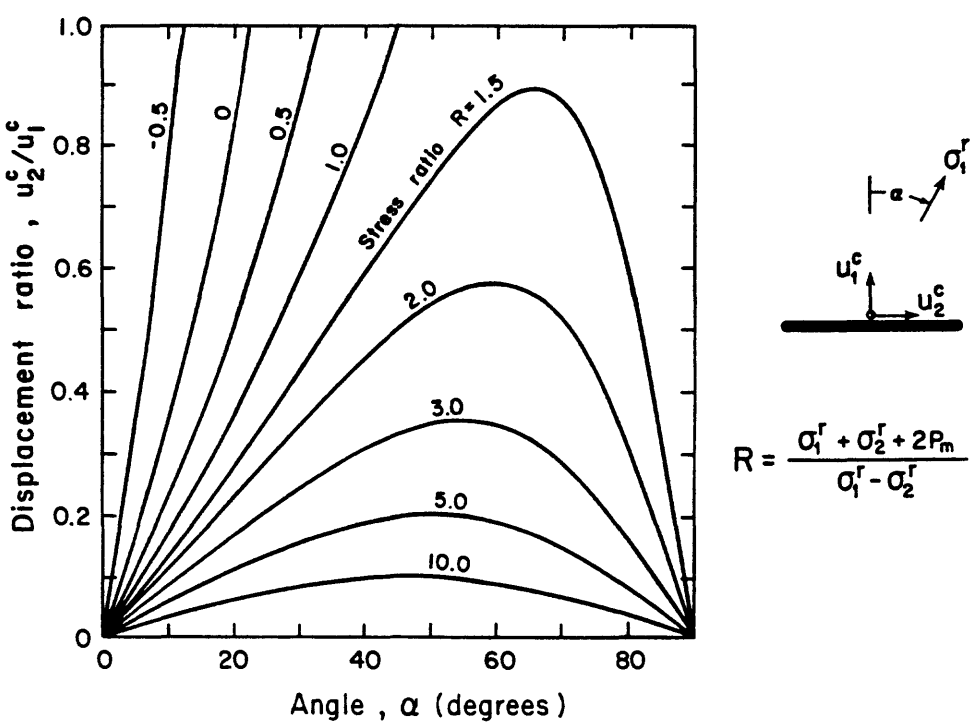

Figure 3

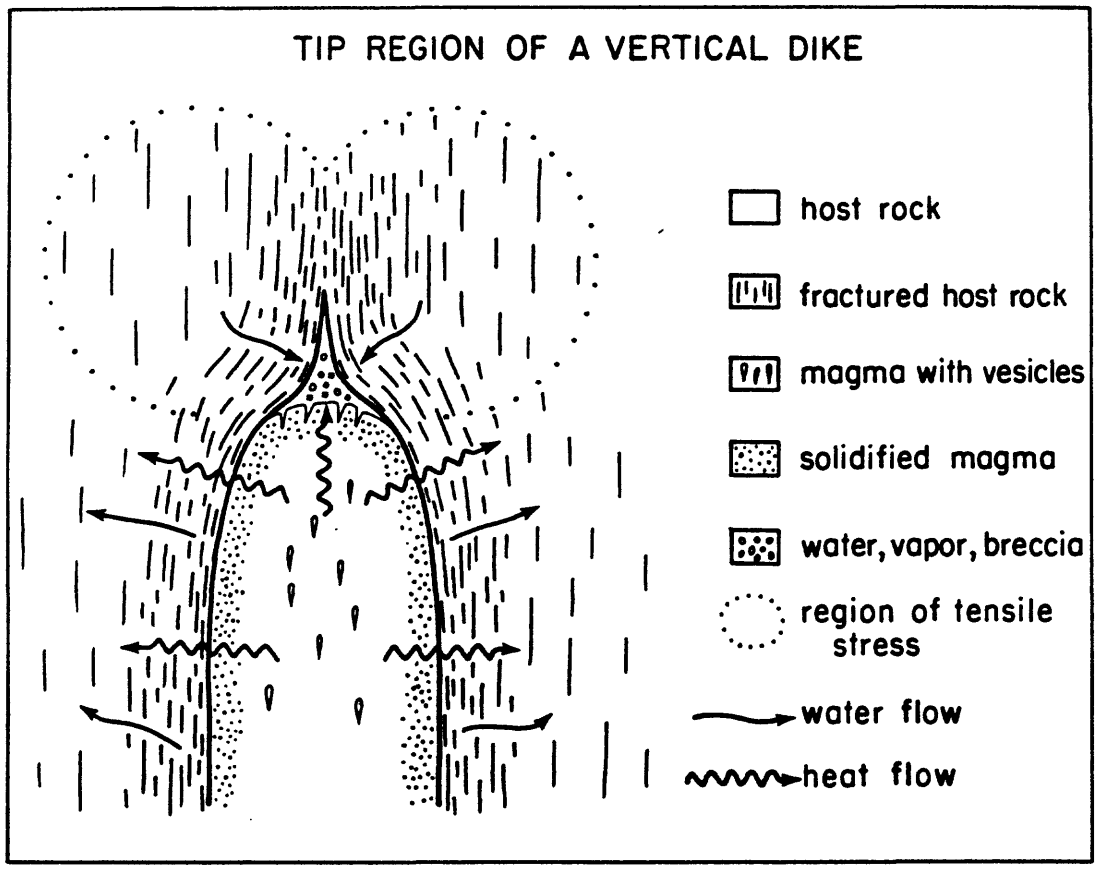

Figure 4

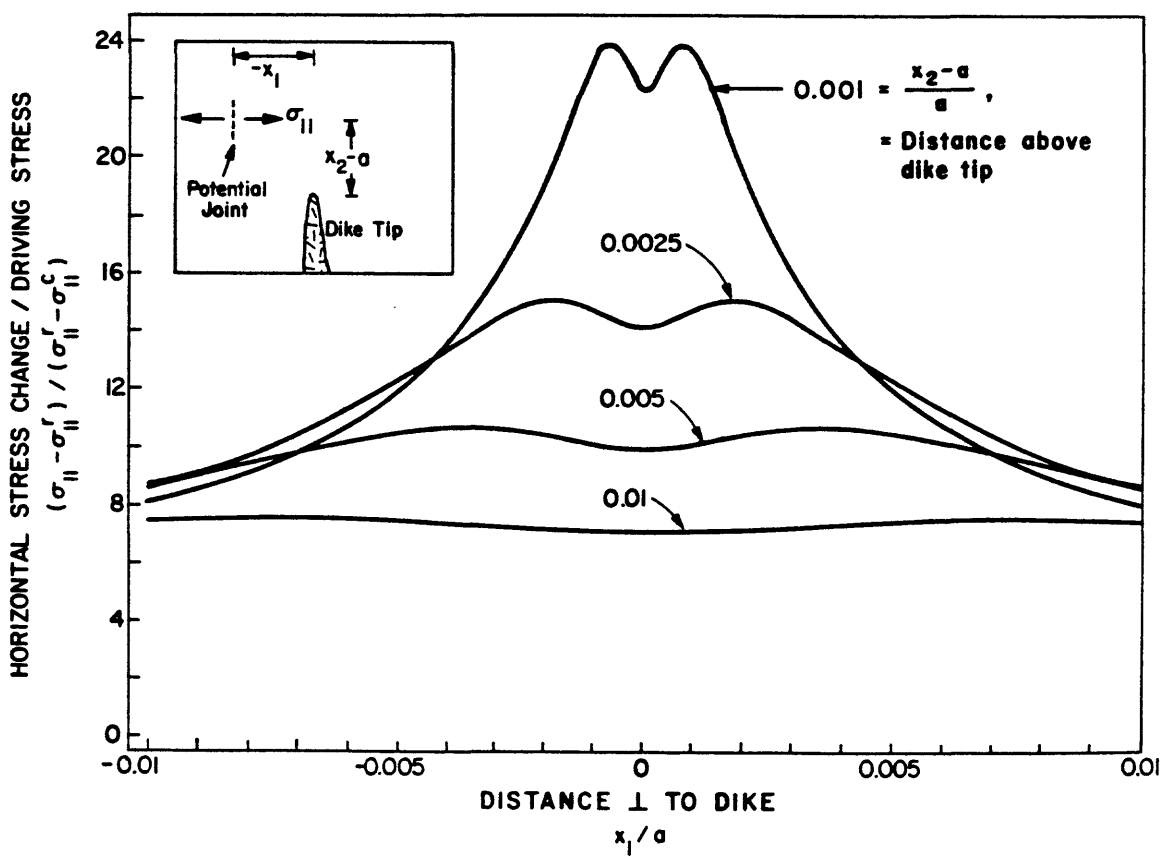

Figure 5

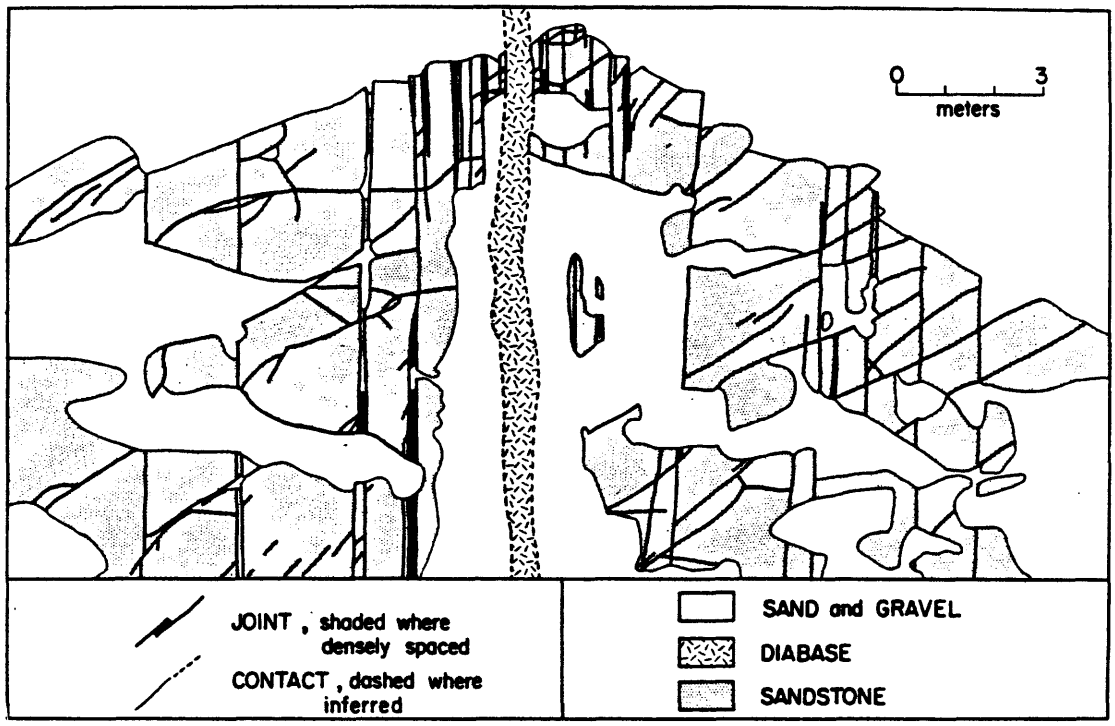

Figure 6

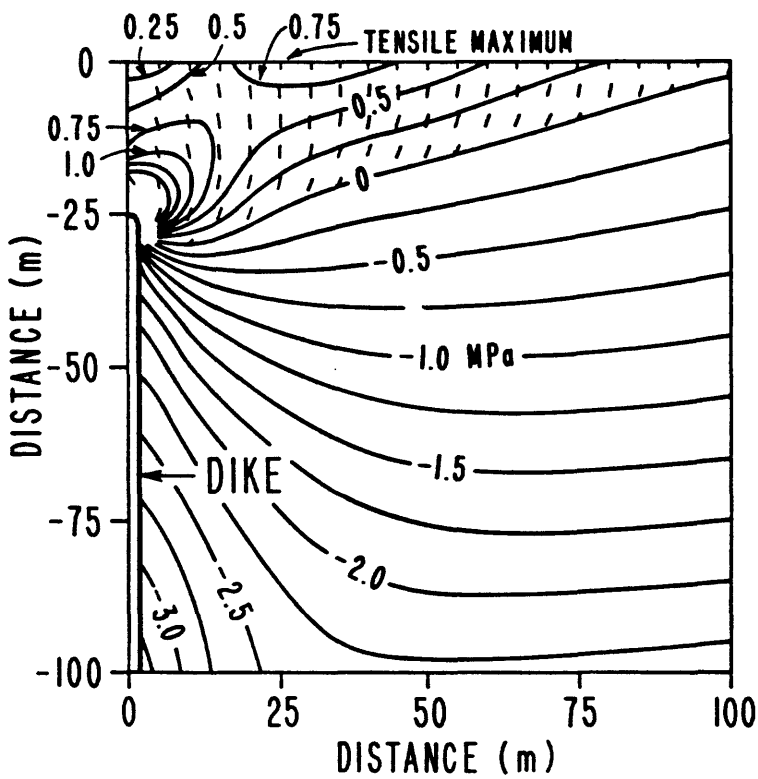

Figure 7

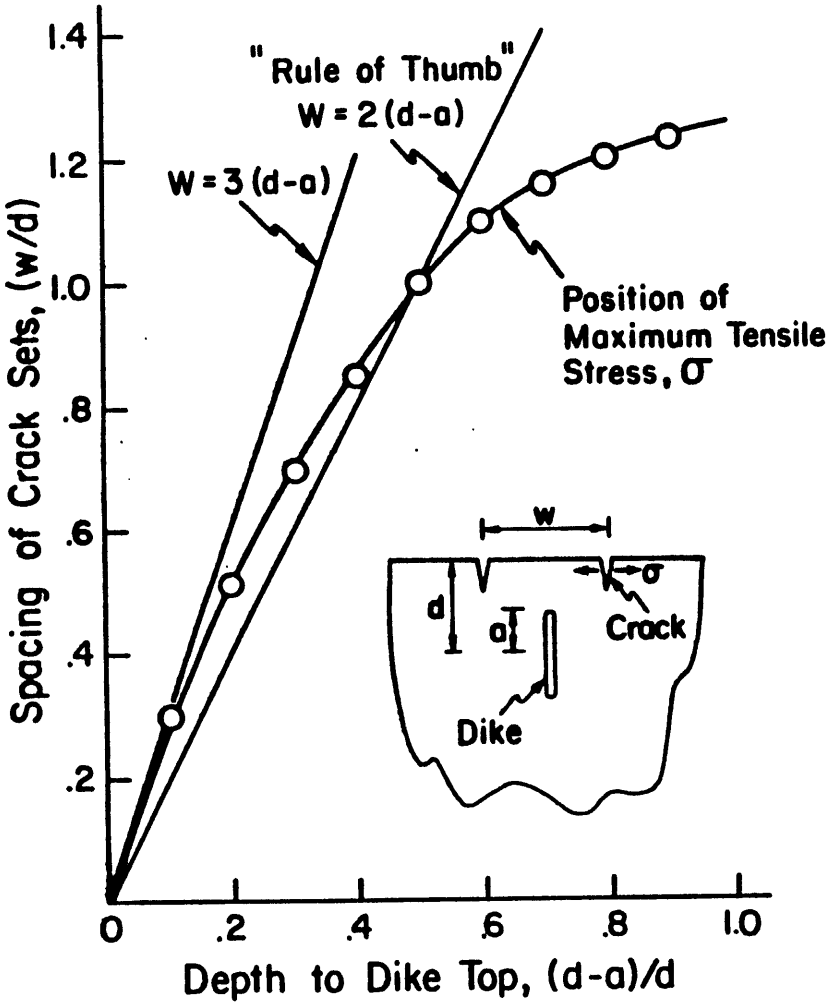

Figure 8

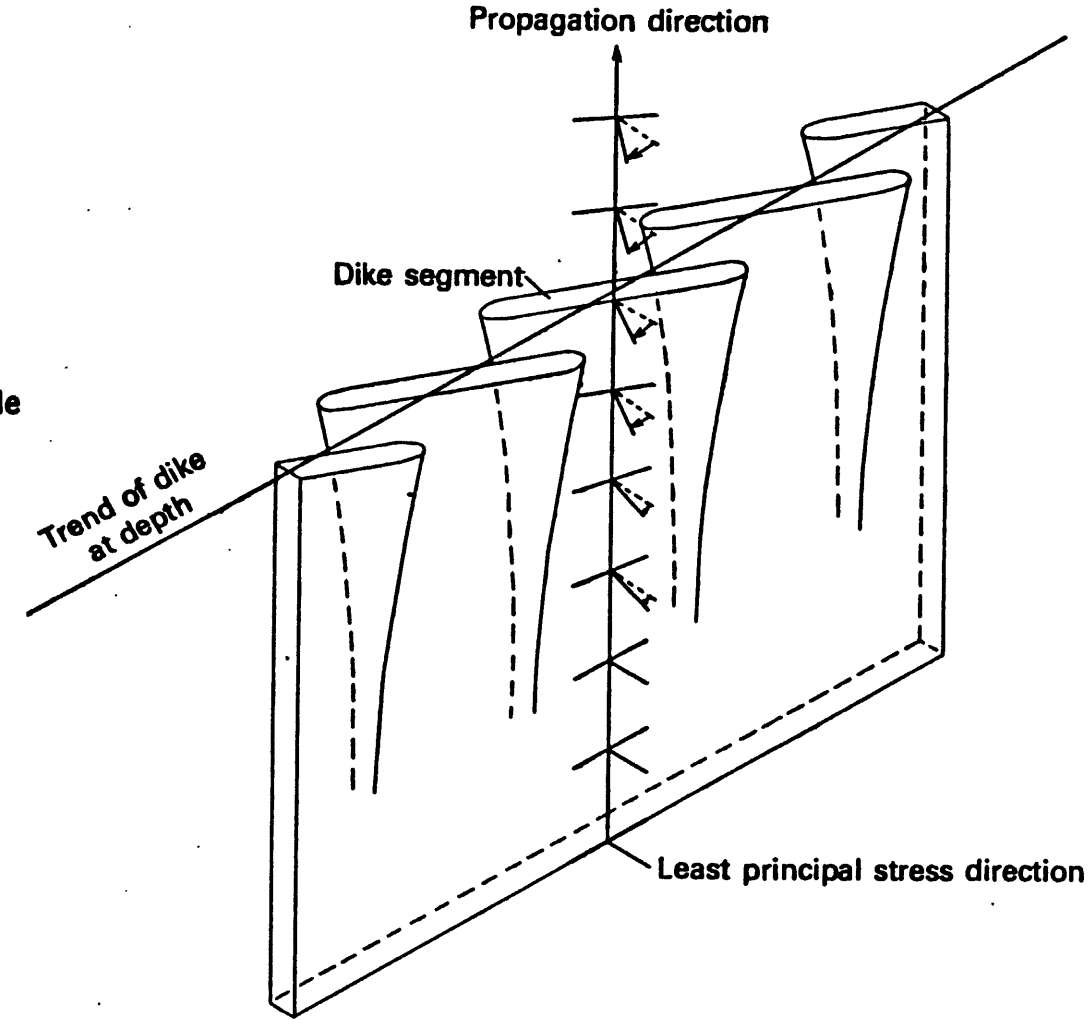

Figure 9

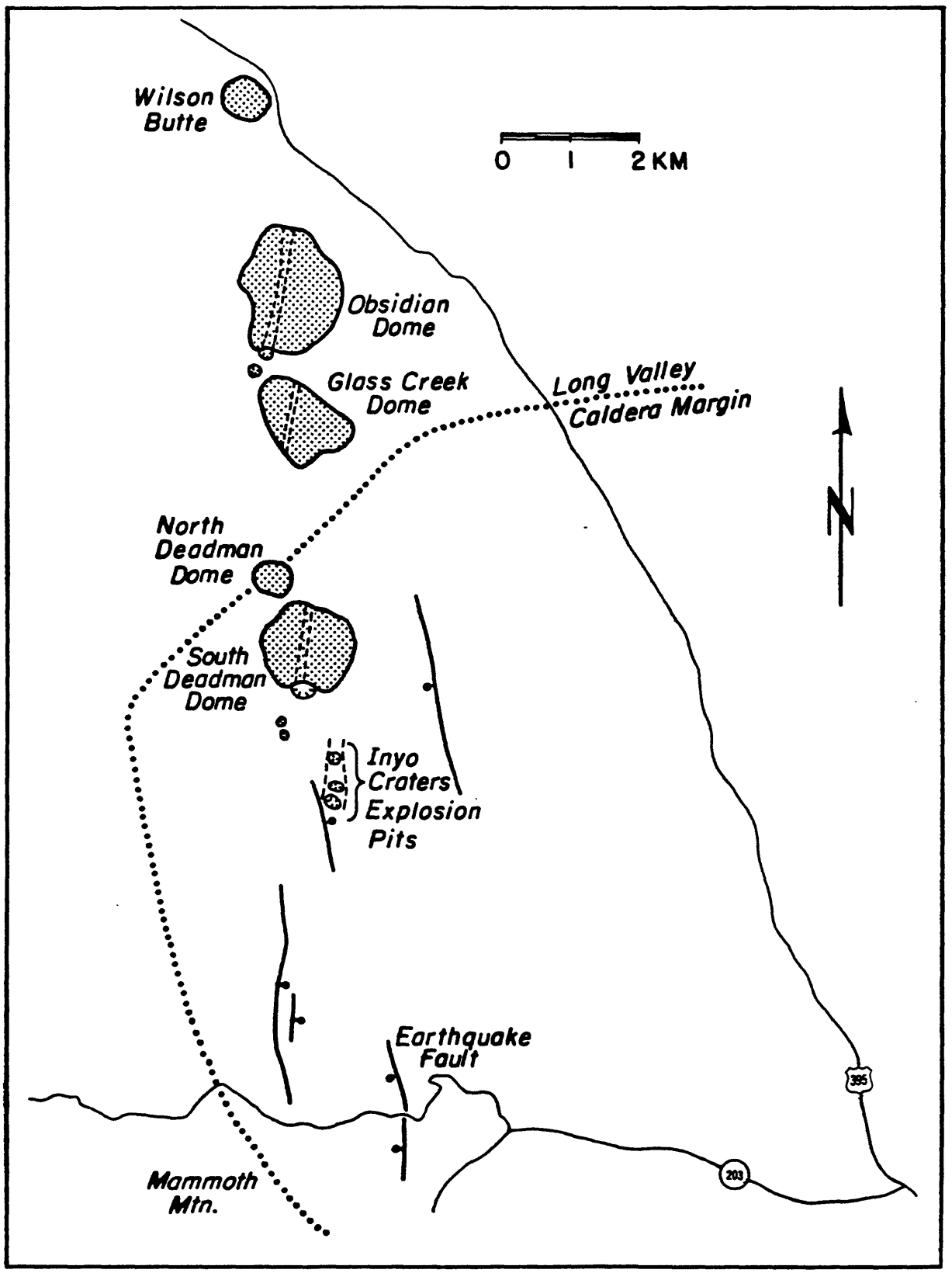
Wilson Butte
0 1 2 KM
Obsidian Dome
Glass Creek Dome
Long Valley Caldera Margin
N
North Deadman Dome
South Deadman Dome
Inyo Craters Explosion Pits
Earthquake Fault
395
203
Mammoth Mtn.

DEGASSING OF MAGMA IN AN OBSIDIAN FLOW AND INFERRED DEGASSING BEHAVIOR AT DEPTH

J. C. Eichelberger and H. R. Westrich
Sandia National Laboratories
Albuquerque, NM 87185

The questions of what volatiles are present in magma and how they are released are closely related to the question of why magmas erupt as they do, sometimes explosively and sometimes effusively. Quenched samples of volatile-bearing magma are provided by dense glasses or obsidians, which represent materials that have been chemically closed since the time of cooling and which occur in tephra as well as flows. Investigation of obsidians from individual small volume rhyolitic sequences, including those of Inyo Domes and Mono Craters, indicate that with the normal progression from explosive to non-explosive events there is a decline in water content from 2-3 wt. % to 0.2 wt. % (Eichelberger and Westrich, 1981) and a corresponding change in hydrogen isotope composition from heavy to light (Taylor et al., 1983; e.g., -65‰ δD to -120‰ δD). The relationship between δD and water content, which can be explained by melt/vapor isotope fractionation, the correspondence of water content of late erupted material with the solubility of water in melt at 1 atmosphere water vapor pressure, and the difficulty in postulating the existence of rhyolitic magma with 0.2 wt. % H_2O suggests that the observed eruption sequences reflect the progressive degassing of rhyolitic magma toward equilibration with surface conditions.

In order to fully describe the end point of this process, a hole was cored through the southern portion of Obsidian Dome in the Inyo chain. The hole penetrated the flow at a site where its thickness is 54.9 m, and continued through Inyo tephra, colluvium, Bishop Tuff, and additional colluvium to bottom in precaldera andesite at 152 m. Except for the upper crust and basal breccia zone, core recovery within the flow was close to 100%.

Stratigraphy of the flow, as defined by distribution of vesicles, fractures, devitrified rhyolite, devitrification textures and orientation of flow banding, is surprisingly complex, although some zones are repeated in the upper and lower portions of the flow. This stratigraphy must reflect the combined effects of downward increasing pressure through the section and inward decreasing cooling rate upon magma which was initially rather uniform. In general, vesicle content decreases downward and glass content decreases inward. The uppermost zone is finely vesicular light gray pumice, characterized by open fractures and steeply dipping flow banding. This material does not occur again in the flow, except as blocks in the basal breccia. At 11.0 m there is an abrupt transition to dense obsidian (actual contact not recovered). This is the same level at which the uppermost obsidian is exposed at the flow margin. At 14.5 m the massive obsidian becomes interbanded with increasing amounts of coarsely vesicular obsidian. In the interval from 17.4 m to 20.4 m no dense glass bands are present. From here downward however, significant changes occur. At 19.5 m, flow banding turns from steep to almost flat over a distance of a few centimeters. At 20.5 m, devitrified material first appears. Density increases abruptly near 21.5 m and the last coarsely vesicular band occurs at 22.6 m. From 21.5 m to 35.3 m is the upper lithophysal zone. This zone is dominantly dense obsidian, although in downward decreasing proportion, and is characterized by pink and gray spheroidal regions of devitrification encasing large, angular, crystal-lined voids. Typical radii of the

lithophysae are 0.5 to 3 cm. Volume-pressure-water content relationships suggest that the voids can be attributed to vapor exsolution during high temperature devitrification. From 22.6 m to 40.2 m the flow is entirely devitrified, but the texture is very different from the lithophysal zones. This interval is finely vesicular and prominently flow banded. Bands of similarly textured material occur above and below this zone and increase in abundance toward it. From 40.2 m to 42.7 m is the lower lithophysal zone, with downward decreasing lithophysae. At 44.5 m, flow banding changes from flat to contorted, probably marking entry into the thoroughly welded portion of the basal breccia. The first obvious welded breccia texture occurs at 46.5 and the first open fractures were encountered at 47.8 m. Finally, from 47.9 m to 54.9 m the flow consists of loose blocks of obsidian and finely vesicular pumice.

In order to determine degassing behavior of extruded magma, obsidian samples were prepared from 2 to 4 cm segments of core (obsidian was hand-picked from devitrified material where necessary) selected at average intervals of 2 m, and analyzed for water content. Four samples were separately prepared from each segment as a test of homogeneity. In general, the span of results for a single core segment was less than 0.05 wt %, although in a few cases (from the zone described below) it was as large as 0.1 wt. %, much larger than analytical error. Except for samples in the interval from 15.6 m to 21.2 m, mean water content is 0.21 $\pm$ 0.02 wt. % (10 core segments; compare with 0.21 $\pm$ 0.03 wt. % for massive obsidian from flow margin). Within the anomalous zone, which corresponds to the occurrence of vesicular bands in the obsidian, mean water contents of dense glass to 0.33 $\pm$ 0.02 wt. % and of vesicular glass to 0.48 $\pm$ 0.05 wt. % occur.

The narrow band of values observed in most of the obsidian corresponds to the solubility of water in melt at 1 atmosphere water vapor pressure and about 800°C. If it is assumed that the solubility of water in melt increases with the square root of water fugacity and that vapor pressure should equal melt pressure within the flow, then the water concentration profile in the flow lies well below the solubility curve except for the vesiculated glass, which lies close to the curve. Thus, water content of the anomalous zone is consistent with vapor saturation and the presence of bubbles, while the bulk of the magma was strongly vapor undersaturated at the time of cooling, and had in fact equilibrated with surface (atmospheric) vapor pressure.

Any process postulated for degassing as represented by this flow must account for the complete absence of bubbles in much of the degassed material and the apparent chemical equilibration of the system at a vapor pressure much less than lithostatic load at the time of cooling. Clearly, the system must have been chemically open during shallow intrusion and/or eruption. The most likely means by which this could occur is for the magma to have been in the form of a permeable foam, as represented by the quenched pumiceous carapace. Water would escape from such a system by diffusing a distance of the order of 10^{-6} m out of bubble walls into a free vapor phase, and then flowing through interconnected bubbles to the surface. Vapor pressure would deline below load on the system provided the foam is sufficiently permeable and rigid so that gas flow is rapid compared to bubble collapse. Once bubble collapse begins, the system becomes chemically closed, vapor pressure rises, and residual vapor is resorbed with the result that the bubbles disappear as pressure equilibrium is approached. The process is analogous to welding in tuff sheets, except that degassing is due solely to permeability of the system rather than permeability and fragmentation. Indeed, water contents observed in the bulk of Obsidian Dome

are essentially identical to those observed in obsidian in young welded tuff (0.20 ± 0.01 wt. %, Wineglass Tuff, Crater Lake).

Data from the Obsidian Dome hole pertain to degassing of magma which was extruded on the surface and emplaced under loads up to 10 bars. One approach to determining degassing behavior of magma at depth is to analyze obsidian from exposed conduits. Data from an exposed vent near Obsidian Dome in Mono Craters indicate degassing to atmospheric pressure at depths up to 110 m or about 20 bars load (Eichelberger and Reece, 1983). However, it is usually difficult to establish the original depth of exposures and to obtain exposed intrusive glass uncontaminated by hydration. A more satisfactory approach is coring young intrusions. An approximately 500 m hole will be slant cored into the conduit of Obsidian Dome in July 1984 and will provide data on degassing of magma at 100 bars.

Pending direct data from depth, it is possible to infer behavior of intrusive magma from Obsidian Dome and Mono Craters results. Obviously, equilibration with atmospheric pressure observed to 100 m can not continue downward indefinitely. Indeed, obsidians with water contents implying vapor pressures of hundreds of bars are ejected during explosive events. On the other hand, disequilibrium between vapor pressure and lithostatic load during degassing would be expected to extend to depth, and appears necessary to explain the existence of the bubble-free obsidian clasts.

The relationship between lithostatic load and vapor pressure in the system is particularly important, because it determines whether an explosive event is possible. In a stagnant system, such as in a lava flow or intrusion, load is constant and loss of vapor causes vapor pressure to decline below the lithostatic value. An explosive eruption cannot then occur, unless the overburden is suddenly removed as happened at Mount St. Helens (e.g., Hoblitt et al., 1981; Eichelberger and Hayes, 1982). There is no evidence in the Inyo and Mono tephras that second boiling following shallow emplacement led to increased vapor pressure and explosive activity.

In an actively rising system, load on the magma declines. Lowering of vapor pressure to achieve new equilibrium can be accomplished by expansion of bubbles and by leakage of vapor from interconnected bubbles. Expansion of bubbles is apparently limited to 70-80 vol. % of the system by interference between neighboring bubbles (Sparks, 1978). Thus, if magma rises from a state of initial equilibrium so that load on the system declines faster than gas flow can bleed off vapor pressure, a condition in which internal vapor pressure exceeds confining pressure can be achieved and lead to fragmentation and explosive eruption. The common sequence from explosive to non-explosive behavior within an episode may therefore be attributed to short residence time of early erupted magma at shallow depth and longer shallow residence (slow rise or prolonged stagnation) of later erupted batches, rather than to initial (pre-intrusion and eruption) variation in volatile content. Based on the highest volatiles contents observed thus far in Inyo and Mono glasses (2 wt. %), degassing should have begun at depths less than 1 km. However, if the magma initially contained more water or significant quantities of other less soluble components such as CO_2, degassing could have begun much deeper.

In summary, data from fresh Inyo and Mono glasses sampled at shallow depth require rapid degassing of intact magma during intrusion and eruption, probably by escape of vapor from permeable magmatic foam. The extent of vapor loss during ascent is the likely cause of changes in eruptive behavior during small to moderate volume rhyolitic eruption episodes.

References

Eichelberger, J. C., and D. B. Hayes, Magmatic model for the Mount St. Helens blast of May 18, 1980, J. Geophys. Res., 87, 7727-7738, 1982.

Eichelberger, J. C., and M. Reece, Degassing of magma in a conduit (abs.), EOS, 64, 895, 1983.

Eichelberger, J. C., and H. R. Westrich, Magmatic volatiles in explosive rhyolitic eruptions, Geophys. Res. Lett., 8, 757-760, 1981.

Hoblitt, R. P., C. D.miller, ,and J. W. Vallance, origin and stratigraphy of the deposit produced by the May 18 direct blast, U.S. Geol. Surv. Prof. Pap., 1250, 401-420, 1981.

Sparks, R. S. J., The dynamics of bubble formation and growth in magma: A review and analysis, J. Volcanol. Geotherm. Res., 3, 1-38, 1978.

Taylor, B. E., J. C. Eichelberger, and H. R. Westrich, Hydrogen isotopic evidence of rhyolitic magma degassing during shallow intrusion and eruption, Nature, 306, 541-545, 1983.

Constraints on the Upper Crustal Structure of the Long Valley-Mono Craters Volcanic Complex, Eastern California, from Seismic-Refraction Measurements

David P. Hill, E. Kissling*, J. H. Luetgert, and U. Kradolfer*

U.S. Geological Survey
345 Middlefield Road
Menlo Park, California

*Permanent address:
Institut fuer Geophysik
ETH - Hoenggerberg
CH-8093 Zuerich
Switzerland

ABSTRACT

Interpretations of four seismic refraction profiles in the tectonically active area between the eastern Sierra Nevada and the Basin and Range Province are presented. The four profiles sample the upper 7-10 km of the crust within the western half of Long Valley caldera, the Mono Craters ring fracture system and the "normal" crust north and northeast of Long Valley. The entire area observed shares a common crystalline basement consisting primarily of Mesozoic granitic rocks. At a depth of 2 km beneath the topographic surface, the P-wave velocity is uniformly 5.6 km/sec beneath which the velocity increases with a gradient of about 0.1 sec^{-1}.

Clear secondary arrivals observed on a profile crossing the west part of the caldera provide further evidence for a reflecting boundary at a depth of 7 to 8 km beneath the west margin of the resurgent dome, which was initially identified and interpreted as the top of a magma chamber by Hill (1976).

Structural details resolved in the upper 2 km of the crust lead to the following conclusions.

1) P-wave velocities in the the crystalline basement at depths shallower than 2 km vary from 3.6 km/sec to 5.0 km/sec. This variation reflects differences in the degree of fracturing of the upper portion of the basement.

2) An apparently homogeneous basement in the upper 7 to 10 km beneath the Mono Craters ring fracture system indicates that any extensive magma chamber must be at least 10 km deep there.

3) The down-dropped crystalline basement beneath the western half of Long Valley caldera dips gently (5 to 10°) to the northeast. Apparent offsets along steeply-dipping caldera-bounding faults are 1.0 to 1.7 km along the northern, western and southern sides of the caldera with largest offsets in the north.

4) Rocks forming the caldera fill fall into essentially three P-wave velocity groups. From the surface downward these velocity groups are: 100 to 400 meters of 1.2 to 1.8 km/sec material corresponding to unconsolidated fluvial or lacustrine deposits or highly fractured rhyolite flows, 200 to 400 meters of 2.8-3.1 km/sec material corresponding to sparsely jointed post-caldera rhyolite, rhyodacite and basalt flows, and approximately 1000 meters of 3.9-4.4 km/sec material corresponding to deposits of Bishop tuff.

INTRODUCTION

Knowledge of the overall crustal structure of the Long Valley-Mono Craters region is one of several critical elements needed for a proper understanding of the tectonic and magmatic processes operating there. As a further step in refining our knowledge of the structure of the upper 5 to 7 km of the crust, we carried out a series of high-resolution seismic-refraction profiles across the Mono Craters region and the Long Valley caldera during the summers of 1982 and 1983. In this initial paper, we present our interpretation of the detailed variations in structure beneath the Mono Craters, a "normal" section of crystalline crust to the east of Mono Craters, and the west-central section of Long Valley caldera. The latter includes new evidence for a reflecting boundary beneath the western margin of the resurgent dome in the caldera. This reflecting boundary was first identified on a 1973 seismic-refraction profile (Hill, 1976) and interpreted as possibly representing the top of the Long Valley magma chamber at a depth of 7 to 8 km.

The basic properties of the shallow crustal structure in the Mono Lake-Long Valley-Owens Valley region were initially defined by a series of seismic-refraction profiles and gravity measurements led by L. C. Pakiser in the late 1950's and 1960's (Pakiser and others, 1960; Pakiser, 1961; Pakiser and others, 1964; and Pakiser, 1970). Two sets of reversed and overlapping seismic-refraction profiles (Hill, 1976) and additional gravity measurements (Kane and others, 1976), which were carried out as part of a multi-disiplinary study of the Long Valley geothermal system in the early 1970's (Muffler and Williams, 1976), served to more tightly constrain the geometry of the caldera floor and the thickness of the overlying volcanic deposits within Long Valley caldera. An integrated analysis of the earlier seismic-refraction and gravity data by Abers (1984) further clarifies the geometry of the caldera boundaries. A teleseismic P-delay study of the caldera by Steeples and Iyer (1976) provided evidence for a large, low-velocity body at mid-crustal depths beneath the west-central section of the caldera, which they interpreted as the Long Valley magma chamber.

The structure of the mid-to-lower crust in the Long Valley region remains poorly defined. The crust along the eastern flank of the Sierra Nevada range is apparently transitional between the 50- to 60-km-thick crust beneath of the high Sierra Nevada (Eaton, 1966; Hill, 1978) and the 30 to 35 km thick crust of the adjacent Basin and Range province. Johnson's (1965) interpretation of a long-range seismic-refraction profile between Mono Lake and Lake Mead, Nevada, suggests that the crust beneath Long Valley is approximatly 40 km thick while an analysis of Pn delays recorded across the region from sources at the Nevada Test Site suggests a crustal thickness of only 30 km just northeast of Long Valley (Priestly and others, 1982).

Here we focus on details in the upper 10 km of the crust beneath the Mono Craters system and the western section of the

Long Valley caldera. Our approach is to first outline the 1982 and 1983 seismic-refraction experiments and then to present our interpretation of four of the 10 lines and fan profiles for which we have data. We conclude with a short discussion of our views on the significance of the results and some of the questions that we hope to address as we work with the data from the remaining profiles.

FIELD WORK

Field work for the seismic-refraction profiles described in this paper was carried out in the summers of 1982 and 1983 as part of a study funded by the Office of Basic Energy Science under the Department of Energy to evaluate the Mono Craters-Long Valley region as a possible site for deep scientific drilling in a thermal regime. Figure 1 shows the distribution of shot points and recording sites occupied during both field seasons. One hundred recording units were used in the 1982 field work (triangles in Figure 1) and a total of 120 recorders were used in 1983 (squares in Figure 1). These instruments are the self-contained, seismic-refraction recording units described by Healy and others (1982) and used in earlier experiments in, for example, Saudi Arabia (Healy and others, 1982), Yellowstone and the eastern Snake River Plain (Smith and others, 1982) and the Imperial Valley (Fuis and others, 1984). The shots were fired in 50- to 60-meter deep drill holes using 1,000 kilograms of class B explosives. A detailed description of the 1982 field work together with a complete set of record sections is provided in a report by Meader and Hill (1983). A similar report for the 1983 field work is in preparation.

The principal target of the 1982 seismic-refraction profiling was the Mono Craters ring fracture system, which Kistler (1966) and Bailey and others (1976) suggested may represent the early stages in the evolution of a major silicic volcanic system of the scale of the more mature Long Valley system. Little previous geophysical work had focused on the Mono Craters system, and an issue of some interest was whether we might find evidence for a large, youthful magma chamber at shallow depths beneath the central section of the ring fracture system.

In part to address this issue, the 1982 experiment was configured as two linear profiles with reversed and overlapping coverage that intersect near the center of the Mono Craters ring fracture system and trend in roughly north-south and east-west directions. As illustrated in Figure 1, the Casa-Mono profile extends northward for 50 km along Highway 395 from the southeast margin of the Long Valley caldera to the west shore of Mono Lake. The six shots along this profile were recorded by 92 stations at 0.5 km-spacing between shot points, and at 1 to 2 km-spacing along the unreversed extension beyond the northernmost and southernmost shot points (shot-points 6 and 1, respectively). The Pumice-Granite profile extends from the west edge of the Mono Craters ring fracture system (shot-point 7 at the base of the

Sierra Nevada escarpment) eastward for 80 km to Basalt, Nevada. Five shot points along this profile were recorded by 90 stations at 0.5-km intervals between shot points and 4 km intervals along the 40-km, unreversed extension of the profile beyond the easternmost shot point (shot point 10). The eastern half of the reversed section of this profile samples "normal" crystalline basement away from both the Mono Craters system and the Long Valley caldera.

The 1983 seismic-refraction profiling was focused on Long Valley caldera to improve resolution of the velocity structure in the seismically active south moat (the moat is the topographic low-land that surrounds the resurgent dome), the caldera-bounding ring-fracture system, and the resurgent dome. Additional objectives included further evidence for the 6 to 7 km-deep reflecting boundary beneath the northwestern margin of the resurgent dome found in the 1973 data (Hill, 1976) and evidence for a cupola-shaped protrusion of the magma chamber extending to within 4.5 to 5 km of the surface beneath the southwestern margin of the resurgent dome indicated by Sander's (1984) analysis of anomalous attenuation patterns of P- and S-waves from local earthquakes.

Of the five reversed profiles established during the 1983 field work, we will consider two in this paper: 1) the 30-km-long Convict-Cowtrack profile that extends northward from shotpoint 15 at the southern margin of the caldera across the east side of the resurgent dome and north moat into the "normal" crystalline crust to the north and shotpoint 9 of the 1982-east-west profile , and 2) the 20-km-long Minaret-Bald profile that extends southwestward from the northern margin of the caldera (shotpoint 16) to Minaret Summit on the western margin of the caldera (shotpoint 11). Nominal station-spacing along both profiles was 0.5 km.

INTERPRETATION

Method

To obtain the models for seismic P-wave velocity structure presented in this paper, we use a two-dimensional, iterative ray-tracing technique in which ray paths and P-wave traveltimes are calculated for successive models until the computed traveltimes provide a satisfactory fit to the observed arrival times. We regard a fit as satisfactory when the difference between computed and observed traveltimes is less than 0.05 sec. Although we did not uniformly achieve this precision for all data points on all profiles, we estimate that 90% of the data are fit to within +/- 0.05 sec.and 99% to within +/- 0.1 sec. On each of the profiles, we were left with a few isolated points that, after reasonable effort, could not be fit any better than +/- 0.2 to 0.3 sec.

The particular ray-tracing algorithm used was developed by one of us (J.H.L.) as an extension of the technique described by Cerveny and others (1977) for calculating the propagation of rays through two-dimensional inhomogeneous media. Under this algorithm, ray paths through regions with continuous variations

in velocity are computed by the stepwise integration of the following system of first-order, ordinary differential equations:

$$dx(t)/dt = V(x,z) * \cos(u)$$
$$dz(t)/dt = V(x,z) * \sin(u)$$
$$du(t)/dt = (dV/dx) * \sin(u) - (dV/dz) * \cos(u),$$

where V(x,z) is the P-wave velocity at distance, x, and depth, z, t is time, and u is the angle of incidence measured with respect to the horizontal. By supplying a definition of V(x,z) and specifying initial values for x, z, t, and u, subsequent values of x, z, t, and u may be calculated by simultaneously integrating these equations over small steps in time. For the models presented here, we used a time step of 0.02 sec. Boundaries between lithologic units in the models may be represented by either first- or second-order discontinuities. When the computations along a specific ray encounter a first-order discontinuity in the model, Snell's law or the law of reflection is applied at the boundary for transmitted waves or reflected waves, respectively, and the step-wise integration of the above equations is then resumed.

The resolution and uniqueness associated with the two-dimensional models resulting from this forward, non-linear modeling process are difficult to quantify in a formal way. This is especially true for two-dimensional models based on linear profiles in a strongly three-dimensional structure such as the Long Valley caldera. Most of the profiles, however, are oriented more-or-less perpendicular to major structural features in the area so that contamination of the two-dimensional velocity structure by structures outside of the profile should not be a serious problem. An exception is the Minaret-Bald profile, which cuts obliquely across the caldera. In this case, the model may be partially contaminated by three-dimensional effects, particularly near the caldera boundaries at either end of the profile.

Based on trial and error perturbations in model parameters, we believe that, on average, P-wave velocities are resolved to about 5% and the depths to boundaries are resolved to about 10%. With the average station-spacing of 0.5 km and dominant P-wave frequency of 4 to 8 Hz, we may resolve, under optimum conditions, the position of pronounced lateral changes in structure to within a few hundred meters. In general, the resolution will differ from these average values with the variation in information density along each of the profiles. Thus, for example, the structure at depths from 1 to 5 km along the Casa-Mono and Pumice-Granite profiles has a better-than-average resolution because of the large number of intermediate shot points along these two profiles. In contrast, structure of the uppermost 200 to 300 meters midway between shot points is much more poorly resolved than the average.

The question of model uniqueness depends strongly on particular choices for phase correlations between groups of adjacent wavelets in the record sections and choices for ray

paths and refracting "layers" to which the groups of wavelets (traveltime branches) are associated. The greatest ambiguity in these choices involves the proper identification of traveltime branches for rays confined to the upper 1.0 to 1.5 km of the crust. There is little question that the first arrivals at distances beyond about 10 km from the shotpoints are associated with the 5.6 to 6.1-km/sec basement refractor. To minimize the ambiguity associated with these choices, we rely on independent information from surface geology and, where available, drillhole logs. We also require that the structures on intersecting profiles show reasonable agreement. Because of locally strong lateral variations within the caldera, however, these constraints are relatively soft. Information on the depth to a lithologic boundary from a drillhole only 0.5 km from a profile, for example, may leave the depth to the same boundary in the plane of the profile in question by perhaps 200 to 300 meters. Similarly, the condition that the models match where profiles cross is blurred because of possible contamination of the two-dimensional models by three-dimensional structures.

A constraint not used in this initial analysis of these selected profiles involves the information contained in the waveform amplitudes. The amplitude data, which we will incorporate in the final interpretation of the complete set of profiles, should help constrain velocity gradients within "layers" as well as the uncertainties in both phase correlations and the assignment of specific phase groups to a given traveltime branch.

Results

The data and interpretation for each of the four profiles considered in this paper are summarized in Figures 2 through 11 in terms of selected record sections, observed and computed P-wave traveltimes and ray diagrams for the associated model. The resulting P-wave velocity models are summarized in Figure 12.

Waveforms on the record sections throughout the region are characterized by impulsive first arrivals out to maximum recording distances of 60 km. The first-arriving P-wavelets are typically the largest phases in the P-wave coda, and on most of the record sections, the P-wave coda shows little coherent energy following the first arrivals. This is particularly pronounced in the record sections over the crystalline terrane north of the caldera indicating that the velocity structure there is dominated by a relatively smooth increase in velocity with depth and the absence of laterally continuous reflecting boundaries.

The first 0.5 to 1.0 sec of the P-wave coda for seismograms recorded within the caldera tends to be somewhat more complex than the comparable coda on seismograms recorded over crystalline terrane to the north. This is consistent with the caldera having a more complex crustal structure. An exceptional example is the record section from Shot Point 16 on the Minaret-Bald profile, which has a sharp, high-frequency arrival (Z 10 Hz) following a relatively low-frequency (Z 3 Hz) first arrival by roughly 0.5

sec at distances between 15 to 20 km from the shot point (Figure 11a). More generally, the record sections inside the caldera show hints of coherent wavelets in the P-wave coda with amplitudes approaching those of the initial wavelet.

Because of the general lack of clear secondary arrivals in the record sections, the interpretation we present here depends largely on the pattern of first-arrival traveltimes on reversed and overlapping traveltime curves along a given profile. In some cases, however, we have used the pattern of later arrivals in the vicinity of the more abrupt bends in traveltime curves as a qualitative constraint on transition zones and boundary sharpness.

Refering to Figure 12, the two most obvious aspects of the velocity structure on a broad scale are 1) the remarkably uniform depth of about 2 km beneath the topographic surface to a P-wave velocity of 5.6 km/sec common to all profiles, and 2) the pronounced lateral change in velocity in the upper 2 km of the crust coincident with the northern boundary of the caldera evident on the Casa-Mono and Convict-Cowtrack profiles in Figure 12 b, c. (Note that depths in the velocity models are with respect to sea level and that the surface elevation in the Long Valley region averages about 2 km above sea level.)

The "boundary" between 5.5 km/sec and 5.6 km/sec velocities that parallels the topographic surface at a depth of about 2 km lies entirely within the crystalline basement, and it most likely corresponds to the depth at which most of the micro-cracks in the crystalline basement are closed by the lithostatic pressure of the overlying rocks. The velocity below this "boundary" increases relatively slowly with a gradient on the order of 0.1 sec^{-1} to a velocity of 6.1 km/sec at a depth below the surface of 7 to 8 km. Above this 5.6 km/sec "boundary", velocities show considerable lateral variation and increase much more rapidly with depth than below the "boundary". The boundary itself seems to involve a small (0.1 to 0.2 km/sec) but abrupt increase in velocity (see for example Fig. 2).

The pronounced lateral change in velocity coincident with the northern boundary of the caldera (Fig. 12b and c) is associated with the large normal faults formed during collapse of the caldera 700,000 years ago (Bailey and others, 1976). The 1.4- to 1.6-km difference in depth to velocities of 4.8- to 5.0 km/sec across this boundary is a measure of the subsidence suffered by the northern section of the caldera floor during collapse of the caldera. To the north of this boundary, the crystalline basement, which consists of Cretaceous granitic rocks of the Sierra Nevada batholith, extends to within a few hundred meters or less of the surface. This terrane is sampled by the northern sections of the Casa-Mono and Convict-Cowtrack profiles and by the entire length of the Pumice-Granite profile. South of this boundary, the Casa-Mono and Convict-Cowtrack profiles and the entire central section of the Minaret-Bald profile sample the post-collapse volcanic rocks that fill the western part of Long Valley caldera.

Crystalline Terrane A veneer of rocks with P-wave velocities between 1.2 and 3.0 km/sec covers much of the crystalline basement north of the caldera. This low-velocity veneer varies in thickness from about 600 meters beneath Pumice Valley and the Mono Craters in the vicinity of Shot Point 5 to negligible accumulations where the granitic rocks are exposed at the surface near Granite Mountain west of Shot Point 9. The lower velocities (< 2.0 km/sec) in this veneer are associated with pumice and unconsolidated clastic deposits and the higher velocities (2.5 to 3.0 km/sec) with lava flows and, perhaps in some cases, partially consolidated sedimentary rocks. The edifice forming Mono Craters, for example, which consist largely of pumice and highly fractured rhyolite flows, has a bulk P-wave velocity of only 1.2 km/sec. Roy Bailey (personal communication, 1984) suggests that the 400 to 600 m of 2.9-to 3.0-km/sec material in Pumice Valley and beneath the Mono Craters probably consists of non-welded Bishop tuff underlain in some places by glacial till.

The absence of coherent secondary arrivals in the profile Pumice-Granite indicates that there exists no laterally extensive reflecting boundary beneath the Pumice Valley-Mono Craters ring fracture system in the uppermost 7 to 10 km. This result excludes the possibility of having a laterally extensive, shallow (<7 km) magma chamber beneath the Mono Craters.

P-wave velocities in the upper 500 to 600 meters of the crystalline basement vary significantly along the Pumice-Granite profile (Figure 12a). Where the granitic rocks are exposed over the local topographic high east of Shot Point 9, the velocities reach 4.0 to 4.1 km/sec immediately at the surface. Further to the east near shot point 10 and near the base of the Sierra Nevada escarpment at the western end of the profile, the top of the crystalline basement, which underlies 100 meters or less of low-velocity veneer, has a velocity of 3.5 to 3.6 km/sec increasing to 3.7 to 3.9 km/sec at depths of 500 to 600 meters. The P-wave velocity at the top of the crystalline basement 600 meters beneath Pumice Valley is a relatively high 4.9 km/sec.

The velocity structure of the crystalline basement on the northern sections of the Casa-Mono and Convict-Cowtrack profiles matches the basement structure along the Pumice-Granite profile at common Shot Points 5 and 9, respectively. In particular, the relatively high 4.9 to 5.0 km/sec velocity at the top of the crystalline basement beneath Pumice Valley continues southward toward Long Valley caldera on the Casa-Mono profile as does the somewhat lower, 4.0-to 4.2-km/sec velocity south of Shot Point 9 on the Convict-Cowtrack profile (Figure 12 b, c). In both cases, the crystalline basement rises beneath the Bald Mountain-Glass Mountain highland along the north side of the caldera with the P-wave velocities reaching 4.8- to 5.0-km/sec at depths of 200 to 400 meters beneath the topographic surface.

This variation in velocity within the upper few hundred meters of the crystalline basement is reflected in the local

Bouguer gravity field (see Oliver and Robbins, 1978), which, for example, shows a 5 to 10 milligal gravity high centered over the highland east of Shot Point 9 where 4.0-km/sec basement is exposed at the surface along the Pumice-Granite profile. Both the local gravity field and the variations in the shallow P-wave velocities most likely reflect differences in fractured state of the shallow crystalline basement.

Long Valley Caldera Within the western section of Long Valley caldera, the top of the crystalline basement has a P-wave velocity of about 5.0 km/sec, and it is covered by 1.5 to 2.0 km of rocks with lower P-wave velocities that represent the caldera-fill (Fig. 12d). The depth to basement is greatest beneath the northwestern margin of the resurgent dome along the Minaret-Bald profile (Figure 12d). Here also, the depth to the 5.6-km/sec boundary within the crystalline basement is nearly one km deeper than the 2-km depth (beneath the topographic surface) common elsewhere in the area.

P-wave velocities of rocks forming the caldera-fill cluster in essentially the same three groups found in the earlier work (Hill, 1976). With increasing depth these velocity groups and the associated rock types are:

1) a 1.2- to 1.8-km/sec surficial layer generally less than 100 meters thick but locally as thick as 400 meters, which corresponds to loose accumulations of pumice, highly fractured rhyolite flows, and unconsolidated fluvial and lacustrine deposits.
2) a 2.8- to 3.1-km/sec layer with thicknesses between 200 and 400 meters, which corresponds to sparsely-jointed, post-caldera rhyolite, rhyodacite, basalt flows, and non-welded Bishop tuff deposits (Bailey and others, 1976).
3) a 3.9- to 4.4-km/sec layer roughly 1 km thick, which corresponds to welded deposits of the Bishop tuff within the caldera.

The above association of velocity groups with rock types is based on both geologic field relations (Bailey and others, 1976) and logs from drill holes that penetrate the Bishop tuff at several sites within the caldera (Sorey and others, 1978; Abers, 1984). The first two of these velocity groups and rock types are also observed in the veneer of low-velocity rocks covering the crystalline basement north of the caldera (Fig. 12a and 13).

The structure within the caldera fill illustrated in Figure 12 re-enforces the general character of the structure inferred from the 1973 profiles (Hill, 1976; Abers, 1984). In particular, relief on the upper surface of the Bishop tuff forms a somewhat exaggerated version of the topographic relief of the resurgent dome. As illustrated in Figure 12b,c, the depth to the top of the welded Bishop tuff (3.9 to 4.4 km/sec) decreases from 600 to 700 meters beneath the north moat to about 300 meters beneath the central part of the resurgent dome. The overlying post-caldera lava flows (2.8 to 3.1 km/sec) and unconsolidated rocks (1.2 to 1.8 km/sec) are thickest within the north moat and in the eastern

part of the south moat. The improved resolution afforded by the 1982 and 1983 data help clarify some of the structural relations left unresolved by the earlier data.

The location of the caldera-bounding faults and the offset of the crystalline basement across these faults at the northern wall of the caldera, for example, is much more tightly constrained by Casa-Mono and Convict-Cowtrack profiles than by the more sparsely-sampled Convict-Sand profile of 1973 (B-B' in Figure 8 in Hill, 1976). We interpret the strongest horizontal gradients in our P-wave velocity models of the north margin of the caldera as marking the approximate position of the caldera-bounding faults. The span of these strong gradients is indicated in Figure 13b,c,d by a double line, and we assume that most of the subsidence of the caldera floor took place along one or more subparallel, steeply-dipping faults within the span defined by these strong gradients. The configuration of the strongest horizontal velocity gradients suggests that the caldera-bounding faults dip steeply toward the center of the caldera and that they intersect the surface near the topographic scarp of the caldera wall (Figure 13). A notable exception to this pattern is the strong horizontal contrast in P-wave velocity in the upper 200 to 300 meters directly beneath shot point 16 on the Convict-Cowtrack profile. This abrupt decrease in velocity from 3.0 km/s north of the shot point to 1.2 km/s south of the shot point occurs approximately 3 km south of the topographic scarp expression of the caldera wall (Figures 8, 12b, 13c). Whether this shallow offset in 2.8 to 3.1 km/sec rocks is related to the major caldera-bounding faults is not clear. Abers (1984) concludes that the caldera-bounding faults are systematically located 3 to 4 km inward from the present-day topographic expression of the caldera wall based on his combined analysis of the 1973 refraction data and gravity data. A combined interpretation of the more recent refraction data and the gravity data should help clarify the relation between the topographic caldera wall and the major caldera-bounding faults. The total offset of the crystalline basement across this fault system along the north wall of the caldera appears to be about 1.7 km, or slightly more than half that suggested in the earlier interpretation of the Convict-Sand profile (Hill, 1976).

The velocity model for the Minaret-Bald profile (Figure 12d) indicate that the greatest depth to the top of both the crystalline basement and the Bishop tuff in the western part of the caldera occurs beneath the north margin of the resurgent dome. Here, the crystalline basement is covered by approximatly 1 km of Bishop tuff, which in turn is covered by approximatly 1 km of post-caldera lava flows and unconsolidated clastic deposits. The Convict-Cowtrack profile indicates that over 300 meters of 1.2-km/sec material underlies the northeastern margin of the resurgent dome. This large thickness of low-velocity and low-density rocks beneath the northern section of the resurgent dome and the southern margin of the north moat is consistent with the position of the most pronounced lows in the Bouguer gravity field

over the caldera (see Kane and others, 1976; Oliver and Robins, 1978). These results indicate that the rhyolite flows that form the topographic high along the north margin of the resurgent dome (the Lookout Mountain complex) are indeed surficial flows underlain by several hundred meters of low-density, unconsolidated material.

The depth to the Bishop tuff and the crystalline basement shallows abruptly at the west edge of the resurgent dome where the Minaret-Bald profile intersects the Casa-Mono profile. This offset may be associated with the medial graben that transects the resurgent dome in a north-northwest direction (Bailey and others, 1976). The west wall of the graben runs subparallel to and within 0.5 km west of the Casa-Mono profile, and the sense of offset across the fault (east side down) is consistent with the geometry of the step in the top of the Bishop tuff and crystalline basement shown in the Minaret-Bald profile.

West of the resurgent dome, results from the Minaret-Bald profile indicate that the depths to all velocity boundaries shallow systematically across the west moat toward the west wall of the caldera. The geometry of the caldera-bounding fault along the west caldera wall is not well constrained by data on the Minaret-Bald profile, although the horizontal velocity gradients as modeled in Figure 12d suggest an offset of approximatly 1 km in the crystalline basement 2 to 4 km east of Minaret summit.

We interpret the pronounced secondary arrival (labeled 'r' on Fig. 11) that follows the first arrival by 0.5 sec at distances of 12 to 20 km west of Shot Point 16 as being reflected by a boundary 7 to 8 km beneath the west margin of the resurgent dome (Figure 11 and 12d). This reflecting boundary dips approximatley 9° to the northeast in the plane of the profile to produce the observed traveltimes. The true P-wave velocities on either side of the boundary are not well resolved by the available data, although we feel that the values shown in Figure 12d are probably within 5% of the true values. The velocity contrast across the boundary (Fig. 12d) is a minimum value necessary to generate reasonable amplitude for the reflected wave, and it is consistent with the velocity contrast for a low-velocity body in the same area found by Kissling and others (1984) in their tomographic study of P-wave traveltimes beneath the Long Valley caldera. This reflected arrival is not obvious on the reversing profile extending to the northeast from Shot Point 11 at Minaret Summit (figure 10). Because of the apparent dip of the reflecting boundary to the northeast, however, common-depth-point rays would only be recorded beyond distances of about 20 km from Shot Point 11 where we have few records. This absence of reflected arrivals on the record section at distances less than 20 km from Shot Point 11 suggests that the reflecting boundary has a limited horizontal extent.

The depth to the reflecting boundary beneath the Minaret-Bald profile is essentially the same as that for the reflecting boundary found beneath the Deadman-Antelope profile in the 1973 data (profile A-A in Figures 4 and 7 of Hill, 1976). The latter

underlies the western margin of the resurgent dome about 4 km to the north of the the Minaret-Bald profile, and it has an apparent dip of about 3° to the west-northwest. Together, the reflected arrivals on the Deadman profile (Hill, 1976) and the Minaret-Bald profile (Figure 11) begin to define the top of a low-velocity body with a convex-upward shape at a depth of approximately 7 km beneath the northwest margin of the resurgent dome. These reflecting boundaries correspond remarkably well with the upper surface of an elongate low-velocity body defined by the tomographic inversion of P-wave traveltimes from local earthquakes by Kissling and others (1984). Their low-velocity body extends nearly 40 km north-northwestward from beneath the high Sierra south of the caldera, through the caldera beneath the western margin of the resurgent dome, and thence beneath the Inyo Craters and southern section of the Mono Craters to the north. The reflecting boundaries also correspond closely to the upper surface of a volume that strongly attenuates seismic body waves defined by Sanders (1984) in a study of attenuation patterns of P and S waves recorded in the Long Valley region from local earthquakes. All of these results are consistent with the interpretation that the reflecting boundaries represent the top of a magma body beneath the western part of the caldera (Fig. 2 in Hill and others, 1984).

CONCLUSIONS

The three major structural blocks in the Long Valley region (Long Valley caldera itself, the rugged high Sierra Nevada south and west of the caldera, and a highland of subdued topography north and east of the caldera) share a common crystalline basement. This basement consists primarily of Mesozoic granitic rocks but includes some metasedimentary and metavolcanic roof pendants of Paleozoic age. The four seismic-refraction profiles described in this paper sample the upper 5 to 7 km of this crystalline basement beneath the western half of Long Valley caldera and beneath the highland to the north and east; the profiles did not extend into the rugged terrain of the high Sierra Nevada.

Results from the interpretation of these seismic-refraction profiles indicate that P-wave velocities in the "typical" crystalline basement of the block north of the caldera varies between 3.6 and 5.0 km/sec at its upper-most surface and increases fairly rapidly with depth to a uniform velocity of 5.6 km/sec at a depth of 2 km beneath the topographic surface. Below a depth of 2 km, the P-wave velocity increases more slowly with a gradient on the order of 0.1 s^{-1}. This variation in velocity with depth is similar to that found in the upper few km of Cretacious granitic rocks exposed in both the Mojave desert of southeastern California (G. Fuis, per. communication, 1984) and in the Gabilan Range in central California (Walter and Mooney, 1982), and it probably reflects the degree to which the rocks are fractured. The laterally uniform velocity beginning at a depth

of 2 km suggests that most of the fractures are closed by lithostatic pressure at depths below 2 km (Moos and Zoback, 1983).

The crystalline basement within the western portion of the Long Valley block is down-dropped by 1.5 to 1.7 km with respect to the highland to the north along steeply-dipping faults that form the north caldera wall and about 1 km along faults that form the west and south caldera wall. The top of the basement appears to be about 2 km deep beneath the northern margin of the resurgent dome. The down-dropped basement of Long Valley dips to the northeast thus making the difference in elevation across the southwestern caldera faults somewhat smaller. Because we do not observe a one-to-one relationship between rock type and p-velocity the exact dip and location of the caldera-bounding faults is poorly resolved.

Rocks that overlie the crystalline basement fall into three distinct P-wave velocity groups: 1) pumice, unconsolidated sedimentary rocks, and highly brecciated lava flows with velocities between 1.2 and 1.8 km/sec; 2) intact rhyolite and basalt lava flows and deposits of non-welded Bishop tuff with velocities between 2.8 and 3.2 km/sec; and 3) deposits of welded Bishop tuff with velocities between 3.9 and 4.4 km/sec. (The velocities for the welded Bishop tuff, which is confined primarily to the caldera, are comparable to those of the more fractured granitic rocks in the upper 2 km of crystalline basement north of the caldera.) A thin layer of rocks made up of the first two velocity groups covers sections of the crystalline basement north and east of the caldera. This layer is thickest beneath Pumice Valley and the Mono Craters, and it is absent in the vicinity of Granite Mountain. Much of the 400 to 500-meter thickness of this layer in Pumice Valley is presumably comprised of non-welded Bishop tuff, which may in places overlie glacial till deposits. The fact that granitic basement is exposed in the Aeolian Buttes just 2 km southeast of the intersection between the Casa-Mono and Pumice-Granite profiles indicates a relief of at least 400 meters on the crystalline basement within the Mono Craters "ring fracture system".

Rocks of all three velocity groups form the fill over the down-droped, crystalline basement within the caldera. The combined thickness of the first and second groups varies from less than 300 meters over the central section of the resurgent dome to 600 to 700 meters within the moat north and south of the resurgent dome. The maximum combined thickness of these low-velocity rocks approaches 1 km beneath the north margin of the resurgent dome. Welded deposits of the Bishop tuff (the third velocity group) form a layer of fairly uniform thickness about 1 km throughout the western half of the caldera. Relief on the top of the welded tuff deposits forms a slightly exaggerated version of the resurgent dome topography.

P-wave velocities by themselves do not provide a unique guide to lithology. Our interpretation of the association of lithologic groups and velocity groups described above is

summarized in the cross sections for each of the profiles in Fig. 13. P-velocities within the Bishop tuff, for example, vary from 2.8 to 3.1 km/s for the non-welded (under Pumice Valley and Mono Craters, see profile Pumice Granite, Fig 13a) to velocities around 4.0 km/s for the densely welded deposits (bottom of Bishop tuff within Long Valley caldera). Because the lower limit of the P-wave velocity coincides with the velocities found for denser rhyolitic flows of the resurgent dome (layer 2 within the caldera) the boundary between the early post-caldera forming rhyolitic flows and the Bishop tuff is poorly constrained where the latter is non-welded. Generally the velocity differences between the Bishop tuff and the underlying basement rocks are pronounced. At the caldera boundary, however, fracturing and weathering of the exposed granitic basement reduces its P-velocity to values around 4.0 km/s thus smoothing the effect of the caldera boundary faults considerably. While in some cases the location of the faults in the upper 0.5 km is clearly defined by the difference for P-velocities between the basement rocks and layer 1 and 2 within the caldera (see for example Fig. 12 c,d), at greater depths the refraction data can only resolve a zone 0.5 to 1.0 km wide where the lateral transition between Bishop tuff and basement rocks takes place.

The reflecting boundary beneath the northwestern resurgent dome at a depth of about 7 km first reported by Hill (1976) has shown up again the Minaret-Bald profile described here. Interpretation of this boundry as the top of a magma body is strengthened by independent seismological data showing anomalous attenuation of body waves (Sanders, 1984) and low p-velocities (Kissling and others, 1984) in a volume immediately beneath the reflecting boundry. The absence of a coherent reflected phase on the record section from Shot Point 1 on the Casa-Mono profile, which passes directly over the reflecting boundry in a northerly direction, may be due in part to a non-planar (upwardly convex) geometry of the boundry in this direction and in part to complexities in the record section at distances we should expect to record the reflected wave (8 to 20 km) associated with the caldera-bounding faults.

With the analysis of these 4 profiles we have improved the overall knowledge of the velocity structure in the Long Valley caldera and in the area to the north where the granitic basement outcrops. In addition, we have examined the geometry of the ring fracture system bounding the caldera at four locations and collected further evidence for the existence of a partial melt zone at depth. With the study of the remaining profiles (Fig. 1) we expect to extend this knowledge to the southern and eastern parts of the caldera. We also expect to establish further constraints on the geometry of caldera bounding faults and the deep reflection horizon from the modeling of amplitude data on all profiles in combination with three-dimensional modeling of the Bouguer gravity field.

Acknowledgments

This project stems from a multi-disciplinary proposal to the Department of Energy initiated by John Rundle for high-resolution geophysical investigations of the Mono Craters-Long Valley magma systems. We wish to express our appreciation to John for his encouragement and continued interest in our work. We are grateful to G. Fuis, P. Meador, V. Sutton, E. Criley, R. McClearn, S. Gallanthine, J. VanSchaack, J. Murphy, L. Hwang, R. Colburn, T. Reed and R. Kaderabek for their invaluable assistence in field work and data processing. We thank S. Johnson and J. Ellefson for carefully typing the manuscript. We are also grateful to W. Mooney for his help throughout the project and thank him and P. Ward for critically reviewing the manuscript. This project was funded by the Office of Basic Energy Science under the Department of Energy. One of us (E.K.) has been supported by the National Science Foundation of Switzerland under project no. 82.998.0.82.

References

Abers, G., The subsurface structure of Long Valley caldera, Mono County, California: a preliminary synthesis of gravity seismic, and drilling information, submitted to J. Geophys. Res., 1984.

Bailey, R. A., G. B. Dalrymple, and M. A. Lanphere, Volcanism, structure, and geochronology of Long Valley caldera, Mono County, California, J. Geophys. Res., 81, 725-744, 1976.

Bailey, R. A., Other potential eruption centers in California: Long Valley - Mono Lake, Coso, and Clear Lake volcanic fields, in: status of volcanic prediction and emergency response capabilities in volcanic hazard zones of California, R. C. Martin and J. F. Darin (eds.), Cal. Dep. Conservation, Div. Mines and Geology, spec. publ. 63, 17-28, 1982.

Cerveny, V., I. A. Molotkov, and I. Psencik, Ray method in seismology, Univ. Korlova, Prague, Charles University Press, 214 pp., 1977.

Eaton, J. P., Crustal structure in northern and central California from seismic evidence, geology of Northern California, edited by E. H. Balley, Calif. Div. Mines Geol. Bull., 190, 419-426, 1966.

Fuis, G., W. D. Mooney, J. H. Healy, G. A. McMechan, and W. J. Lutter, Seismic-refraction studies of the Imperial Valley region, California, J. Geophys. Res., 89, 1165-1189, 1984.

Healy, J. H., W. D. Mooney, H. R. Blank, M. E. Gettings, W. M. Kohler, R. J. Lamson, and L. E. Leone, Saudi Arabian seismic deep-refraction profile: final report: U.S. Geological Survey Saudi Arabian Mission Report 02-37, Jiddah, Saudia Arabia, 629 pp., 1982.

Hill, D. P., Structure of Long Valley caldera from seismic refraction experiments, J. Geophys. Res., 81, 745-753, 1976.

Hill, D. P., Seismic evidence for the structure and Cenozoic tectonics of the Pacific Coast States, in Cenozoic tectonics and Regional Geophysics of the western Cordillera, Smith, R. B. and G. P. Eaton (eds.), Geol. Soc. Am. Mem., 152, 145-174, 1978.

Hill, D. P., A. S. Ryall, and R. A. Bailey, Active tectonic and magmatic processes beneath Long Valley caldera, eastern California: A summary, this volume, 1984.

Johnson, L. R., Crustal structure between Lake Mead, Nevada, and

Mono Lake, California, J. Geophys, Res., 70, 2863-2872, 1965.

Kane, M. F., D. R. Mabey, and R. L. Brace, A gravity and magnetic investigation of Long Valley caldera, Mono County California, J. Geophys. Res., 81, 754-762, 1976.

Kissling, E., W. L. Ellsworth, and R. S. Cockerham, Three-dimensional structure of the Long Valley Caldera, California, region by geotomography, this volume, 1984.

Kistler, R. W., Structure and metamorphism in the Mono Craters quadrangle, Sierra Nevada, California, U.S. Geol. Survey Bull, 1221-E, 1-52, 1966.

Meador, P., and Hill, D. P., Data report for the August 1982 seismic-refraction experiment in the Mono Craters-Long Valley region, California, U.S. Geological Survey Open-File Report 83-708, 53 pp., 1983.

Moos, D. and M. D. Zoback, In situ studies of velocity in fractured crystalline rocks, J. Geophys. Res., 88, 2345-2358, 1983.

Muffler, L. J. P. and D. L. Williams, Geothermal investigations of the U.S. Geological Survey in Long Valley, California, 1972-1973, J. Geophys. Res., 81, 721-724, 1976.

Oliver, H. W. and S. L. Robbins, Bouguer gravity map of California, Mariposa Sheet, California Div. of Mines and Geol. Sacramento, Ca., scale 1:250,000, 1978.

Pakiser, L. C., Gravity, volcanism, and crustal deformation in Long Valley, California, U.S. Geol. Surv. Prof. Pap. 424-B, B250-B253, 1961.

Pakiser, L. C., Structure of Mono Basin, California, J. Geophys., Res., 75, 4077-4080, 1970.

Pakiser, L. C., F. Press, and M. F. Kane, Geophysical investigation of Mono Basin, California, Geol. Soc. Amer. Bull., 71, 415-447, 1960.

Pakiser, L. C., M. F. Kane, and W. H. Jackson, Structural geology and volcanism of the Owens Valley region, California-A geophysical study, U.S. Geol. Surv. Prof. Pap. 438, 68 pp., 1964.

Priestly, K. F., A. S. Ryall, and G. S. Feze, Crust and upper mantle structure in the Northwest Basin and Range province, Seism. Soc. Am. Bull.,72, 911-923, 1982.

Sanders, C. O., Location and configuration of magma bodies beneath Long Valley, California, determined from anomalous earthquake signals, this volume, 1984.

Smith, R. B., M. M. Schilly, L. W. Braile, J. Ansorge, J. L. Lehmann, M. R. Baker, C. Prodehl, J. H. Healy, St. Mueller, and R. W. Greensfelder, The 1978 Yellowstone - Eastern Snake River Plain seismic profiling experiment: crustal structure of the Yellowstone region and experiment design, J. Geophys, Res., 87, 2583-2596, 1982.

Sorey, M. L., R. E. Lewis, and F. H. Omsted, The hydrothermal system for Long Valley caldera, California, U.S. Geological Survey Prof. Pap., 1044-A, 60 pp., 1978.

Steeples, D. W., and H. M. Iyer, Low-velocity zone under Long Valley as determined from teleseismic events, J. Geophys. Res., 81, 849-860, 1976.

Walter, A. W. and W. D. Mooney, Crustal structure of the Diablo and Gabilan ranges, Central California: a reinterpretation of existing data, Seism. Soc. Am. Bull., 72, 1567-1590, 1982.

FIGURE CAPTIONS

Figure 1. Map of the Long Valley Mono Lake region showing the outline of the refraction experiment over the outcrop of granite basement (7), the Long Valley caldera boundary, and the inferred Mono Craters ring fracture system (double dashes). Circles containing a star mark the shotpoints labeled 1 thru 18. Locations of the recording units are shown as triangles for the 1982 profiles and as squares for the 1983 lines. In this report we discuss the crustal structure along the profiles Pumice-Granite, Casa-Mono, Convict-Cowtrack, and Minaret-Bald.

Figure 2. Pumice-Granite profile: Shot Point 7. a) record section, b) traveltimes for observed (circles) and computed (crosses) P-wave arrivals, and (c) ray diagram for the final model. Record section and traveltime curve reduced by x(km)/6.0 (km/s), where x is shot-receiver offset. All distances are given in kilometers and the reduced travel times in seconds. The three digit number above each trace in the record section denote the number of the location while the two digit number above denotes the attenuation setting in db for this particular trace (Meador and Hill, 1983). The velocities of the model are given in Fig. 12.

Figure 3. Pumice-Granite profile: Shot Point 10. a) record section, b) traveltimes for observed (circles) and computed (crosses) P-wave arrivals, and c) ray diagram for the final model. The conventions are the same as in Fig. 2.

Figure 4. Caso-Mono profile: Shot Point 1. a) record section, b) traveltimes for observed (circles) and computed (crosses) P-wave arrivals, and c) ray diagram for the final model. The conventions are the same as in Fig. 2.

Figure 5. Caso-Mono profile: Shot Point 3. b) traveltimes for observed (circles) and computed (crosses) P-wave arrivals, and c) ray diagram for the final model. Traveltime curve reduced by x(km)/6.0 (km/s), where x is shot-receiver offset. The conventions are the same as in Fig. 2.

Figure 6. Caso-Mono profile: Shot Point 6. a) record section, b) traveltimes for observed (circles) and computed (crosses) P-wave arrivals, and c) ray diagram for the final model. The conventions are the same as in Fig. 2.

Figure 7. Convict-Cowtrack profile: Shot Point 15. a) record section, b) traveltimes for observed (circles) and computed (crosses) P-wave arrivals, and c) ray diagram for the final model. The conventions are the same as in Fig. 2.

Figure 8. Convict-Cowtrack profile: Shot Point 16. a) record section, b) traveltimes for observed (circles) and computed (crosses) P-wave arrivals, and c) ray diagram for the final model. The conventions are the same as in Fig. 2.

Figure 9. Convict-Cowtrack profile: Shot Point 9. a) record section, b) traveltimes for observed (circles) and computed (crosses) P-wave arrivals, and c) ray diagram for the final model. The conventions are the same as in Fig. 2.

Figure 10. Minaret-Bald profile: Shot Point 11. a) record section, b) traveltimes for observed (circles) and computed (crosses) P-wave arrivals and c) ray diagram for the model. The conventions are the same as in Fig. 2.

Figure 11. Minaret-Bald profile: Shot Point 16. a) record section, b) traveltimes for observed (circles) and computed (crosses) P-wave arrivals and c) ray diagram for the model. The convention is the same as in Fig. 2. The secondary arrivals modeled as reflection off the top of a low-velocity zone are labeled 'r'.

Figure 12. Resulting P-wave velocity models for the profiles Pumice-Granite (a), Casa-Mono (b), Convict-Cowtrack (c), and Minaret-Bald (d). Velocities are given in km/sec. The depth is calculated with respect to sea level; note that the Long Valley caldera floor is at about-2000m above sea level.

Figure 13. Geologic interpretation of the p-wave velocity models for the refraction seismic profiles Pumice-Granite (a), Minaret-Bald (b), Casa-Mono (c), and Convict-Cowtrack (d). The vertical exaggeration is 2:1.

1: Loose accumulations of pumice, highly fractured rhyolite flows, and unconsolidated fluvial and lacustrine deposits.

2: Post-caldera rhyolite, rhyadacite, basalt flows and possibly some upper un-welded Bishop tuff deposits.

3: Non-welded Bishop tuff underlain in some places by glacial till.

4: Bishop tuff, mostly welded.

5: Granitic basement (includes some Paleozoic metasedimentary and metavolcanic rocks).

6: Fault zone of the caldera ring fracture system.

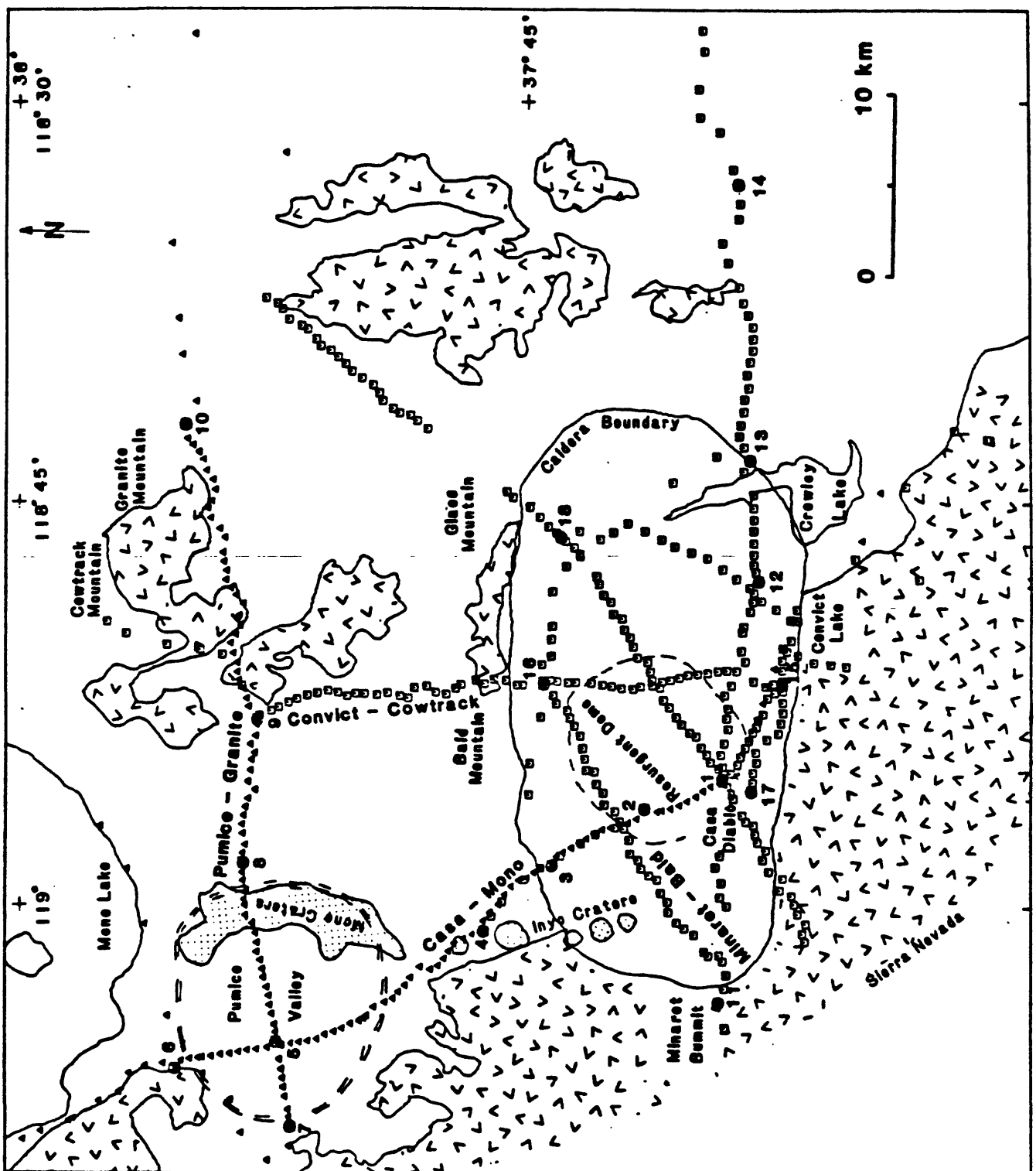
+38°
118° 30'
+37° 45'
N
0
10 km
118° 45'
Granite Mountain
Cowtrack Mountain
Glass Mountain
Caldera Boundary
Crowley Lake
Convict Lake
Convict - Cowtrack
Bald Mountain
Resurgent Dome
Pumice - Granite
Mono Craters
Mono Lake
Pumice Valley
Casa - Mono
Inyo Craters
Minaret - Bald
Casa Diablo
Minaret Summit
Sierra Nevada
+119°

FIGURE 1

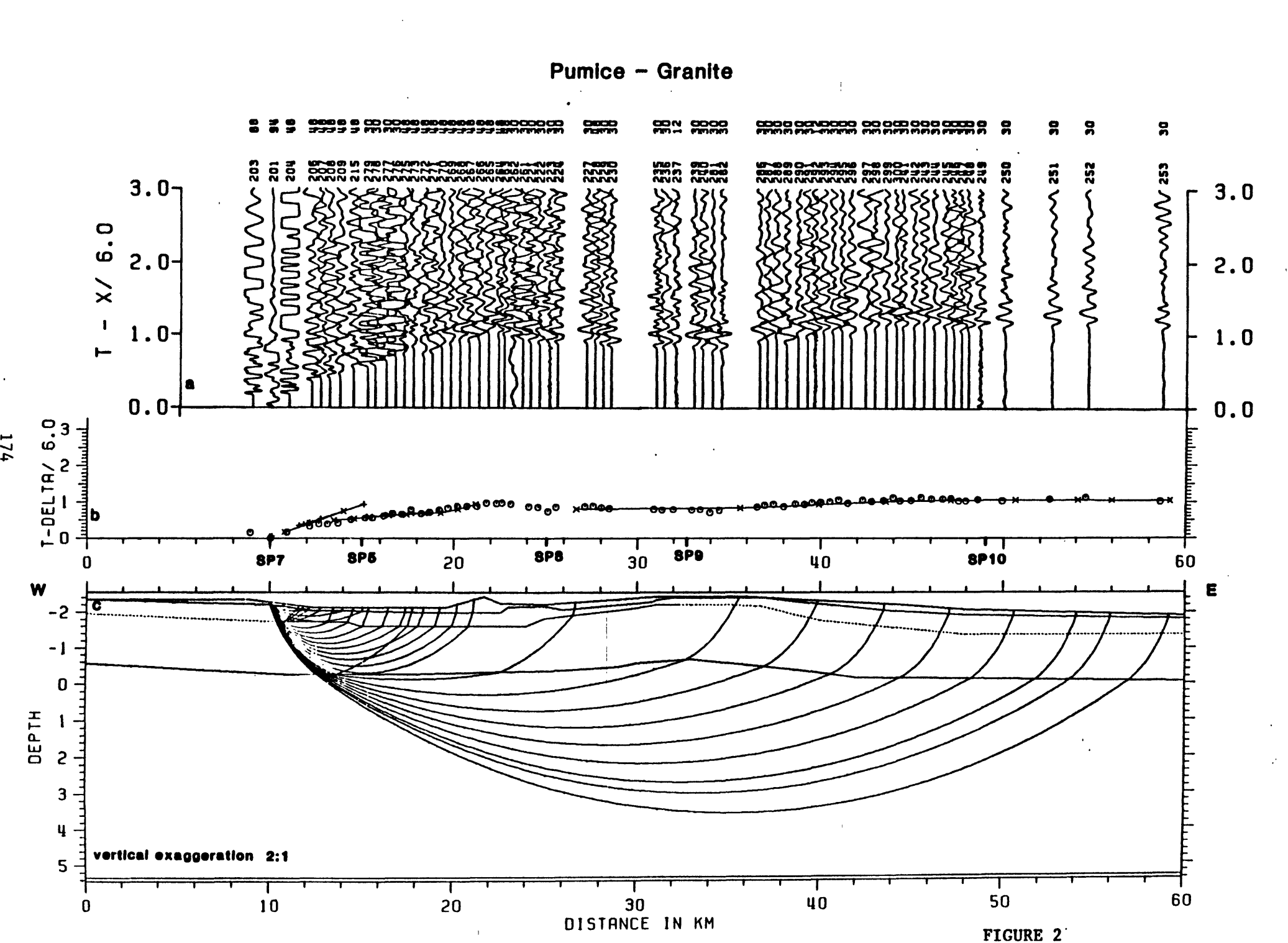
Pumice – Granite
T - X/ 6.0
3.0
2.0
1.0
0.0
a
T-DELTA/ 6.0
b
SP7
SP5
SP8
SP9
SP10
0
20
30
40
60
W
E
c
DEPTH
vertical exaggeration 2:1
10
50
DISTANCE IN KM

FIGURE 2

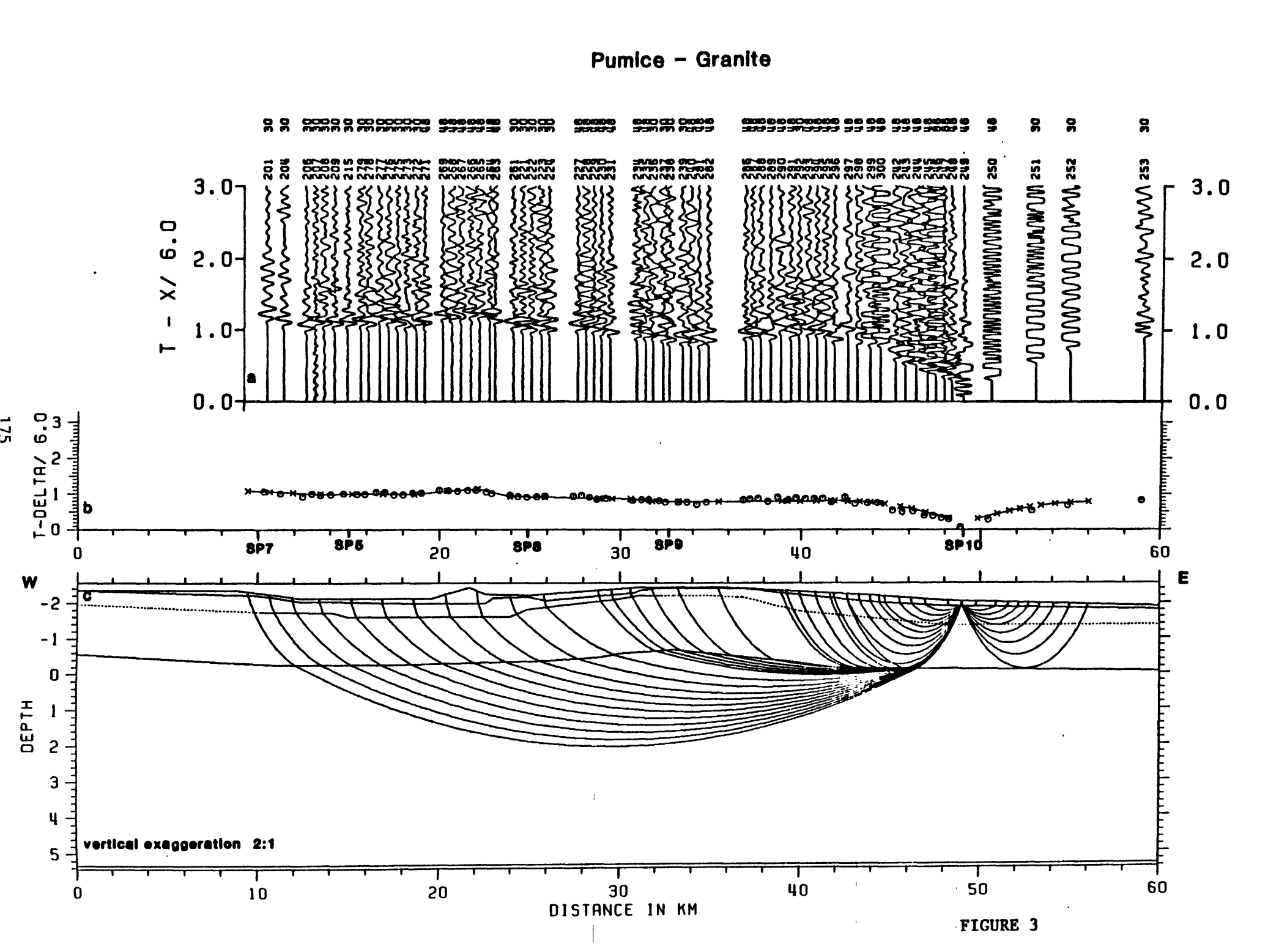
Pumice – Granite
T - X/ 6.0
3.0
2.0
1.0
0.0
a
T-DELTA/ 6.0
b
SP7
SP6
SP8
SP9
SP10
0
20
30
40
60
W
E
c
DEPTH
vertical exaggeration 2:1
10
50
DISTANCE IN KM

FIGURE 3

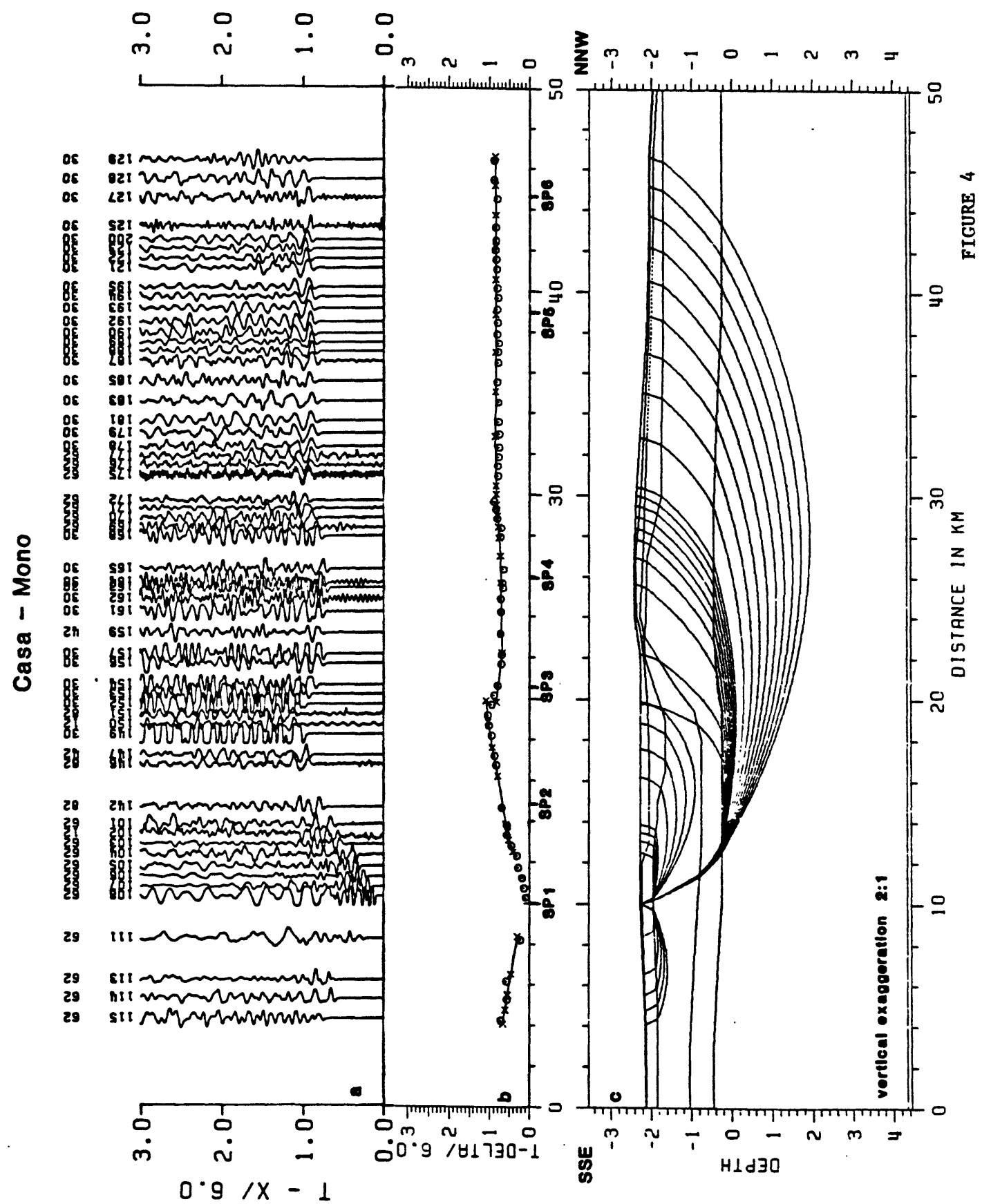
Casa - Mono
T - X/ 6.0
T-DELTA/ 6.0
DEPTH
DISTANCE IN KM
SSE
NNW
SP1
SP2
SP3
SP4
SP5
SP6
vertical exaggeration 2:1
a
b
c

FIGURE 4

Casa – Mono

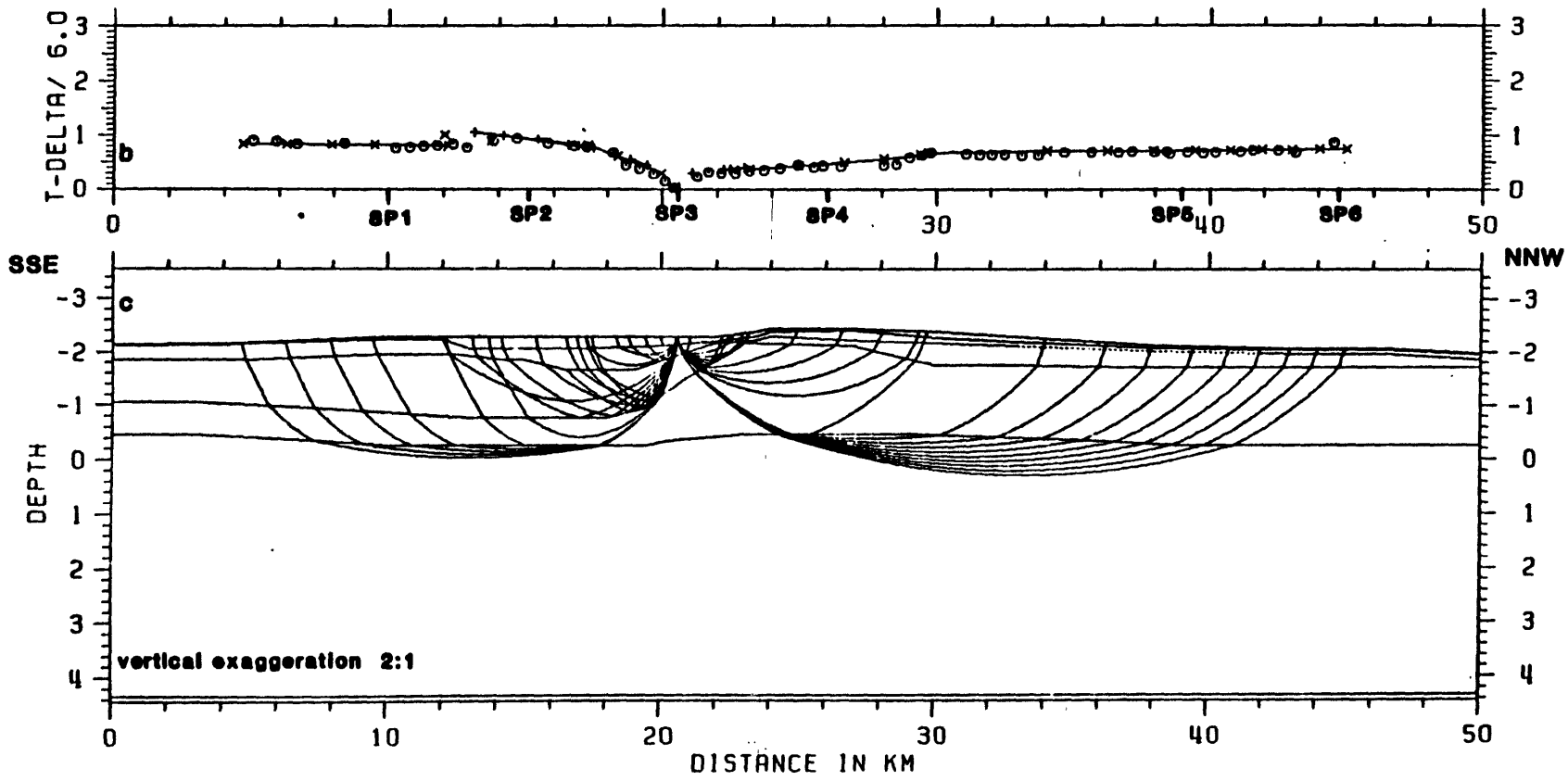

FIGURE 5

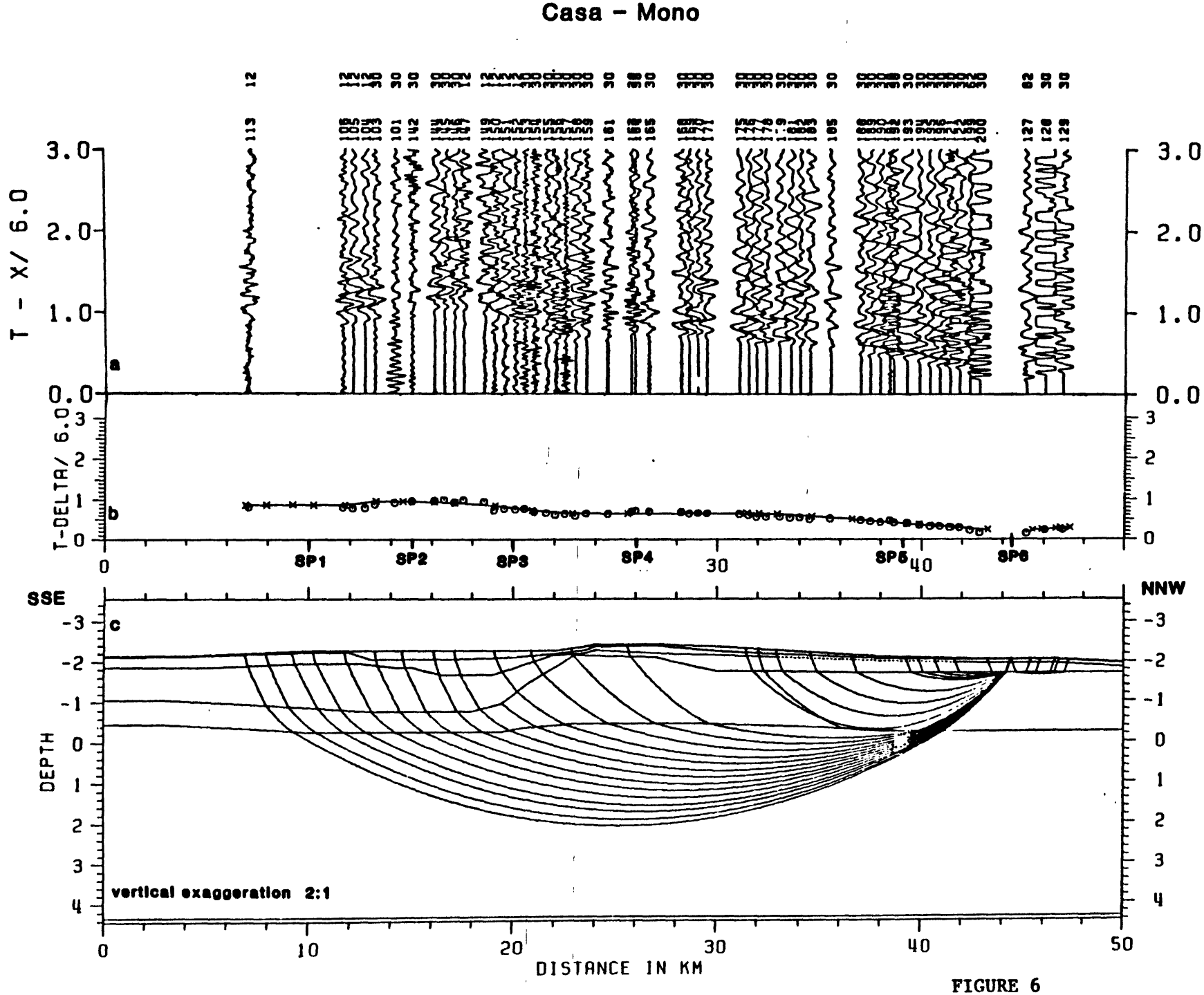
Casa - Mono
T - X/ 6.0
3.0
2.0
1.0
0.0
a
T-DELTA/ 6.0
b
SP1
SP2
SP3
SP4
SP5
SP6
0
30
40
SSE
NNW
c
DEPTH
vertical exaggeration 2:1
10
20
50
DISTANCE IN KM

FIGURE 6

Convict – Cowtrack

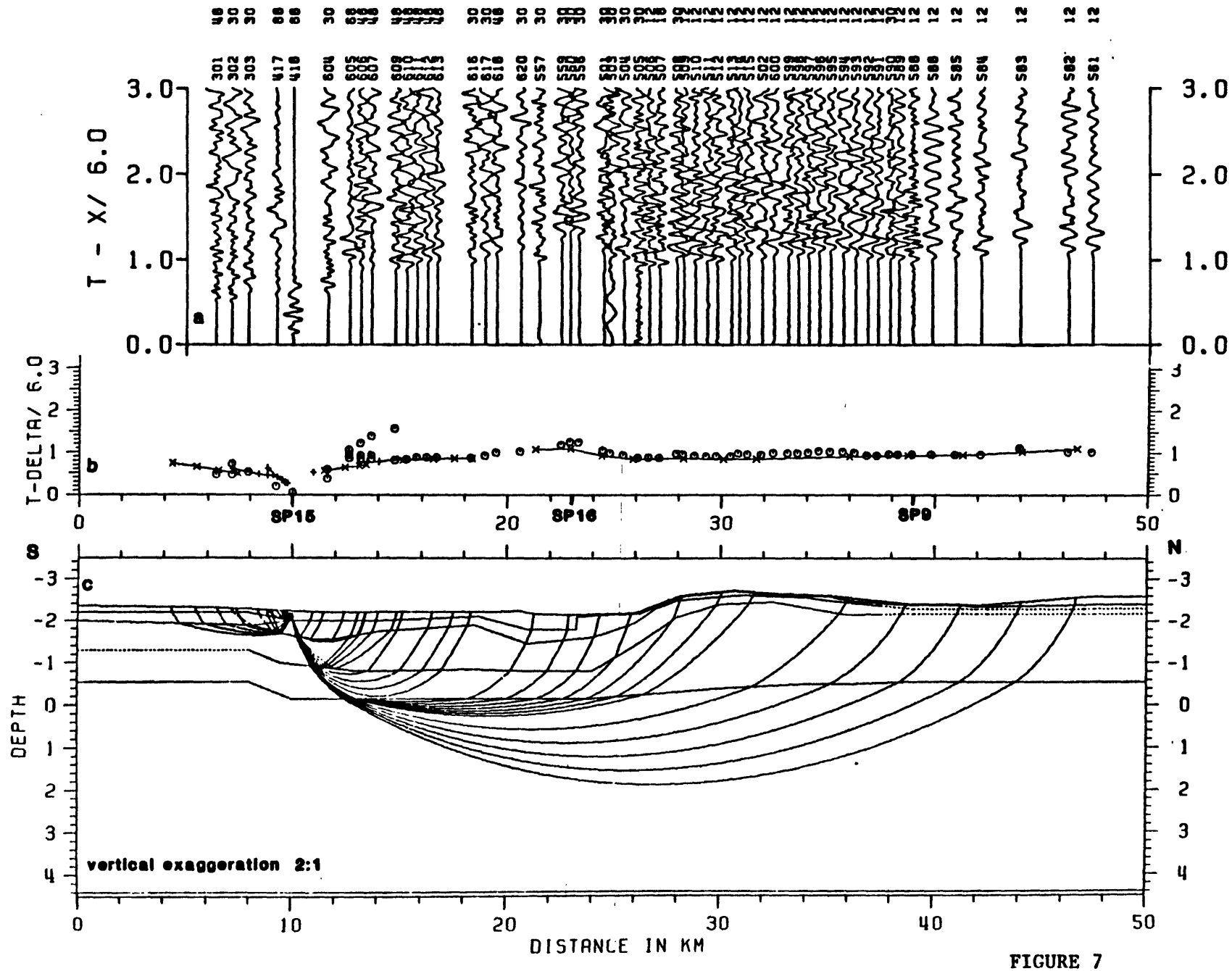

FIGURE 7

Convict – Cowtrack

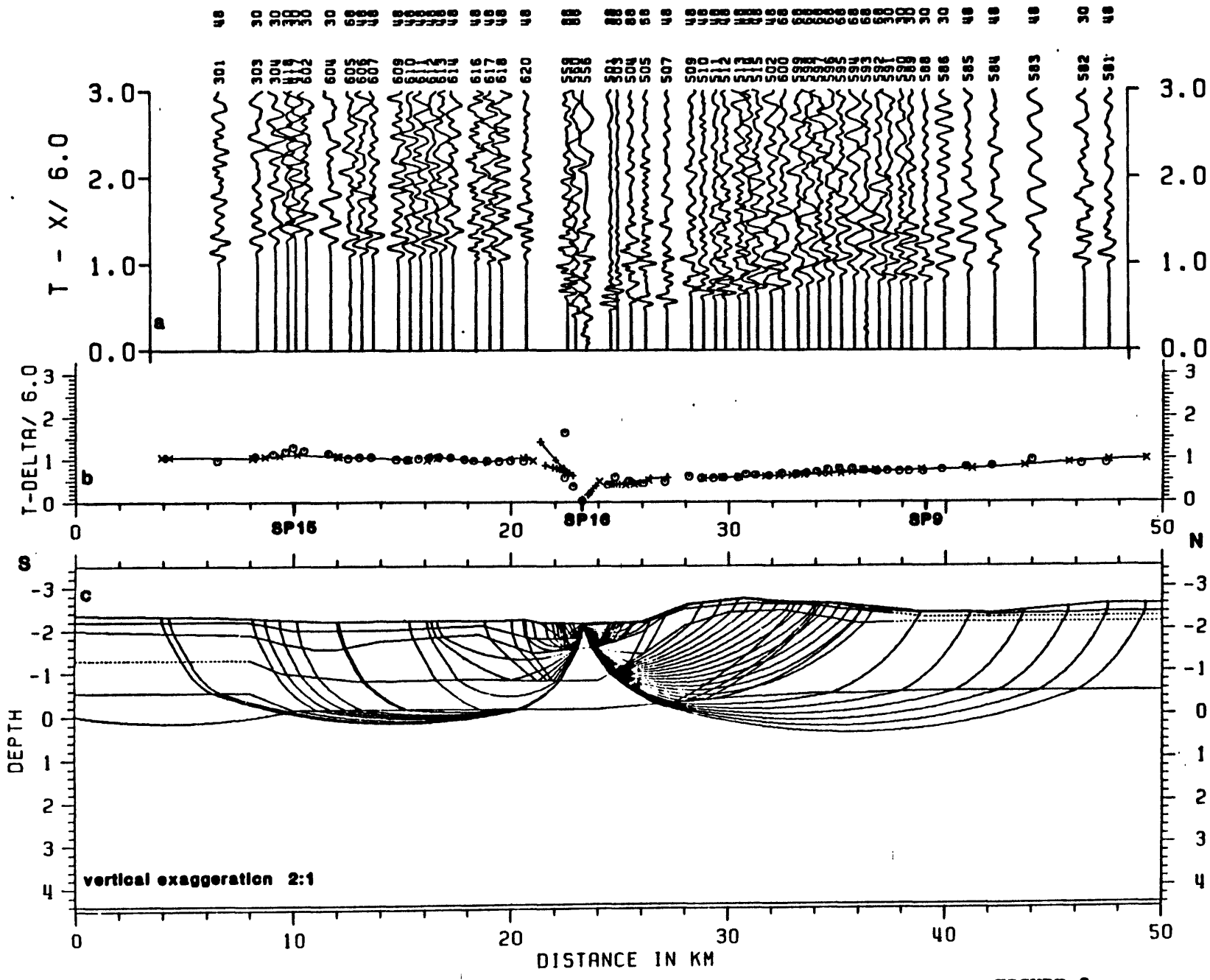

FIGURE 8

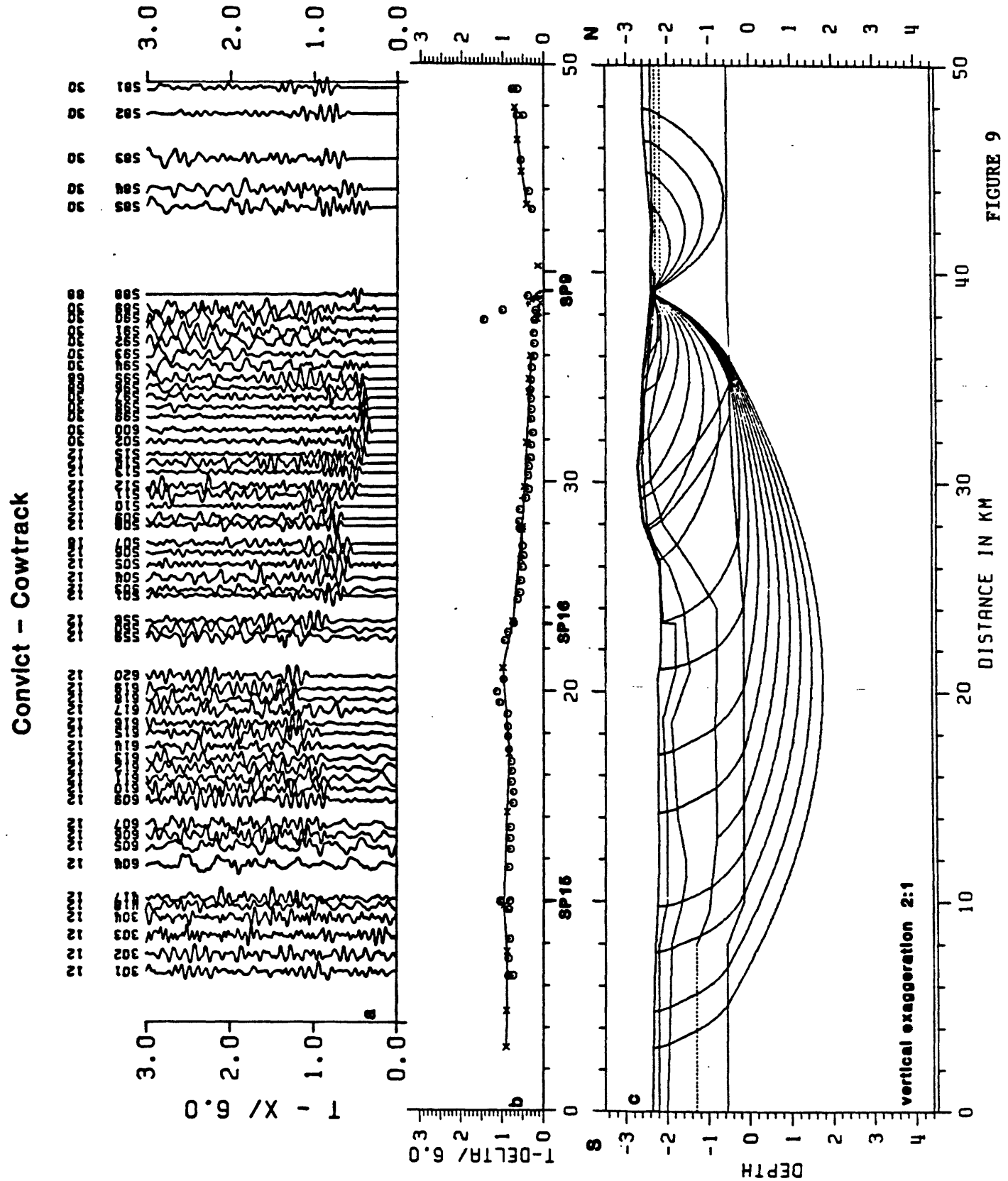
Convict – Cowtrack
T - X/ 6.0
T-DELTA/ 6.0
DEPTH
DISTANCE IN KM
vertical exaggeration 2:1
SP8
SP16
SP15
N
S
a
b
c

FIGURE 9

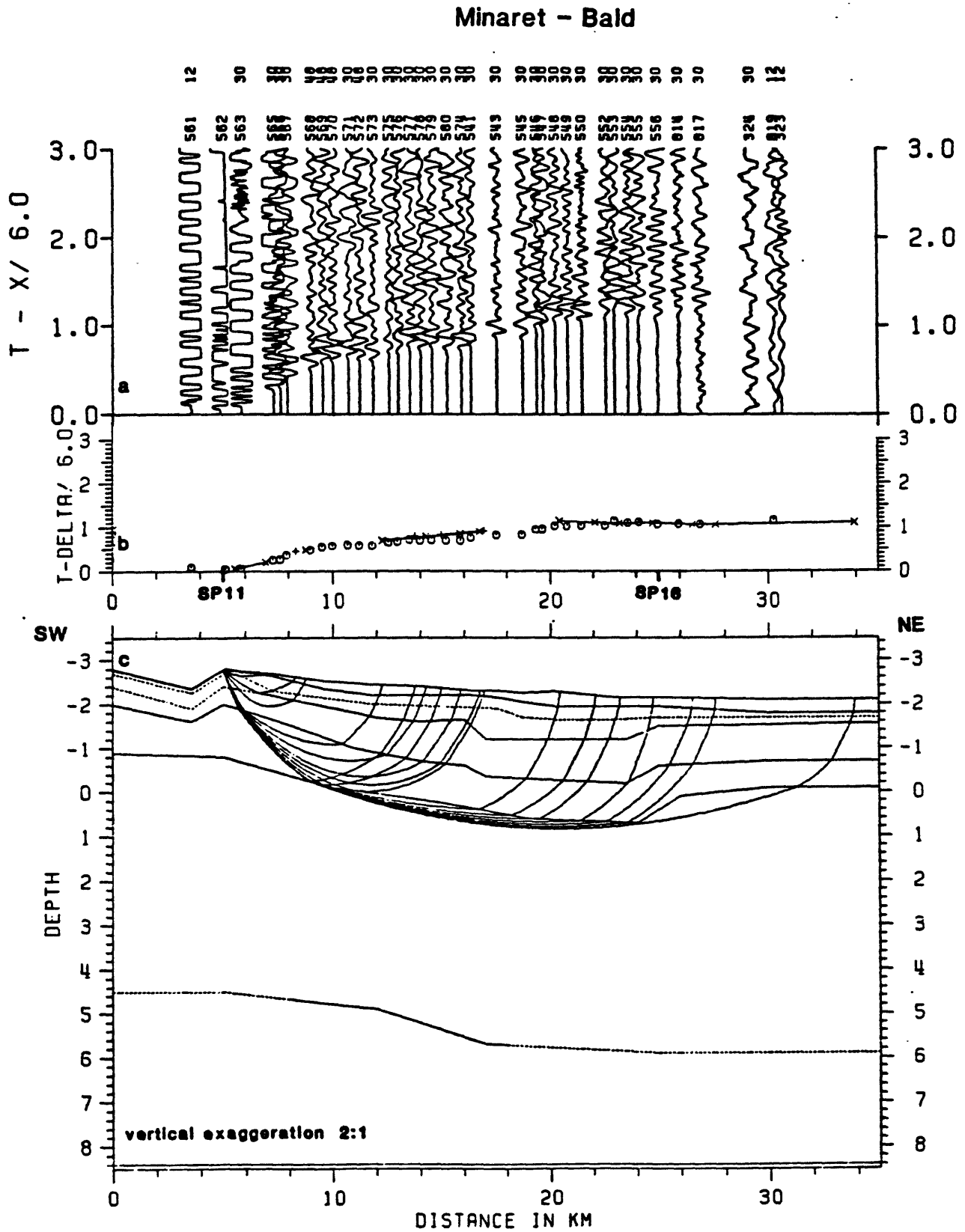
Minaret – Bald
T - X/ 6.0
T-DELTA/ 6.0
a
b
c
SP11
SP16
SW
NE
DEPTH
vertical exaggeration 2:1
DISTANCE IN KM

FIGURE 10

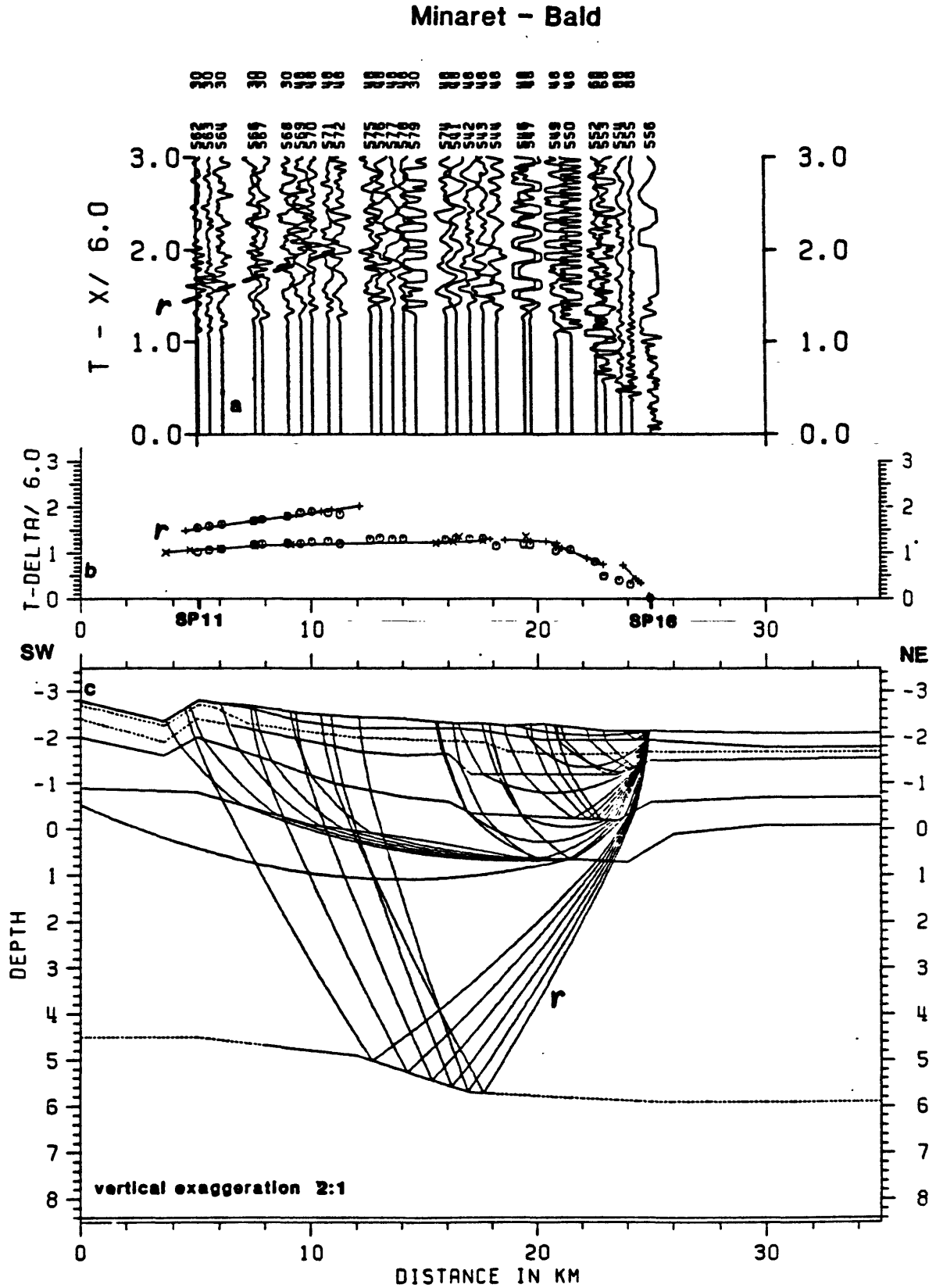
Minaret – Bald
T - X/ 6.0
3.0
2.0
1.0
0.0
r
a
T-DELTA/ 6.0
b
SP11
SP16
0
10
20
30
SW
NE
c
DEPTH
vertical exaggeration 2:1
DISTANCE IN KM

FIGURE 11

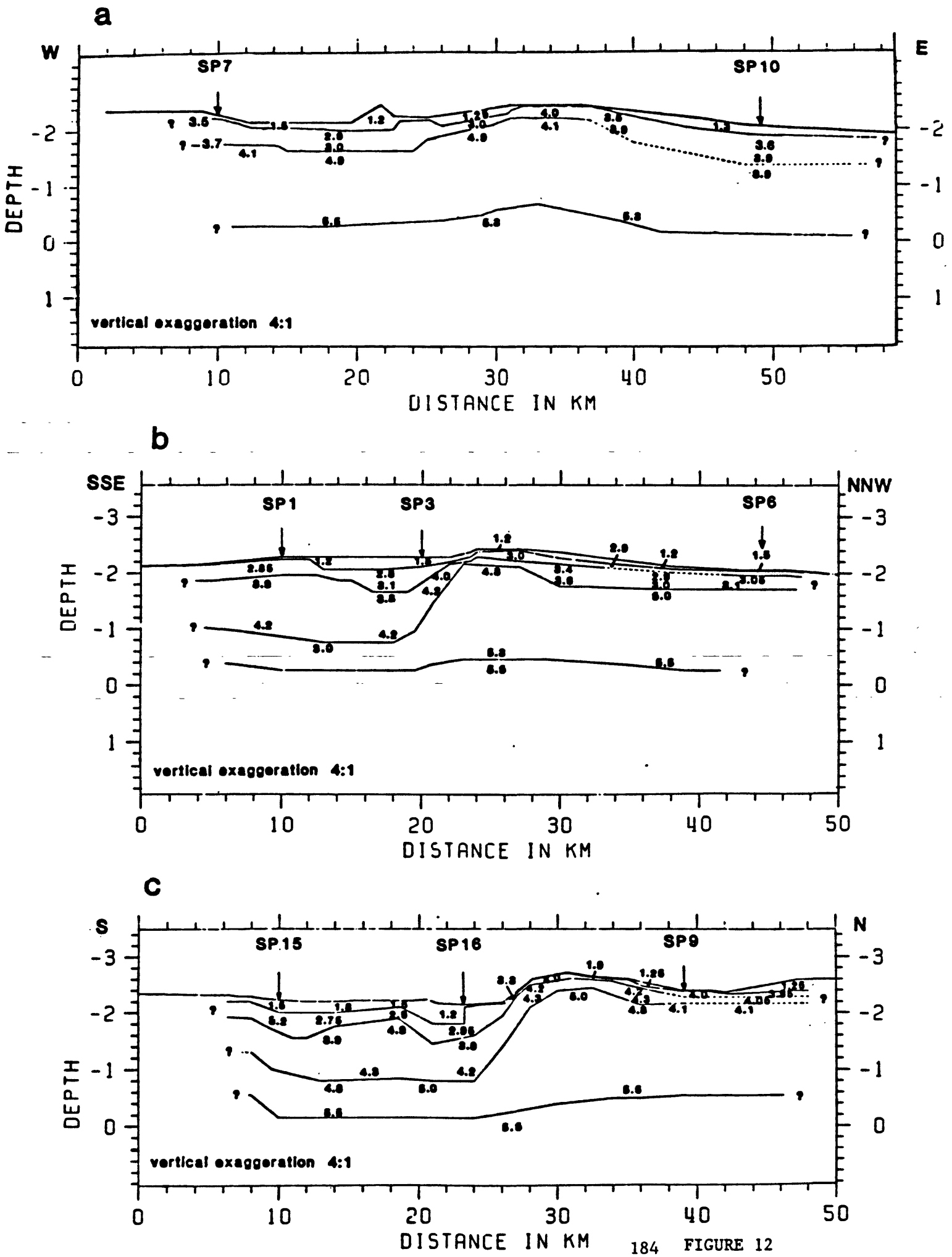

184 FIGURE 12

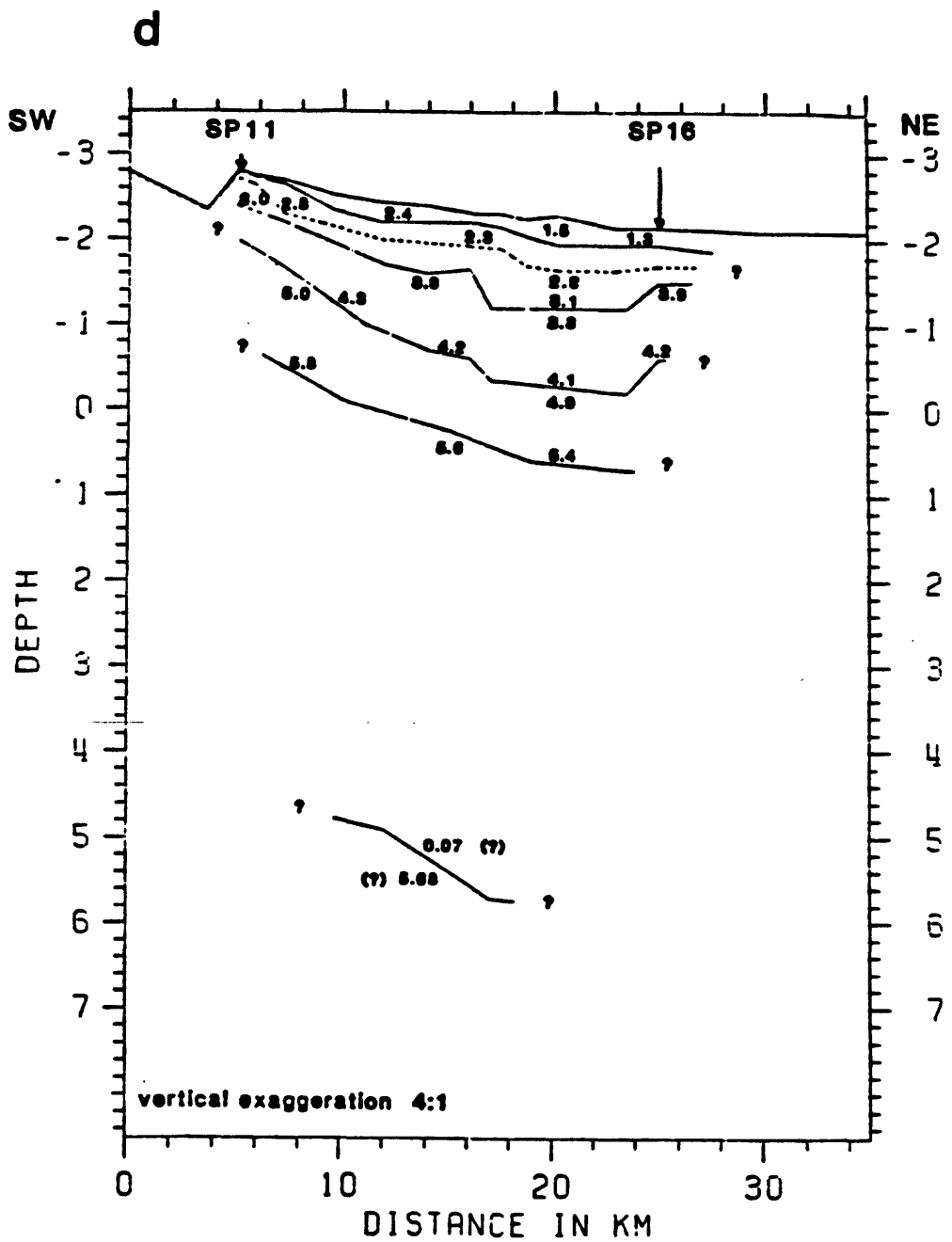
d
SW
NE
SP11
SP16
DEPTH
DISTANCE IN KM
vertical exaggeration 4:1
0
10
20
30
-3
-2
-1
0
1
2
3
4
5
6
7
2.0
2.8
2.4
2.8
1.8
1.8
2.8
2.8
2.1
2.8
2.9
6.0
4.8
4.2
4.2
4.1
4.9
5.8
5.6
5.4
0.07 (?)
(?) 5.88

FIGURE 13

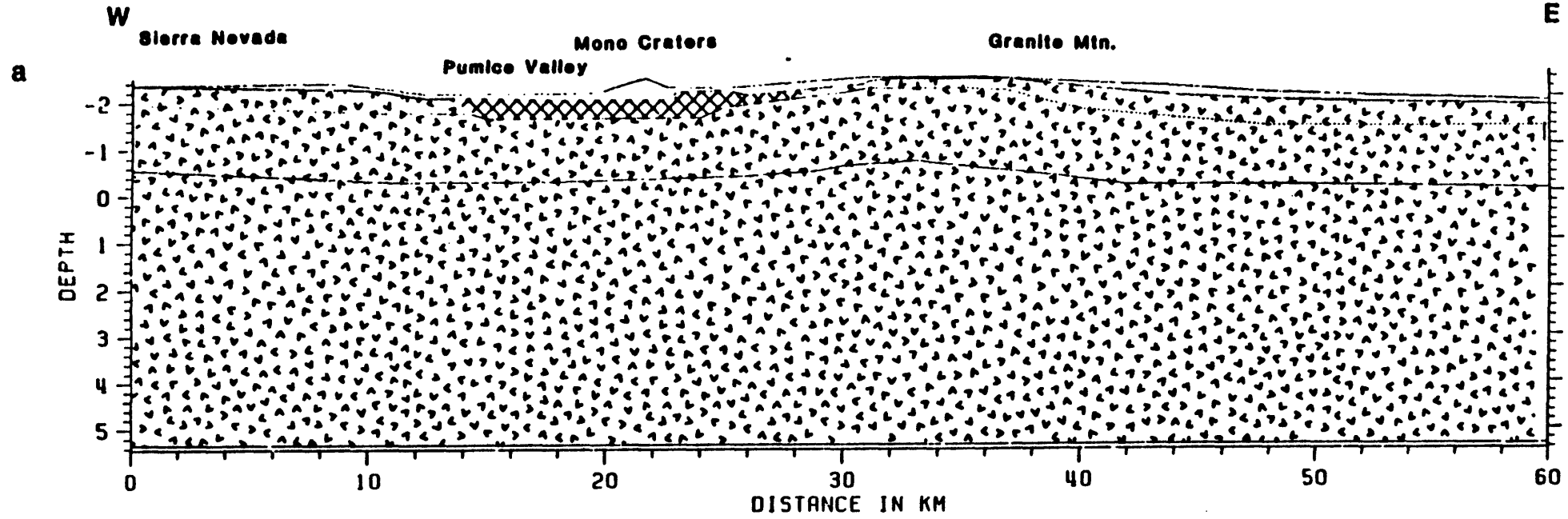
W
E
Sierra Nevada
Mono Craters
Granite Mtn.
Pumice Valley
a
DEPTH
-2
-1
0
1
2
3
4
5
0
10
20
30
40
50
60
DISTANCE IN KM

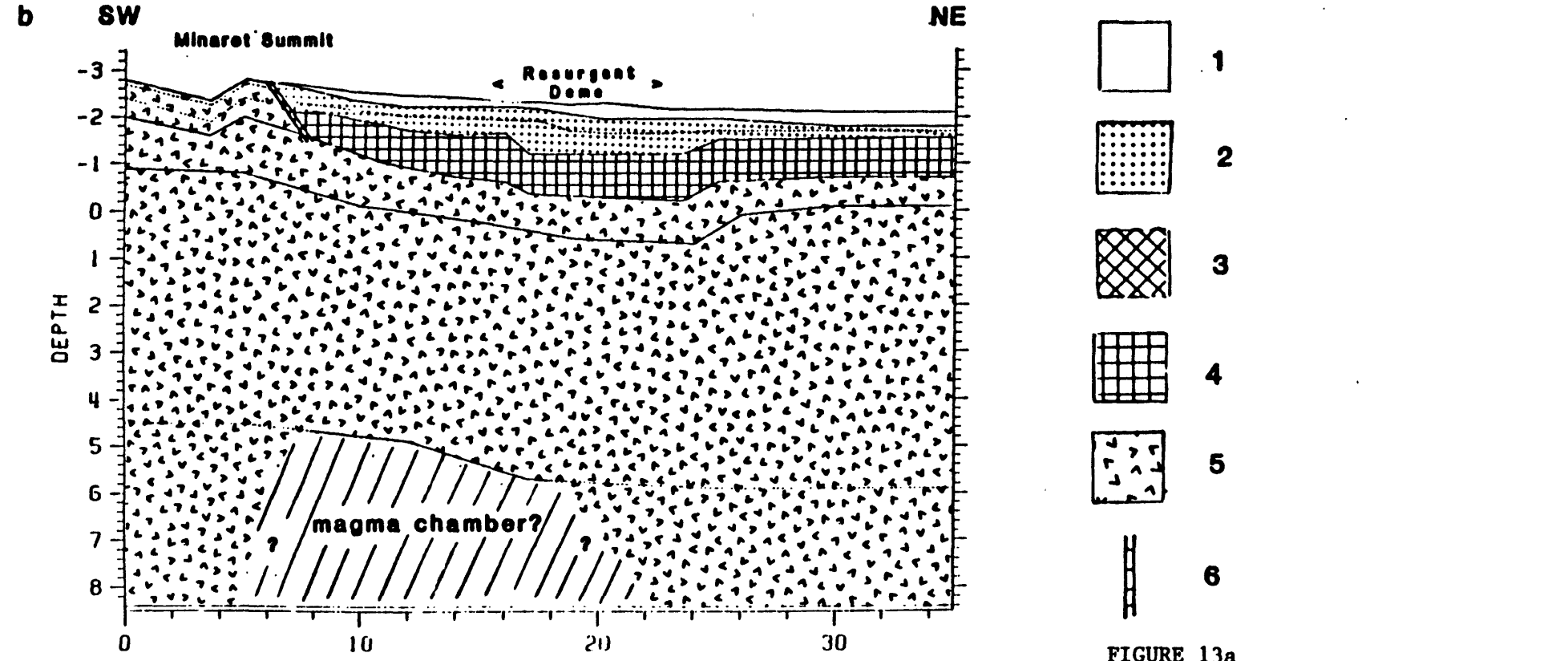
b
SW
NE
Minaret Summit
Resurgent Dome
DEPTH
-3
-2
-1
0
1
2
3
4
5
6
7
8
magma chamber?
?
?
0
10
20
30
1
2
3
4
5
6

FIGURE 13a

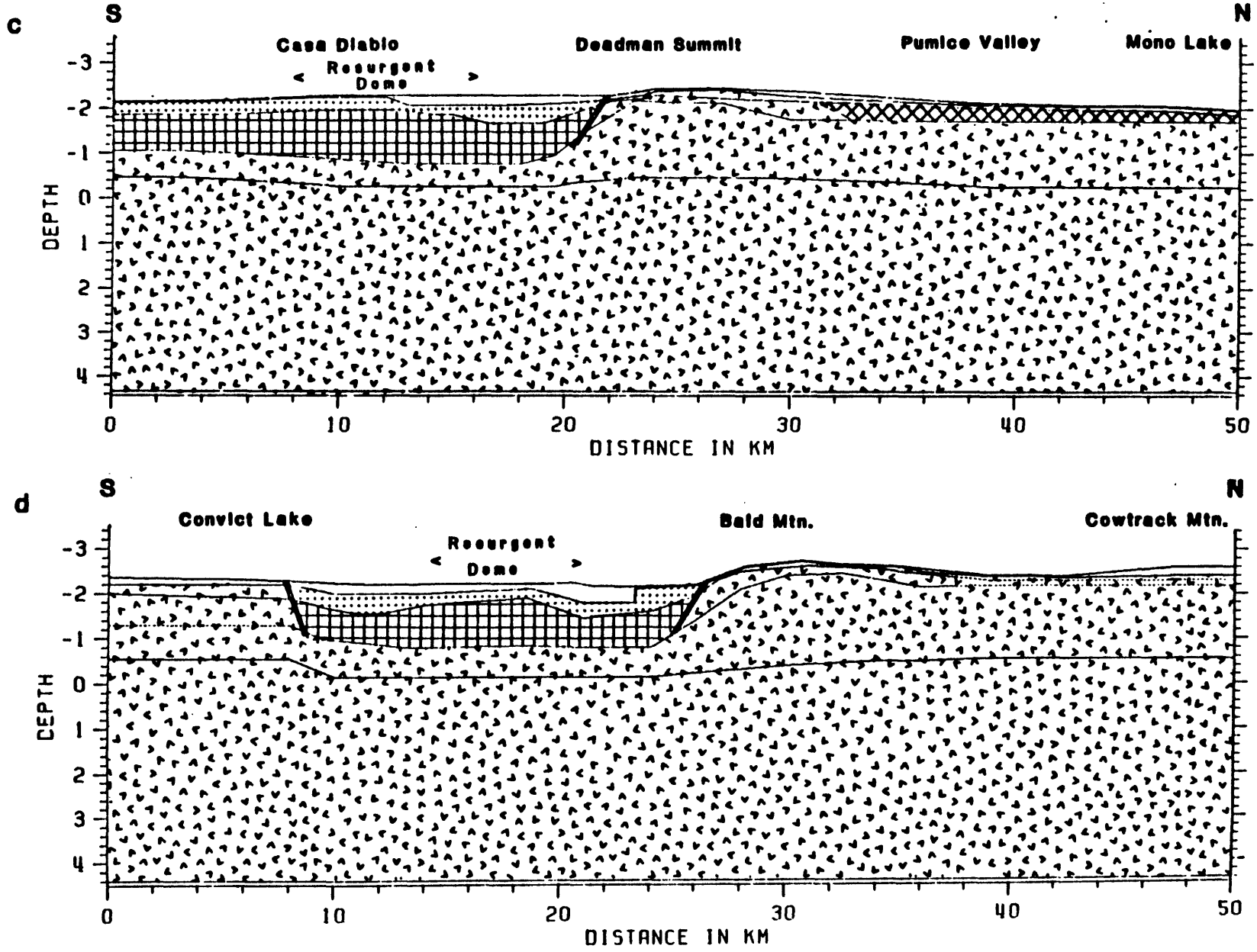
c
S
N
Casa Diablo
Deadman Summit
Pumice Valley
Mono Lake
Resurgent Dome
DEPTH
-3
-2
-1
0
1
2
3
4
0
10
20
30
40
50
DISTANCE IN KM
d
S
N
Convict Lake
Bald Mtn.
Cowtrack Mtn.
Resurgent Dome
DEPTH
-3
-2
-1
0
1
2
3
4
0
10
20
30
40
50
DISTANCE IN KM

FIGURE 13b

THREE-DIMENSIONAL STRUCTURE OF THE LONG VALLEY CALDERA, CALIFORNIA, REGION BY GEOTOMOGRAPHY

E. Kissling*, W. L. Ellsworth, and R. S. Cockerham

U.S. Geological Survey
Menlo Park, California
345 Middlefield Road

* permanent address:
Institut fuer Geophysik
ETH - Hoenggerberg
8093 Zuerich, Switzerland

Abstract

A geotomographic inversion method was used to derive the three-dimensional velocity distribution of Long Valley caldera, California, from local earthquake data. 2450 local events with more than 8 recordings (observations from the 30 permanent and/or 83 temporary stations throughout the area under study) have been selected from the approximately 10,000 events recorded and located between May 1980 and June 1984 by the U.S. Geological Survey. The 31,730 observations were used to determine the velocity perturbations of 3328 blocks thus leading to an overdetermination factor of about 6.5.

The main results of the geotomographic inversion suggest the presence of a zone of low p-velocity (decreased 3%to 5% (0.20 to 0.30 km/s) beneath the southern part of the resurgent dome and the south moat of the caldera between 3km and 7km depth. This anomaly seens to overlie a weaker and broader zone of low p-velocity (decrease of approximately 1%) in the depth range of 5km to 14 km. The latter zone strikes south from beneath the Mono Craters through the Long Valley caldera and runs southeast beneath the south moat and into the Sierran block. While the seismic activity inside the caldera coincides with the area of low p-velocity the majority of the events outride the caldera lies in zones of higher p-velocity.

1. Introduction

The Long Valley caldera and the Inyo-Mono Craters volcanic chain lie at the base of the eastern escarpment of the Sierra Nevada range. The escarpment is formed by large, east-dipping normal faults that define the western margin of the Basin and Range province. This region is the tectonically most active area in eastern California, both in terms of persistent earthquake activity over the last century and frequent volcanism over the last 600,000 years. The large increase in seismicity that occured in January 1983 which coincided with numerous other geophysical phenomena (see other papers this volume) underscores the need for a detailed 3-dimensional image of the upper and middle crust in the Long Valley area. Seismic refraction and gravity studies (Pakiser et al., 1960, 1964; Pakiser, 1961 and 1970; Hill, 1976; Kane et al., 1976) reveal the intracaldera crustal structure of the uppermost 4 km in great detail. In comparison, the information about the velocity distribution below this depth is still sparse and in some cases controversial (Eaton, 1963 and 1966; Johnson, 1965; Steeples and Iyer, 1976; Hill, 1978; Prodehl, 1979).

In this paper we exploit the nearly continuous distribution of seismic activity in the area as a means of probing the middle crust as well as refining the near surface velocity structure. Our approach is to apply geophysical inverse theory to local earthquake travel time data, using some constraints for the uppermost crustal structure gained from the most recent seismic refraction investigation (Hill et al., 1984, this volume).

2. Geotomography

The technique we developed is an extension of the method of Aki and Lee (1976), for determination of three-dimensional velocity structure and hypocenter locations from local earthquakes as refined by Thurber (1981) who added the parameter separation algorithm of Pavlis and Booker (1980) and the ray tracing method of Thurber and Ellsworth (1980). The extension used here was suggested to us by Clayton (Clayton, 1984), and involves the construction of an approximate inverse to a very large system of linear equations. This approximation is similar to the algebraic reconstruction technique commonly used in medical imaging (Herman, 1980), hence the name geotomography.

2.1. Formulation of the Inverse Problem

Following Aki and Lee (1976), the basic set of equations to be solved for the (full) simultaneous inversion of local earthquake travel time data is:

$$t = A\,m + e \qquad (1)$$

where:

t : vector of length n containing the traveltime residuals of n observations

m : vector of length k containing the unknown parameters, i.e. the hypocentral parameters (4*ne = 4* number of events) and the (mo) velocity model parameters. k= 4*ne + mo

A : matrix of size n*k with partial derivatives of travel time with respect to unknowns.

e : error vector.

Methods of solving the large system of linear equations defined by (1) have been the subject of extensive investigation in recent years. One commonly used approach is to solve this system of equations using the damped least squares method (Levenberg, 1944):

$$(\underline{A}\underline{A} + T)m = \underline{A}\, t \qquad \text{and}$$

$$m = (\underline{A}\underline{A} + T)^{-1} \underline{A}\, t \qquad (2)$$

where $\underline{A}$ denotes the transpose of A and T is a diagonal (damping) matrix.

The resolving kernel or resolution matrix R introduced by Backus and Gilbert (1968) for this problem is given as:

$$R = (\underline{A}\underline{A} + T)^{-1} \underline{A}\underline{A} \qquad (3)$$

Wiggins (1972) showed the size of the diagonal elements of this matrix to be a good measure of the resolution. If R is the identity matrix I, the solution is unique.

The principal limitation of this or other methods that determine the solution to (1) by simultaneous inversion of the full system of equations is the size of the matrix A that can be successfully stored and inverted on a given computer. While the size of A or $\underline{A}\underline{A}$ can be controlled by either limiting the number of velocity model parameters (mo) or events (ne) either strategy can severely limit the amount of information that may be learned about the earth.

Given an appropriate amount of a priori information in an area of complex geology a reasonable velocity model might consist of several thousand parameters. The formulation of the problem as an overdetermined system demands an even larger number of equations, each equation being the expression of a traveltime observation. Since the average number of local stations for an

event in an area like Long Valley caldera rarely exceeds 30 but more typically is 10 - 15 stations, we need at least several hundred events. This already leads to a matrix A too large in size to either be stored or inverted in reasonable time . The original method of Aki and Lee (1976) has therefore been modified by several workers to reduce the size of the matrix A.

Pavlis and Booker (1980) developed an algorithm to separate the matrix A in equation (1) into two smaller matrices (H and M) where H contains the partial derivatives of the travel time with respect to the hypocentral parameters and M contains the partial derivatives with respect to the velocity model parameters:

$$A\,m = H\,x + M\,d \qquad (4)$$

m: original vector containing all unkowns (i.e. hypocentral and model perturbations)
x: unknown hypocentral perturbations
d: unknown model perturbations

Their method, known as parameter separation, permits the reformulation of the original problem into another problem that explicitly contains the model parameters as unknowns only:

$$t' = M'\,d + e' \qquad (5)$$

Solutions to this new sets of equations are identical to those for (1) if the hypocenter parameters are determined by least squares. Though the size of the matrix has been reduced considerably, the available data set at places like Long Valley caldera, with broadly distributed seismic activity, may still be an order of magnitude too large to be successfully inverted using full matrix methods. At this point we must either reduce the number of velocity model parameters (and hence M') to a size that can be handled by our computer and sacrifice spatial detail, or construct the solution with an algorithm that does not require random access to the entire matrix.

In this report we are seeking the maximum spatial detail and therefore use an alternate method of solution which we refer to as the geotomographic method. We interpret the results as a first approximation to the three-dimensional velocity structure in Long Valley caldera area.

2.2 Geotomographic Solution Method.

The main advantages of the geotomographic method are the reduction in the amount of computer memory required and in the computational effort needed to construct the solution. The complete conditional equation matrix (M), which contains mo parameters * n observations, requires on the order of mo * mo *n operations to solve it and mo * n words of memory to store it. Here, we store only 2*mo elements, the diagonal elements of the normal equation matrix (M' M + T) and the right hand side vector (M' t'):

$$(M'\,M' + T)d = M'\,t' \qquad (6)$$

Furthermore our solution may be obtained in mo operations (division of each element of vector (M' t') by the respective element of matrix (M' M' + T). This method produces a good approximation to the "correct" solution if the normal equations are diagonally dominant.

The computational burden would be greatly reduced if we neglected the existence of the coupled hypocenter problem, as has been suggested by some investigators. However, we feel that the more conservative approach used here is more appropriate until proven otherwise.

An iterative solution for the model parameters only (Dynes-Lytle algorithm, Dynes and Lytle, 1979) will be obtained by adjusting the velocity model parameters by the results calculated from equation (6) and repeating the whole procedure, beginning with the equation (1). We use the revised three dimensional velocity model in computing the new residuals and raypaths, but retain the original hypocenter locations throughout the procedure.

2.3. Assessment of "Resolution" for the Geotomographic Solution

Resolving kernels may be obtained for the geotomographic solution in the same way as for the full inversion (equation 3). However, the resolution calculation for each block requires construction and storage of the corresponding row of the normal equations. Calculation of the full resolution matrix is therefore impractical. In order to circumvent this problem we define a quantitative measure of the block sampling that can be related to the resolution for each block in a qualitatively simple way.

Intuitively, we know that for a block to be resolved from its neighbors it must be sampled by a unique set of rays (Ellsworth, 1977). If two blocks were sampled in an identical fashion by the same rays we could not separate a velocity change in one from the other. Considering for simplicity sampling of blocks in two-dimensions, it is obvious that two rays passing through a block in directions perpendicular to each other will lead to a better resolution of that block than even a large number of subparallel rays passing through the same block. The same applies of course to a three - dimensional model, only here we need 3 perpendicular rays to achieve optimal resolution. The distribution of all the rays which pass through a block should therefore be a qualitative measure of the resolution of this particular block. If the rays are equally distributed in all directions , or as we refer to it, if the ray density is equal in all directions, the resolution is predicted to be good.

The ray density distribution for each block can be conveniently represented by a tensor (V) defined as the sum of all individual matrices v_n:

$$V = \mathrm{sum}_n (v_n) \qquad (7)$$

$$v'_n = \begin{bmatrix} a & 0 & 0 \\ 0 & 0 & 0 \\ 0 & 0 & 0 \end{bmatrix}$$

v'_n is given in a local coordinate system with its x-axis parallel to the ray. V_n denotes the matrix V'_n in the global coordinate system.

The value of a is proportional to both the length of the ray within the block and the weight given to the observations that lead to this raypath. To calculate the ray density tensor V each v'_n gets transformed into the global coordinate system and added up. One may think of the ray density tensor as the difference between the identity matrix I and the moment of inertia tensor T_n for each ray in the local coordinate system.

$$V'_n = \begin{bmatrix} a & 0 & 0 \\ 0 & 0 & 0 \\ 0 & 0 & 0 \end{bmatrix} = aI - T_n = a \begin{bmatrix} 1 & 0 & 0 \\ 0 & 1 & 0 \\ 0 & 0 & 1 \end{bmatrix} - \begin{bmatrix} 0 & 0 & 0 \\ 0 & a & 0 \\ 0 & 0 & a \end{bmatrix} \quad (8)$$

We can now qualitatively display the resolution for one block (Fig.1) using the eigenvalues (V1,V2,V3 ordered according to their size with V1 as the largest) and eigenvectors of the tensor V and establish some quality categories (see table 1).

Table 1:

eigenvalues of ray density tensor:	resolution:
$V1 = V2 = V3 \neq 0$	excellent
$V1 \simeq V2 > V3 \neq 0$	very good
$V1 > V2 \simeq V3 \neq 0$	good
$V1 > V2 \neq 0,\ V3=0$	fair
$V1 >> V2 \simeq V3 = 0$	poor

Since the ray density may also vary from one block to another, the relative size of the largest eigenvalue of any given block to the largest eigenvalue within the same layer or of all the layers should also be considered when judging the solution (Fig.1). The variable M in the upper left corner of each block (Fig. 7 and following) quantifies this relation (see Fig. 1).

A word of caution is in order at this point, as the ray density tensor contains no information about the presence of side lobes in the resolving kernels, which may be important. For example, a block crossed by three orthogonal rays will yield the "optimal" ray density tensor, but cannot be resolved from a neighboring block that is crossed by only one of the three rays.

3. Application to greater Long Valley caldera area

3.1 Stage 1: Establishing the initial one - dimensional velocity model

Our geotomographic inversion requires both well-located events and a well averaged one-dimensional initial velocity model to get reasonable results with only a few iteration steps. Fortunately, the location program (HYP071, Lee and Lahr,1975) used to locate the events when given the appropriate one-dimensional model and station corrections, yields quite accurate locations, as will be shown.

We calculated both station corrections and one-dimensional velocity model by (full) inversion of travel times from 800 selected events using a procedure written by Roecker and Ellsworth (1978) following the method of Crosson (1976).

To account for the differences in seismic velocities of the upper 2 km inside and outside the caldera we selected two independent subsets of 400 earthquakes each by choosing source - receiver pairs that lead to raypaths entirely within either the caldera or the surrounding Sierran block. The one-dimensional models derived from the full inversion for the coupled hypocenter - structure problem using these two subsets of data match those from the extensive seismic refraction profiling in the same area (Kissling et al., 1983). The difference between the two models is principally in the values of the derived station corrections and in the velocities and layer boundaries of the uppermost 3 km of the crust. While both models give almost identical locations for events within the caldera, the Sierran model is clearly superior with increasing distance from the caldera boundary (Cockerham and Pitt, 1984 , this volume). We therefore concluded the best one-dimensional model for the whole area under study to be a Sierra type model with some refinement in the velocities of the uppermost 3 km. This final model was again derived by full inversion of the traveltimes from 400 selected events .

For the final one-dimensional model (Fig. 2) used as the starting model for the geotomographic inversion, care was taken to introduce enough layer boundaries at appropiate depths to match the drillhole information (Sorey et al., 1978), the seismic refraction data (Hill and others, 1984), and the two one-dimensional models inside and outside the caldera of the previous inversions. This final one-dimensional model is but a crude first approximation to the true velocity distribution in the area. The small relative error in the location of 12 shots from the seismic refraction experiment (Hill et al.,1984) show (Fig.4) that this model used in conjunction with the simultaneously calculated station corrections (Cockerham and Pitt, 1984) for the 113 stations of this study (Fig.3) is appropriate for locating events in the caldera.

3.2 Stage 2 : Model and data specification for geotomographic inversion

In the second stage of our analysis we calculate a first approximation to the three-dimensional velocity distribution by the geotomographic method using the hypocenter and origin times for all the events recorded in the area since August, 1980.

From over 10,000 events we selected some 7229 events that meet the following criteria:

1) seven or more observations of reading quality 2 (Lee and Lahr, 1975) or better
2) root mean square of all p-wave traveltime residuals of each event smaller than 0.15 sec.

The first criteria turned out to be far more important since about 90 percent of the events that failed were ruled out because of insufficent total number of observations that matched the required standard in observation weight and in size of the residual (less than 0.25 sec).

Unfortunately, these 7229 events (Fig.5) are not evenly distributed throughout the study area but tend to cluster in the south moat of the caldera and the adjacent Sierran block (Cockerham and Pitt,1984). They locate within a depth range of 2 to 14 km . Unfrequently though, events also do occur in most other parts of the area under study. As tests with one-step geotomographic solutions calculated for this data set of over 69,000 observations showed the input data could be considerably reduced with hardly any change in the area and depth range sampled as well as in the resulting velocity model. We therefore further selected events in the area of the south moat and directly south of it within the Sierran block where most events cluster (Fig.5). Keeping the 500 events for each of these two areas with the most readings and of about the same depth distribution and requesting a minimum of 8 observations for all events, we end up with the final data set of 2450 events (Fig. 6) and a total of 31,730 observations.

To reduce observational redundancy along densely sampled raypaths we applied to each ray, in addition to the observation weight, a geometric weight (W_g) inversely proportional to the total number (NR) of rays (plus a constant, here 4), that originate from events within the same model block and end at the same station.

$$W_g = \frac{1}{NR + 4} \qquad (9)$$

The starting p-velocity model for the geotomographic inversion is one-dimensional and consists of 6860 blocks of variable size. The block height is equal to the respective layer thickness they subdivide, while the length and width of the blocks is variable. The flexible blocksize serves the demands for very small blocks in well sampled areas with expected large lateral variation of p-velocity and large blocks for poorly sampled areas that allow an approximation of the average velocity. Furthermore, the flexible blocksize permits the separation of the caldera from its surrounding areas quite accurately with only a small increase in the total number of blocks, since the total number of blocks is limited for computational reasons.

The smallest blocks have both a width and length of 2km and were used for the best sampled areas, mainly within the Long Valley caldera. The area outside the caldera (Fig. 3) was divided into blocks ranging from 20 km x 20 km down to 2 km x 2km depending on the number and directions of rays sampling the block and on the available geologic information. Most of this area is poorly sampled and was included in the model only to get better azimuthal coverage with distant stations where local stations were not available. The size of the blocks for the area of interest, Long Valley caldera and adjacent region, is shown for each layer with the ray density distribution (Fig. 7, 8, 9, 10, 12 and 14 upper parts).

In the inversion of local earthquake data, the choice of ray tracing method affects not only the accuracy and stability of the results but also the computation time. Our goal is to establish a three-dimensional velocity model of the upper crust in the greater Long Valley caldera area. However, this does not mean our model could account for reflected and refracted phases off other than horizontal boundaries. The structural model is basically one-dimensional with a three-dimensional velocity grid superimposed. The raytracer used in this procedure exactly calculates the direct and refracted ray for a one-dimensional model with velocities averaged from the 3D - velocity - grid for each layer over the distance between source and receiver (Thurber and Ellsworth, 1980). Once the raypath is established, the travel time is calculated according to the 3D - velocity distribution.

The inversion procedure starts by raytracing all the observations of one event at a time, then performs the hypocentral parameter separation (Pavlis and Booker, 1980) and accumulates the diagonal elements of the normal equations (6). The velocity perturbations are finally calculated by a simple division of the right hand side vector by the diagonal element of the matrix on the left hand side of the equation (6) which includes the damping factor. Velocity perturbations were calculated only for blocks penetrated by at least 3 rays in order to downweight the effects of single anomalous raypaths.

We estimate that a damping factor of 10.0, corresponding to a timing error of 0.03 sec and an inferred root mean square model fluctuation of 1 percent, would produce a particular solution that approximates a stochastic inverse (Franklin, 1970). However, for the results presented in this paper we have chosen a damping factor of 50.0 thus overdamping the system. The variance improvement due to the solution may be approximately determined from information retained in the geotomographic solution (Aki et al., 1977). For the one-step solution with a damping factor of 50.0, the estimated variance improvement of 90 percent overestimates the true variance reduction by about a factor of 2.5, as a second iteration with the Dynes-Lytel algorithum has shown.

4. Velocity distribution of the upper crust in Long Valley caldera area

Layers 1 to 4 (0 to 2 km depth)

The first four layers of the model contain the topography (layer 1) and the uppermost 2km of the crust, taking the caldera floor at 2000 m above sea level as reference plane. In these layers we estimate that we have good resolution (Fig. 7, upper part) for most sampled blocks but we do not sample many blocks in each layer. Probably as a result of the heavy damping and the thin layers, the differences in velocity from block to block are small in most places for the first 4 layers as illustrated by layer 2 (Fig. 7, lower part). Since the base of the Bishop Tuff is approximately 2km below the caldera floor (Sorey et al., 1978; Hill et al., 1984) any lateral velocity variations within the first 4 layers of the caldera may be interpreted as lateral variations in lithology as discussed by Bailey et. al. (1976).

Layer 5 (2km to 3km depth, Fig. 8)

Layer 5 represents the shallowest level in our model that may contain the same lithology inside and outside the caldera, according to refraction modeling (Hill et al., 1984). This layer contains localized regions with velocity variations of about 2 , occasionally as high as 8 superimposed on an otherwise fairly uniform p-velocity of 5.35 km/s. Long Valley caldera is characterized by weakly negative velocity perturbations, with all positive anomalies outside or in the westernmost part of the caldera. The southern boundary of the caldera, an area with abundant data, is particularly well-defined.

Layer 6 (3km to 5km depth, Fig. 9)

The most intense velocity fluctuations in the model are found in this generally well-resolved layer. A pronounced area of low p-velocity underlies the resurgent dome and south moat of the caldera. We question the reality of the deep low beneath the resurgent dome, as leakage of the true anomalies at shallower levels along raypaths from station LMC (Fig. 4) might produce the observed pattern. Further tests are currently in progress to resolve this question. However, we feel confident that the low-velocity region in the south moat is faithfully imaged in our model. Two other zones of lower than average velocity in areas of fair resolution can also be seen, beneath the Mono Craters and Tom's Place.

Layer 7 (5km to 7km depth, Fig. 10)

This layer contains the highest level of earthquake activity within the caldera (Cockerham and Pitt, 1984), and is well sampled by rays from deeper events to the south as well as events at this level. The ray density diagram for this layer (Fig. 10, upper part) indicates that resolution should be good to fair in most areas. The velocity perturbations generally resemble those found in the overlying and underlying layers. Intense low-velocity zones are seen beneath the south moat and southern half of the resurgent dome, with weaker anomalies aligned along a NE-SW trend from Mono Craters to Tom's Place.

Layer 8 (7km to 9 km depth, Fig. 11

The sampling in this layer is good throughout the caldera and in the area to the south and in parts to the east (Fig. 11, upper part). The p-velocity distribution again shows a zone of lower velocity extending from beneath the Mono Craters through the caldera, across the south moat and into the Sierran block to the south-east. Localized anomalies of larger amplitude are superimposed on this general trend. Higher p-velocities are found in the area surrounding the caldera mainly in the east and south. The anomalies are somewhat weaker than in the overlying layers, which might suggest that the base of the south moat low velocity zone is being encountered. However, the amplitude of the perturbations may be controlled by the damping and method of solution rather than earth structure.

Layer 9 (9km to 11km depth, Fig. 12)

The well sampled area for layer 9 encompasses the caldera, part of the Sierran block to the south, and parts of the Sierran block to the south, and parts of the crustal blocks to the east and north of the caldera (Fig. 12, upper part). The percent changes in p-velocity are fairly small (-2% to +2%) compared to shallower layers. As in the overlying layers, a broad, continuous zone of weakly low velocities crosses the caldera from northwest to southeast. Regions of higher p-velocity coincide with the Sierra Nevada in the south and west and the crustal block with outcropping basement east of the caldera.

Layer 10 (11km to 14km depth, Fig. 13)

Due to the small number of events below 14km depth (Cockerham and Pitt, 1984) the area with good sampling shrinks considerably going from layer 9 to layer 10. In layer 10 only the south moat of the caldera and a small part of the sierran block to the south are well sampled leaving the rest with but fair or poor resolution (Fig. 13, upper part). The velocity distribution in layer 10 in general is very similar to the distribution in layer 9 except that the amplitudes have decreased by about a factor of 3.

5. Discussion

The p-wave velocity distribution of the uppermost 3km in Long Valley caldera is fairly uniform with some very local low or high velocity anomalies superimposed (Figs. 7-8). The average velocities for these layers match those measured with refraction seismic experiments (Hill et al., 1984), as expected since the layer thickness has been taken from the results of the refraction experiments. However, the refraction data shows broader lateral variations of the p-velocity within for the uppermost 3 km of the crust (Hill and others, 1984) in contrast to our generally uniform distribution with local anomalies of in some places large amplitudes (a 2% change in p-velocity in layer 5, Fig. 8, equals 0.10 km/s). Considering though the effect of the dominately vertical block sampling in the first 5 layers (see Figs. 7 and 8, upper part) in contrast to the more horizontal sampling by seismic refraction data, on results are not surprising. The anomalies in p-velocity found by the geotomographic inversion in general tend to decrease in amplitude and increase in wavelength when going from shallower to deeper layers. This may reflect basic features of the p-velocity distribution within the earth but is also in part the result of the applied technique. As a result of the depth distribution of the earthquakes, the sampling in the shallowest 3 km is dominantly sub-vertical (see for example Fig. 7, upper part), while at depths greater than 7km the majority of the blocks are sampled by subhorizontal rays (Fig. 11, upper part). The raytracer used in this study has a smoothing effect that is largest for horizontal raypaths thus affecting the layer 8, 9, and 10 more than shallower layers. In contrast to the uppermost 3km of the crust, layers 6 to 10 show rather broad p-velocity anomalies, some of them continuing over two or more layers. The common feature in the depth range of

3km to 14km is a roughly 10 km wide zone of lower p-velocity that extends from beneath the Mono Craters, through the caldera and to the southeast beneath Tom's Place. In layers 6, 7, and 8 this zone widens beneath Long Valley caldera to encompass most of the caldera (Figs. 9, 10 and 11). In several layers (Figs. 9 to 12) this zone of low p-velocity is best defined by several local anomalies of increased velocity that are almost exclusively found in the area surrounding the caldera. On average, the p-velocity within this anomalous zone is 2% to 3% lower than the velocity in the surrounding areas.

In layers 6 and 7 (depth range 3km to 7km) a strong (decrease of 5% in p-velocity) local anomaly underlies the resurgent dome and the south moat. Additional strong local (decreases in p-velocity are found at shallower depth beneath the southern end of the Mono Craters and beneath Tom's Place (Figs. 9 and 10), though these two anomalies are in areas with but fair resolution. Sanders (1984, Fig. 1) defines three areas of high s-wave attenuation within the caldera and another one south of Lake Crowley. In general these zones correspond well with the areas of strongest decreases in p-velocity found in this study. We believe the local discrepancies to be due to the lack of sufficient accuracy in either method as a result of the errors in hypocenter location and of the block model.

The resulting velocity perturbations for the upper 14 km of the Long Valley caldera area calculated from local earthquake data may also be compared with the distribution of delays for teleseismic events described by Steeples and Iyer (1976). While the location of the zone of low velocity matches well, Steeples and Iyer's (1976) model favors a decrease in p-velocity of 10 percent compared with the 2-3 percent decrease for the broad anomaly resulting from this study. This apparent discrepancy might be explained by near surface structure within the caldera. Steeples and Iyer (1976) assumed a delay in traveltime of 0.2 sec to account for the low-velocity material of the uppermost 6 km within the Long Valley caldera. In the light of the extensive new refraction data recorded in 1982 and 1983 throughout the area (Meador and Hill, 1983, and Hill et al., 1984) a delay of 0.3 - 0.4 sec seems to be more appropriate. Thus the amplitude of the anomaly modeled by Steeples and Iyer (1976) may be reduced by half, which would be more compatible with our results. Furthermore, the local anomalies within the caldera found in layers 6 and 7 with up to 5% decrease in p-velocity cause additional delay in traveltime for teleseismic events in the area of the resurgent dome and south moat where Steeples and Iyer (1976) observe the largest delays. While amplitude and horizontal location of the anomalies seem to match fairly well, the depth of the anomalous zones differ considerably. Steeples and Iyer (1976) favor a decrease in p-velocity in the depth range between 6 km and 20 km while our results show evidence for a braod weakly anomalous zone between 5km and 14km with the top of the strong local anomalies beneath the resurgent dome and the south moat as shallow as 3km.

Another finding is that the location of the majority of the earthquakes outside the caldera (Fig. 5) correlates well with areas of higher p-velocity while within the caldera the earthquake activity is almost exclusively found in the southmoat and in the southern part of the resurgent dome (Fig. 5), areas of strongly decreased p-velocity. In addition over 90% of the

earthquakes within the caldera occur at depths shallower than 9km where we observe the strongest decrease in p-velocity inside the caldera (layer 6, 7, and 8), while the seismicity in the Sierra block south of the caldera is spread over a much large depth range (Fig. 14). The principal exception to this correlation is the strong decrease in p-velocity beneath the northern resurgent dome (Fig. 9), where very few, if any earthquakes occur (Fig. 5). However, we suspect that this feature is in part an artifact created by leakage from station LMC (Fig. 4). The seismic refraction data (Hill et al., 1984) reveal an unusually thick sedimentary cover (with p-velocity as low as 2.0 km/s) in this region where we lack good vertical resolution.

6. Conclusions

The geotomographic method allows the inversion of travel timed data from a large number of events for a large number of velocity parameters, resulting in a first-order approximation of the geotomographic inversion to the Long Valley caldera area suggest the presence of a roughly 10km wide zone where p-wave velocity is approximately 2 percent (-0.10 km/sec lower than the surrounding region). The zone strikes N-S from the Mono Craters through the Long Valley caldera and to the southeast into the Sierra at a depth between 5km and 14km from the surface. Superimposed on this zone is a local anomaly of low p-velocity (additional decrease of 3%) beneath the resurgent dome and south moat of the caldera at depth between 3km and 7km.

These results are in plausible agreement with the distribution of delays of teleseismic events (Steeples and Iyer, 1976). In general the zones of strongly decreased p-velocity coincides with areas of high s-wave attenuation (Sanders, 1984) though this geotomographic study lacks good resolution in places outside the caldera, where some of these local anomalies are found.

Inside Long Valley caldera the vast majority of the earthquakes occur within the zone of lower p-velocity in the south moat suggesting fracturing at this crustal volume being at least partly the cause for the decrease in p-velocity. In constrast the seismic activity outside the caldera is almost exclusively found in areas of high p-velocity. Most of the local earthquakes occur in the upper 10km of the crust (Fig. 14), limiting the present study to alert the same depth range.

However, with the addition of information about the p-wave velocity in the middle and lower crust from long range seismic refraction profiles and with the inclusion of additional distant stations and well-located events, the three-dimensional velocity distribution under Long Valley caldera could be illuminated to a greater depth where we have good reason (Steeples and Iyer, 1976) to expect the low p-velocity body continuing under Long Valley caldera.

Fig. 1 Example of ray density distribution (V) for one model block. The ray density tensor V is represented by two ellipses (E1 and E2), that are two perpendicular cross sections of the ellipsoid defined by the three eigenvalues V1,V2,V3 ordered according to their size. The larger the eigenvalue the more rays that passed through the block in this direction.
β : dip of eigenvector of largest eigenvalue
M : size of largest eigenvalue of this block (V1) relative to largest eigenvalue of layer (V_{max}).
$M = -10 \log \left(\frac{V1}{V_{max}}\right)$

Fig. 2 One - dimensional velocity model of greater Long Valley caldera area determined by inversion of local earthquake data (800 selected events). Surface corresponds to elevation of 2000 m, which is approximately the floor Long Valley caldera. The average velocity of topography above this level is 3.50 km/sec in this model.

Fig.3 Area under study for geotomographic inversion. Each star denotes a station (temporary or permanent) used for the inversion.

Fig.4 Comparison of the true locations (large circles) of 11 shots (S1-S11) from refraction seismic experiments (Hill et al., 1984) with the locations (dots) calculated with HYP071 (Lee and Lahr,1975) using the one-dimensional velocity model (Fig.2) and appropriate station corrections. At the time of the shot S10 and S11 (1982) only 5 of the stations shown here were in operation. The calculated locations of the shots S6 and S7 clearly show the effect of the thick quarternary sediments of the caldera fill east of station CSR which are not accounted for in our one-dimensional model.

Fig.5 Distribution of 7229 best located events (dots, Cockerham and Pitt, 1984) and stations (stars) in Long Valley and adjacent Sierran block.

Fig.6 Distribution of 2450 selected events (dots) and stations (stars) in Long Valley caldera area used for the geotomographic inversion.

Fig.7 Distribution of ray density (upper part) and of percentage change in p-velocity (lower part) for layer 2 in Long Valley caldera area. Top of layer 2 is the surface within Long Valley caldera (at 2 km above sea level). The thickness of layer 2 is 0.5 km and the p-velocity used in the one-dimensional model is 3.55 km/sec. The dots mark the location of the stations. Places with changes in p-velocity of 1 percent or larger are marked by underlines. Note the correlation of

negative values (lower p-velocities) with the Long Valley caldera in general thus showing the effect of the thick caldera fill.

Fig.8 Ray density (upper part) and p-velocity distribution (in percent velocity change) for layer 5 (depth range 2-3km) for Long Valley caldera area. The p-velocity used in the one-dimensional model is 5.35 km/s.

Fig.9 Ray density (upper part) and p-velocity distribution (in percent velocity change) for layer 6 (depth range 3-5 km) for Long Valley caldera area. The p-velocity of the one-dimensional-model used for this layer is 5.67 km/s.

Fig.10 Ray density (upper part) and p-velocity distribution (in percent velocity change) for layer 7 (depth range of 5-7km). The p-velocity used in the one-dimensional model for this layer is 5.9 km/s.

Fig.11 Ray density (upper part) and p-velocity distribution (in percent velocity change) for layer 8 representing the depth range of 7 to 9 km. The p-velocity used in the one-dimensional model for this layer is 6.00 km/s.

Fig.12 Ray density (upper part) and p-velocity distribution (in percent velocity change) for layer 9 representing the depth range of 9 km to 11 km. The p-velocity of this layer in the one-dimensional model is 6.07 km/s.

Fig. 13 Ray density (upper part) and p-velocity distribution (in percent velocity change) for layer 10 representing the depth range of 11km to 14km. The p-velocity of this layer in the one-dimensional model is 6.10 km/s.

Fig. 14 Focal depth distribution of earthquakes recorded by U.S Geological Survey between June 1984 and July 1984. A: inside the caldera (Total 7116 events) B: outside the caldera, mainly with Sierra Nevada (total 4060 events).

Acknowledgments

We thank A. Ryall, University of Nevada, Reno, for supplying records from his regional network surrounding Long Valley caldera. We are grateful to many U.S. Geological Survey colleagues for helpful discussions, in particular we thank D. Hill and J. Lahr for their suggestions and D. Oppenheimer and H. M. Iyer for critically reviewing the manuscript. We thank S. Johnson and J. Ellefson for carefully typing the manuscript. One of us (E.K.) was supported by the National Science Foundation of Switzerland under project no. 82.998.0.82.

References

Aki, K. and W. H. K. Lee, Determination of three-dimensional velocity anomalies under a seismic array using first P arrival times from local earthquakes, 1, A homogeneous initial model, J. Geophys. Res., 81, 4381-4399, 1976.

A

References

Aki, K. and W. H. K. Lee, Determination of three-dimensional velocity anomalies under a seismic array using first P arrival times from local earthquakes, 1, A homogeneous initial model, J. Geophys. Res., 81, 4381-4399, 1976.

Aki, K., A. Christofferson, and E. S. Husebye, Determination of the three-dimensional seismic structure of the lithosphere, J. Geophys. Res., 82, 277-296, 1977.

Bailey, R. A., G. B. Dalrymple, and M. A. Lanphere, Volcanism, structure, and geochronology of Long Valley caldera, Mono County, California, J. Geophys. Res., 81, 725-744, 1976.

Clayton, R., Seismic Tomography (abs.), EOS Trans. Amer.Geophys.Union,v.65, p.236,1984.

Cockerham, R., and M. Pitt, Seismic activity in Long Valley Caldera area, California-June 1982 through July 1984; this volume, 1984.

Crosson, R. S., Crustal modelling of earthquake data 1. Simultaneous least squares estimation of hypocenters and velocity parameters, J. Geophys. Res., 81, 3036-3046.

Dynes, K. A., and R. J. Lytle, Computerized geophysical tomography, Proc. IEEE, 6717, 1065-1073, 1979.

Eaton, J. P., Crustal structure from San Francisco, California, to Eureka, Nevada, from seismic refraction measurements, J. Geophys. Res., 68, 5789-5806, 1963.

Eaton, J. P., Crustal structure in northern and central California from seismic evidence, geology of Northern California, edited by E. H. Balley, Calif. Div. Mines Geol. Bull, 190, 419-426, 1966.

Ellsworth, W. L., Three-dimensional structure of the crust and mantle beneath the island of Hawaii, Ph.D. dissertation, Massachusetts Institute of Technology, Cambridge, Massachusetts, 327 pp., 1977.

Franklin, J. N., Well-posed stochastic extensions of ill-posed linear problems, J. Math. Anal. Appl., 31, p. 682-716, 1970.

Herman, G. T., Image reconstruction from projections, The Fundamentals of computerized tomography, Academic Press, New York, 316 pp., 1980.

Hill, D. P., Structure of Long Valley caldera from seismic refraction experiments, J. Geophys. Res., 81, 745-753, 1976.

Hill, D. P., Seismic evidence for the structure and Cenozoic tectonics of the Pacific and states, Geol. Soc. Am. Mem., 152, 145-173, 1978.

Hill, D. P., Contemporary block tectonics: California and Nevada, J. Geophys. Res., 87, 5433-5450, 1982.

Hill, D. P., E. Kissling, and J. H. Luetgert, and U. Kradolfer, Constraints on the upper crustal structure of the Long Valley - Mono Craters volcanic complex, eastern California, from seismic-refraction measurements, this volume, 1984.

Johnson, L. R., Crustal structure between Lake Mead, Nevada, and Mono Lake, California, J. Geophys. Res., 70, 2863-2872, 1965.

Kane, M. F., D. R. Mabey, and R. L. Brace, A gravity and magnetic investigation of Long Valley caldera, Mono County California, J. Geophys. Res., 81, 754-762, 1976.
Kissling E., W. L. Ellsworth, and R. Cockerham, Structure of Long Valley caldera region as interpreted from seismic data (abs.): EOS, Trans. Amer. Geophys. Union, 64, 890, 1983.
Leavenberg, K., A method for the solution of certain non-linear problems in least squares, Quant. Appl. Math., 2, 164-168, 1944.
Lee, W. H. K., and J. C. Lahr, HYPO71 (revised): A computer program for determining hypocenter, magnitude, and first motion pattern of local earthquakes, U.S. Geol. Surv. Open File Rep. 75-3111, 114 pp., 1975.
Meador, P., and Hill, D. P., Data report for the August 1982 seismic-refraction experiment in the Mono Craters-Long Valley region, California, U.S. Geological Survey Open-File REport 83-708, 53 pp., 1983.
Pakiser, L. C., Gravity, volcanism, and crustal deformation in Long Valley, California, U.S. Geol. Surv. Prof. Pap. 424-B, B250-B253, 1961
Pakiser, L. C., Structure of Mono Basin, California, J. Geophys. Res., 75, 4077-4080, 1970.
Pakiser, L. C., F. Press, and M. F. Kane, Geophysical investigation of Mono Basin, California, Geol. Soc. Amer. Bull., 71, 415-447, 1960.
Pakiser, L. C., M. F. Kane, and W. H. Jackson, Structural geology and volcanism of the Owens Valley region, California-A geophysical study, U.S. Geol. Surv. Prof. Pap. 438, 68 pp., 1964.
Pavlis, G. L. and J. R. Booker, The mixed discrete continuous inverse problem: application to the simultaneous determination of earthquake hypocenters and velocity structure, J. Geophys. Res. 85, 4801-4810, 1980.
Prodehl, C., Crustal structure of the Western United States, U.S. Geol. Surv. Prof. Pap. 1034, 74 pp., 1979.
Roecker, S., and Ellsworth, W. L., VELEST, Fortran Program, U.S. Geol. Surv., Menlo Park, California, 1978.
Sanders, C. O., Location and configuration of magma bodies beneath Long Valley, California, determined from anomalous earthquake signals, this volume, 1984.
Sorey, M. L., R. F. Lewis, and F. H. Olmsted, The hydrothermal system of Long Valley caldera, California, U.S. Geol. Surv. Prof. Pap. 1044-A, 60 pp., 1978.
Steeples, D. W., and H. M. Iyer, Low-velocity zone under Long Valley as determined from teleseismic events, J. Geophys. Res., 81, 849-860, 1976.
Thurber, C. H., Earth structure and earthquake locations in the Coyote Lake area, central California, Ph.D. Dissertation, Massachusetts Institute of Technology, Cambridge, Massachusetts, 332 pp., 1981.
Thurber, C. H., and W. L. Ellsworth, Rapid solution of raytracing problems in heterogeneous media, Bull. Seismol. Soc. Am., 70, 1137-1148, 1980.
Wiggins, R. A., The general linear inverse problems: implication of surface waves and free oscillations for Earth structure, Rev. Geophys. Space Phys., 10, 251-10,285, 1972.
Zoback, M. L., and M. Zoback, State of stress in conterminous United States, J. Geophys. Res., 85, 6113-6156, 1980.

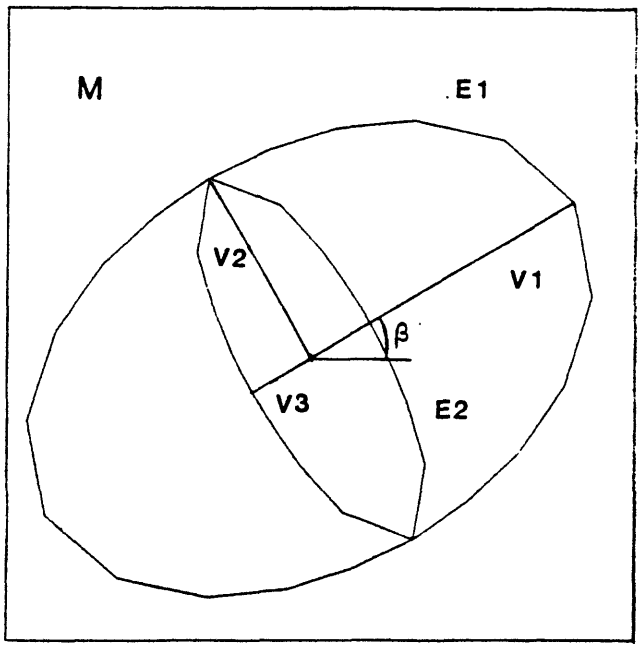

FIGURE 1

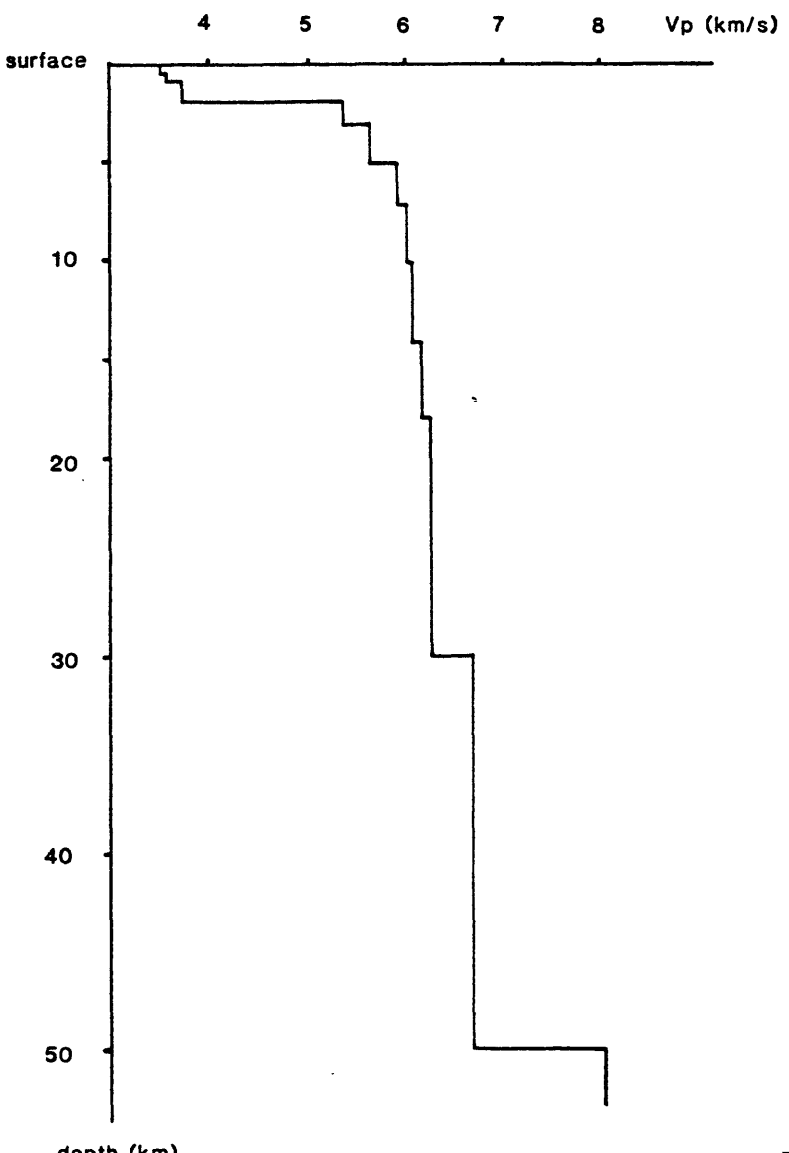

FIGURE 2

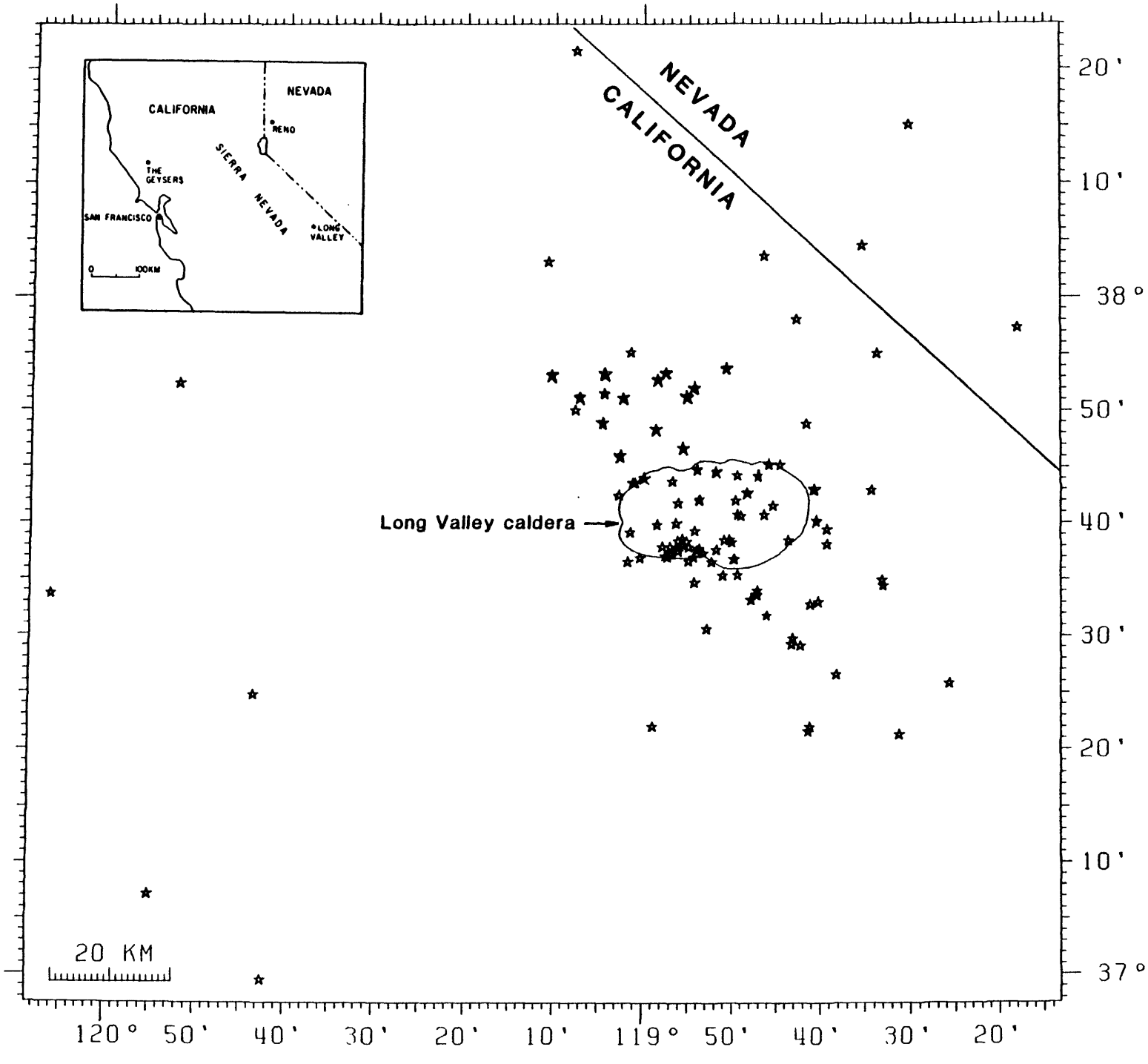
NEVADA
CALIFORNIA
CALIFORNIA
NEVADA
RENO
THE GEYSERS
SIERRA NEVADA
SAN FRANCISCO
LONG VALLEY
0
100KM
Long Valley caldera
20 KM
20'
10'
38°
50'
40'
30'
20'
10'
37°
120° 50' 40' 30' 20' 10' 119° 50' 40' 30' 20'

FIGURE 3

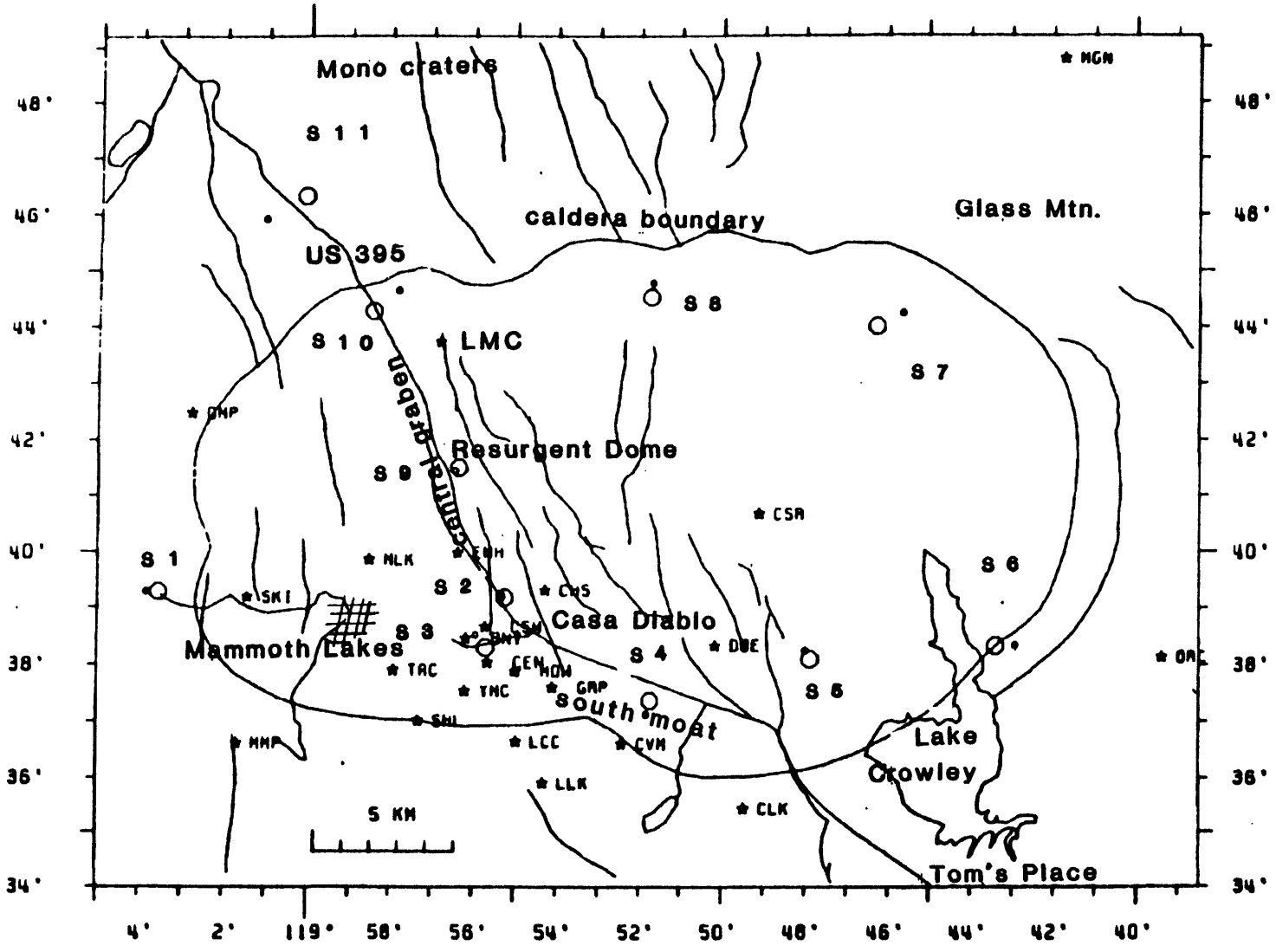
Mono craters
S 1 1
caldera boundary
Glass Mtn.
US 395
S 8
S 10
LMC
S 7
Resurgent Dome
S 9
S 1
S 2
S 3
S 4
S 5
S 6
Casa Diablo
Mammoth Lakes
South moat
Lake Crowley
Tom's Place
5 KM
MGN
OMP
MLK
SKI
CMS
CSM
BMT
CEN
HOM
TAC
TMC
GRP
SHL
MMP
LCC
CVM
LLK
CLK
CSR
DBE
OR
48°
46°
44°
42°
40°
38°
36°
34°
4'
2'
119°
58'
56'
54'
52'
50'
48'
46'
44'
42'
40'

FIGURE 4

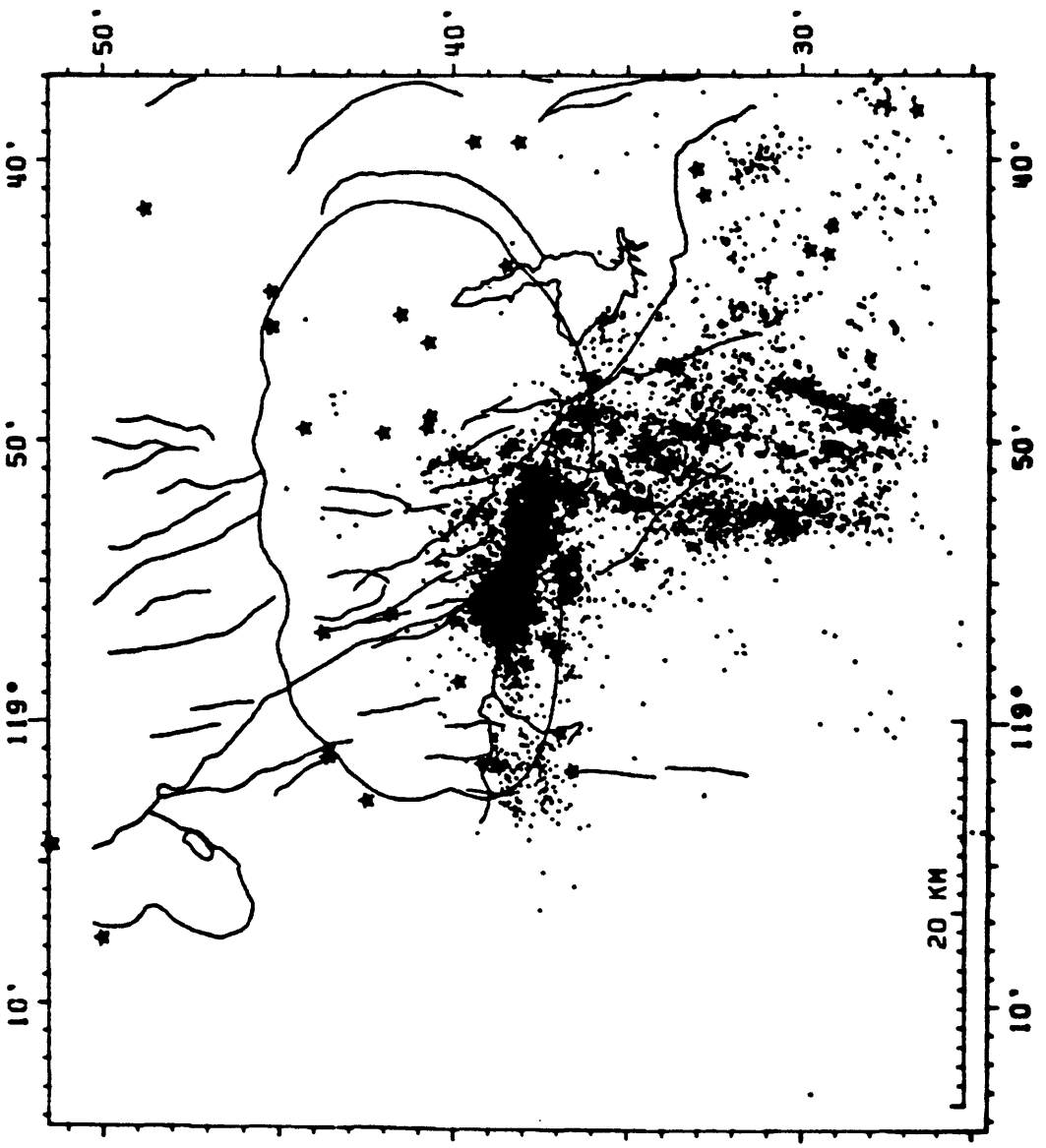

FIGURE 5

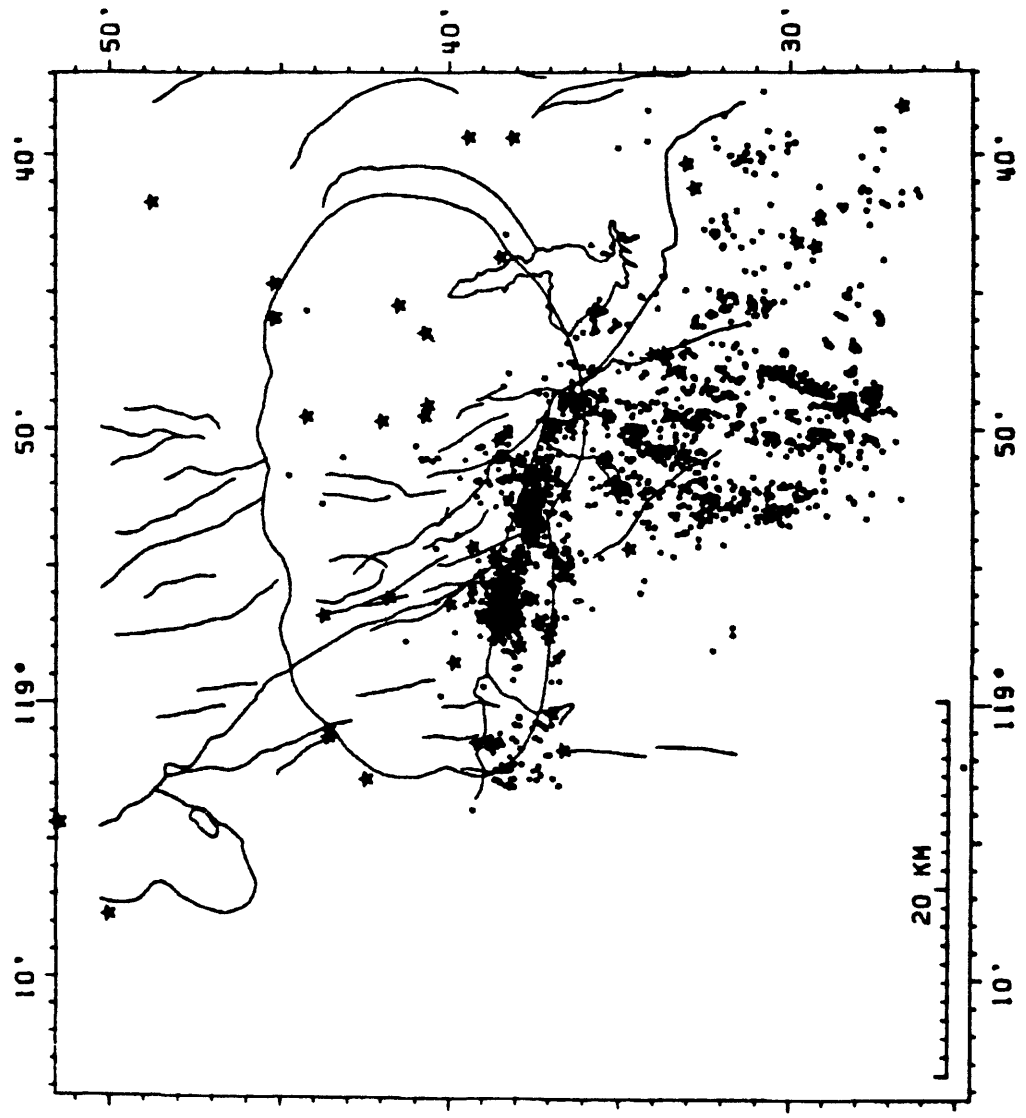

FTGURE 6

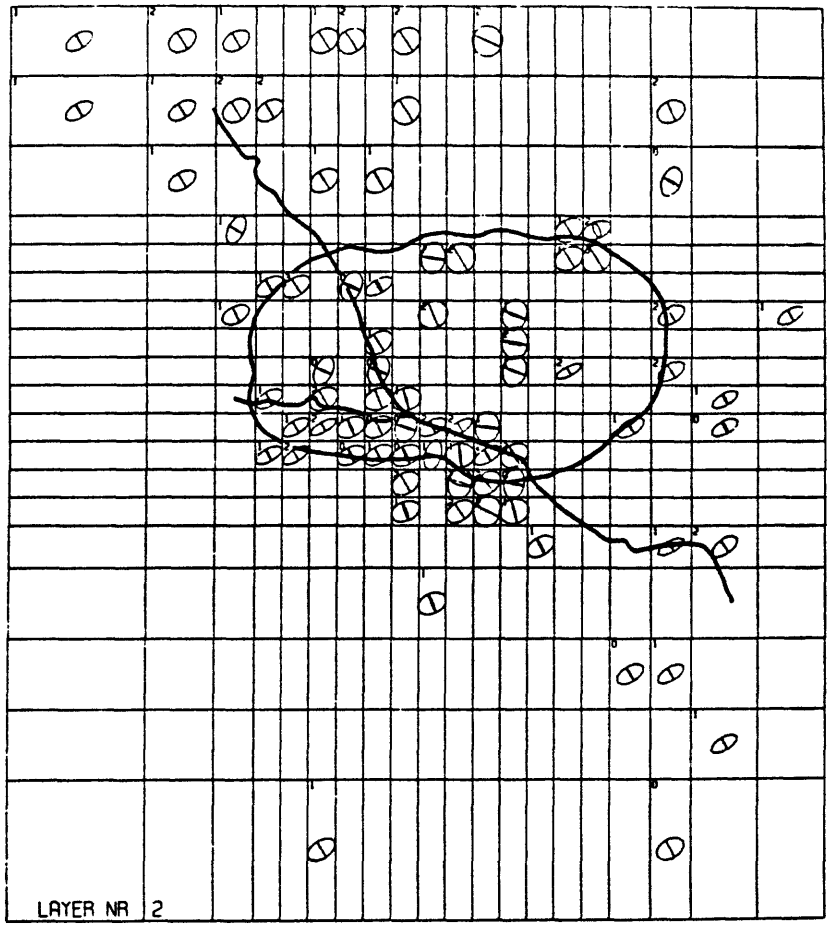

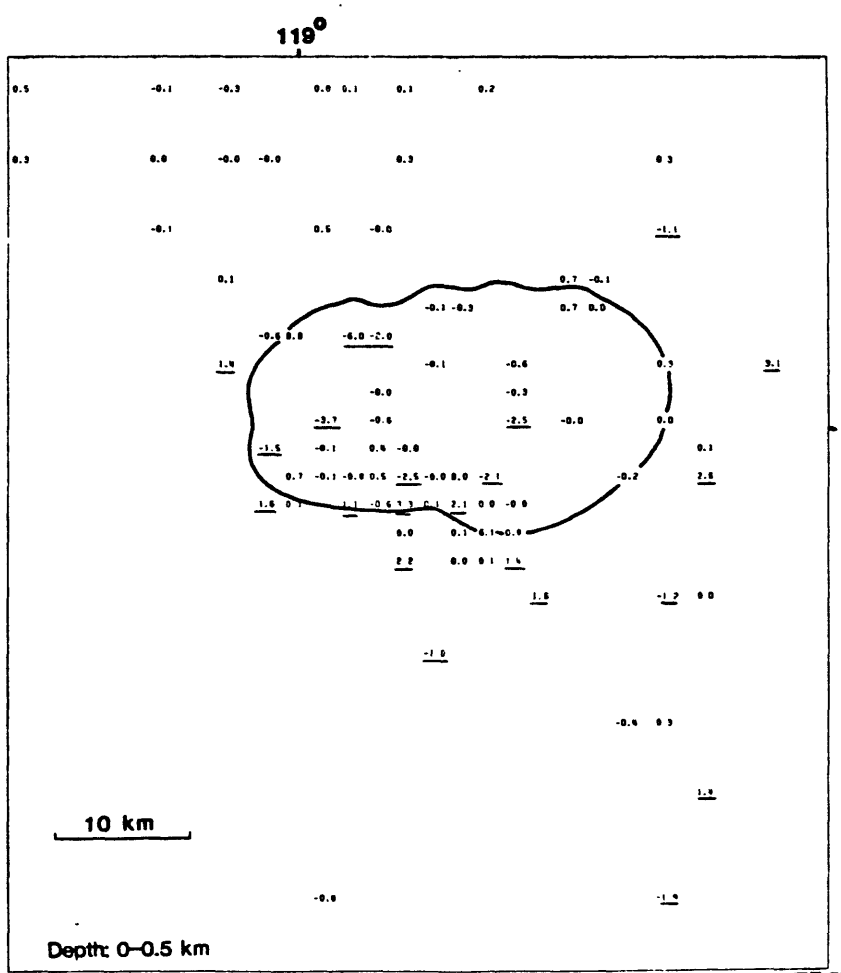

FIGURE 7

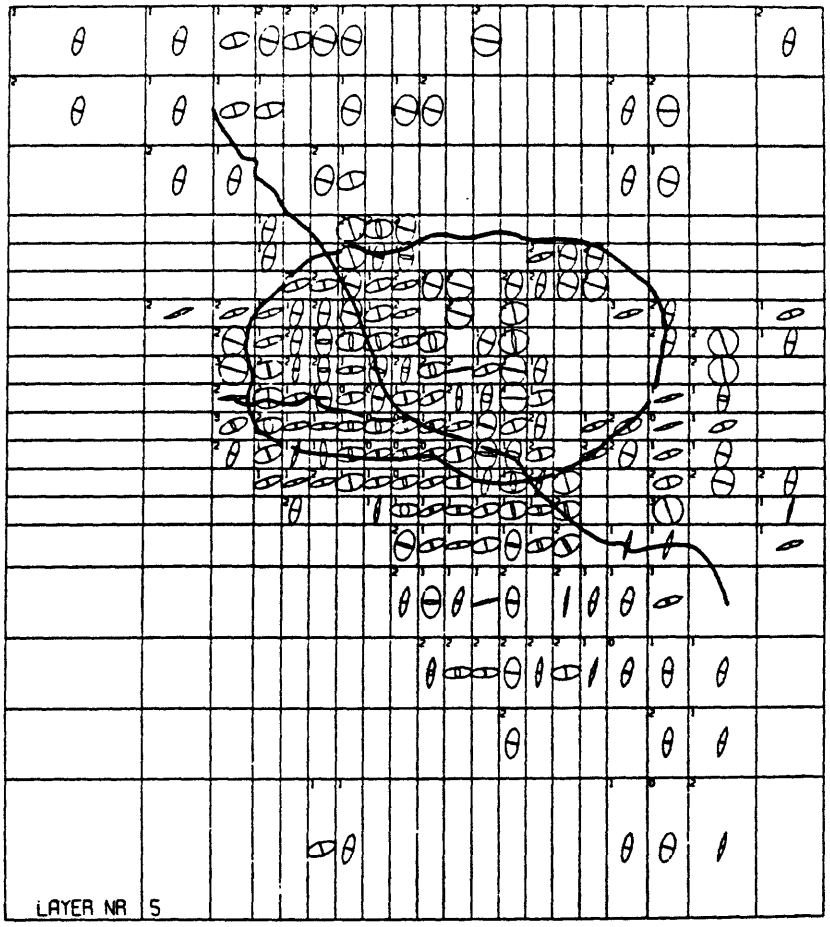

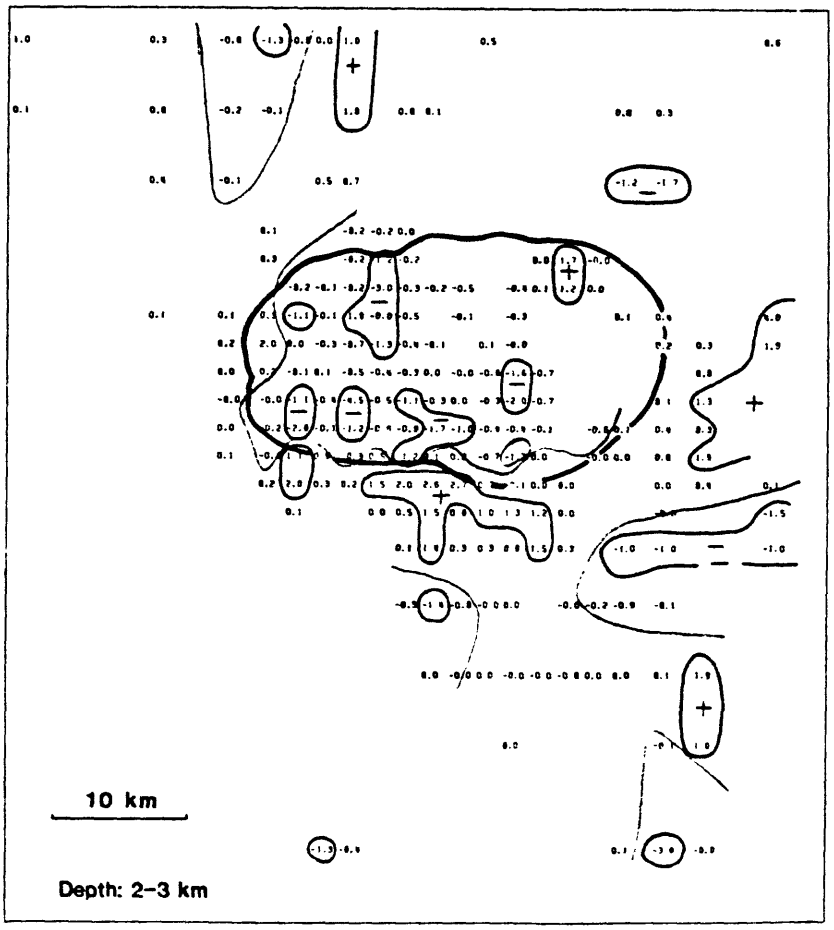

FIGURE 8

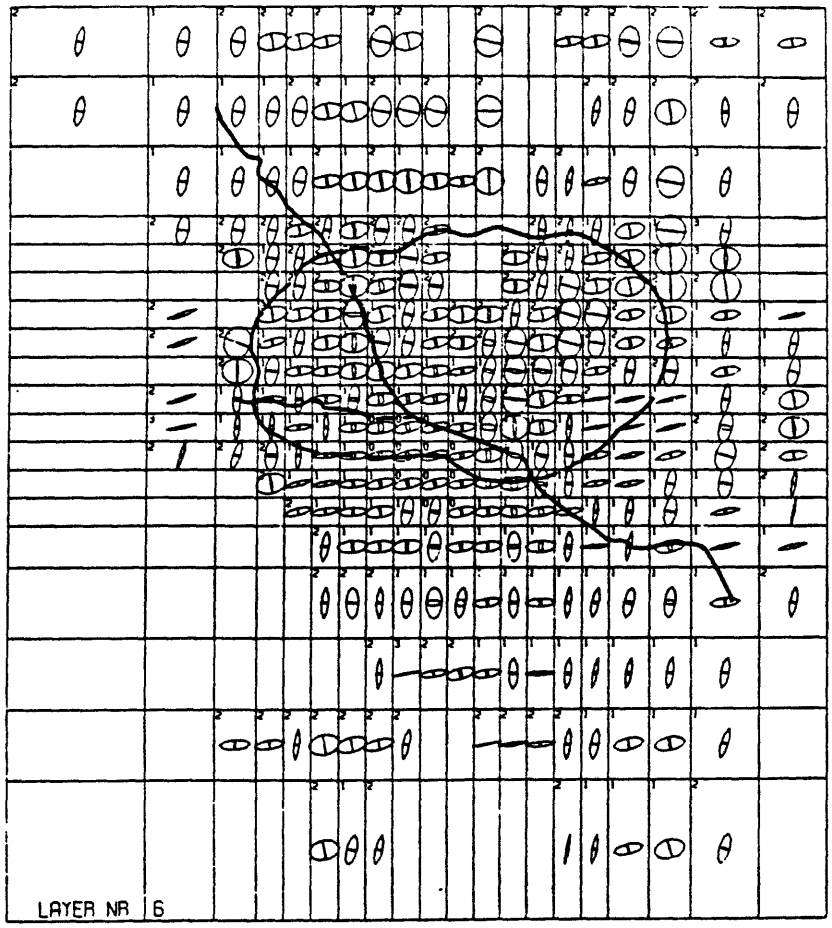

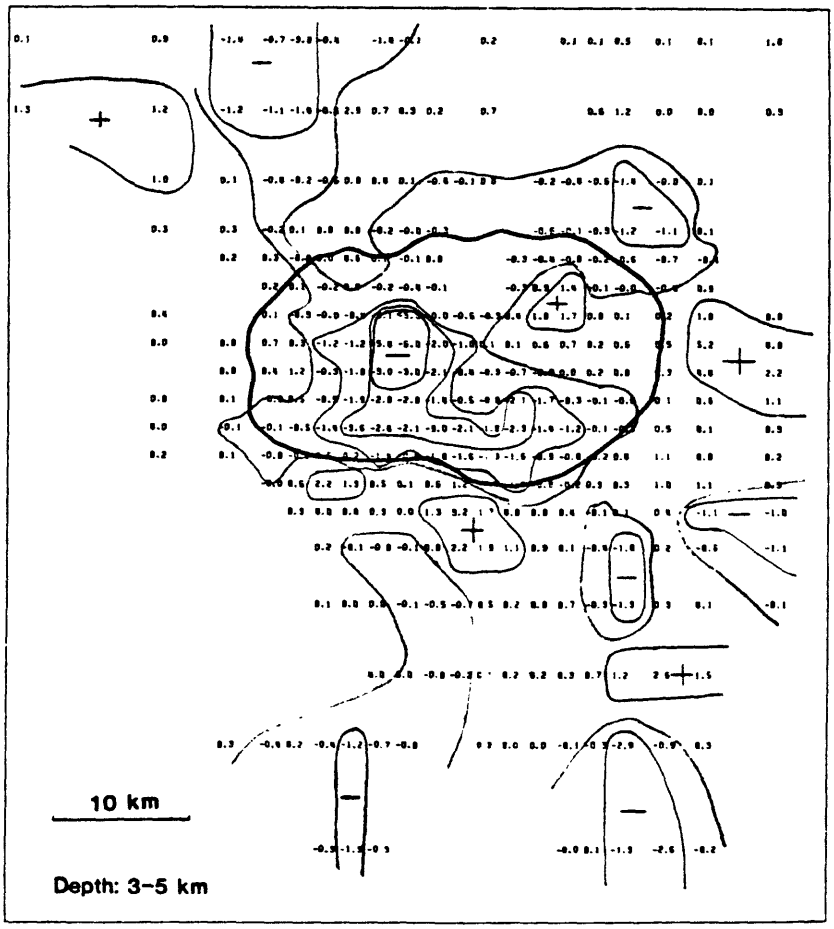

FIGURE 9

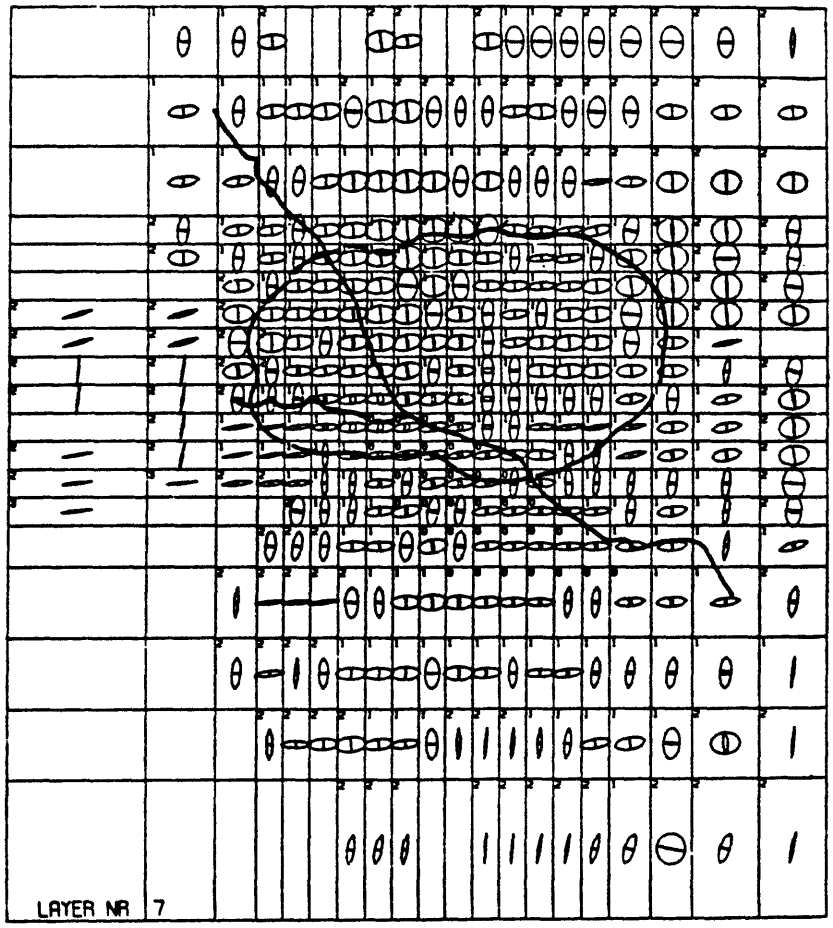

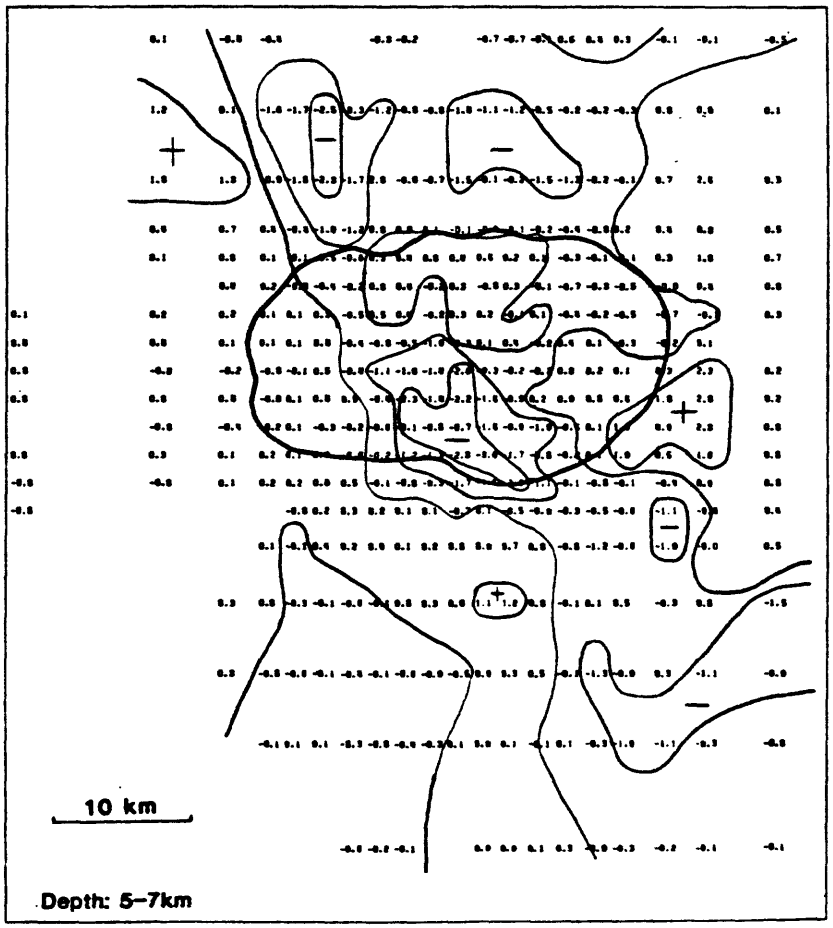

FIGURE 10

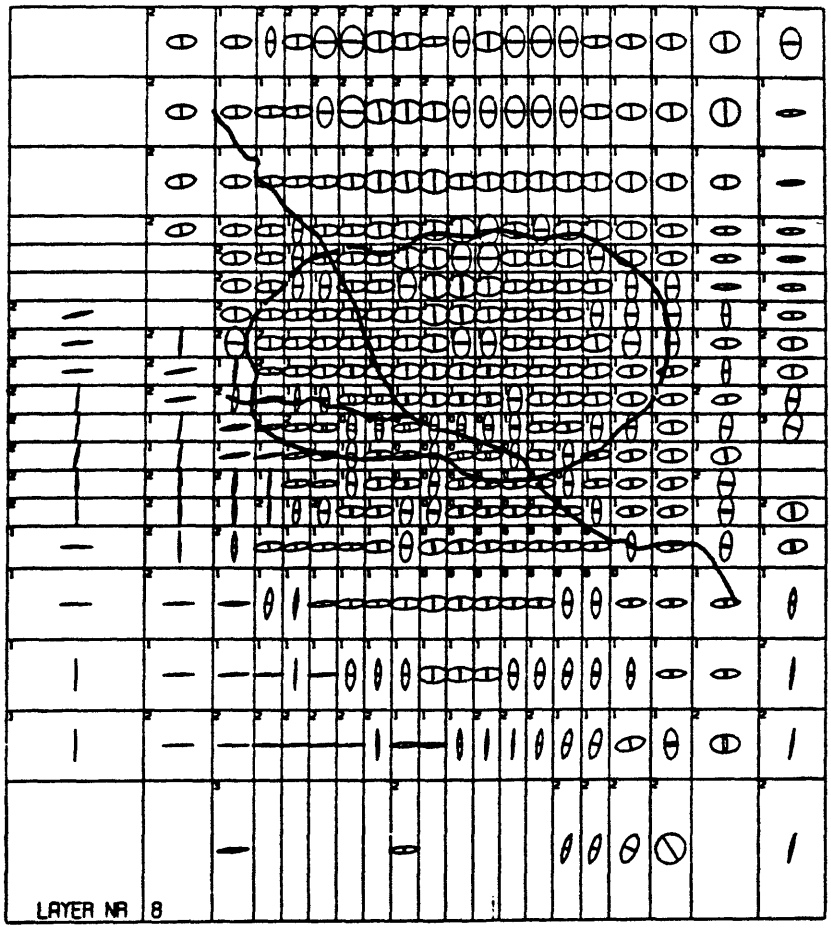
LAYER NR 8

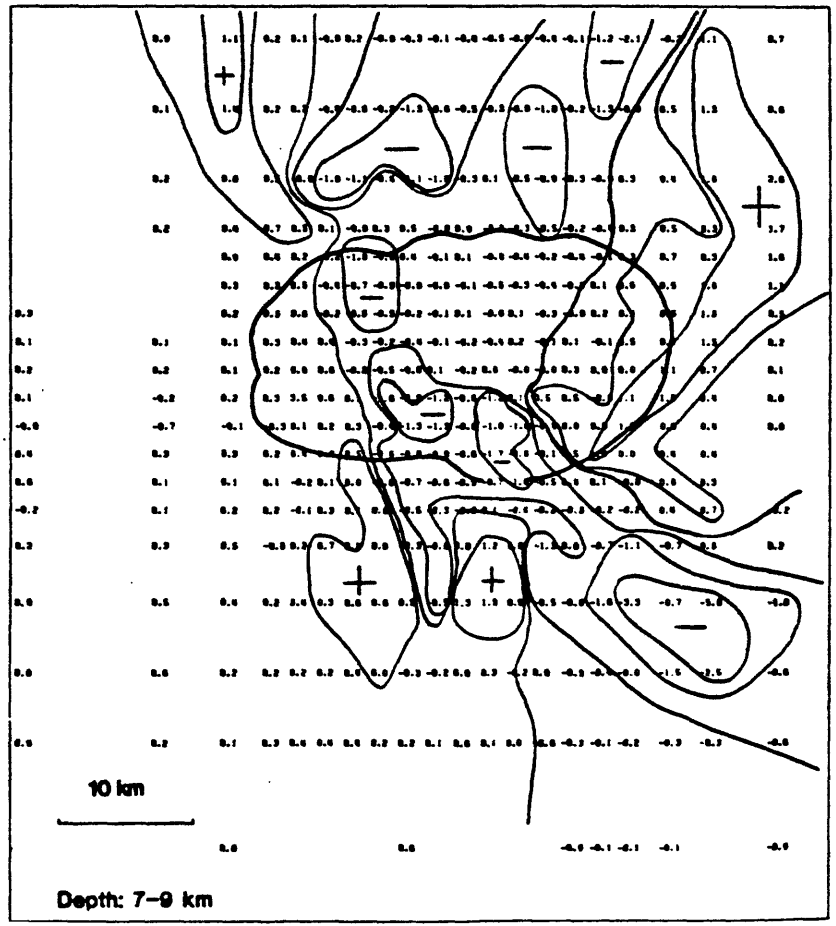
10 km
Depth: 7–9 km

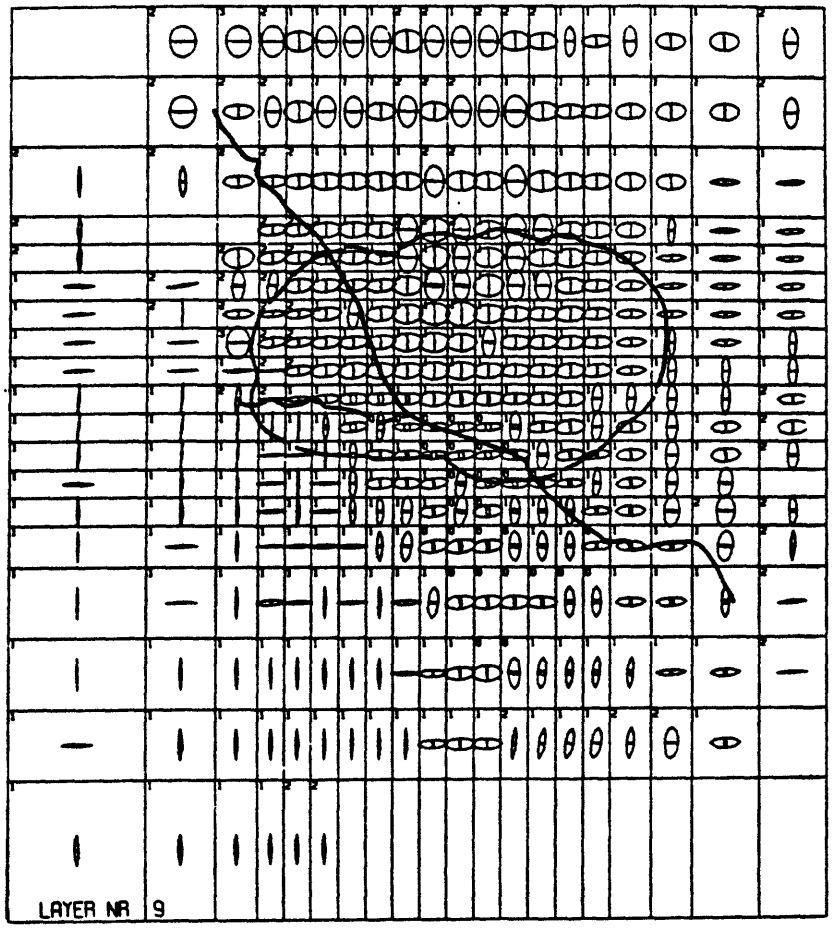

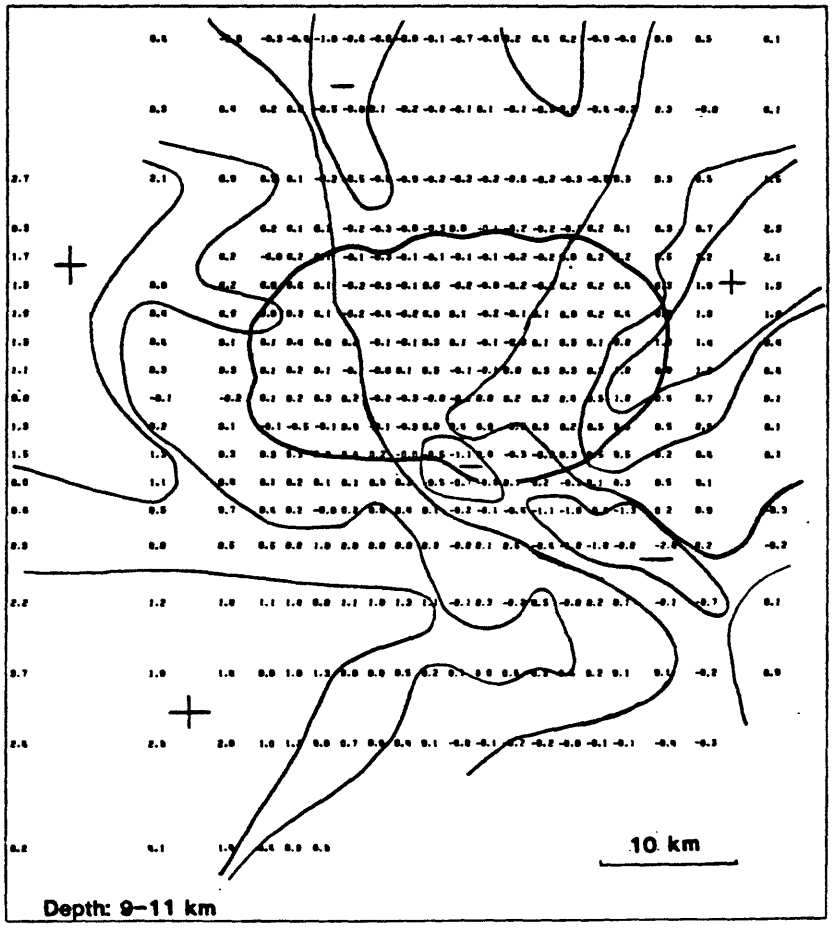

FIGURE 12

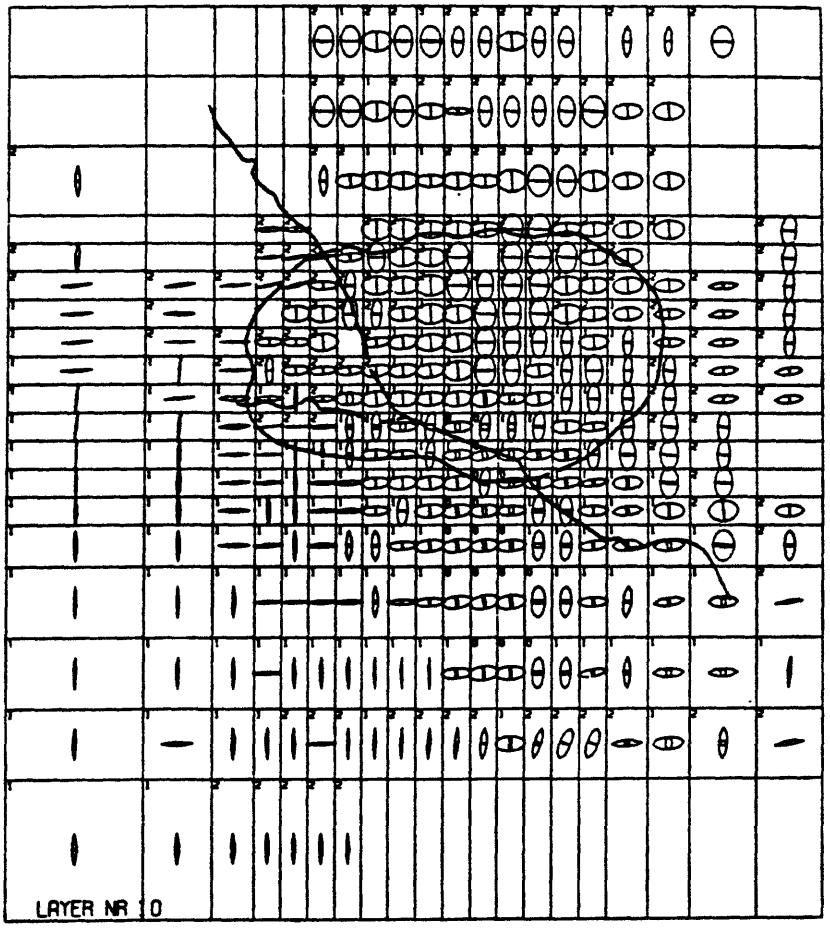
LAYER NR 10

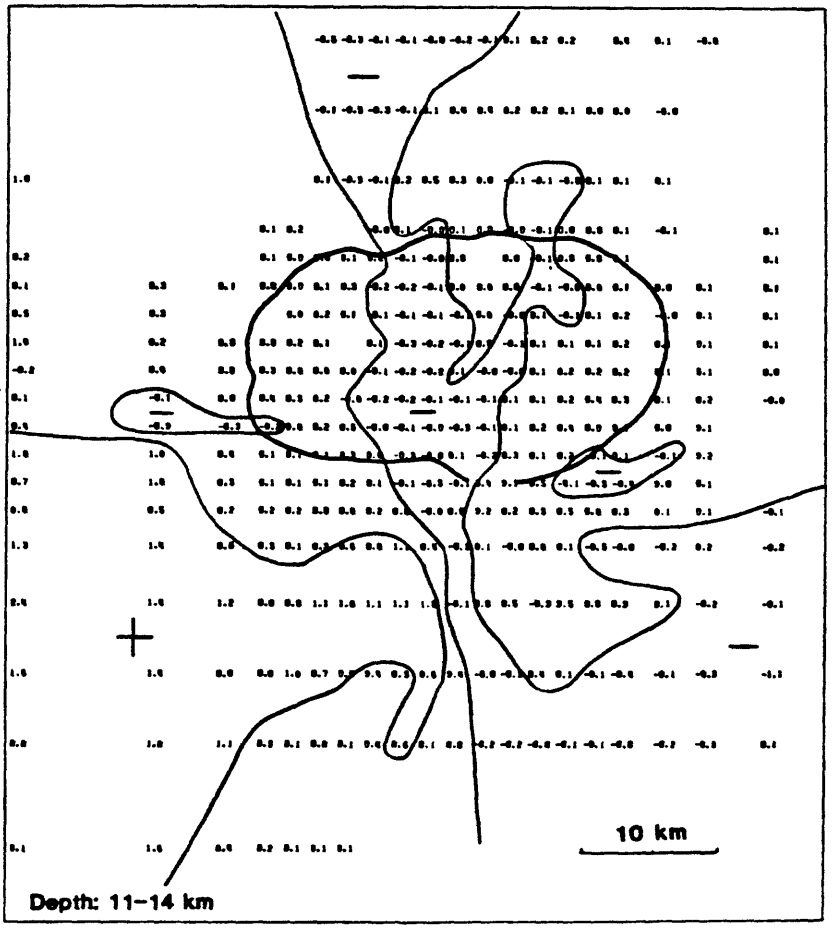
10 km
Depth: 11–14 km

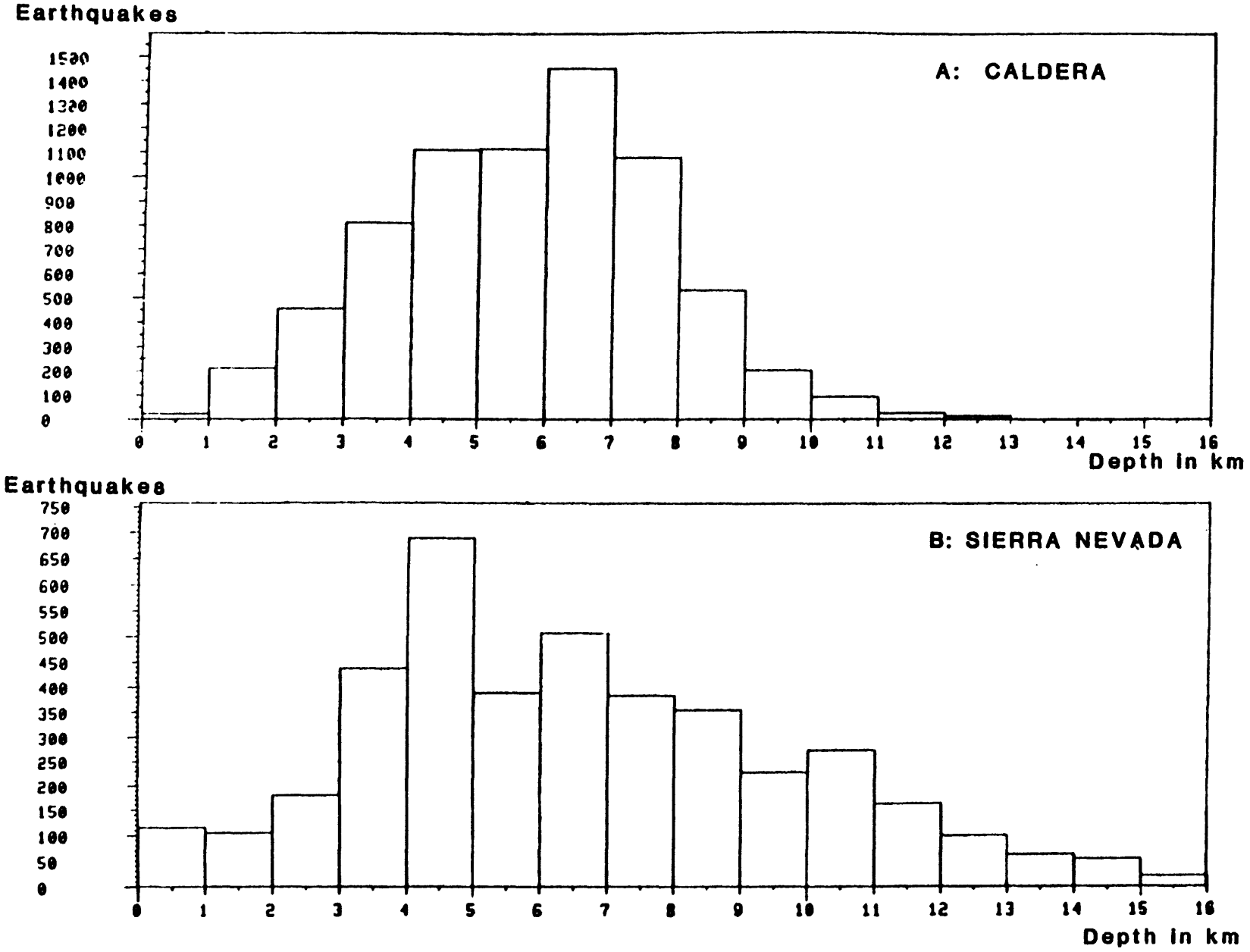
Earthquakes
1500
1400
1300
1200
1100
1000
900
800
700
600
500
400
300
200
100
0
A: CALDERA
0 1 2 3 4 5 6 7 8 9 10 11 12 13 14 15 16
Depth in km
Earthquakes
750
700
650
600
550
500
450
400
350
300
250
200
150
100
50
0
B: SIERRA NEVADA
0 1 2 3 4 5 6 7 8 9 10 11 12 13 14 15 16
Depth in km

FIGURE 14

LOCATION AND CONFIGURATION OF MAGMA BODIES BENEATH LONG VALLEY, CALIFORNIA, DETERMINED FROM ANOMALOUS EARTHQUAKE SIGNALS

Chris O. Sanders

Seismological Laboratory, Mackay School of Mines
University of Nevada, Reno, Nevada 89557

Abstract

Recordings of 281 small earthquakes which occurred recently near the southern edge of Long Valley caldera at depths from 1 to 15 km are used to map the subsurface geometry of shear wave attenuating bodies in the caldera. Signatures of these events recorded northwest, north, northeast, and east of Long Valley with ray paths through the caldera are often anomalous in that *S* wave arrivals have very low amplitudes, and high frequency *P* and *S* wave energy is missing for the same station-event combinations. The volcanic and geothermal history of the region suggests that ray paths for these anomalous signals have passed through magma which absorbed much of the *S* wave energy and also attenuated the higher frequencies. With over 1200 normal and anomalous ray paths through the caldera we have located two apparently massive magma bodies in the central and northwest caldera as well as two more dispersed magma areas in the southern caldera and beneath Crowley Lake. The central magma body extends from 4.5 to at least 13 km beneath the surface, and the northwest body is as shallow as 5.5 km. These two magma bodies are probably connected below about 8 km. Secondary arrivals seen on select seismograms are tentatively interpreted as reverberations inside the central magma chamber and are consistent with the interpreted lateral extent of the magma. The northwest and central magma bodies lie beneath the northwest and southeast corners of the caldera's resurgent dome and probably connect beneath the dome's center. Also the shallower parts of these magma bodies and the southern anomalous area lie beneath the surface expression of the medial graben faults suggesting that structural features seen at the surface of the valley may be related to magma location at depth.

Introduction

This study provides detailed evidence for the existence and location of molten or partially molten rock bodies beneath Long Valley, California. The existence of such bodies has been hypothesized by many geological workers who recognized the young volcanic deposits and landforms and also the widespread hot spring activity in southeast Long Valley and concluded that the molten rock and geothermal heat were most likely supplied from shallow crustal sources.

The Long Valley depression has been recognized as the surface expression of a caldera which collapsed 720,000 years ago following eruption of the voluminous Bishop Tuff [see *Bailey et al.*, 1976, p. 731]. Intracaldera volcanism continued intermittently to about 50,000 years ago, and Holocene rhyolitic and phreatic eruptions have occurred suggesting that residual magma underlay Long Valley as recently as about 700 years ago [*Bailey et al.*, 1976; *Wood*, 1977].

Geophysical work performed in Long Valley in the early 1970's was consistent with the existence at depth of "a hot intrusive mass that may still contain some residual magma" [*Muffler and Williams*, 1976]. In particular, a teleseismic *P* residual study by *Steeples and Iyer* [1976] showed delays of up to 0.36 seconds from which they interpreted the existence of a low velocity zone ("anomalously hot rock") between depths of about 7 and 25 km in the west-central part of the caldera. The approximate upper limit of 7 km was obtained from the refraction profiling results of *Hill* [1976] who interpreted secondary arrivals on one record section as possible reflections from the top of a 7-8 km deep magma chamber in the northwest caldera. The refraction profiles, which ran WNW-ESE and NNW-SSE through the center of the caldera, showed a normal increase in velocity with depth down to 3-4 km with no low-velocity zones in that depth range.

In May 1980 four *M* 6+ earthquakes occurred near the southern rim of the caldera. Immediately following this series of shocks precise geodetic measurements revealed that since 1975 about 250 mm of uplift (doming) had occurred in the vicinity of the resurgent

dome in the west-central caldera. This uplift was not consistent with co-seismic slip on a fault or faults but was modeled by *Savage and Clark* [1982] as due to the inflation of a spherical magma chamber at a depth of about 10 km beneath the dome.

Aftershocks of the large earthquakes were numerous and thousands of small events have continued in the epicentral zone to the present day. During routine analysis of seismograms for arrival times and first motions of the 1980 earthquakes *Ryall and Ryall* [1981] noticed that many of the seismograms had diminished S wave amplitudes and that P and S waves for the same station-event combinations were deficient in frequencies higher than about 2-3 Hz. They compiled the event locations and ray paths for some of these anomalous signals and determined that a region in the south-central caldera deeper than about 7-8 km was responsible for the filtering effects. The selective filtering of S waves suggested that the rays were traveling through a body of molten rock. *Sanders and Ryall* [1983] conducted a similar study using a larger and more detailed data set of anomalous ray paths through the caldera. They were able to define a large magma body in the south-central Long Valley caldera extending from about 4.5 to at least 13 km in depth; a second magma body was outlined and tentatively located in the northwest caldera coincident with *Hill*'s [1976] deep reflection. To obtain depth information *Sanders and Ryall* assumed that the rays leaving the source were nearly horizontal and intersected the nearby magma bodies at the same depth as the event hypocenter.

The study reported herein is a continuation of the study of *Sanders and Ryall* [1983] and includes 50% more data and also information on the ray take-off-angle from the source. This, coupled with a computer routine for plotting ray-intersection cross sections, provides significantly more detail on magma body location and configuration.

Technique

This study uses observations of anomalous shear wave (S wave) arrivals in order to locate shallow crustal magma bodies beneath Long Valley, California. 259 quality A and B and 22 quality C events (see *Lee and Lahr* [1975] for explanation of location quality) located along a 20 km stretch of the southern rim of the Long Valley caldera and in the Sierra Nevada block south of the caldera and having depths of 1 to 15 km are used to obtain a detailed picture of magma bodies beneath Long Valley (Figure 1). These earthquakes occurred between August 1982 (when a high density local seismic array was installed) and June 1983. The technique employed is simple in concept. The 281 small earthquakes (M_L 1 to 3, average 2) are natural sources of compressional and shear wave energy. Seismograms of these earthquakes recorded at regional seismic stations (Figure 2) contain information about the crust through which the rays traveled. Seismograms corresponding to travel paths through the caldera often show S wave arrivals with anomalously low amplitudes. In addition, higher frequency P and S wave energy is often absent. These anomalous ray paths are plotted on surface projections for various depth ranges, and by noting where they intersect the region of crust responsible for the filtering effects is found. In addition, detailed information on the depth configuration of these anomalous regions is obtained from vertical cross sections. These sections are constructed using ray take-off-angles (TOA) calculated by the hypocentral location routine HYP071 [*Lee and Lahr*, 1975] and show the depths at which rays intersect various parts of the caldera. The calculated take-off-angles to the most important stations are usually between 90 and 96 degrees, so the assumption of essentially horizontal take-off-angles by *Sanders and Ryall* [1983] was reasonable. However, valuable depth information from rays to stations at P_n distances (greater than about 120 km, TOA about 50 degrees) and to close-in stations (TOA greater than 100 degrees) is available and is utilized in this study.

More than 1200 seismograms were given ratings from 0 to 3 depending on the visual character of the shear wave arrival -- 0 for normal, 3 for little or no S wave, and 1 or 2 for intermediate S wave arrival quality. Ratings of 0, 2, and 3 are considered very reliable; a

rating of 1 is more uncertain (although most of the seismograms rated 1 did have travel paths through or very near the anomalous regions outlined by the 0, 2, and 3 rays). In order to insure objectivity the seismograms were rated before the exact locations of the earthquakes were known. The data in the form of source-station ray paths with corresponding S wave quality ratings (for the remainder of this discussion quality refers to our rating of shear wave quality and not to location quality) were stored in computer files and then plotted on maps and cross sections for selected ranges of azimuth (select stations), event depth, and S wave quality. These maps and cross sections were then interpreted visually to delineate the Long Valley magma structures.

Error Assessment

The error in location of these bodies, other than that arising from interpretational ambiguity, is due mainly to errors inherent in the earthquake location procedure. Error due to refraction of rays around the low-velocity magma bodies seems to be insignificant, since as will be seen the well-constrained boundaries are sharply defined by ***both*** normal and anomalous rays. The close proximity of the earthquakes to the large bodies probably reduces the possibility of significant lateral refractions. The precision of the hypocenters of most of the earthquakes used in this study is less than a kilometer laterally and vertically (as calculated by the location routine HYPO 71; Lee and Lahr [1975]). Differences in epicentral location are very small if slightly differing velocity structures are used in the location routine. However, consistent differences of about 1.5 km occur between epicentral locations calculated using station time corrections and those determined without using corrections. Since the velocity structure in the immediate vicinity of the caldera is laterally heterogeneous at shallow depth we have chosen to use a Sierra crustal model, with station corrections to account for shallow variations in structure. The corrections were determined from a study of earthquakes and local explosions in the summer of 1982 (A. Ryall, personal communication). At this time we believe that the maximum error in absolute location of the magma (other than possible interpretational errors discussed in the text) is about a kilometer laterally and less than two kilometers vertically.

Source Versus Structure

A possible interpretation of the low shear wave amplitudes seen on certain seismograms is position of the seismic recording stations relative to the pattern of S_v energy radiating from the earthquake source. Low amplitudes are expected near nodal planes of the S_v radiation pattern. To test this possible interpretation of the data we have compared seismograms from several small earthquakes with well-constrained focal mechanisms for those same events. Figure 3 shows seismograms and the source mechanism for a 5.7 km deep event. The seismograms at the stations indicated all have large amplitude shear wave arrivals regardless of position on the S_v radiation pattern. The source mechanism and seismograms for a 6.9 km deep event are shown in Figure 4. The seismogram recorded at station MMC has anomalously low shear wave amplitudes compared with the seismogram from station MON and with the MMC seismogram in Figure 3, even though all are similarly situated on the source radiation pattern. Apparently the ray to MMC from the 6.9 km deep event was affected along its travel path, while the rays to stations MON and BON were not. The selective attenuation of the shear waves, coupled with the known volcanic history of the region, indicates that the ray to MMC passed through a fluid, probably molten rock. Source effects can be ruled out as the cause of the anomalous amplitudes, since rays to stations MON and BON gave normal seismograms.

Molten Rock?

The severe attenuation of the >2 Hz shear waves by anomalous regions beneath Long Valley must be explained by some plausable model. A rough estimate of the attenuation of shear waves in these regions gives a Q_β of less than 30. This is quite low and is similar to the Q_β of about 10 obtained from long period S waves for the partially molten

asthenosphere beneath the mid-Atlantic ridge [*Solomon*, 1973]. The geophysical models which could explain this low Q_β beneath Long Valley range from large volumes of rock saturated with several percent partial melt or other fluids [*O'Connell and Budiansky*, 1977] to actual magma bodies containing a high percentage of melt (the effectiveness of S wave propogation depending on the viscosity and geometry of the bodies). The rhyolitic and rhyodacitic volcanic rocks erupted from Long Valley generally contain less than 30% phenocrysts [*Bailey*, 1976] suggesting that the magmatic sources are at least about 70% molten. Such bodies could easily give the attenuation effects seen. The quantitative attenuation data available, however, are insufficient for discriminating between the possible models.

Other observations may provide some guides or constraints on the most likely composition of the attenuating bodies. *Bailey* [1976] has determined that since the formation of Long Valley caldera by the massive eruption of Bishop Tuff about 700,000 years ago rhyolitic and rhyodacitic magma has continued to erupt into Long Valley during several episodes and probably underlay the valley as recently as 700 years ago [*Wood*, 1977]. In addition, although the post-Bishop Tuff magma chamber has cooled and shrunk in size [*Bailey*, 1976] it has not completely cooled and has probably been rejuvinated with heat supplied from deeper, mafic magmatic sources at least once about 300,000 years ago [*Bailey*, 1983; *Lachenbruch et al.*, 1976*b*]. Hot geothermal waters continue to flow onto the surface of Long Valley. Thus the geological evidence strongly suggests that molten rock still underlies portions of west-central Long Valley.

The shape of the attenuating regions provides another clue about the possible composition of the attenuating bodies. The northwest and central regions have upper surfaces which are concave down, that is they have definite roofs at about 5 km depth and definite sides which seem to widen with depth. If the attenuating bodies were actually fractured/altered volumes of rock saturated with hydrothermal fluids then we would expect the attenuating effects to be observed throughout the vertical extent of the circulation system, from the surface of the valley where geothermal water effuses down to near the source of the heat. This is not seen. Instead the overall shape of these bodies is consistent with the picture of a deeper, broad magma reservoir which has narrower appendages reaching toward the surface possibly along preexistent zones of weakness. In addition, the large bodies lie directly beneath the areas of extensive post-Bishop Tuff volcanism in the west-central caldera and can be viewed as possible sources for the rhyolitic magma which erupted possibly reaching the surface along the major faults in the immediate area.

These observations suggest that the attenuating regions beneath Long Valley most likely contain partially molten rock (% melt unknown) and that use of the term 'magma bodies' to describe them is appropriate.

Results

We have outlined two large magma bodies in the central and northwest areas of Long Valley caldera. In addition, two other areas of anomalous crust, one just south of the central body and the other beneath Crowley Lake, are observed.

Figure 1 shows the locations of the magma bodies in and near the Long Valley caldera. The southwestern and southern boundaries of the central magma body are well-constrained between 5 and 8 km depth and are indicated by the solid depth-contour lines. The rest of the central magma body is located with less precision, and the boundaries are more interpretive. Data suggests that this body contains molten rock as shallow as 4.5 km beneath the surface and at least as deep as 13 km. The probable shape between 4.5 and 7 km is indicated by the dashed depth-contour lines. This body extends to the west and east at depths at least as shallow as 11 and 10 km respectively. Dotted lines indicate the deeper contours. The northern boundary appears to be very sharp and nearly vertical between 5 and at least 8 km.

The location of the northwest caldera magma body is indicated in Figure 1 by the dotted 5.5, 7, and 7.5 km contour lines. The plan view shape of this body is poorly constrained in the north-south direction. This body contains magma from 5.5 to at least 13 km depth.

The southern anomalous area and the Crowley Lake anomalous area are shown by dashed outlines on Figure 1. The southern anomalous area extends from 5.7 to at least 10 km depth and the other from about 5 to at least 15 km beneath Crowley Lake. The data suggests that these areas do not contain large, massive magma bodies but rather may be areas of magmatic intrusion in fractured country rock.

Figure 5 is a subsurface contour map of the depth above which no large, massive magma bodies are present in Long Valley caldera. This map was made by interpreting cross sections which showed where the rays with normal signatures were traveling through the caldera. In particular, the map helps determine where the shallowest magma can be located. The map gives no indication of the existence or non existence of magma below the depths indicated; it only implies that large magma bodies probably do not exist above those depths in the caldera. The four anomalous crustal regions are discussed in detail below.

Central Magma Body and Southern Anomalous Area

The magma body situated in the central caldera (Figure 1) has well-located western and southern boundaries between depths of 5 and 8 km. The body generally narrows upward, as indicated by the depth contour lines. Rays to stations MON, MGN, HCK, BON, ORC, SVP, and JAS (Figure 2) are used to constrain the body geometry between 5 and 8 km. Figures 6, 7, and 8 show the anomalous ray paths and the anomalous and normal rays through the corresponding cross sections to stations north and northeast of the caldera. In each cross section the shape of the central body as seen by rays to the specific station is outlined with solid, dashed, and dotted lines. The solid lines indicate the well-located portion of the body; the dashed and dotted lines are increasingly more interpretive. The anomalous area just south of the central body is outlined by the dashed rectangle.

Figure 6*a* shows the anomalous ray paths to station MON. The short dashed lines are quality 3 rays and the longer dashed lines quality 2 rays, as defined earlier. In order to clarify the presentation quality 0 and 1 ray paths are left off most of these maps. Figure 6*b* shows the quality 1, 2, and 3 rays intersecting section A-A'. The anomalous rays farthest west probably intersect the northwest caldera body about 8 km northeast of this section and, thus do not indicate a westward extension of the central body. Figure 6*c* shows the normal rays to station MON intersecting section A-A''. Figures 7 and 8 show the anomalous ray paths and the anomalous and normal ray intersections to stations BON, HCK, MGN, and other northeastern stations. All have P_g first arrivals except KVN which sees P_n first. The anomalous rays indicate that magma extends to a depth of at least 13 km. The quality 2 ray on the right side of Figures 8*a* and 8*b* is heading toward KVN with a 50 degree take-off-angle. This ray first hits magma about 3 km northeast of its intersection with section C-C' and at a depth of about 11 km. Figure 8*a* shows the two anomalous rays seen at station JAS. One ray helps locate the southwest corner of the magma body, the other may be intersecting magma in the western caldera.

Figure 9 shows the normal ray paths to station ORC. Although no anomalous rays were noted to this station the normal rays help define the southern edge of the central magma body.

Note how in Figures 6 through 9 the well-constrained boundaries are tightly defined by both anomalous and normal rays. This indicates that refraction effects near the edge of the low-velocity magma body do not significantly affect the location of these boundaries.

To all of the stations represented in Figures 6 through 9 very few normal rays pass through the outlined magma body and very few anomalous rays pass outside of it. This is strong evidence indicating the massive nature of the central magma. As is evident the same is not true of the southern anomalous area. The mixing of anomalous and normal rays through this area suggests that the magma structures must be small and local and intruded into solid rock. Magma in this area is most reasonably interpreted to be present in thin, small bodies such as dikes, pipes, and/or sills.

In *Sanders and Ryall* [1983] the central magma body was interpreted to be relatively massive below 7 km and more dispersed between 7 and 4.5 km. Due to the availability at that time of ray maps only (no ray-intersection cross sections) the existence of the southern anomalous area was not known. Thus rays passing through the southern anamolous area were interpreted as passing through part of the central body farther north. These rays along with many normal rays through that same area gave the impression of interspersed magmatic and bedrock regions in the upper part of the central body. The additional earthquakes examined in the study reported here and the ability to plot the data directly on cross sections and obtain more detailed depth information have helped resolve the separate body locations. The central magma body now appears to be relative massive (at least as viewed from the south) through its entire extent.

Considerable data was collected from seismograms recorded at station MMC north-northwest of the caldera (Figure 2). Figure 10*a* shows the anomalous ray paths to station MMC. These rays intersect more than one magma body, and when viewed in cross section (Figure 10*b*) no distinction can be made between the different bodies. Evidence of normal rays received at other stations, however, requires that the northwest and central bodies be separated at least above about 8 km (see Figures 5 and 6).

Many rays to MMC intersect magma between 4.5 and 5 km depth. This shallow magma is most likely part of the central magma body, even though its existence is neither ruled out nor confirmed by rays to other stations. The shape of the body between 4.5 and 5 km is constrained by normal rays to northeastern stations (Figure 5). An elongate north-northeast shape (Figure 1) is required by the anomalous and normal ray data sets. The northern extent of the central body between 5 and 8 km depth is located based on the known shape of the southern part of this body and the required extent of the 4.5 km anomaly.

The shallow magma between 4.5 and 5 km depth is seen by rays to station MMC and is constrained to lie somewhere along those ray paths to MMC. The location we give this shallow zone is the only one possible within the caldera (see Figure 5). A location outside the caldera, however, cannot be ruled out. On their path to station MMC the rays leaving the southern caldera rim travel beneath the Mono Craters and Mono Lake, both sites of geologically recent volcanism, and could intersect magma beneath these volcanoes. Geological studies, a seismic refraction study, a recent *P* delay study (R. Bailey, D. Hill, and H. Iyer, personal communications, 1983) and heat flow modeling [*Lachenbruch et al.*, 1976*a*], though, suggest that magma beneath the Mono Craters must lie much deeper than the Long Valley magma. Thus a Long Valley location for the shallowest magma is the most plausible.

The easternmost anomalous rays to station MMC (Figures 10*a* and 10*b*) suggest extension of the central magma body to the east at a depth of about 8 to 10 km. This is supported by the next-to-the-easternmost anomalous ray to station KVN (Figure 8) which intersects this eastern extension at about 11 km.

The westernmost anomalous rays to station MMC miss the central magma body and intersect a magma body located in the northwest caldera. Figure 10*c* shows normal ray paths to stations located north-northwest of the Long Valley caldera. The normal rays coincident with the anomalous MMC rays at the left side of Figures 10*b* and 10*c* indicate that magma is not located near the plane of this section. These normal rays diverge from the anomalous rays further northwest and help outline the location of a magma body in

the northwest caldera.

Northwest Caldera Magma

The northwest caldera magma body is intersected principally by rays to station MMC. Figure 10*d* shows the anomalous rays to MMC intersecting cross section J-J' (Figure 10*a*) and also shows the normal rays to all of the northwest stations plus MON intersecting the same section. The western half of a magma body is clearly defined by the anomalous and normal rays, and the boundaries are fairly sharp. The dense cluster of normal rays on the right side of Figure 10*d* are rays to station MON. These rays limit the eastern extension of this body in the depth range 6 to 7.5 km. The three anomalous rays on the right side of Figure 10*d* are the westernmost anomalous rays seen at station MON (Figures 6*a* and *b*). These rays lie just beneath the cluster of normal rays to MON and are interpreted to intersect the eastern edge of the northwest magma body. The dashed outline in Figure 10*d* is the interpreted eastern limit of this magma body above 8 km based on the MON data. This is also supported by the extent of the reflection surface reported by *Hill* [1976].

Figure 11*a* shows the anomalous ray paths to five stations located northwest of the caldera. Their intersection with the central magma body along cross section K-K' is shown in Figure 11*b*. The four anomalous rays on the left side of Figures 11*a* and *b* probably intersect only the northwest magma body. The upper two definitely do and indicate that the northwest magma body extends to at least about 13 km depth (Figure 10*d*). These western rays also have a more westerly azimuth than do the rays to MMC and begin diverging from the anomalous MMC rays near the northwest magma body. This supports our location of the northwest body where the diverging anomalous rays are adjacent. In Figure 1 the shallowest (5.5 km) part of the northwest body is drawn coincident with the location of the possible 7-8 km deep reflection seen by *Hill* [1976]. This phase could also possibly be interpreted as a multiple reflection from a shallower layer [*Steeples and Iyer*, 1976]. However, if *Hill*'s interpretation is correct, and the magma is about 7 km deep there, then the 5.5 km top of this body must lie somewhat NNW or SSE of the position given on the map.

Anomalous Region Beneath Crowley Lake

During the course of our investigation several definitely anomalous seismograms were found which later were seen to have ray paths outside of Long Valley caldera. Six of these anomalous rays intersect in a region beneath Crowley Lake at depths of about 5 to 15 km (Figures 12*a* and *b*). Many normal rays also pass through this area indicating that magma present is not in a large, massive body but rather in discrete smaller bodies such as dikes, pipes, or sills intruded into solid rock similar to the small anomalous area just south of the central magma body.

Secondary Arrivals

Large amplitude secondary arrivals are seen on many seismograms corresponding to select source-station ray paths through the central and northwest caldera magma bodies. The spacial association of the bodies with these secondary phases suggests that the phases may result from energy reverberating within the magma chamber. Reflections off the top of the magma body and back to the surface are ruled out, since most of the earthquakes are located deeper than the magma roof. Figure 13 shows the source-station ray paths for the seismograms which have strong secondary arrivals. Seismograms and the source mechanism for one earthquake which produced secondary arrivals at several stations are shown in Figure 14. The secondary phase generally arrives about 1.5 to 2 seconds after the initial P_g phase depending on the station and several seconds before the first shear waves. The arrival time of this secondary phase after the P_g phase does not change when the distance from the source to the magma body increases indicating that the phase is not converted S wave energy but rather P energy which travels a longer path than P_g and/or travels at a lower velocity along part of its

travel path. Some of the seismograms at MON which showed secondary arrivals (Figure 13*a*) also showed good *S* waves suggesting that P_g and S_g energy passed over the magma (TOA about 95 degrees). The energy contained in the second phase, however, must have traveled down to the magma and then back up to MON indicating that a longer travel path accounts for a small part of the observed time lag. Travel within the lower velocity magma body, though, is probably responsible for most of the time lag.

Some earthquakes which produced secondary arrivals at stations MON, MMC, KVN, and HCK (Figures 13*a*, *b*, *c*, and *f*) had ray paths to these stations through the east-central caldera. The generation of these signals in this area of the caldera supports the interpretation of the eastern extension of the central magma body. The western rays to MON and KVN (Figures 13*a*, *e*, and *f*) suggest the existence of a western extension of the central magma body below 8 km and a probable connection with the northwest caldera body. The westernmost rays to MMC and SJC (Figures 13*c* and *d*) may have produced signatures with small secondary arrivals by interaction with the northwest magma body.

The only ray path to eastern station SVP which gave an anomalous seismic signal due to transmission through the central magma body also produced a definite secondary arrival at that station (Figure 13*b*) similar to the secondary arrivals seen at the northwest and northeastern stations. Since this was the only seismogram at SVP which showed the secondary arrival this is good evidence linking the magma bodies with generation of the secondary phase.

Comparison with a *P* delay Study

From a study of teleseismic *P* wave residuals *Steeples and Iyer* [1976] found relative delays of up to 0.36 seconds in the west-central part of the Long Valley caldera after regional and near-surface effects had been removed. They interpreted this delay as evidence for the existence of low-velocity material (velocity contrast 10-15%) beneath the valley floor at depths greater than 7 km and probably less than 25 km. Figure 15 shows the *P* delay anomaly as it would locate at 12 km depth. Superimposed on the *P* delay data points are the depth contour lines of the central and northwest caldera magma bodies as determined by this study. The agreement between the results of the two data sets is very good. The easternmost *P* delays support the eastward extension of the central magma body at about 8 to 10 km depth. In addition, the northern boundary of the central magma body beneath 7 km is tightly constrained by the undelayed teleseismic rays in the north-central caldera. The central magma body appears to fall off steeply at its northern end.

P delays seen in the northwest caldera support the existence and location of the northwest magma body. Undelayed teleseismic signals northwest and southwest of this body provide a constraint on the maximum size of the body in these directions.

Conclusions

From qualitative interpretation of over 1200 seismograms corresponding to source-station ray paths through Long Valley caldera, many of which show anomalous shear wave arrivals, we are able to locate molten rock bodies at depth in the caldera.

A magma body in the central caldera is very well located at its southern and southwestern extent between depths of 5 and 8 km. This body probably contains magma as shallow as 4.5 km. The shape of the northern extension of the central magma body above 8 km is constrained by normal ray paths to northeastern stations and anomalous rays to northwestern station MMC and is elongated in a north-northeast direction. The western and eastern limits of this body below 8 km are not precisely constrained, however several anomalous rays to stations MMC and KVN indicate the presence of magma below 8 km both west and east of the shallower part of the body. Further constraint is provided on the eastern and northern extensions of the central magma body by the *P* delay results of *Steeples and Iyer* [1976]. The *P* delay results are consistent with our

magma body locations and when compared with our data suggest that the northern boundary of the central body is steep and sharp and that the magma extends broadly to the east at about 8 to 10 km depth. The central magma body is seen as deep as 13 km and probably extends to greater depth.

A large magma body exists in the northwest caldera between depths of 5.5 and at least 13 km. Several lines of evidence support the existence and location of this magma body. The westernmost anomalous rays to station MMC cannot be explained by intersection with the central magma body. These rays pass directly through an area in the northwest caldera which was interpreted by *Hill* [1976] to be the source of a possible 7-8 km deep reflection from the roof of a magma chamber. Some anomalous rays to other northwestern stations have paths which diverge from the anomalous MMC rays near this northwest magma body strongly suggesting that the attenuating body is located where the divergent rays are coincident. The *P* delay results of *Steeples and Iyer* [1976] also indicated the existence of low-velocity rock in the northwest caldera.

The westernmost anomalous rays to station MON probably intersect the eastern edge of the northwest caldera body. These anomalous rays and the normal rays to MON, MMC, and the other northwestern stations complete the east-west cross sectional outline of the northwest magma body. No information is available on the north-south areal extent of this magma except for the rough constraint provided by the *P* delay results.

The central and northwest caldera magma bodies appear to be composed of a relatively massive assemblage of molten or partially molten rock. The quality 2 seismograms, whose corresponding rays paths help to define these bodies, and the quality 1 seismograms do show some *S* wave arrivals indicating that often not all shear wave energy is lost during travel through the bodies. This, coupled with the observation of some normal ray paths through the bodies, suggests that above 8 km the magma, at least locally, is best described as partially molten and/or is interspersed with some solid rock.

Two smaller areas of anomalous crust are indicated by our data, one just south of the central magma body extending from about 6 to at least 10 km depth and another beneath Crowley Lake at about 5 to at least 15 km depth. Both normal and anomalous rays pass through these regions indicating that they do not contain large, massive magma bodies but rather small, isolated structures such as dikes, pipes, and/or sills.

The shallower portions of the central and northwest caldera magma bodies and the entire southern anomalous area have a close spacial relationship with the normal faults of the medial graben mapped by *Bailey et al.* [1976] in that they seem to lie directly below the surface expression of the graben. The magma bodies also lie beneath the northwest and southeast corners of the caldera's resurgent dome and probably connect beneath the center of the dome. These relationships suggest that perhaps the structural features seen on the surface of the caldera are related to magma location at depth. This is consistent with the close spacial relationship between the Long Valley caldera structures (rim fracture, normal faults, and resurgent dome) and the post-Bishop Tuff volcanism in the caldera reported by *Bailey* [1976].

Acknowledgements

I thank Alan Ryall and Floriana Ryall for their assistance and support throughout this project. I also thank Ron Sheen who developed the graphics software used to plot the ray maps and cross sections. This research was primarily supported by a U.S. Department of Energy contract number DE-AS08-82ER12802; the work was also partly supported by the U.S. Geological Survey under contract number 14-08-0001-21248.

References

Bailey, R. A., Dalrymple, G. B., and Lanphere, M. A., Volcanism, structure, and geochronology of Long Valley caldera, Mono County, California, *J. Geophys. Res.*, *81*, 725-744, 1976.

Bailey, R. A., Postcaldera evolution of the Long Valley magma chamber, eastern California, *EOS*, *64*(45), 889, 1983.

Hill, D. P., Structure of Long Valley caldera from a seismic refraction experiment, *J. Geophys. Res.*, *81*, 745-753, 1976.

Lachenbruch, A. H., Sass, J. H., Munroe, R. J., and Moses, T. H., Jr., Geothermal setting and simple heat conduction models for the Long Valley caldera, *J. Geophys. Res.*, *81*, 769-784, 1976*a*.

Lachenbruch, A. H., Sorey, M. L., Lewis, R. E., and Sass, J. H., The near-surface hydrothermal regime of Long Valley caldera, *J. Geophys. Res.*, *81*, 763-768, 1976*b*.

Lee, W. H. K., and Lahr, J. C., HYPO71 (revised): A computer program for determining hypocenter, magnitude, and first motion pattern of local earthquakes, *U. S. Geol. Surv. Open File Rep. 75-311*, 113 pp, 1975.

Muffler, L. J. P. and Williams, D. L., Geothermal investigations of the U. S. Geological Survey in Long Valley, California, 1972-1973, *J. Geophys. Res.*, *81*, 721-724, 1976.

O'Connell, R. J. and Budiansky, B., Viscoelastic properties of fluid-saturated cracked solids, *J. Geophys. Res.*, *82*, 5719-5735, 1977.

Ryall, A. and Ryall, F., Attenuation of *P* and *S* waves in a magma chamber in Long Valley caldera, California, *Geophys. Res. Letters*, *8*, 557-560, 1981.

Sanders, C. O. and Ryall, F., Geometry of magma bodies beneath Long Valley, California, determined from anomalous earthquake signals, *Geophys. Res. Letters*, *10*(8), 690-692, 1983.

Savage, J. C., and Clark, M. M., Magmatic resurgence in Long Valley caldera, California: Possible cause of the 1980 Mammoth Lakes earthquakes, *Science*, *217*, 531-533, 1982.

Solomon, S. C., Shear wave attenuation and melting beneath the mid-Atlantic ridge, *J. Geophys. Res.*, *78*, 6044-6059, 1973.

Steeples, D. W. and Iyer, H. M., Low-velocity zone under Long Valley as determined from teleseismic events, *J. Geophys. Res.*, *81*, 849-860, 1976.

Wood, S. H., Distributon, correlation, and radiocarbon dating of late Holocene tephra, Mono and Inyo craters, eastern California, *Geol. Soc. America Bull.*, *88*, 89-95, 1977.

Figure Captions

Fig. 1. (*a*) Map of Long Valley caldera showing epicenters of the earthquakes used in this study, the locations of the central and northwest magma bodies and the southern and Crowley Lake anomalous areas, and related geological features. The earthquake epicenters are indicated by solid dots. The northwest and central caldera magma bodies are outlined at various depth intervals indicated by the large numbers. The smaller numbers near the central body show the shallowest depth at which attenuation is actually seen in those areas. The solid lines indicate well-located boundaries. The dashed contours are more interpretative; the dotted contours are the most interpretative. The 'x' in the SW corner of the central body marks the location of Casa Dablo Hot Springs. The surface projections of the areas of anomalous crust in the southern caldera and beneath Crowley Lake are represented by dashed outlines. Major faults in and near the caldera are drawn with heavy lines, and the area of the resurgent dome is outlined by long, thin dashes. HCF - Hilton Creek Fault, LCF - Laurel-Convict Fault, HSF - Hartley Springs Fault. The late-Holocene Inyo Domes and craters (last active about 700 years ago) are shown in the northwest caldera. The thin, solid line in the northwest caldera encloses the approximate area of the deep "magma roof" reflection seen by Hill [1976]. The location of U.S. Highway 395 is indicated by the line of long and short dashes running diagonally across the map. (*b*) West-east cross section through the Central magma body. (*c*) Northwest-southeast cross section through the Northwest and Central magma bodies.

Fig. 2. Map of western Nevada and eastern California showing the locations of seismograph stations which recorded the Long Valley earthquake signals Long Valley caldera is outlined and labeled, and the epicentral area of the earthquakes we used is shaded. The three lakes shown are from north to south Tahoe, Walker, and Mono.

Fig. 3. Seismograms and source mechanism for a 5.7 km deep Long Valley event. Note the large amplitude shear wave arrivals at the stations indicated regardless of position relative to the source radiation pattern.

Fig. 4. Seismograms and source mechanism for a 6.9 km deep Long Valley event. Note the very low-amplitude shear wave arrival at station MMC and the normal shear wave signals at MON and BON. As the source mechanism indicates the anomalous signal at MMC cannot be explained by source effects (since MON and MMC are located similarly on the radiation pattern) and is probably due to transmission through magma beneath Long Valley. Also compare this MMC signal with the MMC signal in Figure 3.

Fig. 5. Subsurface contour map showing the probable depths above which no large, massive magma bodies exist in Long Valley caldera. The presence or absence of magma below these depths cannot be determined from this map, since the rays do not penetrate deep enough in many parts of the caldera.

Fig. 6. (*a*) Map showing the surface projection of anomalous ray paths through Long Valley to station MON. The earthquake epicenters are shown by solid dots. Short dashed lines represent quality 3 rays; longer dashed lines represent quality 2 rays, as defined in the text. The magma bodies are indicated by the solid, dashed, and dotted outlines. The 5.5 and 7.5 km contours of the northwest body and the 4.5 and 8 km contours of the central body are shown. Other figures will use this same map base. (*b*) Cross-section A-A' showing the intersections of anomalous rays to station MON. Quality 1, 2, and 3 rays are plotted (shear wave quality defined in the text). The horizontal projection of the central magma body is outlined in solid (well-located) and dashed lines. The dashed rectangle shows the position of the southern anomalous area. (*c*) Cross-section A-A" showing the intersection of normal rays (0) to station MON.

Fig. 7. (*a*) Map of anomalous ray paths to station BON. (*b*) Anomalous rays to station BON intersecting section B-B'. The central magma body and southern anomalous area are outlined. (*c*) Normal rays to station BON intersecting section B-B'.

Fig. 8. (*a*) Map of anomalous rays to northeastern stations MGN, HCK, KVN, MNA, LHV, and FER, and to western station JAS. (*b*) Anomalous and normal rays to stations MGN, HCK, KVN, MNA, LHV, and FER intersecting section C-C'. The central magma body and southern anomalous area are outlined.

Fig. 9. (*a*) Map of normal rays to station ORC. (*b*) Normal rays to station ORC intersecting section E-E' near the central magma body and section E''-E''' near the southern anomalous area.

Fig. 10. (*a*) Map of quality 3 rays to station MMC. Note how many of these rays intersect more than one magma body. (*b*) Anomalous rays to station MMC intersecting the central magma body and southern anomalous area along section I-I'. (*c*) Normal rays to station MMC and other northeastern stations intersecting the central magma body and southern anomalous area along section I-I''. (*d*) Anomalous rays to stations MMC and MON intersecting the northwest caldera magma body at section J-J'. The three rightmost rays are to station MON. The approximate source region for the deep reflection seen by Hill [1976] lies below the segment designated "r". (*e*) Normal rays to the northwestern stations and station MON intersecting the northwest caldera magma body at section J-J'.

Fig. 11. (*a*) Map of anomalous rays to several northwest stations. The stations names are printed in the lower left corner of the figure. (*b*) Anomalous rays to several northwest stations intersecting the central magma body at section K-K'. (*c*) Anomalous rays to several northwest stations intersecting the northwest magma body at section L-L'.

Fig. 12. (*a*) Map of anomalous rays to stations KVN, BON, SVP, and PMC which suggest the existence of dispersed magma beneath Crowley Lake. (*b*) Anomalous and normal rays through section M-M' showing the depth distribution of anomalous signals beneath Crowley Lake and also the numerous normal rays through the same area.

Fig. 13. Map showing the locations of earthquakes which produced secondary signals at stations MON (*a*), MMC (*b*), SJC (*c*), HCK and SVP (*d*), large secondary phase at KVN (*e*), and small secondary phase at KVN (*f*). The locations of the magma bodies are plotted, and the bounding ray paths are drawn.

Fig. 14. Five seismograms and the source mechanism from a 8.3 km deep Long Valley earthquake. The seismograms are labeled by station and epicentral distance. The corresponding station position relative to the source radiation pattern is also indicated. Note the large amplitude secondary phase on these records about 2 seconds after the initial *P* arrival. The small arrows indicate the expected shear wave arrival. The shear waves at MON, HCK, and MMC are given quality 2 ratings.

Fig. 15. Map of Long Valley caldera showing the position of relative teleseismic P-delays at 12 km depth (modified from *Steeples and Iyer* [1976]). The small open squares indicate the position of the recording stations operative during the *P* delay study. The solid and dashed lines project from these stations back toward the earthquake source and terminate at 12 km depth in open or solid circles. The open circles and dashed line segments represent non-delayed ray paths. The solid circles and lines indicate the position of delayed rays, the larger circles representing larger relative delays. The depth contours of the northwest and central caldera magma bodies and the southern and Crowley Lake anomalous areas are shown by solid, dashed, and dotted lines as explained in Figure 1.

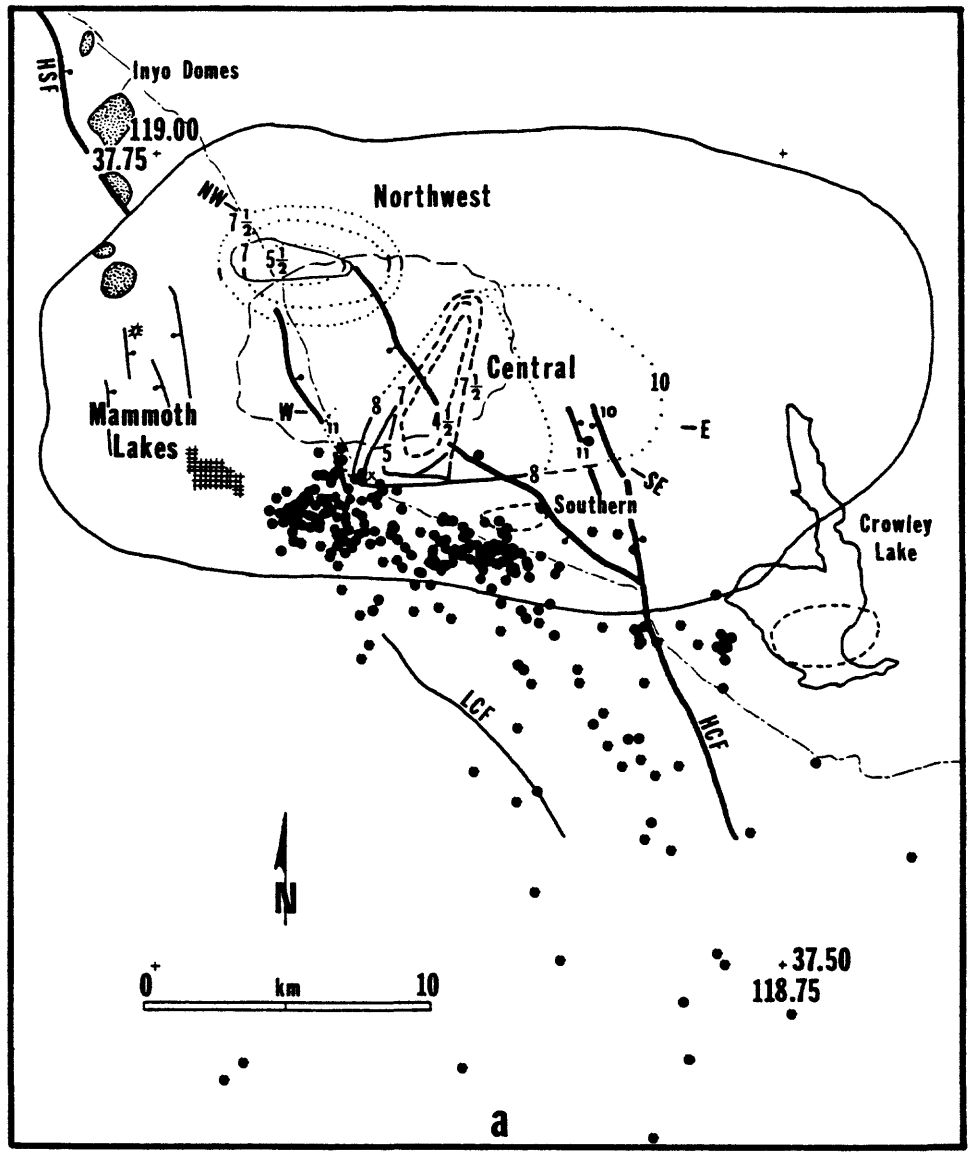
HSF
Inyo Domes
119.00
37.75
NW
Northwest
Central
Mammoth
Lakes
W
E
SE
Southern
Crowley
Lake
LCF
HCF
N
0
km
10
37.50
118.75
a

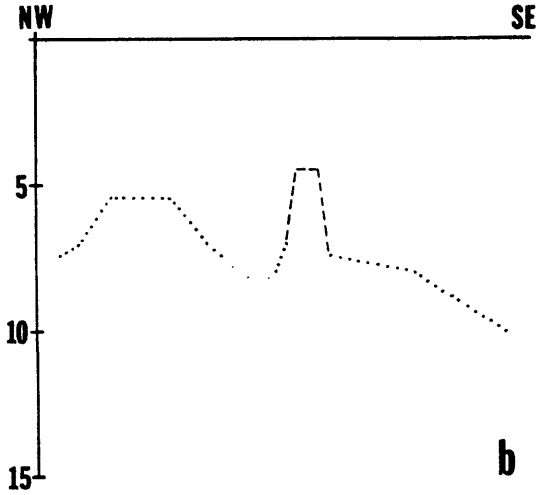
NW
SE
5
10
15
b

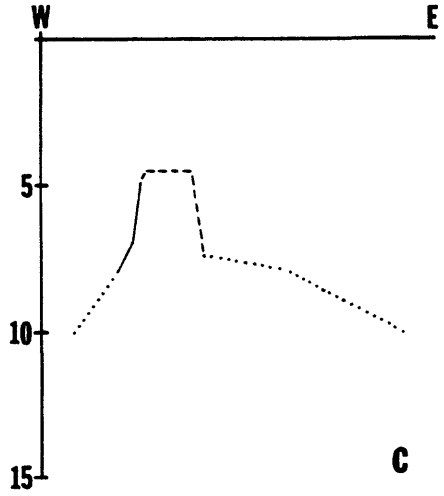
W
E
5
10
15
c

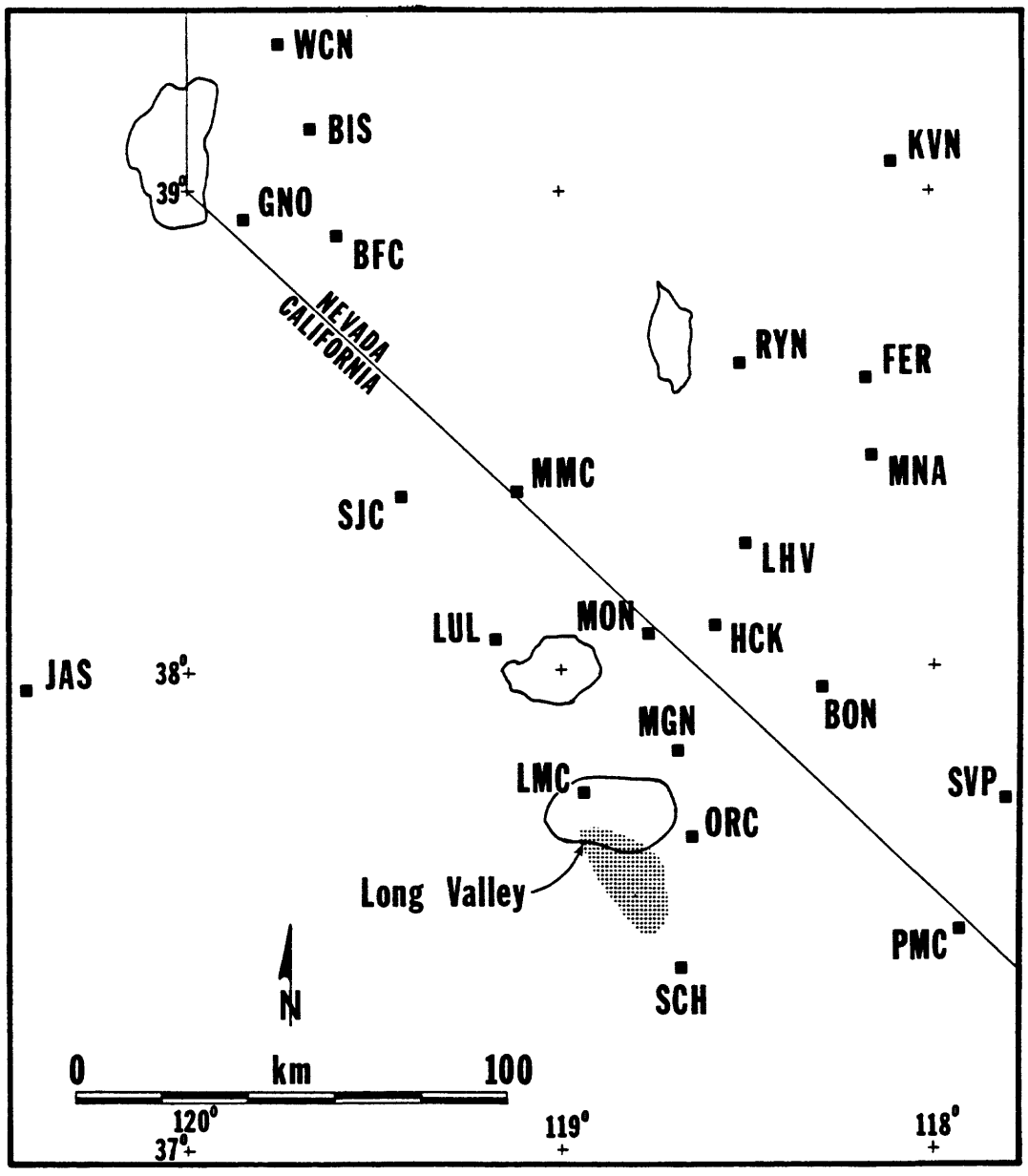
WCN
BIS
KVN
39°
GNO
BFC
NEVADA
CALIFORNIA
RYN
FER
MMC
MNA
SJC
LHV
LUL
MON
HCK
JAS
38°
BON
MGN
LMC
SVP
ORC
Long Valley
PMC
SCH
N
0
km
100
120°
37°
119°
118°

2

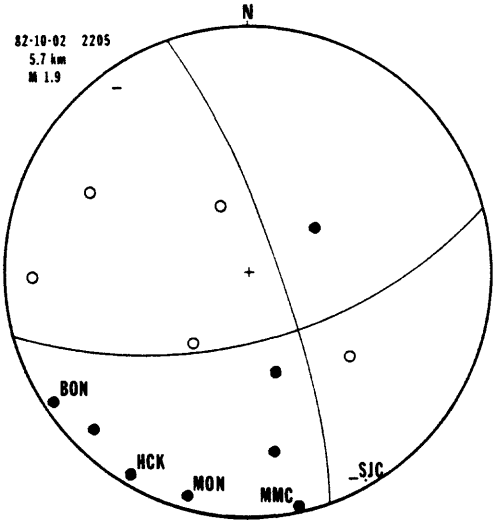
N
82-10-02 2205
5.7 km
M 1.9
BON
HCK
MON
MMC
SJC

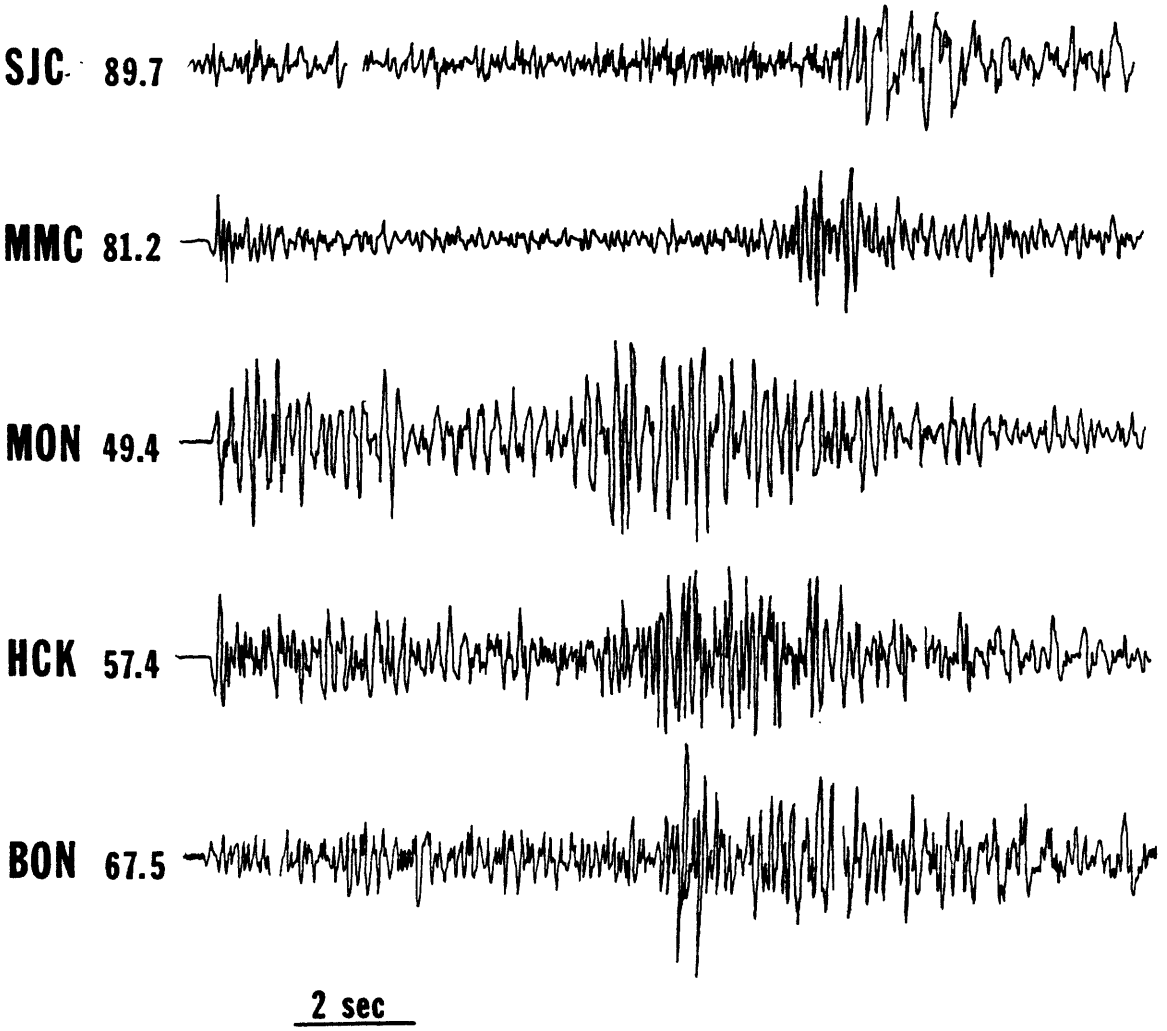
SJC 89.7
MMC 81.2
MON 49.4
HCK 57.4
BON 67.5
2 sec

3

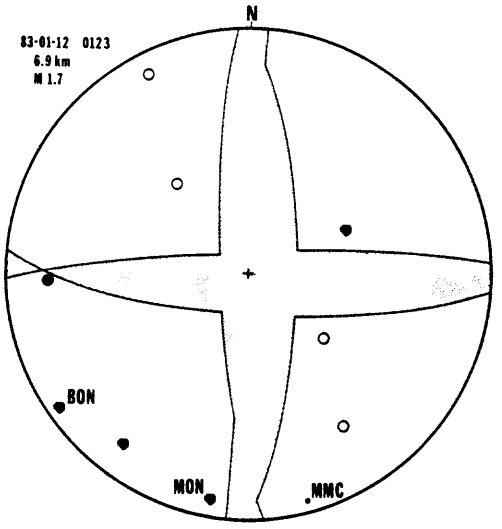

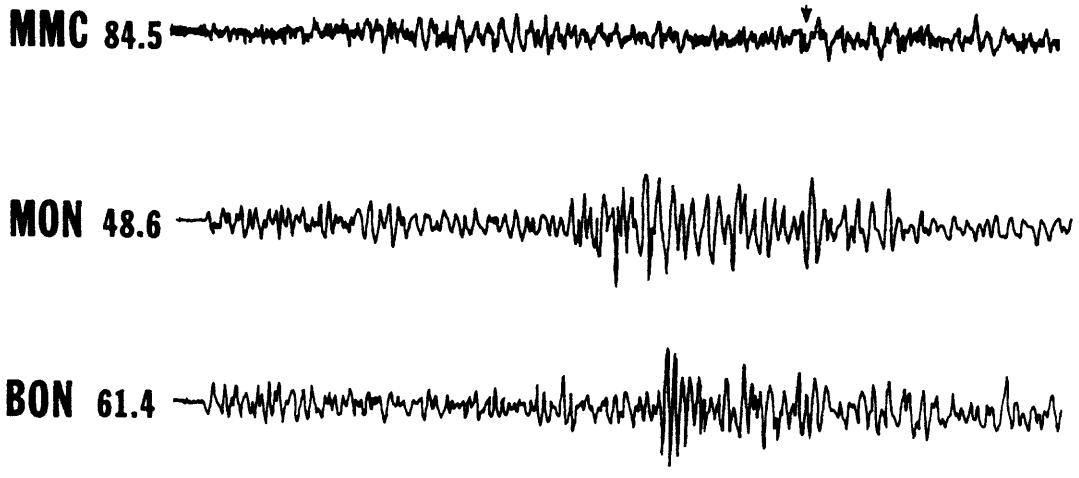

4

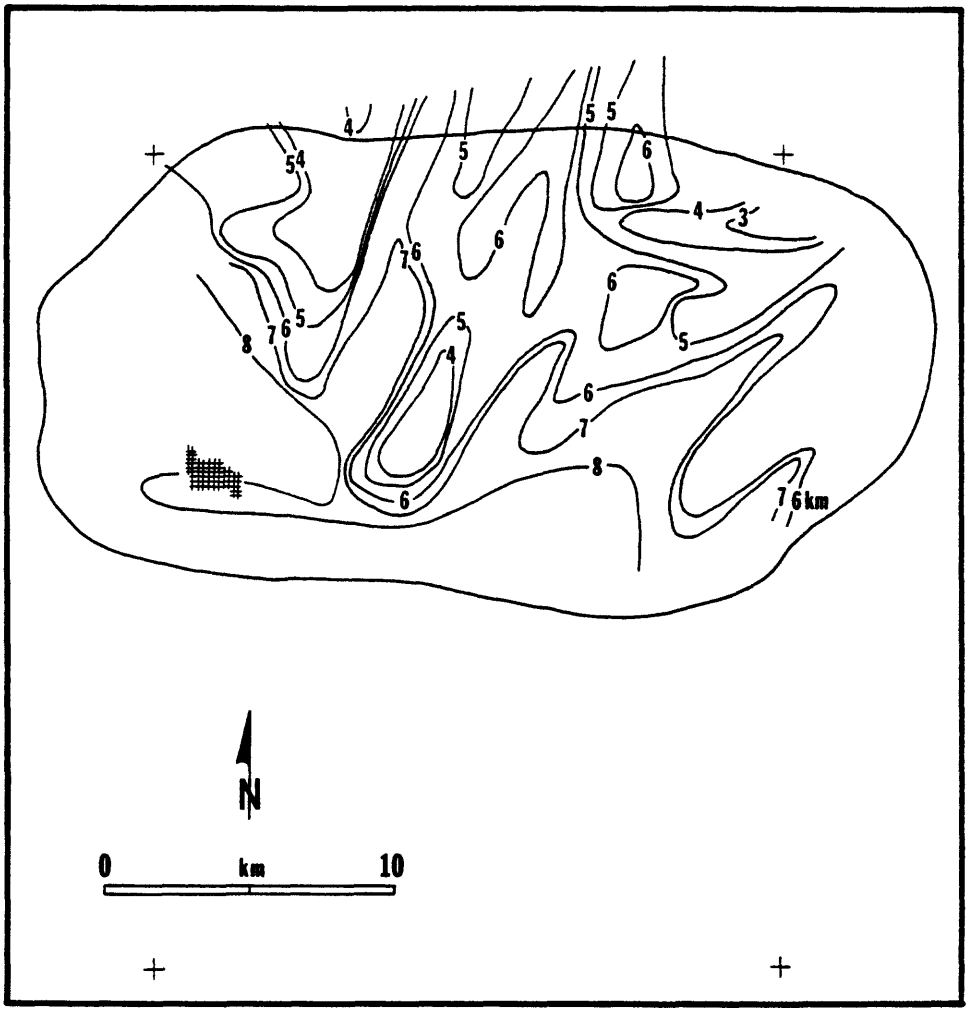

5

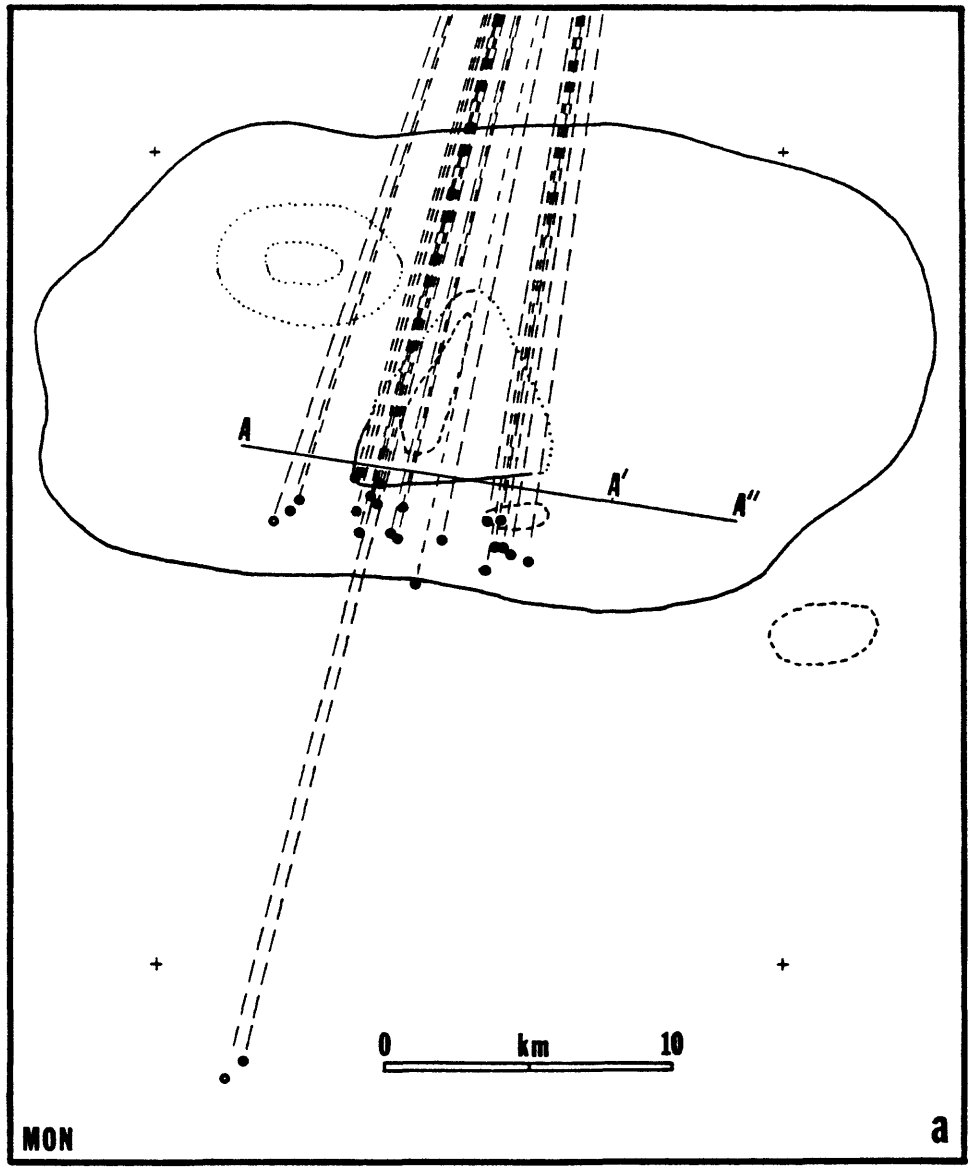

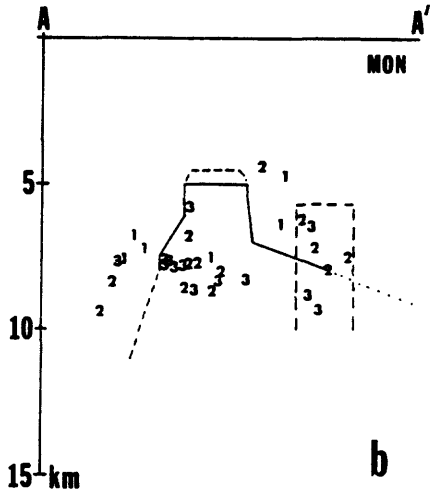

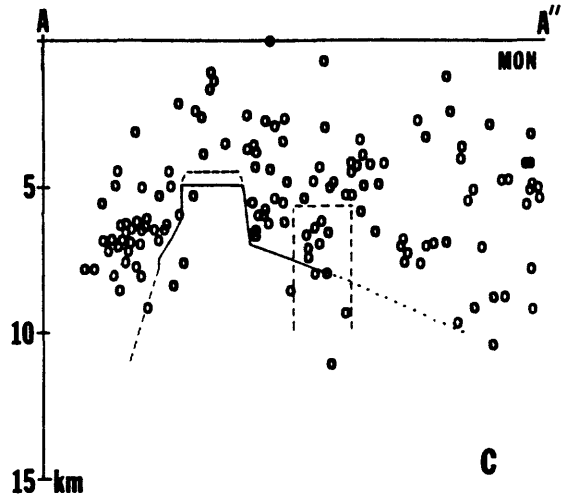

6

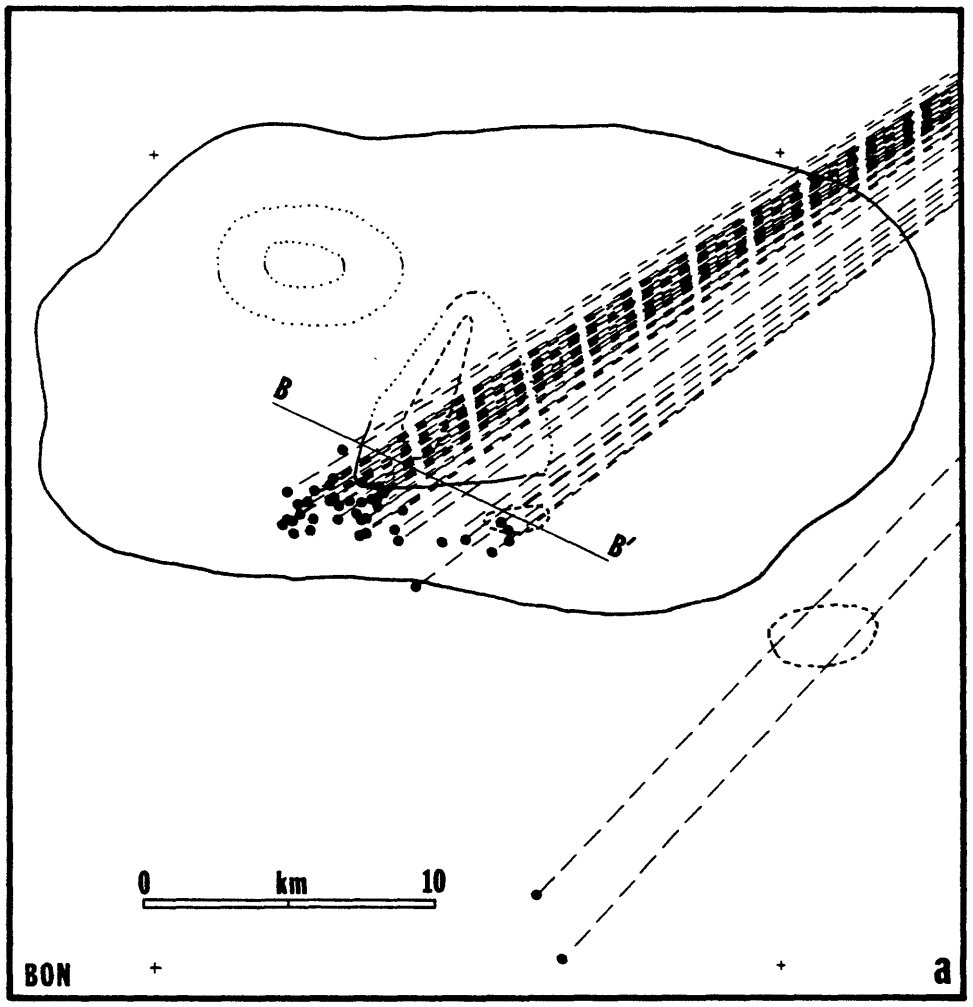

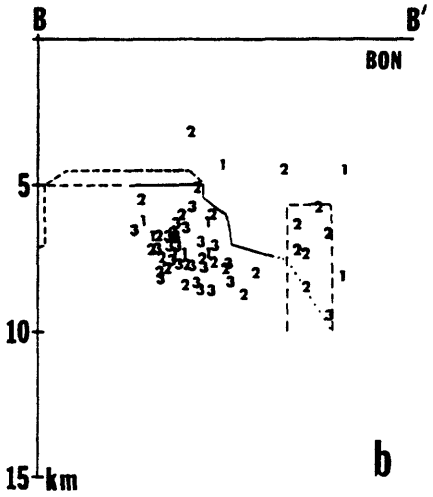

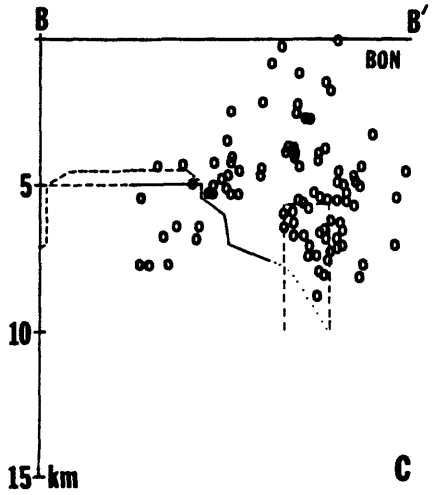

7

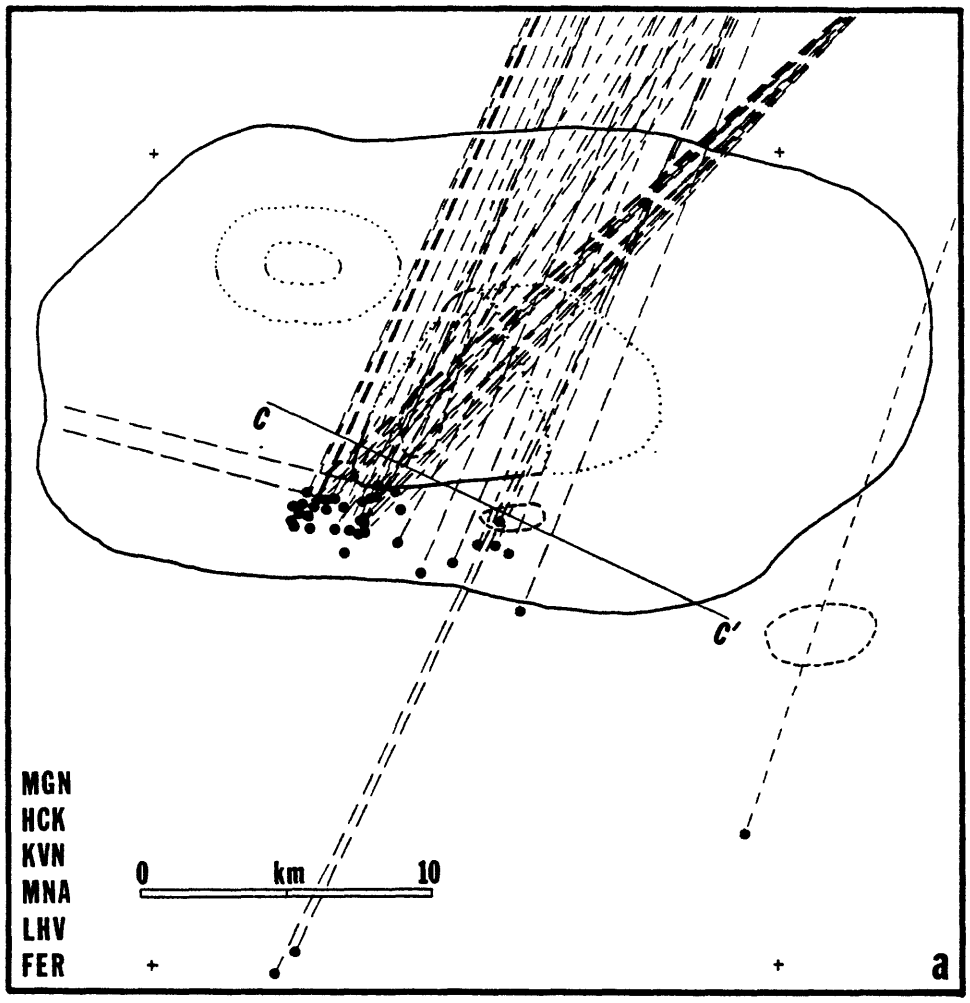

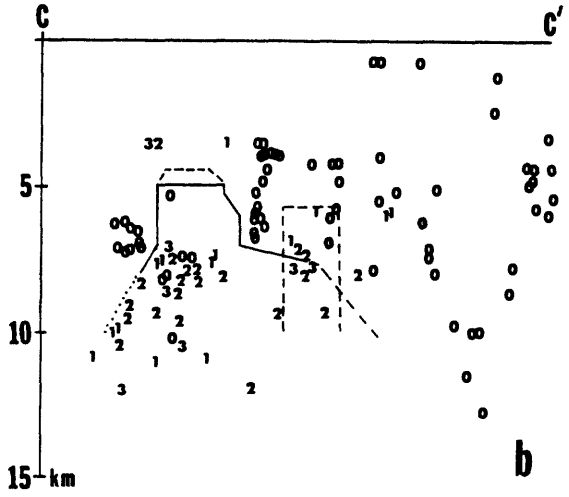

8

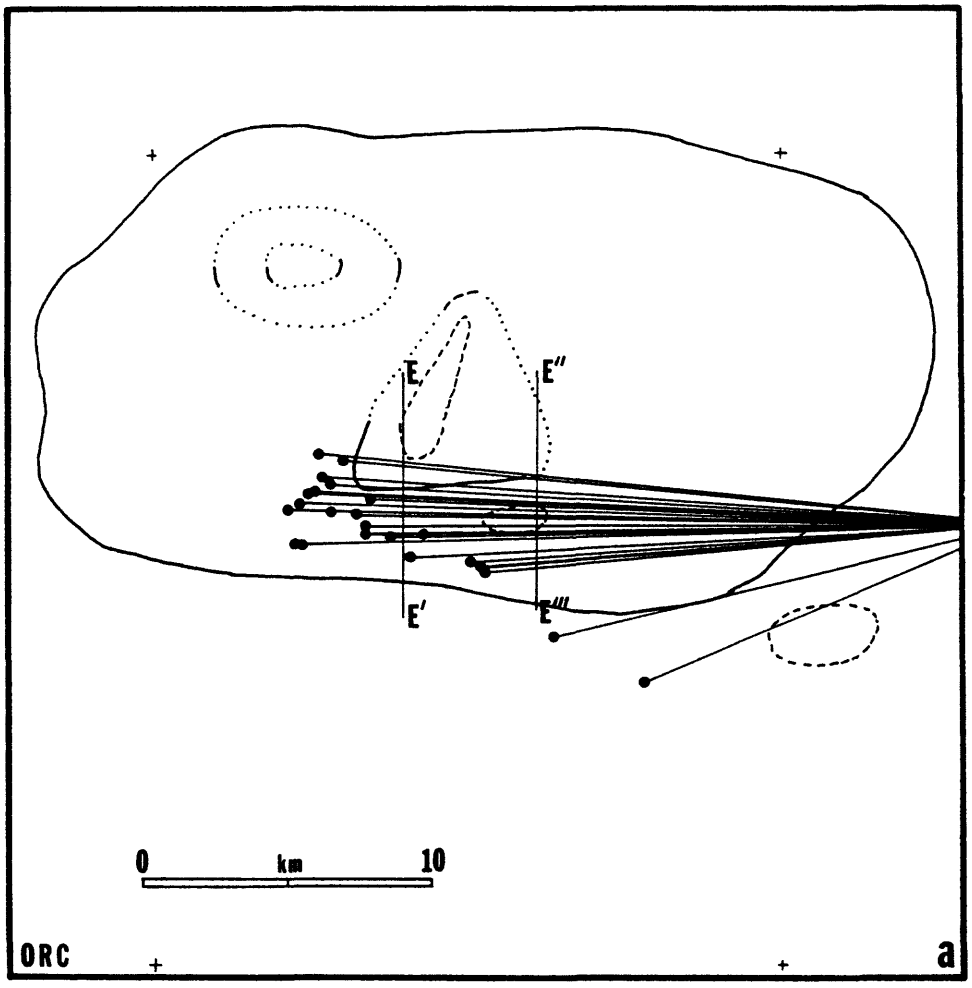

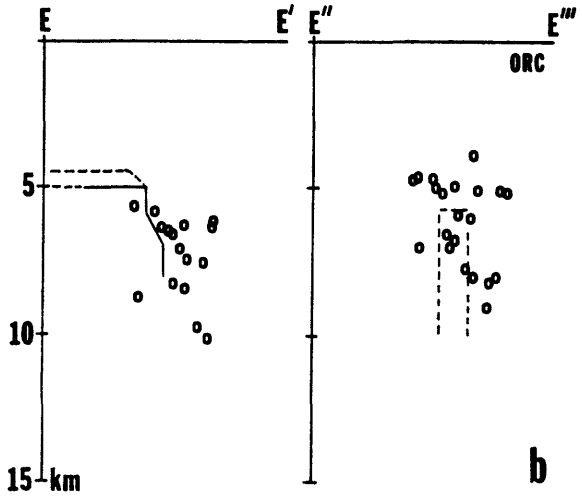

9

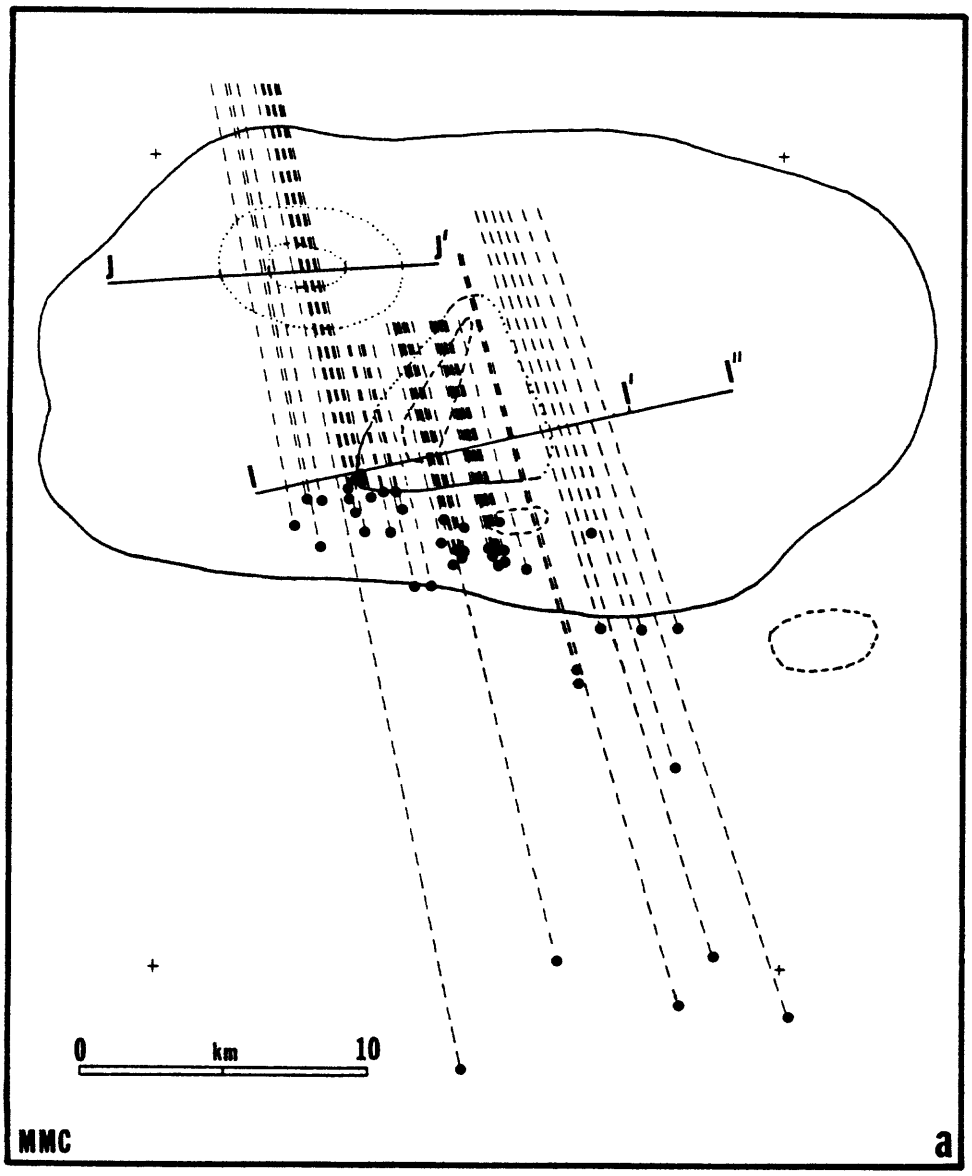
J
J'
I
I'
I''
0
km
10
MMC
a

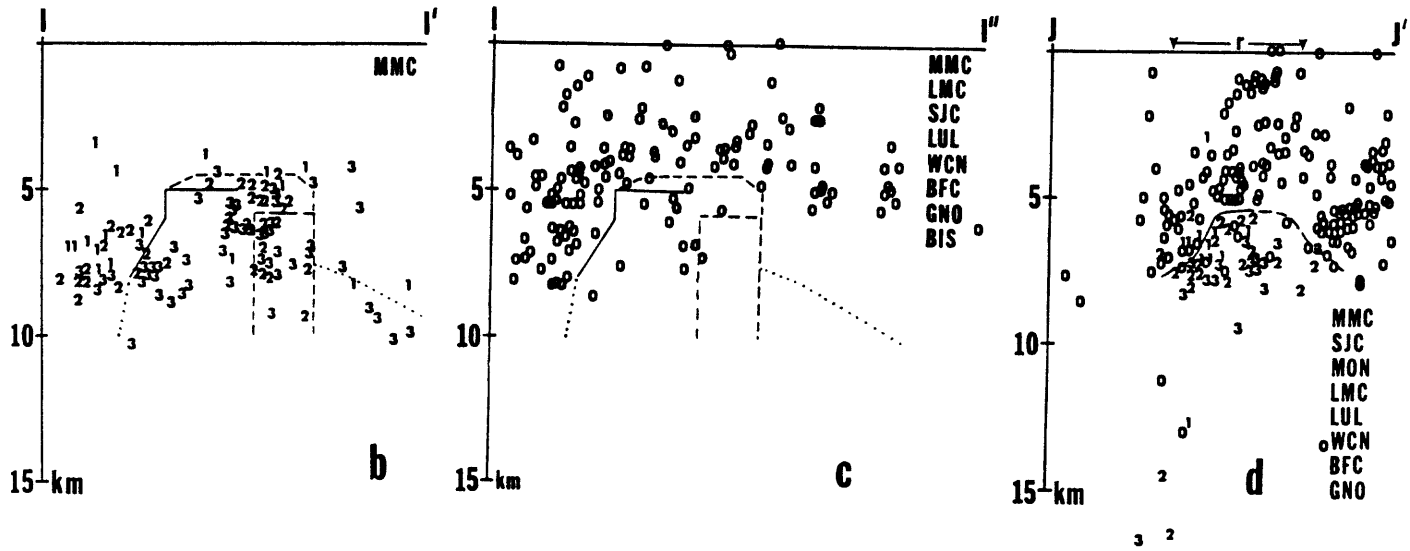
I
I'
MMC
5
10
15
km
b
I
I''
MMC
LMC
SJC
LUL
WCN
BFC
GNO
BIS
5
10
15
km
c
J
J'
MMC
SJC
MON
LMC
LUL
WCN
BFC
GNO
10
15
km
d

10

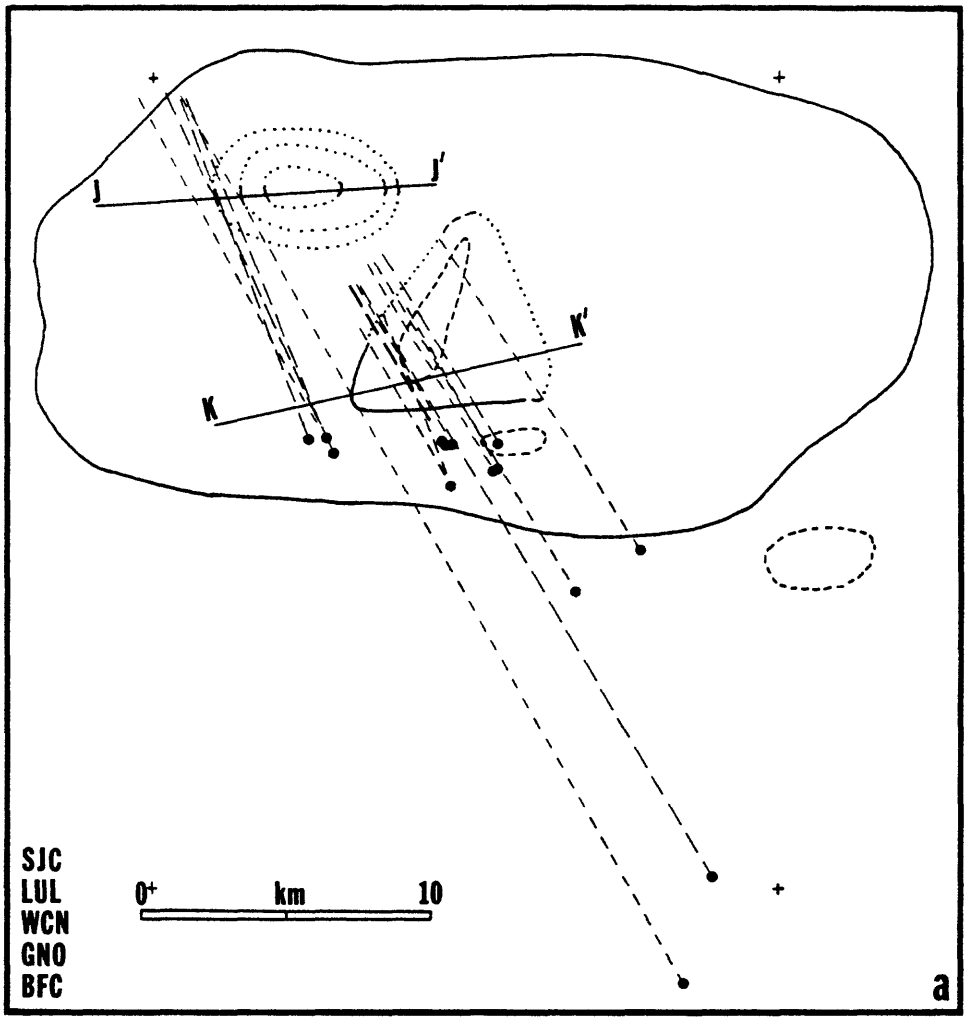
J
J'
K
K'
SJC
LUL
WCN
GNO
BFC
0+
km
10
a

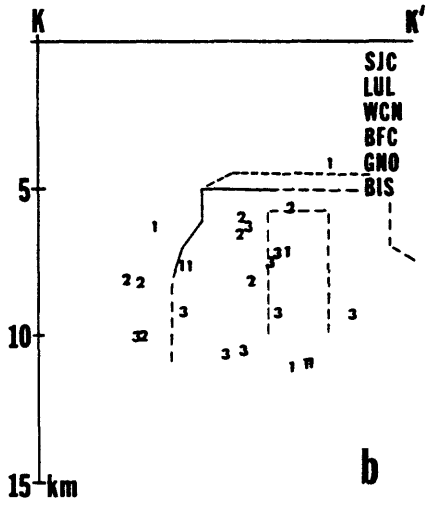
K
K'
SJC
LUL
WCN
BFC
GNO
BIS
5
10
15 km
b

11

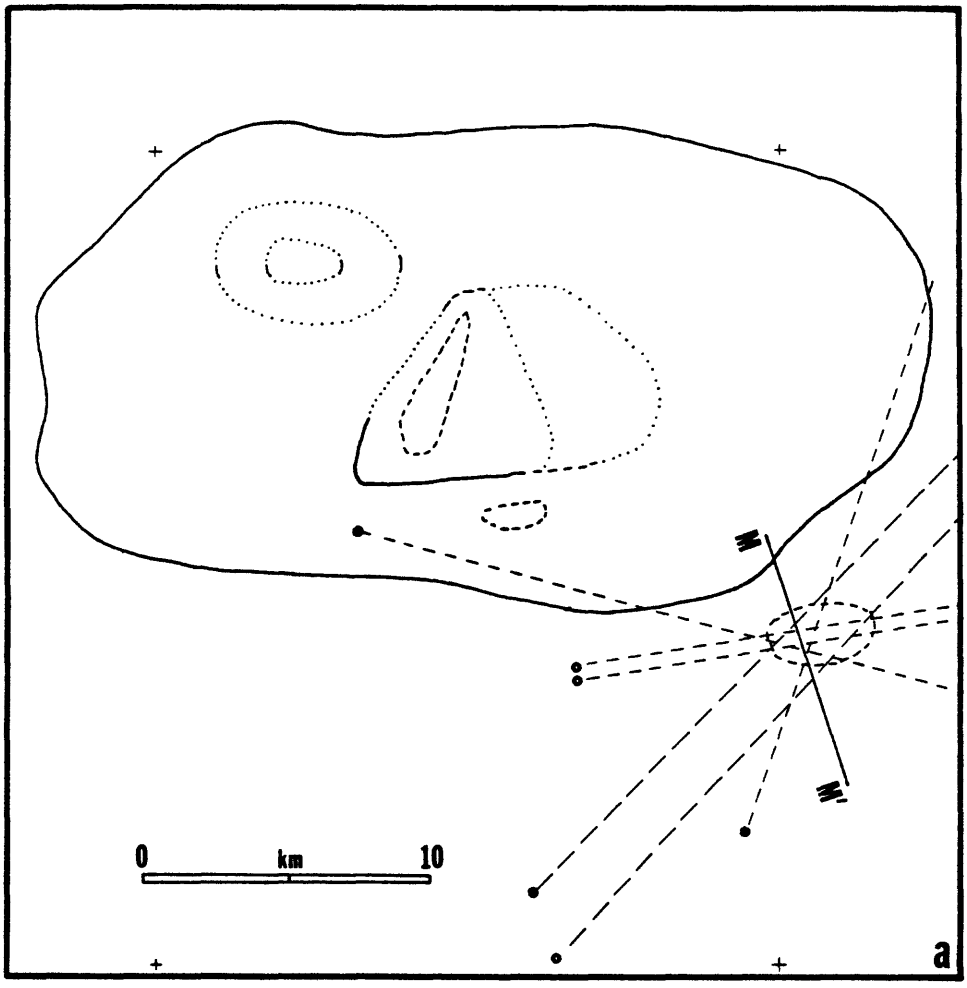

12

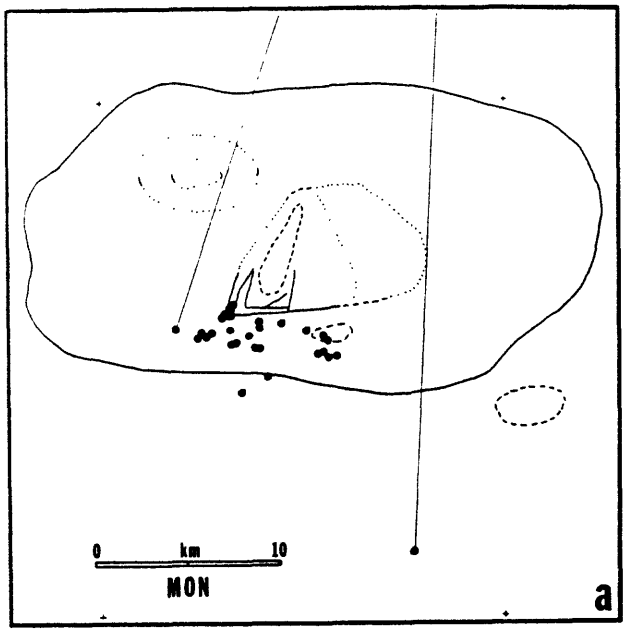
0 km 10
MON
a

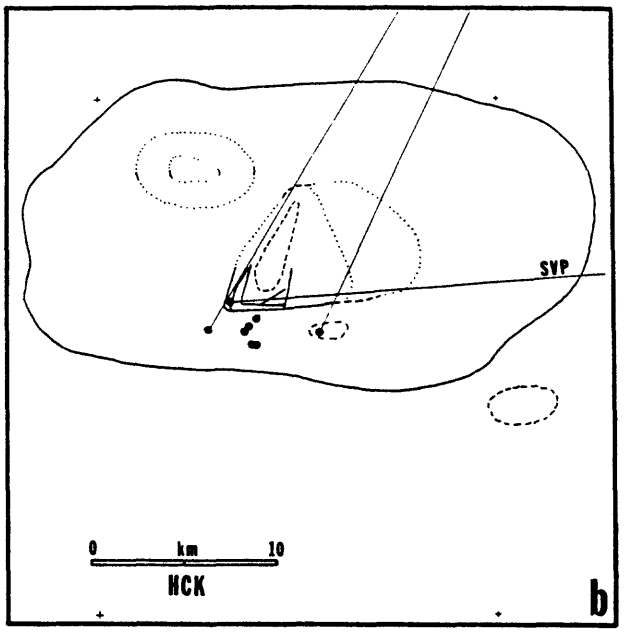
SVP
0 km 10
HCK
b

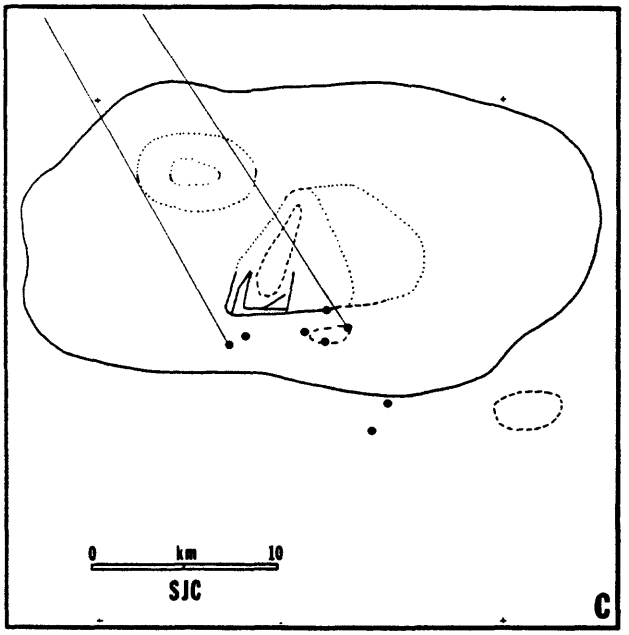
0 km 10
SJC
c

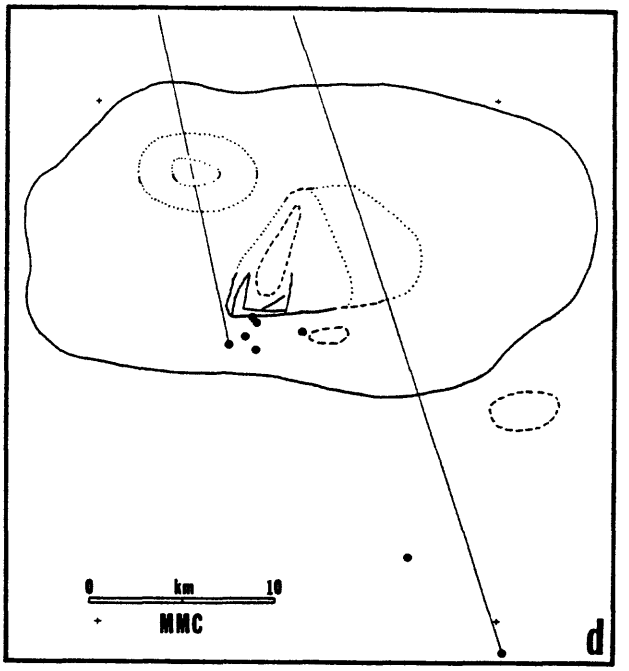
0 km 10
MMC
d

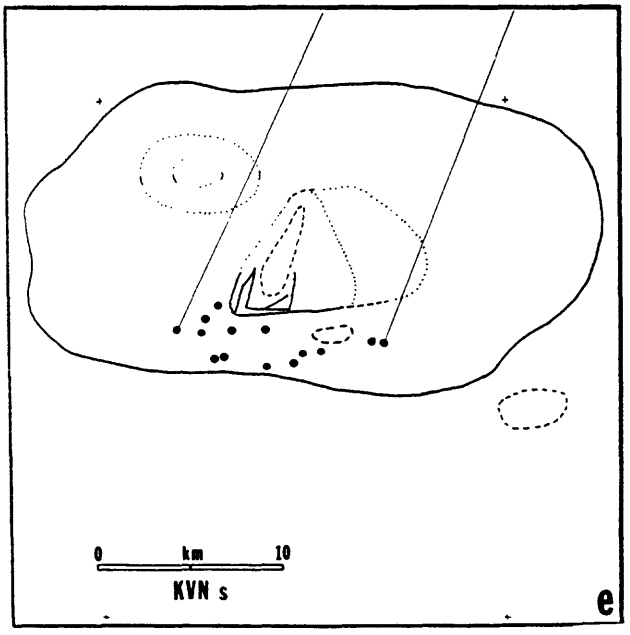
0 km 10
KVN s
e

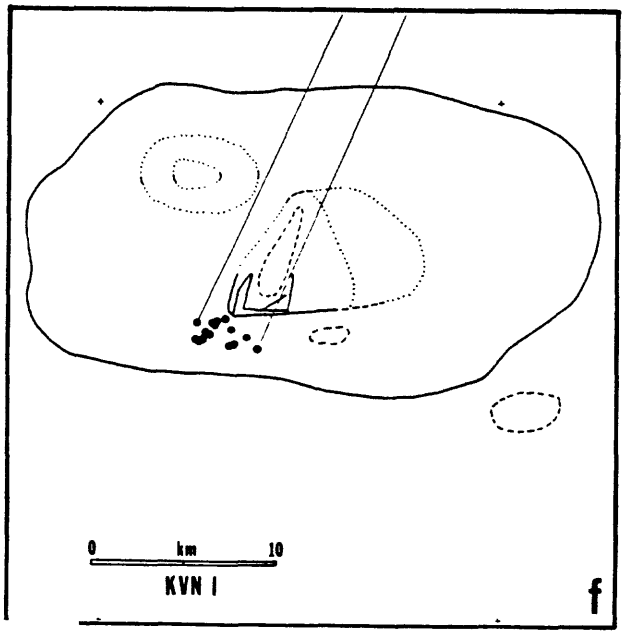
0 km 10
KVN l
f

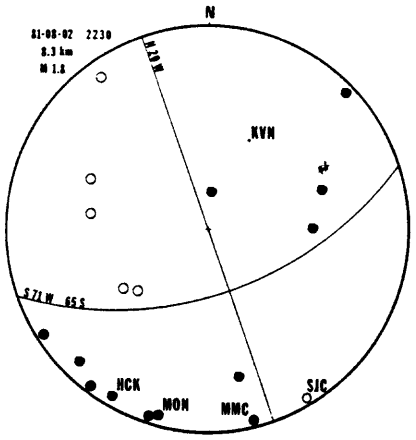
N
81-08-02 2230
8.3 km
M 1.8
KVN
S 71 W 65 S
HCK
MON
MMC
SJC

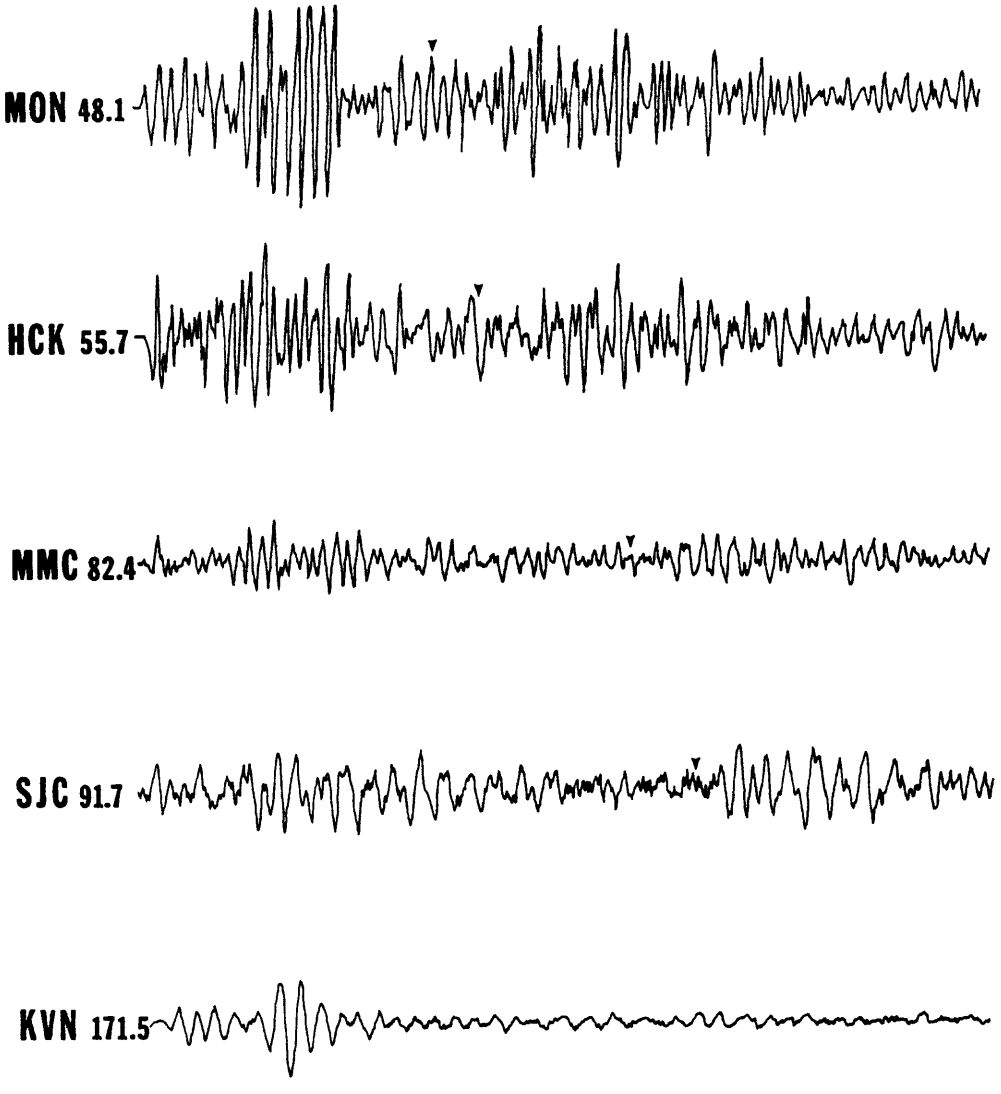
MON 48.1
HCK 55.7
MMC 82.4
SJC 91.7
KVN 171.5
2 sec

14

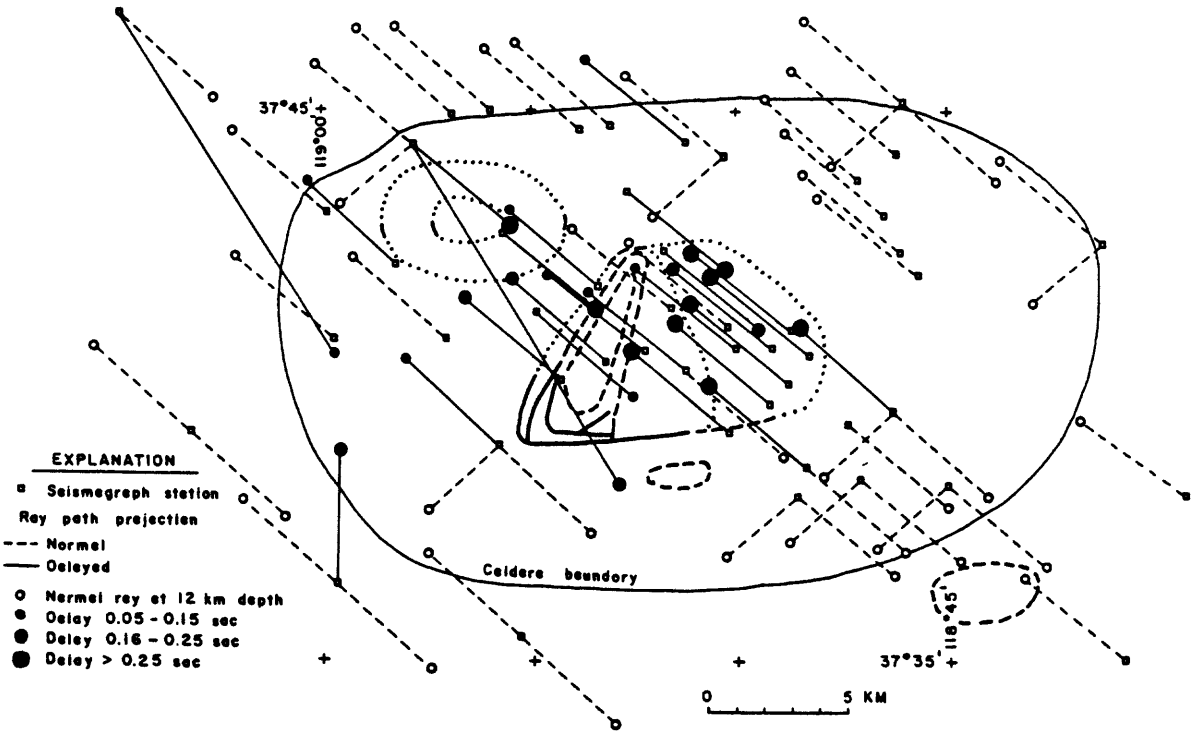
37°45'
118°00'
EXPLANATION
Seismograph station
Ray path projection
Normal
Delayed
Normal ray at 12 km depth
Delay 0.05 - 0.15 sec
Delay 0.16 - 0.25 sec
Delay > 0.25 sec
Caldera boundary
37°35'
118°45'
0
5 KM

15

GRAVITY INVESTIGATIONS AT LONG VALLEY CALDERA, CALIFORNIA

by

Robert C. Jachens and Carter W. Roberts

U.S. Geological Survey

Menlo Park, California

ABSTRACT

Temporal gravity measurements over a broad network in the vicinity of Long Valley caldera, California reveal significant gravity decreases over the interval June 1980-July 1983 at five stations within or close to the caldera. The negative gravity changes reflect the late states of an uplift of the caldera which began before the initial June 5-9, 1980 gravity survey (based on the gravity data) and after July 1979, according to the results of horizontal deformation measurements. Temporal gravity measurements at a more detailed network established within the caldera during June 1982 suggest that a low-amplitude 1982-1983 uplift occurred immediately after the January 1983 south moat earthquake swarm and that the uplift probably was accompanied by the addition of mass at depth. However, these data are complicated by gravity changes due to changes in depth to the water table.

An areal gravity survey of the south moat reveals two local gravity highs of 4-5 mGal amplitude and 2-3 km diameter. These local highs occur directly above two areas that have experienced intense earthquake swarm activity during the past few years and are believed to mark the locations of past intrusions into the south moat.

INTRODUCTION

Investigations of the earth's gravity field have contributed much to our knowledge of the structure and conditions present beneath the surface. Areal gravity surveys have been used for many years to map subsurface density distributions which in turn have been used as the basis for inferring subsurface geology. More recently studies of temporal variations in the earth's gravity field have been used to monitor crustal deformation and to investigate the physical processes involved in tectonic and volcanic activity. During the past few years we have conducted both types of gravity investigations in the vicinity of Long Valley caldera, California as part of the U.S. Geological Survey's Volcano Hazards Program in this region. The results of these investigations show the varied application of such data to the study of the earth's crust and the processes that modify it.

TEMPORAL GRAVITY INVESTIGATION

Regional Network

During early June 1980, about one week after four $M \geq 6$ earthquakes struck in the vicinity of Long Valley caldera, a broad precision gravity network (Figure 1) was established in the region to monitor continuing crustal deformation associated with these events. The 14-station network is centered near Toms Place (primary reference station on Figure 1) and extends from the Sierra Nevada west of Lee Vining, California, southeastward to a station in the White Mountains east of Bishop, California. Most of the stations outside of Long Valley caldera are located on crystalline bedrock outcrops, but the three stations within Long Valley are underlain by caldera fill.

The network has been remeasured four times since June 1980, most recently in July 1983. During all surveys, measurements were made following the procedures described in Jachens (1978) and typically yielded gravity values relative to Toms Place with uncertainties of 4-7μGal (one computed standard error). Therefore, these data are adequate for defining intersurvey gravity changes with uncertainties of 6-9μGal.

Over the interval between June 1980 and July 1983 significant gravity decreases were detected at the five stations located either inside or within a few kilometers of the caldera rim (Figure 2). These negative gravity changes presumably reflect the uplift of the caldera floor and surrounding areas that was identified by comparison of repeated levelling surveys (Savage and Clark, 1982; Messing and others, 1982; Castle and others, 1984). In contrast, over the same period gravity at most other stations showed cumulative changes that either are small relative to the observational uncertainties or are positive. One exception to this simple pattern can be seen at the Sherwin Summit station where gravity decreased by about 25μGal between the 1980 and 1981 surveys and then held steady during all subsequent surveys. The cause of this gravity change is unknown but, because the station is located about 15 km from the caldera rim, it probably is not related to the uplift of the caldera.

Constraints on Timing of Uplift

The precise timing of the uplift with respect to the time of the four $M \geq 6$ earthquakes (May 25-27,1980) has important implications concerning the question of whether the uplift could have caused or triggered the earthquakes. The time that the uplift began is only loosely constrained by the levelling data but is more tightly constrained by other geophysical data. Comparison of results from levelling across Long Valley caldera in

1932, 1957, 1975, and 1980 led Savage and Clark (1982) to conclude that the uplift found in October 1980 could not have begun before the summer of 1975. Horizontal deformation based on repeated trilateration measurement dating back to 1972 indicate that significant changes first occurred only in the interval July 1979-September 1980 thus making it unlikely that the uplift preceeded the July 1979 survey (Savage and Clark, 1982).

An additional constraint on the timing of the uplift can be inferred from the temporal gravity data even though our surveys date back only to early June 1980, 1-2 weeks after the earthquakes. Given a relationship between gravity change and elevation change, an estimate of the amount of uplift that occurred at the gravity stations during the June 1980-July 1983 interval can be made. Because two of the caldera gravity stations are adjacent to level line benchmarks that were surveyed in 1975, 1982, and 1983 and because the levelling and gravity surveys of 1982 and 1983 were coincident in time, it is possible to work backward in time from the 1983 surveys to estimate the amount of uplift that had occurred at these sites prior to the initial gravity survey.

Levelling and gravity surveys prior to the summer of 1982 were not coincident in time so these data cannot be used to define a gravity change versus elevation change relationship for the early stages of the uplift. However, studies in other volcanic areas (Jachens and Eaton, 1980; Dzurisin and others, 1980; Torge and Kanngieser, 1980; Johnsen and others, 1980) have yielded gravity change versus elevation change relationships that generally are consistent with values predicted on the basis of numerical or analytical model studies (Rundle, 1978; Savage, 1984). Assuming that the Long Valley uplift was caused primarily by inflation of a deep magma chamber (Savage and Clark, 1982) and that the inflation was accompanied by injection of magma, the

expected relation between gravity change and elevation change is about -2.3 to -2.4 μGal/cm. These values are close to the value of -2.5 μGal/cm suggested by the gravity and levelling data covering the 1982-1983 interval (see discussion of detailed network below). Using a relation of -2.5 μGal/cm and the 1980-1983 gravity changes near Casa Diablo Hot Springs (station CD in Figure 1) and Whitmore Hot Springs (station WH in Figure 1) (-67 ± 7 μGal and -26 ± 7 μGal, respectively) we estimate that during this interval about 25 cm of uplift accumulated at CD and about 10 cm occurred at WH. Since the estimated uplifts at the two stations for the period covered by the gravity measurements are smaller than the 1975-1983 uplift values defined by the levelling data (about 39 cm at CD and 22 cm at WH), the uplift most likely began before the gravity surveys of June 5-9, 1980.

The gravity data leave unresolved the question of whether the onset of uplift preceeded the M≥ 6 earthquakes because nearly two weeks elapsed between the time of the first earthquake and the start of the first gravity survey, a period during which all of the remaining uplift could have occurred. However, even assuming that no uplift took place during this interval the gravity data do suggest that only 10-15 cm or less of uplift at CD and WH accumulated before the four M 6 earthquakes.

Detailed Network

Following the discovery of the Long Valley uplift by Savage and Clark (1982) and their interpretation of the deformation in terms of magma chamber inflation, about 50 stations were added to the precision gravity network (Figure 1), the majority within Long Valley. Most of the new stations are on level line benchmarks underlain by caldera fill or unconsolidated sediments. The new gravity network was initially measured during June 1982 and partially

remeasured during September 1982, January 1983, and July 1983. The June 1982 and July 1983 surveys were made concurrent with levelling surveys.

Comparison of the results from the June 1982 and July 1983 gravity surveys (Figure 3) reveals a complex pattern of gravity changes (both positive and negative) within the caldera. In general gravity increased at stations in the west and southwest moat and decreased at most other stations. Although many of the changes are small, gravity fluctuations as large as 30-40 μGal were found at some locations. The pattern of gravity change displays relatively short-wavelength components.

In contrast to the complex pattern of gravity change, the 1982 and 1983 levelling surveys reveal a low-amplitude, broad uplift centered on the resurgent dome (Castle and others, 1984). The pattern of uplift is much smoother than that of the gravity change, as illustrated by a plot of gravity change versus elevation change (Figure 4). Although most of the points in Figure 4 fall in the quadrant appropriate for gravity variations accompanying uplift, they do not define a linear relationship as has been seen in other volcanic areas. The considerable scatter evident in this plot suggests either that we seriously underestimated our observational uncertainties or that we measured additional gravity changes due to sources other than the uplift. Direct and indirect evidence supports the idea that the observed gravity changes are real and result both from uplift and from temporal changes in depth to the water table.

Influence of Ground Water Fluctuations

Direct evidence for gravity changes due to water level fluctuations can be seen in Figure 5 which plots gravity change versus changes in elevation of the shallow water table at the few sites where we have information on the

water table elevation. The two quantities are well correlated, with positive gravity changes associated with increased water table elevation and vice versa. Although the data in Figure 5 document conditions at only a few locations, indirect evidence from the entire network also supports the idea that the observed gravity changes partially reflect fluctuations in ground water level. At stations on crystalline bedrock outside the caldera gravity changes determined by comparing the results from the September 1982 and July 1983 surveys with those of June 1982 are distributed with means near zero and standard deviations of about 6 μGal. These results are about what would be expected based on the computed measurement uncertainties of 6-9 μGal. Because the porosity of the crystalline bedrock is low, gravity changes due to ground water fluctuations beneath bedrock stations should be small. In contrast, the non-bedrock stations are underlain by material that generally has high porosity and so the potential for gravity changes due to variations in the height of the water table is greater at these stations. For non-bedrock stations gravity changes June-September 1982 and June 1982-July 1983 are distributed with standard deviations of 11 and 16 μGal, respectively, much larger than the corresponding standard deviations at the bedrock stations. The larger scatter at non-bedrock stations is shown in Figure 6 which also serves to demonstrated that the increased scatter is not due to uplift (compare middle and lower panels of Figure 6).

An attempt was made to determine if the measured gravity changes are quantitatively consistent with changes due to water level fluctuations and uplift alone by examining the temporal gravity, water level, and elevation data at the 10 stations where we have such information for the June 1982-July 1983 interval. Figure 7 shows three gravity time histories at each of the 10 stations; the ones on the left representing the observed changes, the ones in

the center representing gravity changes corrected for water level changes assuming complete saturation or drainage of material with porosity of 0.3, and the ones on the right representing gravity changes corrected both for water level changes and for uplift assuming a gravity change versus elevation change relation of -2.5 μGal/cm. For this test, the uplift was assumed to have occurred after the January 1983 gravity survey. The gravity time histories on the right show consistently smaller temporal fluctuations at all stations than those on the left and at seven of the ten stations show no corrected fluctuations larger than the error bars.

Conclusions from temporal gravity measurements

Two main conclusions can be drawn from the results shown in Figure 7. First, gravity changes resulting from uplift and water level changes can readily account for the measured gravity changes. Second, although only three stations shown in Figure 7 (top three) were measured in January, 1983 the gravity data from them suggest that the 1982-1983 uplift occurred after our measurements on January 8 and 9 taken during the peak of the January earthquake swarm. The uplift was first detected during a levelling survey conducted by the Los Angeles Department of Water and Power (January 13-20, 1983). Thus the combined gravity and levelling data suggest that the uplift occurred immediately after the swarm.

Encouraged by the apparent success of efforts to correct for the effects of water level changes, we attempted to use corrected gravity change data to determine whether the magma chamber expansion represented simple inflation or inflation accompanied by magma injection. Figure 8 shows a plot of gravity change (corrected for water level change) versus elevation change. The data cluster around a value of about -2.5 μGal/cm which suggests that some magma

injection accompanied the uplift. Unfortunately, the uplift was so small compared to observational uncertainties in the gravity data that simple inflation ($\partial g/\partial e$ = -3.1 μGal/cm) cannot be completely ruled out.

AREAL GRAVITY SURVEY

The areal gravity survey was designed to investigate a prominant feature of the recent seismic activity in the vicinity of Long Valley caldera, namely the concentration of numerous earthquake swarms in the southern part of the caldera (Ryall and Ryall, 1983; Cockerham and Pitt, 1984). Cockerham and Pitt (1984) have identified two classes of swarms: class 1 swarms generally contain more than 200 events, last for two or more days, and contain at least one event with M$\geq$ 4; class 2 swarms have 20-200 events, of which the largest rarely exceeds M=3.5, and last from minutes to several hours. Five of the class 1 swarms and many of the class two swarms have occurred beneath a small area located about 4 km east of Mammoth Lakes (Cockerham and Pitt, 1984) (Figure 9). The sixth and most intense class 1 swarm, which took place in January 1983, originated beneath the same small area but subsequently spread east-southeastward along a linear zone roughly 10 km in length. The earthquakes in this swarm were not distributed uniformly along the linear zone but rather formed a "kidney" shaped distribution with the most intense concentration of seismicity located at the western end and a somewhat less intense concentration at the eastern end. This pattern also is evident in the non-swarm seismicity in the south moat (R. S. Cockerham, oral commun. 1984). Most of the earthquakes have focal depths in the 2-10 km range. The swarm-like behavior of the seismicity, the concentration of the swarms within a small volume of crust, and analysis of geodetic data have lead to the

interpretation that the south moat seismicity reflects intrusion of magma into the crust beneath this area (Ryall and Ryall, 1983; Savage and Cockerham, 1984; Cockerham and Pitt, 1984).

Given the possibility that knowledge of the subsurface density distribution in the south moat might provide some insight into the structure controlling the distribution of earthquakes and the physical processes involved in the current activity, a detailed gravity survey of the south moat was conducted during the summer of 1983. Standard techniques were used to reduce the data to Bouguer gravity (Dobrin, 1952) with a reduction density of 2.67 g/cm^3 and terrain corrections carried out to a radius of 166.7 km from each observation site. Uncertainties in the detailed Bouguer gravity data resulting from possible errors in elevation, observed gravity, and terrain correction probably are less than 0.5 mGal. These new data were combined with more widely spaced data of Kane and others (1976) in order to place the new survey in a regional context. Finally, a long-wavelength regional field based on a model of topography isostatically compensated according to the Airy-Heiskanen model was removed from all the data in order to suppress the effects of deep density structure associated with the crustal root beneath the Sierra Nevada (Jachens and Griscom, 1982).

Interpretation of the gravity data

The resulting gravity map (Figure 10) reveals the following major features in the vicinity of the south moat: 1) a steep gradient across which the gravity decreases by more than 20 mGal from south to north and which is part of a continuous feature that encircles the entire caldera; and 2) a narrow east-west alignment of alternating lows (three) and highs (two) that lie at the base of the boundary gradient and have a maximum relief of slightly

more than 4 mGal (Figures 9 and 10). The steep gravity gradient reflects the lateral transition from relatively high density crystalline rocks of the Sierra Nevada to the lower density material within the caldera (Kane and others, 1976). This gradient thus defines the position of the structural boundary of the caldera. We view the aligned gravity lows as reflecting a gravity trough which is interrupted in two places by local gravity highs (Figure 9). Identification of the two highs as localized features superposed on a low background field is based mainly on the fact that the gravity levels at the bottoms of the three lows define a linear gradient and that the two highs are spatially correlated with the distribution of seismicity as discussed below. The cause of the linear gravity low over the south moat is not well constrained by the gravity data but possible sources include a graben-like structure in the floor of the caldera or a narrow zone of very low density material within the south moat fill. Analysis of the detailed seismic refraction data collected in the south moat during the summer of 1983 (E. Kissling, oral commun., 1984) should help to identify the detailed structure in this area.

The locations and characteristic dimensions of the two local gravity highs that interrupt the linear low are correlated with the distribution of recent seismicity in the south moat (Figure 9). The western gravity high occurs directly above the western concentration of seismicity and roughly covers the area of the class 1 swarms that occurred prior to January 1983. Similarly, the eastern gravity high occurs above the eastern lobe of the January 1983 class 1 swarm.

Analysis of the shape and size of a gravity anomaly can provide information on the location and size of the density distribution that gives rise to the anomaly. Of the two gravity highs, the western anomaly is best

suited for this type of analysis because it is reasonably well isolated from the much larger anomaly associated with the boundary of the caldera. However, the similarity in size and shape of the two anomalies suggests that results from analyzing the western anomaly probably also roughly apply to the eastern anomaly. The shape of the western anomaly is similar to that caused by a point source located at a depth of 1.3 km or a spherical source whose center is at this depth. Finite volume sources with other shapes can be found that will cause anomalies similar to the observed data but, because the point source geometry represents the limiting depth case, some parts of all other geometries must lie at depths of less than 1.3 km. Since the caldera floor lies at a depth of about 1.3 km beneath the south moat (E. Kissling, oral commun., 1984) at least some part and possibly all of the anomalous density distribution that causes the western anomaly must be contained within caldera fill.

According to Gauss's theorem (LaFehr, 1965) the total anomalous mass causing a gravity anomaly can be determined from the integral of the gravity anomaly, regardless of the shape of the source. Thus, 1.1×10^{12} kg, which is the mass of a point source at 1.3 km that will cause a maximum gravity anomaly of about 4.5 mGal, should approximate the total anomalous mass responsible for the western gravity high. A more useful number would be an estimate of the volume of the source but this requires knowledge of the density contrast between the source and its surroundings. The density contrast is not known but assuming an average density for the caldera fill of 2.25 g/cm^3 (Kane and others, 1976) the density contrast probably does not exceed 0.8 g/cm^3. This contrast yields a source volume 1.4 km^3 which probably represents a minimum estimate because it assumes that the source has a density of 3.05 g/cm^3 and is located completely within the caldera fill. A source with a lower density or

one that is contained partly beneath the floor of the caldera would lead to a larger volume estimate. Therefore, the total volume for the sources of the two gravity highs probably is of the order of a few cubic kilometers or more.

Discussion and conclusions based on the areal gravity survey

Likely candidates for sources of the two local gravity highs are intrusions that penetrated the caldera fill and solidified at depth. Non-vesicular volcanic rocks with compositions similar to those found at the surface in Long Valley could have densities sufficiently high to cause positive density contrasts with the typical caldera fill (Telford and others, 1976). Basalt was erupted from vents in the west and south moat during the past 0.15 my (Bailey and others, 1976) and the geologic map of Bailey and Koeppen (1977) shows a basaltic vent about 1 km due south of the center of the western gravity high.

Cockerham and Pitt (1984) suggest that the class 1 swarms were caused by repeated magma injection into the crust beneath the south moat. The local gravity highs that are spatially correlated with the recent seismicity also suggest that intrusion has occurred beneath the south moat prior to the last few years. That the gravity data do not primarily reflect the current event is indicated by the locations of the gravity anomaly sources (shallower than the seismicity) and by the volumes of the gravity anomaly sources (at least an order of magnitude greater than the volume changes associated with recent deformation and more that 2 orders of magnitude greater than the volume changes inferred for the south moat area) (Savage and Clark, 1982; Savage and Cockerham, 1984; Rundle and Whitcomb, 1984). Therefore, it appears likely that the area currently experiencing intense earthquake swarm activity has been the site of intrusions in the past and the proposed dike

intrusions during the past few years may be just the latest in a series of such events.

REFERENCES

Bailey, R.A., Dalrymple, G.B., and Lanphere, M.A., 1976, Volcanism, structure, and geochronology of Long Valley caldera Mono County, California: Journal of Geophysical Research, v. 81, p. 725-744.

Bailey, R.A., and Koeppen, R.P., 1977, Preliminary geologic map of Long Valley caldera, Mono County, California: U.S. Geological Survey, Open-file Map 77-468.

Castle, R.O., Estrem, J.E., and Savage, J.C., 1984, Uplift across Long Valley caldera, California: (submitted to Journal of Geophysical Research)

Cockerham, R.S., and Pitt, A.M., 1984, Intra-caldera earthquake swarms in the Long Valley caldera: in Proceedings of Conference __, Active Tectonic and Magmatic Processes in Long Valley Caldera, Eastern California, U.S. Geological Survey Open-File Report

Dobrin, M.B., 1952, Introduction to geophysical prospecting: McGraw-Hill, New York, 435 p.

Dzurisin, D., Anderson, L.A., Eaton, G.P., Koyanagi, R.Y., Lipman P.W., Lockwood, J.P. Okamura, R.T., Puniwai, G.S., Sako, M.K., and Yamashita, K.E., 1980, Geophysical observations of Kilauea volcano, Hawaii, 2, Constraints on the magma supply during November 1975-September 1977: Journal of Volcanology and Geothermal Research, v. 7, p. 241-269.

Jachens, R.C., 1978, Temporal gravity changes as applied to studies of crustal deformation: in Proceedings of Conference VII, Stress and Strain Measurements Related to Earthquake Prediction, U.S. Geological Survey Open-File Report 79-370, p. 222-243.

Jachens, R.C., and Griscom, Andrew, 1982, An isostatic residual gravity map of California: a residual map for interpretation of anomalies from intracrustal sources: Society of Exploration Geophysicists, Technical program Abstracts and Biographies, Fifty-Second Annual International Meeting and Exposition, Dallas, Texas, October 17-21, 1982, p. 299-301.

Jachens, R.C., and Eaton, G.P., 1980, Geophysical observations of Kilauea volcano, Hawaii, 1, Temporal gravity variations related to the 29 November 1975, M=7.2 earthquake and associated summit collapse: Journal of Volcanology and Geothermal Research, v. 7, p. 225-240.

Johnsen, G.V., Bjornsson, A., and Sigurdsson, S., 1980, Gravity and elevation changes caused by magma movement beneath the Krafla caldera, northeast Iceland: Journal of Geophysics, v. 47, p. 132-140.

Kane, M.F., Mabey, D.R., and Brace, R.L., 1976, A gravity and magnetic investigation of the Long Valley caldera, Mono County, California: Journal of Geophysical Research, v. 81, p. 754-762.

LaFehr, T.R., 1965, The estimation of the total amount of anomalous mass by Gauss's theorem: Journal of Geophysical Research, v. 70, p. 1911-1919.

Messing, J., Riley, F.S., and Denlinger, R.P., 1982, Uplift of the Long Valley, California, caldera between 1975 and 1982: Transactions, American Geophysical Union (Eos), v. 63, p. 1132.

Rundle, J.B., 1978, Gravity changes and the Palmdale uplift: Geophysical Research Letters, v. 5, p. 41-44.

Rundle, J.B., and Whitcomb, J.H., 1984, A model for deformation in Long Valley, California, 1980-1983; in Proceedings of Conference ___, Active Tectonic and Magmatic Processes in Long Valley Caldera, Eastern California, U.S. Geological Survey Open-File Report

Ryall, A., And Ryall, F., 1983, Spasmodic tremor and possible magma injection in Long Valley Caldera, eastern California: Science, v. 219, p.1432-1433.

Savage, J.C., 1984, Local gravity anomalies produced by dislocation sources: Journal of Geophysical Research, v. 89. p. 1945-1952.

Savage, J.C., and Clark, M.M., Magmatic resurgence in Long Valley caldera, California: Possible cause of the 1980 Mammoth Lakes earthquakes: Science, v. 217, p. 531-533.

Savage, J.C., and Cockerham, R.S., 1984, Earthquake swarm in Long Valley Caldera, California, January 1983: Evidence for dike intrusion: Journal of Geophysical Research, (in press).

Telford, W.M., Geldart, L.P., Sheriff, R.E., and Keys, D.A., 1976, Applied Geophysics: Cambridge University Press, New York, 860 p.

Torge, W., and Kanngieser, E., 1980, Gravity and height variations during the present rifting episode in northern Iceland: Journal of Geophysics, v. 47, p. 125-131.

FIGURE CAPTIONS

Fig. 1. Map showing network for monitoring temporal variations of gravity near Long Valley caldera. Dashed line indicates approximate boundary of caldera. Large hexigon shows location of primary reference station at Toms Place (TP). Triangles show locations of stations established during June 1980. Dots show locations of stations established during summer of 1982. Station designations: BR-Benton Range; CD-Casa Diablo; LM-Lookout Mountain; LV-Lee Vining; MC-McGee Creek; NR-North Rim; RC-Rock Creek Lake; SR-Southwest Rim; SS-Sherwin Summit; TH-Tungsten Hills; TP-Toms Place; WH-Whitmore Hot Springs; WM-White Mountains.

Fig. 2. Gravity time histories at stations of the broad network established in 1980. Zero reference for each survey is the average of gravity changes at all stations located on crystalline bedrock and more than 5 km from the caldera boundary. Error bars indicate one computed standard error on either side of the plotted points.

Fig. 3. Map showing gravity changes during interval June 1982-July 1983. Open circles indicate gravity decreases, screened circles indicate gravity increases, and the diameters of the circles reflect the magnitudes of the changes.

Fig. 4. Plot of gravity change versus elevation change for interval June 1982-July 1983. Dashed line indicates a $\delta g/\delta e$ relationship of -2.5 μGal/cm.

Fig. 5. Plot of gravity change versus ground water level change for all surveys. Point marked by "greater than" symbol comes from location for which we only know a minimum value of the water level change. This point probably should plot farther to the right. Dashed line indicates a gravity change/ water level change relationship assuming complete saturation and drainage of material with porosity 0.45.

Fig. 6. Gravity change plotted as a function of radial distance from the center of uplift, located approximately 3 km east-northeast of station CD on Figure 1. Dots indicate stations on crystalline basement. Upper panel represents changes over interval June-September 1982 and lower two panels represent changes over interval June 1982-July 1983. Bottom panel shows gravity changes corrected for elevation changes assuming a $\delta g/\delta e$ relationship of -2.5 μGal/cm.

Fig. 7. Time histories of gravity change at all stations where gravity, elevation, and water level data all are available. See text for discussion of the differences between the three time histories at each station.

Fig. 8. Plot of gravity change (corrected for water level fluctuations) versus elevation change for interval June 1982-July 1983. Lower dashed line represents best fit $\delta g/\delta e$ relationship of -2.5 μGal/cm and upper dashed line represents $\delta g/\delta e$ relationship of -3.1 μGal/cm.

Fig. 9. Detailed residual gravity and epicenter (plus signs) map of the south moat area. Contour interval is 1 mGal. Seismicity is for interval

February-May, 1983. Dash-dot line encloses area of class 1 earthquake swarms for interval June 1980-May 1982; dashed line encloses area of January 1983 swarm (after Cockerham and Pitt, 1984).

Fig. 10. Isostatic residual gravity map of Long Valley caldera. Plus signs show locations of gravity measurements. Hachures indicate direction of decreasing gravity. Contour interval is 2 mGal.

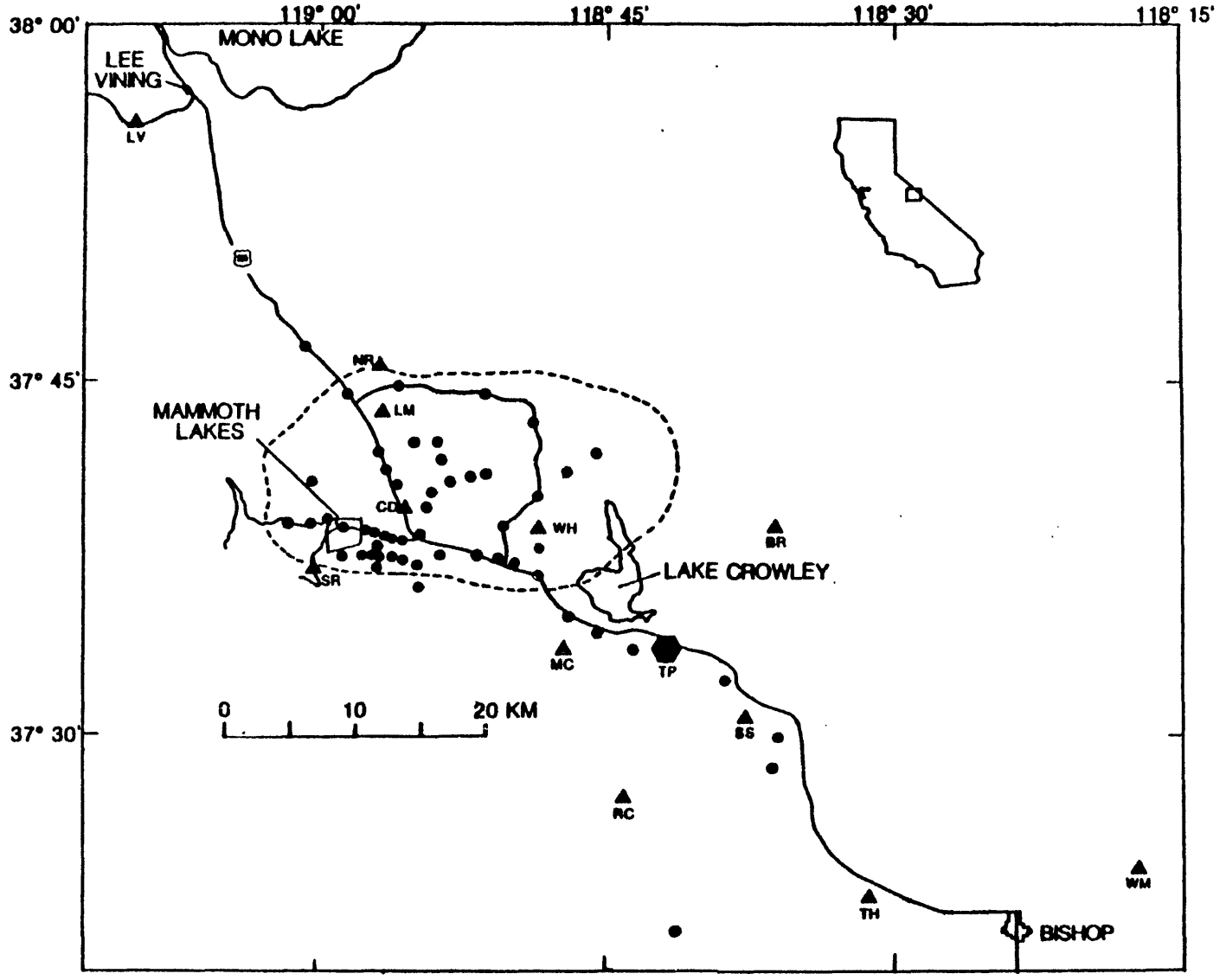
38° 00'
119° 00'
118° 45'
118° 30'
118° 15'
MONO LAKE
LEE VINING
LV
37° 45'
MAMMOTH LAKES
MR
LM
CD
WH
SR
BR
LAKE CROWLEY
MC
TP
0
10
20 KM
37° 30'
SS
RC
TH
WM
BISHOP

FIGURE 1

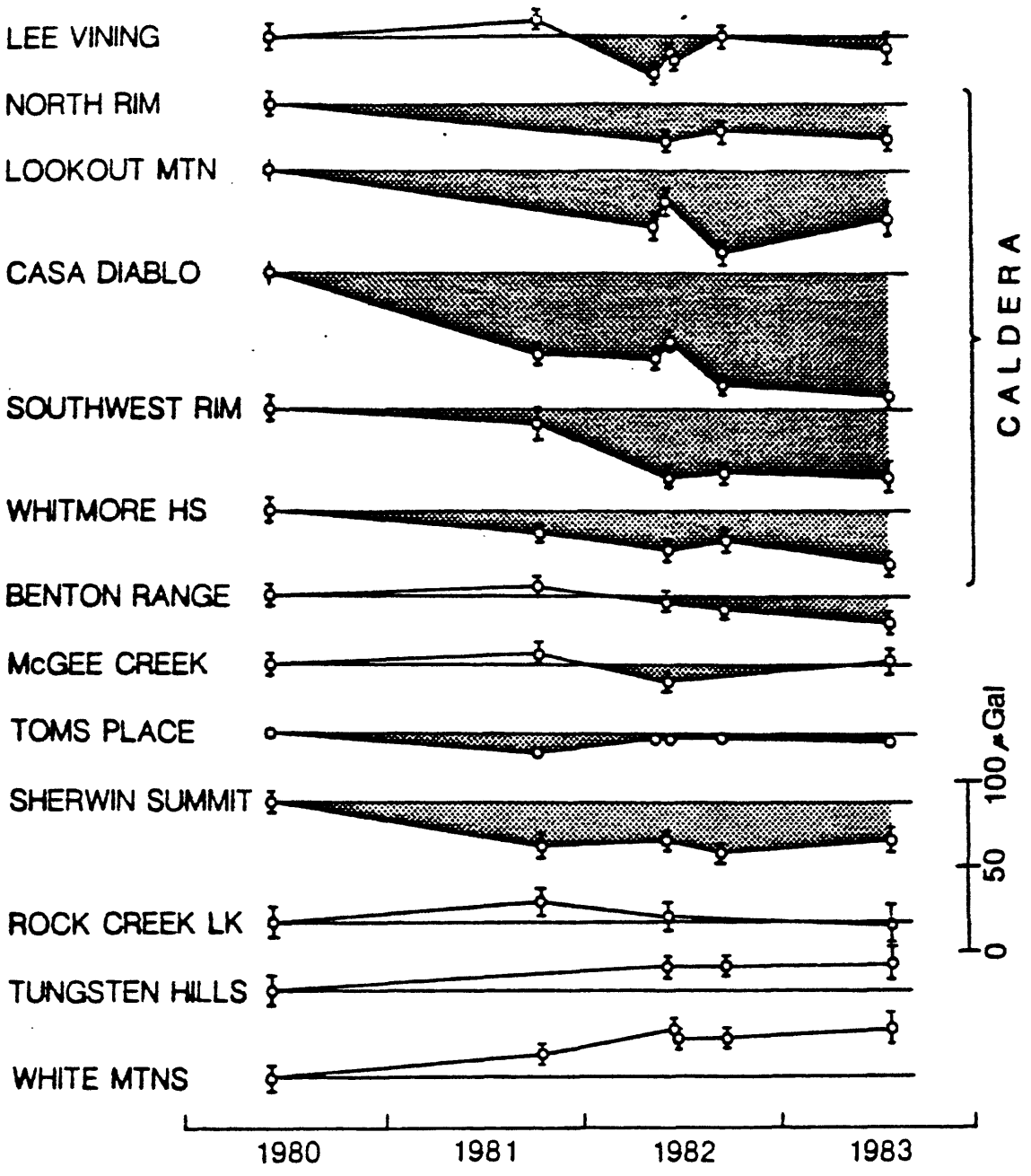
LEE VINING
NORTH RIM
LOOKOUT MTN
CASA DIABLO
SOUTHWEST RIM
WHITMORE HS
BENTON RANGE
McGEE CREEK
TOMS PLACE
SHERWIN SUMMIT
ROCK CREEK LK
TUNGSTEN HILLS
WHITE MTNS
CALDERA
0
50
100 μGal
1980
1981
1982
1983

FIGURE 2

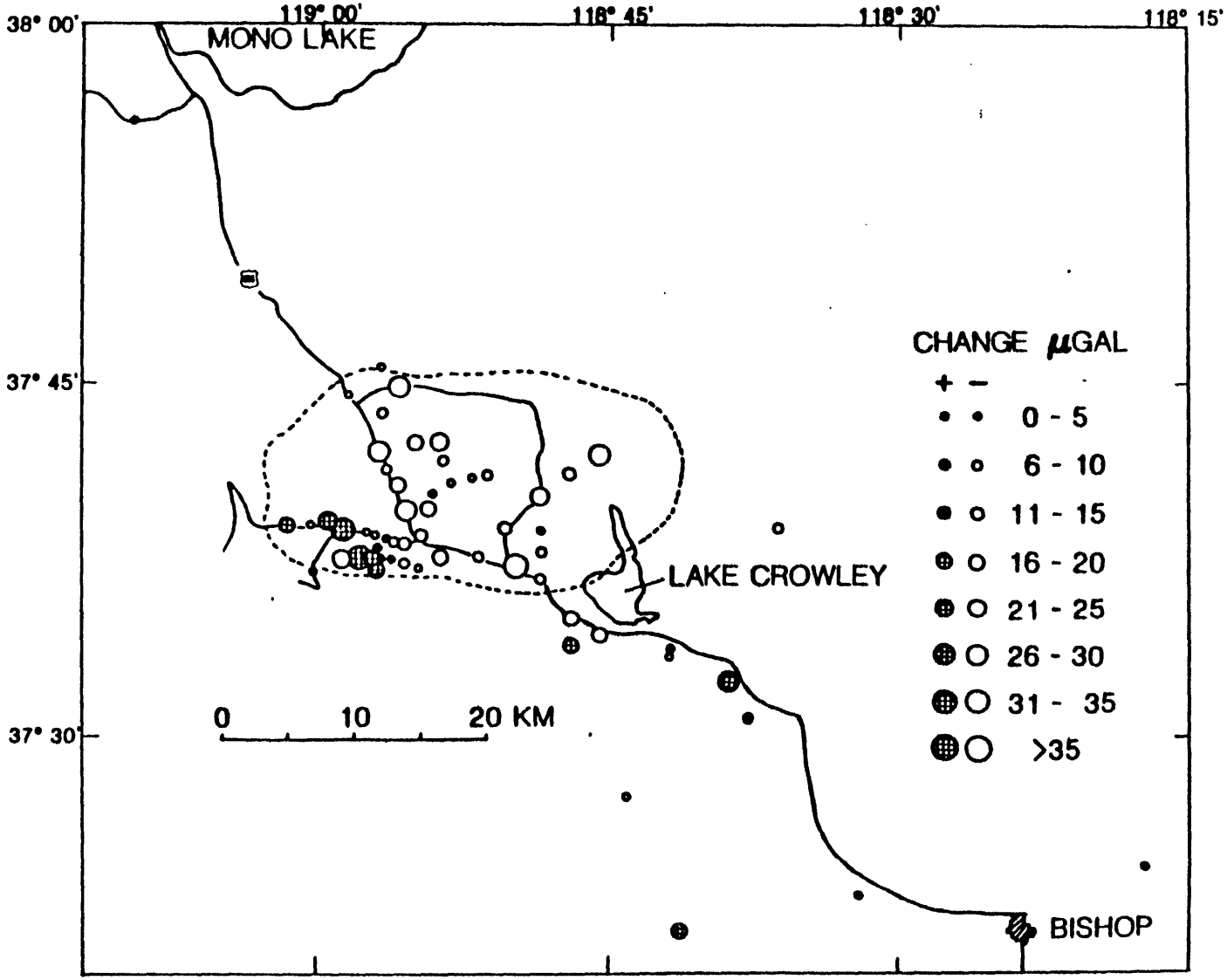
38° 00'
119° 00'
118° 45'
118° 30'
118° 15'
MONO LAKE
37° 45'
37° 30'
LAKE CROWLEY
0 10 20 KM
CHANGE μGAL
+ −
0 - 5
6 - 10
11 - 15
16 - 20
21 - 25
26 - 30
31 - 35
>35
BISHOP

FIGURE 3

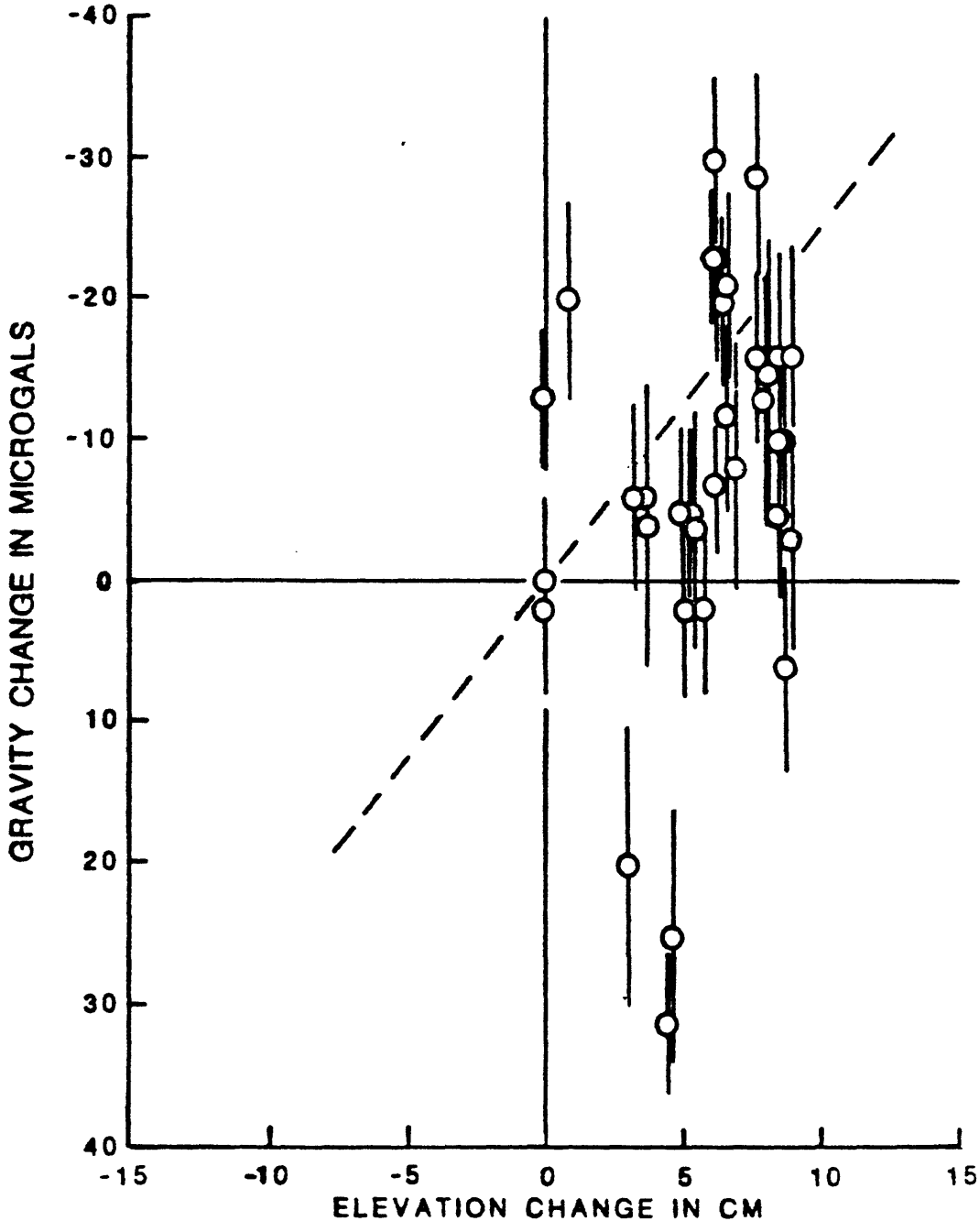
GRAVITY CHANGE IN MICROGALS
-40
-30
-20
-10
0
10
20
30
40
-15
-10
-5
0
5
10
15
ELEVATION CHANGE IN CM

FIGURE 4

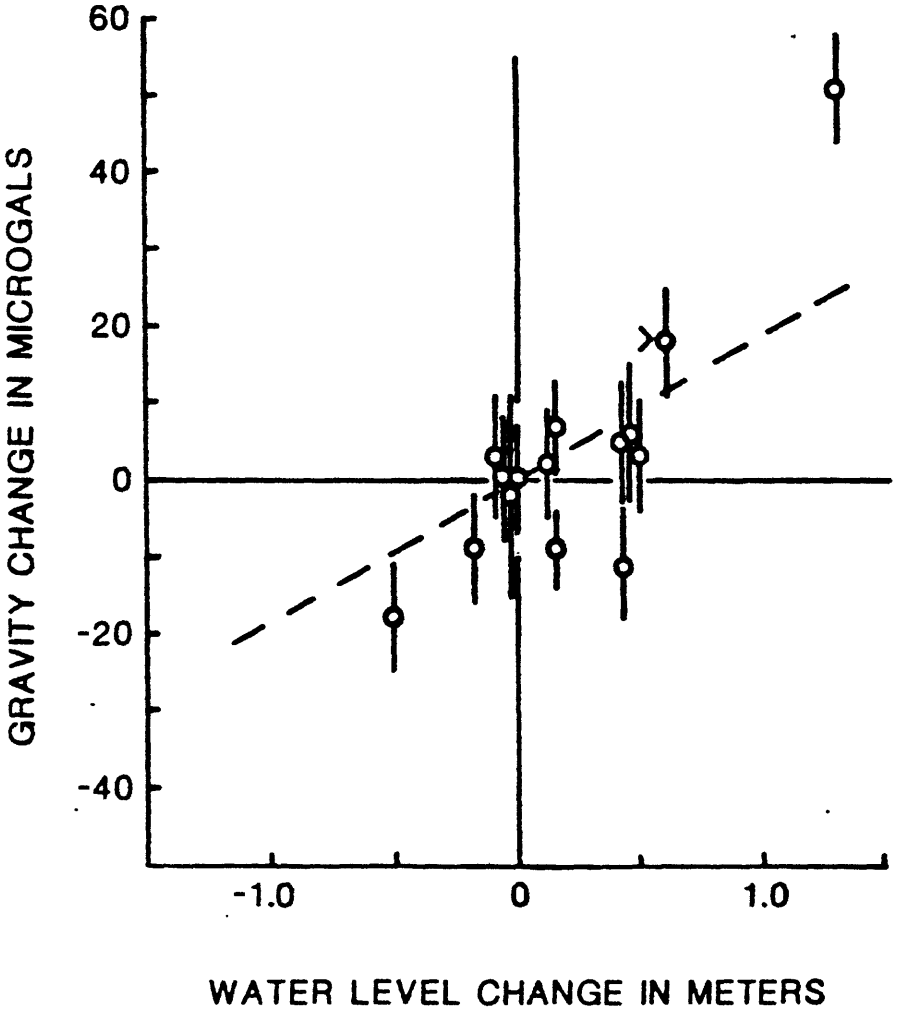
60
40
20
0
-20
-40
GRAVITY CHANGE IN MICROGALS
-1.0
0
1.0
WATER LEVEL CHANGE IN METERS

FIGURE 5

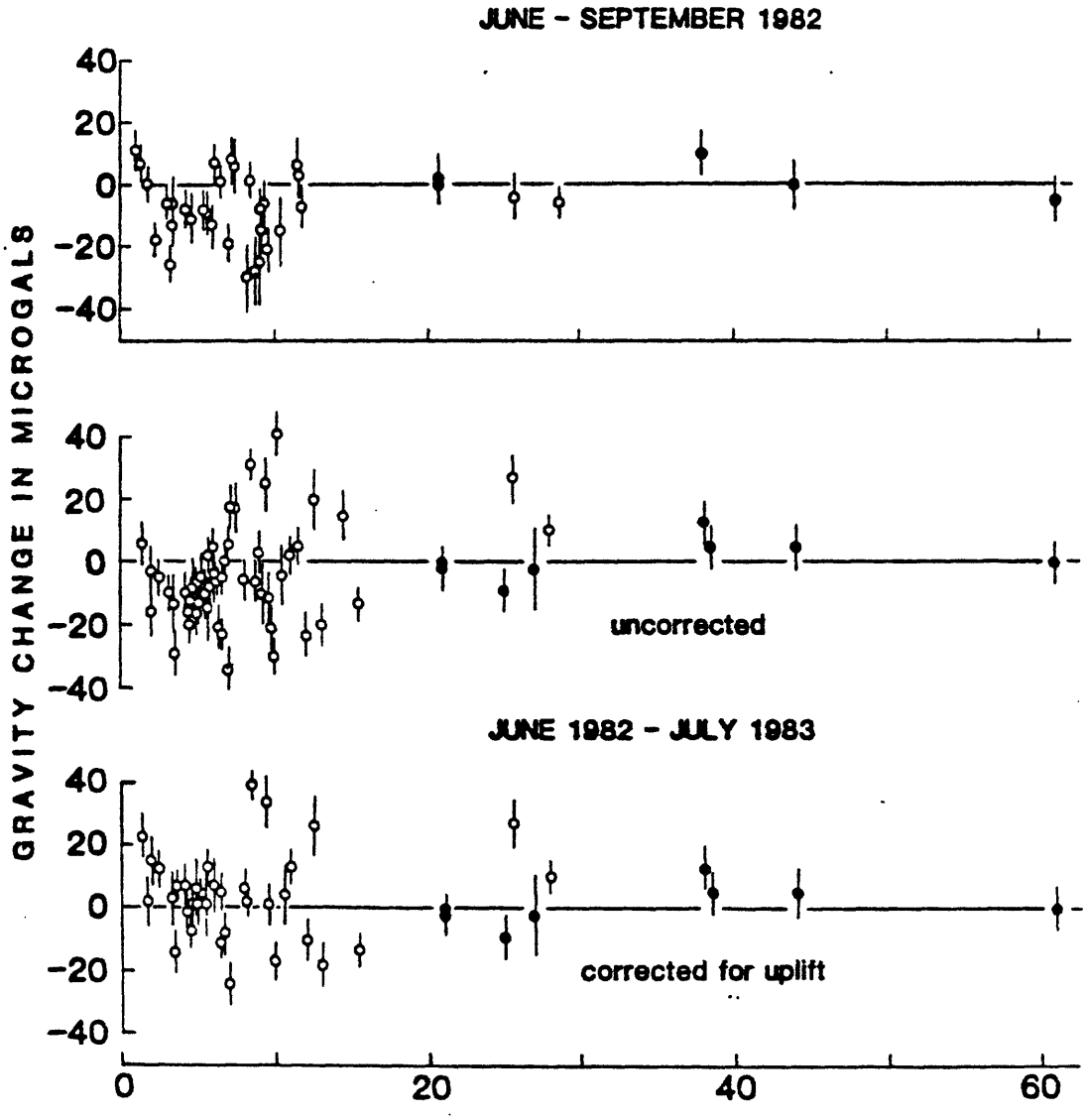
JUNE - SEPTEMBER 1982
GRAVITY CHANGE IN MICROGALS
40
20
0
-20
-40
uncorrected
JUNE 1982 - JULY 1983
corrected for uplift
0
20
40
60

FIGURE 6

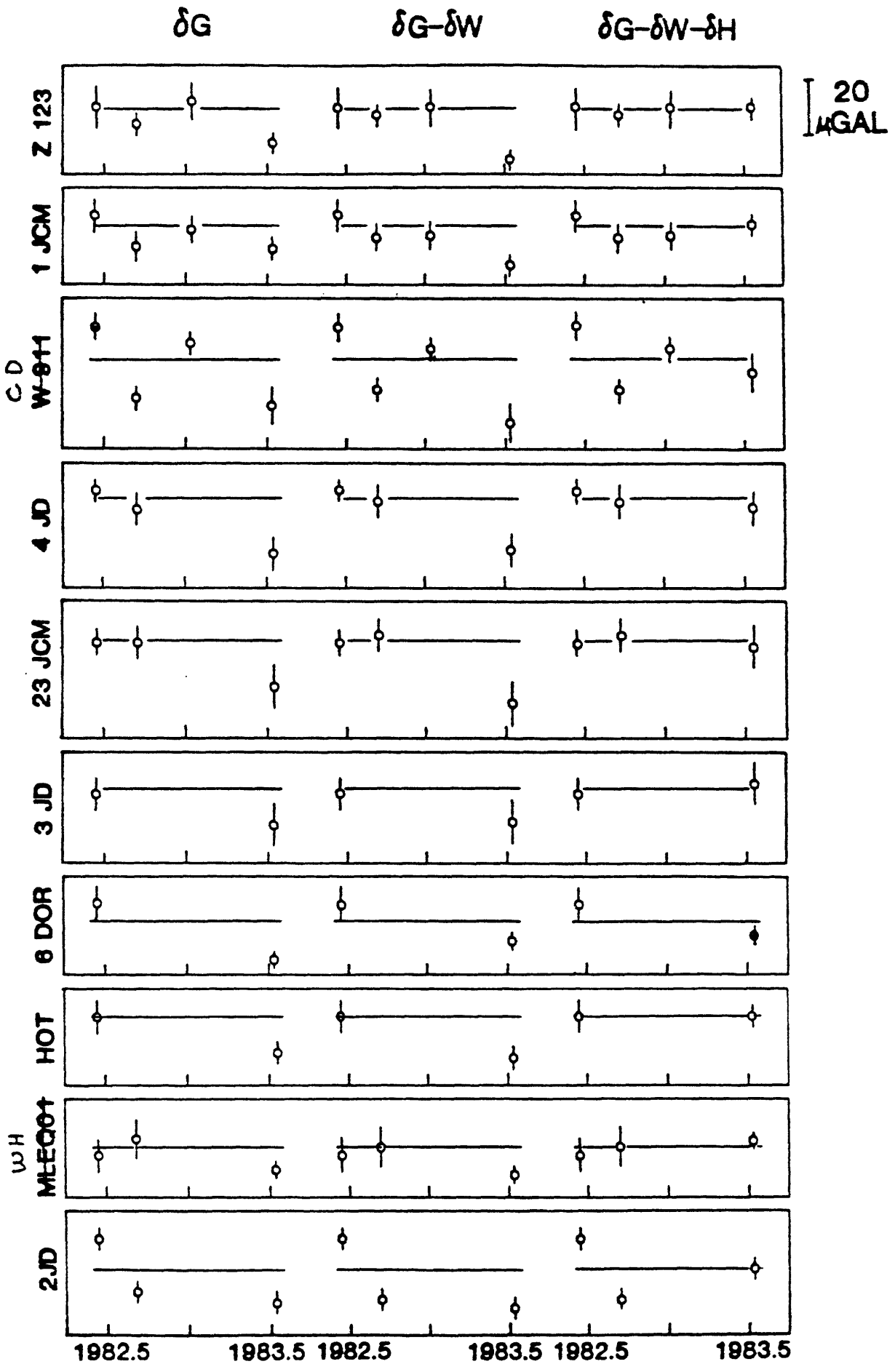
δG
δG-δW
δG-δW-δH
20 μGAL
Z 123
1 JCM
C D
W-811
4 JD
23 JCM
3 JD
6 DOR
HOT
W H
MLEQ01
2JD
1982.5
1983.5
1982.5
1983.5
1982.5
1983.5

FIGURE 7

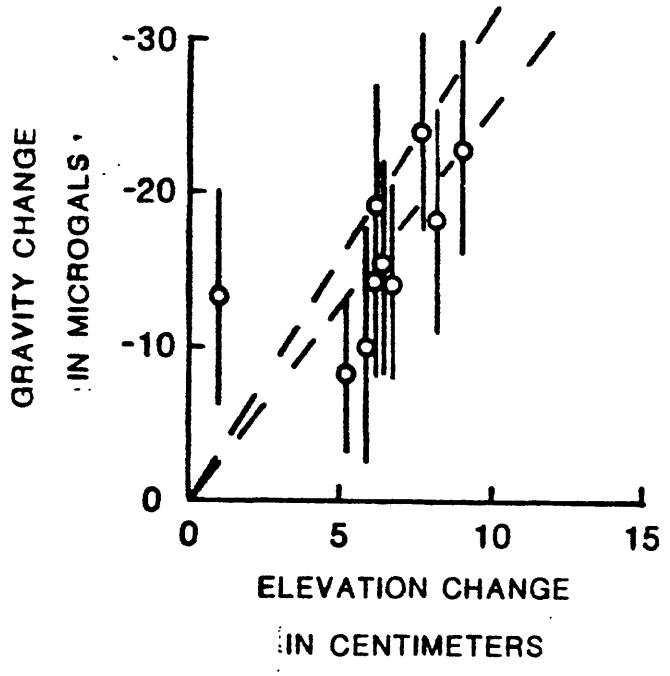
GRAVITY CHANGE
IN MICROGALS
-30
-20
-10
0
0
5
10
15
ELEVATION CHANGE
IN CENTIMETERS

FIGURE 8

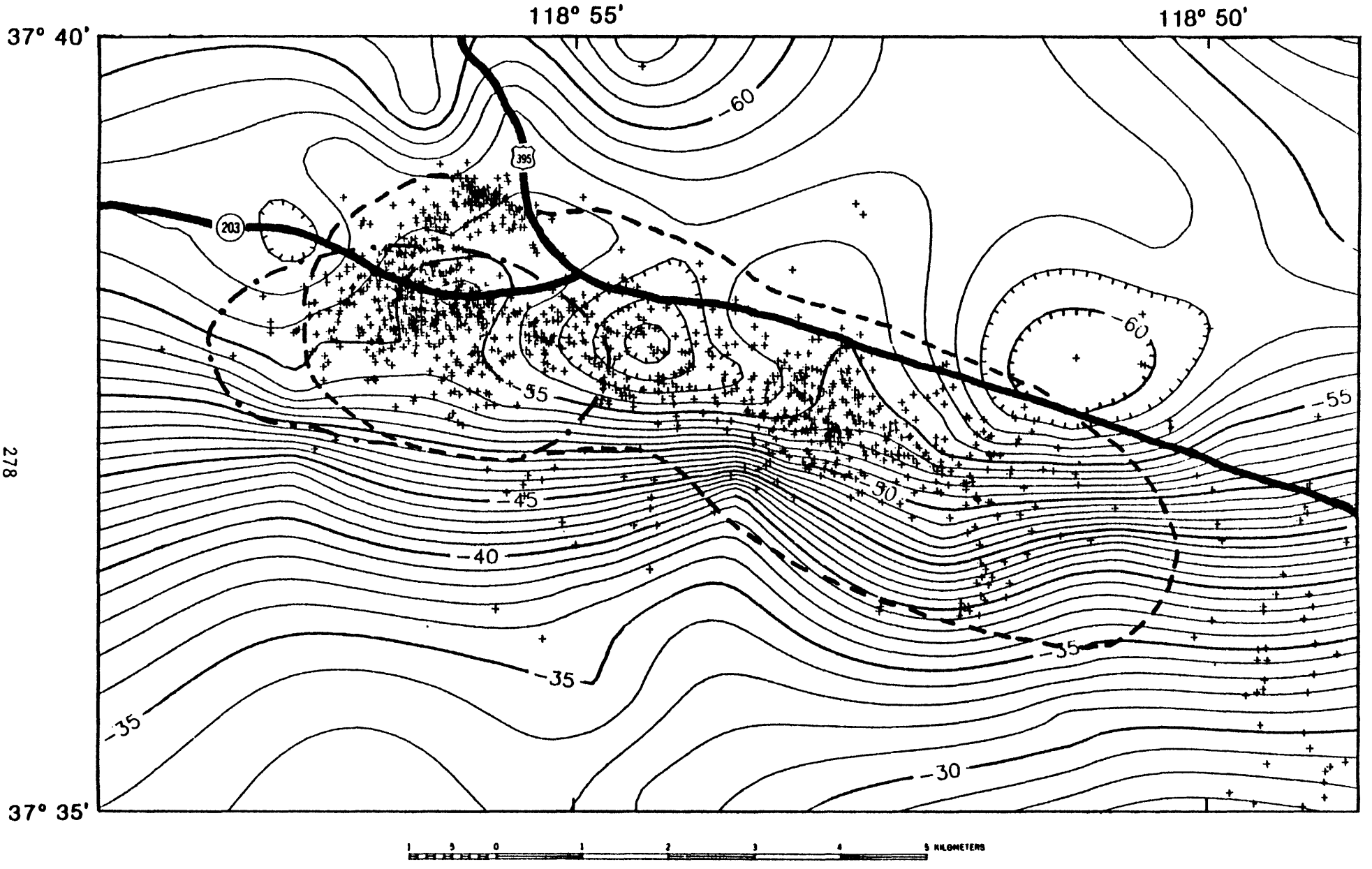
118° 55'
118° 50'
37° 40'
37° 35'
395
203
-60
-55
-50
-45
-40
-35
-30
1 5 0 1 2 3 4 5 KILOMETERS

FIGURE 9

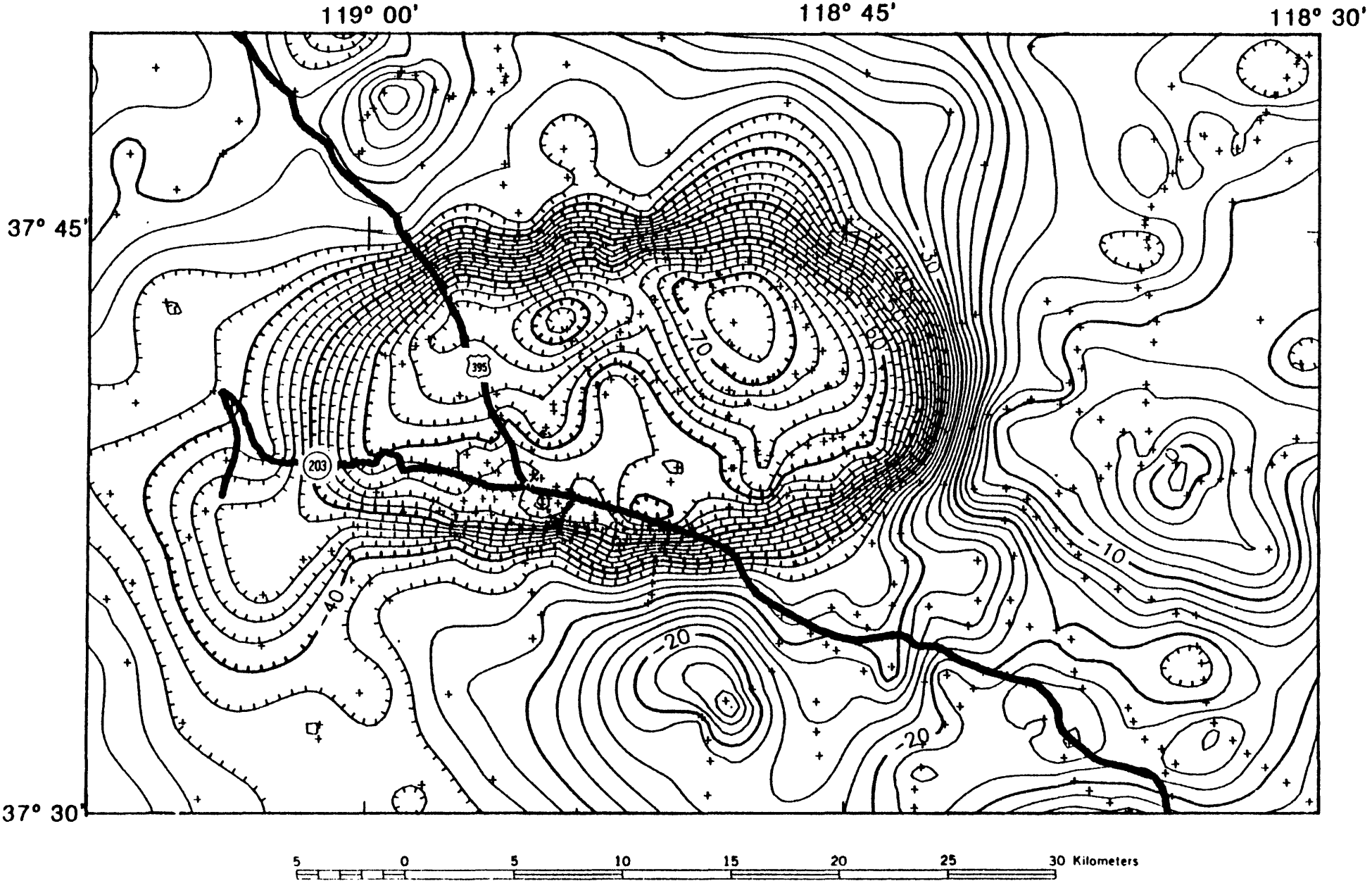
119° 00'
118° 45'
118° 30'
37° 45'
37° 30'
-30
-70
-50
-10
-40
-20
-20
395
203
5 0 5 10 15 20 25 30 Kilometers

FIGURE 10

Gravity Variation in the Mammoth Lakes, Mono Lake and Owens Valley, California Regions

J. H. Whitcomb, (Cooperative Institute for Research in Environmental Sciences, University of Colorado/NOAA, Boulder, CO 80309)
J. B. Rundle (Sandia Laboratories, Albuquerque, NM 87185)

Forty gravity stations were established in the Mammoth Lakes, Mono lake, and Owens Valley regions in August, 1982. A subset of 21 of these stations was reoccupied in October 1982 and a subset of 10 stations was reoccupied in January 1983 shortly after an earthquake swarm containing two magnitude 5.7 events near Mammoth Lakes. All stations were reoccupied in July 1983. A single base station at Mammoth Lakes was used for the entire network and the base station shows no significant gravity change with respect to absolute gravity reference sites in the Owens Valley and Pasadena, California.

In the Long Valley caldera, the gravity decrease (ground uplift) observed at the Sheriff substation and nearby resurgent dome region after the January 1983 swarm is unchanged. However, gravity to the southwest of the dome near Mammoth Lakes and the swarm area which decreased in January has now returned to its July 1982 levels.

Northwest of the Long Valley caldera, comparison of July 1983 gravity with that of July 1982 shows a gravity decrease (24-30 microgals) in the crystalline Sierras. This grades to the east to a gravity increase (17-26 microgals) apparently centered on the north-south Inyo-Mono volcanic structures. One possible interpretation of this gravity change is an injection of fluid in a vertical fracture at depth along the recent Inyo-Mono volcanic domes.

Evidence that supports an Inyo-Mono dike injection hypothesis comes from observations of other geophysical parameters. The 1983-1982 leveling data along highway 395 shows a decrease in elevation over the Inyo-Mono domes trend with increases on either side as would be expected. The total change is of the order of 3-4 cm although there is some question about the 1982 leveling data. The 1983-82 USGS Geodolite network data shows one line, MONO-GLASS, outside the Long Valley distortion regime that has significant strain. This approximately east-west line, which extends from the top of the MONO domes in a WSW direction to Glass mountain, lengthened 24±9 mm or about one microstrain (J. Savage, personal communication) in agreement with east-west expansion of a buried dike. No other proposed model has explained this large strain. Finally, recent tension cracks have been observed on the surface along the Inyo domes trend (Fink and Pollard, 1983). Preliminary analysis of the 1983-1975 leveling along the Tioga Pass road west of the Lee Vining shows no change (J. Savage, personal communication) and, if the data are confirmed, may provide further temporal constraints on the model.

THE LONG VALLEY/MONO CRATERS VOLCANIC COMPLEX;

A PRELIMINARY INTERPRETATION BASED ON TELLURIC FIELD PATTERNS

John F. Hermance
Warren Slocum
Gregory A. Neumann

Geophysical/Electromagnetics Laboratory
Department of Geological Sciences
Brown University
Providence, Rhode Island 02912

Manuscript submitted to the proceedings of the USGS Redbook
Conference on
Tectonic and Magmatic Processes in the Long Valley Region

ABSTRACT

The Long Valley/Mono Basin volcanic complex in eastern California is one of the few major silicic caldera systems in western North America which have exhibited volcanic activity so recently that they may still be potentially active. Whereas, in principle, magnetotelluric measurements offer a significant opportunity to study such systems through mapping subsurface electrical features associated with hydrothermal and magmatic processes in the crust, our studies in this area indicate that such techniques are profoundly affected by the highly three dimensional structures associated with these complicated volcanic terranes.

We argue that while simple plane-layered (1-D) interpretations are likely to be misleading in such a complicated 3-D environment, magnetotelluric observations can in fact delineate important physical features associated with caldera structures; in particular the method can closely determine the location and magnitude of major boundary faults. Because of the high resistivity contrast between basin fill and crystalline basement, these techniques are very useful for characterizing the subsurface hydrologic regime as well. In addition, significant anomalies are associated with areas of known hydrothermal activity at the surface and, through inference, these anomalous patterns seen elsewhere suggest that hydro-magmatic activity is more wide-spread in Long Valley caldera than hitherto realized.

A number of sites have been occupied in the southwest moat of Long Valley caldera; an area that is currently exhibiting a variety of tectonic activity. The telluric field pattern implies the presence of a structurally controlled east-west electric current system at relatively shallow depth in the crust. This elongated E-W zone is aligned along the belt of recent seismic activity in the southwest moat, a zone of seismic shear wave attenuation, and a zone of known hydrothermal alteration at the surface.

Finally, we summarize observations from the vicinity of Pumice Valley (adjacent to Mono Craters) which has been thought to be an incipient caldera in the process of still forming. Since our present data do not indicate an observable decrease in resistivity at shallow depths beneath the valley, we are led to conclude that the parent magma body feeding Mono Craters (and perhaps Inyo domes) is either too thin, too deep, or is significantly displaced from a position beneath the center of the inferred ring fractures.

INTRODUCTION

Long Valley Caldera

The Long Valley volcanic system is one of several young volcanic centers occurring along the western margin of the Great Basin adjacent to the eastern front of the Sierra Nevada (Figure 1; after Hermance, 1983a). Other such centers include Mono Craters and Mono Basin to the north and the Coso volcanic complex (not shown) to the south. These systems occur along a particularly active marginal segment of the Basin and Range province, where seismic activity, high heat flow and recent faulting indicate that relatively rapid east-west crustal extension dominates the tectonic regime.

Bailey (1980) has suggested that the volcanism responsible for forming Long Valley caldera itself has probably completed its evolutionary cycle, culminating in a voluminous ash-flow eruption, caldera collapse and post-caldera structural and magmatic resurgence. In this regard, Long Valley at the present time should be in a stage of development similar to the Valles caldera (Smith and Bailey, 1968; Smith, 1980), although recent volcanism in Inyo Craters, as well as an increasing amount of geophysical evidence, suggests that this system is possibly being reactivated.

Present Tectono-Magmatic Activity

A number of workers have recently stressed the possibility of renewed volcanism in Long Valley caldera (Savage and Clark, 1982; Ryall and Ryall, 1983; Notice of potential volcanic hazard, 1982; Miller et al., 1982; Geotimes, 1982a,b). Manifestations of contemporary tectonic activity are illustrated in the composite diagram of Figure 2 (after Hermance, 1983a). The inferred uplift predicted theoretically by the magma injection model of Savage and Clark (1982) is shown as dashed contours centered on the Long Valley resurgent dome. Also shown as dashed arrows, are the theoretical horizontal displacements predicted by this model, along with those actually observed shown as solid arrows (Savage and Clark, 1982).

This diagram also shows the locations (after Archuleta et al., 1982) and the generalized fault plane solutions (after Cramer and Toppozada, 1980) of the four major earthquakes in May 1980. The shear wave shadow zone reported by Ryall and Ryall (1981) is shown as the hatched area, and the location of the anomalous 1982 earthquake swarm activity is shown as a circle immediately to the east of Mammoth village.

Hermance (1983a) has argued that while the lack of geometric coincidence of some of these features may in some part be due to an artifact of the geophysical technique used to delineate them, this may also suggest, in fact, that certain of these phenomena are unrelated to one another in any direct way. Nevertheless, there is a persuasive (although not compelling) set of evidence to support the hypothesis of renewed volcanic activity in Long Valley caldera.

SUMMARY OF RECENT WORK BY BROWN UNIVERSITY IN LONG VALLEY/MONO CRATERS

Overview. In October 1981, Brown University initiated a regional magnetotelluric survey in east central California in an effort to study the relationship of the active volcanic centers along the eastern front of the Sierra Nevadas to regional extension in the Great Basin. Originally, our field system was deployed during the early winter in Mono Basin and in the Owens Valley region. When work was resumed in April 1982, sites were occupied in the Long Valley volcanic complex. In May, following the Notice of Potential Volcanic Hazard issued by the U.S.G.S., ten sites were occupied in the southwest moat of the caldera straddling the location of the most recent seismic swarm as reported by Alan Ryall (Personal communication, 1982). Our sites were within a circle of 3 km radius centered on 37.63° North, 118.94° West, the area reported by Ryall and Ryall (1983) as having unusual seismic swarm activity which they identified as spasmodic tremor. Useful data were obtained at nine of these sites.

Preliminary Results. A regional map (Figure 3) depicts the location and results from selected sites in our survey. As is clear from the magnitude of the telluric ellipses, Long Valley caldera exhibits anomalously low apparent resistivities at long periods, more than an order of magnitude less than the highly resistive Mono Craters to the north.

In Figure 4 we show a larger scale map of the Long Valley/Mono Basin complex. Here the telluric ellipses show a striking interplay between the effects of regional current systems (as indicated by a general north south orientation of the major axes of the telluric ellipses) and the effects of local conductivity anomalies (as evidenced in the sharp differences in polarization and magnitude between closely spaced telluric sites). It should be clear that within the interior of the caldera, over the resurgent dome, and within the circle of recent seismic activity in the southwest moat, a greatly reduced telluric field is evident representing low resistivities associated with the caldera fill and/or basement, as well as the effects of a large zone of hydrothermal alteration associated with the southern and eastern margins of the resurgent dome.

A still larger scale map of the southwest moat of Long Valley caldera is shown in Figure 5. One should note the high coherency between the orientation and magnitude of the telluric ellipses at these sites as well as the orthogonal orientation of magnetic "induction arrows" (following Schmucker, 1970) relative to the major axes of the telluric ellipses. Both the telluric field and the induction arrows imply the presence of a structurally controlled east-west current system at relatively shallow depth in the crust. This elongated E-W zone is aligned along the belt of seismic activity in the southwest moat, the zone of seismic shear wave attenuation (see Figure 2), and the zone of known hydrothermal alteration.

We have attempted to model the general features of the telluric field data as the effect of telluric distortion from near surface lateral heterogeneities as discussed by Berdichevskiy and Dmietriev (1976). We have been able to explain certain characteristics of the magnetotelluric fields in this region at periods of 20 sec and longer using DC telluric models (Hermance et al., 1984).

A Simple 3-D Model

The static effects of surficial lateral heterogeneities can be simulated at periods from tens to hundreds of seconds by invoking the D.C. or galvanic approximation (e.g. Berdichevskiy and Dimitriev, 1976). This approach has been recently exploited by Hermance (1982, 1983b) to simulate the behavior of magnetotelluric fields in the vicinity of 3-D features at long periods. The thin sheet conduction algorithm of Hermance (1982) has been extended to calculate the magnetic field as well as the telluric field anomalies. The algorithm has been applied to a model which simulates the effects of regional geologic features in the Long Valley/Mono Basin area on local magnetotelluric field observations (Figure 6).

A thin (3 km) layer of heterogeneous resistivity overlies an insulating basement; resistivities in the surface layer are chosen to be representative of the contrasts between "known" electrical features in the regional geology. On the west side of the model in Figure 6, we have represented the granitic batholiths of the Sierra Nevada range with a resistivity of 500

ohm-m. This would correspond to a thin weathered surface layer.

To the east, we simulate the White Mountains, which are also granitic and are assigned the same resistivity as the Sierras. A somewhat lower resistivity, 200 ohm-m, is assigned to the Pleistocene volcanic rhyolite and pyroclastic rocks,with occasional outcrops of granite, which span a region between Owens Valley in the east and Pumice Valley/Mono Basin in the west. We take this value as representative of the north rim of Long Valley caldera as well.

Within the basins and the interior of the caldera, guided by the results of Hoover et al. (1976) and Stanley et al. (1976), we have assigned a value of 100 ohm-m to the somewhat variable alluvial fill and tuff. In addition we account for the effects of the known hydrothermal zone associated with the southern portion of the resurgent dome in Long Valley caldera. This is represented by an arc wrapped around the southern part of the dome having a value of 40 ohm-m (following Hoover et al., 1976). The values represent conductivity contrasts that are depth-integrated to the basement, which we assume has infinite resistivity for the purposes of this model.

The overall dimensions of our model are 200 km on a side. Mesh spacing is 3 km minimum. The portion shown in Figure 6 extends 40 km east-west and 70 km north-south. The width of Owens Valley, for example, is 7 km. We feel our results are representative of periods of 20 s or greater; this is when the skin depth is large relative to the thickness of surface

heterogeneities.

Modelling Results

The results of using a unit amplitude, circularly polarized electric source field at infinity to produce telluric ellipses for each rectilinear element of the model is shown in Figure 7.

We see that the orientation of the telluric ellipses follows the line of the Sierra Nevada batholith on the west as currents are channeled N-S along the sedimentary basins. On the east, they follow the contours of Owens Valley in a general N-S direction. An enlarged view of the region of Long Valley caldera is shown in Figure 8. Within the more conductive region of the Long Valley caldera, especially through the arc of lowest resistivity corresponding to the hydrothermal zone, we see an overall east-west distortion of the telluric field.

Comparison of Field and Thin Sheet Modelling Results

The theoretical telluric ellipses shown in Figures 7 and 8 bear a marked resemblance to our actual field observations in Figures 3 through 5. On a broad regional scale, a consistent pattern emerges between the field data in Figure 3 and the theoretical results in Figure 7 such that a dominant N-S trend exists for the telluric ellipses adjacent to Mono Craters in the north. The large amplitude of the major axes reflects the highly resistive crust beneath these two regions.

The area of Long Valley is characterized by lower telluric

field amplitudes both in the field data of Figures 4 and 5, and the model results of Figure 8. Even some of the detail in the field data from the southwest moat of Long Valley caldera is embodied in the modelling results for the telluric ellipses.

We would emphasize that little fine-tuning in the details of our model has occurred. One should recognize that this is truly a first-cut effort and while it is clear that some improvement could be made with modest adjustments, the results might be misleading considering the gross assumptions underlying the numerical algorithm we are using (see Hermance, 1982, for cautionary notes regarding the algorithm).

Prospects for Mapping Major Boundary Faults in Long Valley caldera

A careful comparison of the field data (Figure 4) and the thin sheet model results (Figure 8) shows that the actual telluric fields are much more discontinuous than allowed for by our model. As we approach Long Valley caldera from the north, the northwest rim is evidenced by a sharp discontinuity in the observed telluric field between sites outside the caldera and those within (see the enlarged view in Figure 9). This is associated with a sharp vertical offset due to normal faulting along the major boundary faults. A vertical throw in the basement of 3 km or more is indicated in both gravity and seismic refraction interpretations (Figure 10 after Kane et al., 1976; Hill, 1976), although a discrepancy exists between the gravity and seismic interpretations of up to 3 km.

We have been able to locate this fault with somewhat greater precision (0.5 km), because of the close spacing of magnetotelluric sites in this region, and have accounted for the discontinuity in the telluric field amplitudes using the simple 3-D azimuthally symmetric model of Hermance (1983b). The caldera is modelled as a 3 km deep basin having a fixed resistivity contrast with respect to the surrounding host medium (Figure 11). Recognizing that Long Valley caldera is elliptical in plan-view, whereas our model is required to be azimuthally symmetric, we have used the local radius of curvature of the caldera (R = 6.5 km) as the radius of the basin in our circular model. In Figure 12 we compare telluric ellipse areas from actual field measurements with results from our model for various resistivity contrasts between the basin fill and the surrounding medium. Suprisingly we can determine the range of possible resistivity contrasts quite well, considering the simplicity of our model. It seems clear that refined surveys in the future offer high promise for detailed studies of caldera structures, in particular for characterizing features associated with major boundary faults. The high resistivity contrast between crystalline basement and basin fill is very favorable for telluric and magnetotelluric mapping experiments.

Magnetotelluric Results from Mono Craters and Mono Basin

Mono Craters and Mono Basin are the northern-most and youngest (1KY) members of a succession of three progressively younger volcanic complexes, each in different stages of evolution.

According to Bailey (1980), Mono Craters may have evolved through the early stages of caldera formation, whereas the centers in Mono Lake form the smallest and youngest complex and seem to be in a relatively youthful stage. Mono Craters are chemically homogeneous which, along with their recent age and frequency of eruption suggests that they were extruded from a single magma chamber, largely molten and perhaps still rising to the surface (Bailey, 1980).

Very little is known concerning the subsurface structure of Mono Craters, although this may be one of the most dramatic elements evolving in the tectonic fabric of the region (Hermance, 1983a). Basically, volcanism is too recent for geologists to have reconstructed a model of temporal evolution.

Present-day volcanism at the surface is, to a marked degree, structurally controlled. Bailey et al. (1976) and Bailey (1980) have argued that the inferred ring-fracture (Figure 1) outlines what may be an incipient magma chamber in the crust. The depth to such a magma body, if it exists, is not clear, however Bailey has drawn on Carmichael's (1967) petrologic study of samples from Inyo Domes, to the south, to suggest a source depth of less than 22 km. Temperatures at the time of extrusion averaged 825^{o}C (Carmichael, 1967).

Little geophysics has been reported from the area of Mono Craters. Regional gravity studies do not indicate the type of strong anomaly patterns that are associated with low-density basin fill beneath Long Valley caldera and Mono Basin proper

(i.e. in the vicinity of Mono Lake). Seismic refraction studies show essentially that the overburden in Pumice Valley is quite thin (Pakiser et al, 1960; Pakiser, 1976). The surface geology confirms this with crystalline basement out-cropping in several places over the floor of the valley. Hence, although the setting is ideal for using gravity to detect a shallow low-density magma body, the data do not indicate that one is present.

Lachenbruch (1982) noted that a preliminary heat-flow estimate of 2.2 HFU from within the inferred Mono ring fracture is not atypical for the Basin and Range province, and argued that there may be no detectable heat flow anomaly over this feature. He concluded that if the background heat flow is, in fact, typical of the Basin and Range, then any magma body must be deeper than 10 km if older than 0.7 - 1 m.y., 8 km if older than 3×10^5 yrs and 6 km if less than 1.5×10^5 yrs. On the other hand, he pointed out that if the background heat flow is more characteristic of the Sierra Nevada province (which is about 1.2 HFU), then the observed heat flow is indeed anomalous by approximately 1 HFU. This could be caused by a magma chamber at 8 km emplaced 5×10^5 yrs ago or a chamber at 6 km emplaced 2×10^5 yrs ago. If such a magma body were present, it should be readily detected using magnetotelluric methods.

Constraints on the regional electrical structure have been provided by the studies of Lienert and Bennett (1977) and Lienert (1979), who inferred low resistivities within the crust from a large-scale controlled source experiment. Their data are

compatible with a relatively resistive upper crust (d < 10 km), but the resistivity drops to values on the order of 30 ohm-m at depths of 15 km or so.

Referring to the map in Figure 3 we see little evidence in the area of the inferred Mono Craters ring-fracture to suggest the presence of a major magma body at shallow depth in the crust. Telluric field amplitudes have generally the same amplitude and are polarized in more or less the same sense to the east and to the south of Mono Craters. We would conclude that if an anomaly were present it must represent less than 20% of the background telluric field pattern or it would be detected in data such as those in Figure 3.

The constraints that this places on a possible magma body are that the body, if present, is either too thin to be resolved in our data, or too deep. Using the 3-D azimuthally symmetric model of Hermance (1983b), we have simulated a variety of situations which can be summarized by Figure 13. We have attempted to identify the limits on resolving a conductive magma body (having a nominal resistivity of 1 ohm-m) in a fairly resistive crust. To be compatible with a variety of telluric, magnetotelluric and active DC resistivity experiments in this region, we assume an average resistivity of 350 ohm-m. The maximum anomaly in the telluric field is defined as the total electric field over the center of the body minus the field which would be observed if the magma body were absent; this difference being divided by the normal reference field at infinity. Referring to Figure 13, we

see for example that if the maximum anomaly is required to be less than 20% (to be consistent with our observed data) the magma body must be less than 500 m thick, if it is at a depth less than 8 km, or, if very thick, it must be deeper than 10 km.

CONCLUSIONS

In conclusion, we find that a quantitative interpretation of the observed data in terms of a 1-D plane layered model is not appropriate for many sites in this region and may be misleading. Nevertheless, several substantive points can be emphasized:

1) A strong influence is exerted by the caldera boundary on the direction and magnitude of the local telluric fields. This suggests that telluric field measurements may be an effective tool to map structural relief in basement topography, particularly those sharp offsets associated with major normal boundary faults.
2) The southwest moat and a significant portion of the resurgent dome and western caldera are underlain by low resistivity material.
3) Telluric fields in the southwest moat show a strong preferential E-W direction, contrasted with the regionally dominant N-S pattern elsewhere along the Sierran front. This can be explained in part by current channeling through a surface hydrothermal zone, although the feature may well extend to appreciable depth. In addition, this elongated (E-W) zone is aligned along the belt of present seismic activity in the southwest moat, as well as along the zone of seismic shear wave attenuation.
4) While the 3-D effects of surficial geology make it difficult (and highly questionable) to put precise limits

on the depth to the conductive feature beneath the southwest moat of Long Valley caldera, if one employs the depth of penetration as a typical scale dimension, then it is possible that a conductive layer may be present beneath the southwest moat of Long Valley caldera at a depth of 3 to 4 km below the surface.

5) Magnetotelluric measurements in the area of the Mono Craters ring fracture, thought to be an incipient caldera in the process of still forming, do not indicate an observable decrease in resistivity at shallow depth beneath Pumice valley. We are led to conclude, therefore, that the parent magma body feeding Mono Craters (and perhaps Inyo domes) is either too thin or too deep to be resolved, or is significantly displaced from a position beneath the center of the inferred ring fractures.

ACKNOWLEDGMENTS

We would like to acknowledge the extended discussions we have had with Roy Bailey on the Long Valley/Mono Craters complex. Several workshops organized by John Rundle and John Eichelberger from Sandia National Laboratory were of enormous value in helping exchange ideas with colleagues. This report summarizes research supported by U.S. Department of Energy Office of Basic Energy Sciences Contract Number DE-AC02-79ER10401.

REFERENCES

Archuleta, R.J., E. Cranswick, C. Mueller, and P. Spudich, Source parameters of the 1980 Mammoth Lakes, California, earthquake sequence, J. Geophys. Res., 87, 4595-4608, 1982.

Bailey, R.A., Structural and petrologic evolution of the Long Valley, Mono Craters, and Mono Lake volcanic complexes, eastern California, EOS, 61, 1149, 1980.

Bailey, R.A., G.B. Dalrymple and M.A. Lanphere, Volcanism, structure and geochronology of Long Valley caldera, Mono County, California, J. Geophys. Res., 81, 725-744, 1976.

Berdichevskiy, M.N., and V.I. Dmitriev, Basic principles of interpretation of magnetotelluric sounding curves, Geoelectric and Geothermal Studies, KAPG geophys. Mono., edited by A. Adams, 165-221, Budapest, 1976.

Carmichael, I.S.E., The iron-titanium oxides of salic volcanic rocks and their associated ferro magnesium silicates, Contrib. Mineral. Petrol., 14, 36-64, 1967.

Clark, M.M. and J.C. Yount, Surface faulting along the Hilton Creek fault associated with the Mammoth Lakes, California earthquakes of May, 1980, Earthquake Notes, 52, 45, 1981.

Geotimes News Notes, Earthquake swarm in Long Valley Caldera, California, 27, 28, August, 1982a.

Geotimes News Notes, Earthquake swarm in Long Valley Caldera, California, 27, 28, September, 1982b.

Hermance, J.F., The asymptotic response of three-dimensional basin offsets to magnetotelluric fields at long periods: The effects of current channeling, Geophysics, 47, 1562-1573, 1982.

Hermance, J.F., The Long Valley/Mono Basin volcanic complex in Eastern California; Status of present knowledge and future research needs, Rev. Geophys. and Space Phys., 21, 1545-1565, 1983a.

Hermance, J.F., Telluric fields in three-dimensions: A refined finite difference simulation using local integral forms, Geophysics, 48, 331-340, 1983b.

Hermance, J.F., W. Slocum and G.A. Neumann, The Long Valley/Mono Basin volcanic complex; A preliminary magnetotelluric and magnetic variation interpretation, Submitted to Jour. Geophys. Res., 1984.

Hill, D.P., Structure of Long Valley Caldera, California, from a seismic refraction experiment, J. Geophys. Res., 81, 745-753, 1976.

Hoover, D.B., F.C. Frischknecht and C.L. Tippens, Audiomagnetotelluric sounding as a reconnaissance exploration technique in Long Valley, CA, J. Geophys. Res., 81, 801-809, 1976.

Kane, M.F., D.R. Mabey and R.L. Brace, A gravity and magnetic investigation of the Long Valley Caldera, Mono County, California, J. Geophys. Res., 81, 754-762, 1976.

Kilbourne, R.T., C.W. Chesterman, S.H. Wood, Recent volcanism in the Mono Basin-Long Valley region of Mono County, California, in, Mammoth Lakes, California earthquakes of May 1980 (R.W. Sherburne, ed.), Cal. Div. Mines and Geol., Spec. Report, 150, 7-22, 1980.

Kistler, R.W., Structure and metamorphism in the Mono Craters quadrangle, Sierra Nevada, California, U.S. Geol. Surv. Bull., 1221-E, 1-52, 1966.

Lachenbruch, A.H., J.H. Sass, R.J. Munroe and T.H. Moses, Geothermal setting and simple heat conduction models for the Long Valley Caldera, J. Geophys. Res., 81, 769-784, 1976.

Lachenbruch, A.H., M.L. Sorey, R.E. Lewis and J.H. Sass, The Near-Surface Hydrothermal Regime of Long Valley Caldera, Jour. Geophys. Res., 81, 763-768, 1976.

Lachenbruch, A.H. and J.H. Sass, Models of an extending lithosphere and heat flow in the Basin and Range province, Geol. Soc. Amer. Memoir 152, R.B. Smith and G.P. Eaton (eds.), 209-250, 1978.

Lachenbruch, A.H., Regional thermal structure in the western U.S., EOS, 61, 1144, 1980.

Lachenbruch, A., Heat flow at Aeolian Butte - constraints on a magma chamber beneath the Mono ring fracture, Contributions to Field Trip Notes: Mono Craters/Long Valley Field Trip; May 5, 1982.

Lienert, B.R., Crustal Electrical Conductivities along the Eastern Flank of the Sierra Nevadas, Geophysics, 44, 1830-1845, 1979.

Lienert, B.R., and J.J. Bennet, High electrical conductivities in the lower crust of the northwestern Basin and Range: an application of inverse theory to a controlled source deep magnetic sounding experiment, in The Earth's Crust, Geophys. Mono. Ser., 20, edited by J.G. Heacock, 531-552, Amer. Geophys. Union, Washington, D.C., 1977.

Mayo, E.B., The Pleistocene Long Valley Lake in eastern California, Science, 80, 95-96, 1934.

Miller, C.D., D.R. Mullineaux, D.R. Crandell and R.A. Bailey, Potential hazards from future volcanic eruptions in the Long Valley-Mono Lake area, East-Central California and Southwest Nevada - A preliminary assessment. U.S. Geol. Survey Circular 877, 10 pages, 1982.

Muffler, L.P.J. and D.L. Williams, Geothermal investigations of the U.S. Geological Survey in Long Valley, California, 1972-1973, Jour. Geophys. Res., 81, 721-724, 1976.

Notice of potential volcanic hazard issued for Eastern California, May 25, 1982, 3 pp., Public Affairs Office, USGS, Reston, VA 1982.

Pakiser, L.C., Gravity and volcanism and crustal deformation in Long Valley, California, U.S. Geol. Surv. Prof. Pap. 424-B, B250-B253, 1961.

Pakiser, L.C., Seismic exploration of Mono Basin, California, Jour. Geophys. Res., 81, 3607-3618, 1976.

Pakiser, L.C., M.F. Kane and W.H. Jackson, Structural geology and volcanism of Owens Valley region, California - A geophysical study, U.S. Geol. Surv. Prof. Pap. 438, 1-68, 1964.

Pakiser, L.C., F. Press, and M.F. Kane, Geophysical investigation of Mono Basin, California, Geol. Soc. Amer. Bull., 71, 415-447, 1960.

Rinehart, C.D., and N.K. Huber, The Inyo Crater Lakes -A blast in the past, Calif. Div. Mines Geol. Miner. Inform. Serv., 18, 169-172, 1965.

Rinehart, C.D. and W.C. Smith, Earthquakes and Young Volcanoes Along the Eastern Sierra Nevada, 62 pp., Edited by G. Smith, Distributed by William Kaufmann, Inc., Los Altos, California, 1982.

Russell, I.C., Quaternary history of Mono Valley, California, U.S. Geol. Survey Ann. Report, 8, 261-394, Reston, VA, 1889.

Ryall, A. and F. Ryall, Spatial-temporal variations in seismicity preceding the May, 1980, Mammoth Lakes, California, earthquakes, California Div. Mines and Geol., Special Report 150, 27-39, 1980.

Ryall, F. and A. Ryall, Attenuation of P and S waves in a magma chamber in Long Valley Caldera, California, Geophys. Res. Lett., 8, 557-560, 1981.

Ryall, A. and F. Ryall, Spasmodic tremor and possible magma

injection in Long Valley Caldera, Eastern California, Science, 219, 1432-1433, 1983.

Savage, J.C., M. Lisowski, W.H. Prescott and N.E. King, Strain accumulation near the epicenters of the 1978 Bishop and 1980 Mammoth Lakes, California, earthquakes, Bull. Seis. Soc. America, 71, 465-476, 1981.

Savage, J.C. and M.M. Clark, Magmatic resurgence in Long Valley Caldera, California: Possible cause of the 1980 Mammoth Lakes earthquakes, Science, 217, 531-533, 1982.

Schmucker, U., Anomalies of geomagnetic variations in the southwestern United States, Bull. Scripps Inst. Oceanography, 13, 165 pp., Univ. of California Press, Richmond, California, 1970.

Smith, R.L. and R.H. Bailey, Resurgent cauldrons, in Studies in Volcanology, Geol. Soc. Amer. Mem. 116, R.R. Coats, R.L. Hay and C.A. Anderson (eds.), 613-632, GSA, Boulder, Colorado, 1968.

Smith, R.L., The Valles Caldera, Jemez mountains, New Mexico, EOS, 61, 1150, 1980.

Sorey, M.L. and R.E. Lewis, Convective heat flow from Hot Springs in the Long Valley Caldera, Mono County, California, J. Geophys. Res., 81, 785-791, 1976.

Sorey, M.L., R.E. Lewis and F.H. Olmsted, The hydrothermal system of Long Valley Caldera, California, U.S. Geol. Surv. Prof. Pap. 1044-a, A1-A60, 1978.

Stanley, W.D., D.B. Jackson and A.A.R. Zohdy, Deep electrical investigations in the Long Valley geothermal area, California, J. Geophys. Res., 81, 810-820, 1976.

Wood, S.H., Mono and Inyo Crater eruptions, eastern California-Radiocarbon dating and trace element correlations of Late Pleistocene tephra, Geol. Soc. Amer. Abstr. Programs, 7, 389, 1975.

FIGURE CAPTIONS

Figure 1. Generalized map of the Long Valley/Mono Basin volcanic complex showing its position relative to the Sierra Nevadas to the west and the Basin Range province to the east (after Bailey et al., 1976). The darkly shaded portions of the map (Inyo Domes, Mono Craters and the volcanic craters in Mono Lake) represent recent (Holocene) volcanism.

Figure 2. Composite diagram showing the interrelationships of various types of recent tectonic activity in the region of the Long Valley/Mono Basin volcanic complex. Long Valley caldera and the incipient Pumice Valley "caldera" are indicated by dashed lines. Mono Craters and the Long Valley resurgent dome are indicated by solid lines. Owens Valley is shown to the east and major faults are shown by heavy lines. This figure illustrates horizontal displacements, the locations and general fault plane solutions for the major earthquake sequence in May 1980, the shear wave shadow zone, and the theoretical contours of the uplift inferred from recent releveling. The circle to the east of Mammoth village outlines the area of 1982 earthquake activity.

Figure 3. Telluric ellipses and induction arrows computed from data in the Long Valley/Mono Craters volcanic complex.

Figure 4. Telluric ellipse patterns in Long Valley caldera.

Figure 5. Telluric ellipses and induction arrows computed from data collected in the southwest moat in Long Valley caldera. The real (solid) and imaginary (dashed) arrows follow a convention such that they are perpendicular to and point away from current concentrations.

Figure 6. Plan view of thin sheet electrical model of Owens Valley and the Long Valley/Mono Basin volcanic complex.

Figure 7. Theoretical telluric ellipses for the thin sheet model in Figure 6.

Figure 8. An enlarged view of the theoretical telluric ellipses from the portion of the thin sheet model in

the region of Long Valley caldera.

Figure 9. Enlarged view of northwest rim of Long valley caldera. This figure corresponds to the boxed area in Figure 4.

Figure 10. Gravity and seismic refraction interpretations along a profile across the northwest rim of the Long Valley caldera (after Pakiser et al., 1964; Kane et al., 1976; Hill, 1976).

Figure 11. Azimuthally symmetric 3-D model used to simulate the effects of basin fill on telluric fields. The depth (D) of basin is fixed at 3 km in keeping with seismic and gravity interpretations. The radius (R) is 6.5 km, appropriate for the local radius of curvature for Long Valley caldera. The resistivity contrast between the basin fill and surrounding material is varied.

Figure 12. Comparison of telluric ellipse area across the caldera rim calculated from field data with various results from our azimuthally symmetric 3-D model for the caldera basin. The basin has a radius of 6.5 km and is 3 km deep. The curves differ in the resistivity contrast assigned between the basin fill and the surrounding medium.

Figure 13. The maximum normalized telluric field anomaly over the center of an imbedded 3-D azimuthally symmetric magma body as a function of depth for various thicknesses (0.5, 1, 2, 4, 8, and 50 (or ∞) km). Its radius is 6.5 km. The magma is assumed to have a nominal resistivity of 1 ohm-m and the resistive crust a resistivity of 350 ohm-m.

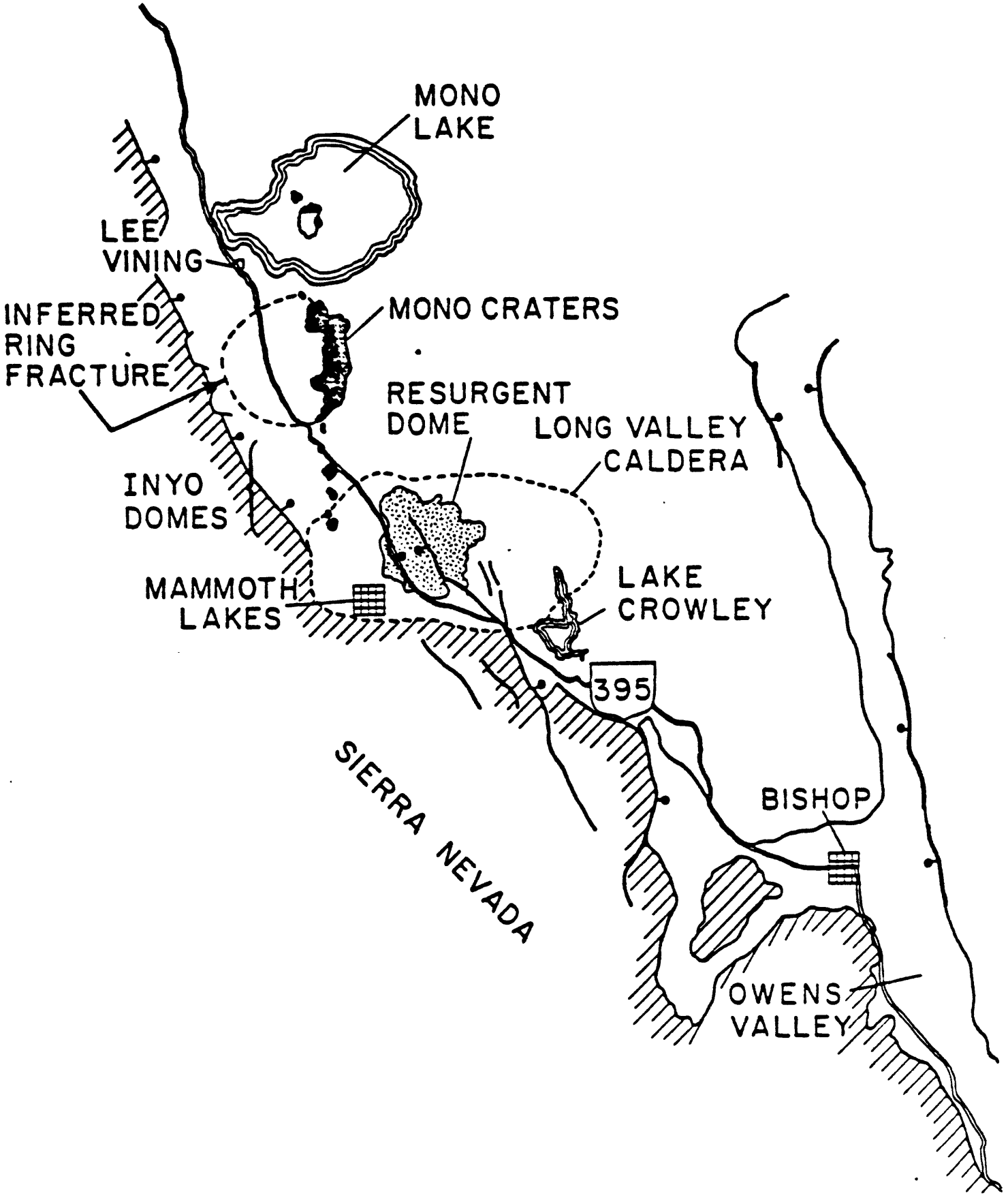
MONO
LAKE
LEE
VINING
INFERRED
RING
FRACTURE
MONO CRATERS
RESURGENT
DOME
LONG VALLEY
CALDERA
INYO
DOMES
MAMMOTH
LAKES
LAKE
CROWLEY
395
SIERRA NEVADA
BISHOP
OWENS
VALLEY

FIGURE 1.

HORIZONTAL DISPLACEMENT
OBSERVED
THEORETICAL
INFERRED UPLIFT
15cm
20
25
SHEAR WAVE SHADOW
MAMMOTH
1982-SWARM
MAY 1980
0 25mm DISPL.
0 5 10KM
37°45'
37°30'
119°00'
CH
D
B
C
G
S
L
T

FIGURE 2.

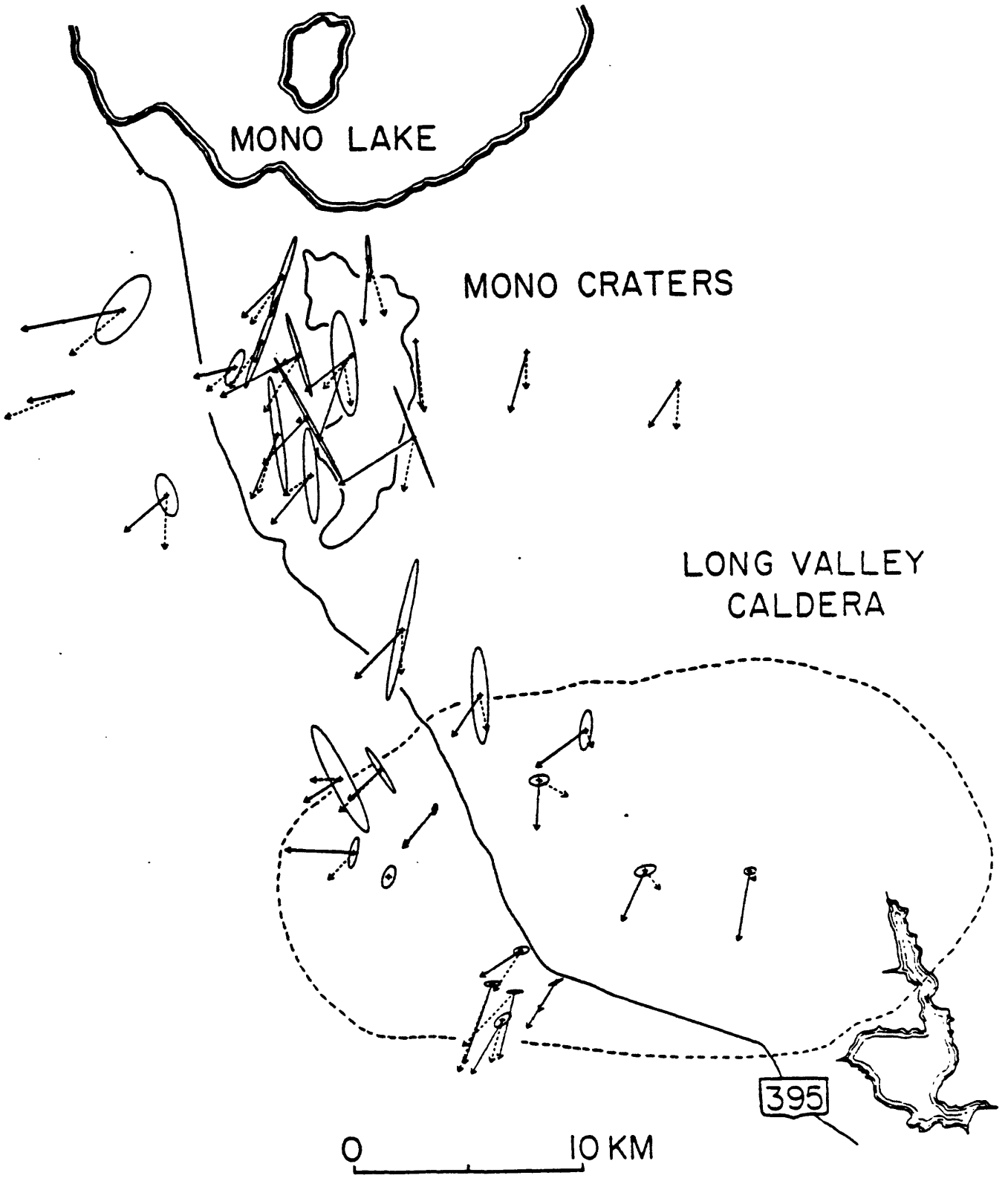

FIGURE 3.

PERIOD:80.00 ARROW 0.00 RHO 25.0 PHASE 60.0

DEADMAN CREEK 80 S

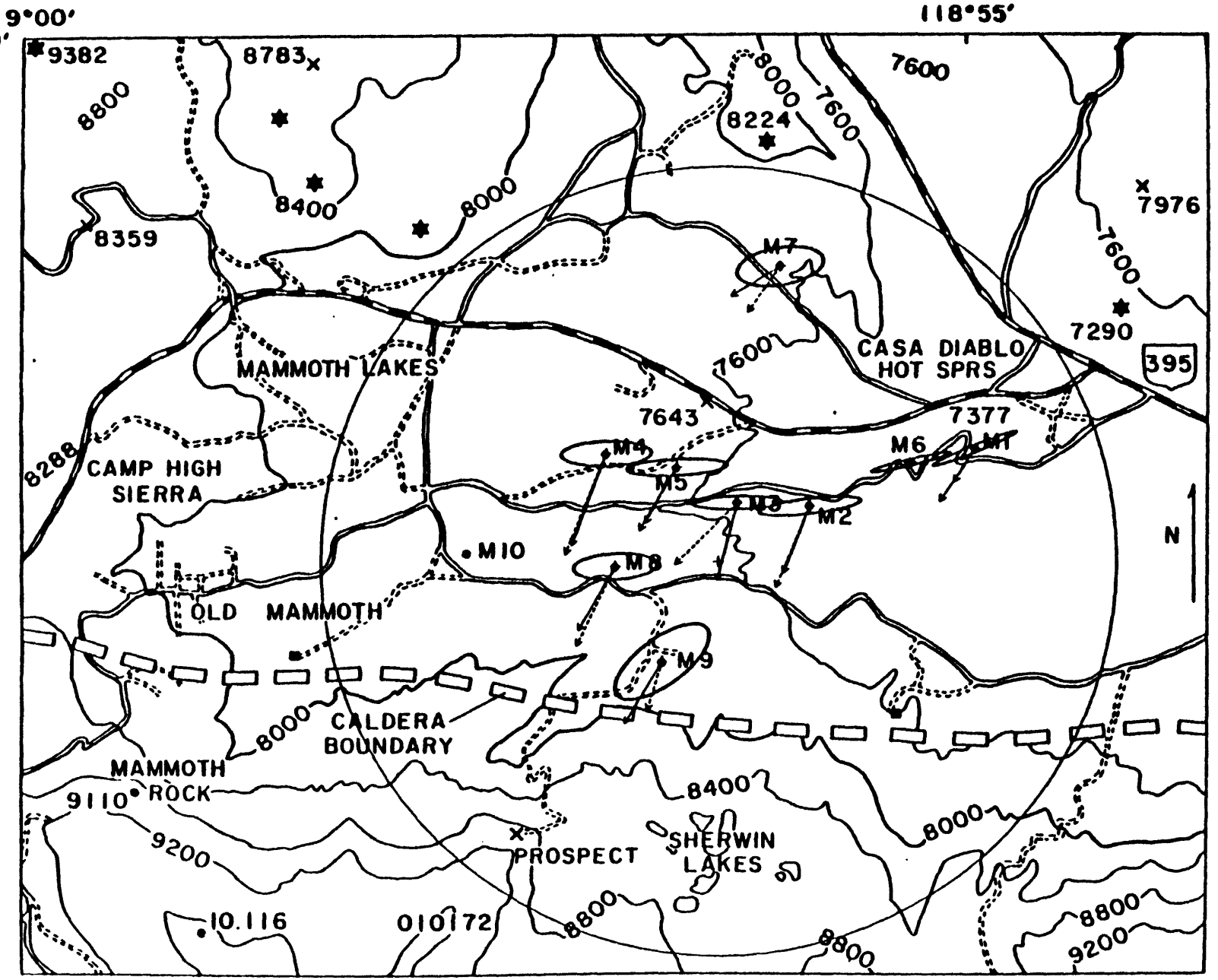
119°00'
37°40'
118°55'
9382
8783
8800
8400
8000
8359
8224
7600
7976
7290
395
MAMMOTH LAKES
CASA DIABLO
HOT SPRS
7643
7377
8288
CAMP HIGH
SIERRA
M1
M2
M4
M5
M6
M7
M8
M9
M10
N
OLD MAMMOTH
CALDERA
BOUNDARY
MAMMOTH
ROCK
9110
9200
10.116
010172
PROSPECT
SHERWIN
LAKES
8800
9200

FIGURE 5.

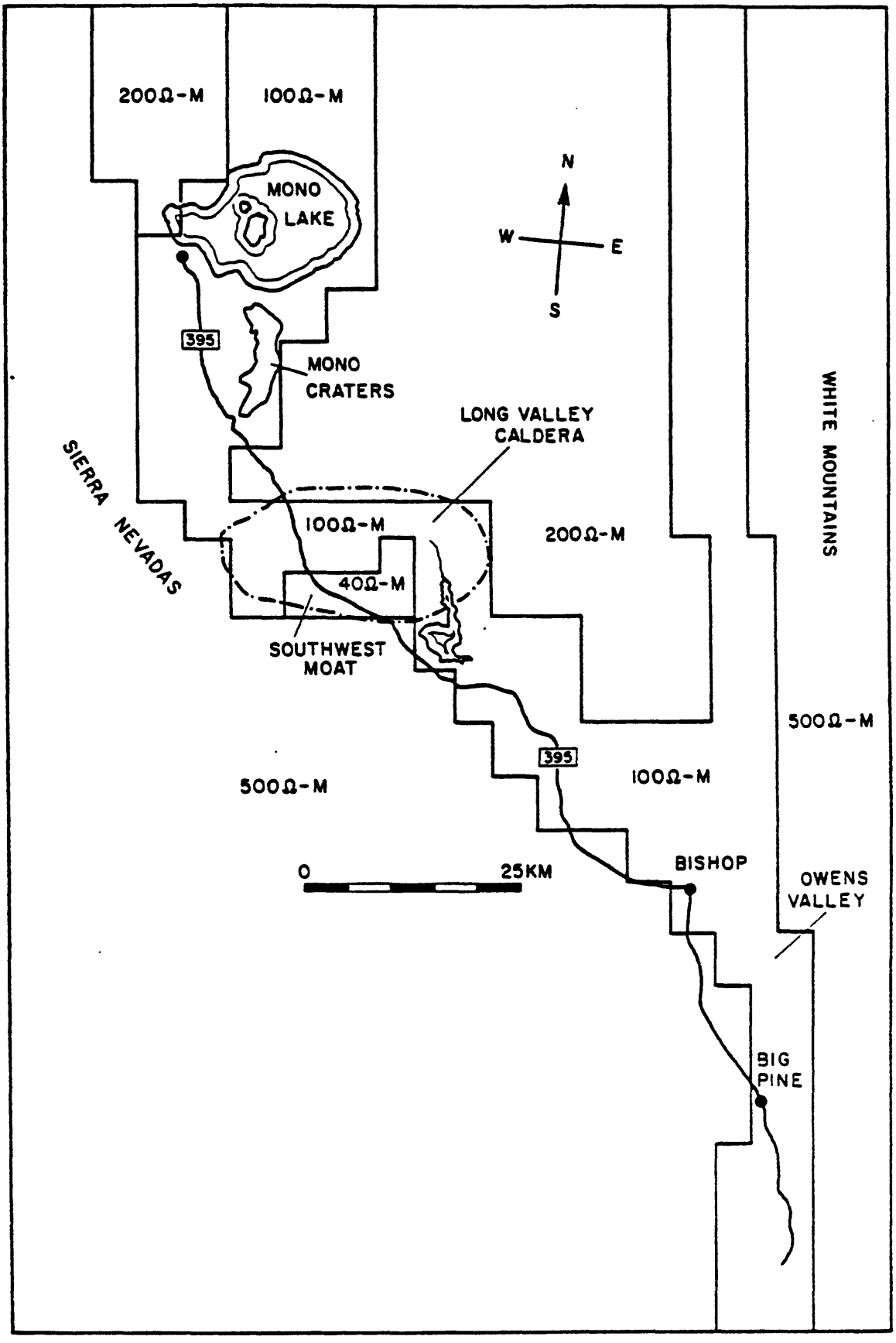
200Ω-M
100Ω-M
MONO
LAKE
N
W
E
S
395
MONO
CRATERS
LONG VALLEY
CALDERA
SIERRA NEVADAS
WHITE MOUNTAINS
100Ω-M
200Ω-M
40Ω-M
SOUTHWEST
MOAT
500Ω-M
395
100Ω-M
500Ω-M
0
25KM
BISHOP
OWENS
VALLEY
BIG
PINE

FIGURE 6.

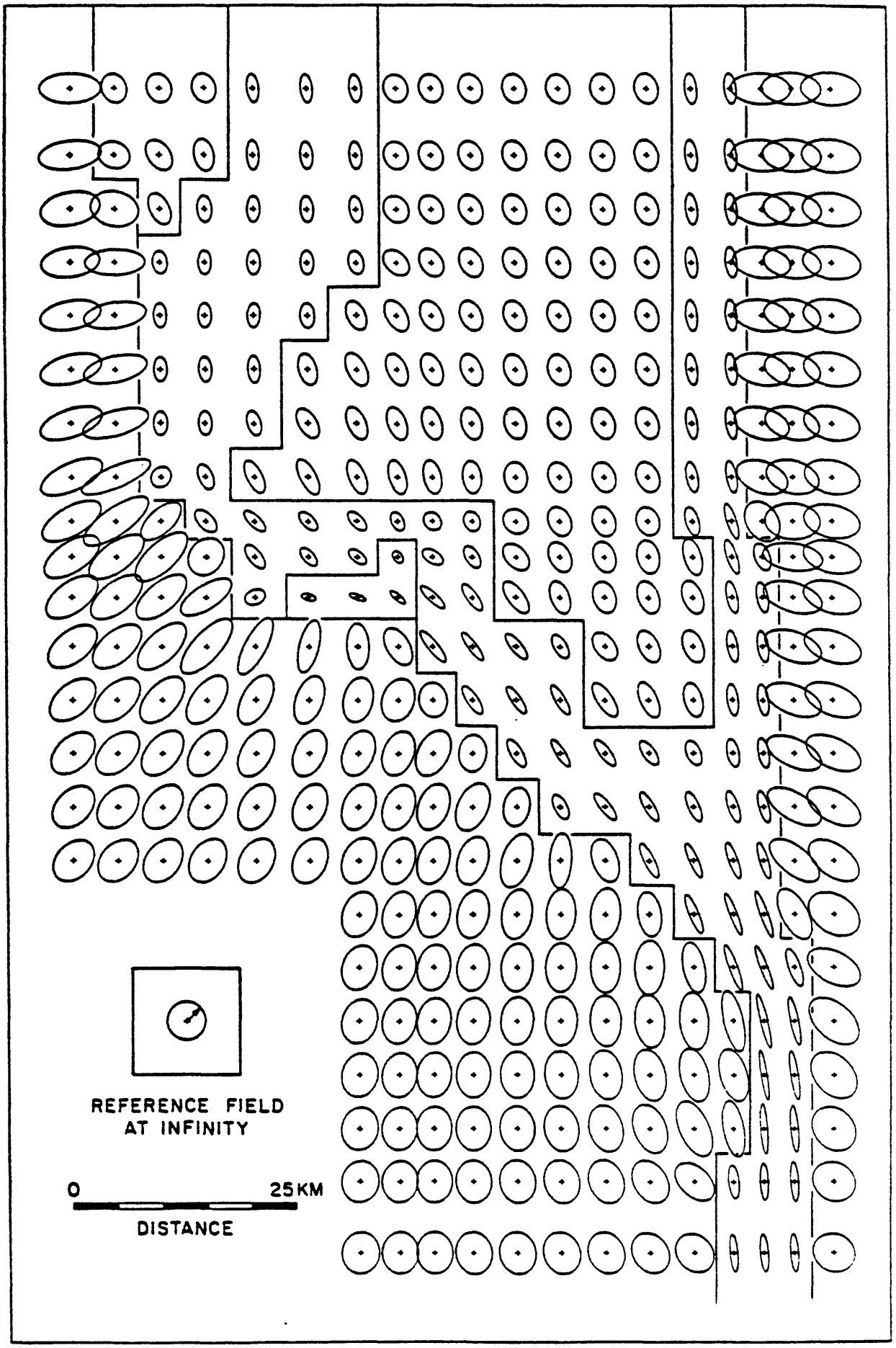

FIGURE 7.

FIGURE 8.

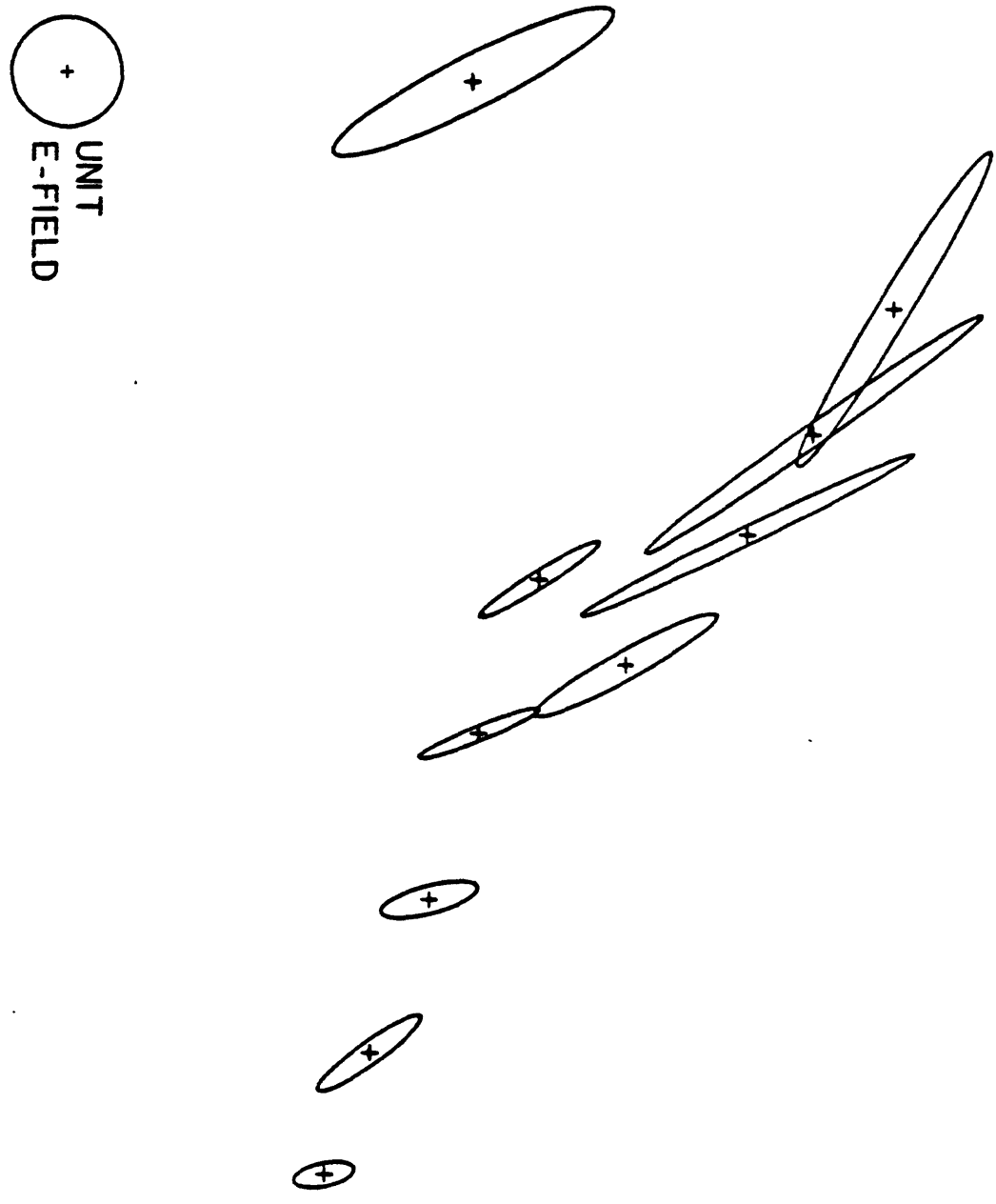

PERIOD: 20.00 ARROW 0.00 RHO 100.0 PH

FIGURE 9.

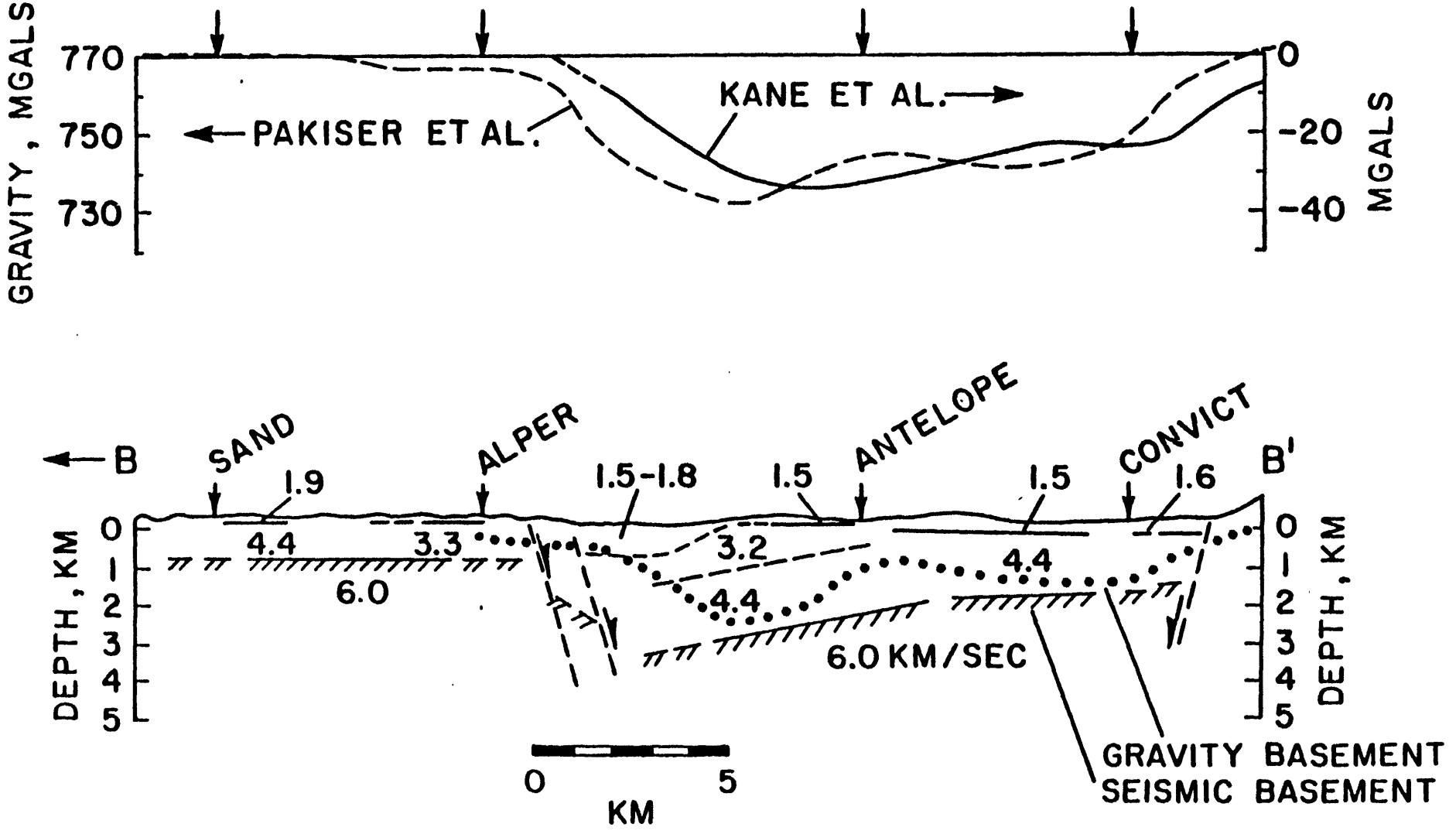
GRAVITY, MGALS
770
750
730
0
-20
-40
MGALS
PAKISER ET AL.
KANE ET AL.
B
B'
SAND
ALPER
ANTELOPE
CONVICT
1.9
1.5-1.8
1.5
1.5
1.6
4.4
3.3
6.0
3.2
4.4
4.4
6.0 KM/SEC
DEPTH, KM
0
1
2
3
4
5
0
5
KM
GRAVITY BASEMENT
SEISMIC BASEMENT

FIGURE 10.

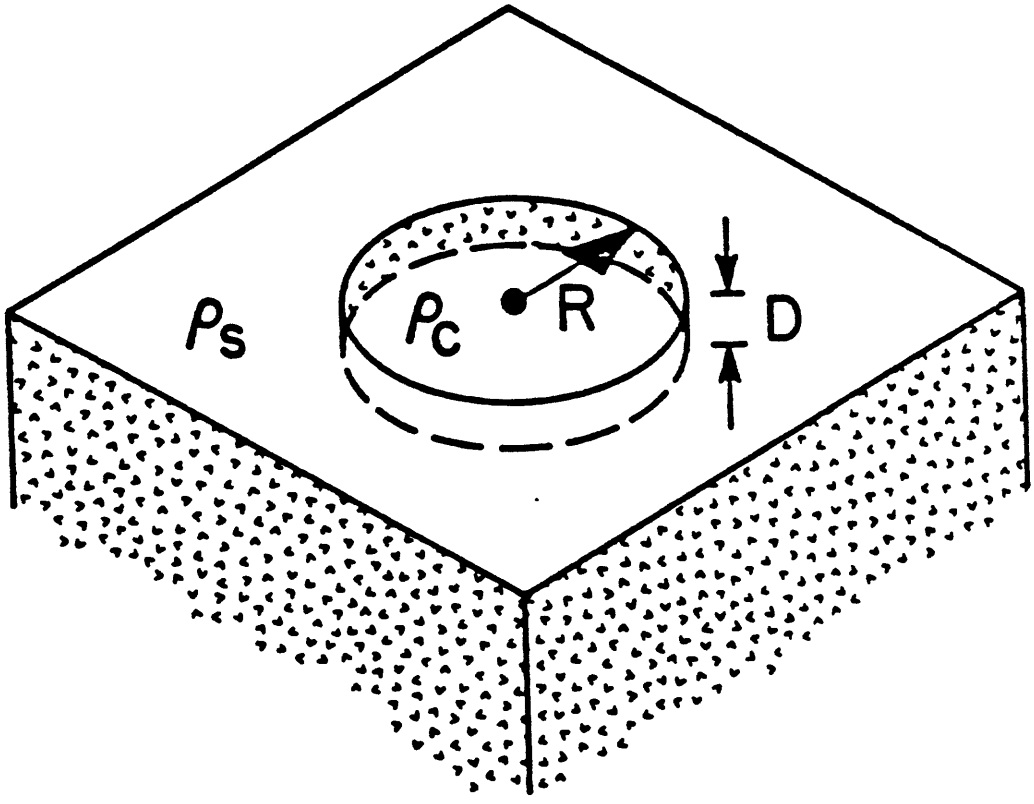

FIGURE 11.

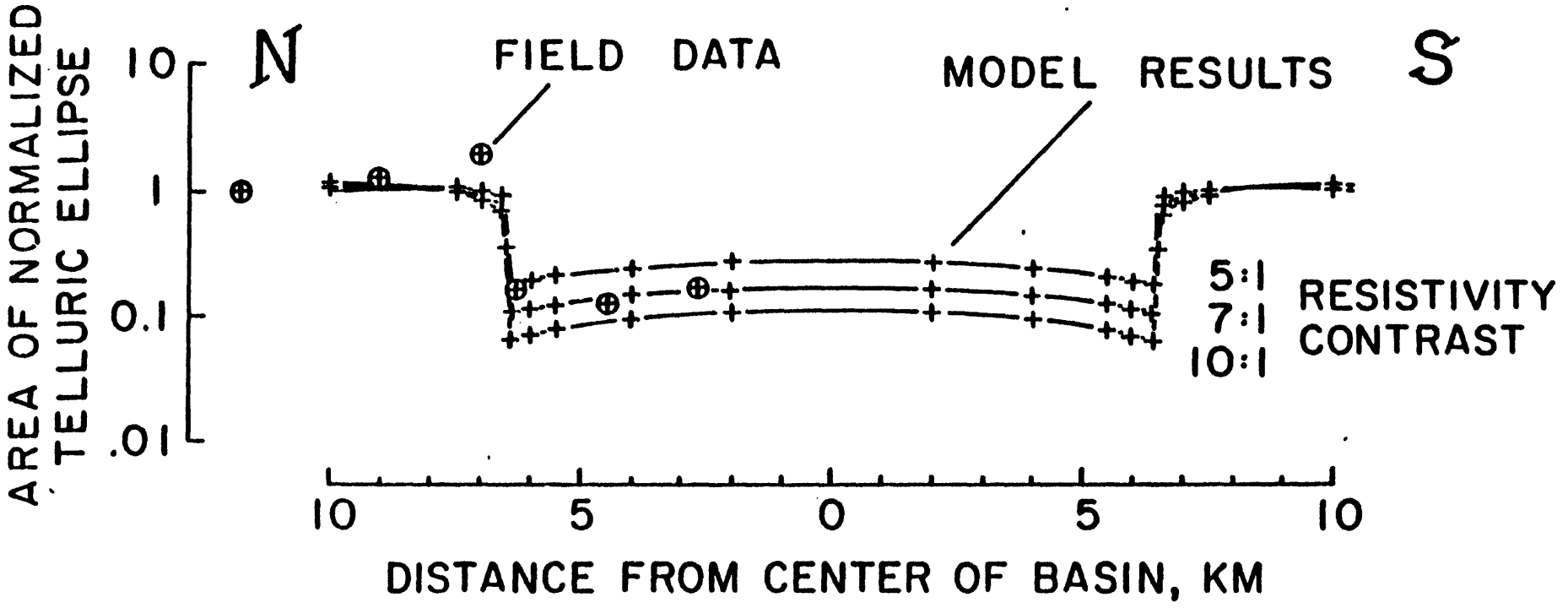
AREA OF NORMALIZED TELLURIC ELLIPSE
10
1
0.1
.01
N
FIELD DATA
MODEL RESULTS
S
5:1
7:1
10:1
RESISTIVITY CONTRAST
10
5
0
5
10
DISTANCE FROM CENTER OF BASIN, KM

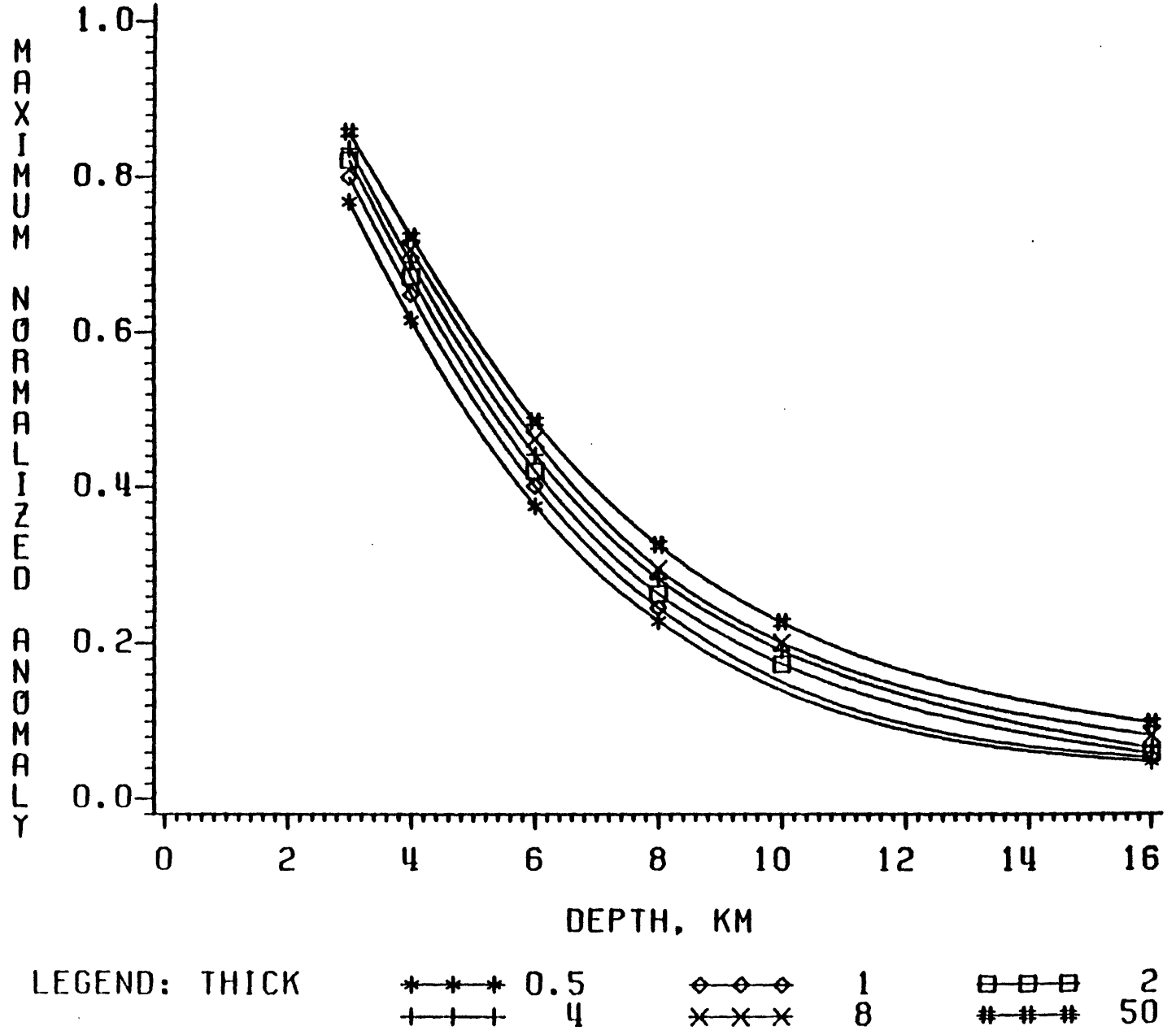
ANOMALY DUE TO AZIMUTHALLY SYMMETRIC BODY
NO BASIN COVER
MAXIMUM NORMALIZED ANOMALY
1.0
0.8
0.6
0.4
0.2
0.0
0
2
4
6
8
10
12
14
16
DEPTH, KM
LEGEND: THICK
0.5
1
2
4
8
50

FIGURE 13.

Earthquake Processes in the Long Valley Caldera Area, California

Bruce R. Julian

U.S. Geological Survey

Mail Stop 77

345 Middlefield Rd.

Menlo Park, CA 94025

Stuart Sipkin

U.S. Geological Survey

Mail Stop 967

Box 25046

Denver Federal Center

Denver, CO 80225

ABSTRACT

At least three of the largest earthquakes in 1978 and 1980 near Long Valley caldera have unusual mechanisms, unlike those appropriate for slip on shear faults. This conclusion is supported by data that include short-period P first motions, long-period P and SH first motions, surface-wave spectral amplitudes and initial phases, and long-period P and SH waveforms. These data can be explained consistently only by equivalent force-systems with large non-double-couple components. Two explanations for these anomalous earthquakes have been proposed: (1) they are caused by simultaneous strike-slip and normal motion on separate faults, and appear unusual only because the distinct sub-events have not been resolved; or (2) they are produced by tensile failure under high fluid pressure.

The best data for evaluating these conflicting hypotheses are the waveforms of body waves, especially if broad-band recordings are available. Using the Multichannel Signal Enhancement (MSE) algorithm, we have inverted P and SH waveforms recorded by the Global Digital Seismograph Network (GDSN) to obtain moment-tensor representations of the earthquakes, and have also generated broad-band seismograms by applying the method of Harvey and Choy (1982) to short- and long-period GDSN data. The largest event (1633:44 UTC 25 May 1980) has a duration of about 10 seconds, and on broad-band records is resolved into two events 6 to 8 seconds apart. However, the moment-tensor inversion results show no change of the mechanism of this event with time, as would

be expected if the sub-events involve different types of faulting. Furthermore, the broadband records for the earthquake of 1450:56 UTC 27 May 1980 are extremely simple, and inconsistent with this being a multiple event.

Thus, analysis of digital waveforms indicates that the non-double-couple mechanisms observed for some Long Valley earthquakes are intrinsic to the source process, and are not artifacts caused by misinterpretation of multiple ruptures as single events. Opening of cracks under high fluid pressure is the most likely possibility for this process, although its dynamics are complex and not yet fully understood.

July 20, 1984

INTRODUCTION

Since October 1978, Long Valley caldera has experienced 4 earthquakes in the magnitude 6 range, and several earthquake swarms involving thousands of smaller events. The most intense activity occurred from May 25 to May 27, 1980, when four of the largest earthquakes occurred, but even today, nearly six years after the earthquakes began, Long Valley remains the most seismically active area in California. This unusual seismic activity, coupled with geodetically detected uplift within the caldera, has aroused fears of a possible volcanic eruption, and has led the U. S. Geological Survey to issue a formal "notice of volcanic hazard" for the area.

Figure 1 is a map of the Long Valley area, showing the epicenters of earthquakes larger than magnitude 4 that occurred in 1980. The three largest earthquakes in 1980 and the largest earthquake in 1978 are also identified on the figure, and their locations and other parameters are given in Table 1. Robert Ccockerham determined the hypocenters and origin times, using local and regional arrival times recorded by the U.S. Geological Survey, the California Institute of Technology, and the University of Nevada. The magnitudes in Table 1 were taken from the Bulletin of the International Seismic Centre. Different types of data and analysis methods were used to derive the seismic moments; the table indicates the approximate period of the waves used in each case. The moments determined in this study will be discussed in more detail in a later section.

For the largest earthquakes, unusually complete data are available, because there are more than 500 short-period seismometers in California and western Nevada, and because the earthquakes were large enough to generate well-observed teleseismic waves. These data have, however, proved difficult to

interpret. Mechanisms derived by applying conventional seismological methods to different subsets of the data are inconsistent with each other, as though the data were internally inconsistent (Given *et al.*, 1982). Various possible reasons for this difficulty have been suggested: spatial or temporal complexity of the rupture process may have led to spurious results when the earthquakes were modelled as simple point sources; seismic-wave propagation anomalies caused by complex earth structure in the area may have biased the analysis; or the earthquakes may have been caused by a process other than slip on faults. Julian (1983), Barker and Langston (1983), and Ekström and Dziewonski (1983) independently pointed out that the difficulty in interpreting the data disappears if a general moment-tensor representation is used, instead of the conventional but more restrictive double-couple force system; all the data can then be explained by mechanisms with large Compensated Linear Vector Dipole (CLVD) components (Knopoff and Randall, 1970). Julian (1983) suggested that such mechanisms would be expected for tensile failure under high fluid pressure, such as would accompany dike intrusion. Other workers, including Ekström (1983) and Wallace *et al.* (1983), attribute the anomalous earthquakes to simultaneous dip-slip and strike-slip motion on different faults. It is obviously important to resolve this disagreement, both because of the potential volcanic hazard at Long Valley and to advance our understanding of seismic and volcanic processes.

In this paper, we examine the available seismological data (short-period P-wave first motions, long-period P and SH-wave first motions, long-period P and SH-waveforms, and long-period surface-wave amplitudes and phases). We analyze the digitally recorded P and SH waveforms in the most detail, because such data can best resolve the geometrical and temporal characteristics that are diagnostic of multiple events.

PREVIOUS STUDIES

Field observations

Surface ruptures in the earthquakes of May 1980 (Taylor and Bryant, 1980, Clark *et al.*, 1982) were distributed in a north-northwest trending region about 20 *km* long and up to 10 *km* wide within Long Valley caldera and extending southeastward from the caldera along the Hilton Creek fault. The pattern of fractures was complex, involving both normal faulting (down to the northeast, usually) and tensional cracking (relative displacements east-west to northeast-southwest) on numerous branching traces, mostly unrelated to known faults, and undoubtedly often complicated by ground failure caused by shaking. Extensional cracking seems to have been the dominant type of faulting: The 82 measurements tabulated by Taylor and Bryant include 25 cases in which vertical offset dominated, 52 cases where extension dominated, and 5 cases in which vertical and extensional offsets were about equal. The largest displacements (both vertical and extensional) were about 25 cm, but most were much smaller. Strike-slip offset was a minor component of the faulting, observed in only a few places, and was right-lateral on north to northwest trending faults.

Previous seismological studies

Several investigators have studied the mechanisms of the largest Long Valley earthquakes seismologically, but their conclusions do not agree. It is now generally agreed that the data can be explained by point sources only if they have large non-double-couple components.

The first seismological studies (Cramer and Toppozada, 1980, Ryall and Ryall, 1981) were based on short-period P-wave first motions at seismographs in California and Nevada. These waves have take-off angles restricted to the range from about 50° to 90° and were interpreted in terms of strike-slip motion on

nearly vertical fault planes. However, neither of the two possible interpretations, involving either left lateral motion on north-south faults or right lateral motion on east-west faults, is supported by the field observations described above.

These strike-slip interpretations were called into question by a later study of the amplitudes and initial phases of 80-200 second surface waves recorded by the Global Digital Seismograph Network (Given *et al.*, 1982). The Rayleigh waves do not have the symmetric four-lobed radiation pattern expected for strike-slip mechanisms, but are largest in the directions N. 68° E. and S. 68° W., and small in the perpendicular directions, much as they are for normal-faulting earthquakes. Given *et al.* carried out a moment-tensor inversion of the surface wave data, in order to determine the mechanism For the periods considered (150–200*s*), the event was effectively at the free surface, so that three components of the moment tensor, M_{xz}, M_{yz}, and M_{zz}, could not be determined. Given *et al.* therefore imposed the constraints $M_{zz} = -M_{xx} - M_{yy}$ (no net volume change) and $M_{xz} = M_{yz} = 0$. The inversion procedure yielded a moment tensor that can be represented as a combination of three orthogonal force dipoles: a vertical compressional dipole with a moment of $1.33 \times 10^{25} dyne\text{-}cm$; a horizontal compressional dipole oriented N. 22° W. with a moment of $1.35 \times 10^{25} dyne\text{-}cm$; and a horizontal extensional dipole oriented N. 68° E. with a moment of $2.68 \times 10^{25} dyne\text{-}cm$. This mechanism is not a double couple; in fact, to well within the probable observational errors, it is a pure CLVD. Given *et al.* (1982) then added M_{xz} and M_{yz} components to the moment tensor to obtain a double-couple solution, which they interpreted as left-lateral oblique normal slip on a fault plane striking N. 12° E. and dipping 50° E. As they acknowledged, however, this double-couple mechanism is inconsistent with short-period first motion observations.

Barker and Langston (1983), Julian (1983), and Ekström and Dziewonski (1983) independently noticed that the apparent inconsistencies in the seismological data do not exist if a general moment tensor source representation is used. In fact, in their study of long-period body wave waveforms recorded by the World-Wide Standardized Seismograph Network (WWSSN), Barker and Langston (1983) found that the non-double-couple moment tensors derived by an objective inversion procedure explain nearly all of the P-wave first motion observations, even though these data were not used in the inversions. The mechanisms they derived for the events of 1633 UTC on May 25 and 1450 UTC on May 27 have non-double components amounting to 61.6 and 61.1 percent of their total moments .

Effects of complex structure

Several investigators (Given *et al.*, 1982, Wallace *et al.*, 1982, Barker and Langston, 1983) have suggested that the difficulty in explaining the seismological observations using double-couple sources is caused by anomalous wave propagation through complex structures associated with Long Valley caldera or the eastern front of the Sierra Nevada, although no quantitative analysis of such effects has been given. In addition to the fact that the difficulty disappears if non-double-couple mechanisms are allowed, several other lines of evidence argue against an explanation in terms of anomalous wave propagation.

The events of 1642:49 UTC 4 Oct 1978, 1633:45 UTC 25 May 1980, and 1450:57 UTC 27 May 1980 all have similar non-double-couple mechanisms, despite the fact that they are situated at different distances from both the

* There are several ways to decompose the non-dilatational part of a moment tensor into double-couple and CLVD components, and the result depends strongly on which method is used. The values given above are calculated using the decomposition scheme of Knopoff and Randall (1970), which assumes that the double couple and non-double-couple components have the same principal axes. Barker and Langston used a different method, which gave values of 36.5 and 36.1 percent for the two events.

caldera and the Sierra Nevada range front, and cannot plausibly be supposed to have suffered identical propagation effects. The 1978 event was within about 3 km of the rangefront and about 15 km from the caldera, whereas the event of 1633:44 UTC 25 May 1980 was within 2 km of both the rangefront and the caldera boundary, and the 27 May 1980 event was 13 km from the rangefront and 15 km from the caldera. Even more difficult to explain as a wave-propagation effect, the event of 1944:51 UTC May 25 1980, which was located in the midst of the three non-double-couple events referred to above, had a double-couple mechanism, as we will show in a later section (Ekstrom and Dziewonski, 1983).

Furthermore, the pattern of anomalies required is not compatible with plausible structures in the area. The surface waves analyzed by Given *et al.* had wavelengths of 700 km or more, and can not have been affected significantly by a caldera 30 km in diameter. Therefore, if the mechanism (of the 1633:44 UTC 25 May 1980 event, for example) is a double couple, it must have an oblique-slip mechanism that is consistent with the surface-wave observations, and the short-period P waves must be strongly distorted by complex structures. In particular, as can be seen from the focal-sphere plot (Fig. 3) waves leaving the source in a southerly direction and in a northeasterly direction must have apparent positions on the focal sphere that have been moved 20° or 30° degrees toward the southwest. For the northerly rays, such an anomaly might concievably be attributed to refraction around a low-velocity region beneath the southeastern corner of the caldera, although there is no evidence for the existence of such a feature. The southerly rays would require a low-velocity region beneath the Sierra Nevada. What is known of the crustal and upper mantle structure in the region, however, suggests that seismic velocities are, if anything, higher beneath the Sierra Nevada than they are further east. For example, seismic refraction measurements (Eaton, 1963, Johnson, 1965) indicate

that the compressional-wave speed at the top of the mantle is about $7.9 km/s$ beneath the Sierra Nevada and $7.8 km/s$ beneath the Basin and Range province. Furthermore, changes in crustal thickness seem inadequate to produce the required effect: Both of the above-mentioned studies conclude that the crustal root of the Sierra Nevada continues eastward at least as far as the California-Nevada border.

Simultaneous multiple ruptures

A possibility suggested by both Barker and Langston (1983) and Ekström (1983) is that the double-couple mechanisms may be artifacts caused by complex ruptures. If two double couples with different orientations are superposed, the resultant force system is, in general, not a double couple. (Conversely, the non-volumetric part of any non-double-couple force system can be decomposed into a pair of double couples; in fact there are infinitely many ways to perform such a decomposition.) Therefore, if two shear-faulting earthquakes happen at nearly the same time, the resultant point source derived from long-period seismic data can have a non-double couple component. In particular, a combination of north-south left-lateral strike-slip faulting and normal faulting on northeast of southwest-dipping planes can produce a non-double-couple mechanism similar to those observed. Such simultaneous events are unlikely to occur accidentally; it is extremely improbable that three of the large Long Valley earthquakes involved such chance occurrences. If the anomalous events are simultaneous slip on multiple faults, they must be caused by some unusual process.

Tensile failure

A much simpler possibility, suggested by Julian (1983), is that the earthquakes are not caused by slip on faults, but by some other process that

has a non-double-couple equivalent force system. Tensile failure under high fluid pressure is such a process, and can be expected to occur in volcanic areas. At depth a void cannot form, and a tensile crack can open only if fluid under high pressure flows into it and holds it open. Indeed, if the fluid pressure is high enough, tensile failure is the only type of failure that can occur (Fig. 17). A simple qualitative argument (see Figure ?) shows that the mechanism of such a process must have a large CLVD component. The equivalent force system for a shear fault is a double couple, whose principal-axis representation is a pair of orthogonal dipoles of equal magnitude and opposite sign. A CLVD, on the other hand, consists of three dipoles, with moments in the ratio 2:-1:-1. Now a opening tensile crack may be represented as a plane across which there is a discontinuity in the normal component of displacement; the equivalent force system consists of three dipoles with moments in the ratio $\lambda+2\mu:\lambda:\lambda$ (Aki and Richards, 1980). If we add an implosive force system that is symmetric about the primary (extensional) dipole and just cancels out the volumetric component, as is required by the fact that large voids cannot form at depth in the earth, we obtain a CLVD. Physically, the compensation is provided by fluid flowing into the crack, and would not be completely symmetric, so the resultant force system would not be a pure CLVD, but would also have a double-couple component. This type of earthquake mechanism was originally proposed in Japan more than 50 years ago by Ishimoto (1932), who attributed most earthquakes to magma movement.

The purpose of this paper is to try to decide between the alternative hypotheses of (a) simultaneous shear-faulting earthquakes and (b) an intrinsically non-double-couple process such as tensile failure, as explanations of the anomalous earthquakes.

BODY-WAVE FIRST MOTIONS

Short-period P waves

Figures 3 and 4 show the observed first motions of short-period P waves for the events of 1633:44 UTC 25 May 1980 and 1450:57 UTC 27 May 1980. These data were taken from Figures 5(b) and 10 of Given *et al.* (1982), and most of them came originally from seismograph networks operated in California and Nevada by the U. S. Geological Survey, the University of Nevada, and the California Institute of Technology. The teleseismic data came originally from the Earthquake Data Reports (EDR) of the U.S. Geological Survey. Also shown in Figures 3 and 4 are the nodal planes corresponding to the double-couple mechanisms proposed by Given *et al.* (1982), as well as the non-planar nodal curves corresponding to non-double-couple mechanisms fitted to the data (see figure captions). As can be seen, the non-double-couple mechanisms fit the short-period first motions much better than the double couples: they have only 4 and 2 inconsistent data for the two events, whereas the double couples have 32 and 16.

To check the reliability of the short-period first motions, we have examined most of the seismograms upon which they are based. On short-period seismograms, the event of 1633:44 UTC 25 May 1980 began more impulsively, and provides more reliable first motions than does the event of May 27. Furthermore, for both events the compressional first motions are more impulsive and reliable than the dilatational ones. The most reliable dilatational first motions are those observed at U.S. Geological Survey stations in the vicinity of Walker Pass and the southern Owens Valley. It is interesting to note that first motions for rays leaving the source in a west-northwesterly direction, approximately tangent to the southern boundary of the caldera, are not in good agreement with the predictions for either double-couple or non-double-couple

mechanisms. This may be an effect of anomalous structure.

An interpretation of the type presented here, based upon both local and teleseismic observations, has been criticized by Ryall (oral communication) on the grounds that the two data sets may not refer to the same part of the source time function. If the readings correspond to different sub-events, they must occur within about one second of each other, because of the consistency of the reported arrival times at both regional and teleseismic distances. The local and regional short-period seismograms show no evidence of an event following the first event by a second or two, although detecting such evidence is made difficult by the fact that many records are clipped after the first few cycles, and by the difficulty of separating source and propagation effects at regional distances. In any case, a majority of "normal" earthquakes have complicated time functions, but it is unusual for them to involve a temporal change in focal mechanism, and conventional first-motion techniques are effective for studying them. As will be discussed in the next section, waveform inversion indicates that the most complex Long Valley event had a temporally stable mechanism. Nevertheless, it is certainly true that the short-period first motions are the least reliable of the various data sets. The most satisfactory way to interpret the short-period signals is to compare the waveforms with ones calculated from dynamic models of the source process. Chouet and Julian (this volume) have formulated such a dynamic model for a propagating fluid-filled crack, and plan to compare the predictions of this model with the observed waveforms.

Long-period P and SH waves

Long-period P and SH-wave first motions are shown in Figure 5. Most of these data come from the Worldwide Standardized Seismograph Network (WWSSN) and the Global Digital Seismograph Network (GDSN). The mechanism shown on Figure 5 was determined by a recently developed technique for using

linear programming methods to determine seismic focal mechanisms from polarity observations (Julian, 1983). The non-double-couple mechanism fits the data better than the double couple does, with the difference being most pronounced for the SH data. In fact, the linear programming analysis demonstrates that these long-period first motions are incompatible with a double-couple mechanism.

Nodal-curve geometry

The nodal surfaces plotted on the focal sphere in Figures 3, 4, and 5 bear little resemblance to the more familiar ones that are appropriate for double couples. To help clarify the difference between the patterns for double-couple and non-double-couple sources, Figure 6 shows the geometry of the nodal surfaces for a pure double couple and a pure CLVD. For a double couple, the surfaces are orthogonal planes whose intersections with the focal sphere are orthogonal great circles that divide the focal sphere into equal quadrants. For a CLVD, on the other hand, the curves are circular cones, whose intersections with the focal sphere are two small circles that divide the focal sphere into three regions. In fact, the Japanese, who first considered mechanisms of this kind referred to them as of "conical type" (Ishimoto, 1932). (The apex angles of these cones are $\cos^{-1}(-1/3) = 109.47°$, the "tetrahedral angle".) For mechanisms intermediate between double couples and CLVDs, the nodal surfaces are more general (not circular) cones; the planar surfaces for a double couple may be considered as limiting cases of such cones, corresponding to vanishing of one of the principal moments.

WAVEFORM INVERSION

Detailed information about earthquake mechanisms and time functions can be obtained by inverting high-resolution digital waveforms of body waves to estimate the parameters in a moment-tensor source representation. We did this for three of the events that occurred in May 1980, applying the multi-channel signal enhancement (MSE) algorithm of Sipkin (1982) to long-period P- and SH-waveforms recorded by the Global Digital Seismograph Network (GDSN).

Method

The MSE algorithm determines an earthquake's mechanism from a suite of observed seismograms, using methods from the theory of optimal filter design. The moment tensor of the source is regarded as an unknown multi-channel filter whose input is a set of Green's functions and whose output is a set of theoretical seismograms. The input Green's functions are taken as known, and the algorithm determines the filter (moment tensor) that makes the output agree as well as possible with the observed seismograms. The moment tensor acts as both a signal-enhancement filter and a noise-rejection filter; features of the seismograms that are not included in the Green's functions (for example, arrivals generated by unmodelled near-receiver or near-source structure) are regarded as noise and have little effect on the solution. The MSE waveform inversion algorithm has the advantages of being more objective (and much faster) than trial-and-error methods, and is less sensitive to lateral heterogeniety in earth structure than are techniques that use long portions of the wave train.

We used two variants of the MSE algorithm. In the first variant, all the elements of the moment tensor are constrained to be similar functions of time, differing only by constant factors, while in the second variant the elements are

allowed to be independent functions of time. This second representation provides information about the time history of the rupture process, and is helpful for identifying multiple earthquakes and for studying such processes as changes in fault orientation or in slip direction. For example, for the Coalinga, California, earthquake of 2 May 1983, a rotation of the fault plane by about 10° was easily resolvable. In both variants of the MSE algorithm, the solutions are constrained to be purely deviatoric, but are not required to be double couples. The Green's functions used here are those for the far field of a point source, and include the effects of reflection at the free surface and attenuation.

The inversion was carried out in several steps. First, the focal depths were estimated, using P waveforms only and constraining the moment tensor elements to be similar time functions, and the depth was varied until the best fit to the data was obtained. Since the P waveforms contain the phases pP and sP, as well as the direct P waves, this procedure is quite sensitive to source depth. The inversion was then repeated with the depth constrained to this value, using both P and SH waveforms. Finally, for the largest event, the more general type of inversion was performed, dropping the similarity restriction on the moment tensor elements.

Results

The MSE waveform inversion technique was applied to (GDSN) data recorded at epicentral distances from 52° to 99° (Figure 7) for the events of 1633:44 and 1944:50 UTC 25 May 1980 and 1450:56 UTC 27 May 1980. A plot of the mean-squared error versus depth for the 1450:56 UTC 27 May 1980 event is shown in Figure 8. The point-source inversion procedure yields source depths of 9, 11, and 7 km, respectively, for the three events considered. The depths were then fixed and the inversions redone using P waves alone and using P and SH waves together. For the event of 1944:50 UTC 25 May there were not enough suitable P

waves, so only a P-SH inversion was performed. The results of these inversions are listed in Table 2 and shown in Figure 13. These results are very similar to those found by Barker and Langston (1983) using WWSSN data and different analysis methods. The fits of the resultant theoretical waveforms to the data are shown in Figure 11 for the 1633:44 UTC 25 May 1980 event and in Figure 12 for the event of 1450:56 UTC 27 May 1980. For the 1633:44 UTC 25 May 1980 and 1450:56 UTC 27 May 1980 events the scalar moments are 1.7×10^{25} and 1.8×10^{25} dyne-cm, corresponding to magnitudes M_w of 6.1. The double-couple parts of the moment tensors are 30 and 35 percent. However, the solution for the 1944:50 UTC 25 May 1980 event is almost a pure double couple, with a non-double-couple part of only 8 percent and a scalar moment of 1.2×10^{25} dyne-cm (M_w=6.0).

The general inversion, without a similarity constraint on the moment-tensor elements, was performed for the 25 May 16:33 event. The principal axes of the resulting moment tensor do not change significantly with time, indicating that the source mechanism did not change during the earthquake. The changes of the principal axes are so slight that a figure displaying them would be uninformative. The scalar moment as a function of time is shown in Figure 9. The source duration is approximately 10 seconds and the source-time function is symmetric. This duration agrees with values inferred from both broad-band waveforms and near-field strong motion records, both of which are discussed in more detail below.

The resolving power of the MSE algorithm depends upon the station distribution, the character of the noise and the bandwidth of the instrument. Given the seimograms to be fit, a noise sample for each seismogram, and the inversion kernel functions, one can use the procedure outlined by Oldenburg (1982) to compute a set of averaging functions from which the available resolution can be inferred. Figure 10 shows one of the averaging functions

computed for this data set. Its width is about 6 sec.; therefore, two sub-events separated by less than this interval would not be resolvable. This estimate is computed under the assumption that all errors are caused by noise; since there are certainly unmodeled errors present, the resolution is probably somewhat greater than 6 sec.

SURFACE WAVES

Surface waves

As was pointed out above, the Long Valley earthquakes are so shallow that the surface waves generated by them provide information about only three of the six moment-tensor elements. As a result, the observed surface-wave spectral amplitudes and initial phases can be explained equally well by many different mechanisms, including a pure double couple and a pure CLVD. It is nevertheless important to verify that any proposed mechanism is quantitatively consistent with the observed surface waves. The event of 1633:44 UTC 25 May 1980 provides the most stringent test, because it had the largest seismic moment and generated the highest-quality surface-wave data. Figure 14 compares the observed spectral amplitudes of Love and Rayleigh waves for this event with the theoretical radiation patterns for the double-couple mechanism proposed by Given *et al.* (1982) and for a non-double-couple mechanism determined in this study by inverting P and SH waveforms. This solution is a weighted combination of the two solutions given in Table 2 for this event (with the P-SH solution having $\frac{2}{3}$ of the total weight. As can be seen, both mechanisms fit the observed amplitudes equally well. The pattern at a period of 150 seconds is quite similar. Thus, surface-wave data, while not powerful enough to ascertain whether or not an event is a double couple, do provide useful information which is independent of that contained in the P and SH waveforms.

BROAD-BAND WAVEFORMS

Long-period seismograms, recorded on relatively narrow-band instruments, are poorly suited for assessing possible complexity of the source process. Records from broad-band instruments are much better for this purpose, but few such instruments are now deployed. However, if digital waveforms of high resolution and accuracy are available, it is possible to combine outputs from short- and long-period instruments to synthesize seismograms of increased bandwidth. Such broadband signals are very powerful for recognizing sub-events within an earthquake, as well as for identifying the depth phases pP and sP.

We used the technique described by Harvey and Choy (1982) to produce broad-band seismograms from data recorded by the Global Digital Seismograph Network (GDSN). Figure 16 shows the broadband displacements from the events of 1633:44 UTC May 25 1980 and 1450:56 UTC 27 May. The broadband waveforms for the 27 May. 1980 event are extremely simple, with an initial dilatation followed by a somewhat larger and broader compressional arrival. The initial arrival is the direct P-wave and the later arrival is a combination of pP and sP (and PcP at station GRFO). There is no evidence in the broadband waveforms of any source multiplicity.

The waveforms for the event of 1633:44 UTC 25 May 1980 are considerably more complex. By comparing these waveforms with the simpler ones for the earthquake two days later, it is possible to identify two events about 6 to 8 seconds apart, as was suggested by Ekström and Dziewonski (1983) and Ekström (1983). Evidence of these two sub-events can also be seen in the near-field strong-motion records displayed by Hartzell (1982). Ekström (1983) and Wallace *et al.* (1983) argued that these sub-events have different mechanisms, by whose superposition they sought to explain the non-double-couple

mechanism of the earthquake. Ekström's analytical technique consisted essentially in specifying a normal-faulting mechanism for the first event and then determining the second (strike-slip) so as to obtain the correct resultant moment tensor. As was mentioned above, such a mathematical decomposition of a moment tensor is always possible, and is not unique. Ekström's interpretation is not required by the data; Wallace *et al.* (1983) explain the same data with a strike-slip event followed by a normal-faulting event. As was shown above, objective inversion of the waveforms indicates that the mechanism is quite stable and does not change with time.

The later phases on the broad-band records can be used to determine the depth of focus for the 1450:56 UTC 27 May 1980 event. The intervals between the arrival times of the initial dilatations and the following compressions fall into two groups, averaging about 4.4 and 6.1 seconds. If it is assumed that the first group represents the pP-P times and the second group represents the sP-P times, and that the crustal compressional and shear-wave speeds are 6.0 and 3.3 km/s, then the source depth is about 12.6 km. Of course, the effect of any lower velocity surficial layers will be to decrease this estimate and make the earthquake shallower. The depth found is close to the 13 km depth determined by the National Earthquake Information Service. This information may be used in conjunction with the 7 km centroidal source depth determined from the long-period body-wave inversion to infer that the source propagated upward.

DISCUSSION

We have shown that the seismological data for some of the largest Long Valley earthquakes can best be explained in terms of tensile failure and the opening of cracks under high fluid pressure.

Another line of support for the tensile-failure hypothesis is provided by

results of a high-resolution seismic experiment carried out with portable seismometers in the southern part of the caldera by Dr. Albert Smith in the summer of 1982. During the experiment, a swarm of small earthquakes occurred, the locations of which (Fig. 17) clearly define a vertical plane striking northwest-southeast, which is the expected orientation of a tensile crack given the stress orientation in the region. Unfortunately, the first-motion data were too sparse to distinguish between double-couple and non-double-couple earthquake mechanisms.

Non-double-couple earthquake mechanisms have from time to time been reported from other areas of volcanism and extensional tectonics. For example, it is often impossible to fit orthogonal nodal planes to P wave first motions from large "normal faulting" earthquakes on the Mid-Atlantic Ridge (Sykes, 1967, Sykes, 1970), although it seems possible to explain these observations adequately in terms of wave-propagation effects (Solomon and Julian, 1974, Trehu *et al.*, 1981). Other examples of anomalous earthquake mechanisms similar to those discussed here have recently been reported for small earthquakes at the Hengill geothermal area in Iceland (Foulger and Long, 1984). It would be worthwhile to re-examine earthquakes from other volcanic areas to see if anomalous mechanisms have been overlooked.

Conditions for tensile failure

Under what conditions would tensile failure be expected occur, as opposed to shear failure? This question can be conveniently analyzed using a Mohr's circle diagram, which gives the relationship between the shear stress, τ, and the normal stress, σ, acting across a plane at a point in a stressed medium (Figure 18). As the plane is rotated between the directions of the maximum and minimum principal stresses, the (σ, τ) values trace out a circle, centered at the point $(\frac{1}{2}(\sigma_1 + \sigma_3), 0)$ and having a diameter of the stress difference $\sigma_1 - \sigma_3$. If

many such circles, corresponding to stress states at failure, are plotted on this diagram, they define a "failure envelope". The condition for failure is that Mohr's circle shall touch this failure envelope, and the orientation of the failure surface is then simply related to the position on the circumference at which the contact occurs. Figure 18 shows a theoretical failure envelope for a brittle material such as rock. This curve corresponds to the Griffith theory of failure, as modified by McClintock and Walsh (Price, 1966), although only its general shape is important in this discussion. In the compressional field ($\sigma > 0$) the straight failure envelope represents the Navier-Coloumb criterion for shear failure. If the mean stress is large, as in the upper part of Figure 18, only shear failure can occur. The approximate effect of fluid pressure is to effectively lower all the principal stresses by the amount p. This effect now makes it possible for shear failure to occur at rather small stress differences if the fluid pressure is comparable to the overburden pressure. The restrictive nature of this condition probably explains why tensile failure in the earth is apparently relatively rare.

Volume of the intrusion

The volume, V, of fluid intruded into a crack can be related to the seismic moment of the associated earthquake. If we assume that the equivalent forces for the fluid flow are confined to the plane of the crack, then these forces do not affect the principal dipole of the CLVD, whose moment is

$$M = (\lambda+2\mu)A\bar{u} \equiv (\lambda+2\mu)V \ ,$$

where A is the area of the crack face and $\bar{u}$ is the average amount of opening of the crack. For the largest earthquake, that of 1633:44 UTC 27 May 1980, $M = 1.7\times10^{25} dyne\ cm$. Taking $\lambda = \mu = 3\times10^{11} dyne\ cm^{-2}$, we get $V = 0.018\, km^3$.

Viscosity of the fluid

It might be thought that some fluids, such as magma, are too viscous to flow into a crack fast enough to cause an earthquake. Approximate calculations show that this is not so. Referring to Figure 19, consider a dike of thickness h, length l and aspect ratio r propagating upward from a source of magma or other high-pressure fluid. The volume of the dike is then

$$V = rh^2 l$$

and, for laminar viscous flow, the flow rate is

$$\dot{V} = \frac{lh^3}{12\eta}\frac{dP}{dx} = \frac{lh^3}{12\eta}\frac{\Delta P}{rh} = \frac{V\Delta P}{12r^2\eta} ,$$

where ΔP is the pressure difference driving the fluid into the crack, and is comparable in magnitude to the strength of the rock. Therefore V varies as $\exp(t/\tau)$, where

$$\tau = \frac{12r^2\eta}{\Delta P} .$$

The crack volume increases exponentially, with a time constant that depends on the driving pressure, the shape of the crack, and the viscosity of the fluid. Of course the crack can not grow indefinitely; the analysis given here ignores effects such as the dynamics of rock failure and the pressure drop in the source reservoir, which would limit crack growth. If we take τ = 10, the approximate duration of the earthquakes, r = 100 to 1000, and ΔP = 1 to 10*kbar*, we get values for η between 170 and 8×10^4 poise, a range that overlaps the viscosities observed for many magmas. This argument merely shows that magma can not be ruled out on viscosity grounds; other fluids, such as water or carbon dioxide remain equally acceptable possibilities. Indeed, the rapid exsolution of such volatile fluids is likely to be an important mechanism increasing the mobility of magma.

Non-double-couple earthquake mechanisms may be important in other

areas of volcanism and extensional tectonics. Earthquakes in such areas are currently under investigation.

CONCLUSIONS

At least three of the largest earthquakes in the Long Valley region in 1978 and 1980 have unusual focal mechanisms, with large non-double-couple components, and unlike the mechanisms appropriate for slip on faults. The suggestion that these earthquakes are caused by simultaneous slip on different faults, and that the non-double-couple mechanisms are artifacts caused by failure to resolve the separate events, is inconsistent with the observed P and SH waveforms. Broad-band waveforms for the event of 1450:56 UTC 27 May 1980 are very simple, and unlike those expected for a multiple event. Furthermore, objective inversion of P and SH waveforms using the multichannel signal enhancement (MSE) algorithm indicates that the mechanisms do not change with time, as would be expected for simultaneous earthquakes with different mechanisms.

The most likely physical explanation of these earthquakes is that they are caused by sudden tensile failure and the opening of cracks under high fluid pressure. If this explanation is correct, earthquake mechanisms may prove be useful for monitoring intrusive processes in active volcanic areas.

ACKNOWLEDGEMENTS

During this study, we had valuable conversations with David Hill, William Ellsworth, James Savage, and Rob Cockerham. We thank Rob Cockerham, and Terry Wallace, for permission to use unpublished data and Peter Ward for help in digitizing published data.

References

Hartzell, Stephen, 1982. Simulation of ground accelerations for the May 1980 Mammoth Lakes, California, earthquakes, *BSSA*, **72**, 2381-2387.

Aki, Keiiti and Paul G. Richards, 1980. *Quantitative Seismology*, W.H. Freeman and Company, San Francisco, 932 pages.

Barker, Jeffrey S. and Charles A. Langston, 1983. A teleseismic body-wave analysis of the May 1980 Mammoth Lakes, California, earthquakes, *BSSA*, **73**, 419-434.

Chouet, Bernard and Bruce R. Julian, 1984. Dynamics of an expanding fluid-filled crack, *JGR (submitted)*.

Clark, M. M., J. C. Yount, P. R. Vaughan, and R. L. Zepeda, 1982. Map showing surface ruptures associated with the Mammoth Lakes, California, earthquakes of May 1980, *U. S. Geological Survey Miscellaneous Field Studies*, **Map MF-1336**.

Cramer, Chris H. and Tousson R. Toppozada, 1980. A seismological study of the May, 1980, and earlier earthquake activity near Mammoth Lakes, California, *Special Report*, **150**, 91-130.

Eaton, Jerry P., 1963. Crustal structure from San Francisco, California, to Eureka, Nevada, from seismic-refraction measurements, *JGR*, **68**, 5789-5806.

Ekstrom, G. and A. M. Dziewonski, 1983. Moment tensor solutions of Mammoth Lakes earthquakes (abstract), *EOS*, **64**, 262.

Foulger, G. and R. E. Long, 1984. Anomalous focal mechanisms: tensile crack formation on an accreting plate boundary, *Nature*, **310**, 43-45.

Given, J. W., T. C. Wallace, and H. Kanamori, Aug 1982. Teleseismic analyis of the 1980 Mammoth Lakes earthquake sequence, *BSSA*, **72**, 1093-1109.

Harvey, D. and G. L. Choy, 1982. Broadband deconvolution of GDSN data, *GJRAS*, **69**, 659-668.

Johnson, Lane R., 1965. Crustal structure between Lake Mead, Nevada and Mono Lake, California, *JGR*, **70**, 2863-2872.

Julian, Bruce R., 1983. Analysis of seismic-source mechanisms by linear-programming methods, *GJRAS (in press)*.

Julian, Bruce R., 1983. Evidence for dyke intrusion earthquake mechanisms near Long Valley caldera, California, *Nature*, **303**, 323-325.

Knopoff, L. and M.J. Randall, 1970. The compensated linear-vector dipole: A possible mechanism for deep earthquakes, *JGR*, **75**, 4957-4963.

Oldenburg, D. W., 1982. Multichannel appraisal deconvolution, *GJRAS*, **69**, 405-414.

Price, Neville J., 1966. *Fault and Joint Development in Brittle and Semi-brittle Rock*, Pergammon Press, Oxford, 176 pages.

Ryall, A. and F. Ryall, Jun 1981. Spatial temporal variations in seismicity preceding the May 1980, Mammoth Lakes, California, earthquakes, *BSSA*, **71**, 747-760.

Solomon, Sean C. and Bruce R. Julian, 1974. Seismic constraints on ocean-ridge mantle structure: anomalous fault-plane solutions from first motions, *GJRAS*, **33**, 265-285.

Sykes, Lynn R., 1967. Mechanism of earthquakes and nature of faulting on the mid-oceanic ridges, *JGR*, **72**, 2131-2153.

Sykes, Lynn R., 1970. Focal mechanism solutions for earthquakes along the world rift system, *BSSA*, **60**, 1749-1752.

Taylor, Gary C. and William A. Bryant, 1980. Surface rupture associated with the Mammoth Lakes earthquakes of 25 and 27 May, 1980, in ***Special Report 150***, pp. 49-67 , ed. Roger W. Sherburne, CDMG.

Trehu, A. M., J. L. Nabelek, and S. C. Solomon, 1981 Fellowship. Source characterization of two Reykjanes Ridge earthquakes: surface waves and moment tensors, P waveforms and nonorthogonal nodal planes, *JGR*, **86**, 1701-1724.

Wallace, Terry, Jeff Given, and Hiroo Kanamori, 1982. A discrepancy between long- and short-period mechanisms of earthquakes near the Long Valley Caldera, *GRL*, **9**, 1131-1134.

Table 1 - Earthquake Parameters

Origin time UTC	Lat.(N) (°)	Long.(W) (°)	Depth (*km*)	Magnitude	Moment$_{(Period)}$ ($10^{25} dyne-cm$)
4 Oct 1978 1642:48.3	37.49	118.67	7	5.3m_b 5.3M_s	0.18$_{(>45)}$(ED)
25 May 1980 1633:44.2	37.60	118.83	8	6.1m_b 6.1M_s	2.9$_{(150)}$(GWK) 1.87$_{(20)}$(BL) 1.8$_{(>45)}$(ED) 1.7$_{(25)}$(JS)
25 MAY 1980 1944:50.71	37.54	118.82	7	5.6m_b 6.0M_s	1.3$_{(80)}$(GWK) 0.8$_{(>45)}$(ED) 1.2$_{(25)}$(JS)
27 May 1980 1450:56.5	37.48	118.80	10	5.7m_b 6.0M_s	1.1$_{(80)}$(GWK) 1.03$_{(20)}$(BL) 0.8$_{(>45)}$(ED) 1.8$_{(25)}$(JS)

GWK - Given *et al.* (1982)
BL - Barker and Langston (1983)
ED - Ekström and Dziewonski (1983)
JS - This study

Table 2 - Source Parameters

Origin Time UTC	Phases	M ($10^{25} dyn-cm$)	Trend (°)	Plunge (°)	DC	CLVD
		-2.58	341	35		
	P	3.33	246	8	55%	45%
1633:44		-0.75	145	54		
25 May 1980						
		-1.43	321	80		
	P,SH	2.05	63	2	39%	61%
		-0.62	154	10		
1944:50		?	?	?		
25 May 1980	P,SH	?	?	?	92%	8%
		?	?	?		
		-2.25	340	6		
	P	3.08	249	10	46%	54%
1450:56		-0.83	101	78		
27 May 1980						
		-0.80	346	40		
	P,SH	1.18	79	4	34%	66%
		-0.39	174	49		

FIGURE CAPTIONS

Figure 1. Long Valley caldera and vicinity, showing all earthquakes in 1980 larger than magnitude 4. Heavy lines: normal faults.

Figure 3. Short-period P-wave first motions for earthquake of 1633:44 UTC 25 May 1980. Data from Figure 5(b) of Given *et al.* (1982). Lower focal hemisphere is shown in equal-area projection. Solid circles, compressions; open circles, dilatations. Light curves, nodal planes for shear fault with strike 12°, dip 50°, and rake -35°, as proposed by Given *et al.* (1982); heavy curves, nodal lines for mechanism fitted to these data (80% CLVD, 20% double couple: principal moments in the ratio 2:-1.2:-0.8 with primary axis extensional and trending N 55° E and plunging 7.5°.).

Figure 4. Same as figure 2 for earthquake at 1450:57 UTC on May 27, 1980. Data from Figure 10 of Given *et al.* (1982). Shear fault has strike 25°, dip 42°, and rake -19°. Heavy curve is for hand-fitted CLVD with horizontal primary axis trending N 58° W.

Figure 5. Long-period P and SH-wave first motions for earthquake at 1633:44 UTC on May 25, 1980. Lower focal hemispheres are shown in equal-area projection. Solid circles, compressions; open circles, dilatations. Light curves, nodal surfaces for shear fault with strike 12°, dip 50°, and rake -35°, as proposed by Given *et al.* (1982); heavy curves, nodal lines for moment tensor fitted to these data (see text).

Figure 6. Top: P-wave nodal surfaces for double couple (left) and CLVD (right) earthquake mechanisms. Bottom: intersections of nodal surfaces with focal sphere.

Figure 7. Azimuthal equidistant projection, centered on Long Valley caldera and showing the GDSN stations used in waveform inversions. The edge of the map is at an epicentral distance of 100 degrees.

Figure 8. Mean-squared error vs. assumed focal depth from MSE inversion for event of 1450:57 UTC 27 May 1980.

Figure 9. Source time-function (scalar moment as a function of time) for the event of 1633:44 UTC 25 May 1980.

Figure10. Averaging function for the $M_{\vartheta\varphi}$ component of the moment tensor for the event at 1633 UTc on 25 May 1980.

Figure 11. Real (solid) and synthetic (dashed) waveforms for event at 1633:44 UTC on May 25: a - P waves; b - SH waves.

Figure 12. Same as figure 8 for event at 1450:57 UTC on May 27.

Figure 13. P and SH nodal curves for mechanisms derived by waveform inversion. Lower focal hemispheres are shown in equal-area projection. above: event at 1633:44 UTC 25 May 1980; below: event at 1450:57 UTC 27 May 1980.

Figure 14. Observed and predicted 200-second surface-wave amplitudes for earthquake at 1633:44 UTC 25 May 1980. Light lines: theoretical curves for shear fault with strike 12°, dip 50° and rake -35° ("solution 2" of Given *et al.*, 1982. Heavy lines: theoretical curves for solution (50% double couple, 50% CLVD) derived in this study.

Figure 15. Broadband displacement waveforms for event of 1633:44 UTC 25 May 1980.

Figure 16. Broadband displacement waveforms from event of 1450:56 UTC 27 May 1980. Vertical lines: peaks of the P, pP, and sP arrivals. Arrows: computed PcP times (peak of arrival).

Figure 17. Epicenters of small earthquake swarm on 9 August 1982, as determined by Smith (1984).

Figure 18. Mohr's circle diagrams, illustrating conditions for shear and tensile failure. Above: at high confining stress with no fluid pressure, only shear failure occurs. Below: high fluid pressure lowers the effective confining stress, and tensile failure occurs at comparatively low stress differences.

Figure 19. Geometry of dike assumed in analyzing viscous flow (see text).

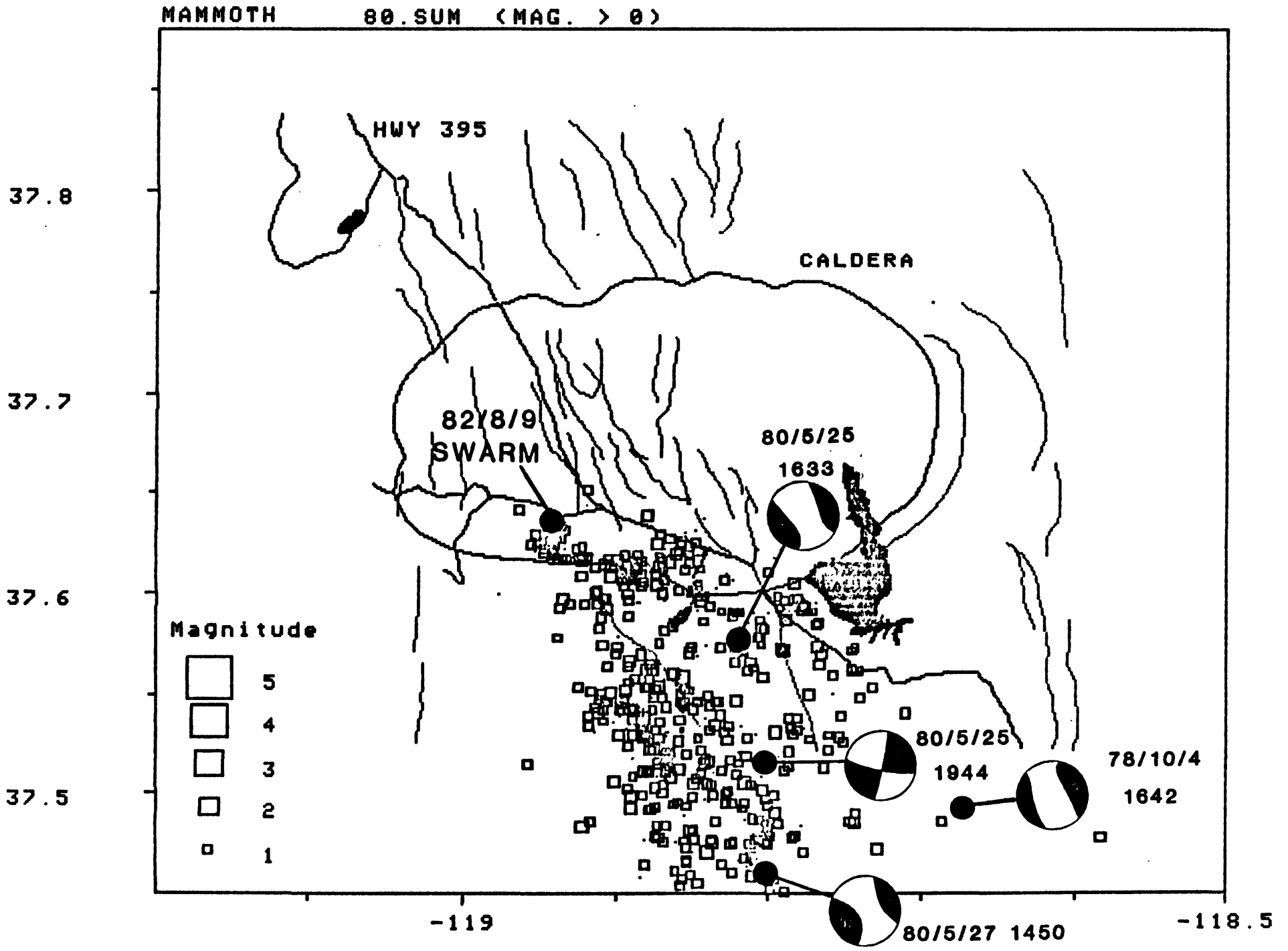
MAMMOTH 80.SUM (MAG. > 0)
HWY 395
CALDERA
82/8/9
SWARM
80/5/25
1633
80/5/25
1944
78/10/4
1642
80/5/27 1450
Magnitude
5
4
3
2
1
37.8
37.7
37.6
37.5
-119
-118.5

FIGURE 1

EQUIVALENT FORCE SYSTEMS

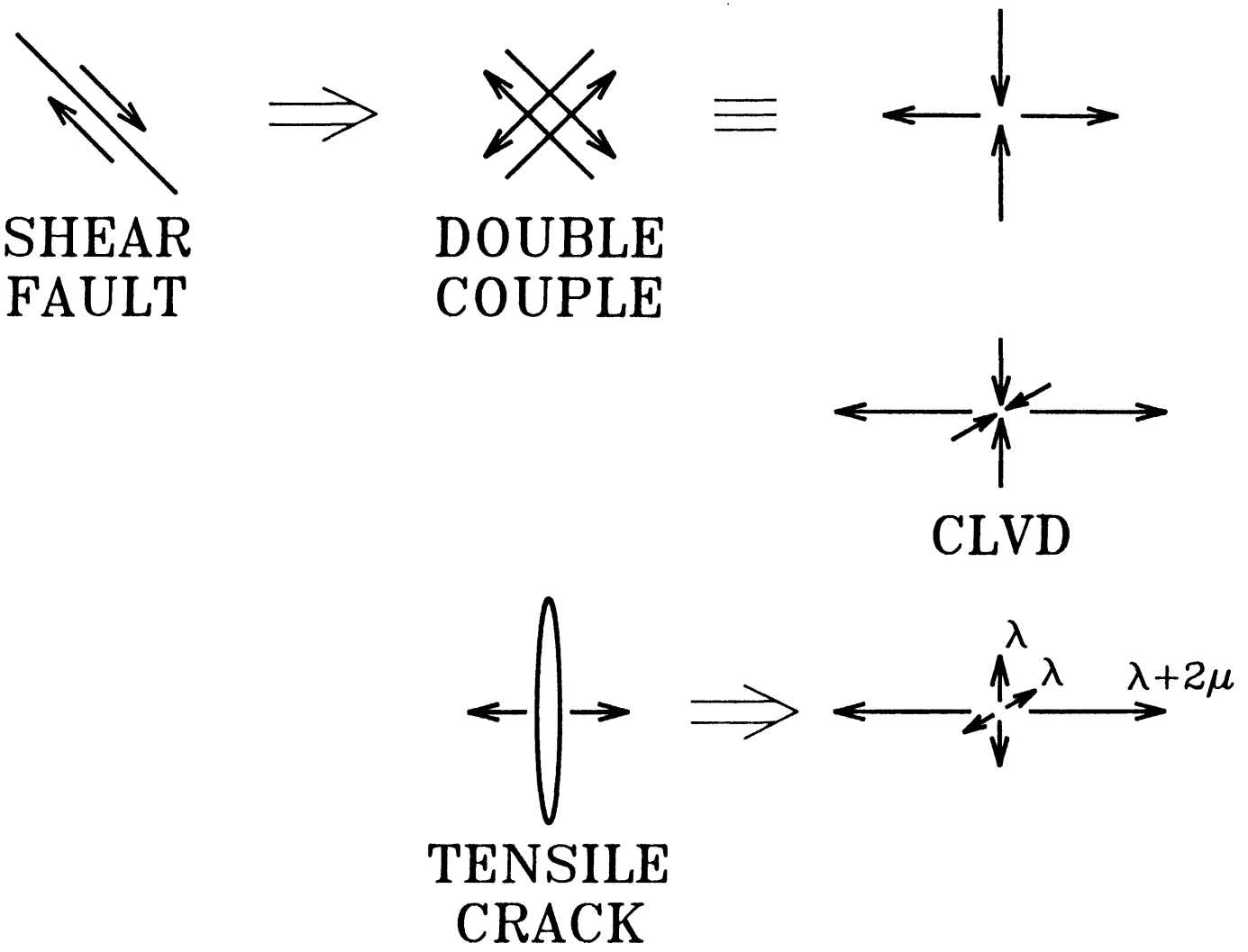

FIGURE 2

SHORT-PERIOD FIRST MOTIONS

25 May 1980 1633:44

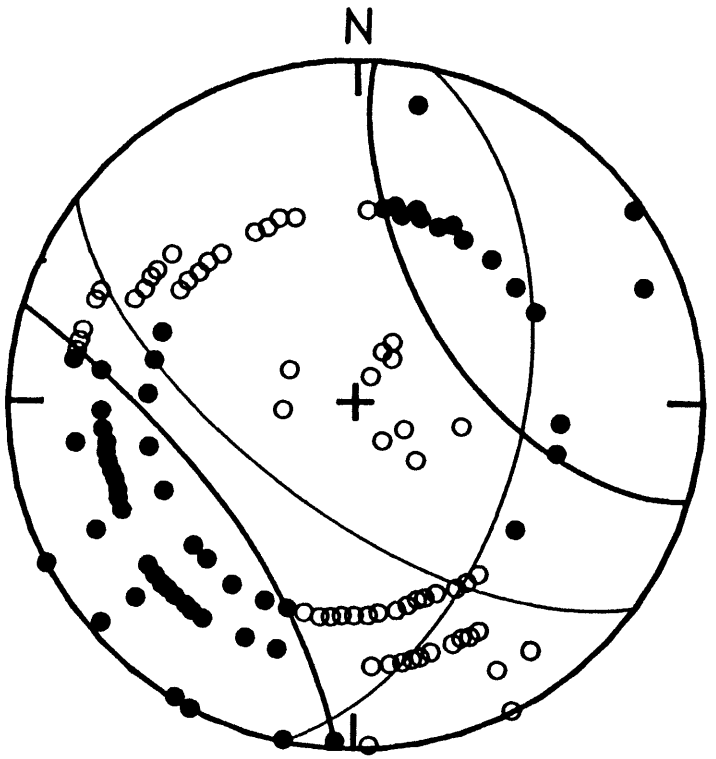

FIGURE 3

27 May 1980 1450:57

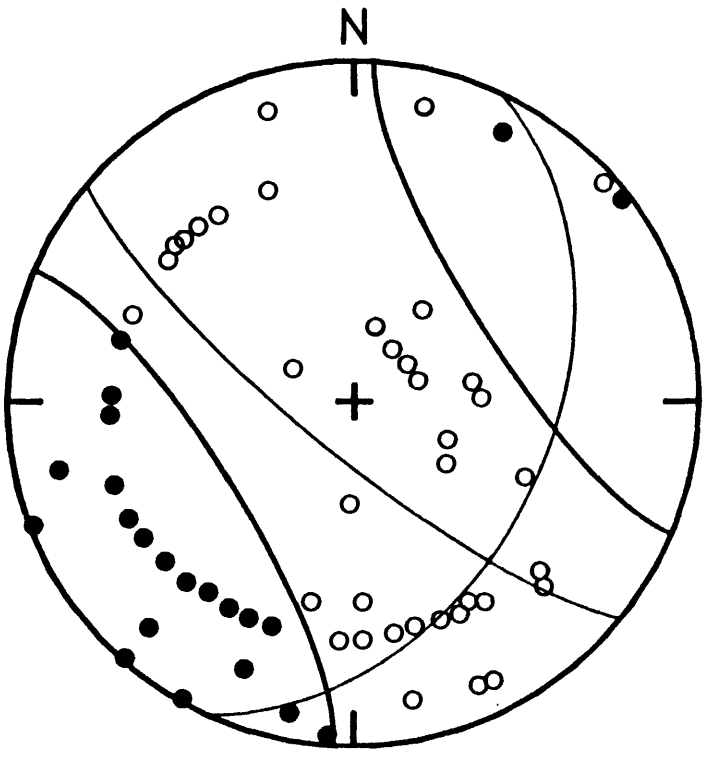

FIGURE 4

LONG-PERIOD FIRST MOTIONS

25 May 1980 1633:44

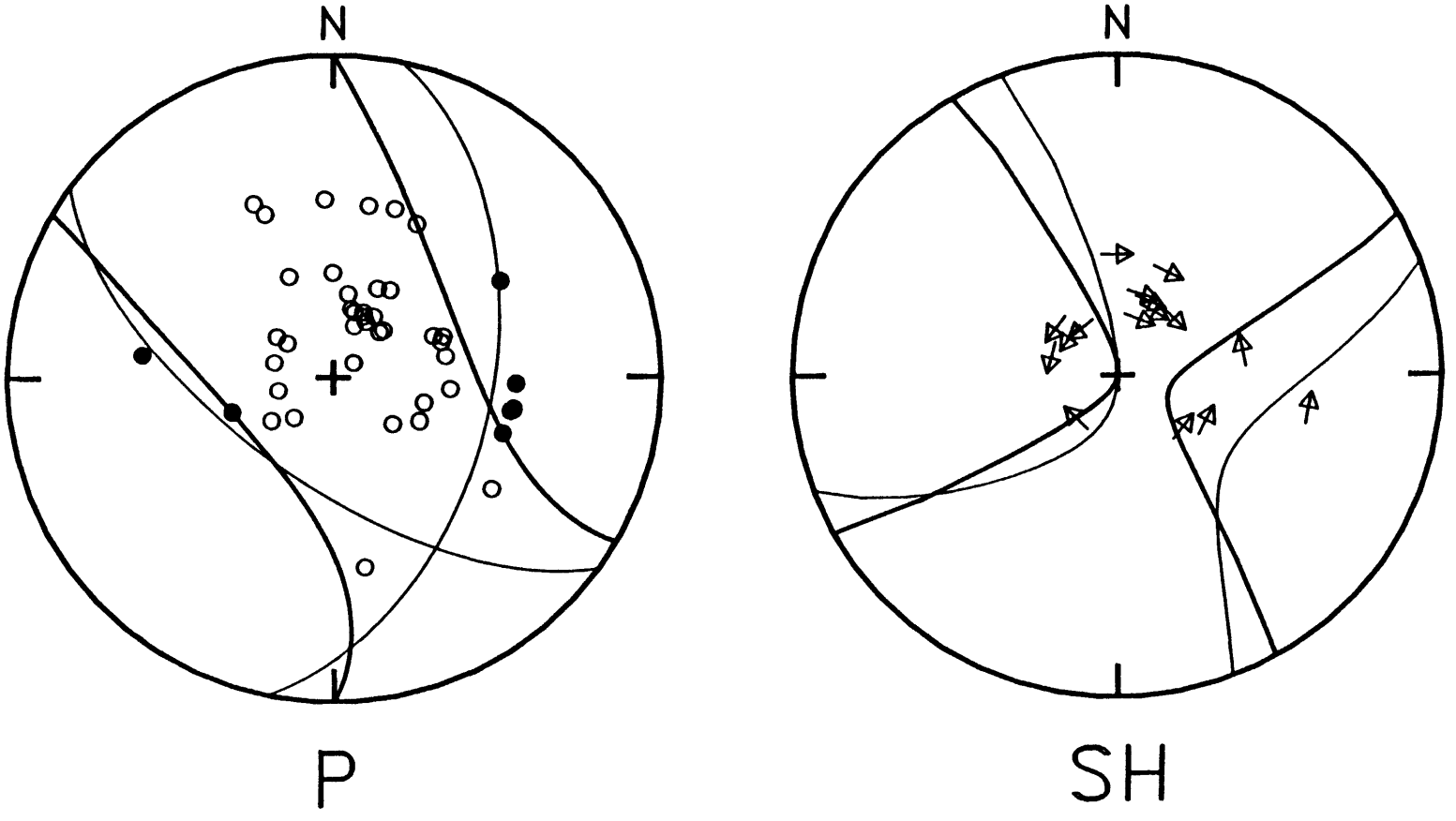

FIGURE 5

NODAL SURFACES

QUADRANTAL

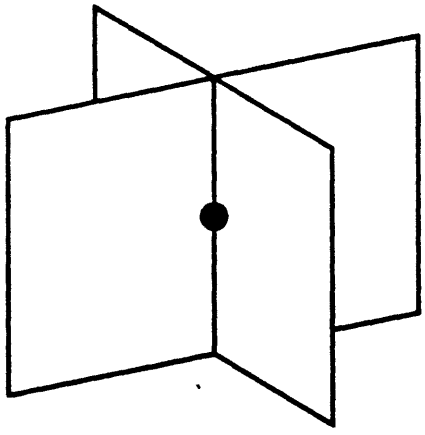

CONICAL

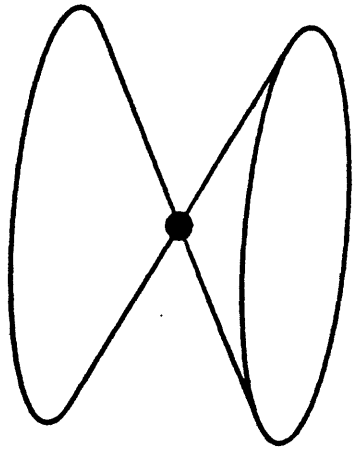

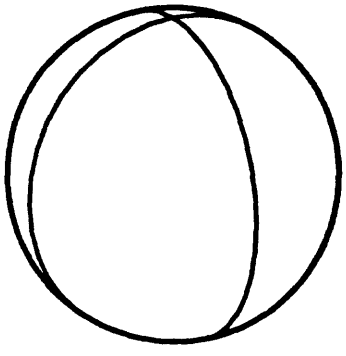

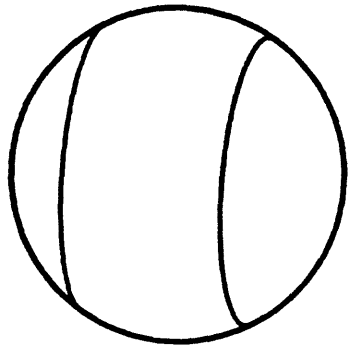

FIGURE 6

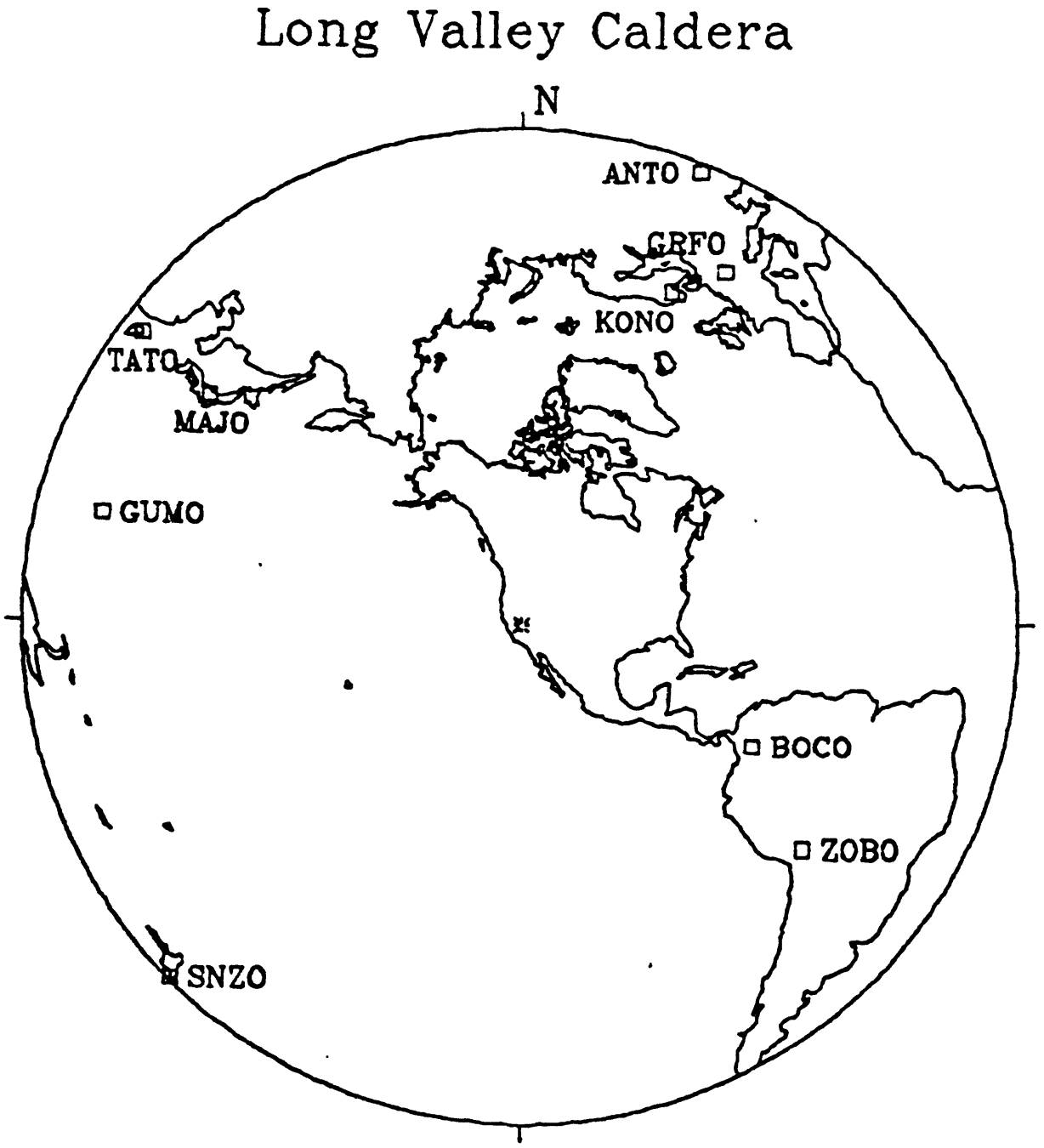
Long Valley Caldera
N
ANTO
GRFO
KONO
TATO
MAJO
GUMO
BOCO
ZOBO
SNZO

FIGURE 7

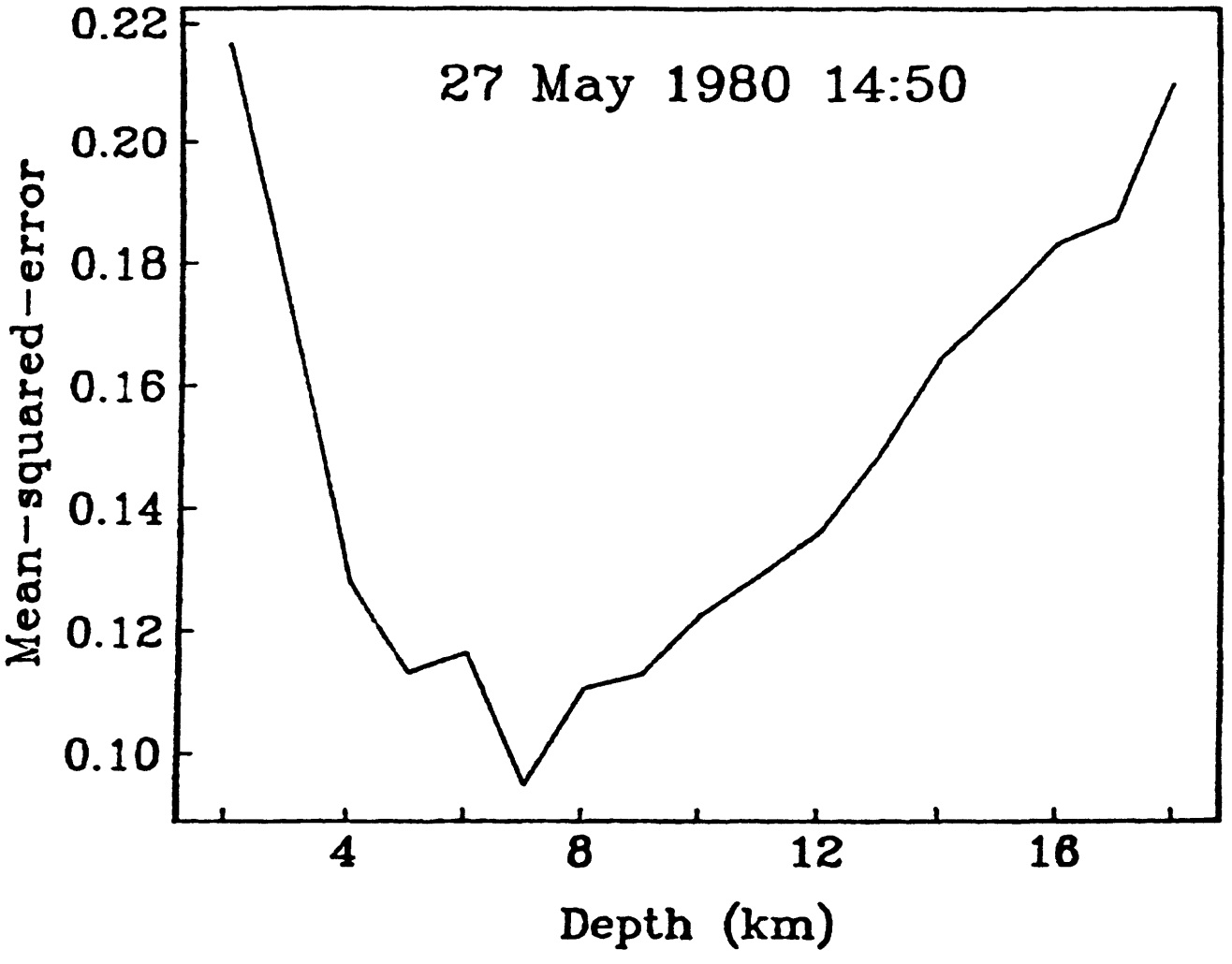
27 May 1980 14:50
Mean-squared-error
0.22
0.20
0.18
0.16
0.14
0.12
0.10
4
8
12
16
Depth (km)

FIGURE 8

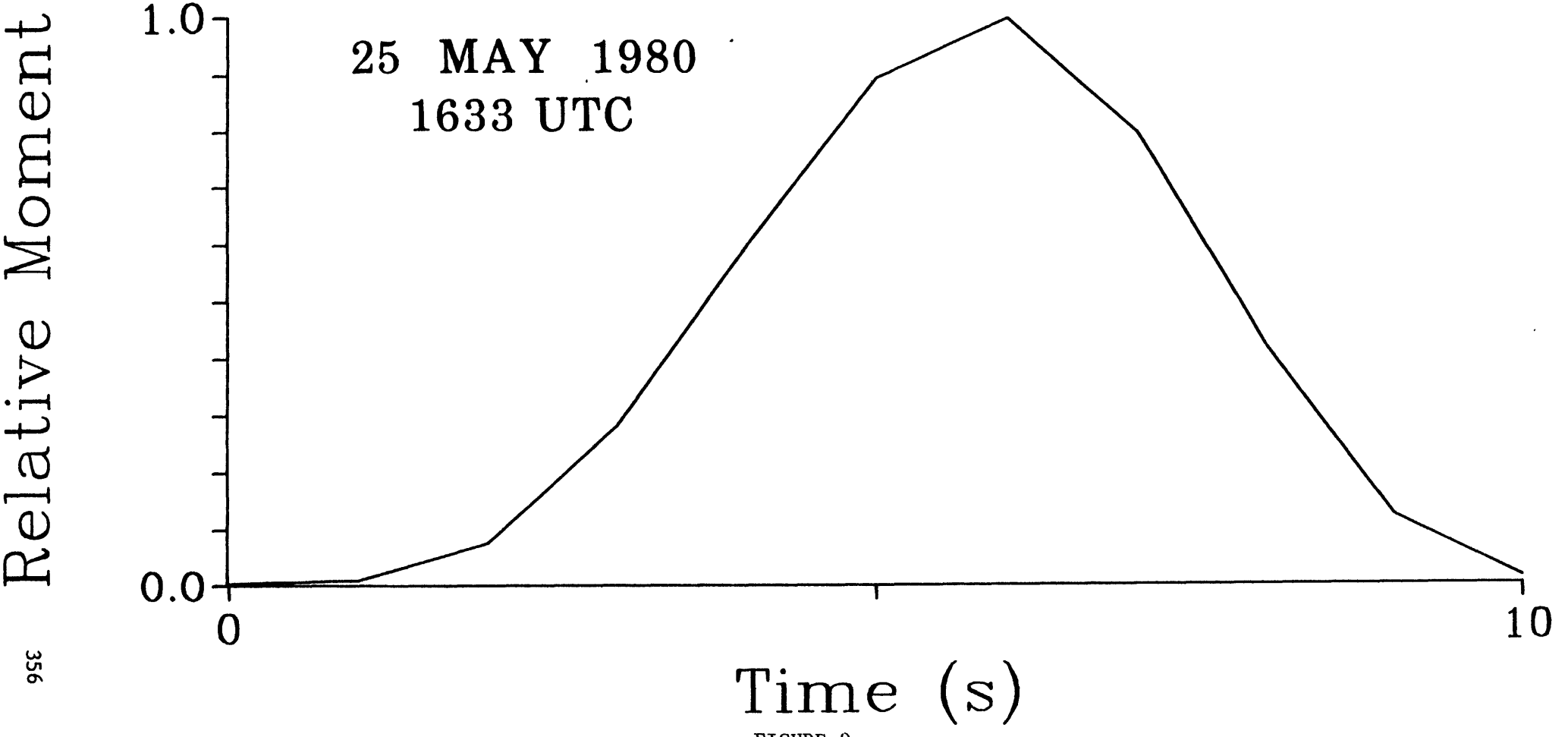

FIGURE 9

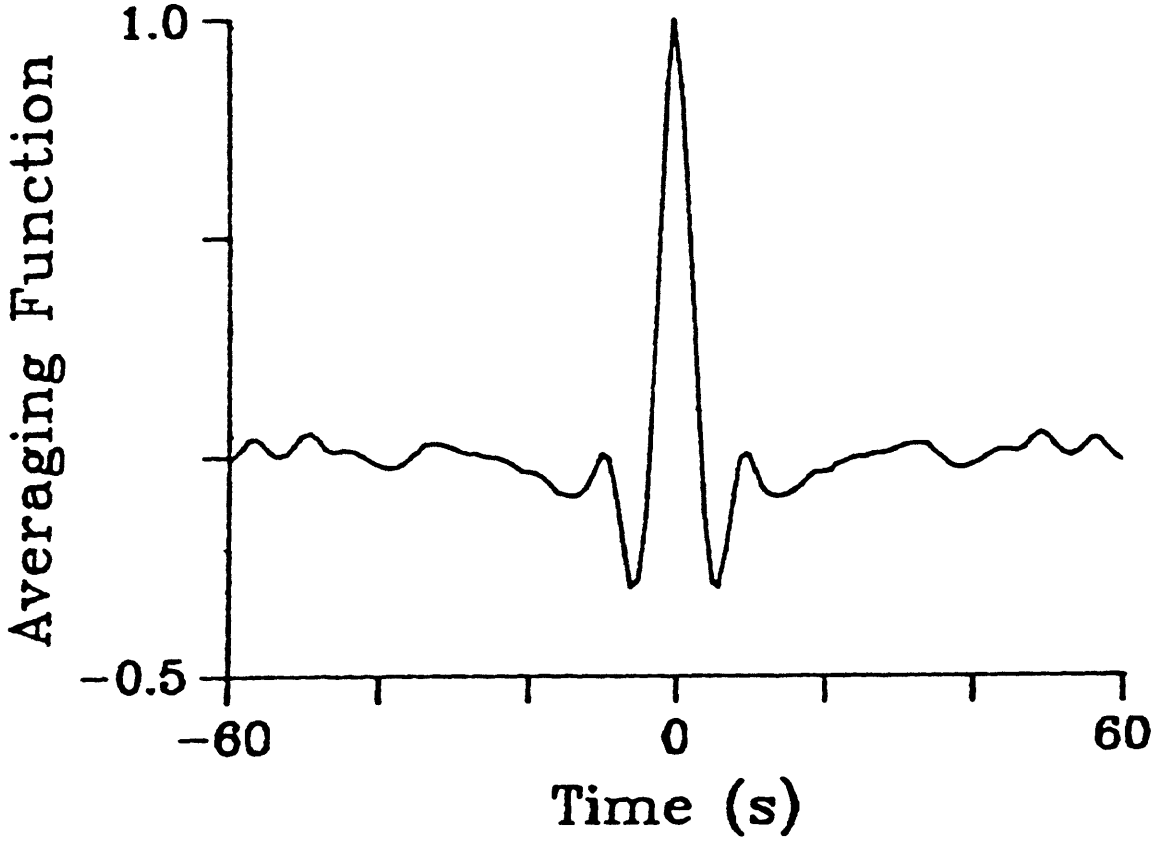

FIGURE 10

25 May 1980
16:33 UTC

P

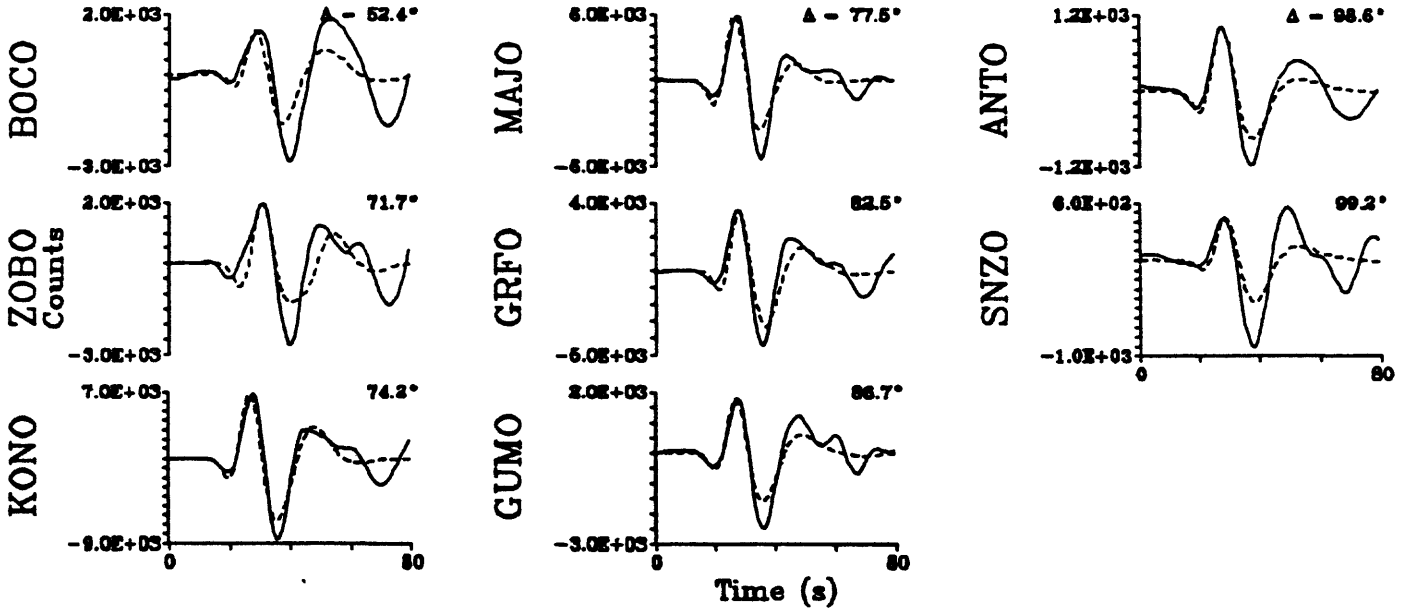

SH

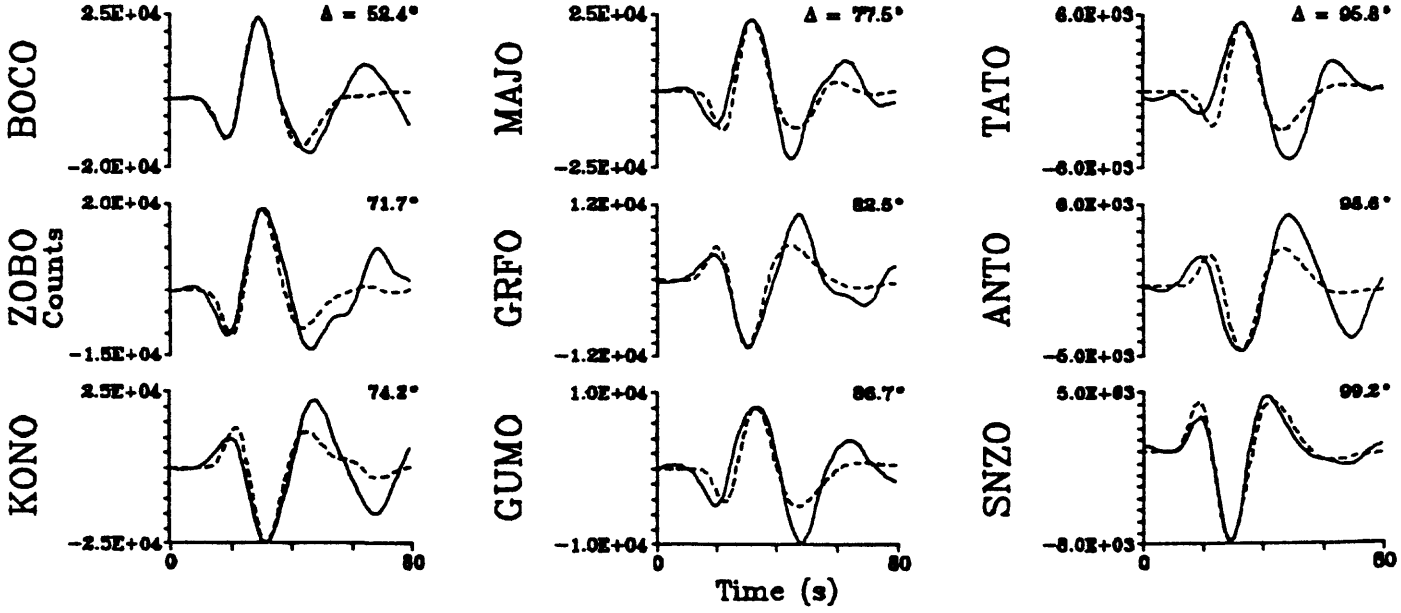

FIGURE 11

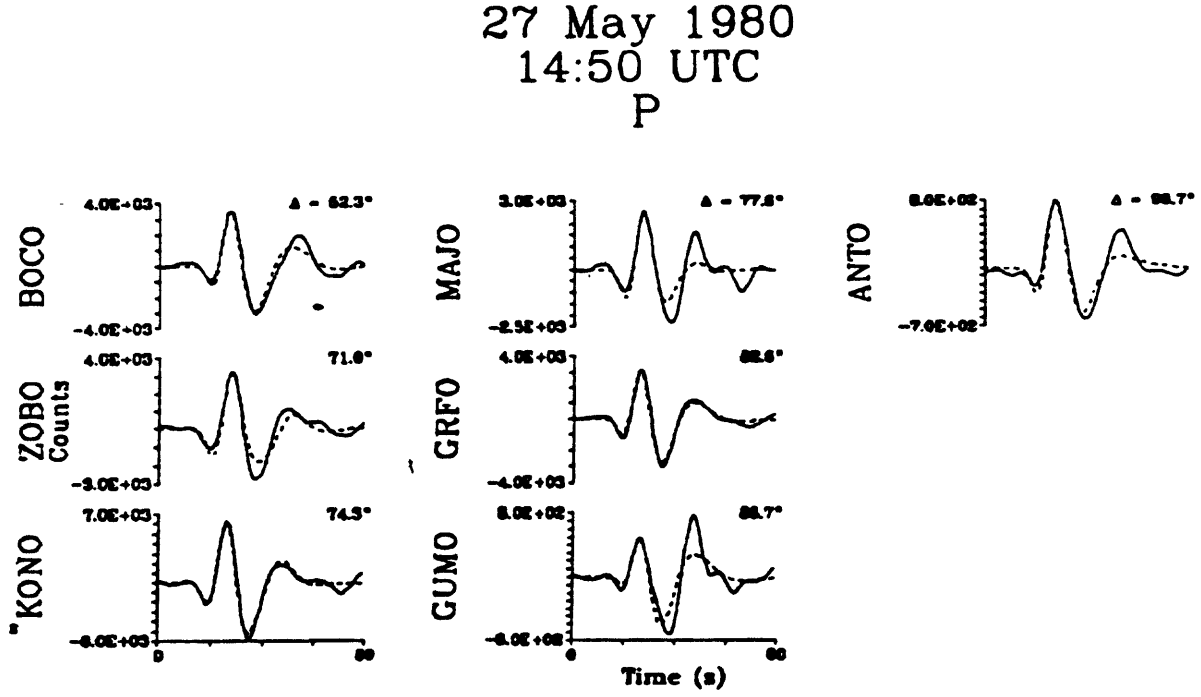
27 May 1980
14:50 UTC
P
BOCO
MAJO
ANTO
ZOBO
GRFO
KONO
GUMO
Counts
Time (s)

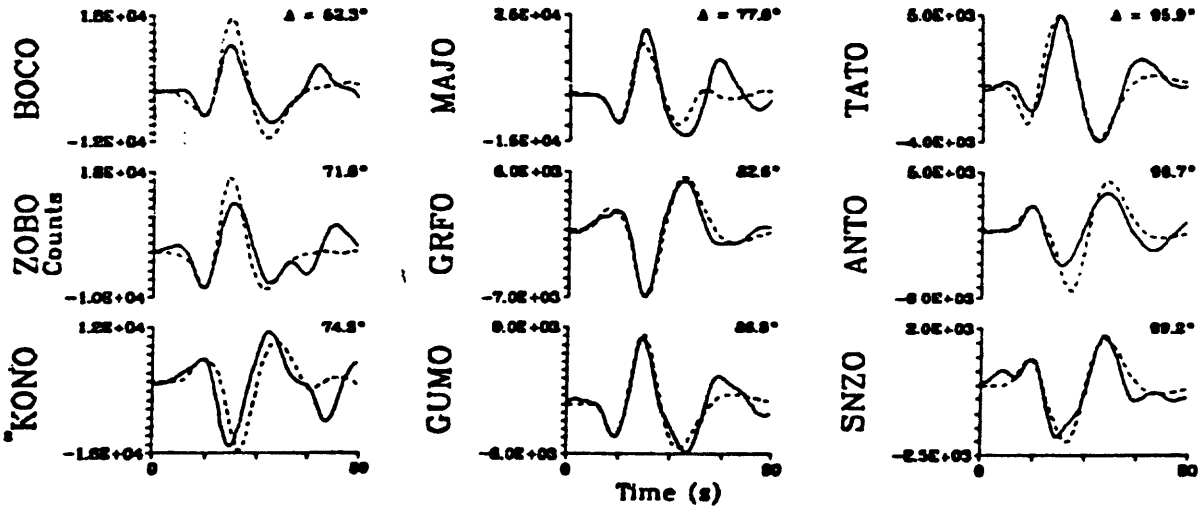
SH
BOCO
MAJO
TATO
ZOBO
GRFO
ANTO
KONO
GUMO
SNZO
Counts
Time (s)

FIGURE 12

25 May 1980
16:33 UTC

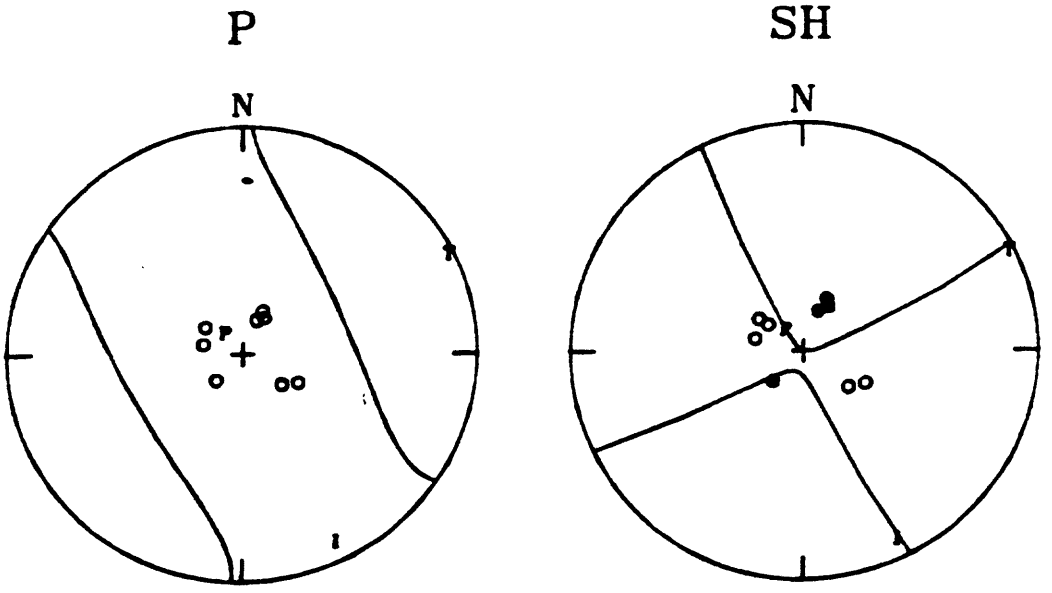

MSE / P, SH

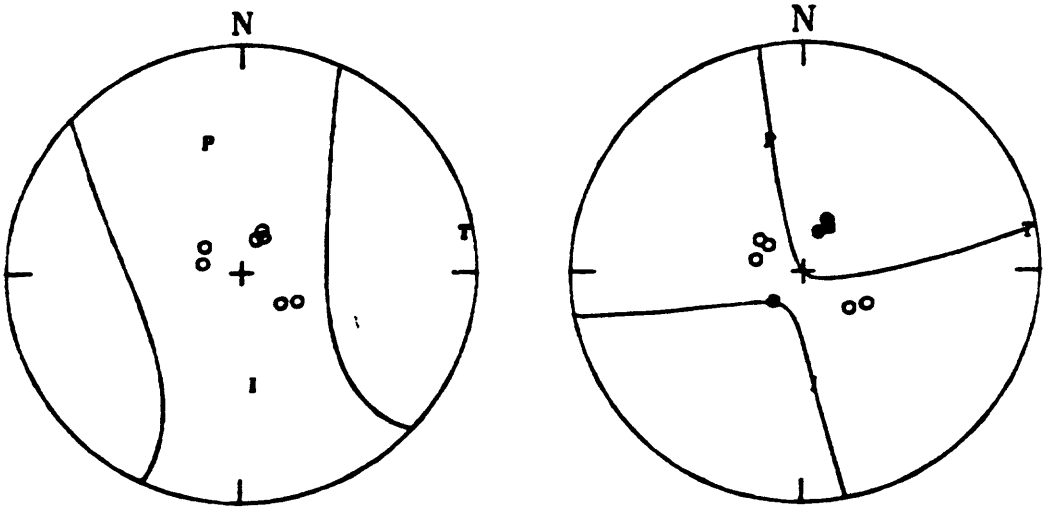

FIGURE 13

SURFACE WAVE AMPLITUDES

1980 May 25 1633:44 UTC

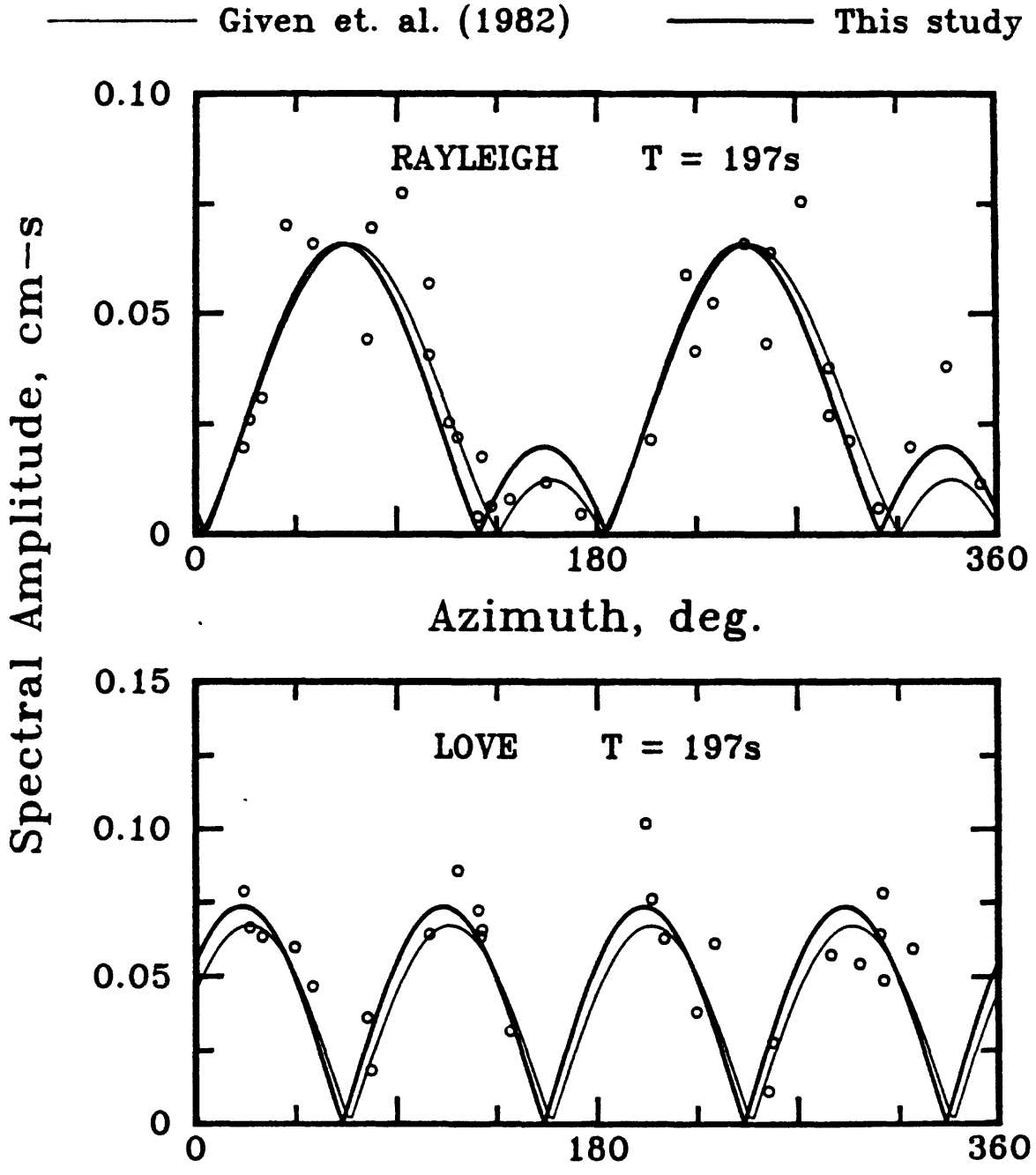

FIGURE 14

25 May 1980 16:33

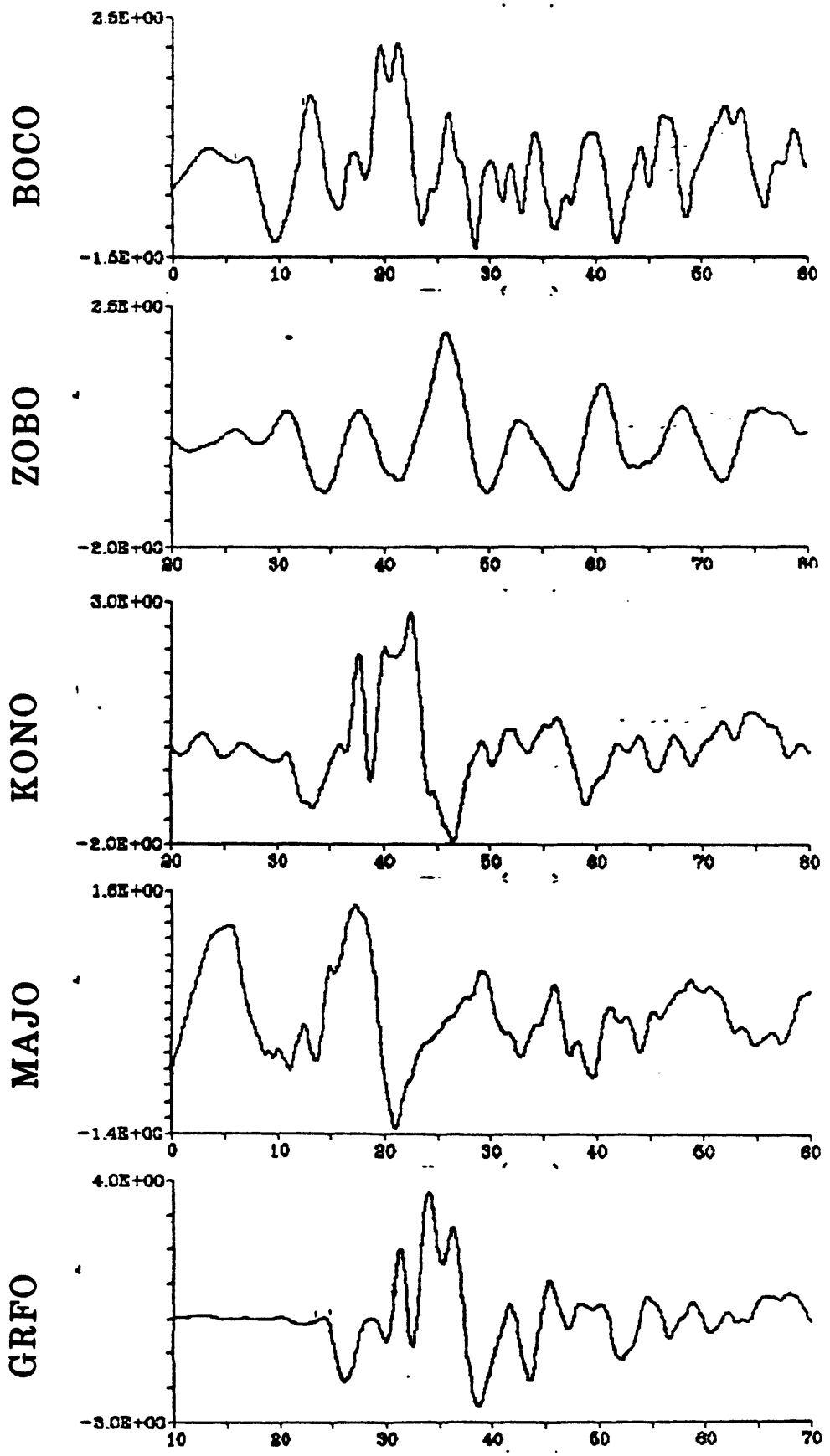

FIGURE 15

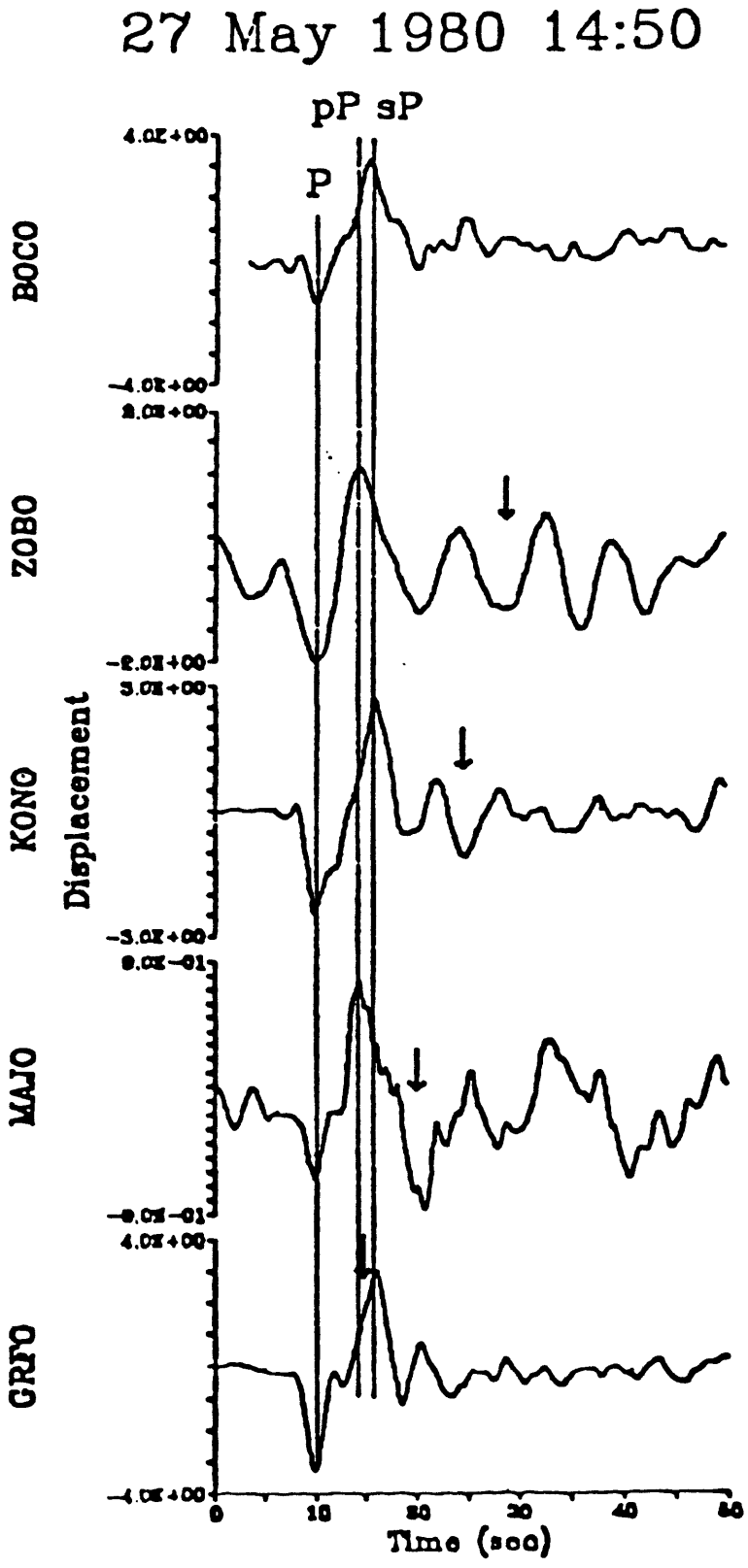
27 May 1980 14:50
pP sP
P
BOCO
ZOBO
KONO
MAJO
GRFO
Displacement
Time (sec)

FIGURE 16

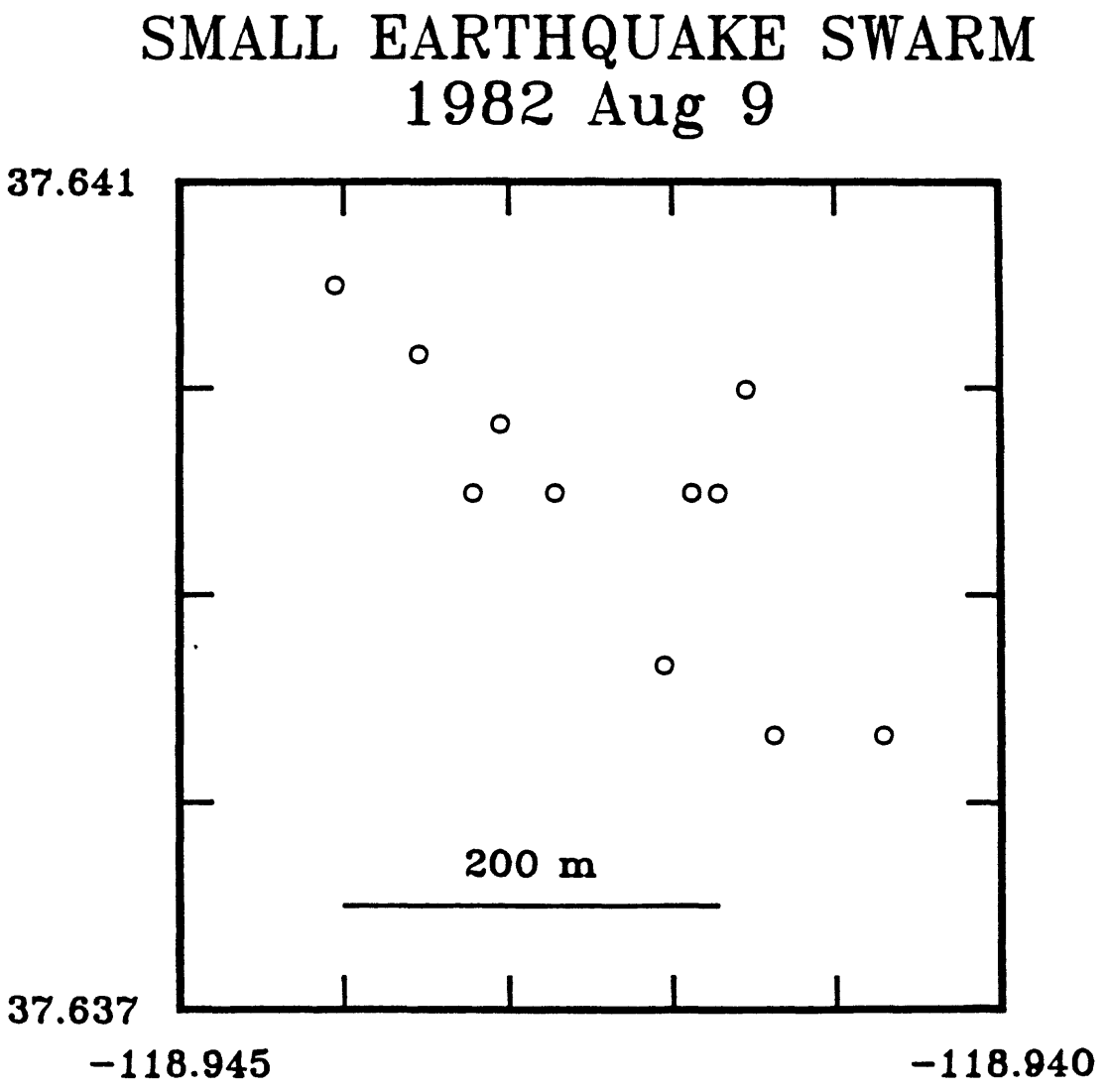

Data courtesy of Dr. Albert T. Smith
Lawrence Livermore National Laboratory

FIGURE 17

MODES OF FAILURE

NO FLUID PRESSURE
(Shear failure)

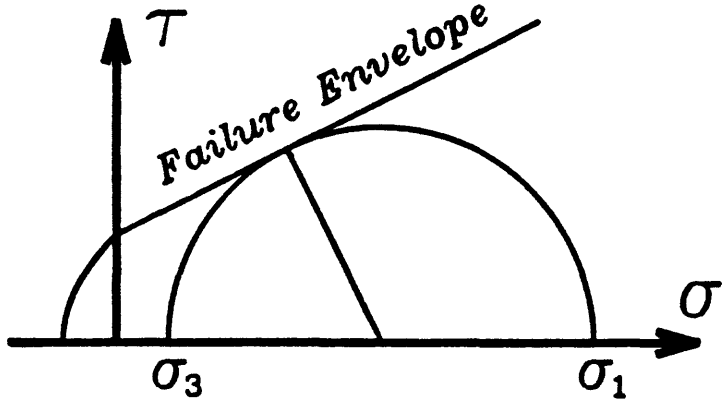

HIGH FLUID PRESSURE
(Tensile failure)

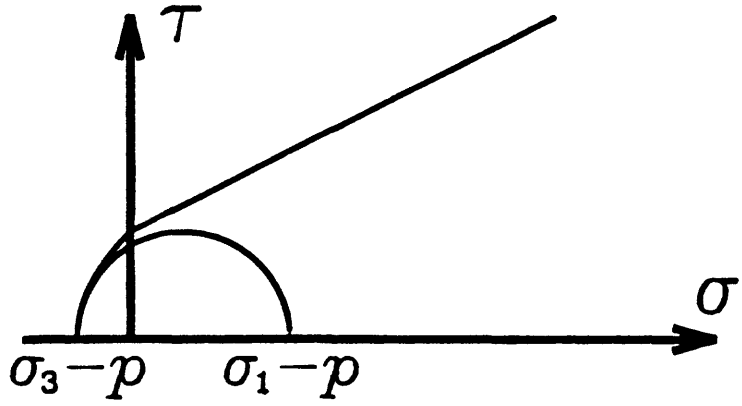

FIGURE 18

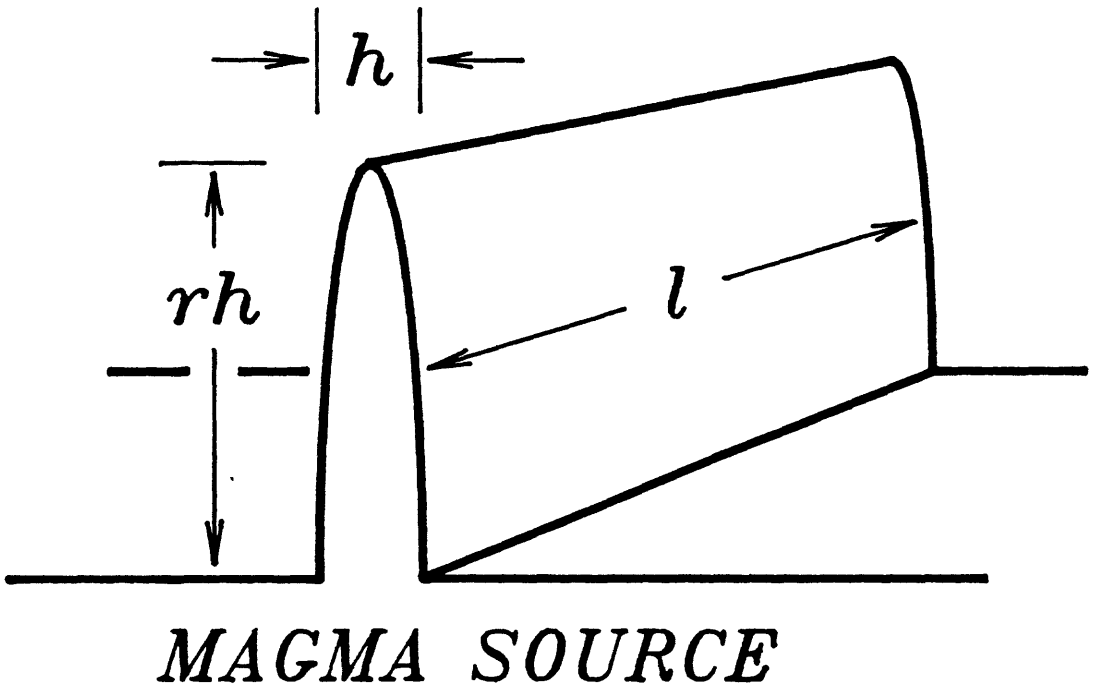

FIGURE 19

DYNAMICS OF AN EXPANDING FLUID FILLED CRACK

by

Bernard Chouet

and

Bruce R. Julian

Mail Stop 77

U.S. Geological Survey

345 Middlefield Rd.

Menlo Park, CA 94025

ABSTRACT

The dike-intrusion mechanism proposed recently by Julian and his colleagues for several large earthquakes at Long Valley caldera has stimulated new interest in the mechanics of fluid injection. This study is an attempt to resolve some of the questions raised by this interpretation by numerically simulating the dynamics of a propagating fluid-filled crack. The computations are based on the two-dimensional finite difference method developed by Madariaga [1976] that was applied by Aki *et al.*[1977] to a similar problem of a fluid-driven crack. We extend this earlier study by improving the boundary conditions applied in the plane of the crack and by analyzing a crack containing a viscous fluid that supports acoustic-wave propagation.

The problem has two time scales: the duration of the rupture, which is proportional to the distance the crack propagates, and the period of the acoustic resonance of the fluid, which is a function of the length of the crack and the acoustic velocity in the fluid. For a small extension of a long crack containing a fluid of low bulk modulus, these time scales are markedly different. The initial motion of the walls near the propagating crack tip is directed outward, so the radiated first motion is compressive everywhere. The increase of the crack-tip volume, however, induces a pressure drop in the fluid which propagates over the length of the crack with the velocity of the acoustic wave, causing a partial collapse of the wall radiated as a long-period dilatation. The dilatation following the short compressional first arrival is well marked in the vicinity of the crack plane, and for a buried vertical crack it is a conspicuous feature of the near-field vertical ground motion close to the crack trace. These properties of the signal suggest that first motion studies of this frequency-dependent source may be delicate without broadband instruments.

Inhomogeneous waves propagating at the liquid-solid interface produce high-frequency vibrations which are observed only in the immediate vicinity of the crack. The source duration depends strongly on the fluid viscosity and associated viscous damping at the crack wall; damping of the motion by the radiation of elastic waves is a comparatively small effect.

INTRODUCTION

Three of the four largest earthquakes in the Long Valley caldera area since 1978 have recently been found to have mechanisms with significant non-double-couple components in their seismic moment tensors [Barker and Langston, 1983; Julian, 1983; Ekström and Dziewonski, 1983]. The physical interpretation of these unusual events is currently a subject of controversy. Ekström and Dziewonski [1983] attribute them to simultaneous slip on normal and strike slip faults with identical tension axes; superposition of double couples will, in general, yield a non-double-couple resultant force system. On the other hand, Sipkin and Julian [1983] and Julian and Sipkin [1984] found that some events have simple source time functions and that the mechanisms do not change orientation with time. They therefore prefer a process that differs fundamentally from shear faulting, and has a non-double-couple equivalent force-system. Julian [1983] proposed that this process is the rapid opening of a crack under high internal fluid pressure. Similar earthquake-generating processes were proposed decades earlier in Japan, notably by Ishimoto [1932], who attributed many earthquakes to subterranean magma movement.

The mechanisms determined for the Long Valley earthquakes involve no significant volume change. Since an opening tensile crack has an equivalent force-system with an explosive component, [Burridge and Knopoff, 1964], an additional implosive component is required. Julian [1983] proposed that this component originates from fluid flowing into the expanding crack. At the high pressures within the earth, large voids cannot form and such fluid flow is required for tensile failure to occur. A similar suggestion was made by Haskell [1964] who pointed out that growth of a fluid-filled tensile crack would cause a sudden decrease in the fluid pressure, which would contribute an implosive component to the source.

Anomalous focal mechanisms are not restricted to the Long Valley region but have also been reported elsewhere – mostly in areas of volcanic activity [Sykes, 1967; Sykes, 1970; Klein *et al.*, 1977; Einarsson, 1979]. In a recent study of the microseismicity of the Hengill geothermal area in the Neovolcanic zone of Iceland, Foulger and Long [1984] observed that about 60% of the recorded events have non-double-couple mechanisms, which they

interpreted as evidence for tensile crack formation.

Aki [1984] has called attention to a difficulty with the interpretation of any of the anomalous earthquake mechanisms as tensile cracking. The opening of a tensile crack produces first motions that are compressional everywhere, whereas for the non-double-couple earthquakes at Long Valley and in Iceland, dilatational first motions are reported in a band of the focal sphere centered on the hypothetical crack plane. Aki suggested that the reason for this inconsistency might be difficulty in determining the true direction of first motion on seismograms. According to the theoretical results of Chouet [1981], the compressional first motion near the crack plane is small and is followed by a large dilatation which might have been misidentified as the first motion.

To evaluate the hypothesis that dike intrusion caused the anomalous earthquakes, we need a realistic model of the radiation of elastic waves from a propagating fluid-filled crack. The calculations of Chouet [1981] are based on the fluid-driven crack model of Aki *et al.*[1977]. This model uses an approximate boundary condition at the crack surface, namely $\sigma_{yy} = (2K/d)v(d/2)$, where σ_{yy} is the normal stress on the crack face, K is the bulk modulus of the fluid, d is the initial crack thickness, and $v(d/2)$ is the normal displacement of the crack face. In this approximation, the fluid behaves as a cushion; the wall stress depends only on the local displacement and the fluid does not flow or support acoustic waves. In the present study we model the fluid more accurately, extending the finite-difference method of Aki *et al.*[1977] and the model of Chouet [1984] to solve the equations for the conservation of mass and momentum in the fluid simultaneously with the elastic equations in the solid.

EQUATIONS OF MOTION

Consider a two-dimensional crack of length L, whose thickness d is much smaller than the seismic wavelengths of interest. The crack is set in the plane $y = 0$ and extends from the origin 0 to a distance L along the x axis and to $\pm\infty$ in the z direction. The displacements and stresses have no z components and are independent of z. Following Madariaga [1976] and Fehler and Aki [1978], we write the equations of motion of the elastic

solid as the hyperbolic system of first-order equations,

$$\begin{aligned}
\frac{\partial}{\partial t}\sigma_{yy} &= \lambda\frac{\partial \dot{u}}{\partial x} + (\lambda+2\mu)\frac{\partial \dot{v}}{\partial y}, \\
\frac{\partial}{\partial t}\sigma_{xx} &= (\lambda+2\mu)\frac{\partial \dot{u}}{\partial x} + \lambda\frac{\partial \dot{v}}{\partial y}, \\
\frac{\partial}{\partial t}\sigma_{xy} &= \mu\left(\frac{\partial \dot{u}}{\partial y} + \frac{\partial \dot{v}}{\partial x}\right), \\
\frac{\partial}{\partial t}\dot{u} &= \frac{1}{\rho_1}\left(\frac{\partial}{\partial x}\sigma_{xx} + \frac{\partial}{\partial y}\sigma_{xy}\right), \quad \text{and} \\
\frac{\partial}{\partial t}\dot{v} &= \frac{1}{\rho_1}\left(\frac{\partial}{\partial x}\sigma_{xy} + \frac{\partial}{\partial y}\sigma_{yy}\right),
\end{aligned} \tag{1}$$

where λ and μ are the Lamé elastic moduli, ρ_1 is the density of the solid, u and v are the x and y components of displacement, and σ_{xx}, σ_{yy} and σ_{xy} are the components of stress.

In the long wavelength limit, the motion of the fluid in the crack is dominantly longitudinal, and is described by the equation of conservation of momentum,

$$\frac{1}{\rho_2}\frac{\partial p}{\partial x} + \frac{2}{\rho_2 d}\tau + \frac{\partial V}{\partial t} = 0, \tag{2}$$

and the equation of continuity,

$$\frac{1}{\rho_2 a^2}\frac{\partial p}{\partial t} + \frac{2}{d}\frac{\partial}{\partial t}v(d/2) + \frac{\partial V}{\partial x} = 0. \tag{3}$$

In these equations, ρ_2 is the fluid density, τ is the viscous shear stress at the crack wall, p is the fluid pressure, V is the flow velocity, t is time, a is the acoustic wave velocity in the fluid, and $v(d/2)$ is the transverse displacement of the crack wall. Note that we neglect convective terms such as $V\partial V/\partial x$ in (2) and $V\partial\rho_2/\partial x$ and $V\partial v/\partial x$ in (3) under the assumption that the flow velocities are small compared to the acoustic velocity in the fluid. In addition, we relate the shear stress at the crack wall to the fluid velocity by assuming a laminar flow:

$$\tau = \frac{6\eta V}{d}, \tag{4}$$

where η is the viscosity of the fluid.

To deal with the flow of the fluid, we first transform equations (2) and (3) into ordinary differential equations using the method of characteristics. Multiplying equation (3) by an undetermined coefficient Λ and adding the result to equation (2), we get

$$\frac{\Lambda}{\rho_2 a^2}\left(\frac{\partial p}{\partial t}+\frac{a^2}{\Lambda}\frac{\partial p}{\partial x}\right)+\left(\frac{\partial V}{\partial t}+\Lambda\frac{\partial V}{\partial x}\right)+\frac{12\eta}{\rho_2 d^2}V+\frac{2\Lambda}{d}\dot{v}(d/2)=0. \tag{5}$$

Now if we choose $\Lambda=\pm a$, then the parenthesized expressions become

$$\frac{\partial p}{\partial t}\pm a\frac{\partial p}{\partial x} \quad \text{and} \quad \frac{\partial V}{\partial t}\pm a\frac{\partial V}{\partial x},$$

which are in the form of total derivatives along the characteristic curves $x\mp at=constant$. The desired ordinary differential equations are

$$\frac{1}{\rho_2 a}\frac{dp}{dt}+\frac{dV}{dt}+\frac{12\eta}{\rho_2 d^2}V+\frac{2a}{d}\dot{v}(d/2)=0 \quad \text{along} \quad x-at=constant, \tag{6}$$

and

$$-\frac{1}{\rho_2 a}\frac{dp}{dt}+\frac{dV}{dt}+\frac{12\eta}{\rho_2 d^2}V-\frac{2a}{d}\dot{v}(d/2)=0 \quad \text{along} \quad x+at=constant. \tag{7}$$

These equations are to be solved together with equations (1) under appropriate initial and boundary conditions.

INITIAL AND BOUNDARY CONDITIONS

In the solid medium, the stress σ_{xy} and the transverse displacement v are both odd functions of y and thus vanish in the plane of the crack. The normal stresses σ_{xx}, σ_{yy}, and the displacement u, on the other hand, are even functions of y. These symmetries reduce the problem to solving equations (1) in the upper half-plane $(y>0)$ subject to the following boundary conditions on $y=0$:

$$\sigma_{xy}=0 \quad \text{for} \quad x<0 \quad \text{and} \quad x\geq L-\Delta l;$$

$$\sigma_{xy}=-\tau \quad \text{and} \quad \sigma_{yy}=-p \quad \text{for} \quad 0\leq x<L-\Delta l;$$

$$\sigma_{yy}=2K\frac{v(d/2)}{d} \quad \text{for} \quad L-\Delta l\leq x\leq L; \tag{8}$$

$$u = V \qquad \text{for} \quad x = 0;$$

$$v = 0 \qquad \text{for} \quad x \leq 0 \quad \text{and} \quad x \geq L.$$

where Δl represents the length of the incremental crack extension. The solution of the flow problem requires an additional condition describing the flow at the expanding crack tip. This condition is provided by the equation of continuity,

$$V\Big|_{x=L-\Delta l} = \frac{2\Delta l}{d}\dot{v}(d/2), \tag{9}$$

which expresses the equality between the rate of fluid flow into the crack tip and the rate of increase of the crack-tip volume.

We follow Aki *et al.*[1977] in formulating the initial conditions. Suppose the crack contains a fluid whose pressure exceeds the ambient compressive stress in the surrounding medium. As Aki *et al.*[1977] discussed, the crack tip may propagate rapidly if the internal pressure is high enough and if either (1) the material strength varies from place to place, or (2) the dynamic value of the critical stress-intensity factor for failure is lower than its static value. In either case, the crack area increases suddenly by ΔS. The stress in the solid, which was initially tensional ahead of the crack tip, drops suddenly to zero and then quickly becomes compressive as fluid flows into the newly-formed part of the crack. The dynamic motion of the crack surface triggered by the extension of the crack tip may then be considered as the response of the crack to a pressure step of amplitude ΔP applied over the incremental area ΔS. Although we realize that the viscosity of the fluid must be a rate-limiting factor in the rupture process, we do not dwell on the complexities of crack tip dynamics here. Rather, we assume that the rupture front propagates with infinite velocity and that the pressure step is applied instantaneously over ΔS.

METHOD OF COMPUTATION

To solve the equations of motion (1) and the flow equations (6) and (7) with the boundary conditions (8) and (9) we use the method of finite differences. Since $\partial x/\partial t = a$ represents a characteristic over which (6) is valid while $\partial x/\partial t = -a$ similarly applies to

(7), the solution for pressure and flow velocity is obtained by the intersection of these characteristics in the $x-t$ plane. We can transform equations (6) and (7) into the difference equations

$$\frac{1}{\rho_2 a}(p_P - p_A) + V_P - V_A(1 - \frac{12\eta}{\rho_2 d^2}\Delta t) + \frac{2a}{d}\Delta t \dot{v}_A(d/2) = 0, \tag{10}$$

and

$$\frac{-1}{\rho_2 a}(p_P - p_B) + V_P - V_B(1 - \frac{12\eta}{\rho_2 d^2}\Delta t) - \frac{2a}{d}\Delta t \dot{v}_B(d/2) = 0, \tag{11}$$

with the solutions

$$p_P = \frac{1}{2}\left\{\rho_2 a(1 - \frac{12\eta}{\rho_2 d^2}\Delta t)(V_A - V_B) + p_A + p_B - \frac{2K}{d}\Delta t[\dot{v}_A(d/2) + \dot{v}_B(d/2)]\right\} \tag{12}$$

and

$$V_P = \frac{1}{2}\left\{(1 - \frac{12\eta}{\rho_2 d^2}\Delta t)(V_A + V_B) + \frac{1}{\rho_2 a}(p_A - p_B) - \frac{2a}{d}\Delta t[\dot{v}_A(d/2) - \dot{v}_B(d/2)]\right\}, \tag{13}$$

in which

$$\begin{aligned} p_A, V_A &= p, V(x, t), \\ p_B, V_B &= p, V(x + 2\Delta x, t), \text{ and} \\ p_P, V_P &= p, V(x + \Delta x, t + \Delta t), \end{aligned} \tag{14}$$

where Δx and Δt denote the grid intervals in space and time. Using the particle velocities $\dot{v}$ obtained from (1), together with (9) and the condition $u = V$ in (8) completely defines the solutions (12) and (13).

An effective numerical method for solving the system of equations (1) is the leap-frog finite-difference scheme developed by Madariaga [1976] and used by Aki *et al.*[1977] and Fehler and Aki [1978]. We let the crack tip propagate by one grid space and simulate this initial condition by applying a pressure step ΔP at this grid point. Using the finite-difference method we then compute the particle velocities and the time derivatives of stresses. Displacements and stresses are obtained by integrating these solutions with respect to time. The resulting static field thus represents the opening of the crack relative to its initial thickness prior to the extension. Setting $\Delta x = \Delta y = \Delta$, the grid spacing, the

velocity $\dot{u}$ is obtained at the position $[n\Delta, m\Delta]$, the velocity $\dot{v}$ at $[(n+\frac{1}{2})\Delta, (m+\frac{1}{2})\Delta]$, the stresses σ_{xx} and σ_{yy} at $[(n+\frac{1}{2})\Delta, m\Delta]$, and the stress σ_{xy} at $[n\Delta, (m+\frac{1}{2})\Delta]$. The boundary conditions for $\dot{v}$ and σ_{xy} must be imposed one-half grid-space away from the crack, at $y = \Delta/2$, whereas those for $\dot{u}$, σ_{xx} and σ_{yy} are imposed on the crack wall, at $y = 0$. Thus the crack stiffness effectively includes the elasticity of layers of rock, one half grid space thick, on either side of the crack. The effect of this layer of rock is the main limitation on the accuracy with which we can describe the crack parameters with this numerical scheme.

In the model used by Aki *et al.*[1977], the boundary conditions in the plane $y = 0$ are $\sigma_{xy} = 0$ for $-\infty \leq x \leq \infty$ and $\sigma_{yy} = (2K/d)v(d/2)$ for $0 \leq x \leq L$. These conditions are approximated in the numerical grid by setting $\sigma_{xy}[n\Delta, \frac{\Delta}{2}] = 0$ for all x, $\sigma_{yy}[(n+\frac{1}{2})\Delta, 0] = (2K/d)v[(n+\frac{1}{2})\Delta, \frac{\Delta}{2}]$ for $0 \leq x \leq L$, and $\sigma_{yy}[(n+\frac{1}{2})\Delta, 0] = 0$ for $x < 0$ and $x > L$. The stress $\sigma_{xx}[(n+\frac{1}{2})\Delta, 0]$ and velocity $\dot{u}[n\Delta, 0]$ are both set to zero on the crack plane, while the velocity $\dot{v}[(n+\frac{1}{2})\Delta, \frac{\Delta}{2}]$ is only calculated for $0 \leq x \leq L$ and assumed to be zero for $x < 0$ and $x > L$.

These boundary conditions can be improved by computing $\dot{u}$, σ_{xx}, and σ_{yy} on the plane $y = 0$ and using the antisymmetry of σ_{xy} and $\dot{v}$ about this plane. Instead of setting $\sigma_{yy}[(n+\frac{1}{2})\Delta, 0] = 0$ and $\dot{v}[(n+\frac{1}{2})\Delta, \frac{\Delta}{2}] = 0$ for $x < 0$ and $x > L$, and $\sigma_{xx}[(n+\frac{1}{2})\Delta, 0] = 0$ for $-\infty \leq x \leq \infty$, we calculate these values in the normal fashion using the relation $\dot{v}[(n+\frac{1}{2})\Delta, \frac{\Delta}{2}] = -\dot{v}[(n+\frac{1}{2})\Delta, -\frac{\Delta}{2}]$. Likewise, the velocity $\dot{u}$ is obtained on the crack plane by using the relation $\sigma_{xy}[n\Delta, \frac{\Delta}{2}] = -\sigma_{xy}[n\Delta, -\frac{\Delta}{2}]$. Once $\dot{u}[n\Delta, 0]$ is known, the stress $\sigma_{xy}[n\Delta, \frac{\Delta}{2}]$ is fixed for all x and the earlier approximation $\sigma_{xy}[n\Delta, \frac{\Delta}{2}] = 0$ is no longer required.

In Figure 1, the results obtained by Aki *et al.*[1977] are compared with those obtained using this modified approach for the cases of a dry and a wet crack. These plots show the normal displacement calculated at 20 points on the crack surface as a function of time for an increment $\Delta l = L/20$ in the crack length. Here and in subsequent figures, the quantity plotted is the dimensionless combination $\mu v/(L\Delta P)$, termed the dimensionless displacement, and the independent variable is the dimensionless time, $\alpha t/L$, where α denotes the compressional velocity of the solid. The fluid does not flow or support acoustic

waves in these models, and its effect is characterized by the parameter $C = (K/L)(\mu/d)$, called the crack stiffness. The value $C = 0$ represents a dry crack, while the value $C = 5$ corresponds to a crack filled with magma (see Aki *et al.*[1977] and Chouet [1981], for details). The two approaches give significantly different results. The main features of interest in our model are the absence of ringing of the crack wall, the smaller overshoot of the initial opening for the wet crack and the absence of overshoot for the dry crack, the distinct closure of the crack wall caused by the the shear wave radiated from the propagating tip, and the reduced amplitude and broader shape of the static opening. The Rayleigh wave dominates the dynamic response after the first reflection at the stable tip of the dry crack. The long-period motion associated with the multiple reflections of this wave are not seen in Aki's model. For the wet crack the reflected phases are small, and apart from the difference in the ringing characteristics, the variations between the solutions are less obvious.

There is, however, an additional constraint on the numerical solution, which cannot be exactly met with the above scheme when the boundary conditions (8) are used. Clearly, to include the effect of the viscous shear stress at the crack wall, we cannot simply use the antisymmetry of σ_{xy}. Instead, we set $\sigma_{xy}[n\Delta, \frac{\Delta}{2}] = -\tau$, which is actually the stress on the crack face. Thus, we are unable to fully account for the finite thickness of the crack in our numerical representation. As discussed by Fehler and Aki [1978] this approach to the crack problem appears to be adequate as long as $K/\mu \ll 1$ and the crack thickness d is small. A complete two-dimensional treatment of the visco-elastic field in the crack must be undertaken when these conditions are not met.

Defining $H = \Delta t/\Delta$, the condition for stability of the numerical solution in the solid is given by [Madariaga, 1976]

$$H \leq \frac{1}{\sqrt{2}\alpha}. \tag{15}$$

For the acoustic field in the crack the grid spacing and time step are related by

$$H_a = \frac{\Delta t_a}{\Delta x_a} = \frac{1}{a}. \tag{16}$$

Taking $\Delta t_a = \Delta t$ then provides the condition $\Delta x_a = aH\Delta$, and choosing $H = 1/(2\alpha)$

we obtain

$$\Delta x_a = \frac{a}{2\alpha}\Delta. \tag{17}$$

To satisfy this requirement when $a \leq \alpha$ we interpolate between the values of $\dot{v}$ at $[(n + \frac{1}{2})\Delta, \frac{\Delta}{2}]$ using the method of Wiggins [1976].

Various tests of the validity and convergence of the leap-frog finite difference scheme used in the computation of the elastic field can be found in Madariaga [1976] and Fehler and Aki [1978]. These tests show that the solution is accurate for wavelengths longer than about 5 grid spacings, but exhibits spurious dispersion for shorter wavelengths. The numerical solution is thus reliable for wavelength $\lambda > 5L/n$, or wavenumber $k = 2\pi/\lambda < 2n\pi/(5L)$, where n is the number of grid points over the length of the crack. The finite-difference solution of the flow equations (12) and (13) is inherently stable, so the accuracy of the computed acoustic field in the crack depends only on the accuracy of the interpolation between sampled values of the elastic solution. This accuracy can be improved by increasing the density of grid points. To avoid spurious effects caused by the boundary of the mesh, we make the size of the grid space large enough so that no waves reflected from the boundary arrive back at the crack during the time interval of interest.

RESPONSE OF THE CRACK TO AN INCREMENTAL EXTENSION OF ITS TIP

Examples of the response of the crack wall to a sudden extension of the crack tip are shown in Figures 2 through 8. These examples were calculated assuming a Poisson's ratio of $\frac{1}{4}$ in the solid and $K/\mu = 0.1$. The effect of the fluid in the crack depends on three dimensionless parameters: the crack stiffness $C = (K/\mu)(L/d)$, the viscous damping loss $F = 6(\eta/K)(a/d)$, and the velocity ratio $G = \alpha/a$. Table I summarizes the values of these parameters for the cases displayed in the figures.

The value of 0.1 for the ratio K/μ is appropriate for a liquid containing a small concentration of bubbles (see Aki *et al.*[1978] for a discussion). We assume that bubbles exsolve from the liquid as a result of the pressure drop induced by the opening of the crack. Adequate data on the physical properties of magma in situ are not available, so this

value is only a rough guess. The ratio K/μ determines the crack stiffness factor and also the ratio between the velocities of the compressional wave in the solid and the acoustic wave in the fluid. The aspect ratio L/d observed for dikes in nature ranges from 10^3 to values perhaps as low as 10. Hence the crack stiffness can vary between 10^2 and 1 for our choice of K/μ. Unfortunately, because the grid is offset by half a unit from the crack face, we cannot model cracks that are very stiff. Here we have taken the value $C = 5$ as the upper limit compatible with our representation of the crack.

The choice of the parameter G is limited by the number of grid spaces used to discretize the crack (see equation (17)) which strongly affects the amount of computational labor required to solve the equations. We have limited our consideration to ratios α/a of 2 and 4, which are the lowest values compatible with our choice of K/μ.

Figure 2 displays the normal component of the particle velocity at the crack surface as a function of time and distance across the crack. The source parameters are $C = 5$, $F = 0$ (i.e., the fluid is inviscid) and $G = 2$. The crack is initially 39 grid spaces long and propagates by $\Delta l = L/40$. The opening velocity is depicted over $1\frac{1}{4}$ cycles of motion, clearly showing the onset of the disturbance at the expanding tip and its propagation over the crack wall. The motion of the crack faces is dominated by the acoustic wave, which consists of a train of short-period low-amplitude wavelets followed by a larger longer-period oscillation. This large low-frequency wave has the characteristics of the long-period Stoneley waves observed in fluid-filled boreholes [Biot, 1952; Cheng and Toksöz, 1981] and corresponds to the "water hammer" wave in pipes [Wylie and Streeter, 1978]; its arrival is delayed by elastic yielding of the crack wall. This is in harmony with the approximation made in the study of tube waves at low frequencies, where the elasticity of the pipe effectively lowers the acoustic velocity [Halliwell, 1963; White, 1965]. Except in the immediate vicinity of the expanding tip, the motion associated with the arrival of this dominant long-period wave is clearly negative, corresponding to a closure of the crack.

The normal displacement of the crack face is shown in Figure 3 for an extension $\Delta l = L/20$. As in figure 1, the value plotted is a dimensionless combination of the applied pressure step, the crack length, and the rigidity and compressional velocity of the rock matrix. Of particular interest in this figure is the direction of the dominant motion

following the first arrival at various locations on the crack surface. The initial motion at the propagating tip of the crack is an opening. Elsewhere, however, the dominant motion immediately following the onset of the signal clearly corresponds to a closure of the crack faces. This closure occurs because the opening of the crack tip produces a pressure drop in the fluid, which propagates across the crack at the Stoneley-wave velocity. This phenomenon is different from the closure seen for a dry crack (Fig. 1), which is caused by the shear wave radiated by the rupture. Figure 4 is the same as Figure 3, but covers a longer interval and suggests that the pattern of static displacement of the crack face is similar to that of the dynamic motion, with a net closure near the stable tip and opening near the propagating tip.

For a crack containing a non-viscous fluid, the only mechanism of energy loss is elastic-wave radiation into the solid. The effect of this loss is obvious in Figures 3 and 4 for high frequencies, which are rapidly damped. The lower frequencies, on the other hand, are only weakly damped by radiation losses, indicating that the elastic energy is a trivial part of the available acoustic energy in the fluid at these frequencies, and confirming the assumption made earlier by Chouet [1984].

The effect of viscous dissipation in the fluid is illustrated in Figure 5. Here the viscous damping is given by the parameter $F = 0.01$. The factors C and G and the extension Δl are kept unchanged, so this figure offers a direct comparison with the case of an inviscid fluid depicted in Figure 3. The fluid viscosity does not affect the amplitude of the first motion at the expanding tip or the static opening of the crack. The energy loss caused by viscous dissipation at the wall, however, strongly affects the duration of the dynamic motion. This loss effectively decreases the amplitude of the negative first motion near the stable tip of the crack but does not markedly modify the shape or period of the signal over the first few cycles of oscillation.

The motion of the crack has two time scales: that of the tensile failure, which depends on the distance Δl the crack extends, and that of the acoustic resonance, which is proportional to the length L of the crack. This is best demonstrated by comparing the motion shown in Figure 3 with that depicted in Figure 6 for a crack extending by $\Delta l = L/40$, that is, one half of the value assumed earlier. The length of the crack is

unchanged, so the period of the acoustic resonance is the same in both cases. The period of the high-frequency response of the wall associated with the crack extension, on the other hand, is reduced by a half in direct proportion to the distance the crack propagates. Also, the amplitude of the maximum crack opening is smaller by a factor of 1.76 when Δl is halved.

Figures 7 and 8 show the effect of lowering the acoustic velocity in the fluid. Keeping all other source parameters identical to those of Figure 6, we set $G = 4$ and first consider the wall response to an extension $\Delta l = L/40$ (Figure 7). Before the acoustic arrival, another wave is clearly identifiable propagating across the crack with a velocity slightly lower than the shear velocity in the solid and attenuating rapidly on reflection at the non-expanding tip. This wave train consists of pseudo-Rayleigh waves similar to the guided waves that propagate along the solid-fluid interface in a fluid-filled borehole [e.g., Cheng and Toksöz, 1981]. A better picture of these waves is offered in Figure 8, which displays the transverse particle velocity at 160 locations on the surface of a crack extending by $\Delta l = L/160$. They are highly dispersive, having phase velocities bounded by the shear velocity of the rock at low frequencies and approaching the acoustic velocity of the fluid at higher frequencies. Also apparent in the figure is the weak P wave, which rapidly attenuates away from the propagating tip of the crack. The effects of both the P wave and the pseudo-Rayleigh wave are limited to the immediate vicinity of the crack. (In the far field, the main result of halving the speed of the acoustic wave is to double the period of acoustic resonance of the crack.)

NEAR FIELD GROUND MOTION

We have used the discrete wave-number method [Bouchon, 1979; Chouet, 1981, 1982] to calculate the near-field ground motion corresponding to one of the crack models discussed above. The models we have treated in this paper are two-dimensional, extending to infinity in the $\pm z$ directions. The theoretical waveforms for such infinite cracks, however, have artificial and unrealistic features, so we arbitrarily limit the dimension of the crack to a finite value. In doing this, we implicitly neglect the effect of the ends of the crack upon the

motion. Our calculation is carried out for a vertical crack with the horizontal dimension of $2\,km$ and depth extent of $1\,km$, buried $5\,km$ below the surface of a homogeneous elastic half space with compressional velocity $\alpha = 3\ km/s$, shear velocity $\beta = \alpha/\sqrt{3}\,km/s$ and density $\rho = 2.7\ g/cm^3$. The crack is oriented so that its motion depends on the horizontal coordinate only, and is independent of depth on the crack plane. The source considered is shown in Figure 5, and corresponds to a crack extension $\Delta l = 100\ m$.

The configuration of the problem is depicted in Figure 9. The representation of the displacements is carried out at 15 locations set along 5 transverse profiles spaced at equal intervals of $1.5\,km$ in the longitudinal direction. The crack trace extends between the coordinates $[0,0]$ and $[2,0]$, with the epicenter located at the latter position, so that profile 3 bisects the crack plane while profiles 2 and 4 are positioned $0.5\,km$ beyond the crack tips. Each profile has three receivers, positioned at 0, 1.5, and $3\,km$ from the crack plane. The u and v components are the horizontal displacements parallel and normal to the crack, respectively, and w is the vertical displacement.

The three components of the ground motion, normalized to a pressure step ΔP of unity, are shown in Figure 10. The records start at the arrival of the compressional wave and are about $4s$ in duration. The arrival times of various compressional (P) and shear (S) phases are indicated by arrows. Waves generated at the propagating end of the crack are marked by the subscript "0", and those generated by the first reflection of the acoustic wave at the opposite end are indicated by the subscript "1". In addition, a superscript "0" identifies arrivals from the upper edge of the crack and a superscript "1" identifies those from the lower edge.

Because the transverse displacement is antisymmetric about the crack plane, the normal component of horizontal motion vanishes on the crack trace. The first motion, naturally, is everywhere compressive, since the onset of the signal is produced by the initial opening at the propagating crack tip. The duration of this compressive pulse is the interval between the arrivals P_0^0 and P_0^1 from the top and bottom of the propagating crack edge. Note that the first motion is negative on the longitudinal component over the first three profiles because these are located to the left of the epicenter; in all cases the motion is away from the epicenter.

The next arrival of importance is the shear phase from the propagating crack edge. Its duration is controlled by the arrivals S_0^0 and S_0^1. This phase is characterized by a strong outward motion on the transverse horizontal component and by a somewhat weaker inward motion on the parallel component. Vertical motion exhibits a reversal of polarity for this arrival, from a clear upward onset on the crack trace to a strong downward motion at some distance from the crack plane. Another phase with similar characteristics follows the shear arrival S_1^1. This wave is generated by the acoustic wave in the fluid impinging on the stable crack tip, and is well developed on the transverse and vertical components at increasing distances from the source.

The phases $[P_0^0, P_0^1]$ and $[S_0^0, S_0^1]$ are both followed by a longer-period signal of opposite polarity, generated by the closure of the crack faces as fluid flows toward the expanding crack tip. In the immediate vicinity of the source, this motion of the crack wall produces a long-period dilatation on all three components. This dilatation is strongest on the vertical component near the rupture front, where it lasts about five times longer than the initial compression. The downward motion of the ground above the expanding tip of the crack resembles the static displacement [Chouet, 1981] and appears to be dominantly a near field property. The dilatation quickly diminishes in size with distance from the crack plane, becoming a compression a few kilometers away. At these distances the compressional first motion observed on the vertical displacement lasts until the arrival of the shear phase S_0^0. For a shallower source (Figure 11), the dilatation is larger, but its spatial extent is reduced. This is again in harmony with the reduced but more sharply marked area of static deformation above the source.

FAR FIELD COMPRESSIONAL WAVE

In this section, we compute theoretical far-field waveforms of compressional waves radiated by a propagating fluid-filled crack, starting from the results computed earlier for the motion of the walls. Consider a vertical crack that lies in the $x-z$ plane of a Cartesian coordinate system and whose upper edge propagates upward (see Figure 12). We assume that the crack has a finite width in the x direction. Following Burridge and Knopoff [1964]

and Madariaga [1976], we express the radial displacement in the far-field as an integral over the crack surface:

$$u(\vec{R},t) = \frac{1}{4\pi\rho\alpha^3 R} S_{\theta\phi} \int\int dS\, \Delta\dot{u}_y \left(\vec{r},\, t - \frac{R - (\hat{R}\cdot\vec{r})}{\alpha} \right), \tag{18}$$

where $\vec{R}$ defines the observation point, $R = |\vec{R}|$, $\hat{R}$ is the unit vector in the $\vec{R}$ direction, $\vec{r}$ defines position on the crack surface, and $S_{\theta\phi} = \lambda + 2\mu \sin^2\theta \sin^2\phi$ is the radiation pattern for a tensile crack (e.g., Chouet [1979]). Since the motion of the crack face, Δu_y, is independent of x, the waveform can be expressed as

$$\begin{aligned} u(\vec{R},t) &= \frac{1}{4\pi\rho\alpha^3 R} S_{\theta\phi} \int dx \int dz\, \Delta\dot{u}_y \left(z,\, t - \frac{R - x\sin\theta\cos\phi - z\cos\theta}{\alpha} \right) \\ &= \frac{1}{4\pi\rho\alpha^3 R} S_{\theta\phi} \int dx\, F\left(t - \frac{R - x\sin\theta\cos\phi}{\alpha} \right), \end{aligned} \tag{19}$$

where

$$F(t) \equiv \int dz\, \Delta\dot{u}_y \left(z,\, t + \frac{z\cos\theta}{\alpha} \right). \tag{20}$$

Thus each element dx of width of the crack makes an identical contribution $F(t)$ to the total waveform, but the contribution is delayed by the amount $(x/\alpha)\sin\theta\cos\phi$. In other words, the effect of the finite crack width is to smooth the waveforms by convolving them with a "boxcar" function of duration $(W/\alpha)\sin\theta\cos\phi$. For this qualitative discussion, we avoid this complication and display only $F(t)$, the contribution of a single element of infinitesimal width. In this case, the shape of the waveform depends only on θ, although its amplitude depends on both θ and ϕ.

The computed waveforms are shown in Figures 13 through 16, each of which displays the function $F(t)$ for several values of θ between 0 and 180°. High-frequency components that are contaminated by numerical noise have been supressed by filtering the waveforms with recursive digital filters with a 3-pole low-pass Bessel (maximally flat delay) response and a corner frequency of $2\,Hz$.

Figure 13 shows the waveforms for a crack of stiffness $C = 5$ and velocity ratio $G = 2$ that contains an inviscid fluid. The crack tip propagates a distance of one twentieth of the total crack length ($\Delta l = L/20$). The motion on the crack faces for this case is shown

above in Figures 3 and 4. The waveforms displayed in Figure 13 all begin with a strong but brief compression which originates at the propagating crack tip. This compression is followed by a weak dilatation that persists for the entire duration of the displayed signal, but is interrupted by pulses generated by successive Stoneley waves impinging on the ends of the crack. The shape of this dilatation depends on the direction to the observer; in the direction of the propagating tip of the crack, the dilatation is largest between the first and second Stoneley-wave pulses, whereas in the opposite direction it is largest immediately following the initial compression.

Figure 14 shows the waveforms for a crack containing a viscous fluid. Except for the dimensionless viscosity F, which is taken to be 0.01, the parameters are the same as those of figure 13. The motion on the crack for this case is shown in Figure 5. The waveforms are similar to those for the case of a non-viscous fluid, but the pulses generated by the Stoneley-wave reflections are smaller.

Figure 15 shows the far-field waveforms for a crack whose tip propagates a shorter distance $\Delta l = L/40$. Otherwise, this case is the same as that in Figure 13. The motion of the crack face, from which the waveform was computed, is shown in Figure 6. The main effect of the smaller value of Δl is to decrease the duration of the pulses that compose the signal, and to enrich their high-frequency content.

Figure 16 shows waveforms calculated for a crack extension of $\Delta l = L/40$ and a lower acoustic velocity in the fluid $(a = 0.25\alpha)$, corresponding to the crack motion shown in Figure 7. In this case, the pseudo-Rayleigh wave and the acoustic wave propagating along the crack have very different velocities, and the arrival times and shapes of the pulses composing the waveforms are therefore different. Furthermore, the dilatational portions of the wave are considerably smaller in amplitude.

Are these theoretical waveforms compatible with those observed for the non-double-couple earthquakes at Long Valley? The observed first motions come mostly from the lower focal hemisphere and are dilatational in a band centered on the plane of the hypothetical crack, and compressional elsewhere. The theoretical waveforms, on the other hand, all begin with unambiguous compressions, which are followed by dilatations that are smaller and of longer duration. As pointed out by Aki [1984] in the case of the Mammoth Lakes

earthquakes, there are numerous reports of compressional first motion for short-period P waves at stations where the long-period P waves are clearly dilatational. Aki suggests that these observations can be explained if the compressional first motions are weak and of high-frequency content in the direction where long-period P waves are dilatational so that the reported dilatations refer to cases where true first motions went undetected. Although this seems unlikely on the basis of the theoretical data presented in Figures 13 – 15, there are several factors which have not been taken into account in our analysis, whose effects may possibly lend credence to Aki's hypothesis. These factors are : (1) the path effects, such as attenuation, which may affect the initial short-period compression more strongly than the following long-period dilatation; (2) the interference between direct waves and waves reflected from the earth's surface; (3) the azimuthally-varying smoothing of the waveform associated with a finite crack width; and (4) the response of the recording instruments. Thus, it is perhaps conceivable that the large difference in the duration of the compressional and dilatational portions of the waveform may result in the experimentally-determined polarity being dependent on the frequency response of the instrument used to record the waves.

CONCLUSIONS

This study of the dynamics of a propagating fluid-filled crack extends the finite-difference calculation made by Aki et al. [1977], improving the boundary conditions and treating the case of a viscous fluid that supports acoustic-wave propagation.

Two different time scales characterize the motion in this model: the duration of brittle failure at the propagating crack tip and the period of resonance of the fluid-filled crack. The failure at the crack tip has a duration proportional to the distance Δl that the crack propagates, and is responsible for exciting the crack into resonance. The resonant period is proportional to the length L of the crack and varies inversely with the acoustic velocity a in the fluid; it is generally much greater that the duration of brittle failure.

The initial displacement of the crack at the propagating tip is an opening, and the first motion radiated is strongly compressive in all directions. Flow of fluid into the opening

crack tip, however, causes a pressure drop in the fluid which propagates across the crack with the acoustic-wave velocity, causing the crack wall to close partially and radiate a dilatation. In the near field of the crack, this long period dilatation is most pronounced near the plane of the crack, and is especially well marked in the vertical ground displacement observed along the crack trace for a buried vertical source. The width of the zone over which this effect is important depends on the depth of burial and stiffness of the crack.

For small incremental extensions of cracks with low acoustic velocities, the time scale of the acoustic resonance may greatly exceed the duration of the brittle failure. The resulting radiated waveforms are frequency dependent, and analyses of them based on conventional narrow-band instruments may be misleading.

When the fluid viscosity is low and the viscous damping is small, the main mechanism of dissipating energy is elastic-wave radiation into the solid. This radiation loss strongly affects the high-frequency motion of the source but has only a weak effect on lower frequencies. Vibration of the crack in its fundamental mode can thus persist for a considerable amount of time, with the crack acting as a high-Q oscillator. Inhomogeneous waves trapped near the liquid-solid interface produce high-frequency motion in the immediate vicinity of the crack.

ACKNOWLEDGEMENTS

Michael Fehler kindly gave us the finite-difference computer program that was the starting point for this study. We thank Professor Keiiti Aki for providing a manuscript of his paper in advance of its publication, and for many helpful discussions. We also gratefully appreciate the careful reviews of a preliminary draft by Ralph Archuleta and Art McGarr.

REFERENCES

Aki, K., M. Fehler, and S. Das, Source mechanism of volcanic tremor : fluid-driven crack models and their application to the 1963 Kilauea eruption, *J. Volcanol. Geotherm. Res.*, **2**, 259–287, 1977.

Aki, K., B. Chouet, M. Fehler, G. Zandt, R. Koyanagi, J. Colp, and R.G. Hay, Seismic properties of a shallow magma reservoir in Kilauea Iki by active and passive experiments, *J. Geophys. Res.*, **83**, 2273–2282, 1978.

Aki, K., Evidence for magma intrusion during the Mammoth lakes earthquakes of May, 1980 and implications for the absence of volcanic (harmonic) tremor, *submitted to J. Geophys. Res.*, 1984.

Barker, J.S., and C.A. Langston, A teleseismic body-wave analysis of the May 1980 Mammoth Lakes, California, earthquakes, *Bull. Seismol. Soc. Am.*, **73**, 419–434, 1983.

Biot, M.A., Propagation of elastic waves in a cylindrical bore containing a fluid, *J. Appl. Phys.*, **23**, 997–1005, 1952.

Bouchon, M., Discrete wave number representation of elastic wavefields in three-space dimensions, *J. Geophys. Res.*, **84**, 3609–3614, 1979.

Burridge, R., and L. Knopoff, Body force equivalents for seismic dislocations, *Bull. Seismol. Soc. Am.*, **54**, 1875–1888, 1964.

Cheng, H.C., and M.N. Toksõz, Elastic wave propagation in a fluid-filled bore-hole and synthetic acoustic logs, *Geophysics*, **46**, 1042–1053, 1981.

Chouet, B., Sources of seismic events in the cooling lava lake of Kilauea Iki, Hawaii, *J. Geophys. Res.*, **84**, 2315–2330, 1979.

Chouet, B., Ground motion in the near field of a fluid-driven crack and its interpretation in the study of shallow volcanic tremor, *J. Geophys. Res.*, 86, 5985–6016, 1981.

Chouet, B., Free surface displacements in the near field of a tensile crack expanding in three dimensions, *J. Geophys. Res.*, **87**, 3868–3872, 1982.

Chouet, B., Ground response generated by the magmatic excitation of a buried volcanic pipe, a source model for shallow long-period volcanic events and harmonic tremor, *submitted to J. Geophys Res.*, 1984.

Einarsson, P., Seismicity and earthquake focal mechanisms along the mid-Atlantic plate boundary between Iceland and the Azores, *Tectonophysics*, **55**, 127–153, 1979.

Ekström, G., and A. M. Dziewonski, Moment tensor solutions of Mammoth lake earthquakes, *Eos Trans. Amer. Geophys. Union*, **64**, 262, 1983.

Fehler, M., and K. Aki, Numerical study of diffraction of plane elastic waves by a finite crack with application to location of a magma lens, *Bull. Seismol. Soc. Am.*, **68**, 573–598, 1978.

Foulger, G. R., and R.E. Long, Anomalous fault plane solutions : evidence for tensile crack formation on an accreting plate boundary, *submitted to Nature*, 1984.

Halliwell, A.R., Velocity of the water-hammer wave in an elastic pipe, *J. Hydr. Div., Proc. Amer. Soc. Civ. Eng.*, **89, HY4**, 1–21, 1963.

Haskell, N.A., Total energy and energy spectral density of elastic wave radiation from propagating faults, *Bull. Seismol. Soc. Am.*, **54**, 1811–1841, 1964.

Ishimoto, M., Existence of a quadrupole source at the seismic focus according to the study of the distribution of initial movements of seismic shocks, *Bull. Earthquake Res. Inst., Tokyo*, **10**, 449, 1932.

Julian, B. R., Evidence for dyke intrusion earthquake mechanisms near Long Valley caldera, California, *Nature*, **303**, 323–325, 1983.

Julian, B.R., and S.A. Sipkin, Earthquake processes in the Long Valley caldera area, California, *J. Geophys. Res., (submitted)*.

Klein, F.W., P. Einarsson, and M. Wyss, The Reykjanes Peninsula, Iceland earthquake swarm of September 1972 and its tectonic significance, *J. Geophys. Res.*, **82**, 865–888, 1977.

Knopoff, L., and M.J. Randall, The compensated linear vector dipole : a possible mechanism for deep earthquakes, *J. Geophys. Res.*, **75**, 4957–4963, 1970.

Madariaga, R., Dynamics of an expanding circular fault, *Bull. Seismol. Soc. Am.*, **66**, 639–666, 1976.

Sykes, L.R., Mechanism of earthquakes and the nature of faulting on the mid-ocean ridges, *J. Geophys. Res.*, **72**, 2131–2153, 1967.

Sykes, L.R., Focal mechanism solutions for earthquakes along the world rift system,

Bull. Seismol. Soc. Am., **60**, 1749–1752, 1970.

White, J.E., *Seismic Waves, Radiation, Transmission, and Attenuation*, pp 148–151, McGraw-Hill, New York, 1965.

Wiggins, R.A., Interpolation of digitized curves, *Bull. Seismol. Soc. Am.*, **66**, 2077–2081, 1976.

Wylie, E.B., and V.L. Streeter, *Fluid Transients*, McGraw-Hill, New York, 1978.

TABLE 1 PARAMETERS OF CRACK MODELS

Figures	No. of points	Stiffness C	Viscosity F	Velocity ratio G
2	40	5	0	2
3,4,13	20	5	0	2
5,10,11,14	20	5	0.01	2
6,15	40	5	0	2
7,16	40	5	0	4
8	160	5	0	4

FIGURE CAPTIONS

Fig. 1. Transverse displacement of the crack surface plotted as a dimensionless function of dimensionless time. The crack is 20 grid intervals long and extends by $\Delta l = L/20$. The original solution derived by Aki *et al.*[1977] is reproduced at the left for comparison with our results shown at the right. Two cases are represented using different time scales. These are the response of a dry crack, characterized by the stiffness $C = 0$ (top), and that of a wet crack with the stiffness $C = 5$ (bottom). The fluid in the wet crack model does not flow or support acoustic waves. (See text for explanation of symbols).

Fig. 2. Normal component of the particle velocity plotted as a function of time and position on the surface of the crack. The crack is 40 grid steps long and the motion is calculated for 501 time steps. The number of time samples has been decimated by a factor of two to improve the clarity of the figure. These results represent the case of an inviscid fluid in a crack characterized by the stiffness $C = 5$. The acoustic velocity in the fluid is half of the P-wave velocity in the solid and the acoustic arrival is denoted by an arrow.

Fig. 3. Transverse displacement of the crack surface in dimensionless units for a crack 20 grid intervals long which expands by $\Delta l = L/20$. The crack parameters are listed at the top (see text for details).

Fig. 4. Same as Figure 3, but showing $2\frac{1}{2}$ cycles of the acoustic resonance of the fluid.

Fig. 5. Same as Figure 3 for a viscous fluid characterized by $F = 10^{-2}$.

Fig. 6. Dimensionless transverse displacement of the crack surface for a crack 40 grid steps long and propagating a distance $\Delta l = L/40$. The other parameters are identical to those used in Figure 3.

Fig. 7. Same as Figure 6 with an acoustic velocity half as large.

Fig. 8. Normal component of the particle velocity plotted at 160 locations on the surface of a crack that extends by $\Delta l = L/160$. The motion is calculated over 501 grids in time and is plotted every fourth sample to improve the clarity of the plot. The case represented is that of an inviscid fluid in a crack characterized by the stiffness $C = 5$. The acoustic velocity in the fluid is $\frac{1}{4}$ of the compressional velocity in the solid. Note the

individual wavefronts denoted by arrows.

Fig. 9. Configuration of the source, medium, and receivers used in the computation of the ground motion generated by the propagating crack. The source is represented by the vertical rectangular plane with the dimensions of $2 \times 1 km$. The ground displacements are calculated at 15 locations over an area of $3 \times 6 km$. Each of these locations is represented by one grid point in the figure. The separation between stations is 1.5 km in both transverse and longitudinal directions. The profiles referred to in the text are numbered 1 through 5 and the number in parentheses denote the horizontal coordinates of individual stations. The crack trace extends from the coordinates $(0,0)$ and $(2,0)$. The positive direction of the three components of motion u, v, w is indicated by vectors. Another vector points to the direction of propagation of the crack.

Fig. 10. Synthetic seismograms of the three components of ground displacement at 15 stations along 5 transverse profiles for the source depicted in Figure 5. The crack is buried at a depth of $5 km$ in a homogeneous half space. The disposition of the source and receivers is given in Figure 9 and the x and y coordinates of the stations are shown at the top and right of the figure, respectively. The records start with the arrival of the P wave from the hypocenter and are about $4\ s$ in duration. The displacement amplitudes have been normalized to a ΔP of unity.

Fig. 11. Same as Figure 10 for a crack opening at a depth of $2.5 km$ in a homogeneous half space. The other source parameters are identical to those used in Figure 10.

Fig. 12. Crack geometry and coordinate system used in calculating far-field waveforms.

Fig. 13. Far-field compressional waveform for a crack of stiffness $C = 5$, containing an inviscid fluid with acoustic wave speed $a = 0.5\alpha$. The crack tip propagates by $\Delta l = L/20$. Numbers to the left of the waveforms give the values of the angle θ.

Fig. 14. Same as Figure 13, with $F = 10^{-2}$.

Fig. 15. Same as Figure 13, with $\Delta l = L/40$.

Fig. 16. Same as Figure 13, with $a = 0.25\alpha$ and $\Delta l = L/40$.

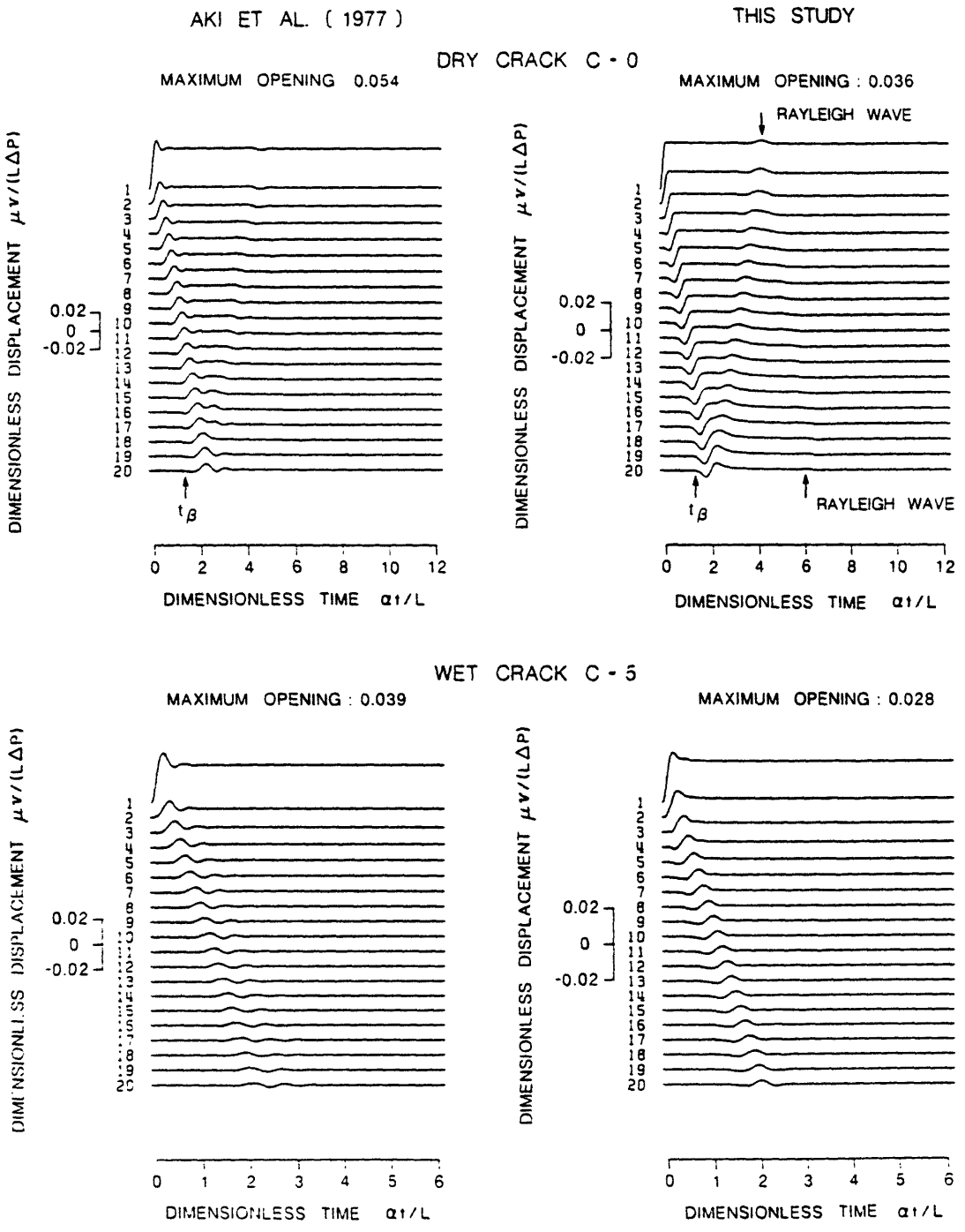
AKI ET AL. (1977)
THIS STUDY
DRY CRACK C - 0
MAXIMUM OPENING 0.054
MAXIMUM OPENING : 0.036
RAYLEIGH WAVE
DIMENSIONLESS DISPLACEMENT μv/(LΔP)
0.02
0
-0.02
t_β
RAYLEIGH WAVE
0 2 4 6 8 10 12
DIMENSIONLESS TIME αt/L
WET CRACK C - 5
MAXIMUM OPENING : 0.039
MAXIMUM OPENING : 0.028
0 1 2 3 4 5 6

Fig. 1

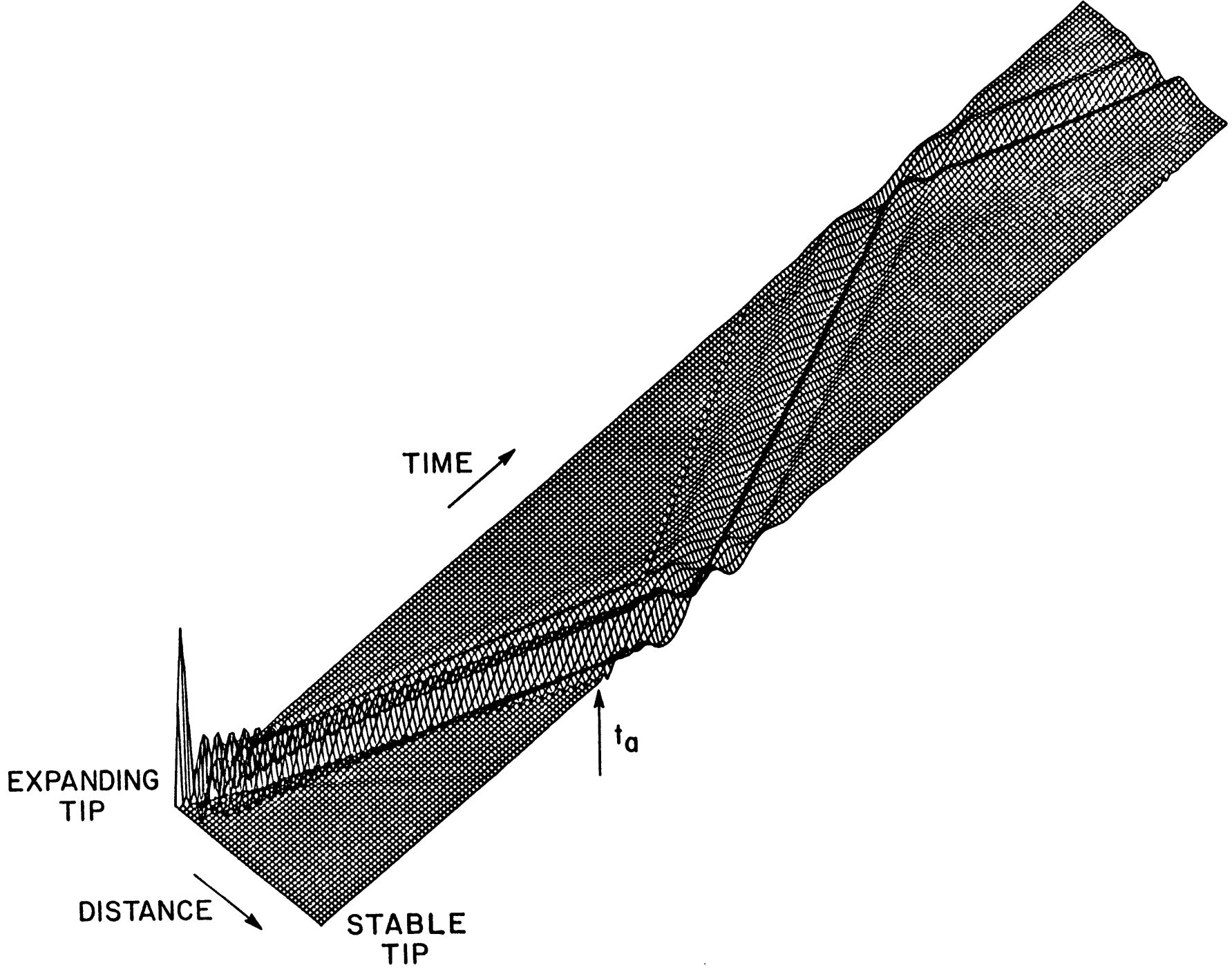

Fig. 2

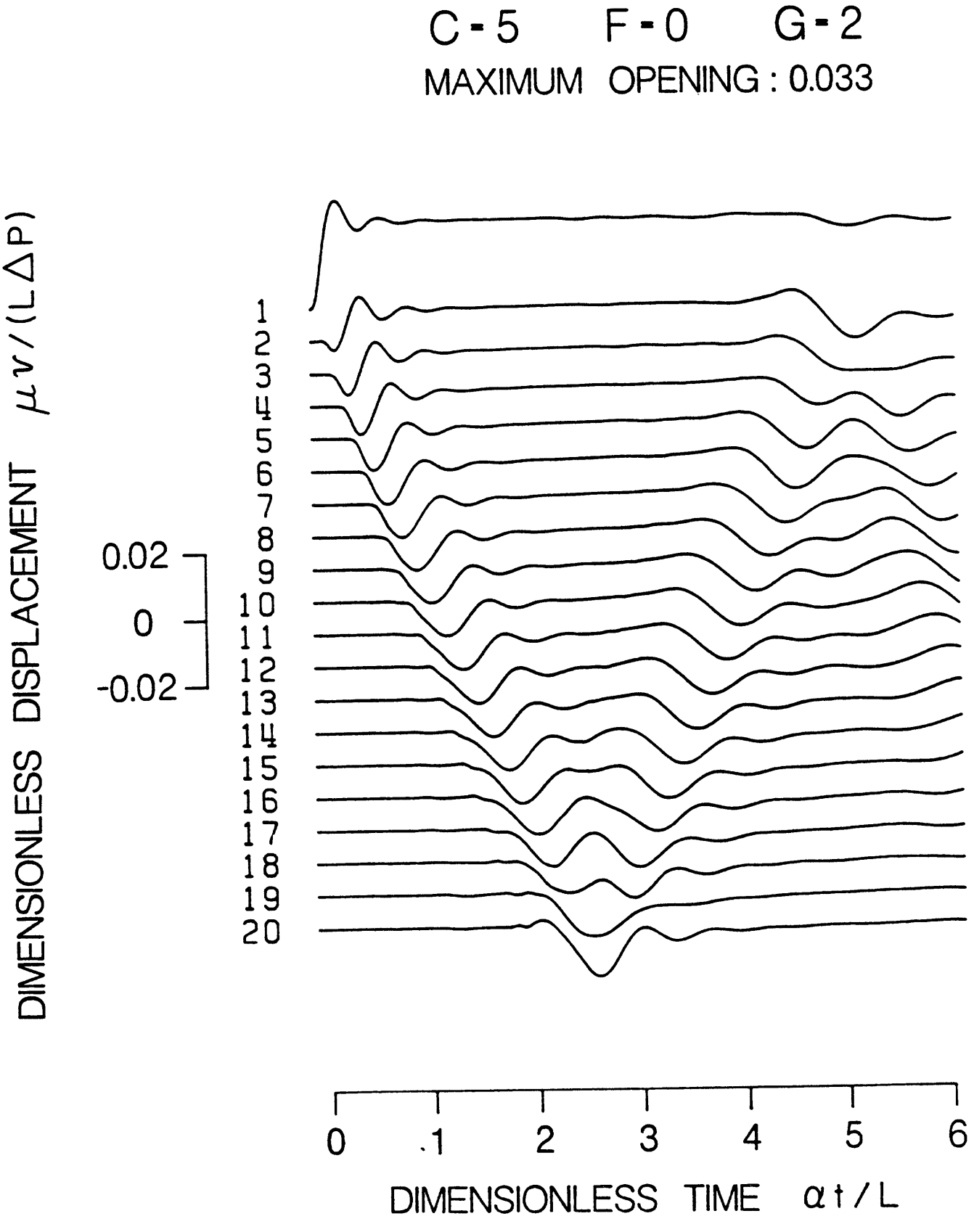
C - 5 F - 0 G - 2
MAXIMUM OPENING : 0.033
DIMENSIONLESS DISPLACEMENT μv/(LΔP)
0.02
0
-0.02
1
2
3
4
5
6
7
8
9
10
11
12
13
14
15
16
17
18
19
20
0
.1
2
3
4
5
6
DIMENSIONLESS TIME αt/L

Fig. 3

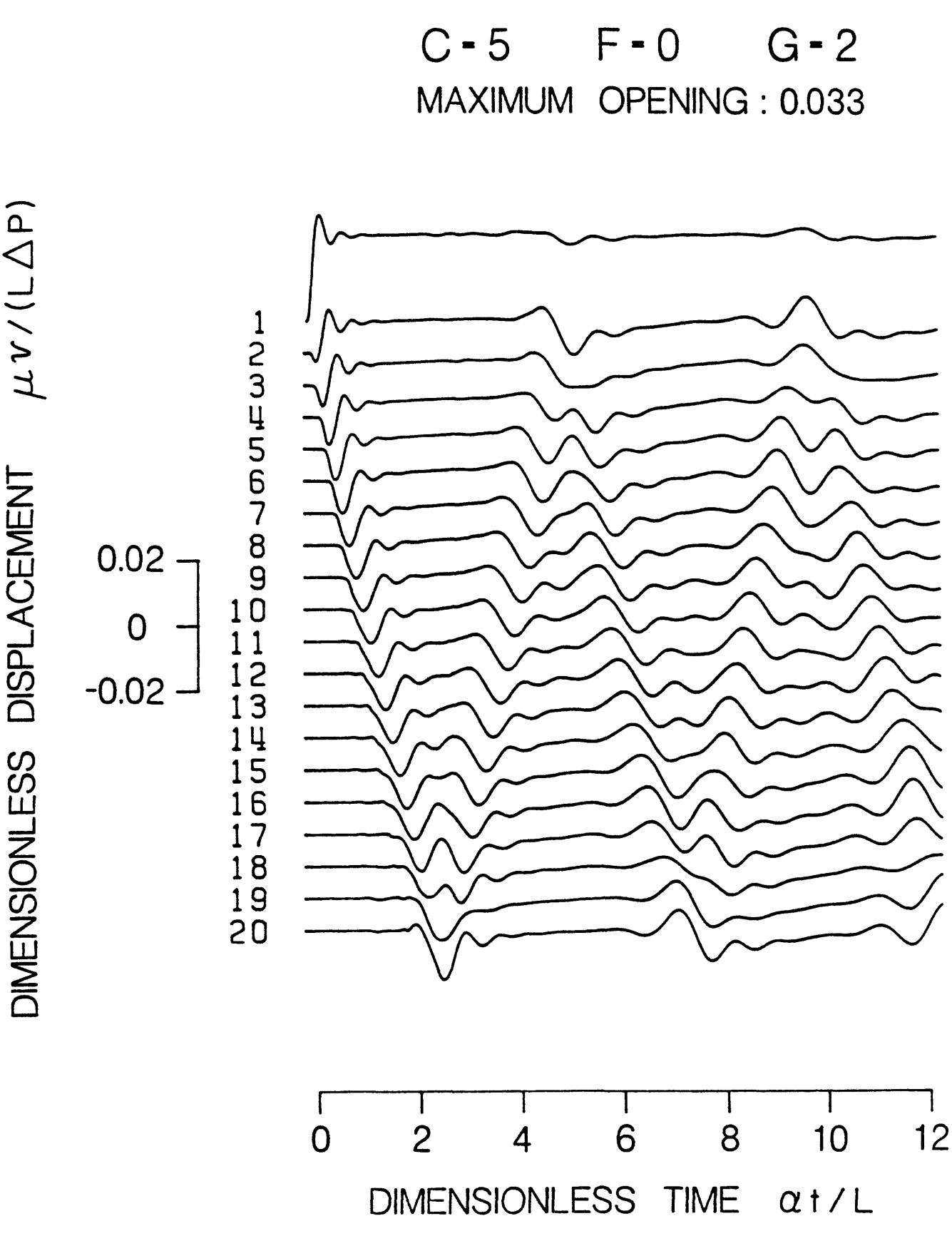
C - 5 F - 0 G - 2
MAXIMUM OPENING : 0.033
DIMENSIONLESS DISPLACEMENT μv/(LΔP)
0.02
0
-0.02
1
2
3
4
5
6
7
8
9
10
11
12
13
14
15
16
17
18
19
20
0
2
4
6
8
10
12
DIMENSIONLESS TIME αt/L

 Fig. 4

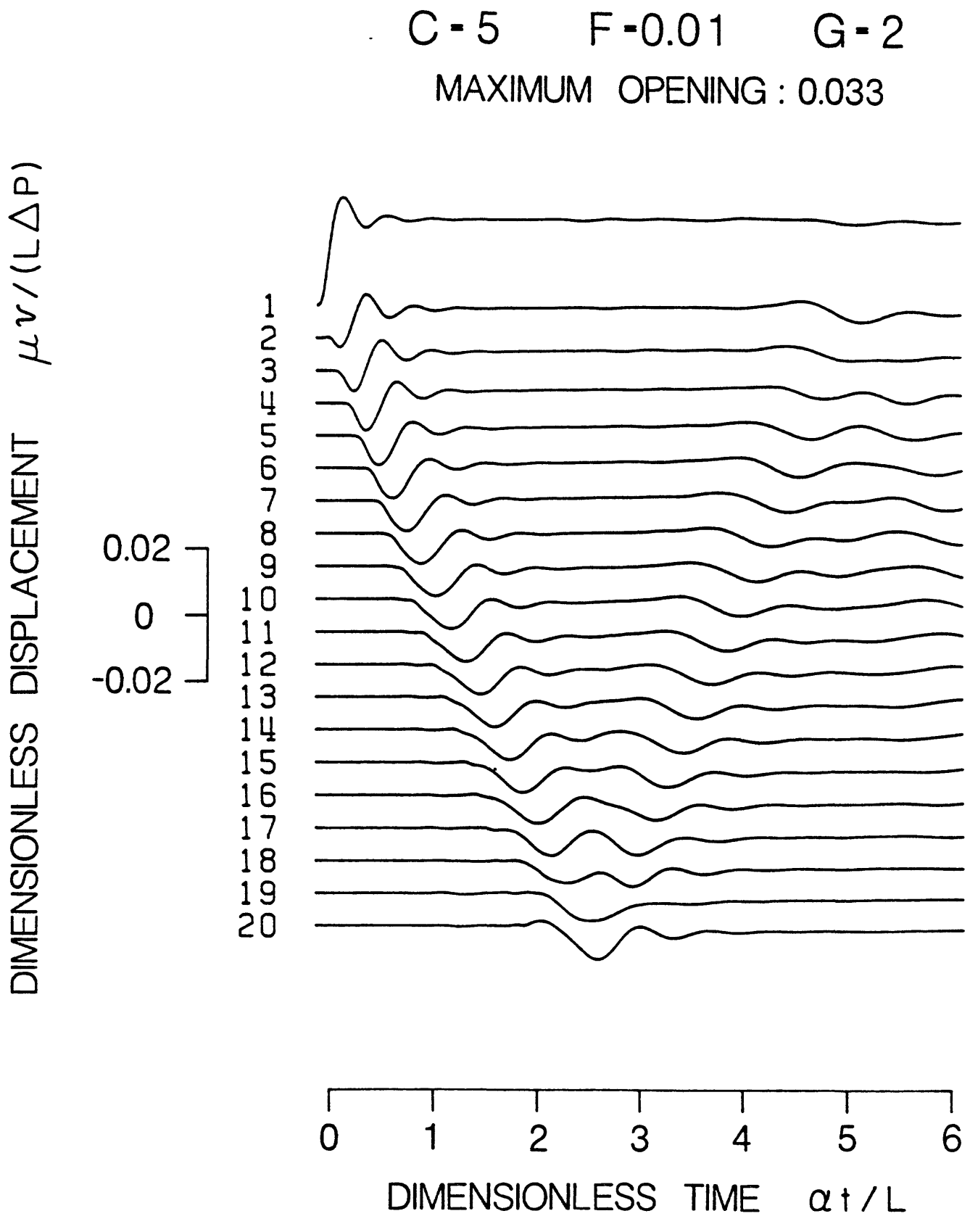
C - 5 F - 0.01 G - 2
MAXIMUM OPENING : 0.033
DIMENSIONLESS DISPLACEMENT μv/(LΔP)
0.02
0
-0.02
1
2
3
4
5
6
7
8
9
10
11
12
13
14
15
16
17
18
19
20
0
1
2
3
4
5
6
DIMENSIONLESS TIME αt/L

Fig. 5

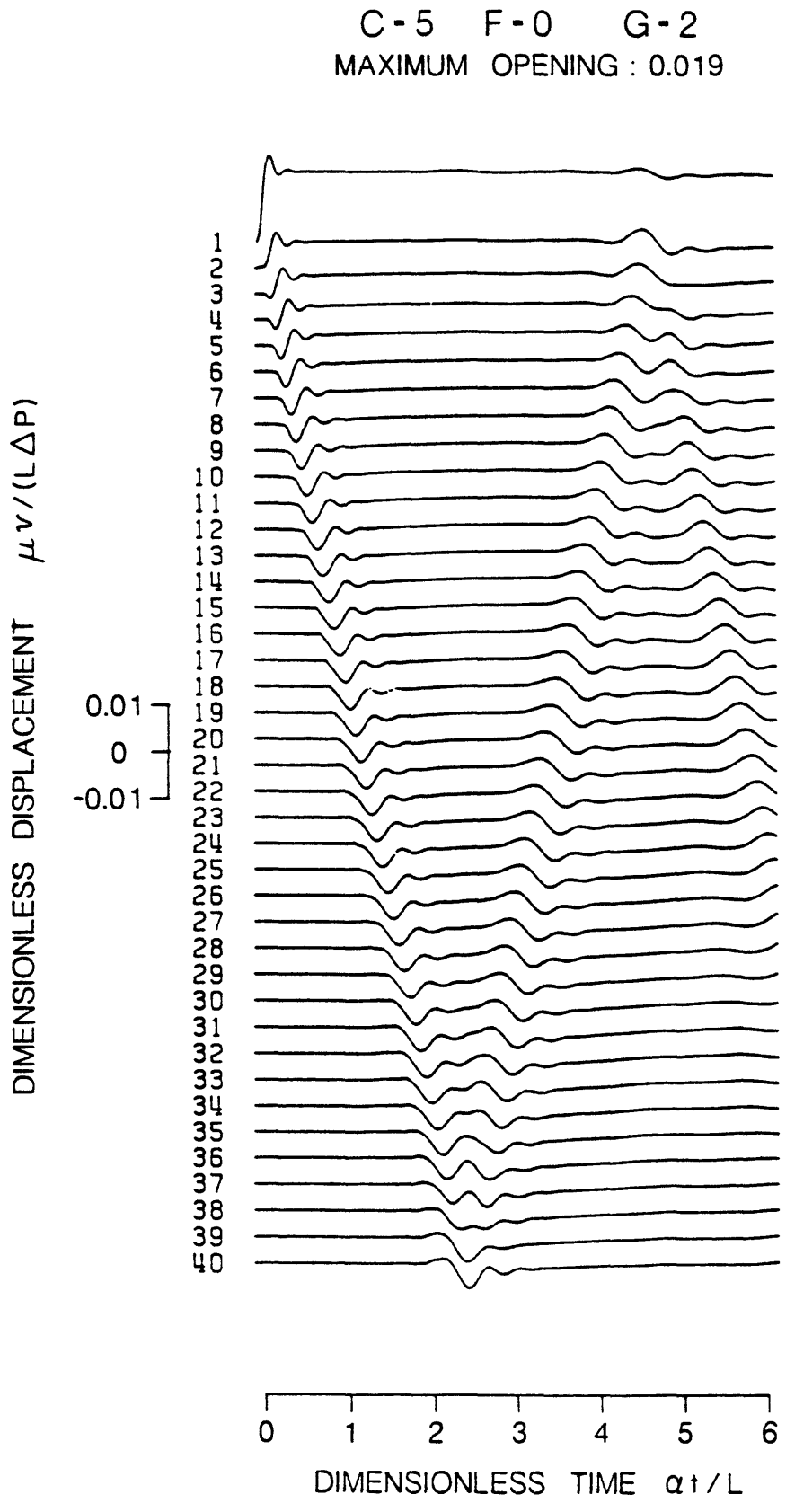
C-5 F-0 G-2
MAXIMUM OPENING : 0.019
DIMENSIONLESS DISPLACEMENT μv/(LΔP)
0.01
0
-0.01
1
2
3
4
5
6
7
8
9
10
11
12
13
14
15
16
17
18
19
20
21
22
23
24
25
26
27
28
29
30
31
32
33
34
35
36
37
38
39
40
0
1
2
3
4
5
6
DIMENSIONLESS TIME αt/L

Fig. 6 398

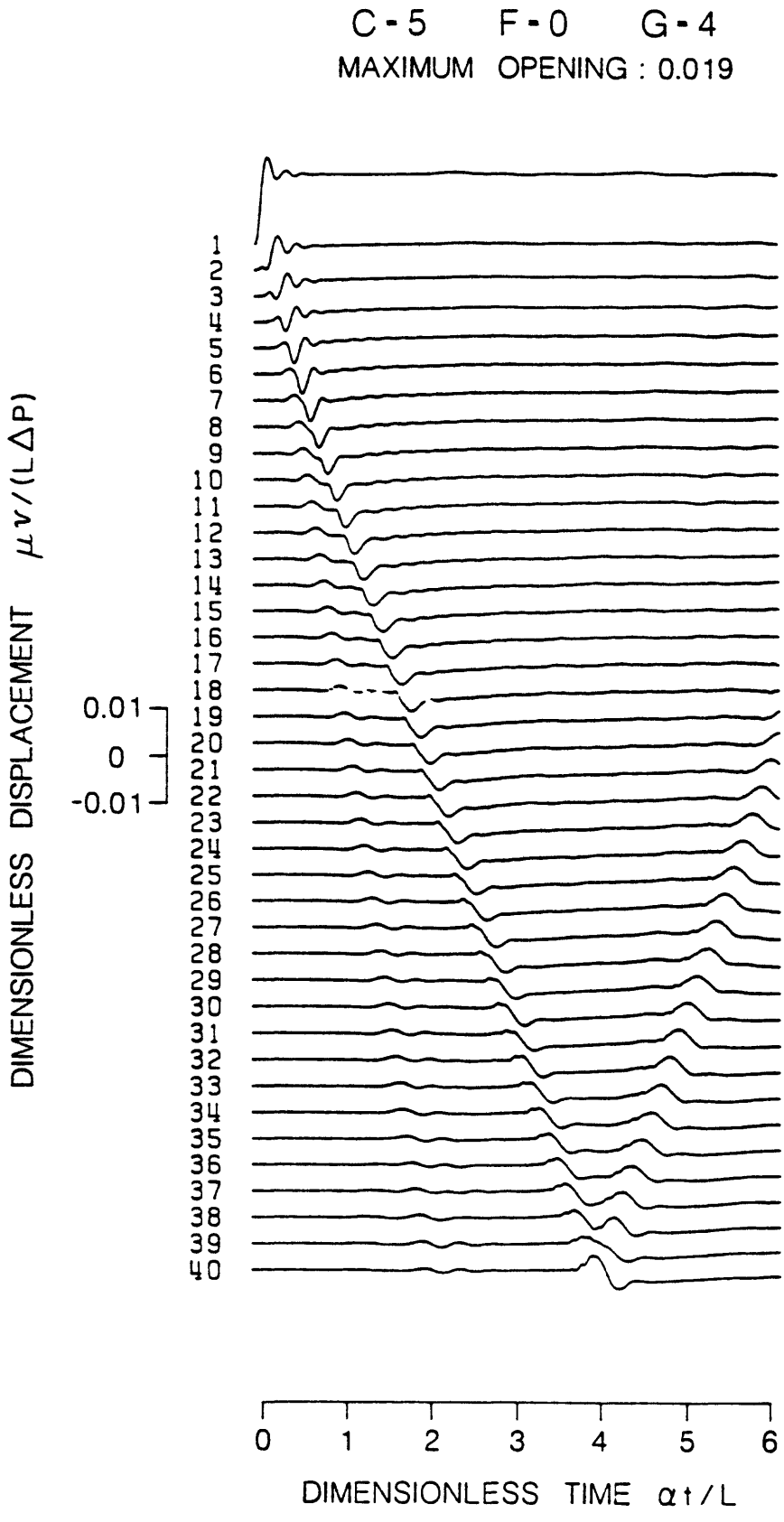
C - 5 F - 0 G - 4
MAXIMUM OPENING : 0.019
DIMENSIONLESS DISPLACEMENT μv/(LΔP)
0.01
0
-0.01
1
2
3
4
5
6
7
8
9
10
11
12
13
14
15
16
17
18
19
20
21
22
23
24
25
26
27
28
29
30
31
32
33
34
35
36
37
38
39
40
0
1
2
3
4
5
6
DIMENSIONLESS TIME αt/L

Fig. 7

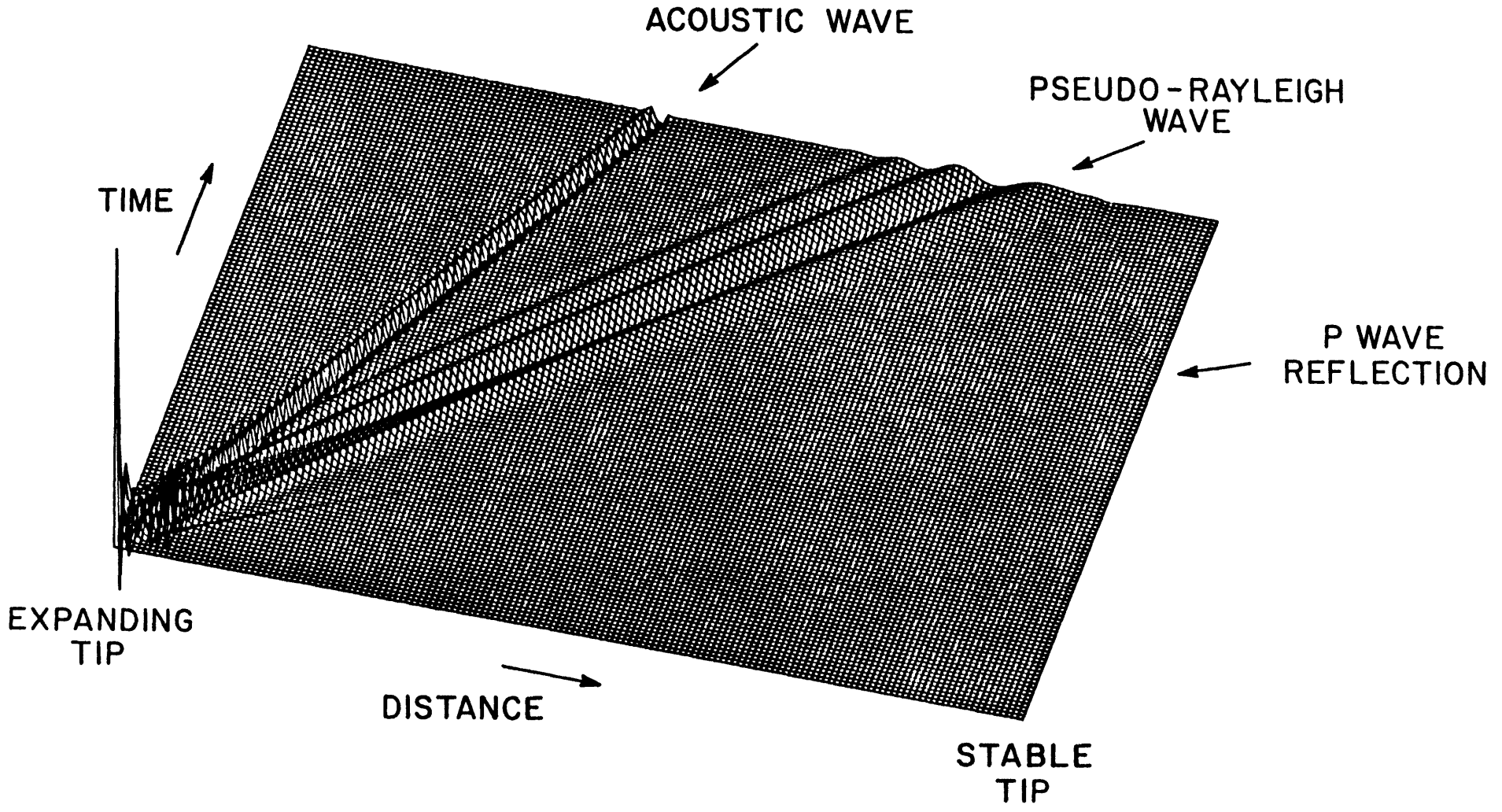
ACOUSTIC WAVE
PSEUDO-RAYLEIGH WAVE
TIME
P WAVE REFLECTION
EXPANDING TIP
DISTANCE
STABLE TIP

400

Fig. 8

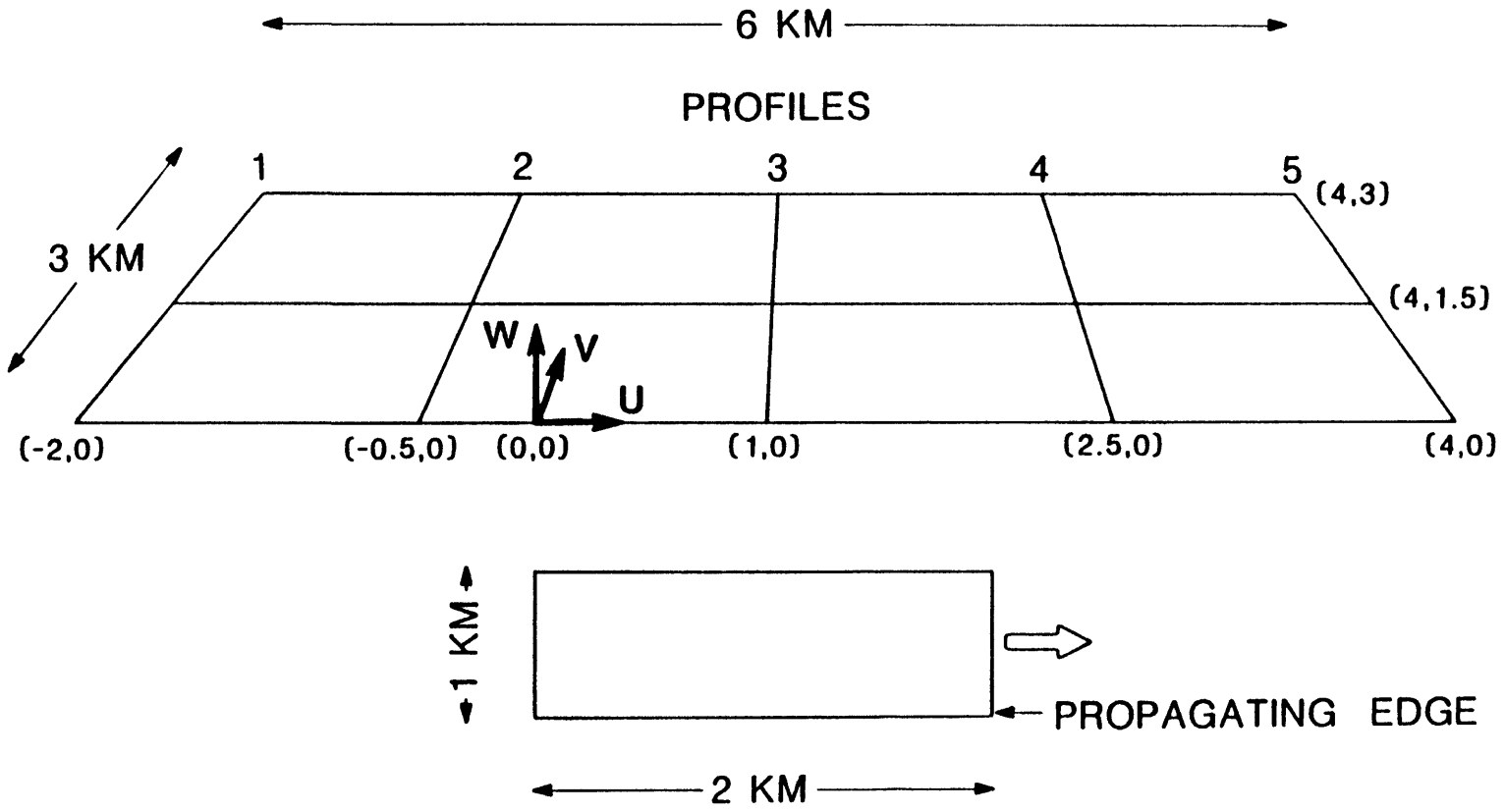
6 KM
PROFILES
1
2
3
4
5
(4,3)
3 KM
(4,1.5)
W
V
U
(-2,0)
(-0.5,0)
(0,0)
(1,0)
(2.5,0)
(4,0)
1 KM
PROPAGATING EDGE
2 KM

Fig. 9

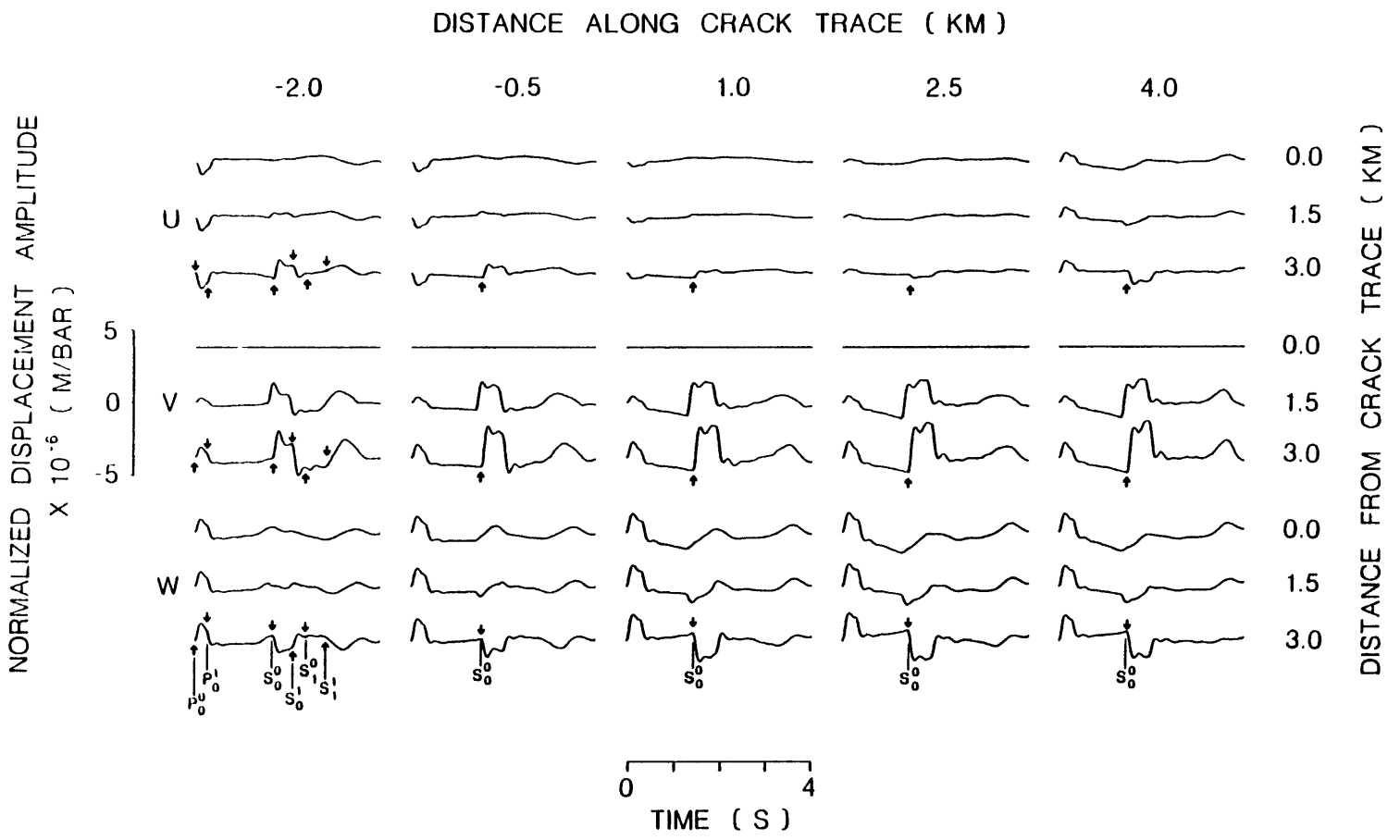
DISTANCE ALONG CRACK TRACE (KM)
-2.0
-0.5
1.0
2.5
4.0
NORMALIZED DISPLACEMENT AMPLITUDE
X 10⁻⁶ (M/BAR)
5
0
-5
U
V
W
0.0
1.5
3.0
DISTANCE FROM CRACK TRACE (KM)
0
4
TIME (S)

Fig. 10

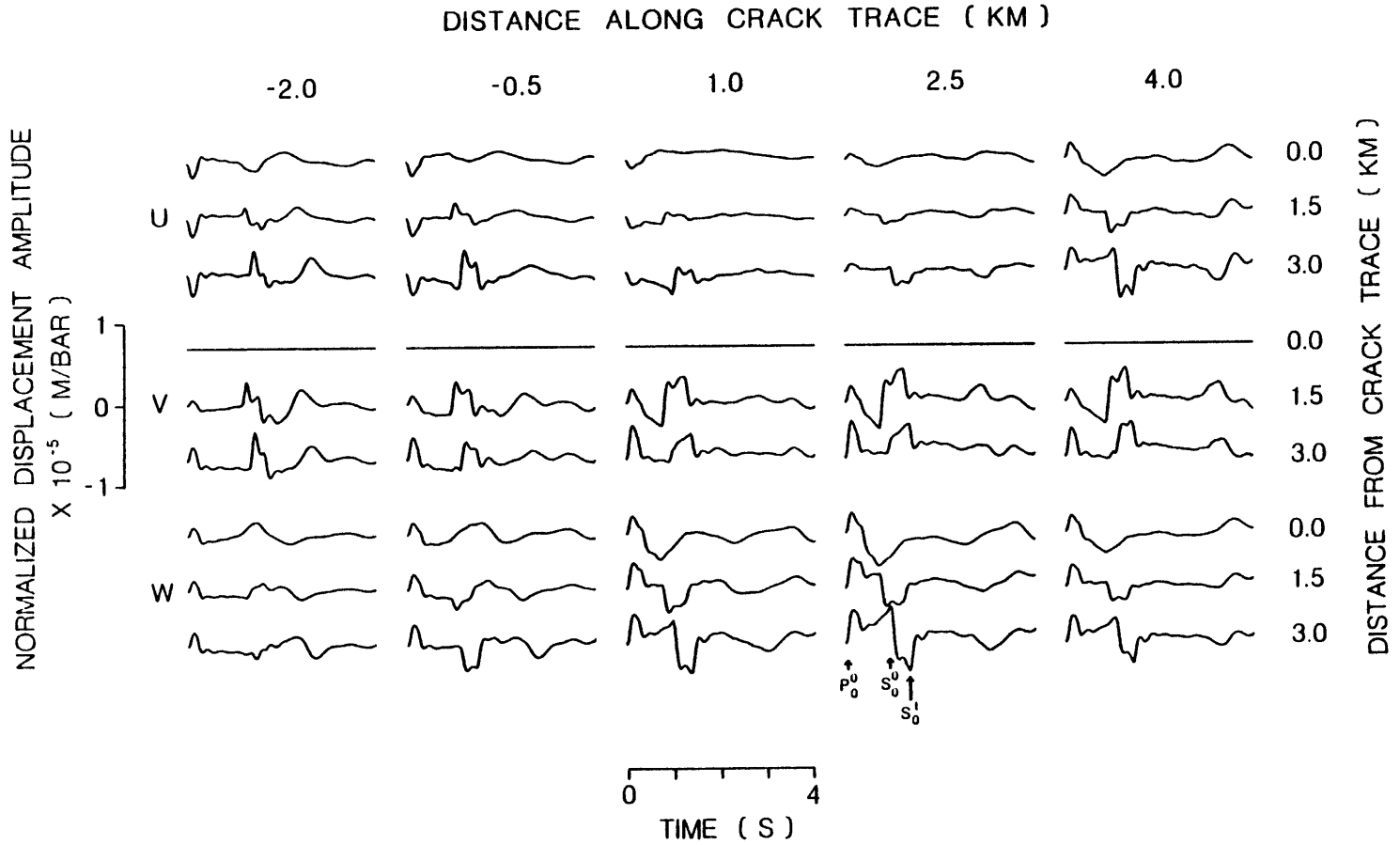
DISTANCE ALONG CRACK TRACE (KM)
-2.0
-0.5
1.0
2.5
4.0
NORMALIZED DISPLACEMENT AMPLITUDE
X 10⁻⁵ (M/BAR)
1
0
-1
U
V
W
0.0
1.5
3.0
0.0
1.5
3.0
0.0
1.5
3.0
DISTANCE FROM CRACK TRACE (KM)
P₀⁰
S₀⁰
S₀¹
0
4
TIME (S)

Fig. 11

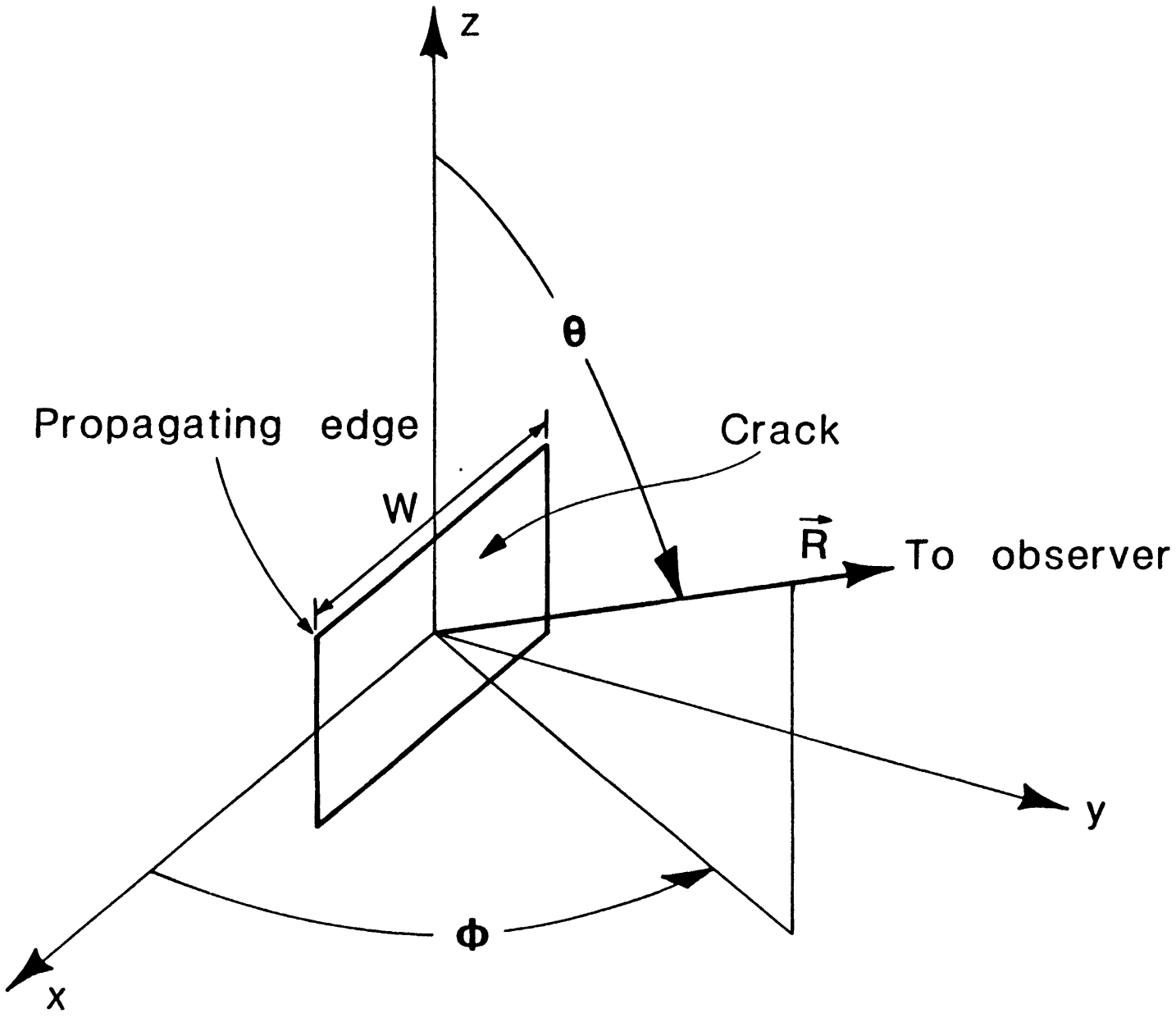

Fig. 12

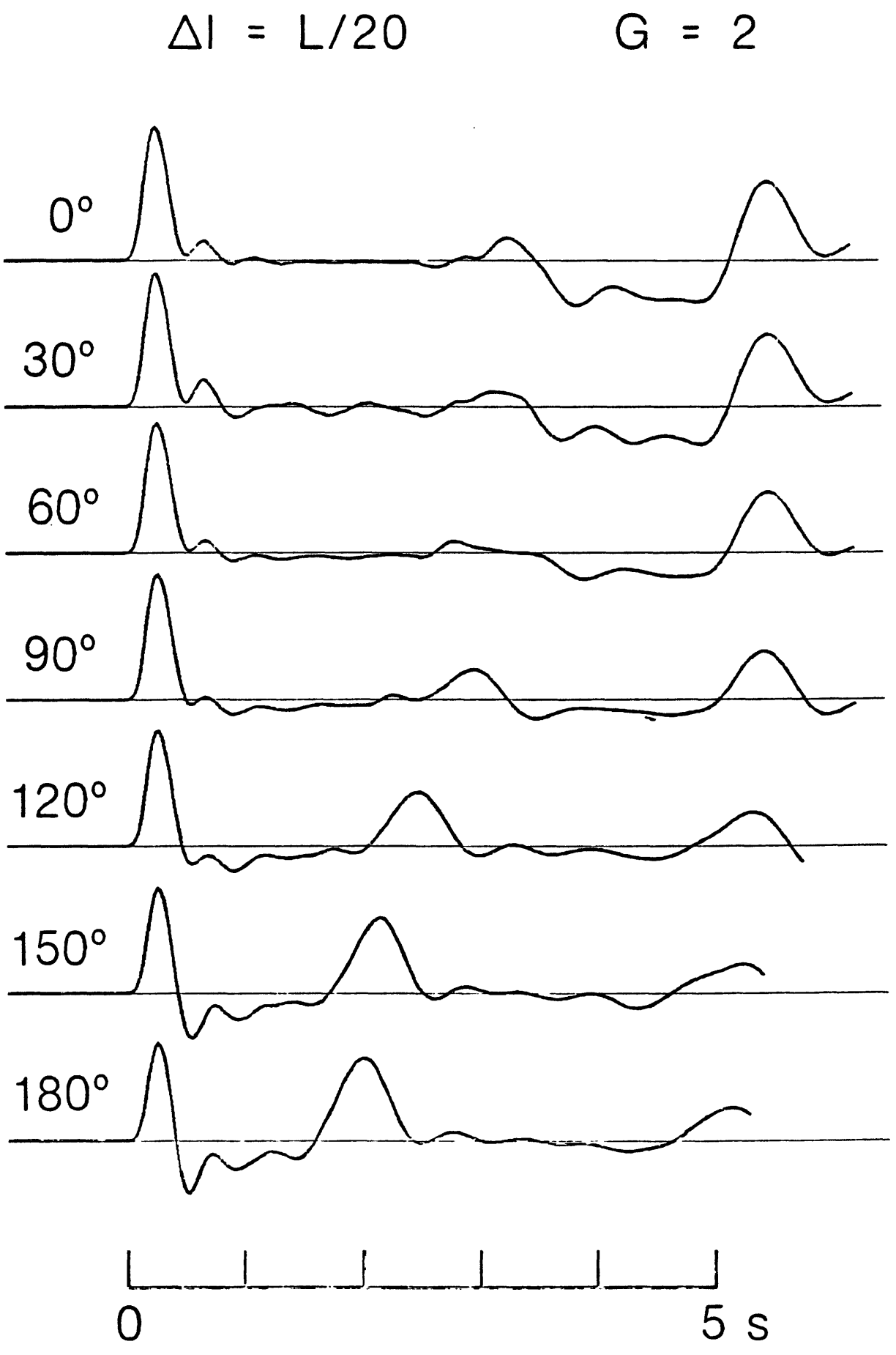

Fig. 13

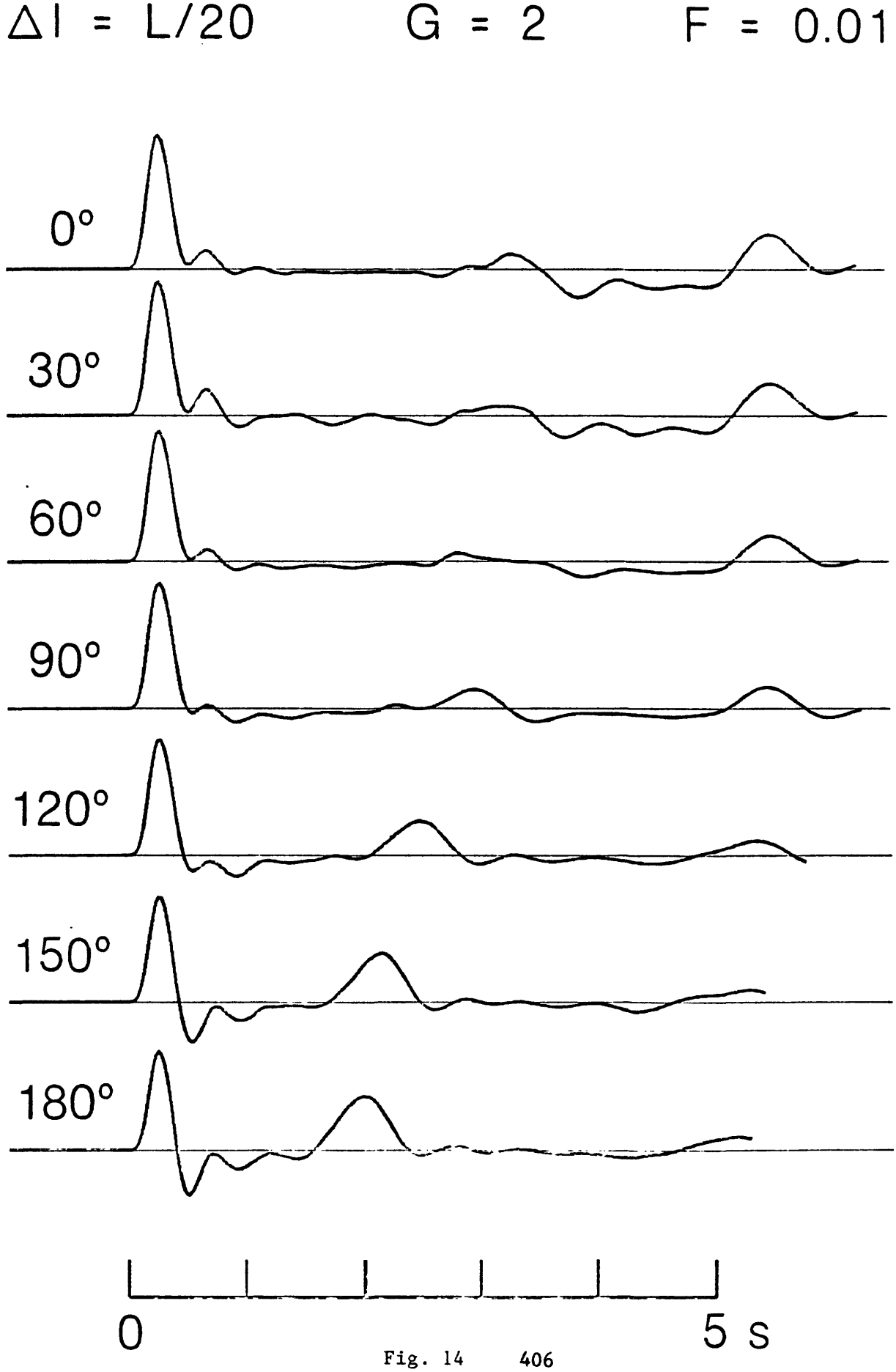

Fig. 14

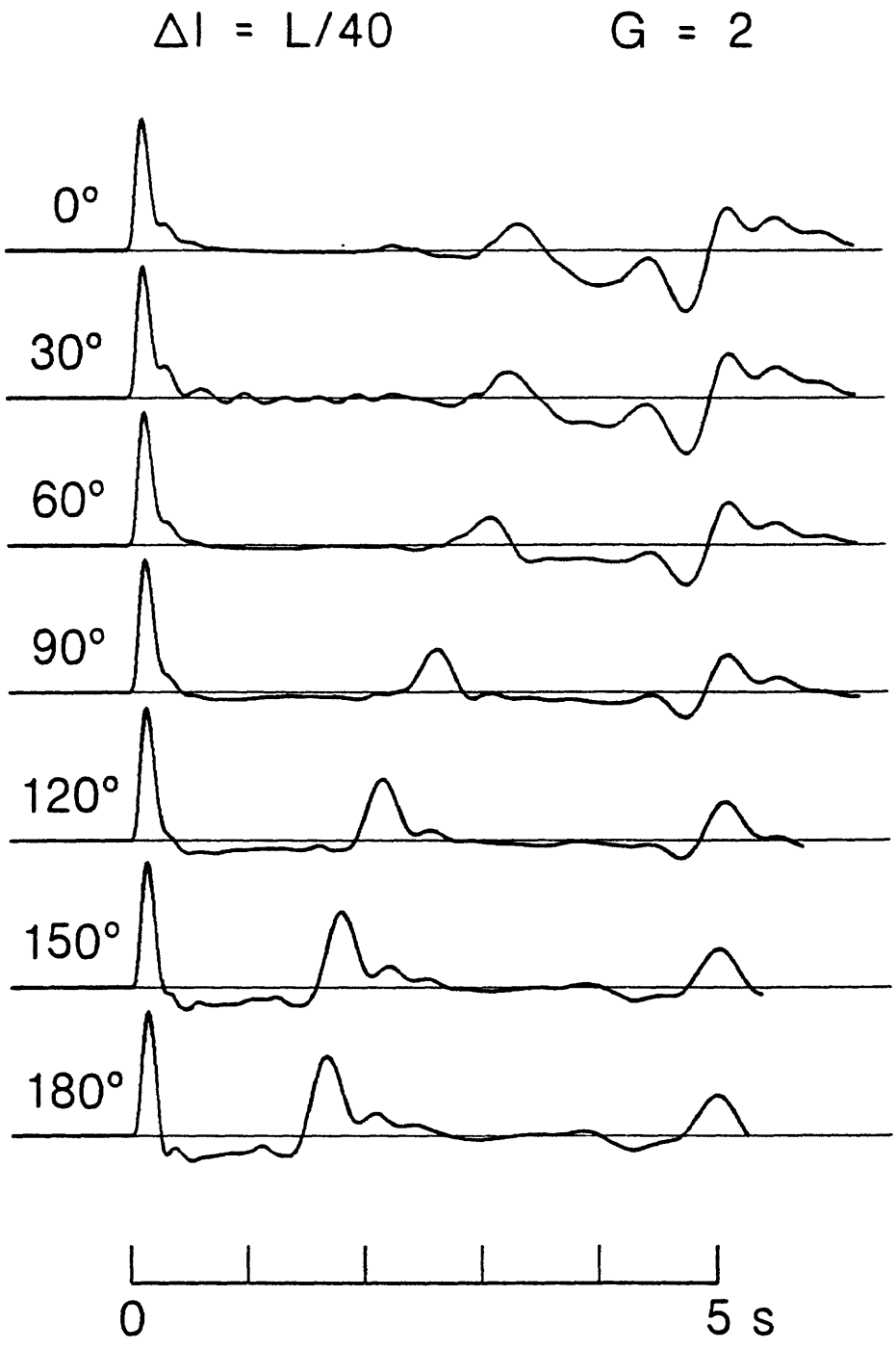

Fig. 15

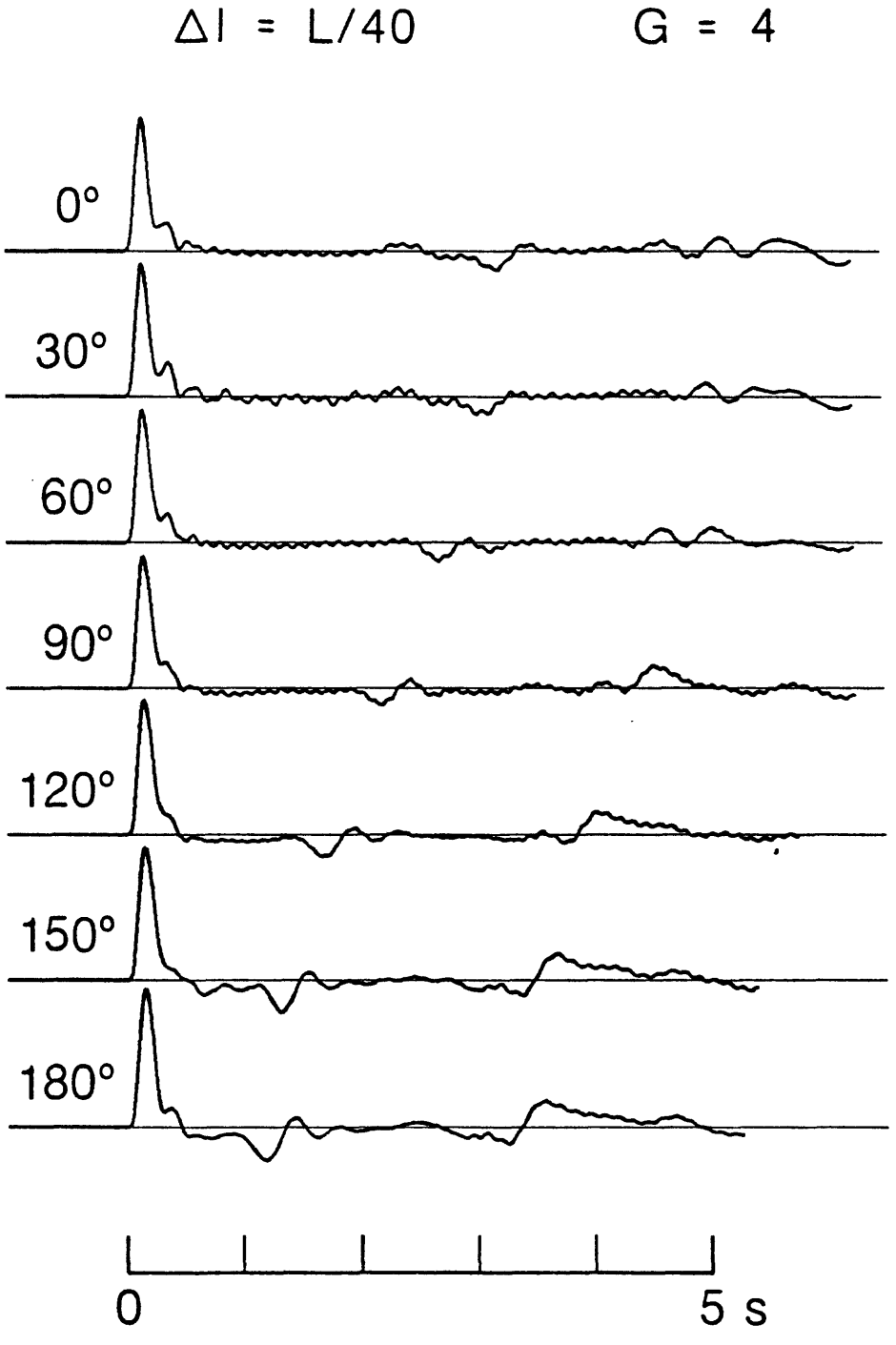

Fig. 16

A RE-EXAMINATION OF THE MOMENT TENSOR SOLUTIONS OF THE 1980 MAMMOTH LAKES EARTHQUAKES

Terry C. Wallace
Department of Geosciences
University of Arizona
Tucson, Arizona 85721

Contribution to U.S.G.S. Redbook Conference
"Active Tectonic and Geologic Processes, Long Valley, California,"
Jan. 24-27, 1984

Abstract

The moment tensor solutions determined from both long period body and surface waves for most of the large earthquakes in the 1980 Mammoth Lakes sequence have substantial deviations from a pure double couple mechanism. Julian (1983) and Aki (1984) argue that these deviations require non-shear faulting sesimic sources such as a CLVD which could represent magmatic dike injection. Here we re-examine the moment tensor solutions and investigate the effects of the non-double couple source on body wave synthetics. An error function which is based on the cross-correlation of a synthetic and an observed waveform was used to assess the difference in fit between the complete moment tensor solution and one constrained to be a double couple. For the mainshock (May 25, 1980; 16:33) the sum of the errors differed by less than 5% for the two models. Similarly, the errors differed by only 3% for the aftershock on May 27, 1980. The conclusion is that the CLVD mechanism is not resolved in the long-period data. In addition, the complete moment tensor solution has an extra parameter; a χ^2 test was applied to normalize the number of parameters, and it was found that the complete solution was slightly less significant than the double couple solution. Finally, the complete solution was compared to a pure CLVD solution; for all the events examined the total moment tensor is as far removed from a CLVD as it is a double couple. Although this does not rule out the possibility of dike injection, it strongly suggests that faulting can account for the long-period seismic observations in the 1980 swarm.

Introduction

The nature of the source mechanisms of the largest events in the 1980 Mammoth Lakes earthquake sequence has been controversial from the beginning and yet it is a very important problem in terms of deciphering the active tectonics of the Long Valley caldera region. Discrepancies between short- and long-period polarities, moment tensor inversions of teleseismic waveforms which yield non-double couple force systems and apparent non-correlation of the epicenters and mechanisms with Holocene faulting features make the source mechanisms difficult to interpret. Three basic models have been suggested to explain the complexity; (1) faulting complexity and stress heterogeneity, (2) velocity structure heterogeneity and (3) dike or fluid injection. Here we re-examine the long period moment tensor solutions in an attempt to differentiate between these models.

During a 48 hour period which began on May 25, 1980, four earthquakes with $M_L > 6$ occurred south of the Long Valley caldera. Aftershock activity was protracted over a two year period (a large aftershock, $M_L = 5.8$, occurred on 30 September 1981), and swarm activity has continued to occur along the southwestern margin of the caldera. Figure 1 shows the epicenters of the three largest events in the 1980 sequence, two large aftershocks, and the 1978 Wheeler Crest earthquake. The Hilton Creek Fault is the most important fault in the epicentral region and shows spectacular surface expression of Holocene normal faulting. A direct association between the Hilton Creek Fault and the 1980 sequence is unlikely; first, the hypocenters are 8 km west of the projected fault plane at depth and secondly, all the fault mechanisms (short- and long-period) are inconsistent with the fault trend. The initial fault mechanisms of the three largest events (B, C and D in Figure 1) were based on local short-period first motions and indicated pure strike-slip motion on vertical,

north-south planes (Ryall and Ryall, 1981; Cramer and Toppozada, 1980). This contrasts with the modeling of the long-period teleseismic body and surface waves; when the moment tensor is constrained to be a double couple, the fault mechanism is oblique-slip on moderately dipping (~45°), north-south planes (Given et al., 1982; Barker and Langston, 1983). When the constraint of double-couple is removed, the moment tensors show a significant deviation from a simple double couple (Barker and Langston, 1983; Ekström and Dziewonski, 1983). It is possible to interpret the non-double couple solutions in terms of a Compensated Linear Vector Dipole (CLVD). Julian (1983) argues that the CLVD is the result of dike injection, and is likely in the tectonic setting of magmatic resurgence in the Long Valley caldera (Savage and Clark, 1982). Ekström and Dziewonski (1983) inverted the worldwide SRO data for the 1978 Wheeler Crest earthquake and found that the moment tensor solution for this event also showed a significant deviation from a simple double couple.

Figure 2 shows the short-period, constrained long-period and total moment tensor solutions for three of the earthquakes in the Mammoth Lakes region. The biggest difference between the short- and long-period solutions is the polarity expected near the center of the focal sphere. Julian (1983) suggests that the "baseball" type nodal lines for a CLVD source could explain both the short- and long-period polarities. However, Wallace et al. (1982) showed that for a number of the teleseismic stations the long-period P-wave was clearly dilational but the short-period was compressional. This has to represent source complexity. Aki (1984) suggests that this is what should be expected for magma intrusion: a compressional short-period arrival everywhere. At long periods the source should approximate a CLVD if the seismic source process time is long compared to the filling of dike. This is still in conflict with the local short-period focal mechanisms which show four quadrant

radiation patterns. Ryall (1984, personal communication) feels that these focal solutions are well constrained. An alternative hypothesis is that the source complexity actually represents multiple shear faulting events.

The confusion about interpreting the short-period arrivals is largely a result of the long-period moment tensor inversion results. Clearly, if the solution had been close to a double couple the discrepancy between long- and short-period polarities would have been interpreted differently. Since the interpretation of the moment tensor results are so important we must re-examine the resolution of the inversion.

Interpretation of a Moment Tensor

The seismic moment tensor is a convenient way to represent most seismic sources. Gilbert (1971) gives the moment tensor in terms of $\hat{n}$, a unit normal to fault plane, and $\hat{e}$, a unit slip vector ($\hat{n}$ and $\hat{e}$ are mutually perpendicular):

$$M_{ij} = M_o (n_j e_j + n_j e_j) \tag{1}$$

M_o is the scalar seismic moment which is proportional to the product of the fault area and the average displacement. As an example, consider a strike-slip fault orientated perpendicular to n_1. Then the moment tensor has the form

$$\underline{M} = M_o \begin{pmatrix} 0 & M_{12} & 0 \\ M_{21} & 0 & 0 \\ 0 & 0 & 0 \end{pmatrix} \tag{2}$$

Since the moment tensor is symmetric it can be rotated into a principal coordinate system and it is most easily characterized by its eigenvalues. These eigenvalues correspond to the principal stress-drop axes: P (maximum compressive), T (minimum compressive) and I (intermediate). Table 1 gives the characteristic eigenvalues for three sources with no volume change (Geller, 1976).

A synthetic seismogram is a linear function of the moment tensor elements. This implies that by using the moment tensor representation it is possible to invert a set of seismic observations to determine the seismic source without first specifying a specific source model; for example, a double couple or an explosion. In general, the moment tensor inversion yields three unequal eigenvalues ($|\lambda_1| > |\lambda_2| > |\lambda_3|$). If the source were a perfect double couple, then $\lambda_1 = -\lambda_2$ and $\lambda_3 = 0$, but in practice this is never the case because of noise in the data or unaccounted complexity in travel path structure or source. If $\lambda_1 \approx -\lambda_2$ and $|\lambda_1| \gg |\lambda_3|$, then the solution is usually interpreted in terms of a shear fault and λ_3 is considered noise. For a shallow source (the source depth is much less than the wavelength of the observation) it is impossible to resolve the isotropic, or volume change, component of the moment tensor (see Burridge et al., 1964; Kanamori and Given, 1981). For this reason the volume change is usually constrained to be zero. This constraint means that the trace of the moment tensor be zero: $\lambda_1 + \lambda_2 + \lambda_3 = 0$. The process of interpreting the nature of the seismic source amounts to decomposing this system of eigenvalues into a set of double couples or compensated linear vector dipoles.

The decomposition of the eigenvalues can be done many different ways. If we consider an ordering of eigenvalues of the form ($|\lambda_1| > |\lambda_2| > |\lambda_3|$) and $\lambda_1 > 0$, then we have two double couples:

$$\lambda_1 \left(1, \frac{\lambda_2}{\lambda_1}, \frac{\lambda_3}{\lambda_1}\right) = \lambda_1(1, -1+f, -f) = \lambda_1 \underset{\text{MDC}}{(1, -1, 0)} + \lambda_1 \underset{\text{mDC}}{(0, +f, -f)} \qquad (3)$$

where MDC is the major double couple and mDC is the minor, or smaller, double couple. This decomposition maximizes the MDC; the mDC is usually interpreted in terms of noise due to laterally varying structure. It is possible to interpret the sum of double couples as two faulting events, but note that the T axes are perpendicular for the two events. If we wanted to preserve the T axes we could do the following decomposition:

$$\lambda_2 \left(\frac{\lambda_1}{\lambda_2}, 1, \frac{\lambda_3}{\lambda_2}\right) = \lambda_2 (-1-f, 1, +f) = \lambda_2 (-1, 1, 0) + \lambda_2 (-f, 0, f) \qquad (4)$$

The MDC in (4) has the same orientation as the MDC in (3) but its size is reduced by $\frac{\lambda_2}{\lambda_1}$. In (4) the mDC is now maximized.

It is possible to decompose the system into a CLVD and a double couple. In the principal coordinate system the eigenvalues for a CLVD are (-2, 1, 1). For a tensile crack opening in an isotropic media the eigenvalues would be $((\Lambda+2\mu), \Lambda, \Lambda)$, where Λ and μ are the Lamé elastic moduli. Since Λ and μ are non-negative there is a volume expansion. However, if the volume expansion is subtracted from the moment tensor for a tensile crack a CLVD is the remainder. If volume can be preserved in the opening of the tensile crack, such as would be the case for rapid filling from a magmatic reservoir, then a CLVD should be the resultant seismic source. Now consider the case of the three unequal eigenvalues:

$$\frac{\lambda_1}{2} \left(2, \frac{2\lambda_2}{\lambda_1} \frac{2\lambda_3}{\lambda_1}\right) = -\frac{\lambda_1}{2} (-2, 1-f, 1+f) = -\frac{\lambda_1}{2} \underset{\text{CLVD}}{(-2, 1, 1)} + \frac{\lambda_1}{2} \underset{\text{mDC}}{(0, -f, f)} \qquad (5)$$

With this decomposition the CLVD is maximized, and again the mDC can be interpreted as noise. With the opening of a tensile crack or a CLVD the dominant stress direction is the T axis, and hence, it is difficult to interpret the mDC as shear slip which is complimentary to the CLVD since the T direction of the mDC is rotated 90° with respect to the T deflection of the CLVD.

Moment Tensor Solutions for the Mainshock (5/25/80; 16:33)

Three different types of data have been inverted to determine the moment tensor of the mainshock in the Mammoth Lakes earthquake sequence. Given et al. (1982) used very long-period surface waves (~200 seconds) as recorded on the global digital station network (IDA, SRO and ARSO). Ekström and Dziewonski (1983) inverted the body and mantle waves for the GDSN in the period range of 40 to 80 seconds. Finally, Barker and Langston (1983) inverted the body waves recorded on the WWSSN (5 to 20 seconds). Table 2 summarizes the results. Since the solutions are all very similar only the direction of the least compressive stress is given.

On first appearance the Given et al. (1982) solution is very close to a CLVD, but they did not invert for M_{XZ} or M_{YZ}, but rather constrained these elements to be zero. This is because at the long-periods of the inversion (~200 seconds) and the shallow depth of the event (~10 km) M_{XZ} and M_{YZ} are not resolvable. This constraint amounts to requiring the stress axes to be horizontal or vertical; in terms of a double couple this would mean pure strike-slip on a vertical fault or pure dip-slip on a fault dipping 45°. If the actual source mechanism has a large component of oblique slip this constraint will lead to considerable error in the moment tensor. Given et al. (1982) interpreted this to be the case for the May 25, 1980, event, and searched for a double couple which was consistent with the moment tensor and had a minimum

scalar moment. The resultant faulting mechanism is shown in Figure 2. It is important to note that the error Given et al (1982) determined for their two different solutions are nearly identical (only 1% different).

In terms of investigating the possibility of a CLVD it is best to examine the other two moment tensor solutions in Table 2. In both of these cases M_{XZ} and M_{YZ} are not constrained. The solutions are very similar, and the T axes agrees well with Given et al. (1982) (if the plunge is neglected the T axes strike N68°E, N72°E, and N64°E respectively). Table 3 gives the decomposition of these moment tensors into a system that maximizes the double couple and one which has a maximum CLVD. Note that both decompositions have a significant mDC.

The Quality of the Moment Tensor Solutions

Before it is possible to choose between either decomposition in Table 3 it is important to determine what features in the observed seismic waveforms are causing the moment tensor to deviate from a pure double couple. We attempted to do this by comparing synthetic seismograms for the whole moment tensor solution and a constrained double couple to the observed body waves. Figure 3 shows a representative suite of P and S waves for the mainshock. The top trace at each station is the synthetic for the moment tensor (taken from Barker and Langston, 1983) while the bottom trace is the synthetic for the double couple (Given et al., 1982). The time function was taken from Given et al.; Barker and Langston's time function is very similar. The difference in 'fit' of the two models is subtle, and which source model is better is not obvious. As a quantitative measure of the quality of fit we used an error function which is based on the cross correlation of the data and the synthetics:

$$e = 1 - \frac{\int fg}{\left(\int f^2\right)^{1/2}\left(\int g^2\right)^{1/2}} \qquad (6)$$

where f is the synthetic and g is the observation. The limits of integration are the time window of the comparison, which is 30 seconds for the P waves and 40 seconds for the S waves. We used 12 P waves and 4 S waves and summed the errors. For the complete moment tensor the average error was 0.324, while the constrained double couple solution had an average error of 0.338. The difference in the errors is less than 5 percent. The complete moment tensor has five degrees of freedom; only the condition that the trace be zero is imposed. On the other hand, for a constrained double couple solution the condition that the intermediate stress-drop be zero reduces the degrees of freedom to four. Strelitz (1978) points out that it is not correct to assess which solution is optimum unless the number of unknowns is taken into consideration. The number of unknowns can be approximately normalized with a χ^2 test. Using the average error a value for χ^2 is determined. The χ^2 for the double couple solution signifies confidence in the 90-95% level while the entire moment tensor is at the 75-90% level. It is possible to interpret this to mean that the constrained double couple solution is slightly more "significant" than the three couple solution (the entire moment tensor). A more conservative assessment would be that it is not possible to reject the source mechanism of a single, shear fault as the source for the mainshock on the basis of the long-period data.

Neither the moment tensor or the double couple sources do a good job in fitting the observations in Figure 3. Both are inadequate in modeling the large backswing in the P waves. Given et al. (1982) modeled this as a complicated source: two events with identical mechanisms separated by 4 seconds.

If there is sufficient complexity in the source the assumption of a single point source used in the various moment tensor inversions will result in significant errors. For this reason one might suspect that the mainshock is not necessarily a good example for resolving the CLVD. Event D in Figure 1 is an aftershock (M_L = 6.0) which appears to be quite simple. A similar analysis of the quality of fit similar to that done for the mainshock was done for this event. Table 4 gives a summary of the moment tensor inversion results, and Table 5 gives the decompositions.

Figure 4 shows a representative suite of P and SH waveforms for the May 27 event. Again the top trace at each station is the synthetic for the moment tensor (taken from Barker and Langston, 1983) and the bottom trace is the synthetic for the double couple (Given et al., 1982). The time function was taken from Given et al. (1982). The visual difference between the synthetics for the two different types of models is very small. We again used 12 P waves and 4 SH waves to determine the average error of the fit. For the complete normal tensor the average error is 0.231, while the constrained double couple is 0.237. The difference in the error is only 3 percent, and χ^2 test signifies confidence for both solutions in the 90 to 95% level. As with the mainshock it is apparent that it is not possible to differentiate between the two types of source models.

Discussion

The controversy concerning the nature of the source mechanisms of the 1980 Mammoth Lakes earthquake sequence arose largely because the original long-period inversion results (Given et al., 1982) for the mainshock indicated a force system that was consistent with a CLVD. Unfortunately, the inversion required that two elements of the moment tensor be constrained to zero.

Subsequent inversion of higher frequency body and mantle waves (Barker and Langston, 1983; Ekström and Dziewonski, 1983) indicated force systems that had significant deviations from a double couple source, but on the other hand, also deviated from a simple CLVD.

Although the moment tensor representation of the source does not require that a source model be specified, it is not a suitable technique for deciding what the most appropriate source model is for a given set of data. Since a constrained double couple has one fewer parameter than the entire moment tensor (with no volume change), so it is expected that the entire moment tensor will give a better fit to the data. Strelitz (1978) proposed that to determine the optimal solution, the best solutions for the various source types should be compared with a χ^2 test. In the case of the Mammoth Lakes sequence mainshock the constrained double couple cannot be rejected on the basis of the available data. The same thing is true for the aftershock on May 27, 1980. Therefore, the nature of the source must be resolved with other data or techniques.

The fact that the Long Valley caldera is a site of magmatic resurgence (Savage and Clark, 1982) suggests that a relationship exists between intrusion and the earthquakes. A direct causal relationship can be questioned though because of the Wheeler Crest earthquake. This event is far removed from the resurgent dome in the western part of the caldera, and is more than 10 km from the large events in the 1980 sequence (see Figure 1). The location of the event is not near any recent evidence of magmatic activity. Yet the moment tensor solution of Ekström and Dziewonski (1983) is very similar to the solutions of the 1980 events; it deviates significantly from a double couple (the eigenvalues are -2.1, 0.6, 1.5 x 10^{24} dyne-cm). There is also a discrepancy between the short- and long-period polarities (see Figure 2; the

long-period mechanism was determined by Wallace and Helmberger, 1981). If one accepts an explanation of source or structural complexity for the Wheeler Crest event, then the same explanation must be considered for the 1980 sequence.

The most consistent result in the moment tensor inversions is the direction of the tension axes. In Figure 1 the lines at each epicenter point in the direction of the T axes; the plunges are all small, less than 15°. The least compressive stress seems to be the dominate or controlling feature in the seismic sources. This is consistent with work by Vetter and Ryall (1983) which showed that for aftershocks in the Mammoth Lakes region the tension axes remained constant, although the faulting mechanisms changed from pure strike-slip to 45° normal slip at 8 km depth. This indicates that the maximum and intermediate compressive stresses are approximately equal at the hypocentral depth of the 1980 events. It seems likely that if these two stresses are approximately equal the source complexity will result; as the fault ruptures spatially the relationship between the P and I axes could change. Wallace et al. (1982) suggested that this is the reason for the discrepancy between the short- and long-period polarities. The faulting began by a small strike-slip event and continued as a more moderate dipping oblique slip event. The size of the initial event must be small since it does not effect the long periods, and therefore it probably is not affecting the long-period moment tenor results.

If we decouple the polarity discrepancy problem from the moment tensor solutions, the question is how can we improve the source model to fit the moment tensor results. The two biggest assumptions in the moment tensor inversions are (1) the point source and (2) adequate Green's function to describe the response of the earth structure. In the case of the mainshock

there is no question that it represents a multiple event source. In an attempt to improve the fit to waveforms we therefore used two double couples. Figure 5 shows a comparison of synthetics for the multiple event source and the constrained double couple source used in Figure 3. The model consists of a source at 9 km followed by the second source at 14 km, 4 seconds later. The mechanism for the first source is that determined by the constrained moment tensor inversion, while the second event is a steeply dipping normal event. This model was found purely by trial and error with one condition imposed: the tension axis of the second event must strike ~N65°E and plunge less than 30°. The moment of the first event is 2 times larger than the second. This two-source model has improved the fit to the P waves by increasing the ratio of the amplitude of the backswing to that of the first arrival. Using the same 12 P waves and 4 SH waves as before an average error was determined. The error for the two-event source is 0.246 or approximately 30% less than for the moment tensor solution. Again there is the problem that there are more parameters in the two-source model, but the dramatic improvement suggests that the multiple source model is a strong possibility.

The two source model shown in Figure 5 is by no means unique. Ekström (1983) also modeled the 1980 mainshock with two events. Ekström has a normal fault followed by a strike-slip fault (delayed by 6.9 seconds). The strike-slip fault mechanism is consistent with the short-period mechanism. The resultant model reduces the variance of his solution from 0.182 to 0.129. Again the two source model indicates a significant improvement of fit to the waveforms.

It is interesting to compare the moment tensor that would be expected for the two-source model (oblique slip followed by normal slip) to the moment tensor derived from the mantle waves. Ekström and Dziewonski's moment tensor

inversion is performed at periods between 40 and 80 seconds, and sources that were separated by only 4 seconds should simply add. Figure 6 shows a comparison of the long-period moment tensor and the sum of the moment tensors for the two sources. The comparison is good, and indicates the uncertainty in the original assumption of the moment tensor inversion that the source could be represented as a point source.

Although the mainshock appears complicated, the aftershock on May 27 is much simpler. The waveforms in Figure 4 do not show a systematic signature of a second source. It is possible to improve the fit to the moment tensor by adding a second source, but it is not resolvable in the error of the waveform fit. On the other hand, it is interesting to test the role structure may be playing in the inversion. Patton and Aki (1979) showed that focusing or multipathing due to structure can lead to significant misestimation of the moment tensor elements. As a simple experiment, we presumed that body waves which traveled through the caldera would have reduced amplitudes. So we increased the amplitude of the P and SH waveforms that had take off azimuths between N15°W and N15°E by 15% and repeated the inversion. The eigenvalues became much closer to a double couple:

(-9.7, 4.3, 5.5)	(-12.0, 2.6, 9.4)	(7)
before	after	

Of course this does not imply that structure is the cause of the non-double couple component of the moment tensor, but it adds to the uncertainty in resolving a CLVD source.

Conclusions

The long-period waveforms which have been inverted for the moment tensor solutions of the 1980 Mammoth Lakes sequence cannot resolve a CLVD source or reject a double couple as the mechanism. A causal relationship between dike injection and the 1980 sequence will only be determined by other data, perhaps at higher frequencies. Both source and structural complexity can improve the fit of the moment tensor solution to the data, but the lack of uniqueness does not allow a single, simple model which will explain all the observations.

Interpretation of the source processes for the 1980 events is left mainly to the various investigators' prejudices. If one assumes that a double couple should represent the source, then the data is consistent as long as the large minor double couples are interpreted as noise or multiple sources. On the other hand, it is not possible to reject a CLVD, but the source representation does not improve the fit of the solution.

Acknowledgments

This work is largely the result of interaction with H. Kanamori at Caltech and J. Barker at Woodward Clyde. The author has also benefited from discussions with B. Julian and others at the U.S.G.S. Redbook Conference on "Active tectonics and geologic process, Long Valley, California" in January of 1984. Parts of this work were supported by DOE Contract DE-AC03-82ER13014 at the Pasadena office of Woodward Clyde.

References

Aki, K. (1984). Evidence for magma intrusion during the Mammoth Lakes of May, 1980 and implications of the absence of volcanic (harmonic) tremor, J. Geophys. Res., in press.

Barker, J.S. and C.A. Langston (1983). A teleseismic body wave analysis of the May 1980 Mammoth Lakes, California, earthquakes, Bull. Seism. Soc. Am., 73, 419-434.

Burridge, R., E.R. Lapwood and L. Knopoff (1964). First motions from seismic sources near a free surface, Bull. Seism. Soc. Am., 54, 1889-1913.

Cramer, C.H. and T.R. Toppozada (1980). A seismological study of the May 1980 and earlier earthquake activity near Mammoth Lakes, California, Special Report No. 150, California Division of Mines and Geology, R.W. Sherbourne, Ed., 91-130.

Ekström, G. (1983). Evidence for source complexities of 1980 Mammoth Lakes earthquakes, EOS, 64, 769.

Ekström, G. and A.M. Dziewonski (1983). Moment tensor solutions of Mammoth Lakes earthquakes, EOS, 64, 262.

Geller, R.J. (1976). Body force equivalents for stress-drop seismic sources, Bull. Seism. Soc. Am., 66, 1801-1804.

Gilbert, F. (1970). Excitation of the normal modes of the earth by earthquake sources, Geophys. J. R. Astr. Soc., 22, 223-226.

Given, J.W., T.C. Wallace and H. Kanamori (1982). Teleseismic analysis of the 1980 Mammoth Lakes earthquake sequence, Bull. Seism. Soc. Am., 72, 1093-1109.

Julian, B.R. (1983). Evidence for dyke intrusion earthquake mechanisms near Long Valley caldera, California, Nature, 303, 323-325.

Kanamori, H. and J.W. Given (1981). Use of long-period surface waves for rapid determination of earthquake-source parameters, Phys. Earth Planet Int., 27, 8-31.

Patton, H. and K. Aki (1979). Bias in the estimate of seismic moment tensor by the linear inversion method, Geophys. J. R. Astr. Soc., 59, 479-495.

Ryall, A. and F. Ryall (1981). Spatial-temporal variations in seismicity preceding the May 1980 Mammoth Lakes, California, earthquakes, Bull. Seism. Soc. Am., 71, 747-760.

Savage, J. and M. Clark (1982). Magmatic resurgence in Long Valley caldera, California: Possible cause of the 1980 Mammoth Lakes earthquakes, Science, 217, 531-533.

Strelitz, R.A. (1978). Moment tensor inversions and source models, Geophys. J. R. Astr. Soc., 52, 359-364.

Vetter, U. and A. Ryall (1983). Systematic change of focal mechanism with depth in the western Great Basin, 88, 8237-8250.

Wallace, T.C. and D.V. Helmberger (1981). Evidence for a S-wave anomaly in the Long Valley caldera from long period regional body waves, EOS, 62, 970.

Wallace, T.C., J.W. Given and H. Kanamori (1982). A discrepancy between long and short-period mechanisms of earthquakes near the Long Valley caldera, Geophys. Res. Let., 9, 1131-1134.

Table 1

Non-Volume Sources and their Eigenvalues

Source	Eigenvalues
Double couple	$(\lambda_1, -\lambda_1, 0)$
Compensated linear vector dipole	$(-\lambda_1, \frac{\lambda_1}{2}, \frac{\lambda_1}{2})$
Three couple	$(\lambda_1, \lambda_2, -(\lambda_1+\lambda_2))$

Table 2

Summary of the Moment Tensors for 5/25/80

Tension Axes			
Eigenvalues	Strike	Plunge	References
(-2.68, 1.33, 1.35)*	N68°E	0°	Given et al. (1982)
(-2.2, .8, 1.4)	N252°E	10°	Ekström and Dziewonski (1983)
(-2.12, .65, 1.47)	N244°E	10°	Barker and Langston (1983)

*Moments given in 10^{25} dyne-cm

Table 3

Decomposition of Moment Tensor Solutions 5/25/80

Eigenvalues	Maximum DC		Maximum CLVD	
(-2.2,.8,1.4)*	(-2.2,0,2.2)+(0,.8,-.8)		(-2.2,1.1,1.1)+(0,-.3,.3)	
	MDC	mDC	CLVD	mDC
(-2.12,.65,1.47)	(-2.12,0,2.12)+(0,.65,-.65)		(-2.12 1.06,1.06)+(0,-.41,.41)	

*Units in 10^{25} dyne-cm

Table 4

Summary of the Normal Tensors for 5/27/80

Eigenvalues	Tension Axes Strike	Plunge	References
(-9.7, 4.3, 5.5)*	N258°E	4°	Ekström and Dziewonski (1982)
(-11.6, 3.6, 8.0)	N249°E	13.4°	Barker and Lanston (1983)

*Moments given in 10^{24} dyne-cm

Table 5

Decomposition of Moment Solutions 5/27/80

Eigenvalues	Maximum DC		Maximum CLVD	
(-9.7,4.3,5.5)	(-9.7,0,9.7)+(0,4.3,-4.3)		(9.7,4.9,4.9)+(0,0.6,0.6)	
	MDC	mDC	CLVD	mDC
(-11.6,3.6,8.0)	(-11.6,0,11.6)+(0,3.6,-3.6)		(-11.6,5.8,5.8)+(0,-2.2,2.2)	

Figure Captions

Figure 1: Location map of epicenters in the Long Valley region all the events shown have moments greater than $1x10^{24}$ dyne-cm. The lines from the stars point in the direction of the T axes determined from the long-period focal mechanisms.

Figure 2: Three different groups of mechanisms for some of the earthquakes in the Long Valley region. The short-period fault plane solutions are from local first motions (Ryall and Ryall, 1981; Cramer and Toppozada, 1980). The long-period fault planes are from moment tensor inversions in which the solution is constrained to be a shear fault. The moment tensor solutions are nodal surfaces from Ekström and Dziewonski (1983) and Barker and Langston (1983).

Figure 3: A comparison of body wave synthetics and observations for a characteristic group of seismograms for the mainshock (May 25, 1980; 16:33). The top trace in each group is a synthetic for the entire moment tensor solution, while the bottom trace is a synthetic for the constrained solution shown in Figure 2. The time function is two trapezoids (Given et al., 1982).

Figure 4: A comparison of body wave synthetics and observations for a characteristic group of seismograms for the event of May 27, 1980 (14:50). The top trace at each station is a synthetic for the entire moment tensor solution, while the bottom trace is a synthetic for the constrained solution shown in Figure 2. The time function is from Given et al. (1982).

Figure 5: A comparison of body wave synthetics and observations for a one and two event source for the Mammoth Lakes mainshock. The top trace in each group is the two source synthetic, while the bottom trace is

the synthetic for the constrained solution shown in Figure 2. The mechanisms shown to the left are for the two source model; the first event is at 9 km and the second is delayed 4 seconds and is at a depth of 14 km. The first event has a moment twice as large as the second event; the time function used for both sources is a trapezoid with a 2 second rise, top and fall.

Figure 6: A comparison at the moment tensor elements for the mainshock as determined by Ekström and Dziewonski (1983) (large circles) and those predicted by the two event source.

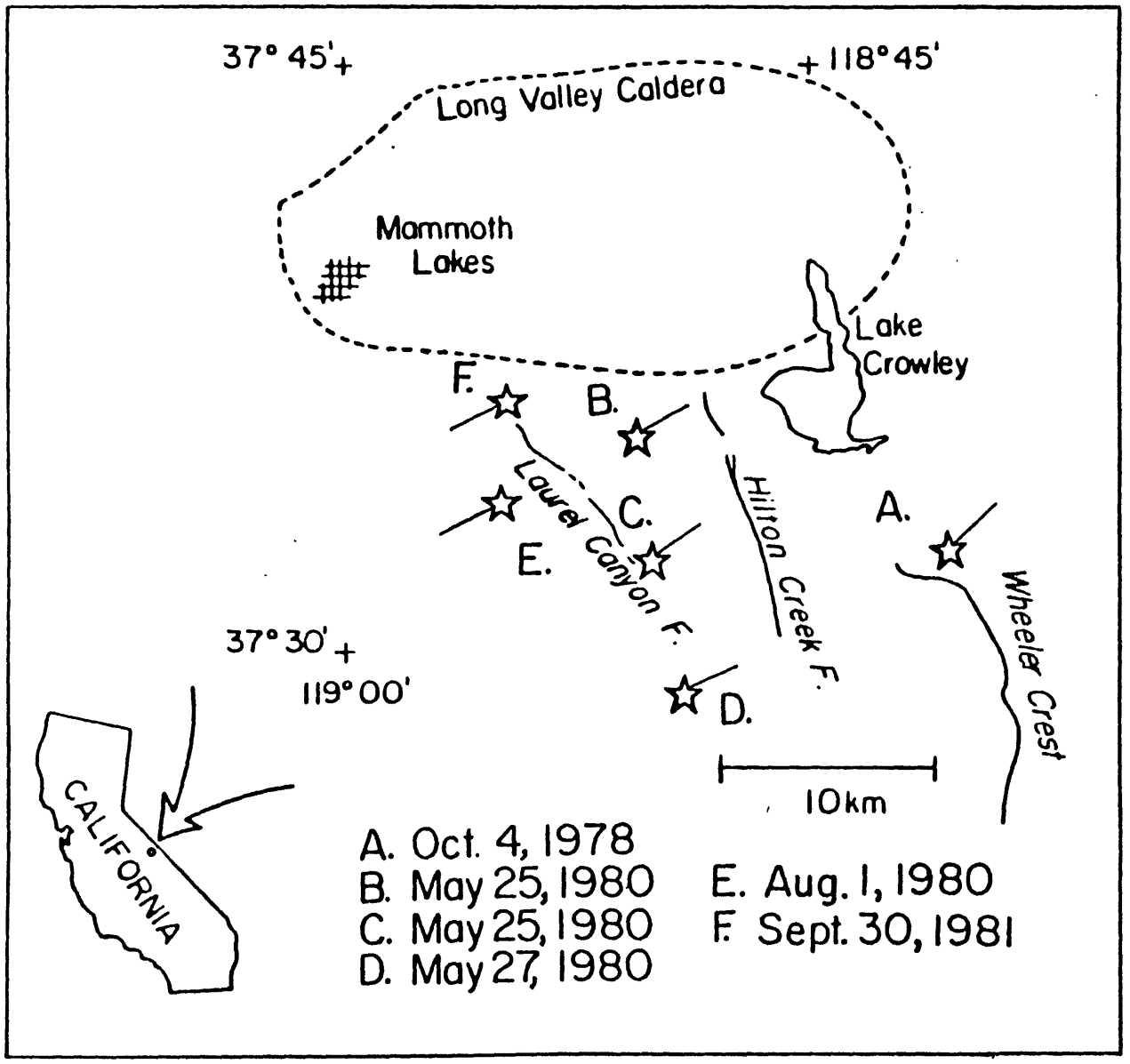
37° 45'
118° 45'
Long Valley Caldera
Mammoth Lakes
Lake Crowley
F.
B.
C.
E.
A.
Laurel Canyon F.
Hilton Creek F.
Wheeler Crest
37° 30'
119° 00'
D.
10km
CALIFORNIA
A. Oct. 4, 1978
B. May 25, 1980
C. May 25, 1980
D. May 27, 1980
E. Aug. 1, 1980
F. Sept. 30, 1981

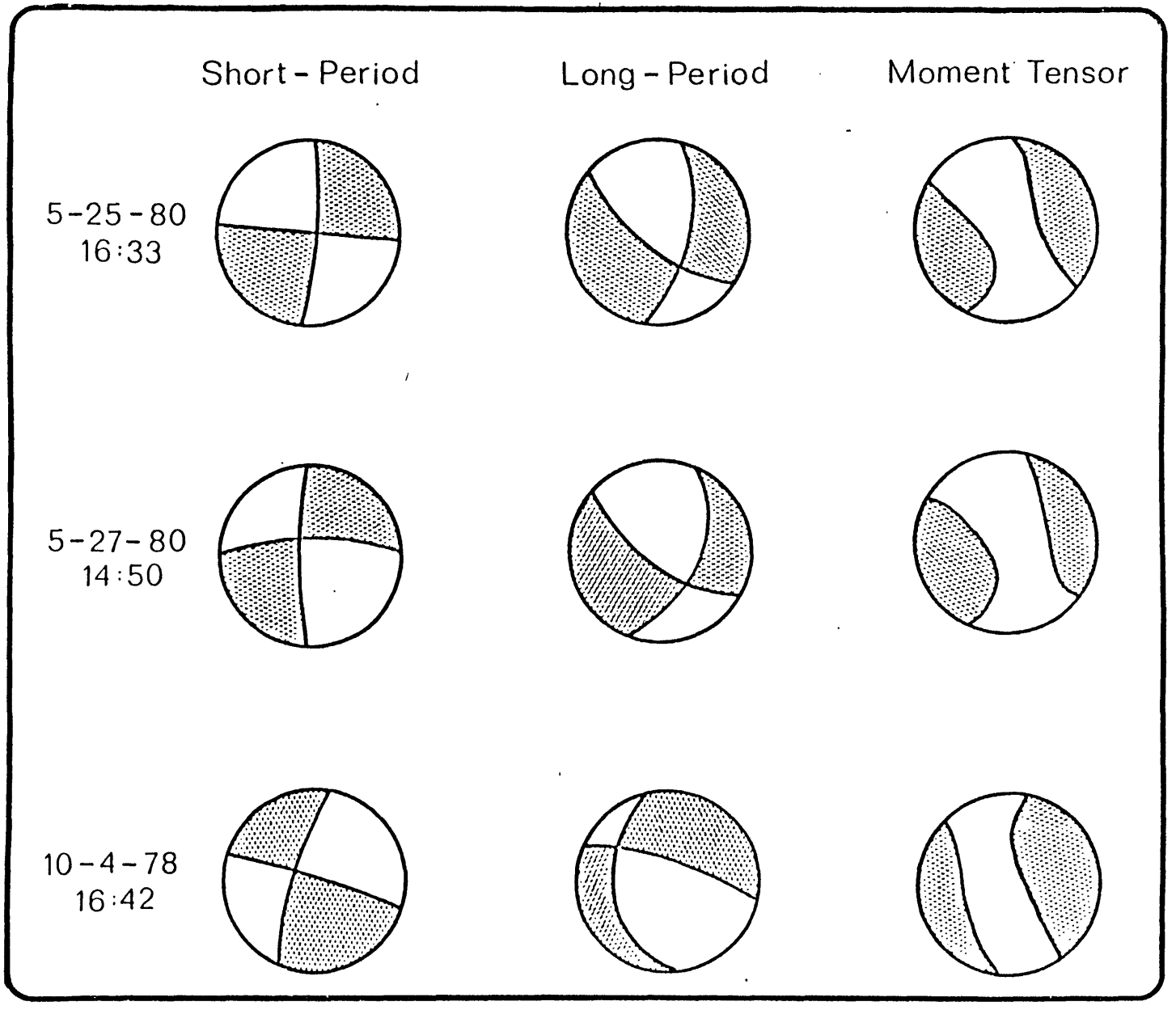
Short - Period
Long - Period
Moment Tensor
5-25-80
16:33
5-27-80
14:50
10-4-78
16:42

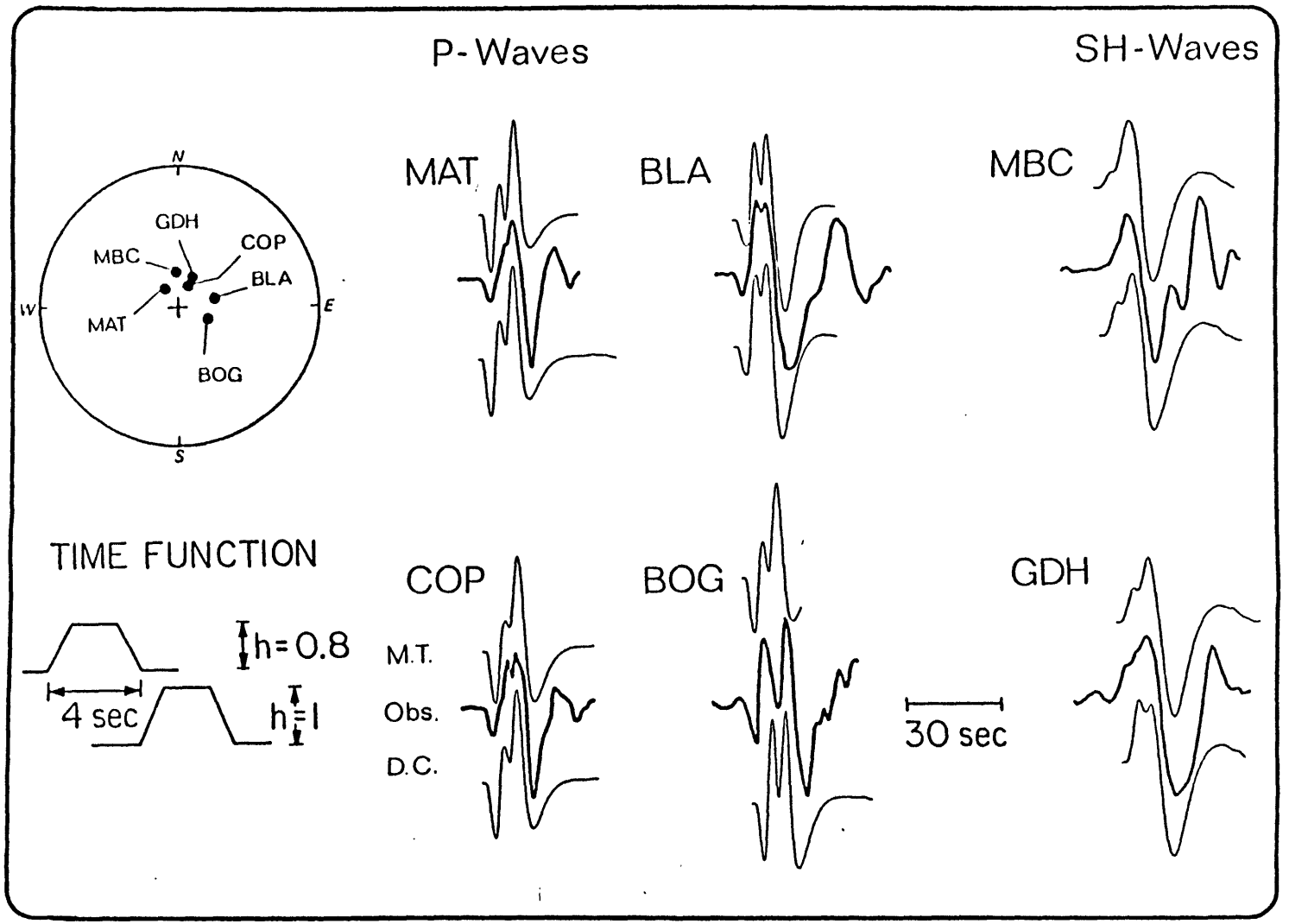
P-Waves
SH-Waves
N
W
E
S
GDH
MBC
COP
BLA
MAT
BOG
MAT
BLA
MBC
TIME FUNCTION
h=0.8
4 sec
h=1
COP
BOG
GDH
M.T.
Obs.
D.C.
30 sec

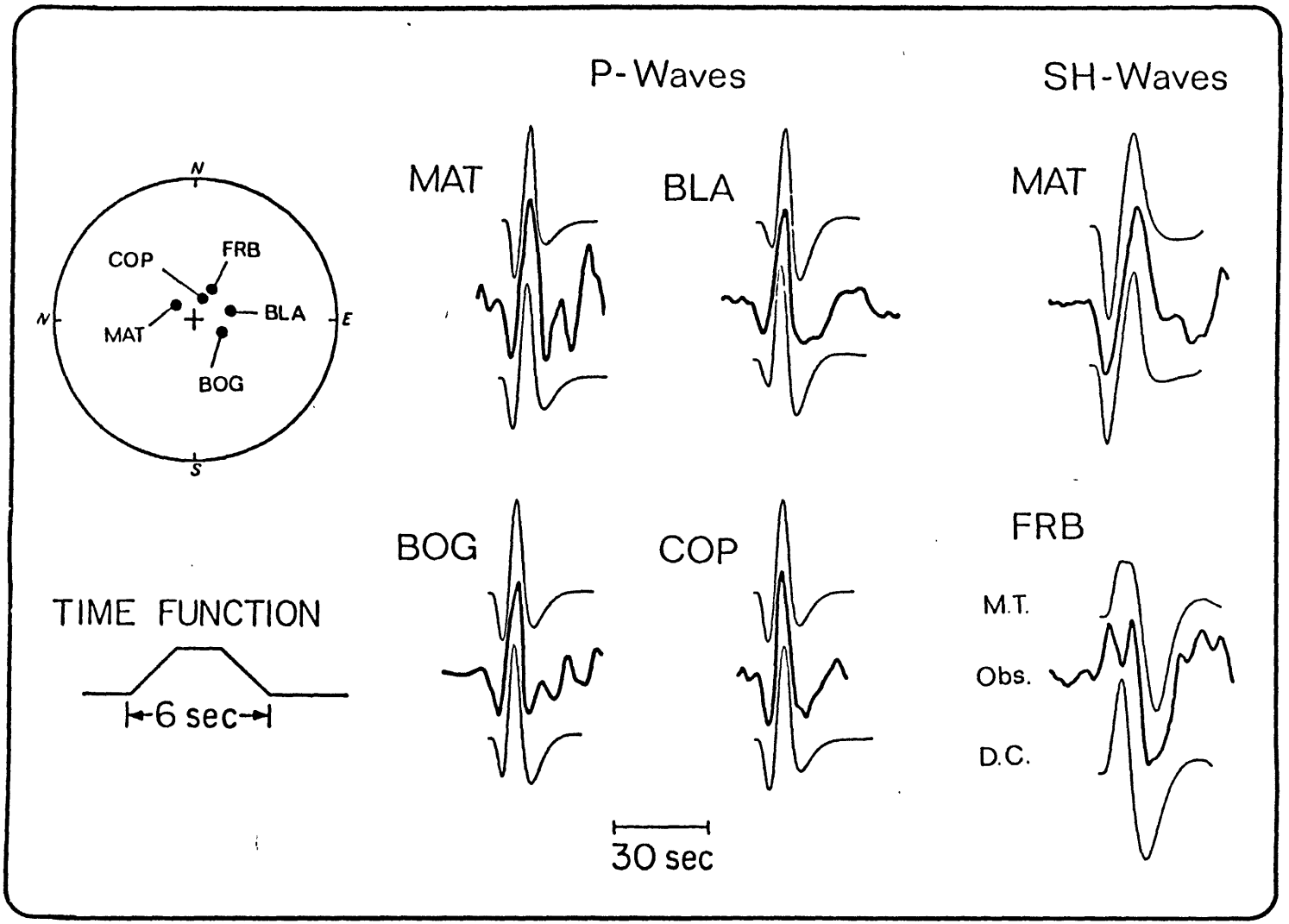
P-Waves
SH-Waves
N
COP
FRB
W
MAT
BLA
E
BOG
S
MAT
BLA
MAT
BOG
COP
FRB
M.T.
Obs.
D.C.
TIME FUNCTION
6 sec
30 sec

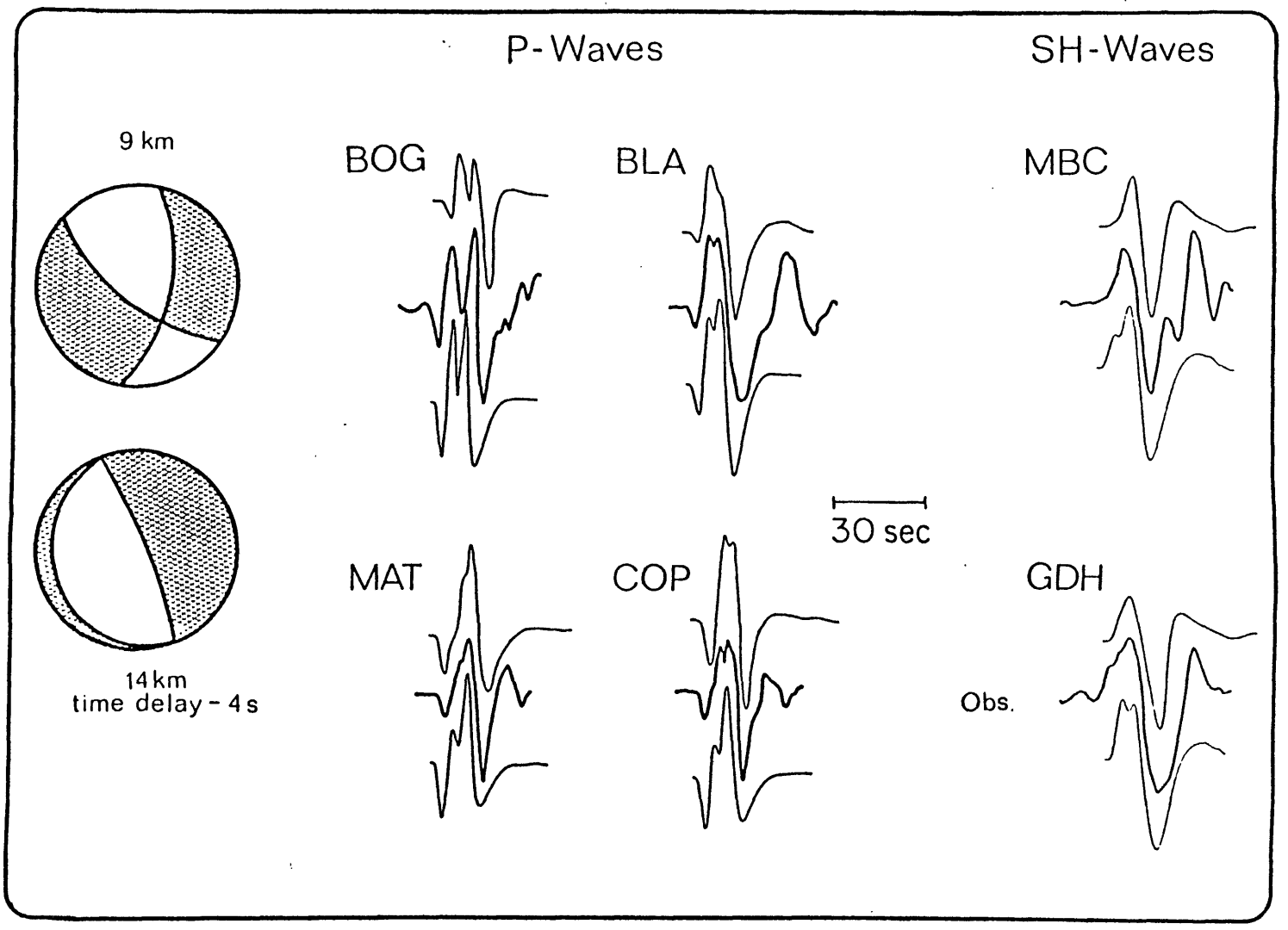
P-Waves
SH-Waves
9 km
14 km
time delay - 4 s
BOG
BLA
MBC
MAT
COP
GDH
Obs.
30 sec

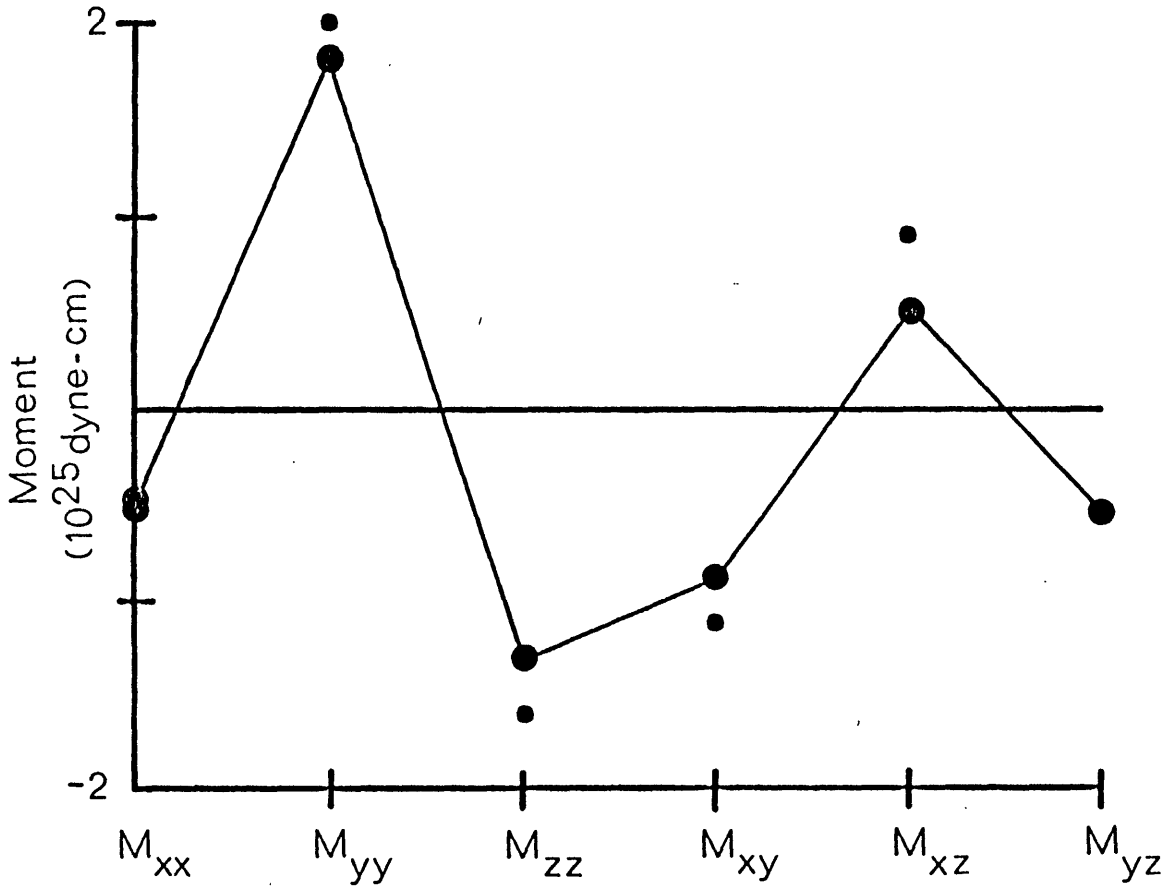
2
-2
Moment
(10^{25} dyne-cm)
M_{xx}
M_{yy}
M_{zz}
M_{xy}
M_{xz}
M_{yz}

RELATIONSHIP BETWEEN AFTERSHOCK LOCATIONS AND MECHANISMS OF THE MAY, 1980 MAMMOTH LAKES EARTHQUAKES

Chester S. Lide and Alan S. Ryall

Seismological Laboratory
University of Nevada
Reno, NV 89557-0018

Abstract. Precise locations of 344 aftershocks of the May 1980 Mammoth Lakes earthquakes indicate that the hypocentral region was bounded on the east side by vertical zones striking NNE, on the north by vertical zones striking WNW and on the bottom by a plane striking NNW and dipping east. These structures support the idea of complex faulting, as do complex waveforms of the larger shocks. The data do not, however, support the interpretation that the large shocks were associated with rapid formation of NNW-striking, vertical dikes.

Introduction

On 25 and 27 May 1980 four magnitude (M_L) 6+ earthquakes occurred near the town of Mammoth Lakes, California. Mammoth Lakes is located in the southwest part of Long Valley caldera, a 17 x 32 km depression formed 0.7 mybp by the eruption of 600 km^3 of ash and tuff (Bailey *et al.*, 1976). The 1980 events were part of a major earthquake sequence that started in the fall of 1978 and has continued to the present time. This swarm has not been associated with a single fault but appears instead to involve complex brecciation of an irregular-shaped crustal block, extending 30 km in a NW-SE direction and about an equal distance from north to south (Ryall and Ryall, 1983). Uplift and horizontal deformation of the surface, intensive swarm activity similar to spasmodic tremor reported in volcanic areas and new fumarole activity have been interpreted as indications of magmatic involvement in the earthquake sequence (US Geological Survey, 1982; Savage and Clark, 1982; Ryall and Ryall, 1983).

An interesting controversy has surrounded the P-wave radiation pattern and moment-tensor solutions for focal mechanisms of the largest Mammoth Lakes events. First-motion plots for short-period P-waves recorded at regional seismic stations indicated that the M_L 5.7-6.2 shocks on 4 October 1978 (1642 GMT), 25 May 1980 (1633, 1649 and 1944 GMT) and 27 May 1980 (1450 GMT) involved primarily strike-slip faulting -- left-lateral slip on vertical planes striking NNE or right-lateral slip on planes striking WNW (Cramer and Toppozada, 1980; Ryall and Ryall, 1981). On the other hand, moment-tensor inversion of long-period body and surface waves requires a different type of mechanism for four of these events -- variously interpreted as left-oblique slip on planes striking NNW and dipping E (Given *et al.*, 1982; Wallace, 1983, 1984) or a non-double-couple mechanism (Barker and Langston, 1983; Julian, 1983; Ekstrom and Dziewonski, 1983; Sipkin and Julian, 1983; Aki, 1984). In several of these papers the data have been explained in terms of the formation of NNW-striking vertical dikes.

While there is other evidence for magmatic activity associated with this sequence, the seismological data are not compelling in terms of interpreting the large shocks as dike injection rather than fault movement. In this regard Wallace (1983, 1984) has shown that the discrepency between short- and long-period radiation patterns could be due either to structural complexity or to source complexity. In the first instance ray paths would be deflected by low-velocity zones below the caldera, leading to misinterpretation of the source geometry. In the second, he presents evidence that large events of the Mammoth Lakes sequence were multiple shocks, starting with a small, high stress-drop event that "may represent the failure of an asperity which, when broken, allows the regional strain to be relieved with the mechanism determined from the long-period data."

In this paper we present results of a master-event relocation of several hundred aftershocks of the May 1980 sequence. Results of this analysis show clear lineups of events along vertical, NNE- and WNW-striking planes that agree with the interpretation of strike-slip faulting, but not with the idea of dike injection along vertical NNW-striking fissures. In addition, P-waveforms of the larger events at local and regional seismic stations support Wallace's suggestion of complex rupturing -- with relatively small strike-slip shocks on vertical planes triggering larger events on faults that could have some other orientation.

Analysis and Results

Aftershock distribution. The data set used in this part of the study included recordings from five stations of the University of Nevada Seismological Laboratory (UNSL) telemetry network, six UNSL field stations and one USGS field station -- all in the area around Long Valley caldera -- plus one station of the University of California, Berkeley (UCB) network on the western slope of the Sierra Nevada. Ten of these stations are shown by triangles on Figure 1. Events selected for analysis were primarily $M_L \geq 3.0$ events (UCB, 1980) for the period 31 May - 4 June 1980, when the UNSL and USGS field stations were operational. For one station (EDL) P-wave arrival times were read using a digitizing tablet, to a precision of about ± 0.02-0.04 second. For other stations times were measured to the same accuracy from strip-chart playbacks of the original tape recordings.

The hypocenter location program developed for this study used Geiger's least-squares method without the weighting or depth-fixing features incorporated into other location routines. Because station elevation differences in the area of interest were large (up to 650 meters) elevations were used in the calculation to avoid problems associated with programs that assume planar station geometry. Use of the three-dimensional station distribution improved the precision of the hypocenter calculations, from an average rms deviation of ±0.08 second for previous solutions using the program HYPO71 (Lee and Lahr, 1975) to average rms of ±0.04 second. The 3D calculation also gave better convergence for events with shallow depth. For simplicity an average velocity of 5.8 km/sec was used for the Sierran crustal block south of the caldera. This velocity was initially determined from the recording of several blasts in the distance range 2-22 km along profiles in the Sierra Nevada. In addition calculations with a range of average velocities indicated that this value yielded minimum residuals in hypocenter determinations.

A master event (31 May 1980, 08h 05m) was selected based on several criteria: 1) the event was centrally located within the epicentral area; 2) it occurred at a time when station distribution was such that it could be located using only stations in the Sierran block; and 3) the event was located at short

distance (1.2 km NW) from a three-component digital event recorder operating at Buzztail Spring in McGee Canyon. This station recorded very clear P and S arrivals which constrained the focal depth to 9.2 km. Using only Sierran stations in the master-event location we avoided bias that might result from including data from stations on low-velocity material within the caldera. Traveltime residuals for stations used in the master-event location ranged from -0.05 to +0.06 and gave an rms deviation of ± 0.03 second. The traveltime residual at each station for the master event was used as a correction in locating other earthquakes relative to the master event.

The large earthquakes on 25-27 May 1980 occurred before most of our field equipment was operating; they were relocated using the program HYPO71 with station corrections determined from the master event procedure. Epicenters for these events are somewhat less reliable than those for the aftershocks, but probably more reliable than previously published values (Cramer and Toppozada, 1980). The latter included readings from stations out to distances greater than 200 km and mixed readings from sensitive seismic stations with trigger times of strong-motion instruments. Because the large shocks were multiple events (see below) it is probable that arrival times at different distance ranges, or from recordings of instruments with very different magnification, corresponded to different events within the P coda.

Figure 1 shows the location of 344 events in the area of interest. The rms values of the residuals for all of the hypocenter determinations were less than 0.1 second, and the events are considered to be located to an accuracy of a few hundred meters relative to the master event. The figure shows clear NNE trends in the Sierran block south of Long Valley caldera, as well as WNW trends along the southern boundary of the caldera. Two of the four M_L 6+ events on May 25 and May 27 (solid circles on Figure 1) were located in or near the NNE-trending aftershock zones, the third was at the intersection of a NNE zone with the caldera boundary, and the fourth was at the western end of a WNW-trending cluster. Figure 2 shows a cross-section viewed in the direction N20°E for the area south of the caldera. The figure indicates clearly that the eastern edge of the hypocentral zone is a vertical plane striking NNE, and it also suggests that the western boundary of the zone is a plane dipping east.

The fracture pattern is perhaps better seen in a 3-dimensional projection (Figure 3) which when viewed with a stereoscope shows a vertical zone of hypocenters trending WNW along the caldera boundary, several NNE-trending vertical clusters, and -- underlying the hypocentral zone -- a plane striking NNW and dipping moderately to the east. The latter is parallel to, and on line with, the Hartley Springs fault which is the main frontal fault northwest of Long Valley caldera.

Waveforms of large shocks. Interpretation of first-motion data to determine mechanisms for the M_L 6+ earthquakes on 25 and 27 May 1980 is complicated because the large events were multiple shocks. Evidence for this is shown by several playbacks (Figure 4) from a wideband digital event recorder that was operating at the Mammoth Lakes Forest Service Visitor Center during the period of interest. All of the traces shown on the figure are *displacement* recordings, uncorrected for instrument response. On the left side are shown playbacks of the vertical-component instrument, at identical gain settings, for the M_L 6.1 shock at 16h 33m GMT on 25 May and for an M_L 4.6 aftershock at 17h 06m GMT on 25 May. Comparison of the two recordings indicates that the M_L 6.1 P onset was smaller than that of the M_L 4.6 aftershock; 0.3 second after the P onset another arrival is observed which had opposite polarity from the first one and much larger amplitude. On the right side of Figure 4 are playbacks for the largest (M_L 6.2) event of the sequence, at 14h 50m GMT on 27 May, compared with an

M_L 4.0 aftershock of that event. Within the P-wave of the M_L 6.2 event can be seen several pulses with drastically different amplitudes. The first, labeled "1" on the figure, is about comparable to the P-amplitude for the M_L 4.0 aftershock, although the latter has a sharper onset. A second event ("2") occurs about 0.3 second after the initial P-wave, and a third ("3") at about 0.7 second after the first arrival. Taking into account the differences in gain for the playbacks, the third event had almost 50 times the amplitude of the first one.

Complexity in the P-wave group for the large events leads to some concern about fault-plane solutions based on data from different distance ranges. Because successive P-arrivals increase in amplitude, arrivals at larger distance could correspond to the later pulses (i.e., pulse "2" or "3" for the M_L 6.2 event shown on Figure 4). To combine first-motion measurements at different distance ranges into one fault-plane solution requires the assumption that all of the pulses represent coherent motion on a fault, with amplitude increasing as a function of time (i.e., breaking of larger asperities with time). For the M_L 6.2 shock on 27 May this assumption may be valid: The pulses labeled for this event on Figure 4 all have the same polarity, and a first-motion plot using more than 150 observations in the California-Nevada region is, although not well constrained, consistent with a fault-plane solution that could range from strike- to oblique-slip (E. J. Corbett, personal communication). However, as noted above the second pulse on the recording of the M_L 6.1 event on the left side of Figure 4 has opposite polarity from the first pulse, which suggests that it was caused by an event with a different mechanism.

Discussion

In a study of steeply-dipping joint systems in the Sierra Nevada Mayo (1937) found that trends of N30-50°E and N30-50°W predominated to the west and northwest of the Rock Creek salient, which contains the eastern edge of the hypocentral zone shown on Figures 1 and 3. Within that block, however, swarms of fractures striking N10-20°E predominate. Figure 5 is a plot of rose diagrams showing the strike of fractures as mapped by Mayo; note the predominance of joints striking N10-20°E in the southeast quadrant. Lockwood and Moore (1979) also identified NNE-trending *microfaults* in an area near the southern end of the epicentral zone on Figure 1, and associated left-lateral strike-slip motion with these fractures.

There is excellent agreement between the NNE-striking nodal planes determined by Cramer and Toppozada (1980) and Ryall and Ryall (1981) for the large shocks in 1978 and 1980, vertical zones of hypocenters determined in this study, and the predominant strike of joints and fractures in the area of interest (Mayo, 1937; Lockwood and Moore, 1979). We conclude that the 1978 event and at least the first of the large 1980 shocks were initiated by left-lateral strike-slip motion on vertical planes striking NNE. From the distribution of aftershocks the large shock within the caldera appears to have resulted from right-lateral strike-slip along the WNW-striking vertical zone associated with the southern boundary of the caldera, and the large event near the intersection of these zones could have been associated with either of these types of faulting. We see no evidence for vertical NNW-striking hypocentral zones and as a result conclude that our analysis does not support the idea (Julian, 1983; Aki, 1984) that the large shocks were caused by the rapid formation of dikes with that orientation.

It appears that a fault parallel to the rangefront may also have played a part in the Mammoth Lakes sequence, evidenced by the NNW-striking, east-dipping plane that appears to form the southwestern boundary of the

hypocentral zone on Figure 3. One possibility is that the plane represents a southerly extension of the Hartley Springs fault. Crustal extension in an ENE-WSW direction could result in normal or oblique slip on that fault, as well as left-lateral or right-lateral strike-slip, respectively, on vertical planes striking NNE or WNW (Vetter and Ryall, 1983).

From examination of the P-waveforms for two of the largest earthquakes of the sequence we conclude that these shocks started as small-to-moderate events, initiating a complex rupture process that increased in amplitude and at least in one case changed in orientation with time. In the case of the M_L 6.1 shock at 16h 33m GMT on 25 May the initial event had magnitude greater than 4 and a fault-plane solution corresponding to a vertical strike-slip fault (Ryall and Ryall, 1981). For the M_L 6.2 shock on 27 May, local and regional observations of P-wave first-motion direction could be consistent with either strike- or oblique-slip motion, respectively on a vertical plane striking N or on a plane striking NNW and dipping W (E. J. Corbett, personal communication). Since the initial P waves for these events would not have been detected by long-period teleseismic stations, mechanisms inferred from the inversion of data from such stations reflect the release of regional strain -- possibly by oblique slip on planes striking NNE and dipping E, as suggested by Given *et al.* (1982). Evidence from the mechanism of the initial shock for the M_L 6.1 event on 25 May, and from the distribution of aftershocks shown on Figures 1-3, suggests that the large earthquakes may have been triggered by small strike-slip events on vertical fractures (Wallace, 1983; 1984). Recordings of the UNSL network indicate that complex rupturing is not uncommon for the Mammoth Lakes sequence, even for relatively small events.

Acknowledgements

W. A. Peppin and E. J. Corbett reviewed the manuscript and made helpful suggestions. Some of the data used to determine aftershock distribution was supplied by the U. S. Geological Survey and the University of California, Berkeley. This research was partly supported by the U. S. Department of Interior, Geological Survey, under contract 14-08-0001-21863, and partly by the U. S. Department of Energy under contract DE-AS08-82ER12082.

References

Aki, K., Evidence for magma intrusion during the Mammoth Lakes earthquakes of May, 1980 and implications of the absence of volcanic (harmonic)tremor, submitted to *Jour. Geophys. Res.*, 1984.

Bailey, R. A., Dalymple, G. B. and Lanphere, M. A., Volcanism, structure and geochronology of Long Valley caldera, Mono County, California, *Jour. Geophys. Res.*, *81*, 725-744, 1976.

Barker, J. S., and Langston, C. A., A teleseismic body wave analysis of the May 1980 Mammoth Lakes, California, earthquakes, *Bull. Seismol. Soc. Am.*, *73*, 419-434, 1983.

Cramer, C. H., and Toppozada, T. R., A seismological study of the May 1980 and earlier earthquake activity near Mammoth Lakes, California, *Calif. Div. Mines Geol. Spec. Rep.*, *150*, 91-130, 1980.

Ekstrom, G., and Dziewonski, A. M., Moment tensor solutions of Mammoth Lakes earthquakes, *EOS, Trans. Am. Geophys. Un.*, *64*, 262, 1983 [abstract].

Given, J. W., Wallace T. C., and Kanamori, H., Teleseismic analysis of the 1980 Mammoth Lakes earthquake sequence, *Bull. Seismol. Soc. Am.*, *72*, 1093-1109, 1982.

Julian, B. R., Evidence for dyke intrusion earthquake mechanisms near Long Valley caldera, California, *Nature, 303*, 323-325, 1983.

Lee, W. H. K. and Lahr, J.C., HYPO71: a computer program for determining hypocenter, magnitude and first motion pattern of local earthquakes, *U. S. Geol. Survey, Open-File Rept. 75-311*, 113 pp., 1975.

Lockwood, J. P. and Moore, J. G., Regional extension of the Sierra Nevada, California, on conjugate microfault sets, *Jour. Geophys. Res.*, *84*, 6041-6049, 1979.

Mayo, E. B., Sierra Nevada pluton and crustal movement, *Jour. Geol.*, *45*, 169-192, 1937.

Ryall, A., and Ryall, F., Spatial-temporal variations in seismicity preceding the May, 1980, Mammoth Lakes, California, earthquakes, quakes, *Bull. Seism. Soc. Am.*, *71*, 27-39, 1981.

Ryall, A., and Ryall, F., Spasmodic tremor and possible magma injection in Long Valley Caldera, eastern California, *Science, 219*, 1432-1433, 1983.

Savage, J. C., and Clark, M. M., Magmatic resurgence in Long Valley caldera, California: Possible cause of the 1980 Mammoth Lakes earthquakes, *Science, 217*, 531-533, 1982.

Sipkin, S. A. and B. R. Julian, Evidence for non-double couple earthquake mechanisms, *EOS, Trans. Am. Geophys. Un.*, *64*, 262, 1983 [abstract].

Sorey, M. L., Lewis, R. E., and Olmstead, F. H., *The Hydrothermal System of*

Long Valley Caldera, California, US Geol. Survey Prof. Paper 1044-A, 60 pp., 1978.

Univ. Calif., Berkeley, *Bull. Seismogr. Stations, 50*, 87 pp., 1980.

U. S. Geol. Survey, *Volcano Hazards Assessed for California's Long Valley-Mono Lake Area*, press release, 5 pp., 1982.

Vetter, U. R. and A. S. Ryall, Systematic change of focal mechanisms with depth in the western Great Basin, *Jour. Geophys. Res., 88*, 8237-8250, 1983.

Wallace, T. C., *Long Period Regional Body Waves*, Calif. Inst. Technology, PhD Dissertation, 180 pp., 1983.

Wallace, T. C., A re-examination of the moment tensor solutions of the 1980 Mammoth Lakes earthquakes, *Active Tectonic and Magmatic Processes in Long Valley Caldera, US Geol. Survey Open-File Rept.*, 1984.

Figure Captions

Figure 1. Map of Long Valley caldera showing caldera margin, mapped faults (from Sorey *et al.*, 1978), town of Mammoth Lakes (in SW part of caldera), Lake Crowley (crossing SE part of caldera), seismic stations used in the present study (triangles), epicenters of M_L 6+ shocks in 1980 (solid circles) and locations of 344 aftershocks (crosses).

Figure 2. Depth section showing 227 events south of Long Valley caldera. View is N20 E. Note vertical zone at right (eastern) side of hypocentral zone and suggestion of an east-dipping zone (upper left to lower right).

Figure 3. Three-dimensional plot of hypocentral zone, showing the 344 aftershocks on Figure 1. North is toward the top of the figure, the viewpoint is 15 km directly above the earth's surface, and the dimensions of the box are 33 km N-S, 22 km E-W and 16 km in depth. With the aid of a stereoscope the figure shows vertical planes trending NNE in the eastern part of the hypocentral zone, vertical planes trending WNW along the northern edge of the zone (southern boundary of the caldera) and a deeper plane striking NNW and dipping east.

Figure 4. *Left-side*: Playbacks from a digital event recorder at the Mammoth Lakes Forest Service Visitors Center, for the first M_L 6.1 event at 16h 33m GMT on 25 May 1980, and for an M_L 4.6 aftershock at 17h 06m on the same date. Distance to the station is 12.77 km for the 1633 event and 13.00 km for the aftershock. Playbacks were made at the same gain setting and up on both records corresponds to ground motion up. *Right side*: Playbacks at three different gain settings for the M_L 6.2 earthquake at 14h 50m on 27 May 1980, compared with an M_L 4.0 aftershock at 15h 42m on the same date. Relative gain settings are indicated at the side of each playback. Numbers indicate successive pulses within the P wave for the 1450 event. The large earthquake and the aftershock were within a kilometer of each other. The traces correspond to ground *displacement* and are uncorrected for instrument response.

Figure 5. Rose diagrams showing frequency of various orientations of steeply dipping joints and fractures for four areas south of Long Valley caldera, from Mayo (1937). The four areas are separated by lines at latitude 37.5 N and longitude 118.94 W. The southern boundary of the caldera, Lake Crowley and several mapped faults are also shown.

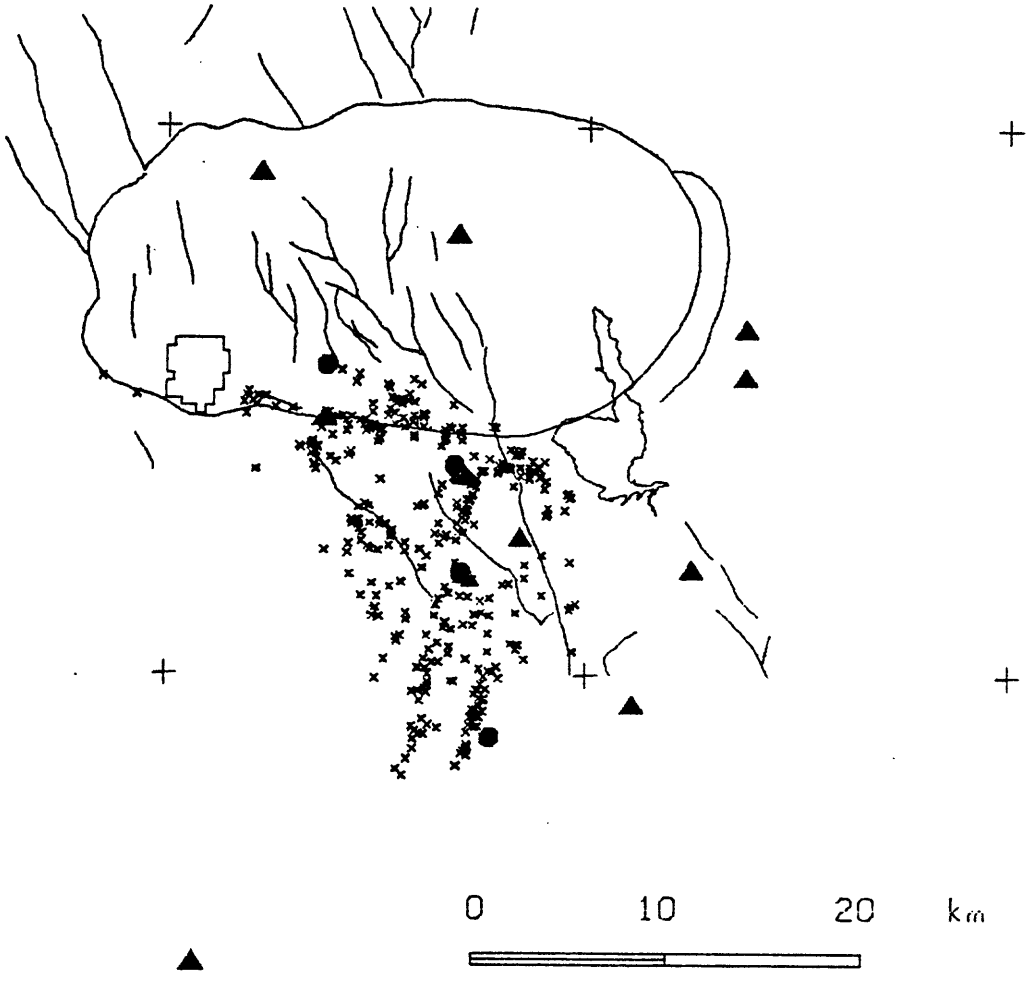

Figure 1

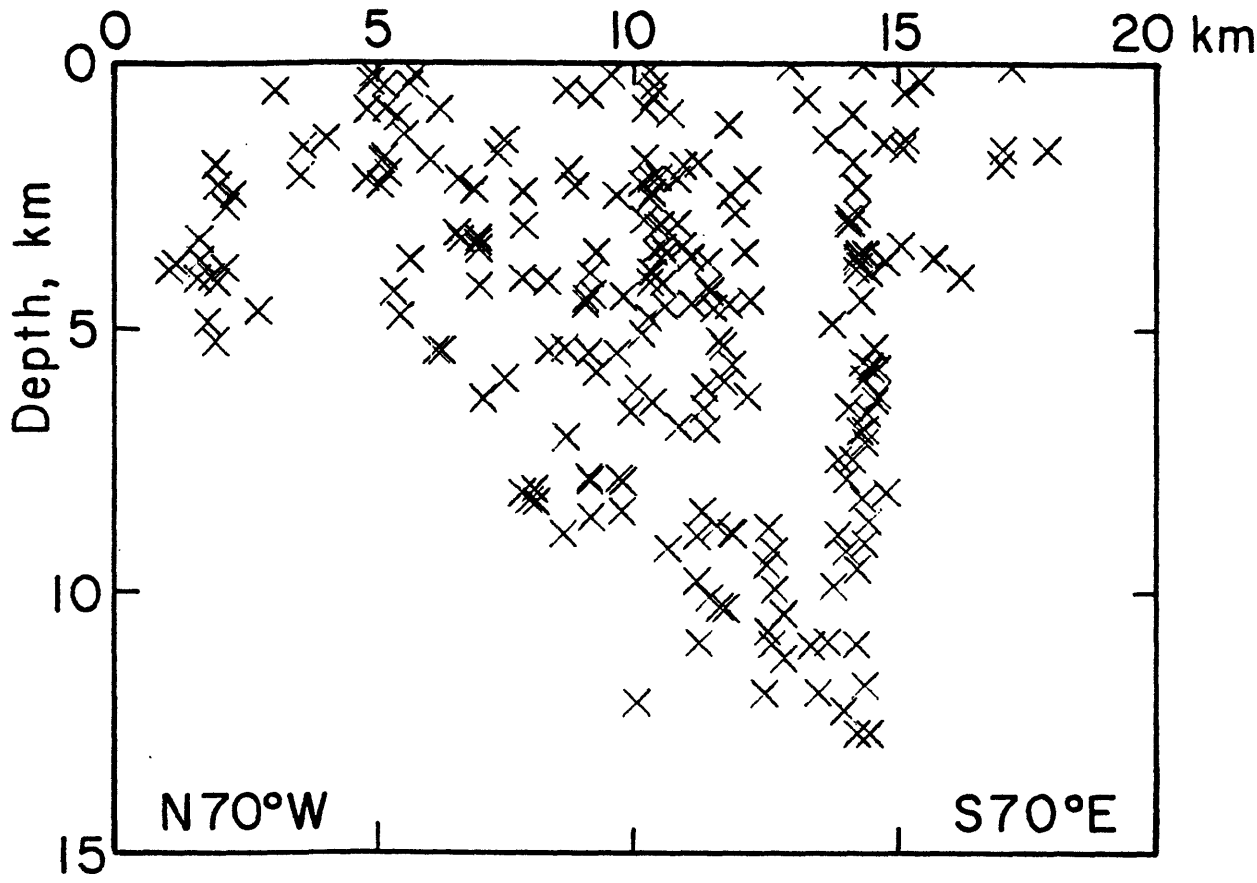

Figure 2

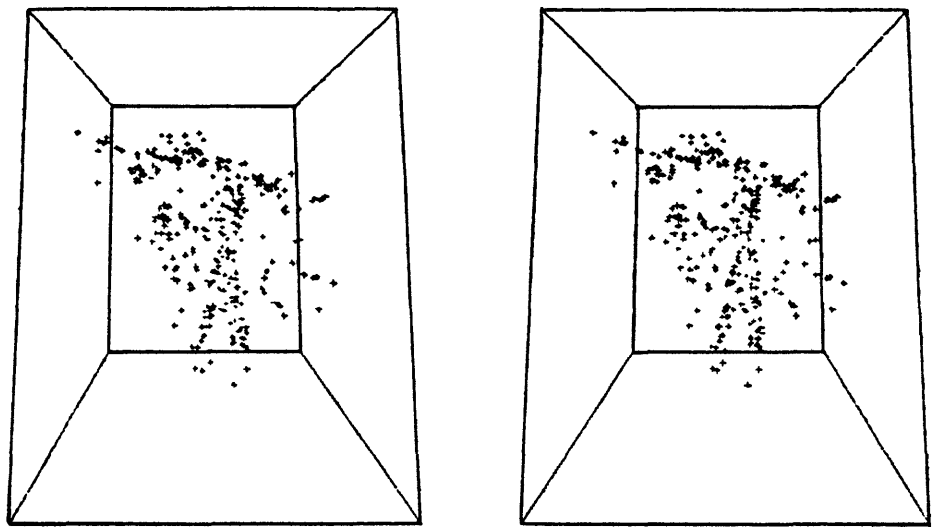

Figure 3

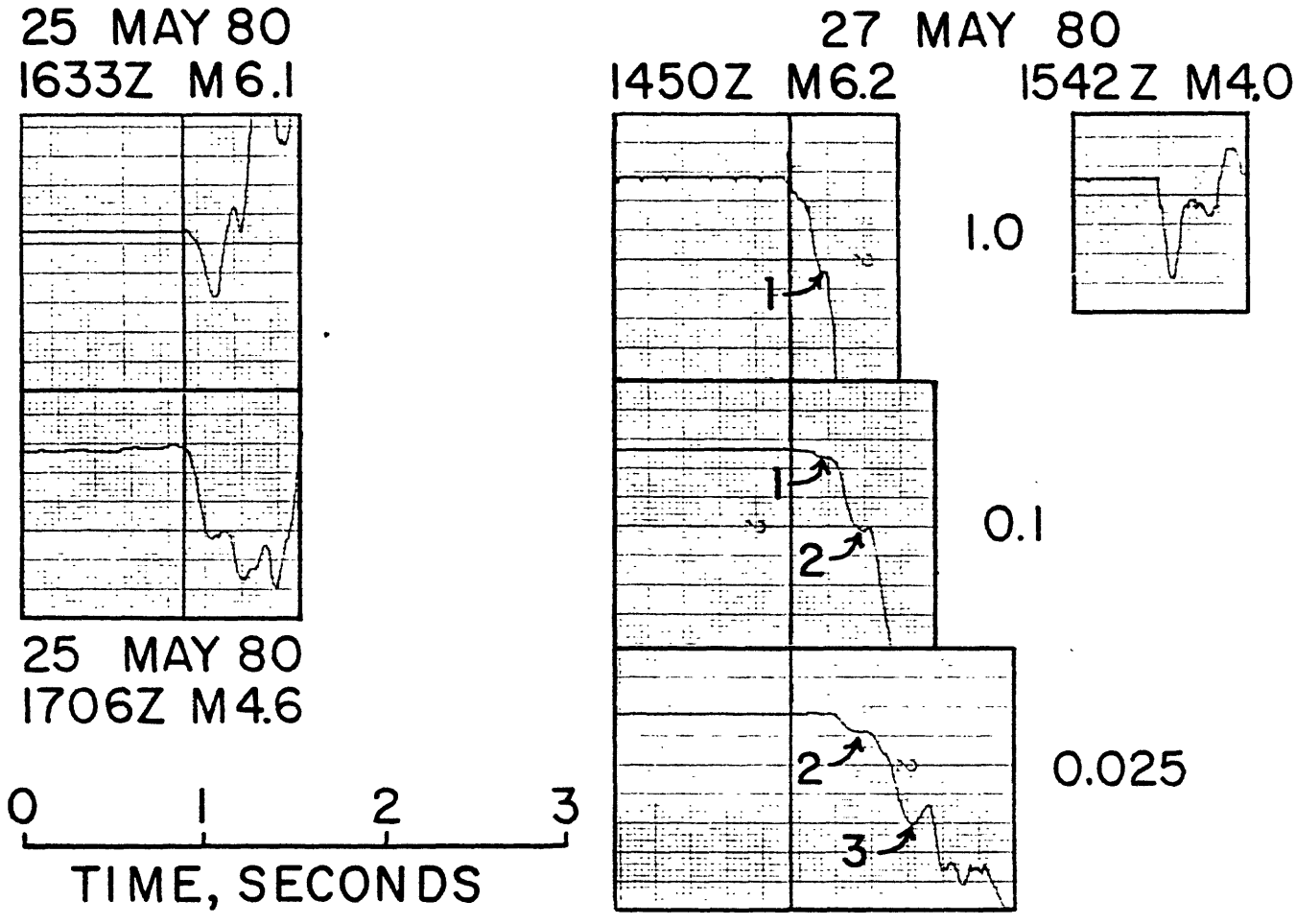
25 MAY 80
1633Z M6.1
25 MAY 80
1706Z M4.6
0
1
2
3
TIME, SECONDS
27 MAY 80
1450Z M6.2
1542Z M4.0
1.0
0.1
0.025
1
1
2
2
3

Figure 4

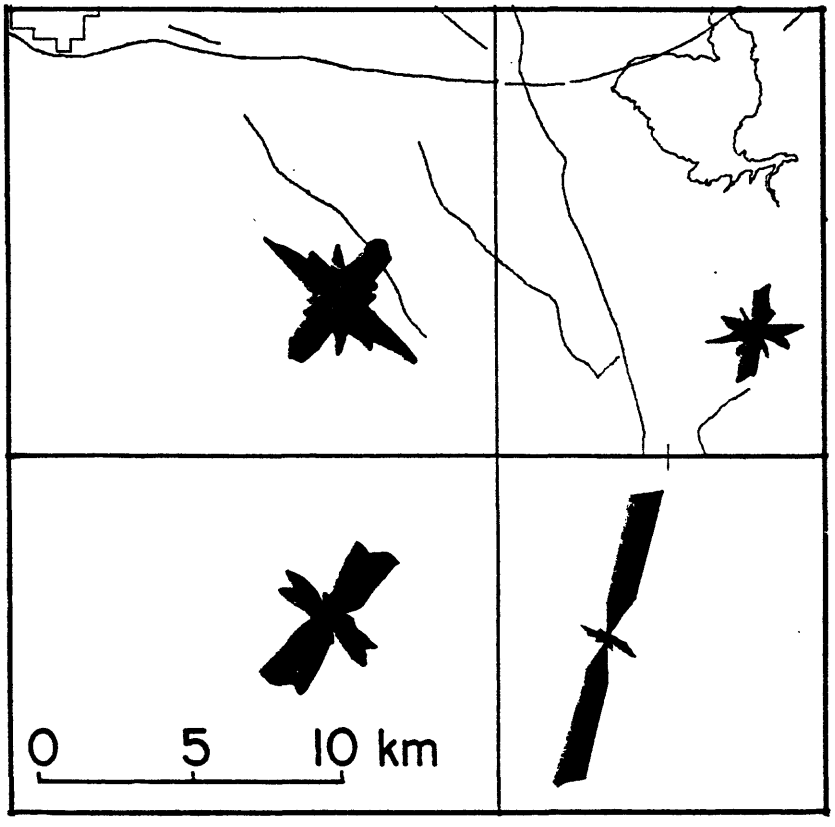

Figure 5

FOCAL MECHANISMS AND FREQUENCY-DEPTH DISTRIBUTION OF EARTHQUAKES IN THE MAMMOTH LAKES AREA

Ute R. Vetter

Seismological Laboratory
University of Nevada
Reno, NV 89557-0018

ABSTRACT

Fault-plane solutions for more than 100 Mammoth Lakes earthquakes indicate that earthquake mechanisms change systematically with depth, as we have also observed for western Nevada earthquakes: the shallow earthquakes have mainly strike-slip mechanisms, the deeper ones oblique and normal slip. The change takes place in the depth range of 6-9 km. On the basis of this change in mechanism a rough estimate of the principal stress components and their variation with depth can be made. Using published temperature-depth curves for the Basin and Range province and the frequency-depth distribution of earthquakes in the same area, a temperature-depth curve for the Mammoth region can be derived under the assumptions that the two tectonically similar regions have the same temperature at their respective maximum seismogenic depth, and that the respective geotherms have the same shape. In this way, the frequency-depth distribution of earthquakes in the Mammoth Lakes region implies a temperature of $400-500^{\circ}C$ at 11 km depth.

While each region exhibits extensional tectonics, the focal mechanisms indicate a significant difference in the direction of maximum extension: ENE-WSW for Mammoth Lakes and NW-SE for the western Great Basin.

INTRODUCTION

The primary tectonic process in the Basin and Range province is lithospheric extension, with the average extension direction being E-W to NW-SE, resulting in the brittle fragmentation of a crustal slab above a plastically extending lower medium. The Mammoth Lakes area is located within the Sierra Nevada Great Basin boundary zone, where significant changes in crustal structure, crustal thickness and also in heat flow are known to occur. The Long Valley caldera (outlined on Figs. 1-6) collapsed 720,000 years ago, following the eruption of the Bishop Tuff (Bailey et al., 1976). Intracaldera volcanism and volcanic eruptions along other parts of the eastern front of the Sierra Nevada have occurred at least as recently as a few hundred years ago. Focal mechanisms from earthquakes in the Mammoth Lakes area indicate extension in a NE-SW direction which is locally restricted to this area. In contrast, earthquakes east of Mono Lake exhibit the Basin and Range (NW-SE) extension direction while those around Bishop, south of the Mammoth Lakes area, show both extension directions, as do earthquakes occurring in the eastern Sierra north and south of the Mammoth Lakes area.

In previous reports (Ryall and Vetter, 1982; Vetter and Ryall, 1983) we compared P-wave fault-plane solutions for different areas within the western Great Basin and Mammoth Lakes area and for different depth ranges. The results of this comparison indicated that focal mechanisms correlate with focal depth, with shallow events having primarily strike-slip motion while many of those at mid-crustal depths were characterized by normal or oblique faulting.

Stability of Solutions. More than 100 focal mechanisms were analyzed from the Mammoth Lakes area. The location of the earthquakes was done with the HYP071 algorithm of Lee and Lahr (1975) using a four layer crustal structure together with a set of station adjustments determined from a large number of Mammoth events. Test calculations were done with a USGS crustal model, which gave in general the same location but a greater focal depth by up to 4 km. Since the depth variation appeared to be rather systematic (i.e., the depth was shifted in the same direction for all earthquakes) the relative depth relation between earthquakes did not change significantly. The absolute depth given for the occurrence of strike-slip or normal events may be incorrect by up to 2 km, but the fact that strike-slip events are characteristic for shallower depths and oblique and normal events for greater depths, is independent of the crustal models selected. Test plots of focal mechanisms using different depths were tried. For example, the earthquakes ## 28 and 32 (Table II) were tested for depths between 5 and 12 km and their mechanisms did not change. Only in very few cases did the fault planes change or could a solution not be found after a rather dramatic change of the depth. Earthquakes which had such unstable solutions were not used in this study.

RESULTS OF DATA ANALYSIS

Eighty-nine of the Mammoth Lakes focal mechanisms are shown in Figures 1 through 6 and listed in Tables I, II, and III. Numbers beside each focal mechanism correspond to values given in the earthquake list (in order of increasing depth). Figures 1 and 2 show mainly earthquakes from the time period May 1980 to September 1981 where are shown the mechanisms of events shallower and deeper than 9 km, respectively. Figures 3 and 4 show mainly earthquakes from the January 1983 swarm which was concentrated inside the caldera and shallow in comparison to earlier activity south of the caldera. Figure 3 shows the focal mechanisms for earthquakes shallower than 6 km and Figure 4 for earthquakes deeper than 6 km from the last mentioned sequence. Figures 5 and 6 show focal mechanisms from earthquakes that occurred later in 1983: in Figure 5 earthquakes from 1 to 8 km depth are shown and in Figure 6 deeper than 8 km.

For each time period the mechanisms change from strike slip toward oblique/normal slip with increasing depth, although, because of the restricted depth range, the 1980-swarm events show the tendency least clearly (Figures 3 and 4). An example of this change in focal mechanism is shown in Figure 7, with two earthquakes occurring in August 1981 at the same place, 9 minutes apart in time but at different depths: the second event was 6 km deeper than the first. The change from a strike-slip mechanism at 8 km depth to oblique slip at 14 km is quite well constrained and obvious. The shallowest earthquake with normal-slip focal mechanism is about 8 km deep. Strike-slip earthquakes deeper than 10 km occurred but but normal-slip earthquakes were not observed at shallow depth.

Focal mechanisms of Mammoth Lakes earthquakes from 1 to 8 km depth show 73% strike slip, 16% strike slip to oblique slip, 9% oblique, and 2% normal slip. Deeper than 8 km they show only 9% strike slip, 24% strike slip to oblique slip, 29% oblique, and 38% normal slip. In the report by Vetter and Ryall (1983) we modeled the change in focal mechanisms by increasing overburden pressure with depth, with the overburden pressure having a larger gradient than the maximum and minimum horizontal stresses. Figure 8 shows this model for the idealized case in which normal faulting prevails for depths greater than about 10 km, where the overburden pressure represents the maximum compressive stress.

The figure is based on measurements of the maximum deviatoric stress in hard rock, extrapolated downward (McGarr, 1980), as shown by the line labelled (S1-S3). The minimum principal stress S3 is assumed to be horizontal at all depths in this model, corresponding to the known extension of the Great Basin region (Zoback and Zoback, 1980). The T-axes of the focal mechanisms deviate by a maximum of 45° from the horizontal but are mostly within 20° of horizontal. However, the maximum principal stress S1, represented by the P-axes, ranges from horizontal at shallow depth to 45–85° in the middle crust. At depth greater than 8 km 67% of the focal mechanisms in the Mammoth Lakes area are oblique and normal; for the western Great Basin this figure is about 80% and the normal slip mechanisms contribute 57%. Consequently the diagram on Figure 8 is more accurate for conditions in the western Great Basin than in the Mammoth Lakes area, where we find strike-slip, oblique- and normal-slip earthquakes at depth greater 8 km in about equal numbers, which suggests that the greatest and the intermediate principal stresses are similar in value.

Seventy-four percent of the seismic activity of the Mammoth Lakes region occurs in the uppermost 8 km of the crust; in the caldera this figure reaches 82% (Figure 9). The maximum focal depth (=MFD) in a region, defined by Strehlau and Meissner (1984) as the depth value above which 95% of the hypocenters are located, is 11 km for the whole Mammoth Lakes area and 9.6 km for the caldera. The level of 8 km, where most earthquakes occur, seems to coincide with the region of maximum shear strength in the crust, which also indicates the bottom of the brittle layer (Strehlau and Meissner, 1984, Figs. 6 and 9; Meissner and Strehlau, 1982; Sibson, 1982). Below this brittle layer follows a transition zone to the plastic region which starts below the MFD. It is interesting to note that strike-slip earthquakes are characteristic for the brittle layer, while oblique- and normal-slip earthquakes are concentrated in the transition zone between brittle and plastic behavior. This points to a relationship between focal depth, focal mechanism, and the temperature-depth distribution. When the seismicity is restricted to a certain temperature range it seems reasonable to assume that this temperature range should be similar everywhere with some variations determined by the type of faulting in different geologic regions. Strehlau and Meissner (1984) have shown that for intra- and interplate seismic zones of continents normal faulting extends to greater depth than strike-slip, and that thrust faulting should end at the shallowest depths for the same temperature range and creep rate. The influence of the rising temperature with increasing depth supports increasing normal faulting with depth (Strehlau and Meissner, 1984, Figs. 6 and 9).

Since faulting in both the western Great Basin and the Mammoth Lakes area is related to crustal extension, the MFD in each region should be associated with the same temperature. Based on the temperature-depth curves calculated from Lachenbruch and Sass (1978) for the Basin and Range province for a surface heat flow varying between 1.7 and 2.1 HFU, the temperature at the MFD in this region (17 km) ranges between about 400–500°C. As compared to the Mammoth MFD of 11 km and the caldera MFD of 9.6 km this implies a temperature of 400–500°C at these depths which leads to the temperature-depth profiles shown in Figure 10. Assuming a linear temperature gradient, values of 23–29°C/km for the Basin and Range province, 36–46°C/km for the whole Mammoth Lakes region and 42–52°C/km for the caldera can be estimated. Seventy-five percent of the seismicity occurs in a temperature level above 280–350°C according to this temperature model.

Figure 11 shows fault-plane parameters for 85 Mammoth Lakes events. Fig. 11a shows the directions of the fault and auxiliary planes for all earthquakes

with depths shallower than 8 km, Fig. 11b shows the same for events deeper than 8 km and Fig 11c shows the T axis directions, which do not differ for both groups shown in a and b. For the same events, the mean inclination of the fault planes was 78° for events 0-6 km deep, 75° for events 6-7 km deep, 71° for events 7-8 km deep, and 58° for events exceeding 8 km. The mean plunge of the P axes changed from 14° for depths of 0-6 km, 16° for 6-7 km, 24° for 7-8 km, to 50° for depths exceeding 8 km. The plunge of the T axes showed no systematic change and had a mean value of 11° for all 85 earthquakes.

These numbers, together with the three plots on Figure 11 indicate that earthquakes occurring in the upper 8 km of the crust are mainly strike slip while below that depth strike slip, oblique slip and normal slip earthquakes occur, resulting in a P axis direction deviating significantly from horizontal and a greater scatter of the fault plane directions.

DISCUSSION

The Mammoth Lakes data support our previous conclusion regarding the prevalence of strike slip movement in the uppermost crust and a tendency toward normal faulting at depth (Vetter and Ryall, 1983). Indications for a change of focal mechanisms toward normal faulting with increased depth has also been observed by other authors in comparable tectonic regimes. Klein et al. (1977) found that the focal mechanisms for an earthquake swarm occurring during 1972 on the Reykjanes Peninsula of Iceland were strike-slip for depths less than 3 km but mostly normal for greater depth. Pitt and Steeples (1975) studied microearthquakes in the Mono Lake-northern Owens Valley region. They made a composite focal mechanisms for 34 events with depths less than 10 km resulting in a strike-slip solution with E-W extension axis. No solution was possible from a composite of 17 events deeper than 10 km. This might be expected if earthquakes deeper than 10 km have variable mechanisms as we have seen. Thus, our principal result has been observed elsewhere by others.

The occurrence of numerous strike-slip earthquakes in the western Great Basin may be surprising since surface faulting, the expression of strong earthquakes in the past, generally shows a substantial vertical component of motion. Even if significant strike-slip motion attends these Holocene events, the evidence for it may simply have been obscured by erosion. Moreover, recent observations do confirm strike-slip motion at the surface. A field study done after the May 1980 earthquakes in the Mammoth area (Clark et al.,1982) showed indications of horizontal and vertical movements of about equal amount. Lockwood and Moore (1979) show evidence for left-lateral motion on ENE faults and right-lateral movements on NNE faults in the Sierra Nevada, but near the Mammoth Lakes area they show left-lateral motion on NNE striking microfaults. Precise relocation of the May 1980 aftershocks in the Mammoth area by Lide (1984) shows strong epicenter lineups along vertical, NNE-striking fault zones down to about 9 km depth south of the Long Valley caldera, which agrees with our NNE-striking nodal planes for strike-slip earthquakes. Along the caldera boundary epicenters line up along steeply dipping WNW zones which coincides with the WNW-striking nodal planes of our strike-slip events. The deeper events occur mainly in a narrow zone south of the caldera which is approximately perpendicular to the T- axis direction (NE to ENE). Hill (1977) proposed a model to explain the predominance of strike-slip earthquakes in the uppermost crust in volcanic areas, in which conjugate shear failures accompany the formation of magma-filled dikes. A recent study by Sanders (1983) on the shadowing of seismic S-waves by assumed magma bodies in the Mammoth Lakes area delineates the upper boundary of an energy absorbing body, possibly magma, at a depth of

4.5-5.5 km. However at this shallow depth the absorbing body appears to be dispersed (e.g., in form of dikes) rather than continuous. At about 7 km depth the body appears to be more continuous. The deeper configuration of the structure cannot be determined by S-wave shadowing since the depth range of the earthquakes is restricted.

Recently, Wiens and Stein (1984) studied intraplate seismicity in young oceanic lithosphere of the Atlantic, Pacific, and Indian Ocean. They compared 27 focal mechanisms and found that the normal-slip earthquakes occur at greater depths than the thrust and strike-slip events. They concluded that in young oceanic lithosphere thrust and strike-slip earthquakes are restricted to the temperature regime above the $600°C$ isotherm, while normal-slip earthquakes reach downwards to the depth region of the $750°C$ isotherm. Strehlau and Meissner (1984) collected data from numerous seismically active continental areas and concluded that in areas characterized by thrust, strike-slip, and normal-faulting the seismicity bottoms where the temperature reaches $400°C$, $450°C$, and $500°C$, respectively. The temperature values of $400-500°C$ estimated from the MFD of earthquakes in the western Basin and Range province are in good agreement with their temperatures for earthquake zones in which both normal- and strike-slip earthquakes occur. Strehlau and Meissner gained their results from theoretical shear strength-depth curves, calculated for wet quartz-bearing rock material, and found very good agreement with published MFD data. Such studies as those by Wiens and Stein (1984) and Strehlau and Meissner (1984), together with our results, suggest that in intraplate regions focal mechanisms of earthquakes depend on focal depth, possibly because of the mechanism we have proposed for stress change with depth. There can be little doubt that a transition zone from brittle to plastic behavior exists under Mammoth Lakes, because about 25% of the seismicity occurs below the depth of the stress maximum as defined by the depth of maximum earthquake occurrence. If there were no transition, seismicity should end abruptly below this maximum (Sibson, 1982).

CONCLUSION

Focal mechanisms, frequency-depth distribution, and maximum focal depth of the Mammoth Lakes seismicity have been studied. As in our previous research, we find a striking change in focal mechanism of the earthquakes: in the depth range 8 km or less, representing about 75% of the total seismicity, 73% of the focal mechanisms are strike-slip and only 2% are normal. The far less abundant seismicity in the depth range 8-11 km showed only 9% pure strike-slip and 38% normal-slip events. A maximum in the occurrence of earthquakes around 8 km depth suggests that this is the depth range of the maximum shear strength under the Mammoth Lakes area.

Temperature-depth profiles have been estimated for the whole Mammoth Lakes region and for Long Valley caldera. These were constructed on the assumptions that in tectonic similar regions the maximum depth of the seismicity has about the same temperature and that the shape of the geotherm is similar to that of the Basin and Range geotherm. Then the temperature gradients for the caldera and the whole Mammoth Lakes area have values of $42-52°C/km$ and $36-46°C/km$ respectively, as compared with the Basin and Range value of $23-30°C$ /km.

ACKNOWLEDGMENTS

This research was partly supported by the U. S. Geological Survey under contract 14-08-0001-21863, and partly by the U. S. Department of Energy under contract DE-AS08-82ER12082. It was further partly supported by the Defense Advanced Projects Agency of the Department of Defense and monitored by the Air Force Office of Scientific Research under contract F49620-83-C-0012. The author wishes to thank W. Peppin and A. Ryall for careful reviewing the manuscript, and the U. S. Geol. Survey for providing data.

REFERENCES

Bailey, R. A., Dalrymple, G. B., and Lanphere, M. A., Volcanism, structure, and geochronology of Long Valley caldera, Mono County, California, *J. Geopys. Res.*, *81*, 725-744, 1976.

Clark, M. M., Yount, I. C., Vaughan, P. R., and Zepeda, R. L., Ruptures associated with the Mammoth Lakes, California, earthquakes of May 1980, Map, U.S. Geol. Survey, Denver, 1982.

Hill, D. P., A model for earthquake swarms, *J. Geophys. Res.*, *82*, 1347-1352, 1977.

Klein, F. W., Einarsson, P., and Wyss, M., The Reykjanes Peninsula, Iceland, earthquake swarm of September 1972 and its tectonic significance, *J. Geophys. Res.*, *82*, 865-888, 1977.

Lachenbruch, A. H. and Sass, J. H., Models of an extending lithosphere and heat flow in the Basin and Range province, in Cenocoic Tectonics and Regional Geophysics of the Western Cordillera; R. B. Smith and G. P. Eaton, eds., *Geol. Soc. Am. Mem.*, *152*,209-250,1978.

Lee, W. H. K., and Lahr, J. C., HYP071 (revised): A computer program for determining hypocenter, magnitude, and first motion pattern of local earthquakes, *U. S. Geol. Surv. Open File Rep. 75-311*, 113 pp, 1975.

Lide, C.S., Precise relocation of aftershocks of the May 1980 Mammoth Lakes earthquakes, Univ. Nevada MS Thesis, 1984.

Lockwood, J. P and Moore, J. G., Regional deformation of the Sierra Nevada, California, on conjugate microfault sets, *J. Geophys. Res.*, *84*, 6041-6049, 1979.

McGarr, A., Some constraints on levels of shear stress in the crust from observations and theory, *J. Geophys. Res.*, *85*, 6231-6238, 1980.

Meissner, R. and Strehlau, J., Limits of stresses in continental crusts and their relation to the depth-frequency distribution of shallow esrthquakes, *Tectonics*, *1*, 73-89, 1982.

Pitt, A. M. and Steeples, D. W., Microearthquakes in the Mono Lake- northern Owens valley, California, region from September 28 to October 18, 1970, *Bull. Seism. Soc. Am.*, *65*, 835-844, 1975.

Ryall, A. S., and Vetter, U. R., *Seismicity Related to Geothermal Development in Dixie Valley, Nevada*, Final Rept. on USDOE Contr. DE-AC08-79NV10054, Univ. of Nevada, Reno, 102 pp., 1982.

Sanders, C. O., Location and configuration of magma bodies beneath Long Valley, California, determined from anomalous earthquake signals, *J. geophys. Res.*, 1984 (in press).

Sibson, R. H., Fault zone models, heat flow and the depth distribution of earthquakes in the continental crust of the United States, *Bull. Seism. Soc. Am.*, *72*, 151-163, 1982.

Strehlau, J. and Meissner, R., Earthquakes in continental crust: temperature dependence of maximum focal depth, *J. Geophys. Res.*, 1984 (in press).

Vetter, U. R. and Ryall, A. S., Systematic change of focal mechanisms with depth in the western Great Basin, *J. Geophys. Res.*, *88*, 8237-8250, 1983.

Wiens, D. A. and Stein, S., Intraplate seismicity and stresses in young oceanic lithosphere, *J. Geophys. Res.*, 1984 (in press).

Zoback, M. L., and Zoback, M. D., Faulting patterns in north-central Nevada and strength of the crust, *J. Geophys. Res.*, *85*, 275-284, 1980.

FIGURE CAPTIONS

Figure 1. Fault plane solutions for Mammoth Lakes earthquakes (Table I) with depth less than 9 km; time period 1980-81 (Lower hemisphere, equal-angle projection; shaded areas - compression). The map shows the Long Valley caldera margin, the town of Mammoth Lakes (in SW part of Caldera), Lake Crowley (crossing SE part of caldera) and some mapped faults S of the caldera.

Figure 2. Same as Figure 1 with depth greater than 9 km.

Figure 3. Fault plane solutions for Mammoth Lakes earthquakes (Table II) with depth less than 6 km; time period January 1983.

Figure 4. Same as Figure 3 for depth greater 6 km. (Two of the earthquakes, # 30 and 31, are from July 1983)

Figure 5. Fault plane solutions for Mammoth Lakes earthquakes (Table III) with depth less and equal to 8 km; time period Aug. - Nov. 1983; (triangles mark seismograph stations).

Figure 6. Same as Figure 5 for depth greater 8 km.

Figure 7. Fault plane solutions for two Mammoth Lakes events that occurred on Aug. 9, 1981, at the same epicentral location. Time (GMT), coordinates, depths (D), magnitudes (M), and quality (B) are given. Closed circles -- compression, open circles – dilatation; T -- T axes, P -- P axes.

Figure 8. Estimated principal stresses as a function of depth to explain a change of focal mechanism with depth. S1-S3 – twice the maximum shear stress measured for hard rocks and extrapolated downward (McGarr, 1980); Sh=S3 -- smallest horizontal principal stress, shaded area shows range of S3; SH – greatest horizontal principal stress (assumed on the basis of pure strike-slip at shallow depth and a crossover with SV around 10 km); SV -- overburden pressure.

Figure 9. Seismicity as a function of depth for the Mammoth area and the Long Valley caldera in comparison to the western Great Basin; focal mechanisms for depths shallower and greater 8 km are indicated for Mammoth Lakes area and western Great Basin; SNGB = Sierra Nevada- Great Basin boundary zone; SS – strike slip; obl -- oblique; N – normal.

Figure 10. Temperature-depth model for the Mammoth area and for the Long Valley caldera alone based on the temperature curves for the Basin and Range province from Lachenbruch and Sass (1978) and on the frequency-depth distribution of earthquakes. The 95% lines mark the MFD, the broken lines labelled 73% and 74%, respectively mark the depth range of the maximum shear strength.

Figure 11. a) Rose diagram showing the orientation of the fault planes for earthquakes shallower than 8 km, b) deeper than 8 km, and c) T axis directions for all depths.

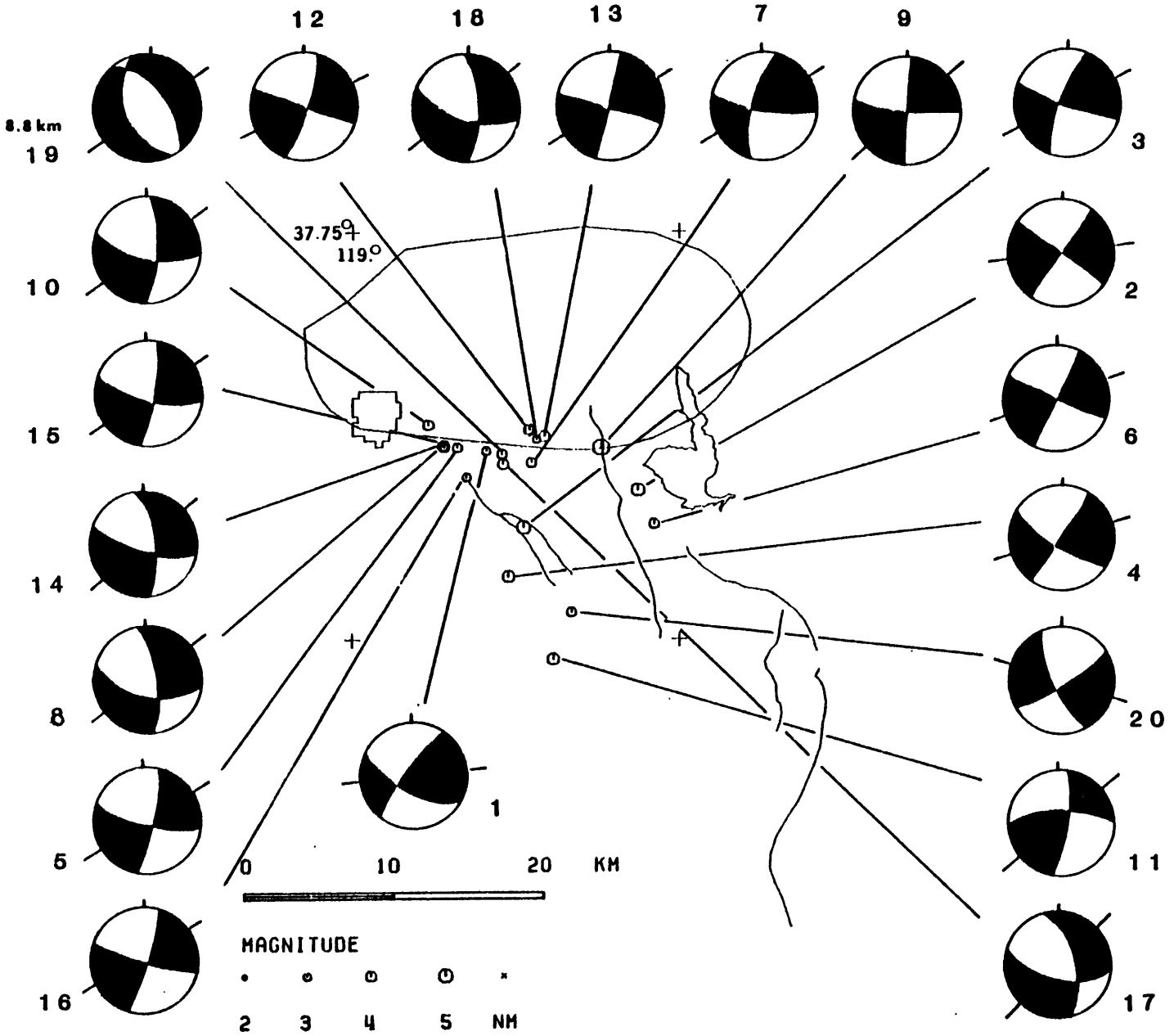
12
18
13
7
9
8.8km
19
3
37.75°
119.°
10
2
15
6
14
4
8
20
1
5
11
0
10
20
KM
MAGNITUDE
2
3
4
5
NM
16
17

Figure 1

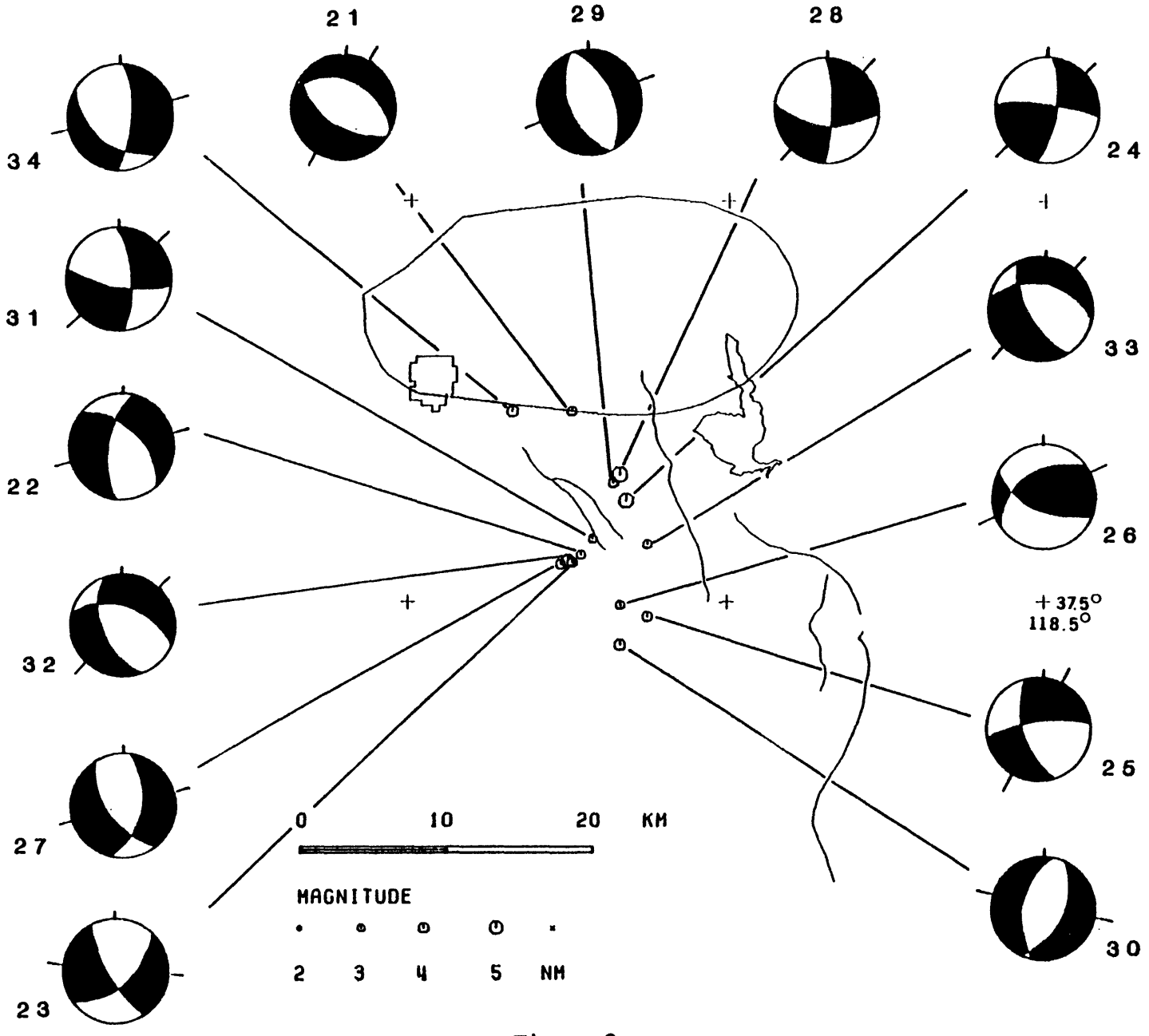
21
29
28
34
24
31
33
22
26
32
+37.5°
118.5°
25
27
30
23
0
10
20
KM
MAGNITUDE
2
3
4
5
NM

Figure 2

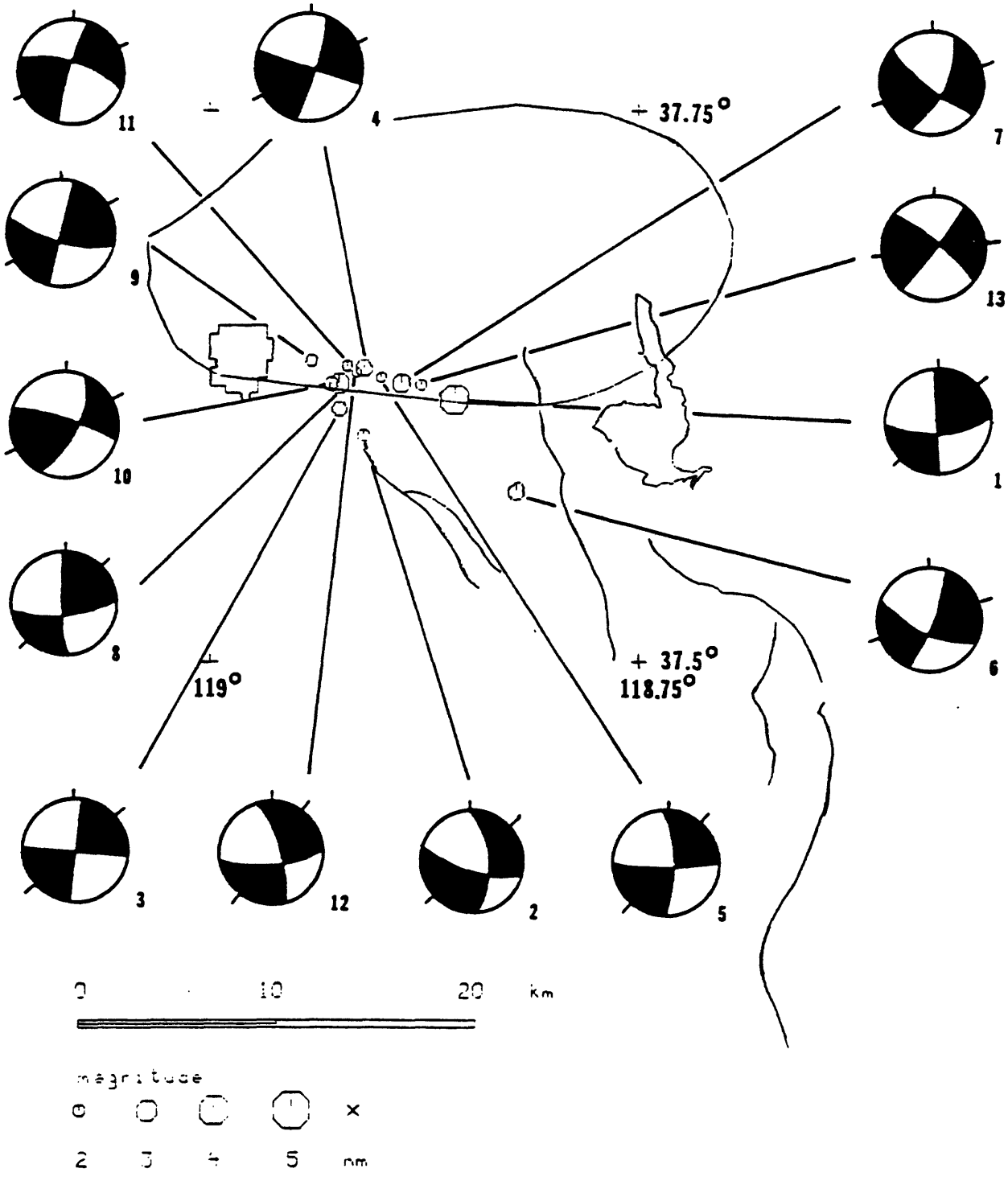
11
4
7
9
13
10
1
8
6
3
12
2
5
+ 37.75°
+ 119°
+ 37.5°
118.75°
0
10
20
km
magnitude
2
3
4
5
nm

Figure 3

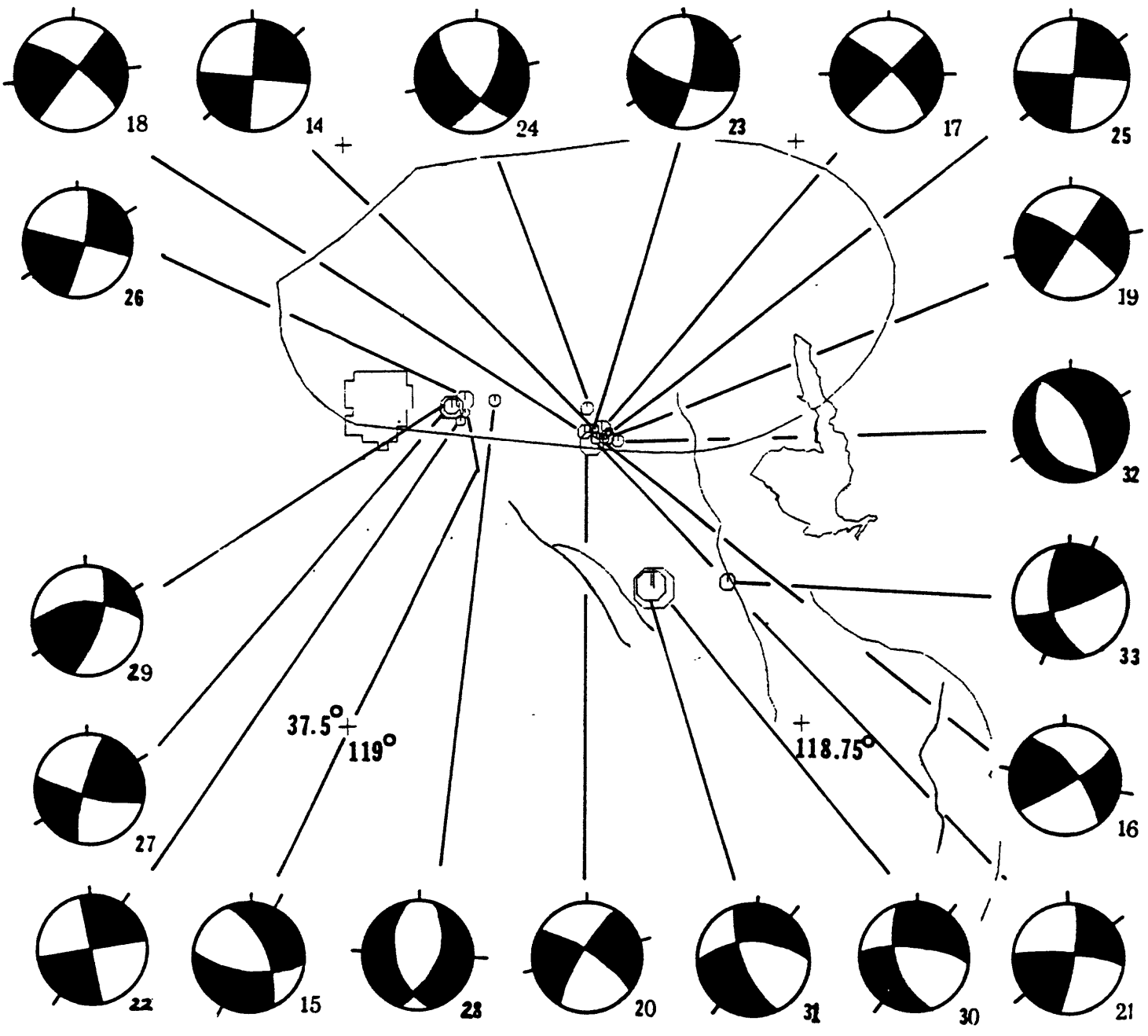
18
14
24
23
17
25
26
19
32
29
33
37.5°
119°
118.75°
27
16
22
15
28
20
31
30
21
0
10
20
km
magnitude
2
3
4
5
nm

Figure 4

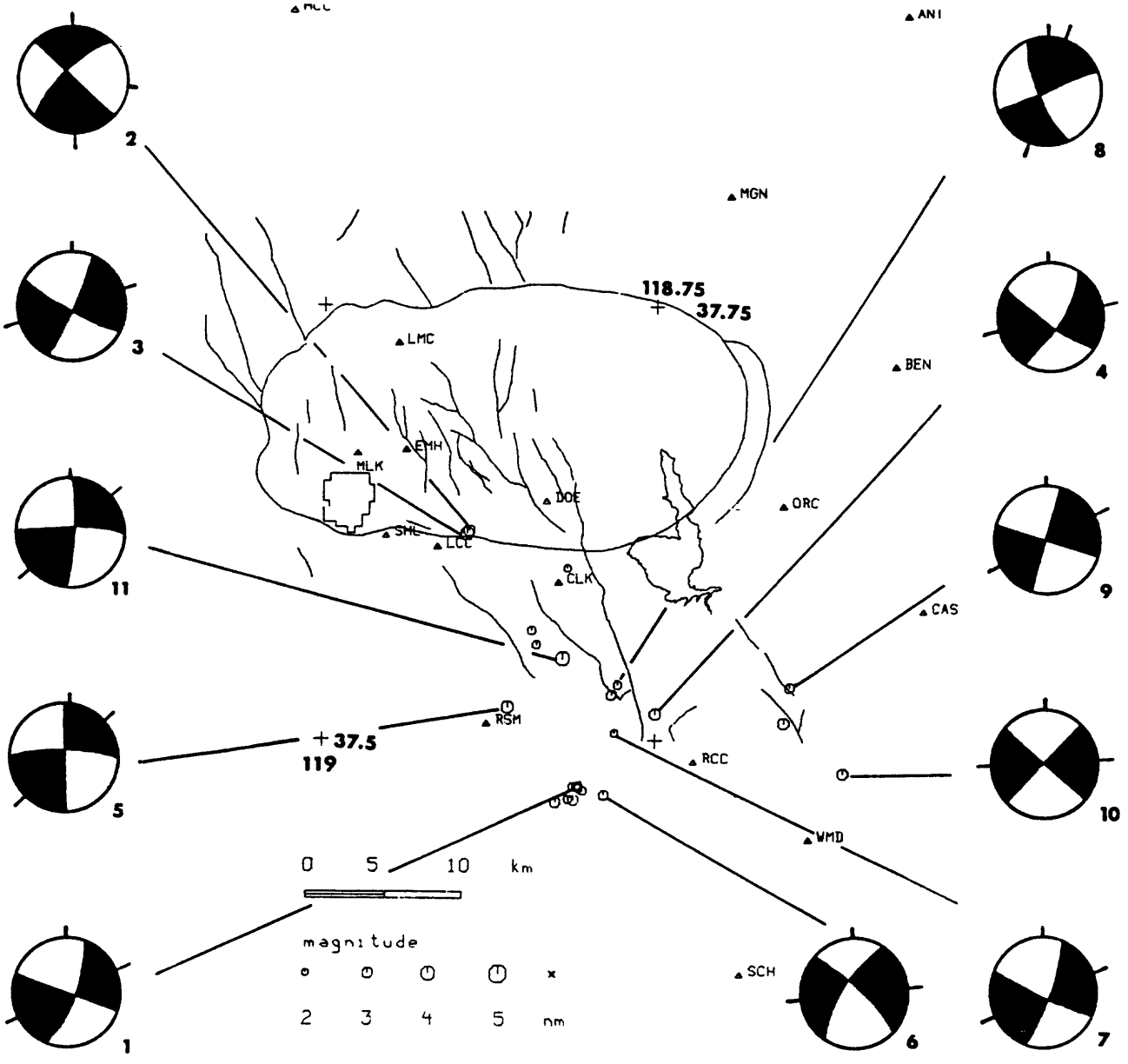
ANI
MGN
118.75
37.75
LMC
BEN
EMH
MLK
DOE
ORC
SML
LCC
CLK
CAS
RSM
+37.5
119
RCC
WMD
0 5 10 km
magnitude
2 3 4 5 nm
SCH
1
2
3
4
5
6
7
8
9
10
11

Figure 5

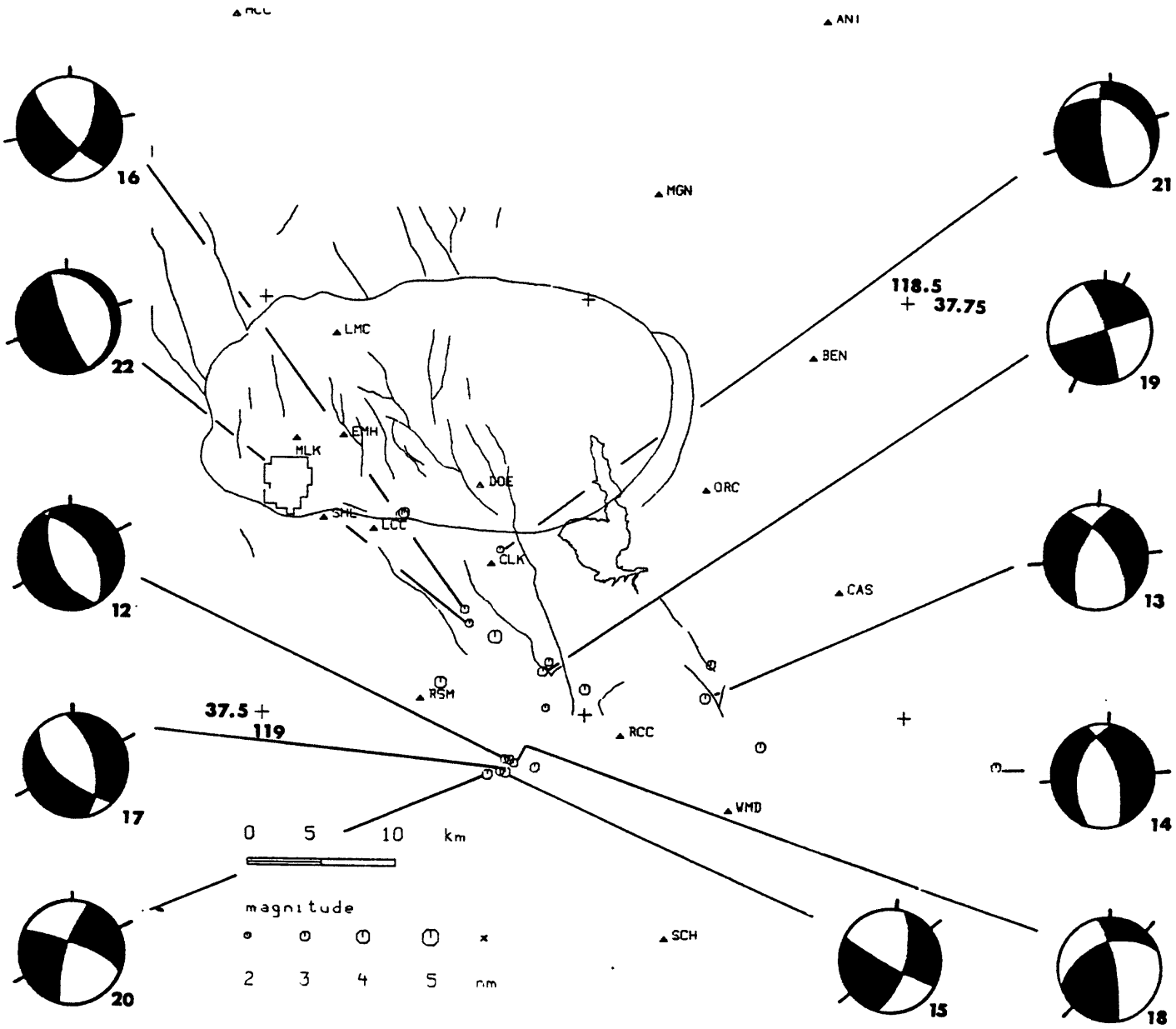
ANI
MGN
LMC
BEN
EMH
MLK
DOE
ORC
SHC
LCC
CLK
CAS
RSM
RCC
VMD
SCH
118.5
37.75
37.5
119
0 5 10 km
magnitude
2 3 4 5 nm
16
21
22
19
12
13
17
14
20
15
18

Figure 6

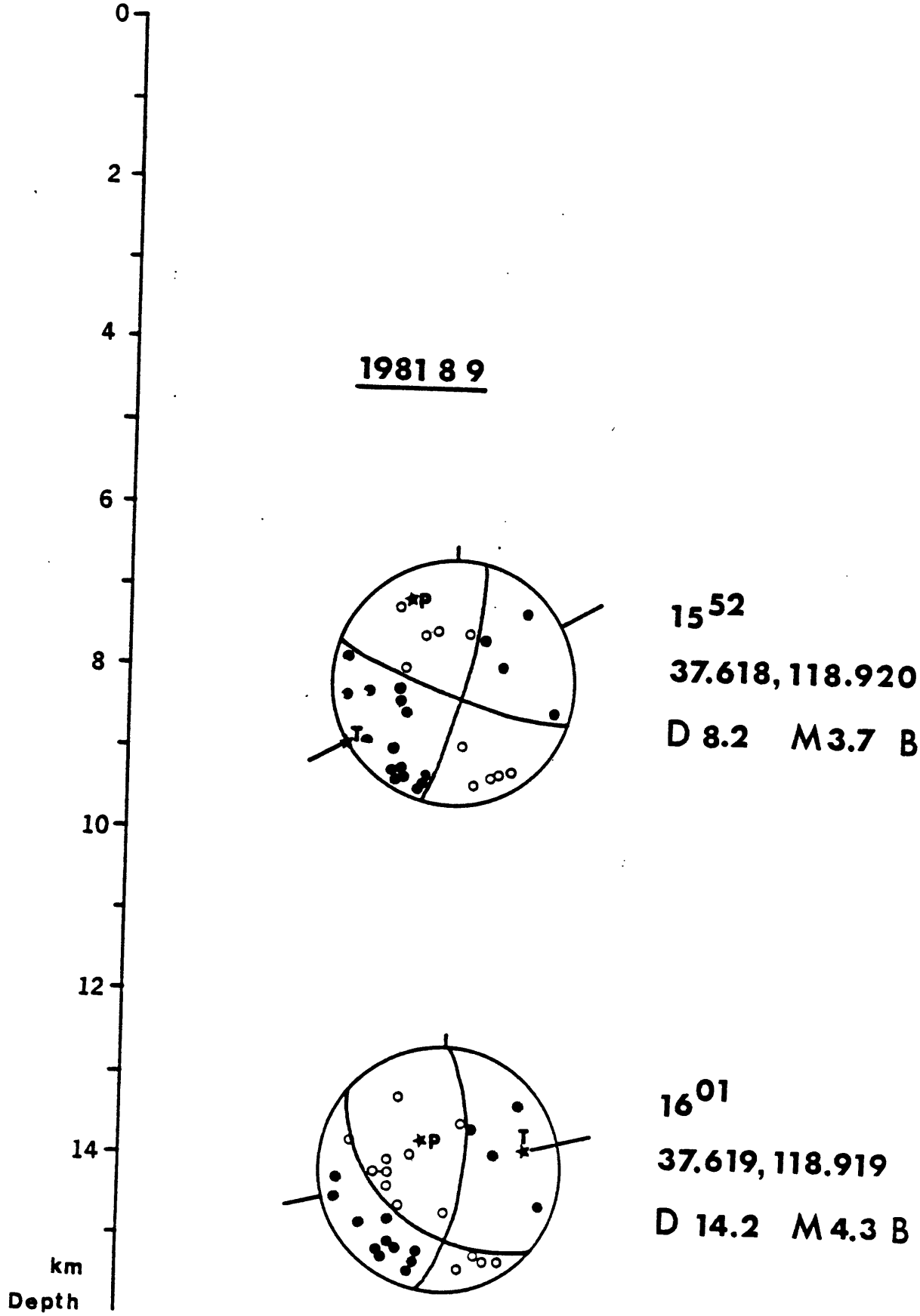
0
2
4
6
8
10
12
14
km
Depth
1981 8 9
P
I
15 52
37.618, 118.920
D 8.2 M 3.7 B
16 01
37.619, 118.919
D 14.2 M 4.3 B

Figure 7

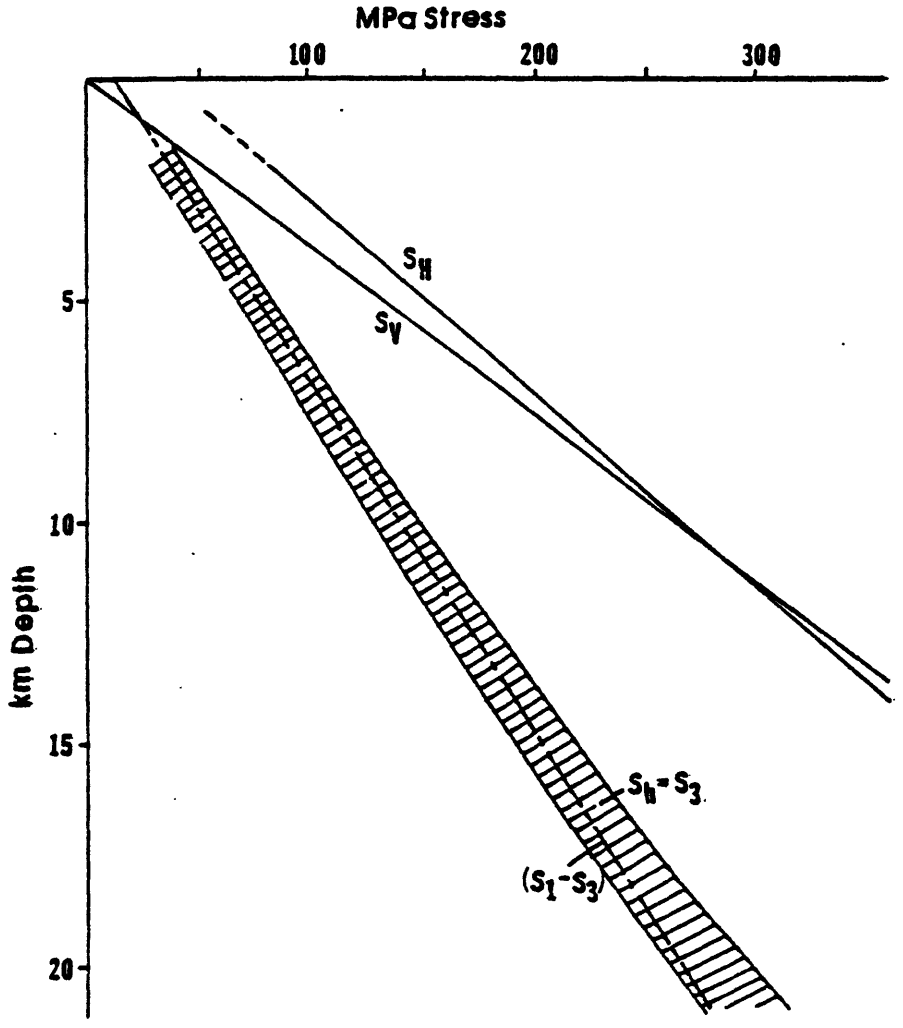

Figure 8

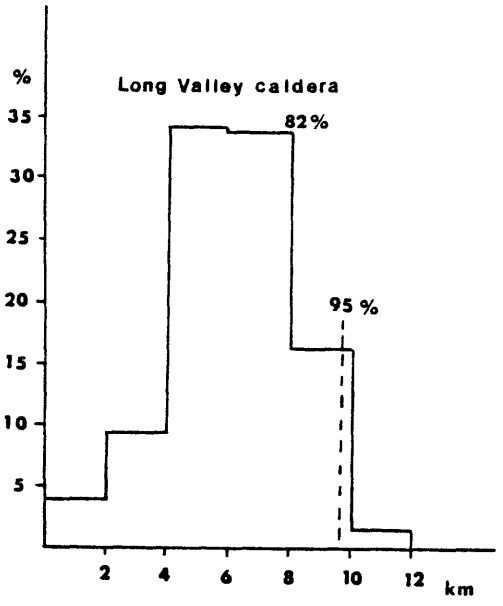

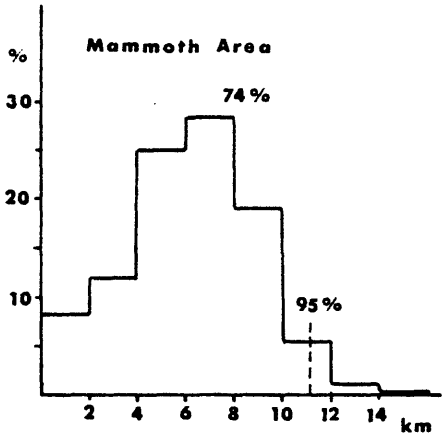

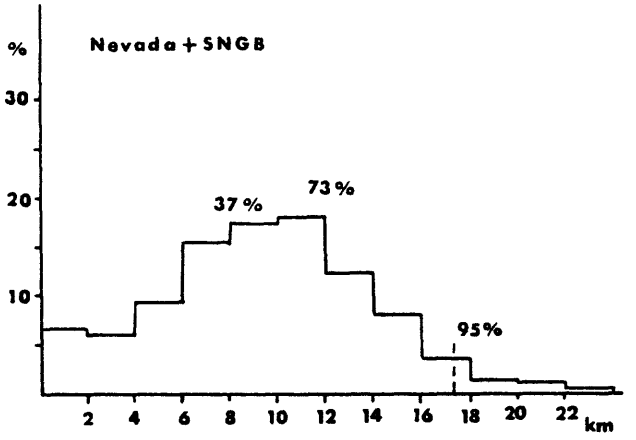

73 % SS	9 % SS
16 % SS/obl	24 % SS/obl
9 % obl	29 % obl
2 % N	38 % N

86% SS	5 % SS
14 % SS/obl	14 % SS/obl
	24 % obl
	57 % N

Figure 9

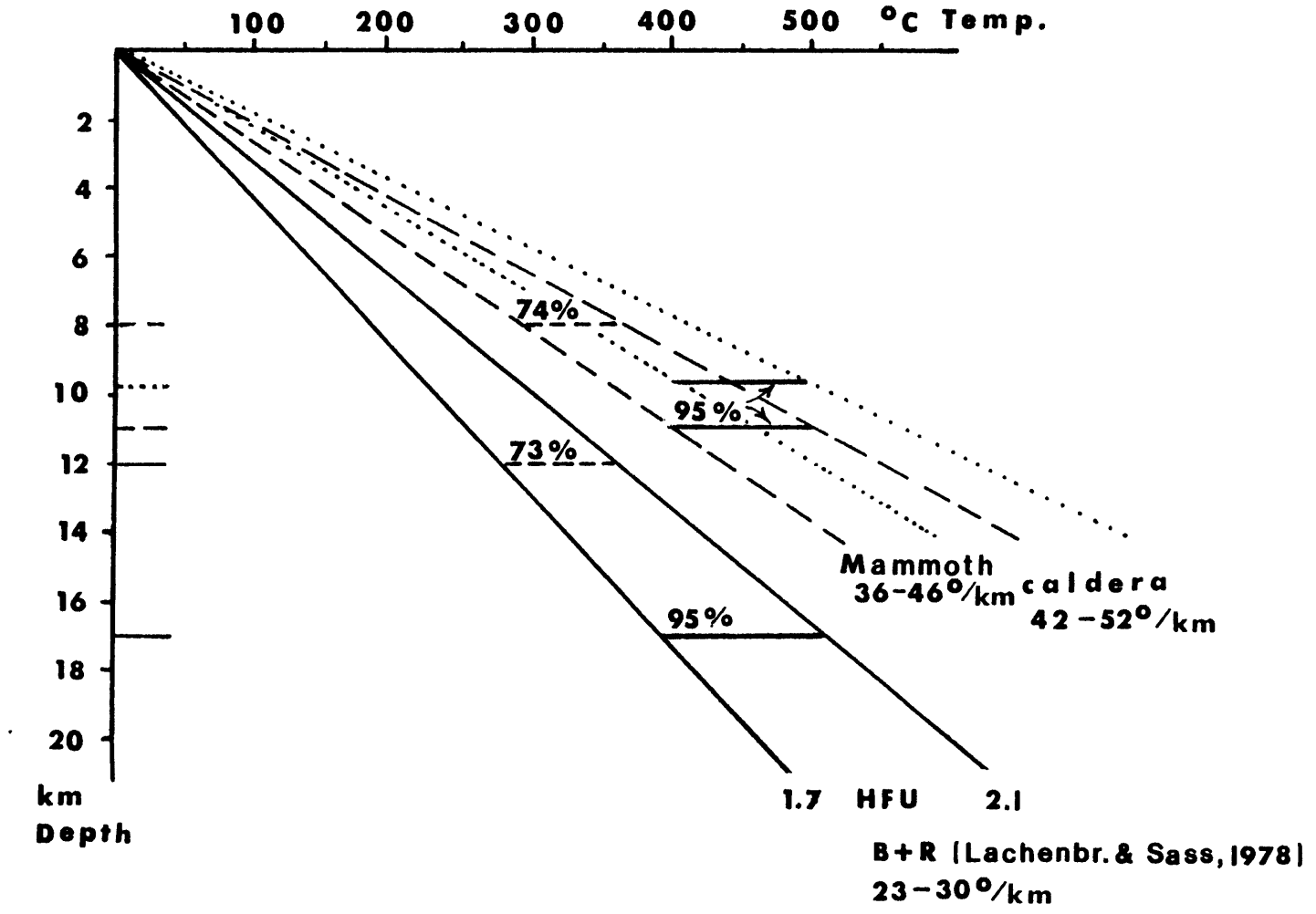
100
200
300
400
500
°C Temp.
2
4
6
8
10
12
14
16
18
20
km
Depth
74%
95%
73%
95%
Mammoth caldera
36-46°/km
42-52°/km
1.7 HFU 2.1
B+R (Lachenbr. & Sass, 1978)
23-30°/km

Figure 10

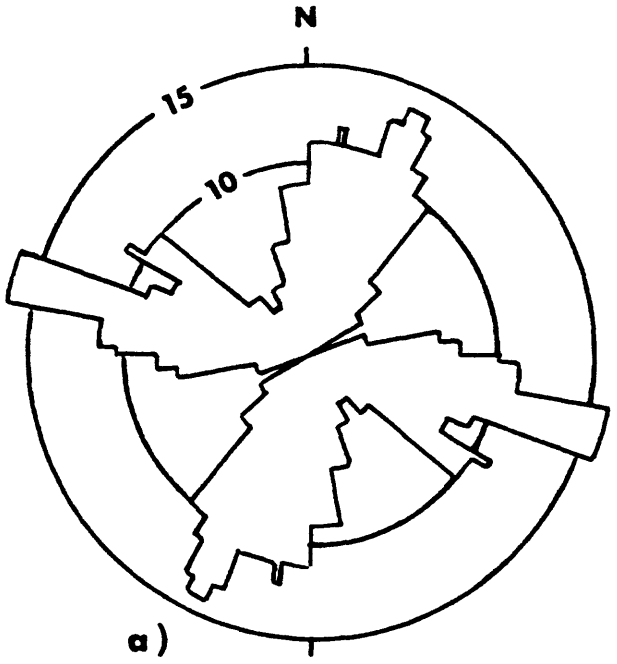

a)

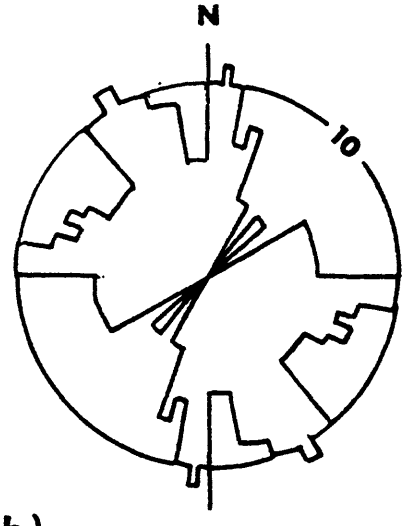

b)

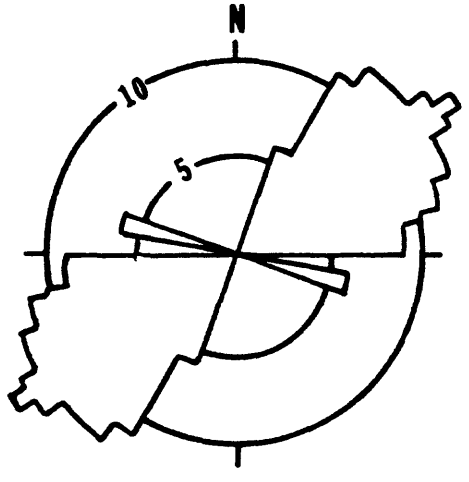

c)

Figure 11

TABLES

Table I. List of the Mammoth Lakes earthquakes shown on Figures 1 and 2, listed in order of increasing depth; time period: 1980 and 1981. The labellings are: (a) -- number; (b) -- date; (c) -- time, GMT; (d) -- latitude, ° N; (e) -- longitude, ° W; (f) -- focal depth, km; (g) -- M_L; (h) quality; (i) -- strike and dip of fault plane A; (j) -- strike and dip of fault plane B.

Table II. List of the Mammoth Lakes earthquakes shown on Figures 3 and 4; time period January 1983, 2 earthquakes from July 1983. Labelling: same as Table I; (k) -- strike of T axis; (l) -- strike of P axis.

Table III. List of the Mammoth Lakes earthquakes shown on Figures 5 and 6; time period Aug. to Nov. 1983. Labelling: as Tables I and II; (k) -- strike and plunge of T axis.

Table I Mammoth Lakes Area

(a)	(b)	(c)	(d)	(e)	(f)	(g)	(h)	(i)	(j)
1	1982 8 5	1538	37.616	118.898	2.8	3.4	B	N 36 E 79°	N 60 W 60°
2	1980 5 27	1901	37.592	118.781	3.9	4.8	B	N 36 E 90°	N 54 W 90°
3	1981 9 30	1153	37.569	118.689	4.0	5.2	B	N 20 E 79°	N 71 W 82°
4	1980 6 11	440	37.539	118.881	4.3	4.6	B	N 31 E 90°	N 59 W 73°
5	1980 6 4	2100	37.600	118.913	4.5	3.3	A	N 17 E 80°	N 71 W 85°
6	1980 6 1	1727	37.571	118.769	4.9	3.9	A	N 22 E 90°	N 67 W 86°
7	1981 9 30	1433	37.609	118.863	5.7	3.8	B	N 17 E 70°	N 75 W 82°
8	1981 11 13	350	37.618	118.930	6.0	3.3	B	N 06 W 66°	N 76 W 50°
9	1980 5 25	1633	37.618	118.809	6.5	6.1	B	N 03 E 86°	N 86 W 86°
10	1982 5 8	357	37.632	118.942	6.9	4.1	A	N 04 E 68°	N 76 W 68°
11	1980 5 31	058	37.488	118.846	7.1	4.5	B	N 11 E 73°	N 88 W 65°
12	1981 10 9	1101	37.629	118.865	7.6	4.1	B	N 18 E 80°	N 73 W 90°
13	1981 10 2	737	37.625	118.853	7.7	4.2	B	N 14 E 90°	N 76 W 90°
14	1981 11 13	307	37.619	118.930	7.8	4.2	B	N 11 W 62°	N 76 W 50°
15	1981 11 13	300	37.619	118.931	7.9	4.0	B	N 16 E 86°	N 74 W 70°
16	1981 8 9	1552	37.618	118.920	8.2	3.7	B	N 15 E 80°	N 74 W 80°
17	1981 8 24	452	37.608	118.885	8.4	4.0	B	N 11 W 56°	N 77 W 58°
18	1981 9 30	1427	37.623	118.859	8.6	3.1	B	N 04 W 64°	N 76 W 60°
19	1981 8 22	2054	37.614	118.886	8.8	3.8	B	N 22 W 51°	N 40 W 40°
20	1981 8 6	2231	37.517	118.832	8.9	3.8	B	N 60 E 78°	N 26 W 70°
21	1980 6 1	2230	37.619	118.882	9.2	3.7	B	N 65 W 46°	N 72 W 44°
22	1981 3 25	401	37.530	118.864	9.6	3.7	B	N 11 E 60°	N 43 W 45°
23	1981 9 25	648	37.525	118.871	9.9	3.9	B	N 46 E 50°	N 32 W 75°
24	1980 6 23	632	37.564	118.829	10.6	5.5	B	N 05 E 64°	N 90 W 82°
25	1980 6 13	2323	37.491	118.812	10.9	4.0	B	N 78 E 75°	N 22 W 56°
26	1980 6 14	735	37.498	118.833	11.0	3.5	B	N 65 E 37°	N 63 W 66°
27	1981 3 5	528	37.524	118.880	11.1	3.9	B	N 10 E 47°	N 37 W 54°
28	1980 6 23	516	37.580	118.834	11.1	5.6	B	N S 80°	N 85 W 60°
29	1980 6 27	129	37.575	118.839	11.1	3.7	B	N 21 W 40°	N 21 W 50°
30	1980 6 8	2322	37.473	118.833	11.4	4.3	B	N 10 E 50°	N 19 E 40°
31	1981 9 17	1236	37.540	118.855	12.4	3.5	B	N S 60°	N 79 W 70°
32	1980 5 26	1224	37.526	118.874	12.4	5.1	B	N 19 W 50°	N 70 W 52°
33	1981 11 5	330	37.537	118.812	13.7	3.5	B	N 34 W 63°	N 82 W 38°
34	1981 8 9	1601	37.619	118.919	14.2	4.3	B	N 03 E 64°	N 50 W 38°

TABLE II Mammoth Lakes Area

(a)	(b)	(c)	(d)	(e)	(f)	(g)	(h)	(i)	(j)	(k)	(l)
1	1983 1 7	0511	37.620	118.858	1.0	4.0	A	N 86 E 67° S	N 3 W 90°	N 44 E	N 51 W
2	1983 1 11	0806	37.603	118.911	1.5	2.1	B	N S 50° E	N 73 W 70° S	N 58 E	N 31 W
3	1983 1 15	0718	37.615	118.925	2.1	2.3	B	N 8 E 90°	N 83 W 90°	N 52 E	N 39 W
4	1983 1 13	0758	37.634	118.910	2.5	2.5	B	N 16 E 85° SE	N 75 W 90°	N 60 E	N 30 W
5	1983 1 7	0404	37.630	118.901	2.9	1.3	A	N 84 E 85° S	N 7 W 70° E	N 37 E	N 50 W
6	1983 1 11	1849	37.578	118.822	3.7	2.6	B	N 20 E 84° E	N 66 W 60° S	N 70 E	N 27 W
7	1983 1 17	1820	37.627	118.889	4.0	2.7	A	N 23 E 60° SE	N 61 W 80° SW	N 68 E	N 16 W
8	1983 1 9	0744	37.627	118.925	4.4	2.9	B	N 81 E 66° S	N 5 W 86° W	N 42 E	N 53 W
9	1983 1 13	0231	37.637	118.941	4.7	2.0	C	N 11 E 90°	N 79 W 71° S	N 57 E	N 35 W
10	1983 1 13	0135	37.626	118.929	4.7	2.2	C	N 20 E 60° E	N 78 W 76° N	N 57 E	N 26 W
11	1983 1 13	2256	37.635	118.920	5.2	1.9	B	N 13 E 86° W	N 74 W 70° N	N 62 E	N 32 W
12	1983 1 13	2249	37.632	118.915	5.7	2.5	B	N 84 E 60° S	N 19 W 71° E	N 36 E	N 59 W
13	1983 1 11	0019	37.626	118.878	5.8	2.1	B	N 36 E 85° SE	N 54 W 82° NE	N 81 E	N 9 W
14	1983 1 12	0123	37.628	118.863	6.0	2.3	B	N 8 E 90°	N 83 W 90°	N 49 E	N 41 W
15	1983 1 15	0025	37.365	118.935	6.1	2.3	B	N 26 W 50° NE	N 86 W 60° S	N 28 E	N 53 W
16	1983 1 11	0544	37.623	118.858	6.3	2.1	B	N 58 E 80° SE	N 38 W 60° NE	N104 E	N 7 E
17	1983 1 11	0332	37.627	118.859	6.3	2.8	B	N 40 E 90°	N 50 W 75° NE	N 86 E	N 6 W
18	1983 1 9	1117	37.626	118.868	6.4	2.2	B	N 34 E 90°	N 56 W 72° NE	N 30 E	N 13 W
19	1983 1 14	1034	37.624	118.856	6.5	2.7	B	N 32 E 90°	N 58 W 74° NE	N 78 E	N 14 W
20	1983 1 11	0546	37.621	118.865	6.8	3.3	B	N 30 E 80° NW	N 57 W 78° NE	N 77 E	N 13 W
21	1983 1 11	0236	37.623	118.862	6.9	2.3	B	N 8 E 80° E	N 84 W 80° N	N 51 E	N 36 W
22	1983 1 12	1222	37.631	118.937	6.9	2.1	B	N 78 E 90°	N 12 W 85° E	N 33 E	N 56 W
23	1983 1 12	1827	37.627	118.863	7.3	1.8	B	N 10 E 70° E	N 71 W 66° S	N 59 E	N 31 W
24	1983 1 15	2237	37.635	118.874	7.3	2.6	A	N 23 E 50° E	N 43 W 64° SW	N 75 E	N 3 W
25	1983 1 12	2254	37.626	118.855	7.4	2.1	B	N 6 E 90°	N 84 W 90°	N 52 E	N 38 W
26	1983 1 9	0118	37.640	118.935	7.4	2.6	B	N 16 E 72° E	N 74 W 90°	N 59 E	N 28 W
27	1983 1 17	0122	37.637	118.942	7.4	3.1	C	N 16 E 80° NW	N 75 W 80° S	N 60 E	N 29 W
28	1983 1 16	0008	37.640	118.918	7.8	3.2	A	N 16 E 50° E	N 14 W 44° W	N 91 E	N 15 W
29	1983 1 15	1952	37.638	118.942	7.9	2.3	B	N 20 E 62° E	N 97 W 50° N	N 57 E	N 10 W
30	1983 7 3	1840	37.559	118.831	8.0	5.1	B	N 92 E 65° N	N 21 W 50° SW	N 33 E	N 48 W
31	1983 7 3	1650	37.560	118.833	8.3	3.9	B	N 88 E 50° N	N 25 W 65° SW	N 34 E	N 65 W
32	1983 1 13	2041	37.620	118.855	8.5	3.0	B	N 33 W 60° NE	N 33 W 30° SW	N 56 E	N 56 E
33	1983 1 17	2314	37.557	118.795	12	2.4	B	N 70 E 80° S	N 13 W 50° W	N 23 E	N 53 W

Table III Mammoth Lakes Area

(a)	(b)	(c)	(d)	(e)	(f)	(g)	(h)	(i)	(j)	(k)
1	1983 8 3	0534	37.4730	118.8083	1	2.8	B	N 21 E 74° E	N 70 W 90°	N 65 E 11° SW
2	1983 11 15	0336	37.6205	118.8915	2.9	3.3	A	N 38 E 90°	N 53 W 64° SW	N 82 E 4° E
3	1983 11 15	0329	37.6190	118.8932	3	3.8	A	N 26 E 86° SE	N 63 W 80° SW	N 73 E 4° E
4	1983 11 19	1142	37.5152	118.7500	3.4	3.2	B	N 32 E 70° SE	N 54 W 80° SW	N 78 E 6° W
5	1983 11 23	0639	37.5190	118.8620	6.6	3.5	B	N 85 E 75° N	N 6 W 90°	N 42 E 10° SW
6	1983 10 31	0405	37.4685	118.7888	6.7	2.9	B	N 38 E 64° NW	N 46 E 76° NE	N 85 E 8° E
7	1983 10 04	0053	37.5042	118.7807	8	2.3	B	N 20 E 75° SE	N 68 W 80° SW	N 66 E 3° SW
8	1983 09 16	1430	37.5317	118.7784	8	2.5	C	N 68 E 90°	N 22 W 66° SW	N 20 E 17° N
9	1983 08 25	0922	37.5308	118.6505	8	2.8	B	N 18 E 90°	N 72 W 90°	N 63 E 0°
10	1983 09 28	2222	37.4818	118.6113	8	3.2	C	N 40 E 90°	N 50 W 90°	N 85 E 0°
11	1983 09 30	1614	37.5467	118.8205	8	4.0	B	N-S 80° E	N 88 E 80° N	N 44 E 14° SW
12	1983 11 12	0201	37.4732	118.8123	8.3	2.5	B	N 22 W 50° W	N 31 W 40° E	N 62 E 4° SW
13	1983 08 09	2311	37.5105	118.6548	8.4	3.2	C	N 13 E 54° W	N 39 W 50° E	N 78 E 1° W
14	1983 08 14	0745	37.4710	118.4282	9	2.8	C	N 8 E 38° W	N 25 W 56° E	N 79 E 10° E
15	1983 11 12	0147	37.4655	118.8117	9	3.2	B	N 11 E 56° E	N 70 W 78° S	N 46 E 6° SW
16	1983 11 20	1741	37.5630	118.8442	9.6	2.5	B	N 30 E 52° SE	N 44 W 70° SW	N 79 E 10° W
17	1983 11 08	2338	37.4660	118.8157	9.7	2.5	B	N 8 W 46° E	N 43 W 50° SW	N 67 E 1° W
18	1983 11 12	0031	37.4710	118.8050	10	2.5	B	N 60 E 34° N	N 14 W 80° E	N 42 E 45° SW
19	1983 09 16	1423	37.5260	118.7830	10	2.9	B	N 65 E 90°	N 26 W 80° NE	N 19 E 7° SW
20	1983 11 04	1909	37.4642	118.8255	10	3.0	B	N 18 E 70° W	N 65 W 70° N	N 66 E 0°
21	1983 10 31	0117	37.5992	118.8170	11	2.3	A	N 10 W 76° W	N 79 W 25° NE	N 65 E 28° SW
22	1983 10 29	2145	37.5545	118.3405	11	2.5	B	N 23 W 80° SW	N 23 W 10° NE	N 67 E 32° SW

APPENDIX
Earthquake Focal Mechanisms
From Tables II and III

Table II.

APPENDIX

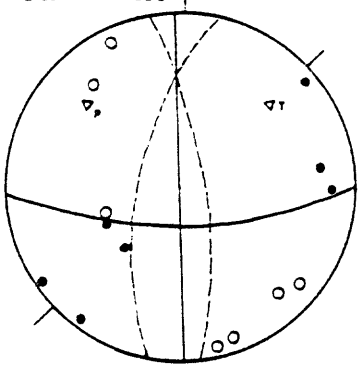
1

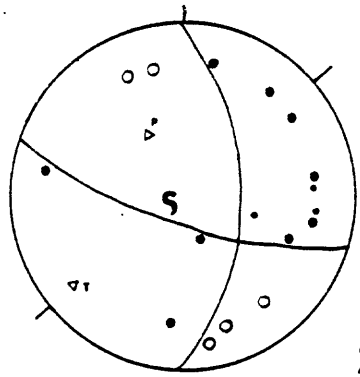
2

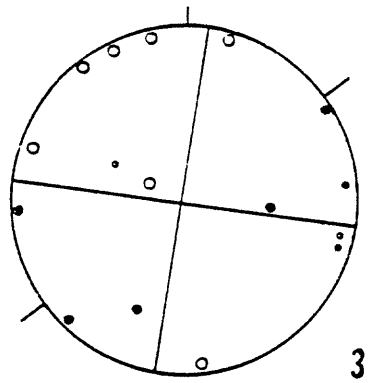
3

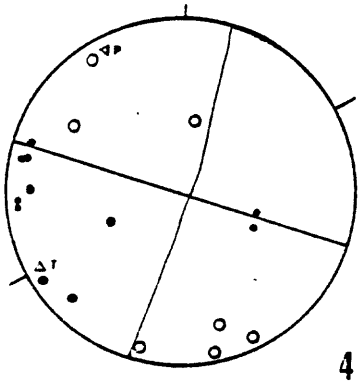
4

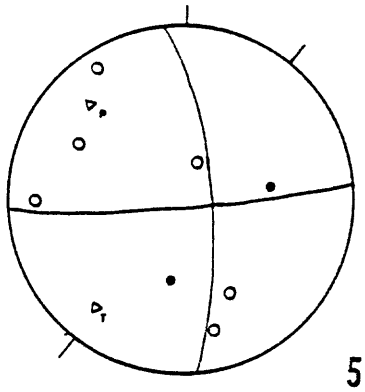
5

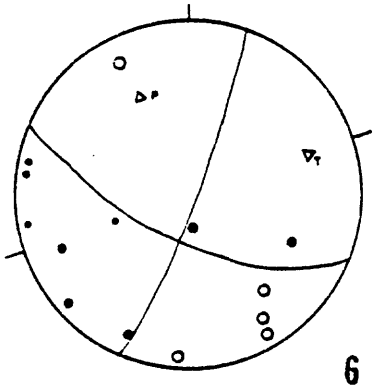
6

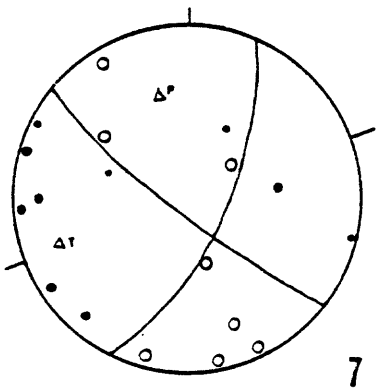
7

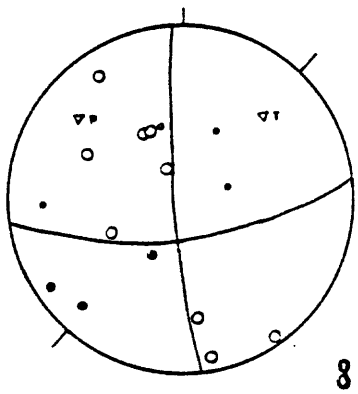
8

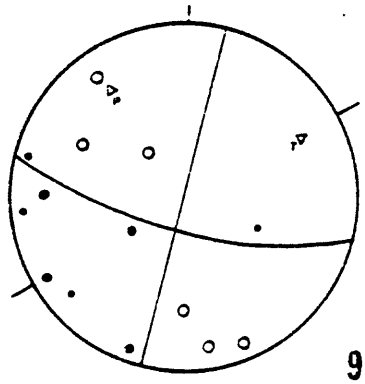
9

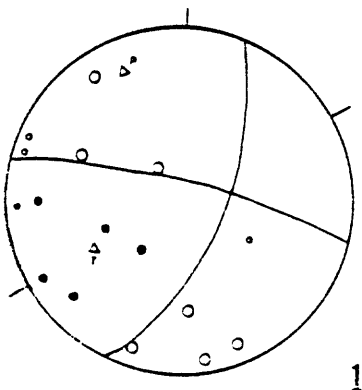
10

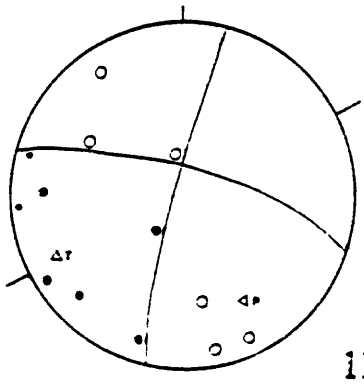
11

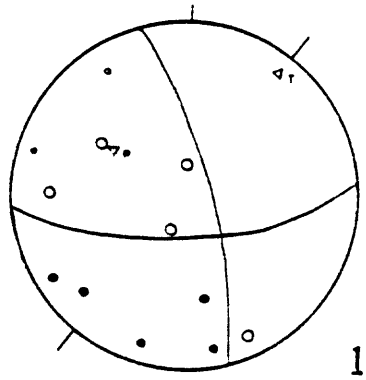
12

Table II contd.

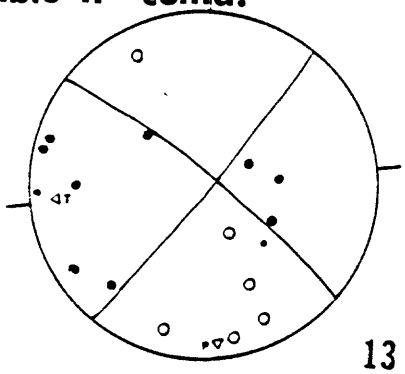
13

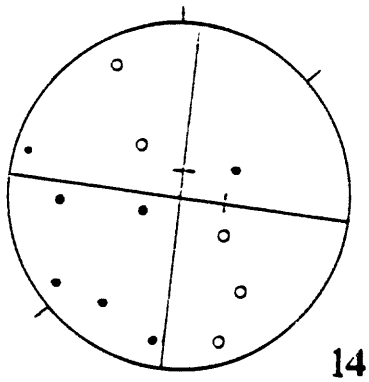
14

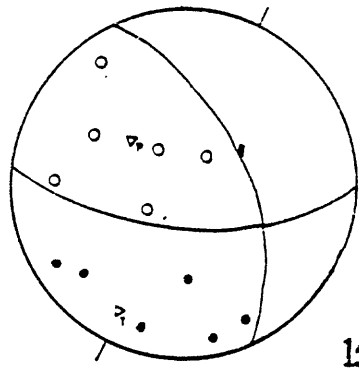
15

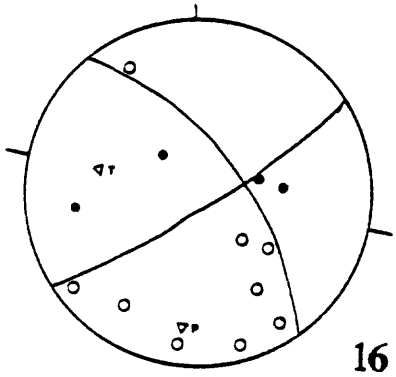
16

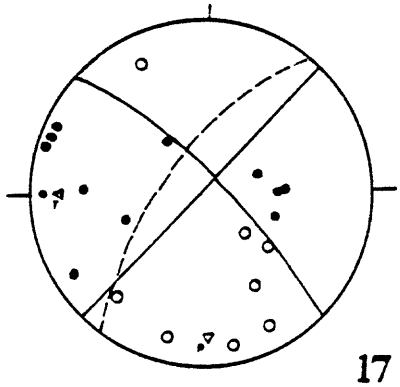
17

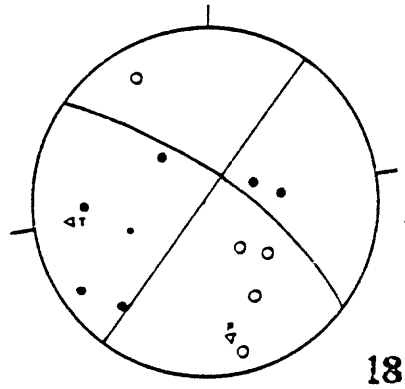
18

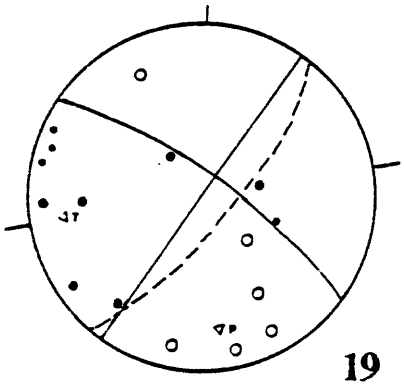
19

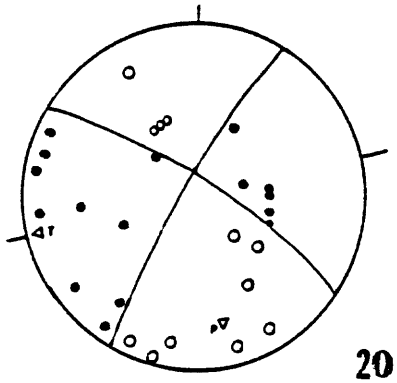
20

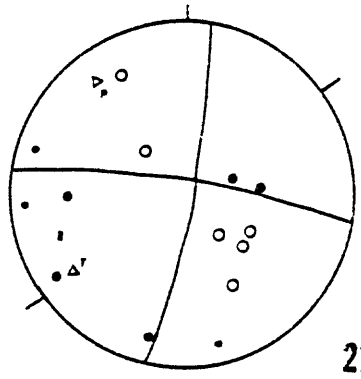
21

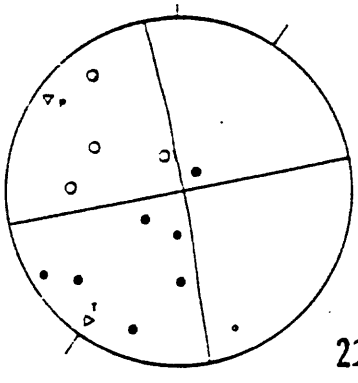
22

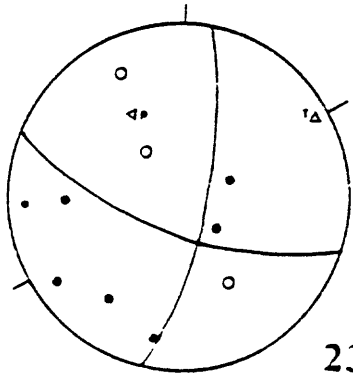
23

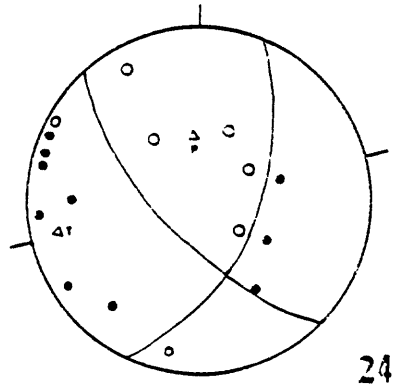
24

Table II contd.

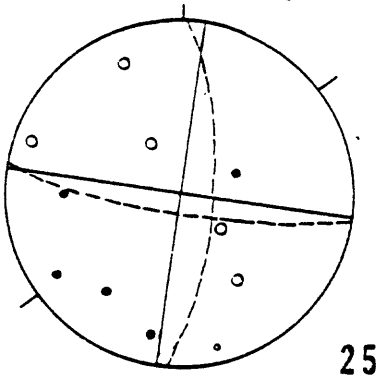
25

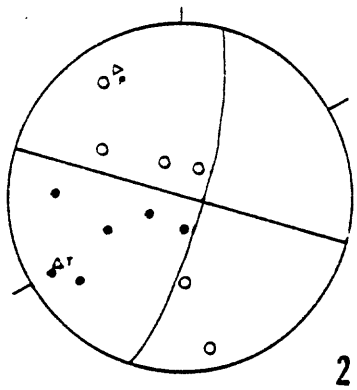
26

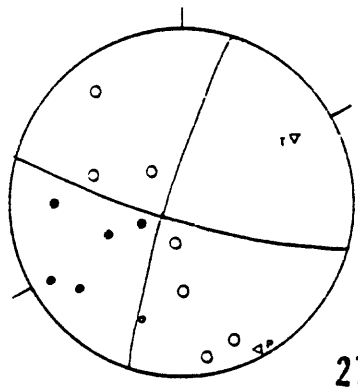
27

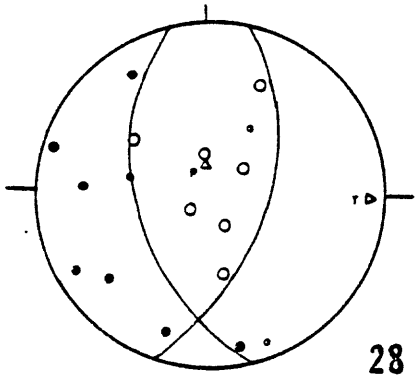
28

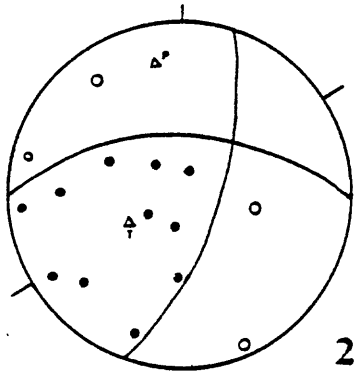
29

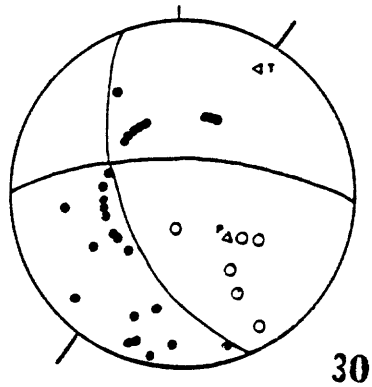
30

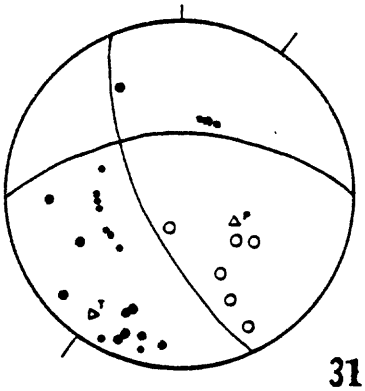
31

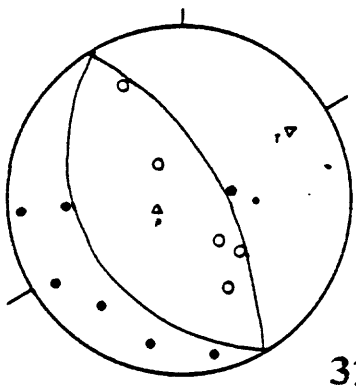
32

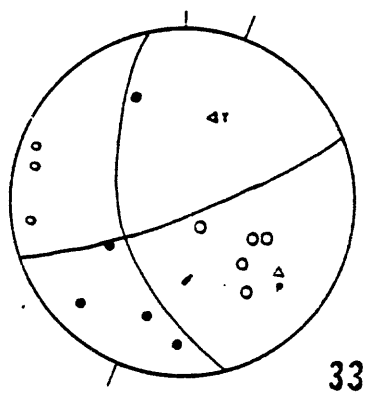
33

Table III.

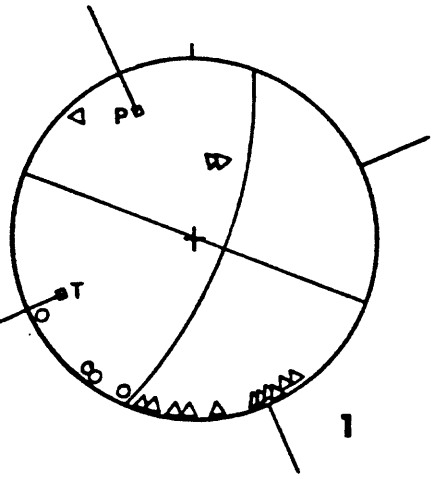

1

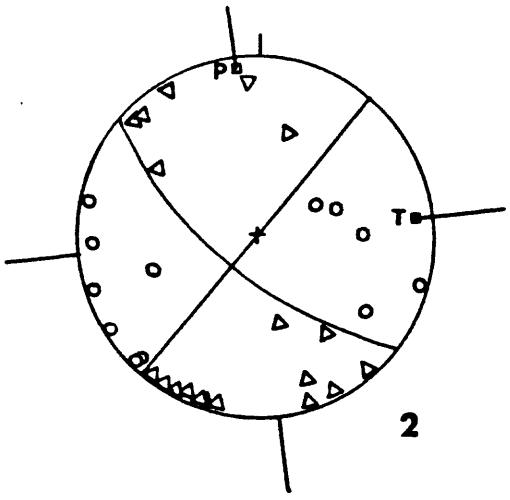

2

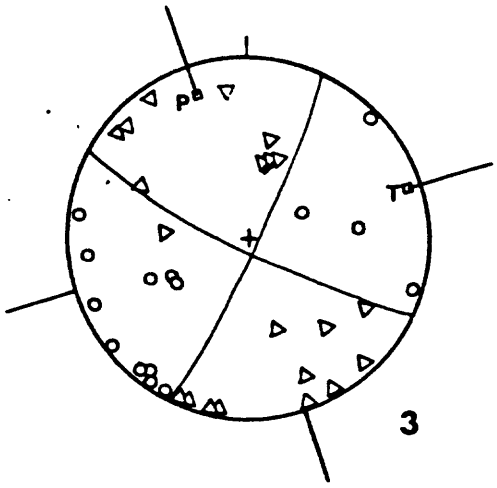

3

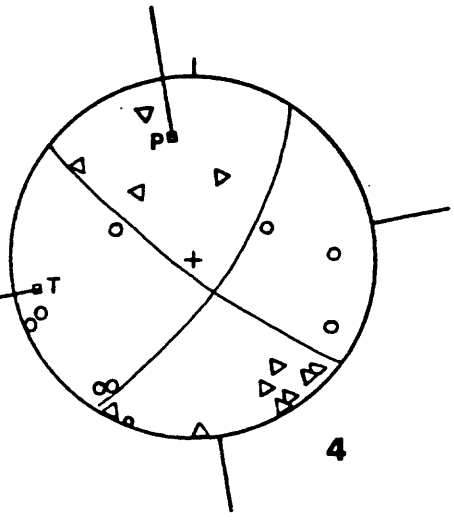

4

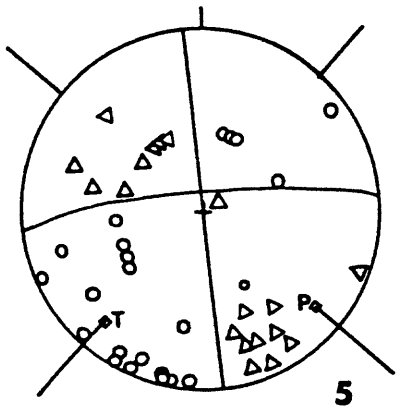

5

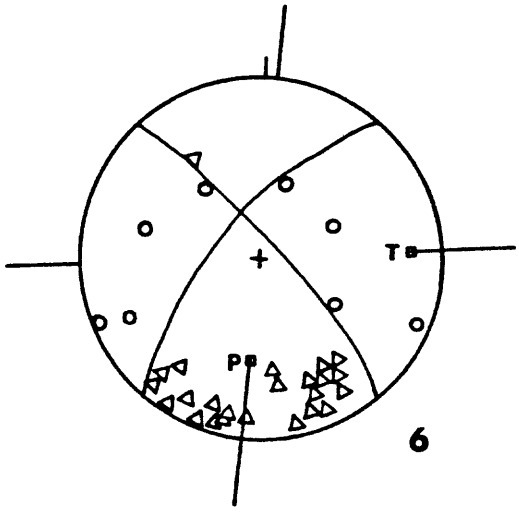

6

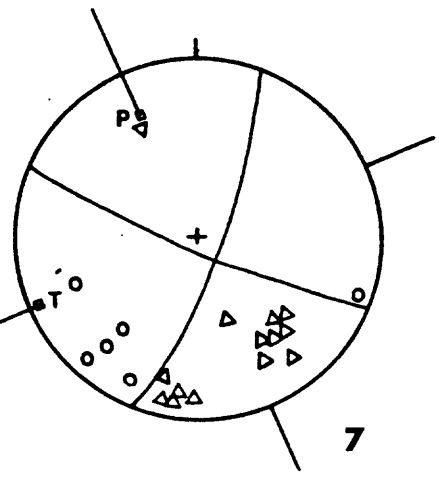

7

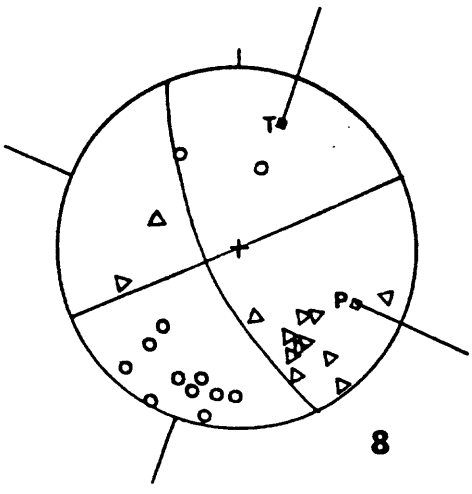

8

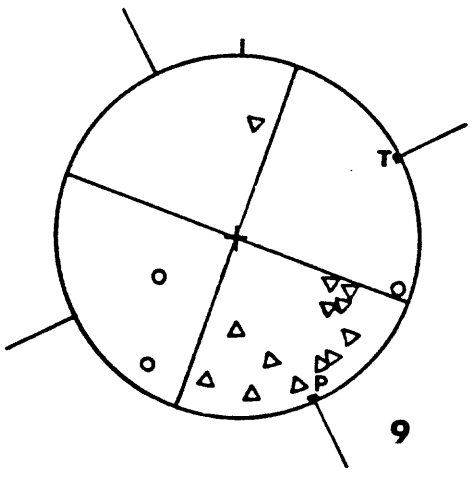

9

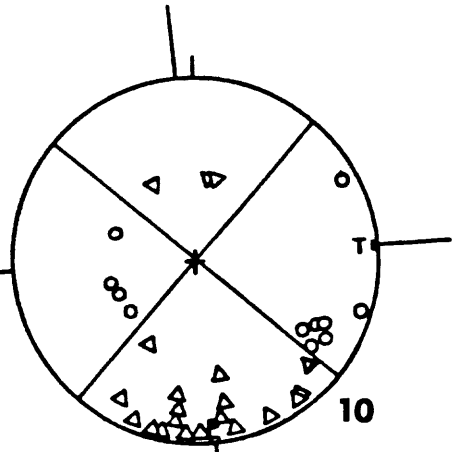

10

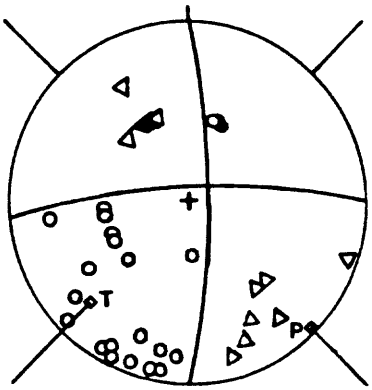

11

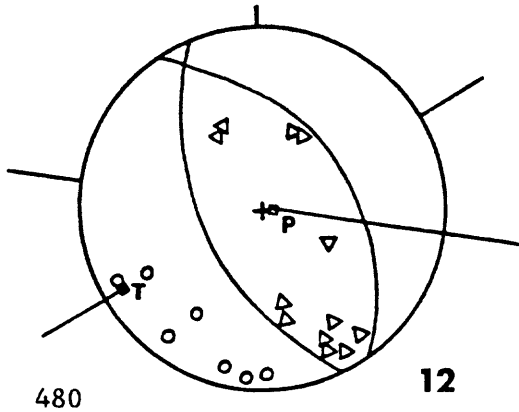

12

Table III contd.

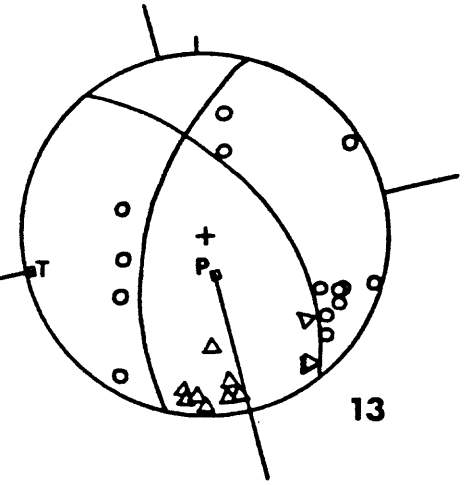

13

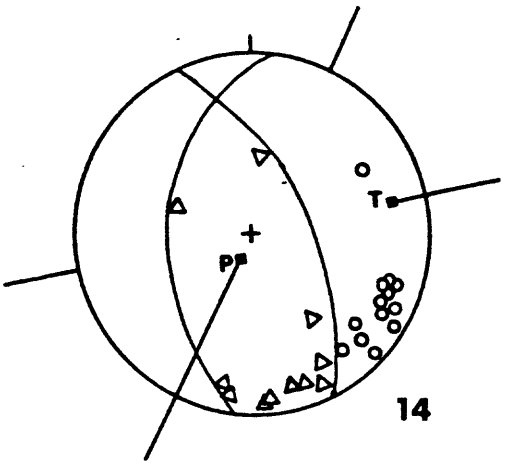

14

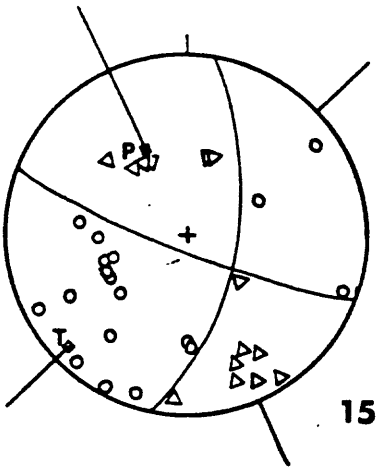

15

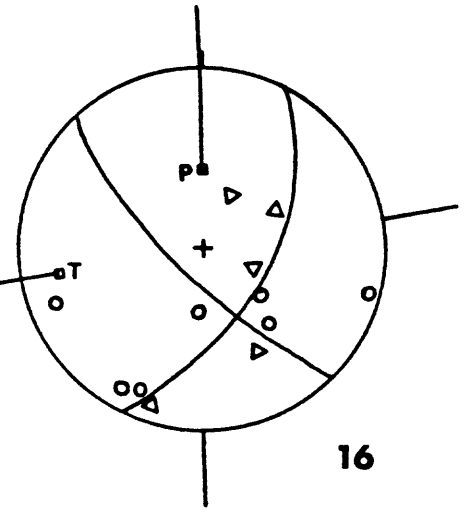

16

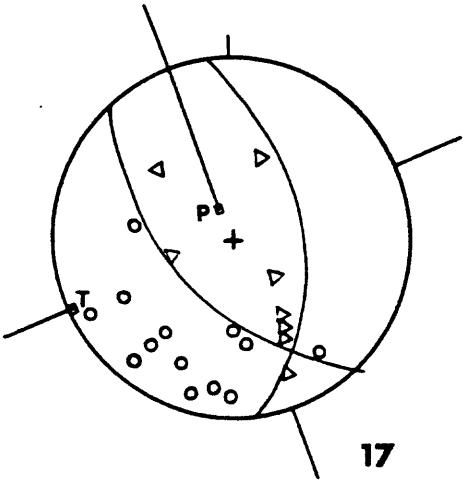

17

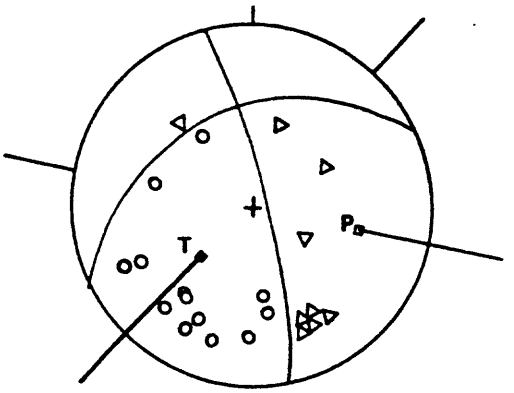

18

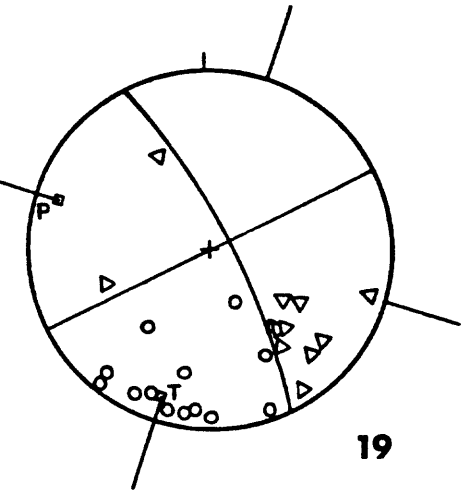

19

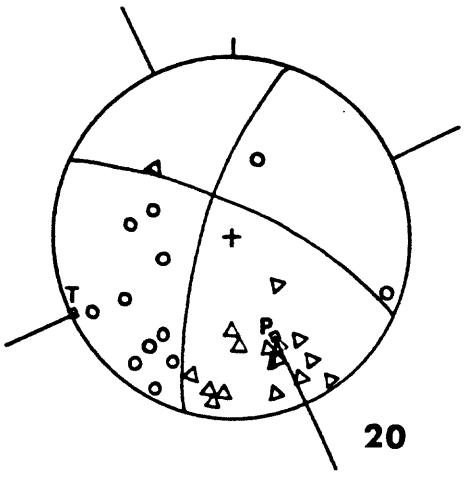

20

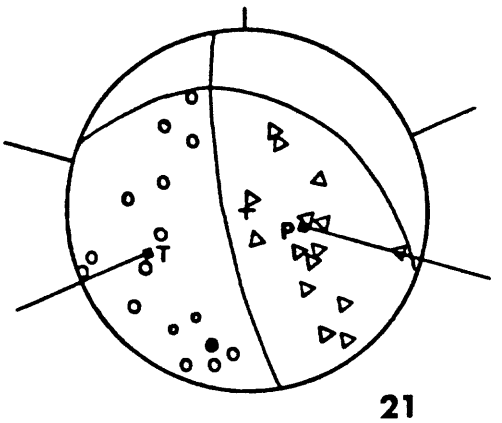

21

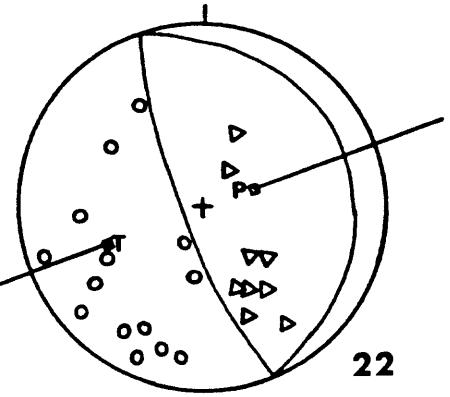

22

THREE DIFFERENT MECHANISMS FOR ELONGATE DISTRIBUTION OF SHALLOW EARTHQUAKE EPICENTERS

Kazuaki Nakamura

Earthquake Research Institute, University of Tokyo, Tokyo 113

ABSTRACT

There are at least three different mechanisms to give a linear distribution of earthquake epicenters : 1. Earthquakes associated with a steeply dipping strike-slip fault movement, 2. Those confined within a rock body capable of brittle fracturing and areally surrounded by more ductile rocks (1965-'67 Matsushiro earthquakes), 3. The epicenters elongate in a horizontal P axis direction of the ambient stress field (1962 Miyakejima, 1974 Chokai and 1980 Izu earthquakes). Examples for cases 2 and 3 are given as indicated in the parenthesis.

A new interpretation is given for the Matsushiro earthquakes as the seismic aspect of a water-eruption event.

INTRODUCTION

When the distribution of earthquake epicenters shows an elongate pattern, it is ususally assumed that the attitude of the fault plane is responsible for it. The common case of this kind of elongate earthquake pattern is an almost linear epicenter distribution associated with a vertical strike-slip faulting. There are, however, at least two other mechanisms that are capable of producing an elongate epicenter distribution. These are ;

1) the case where there is an elongately distributed rock mass which is capable of fracturing brittly to cause earthquakes while the surrounding rocks are more ductile and incapable of brittle fracturing. An example of this is the 1965-1967 Matsushiro Earthquakes in central Honshu.

2) the case where the epicneter distribution of earthquakes is elongated in the P direction of the ambient stress field as indicated with the focal mechanism solutions of earthquakes. Examples of this kind are volcanic earthquakes associated with the 1974 and 1962 activities of the Chokai and the Miyakejima Volcanoes, respectively, and the 1980 earthquake swarm east of the Izu Peninsula.

In the following pages, the above-mentioned four earthquakes are briefly described and discussed.

Manuscript submitted to the proceedings of the USGS Redbook Conference on
Active tectonic and magmatic processes, Long Valley Caldera, California
January 24 - 27, 1984

THE MATSUSHIRO EARTHQUAKES

The 1965-1967 Matsushiro earthquakes are interpreted as the seismic aspect of a 'water eruption' event in contrast to a magma eruption which is a normal volcanic eruption (Nakamura, 1971; Hagiwara, 1972; Ohtake, 1975).

The earthquake activity started in August, 1965. The daily number of felt shocks attained the second maximum of over 400/day at the end of August 1966 (Fig. 1, J.M.A., 1968). During September 1966, an areal outflow of underground water took place in the middle of the epicenter region (Fig. 2) causing several landslides. The water erupted to the surface not only through the existing wells but also from numerous sites on the ordinary ground surface. Prior to this 'water eruption' event, inflation of the epicentral region continued and the epicenters spread gradually to the NE and SW (Hagiwara•Iwata, 1968; Kasahara, 1970; Tsubokawa et al., 1968). After this 'water eruption', the deflation of the same area proceeded (Fig. 3) for years with the same center as that of the earlier inflation (F.O.S., ERI, 1970, Okada, 1970). The total volume of this deflation (Okada, 1970; Kisslinger, 1975) nearly equaled the volume of the outflown water (ca $10^7 m^3$, Iijima, 1969). During the deflation period, the epicenter distribution further spread to the NE and SW to form a 30 km long and 10 km wide straight zone (Hagiwara•Iwata, 1970, Fig. 4). Focal mechanism solutions of the strike-slip type with E-W compression remained nearly the same all through the activity (Ichikawa, 1967). A zone of NW-SE striking surface breaks (Fig. 2), caused by an underground left lateral strike-slip fault occurred prior to the 'water eruption' (Tsuneishi•Nakamura, 1970). Therefore the long axis of the epicenter distribution did not coincide with the strike of the earthquake fault.

Thus, the whole crustal activity may be well interpreted as the water-eruption event in contrast to the magma-eruption event (i.e. volcanic eruption). In the water-eruption, the water played the role of magma in volcanic eruptions and the seismic activity was one of the aspects associated with the event. The increased water pressure triggered the release of tectonic stress (E-W compression) causing concentrated seismicity in and near the reservoir on one hand, and it caused inflation of the ground surface with the subsequent deflation after the water eruption, on the other. Water migrated from the initial center during the entire period, causing earthquakes selectively within the belt of uplift where the rock was brittle enough to generate earthquakes (Nakamura, 1971).

The areal distribution of epicenters associated with this 'water eruption' was confined within the 'belt of uplift' intruded by Miocene quartz diorite (Tsuneishi•Nakamura, 1970, Fig. 5). In this belt the seismic velocity layer with Vp = 6.0 km/sec. forms a horst a few to several km higher than the surrounding softer (and therefore probably incapable of brittle fracturing) Pliocene-Quaternary sedimentary rocks (Fig. 6). Apparently, the earthquakes spread within this 6.0 km/sec layer.

THE 1974 CHOKAI EARTHQUAKES

The first example of the P direction mechanism is the volcanic earthquakes associated with the 1974 eruption of the Chokai Volcano in NE Honshu (Nakamura and Ui, 1974; Ueki et al., 1975; Ui and Nakamura, 1976). Mt. Chokai is an active, 2000 meter high stratovolcano located 400 km north of Tokyo. The phreatic eruptions from the summit crater, most probably caused by a shallow intrusion of magma, took place during March and April 1974. Volcanic earthquakes were associated with this activity. At the beginning of the activity, these earthquakes were distributed near the volcanic ediffice but the earthquake activity spread later toward the NW and SE (Fig. 7). It was impossible to obtain composite focal mechanism solutions during the period of eruptive activity (Fig. 8, A) but after the cessation of surface activity, the mechanism became stable with NW-SE trending P axes (Fig. 8, B).

These observations may be interpreted as follows. During the period of the active eruption, earthquake generating stresses were caused mostly by strain change directly associated with the magma movement including the inflation of the volcanic edifice. Because these magma-related strain field was of an approximate point source in plan view, it was impossible to obtain a composite mechanism solution. After the eruption, the magma-caused deformation was relieved due to the eruption, the pressurized fluid, (probably volcanic gas or magma-heated underground water) propagated through cracks in the P direction of the tectonic stress causing the spread of the earthquakes. WNW striking P direction of tectonic stress was shown by the flank crater distribution of the volcano and by the tectonic earthquakes near the volcano.

THE 1962 MIYAKE-JIMA EARTHQUAKES

The Miyake-jima earthquakes of the present concern are those associated with the 1962 eruption. Miyake-jima is an insular basaltic stratovolcano, 814.5 m a.s.l. and located about 200 km south of Tokyo. The volcano erupted August 24 to 26 after 22 years of quiescence. The eruption was a flank eruption from a curved 2.5 km long radial fissure. The eruption continued for less than 30 hours and ended early in the morning of August 26 (Matsuda-Morimoto, 1962).

The eruption-associated swarm earthuqakes began about one hour before the onset of the eruption and lasted over a month. The peak seismicity was observed on August 30, several days after the cessation of the eruption. The hypocenter distribution is shown in Fig. 9. The earthquakes are radially distributed from the summit ranging 1 to 4 km in depth.

The focal mechanism solution of an earthquake (M 5.9) of the above swarm (Fig. 10) was a strike-slip type with P axis in the NW-SE direction, coinciding with the axis of epicenter elongation. This mechanism is common to those of the earthquakes occurring from time to time near the Miyake-jima island and is interpreted to be caused by the bending of the Philippine

Sea plate associated with its subduction at the Sagami trough running NW-SE (Nakamura et al., 1984). The pattern of the 1962 eruptive fissure as well as those of 1983 and older ones also indicate the NW-SE σHmax by their bending towards NW or SE (Fig. 1 of Nakamura, 1977). Thus, almost the same interpretation as the case of Chokai is possible for this case. Apparently, volcanic fluid migrated from the summit reservoir in the P direction of the ambient stress field causing earthquakes.

THE 1980 IZU EARTHQUAKES

The third example of the epicentral distribution of earthquakes in the maximum pressure direction of the crustal stress field is a swarm event during 4 days immediately before the main shock of magnitude 6.7, 1980 Izu Hanto Toho Oki Earthquake (Imoto et al., 1981; Ishida, 1984). This 4 days event occurred beneath the sea a few kilometers east of Izu Peninsula. The epicentral area was elongated in a NW-SE direction and was 3 km long and 1.5 km wide (Fig. 11). The main shock occurred on the southeastern tip of the area and was of a strike-slip type with P axis in a N55°W direction (Fig. 12). Thus, the elongate direction of the epicenters of the 4 days foreshocks coincides with the direction of the P axis of the main shock. Its aftershocks spread to the south, indicating that the N10°W nodal plane corresponds to the actual fault plane of the main shock.

I concur with Ishida (1984) who suggested that an increase in pore fluid pressure caused the foreshocks and helped pore fluid to migrate to the SE (P direction) eventually triggering the main shock.

ACKNOWLEDGEMENT I thank Yukio HAGIWARA for a critical comment on the geodetic data of Matsushiro, Mizuho ISHIDA for her discussion about Izu earthquakes, Robert MACABE for helpful advice to the earlier draft and Akiko ISHII for help to prepare the manuscript.

REFERENCES

Asano, S., S. Kubota, H. Okada, M. Nogoshi, H. Suzuki, K. Ichikawa and H. Watanabe, 1969, Explosion seismic studies of the underground structure in the Matsushiro earthquake swarm area, Jour. Phys. Earth, 17, 77-90.

Field Observation Section, Earthquake Research Institute, 1970, Levelling resurvey associated with the area of Matsushiro earthquake swarms (3), Bull. Earthq. Res. Inst., Univ. Tokyo, 48, 341-344. *

Geographical Survey Institute, 1967, Geodetic surveys in the area of Matsushiro earthquake swarm, Bull. Geographical Survey Institute, 12 (2), 20-25.

Hagiwara, T. and T. Iwata, 1968, Summary of the seismographic observation of Matsushiro swarm earthquakes, Bull. Earthq. Res. Inst., 46, 485-515.

Hagiwara, T., 1972, Cause of shallow earthquakes occuring in the earth's crust as suggested by the accompanying land deformation, Phys. Earth Planet. Interior, 6, 250-255.

Ichikawa, M., 1967, Statistical study of the focal mechanism of Matsushiro earthquake swarm, Zisin, 20, 116-127 *

Iijima, H., 1969, Surface geology of Matsushiro area and disasters by the Matsushiro earthquake swarm, in Studies on the Matsushiro earthquake swarm : Tokyo, National Research Center for Disaster Prevention, p. 103-115. *

Imoto, M., I. Karakama, S.R. Matsu'ura, F. Yamazaki, A. Yoshida and K. Ishibashi, 1981, Focal mechanisms of the 1980 Earthquake Swarm off the east coast of the Izu Peninsula, Japan, Zisin, 34, 481-493. *

Ishida, M., 1984, Spatial-temporal variation of seismicity and spectrum of the 1980 earthquake swarm near the Izu Peninsula, Japan, Bull. Seis. Soc. Amer., 74, 199-221.

Izutsuya, S., 1975, Revised results of levelling surveys during the Matsushiro earthquake swarm, Bull. Earthq. Res. Inst., Univ. Tokyo, 50, 273-280. *

Japan Meteorological Agency, 1968, Report on the Matsushiro earthquake swarm, August 1965-December 1967, Tech. Report JMA, 62, 556p. *

Kasahara, K., 1970, The source region of Matsushiro swarm earthquakes, Bull. Earthq. Res. Inst., Univ. Tokyo, 48, 581-602.

Kisslinger, C., 1975, Processes during the Matsushiro, Japan, earthquake swarm as revealed by levelling, gravity, and spring-flow observations, Geology, 3, 57-62.

Matsuda, T. and R. Morimoto, 1962, 1962 August eruption of Miyake-jima, Kagaku, 32, 578-585 (in Japanese).

Minakami, T., 1964, The 1962 Eruption of Miyake-sima, one of the seven Izu islands, Japan, Bull. Volcanol. 27, 225-234.

Nakamura, K., 1971, What was the Matsushiro earthquakes? Kagaku Asahi, 10, 127-133, (in Japanese).

Nakamura, K., 1977, Volcanoes as possible indicators of tectonic stress orientation. J. Volcanol. Geotherm. Res. 2, 1-16.

Nakamura, K., K. Shimazaki and N. Yonekura, 1984, Subduction, bending and eduction-Present and Quaternary tectonics of the northern border of the Philippine Sea plate, Bull. Soc. Geol. Fr. (in press).

Nakamura, K. and Y. Tsuneishi, 1967, Ground cracks at Matsushiro probably of underlying strike-slip fault origin, II - The Matsushiro earthquake fault, Bull. Earthq. Res. Inst., Univ. Tokyo, 45, 417-471.

Nakamura, K. and T. Ui, 1975, Possible role of pore pressure in 1974 volcanic earthquakes of Chokai Volcano, Bull. Volcanol. Soc. Japan, 20, 103-104, (in Japanese).

Ohtake, M., 1976, The Matsushiro earthquakes, after 10 years, Kagaku, 46, 306-313, (in Japanese).

Okada, A., 1970, The vertical crustal movement in the area of Matsushiro earthquake, Bull. Earthq. Res. Inst., Univ. Tokyo, 48, 345-349. *

Tsubokawa, I., A. Okada, S. Izutsuya, Y. Ito and K. Kadono, 1968, Levelling resurvey associated with the area of Matsushiro earthquake swarms (2), Bull. Earthq. Res. Inst., Univ. Tokyo, 46, 417-429. *

Tsuneishi, Y. and K. Nakamura, 1970, Faulting assoicated with the Matsushiro swarm earthquakes, Bull. Earthq. Res. Inst., Univ. Tokyo, 48, 29-51.

Ueki, S., T. Hasegawa, S. Hori and A. Takagi, 1975, 1974 Eruption of Chokai Volcano and its seismic activity (A preliminary report), Progress Report on Disaster Science Research on Tohoku District, 1974 Fiscal Year, 51-54, (in Japanese).

Ui, T., K. Nakamura and K. Shibahashi, 1976-1977, 1974 Activity of Chokai volcano, Japan, Bull. Volcanol., 40, 1-8.

* in Japanese with English abstract.

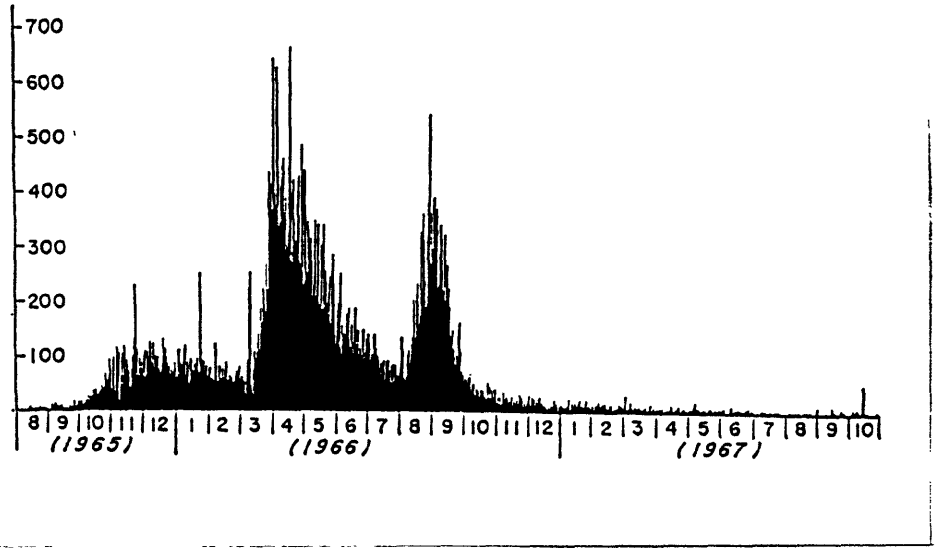

Fig. 1. Daily frequency of felt shocks of the Matsushiro earthquakes recorded at the Matsushiro observatory, J.M.A. (J.M.A., 1968).

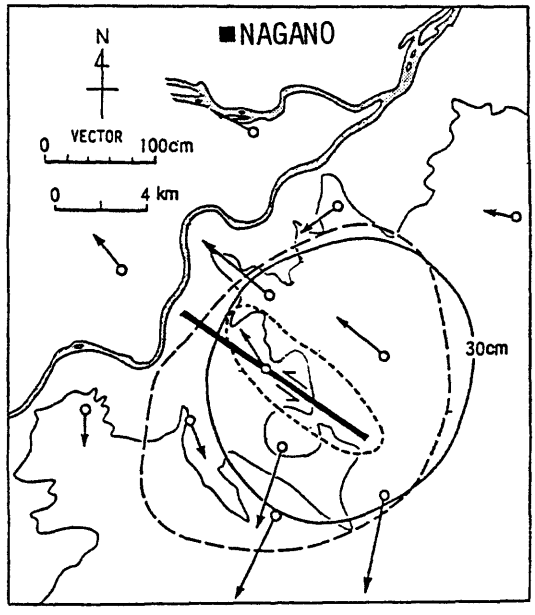

Fig. 2. Horizontal and vertical deformation at Matsushiro from 1965 through September, 1966, the surface breaks and the outline of the water eruption area (Nakamura, 1971).
Horizontal deformation (G.S.I., 1967) is shown by an arrow with a circle (triangulation point). Vertical deformation (Tsubokawa, et al., 1968) is represented by the 30 cm uplift contour line. Approximate limits of the areal outflow of normal underground and concentrated water are shown by longer and shorter broken lines, respectively. Note : The result of the levelling was later revised by Izutsuya (1975) and the 30 cm contour line appears to be larger than the revised one by about 500 m in radius.

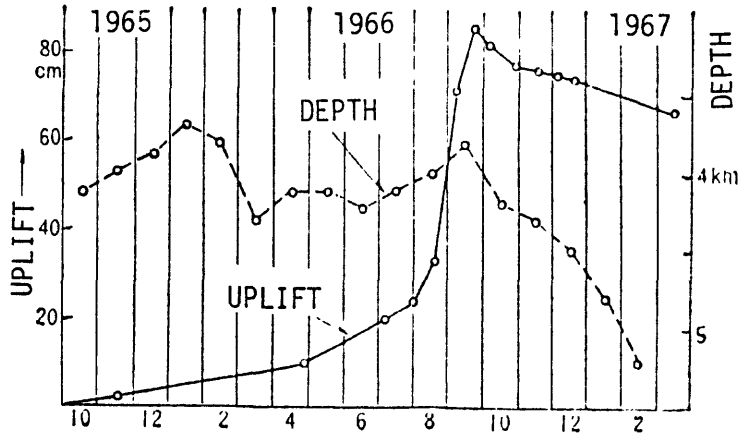

Fig. 3. Vertical movement of the bench mark located near the center of the uplift (Tsubokawa et al., 1968) and the average depth (E.R.I.) of the felt shocks (Nakamura, 1971). The maximum amount of uplift was later found by Izutsuya (1975) to be about 70 cm, rather than 85 cm.

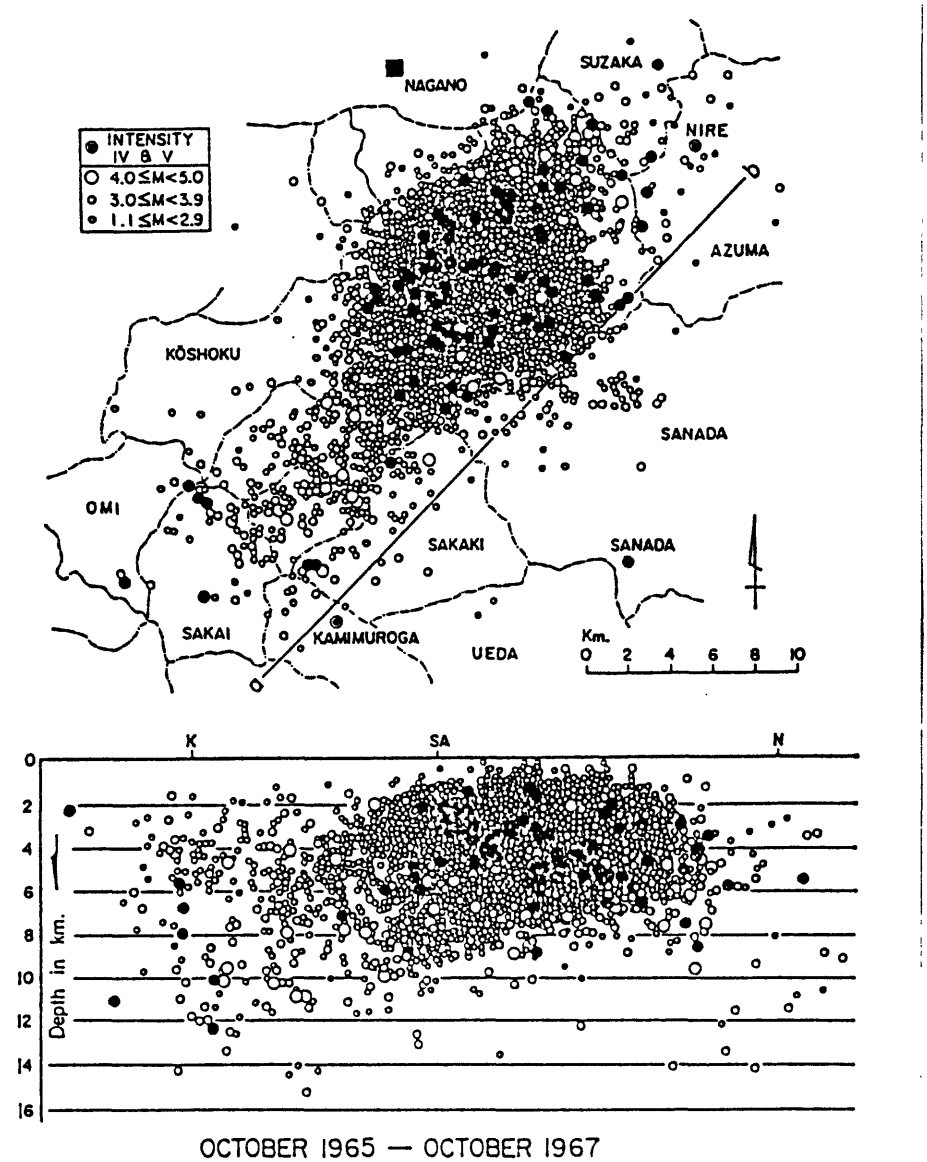

Fig. 4. Distribution of the Matsushiro earthquakes from October 1965 through October 1967 (Hagiwara and Iwata, 1968).
Top : map view, Bottom : NE-SE cross sectional view.

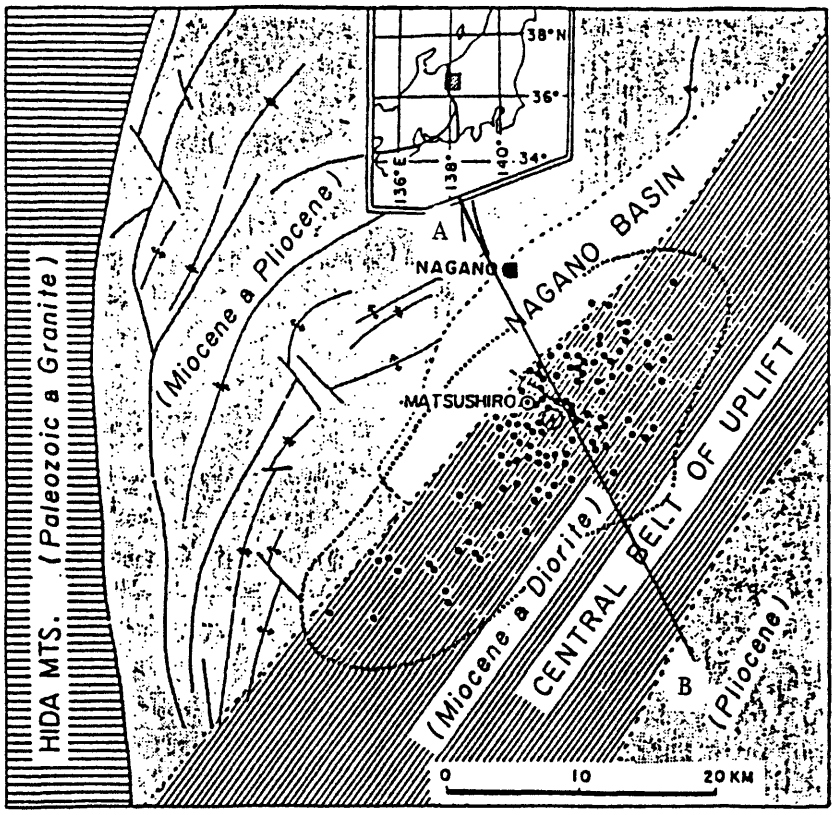

Fig. 5. Map showing the location of Matsushiro (inset) and the Central belt of uplift (Tsuneishi and Nakamura, 1970).
A - B : The cross sectional line for the crustal velocity structure in Fig. 6. Dot : larger shocks (Hagiwara and Iwata, 1968). The elongate area surrounded by dotted line : outline of the area of ultra-micro earthquakes.

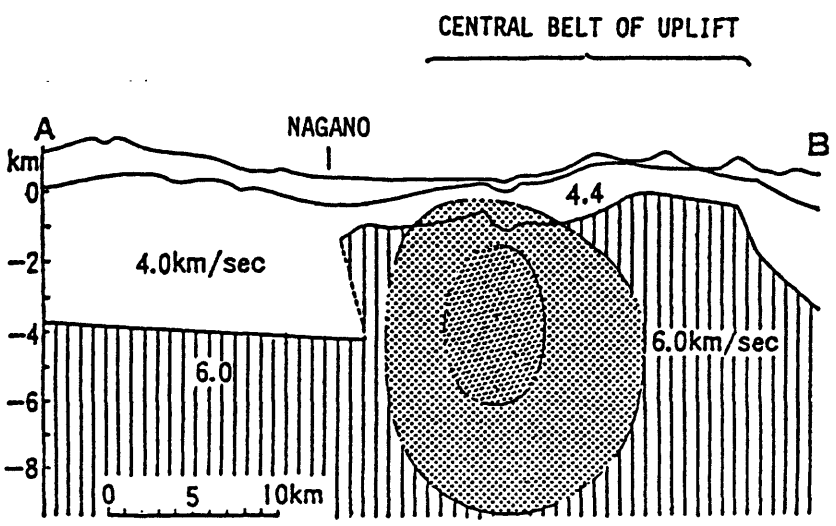

Fig. 6. A NW-SE cross section of the crustal velocity structure (Asano et al., 1969) and of the hypocentral region (stippled area, Hagiwara-Iwata, 1968) of the Matsushiro earthquakes (Nakamura, 1971). The cross sectional line in Fig. 5.

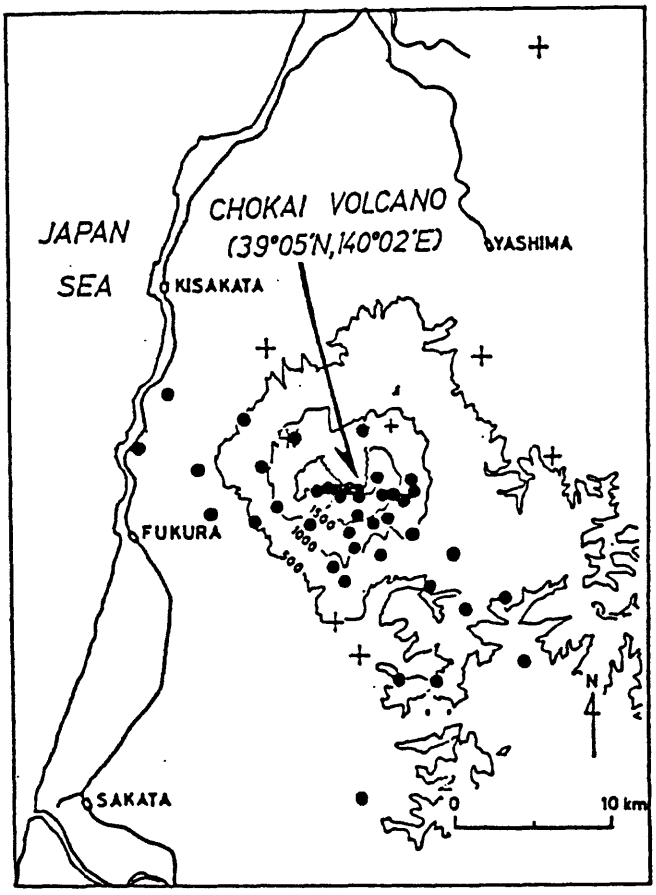

Fig. 7. Epicenter distribution of volcanic earthquakes associated with the 1974 activity of Chokai Volcano (Ueki et al., 1975). Crosses are seismograph stations.

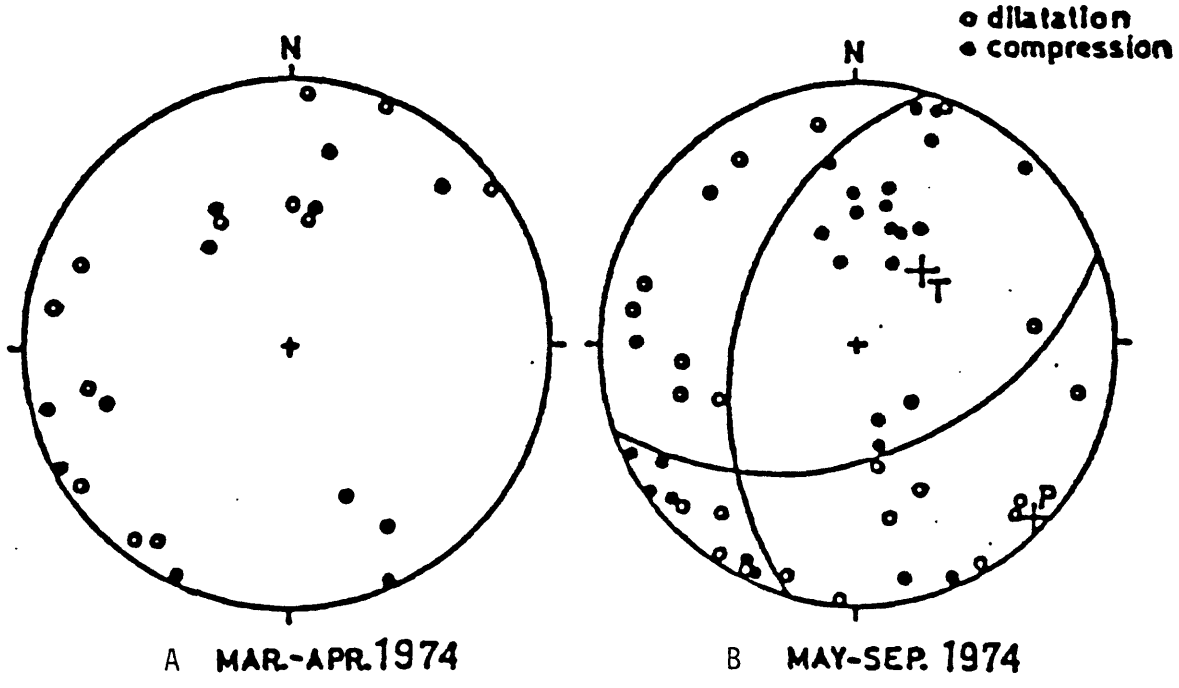

Fig. 8. Equal area projection of the first motions of the volcanic earthquakes on the lower hemisphere (Ueki et al., 1975).

A : during the eruptive period. B : after the cessation of the eruption.

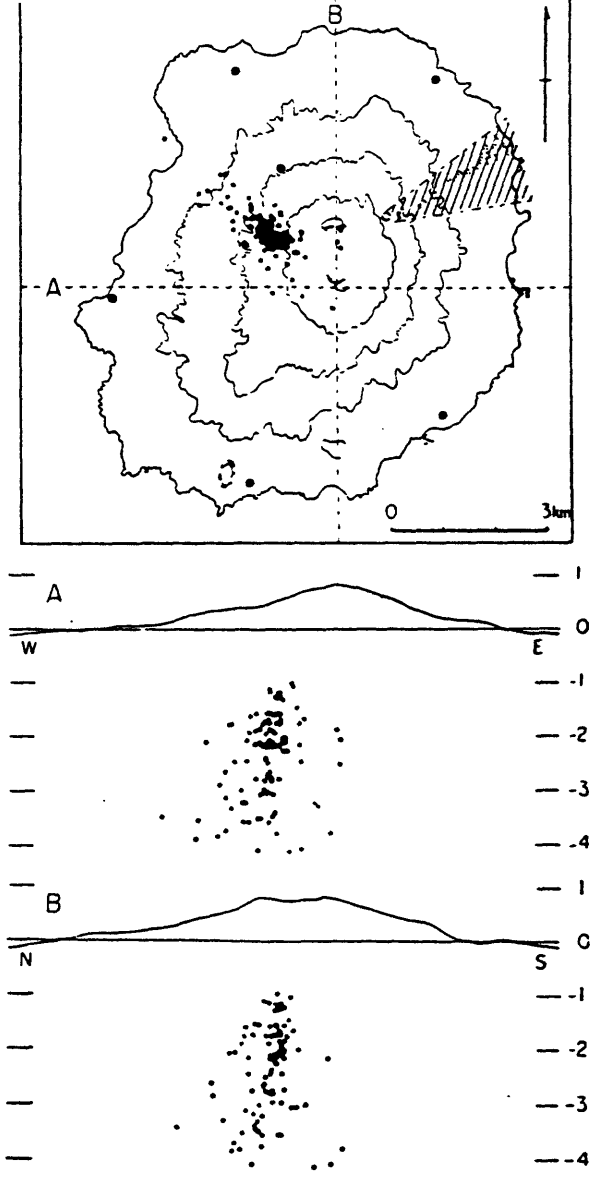

Fig. 9. Hypocenter distribution of Miyake-jima earthquakes right after the 1962 eruption (Minakami, 1964). Ruled area in the map shows approximate flank eruption sites.

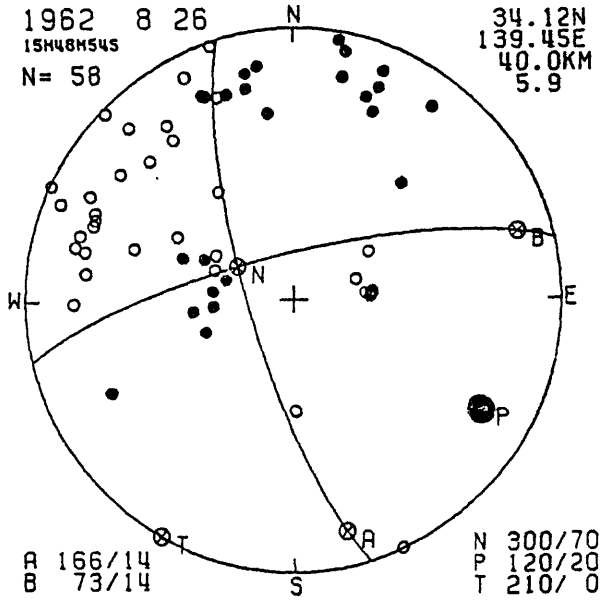

Fig. 10. Focal mechanism solution (lower hemispher) of the 1962 Miyake-jima earthquakes (MAKI, 1983, personal communication).

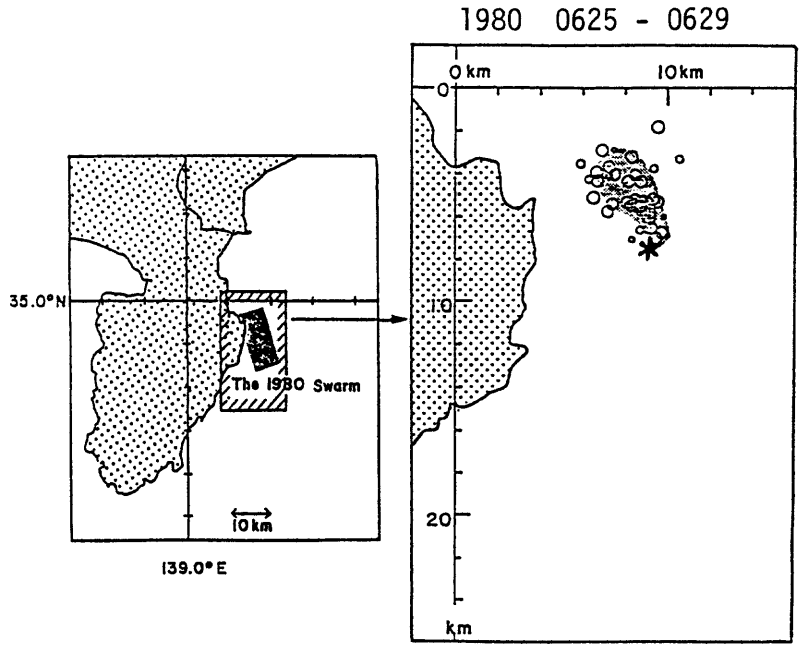

Fig. 11. Distribution of the swarm event east off Izu Peninsula during 4 days immediately before M 6.7 main shock (asterisk) (Ishida, 1984).

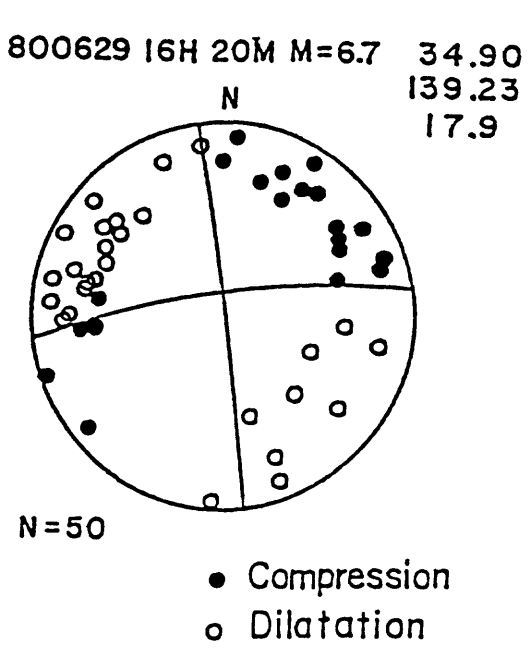

Fig. 12. Focal mechanism solution of the 1980 Izu Hanto Toho oki earthquake of M 6.7 (Imoto et al., 1984).

UNITED STATES DEPARTMENT OF THE INTERIOR

GEOLOGICAL SURVEY

PROCEEDINGS OF

WORKSHOP XIX

ACTIVE TECTONIC AND MAGMATIC PROCESSES BENEATH LONG VALLEY CALDERA, EASTERN CALIFORNIA
VOLUME II

24 - 27 January 1984

Sponsored by

U.S. GEOLOGICAL SURVEY

VOLCANO HAZARDS PROGRAM

Editors and Convenors

David P. Hill
U.S. Geological Survey
Menlo Park, California 94025

Roy A. Bailey
U.S. Geological Survey
Menlo Park, California 94025

Allan S. Ryall
University of Nevada
Reno, Nevada 89557-0018

OPEN-FILE REPORT 84-939

Compiled by
Muriel Jacobson

MENLO PARK, CALIFORNIA
1984

PROCEEDINGS OF WORKSHOP XIX - ACTIVE TECTONIC AND MAGMATIC PROCESSES BENEATH LONG VALLEY CALDERA, EASTERN CALIFORNIA VOL.II

CONFERENCES TO DATE

Conference I	Abnormal Animal Behavior Prior to Earthquakes, I Not Open-Filed
Conference II	Experimental Studies of Rock Friction with Application to Earthquake Prediction Not Open-Filed
Conference III	Fault Mechanics and Its Relation to Earthquake Prediction Open-File No. 78-380
Conference IV	Use of Volunteers in the Earthquake Hazards Reduction Program Open-File No. 78-336
Conference V	Communicating Earthquake Hazard Reduction Information Open-File No. 78-933
Conference VI	Methodology for Identifying Seismic Gaps and Soon-to-Break Gaps Open-File No. 78-943
Conference VII	Stress and Strain Measurements Related to Earthquake Prediction Open-File No. 79-370
Conference VIII	Analysis of Actual Fault Zones in Bedrock Open-File No. 79-1239
Conference IX	Magnitude of Deviatoric Stresses in the Earth's Crust and Upper Mantle Open-File No. 80-625
Conference X	Earthquake Hazards Along the Wasatch and Sierra-Nevada Frontal Fault Zones Open-File No. 80-801
Conference XI	Abnormal Animal Behavior Prior to Earthquakes, II Open-File No. 80-453
Conference XII	Earthquake Prediction Information Open-File No. 80-843
Conference XIII	Evaluation of Regional Seismic Hazards and Risk Open-File No. 81-437

Open-File Service Section
Branch of Distribution
U.S. Geological Survey
Box 25425, Federal Center
Denver, Colorado 80225

CONFERENCES TO DATE

Workshop XV	Preparing for and Responding to a Damaging Earthquake in the Eastern United States Open-File No. 82-220
Workshop XVI	The Dynamic Characteristics of Faulting Inferred from Recordings of Strong Ground Motion Open-File No. 82-591
Workshop XVII	Hydraulic Fracturing Stress Measurements Open-File No. 82-1075
Workshop XVIII	Continuing Actions to Reduce Losses from Earthquakes in the Mississippi Valley Area Open-File No. 83-157
Workshop XIX	Active Tectonic and Magmatic Processes Beneath Long Valley Caldera, Eastern California Open-File No. 84-939
Workshop XX	The 1886 Charleston, South Carolina, Earthquake and its Implications for Today Open-File No. 83-843
Workshop XXI	A Workshop on "Continuing Actions To Reduce Potential Losses from Future Earthquakes in the Northeastern United States" Open-File No. 83-844
Workshop XXII	A Workshop on "Site-Specific Effects of Soil and Rock on Ground Motion and the Implications for Earthquake-Resistant Design" Open-File No. 83-845
Workshop XXIII	A Workshop on "Continuing Actions to Reduce Potential Losses from Future Earthquakes in Arkansas and Nearby States" Open-File No. 83-846
Workshop XXIV	A Workshop on "Geologic Hazards in Puerto Rico" Open-File No. 84-761
Workshop XXV	A Workshop on "Earthquakes Hazards in the Virgin Island Region" Open-File No. 84-762
Workshop XXVI	A Workshop on "Evaluating the Regional and Urban Earthquakes Hazards in Utah" Open-File No. 84-763

Open-File Service Section
Branch of Distribution
U.S. Geological Survey
Box 25425, Federal Center
Denver, Colorado 80225

TABLE OF CONTENTS

VOLUME I

GEOLOGY

GEOPHYSICS

RECENT ACTIVITY

VOLUME II

THE GEOTHERMAL SYSTEM

RELATED MAGMATIC SYSTEMS

SEISMIC ACTIVITY IN LONG VALLEY CALDERA, EASTERN CALIFORNIA, U.S.A.: June 1982 through July 1984

by

Robert S. Cockerham and A. M. Pitt

Office of Earthquakes, Volcanoes, and Engineering

U.S. Geological Survey

Menlo Park, California

INTRODUCTION

In October 1978 a M_L = 5.8 earthquake occurred near Wheeler Crest, 12 km south-southeast of Lake Crowley that heralded the beginning of an unusual sequence of earthquakes for the Long Valley caldera area (LVC), which has continued to present. This sequence, following a northwestward migration from Wheeler Crest towards LVC [Ryall and Ryall 1980, 1981], culminated with the occurrence of four $M_L \geq 6.0$ [Uhrhammer and Ferguson, 1980] earthquakes within a period of 48 hours during May 25 - 27, 1980. Cramer and Toppazada [1980] and Ryall and Ryall [1980, 1981] have demonstrated that there was little seismic activity in LVC between October 1978 and July 1979. In addition, during the 1970 and 1973 studies of Pitt and Steeples [1975] and Steeples and Pitt [1976] only 10 earthquakes total were detected in LVC.

Long Valley caldera an elliptical depression (Fig. 1) 32 km long and 17 km wide, formed by collapse of a magma chamber following a catacylismic eruption that ejected 600 km^3 of rhyolitic magma [Bailey et al., 1976], was recently

identified (May 27, 1982) as the site of a potential volcanic hazard [Miller et al., 1982; Kerr, 1982]. This heightened concern was the result of the scientific community's focused attention upon 3 geophysical phenomena occurring within LVC: (1) an increase in seismic activity [Ryall and Ryall, 1980, 1981]; (2) an increase in ground deformation [Savage and Clark, 1982]; and (3) increased and new fumarolic activity [Miller et al., 1982].

Since May 1980, thousands of earthquakes have occurred within LVC and the Sierran block to the south (Fig. 2). The purpose of this report is to describe the spatial distribution of seismicity in the LVC area during the period June, 1982 through July 1984.

To provide the reader as much "visible" access to the data as space permits we have attempted to supply as many viewing directions and methods as possible. The figures presented in this report best display the general character of the seismicity in the LVC and the Sierran block from June 1982 through July 1984.

SEISMIC NETWORK HISTORY

The U.S. Geological Survey (USGS) seismic microearthquake network in the LVC area is comprised of 22 high-gain short-period vertical component seismometers (Fig. 1b). The analog data from these instruments are telemetered to Menlo Park and recorded on 16mm film and magnetic tape. The frequency response of the seismic system is described by Eaton [1977]. Station locations are listed in Table 1.

TABLE 1: Station delays calculated by program VELEST for the seismic stations used in locating LVC area events. These delays are relative to the model listed in Table 1.

Station	Latitude	Longitude	Elevation	Delay	Organization
BEN	37° 42.93' N	118° 34.40' W	2463 m	-0.16 s	UNR
BNY	37 38.45	118 56.15	2325	-0.01	USGS
CAS	37 34.49	118 33.09	2107	0.00	UNR
CEN	37 38.03	118 55.63	2280	0.11	USGS
CHS	37 39.30	118 54.27	2420	0.09	USGS
CLK	37 35.41	118 49.45	2630	-0.07	USGS
CSR	37 40.66	118 49.10	2122	0.21	USGS
CSW	37 38.65	118 55.69	2280	0.02	USGS
CVM	37 36.59	118 52.40	2260	-0.09	USGS
DMP	37 42.48	119 2.75	2550	-0.14	USGS
DOE	37 38.32	118 50.13	2220	0.12	USGS
EMH	37 39.98	118 56.35	2495	0.09	USGS
GRP	37 37.59	118 54.08	2208	0.06	USGS
LCC	37 36.63	118 54.95	2550	-0.06	USGS
LLK	37 34.73	118 54.30	3030	-0.13	USGS
LMC	37 43.70	118 56.79	2540	0.34	USGS
MAT	37 52.40	119 52.00	1353	-0.51	USGS
MDW	37 37.88	118 54.97	2350	0.11	USGS
MGN	37 48.80	118 41.73	2472	0.16	UNR
MLK	37 39.84	118 58.50	2670	0.18	USGS
MMP	37 36.60	119 1.68	2870	-0.15	USGS

Station	Latitude	Longitude	Elevation	Delay	Organization
MNP	37° 24.82	119° 43.51	975	-0.41	USGS
ORC	37 38.12	118 39.36	2301	-0.03	UNR
RCC	37 29.26	118 43.30	2804	-0.18	UNR
RSM	37 30.52	118 52.58	3670	-0.07	USGS
SCH	37 21.95	118 41.22	2365	-0.25	UNR
SHL	37 37.00	118 57.30	2530	-0.04	USGS
SKI	37 39.18	119 1.44	2660	0.07	USGS
TAC	37 37.90	118 57.90	2398	0.10	USGS
WMD	37 26.61	118 38.22	1683	-0.30	UNR
YMC	37 37.52	118 56.16	2340	0.06	USGS

Prior to May, 1982, three seismic stations (LMC, CLK and ORC; Fig. 1a) were operating in the LVC area on a permanent basis. The data from these stations were telemetered to the University of Nevada at Reno (UNR) and then to the USGS in Menlo Park. During the period from May 7 to August 5, 1982, 5 new seismic station (SHL, MLK, EMH, CHS, LCC) were installed around the seismically active south moat area of the caldera (Fig. 1b). During the January, 1983 seismic swarm (Savage and Cockerham, 1984; this volume) a sixth caldera station, DOE, was installed. In August, 1983, 7 additional caldera stations (BNY, CSW, CEN, MDW, GRP, YMC, CVM) were installed in the south moat in order to concentrate coverage directly above the area of most intense seismic activity. In addition, three stations were installed to monitor the Mammoth Mountain area and possible Inyo Dome seismicity (MMP, SKI, DMP) and three stations were installed for more complete areal coverage (Fig. 1b) within the Sierran block (RSM and LLK) and the eastern caldera area (CSR). This dense local network is supplemented at the regional level by 7 seismic stations operated by UNR (SCH, CAS, ORC, MGN, RCC, WMD, BEN; Fig. 1a) and two USGS seismic stations on the western side of the Sierra Nevada Mountains (MNP and MAT; Fig. 1a).

CRUSTAL MODEL

Eaton [1966] derived a crustal model for the Mono Lake - Owen Valley region from seismic refraction data. This model was refined for shallow depth in LVC by Hill [1976]. The crustal model (Table 2) has been derived by a

TABLE 2. P-wave velocity model used in this study. Vp is the P-wave velocity in km/s and Z is the depth in km to the top of the layer.

Vp	Z
3.55	0.0
3.57	0.5
3.72	1.0
5.35	2.0
5.67	3.0
5.90	5.0
6.02	7.0
6.07	10.0
6.13	14.0
6.19	18.0
6.67	30.0
8.00	50.0

full inversion (computer program VELEST) of P-wave arrival times from 800 local earthquakes using a procedure written by Roecker and Ellsworth [1978] following the method of Aki and Lee [1976]. The starting model was a combination of the Hill and Eaton models. Initially two models were determined, one for inside LVC and the other for the Sierran block. The principle differences between the two models are the station corrections and the layer boundaries in the uppermost 3 km of the crust. The final crustal model is a combination of the LVC and Sierran models with layer boundaries at

appropriate depths to match drillhole data [Sorey et al., 1978] and seismic refraction data [Hill, 1976; Hill, et al., 1984, volume]. The accuracy of hypocentral locations using our model and station corrections can be tested by comparing calculated refraction shot locations with the actual location (Fig. 3). Where we have good seismic station coverage around the shot point the difference in calculated and actual shot location is 0.5 km or less both vertically and horizontally (shots S2, S3, S4, S5, S6, S9 in Fig. 3). The solutions S1 and S8 are also to within 0.5 km even with relatively poor station coverage around the shot-point. Stations MNP and MAT on the western side of the Sierra Nevada Mountains recorded shot S1 well which helps constrain the solution for this shot-point. Shot-points S7 and S10 like S11 are just outside the local network and were not recorded by regional stations, and they have a different near-surface structure (0-500m) than the other shot points. Both factors contribute to the larger difference ($\geq$ 1 km) between the calculated and actual location of these shot-points. Furthermore, the crust beneath shot-points S1 and S8, which are very near earthquake source areas in the south moat (Fig. 2) is well sampled by ray-paths in the P-wave inversion procedure. The crust beneath S7, S10 and S11, however, is poorly sampled by ray-paths due to the lack of sources and stations. Thus the underlying crustal structure is poorly known.

SELECTION OF DATA SET

The telemetered analog data are passed through a real time processor (RTP; Allen, 1982), which produces phase data for each earthquake it detects. From May 27, 1982 through October 1982 most of the phase data were read from 16 mm film or paper records obtained from magnetic tape. Beginning on November 1, 1982 the phase data supplied by the RTP constituted the primary data set. Of

these data, only the phase data from the 18 stations recorded on 16 mm film are routinely checked for timing errors. We have also checked the phase data on all of the stations for selected earthquakes by comparing RTP P-wave arrival times with those timed from tape playback records. Hypocenters and magnitudes from coda durations [Lee et al., 1972] for all earthquakes in this study were determined using computer program HYPO71 [Lee and Lahr, 1975].

EARTHQUAKE DISTRIBUTION

In this section we discuss the spatial and temporal seismic patterns for 1982 (June 1 - December 31), 1983, and 1984 (January 1 - July 31). For the period May 1980 through May 1982 (Fig 4a) only earthquakes of $M \geq 3.0$ where routinely located by the USGS in Menlo Park. The USGS began daily location of earthquakes, $M \geq 1.0$ in the LVC and of $M \geq 1.5$ in the Sierran block on May 26, 1982.

In all map-view figures of the LVC area the plotted caldera boundary represents the current topographic margin of LVC. This escarpment is mostly a result of slumping of the caldera wall after caldera collapse and subsequent erosion [Bailey et al., 1976]. The main boundary fault along which collapse took place probably lies 1 to 3 km inward from the topographic boundary [Bailey et al., 1976].

EPICENTRAL DISTRIBUTION

The overall seismicity pattern (Fig. 2) is comprised of:

1) a prominent west-northwest striking zone of earthquakes in the south moat area of LVC,

2) A broad zone of sub-parellel north-northeast striking zones of epicenters in the Sierran block, south of LVC, and

3) a diffuse scattering of epicenter clusters west and east of the south moat epicentral zone, and east of the main Sierran block seismic activity.

Figure 4 shows seismicity patterns for the time intervals May 1980 through May 1982 (4a), June 1982 through December 1982 (4b), 1983 (4c) and January through July 1984 (4d).

1980 - 1982a (Fig. 4a):

During this period earthquakes of M 1.5 to 2.0 and greater were routinely located by the University of Nevada, Reno. (Flori Ryall, unpublished data, pers. commn.). The U.S. Geological Survey routinely located only M3+ earthquakes in the LVC area. Even though the station coverage was sparse (as discussed earlier) the seismicity pattern appears similar to those in subsequent years (Figs. 4b, 4c and 4d) when station density and distribution provides better hypocentral control.

1982b (June - December; Fig. 4b):

The increase in station coverage during the last 7 months of 1982 resulted in improved resolution of hypocenter locations and a more sharply focussed seismicity pattern.

In LVC the predominant pattern is clusters of epicenters scattered throughout the south moat of the caldera. Each cluster represents a swarm of earthquakes, spatially and temporarily independent from other clusters .

In contrast, the seismic activity south of LVC, within the Sierran block, is characterized by strings of sub-parallel, quasi-linear trends that strike to the north-northeast. Embedded within these linear zones of seismicity are clusters of earquakes, which, as in LVC, represent discrete swarms of activity.

1983 (Fig. 4c):

The dominant trend here is the west-northwest zone of epicenters in the south moat of LVC. This large cluster represents an intense earthquake swarm that began on January 6 and lasted through April, 1983. This swarm is discussed in Savage and Cockerham (1984; this volume) and Hill et al. [1984]. In the vicinity of Mammoth Mountain and the area northeast of Hwy 395, the pattern of seismic activity within the caldera for 1983 differs from that of 1982. Firstly, the area east of Highway 395 is seismically quiet compared with 1982; the areas that had swarm (cluster) activity in 1982 lacked seismic activity in 1983. Secondly, the seismically active area near Mammoth Mountain (southwestern part of LVC) moved from the southwestern flank to the northeastern flank of Mammoth Mountain. Even though seismic stations MMP and SKI were not operational until late 1983, stations SHL and MLK, (Fig. 1b) and western Sierra Nevada foothills stations MNP and MAT (Fig. 1a) provided good azimuthal control of the epicentral locations. MMP and SKI have mainly provided depth control for earthquakes occuring near Mammoth Mountain.

Within the Sierran block the epicentral pattern generally followed that of 1982 showing several sub-parallel zones striking north-northeast. Several distinct clusters in this pattern are noteworthy: the cluster at the southwest end of Convict Lake and the clusters southeast of Convict Lake.

1984 (Fig 4d):

The trends previously discussed persist in 1984 with two noteable differences. [The reader is reminded that we are comparing different lengths of time in these figures (7 months for Fig. 4b; 12 months for Fig. 4c; 6.5 months for Fig 4d)]. Comparing 1984 with 1982 and 1983 one observes another shift in seismic activity in the Mammoth Mountain area (southwestern part of LVC). In 1984 the seismic activity moved to the northwest and the southeast flanks of Mammoth Mountain; each cluster, again, representing a discrete swarm of earthquake spatially and temporarily.

The second major difference involves the seismic activity east of Highway 395. The first substantial earthquake activity in this area since 1982 was a swarm near Whitmore Hot Spring, which occurred on June 3, 1984.

Within the Sierran block the seismicity pattern remained similar to that of 1983.

HYPOCENTRAL DISTRIBUTION

To illustrate the hypocentral distribution of earthquakes we use a series of cross-sections (Figures 6, 7, and 8). Each cross-section is based on all hypocenters located within a 5 km wide box (Fig. 5). The hypocenters within a given box were then projected on to cross-sections as a function of viewing azimuth from 320° to 40° in 10° increments. From these cross-sections clear azimuthally-dependent trends emerge, particularly within the Sierran block. To conserve space we have selected cross-sections in the viewing directions of 340° (Fig. 6), 0° (Fig. 7), and 20° (Fig. 8). Also, we have used only the "best located" according to the following criteria:

- o magnitude $\geq$ 1.0
- o number of stations used in location $\geq$ 8
- o RMS of the traveltime residuals $\leq$ 0.15 s
- o GAP, largest azimuthal separation between azimuthally adjacent stations, $\leq$ 135
- o estimated horizontal and verticle errors of $\leq$ 3 km.

The events satisfying these criteria number approximately 8,000 events.

Long Valley Caldera:

Cross-sectional views of caldera seiemicity are shown in Figures 6, 7, and 8 (parts A and B in each figure). The dominant pattern within LVC is a "donut-like" structure with a radius for the "hole" of 3 to 4 km. (Figs. 6B, 7B, 8B). The overall shape of the donut changes little with viewing azimuth. The donut is composed of many individual clusters and "strings" of earthquakes, each representing a distinct seismic swarm. These individual clusters are generally elongated in a northwest-southeast or east-west direction [Savage and Cockerham, 1984]. The January 1983 swarm accounts for most of the outline of the donut (Savage and Cockerham, 1984; this volume). The 1982 and 1984 earthquakes concentrate within the western half of the donut with 1982 data hypocenters showing a tendacy to form clusters and "strings".

East of the donut is an example of a "string" of seismicity (Fig. 6a). This feature is composed of two swarms, the first and shallower occurred in September 1982 and the second and deeper in November 1982. Both swarms occurred approximately 1.2 km west of the Hot Creek swimming area, probably

along a intracaldera segment of the Hilton Creek fault. By comparing this feature in Fig. 6a with that in Fig. 8a, it appears that the structure along which these events occurred has a northwesterly strike.

Sierran block:

Cross-sectional views of the seismicity south of LVC are presented in Figures 6, 7, and 8 (parts C, D, and E). The Sierran block seismicity is dominated by 3 east dipping, north-northwest striking zones (Fig. 6C and 6D). When viewed in a north-northeasterly direction (Fig. 8C and 8D) these zones are not as sharply focused or linear as when viewed in a northwest direction. The western-most zone projects to the surface southwest of the Laurel-Convict fault (LCF; Fig. 5), the middle zone projects onto the LCF (Fig. 5), and the third zone projects onto a northwest-southeast striking line through Convict Lake. These three zones appear to define 3 planes that do not have seismic activity continuously over their entire surface but typically have clusters of events at varying depths along the planes.

In Figure 5 two or possibly three north-northeast to south-southwest striking trends are apparent. However, in cross-section these trends are only weakly apparent at best (Fig. 8D and 8E). There is some focusing of events into linear features when viewed in a northeast direction (Figs. 7E, 8D, and 8E) suggesting the interpretation of a nearly vertical north-northeast to southwest-southwest striking eastern boundary to the Sierran block seismicity.

To obtain an independent check on hypocentral location errors produced by HYPO71 and to evaluate the possible influence of such errors on the elongation of clusters (Fig. 2), we relocated all the events using program

HYPOINVERSE [Klein, 1984]. This program calculates an error ellipsoid of the horizontal and vertical errors for each hypocenter. The principal axes of the ellipsoid can then be plotted in map view and in cross-section. The results showed no preferential alignment of the largest error axis (typically of $\pm$ 2 km) in a northwesterly direction. However, there is a small, but, clear alignment of the largest error axis in a northeastly direction; particulary for the southernmost clusters in Figure 5, box E. This suggests that north-northeasterly trends present in the epicenter plots may to some degree be a result of preferential alignment along the direction of least control.

To investigate further the significance of the north-northeast epicentral trench is evident in map view and the north-northwest trends observed in the cross-section we made stero plots of the hypocentral data (Fig. 9). The north-northwest striking, northeast dipping planes are clearly observed in Figs. 9E and 9D. When view in north-northeast or south-southwest directions the spatial extent of seismic activity along the planes is observed, but the alignment of clusters is not clearly observed. Thus, the stero plots suggest that the north-northeast lineation of epicenter are a two-dimensional illusion of a three-dimensional distribution.

Ryall and Ryall (1981), Cramer and Toppozada (1980) and Cramer and Toppazada (1980), Ryall and Ryall (1981), Given et al., (1982) have presented focal mechanism solutions for three of the M ~ 6 events in May 1980 suggesting left-lateral strike-slip on NNE striking planes. Vetter and Ryall (1983) showed 33 new focal mechanism solutions for earthquakes of $3.0 < M < 6.0$ in the LVC area; many of which also suggest left-lateral strike-slip on NNE striking planes. Our observations reported here appear to be at odds with the focal mechanism results. Vetter and Ryall (1983) however, show focal

mechanism for 9 events (their numbers 8, 14, 17, 19, 21, 22, 29, 32, 33 in Figs. 3 and 4) within the Sierra block that have 1 nodal plane with a dip and strike approximately coincident with the trends shown in the Figure 9c.

Finally, the epicenters within the Sierran block correspond very closely with the mapped area of the Mt. Morrison roof pendant [Rinehart and Ross, 1964]. The predominant strike of the strata comprising the roof pendant is northwest to north-northwest with vertical to nearly vertical dips. Mayo [1937], in a joint system study of the Sierra Nevada, found steeply-dipping joints with strikes of north-northeast to northeast within the Sierra block south of LVC. Rinehart and Ross [1964] also mapped similar joint patterns within the granitic rocks surrounding and intruding the Mt. Morrison roof pendant. A possible explanation of the apparent discrepency between the north-northeast epicenter lineations in map view and the north-northwest trends evident in cross-section and stereo plots is that the hypocenters are controlled by the intersection of the joint systems and the north-northwest striking stratagraphic boundaries in the Paleozoic roof pendant.

In summary, we suggest that the north-northeast striking epicenter lineations apparent in map view are actually two-dimensional projections of hypocenters distributed along north-northwest striking planes which dip to the northeast. Some but not all focal mechanism data support our findings, however, most focal mechanism solutions for Sierran block earthquakes are not well constrained. This is due primarily to lack of adequate azimuthal station coverage (refer to Fig. 1), particularly for the upper part of the focal sphere.

REFERENCES

Aki, K. and Lee, W. H. K., Determination of three-dimensional velocity anomalies under a seismic array using first P arrival times from local earthquakes, I, A homogeneous initial model, J. Geophys. Res., 81, 4381-4399, 1976.

Allen, R., Automatic Phase Pickers: their present use and future prospects, Bull. Seis. Soc. Amer., 72 (b), 5225-5242, 1982

Bailey, R. A., G. B. Dalrymple and M. A. Lanphere, Volcanism, structures and geochronology of Long Valley caldera, Mono County, California, J. Geophys. Res., 81, 725-744, 1976.

Cramer, C. H. and T. R. Toppozada, A seismological study of the May, 1980, and earlier earthquake activity near Mammoth Lakes, California, in, Sherburne, R. W., ed., Mammoth Lakes, California earthquakes of May 1980, Calif. Div. Mines and Geol., Spec. Rept. 150, 91-130, 1980.

Eaton, J. P., Crustal structure in northern and central California from seismic evidence, Calif. Div. Mines Geol. Bull. 190, 419-426, 1966.

Eaton, J. P., Frequency response of the USGS short period telemetered seismic system and its suitability for network studies of local earthquakes, U.S. Geological Survey Open-File Report 77-844, 45 p., 1977.

Given, J. W., T. C. Wallace, and H. Kanamori, Teleseismic analysis of the 1980 Mommoth Lakes earthquake sequence, Bull. Seis. Soc. Amer., 72 (4), 1093-1109, 1982.

Hill, D. P., Structure of the Long Valley caldera, California, from a seismic refraction experiment, J. Geophys. Res., 81, 745-753, 1976.

Hill, D. P., R. E. Wallace and R. S. Cockerham, Review of evidence on the potential for major earthquakes and volcanism in the Long Valley-Mono craters-White mountains regions of eastern California, Earthquake Prediction Research, in press, 1984.

Hill, D. P., E. Kissling, J. H. Luetgert, and U. Kradolfer, Constraints on the upper crustal structure of the Long Valley-Mono crater volcanic complex, eastern California, from seismic refraction measurements, this volume.

Kerr, R. A., Volcanic hazard alert issued for California, Science, 216, 1302-1303, 1982.

Kissling, E., W. L. Ellsworth and R. S. Cockerham, Three-dimensional structure of the Long Valley caldera, California, region by geotomography, this volume, 1984.

Klein, F. W., User's guide to HYPOINVERSE, a program for VAX and PC350 computers to solve for earthquake locations, U.S. Geol. Survey Open -File Report. in preparation 1984.

Lee, W. H. K. and J. C. Lahr, HYP071 (Revised): a computer program for determining hypocenter, magnitude, and first motion pattern of local earthquakes, U.S. Geol. Survey Open-File Rept. 75-311, 114 p., 1975.

Lee, W. H. K., R. E. Bennett, and K. L. Meagher, A method of estimating magnitude of local earthquakes from signal duration, U.S. Geol. Survey Open-File Report, 28 p., 1972.

Mayo, E. B., Sierra Nevada pluton and crustal movement, Jour. Geology, 45, 169-192, 1937.

Miller, C. Dan, D. R. Mullineaux, D. R. Crandell, and R. A. Bailey, Potential hazards from future volcanic eruptions in the Long Valley-Mono Lake area, east-central California and southwest Nevada - a preliminary assessment, U.S. Geological Survey Circular 877, 10 p., 1982.

Pitt, A. M. and D. W. Steeples, Microearthquakes in the Mono Lake - northern Owens Valley, California, region from September 28 to October 18, 1970, Bull. Seis. Soc. Amer., 65(4), 835-844, 1975.

Rinehart, C. D. and D. C. Ross, Geology and mineral deposits of the Mount Morrison Quadrangle Sierra Nevada, California, U.S. Geol. Survey Prof. Paper 385, 106 p., 1964.

Roecker, S. and Ellsworth, W. L., VELEST, Fortran Program, U.S. Geol. Survey, Menlo Park, CA, 1978.

Ryall, A. and F. Ryall, Spatial-temporal variations in seismicity preceeding the May 1980, Mammoth Lakes, California, Earthquakes, Bull. Seism. Soc. Amer., 71(3), 747-760, 1981.

Ryall, A. and F. Ryall, Spasmodic tremor and possible magma injection in Long Valley caldera, eastern California, Science, 219, 1432-1433, 1983.

Savage, J. C. and M. M. Clark, Magmatic resurgence in Long Valley caldera, California: possible cause of 1980 Mammoth Lakes earthquakes, Science, 217, 531-533, 1982.

Savage, J. C. and R. S. Cockerham, Earthquake swarm in Long Valley Caldera, California, January 1983: Evidence for dike inflation, Jour. Geophys. Res., 89(B10), 8315-8324, 1984.

Steeples, D. W. and A. M. Pitt, Microearthquakes in and near Long Valley, California, Jour. Geophys. Res., 81(5), 841-847, 1976.

Uhrhammer, R. A. and R. W. Ferguson, The 1980 Mammoth Lakes Earthquakes Sequence, in, Sherburne, R. W., ed., Mammoth Lakes, California Earthquake of May 1980, Calif. Div. Mines Geol. Special Rept. 150, 131-136, 1980.

Vetter, U. R., and A. S. Ryall, systematic change of focal mechanism with depth in the Western Great Basin, J. Geophys. Res., 88 (B10), 8237-8250, 1983.

-FIGURE CAPTIONS-

Figure 1. (a) Location of USGS and UNR seismic stations in the Long Valley caldera region and (b) details of seismic station locations relative to key geologic and cultural features within Long Valley caldera. UNR seismic stations are underlined (i.e., WMD). Outline of Long Valley caldera and prominent faults are shown by light lines and the principal highways by heavy lines.

Figure 2. Epicentral locations of approximately 13,000 earthquakes located by the USGS from June 1, 1982 through July 1984. Geologic and cultural features same as in Fig. 1.

Figure 3. Location of explosion sources (+) used by Hill et al. (this volume) and relocated explosion locations (O) station delays and crustal model in Tables 1 and 2. Stars are seismic station locations. Geologic and cultural features same as in Figure 1.

Figure 4. (a) Epicentral locations of earthquakes during May 1980 through May 1982, (b) June, 1982 through December 1982, (c) 1983, and (d) January 1984 through July 1984. Geologic and cultural features same as in Fig. 1.

Figure 5. Boxes used in selecting the earthquakes to be plotted in cross-section. Each box is 5 km in width and only earthquakes within a box are plotted in the respective cross-sections in Figures 6, 7 and 8. LCF is the Laurel-Convict fault [Rinehart and Ross, 1964].

Figure 6. Hypocentral distribution viewed in the direction of 340° (NNW). No vertical exaggeration. Boxes A through E correspond to those outlined in Figure 5.

Figure 7. Hypocentral distribution viewed in the direction of 0°. No vertical exaggeration. Boxes A through E correspond to those outlined in Fig. 5.

Figure 8. Hypocentral distribution viewed in the direction of 20° (NNE). No vertical exaggeration. Boxes A through E correspond to those outlined in Fig. 5.

Figure 9. Stereoscopic views of the Sierran block earthquake plotted in Fig. 5. The box is bounded by 37° 40' and 37' 26' N latutudes and 118° 57.23 and 118° 43.5' W longitude, between the surface and 15 km kepth with depth intervals of 5 km. A cube with 1 km long sides is shown for reference. (A) view from above, (B) view from the south at -7.5 km, (C) a view from the south-southeast at -3.0 km, (D) a view from the north-northwest at -3.0 km, (E) a view from the south-southwest at -3.0 km, (F) and (G) are views from the north-northeast at -3.0 km and 10 km, respectively.

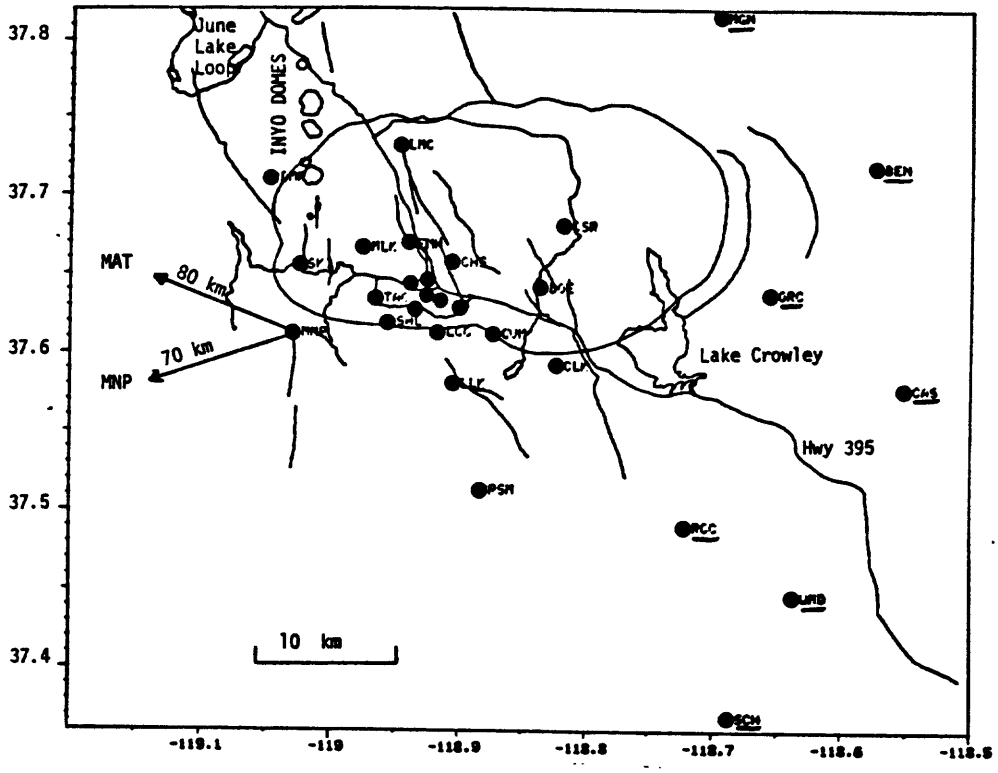
June Lake Loop
INYO DOMES
MAT
80 km
70 km
MNP
Lake Crowley
Hwy 395
10 km
37.8
37.7
37.6
37.5
37.4
-119.1
-119
-118.9
-118.8
-118.7
-118.6
-118.5

A

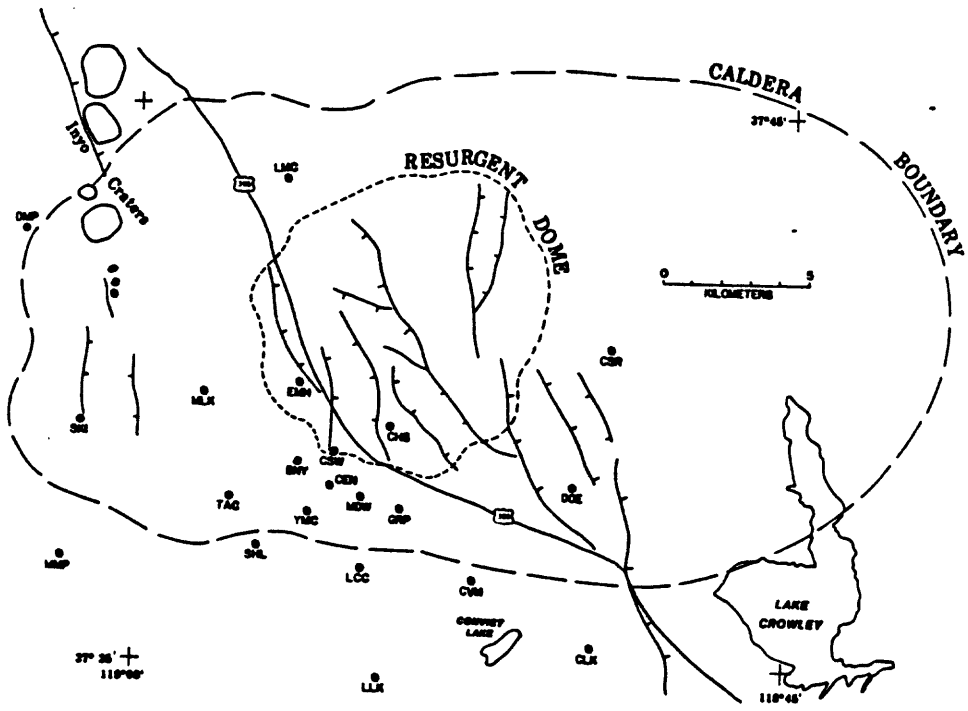
CALDERA
BOUNDARY
RESURGENT DOME
Inyo Craters
LAKE CROWLEY
KILOMETERS

B

FIGURE 1

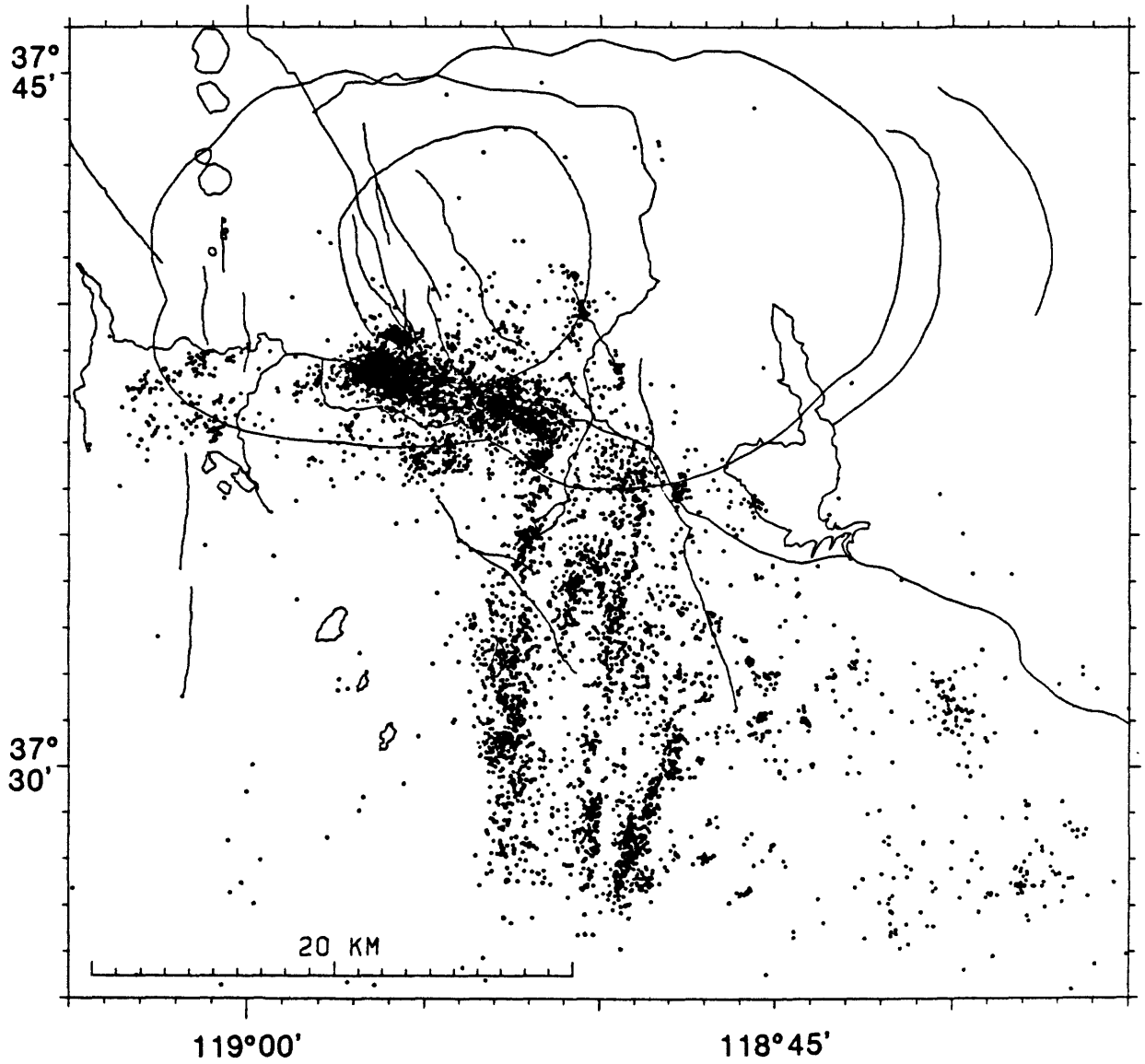

FIGURE 2

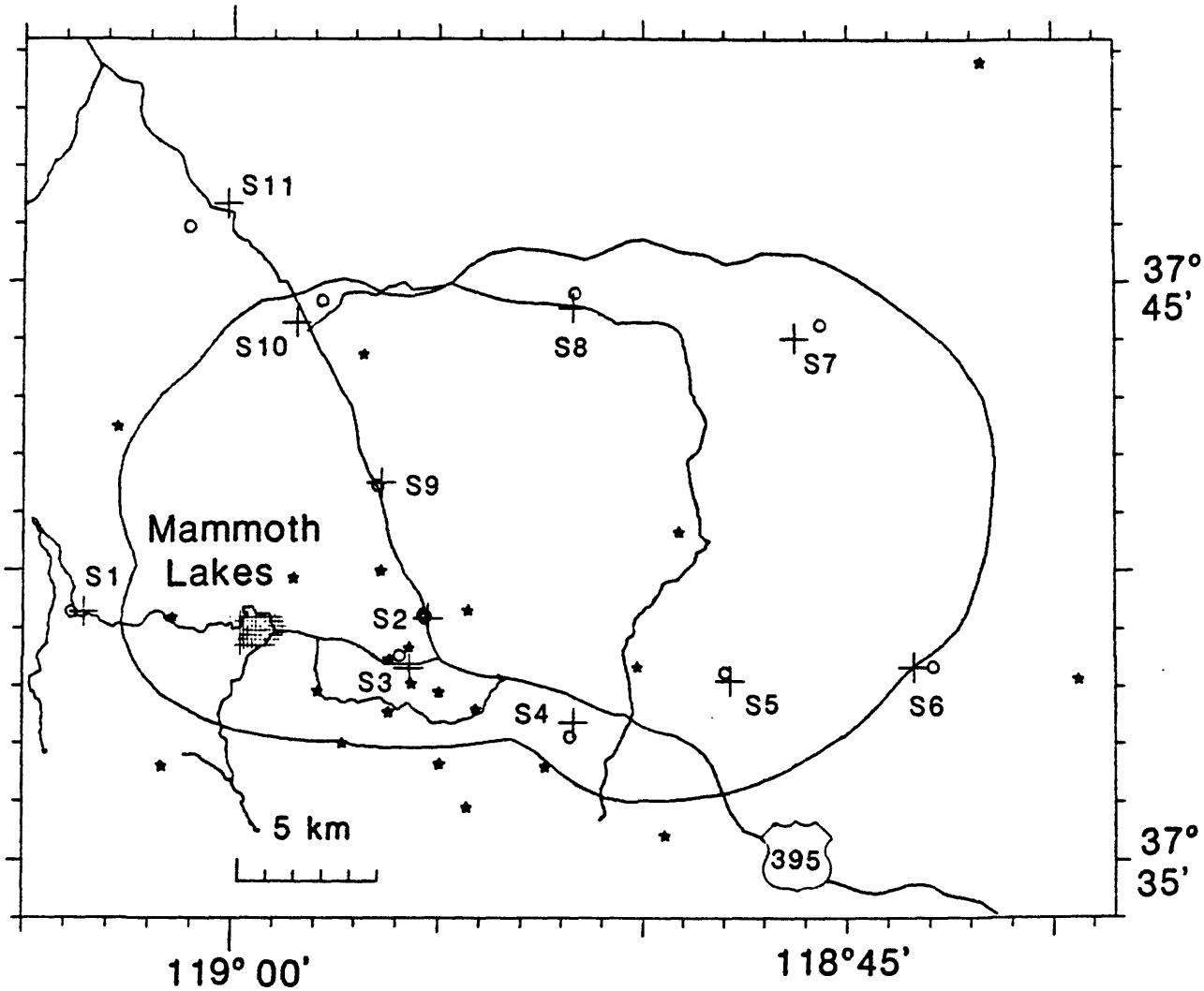
S11
S10
S8
S7
S9
Mammoth
Lakes
S1
S2
S3
S4
S5
S6
5 km
395
37°
45'
37°
35'
119° 00'
118°45'

FIGURE 3

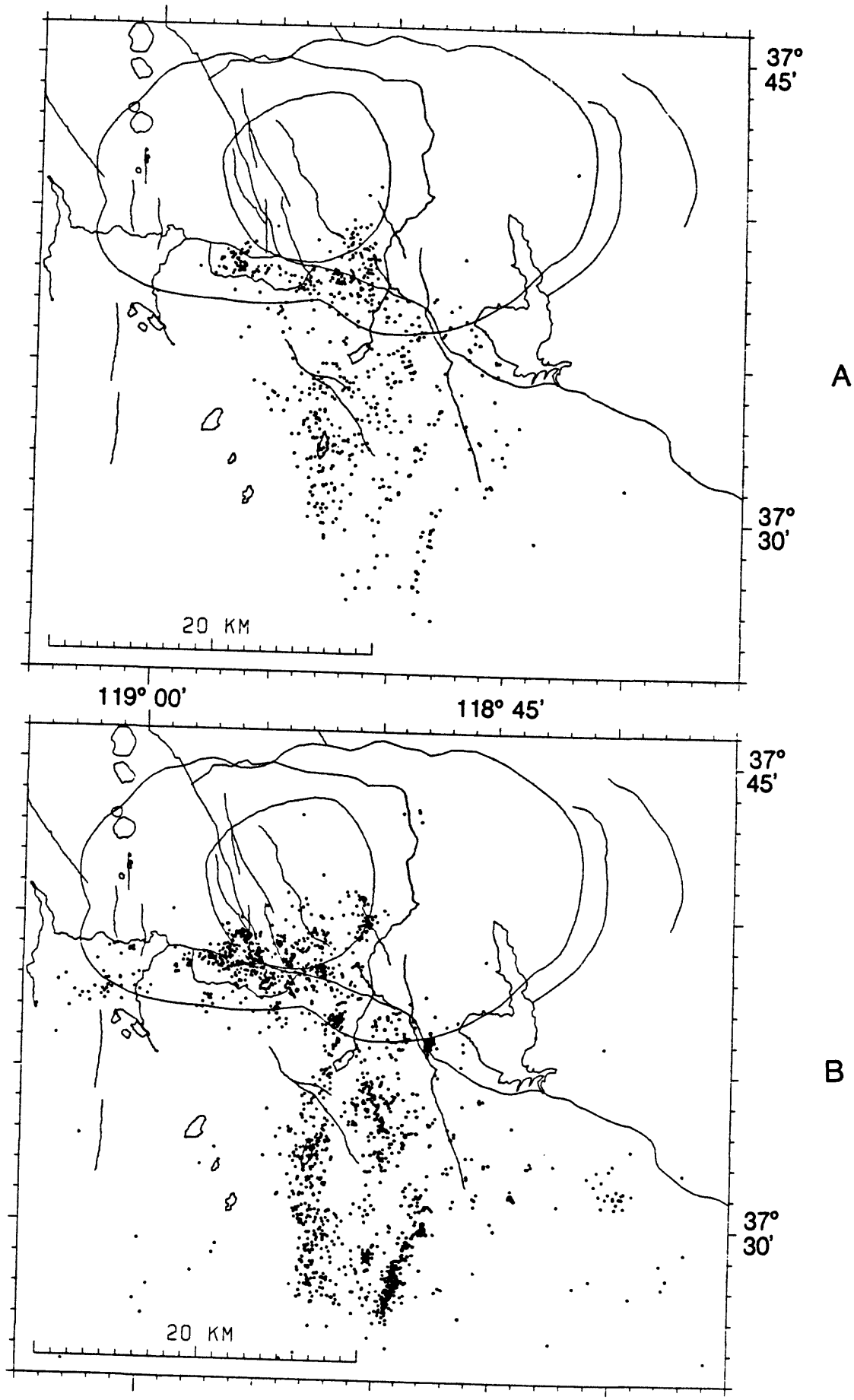

FIGURE 4

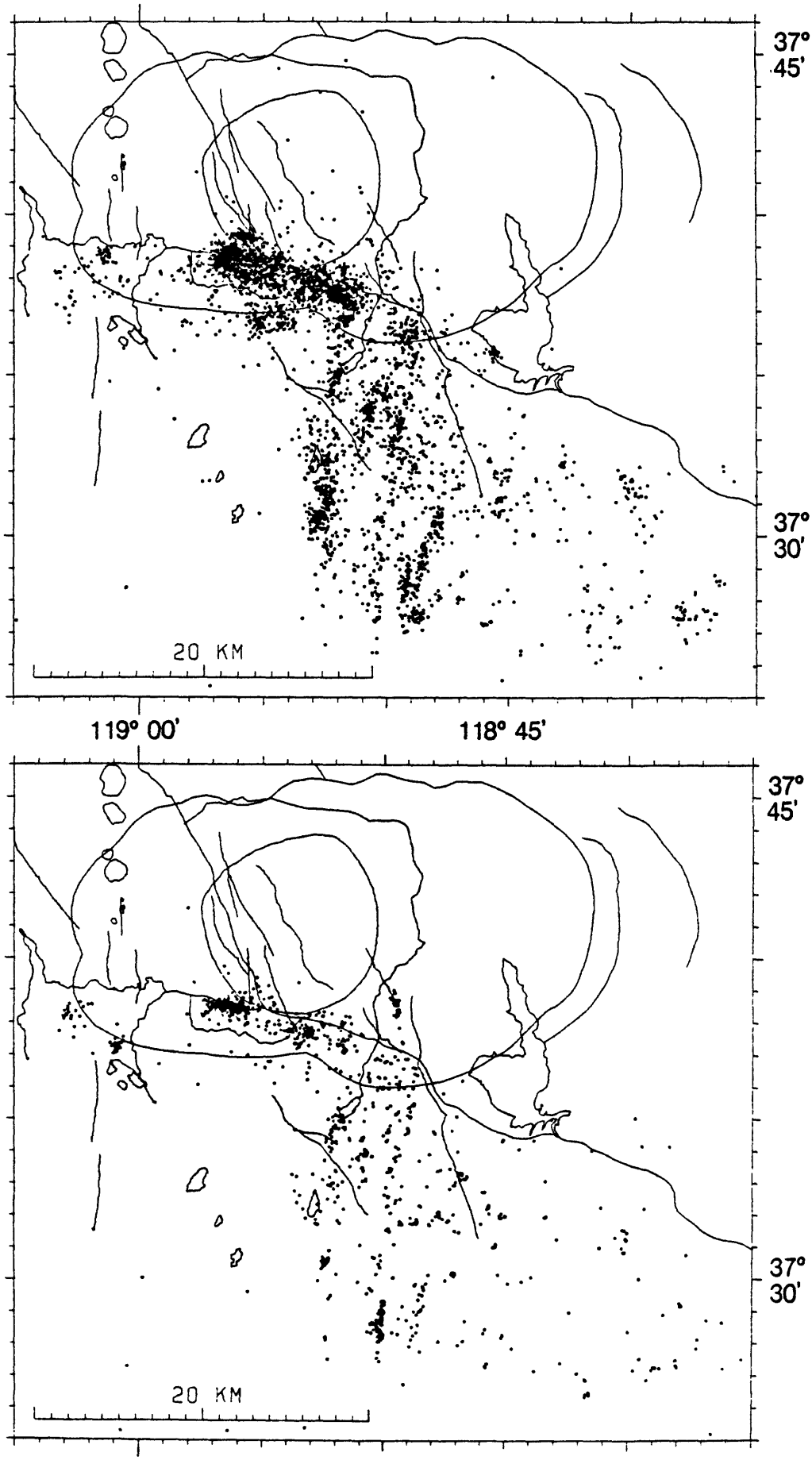

C

D

FIGURE 4

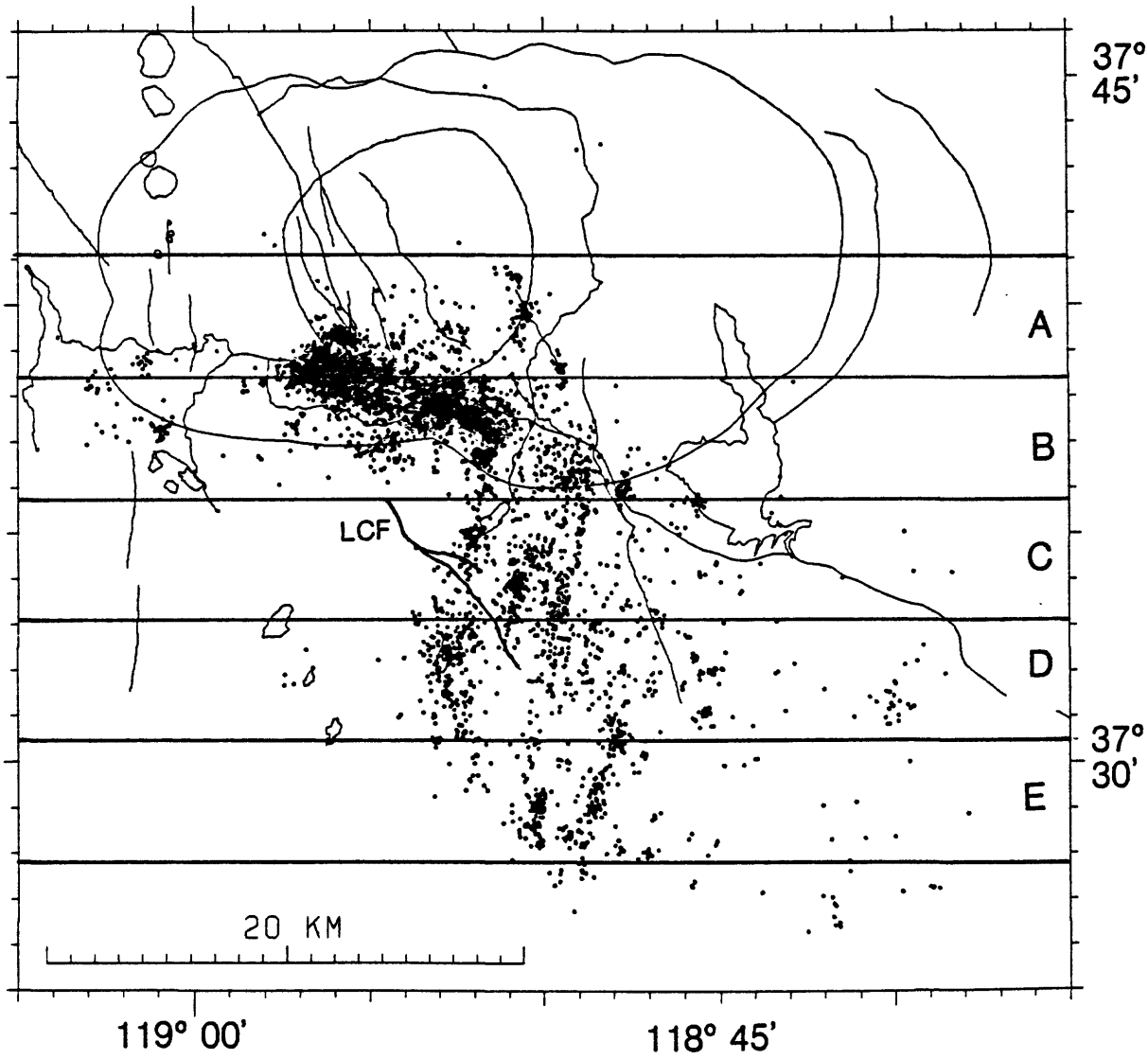

FIGURE 5

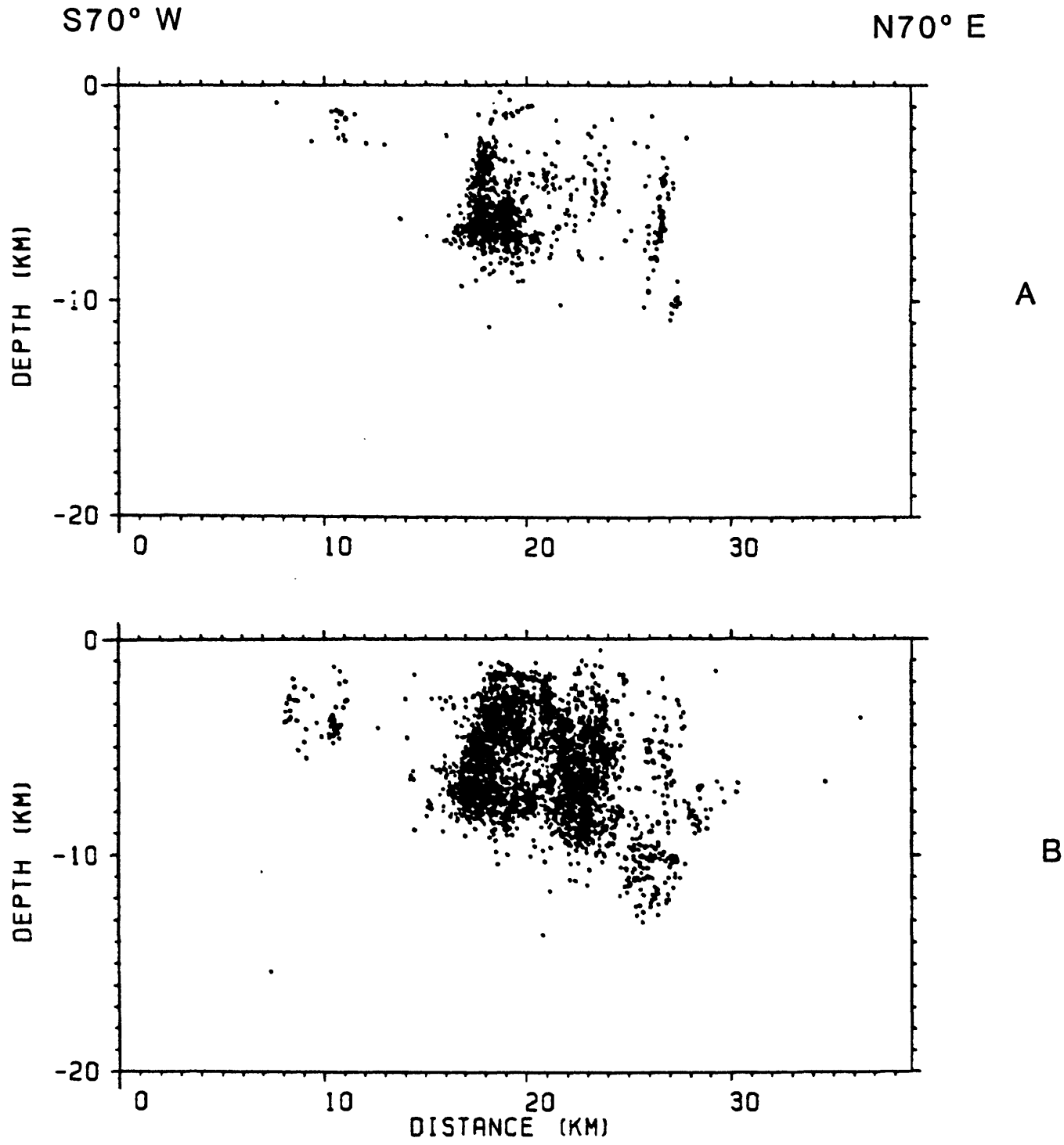
S70° W
N70° E
0
-10
-20
DEPTH (KM)
0
10
20
30
A
0
-10
-20
DEPTH (KM)
0
10
20
30
DISTANCE (KM)
B

FIGURE 6

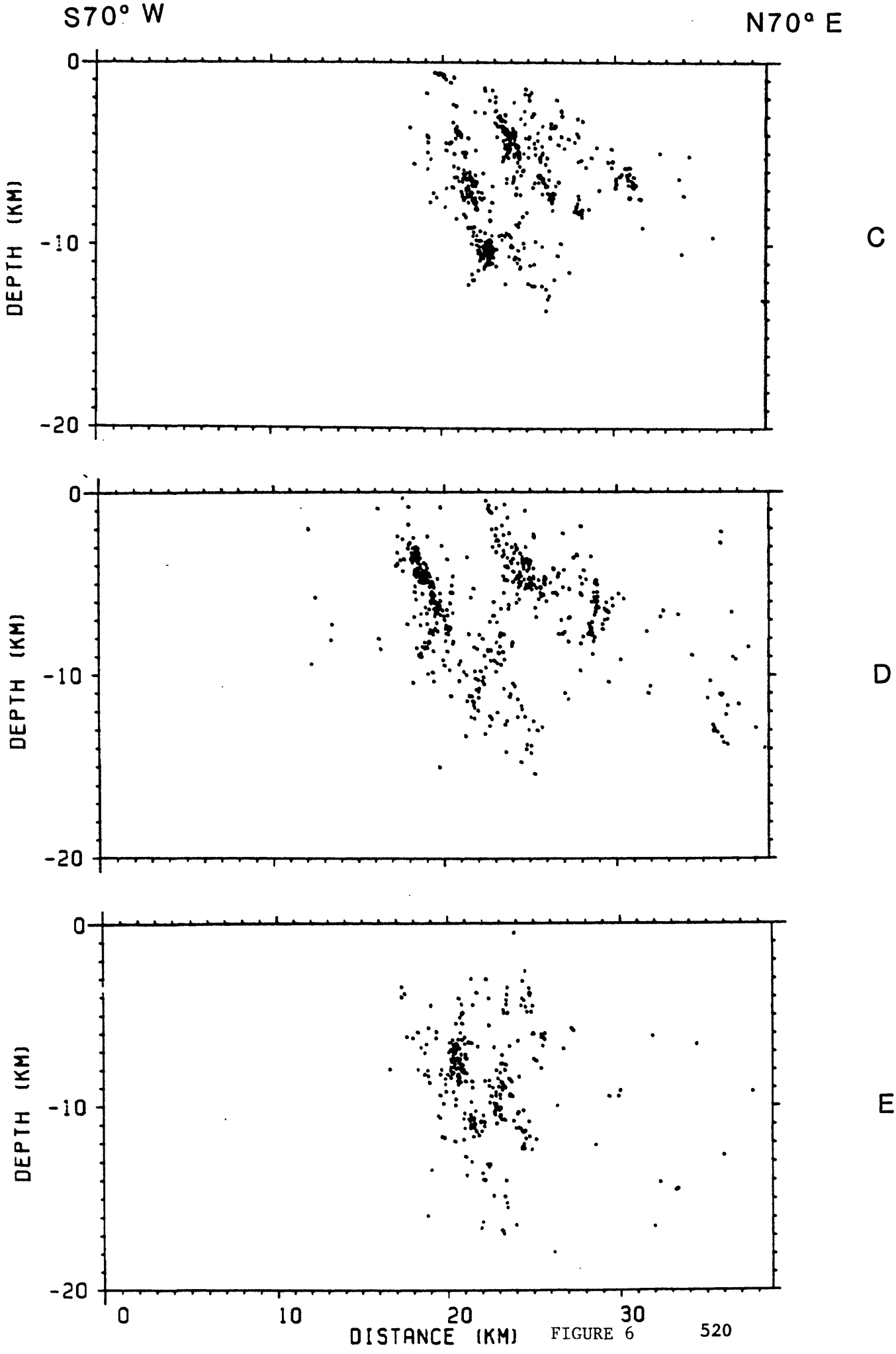

FIGURE 6

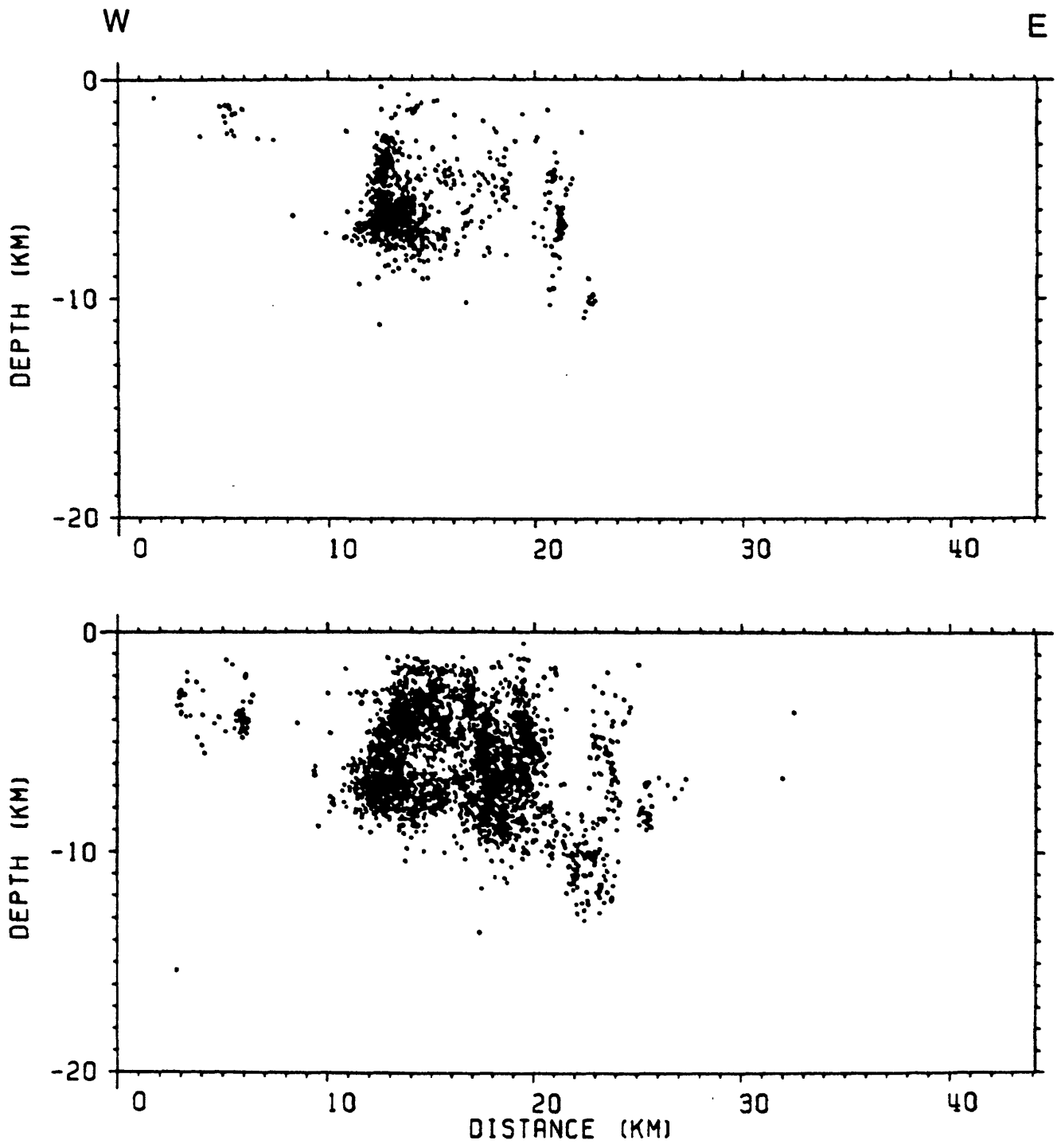

FIGURE 7

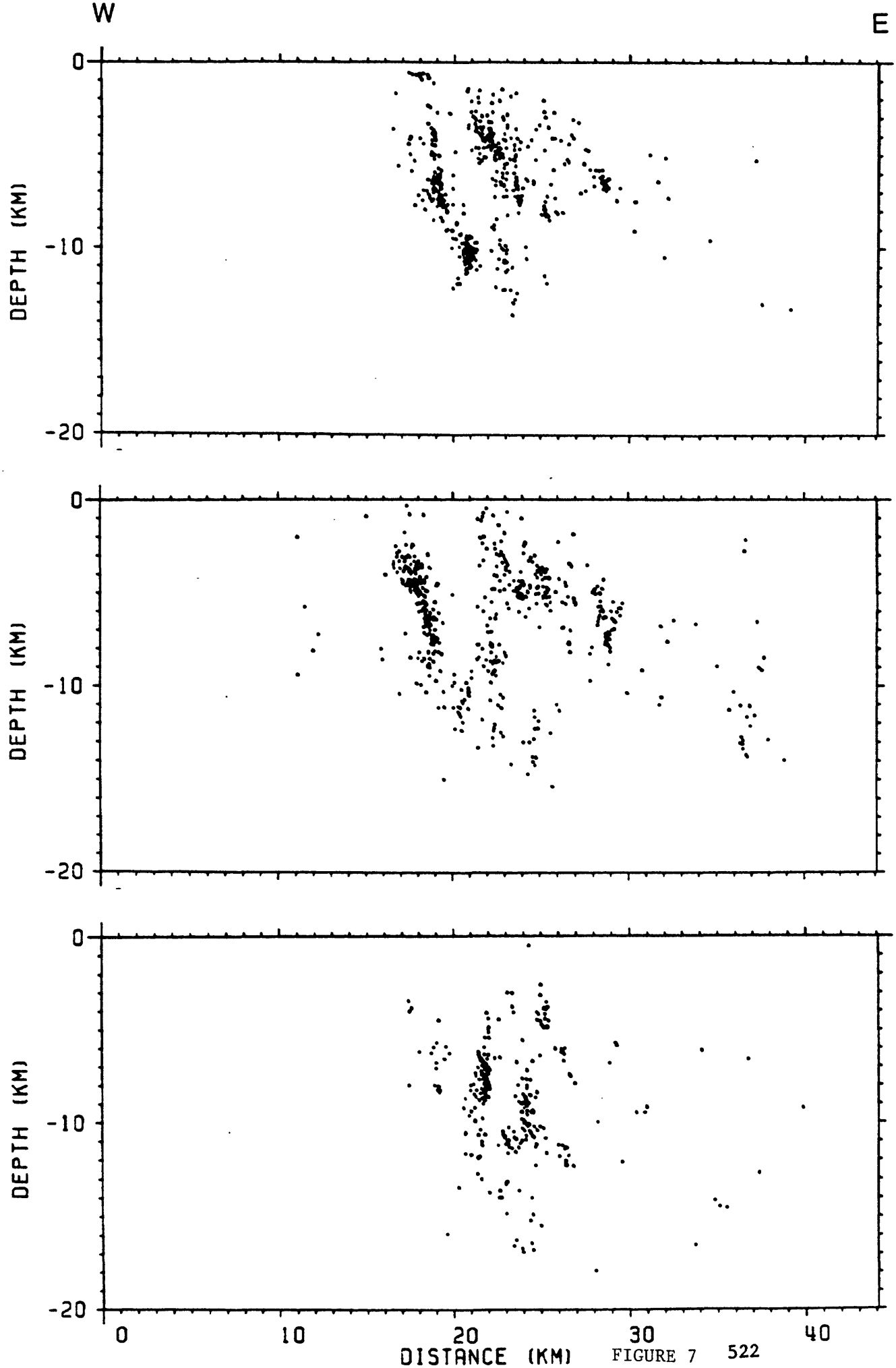
W
E
0
-10
-20
DEPTH (KM)
0
-10
-20
DEPTH (KM)
0
-10
-20
DEPTH (KM)
0
10
20
30
40
DISTANCE (KM)

FIGURE 7

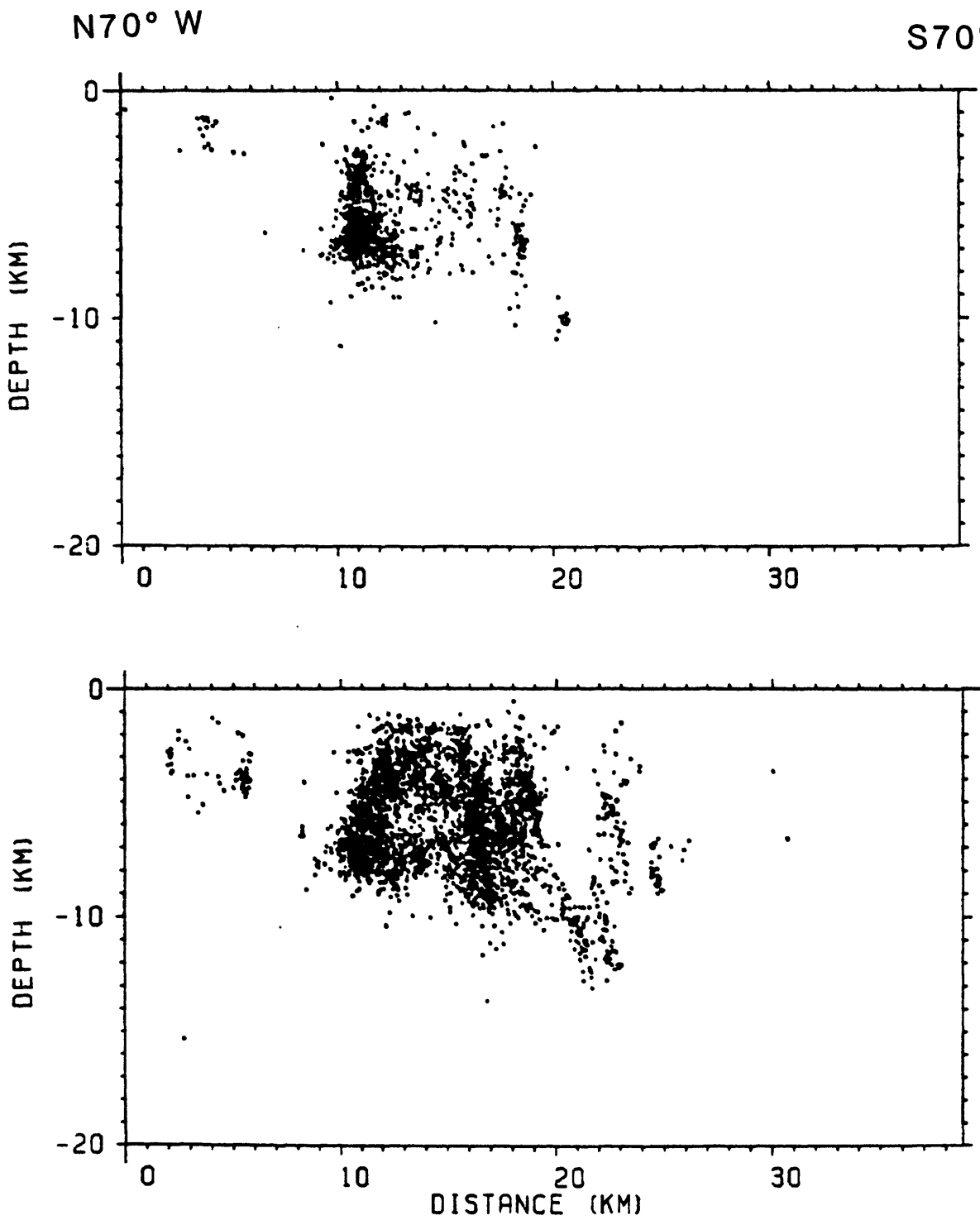

FIGURE 8

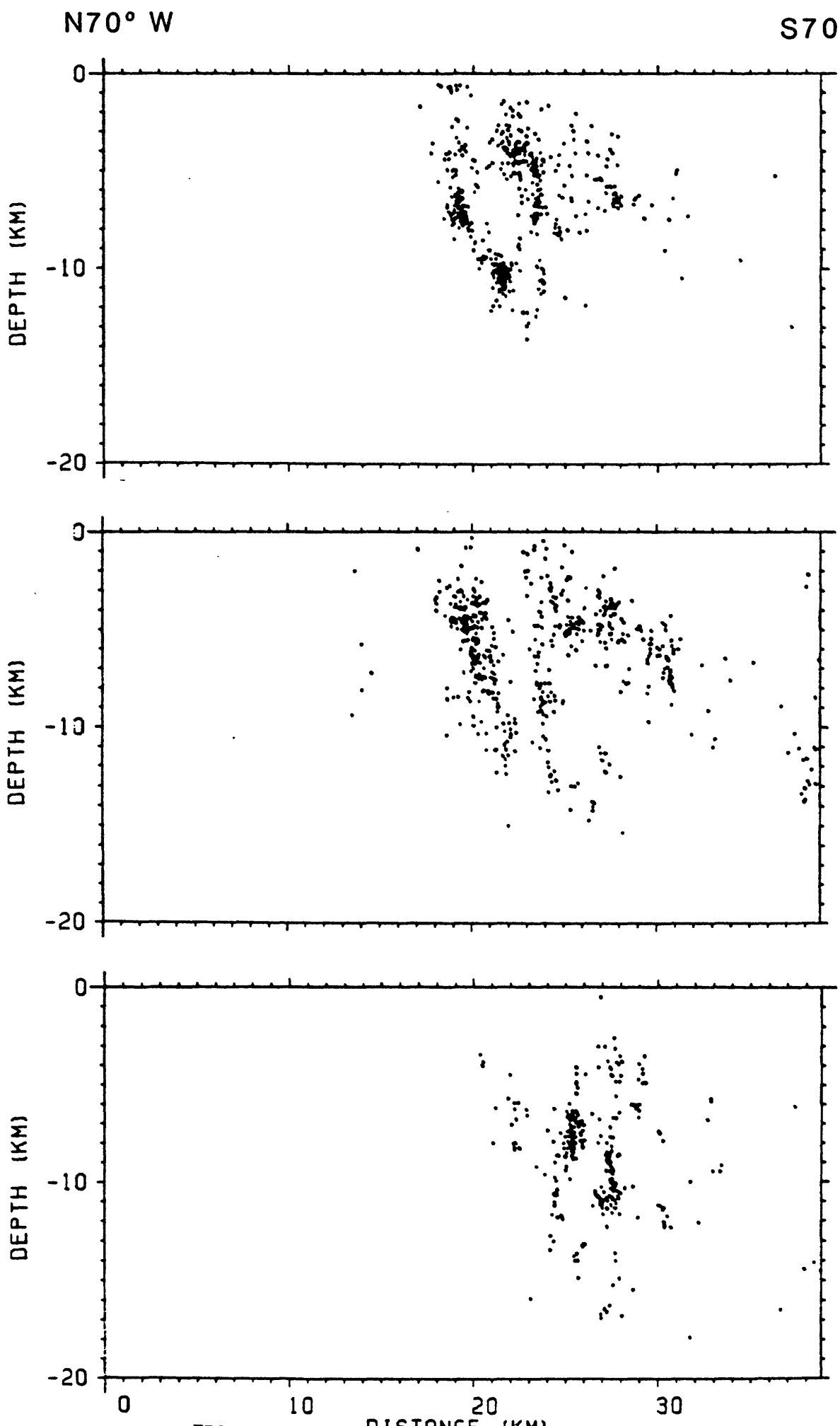
N70° W
S70°
0
-10
-20
DEPTH (KM)
0
-10
-20
DEPTH (KM)
0
-10
-20
DEPTH (KM)
0
10
20
30
DISTANCE (KM)

FIGURE 8

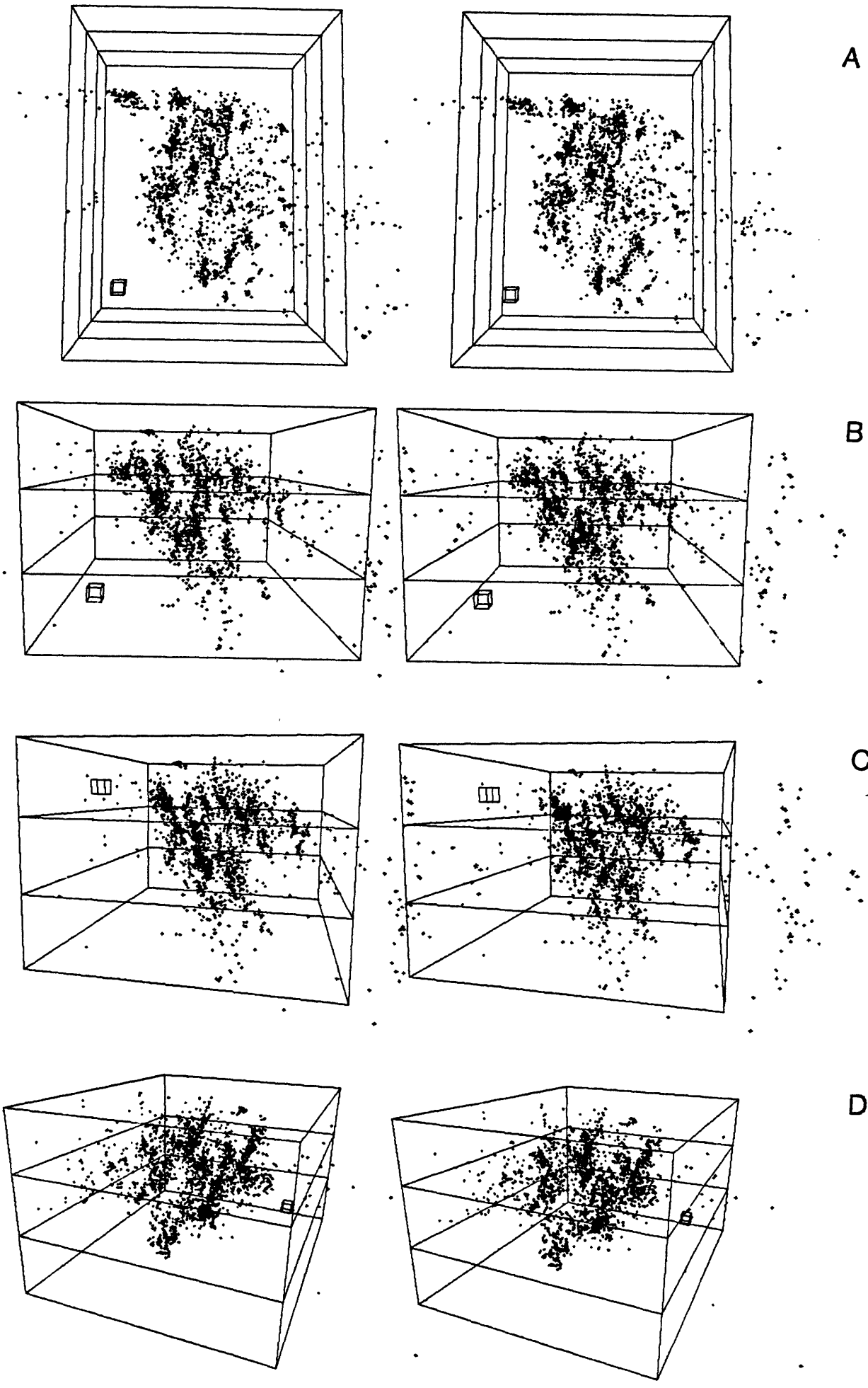

FIGURE 9

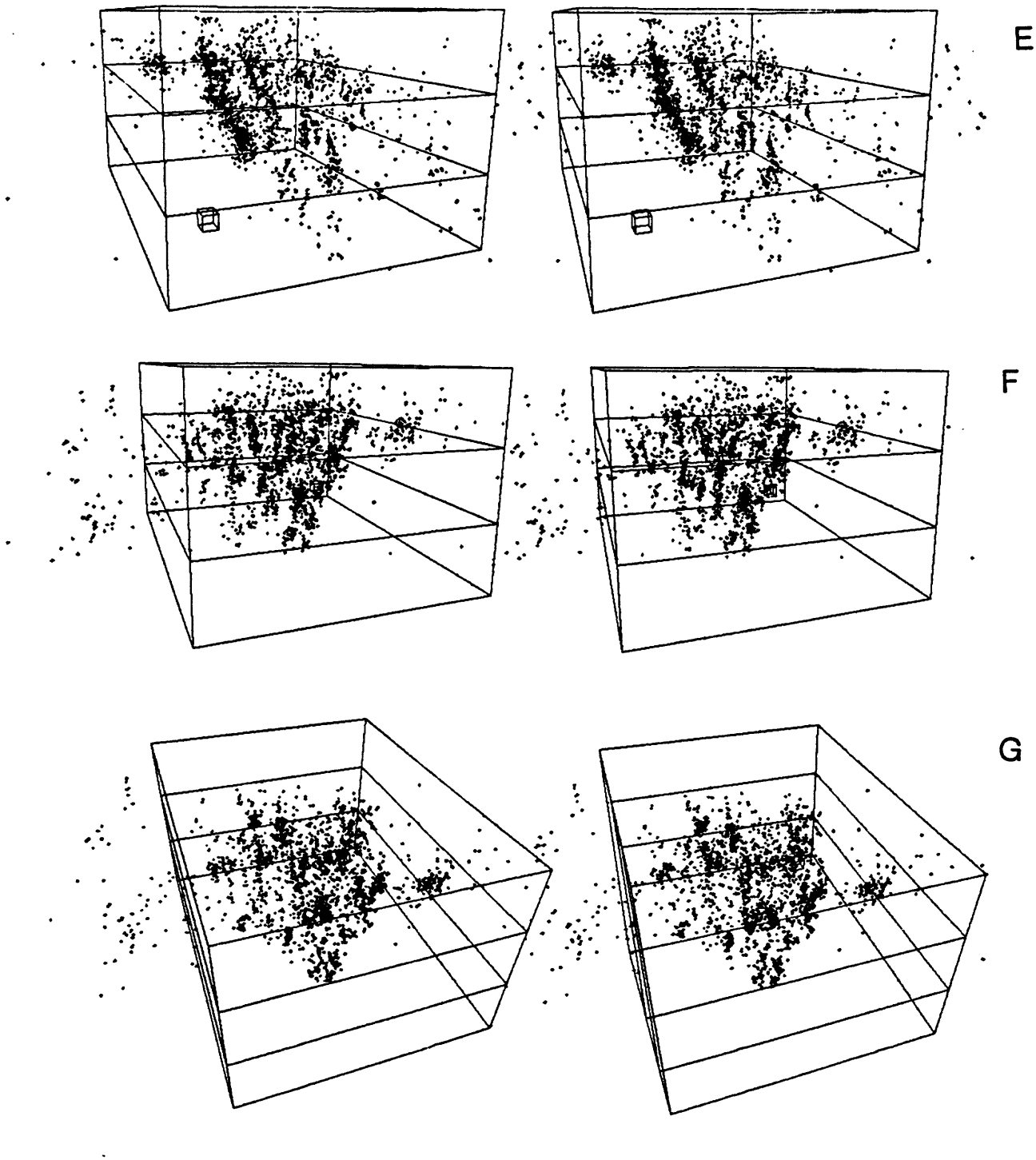

FIGURE 9

HIGH-RESOLUTION MICROSEISMICITY STUDY OF POSSIBLE MAGMATIC INTRUSION IN THE LONG VALLEY CALDERA

Albert T. Smith
Lawrence Livermore National Laboratory
P.O. Box 808
Livermore, California 94550

Abstract. During August 1982, a dense network of 14 seismic stations was deployed in the southwest moat of the Long Valley Caldera. Ten sites used three component seismometers, and all sites used digital event recorders sampling at 200 samples/s with an array trigger criterion to reject local noise and to ensure accurate relative timing. The network recorded microseismicity to magnitude zero, the USGS shots from Casa Diablo to Mono Lake and Adobe Hills, and small local shots to constrain the near surface velocity structure. Hypocenters, station corrections, and velocity structure were simultaneously determined using all this data. The analysis concentrated on a swarm of earthquakes which occurred during August 9, along a vertical plane which was tangent to the resurgent dome. The events occurred along a 0.5 km segment of the plane between depths of 2.5 to 3.5 km. Additional events occurred to depths of 9 km, but not directly beneath the swarm: the deeper events are located from 0.5 to 1.0 km from the swarm epicenters. The configuration suggests intrusion of magma or volatiles: the shallow swarm was above the intrusion; the deeper events occurred along the perimeter of the upwelling. Focal mechanisms of events within the swarm support this interpretation, and indicate that the tensional axis is perpendicular to the plane of seismicity.

Introduction

Since 1978, the vicinity of Mammoth Lakes in the Long Valley Caldera has been the site of both unusual seismicity and surface deformation. The region has a long history of volcanic activity ranging from recent explosive eruptions of rhyolite to a major caldera eruption about 700,000 years ago. Ryall and Ryall (1982) observed spasmodic tremors which they considered as indicative of magma movement. In addition, recent surface deformation has been modelled as uplift induced by inflation of a magma chamber beneath Long Valley (Savage and Clark, 1982). This evidence has prompted concern of a possible volcanic eruption and the issuance of a Volcano Watch by the U.S. Geological Survey during May 1982 (Miller et al., 1982).

The seismicity near Mammoth Lakes represents a unique opportunity to monitor magmatic intrusion with unprecendented resolution: precise locations of the earthquakes together with focal mechanisms and attenuation studies made possible by this high resolution may define the intrusion and its tectonic setting. To determine the feasibility of this approach, a network of 14 seismic stations was occupied during August 1982 near Mammoth Lakes, California. Preliminary analysis of the data collected suggests that the microearthquakes are associated with an intruding dike.

Experimental Details

To use microseismicity as a high-resolution probe of the tectonics and the state of stress requires a dense network of stations, accurate timing, and three-component data. During August 1982, a network of 14 seismic stations was occupied at the site of recent swarm activity reported by Ryall and Ryall (1982). Figure 1 illustrates the locations of the stations and the epicentral area. Each site was surveyed using a geodetic baseline established by Riley et al. (1982). Ten sites used three-component, 4.5 Hz or 2 Hz seismometers, and three sites used 4.5 Hz vertical seismometers deployed by Lawrence Berkeley Laboratory as part of their ASP system (Automatic Seismic Processor). A force-balanced accelerometer and a 1 Hz, L4-3D seismometer were also fielded at a central station in the network. All sites used Sprengnether DR-100 digital event recorders sampling at 200 samples s. To reduce spurious triggers and to ensure accurate relative timing between recorders, all digital event recorders were interconnected through an array trigger: three stations must declare an event within a one second window in order to trigger and record the event simultaneously at all stations in the network. Finally, smoked-drum recorders provided continuous monitoring of two widely spaced stations for quality control.

The network recorded natural microseismicity to magnitude zero, and USGS timed explosions from Casa Diablo to Mono Lake and east to Adobe Hills. To provide additional constraints on the near surface velocity structure, small shots were detonated at most of our seismic stations. The events were located using Roecker's (1982) simultaneous inversion for velocity structure, station corrections, and hypocenters. The initial velocity structure for the inversion used Hill's(1976) refraction profiles and was the USGS model for hypocenter location for this area. The data collection and interpretation strategy produced a significant improvement in hypocentral location compared to the USGS permanent network (R. Cockerham, personal communication, 1983).

Results

The preliminary analysis has concentrated on events associated with a minor swarm on August 9, 1982. The maximum USGS coda magnitude for these events was 1.5. Two USGS shots at the edge of the network on August 5, 1982, (SP 1 and 2) are used as velocity control. In addition, the local velocity structure was constrained with shots at 5 stations. Numerical experiments using different starting velocities and shot combinations suggest an absolute location error of 300 meters using the variation between the models; however, the relative hypocentral locations vary less than 100 meters.

The swarm on August 9 plotted in Figure 2 was located along a vertical plane centered at 118° 56.5' W, 37° 38.3' N, and tangential to the center of uplift observed over the resurgent dome by Savage and Clark (1982). The events occurred during a three hour period along a 0.5 km segment of the plane and between depths of 2.5 km and 3.5 km. No spatial progression in the occurrence of the events was apparent, but events still occurred on the plane ten days later (e.g. event 8). Additional earthquakes occurred to depths of 9 km, but not directly beneath the swarm: the deeper epicenters are located between 0.5 to 1.0 km from the swarm epicenters. Cross sections in Figure 3 suggest that the deeper events outline the vertical NW-SE, planar intrusion. The section perpendicular to A-A' indicates a gap in activity directly beneath the swarm. This pattern is analogous to one observed at Kilauea volcano which indicates intrusion of magma along a conduit outlined by seismicity (Ryan et al., 1981). In our case, the shallow swarm may occur above the planar intrusion where the deviatoric stresses are greatest; the deeper events are possibly induced along the perimeter of the upwelling by the outward pressure of the magma or volatiles. Geological field studies indicate that deformation of the host rock does occur adjacent to a sheet intrusion (Delaney and Pollard, 1982; Pollard et al., 1983).

The focal mechanism shown in Figure 4 is consistent with this interpretation. Magmatic injection may act as a wedge and produce extensional-shear failure. The minimal compressive or "tensional" stress axis will lie perpendicular to the plane of the dike (Pollard, 1973). This is observed in the focal mechanisms: the tensional axis is perpendicular to the plane of the seismicity, while the plane of seismicity does not coincide with a nodal plane. These observations are consistent with extensional or shear failure above an advancing sheet intrusion, rather than shear failure along a fault plane coinciding with the plane of seismicity.

Discussion

The recent horizontal and vertical deformation in Long Valley Caldera indicates inflation of the magma chamber and resulting changes in the stress field (Savage and Clark, 1982). The axisymmetic perturbations to the stress field from the inflation may control the preferred orientation of sheet intrusions in the form of cone-sheets (Anderson, 1936). At shallow depths above the magma chamber, the minimal compressive or "tension" stress is radial to the point of inflation; at deeper depths the radial stress is compressive (Anderson, 1936; Thatcher and Savage, 1982). This induced stress field represents a perturbation to the regional field. In the Long Valley region, focal mechanisms are characterized by NE-SW "tension" (Cramer and Toppozada, 1980). Stress measurements to the east suggest that the least principal horizontal stress lies near N60W (Zoback and Zoback, 1980). Our focal mechanism solutions indicate a tensional stress radial to the resurgent dome at N30E for shallow events. The implication is that inflation of the magma chamber and the resulting

strain determine the local stress regime and produce radial tension. If the existing regional stress field is "tensional" along NE-SW, the perturbation from inflation of the magma chamber would give a maximum "tensional" stress field at the observed location of the swarm and oriented NE-SW. The plane of the dike is normal to this least principal stress axis; consequently, its orientation is consistent with an opening crack (Pollard, 1973). The trend observed in the regional seismicity, however, lies more east-west than the plane of the swarm (R. Cockerham and D. Hill, personal communication, 1983). Hill's(1977) swarm model for en echelon faulting suggests the occurrence of a left-stepping en echelon dike complex as illustrated in Figure 5. The plane of seismicity reported here may represent one dike of an en echelon complex. This pattern would satisfy the essential elements of the seismicity: individual segments of seismicity are tangent to the center of uplift, while the broad trend of seismicity follows the left-stepping dikes and extends more nearly east-west. Seismicity would occur where the strain perturbation induced by the inflating magma chamber reinforces the regional strain field.

Upwelling magma along a cone-sheet could trigger the swarm at its apex and events along its perimeter, but a number of alternatives exist for the precise mechanism inducing the seismicity. The magma may act as a wedge creating high stresses at the apex of the dike. The mode of fracturing could be extensional, brittle or ductile shear failure (Pollard, 1973). The focal mechanisms presented here are consistent with shear failure and a double couple solution: however, extensional failure represented by a compensated linear-vector dipole may be an alternative (Julian, 1983). The magma may not be the actual fluid triggering the events: high pore pressure from volatiles is a likely alternative (Delaney, 1982). Events associated with the swarm extend over depths of one kilometer which suggests a highly mobile fluid inducing the events. One possibility would be magmatic intrusion into a water-saturated host rock which produces high pore pressures and fracturing. This could induce seismicity which both outlines and preceeds the intrusion. High pressure volatiles preceeding the magma would have significant implications for the evolution of the structure. Resolution of this question will require further analysis of existing data sets and additional deployments to monitor the evolution of the intrusion.

Summary

Microseismicity has given a high-resolution image of a zone of possible magmatic intrusion. The orientation and state of stress are consistent with inflation of the magma chamber beneath the Long Valley Caldera. Resulting strain concentrations could provide a path for intrusion of a cone-sheet perpendicular to the least principal stress. In addition, the overview of the seismicity given by the permanent network of the University of Reno, Nevada and the U.S. Geological Survey suggests that this dike lies at the northwestern tail of an en echelon fracture zone extending to S80E in concurrence with Hill's (1977)

model of swarm activity near Kilauea volcano. The mechanism triggering the events is consistent with intruding magma; however, the focal mechanisms are as yet unable to resolve extensional mechanisms from shear failure at the apex of the intrusion. Volatiles released by the magma or high pore pressures induced by intrusion into water-saturated rock may represent the mechanism inducing the seismicity.

Acknowledgement. The field deployment was only possible through the assistance of George Smith, EG&G, Las Vegas, and Calvin Broadwater, Robert Geil, and Don Watwood of LLNL. Kelley Look transferred the data to our computers. Jim Scheimer provided useful suggestions during the simultaneous inversions. Robert Cockerham kindly furnished the first motion data from the USGS seismic network. This work was performed under the auspices of the U.S. Department of Energy by the Lawrence Livermore National Laboratory under contract number W-7405-ENG-48.

Figure Captions

Figure 1:

Map of the Mammoth Lakes - Long Valley region in Eastern California showing the epicenters and seismic stations used in the microearthquake survey. The map covers a region approximately 9 km square and includes the principal highways and the town of Mammoth Lakes. The line extending east-west across the plot represents the southern boundary of the Long Valley Caldera.

Three component, digital stations are shown by squares. Single component, vertical stations installed by Lawrence Berkeley Laboratory are denoted by triangles. All these stations use 4.5 Hz seismometers except one which uses a 2 Hz seismometer. The central station in the network also includes a 1 Hz three-component seismometer and a forced-balanced accelerometer. The nearest University of Nevada, Reno and USGS stations used for the first motion studies are SHL, EMH, CHS, LCC, and MLK.

Epicenters of earthquakes used in the microseismicity survey are indicated by asterisks. A swarm on August 9 is apparent as a cluster of events near the center of the map. The box near the center indicates the region covered by Figure 2, while the depth sections in Figure 3 extend from A to A'.

Figure 2:

Expanded view of the swarm region on August 9, 1982. The map covers a 3 kilometer square as shown in Figure 1.

The epicenters are indicated by letters representing their order of occurrence: **A** through **Z**, **a** through **z**, and **0** to **9**. Events **h** through **r** occurred during a three hour period starting at 0500. These events define a segment of a vertical plane oriented from **A** to **A'**. The maximum coda magnitude for these events was 1.5.

Figure 3:

Depth sections from **A** to **A'** and perpendicular to **A-A'** in Figures 1 and 2. The hypocenters use the same symbols as Figure 2 and no exaggeration is used in the plots. The plot on the left shows a depth section along the trend of seismicity, **A** to **A'**. The swarm now appears between depths of 2.5 to 3.5 km, while deeper events may delineate a vertical sheet intrusion. Looking from **A'** to the NW along the trend of the swarm, the plot on the right indicates that the deeper events do not lie directly below the swarm, but outline the possible intrusion.

Figure 4:

Focal mechanism of event **k** within the swarm. First motions are plotted on a lower hemisphere where C indicates compression and D represents dilatation. The plot combines the digital stations and UNR/USGS stations. A double couple mechanism is plotted suggesting that the least compressive axis, T, is well constrained. A compensated linear

vector dipole would also give an azimuth of approximately N30E for the T axis. The shallow events **j**, **l**, **m**, and **p**, plus the deeper event **x**, are also consistent with this mechanism, although not as well constrained. The deeper event **6**, however, has a component of reverse slip.

Figure 5:

A cartoon after Hill (1977) and Pollard (1973) showing a map view of an en echelon dike structure which may explain the swarm activity near Mammoth Lakes. A series of left stepping dikes would allow a more northernly orientation of individual dikes relative to the east-west trend in seismicity observed by the USGS (Cockerham and Hill, personal communication, 1983). The August 9 swarm represents activity on just one dike structure, while activity on the other dikes and strike-slip offsets may account for the more east-west trend of seismicity. The permanent UNR/USGS network is unable to resolve the activity on individual dikes, but instead outlines a diffuse N80W trend.

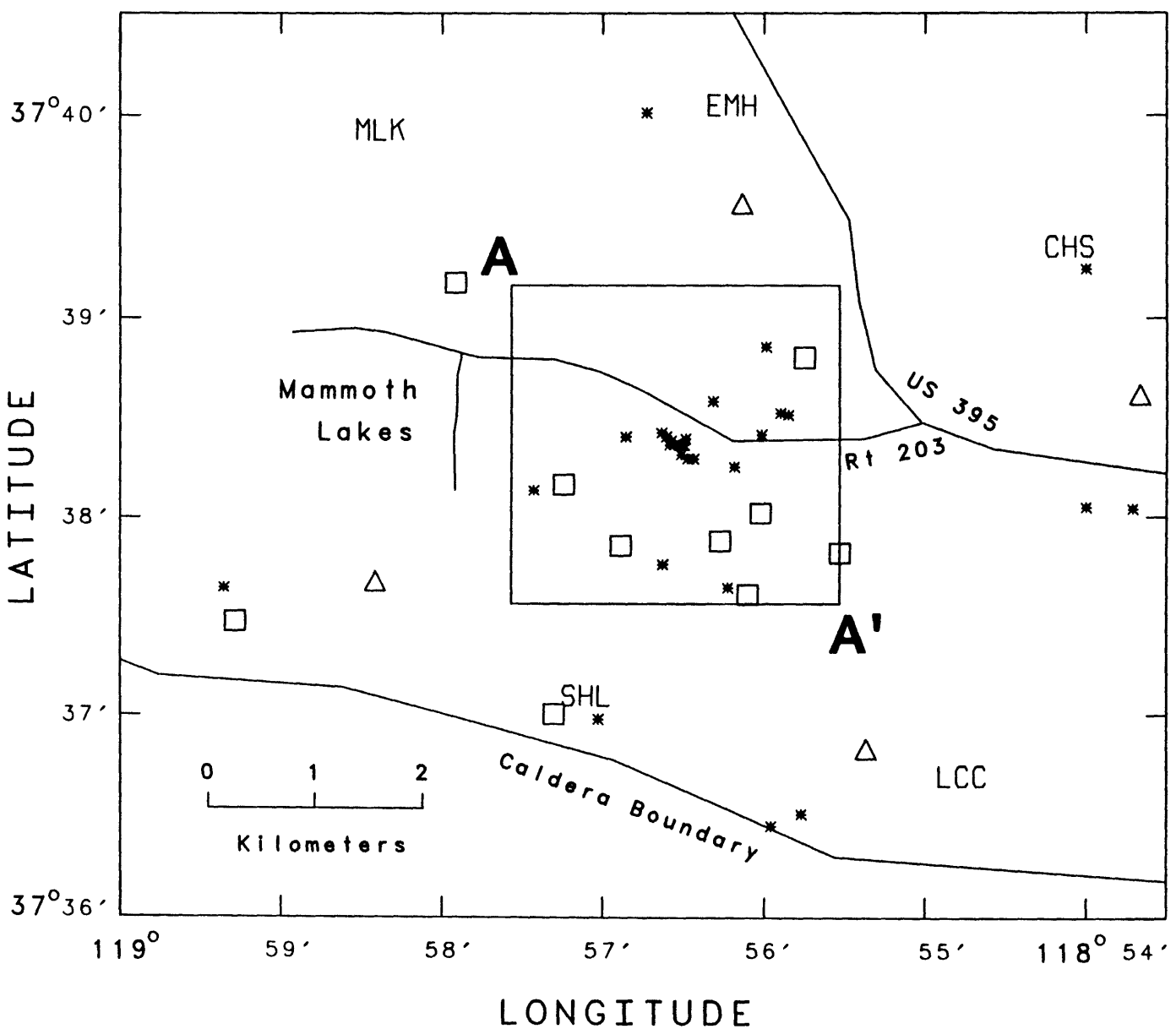
37°40′
39′
38′
37′
37°36′
LATITUDE
119°
59′
58′
57′
56′
55′
118° 54′
LONGITUDE
MLK
EMH
CHS
A
A'
Mammoth
Lakes
US 395
Rt 203
SHL
LCC
0 1 2
Kilometers
Caldera Boundary

Figure 1

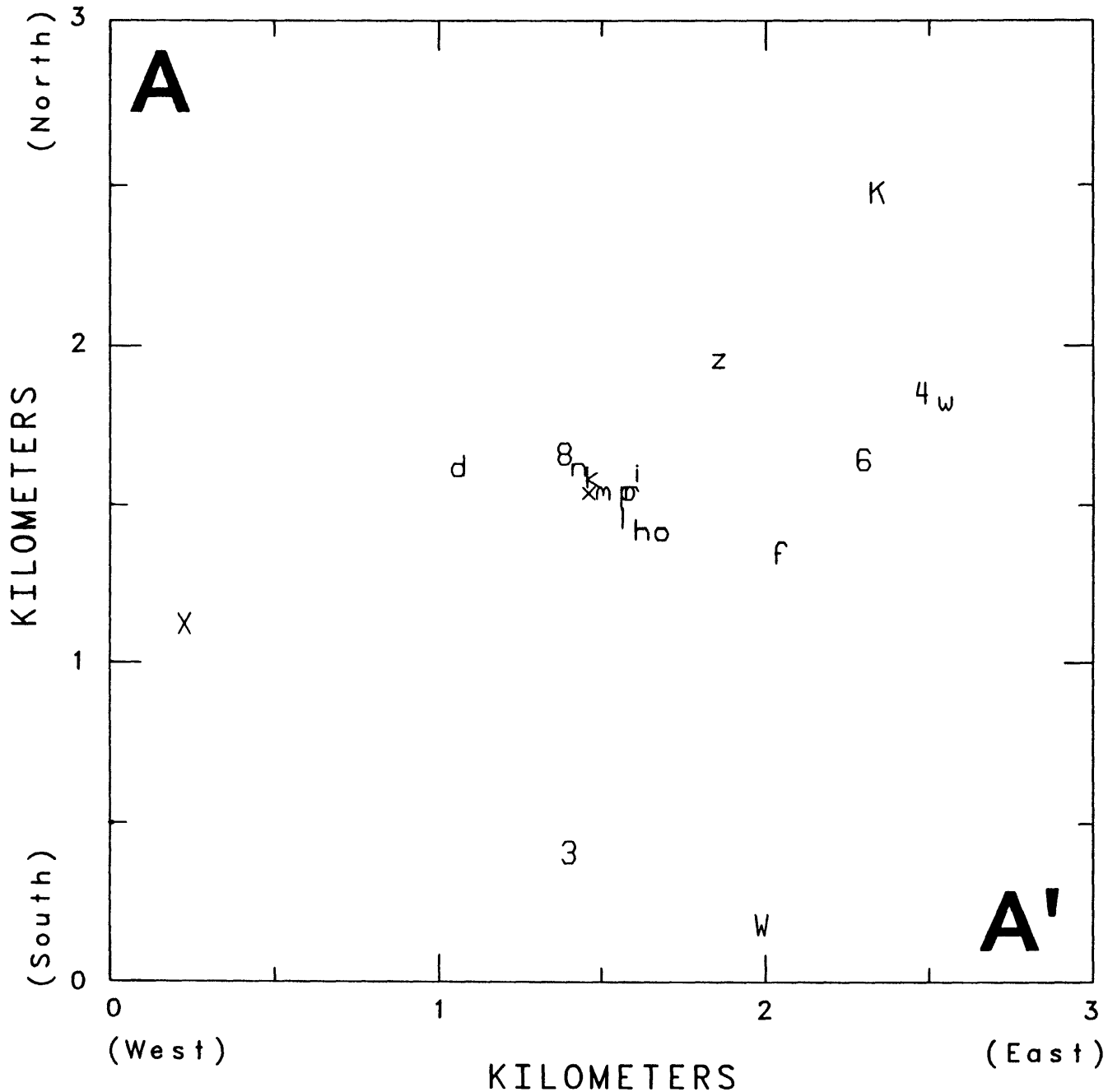
A
A'
(North)
(South)
(West)
(East)
KILOMETERS
KILOMETERS
0
1
2
3
K
z
4
w
d
8
6
ho
f
X
3
W

Figure 2

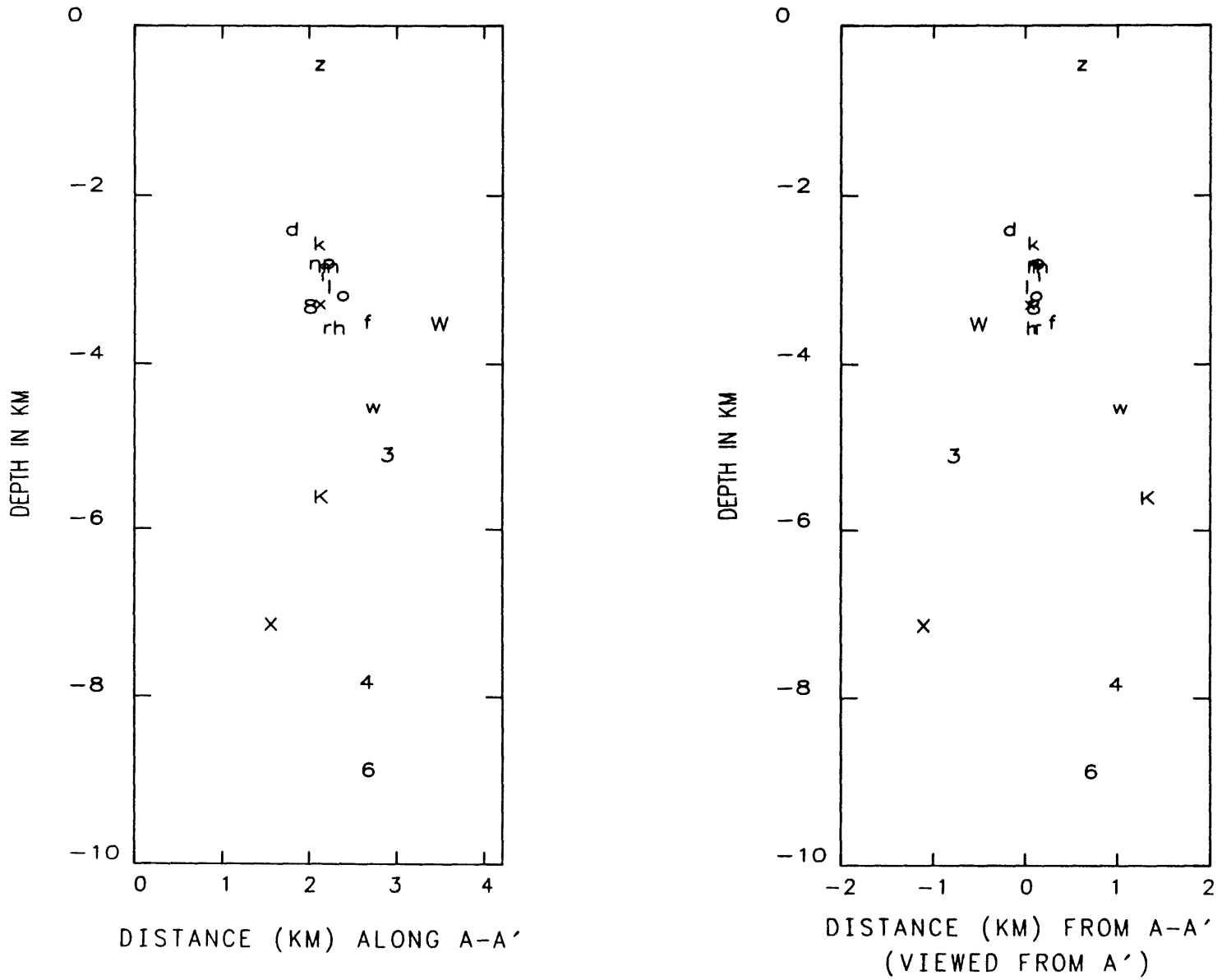
DEPTH IN KM
0
-2
-4
-6
-8
-10
0
1
2
3
4
DISTANCE (KM) ALONG A-A'
z
d
k
rh
f
W
w
3
K
X
4
6
DEPTH IN KM
0
-2
-4
-6
-8
-10
-2
-1
0
1
2
DISTANCE (KM) FROM A-A'
(VIEWED FROM A')
z
W
f
w
3
K
X
4
6

Figure 3

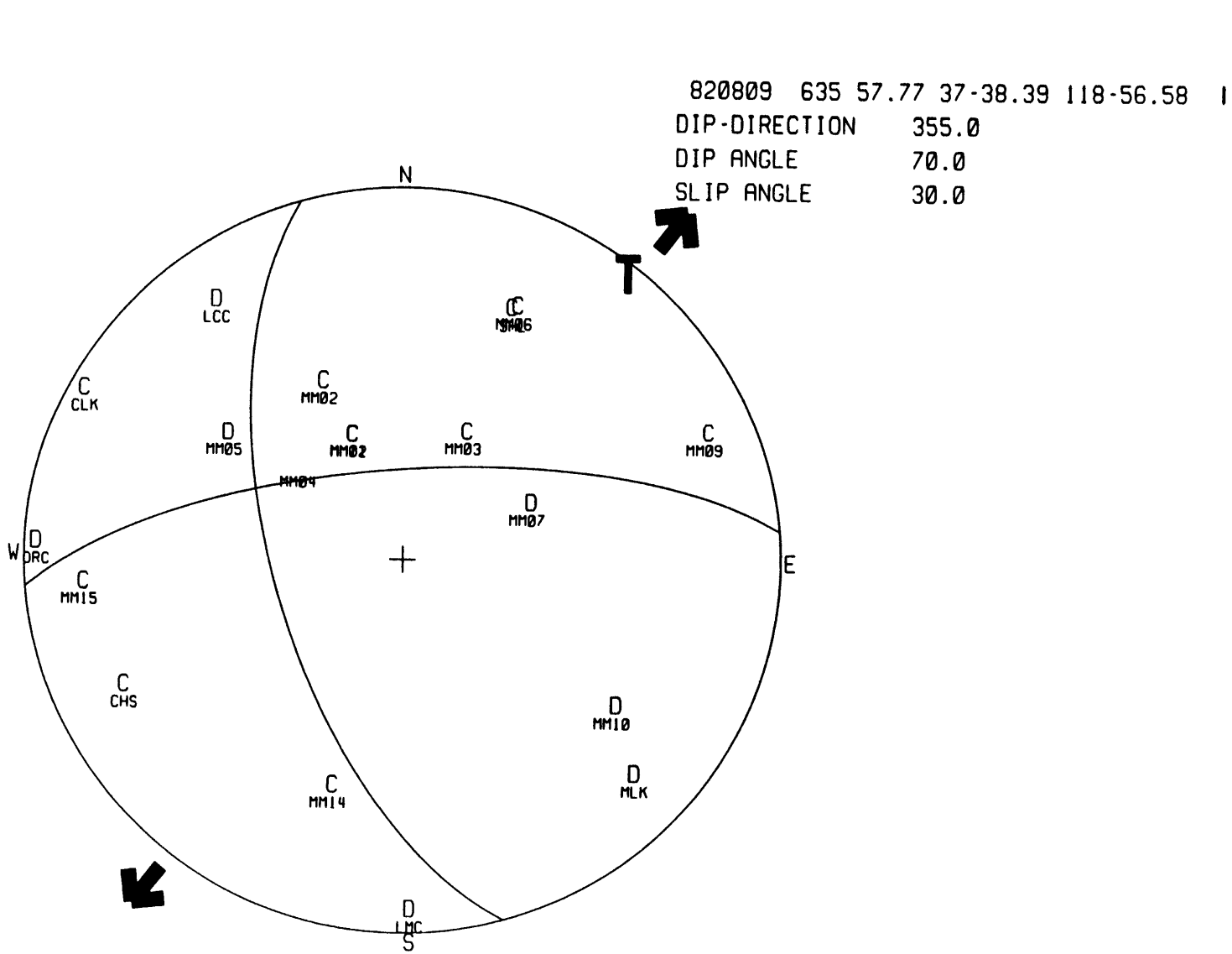
820809 635 57.77 37-38.39 118-56.58 I
DIP-DIRECTION 355.0
DIP ANGLE 70.0
SLIP ANGLE 30.0
N
W
E
S
T
D LCC
C CLK
C MM02
D MM05
C MM03
C MM09
D MM07
D ORC
C MM15
C CHS
D MM10
C MM14
D MLK
D LMC

Figure 4

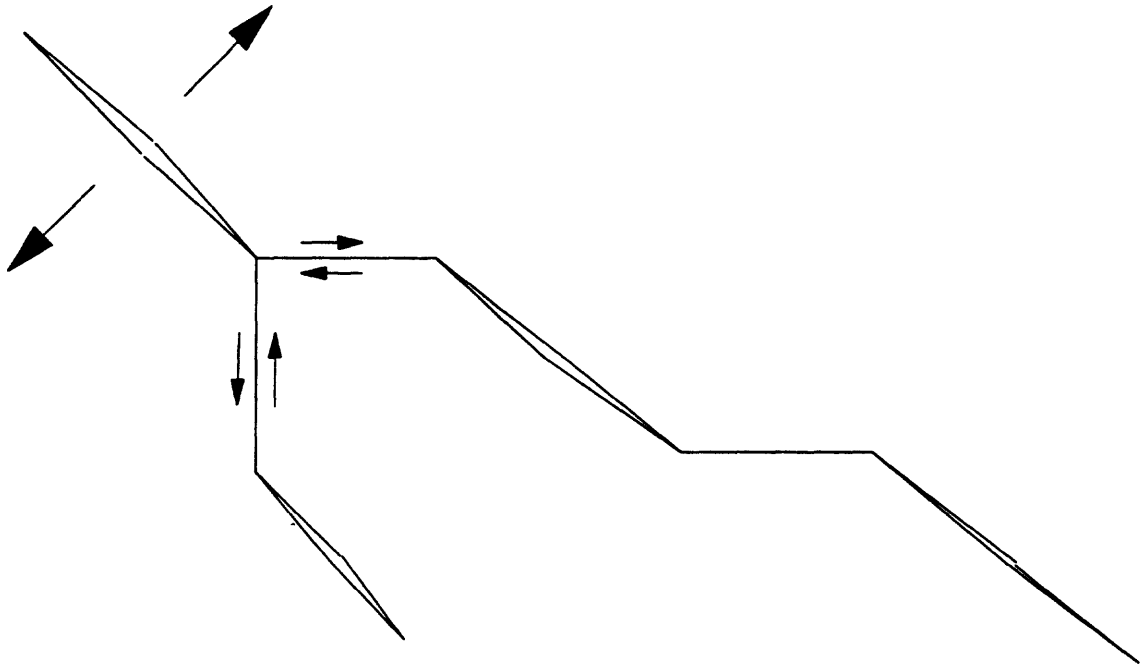

after Pollard (1973) and Hill (1977)

References

Anderson, E. M., 1936. The dynamics of the formation of cone-sheets, ring-dykes, and Caldron-subsidences, *Proceedings of the Royal Society of Edinburgh, 56*, 128-163.

Cramer, C. and T. Toppozada, 1980, A seismological study of the May, 1980, and earlier earthquake activity near Mammoth Lakes, California, *in Mammoth Lakes, California earthquakes of May, 1980, California Division of Mines and Geology Special Report 150*, 91-136.

Delaney, P. T., 1982, Rapid intrusion of magma into wet rock: groundwater flow due to pore pressure increases, *J. Geophys. Res., 87*, 7739-7756.

Delaney, P. T. and D. D. Pollard, 1982, Deformation of host rocks and flow of magma during growth of minette dikes and breccia-bearing intrusions near Ship Rock, New Mexico, *U.S. Geol. Surv. Prof. Paper 1202*, 61p.

Hill, D. P., 1976, Structure of Long Valley Caldera, California, from a seismic refraction experiment, *J. Geophys. Res., 81*, 745-753.

Hill, D. P., 1977, A model for earthquake swarms, *J. Geophys. Res., 82*, 1347-1352.

Julian, B. R., 1983, Evidence for dyke intrusion earthquake mechanisms near Long Valley caldera, California, *Nature, 303*, 323-325.

Miller, C. D., Crandell, D. R., Mullineaux, D. R., Hoblitt, R. P., and Bailey, R. A., 1982, Preliminary assessment of potential volcanic hazards in the Long Valley- Mono Lake area, east-central California and southwest Nevada, *U.S. Geological Survey Open-File Report 82-583*.

Pollard, D. D., 1973, Derivation and evaluation of a mechanical model for sheet intrusions, *Tectonophysics, 19*, 233-269.

Pollard, D. D., P. T. Delaney, W. A. Duffield, E. T. Endo, and A. T. Okamura, Surface deformation in volcanic rift zones, *Tectonophysics, 94*, 541-584, 1983.

Riley, F. S., Massey, B. L., Boling, J. K., Denlinger, R. P., and Carpenter, M. C., 1982, Horizontal Strain within the Long Valley, California, Caldera between 1975 and 1982, *EOS, 63*, 132.

Roecker, S. W., 1982, Velocity structure of the Pamir-Hindu Kush region: possible evidence of subducted crust, *J. Geophys. Res., 87*, 945-959.

Ryall, A. S., 1982, Seismicity and magma injection near Mammoth Lakes, California, in the context of regional tectonics, *EOS, 63*, 1132.

Ryall, F. and Ryall, A., 1982, Propagation effects and seismicity associated with magma in Long Valley Caldera, eastern California, *Earthquake Notes, 53*, 46-47.

Ryan, M., Koyanagi, R. Y., and Fiske, R. S., 1981, Modeling the three-dimensional structure of macroscopic magma transport systems: applications to Kilauea Volcano, Hawaii, *J. Geophys. Res.*, *86*, 7111-7129.

Savage, J. C., and Clark, M. M., 1982, Magmatic resurgence in Long Valley Caldera, California: Possible cause of the 1980 Mammoth Lakes Earthquakes, *Science, 217*, 531-532.

Thatcher, W., and Savage, J. C., 1982, Triggering of large earthquakes by magma-chamber inflation, Izu Peninsula, Japan, *Geology, 10*, 637-640.

Zoback, M. L., and Zoback, M., 1980, State of stress in the conterminous United States, *J. Geophys. Res.*, *85*, 6113-6156.

Earthquake Swarm in Long Valley Caldera, California, January 1983: Evidence for Dike Inflation

J. C. Savage and R. S. Cockerham

U.S. Geological Survey, Menlo Park, CA 94025

Short Title: 1982-83 Dike Inflation in Long Valley

ABSTRACT

The 1982-1983 deformation observed by trilateration and leveling surveys across the Long Valley caldera is apparently related to the 8.5-km-long by 8-km-deep vertical rupture surface defined by the January 1983 earthquake swarm that occurred in the south moat of the caldera. The observed deformation can be explained as follows: In late 1982 0.03 km^3 of magma was injected into a dike that dips 30° northward from the bottom of the rupture surface. The down-dip dimension of this dike is 8 km. The dike inflation accounts for the uplift observed across the caldera as well as some of the horizontal deformation. Inflation of the dike generated a tension of about 3 bars across the vertical plane that was to become the rupture surface of the January swarm. This reduced the frictional stress on the rupture plane and perhaps triggered the slip that caused the January swarm. Right-lateral slip (0.22 m) on the uppermost 2 km of the rupture plane during and after the January swarm accounts for the additional horizontal deformation observed. The model can be improved marginally if strike slip is admitted over the entire rupture surface and 0.006 km^3 of magma is injected along that surface in the depth interval 3 to 8 km. The improvement in the model fit, however, is not sufficient to require shallow injection of magma. Thus, we conclude that inflation of a dike at depth (8 to 12 km) dipping northward beneath the resurgent dome plus shallow right-lateral slip on the rupture surface is a simple, but not unique, explanation of the observed deformation and seismicity.

INTRODUCTION

Long Valley caldera (Figure 1), an elliptical depression 30 km long and 15 km wide near Mammoth Lakes, California, was recently identified as the site of a potential volcanic hazard [Kerr, 1982; Miller et al., 1982]. Interest focused on the area as a result of an unusual sequence of earthquakes that began in October 1978 and has continued to the present. The sequence culminated in May 1980 with the occurrence of four $M_L > 6$ earthquakes. Subsequently, it was discovered that some time between July 1979 and September 1980 the resurgent dome within the caldera had bulged upward about 0.25 m and expanded outward suggesting inflation of a magma chamber at depth [Savage and Clark, 1982]. After May 1980 intense swarms of earthquakes that might be identified as the volcanic phenomenon called spasmodic tremor were observed within the south moat of the caldera [Ryall and Ryall, 1983]. Finally, the nodal plane solutions for two of the May 1980 $M_L > 6$ earthquakes [Julian, 1983] as well as the initial October 1978 shock [Ekstrom and Dziewonski, 1983] have been identified as appropriate to dike intrusion (compensated-linear-vector-dipole mechanism) rather than slip faulting (double-couple mechanism). (An alternate interpretation [Ekstrom, 1983; Wallace, et al., 1983] of these solutions is that they result from near simultaneous faulting on two distinct planes, shallow strike slip and deeper dip slip.) These observations taken together with the unusually long duration, the migration of activity, and the swarm-like character of the seismicity since October 1978 suggest that the earthquake sequence may be a manifestation of the movement of magma at depth rather than an ordinary tectonic event. In particular, the swarms occurring

in the south moat of the caldera may be associated with local intrusions of magma [Kerr, 1983b; Ryall and Ryall, 1983].

In this paper we are concerned with the horizontal and vertical deformation that occurred in the interval July-August 1982 to July-August 1983. The seismicity in that interval was dominated by very intense swarm activity in the south moat of the caldera during early January 1983 (Figure 1). The hypocenters of that swarm defined a vertical rupture surface 8.5 km long and 8 km deep, and it is probable that some of the 1982-1983 deformation is associated with slip on that surface. However, it appears that inflation of a magma chamber beneath the resurgent dome is required to account for the observed 1982-1983 uplift. In this paper that magma chamber is modeled as a tabular body (dike) dipping 30° northward from the bottom of the rupture surface. It is shown that inflation of the magma chamber decreases the normal pressure across the rupture surface making slip, and perhaps magma intrusion, on that surface more likely. Thus, the model affords a comprehensive, though not unique, explanation of the seismicity and deformation in the caldera in 1982-1983.

Although we [Cockerham and Savage, 1983] had earlier argued that the observed 1982-1983 deformation in the caldera indicated dike intrusion along the January rupture surface to within 3 km of the free surface, we now conclude that the more complete set of 1982-1983 deformation data neither excludes nor requires shallow dike intrusion. This lack of uniqueness in the modeling is illustrated further by a model proposed by Rundle and Whitcomb [1983]. In their model deformation is attributed primarily to inflation of two spherical magma chambers, one at a depth of 5 km about 1.5 km west of station Casa and the other at a depth of 9 km about 5.5 km north-northwest of that station,

plus right-lateral slip on the January rupture surface. Their model appears to account for the 1982-1983 deformation essentially as well as the models proposed in this paper. Although the model proposed by Rundle and Whitcomb differs in details from the models proposed here, all models require inflation of a magma reservoir beneath the resurgent dome in the caldera and right-lateral slip on the January rupture surface.

SEISMICITY

In early January 1983 a particularly intense swarm of earthquakes occurred within the caldera a few kilometers southeast of Mammoth Lakes [Kerr, 1983a]. Approximately 7,000 earthquakes in the swarm were automatically located by an on-line computer between January 7 (beginning of swarm) and January 31. About 2,300 of these locations were reprocessed by hand to improve the accuracy; the resulting locations are shown in Figures 2b and 3. The layered earth model used to locate the earthquakes is shown in Table 1 [Cockerham, Pitt, and Kissling, in preparation]. Only the 15 stations shown in Figure 2a were used in locating the earthquakes. A traveltime delay appropriate to the model was used at each station. The epicenters of the January swarm (Figure 2b) cluster closely along an 8.5-km-long linear trend striking east-southeast and the hypocenters cutoff abruptly at about 8 km (Figure 3). Thus, the swarm hypocenters define a 8.5-km-long by 8-km-deep vertical rectangle that we shall call the January rupture surface. Within this rupture surface there are two relatively aseismic strips, one horizontal and one vertical. The horizontal strip occupies the depth interval 0 to 2 km and the vertical strip extends from the surface to a depth of 8 km near the center of the hypocentral

distribution (Figure 3). The two largest earthquakes in the swarm, both of magnitude (M_L) about 5.2, were located near the northwest end of the epicentral area. These were the largest earthquakes to occur within the caldera since May 1980.

Although we will not use this refinement in our subsequent models, a more detailed examination of the earthquake epicenters in Figure 2b suggests that there are two separate trends, one to the west of the central seismic gap and the other to the east. The western epicenters appear to define an east-west trend whereas the eastern epicenters trend to the south-southeast. Thus, the January rupture surface is, in fact, a vertical dihedral (vertex angle of about 160°) with a deficiency of seismicity along the vertex.

Nodal plane solutions consistent with slip faulting have been found for 60 earthquakes in the swarm. Some of these solutions may also be consistent with mechanisms other than slip faulting (e.g., crack opening as found by Julian [1983]), but the data do not require other mechanisms. Nineteen examples of the more tightly constrained solutions are shown in Figure 4. The earthquakes (Table 2) associated with these solutions fall naturally into two distinct groups: those with epicenters on the western limb of the dihedral rupture surface and those with epicenters on the eastern limb. The earthquakes from the western limb of the rupture surface exhibit both strike-slip and dip-slip solutions (Figure 4a). In most cases one nodal plane for these solutions coincides very closely with the east-west trend of the western limb of the rupture surface. The earthquakes from the eastern limb of the rupture surface all appear to be consistent with right-lateral slip on that limb (Figure 4b). A summary of the P and T axes for these 19 solutions is shown in Figure 4c. The T axes are nearly horizontal for all but one solution. The strike of the

T axes for earthquakes on the western limb of the dihedral rupture surface range from north to northeast, whereas the strike of the T axes for earthquakes on the eastern limb range from northeast to east-northeast. The P axes, on the other hand, appear to be concentrated along one quadrant of the girdle that lies in the plane perpendicular to the T-axis trend.

There is no obvious dependence of focal mechanism upon depth in these nodal plane solutions. The focal mechanisms for earthquakes on the eastern limb of the dihedral rupture surface appear to be predominantly strike-slip at all depths. Although a variety of mechanisms are displayed by earthquakes on the western limb, there is no obvious variation of mechanism with depth. Vetter and Ryall [1983] had previously noted a tendency for strike-slip earthquakes to predominate at shallow depths with slip becoming increasingly oblique with depth in the Mammoth Lakes area. Apparently, the January 1983 earthquake swarm did not conform to this pattern.

The January 1983 seismicity suggests right-lateral slip on both limbs of the dihedral rupture surface with a more complicated rupture mechanism superimposed on the western limb. Given the independent arguments for magma intrusion [Kerr, 1983b], it seems reasonable to consider magma intrusion along the western limb as a possible source of the complexity in focal mechanisms noted there. This is not to say that the mechanisms necessarily correspond to crack opening but rather that the dip slip mechanisms may be a response to dike intrusion.

DEFORMATION

In late July 1982, a 21-line trilateration network was established around the caldera (Figure 1). On January 10, 1983, following the most intense

earthquake swarm activity, seven of those lines and one additional line (Casa-Mammoth) were measured. Finally, in July 1983 all 22 lines were remeasured. In each survey the distances were measured with a Geodolite, a very precise distance-measuring instrument, and the atmospheric-refractivity correction was determined from an aircraft flying along the line of sight at the time of ranging (see Savage and Prescott [1973] for details on the procedures and precision). Line length changes for the July 1982 to July 1983 interval are given in Table 3, and plots of the line-lengths as a function of time are shown in Figure 5 for each of the eight lines measured in the January 10 survey. Because the length Casa-Mammoth was not measured directly in July 1982 but rather deduced from a network adjustment, the length change for Casa-Mammoth in the July 1982 to January 1983 interval is shown by a dashed line in Figure 5. Strictly, the length changes in Figure 5 are changes in the slope distances between the station marks, but except for one case (Casa-Laurel) those changes should be virtually the same as to the changes in horizontal distance. The exceptional case (Casa-Laurel) is such a steep line (1.2 km change in elevation in 7.1 km horizontal distance) that changes in elevation at station Casa produce a change in slope distance that would not appear as a change in horizontal distance. An approximate correction for this effect has been calculated, and the dashed segment of the line for Casa-Laurel in Figure 5 represents the calculated change in horizontal distance.

Displacements of the individual stations in the interval July 1982 to July 1983 can be calculated directly from the observed changes in line length subject to some constraint upon the rigid-body motion of the network as a whole. The displacement solution shown in Figure 6 corresponds to the constraint that the rigid-body motion must be such that the sum of the squares

of the displacements is a minimum (the so-called "inner-coordinate" solution; see Welsch [1979, p. 176]). Except at stations Laurel, Casa, Convict, and Bald, the displacements in Figure 6 do not much exceed the uncertainties indicated by the 95% confidence ellipses. The largest displacements are at Casa and Laurel, the two stations closest to the epicenters of the January 1983 swarm (Figure 1), and it seems reasonable to attribute those displacements to slip on a fault that coincides with the rupture surface defined by the hypocenters of the events in the January 1983 swarm. The displacements at Casa and Laurel suggest right-lateral slip on such a fault.

In July and August of 1982 and again in July and August of 1983 an extensive leveling network covering the Long Valley caldera was surveyed using second-order procedures. The 1982-1983 elevation changes deduced from a comparison of these leveling surveys is shown in Figure 7. (See Castle et al. [1984] for a more detailed discussion of the leveling and elevation changes.) The uplift is approximately centered on the resurgent dome (the outline of the resurgent dome roughly coincides with the 70 mm uplift contour), but it is not symmetric about that center. Rather the uplift has the appearance of a tilted block with the steep gradient on the south flank and the more gentle slope on the north. The general appearance of the uplift is quite similar to the trap-door domes associated with igneous intrusions [Moon, 1953, p. 85] except the bounding faults are not clearly defined at Long Valley. In any case, the overall appearance of the uplift is about what might be expected from the inflation of a northward dipping dike beneath the uplift [Davis, 1983, Figure 6].

The leveling route along the south edge of the caldera from 6000R (southeasternmost data point in Figure 7) to 3000M (eastern outskirts of the

town of Mammoth Lakes) was also surveyed by second-order procedures in the interval January 13 to 20, 1983. The elevation changes for the August 1982 to January 1983 are compared to the elevation changes for August 1982 to August 1983 in Figure 8. The two elevation changes are very similar except in the immediate vicinity of the rupture trace (defined by a heavy bar in Figure 8) of the January 1983 swarm where it appears that there has been a partial post-January collapse of the pre-January uplift.

SOURCE MODELS

The deformation of the earth's surface can be modeled by the deformation of the surface of an elastic half space in which idealized sources have been embedded. One of the simplest of these models is an expanding spherical source that is intended to represent the effects of magma-chamber inflation within the earth (e.g., Savage and Clark [1982]). In this paper we will be concerned with dislocation sources, that is, sources that can be represented by a displacement discontinuity across a planar surface. These sources are appropriate representations of slip faulting and dike intrusion. The surface displacements generated by such sources embedded in an elastic half space are readily calculated from the equations given by Comninou and Dundurs [1975].

As suggested earlier the 1982-1983 deformation can be explained approximately as the result of magma intrusion into a dike dipping northward from the bottom of the rupture surface beneath the resurgent dome. (The rupture surface here and in what follows is taken to be planar; the dihedral configuration will not be considered further.) The strike of this dipping dike and its along-strike dimension (8.5 km) are taken to be identical to that of the rupture

surface itself. The dip (30°), the downdip dimension (8 km), and the opening of the dike (0.44 m) were chosen to fit the deformation data. The surface projection of this source is shown in Figure 9. The quality of the fit can be judged in Figures 9 and 10 where the residual displacements (observed displacement less the displacement calculated for the dipping dike) are shown. The residual horizontal displacements are reasonably small except as stations Casa and Laurel where those displacements suggest shallow right-lateral slip on the January rupture surface. (The trace of the rupture surface coincides with the south-southwestern edge of the dipping dike in Figure 9.) The fit to the vertical deformation data is reasonably good except for a regional tilt down to the south-southwest. There is reason to believe that this regional tilt is an artifact of surveying error in the 1982 leveling [Castle et al., 1984]. The type of level used in 1982 is known to be subject to a magnetic deflection that would produce an apparent tilt parallel or antiparallel to magnetic north (N17°E). The magnitude and orientation of the regional tilt in Figure 10 is within the range that could be explained by such a systematic error. Thus, it would appear that the greatest part of the 1982-1983 observed deformation (Figures 6 and 7) can be accounted for simply by the inflation of a dike dipping 30° north-northeast from the bottom of the rupture surface.

The most obvious deficiency of the dipping dike model is the failure to account for the observed displacements at Casa and Laurel (Figure 9). Since both of these displacements are essentially parallel to the strike of the January rupture surface (the trace of the rupture surface coincides with the south-southwestern edge of the buried dike in Figure 9), right-lateral slip on the rupture surface should account for those displacements. We determined the amount and distribution of strike slip on the rupture surface which in

combination with the inflation of the dipping dike would best explain the observed 1982-1983 deformation. The best-fit model is shown in Figure 11a. Notice in that model slip on the rupture surface is confined to the uppermost 2 km, an interval in which seismicity is relatively low (Figure 3). Although the model requires 0.22 m of shallow right-lateral slip along the rupture surface, no obvious ground breakage was observed there. The area was, however, covered by snow at the time of the January 1983 earthquake swarm. The fit of the model to the observed displacements can be judged from the residuals shown in Figures 12 and 13 and Table 3. The fit to the data is reasonably good except for the regional tilt in Figure 13, the same as that in Figure 10 which we have tentatively attributed to survey error. A direct comparison of the observed and predicted elevation changes near the rupture trace is shown in Figure 8 (compare the dashed curve to plotted circles which represent the observed elevation changes). The fit is reasonably good except at the bench marks (983, 2JCM, 3JCM, LC2, and LC3) closest to the trace of the rupture surface.

A third model of the deformation has been constructed in which dip slip and dike intrusion along the rupture surface have been admitted in addition to strike slip. Intrusion along the dipping dike is, of course, also included in this model. The best-fit parameters for a model of this type are shown in Figure 11b, and the residual displacements (observed less model predicted) are shown in Figures 6 and 14. (See also Table 3 for the residual line length changes.) In addition, Figure 8 shows a comparison of the observed (plotted points) and model predicted (solid line) uplift in the vicinity of the rupture surface. In general, the fits provided by the two models in Figure 11 are quite comparable. The most notable difference is the significantly better fit

of the model in Figure 11b to the August 1982 to August 1983 elevation changes along the spur line 11DOR to LC3 (Figure 8 center right).

Two major discrepancies were noted in fitting the models to the observed 1982-1983 elevation changes (see Figures 10, 13, and 14). The first of these is a regional tilt down to the south-southeast (magnetic south) that may be associated with magnetic deflection of the compensator in the level used in the 1982 survey. The second discrepancy involves an uplift (20 mm contour in Figures 10, 13, and 14) a few kilometers west of Mammoth Lakes. This same discrepancy is shown in Figure 8 where the quality of the model fit decreases progressively to the west of Casa Az. A possible explanation of that discrepancy is a local uplift associated with the persistent, shallow, earthquake swarm activity beneath Mammoth Mountain (5.5 km south-southwest of Mammoth Lakes).

Except in the immediate vicinity of the rupture surface, most of the 1982-1983 deformation appears to have occurred before the January 1983 surveys (January 10 for the trilateration and January 13-20 for the leveling). This is seen most clearly in Figure 8 where the agreement between the January 1983 (shown by X's) and August 1983 (open circles) leveling surveys is excellent except at the stations (bench marks 983, 2JCM, 3JCM, LC2 and LC3) within 1 km of the rupture surface. Those exceptional bench marks appear to have been uplifted between August 1982 and January 1983 and then partially subsided. In the distance measurements (Figure 5) only the lines Casa-Laurel and Casa-Bald show really significant post-January line-length changes although changes in length of Bald-Laurel and Bald-Glass are near the level of significance (two standard deviations). The line-length changes in Figure 5 are then consistent with all stations remaining approximately fixed after January 1983 except Casa

which must have moved southward about 24 mm. The only significant horizontal movement required is at Casa, the station closest (2 km) to the rupture surface.

The conclusion that the post-January deformation involved only those stations closest to the rupture surface suggests that deep-seated sources were not involved in that deformation. Rather the source of the deformation would appear to be shallow displacement discontinuities on the rupture surface itself. Thus, if the 1982-1983 deformation is accounted for by the model of Figure 11a, one might expect the post-January deformation to be explained by strike slip on the uppermost 2 km of the rupture surface. The best fit for such a model (64 ± 27 mm right-lateral slip) provided only a very marginally acceptable fit to the observed deformation. The model fails to account for the subsidence near the rupture and the residuals for the line length changes are rather large (e.g., Bald-Casa 19.7 mm, Bald-Laurel 16.2 mm, Casa-Laurel -14.4 mm).

DISCUSSION

The injection of magma into the dipping dike in Figure 11 would generate tension across the January rupture surface which in turn would facilitate both slip and magma injection along that surface. That tension across the rupture surface would be generated by opening of the dipping dike is most easily demonstrated by using a two-dimensional model in which both the rupture surface and dipping dike are assumed to be infinitely long in the direction of strike. The dipping dike can then be represented by two edge dislocations as shown in Figure 15, and the stress across the rupture surface calculated from

the equations given by Mura [1968, p. 95]. As shown in Figure 15 a tension across the rupture surface in excess of 3 bars (0.3 MPa) is generated by a 0.4 m thickening of the dipping dike. That tension would, of course, facilitate slip and magma injection on the rupture surface. The normal stress on the downward extension of the rupture surface below the dipping dike is compressive which should inhibit slip on that part of the surface. This compression could account for the abrupt cutoff in seismicity below 8 km in Figure 3. The stresses on the rupture plane for the three-dimensional models in Figure 11 would be somewhat less than those given by the two-dimensional calculation (Figure 15). As an example, we have calculated from the equations of Comminou and Dundurs [1975] the normal stress across the rupture plane at the center of its surface trace for the inflation of the three-dimensional dipping dike used in the models of Figure 11. The three-dimensional model yields 2.54 bars versus 3.18 bars for the two-dimensional model.

In the models in Figure 11 it should be understood that the dikes are intended to represent pre-existing magma chambers of appreciable width (perhaps, several hundred meters). The indicated opening (0.4 m for the dipping dike and 0.15 m for the January rupture surface) is to be interpreted as the 1982-1983 increment in the dike width. We recognize that injecting magma through channels as narrow as a fraction of a meter would be restricted to short distances due to the viscosity of the magma and its tendency to freeze when in contact with the wall rock. Thus, the models of Figure 11 do not envisage the formation of new dikes but rather the inflation of existing tabular magma chambers. Moreover, these magma chambers need not be totally fluid volumes. Rather a magma chamber may consist of a network of interconnected volumes separated by competent rock. The seismicity could then

correspond to rupture of the competent rock. Obviously, gross observations of deformation at the surface cannot define the detailed structure of sources at depth.

CONCLUSION

A plausible model that accounts for the seismicity and deformation observed in the Long Valley caldera in 1982-1983 is as follows: In late 1982 a tabular magma reservoir dipping 30°N beneath the resurgent dome was inflated by about 0.03 km^3 of magma. This inflation relieved the normal pressure on the vertical plane that was to become the rupture surface for the January swarm. This relaxation of normal stress reduced the frictional stress and allowed slip events (the January 1983 swarm) to occur on the rupture surface. Both deformation and seismic focal plane solutions indicate right-lateral slip was involved in the January swarm. Whether magma injection along the rupture surface was involved is less clear. The focal mechanism solutions along the western half of the rupture surface (Figure 4a) suggest a pattern of deformation considerably more complicated than one would associate with simple right-lateral slip. Moreover, the seismic phenomenon of spasmodic tremor had earlier been tentatively identified near the area that became the west end of the rupture surface [Ryall and Ryall, 1983]. Finally, the 1982-1983 deformation is consistent with a model (Figure 11b) that involves magma intrusion along the rupture surface. All of these observations are suggestive of magma intrusion along the west end of the rupture surface, but they are not sufficiently definitive to prove that it occurred.

REFERENCES

Castle, R.O., J.E. Estrem, and J.C. Savage, Uplift across Long Valley caldera, California, submitted to J. Geophys. Res., 1984.

Cockerham, R., and J. Savage, Earthquake swarm - Long Valley caldera, California, January 1983, EOS Trans. Am. Geophys. Un., 64, 890, 1983.

Comminou, M., and J. Dundurs, The angular dislocation in a half space, J. Elasticity, 5, 203-216, 1975.

Davis, P.M., Surface deformation associated with a dipping hydrofracture, J. Geophys. Res., 88, 5826-5834, 1983.

Ekstrom, G., Evidence for source complexities of 1980 Mammoth Lake Earthquakes, EOS Trans. Am. Geophys. Un., 64, 769, 1983.

Ekstrom, G., and A.M. Dziewonski, Moment tensor solutions of Mammoth Lake Earthquakes, EOS Trans. Am. Geophys. Un., 64, 262, 1983.

Julian, B.R., Evidence for dyke intrusion earthquake mechanisms near Long Valley caldera, California, Nature, 303, 323-325, 1983.

Kerr, R.A., Volcanic hazard alert issued for California, Science, 216, 1302-1303, 1982.

Kerr, R.A., Mammoth Lakes quiet but concern persists, Science, 219, 373-374, 1983a.

Kerr, R.A., New signs of Long Valley magma intrusion, Science, 220, 1138-1139, 1983b.

Lee, W.H.K., R.E. Bennett, and K.L. Meagher, A method of estimating magnitude of local earthquakes from signal duration, U.S. Geol. Survey Open-File Report, 28 p., 1972.

Lee, W.H.K., and J.C. Lahr, HYPO71 (Revised): A computer program for determining hypocenter, magnitude, and first motion pattern of local earthquakes, U.S. Geol. Survey Open-File Report 75-311, 114 p., 1975.

Miller, C.D., D.R. Mullineaux, D.R. Crandell, and R.A. Bailey, Potential hazards from future volcanic eruptions in the Long Valley-Mono Lake area, east-central California and southwest Nevada -- a preliminary assessment, U.S. Geological Survey, Circular 77, 1-10, 1982.

Moon, C.G., Geology of Agua Fria quadrangle, Brewster County, Texas, Bull. Geol. Soc. Am., 64, 151-196, 1953.

Mura, T., The continuum theory of dislocations, Advances in Materials Research, 3, 1-417, 1968.

Rundle, J.B., and J. Whitcomb, A new model for the deformation in Long Valley caldera, 1980-1983, EOS Trans. Am. Geophys. Un., 64, 891, 1983.

Ryall, A.S., and F. Ryall, Spasmodic tremor and possible magma injection in Long Valley caldera, eastern Californa, Science, 219, 1432-1433, 1983.

Savage, J.C., and M.M. Clark, Magmatic resurgence in Long Valley caldera, California: Possible cause of the 1980 Mammoth Lakes earthquakes, Science, 217, 531-533, 1982.

Savage, J.C., and W.H. Prescott, Precision of Geodolite distance measurements for determining fault movements, J. Geophys. Res., 78, 6001-6008, 1973.

Vetter, U.R., and A.S. Ryall, Systematic change of focal mechanism with depth in the western Great Basin, J. Geophys. Res., 88, 8237-8250, 1983.

Wallace, T.C., L.J. Burdick, and H. Kanamori, Faulting and crustal structure complexity: a possible explanation for the moment tensor solutions of the 1980 Mammoth Lakes earthquakes, EOS Trans. Am. Geophys. Un., 64, 769, 1983.

Welsch, W., A review of the adjustment of free networks, Surv. Rev., 30, 167-180, 1979.

FIGURE CAPTIONS

Fig. 1. Map of Long Valley caldera and vicinity showing the location of geodetic stations (triangles), the lines observed in the trilateration network, caldera boundary (dotted oval), and epicenters of the January 1983 earthquake swarm (heavy bar east of the town site of Mammoth Lakes).

Fig. 2. a) Location of the 15 stations (stars) used to locate the seismic events in the January swarm, and b) the epicenters for the interval January 7 through January 31 (UTC), 1983. The box encloses the earthquakes plotted in cross-sectional views shown in Figure 3. Outline of Long Valley caldera and prominent faults are shown by light solid lines and the principal highways by heavy lines.

Fig. 3. Projections of the hypocenters of earthquakes shown within the box in Figure 2 onto vertical planes striking west-northwest and south-southwest. Cross section A-A' is parallel to the long dimension of the box with A at the west-northwest edge, and the other cross section is perpendicular to A-A'.

Fig. 4. a) P-wave first motion focal plane solutions (lower hemisphere, equal-area projection) for events in the western half of the box in Figure 2b. Solid circles are compressional first motion, open circles are dilational, P and T represent calculated compressional and extension axes. The events are labeled by date, origin time, and depth.

b) Composite solution of events in the eastern half of the box in Figure 2b. Symbols and projections are the same as on Figure 4a.

c) Summary plot of P- and T-axes from Figures 4a and 4b shown on a lower-hemisphere, equal-area projection.

Fig. 5. Line lengths L less a nominal constant length L_o for each of the eight lines observed in the January 10, 1983 survey plotted as a function of time. The main part of the January 1983 earthquake swarm occurred a few days prior to the January 10, 1983 measurement. The error bars represent one standard deviation on either side of the plotted point.

Fig. 6. Map of Long Valley caldera (dotted oval) and vicinity showing the displacements (solid arrows) of the trilateration station in the July 1982 to July 1983 interval. The error bars represent the principal axes of the 95% confidence ellipse for each station displacement. The dashed arrows show the residual displacements at the trilateration stations after the displacements generated by the source model of Figure 11b have been removed. The heavy diagonal line segment below station Casa is the locus of the epicenters of the January 1983 earthquake swarm.

Fig. 7. Contour map of the 1982-1983 uplift in millimeters after Castle et al. [1984]. The dotted oval locates the boundary of the Long Valley caldera, and the black dots locate bench marks at which elevation changes were available.

Fig. 8. Relative elevation-change profiles along Highways 395 and 203 (center left) and along the spur line (center right) for the 1982-1983 interval. The solid and dashed lines show relative elevation change predicted by the dislocation models of Figure 11, the X's show the observed relative elevation change at each bench mark for the August 1982 to January 1983 interval, and the plotted points show the elevation change for the interval August 1982 to August 1983. The location of the bench marks relative to the trace of the rupture surface (heavy line segment) is shown at the top of the figure. The elevation profiles along the leveling routes are shown at the bottom.

Fig. 9. Map of Long Valley caldera (dotted oval) and vicinity showing the residual displacements at the trilateration stations after the displacements generated by the source model of a dipping dike at depth (surface projection shown as dashed rectangle) have been subtracted. The error bars represent the principal axes of the 95% confidence ellipse for each station displacement.

Fig. 10. Contour map of residual 1982-1983 uplift in millimeters after the uplift predicted by the simple model of a dipping dike at depth (surface projection shown as a dashed rectangle) have been subtracted. The dotted oval locates the boundary of the Long Valley caldera, and the black dots locate bench marks at which elevation changes were available.

Fig. 11. South-southwest to north-northeast cross sections through two source models that reproduce the observed surface deformation relatively well. The vertical projections of these models upon the earth's surface are shown in Figures 13 and 14. The vertical surface represents the rupture surface defined by the January swarm whereas the surface dipping down to the right represents a tabular magma reservoir. The speckled areas represent regions where magma has been intruded, and numbers indicating the thickness of the speckled areas represent the increment in the width of the tabular magma reservoirs. The amounts of strike slip and dip slip on the rupture surface are also indicated for each model.

Fig. 12. Map of Long Valley caldera (dotted oval) and vicinity showing the residual displacements at the trilateration stations after displacements generated by the source model of Figure 11a (surface projection of that model shown as a rectangle within the caldera) have been subtracted. The error bars represent the principal axes of the 95% confidence ellipse for each station displacement.

Fig. 13. Contour map of the residual 1982-1983 uplift in millimeters after the uplift predicted by the source model of Figure 11a (surface projection of that model shown as a rectangle within the caldera) have been subtracted. The dotted oval outlines the boundary of the Long Valley caldera, and the black dots locate bench marks at which elevation changes were available.

Fig. 14. Contour map of the residual 1982-1983 uplift in millimeters after the uplift predicted by the source model of Figure 11b (surface projection of that model shown as a rectangle within the caldera) have been subtracted. The dotted oval outlines the boundary of the Long Valley caldera, and the black dots locate bench marks at which elevation changes were available.

Fig. 15. A two-dimensional analog (left) of the dipping-dike source in Figure 11 and the normal stress (right) exerted across the plane of the rupture surface by the inflation of this source as a function of depth. The stress has been calculated for a 0.4-m thickening of the dipping dike, the approximate value found for the models in Figure 11.

Table 1. Earth model used in locating earthquake hypocenters

Depth to Layer Top km	P-wave Velocity km/s
0.0	2.25
0.5	3.20
1.0	4.60
2.0	5.25
3.0	5.60
7.0	5.85
18.0	6.20
30.0	6.80
50.0	8.00

TABLE 2

Microearthquakes in Long Valley caldera from January 7 to January 29 used for P-wave focal mechanism study.

DATE	ORIGIN TIME	NORTH LATITUDE	WEST LONGITUDE	FOCAL DEPTH km	MAG	N	GAP deg	DMIN km	RMS s	ERH km	ERZ km	Q
Jan 13	758 42.26	37 38.21	118 54.73	2.15	2.76	12	7Ø	Ø.8	Ø.Ø3	Ø.1	Ø.2	AA
Jan 1Ø	6Ø3 36.26	37 37.69	118 54.87	2.63	2.64	9	67	2.Ø	Ø.Ø9	Ø.5	Ø.9	AA
Jan 13	231 12.87	37 38.36	118 56.Ø4	2.99	2.Ø7	15	63	1.3	Ø.Ø2	Ø.1	Ø.1	AA
Jan 15	Ø25 16.49	37 38.27	118 56.14	3.91	2.42	15	61	Ø.9	Ø.Ø5	Ø.2	Ø.2	AA
Jan 13	2249 42.87	37 38.Ø5	118 55.16	4.31	2.54	15	65	Ø.7	Ø.Ø3	Ø.2	Ø.2	AA
Jan 13	731 59.52	37 38.19	118 56.38	4.47	2.43	13	1ØØ	1.8	Ø.Ø4	Ø.2	Ø.3	AB
Jan 15	1952 53.61	37 38.35	118 56.37	5.ØØ	2.82	16	62	1.1	Ø.Ø4	Ø.2	Ø.3	AA
Jan 13	438 12.4Ø	37 38.38	118 56.Ø6	5.Ø4	1.52	1Ø	63	1.3	Ø.Ø2	Ø.2	Ø.2	AA
Jan 15	2316 2.16	37 38.24	118 56.51	5.19	2.4Ø	16	63	Ø.9	Ø.Ø4	Ø.2	Ø.3	AA
Jan 15	1337 25.Ø9	37 38.28	118 56.83	6.Ø5	1.55	1Ø	74	1.3	Ø.Ø3	Ø.3	Ø.5	AA
Jan 16	ØØ8 51.35	37 38.29	118 55.63	6.18	2.45	16	61	Ø.7	Ø.Ø4	Ø.2	Ø.2	AA
Jan 29	15Ø6 Ø.68	37 38.29	118 55.89	7.75	3.24	1Ø	65	3.Ø	Ø.Ø3	Ø.3	Ø.4	AA
Jan 13	849 5Ø.79	37 37.15	118 51.11	1.51	1.99	9	117	2.6	Ø.Ø3	Ø.2	Ø.2	AB
Jan 13	4Ø3 21.63	37 37.35	118 52.78	4.25	1.8Ø	1Ø	121	3.5	Ø.Ø2	Ø.1	Ø.3	AB
Jan 14	2311 2Ø.78	37 37.48	118 52.42	5.Ø3	1.55	1Ø	116	3.7	Ø.Ø3	Ø.2	Ø.5	AB
Jan 13	739 57.36	37 37.29	118 51.67	5.11	2.Ø3	8	119	3.Ø	Ø.Ø1	Ø.1	Ø.3	AB
Jan 13	357 55.13	37 36.85	118 51.93	5.42	1.59	1Ø	139	3.8	Ø.Ø3	Ø.3	Ø.7	AC
Jan 13	1259 58.84	37 37.64	118 53.Ø9	5.66	1.66	1Ø	1Ø8	3.3	Ø.Ø2	Ø.1	Ø.3	AB
Jan 12	652 52.42	37 37.5Ø	118 52.56	7.4Ø	2.ØØ	1Ø	115	3.9	Ø.Ø3	Ø.3	Ø.5	AB

ORIGIN TIME is in hours, minutes, and seconds. LATITUDE and LONGITUDE are in degrees and minutes. MAG is the coda magnitude of the earthquake (Lee et al.,1972); N is the number of stations used in locating the earthquake; the GAP is the largest azimuthal separation between stations; DMIN is the epicentral distance to the nearest station; RMS is the root-mean-square error of the travel-time residuals; ERH and ERZ are the standard errors in horizontal distance and depth, respectively (Lee and Lahr,1975).

Q is the solution quality of the hypocenter (given as two letters) based on both the statistical measure of the solution and the nature of the station distribution with respect to the earthquake. Each of these two factors is rated independently according to the following scheme. For the statistical measure (first letter), for A: RMS < Ø.15, ERH < 1.Ø, and ERZ < 2.Ø. For B: RMS <Ø.3Ø, ERH < 2.5, and ERZ < 5.Ø. For C: RMS <Ø.5Ø, and ERH < 5.Ø. For the station distribution (second letter), for A: N > 6, GAP < 9Ø, and DMIN < DEPTH or 5 km. For B: N > 6, GAP < 135, and DMIN < 2 times DEPTH or 1Ø km. For C: N > 6, GAP < 18Ø, and DMIN < 5Ø.

The upper group of locations are for the mechanisms shown in Figure 4a; the lower group of locations are the individual earthquakes used to make the composite mechanism shown in Figure 4b.

Table 3. Observed line length changes July 1982 to July 1983 and residuals (O-C) for the two models in Figure 11.

		Length km	ΔL mm	σ mm	O-C, mm Figure 11a	O-C, mm Figure 11b
Bald	Casa	15.5	46	6	0	8
	Glass	17.0	11	6	- 2	- 3
	Laurel	22.6	29	8	12	11
	Mammoth	20.6	31	7	4	- 3
	Mono	14.0	1	6	14	14
Banner	Glass	14.1	0	6	0	0
	Laurel	30.6	25	10	16	10
	Sherwin	23.9	-8	8	-11	-12
Casa	Convict	8.2	-32	5	-15	-18
	Glass	22.1	-4	8	- 4	- 1
	Laurel	7.2	-33	5	- 2	-11
Convict	Laurel	8.2	36	5	14	6
Glass	Mono	28.7	24	9	14	14
	Horse	24.4	5	8	7	8
	Laurel	27.0	29	9	15	9
	Mammoth	32.8	11	10	-12	-22
	Sherwin	30.3	-4	10	-13	14
Horse	Mono	20.7	-8	7	-10	-10
Laurel	Mammoth	13.7	-7	6	- 3	- 4
	Sherwin	20.2	10	7	0	- 3
Mammoth	Mono	27.6	6	9	- 2	- 4

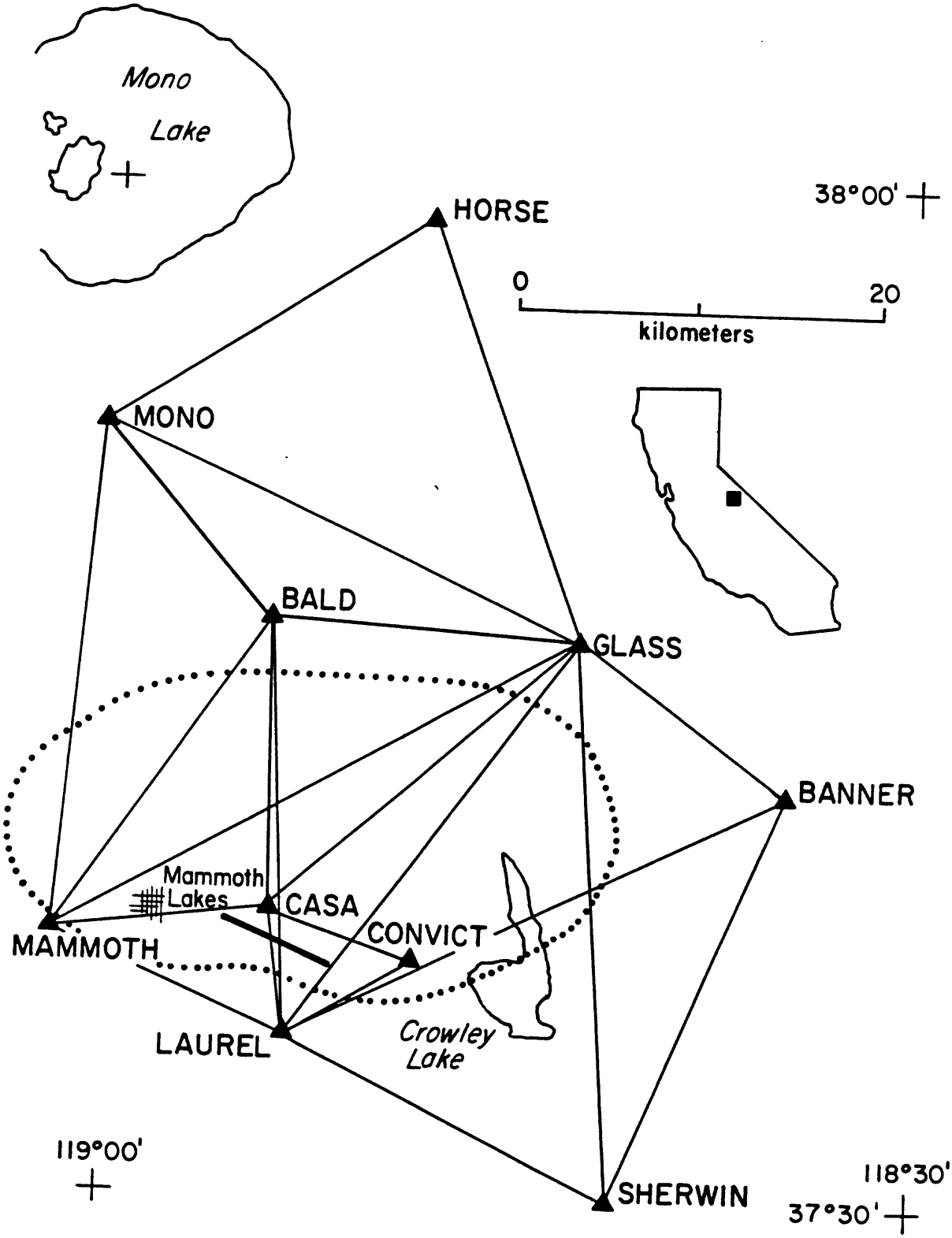
Mono
Lake
38°00'
HORSE
0
20
kilometers
MONO
BALD
GLASS
BANNER
Mammoth
Lakes
CASA
CONVICT
MAMMOTH
LAUREL
Crowley
Lake
119°00'
SHERWIN
118°30'
37°30'

Figure 1

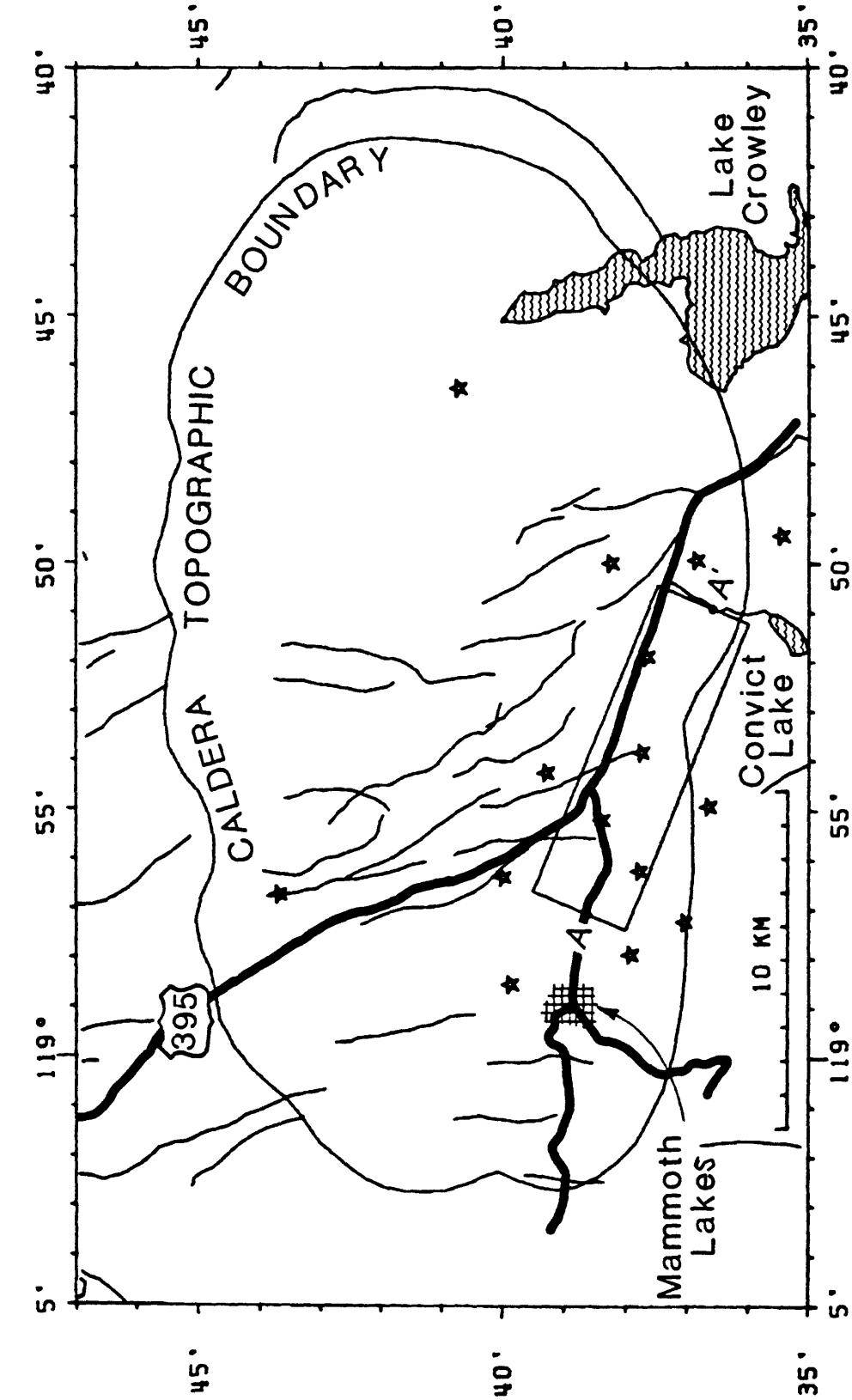
CALDERA TOPOGRAPHIC BOUNDARY
Lake Crowley
Convict Lake
Mammoth Lakes
395
A
A'
10 KM
40'
45'
50'
55'
5'
119°
35'

Figure 2a

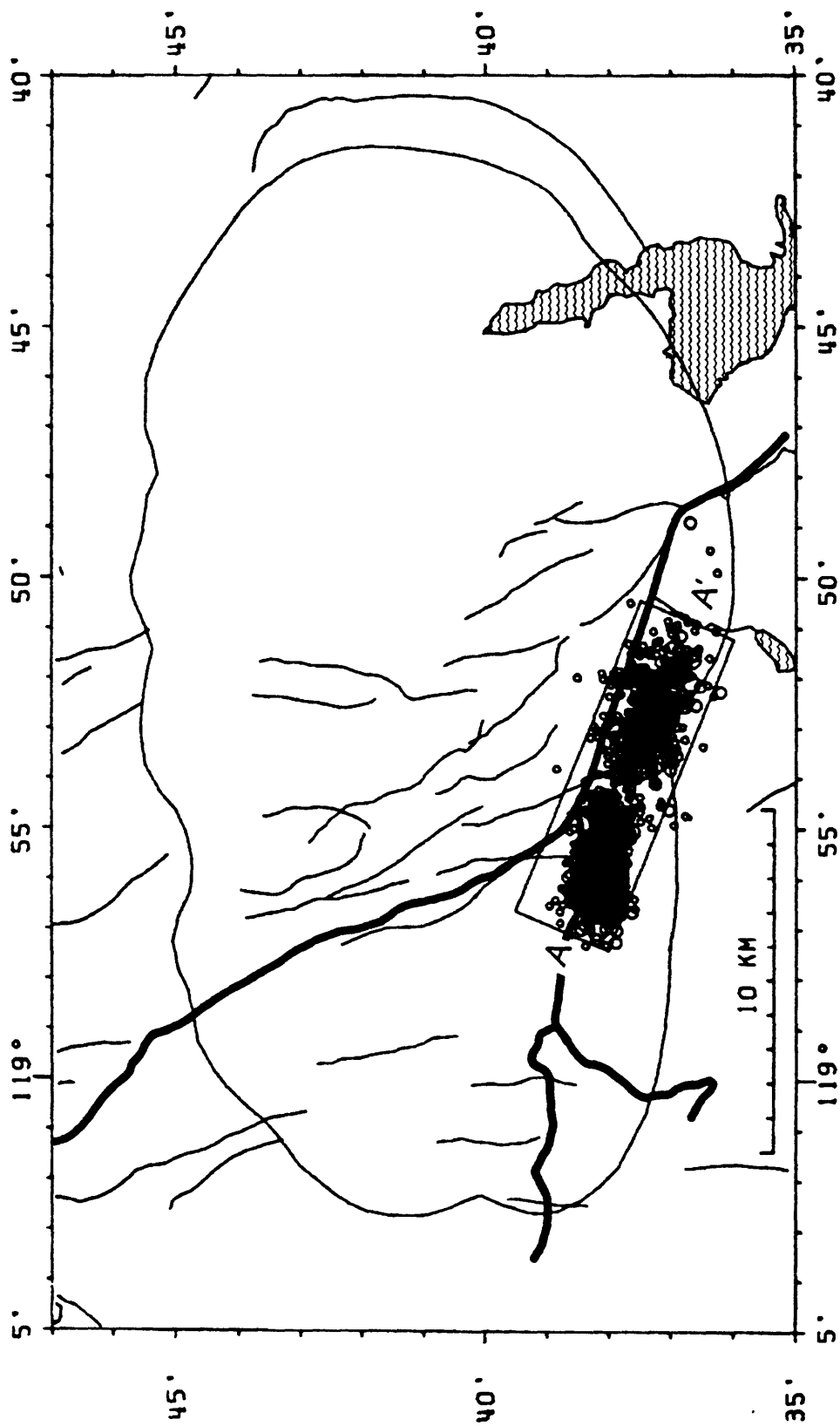

Figure 2b

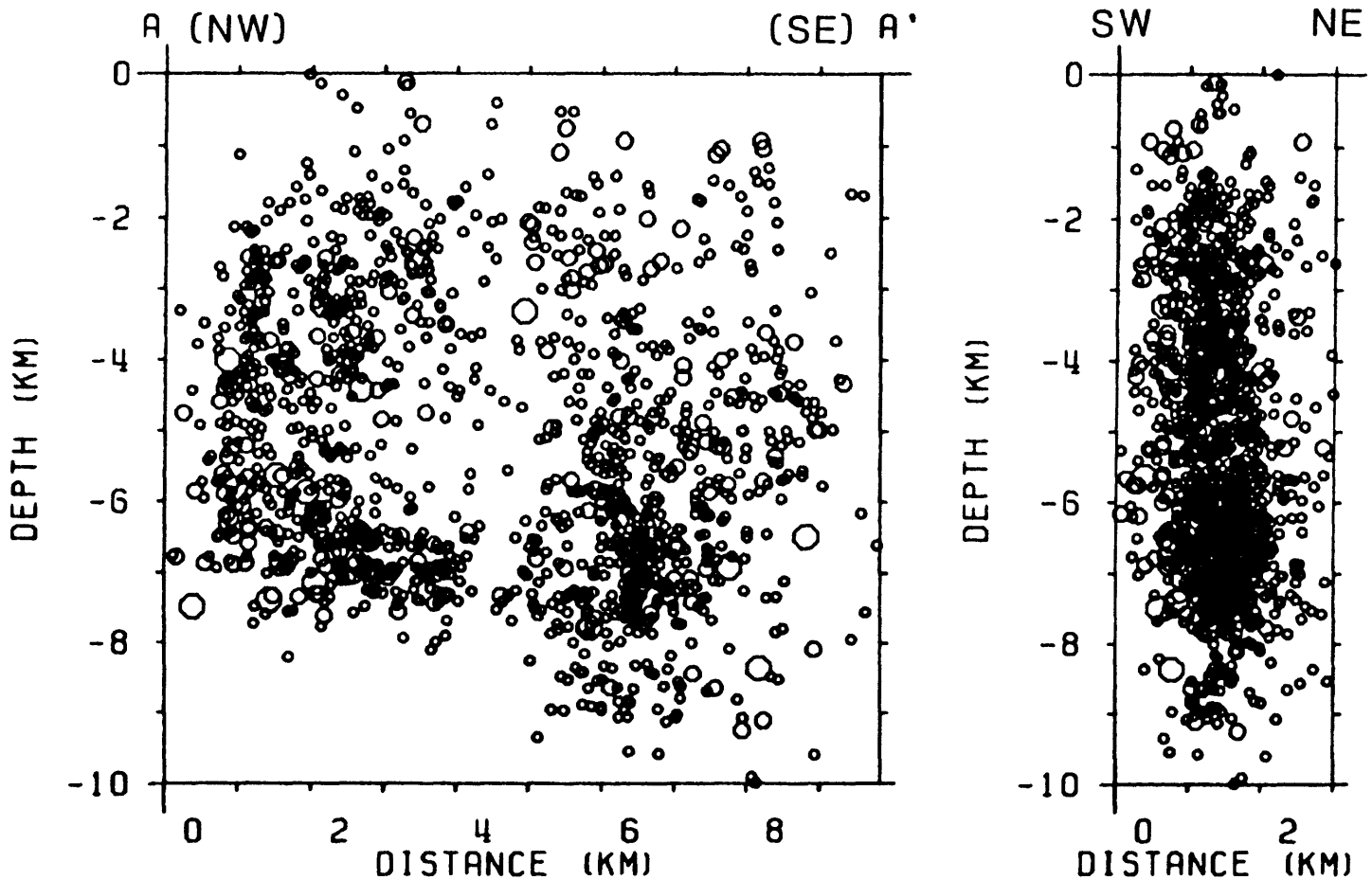
A (NW)
(SE) A'
0
-2
-4
-6
-8
-10
DEPTH (KM)
0
2
4
6
8
DISTANCE (KM)
SW
NE
0
-2
-4
-6
-8
-10
DEPTH (KM)
0
2
DISTANCE (KM)

Figure 3

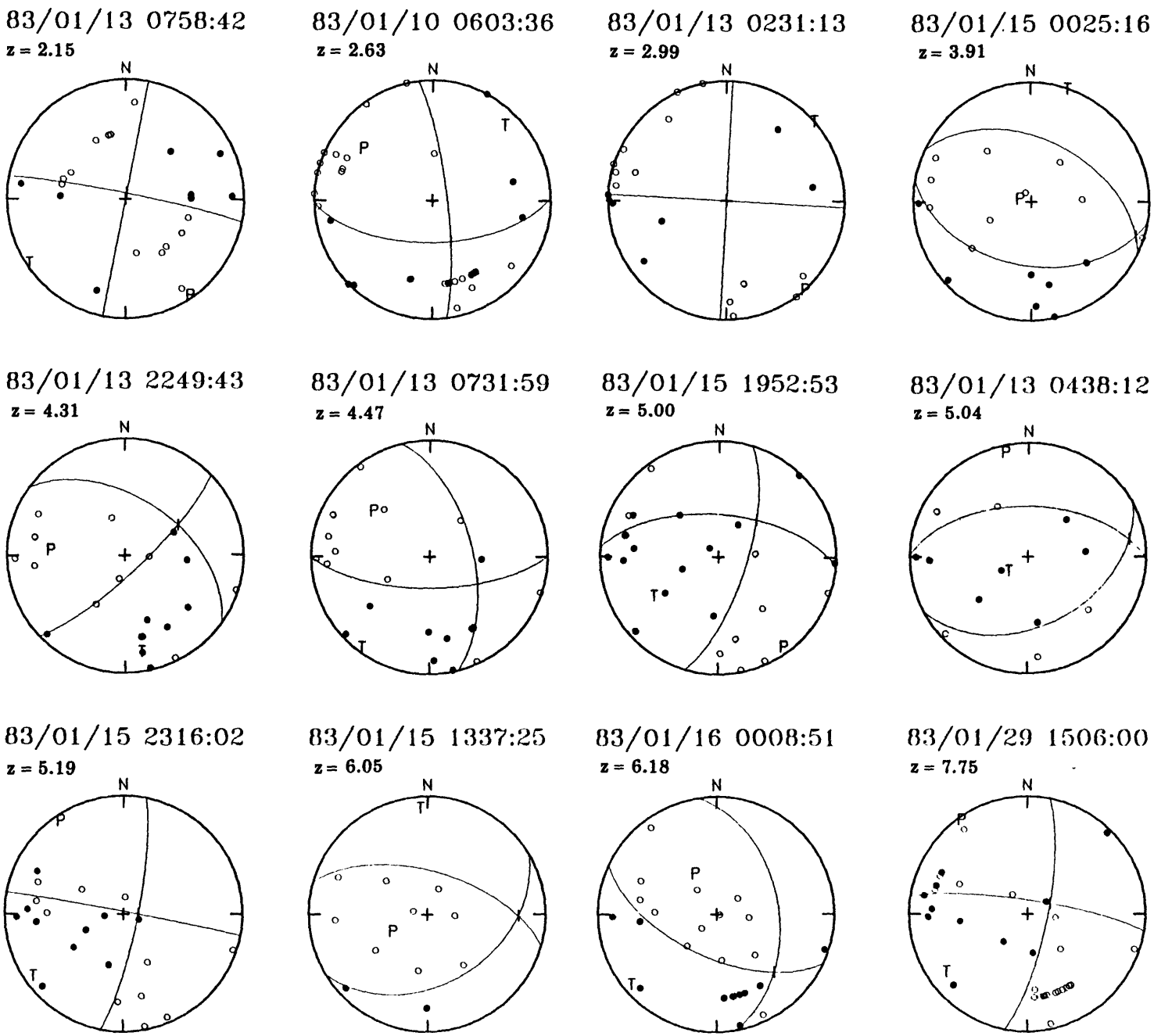
83/01/13 0758:42
z = 2.15
83/01/10 0603:36
z = 2.63
83/01/13 0231:13
z = 2.99
83/01/15 0025:16
z = 3.91
83/01/13 2249:43
z = 4.31
83/01/13 0731:59
z = 4.47
83/01/15 1952:53
z = 5.00
83/01/13 0438:12
z = 5.04
83/01/15 2316:02
z = 5.19
83/01/15 1337:25
z = 6.05
83/01/16 0008:51
z = 6.18
83/01/29 1506:00
z = 7.75
N
P
T

Figure 4a

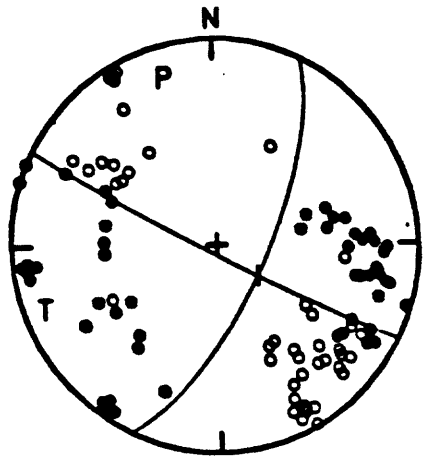

Figure 4b

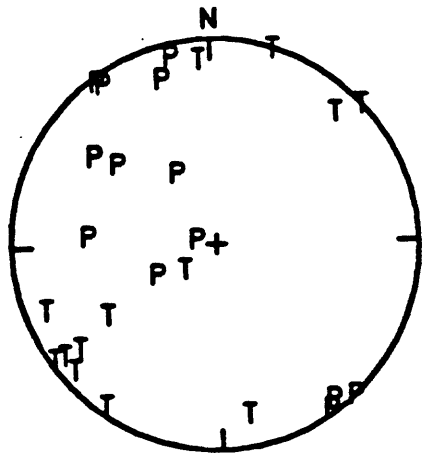

Figure 4c

Figures 4b and 4c

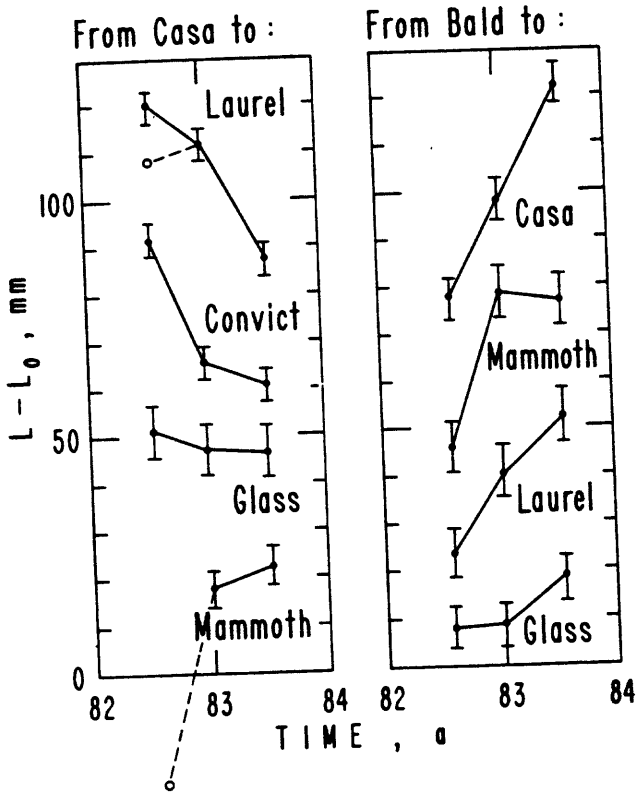
From Casa to :
From Bald to :
Laurel
Convict
Glass
Mammoth
Casa
Mammoth
Laurel
Glass
100
50
0
L - L0 , mm
82
83
84
TIME , a

Figure 5

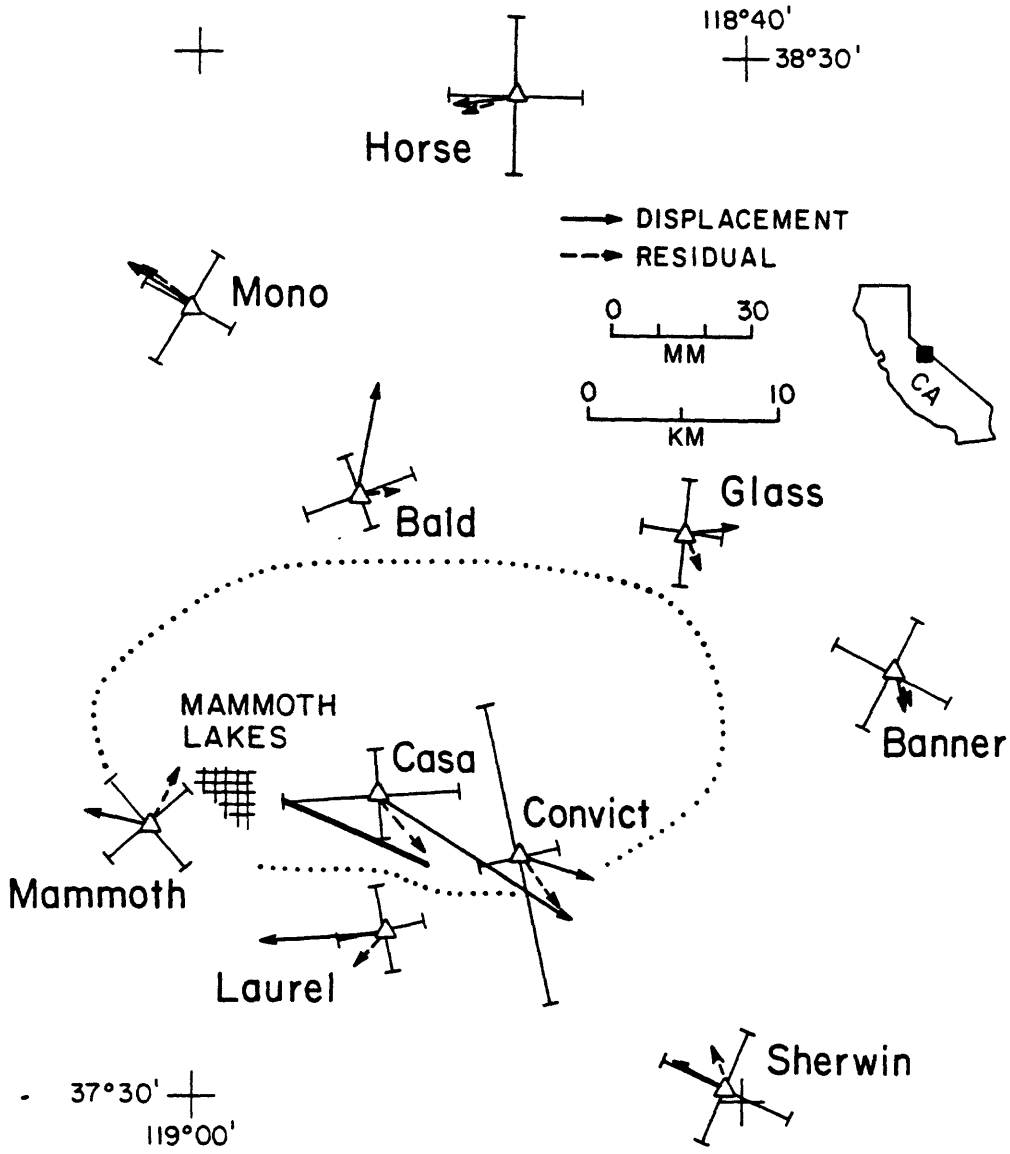
118°40'
38°30'
Horse
DISPLACEMENT
RESIDUAL
Mono
0
30
MM
0
10
KM
CA
Bald
Glass
Banner
MAMMOTH
LAKES
Casa
Convict
Mammoth
Laurel
Sherwin
37°30'
119°00'
1982-1983

Figure 6

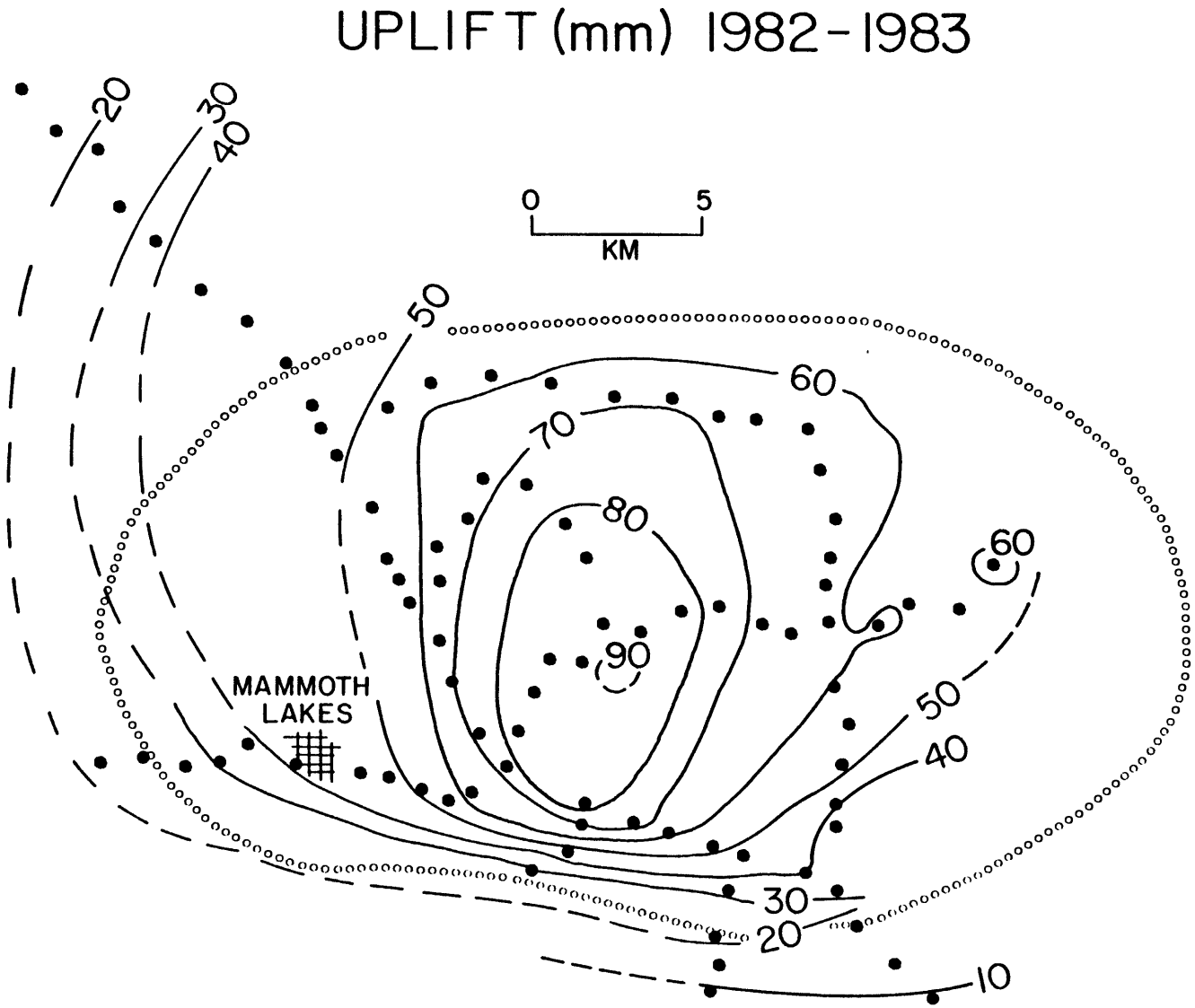
UPLIFT (mm) 1982-1983
0
5
KM
MAMMOTH
LAKES
10
20
30
40
50
60
70
80
90

Figure 7

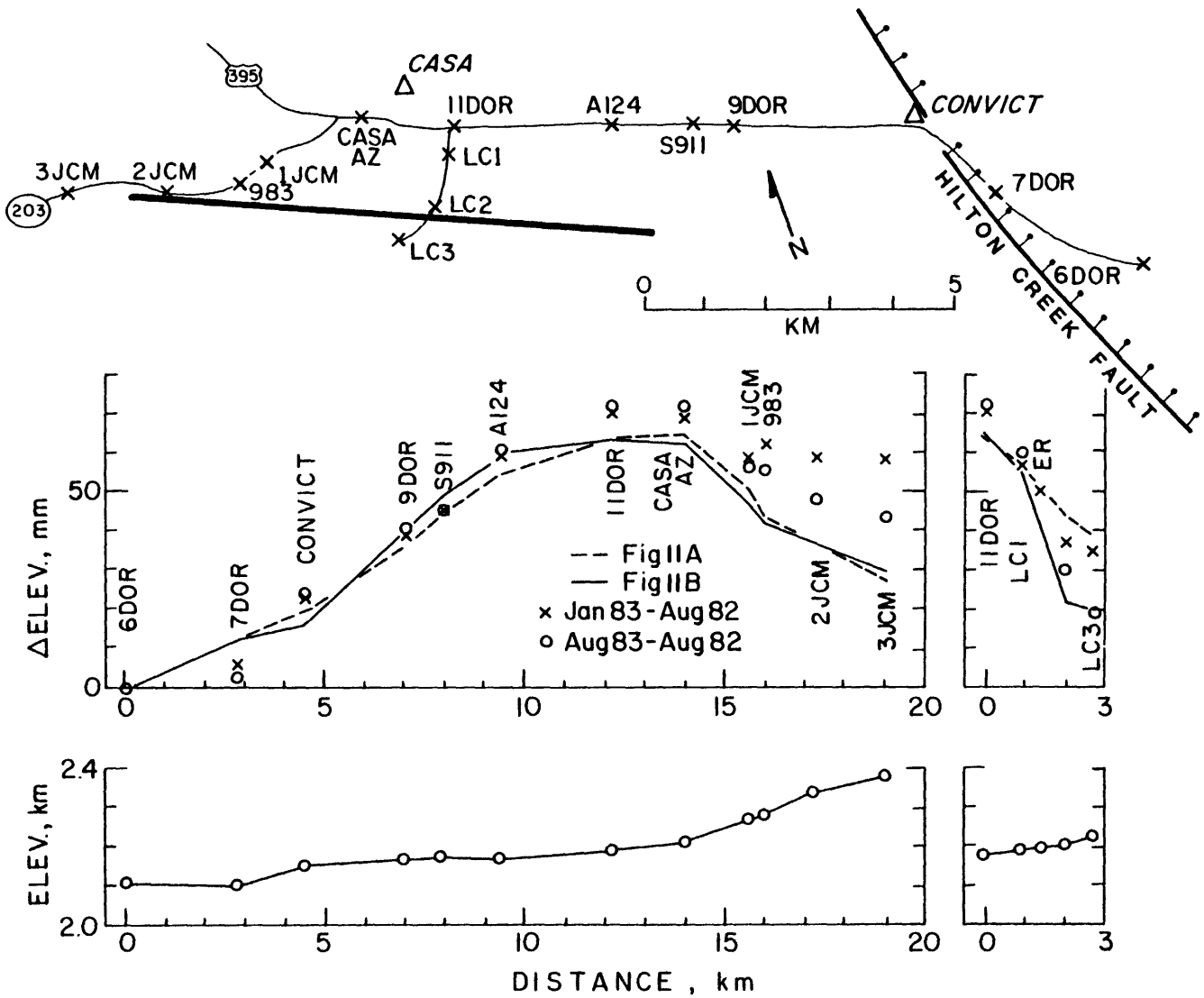
CASA
395
11DOR
A124
9DOR
CONVICT
CASA AZ
LC1
S911
3JCM
2JCM
1JCM
983
LC2
LC3
203
N
0
5
KM
7DOR
HILTON CREEK FAULT
6DOR
ΔELEV., mm
50
0
6DOR
7DOR
CONVICT
9DOR
S911
A124
11DOR
CASA AZ
1JCM
983
2JCM
3JCM
Fig11A
Fig11B
Jan83-Aug82
Aug83-Aug82
0
5
10
15
20
11DOR
LC1
ER
LC3
0
3
ELEV., km
2.4
2.0
DISTANCE , km

Figure 8

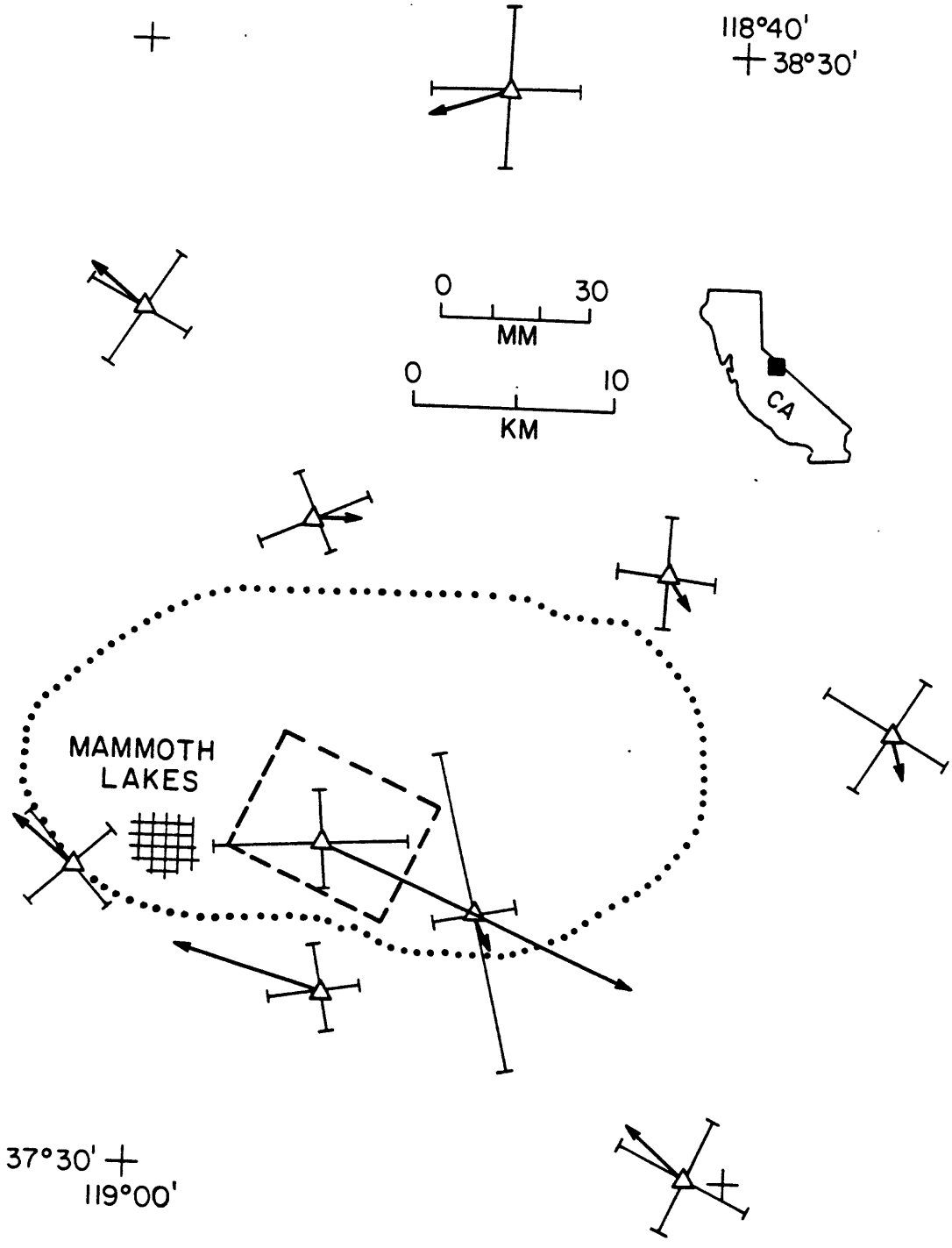

Figure 9

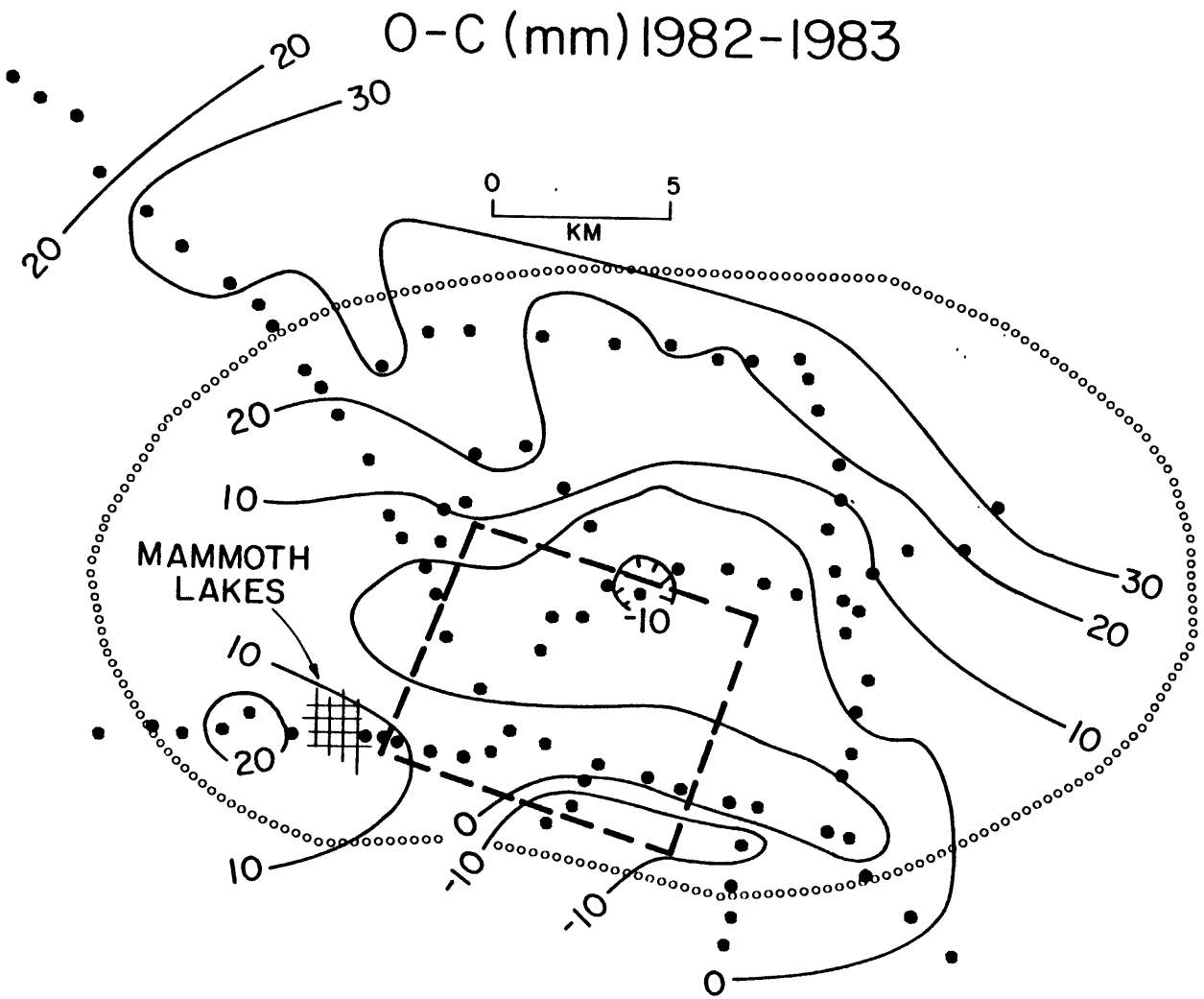
O-C (mm) 1982-1983
0
5
KM
MAMMOTH
LAKES
20
30
20
10
10
-10
30
20
10
20
10
0
-10
-10
0

Figure 10

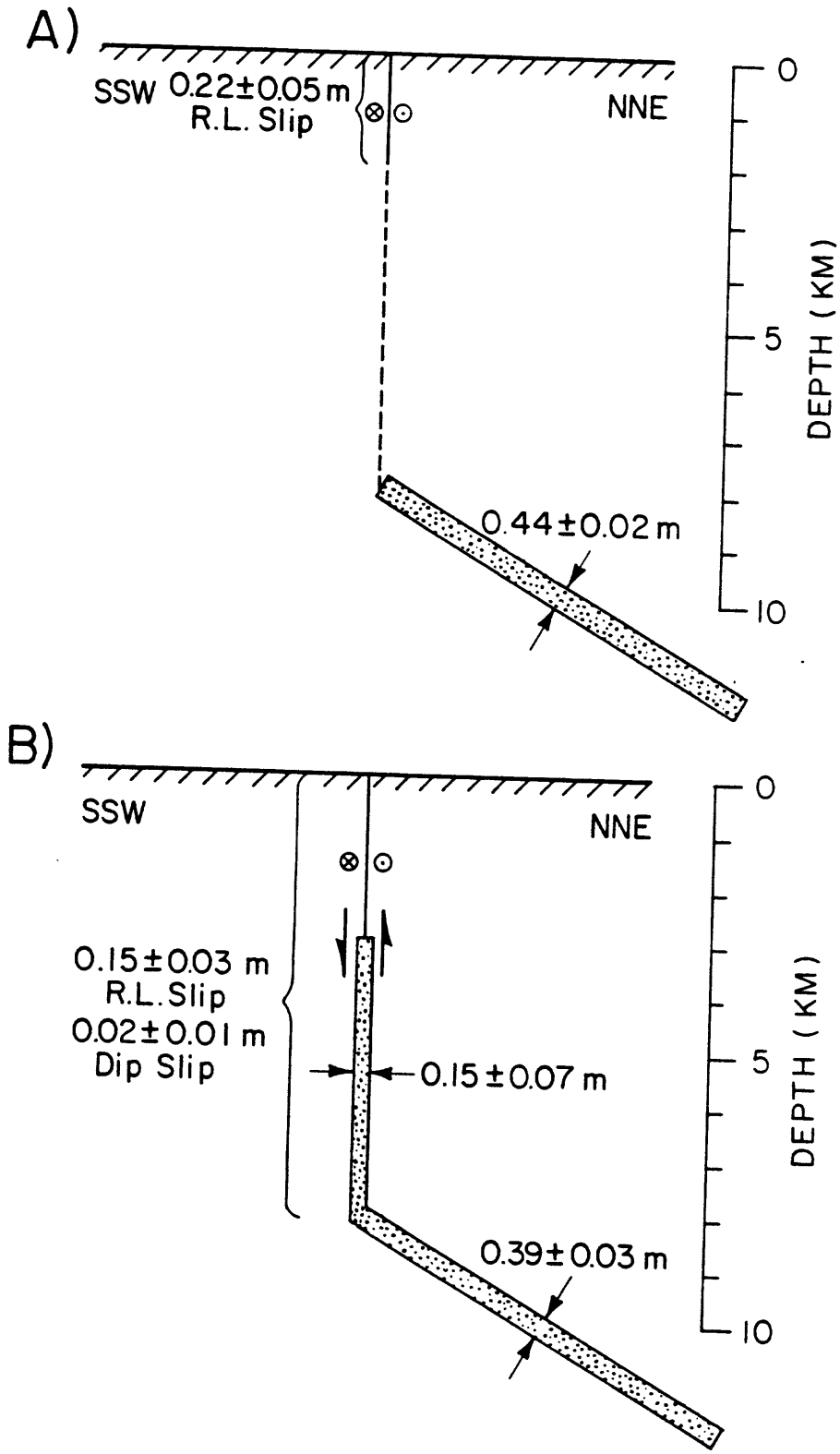
A)
SSW
0.22±0.05 m
R.L. Slip
NNE
0
5
10
DEPTH (KM)
0.44±0.02 m
B)
SSW
NNE
0.15±0.03 m
R.L. Slip
0.02±0.01 m
Dip Slip
0.15±0.07 m
0.39±0.03 m
0
5
10
DEPTH (KM)

Figure 11

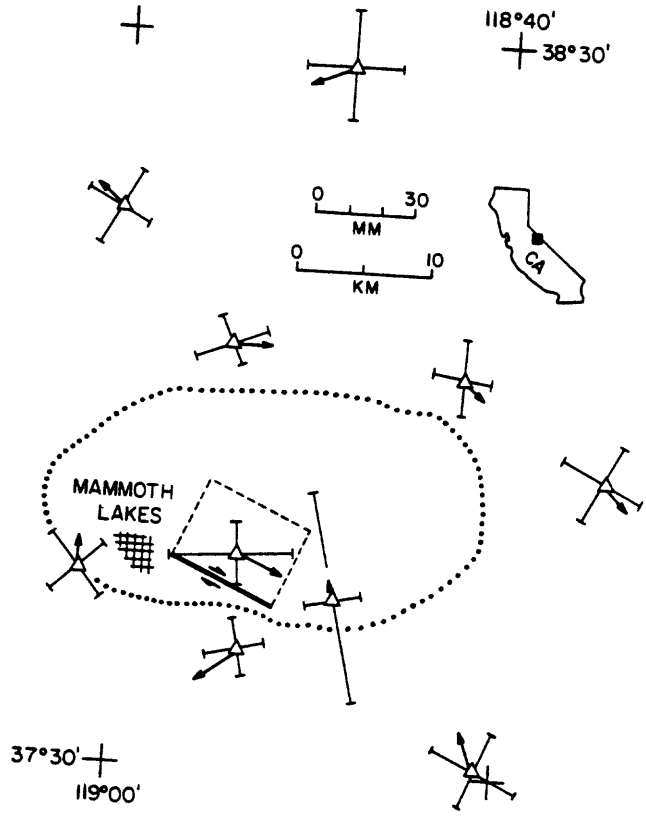

Figure 12

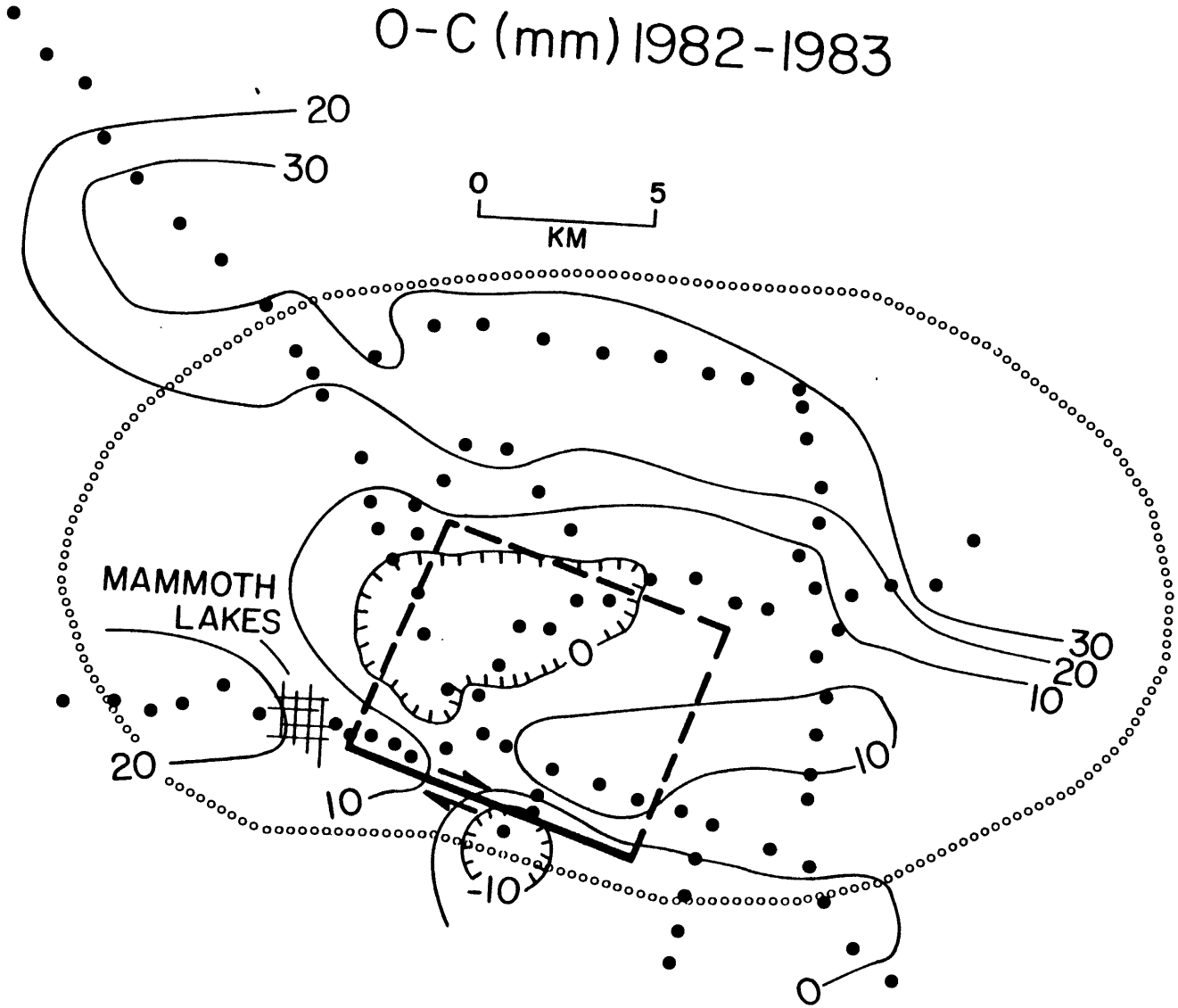

Figure 13

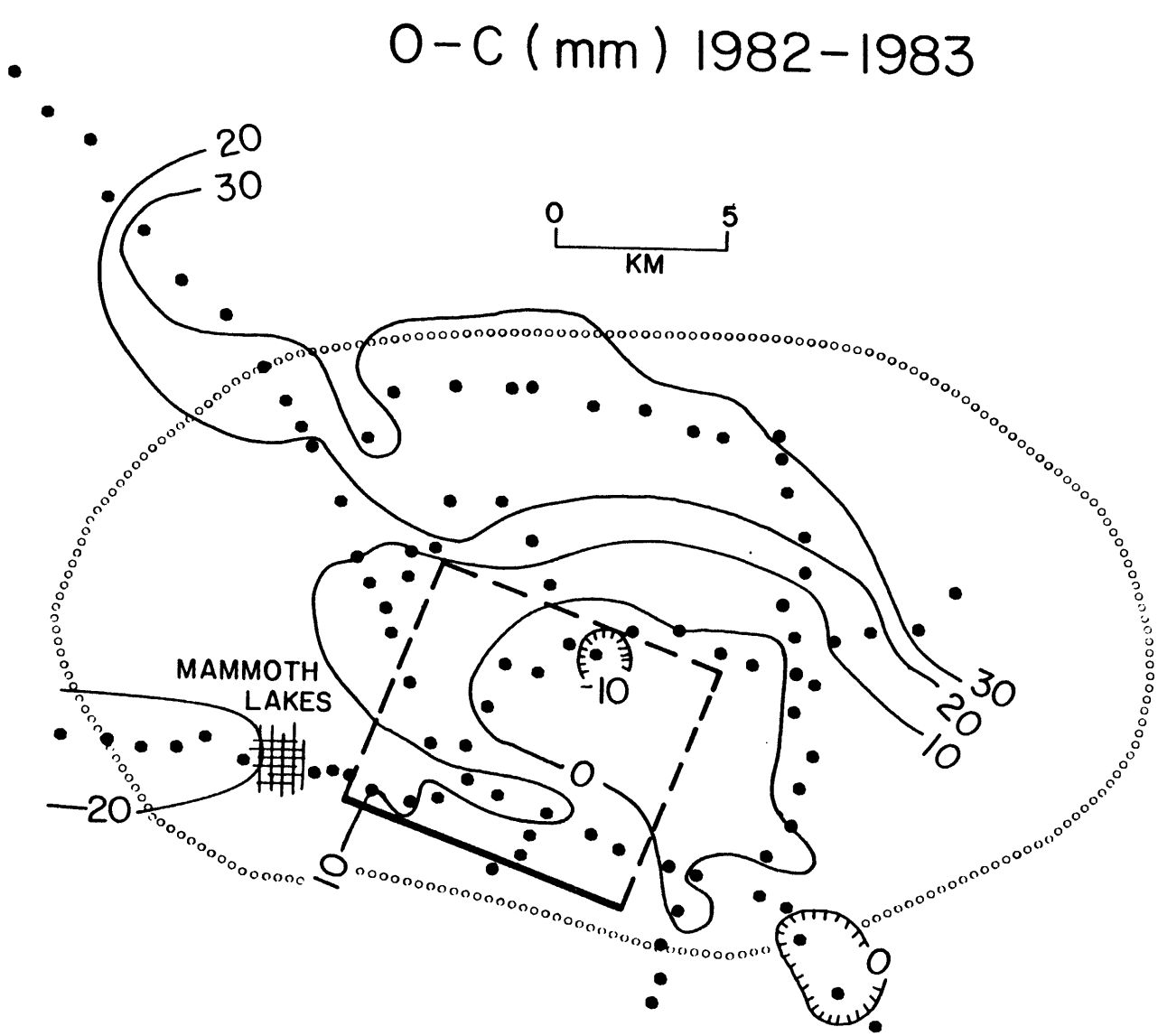

Figure 14

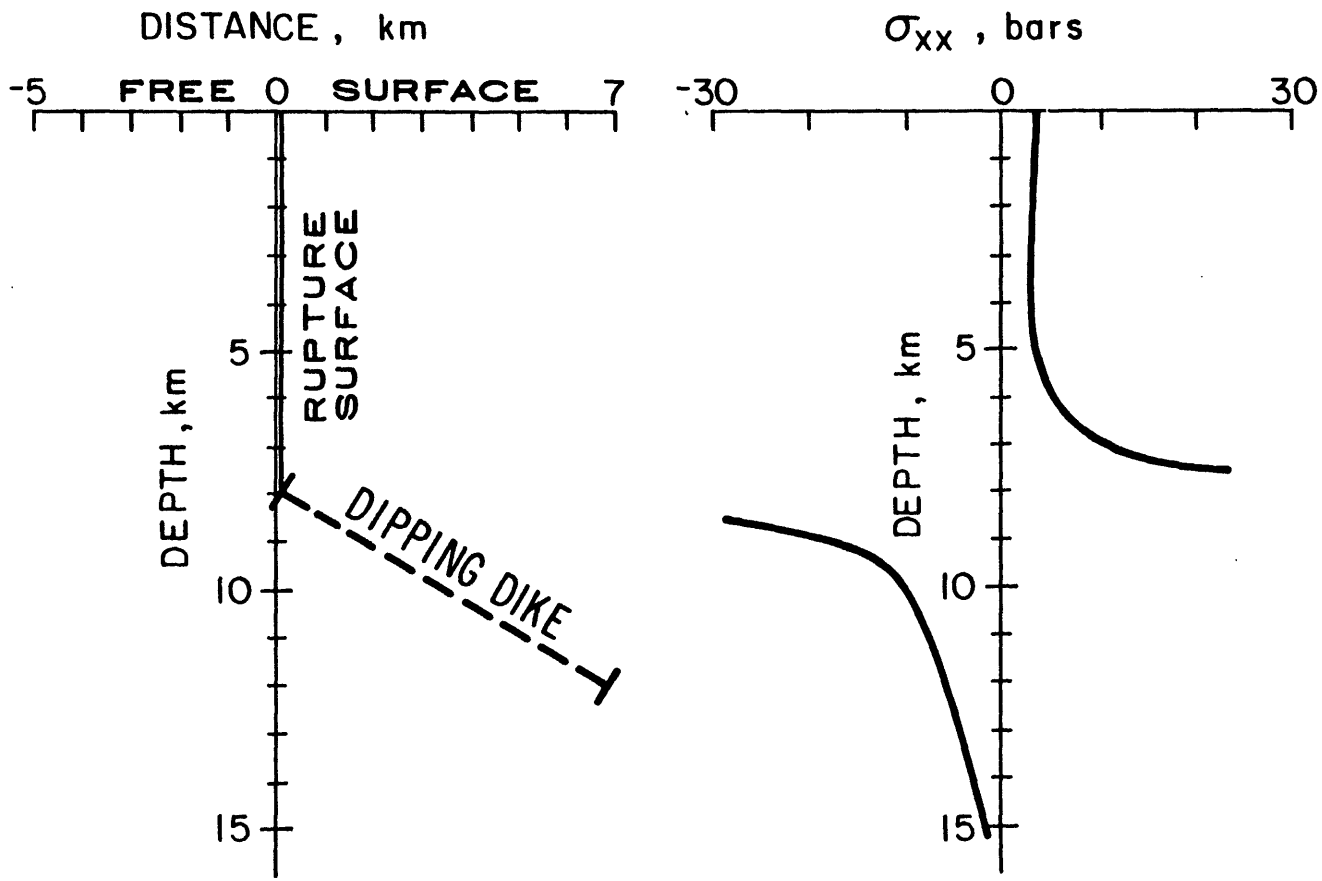
DISTANCE , km
-5
FREE
0
SURFACE
7
RUPTURE SURFACE
DEPTH, km
5
10
15
DIPPING DIKE
σ_{xx} , bars
-30
0
30
DEPTH, km
5
10
15

Figure 15

*A Model for Deformation in Long Valley, California, 1980-1983**

John B. Rundle
Geophysics Division 1541
Sandia National Laboratories
Albuquerque, New Mexico 87185

James H. Whitcomb
University of Colorado
Boulder, Colorado 80302

ABSTRACT

Geodetic data collected in Long Valley, California, from 1975 through 1983 define a pattern of uplift and strain which is evidently associated with a sequence of earthquakes occurring in May, 1980, and subsequent swarm activity continuing until the present. We have constructed a model to explain the deformation observed since May, 1980, in terms of inflation of two subsurface magma chambers, faulting in the south moat region of the caldera on a graben structure, and slip on the Hilton Creek fault. The most significant new feature of the model is the shallow magma chamber, at 5 km depth, located a few hundred meters to the east of the Casa Diablo hot spring area. Inflation of this chamber causes stresses which show consistency with various aspects of the seismicity in the south moat of the caldera. Calculations of stress across vertical planes over the magma chamber can be used together with failure criteria to estimate the inflation volume at which the rock layers intervening between the chamber and the surface will fail by extensional fracture.

* **This work performed at Sandia National Laboratories supported by the U.S. Department of Energy under contract number DE-AC04-76DP00789.**

1. Introduction

In May, 1980, an unusual sequence of earthquakes occurred in Long Valley, California, involving four events with local magnetude M_L of 6 or greater (figure 1). Three of the events occurred a few km west of the Hilton Creek fault, and were characterized by focal mechanisms involving NE-SW tension (Cramer and Toppozada, 1980). The other event occurred in or near the south moat of the caldera, and also involved NE-SW tension. All events had local first motions which suggested strike slip, and all followed a history of recent activity which suggested that these events may have had precursors (Ryall and Ryall, 1980), and that they may have been related to magma injection at depth (Ryall and Ryall, 1983). A leveling survey conducted after the events during the summer of 1980 along highway 395, from Tom's place to Crestview (figures 2,3), revealed the existence of substantial uplift, reaching as much as 25 cm, and occurring presumably at the time of the earthquakes (Savage *et al.*, 1983). Geodolite data (Savage and Clark, 1982) was also obtained which spanned the time period during which the events took place, from 1979 to summer, 1980. Modeling of these data by Savage and Clark(1982) demonstrated that, while the uplift data could be fit rather well by a deformation model involving inflation of a magma chamber at 11 km depth underneath the old resurgent dome of Long Valley caldera, the horizontal strain data could not be fit as well. The worst misfit occurred on the line Laurel-Glass, where the model predicted a line length change of about 125 mm, compared to the observed change of 52 mm. The other length changes generally compared more favorably to the observations.

Subsequent analysis of seismic data by Ryall and Ryall (1981) suggested that a zone of highly attenuating material lay at relatively shallow depth in the south moat region. Using raypaths that they judged to be either normal or anomalous, depending on the character of the S-wave energy in the waveform, Ryall and Ryall (1981) concluded that magma existed in Long Valley at depths as shallow as 7-8 km, in the south central part of the caldera. More recent analysis of 1200 raypaths by Sanders (1983) has delineated two major zones of high attenuation, presumably magmatic intrusions, located in the northwest and south-central part of Long Valley. Depth to the latter intrusion is as shallow as 4.5 km, just to the east of Casa Diablo hot springs. Depths to the more northerly intrusion, where Hill (1976) observed an anomalous reflection in a seismic refraction experiment, possibly from a low velocity reflector at 7-8 km, are as shallow as 5.5 km.

Following the events of May, 1980, swarm activity continued in the south moat area and near it, with events showing a slight trend toward shallower hypocentral depths with time. Leveling data obtained during the summer of 1982, although possibly contaminated by survey error (Savage *et al.*, 1983; figure

3) showed that uplift had continued in association with the swarm activity during the years 1980-1982. Then, on January 7, 1983 a major swarm occurred which included two moderate events, one of magnetude 5.3, and one of magnetude 5.6 (Pitt and Cockerham, 1983), with all events contained at first in a tightly defined, elongate zone in the south moat (figure 2). Focal mechanisms of these events were much the same as those found for the major events of May, 1980, involving strike slip with tension axis oriented NE-SW. Shortly after the major events, the Los Angeles Department of Water and Power ran a second order leveling survey from benchmark 6DOR just east of the Hilton Creek fault, to benchmark 3JCM at the Forest Service Visitor Center in Mammoth Lakes, and from 11DOR near the sheriff's substation up Laurel Canyon to benchmark LC3 (figure 2). This survey, when referenced to the (possibly contaminated) survey of September, 1982, showed an uplift of 70 mm of benchmark 11DOR relative to 6DOR. A subsequent first order survey completed in September, 1983 (figure 3) confirms the existence of the uplift. Figure 4 is a composite of the leveling profile, with the uplift from 6DOR to CASA AZ observed in September, 1983 joined to the profile into Mammoth Lakes which was observed in January, 1983. A composite profile has been used because we feel that it is best to use first order, double run leveling where possible. Figure 4 also shows the line from 11DOR to LC3 which was measured in January, 1983. Strain data collected in January and in July also show significant changes, which have been modeled using both right lateral strike slip on a WNW oriented fault in the south moat, as well as an additional component of extension, due to dike formation, across the fault plane (Savage and Cockerham, 1983).

In evaluating the quality of the fit of models that have been proposed to date to explain the geodetic data, we feel that some improvement is possible. For example, although the fit to the 1980-1975 leveling data shown in Savage and Clark (1982) is good, the large misfit of the model to the line Laurel-Glass causes us concern. Moreover, the model for the events of January, 1983 shown in Savage and Cockerham (1983) ignores the (possibly contaminated) leveling data, but since the uplift from both a strike slip fault and a vertical dike in the south moat would produce little uplift, it seems unlikely that the model could fit a leveling data set which is more or less symmetric about the Casa Diablo area. Finally, the model shown in Savage *et al.* (1983) is for the 1983-1975 period for which no continuous strain data are evidently available. We feel that it would be very desirable, therefore, to construct a model which is capable of fitting the geodetic data epoch by epoch, so to speak, when both uplift and strain data are simultaneously available. In this way, we feel that stronger constraints can be placed on the deformation mechanisms. The ultimate goal of such a modeling

effort is to understand, if possible, the relationship between the uplift and the faulting in the south moat. That these two phenomena occur together seems clear from both the events of 1980 and 1983.

2. Model

Figure 5 shows the elements of the model, which are held constant for all epochs. A magma chamber at 9 km depth is the northernmost feature. Expansion of this chamber is principally responsible for the uplift that was observed in 1980. A second, shallower chamber at 5 km depth is shown near the Casa Diablo hot spring area. The locations of both chambers are consistent with the locations of high S-wave attenuating regions found recently by Sanders(1983). Expansion of this chamber is primarily responsible for the uplift that occurred in January, 1983. As is customarily the case in analyses of this type, we employ dislocation theory to represent the displacements due to expanding spherical cavities (the magma chambers), and so the solid circles represent the center of the chambers. The applicable dislocation is the amount of volume change; the radius of the chamber plays no role in the calculation (see for example Rundle, 1978). The remaining deformation-causing features in the model are faults in the south moat and an idealized fault whose surface expression coincides with the Hilton Creek fault trace. The faults in the south moat form, in our model, a graben-like feature, that is to say, faulting with the included block subsiding. The northern boundary of the graben we call the South Moat fault; the southern boundary we call the Caldera Boundary fault. In addition to vertical motion on the South Moat fault, we also admit the possibility of right lateral strike slip. The Hilton Creek fault we assume to be capable of both normal and left lateral strike slip motion.

We note that the faults used in the model are all assumed to be vertical faults. In the case of the south moat graben faults, there is some justification for assuming this, given the essentially vertical distribution of the seismicity there (see Savage and Cockerham, 1983). The Hilton Creek fault was also assumed vertical for simplicity, although the data fits could almost certainly be improved by choosing a non zero dip angle, that is to say, allowing for more flexibility in fitting the model to the data. As we will show, the inflating magma chambers produce a stress field which drives the right lateral and normal faulting in the south moat, and which drives both left lateral and normal faulting on the Hilton Creek fault. Hence, from a mechanistic point of view, the faulting and seismicity appear to be driven by the injection of magma, which is the predominant cause of the uplift.

In fitting the uplift data, we choose to fix benchmark 6DOR near McGee Creek. Examination of uplift data given in figure 3 shows that there is no uplift between Tom's Place and 6DOR to within the accuracy of the data. Moreover, since the epochs examined in detail are 1979 to September 1980, September 1982 to January 1983, January 1983 to September 1983, and September 1980

to September 1983, we do not use any of the benchmarks north of Crestview. Obviously, the 1980 survey was only a partial survey, from Tom's Place to Crestview, so epochs involving 1980 are of necessity truncated. However, as figure 3 shows, the uplift north of Crestview decreases monotonically, and since there are only 4-5 more benchmarks at which uplift is significantly different from zero in the 1983 survey. The model, whose predicted uplift also decreases monotinically north of Crestview, would clearly not change appreciably were the (unknown) uplift at the rest of the benchmarks to be included. Also, epochs involving the 1982 survey suffer because of the apparent systematic error in that releveling (see Savage *et al.*, 1983 for a detailed discussion of these data). Hence, we have found it impossible to obtain satisfactory fits to the 1983-(unadjusted)September 1982 uplift if benchmarks north of CASA AZ are included in the data. However, by virtue of successful fits to the September 1980-1979 uplift and strain data, and fits to the September 1983-September 1980 uplift data, we feel confident that, were the 1982 profile adjusted artificially to give Lee Vining no elevation change relative to Tom's Place for 1982-1975, this data set could be fit within the confines of the model elements shown in figure 5.

Figures 6-10 show the fit of the models for the various epochs to the uplift and strain data. Given in the upper right hand corner are the root mean square (rms) residuals computed for the fits. With the exception of 1 benchmark in figure 6 (Convict, in the Hilton Creek fault zone); 1 line in figure 7 (Diablo-Chalfant); and 2 lines in figure 10 (Mono-Glass and Mammoth-Laurel), the model can be fit to the data quite well. All of the "reduced" residuals (rms values with the objectionable lines or benchmarks removed) are at or near the expected formal error of measurement. The dislocations and injected volumes can be discussed in terms of a chronology of tectonic activity:

- August,1979-September, 1980: A deep source underlying the caldera injected .066 km^3 into the deep chamber, and .0154 km^3 into the shallow chamber near Casa Diablo hot springs. Stresses generated by the expansion of these chambers (discussed below) in turn triggered faulting in the south moat and on the Hilton Creek fault. Dislocations on the Hilton Creek fault were 7 cm left lateral strike slip and 14 cm normal (west side up) slip, both from the surface to 6 km depth. Dislocations for the south moat fault were 2.5 m right lateral strike slip and 2 cm normal slip (north side up), from 2 to 8 km depth. Finally, normal slip amounting to 5.5 cm ocurred on the Caldera Boundary fault from 2 to 8 km depth (south side up).
- September, 1980-September, 1983: Over these three years, only uplift data is available, so it is only possible to constrain the amount of injected

magma and the vertical component of slip on the Hilton Creek fault. Injection into the deep chamber was .02 km^3, and into the shallow chamber, .012 km^3. Normal slip on the Hilton Creek fault (west side up) was about 3 cm from near the surface to 4 km depth, and about 17 cm from 4 km to 10 km. Slip on the Hilton Creek during this period must have been driven by after-effects of the 1980 events, as well as stress generated by the expanding magma chambers (discussed below).

- September, 1982-January, 1983: The deep chamber was inflated by .0025 km^3, the shallow chamber by .0085 km^3. The stress produced by these events drove right lateral strike slip faulting on the South Moat fault with a dislocation of 14 cm, extending from near the surface to 6 km depth. Additional normal slip (north side up) of 2.5 cm was also induced. Normal slip of about 4.5 cm (west side up) on the Hilton Creek fault, from 1 to 6 km depth was also driven by the injection, as well as 3 cm (south side up) on the Caldera Boundary fault. Note that figure 8, which shows the fit to the uplift data for this period, shows the most discrepancies along highway 203 into Mammoth Lakes. We have found that block normal faulting of several cm on a western extension of the South Moat fault can measurably improve the model fit here, but given the size of the residuals, this seems to be a needless refinement. We point out that the trend of the magma injection apparent in the three epochs discussed so far has been to partition progressively more of the magma into the shallow chamber near Casa Diablo, rather than into the deeper chamber.

- January, 1983-September, 1983: During this period of time, strike slip faulting on the South Moat fault continued, but on only the eastern portion of the fault, from B to C in figure 5, and at shallower depths, from near the surface to 4 km depth. The dislocation for this period is about 8.5 cm of right lateral slip. This pattern of slip can be understood as a delayed stress relaxation after-effect of the inflation event in January, since it is consistent with the result (discussed below) that not all of the stress produced by the injection event across the South Moat fault was relieved in the month or so following the injection.

The data fits summarized in figures 6-10 therefore provide a kind of logical chronology of the deformation events from 1979 to now. In order to understand these events mechanically, it is necessary to compute the stresses produced by both the inflation events and the faulting, and this we do in the next section. Computation of the stress distribution due to injection across material planes of various orientations in fact provides a series of tests of the model, since various qualitative and quantitative phenomena observed in Long Valley since the earthquake activity began can be checked for consistency with the predictions of the model.

3. Stress Calculations

As a first step, recall that the dilatation Δ due to a point center of dilatation is:

$$\Delta = \frac{\delta V}{4\pi}\left[\frac{4}{R^3} - \frac{6r^2}{R^5}\right] \tag{1}$$

where δV is the increment of volume change, r, z define a cylindrical polar coordinate system with z down, h is the source depth, and

$$R = \sqrt{r^2 + (z+h)^2} \tag{2}$$

(Rundle, 1978) . Equation (1) yields the result that the locus of zero dilatation is given by

$$r = \sqrt{2}(z+h). \tag{3}$$

Hence, for the magma chamber at Casa Diablo, the radius of zero dilatation is 7.1 km. Thus, for example, the south moat graben is within the radius defining extension.

Inserting appropriate values into (1) and multiplying by a bulk modulus of 5×10^5 bar gives 11 bar (extension) directly over the Casa Diablo chamber, and 6×10^{-3} bar (compression) at a location corresponding to Hot Creek, some 9 km away. Hence, expansion of the Casa Diablo chamber in January of 1983 could reasonably have caused the drop in water level seen in fumaroles near the intersection of highway 395 and 203 during the January events (Mark Clark, personal communication, 1983). The compressional stress calculated at Hot Creek is too small to have produced the mud geysering observed as well. However, right lateral slip on the South Moat fault would have produced perhaps 5 bars of extension at the Casa Diablo fumarole location, and about 1 bar of compression at Hot Creek (Chinnery, 1963). Stress from the Hilton Creek fault would have been smaller, because the Hot Creek fumaroles lie nearly on the nodal plane. Hence we conclude that both faulting and magma chamber inflation can produce extension at the intersection of highways 203 and 395, but only faulting in the south moat can reasonably produce compression and geysering at Hot Creek.

Let us now compute the normal and shear stresses on the plane $A-A'$ shown in figure 5, as a function of depth, using the expression for the displacements given, for example, in Rundle (1978). Using an average crustal value for the shear modulus of 3×10^5 bar, and a Poisson's ratio of .25, we obtain the contour plot

shown in figure 11. Plotted horizontally is distance from point A, and plotted vertically is depth, with values of stress contoured in bars. The upper part of the figure is the total normal stress, both that due to the inflating chamber, and the stress due to lithostatic pressure. Plotted below is the shear stress, with right lateral shear stress contoured in solid lines, and left lateral stress contoured in dashed. The extent of the fault plane used in modeling the surface displacements which occurred in January, 1983 is shown by the hatched rectangle. The value for the injected volume at Casa Diablo is that appropriate for the original 1980 inflation, .0154 km^3.

By far the most prominent feature on the normal stress plot is the existence of a large compressional stress "bull's eye" centered on the orthogonal projector from the magma chamber to the plane $A-A'$. The nodal line in the vertical plane for the inflation normal stress (***not*** total normal stress) is roughly a circle (actually an ellipse) about the center of the bull's eye, with a radius of about 2.2 km. From about 3 km to the surface, the inflating magma chamber produces extension across the vertical plane of about 10-20 bars, shown in the top of figure 11 by the fact that the zero stress line is actually at a depth 100-200 meters.

We believe that this prominent bull's eye is reflected in the seismicity observed in the south moat during the past year. Figure 12 shows a map view (Savage and Cockerham, 1983) of epicentral locations in Long Valley for events which occurred from January 7 to January 31, 1983. The box shows the events which are plotted in cross-sectional view in figure 13. The large cross and arrows in figure 12 indicate the location of the Casa Diablo magma chamber on the map. On figure 13, the arrows and cross indicate the location of the orthogonal projector from the magma chamber. As can be seen, the location of the projector is, within the accuracy of location of the events, coincident with the location of the center of the anomalous gap in seismicity. Since the azimuth of Savage and Cockerhams' plane $A-A'$ differs from the azimuth of the plane $A-A'$ in figure 3 by only 4°, we conclude that the inflating magma chamber is probably responsible for this feature of the seismicity. Evidently, this gap is a continuing feature of the seismicity now (R. Cockerham, personal communication, 1983), as we would expect from the fact that there has been no deflation up until now. Moreover, if inflation of the chamber continues, we would expect this gap to become even more prominent, and to move up or down should the center of the magma chamber move up or down. Generally, the seismicity should follow the motion of the magma, up or down.

The focal mechanisms reported by Savage and Cockerham (1983) can be summarized by the following: in the eastern part of the box shown in figure 12, events are relatively simple, being almost entirely right lateral strike slip

mechanisms. In the western part of the box, events are more complex, being a combination of right lateral and normal faulting mechanisms. The former mechanisms, in the eastern half, are certainly consistent with the shear stress generated by the magma chamber, as can be seen by examination of the lower part of figure 11. However, if the driving shear stress were only due to the magma chamber at Casa Diablo, then we would expect left lateral faulting instead of right lateral faulting to the west.

We cannot explain this discrepancy simply, but it is clear that there are other factors at work that serve to modify the shear stress from the simple pattern shown in figure 11. For example, calculation of the stress across the South Moat fault due to inflation for both the shallow and deep magma chambers in 1980 gives right lateral shear averaged over the fault plane of a few tens of bars. Yet the stress drop for a slip dislocation of 2.5 m over this size fault plane gives a stress drop of perhaps 200 or more bars. Hence, it seems clear that the 1980 event was triggered, in the sense that there must have been (and perhaps still is) a pre-existing right lateral shear stress field of significant size. Calculation of the stress field across the Hilton Creek fault due to the inflation events in 1980 yields a few bars of left lateral and normal stress, again too small for the size events indicated by the slip magnetude. Hence, we again conclude that significant shear stresses must have pre-existed in 1980. Moreover, it is clear that the deep chamber to the north of Casa Diablo contributes a right lateral shear stress across the entire profile $A-A'$ during an inflation event, although the magnetude is perhaps 10 bars at most near the surface for an inflation event of the size which occurred in 1980. Thus, there will be a bias of the average stress along the profile $A-A'$ toward right lateral shear and hence toward right lateral slip. The highest shear stresses, right lateral as well as left lateral, are effectively useless in promoting average slip due both to their mutual proximity and to the locking effect of the normal stress within the bull's eye. We believe that the lower shear stresses, more significantly affected by this right lateral bias, dominate. Thus the east half of $A-A'$ is induced to slip in a right lateral sense, and the west half in essence follows it.

Another possibility suggested by the model is that nearly aseismic slip on the eastern half of $A-A'$ in delayed response to the inflation of the Casa Diablo chamber is an ongoing feature of deformation in Long Valley, between episodes of sudden injection. This right lateral slip would have the effect of adding a significant component of right lateral shear stress to the western half of $A-A'$, and thus a right lateral "slip deficiency" would steadily accumulate there, as appears to be the case since January, 1983. This slip deficiency could then be filled by triggered slip during the next inflation event. Triggering of small events

on the western half by the ongoing slip on the eastern half could also account for the small magnetude swarms which are a regular feature of the seismicity in the western half (Ryall and Ryall, 1982).

Whatever the reason, we must regard the focal mechanisms as to some extent unexplained. The smaller magnetude shear stress field on the western half of the plane $A - A'$ probably enhances the relative importance of the normal stress component in the focal mechanisms there. Also, there ought to be more normal faulting in the eastern half of $A - A'$ at sufficiently shallow depths than has been observed. In any event, we anticipate that faulting in the eastern half of the box shown in figure 12 should have relatively simpler focal mechanisms than faulting in the western half of the box.

Finally, we note that the average inflation shear stress across the fault plane shown in figure 11 was about 30 bars for the injection event of January, 1983. However, the stress drop corresponding to a slip of 14 cm across the same fault plane was about 20 bars (Chinnery, 1963). Hence, there was a component of unrelieved shear stress left over, which was available to drive continued slip on the right portion of the fault plane. This feature of the model is therefore consistent with the result of continued right lateral slip on the eastern half of the fault plane, needed to fit the line length changes observed from January, 1983 to July, 1983.

4. Failure Analysis

Consistency between the model and aspects of the seismicity distribution prompt us to examine the model for information it may contain on the failure process for rock layers overlying the magma chamber at Casa Diablo. In figure 14 we show the normal stress on vertical planes, or cracks, directly over the magma chamber as a function of depth. The solid line is the lithostat, whose contribution to the stress is entirely compressional, or stabilizing, since it tends to close up cracks that may be open, or to keep them from opening if they are closed. This component of the stress increases linearly with depth. The family of dashed lines represents entirely extensional stress generated by the inflation of the magma chamber. Each dashed line represents the stress appropriate to the inflation volume shown at the top. Thus, for example, at an inflation volume of .05 km^3 a region of net tension exists down to about 1 km, then a region of net compression down to about 3 km, then a region of net extension down to the depth of the chamber. This implies, for example that near the surface, the fumaroles are a product of surface tapping of groundwater-hydrothermal system waters. The isotopic composition of these waters ought to reflect that of meteoric

water, not magmatic water, and this is evidently the case (B. Taylor, personal communication, 1983).

If inflation continues, figure 14 indicates that a point will be reached, at about .1 km^3, when the extensional stress everywhere exceeds the compressional stress. Since rocks have at most a finite strength in extension, failure will ultmately result when the yield strength of the rocks is exceeded. At this point, vertical cracks will begin to open and propagate from the magma chamber to the surface. One can therefore apply various criteria to figure 14 in an attempt to calculate when cracks might begin to propagate. Figure 15 is therefore a calculation of when failure might occur, under various criteria, as a function of future average magma injection rate into the chamber at Casa Diablo. The lower curve is based on the assumption that cracks propagate from the surface to 5 km depth when the stress at all depths becomes net extensional. The upper curve is based on an extensional yield strength of about 150 bars. Also shown on the figure is the range of values one gets for past average magma injection rate, depending on whether all magma in the system is counted, or on whether only magma in the Casa Diablo chamber is counted, and exactly what time interval is used to calculate the rate. If *past* rates of injection are indicative of *future* rates of injection, then rock failure could take place in the 1984-1987 time frame. However, if future injection rates are sufficiently low ($\ll .01\ km^3\ yr^{-1}$), then failure will never occur. It should be added that further uplift would accompany more injection, and in fact about .5-1 meter of additional uplift near Casa Diablo should probably occur prior to failure. These numbers need to be refined with more realistic finite element calculations, however, in which rock rheology is allowed to be inelastic.

It must be kept in mind that figure 15 is, at this point, simply a parametrization of one unknown, the time of failure, in terms of another unknown, the future injection rate, and cannot be regarded as a prediction or forecast. There are three major assumptions upon which the validity of figure 15 depends. First, the model may simply not be correct. Other models for the geodetic data have been discussed above which may ultimately prove to be correct, or in fact some other model not yet considered may be found to explain the data better than the present ones. Second, future injection rates are obviously not known. One can project the past rates into the future, but whether this yields a meaningful result cannot be judged at this time. Finally, the extensional stresses shown in figure 15 depend linearly on the shear modulus assumed. We have used a value of 3×10^5 bar, an average crustal value. However, if half this value of shear modulus is used then all extensional stress in figure 14 should be halved, and all times in figure 15 should be doubled.

5. Discussion

An apparent inconsistency in the discussion above stems from the result that the South Moat fault may be locked in the region of the compressional stress bull's eye, yet we have used a rectangular dislocation in modeling the data which has non-zero slip there. To resolve this problem, we tried models which allowed no slip within the bull's eye. At most, the residuals were altered by a few hundreths of a millimeter, so for all practical purposes, they were unchanged.

Another facet of the model which needs to be pointed out is that the South Moat fault occupys a more restricted area than the extent of the seismicity in the south moat. We regard the South Moat fault as the surface upon which the majority of the slip takes place. Lesser amounts of slip on extensions of the fault can be allowed without changing the residuals appreciably. Alternately, even fairly large amounts of slip can be allowed on additions to the fault plane, if the additions are small in relative area, as the previous paragraph makes clear.

We also point out that the value of Poission's ratio used here, .25, may not be appropriate, although this value is almost always used in problems of this type. We have found that if greater values of this ratio are used instead, the effect is stabilizing, in the sense that a greater inflated volume is necessary for failure to occur. For example, using a value for Poisson's ratio of .33 instead, we find that 50%more inflation can be accomodated prior to failure. The converse is also true, that a smaller Poisson's ratio promotes failure at an earlier time. As a matter of interest, we can also determine how much inflation precedes failure at a variety of source depths: a general rule of thumb is that for each 5 km increase in depth of the chamber, the failure volume increases by an order of magnetude.

Last, we note that the the inflation volume for the time period 1975 to 1983 could have been calculated at once, rather than in two separate epochs, 1975 to 1980, and 1980 to 1983. In this way, we also have the advantage of being able to use more benchmarks, from Tom's Place to Lee Vining. When an inversion is performed, with both Tom's Place and Lee Vining fixed as invariant in elevation, uplifts at the various benchmarks are obtained, which are shown in figure 16. Clearly, the worst agreement between the model and the data is in the Hilton Creek fault zone, where ground deformation is expected to be complex. However, the rms misfit is still good, about 22.5 mm. The dislocations and volume changes are: Casa Diablo magma chamber, .0284 km^3; deep magma chamber, .116 km^3; normal slip on the Hilton Creek fault of 3.7 cm at the surface increasing uniformly to 35 cm at 5 km depth; and right lateral slip on the South Moat fault of 2.3 m. For this inversion, the Hilton Creek fault has been given a dip of 80°to the west, rather than being vertical, to improve the fit slightly.

Note that the the volume changes and dislocations are nearly the same as what was found from the analysis before, particularly the volume change for the Casa Diablo magma chamber, .0284 km^3 here against .0274 km^3 before.

In summary, we feel that the model discussed here for the activity in Long Valley provides an alternative to the models proposed by Savage and Clark (1982), Savage and Cockerham (1983), and Savage *et al.*, (1983). Our model is predictive in the technical sense, meaning that it can be tested against various quantitative and qualitative data sets. We regard the fit to the available data as generally good so far, but whether it remains so under further testing is an open question.

6. Acknowledgements

We would like to thank J.C. Savage for supplying most of the geodetic data used here, and we would like to thank R. Cockerham for the seismicity plots. We would also like to acknowledge useful discussions with A. Ryall, J.C. Savage, J. Langbein, R. Jachens, and D. Hill.

REFERENCES

Chinnery, M.A., The stress changes that accompany strike-slip faulting, *Bull. Seism. Soc. Am., 53*, 921-932, 1963.

Cramer, C. and T. Toppozada, A seismological study of the May, 1980, and earlier earthquake activity near Mammoth Lakes, California, *in Mammoth Lakes, California earthquakes of May, 1980, California Division of Mines and Geology Special Report 150*, 91-136, 1980.

Hill, D.P., Structure of Long Valley caldera, California, from a seismic refraction experment, *J. Geophys. Res., 81*, 745-753, 1976.

Pitt, A.M. and R.S. Cockerham, Long Valley caldera earthquake swarm: January 7, 1983, *Earthquake Notes, 54*, 73, 1983.

Rundle, J.B., Gravity changes and the Palmdale uplift, *Geophys. Res. Lett., 5*, 41-44, 1978.

Ryall, A. and F. Ryall, Spatial-temporal variations in seismicity preceding the May, 1980, Mammoth Lakes, California, earthquakes, *in Mammoth Lakes, California earthquakes of May, 1980, California Division of Mines and Geology Special Report 150*, 27-39, 1980.

Ryall, A. and F. Ryall, Attenuation of P and S waves in a magma chamber in Long Valley caldera, California, *Geophys. Res. Lett., 8*, 557-560, 1981.

Ryall, A. and F. Ryall, Spasmodic tremor and possible magma injection in Long Valley caldera, eastern California, *Science, 219*, 1432-1433, 1983.

Sanders, C.O., Location and configuration of magma bodies beneath Long Valley, California determined from anomalous earthquake signals, *submitted to J. Geophys. Res.*, 1983.

Savage, J.C. and M.M. Clark, Magmatic resurgence in Long Valley caldera, California: Possible cause of the 1980 Mammoth Lakes earthquakes, *Science, 217*, 531-533, 1982.

Savage, J.C. and R.S. Cockerham, Earthquake swarm in Long Valley caldera, California, January, 1983: Evidence for dike intrusion, *submitted to J. Geophys. Res.*, 1983.

Savage, J.C., Estrem, J.E. and R.O. Castle, Uplift across Long Valley, California, caldera 1975-1983, *submitted to J. Geophys. Res.*, 1983.

FIGURE CAPTIONS

1. Map showing Long Valley, together with major faults and focal mechanisms for largest events from 4 October, 1978 to 25 May, 1980 (*from Cramer and Toppozada, 1980*).

2. Map of Long Valley showing 1983 earthquake swarm area (dotted area), and selected benchmarks along highways 395 and 203.

3. Change in elevation along highway 395, from Tom's Place to Lee Vining, during the years 1975-1983 (*from Savage et al., 1983*)

4. Composite of the change in elevation from September, 1982 to 1983. Profile from 6DOR to CASA AZ was observed in September, 1983, using first order, double run techniques. Remainder of the data was observed in January, 1983 using second order techniques. Comparison of the highway 395 data from January to September, 1983 shows no change in the uplift during that time above the level of random error.

5. Map showing southwest part of Long Valley with superimposed locations of magma chambers and faults in the model described in the text.

6. Fits to the leveling data for the epochs 1975-1980, and for 1980- September, 1983. Solid circles are the benchmarks used, line is the model prediction.

7. Fit to the horizontal strain data for the period July, 1979-September, 1980. Observed and (calculated) are shown.

8. Fit to the leveling data for the epoch September, 1982-1983 (composite).

9. Fit to the horizontal strain data for the period July, 1982-January, 1983. Observed and (calculated) are shown.

10. Fit to the horizontal strain data for the period July, 1982-July, 1983. Observed and (calculated) are shown.

11. Normal and shear stresses across the plane $A - A'$ shown in figure 5 due to the magma chamber at Casa Diablo. Top figure is total normal stress (magmatic plus lithostatic). Bottom figure is shear stress. An inflation volume of .0154 km^3 is assumed.

12. Map of epicenters for the period January 7-January 31, 1983 (*from Savage and Cockerham, 1983*). Arrows and cross indicate the position of the magma chamber near Casa Diablo.

13. Hypocenters of events shown in figure 12. Note distinct gap in seismicity centered at 4.7 km depth. Arrows and cross indicate the position of the orthogonal projector from the Casa Diablo magma chamber.

14. Stress across vertical planes as a function of depth over the Casa Diablo magma chamber. Family of dashed lines represents extensional stress due to the amount of magma chamber inflation shown at the top in km^3. Solid line is the compressional stress due to lithostatic pressure.

15. Curve for failure time of rock layers overlying the Casa Diablo chamber, as a function of future magma injection rate. Also shown is the range of injection rates for the past, under a variety of assumptions about partitioning of magma into the two chambers, and applicable time period.

16. Fit of model to the 1975-1983 leveling along Highway 395, with both Tom's Place and Lee Vining fixed.

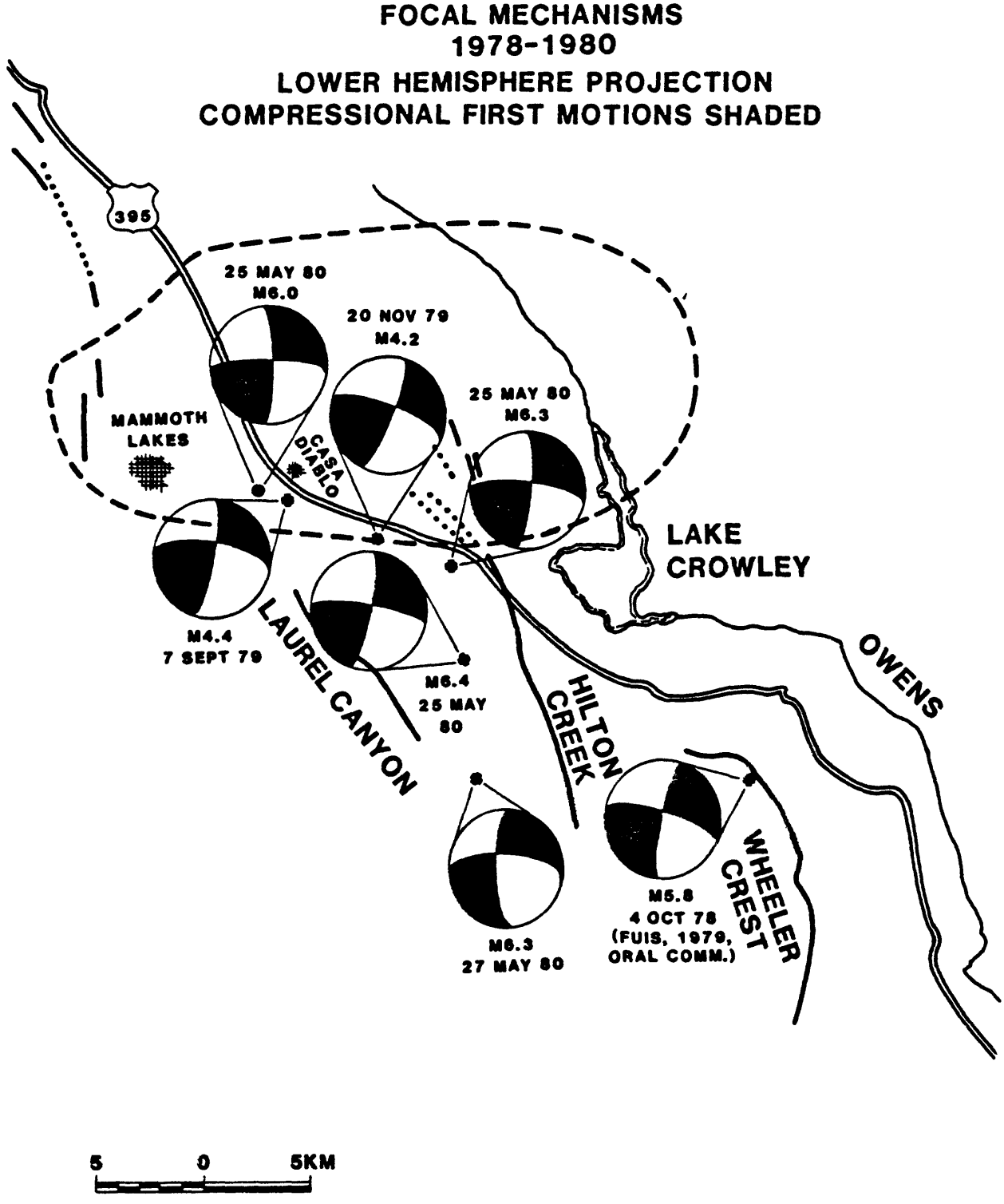
FOCAL MECHANISMS
1978-1980
LOWER HEMISPHERE PROJECTION
COMPRESSIONAL FIRST MOTIONS SHADED
395
25 MAY 80
M6.0
20 NOV 79
M4.2
25 MAY 80
M6.3
MAMMOTH
LAKES
CASA
DIABLO
LAKE
CROWLEY
M4.4
7 SEPT 79
LAUREL CANYON
M6.4
25 MAY
80
HILTON
CREEK
OWENS
M6.3
27 MAY 80
M5.8
4 OCT 78
(FUIS, 1979,
ORAL COMM.)
WHEELER
CREST
5
0
5KM

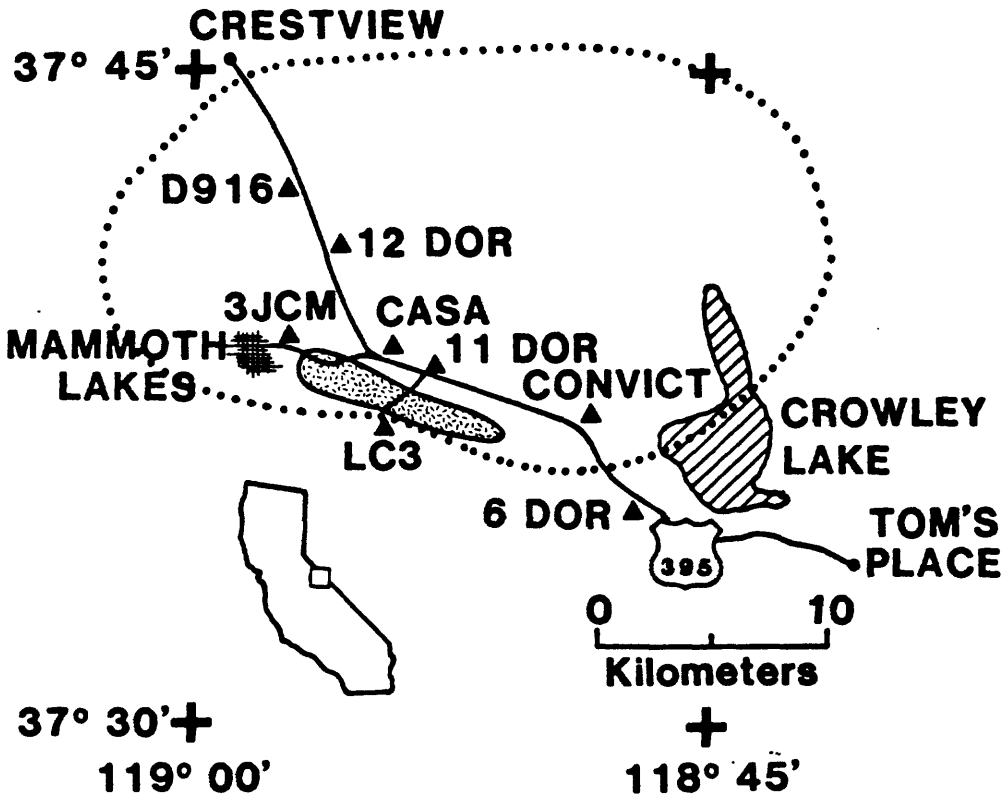
CRESTVIEW
37° 45'
D916
12 DOR
3JCM
CASA
MAMMOTH
LAKES
11 DOR
CONVICT
CROWLEY
LAKE
LC3
6 DOR
TOM'S
PLACE
395
0
10
Kilometers
37° 30'
119° 00'
118° 45'

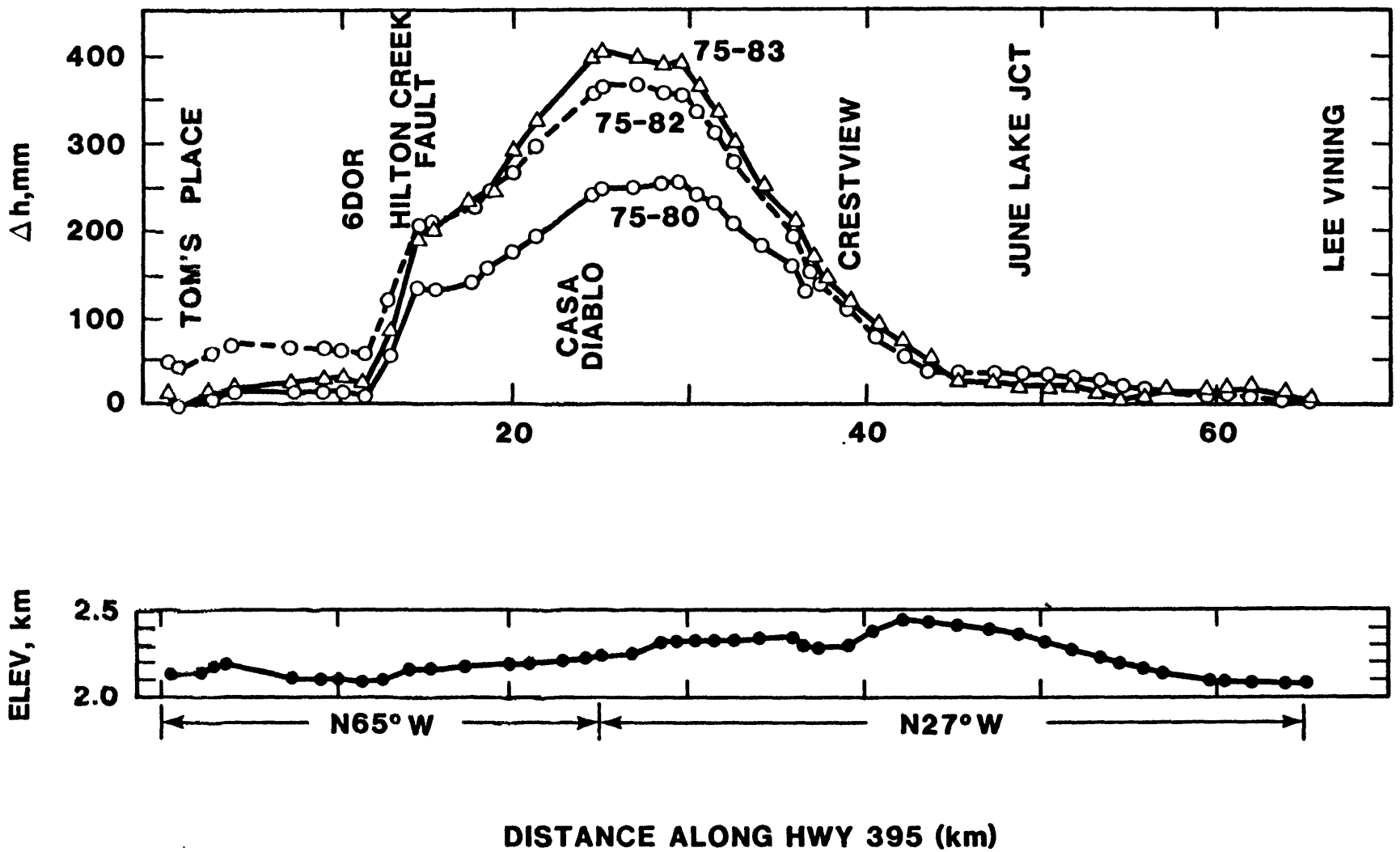
Δh,mm
400
300
200
100
0
TOM'S PLACE
6DOR
HILTON CREEK FAULT
CASA DIABLO
CRESTVIEW
JUNE LAKE JCT
LEE VINING
75-83
75-82
75-80
20
40
60
ELEV, km
2.5
2.0
N65° W
N27° W
DISTANCE ALONG HWY 395 (km)

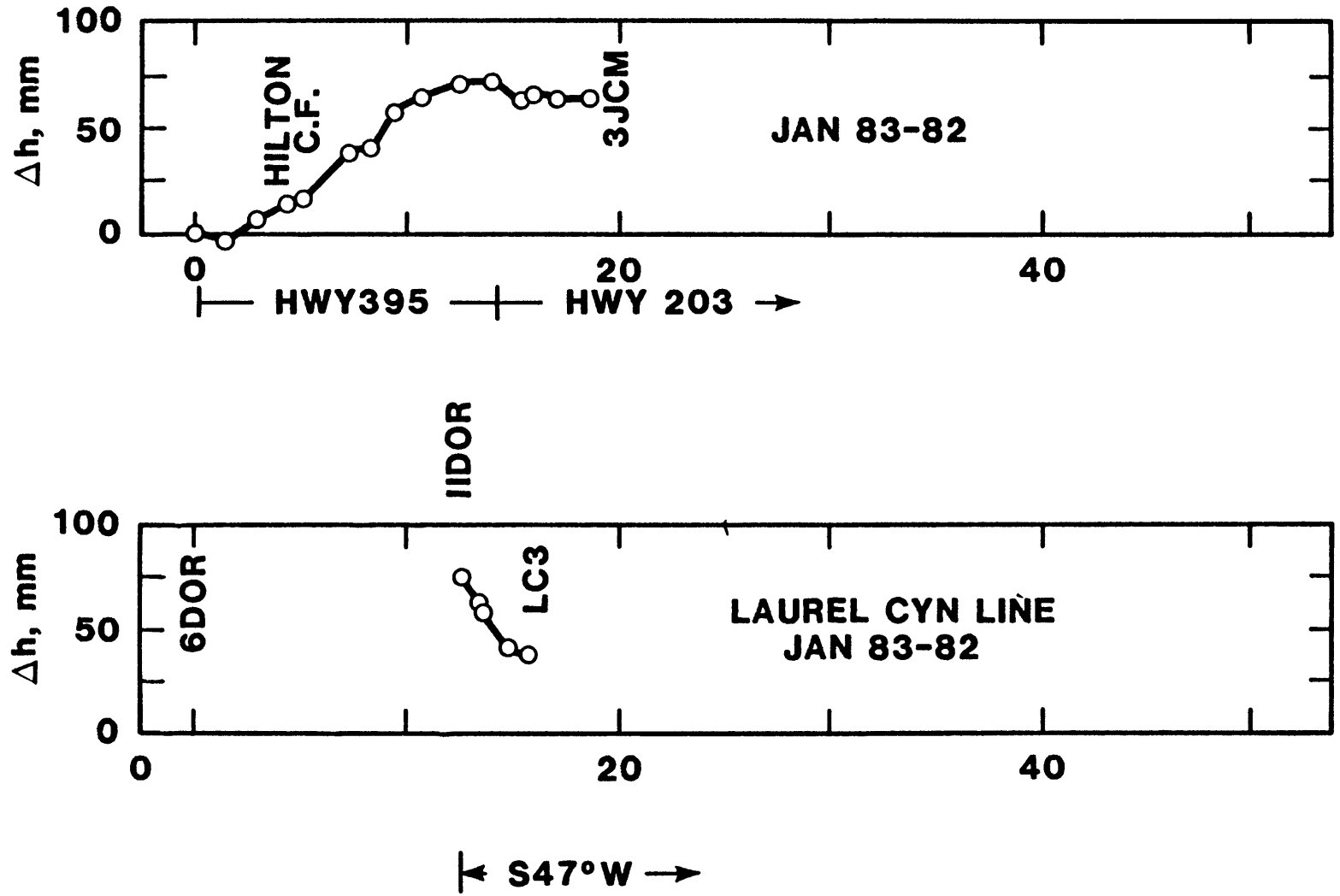
100
50
0
Δh, mm
HILTON C.F.
3JCM
JAN 83-82
0
20
40
HWY395
HWY 203
IIDOR
6DOR
LC3
LAUREL CYN LINE
JAN 83-82
S47°W

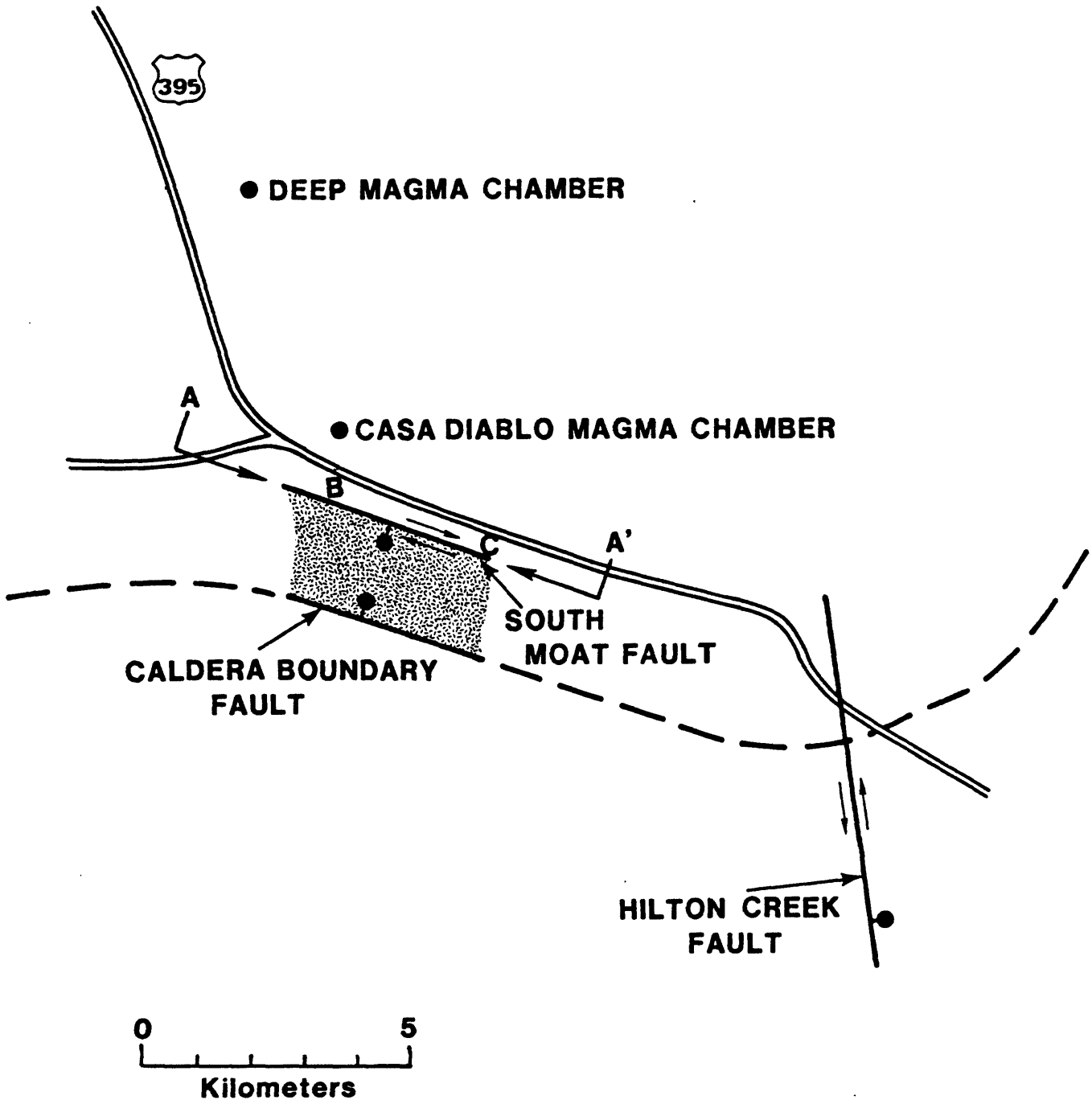
395
DEEP MAGMA CHAMBER
A
CASA DIABLO MAGMA CHAMBER
B
C
A'
SOUTH
MOAT FAULT
CALDERA BOUNDARY
FAULT
HILTON CREEK
FAULT
0
5
Kilometers

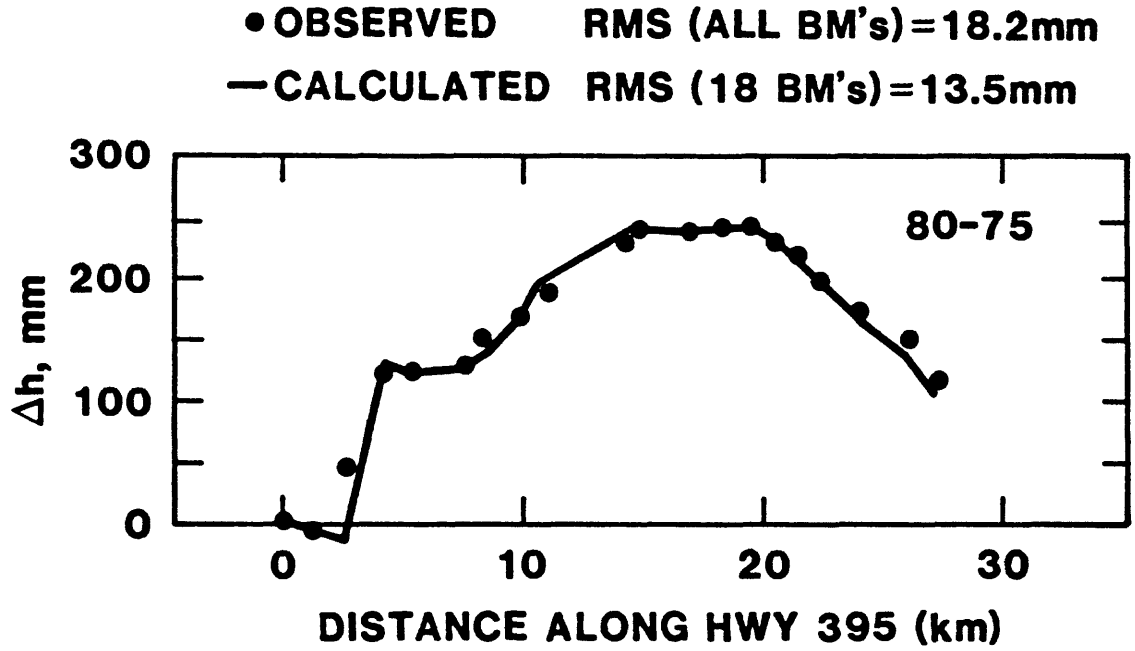
● OBSERVED RMS (ALL BM's)=18.2mm
— CALCULATED RMS (18 BM's)=13.5mm
80-75
Δh, mm
300
200
100
0
0
10
20
30
DISTANCE ALONG HWY 395 (km)

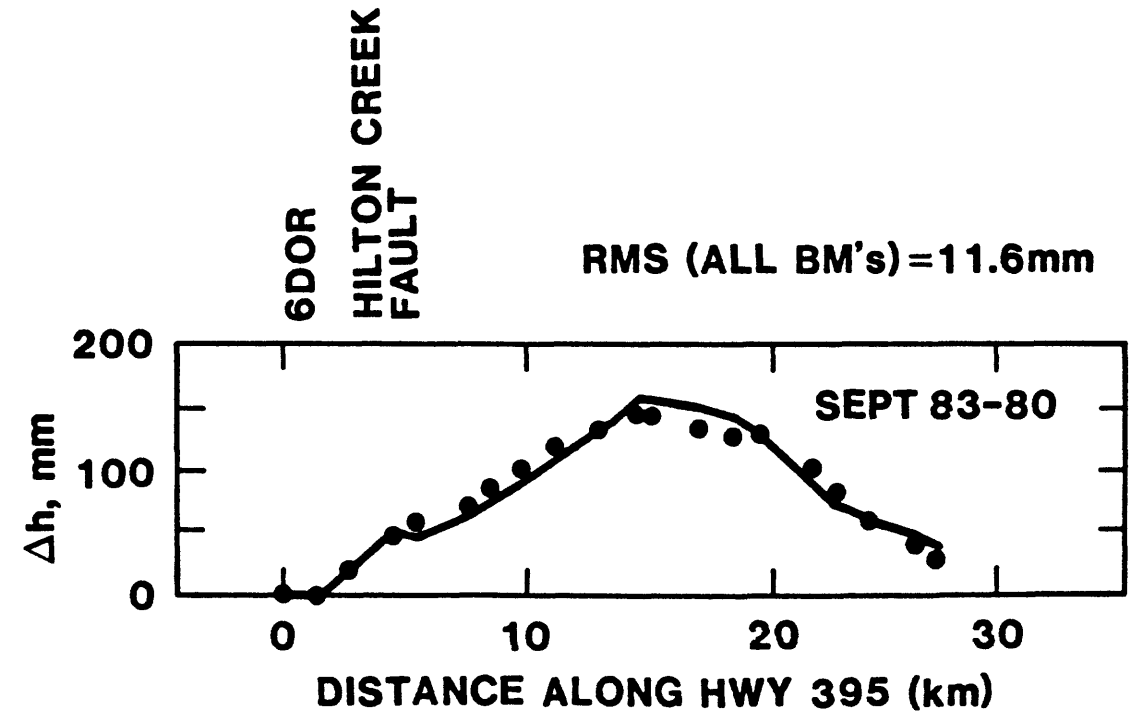
6DOR
HILTON CREEK FAULT
RMS (ALL BM's)=11.6mm
SEPT 83-80
Δh, mm
200
100
0
0
10
20
30
DISTANCE ALONG HWY 395 (km)

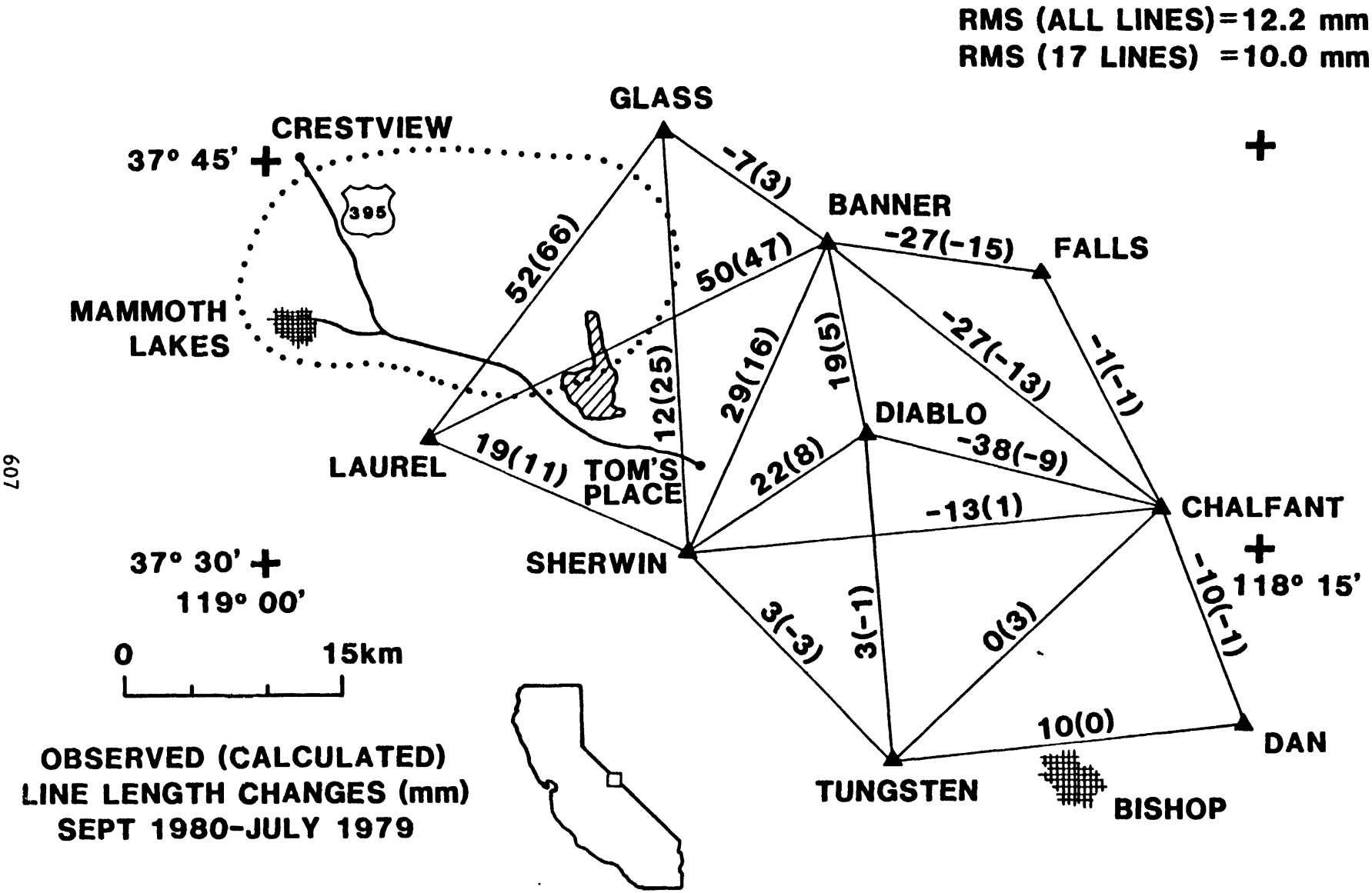
RMS (ALL LINES)=12.2 mm
RMS (17 LINES) =10.0 mm
GLASS
CRESTVIEW
37° 45'
395
BANNER
FALLS
-7(3)
-27(-15)
52(66)
50(47)
MAMMOTH
LAKES
12(25)
29(16)
19(5)
-27(-13)
-1(-1)
DIABLO
LAUREL
19(11)
TOM'S
PLACE
22(8)
-38(-9)
-13(1)
CHALFANT
37° 30'
119° 00'
SHERWIN
118° 15'
-10(-1)
3(-3)
3(-1)
0(3)
0
15km
10(0)
DAN
TUNGSTEN
BISHOP
OBSERVED (CALCULATED)
LINE LENGTH CHANGES (mm)
SEPT 1980-JULY 1979

607

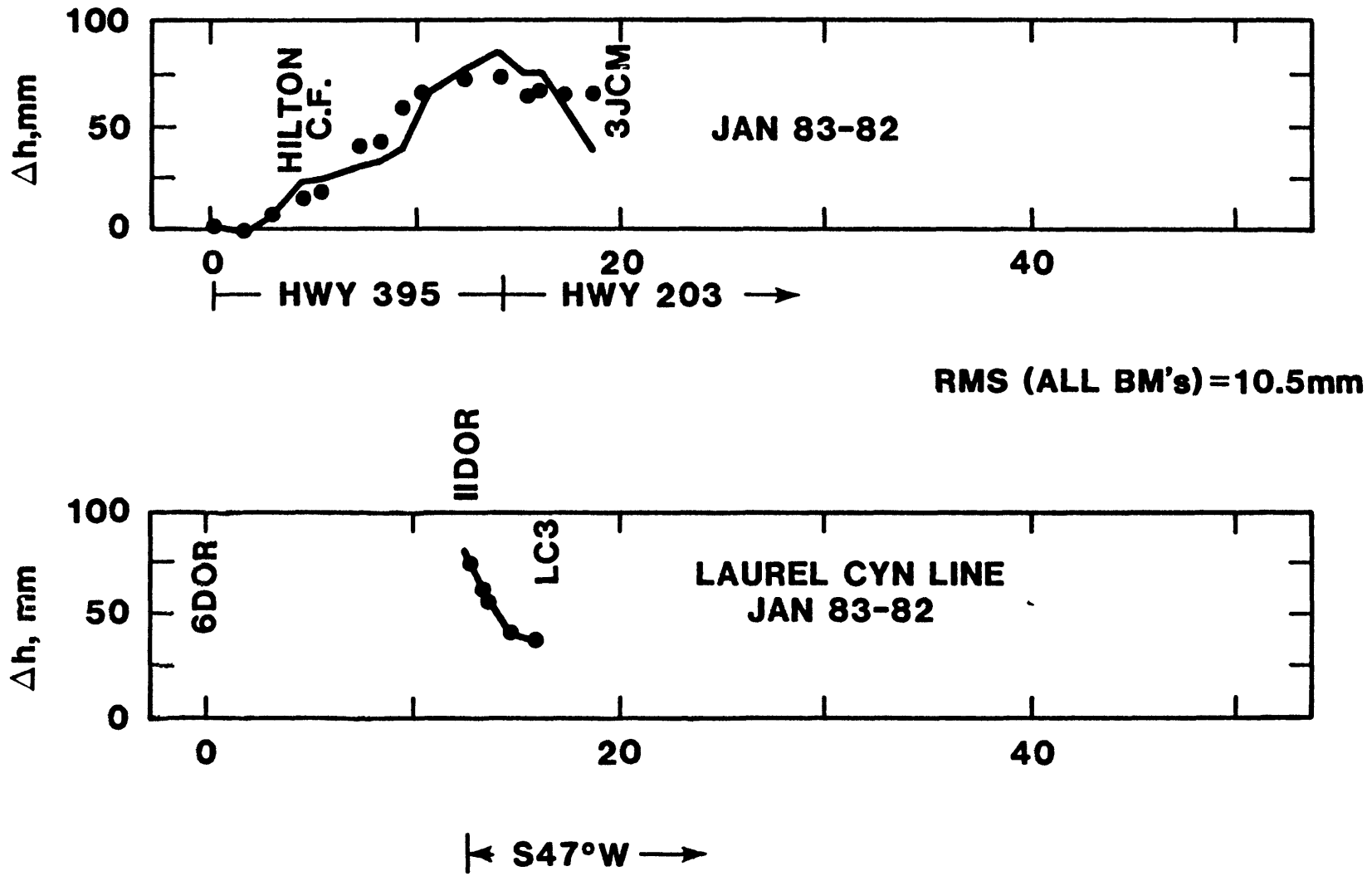
100
50
0
Δh,mm
HILTON C.F.
3JCM
JAN 83-82
0
20
40
HWY 395
HWY 203
RMS (ALL BM's)=10.5mm
IIDOR
6DOR
LC3
LAUREL CYN LINE
JAN 83-82
Δh, mm
S47°W

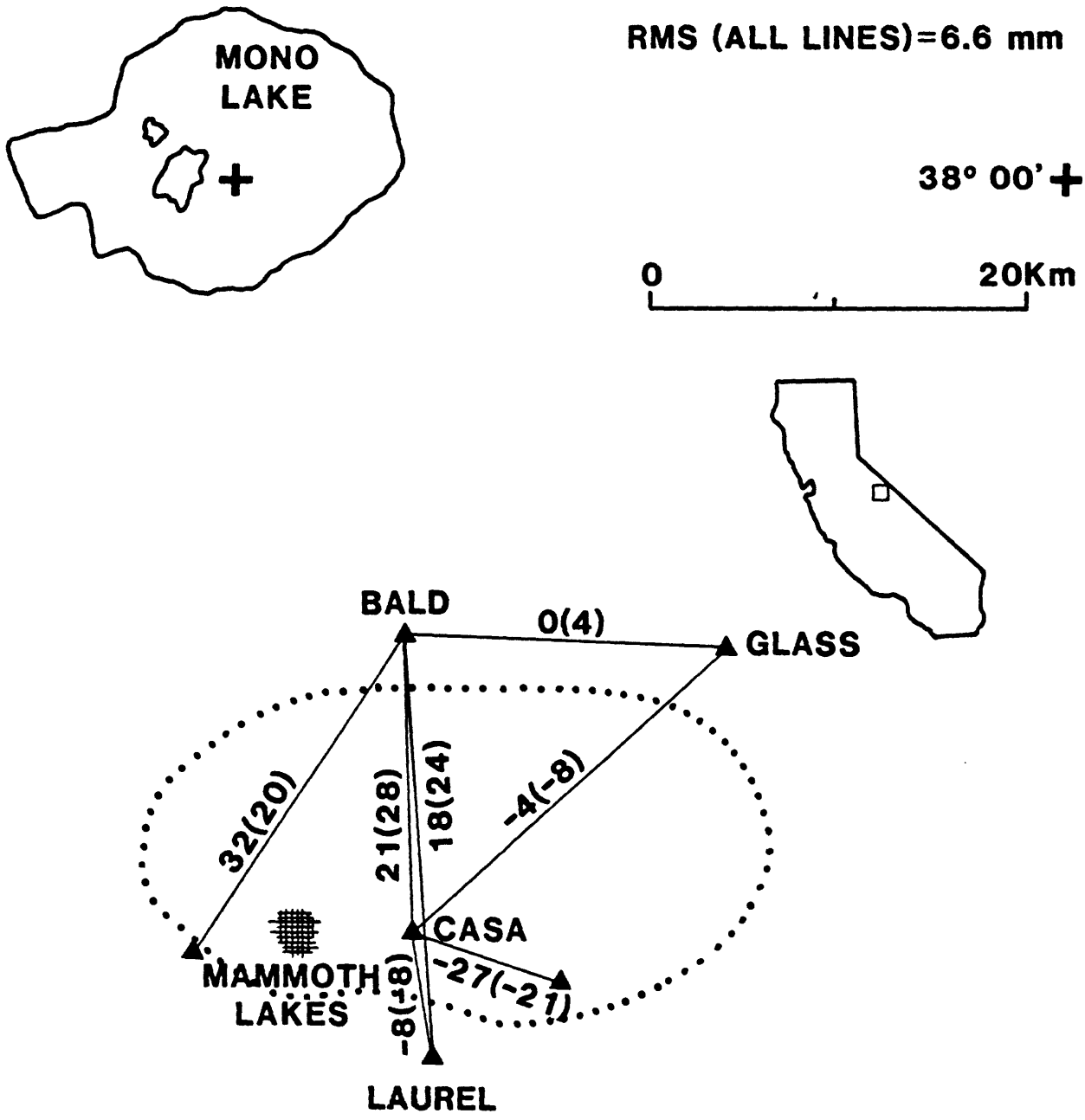

OBSERVED (CALCULATED)
LINE LENGTH CHANGES (mm)
JANUARY 1983-JULY 1982

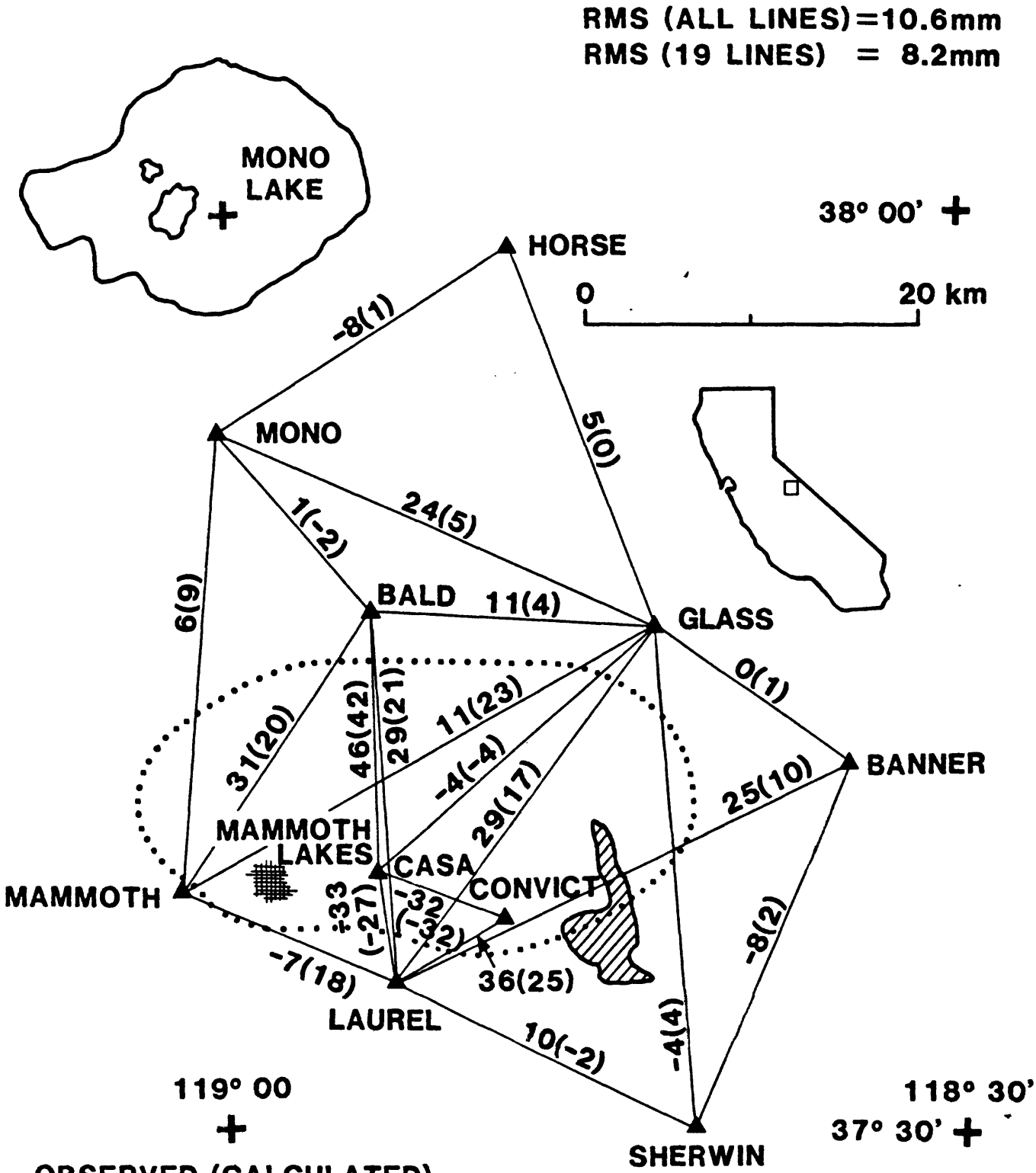
RMS (ALL LINES)=10.6mm
RMS (19 LINES) = 8.2mm
MONO LAKE
38° 00'
HORSE
0
20 km
-8(1)
5(0)
MONO
24(5)
1(-2)
6(9)
BALD
11(4)
GLASS
0(1)
11(23)
31(20)
46(42)
29(21)
-4(-4)
29(17)
25(10)
BANNER
MAMMOTH LAKES
CASA
CONVICT
MAMMOTH
+33
(-27)
-32
(-32)
(2)
-7(18)
36(25)
-8(2)
LAUREL
10(-2)
-4(4)
119° 00
118° 30'
37° 30'
SHERWIN
OBSERVED (CALCULATED)
LINE LENGTH CHANGES (mm)
JULY 1983-JULY 1982

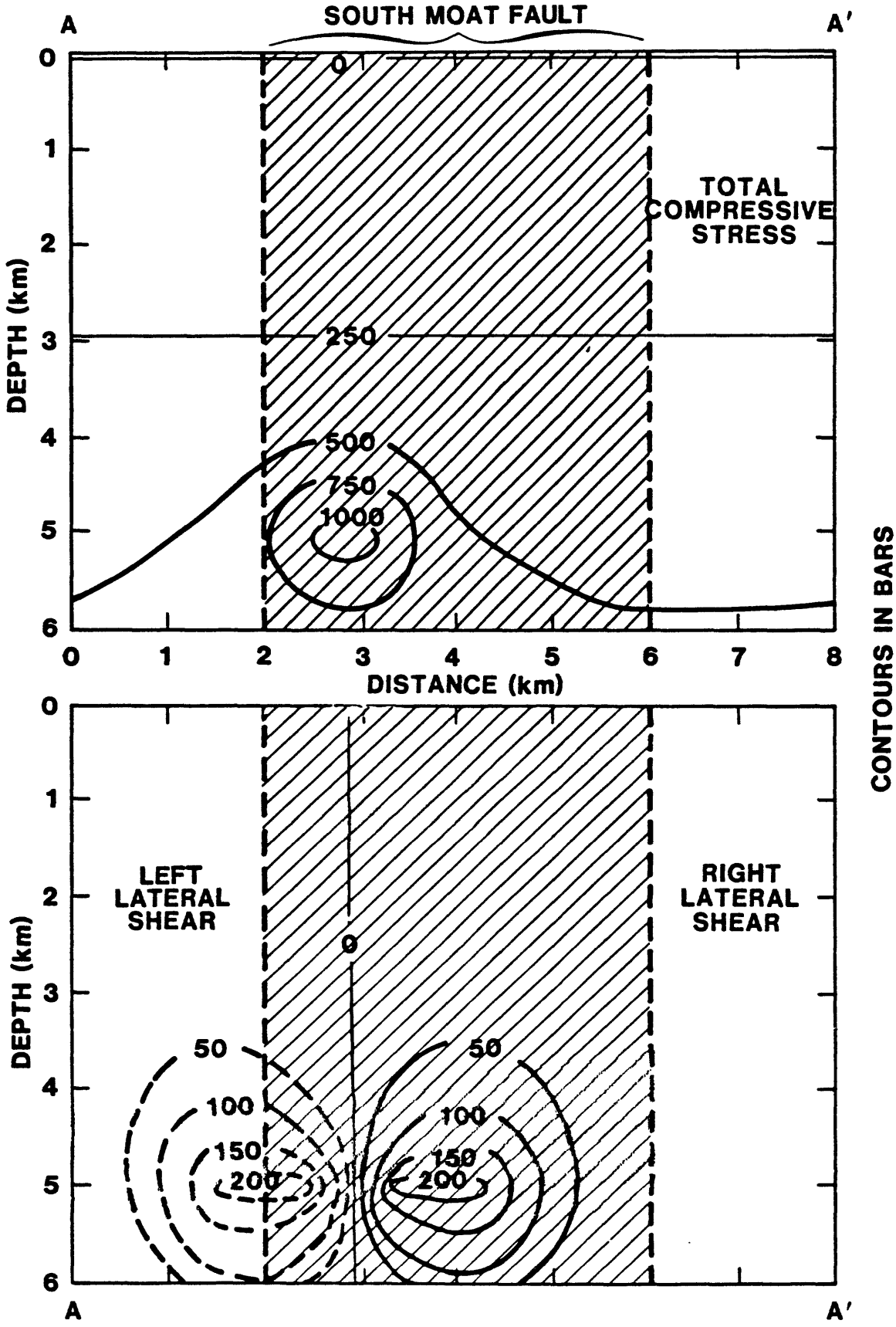
A
SOUTH MOAT FAULT
A'
0
250
500
750
1000
TOTAL
COMPRESSIVE
STRESS
DEPTH (km)
0
1
2
3
4
5
6
0
1
2
3
4
5
6
7
8
DISTANCE (km)
CONTOURS IN BARS
LEFT
LATERAL
SHEAR
RIGHT
LATERAL
SHEAR
0
50
100
150
200
50
100
150
200
DEPTH (km)
A
A'

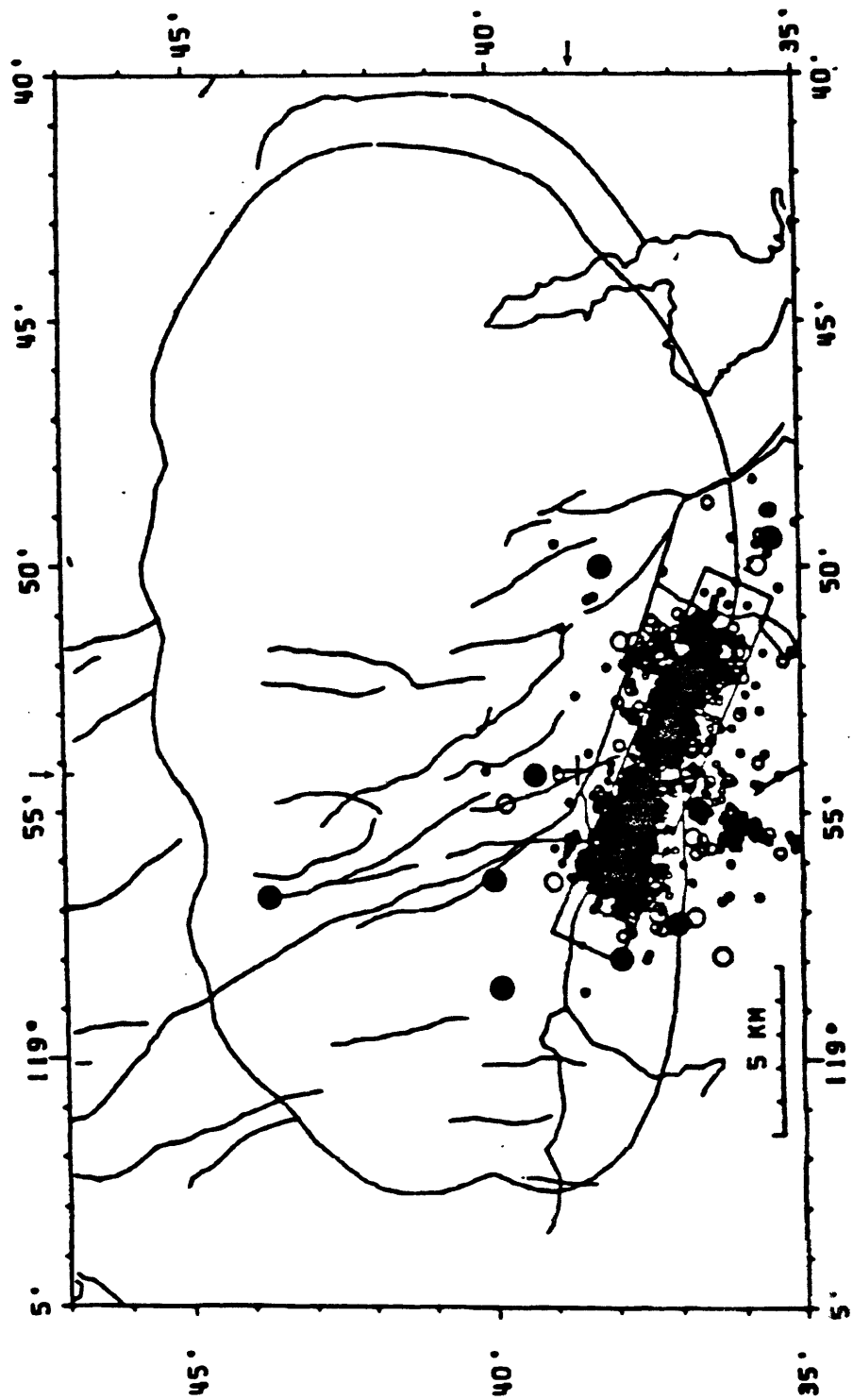
40°
45'
50'
55'
119°
5'
45'
40'
35'
5 KM

B'
B
0
-2
-4
-6
-8
-10
DEPTH (KM)
0
2
DISTANCE (KM)

A'
A
0
-2
-4
-6
-8
-10
DEPTH (KM)
0
2
4
6
8
10
DISTANCE (KM)

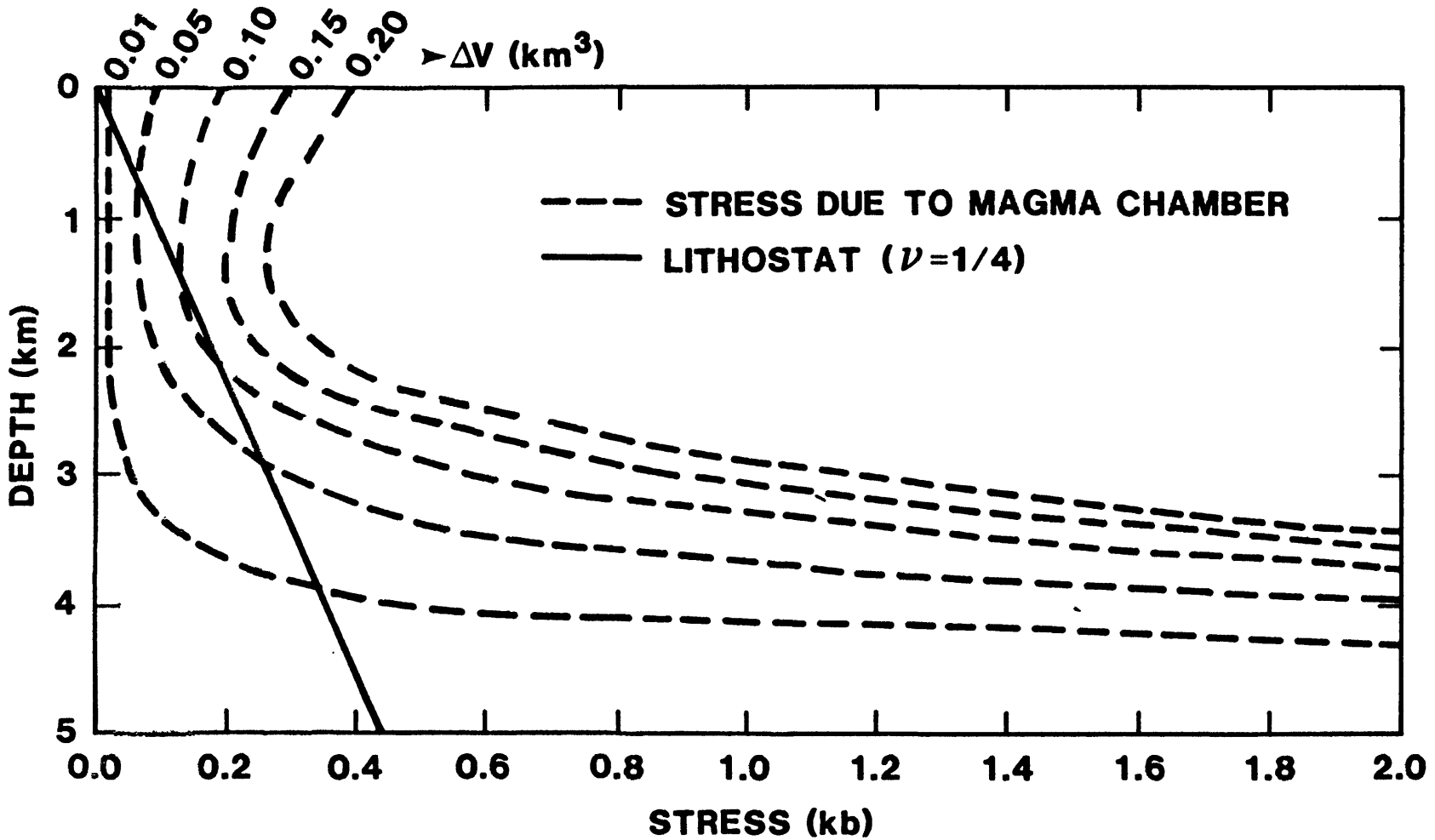
0.01
0.05
0.10
0.15
0.20
ΔV (km³)
STRESS DUE TO MAGMA CHAMBER
LITHOSTAT (ν=1/4)
DEPTH (km)
0
1
2
3
4
5
0.0
0.2
0.4
0.6
0.8
1.0
1.2
1.4
1.6
1.8
2.0
STRESS (kb)

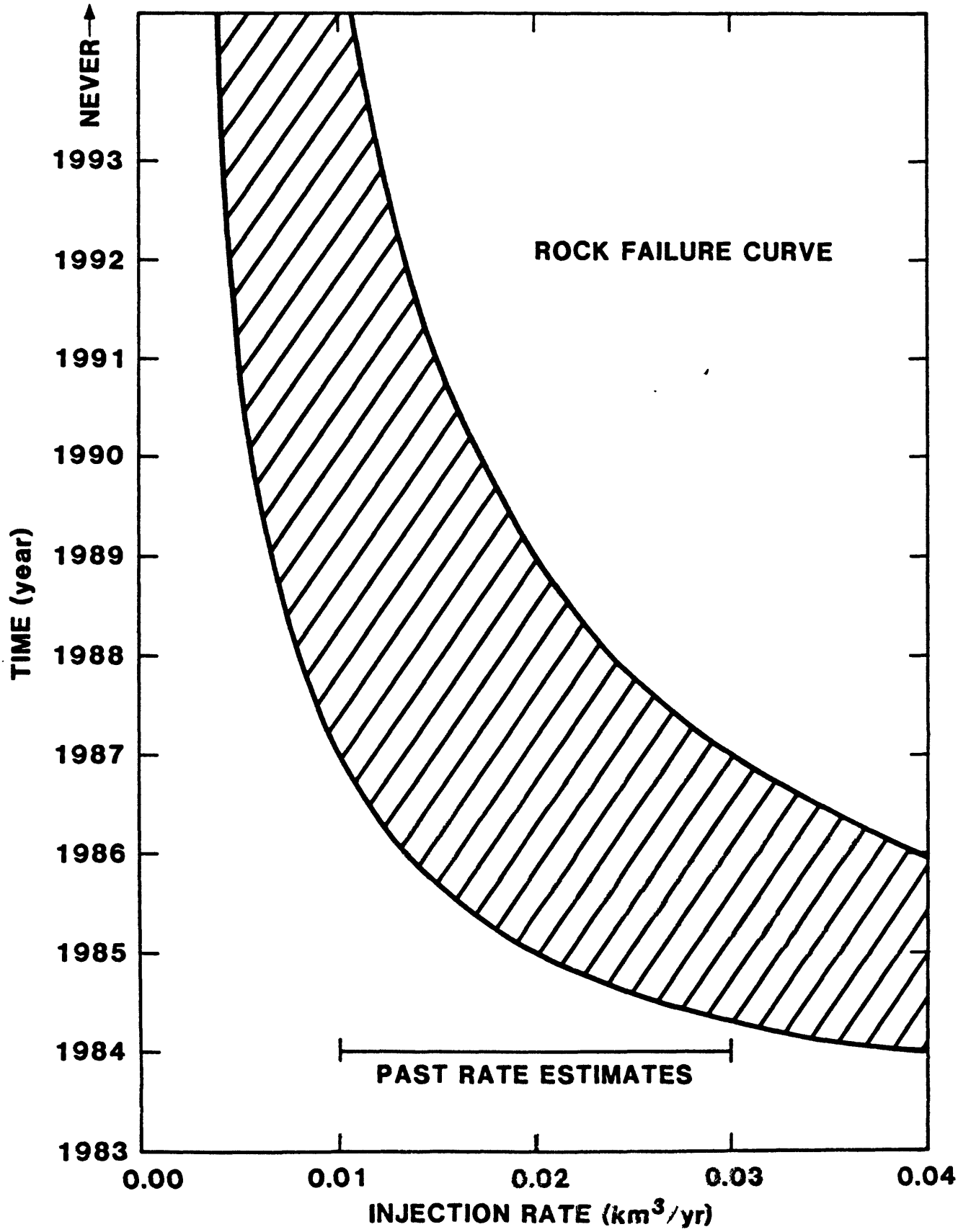
NEVER
1993
1992
1991
1990
1989
1988
1987
1986
1985
1984
1983
TIME (year)
ROCK FAILURE CURVE
PAST RATE ESTIMATES
0.00
0.01
0.02
0.03
0.04
INJECTION RATE (km³/yr)

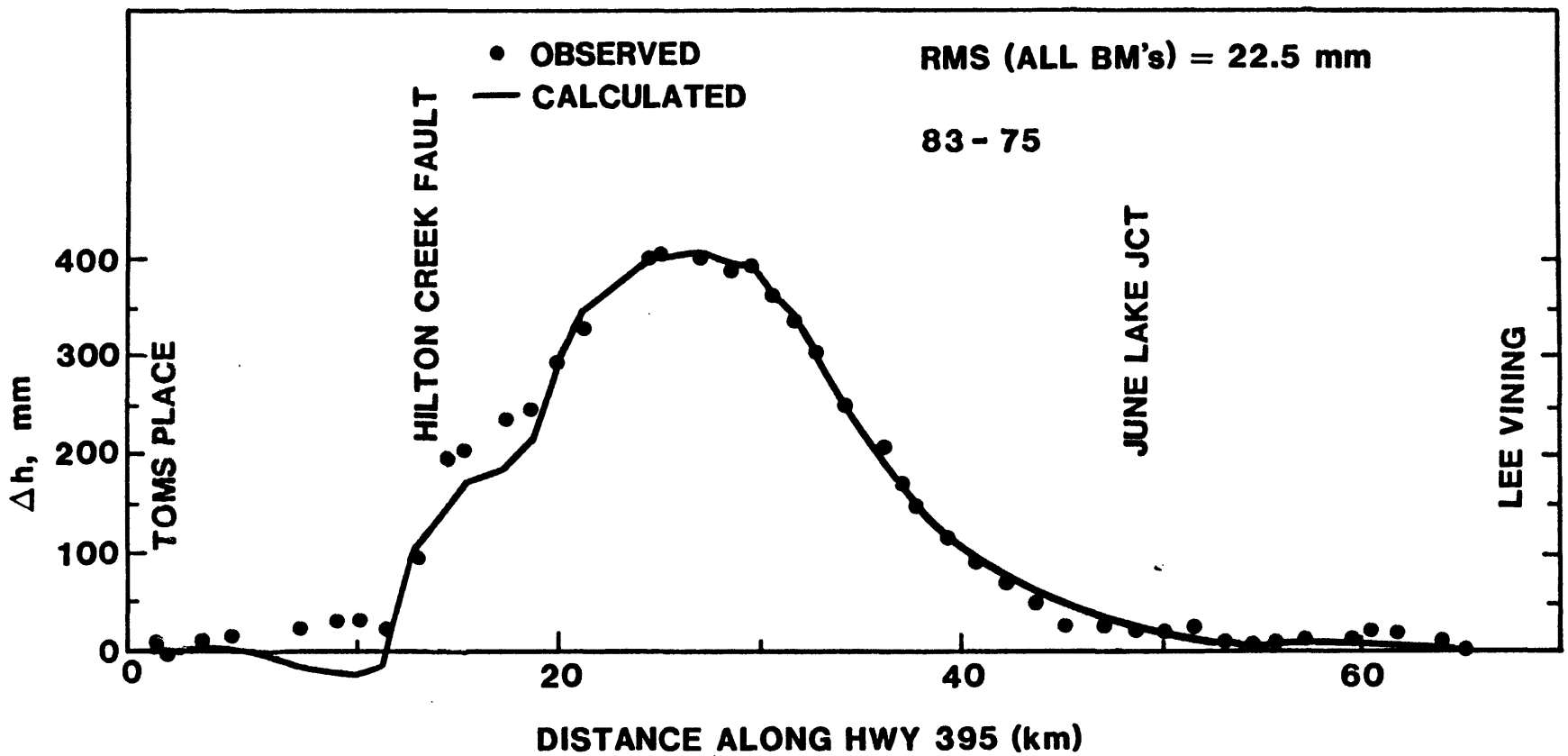
OBSERVED
CALCULATED
RMS (ALL BM's) = 22.5 mm
83 - 75
HILTON CREEK FAULT
TOMS PLACE
JUNE LAKE JCT
LEE VINING
Δh, mm
400
300
200
100
0
0
20
40
60
DISTANCE ALONG HWY 395 (km)

EVOLUTION AND PRESENT STATE OF THE HYDROTHERMAL SYSTEM IN LONG VALLEY CALDERA

Michael L. Sorey

U.S. Geological Survey, Menlo Park, CA

ABSTRACT

Present-day rates of discharge of fluid (250 kg/s) and heat (7×10^7 cal/s) from the hydrothermal system in Long Valley caldera are less than at the Yellowstone caldera but greater than at the Valles caldera. In contrast to observed subsurface conditions within the Yellowstone and Valles calderas, the present-day hydrothermal system in Long Valley appears to consist of two principal zones in which hot water flows laterally from west to east at depths less than about 1 km. Maximum measured temperatures within these zones are near 170°C, but estimates from chemical geothermometers and extrapolation of a high temperature gradient measured in a recent drill hole indicate that a source reservoir at temperatures near 240°C may exist within the Bishop Tuff beneath the west moat.

A tentative outline of the postcaldera evolution of the hydrothermal system is presented, based on analysis of the measured temperature regime at depths of 1-2 km and the record of mineral discharge from Long Valley contained in the saline deposits of Searles Lake. These data indicate that between 0.3 and 0.13 m.y. B.P. hydrothermal activity was more intense than at present and probably involved circulation to depths of several kilometers with heat supplied by the Long Valley magma chamber. As the magma chamber cooled and crystallized downward, the heat source for deep hydrothermal circulation may have shifted to the Inyo-Mono magmatic

system beneath the west moat. During the past 40,000 years or more, the hydrothermal system may have included zones of deep fluid circulation beneath the west moat and shallower zones of lateral flow of hot water within the Bishop Tuff beneath the resurgent dome. Regions of silicic melt detected by shear-wave attentuation at depths of 4 - 5 km beneath the resurgent dome have probably not been in place long enough to sensibly influence the overlying thermal regime within the upper 2 km of caldera fill.

INTRODUCTION

Hydrothermal systems in many silicic Pleistocene calderas appear to have persisted for periods of hundreds of thousands of years and to include regions where temperatures exceed 300°C at depths of less than 2 km. Such is the case at the 0.6 m.y.-old Yellowstone caldera in Wyoming (Fournier, White, and Truesdell, 1976; Christiansen, this volume) and the 1.1 m.y. old Valles caldera in New Mexico (Smith and Bailey, 1968; Grant and Garg, 1981). Necessary conditions for such activity include resupply of magma to sustain continued volcanism and high convective heat flow, and active faulting to provide open channels for fluid convection. Although these conditions appear to be met in the case of the 0.7 m.y.-old Long Valley caldera (LVC) (Sorey, Lewis, and Olmsted, 1978), temperature measurements in wells drilled to depths of 2 km in LVC include maximum values of only about 170°C at depths near 0.15 km and cooler temperatures at greater depths. This suggests either that the present state of the hydrothermal system in LVC differs significantly from conditions at Yellowstone and Valles calderas, or that regions of higher temperture at drillable depths remain undiscovered.

In this paper various lines of evidence, including subsurface temperature measurements, heat-flow determinations, and records of mineral deposits in Searles Lake, are discussed in terms of constraints on the evolution and present state of the Long Valley hydrothermal system. It should be emphasized that any model of this system developed from the limited available data is considered tentative and useful primarily as a guide to the collection and interpretation of additional information from ongoing programs of geothermal exploration, volcanic hazards assessment, and deep continental scientific drilling.

NATURAL DISCHARGE OF FLUID AND HEAT

The rate of natural discharge of heat from LVC was estimated by Sorey, Lewis, and Olmsted (1978) to be 6.9×10^7 cal/s. This represents the sum of heat discharged by thermal springs, subsurface flow of thermal water into Lake Crowley (figure 1), and near-surface heat conduction. If heat were supplied at this rate from a magma chamber underlying the entire 450 km^2 topographic floor of the caldera, the conductive heat flux would average 15 HFU (15×10^{-6} cal $s^{-1} cm^2$). Estimates of the rate of fluid flow through the hydrothermal system range from 190 kg/s to 250 kg/s, depending on assumed values for the chemical composition of the thermal component in the hot-spring waters (Sorey, Lewis, and Olmsted, 1978). Comparison of these measures of the intensity of hydrothermal circulation with values for other calderas (table 1) suggests that the present-day Long Valley system is intermediate in intensity between Yellowstone (most intense) and Valles caldera (least intense).

Areas of present-day hot spring discharge in LVC (figure 1) are distributed primarily around the southern and southeastern sides of the resurgent dome and to the east of the intra-caldera extension of the Hilton Creek Fault. With the exception of the latter group of springs and Reds Meadow Hot Springs on the southwest side of Mammoth Mountain, the hot springs occur along northwest-trending normal faults. Areas of present-day steam discharge in fumaroles and diffuse seepage through soil occur along these northwest-trending faults in the general vicinity of Casa Diablo Hot Springs, and on the northern and southern flanks of Mammoth Mountain. The occurence of hot springs and fumaroles along normal faults has been taken to imply that such faults act as conduits for upward flow from reservoirs at relatively great depth. In contrast, temperature measurements in wells and geochemical considerations indicate that the springs east of the extension of the Hilton Creek Fault are fed by upward flow from relatively shallow lenses of thermal water moving in a southeasterly direction toward Lake Crowley (Bailey, Dalrymple, and Lanphere, 1976; Sorey, Lewis, and Olmsted, 1978).

Two areas where significant hydrothermal activity occured in the past but which are no longer active are denoted Clay Pit and Blue Chert in figure 1. Both areas are on the east side of the resurgent dome at altitudes near 2,230 m (7300 ft), whereas most of the present-day discharge of hot water occurs at altitudes near 2,130 m (7,000 ft). Intense argillic development at Clay Pit resulted from hydrothermal alteration by acidic hot-spring and fumarolic activity (Bailey, Dalrymple, and Lanphere, 1976). Regions of steam flow may still underlie the Clay Pit area at depths of 50-100 m and feed weak fumarolic discharges (Ken Puchlich, Shreveport Mining Company,

personal communication, 1984). At the Blue Chert outcrop (Lipshie, 1976), extensive deposits of siliceous sinter evidence the discharge of hot water that may have been more mineralized than present-day hot-spring waters, which commonly deposit travertine rather than siliceous sinter. Extensive development of hydrothermal alteration in lacustrine deposits that are interbedded with the 0.28 m.y.-old Hot Creek rhyolite flow suggests that the hydrothermal system reached maximum development at about 0.3 m.y.B.P. (Bailey, Dalrymple, and Lanphere, 1976).

Geochemical Considerations

Chemical analyses for selected spring waters reported in table 2 show that the present-day hot springs and thermal wells discharge slightly saline sodium bicarbonate-chloride waters. Nonthermal springs (<15°C), of which Big Springs is typical, discharge nonsaline sodium bicarbonate waters with proportionately more calcium, more magnesium, and less chloride than the thermal springs. The total flow of water in all thermal springs is about 360 L/s (Sorey and Lewis, 1976). An additional 120 L/s of water at temperatures between 40° and 90°C may flow laterally toward Lake Crowley in shallow aquifers within lacustrine sediments east of Hot Creek (Sorey, Lewis, and Olmsted, 1978).

Concentrations of elements such as boron and chloride, which are typically associated with neutral-pH hot-spring waters, generally decrease from west to east as the ratio of thermal to non-thermal water in the springs decreases. The most concentrated hot-spring water occurs at Colton Spring, in an area of fossil sinter deposition through which discharge was reactivated in 1982. Two kilometers to

the northwest at Casa Diablo Hot Springs, thermal-fluid discharge occurs in high-chloride hot springs and in fumaroles and mudpots. The acid-sulfate spring on the east side of old Highway 395 (table 2) was sampled in 1973 but no longer flows. Fluid sampled from the well at Casa Diablo was produced from an aquifer at depths of 120 - 150 m where the measured temperatures are about 170°C. The similarity in chemical composition between the well water and water from the high-chloride springs at Casa Diablo suggests that the springs are fed by upflow from this shallow aquifer along conduits provided by the fault along which the springs are aligned. A similar situation exists in Hot Creek Gorge, where hot springs discharge waters that are chemically identical to water produced from an aquifer penetrated at a depth of about 30 m in several wells drilled 1 km southeast of the Gorge (unpublished data).

Temperatures measured in areas of steam discharge are at or below the boiling point for local land surface altitudes (93°C). The most active fumaroles, which occur on the eastern side of the Casa Diablo Hot Springs area, discharge approximately 99.4 molar percent H_2O and 0.5 molar percent CO_2 (Taylor and Gerlach, 1983). Although ^{13}C values and $^{3}He/^{4}He$ ratios suggest that there may be a component of magmatic origin in the fumarolic gases (Taylor and Gerlach, 1983; Rison and others, 1983), steam discharge in LVC is most likely derived from underlying hot-water reservoirs.

Calculations based on chemical geothermometers (table 2) indicate that temperatures in reservoirs feeding the hot springs and the shallow aquifer at Casa Diablo may exceed 200°C. The highest geothermometer estimates (219° - 238°C) are obtained for water from

the Casa Diablo well. Although publically available temperature data from five wells drilled to depths of 600 - 2,100 m show no direct evidence of reservoirs at temperatures above those measured in the shallow aquifer at Casa Diablo, these data do suggest that zones of higher temperature may exist within the Bishop Tuff beneath the west moat, as discussed in a later section. Concentrations of deuterium and ^{18}O in thermal and nonthermal waters show that the recharge area for the hydrothermal system is around the western rim, consistent with a general model involving downflow and heating in the west and lateral flow of thermal water from west to east (Sorey, Lewis, and Olmsted, 1978; Fournier and others, 1979). Thus, the geothermometer estimates for the Casa Diablo well may represent maximum reservoir temperatures attained within the present-day hydrothermal system beneath the west moat. Lower estimated temperatures for hot-spring waters discharging at Casa Diablo and to the east could result from the effects of mixing and chemical reequilibration as thermal water flows eastward and upward along fault conduits.

Saline Deposits in Searles Lake

Hot springs discharging in the LVC appear to have been the chief source of many of the mineral components in the evaporite deposits delineated from coring beneath Searles Lake (figure 2), one of a series of now-dry lakes connected by the ancestral Owens River system along the east side of the Sierra Nevada (Smith and others, 1983). Although the ancestral Owens River terminated in Owens Lake, when filled, that lake overflowed into Indian Wells Valley to form China Lake. China Lake, in turn, overflowed eastward into Searles Valley to form Searles Lake. At their highest stages, Searles and China Lakes

coalesced into one large lake that drained southeastward into Panamint Lake, which overflowed into Death Valley only during the wettest pluvial episodes. Calculations by Smith (1976) and Smith and others (1983), based on probable evaporation rates and measured lake areas, show that Searles Lake received water from upstream sources (including Long Valley) during times when the flow of the Owens River was 2-3 times larger than at present. These calculations also show that 4-6 times the present flow would have caused Searles Lake to overflow and thus remain, or evolve into, a freshwater lake. When the pluvial periods of the Pleistocene ended, large amounts of salts that were trapped in the basins crystallized as layers on the valley floors. Drilling has shown that no layers of salts accumulated in the upper several hundred meters of Owens Lake and China Lake, that only halite and gypsum accumulated in Panamint Lake, and that major quantities of salts containing uncommon elements such as boron and lithium accumulated only in Searles Lake (Smith and Pratt, 1957). Smith (1976) concludes that hot-spring discharge from LVC was the chief source of many of the components of the salts and brines in Searles Lake because of the relative abundance in the hot-springs waters of many of the uncommon elements found in the Searles Lake deposit, and the apparent balance between tonnages of certain elements contributed by the hot springs to the Owens River and tonnages of these elements in the saline layers beneath Searles Lake. Consequently, analyses of core samples from Searles Lake provide a valuable record of discharge from the hydrothermal system in LVC.

Stratigraphic units and age relationships for the sediments beneath Searles Lake are listed in table 3. Ages of younger units (above the Bottom Mud) are based on ^{14}C dates and on estimates of

sedimentation rates derived from them (Stuiver and Smith, 1979); ages of older units are based on the paleomagnetic stratigraphy (Liddicoat and others, 1980). Although saline deposits are present throughout the sedimentary section, their distribution and mineralogy suggest that only after about 0.31 m.y.B.P. did high-pH lakes, containing large amounts of $NaCO_3$ in their waters, occupy the basin. Smith and others (1983) attribute this compositional change to hydrothermal activity in LVC that Bailey, Dalrymple, and Lanphere (1976) infer to have reached its peak about 0.3 m.y.B.P. Units A and B of the Mixed Layer, which formed between 0.31 and 0.13 m.y.B.P., contain saline beds deposited during periods when lake salinities rarely exceeded about 20 percent and mostly remained in the 5-15 percent range, allowing winter cooling to generate successions of monomineralic layers of crystals. Within this time interval, some rises in lake-level also resulted in short periods when lake waters had lower salinities so that no salts precipitated.

The mud layer above the Mixed Layer (the Bottom Mud) also contains a few thin saline layers composed of minerals indicating that Na and CO_3 continued to predominate in the lake waters. During much of the interval over which this mud layer was deposited (0.13 - 0.032 m.y.B.P.), lake levels in Searles Valley were high enough for water to overflow to Panamint Lake. This overflow should have removed some of the sodium carbonate minerals in solution that were contributed from Long Valley, but deposits of such minerals have not been detected beneath Panamint Lake or in Death Valley. Assuming that the Long Valley hydrothermal system remained active during this period, the corresponding dissolved mineral load may have been

precipitated at later times in the overlying salt layer, as suggested for the Parting Mud by the mineral balances discussed below.

Extensive saline deposits containing sodium borate and sodium carbonate minerals in Searles Lake units younger than 0.032 m.y.B.P. indicate active discharge from the Long Valley hydrothermal system for much of the past 30,000 - 40,000 years. Further evidence for such discharge is provided by the balance between tonnages of certain elements now found in the Upper and Lower Salts of Searles Lake and tonnages of these elements that could have been contributed by hot springs in LVC to the Owens River over the past 32,000 years (Smith, 1976). The balance between these two quantities (figure 3) is remarkably close for boron, potasium, and sulfate, whereas for sodium and chloride, the amounts in the Upper and Lower Salts in Searles Lake are two to three times greater than the Owens River seems likely to have supplied. Smith and others (1983) and Holser (1970) attribute the excess in Searles Lake to contributions from erosion of older lake beds and from atmospheric sources. Deficiences of other elements such as lithium and fluorine in Searles Lake suggest loss during transport by adsorption on clays or fixation by biological processes.

Post-depositional dilution and loss of salt and brine from Searles basin is indicated by large crystal cavities in certain salt-layer horizons and decreases in the deuterium-hydrogen ratios in the salts and brines from values in the parent brine (Freidman, Smith, and Matsuo, 1982). Calculations by these authors indicate that at least half of the original volumes of saline minerals have been dissolved and exported downward and outward from Searles Valley to Panamint Valley. Thus, some combination of a longer period of mineral discharge and/or a greater rate of mineral discharge in the past from

LVC is required to maintain the tonnage balance. Mineral assemblages within the Upper and Lower Salts and the upper part of the Bottom Mud differ from those in saline layers of older units by including significantly greater amounts of borate, potassium, and sulfate-bearing minerals. This presumably reflects a difference in the chemical composition of thermal waters discharged from LVC between the earlier period of accumulation of saline layers in Units A and B and the more recent period during which the Upper and Lower Salts formed.

The total quantity of boron in the Upper and Lower Salts and the Overburden Mud of Searles Lake is approximately 10^{10} kg (Smith, 1976; Smith, 1979). Calculations by Sorey, Lewis, and Olmsted (1978), based on the mineral content of unaltered samples from the Bishop Tuff, show that leaching by hydrothermal fluids of 50-75 percent of the original boron in 100-150 km^3 of rock would be required to supply this amount of boron. Such volume requirements are met if hydrothermal circulation has occurred throughout a substantial thickness of the Bishop Tuff in the western half of the caldera over the past 40,000 years or more. This possibility is consistent with the interpretation of Williams (1976) that lower magnetic susceptibility over the western half of the caldera reflects extensive hydrothermal alteration within the Bishop Tuff. An unknown fraction of the discharge of boron and other elements could represent direct contributions to the hydrothermal system from magmatic gases.

Bailey, Dalrymple, and Lanphere (1976) found evidence in the form of calcareous cement and tufa deposits in lower lake terraces of increased alkalinity and salinity with time in waters of Pleistocene Long Valley Lake. Rough estimates from ages of associated volcanic

units place the level of the caldera lake at about 2,195 m (7,200 ft) at 0.3 m.y.B.P. and at 2,135 m (7,000 ft) at 0.1 m.y.B.P., with complete drainage of the lake occuring sometime within the last 0.1 m.y. Additional data with which to refine the record of lake level and salinity could come from absolute dating of lake terraces using hydration-rind techniques (Friedman and Smith, 1960). Efforts to date hydrothermal alteration products at the Clay Pit and to analyze alteration mineralogy, fluid inclusions, and isotopic exchange in drill cores could also prove useful in delineating various aspects of the evolution of the hydrothermal system in LVC.

Heat Requirements from Magmatic Sources

Heat needed to sustain periods of hydrothermal circulation during the past 0.3 - 0.4 m.y. could have come from several sources. Bailey, Dalrymple, and Lanphere (1976) infer from the paucity of hydrothermal alteration directly associated with the moat rhyolites that the hydrothermal system is related to the main magma chamber rather than to individual postcaldera eruptive groups. Although hydrothermal activity is not spatially related to the postcaldera eruptive groups, additions of heat to the magma chamber from mantle sources may have preceeded the moat eruptions and been accompanied by inflation and shallowing of melt in the chamber which would in turn enhance the rate of heat loss to the hydrothermal system. Heat-conduction models discussed in a later section of this paper indicate that under steady-state conditions the thickness of the conductive roof between the base of the hydrothermal system and the top of the magma chamber would be about 2 km if the rate of heat loss to the hydrothermal system were 15 HFU. Thus, for heat supply from magma at say 6 km, rapid fluid

circulation to depths of 4 km would be required if the present-day heat discharge has persisted long enough for thermal equilibrium to be established (about 0.3 m.y.).

In contrast, the subsurface temperature data discussed in the next section indicate that the present-day hydrothermal system may be heated in large part by one or more relatively shallow intrusions beneath the west moat. The required rate of emplacement of silicic intrusives that cool from 800°C to 300°C to supply heat to fluid convecting at present-day rates is on the order of 3 km^3 / 1000 years. The analysis of Blackwell (this volume) based on the shapes of temperature profiles in wells indicates that thermal fluid has circulated through two distinct aquifers within and above the Bishop Tuff for periods of 3,100 and 700 years, respectively. The volume of silicic intrusives required to supply this convective heat flow over such periods could reasonably be accomodated at relatively shallow depths within the west moat.

The record of saline deposits in Searles Lake suggests, however, that the hydrothermal system in LVC has been active at near present-day rates for much of the past 40,000 years or more. Volumes of silicic intrusives needed to supply convective heat flow at the present-day rate for a period of 40,000 years are on the order of 100 km^3. This estimate could be reduced by about 50 percent if all the required heat were supplied by basaltic intrusions cooled from 1,100°C to 300°C. In either case, the required volumes are unreasonably large for shallow intrusions beneath the west moat, implying that deeper, more extensive magma systems are involved. Deeper heat sources also imply deeper levels of fluid circulation.

Magma from both the Inyo-Mono system and the Long Valley chamber may have provided the necessary heat, since both systems have produced volcanism in the west moat during the past 0.1 m.y. (Bailey, this volume). Thus, it appears likely that during at least the past 40,000 years, the hydrothermal system within LVC has involved both shallow and deep components which have derived heat from both shallow sources (dike intrusions) and deep sources (the Long Valley magma chamber and/or the Inyo-Mono magma chamber).

THERMAL REGIMES

Present-day Hydrothermal System

More than 70 wells have been drilled in LVC since 1960 by government agencies and private industry. Well depths range from about 3 to 2,100 m; over that interval, aquifers at temperatures ranging from 5°C to 175°C have been encountered. Temperature profiles in core holes and shallow peizometer holes less than 300 m deep (figure 4) were divided into three groups on the basis of near-surface gradients by Lachenbruch and others (1976a): Group I profiles are characteristic of the outer margins of the caldera where hydrologic recharge produces nearly isothermal conditions; Group II profiles show little influence of fluid convection to the depth penetrated; Group III profiles show large near-surface gradients and considerable variability with depth that are characteristic of areas of subsurface flow of thermal water around the southern side of the resurgent dome and east of Hot Creek.

Locations of wells labeled CH, which are core holes completed with steel casings and cemented annuli, are shown in figure 5 along with locations of seven deeper wells drilled by private industry. Temperature profiles for all but one of the deeper wells are plotted in figure 6; data for well LC at the head of Long Canyon are still proprietory. Temperature profiles for wells along section AA' are plotted by position and altitude in figure 7. Profiles for wells P2, CP, and RG are also projected onto this section and drawn as dashed lines.

The temperature profiles shown in figures 6 and 7 show that the type of variability in gradient noted for the shallow wells in Group III (figure 4) also exists at deeper levels within the caldera. Most

notable are the reversals in temperature gradient which reflect the effects of lateral convective heat transfer. Such reversals can be caused by the transient thermal regime set up by lateral flows of hot or cold water, or can represent steady-state conditions associated with flow in adjacent aquifers at different temperatures. In some cases gradient reversals of a similar nature are produced by the loss of drilling fluid in permeable zones, as in the profile for well P1 run only 6 days after drilling was completed.

Along section AA' there appears to be a continuous zone of hot water flowing laterally from Casa Diablo eastward at altitudes near that of Lake Crowley (2,070 m). Temperatures in this zone decrease from about 170°C under Casa Diablo (well M1) to less than 70°C near Lake Crowley. Hydrologic continuity for such flow could be provided within lacustrine sediments that underlie this region, although some complexity must be introduced by the normal faults crossing the section. As noted previously, these faults provide conduits for upflow from thermal aquifers to hot springs and fumaroles. It should also be pointed out that this zone of thermal water flow lies below the shallow water-table aquifer that transmits relatively cold groundwater to discharge points such as the springs at the (Hot Creek) Fish Hatchery (figure 1).

Temperature profiles in wells to the north of section AA' show that the thermal flow zone near 2,070 m altitude is not continuous under the resurgent dome, but that additional zones of thermal-water flow at shallow depths occur east of Hot Creek. The total rate of flow in such zones east of Hot Creek was estimated by Sorey, Lewis, and Olmsted (1978) to be 120 L/s at an average temperature of 50°C.

Temperature profiles in wells west of Casa Diablo show no evidence of the thermal flow zone near 2,070 m altitude, although data is not yet available from several industry wells drilled in the west moat north of section AA'. A zone of high temperature gradient was measured in well P1 below a depth of 550 m; an extrapolated profile beneath this well would reach a temperature of 240°C near the top of the Bishop Tuff, estimated from seismic and gravity data to lie at an altitude of 1520 m in this vicinity. This suggests that the source of hot water flowing at shallow depths beneath the Casa Diablo area and to the east may be within the Bishop Tuff under the west moat, where the associated heat source could be recent dike intrusions. The occurrence of fumaroles and hot springs on the flanks of Mammoth Mountain (figure 1) may be related the postulated hot-water reservoir beneath the west moat or may instead be associated with a more localized, shallow-rooted circulation system.

The inferred source reservoir may be continuous with the deeper thermal flow zone delineated by the temperature reversal at an altitude of 1590 m in well M1 at Casa Diablo. A plausible model that fits the available temperature data involves eastward flow of hot water in the Bishop Tuff beneath the west moat to the general vicinity of the fault bounding the medial graben, 1 km west of Casa Diablo (figure 1). As shown in figure 7, a portion of this deeper flow could move up this fault and then flow eastward in the shallow flow zone around the southern side of the resurgent dome. Fumarolic discharge at several locations west of Casa Diablo (figure 1) could be related to such a zone of upflow. Continuity of flow in the deeper aquifer east of Casa Diablo cannot be delineated because of a lack of data from deep drill holes. If it extends within the Bishop Tuff under the

resurgent dome, upflow from this zone may feed the springs at the head of Little Hot Creek (figure 1).

Temperatures measured in well RG in the east moat suggest lateral flow of thermal water at temperatures near 70°C above the Bishop Tuff and lateral flow of cooler water within the Bishop at altitudes near 800 m. Because measured temperatures at this altitude are higher to the west, Blackwell (this volume) proposes a model involving large-scale convection of groundwater westward within the Bishop Tuff and eastward in sediments and volcanics above the tuff. However, hydraulic-head differences based on water table altitudes and stable isotope relationships are not consistent with such a deep flow system (Sorey, Lewis, and Olmsted, 1978). Instead, a separate convection system is postulated for the east moat with recharge along the ring fracture, most likely around the northeast rim, and upflow in the vicinity of the intra-caldera extension of the Hilton Creek Fault.

Evidence for Deep Circulation

Contraints provided by the amounts and ages of various saline mineral deposits in Searles Lake, by dating of areas of extensive fossil hydrothermal alteration within LVC, and heat requirements associated with hot-spring discharge that continues over periods much greater than about 1,000 years indicate that the hydrothermal system in LVC has involved deeper circulation and deeper heat sources in the past than at present. This deeper circulation system may have extended to depths of several kilometers beneath some areas of the caldera. During periods when such a system was active, the thermal regime within zones of upflow should have been affected in a manner similar to that of the present thermal regime within parts of the

Valles Caldera, where temperatures exceeding 300°C and upward doming of isotherms are detected within the Bandelier Tuff (Grant and Garg, 1981).

The available temperature data for LVC are as yet too limited to adequately delineate the temperature distribution below depths of about 1 km. However, a plot of bottom-hole temperatures versus depth for the three wells that penetrate the Bishop Tuff (figure 8) permits general trends to be identified beneath the resurgent dome and east moat. Assuming that bottom-hole temperatures in wells M1 and CP on the resurgent dome are not significantly affected by convective heat flow in aquifers at shallower depths, an average gradient of about 75°C/km is suggested for the background thermal regime upon which the effects of short-term convective heat flow are superimposed. This result implies that fluid temperatures close to the inferred maximum values attained in the present-day hydrothermal system (240°C) may be present within the basement rocks at depths of a few kilometers under the resurgent dome.

The bottom-hole temperature in well RG in the east moat plots below the line corresponding to a gradient of 40°C/km and a heat flow of 2 HFU, the regional heat flow reported by Lachenbruch and others (1976b) for wells east of the caldera rim. This comparison and the shape of the measured temperature profile in well RG (figure 6) suggest that temperatures at depths of at least 2.1 km beneath the east moat are being cooled by the postulated circulation of ground-water within the Bishop Tuff in that region. It should be noted also that Lachenbruch and others (1976b) inferred from the observed heat

flow near the eastern rim that magma from the part of the Long Valley chamber beneath the east moat may have been exhausted with the eruption of the Bishop Tuff. With no resupply of heat beneath this region, a residual magma chamber more circular in plan could have developed under the western part of the caldera.

The temperature-depth trend depicted in figure 8 as the background thermal regime beneath the resurgent dome could be interpreted in terms of two end-member models. If a deep circulation system had persisted beneath this area until a few thousands years ago, the model of Lachenbruch and Sass (1977) for the effective depth to magma could be applicable. Under steady-state conditions, if D is the actual depth of a magma chamber and D_c is the depth over which hydrothermal circulation affects the thermal regime, the relationship between D and D_c is given by

$$D - D_c \left(\frac{N - 1}{N}\right) = \frac{K - T_m}{q} \qquad (1)$$

where K = mean thermal conductivity of the overburden, NK = the effective thermal conductivity in the zone of hydrothermal convection, T_m = temperature of magma, and q = mean combined heat flux above the magma chamber (and at the land surface). As indicated in figure 8, if this model were applied to the LVC with a heat flux of 15 HFU assumed to come from the Long Valley magma chamber, the bottom-hole temperature data for the resurgent dome would be consistent with magma at approximately 5 km and fluid circulation extending to a depth of 3 km. The value of N in this case would be approximately 3. In this one-dimensional model, the temperature vs depth trend defined by the bottom-hole temperature data would represent an average thermal regime between cooler conditions in zones of downflow and hotter conditions

in zones of upflow. Similar, but more detailed results were obtained by Sorey, Lewis, and Olmsted (1978) from three-dimensional numerical simulations of the effects of deep circulation. Although D = 5 km is not unreasonable in view of recent studies detecting magma at similar depths under parts of the resurgent dome (Sanders, this volume), the time required to reach such a thermal steady state is on the order of 0.3 m.y. (Sorey, Lewis, and Olmsted, 1978). If the average depth to magma in the Long Valley chamber was greater than 5 km over most of the past 0.3 m.y., fluid circulation to depths greater than 3 km would have been required to maintain a heat flux of 15 HFU.

An alternative model for the temperature vs depth trend for the resurgent dome is that it represents a condition close to steady-state for heat conduction from a magma chamber at depths of about 10 km, with no deep fluid circulation. Assuming that the deep thermal regime is not affected by convective heat transport, the indicated conductive heat flux would be about 4 HFU. This would be the preferred interpretation if the deep hydrothermal system beneath the resurgent dome had been dormant for most of the past 0.3 m.y., during which time the magma chamber had cooled to depths of 10 km. To the extent that such conditions have been approached, more recent reinflation of the magma chamber to produce regions of melt at depths of 5-8 km would not significantly distort the thermal regime at depths above 3 km for periods of about 60,000 years. This follows from the magnitude of the thermal time constant and its relationship to the distance over which temperatures are affected by conduction from a heat source (Lachenbruch and others, 1976b). However, the conductive

heat flux of 4 HFU suggested by this model is well below the integrated heat flux measured today; the difference could be supplied to the shallow convection system by magma beneath the west moat.

The actual thermal regime at depths below 3 km beneath the resurgent dome probably lies somewhere between the extrapolations in figure 8 because the assumptions required in each model are not met. Obviously more data from deep wells are needed to refine the picture. If there had been a deep circulation system in this region up until a few thousand years ago, evidence of upflow beneath areas of surficial thermal-fluid discharge should still be apparent in the form of elevated temperatures, unless subsequent intrusions of cold water have removed such effects. Alternatively, deep circulation may have been confined to portions of the west moat during the past 40,000 years or more with fluid circulation under the resurgent dome restricted to permeable zones at shallower depths within and above the Bishop Tuff. This situation is illustrated in figure 7 by the larger flow arrows. Heat for such a system would be provided by the Inyo-Mono magma chamber and overlapping parts of the Long Valley chamber.

EVOLUTION OF THE HYDROTHERMAL SYSTEM

A tentative outline for postcaldera development of the Long Valley hydrothermal system is presented in table 4. Selection of the time periods shown was based primarily on the ages of the Searles Lake evaporites; they are intended only as approximate indicators of times when significant changes occured in hydrothermal activity and related hydrologic and thermal processes. It should also be pointed out that concepts of both a deep hydrothermal system, that at one time involved circulation to depths of at least several kilometers over parts of the western half of the caldera, and a shallow hydrothermal system, involving more restricted circulation within and above the Bishop Tuff, may represent oversimplifications of the actual distributions of fluid circulation that existed during the postcaldera period.

Fluid discharge and hydrothermal alteration that reached a peak 0.3 m.y. ago appear to have been related to the deep hydrothermal system and to the main Long Valley magma chamber, possibly during a period when silicic melt persisted at relatively shallow depths. Major areas of hot-water and steam discharge associated with this activity occured at somewhat higher elevations than at present. Subsequent decreases in the intensity of activity within the deep hydrothermal system may have occurred due to cooling and downward crystallization of the magma chamber as well as sealing of fluid conduits by chemical precipitation.

Within the past 0.2 m.y. the eruptive products from both the Long Valley and Inyo-Mono magmatic systems have been confined to the western and southwestern moat areas (Bailey, Dalrymple, and Lanphere, 1976; Bailey, this volume). This fact and the recharge potential provided by the proximity of the Sierra Nevada to the caldera ring

fracture suggest that hydrothermal activity within the past 40,000 years or longer may have been associated with intrusions of magma at various depths beneath these peripheral areas. Intrusive volumes required to supply 40,000 years of convective heat flow at present-day rates are 50 - 100 km^3. This implies that although the heat contained in shallow dikes of limited dimension could drive the present-day system for short periods of time, hydrothermal circulation must have extended to deeper levels and received heat from larger volumes of melt within the Inyo-Mono or Long Valley magmatic systems in the past.

The shift in chemical composition of thermal waters from LVC indicated by the quantities of borate, sulfate, and potassium-bearing minerals within the Upper and Lower Salts and the upper part of the Bottom Mud in Searles Lake, may have been accompanied by a redistribution of flow paths within the Long Valley hydrothermal system. Such a redistribution could have involved the development of zones of deep circulation beneath the west moat and zones of lateral flow through the Bishop Tuff under the resurgent dome. The general distribution of temperature with depth within the lower section of the Bishop Tuff beneath the resurgent dome, based on bottom-hole temperature measurements in two wells, may be relatively unaffected by convective heat transport from such a deep circulation system. The average gradient defined by the bottom-hole temperature data (75°C/km) implies a conductive heat flux of about 4 HFU, which is smaller by a factor of about 4 than the present-day rate of heat loss. Therefore, either the gradient and heat flux below the depth of fluid circulation are 4 times greater or the shallow zone is losing heat provided from somewhere else.

The present-day hydrothermal system apparently consists of several relatively thin zones of hot water flowing laterally from west to east at depths of less than about 1 km. Maximum measured temperatures of about 170°C occur within an upper flow zone at depths of 120 - 150 m beneath Casa Diablo. Flow in this zone may continue eastward around the south side of the resurgent dome to Lake Crowley. A lower flow zone within the Bishop Tuff can also be delineated beneath Casa Diablo. Evidence from a high temperature gradient measured in a well within the west moat and the existence of fumaroles and hot springs on the flanks of Mammoth Mountain indicate that this lower flow zone may originate beneath the west or southwest moat where reservoir temperatures near 240°C are suggested by geothermometer calculations. Upflow of a portion of the flow in this lower zone along fault conduits west of Casa Diablo is suggested as the mechanism for charging the shallow thermal flow zone under Casa Diablo. The original source of recharge for the hydrothermal system is most likely meteoric water moving down the ring fracture around the west and southwest rim of the caldera. Beneath the eastern side of the caldera, temperature measurements and hydrologic and isotopic considerations indicate the existence of a deeply rooted circulatory pattern of convection, possibly recharged around the northeast rim by downflow along the ring fracture.

Additional information is needed to refine this model of the hydrothermal system in LCV. Data from deeper drilling in the west moat could confirm the existence of high-temperature reservoirs within and perhaps below the Bishop Tuff. Analyses of fluid samples from such reservoirs and from thermal flow zones beneath Casa Diablo and Long Canyon would further delineate the degree of lateral continuity

within these zones. Deep drilling in the west moat could also provide information needed to refine seismic-velocity profiles within the caldera fill and delineate the extent of shallow dike intrusion associated with the Inyo-Mono magmatic system. Temperature data from deeper drilling beneath the resurgent dome is needed to determine the thermal regime below the caldera fill, which in turn may provide information about previous periods of deep hydrothermal circulation and the locations and ages of zones of shallow magma. Finally, analyses of hydrothermal-alteration mineralogy, mineral leaching, and isotopic exchange in cores and cuttings from existing wells could allow better definition of the extent and duration of previous periods of hydrothermal circulation.

REFERENCES

Bailey, R.A., Dalrymple, G.B., and Lanphere, M.A., 1976, Volcanism, structure, and geochronology of Long Valley caldera, Mono County, California: Journal of Geophysical Research, v. 81, no. 5, p.725-744.

Bailey, R.A., and Koeppen, R.P., 1977, Preliminary geologic map of Long Valley caldera, Mono County, California: U.S. Geological Survey open-file map, 2 p.

Faust, C.R., Mercer, J.W., and Thomas, S.D., 1983, Quantitative analysis of geothermal development in the Jemez Mountains: Final report to the Bureau of Indian Affairs, Albuquerque, New Mexico, by Geotrans, Inc, 87 p. plus Appendices.

Fournier, R.O., White, D.E., and Truesdell, A.H., 1976, Convective heat flow in Yellowstone National Park: Second United Nations Symposium on the development and use of geothermal resources, Proceedings, p. 731-739.

Fournier, R.O., Sorey, M.L., Mariner, R.H., and Truesdell, A.H., 1979, Chemical and isotopic prediction of aquifer temperatures in the geothermal system at Long Valley, California: Journal of Volcanology and Geothermal Research, v. 5, p. 17-34.

Fournier, R.O., 1981, Application of water geochemistry to geothermal exploration and reservoir engineering: in Geothermal systems: principles and case histories, ed., Rybach, L. and Muffler, L.J.P., p.109-126.

Friedman, I. and Smith, R.L., 1960, A new dating method using obsidian, 1, the development of the method: American Antiquity, v. 25, p. 476-493.

Friedman, I., Smith, G.I., and Matsuo, S., 1982, Economic implications of the deuterium anomaly in the brine and salts of Searles Lake, CA, Economic Geol. v. 77, no. 3, p. 694-702.

Goff, F.E., and Sayer, S., 1980, A geothermal investigation of spring and well waters of the Los Alamos region, New Mexico: Los Alamos Scientific Laboratory report LA-8326-MS, 21 p.

Grant, M.A., and Garg, S.K., 1981, Interpretation of downhole data from the Baca geothermal field: status as of June 1981: Geothermal Resources Council, Transactions, v. 5, p. 337-340.

Holser, W.T., 1970, Bromide geochemistry of some non-marine salt deposits in the southern Great Basin: Mineralogical Society of America Special Paper 3, p. 307-319.

Lachenbruch, A.H., and Sass, J.H., 1977, Heat flow in the United States and the thermal regime of the crust: American Geophysical Union Geophysical Monograph 20, p. 626-675.

Lachenbruch, A.H., Sorey, M.L., Lewis, R.E., and Sass, J.H., 1976a, The near-surface hydrothermal regime of Long Valley caldera: Journal of Geophysical Research, v. 81, no. 5, p. 763-768.

Lachenbruch, A.H., Sass, J.H., Munroe, R.J., and Moses, T.H., 1976b, Geothermal setting and simple heat-conduction models for the Long Valley caldera: Journal of Geophysical Research, v. 81, no. 5, p. 769-784.

Lewis, R.E., 1974, Data on wells, springs, and thermal springs in Long Valley, Mono County, California: U.S. Geological Survey open-file report, 52 p.

Liddicoat, J.C., Opdyke, N.D., and Smith, G.I., 1980, Paleomagnetic polarity in a 930-m core from Searles Valley, California: Nature, v. 286, no. 5768, p. 22-25.

Lipshie, S.R., 1976, Geologic guidebook to the Long Valley - Mono Craters region: GSUCLA Field Guide No. 5 for field trip of the Geological Society of UCLA, University of California at Los Angeles, 184 p.

Mariner, R.H., and Willey, L.M., 1976, Geochemistry of thermal waters in Long Valley, Mono County, California: Journal of Geophysical Research, v. 81, no. 5, p. 792-800.

Rison, W., Welham, J.A., Poreda, R., and Craig, H., 1983, Long Valley: increase in the $^{3}He/^{4}He$ ratio from 1978 to 1983: Abstract in Transactions of the American Geophysical Union, v. 64, no. 45, p. 891.

Smith, G.I., 1976, Origin of lithium and other components in the Searles Lake evaporites, California in Vine, J.D., ed., Lithium resources and requirements by the year 2000: U.S. Geological Survey Professional Paper 1005, p. 92-103.

Smith, G.I., 1979, Subsurface stratigraphy and geochemistry of late Quaternary evaporites, Searles Lake, California: U.S. Geological Survey Professional Paper 1043, 103 p.

Smith, G.I., Barczak, V.J., Moulton, G.F., and Liddicoat, J.C., 1983, Core KM-3, a surface-to-bedrock record of Late Cenezoic sedimentation in Searles Valley, California: U.S. Geological Survey Professional Paper 1256, 24 p.

Smith, G.I., and Pratt, W.P., 1957, Core logs from Owens, China, Searles, and Panamint basins, California: U.S. Geological Survey Bulletin 1045-A, p. 1-62.

Smith, R.L., and Bailey, R.A., 1968, Resurgent cauldrons: Geological Society of America Memoir 116, p. 613-662.

Sorey, M.L., and Lewis, R.E., 1976, Convective heat flow from hot springs in the Long Valley caldera, Mono County, California: Journal of Geophysical Research, v. 81, no. 5, p. 785-791.

Sorey, M.L., and Lewis, R.E., and Olmsted, F.H., 1978, The hydrothermal system of Long Valley caldera, California: U.S. Geological Survey Professional Paper 1044-A, 60 p.

Stuiver, M., and Smith, G.I., 1979, Radiocarbon ages of stratigraphic units, in Smith, G.I., Subsurface stratigraphy and geochemistry of Late Quaternary evaporites, Searles Lake, California: U.S. Geological Survey Professional Paper 1043, p. 68-73.

Taylor, B.E., and Gerlach, T.M., 1983, Chemical and isotopic composition of Casa Diablo Hot Spring: magmatic CO^2 near Mammoth Lakes, California: Abstract in Transactions of the American Geophysical Union, v. 65, no. 7, p. 58.

Williams, D.L., 1976, Implications of a magnetic model of the Long Valley caldera, California: U.S. Geological Survey open-file report 76-439, 7 p.

Table 1. Comparisons of different measures of the intensity of hydrothermal activity at several young silicic calderas.

Caldera (age)	Fluid discharge[1] kg/s	Heat discharge[2] 10^7 cal/s	Heat flux[3] HFU
Yellowstone[4] (0.6 m.y.)	3,000	100	50
Long Valley[5] (0.7 m.y.)	250	6.9	15
Valles[6] (1.1 m.y.)	35	1.8	12

[1]Discharge of high-chloride thermal water in hot springs and river seepage.

[2]For Yellowstone caldera, heat discharge represents convective heat flow in in deep reservoirs from which thermal water discharges at the land surface within part of the caldera draining east of the Continental Divide. For Long Valley caldera, heat discharge represents the surficial discharge of heat by conduction and convection within the caldera area. For Valles caldera, heat discharge represents the sum of conductive and convective heat flow within the caldera area and convective heat flow in subsurface outflow of thermal water that discharges in springs and river seepage outside the caldera.

[3]Calculated as heat discharge divided by caldera area (2,023 km^2 for Yellowstone, 450 km^2 for Long Valley, and 150 km^2 for Valles).

[4]Data from Fournier, White, and Truesdell (1976) and Christiansen (this volume).

[5]Data from Sorey, Lewis, and Olmsted (1978).

[6]Data from Faust, Mercer, and Thomas (1983) and Goff and Sayer (1980).

Table 2. Chemistry of thermal (>15 °C) and nonthermal waters in the vicinity of Long Valley caldera.

Feature	Date sampled	T	PH	ALK[11]	Cl	B	As	Li	F	SiO_2	SO_4	Na	K	Ca	Mg	Fe	Hg	Zn	Geothermometers[12] Quartz	Na-K-Ca
		°C			mg/L	mg/L	mg/L	mg/L	mg/L	mg/L	mg/L	mg/L	mg/L	mg/L	mg/L	ug/L	ug/L	ug/L	°C	°C
Casa Diablo well[1]	5/72	94	9.4	368	280	15	2.2	2.8	12	340	130	390	45	0.9	0.1	50	0.1	190	219	238
Casa Diablo Hot Springs[2] (west of old 395)	10/4/83	91	6.8	47	260	12	1.9	1.1	9.3	220	160	240	23	9.1	1.2	15	0.3	53	186	192
Colton Spring[3]	10/6/83	92	8.3	122	260	11	1.6	2.8	11	240	140	370	24	1.3	0.3	5	0.1	3	193	193
Hot Creek Gorge Spring[4]	10/4/83	91	8.1	500	230	11	1.2	2.5	9.9	140	99	390	25	2.0	0.2	5	0.5	4	157	192
Little Hot Creek Springs[5]	10/4/83	82	6.7	593	210	8.9	0.6	2.9	8.6	85	100	400	28	23	0.7	-	0.1	3	128	165
Meadow Spring[6]	10/6/83	64	6.2	122	190	8.5	2.0	1.3	7.2	190	120	210	36	4.1	0.6	9	0.1	17	176	205
Reds Meadow Hot Springs[7]	7/25/84	46	7.3	423	6.7	1.8	-	0.9	4.8	150	33	140	6.2	61	2.5	20	0.2	110	161	130
Casa Diablo Hot Springs[8] (east of old 395)	8/16/73	93	3.7	-	20	.05	0.005	-	0.4	160	1500	27	17	19	41	7400	-	-	-	-
Big Springs[9]	5/21/71	11	6.8	74	5.7	0.04	0.02	0.04	0.5	58	8	23	4.0	5.1	5.9	30	0.1	45	-	-
Laurel Spring[10]	5/10/84	12	8.9	39	0.5	0.02	0.004	0.006	0.1	19	20	6	1.4	15	0.6	3	0.1	3	-	-

[1] Well Magma Ritchie 5, sampled to include total flow of water and steam. Data from Mariner and Willey (1976).

[2] Northernmost spring along base of fault scarp. Analysis by USGS Central Laboratory, Denver, Colorado.

[3] Analysis by USGS Central Laboratory, Denver, Colorado.

[4] Spring along east bank of Hot Creek about 150 m below bridge. Analysis by USGS Central Laboratory, Denver, Colorado.

[5] Hottest spring, at southwest corner of area containing 4 main vents. Analysis by USGS Central Laboratory, Denver, Colorado.

[6] Analysis by USGS Central Laboratory, Denver, Colorado.

[7] Analysis by USGS Central Laboratory, Denver, Colorado.

[8] Data from Lewis (1974).

[9] Data from Mariner and Willey (1976).

[10] Analysis by USGS Central Laboratory, Denver, Colorado.

[11] Alkalinity calculated as calcium carbonate.

[12] Calculated from equations given by Fournier (1981) for empirically derived relationships between SiO_2 concentrations and cation ratios and and equilibrium temperatures. Quartz geothermometer calculations assume conductive cooling; cation geothermometer calculations corrected for Mg concentration, except for the Casa Diablo spring, where most of the dissolved Mg is assumed to come from surficial sources.

Table 3. Age and thickness of stratigraphic units in Searles Lake (modified from Smith and others, 1983).

Unit	Depth to base (m)	Lithology	Age of base m.y.B.P.
Overburden Mud	6	Mud and salines	0.006
Upper Salt	20	Salines	0.01
Parting Mud	25	Mud and salines	0.024
Lower Salt	38	Salines	0.032
Bottom Mud	69	Mud and salines	0.13
Mixed Layer Units A-B	114	High-pH salines and mud	0.31
Units C-1	693	Neutral-pH salines and mud	3.18
Alluvium	916	Sand and gravel	?
Bedrock	-	Quartz monzonite	?

Table 4. Tentative outline of the evolution of the hydrothermal system in Long Valley caldera and related hydrologic and magmatic processes.

Time period m.y.B.P.	Significant events
0.7 - 0.3	Development of conduits for deep hydrothermal circulation, with maximum rate of discharge attained by 0.3 m.y. Cooling and crystallization of Long Valley magma chamber to depths of 6-9 km. Decline in level of caldera lake from 7,600 to 7,200 ft. a.s.l.
0.3 - 0.13	Active discharge from deep hydrothermal system. Extensive development of acidic hydrothermal alteration at Clay Pit and siliceous sinter at other locations around the margins of the resurgent dome. Discharge from Long Valley hot springs dominated by sodium carbonate minerals carried by ancestral Owens River system to eventual deposition in saline Units A and B of Searles Lake. Initiation of mafic volcanism in west moat associated with the Inyo-Mono magmatic system and rejuvenation of the Long Valley magma chamber resulting in eruption of 0.28 m.y. old rhyolites in the southeast moat. Decline in level of caldera lake from 7,200 to 7,000 ft. a.s.l. and corresponding increase in alkalinity and salinity of lake waters.
0.13 - 0.04	Active discharge from deep hydrothermal system, involving a shift in chemical composition of thermal waters toward greater concentrations of boron, potassium and sulfate. Deposition of the Bottom Mud in Searles Lake during times of high Lake levels and low salinities. Continued mafic volcanism in west moat from Inyo-Mono magmatic system and rhyolitic volcanism from Long Valley chamber at 0.1 m.y. Draining of caldera lake.
0.04 - 0	Discharge at near present-day rates from hydrothermal system involving zones of shallow and deep circulation, with heat provided by parts of the Inyo-Mono and Long Valley magmatic systems beneath the west moat. Deposition of salines in the Upper and Lower Salts of Searles Lake containing borate and sulphate minerals contributed by hot springs in the Long Valley caldera. Development of zones of hydrothermal alteration through a substantial thickness of the Bishop Tuff within the western half of the caldera. Reinflation of the Long Valley magma chamber to depths of 4-5 km beneath parts of the resurgent dome.

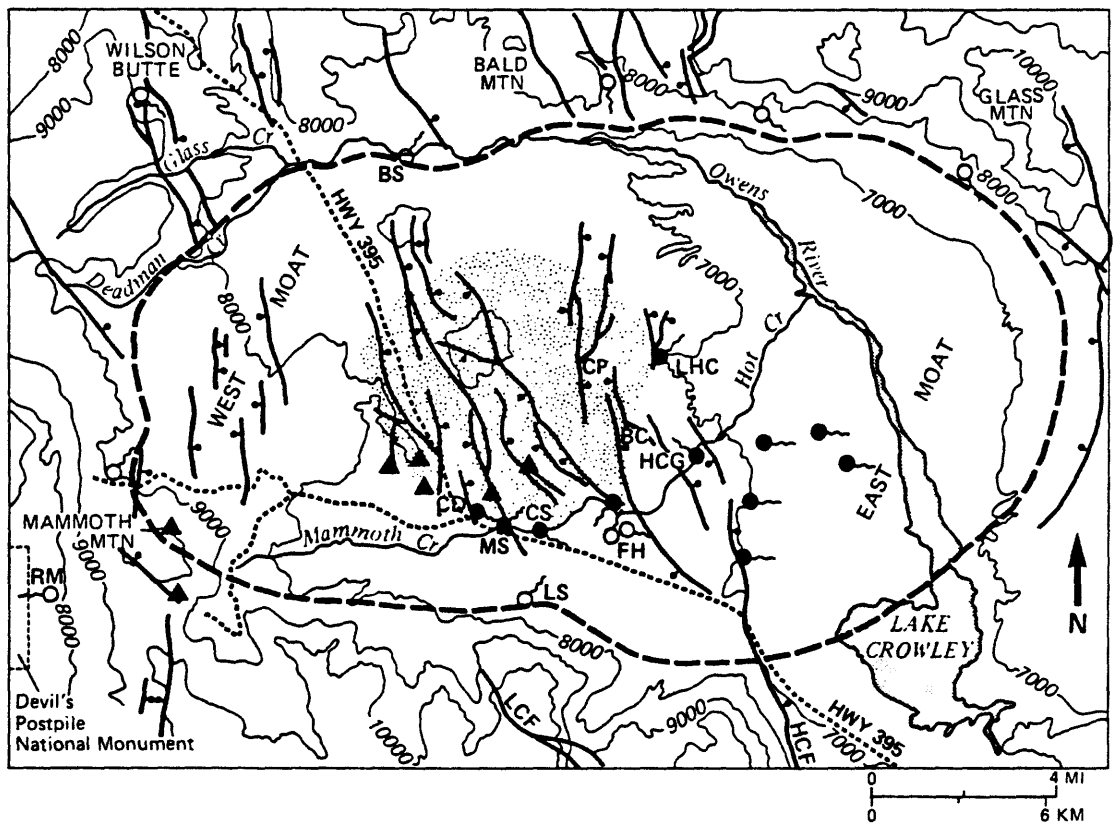

Figure 1. Map of Long Valley caldera (heavy dashed line outlines caldera floor) showing locations of active thermal springs (filled circles with tails), nonthermal springs (open circles with tails), fumaroles (triangles), and areas of fossil hydrothermal alteration noted in text (CP = Clay Pit, BC = Blue Chert). Also shown are principal faults as mapped by Bailey and Koeppen (1977) (HCF = Hilton Creek Fault, LCF = Laurel-Convict Fault), contours of land-surface altitude (in feet), paved roads (dotted lines), and the structural outline of the resurgent dome (patterned area. Springs for which chemical analyses are reported in table 2 are labled RM (Reds Meadow Hot Springs), CD (Casa Diablo Hot Springs), MS (Meadow Spring), CS (Colton Spring), LS (Laurel Spring), HCG (Hot Creek Gorge Spring), LHC (Little Hot Creek Spring), and BS (Big Springs). FH denotes springs at the Fish Hatchery.

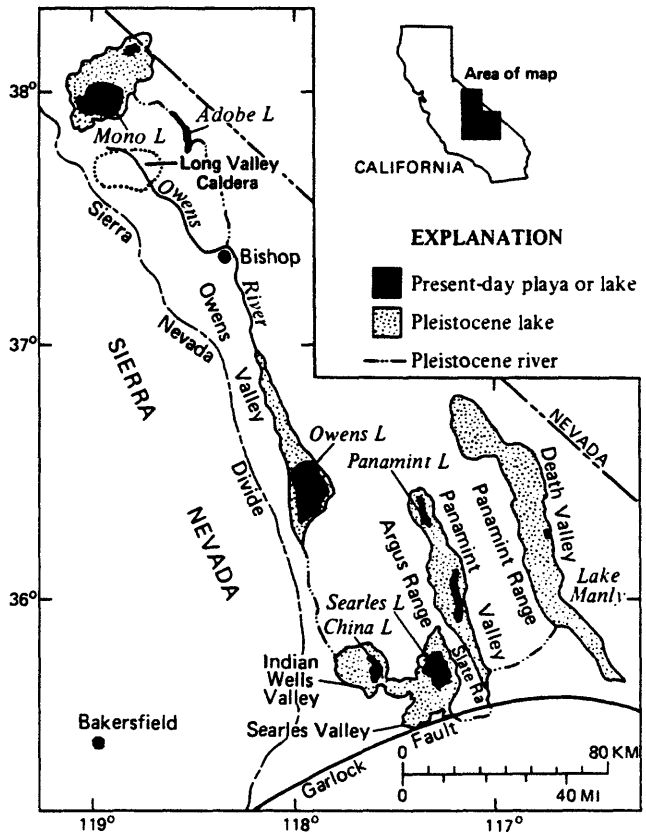

Figure 2. Locations of late Pleistocene and present-day lakes in the chain that includes Searles Lake and Long Valley caldera (modified from Smith and others, 1983).

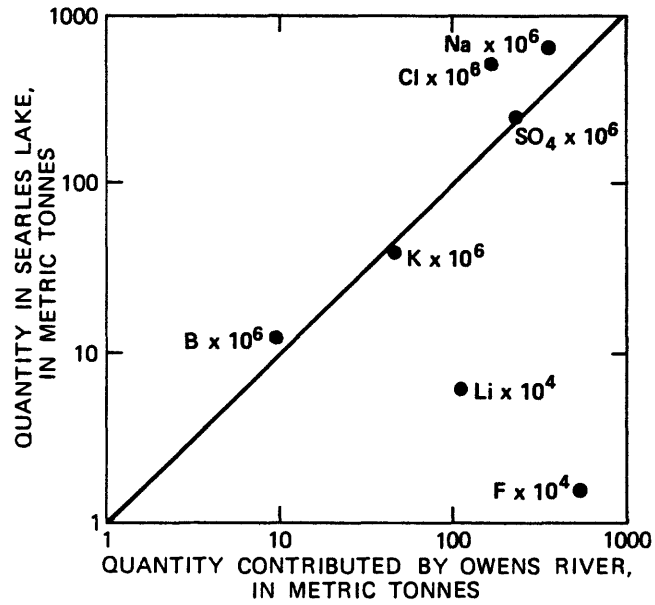

Figure 3. Diagram showing relations between tonnages of selected components carried by the present Owens River in 32,000 years and tonnages in the Upper and Lower Salt of Searles Lake. Quantities expressed as tonnes multiplied by indicated exponent. Diagonal line indicates 1:1 relation. For Li and F, plotted points apply to 24,000 years of flow and corresponding quantities in the Upper Salt. Modified after Smith (1976).

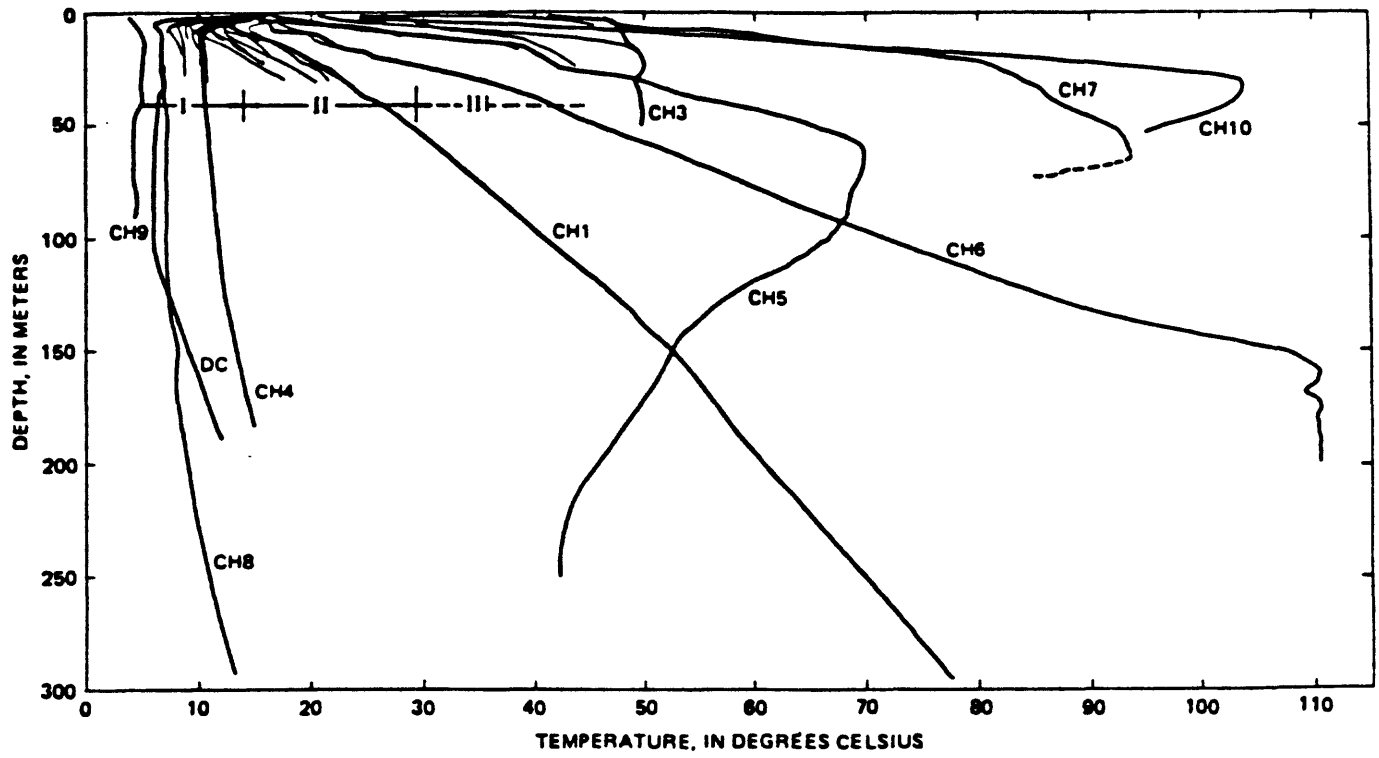

Figure 4. Temperature profiles in core holes and shallow peizometer holes (unlabeled) in Long Valley caldera (from Sorey, Lewis, and Olmsted, 1978). Roman numerals identify groups of profiles associated with similar hydrologic conditions, as discussed in text.

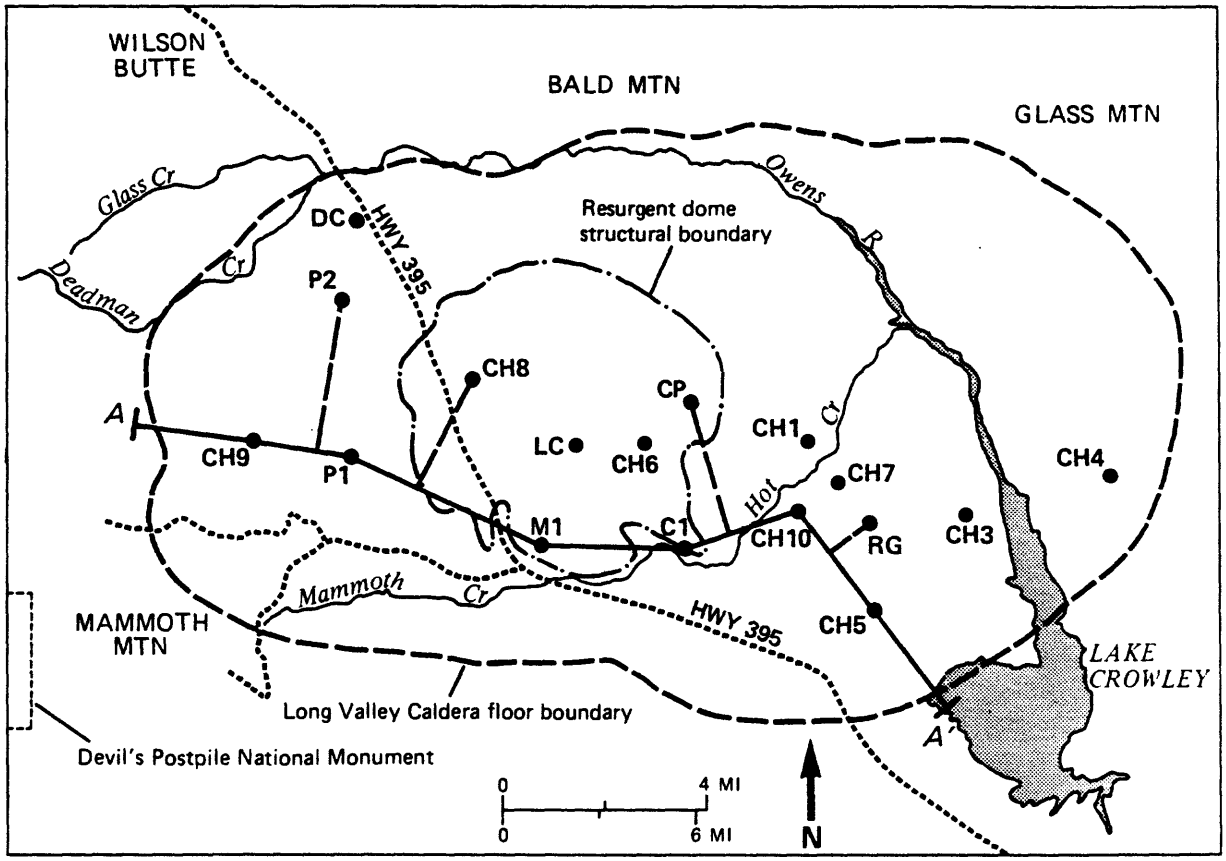

Figure 5. Map of Long Valley caldera showing locations of core holes (labeled CH) for which temperature profiles are plotted in figure 4, and deeper wells lying along or projected onto section AA' for which temperature profiles are plotted in figure 6. Data for well LC are still proprietory. Paved roads shown as dotted lines.

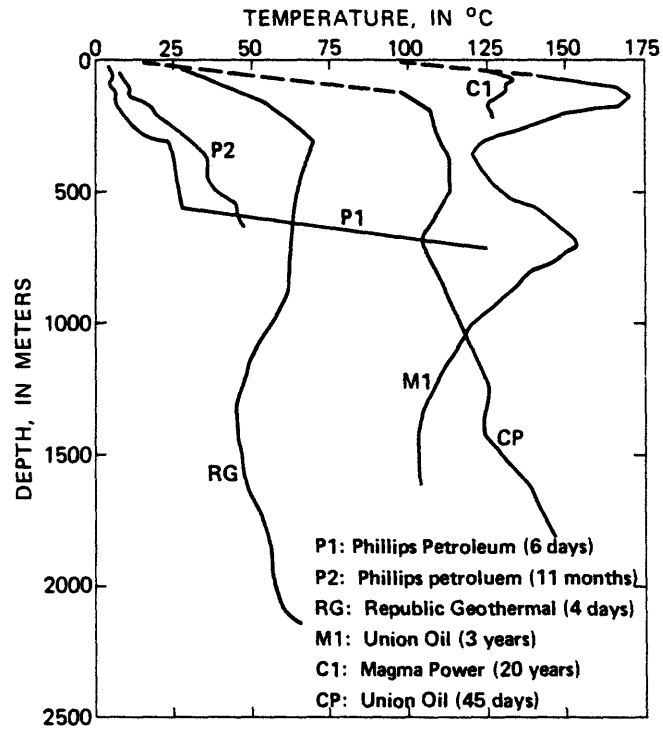

Figure 6. Temperature profiles for deep wells drilled by private industry in Long Valley caldera (see figure 5 for location of wells). Extrapolations above the depth of first measurement indicated by dashed lines. Elapsed times between well completion and time of temperature measurements shown in parentheses.

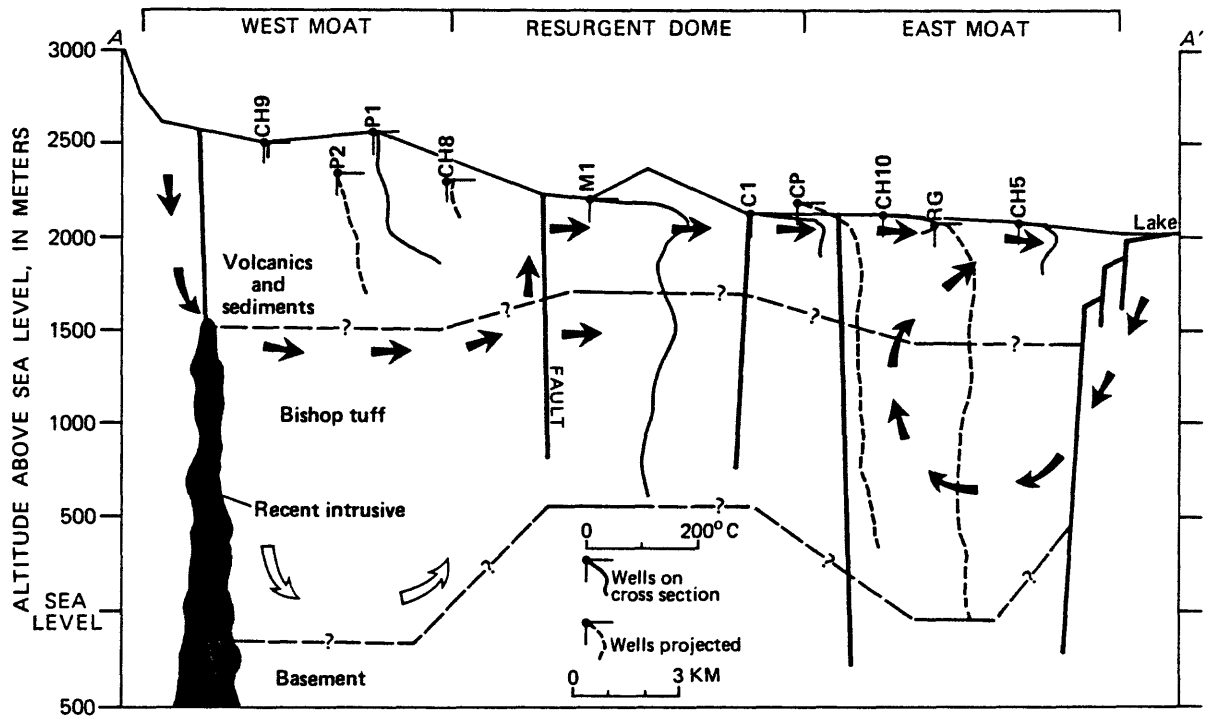

Figure 7. Temperature profiles in wells located in Long Valley caldera along or projected onto section AA' (figure 5). Contacts at the top and bottom of the Bishop Tuff are shown as solid lines where control is provided by well data and by dashed lines where control is provided by seismic and gravity data. Inferred directions of fluid flow in the present-day hydrothermal system indicated by dark arrows. Deeper circulation beneath the west moat during previous periods of activity indicated by light arrows.

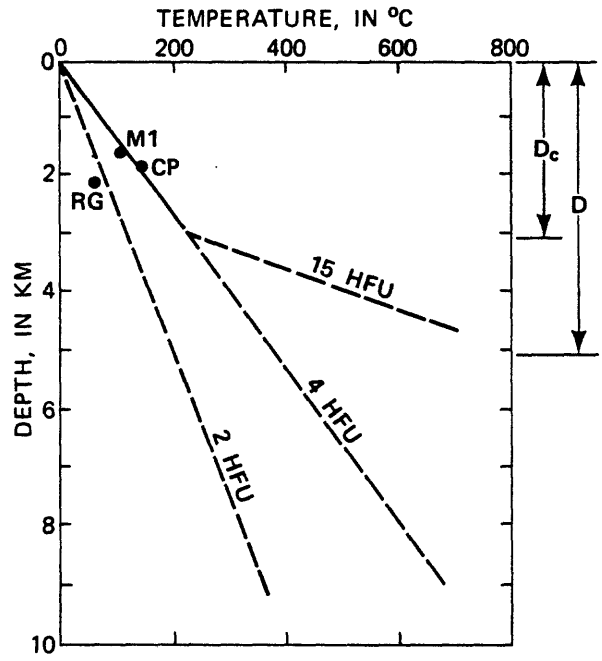

Figure 8. Plots of temperature versus depth for conductive heat flow at various rates (thermal conductivity = 5 mcal/(s°C cm) and bottom-hole temperatures in deep wells in Long Valley caldera. Solid line represents the inferred background temperature gradient beneath the resurgent dome, based on data for wells M1 and CP. D is the depth to magma at 800°C that would produce a heat flux of 15 HFU under steady-state conditions beneath a zone of fluid convection of thickness D_c.

A TRANSIENT MODEL OF THE GEOTHERMAL SYSTEM OF THE LONG VALLEY CALDERA, CALIFORNIA

David D. Blackwell

Department of Geological Sciences

Southern Methodist University

Dallas, Texas 75275

ABSTRACT

The present-day geothermal system underlying the southern one-third of the Long Valley Caldera is discussed, based on interpretation of the complex shapes of temperature-depth curves and the correlation of this interpretation with hydrologic and geologic data. The results give information on the transient nature of the geothermal system operating in the Long Valley caldera. At the present time there is major west-east flow of hot fluid in two aquifers. The first aquifer is just below (and in places may be) the shallow groundwater table aquifer. Water is recharged at a temperature greater than 175°C west of Casa Diablo Hot Springs, and flows eastward at a velocity on the order of 100 to 200 m/yr to exit in the hot springs along Hot Creek and at the edges of Lake Crowley. Temperatures systematically decrease eastward in the shallow aquifer. In order to interpret the temperature data in Long Valley caldera, a model of the thermal effects of flow in a shallow aquifer is discussed, and the results are found to be consistent with geologic and hydrologic information. The shape of overturns of temperature versus depth curves indicate that the age of this aquifer ranges between 200-700 years; the best estimate is 500-700 years. The initiation of hot water flow in the shallow aquifer coincides with intrusive activity associated with the Mono/Inyo Crater chain of rhyolitic centers, which was active over a linear distance of about 40 km during the period 500-600 years ago. A second aquifer occurs just below the top of the Bishop Tuff at a depth of approximately 700 m in hole Mammoth #1. Less is known about the flow velocity and other characteristics of this aquifer. Modeling of the temperature-depth suggests that this aquifer is on the order of 3000 years old. Temperatures associated with both aquifers are evidence for transient events which caused a sudden

input of hot water along the west side of the caldera into an existing geothermal system that was circulating at temperatures below 120°C. Apparently, previous to the input of hot water into these aquifers, the geothermal system in the caldera may have been in a waning phase. The waning of the system may have been due to loss of porosity and permeability by mineral deposition in the circulation pathways and/or cooling of the caldera and subjacent intrusive rocks and a decrease in the thermal drive. There is no evidence of a recent large-scale, high-temperature geothermal system associated with the magma chamber identified by seismic studies beneath the resurgent dome. Whether the high temperatures in the current geothermal system reflect cooling of magma associated with Mono/Inyo Craters, or merely fracturing and reconnection of a pre-existing source of hot water to the shallow subsurface, is not known. Although the shallow flow of hot water is from west to east, deep temperature data suggest deep return flow of cold water from east to west in the caldera fill below the deep aquifer in the eastern part of the caldera. The velocity of this return flow is probably on the order of a meter per year, or two orders of magnitude below the velocity of flow in the shallow aquifers.

INTRODUCTION

The Long Valley Caldera is a 450 km^2 elliptical depression along the eastern front of the Sierra Nevada Mountains in east central California. It occurs along the boundary between the Basin and Range province to the east and the Sierra Nevada province to the west. Cenozoic volcanism in the vicinity began about 3.2 my ago and has continued until very recent times. The caldera was formed about 0.7 my ago by the eruption of approximately 600 km^3 of Bishop Tuff. The eruption of the rhyolitic Bishop Tuff resulted in the collapse of the roof of the magma chamber along steep ring fractures and deposition of about 1 km of infill tuff on the previous basement (Sierra Nevada granite and metamorphic rocks). Subsequent intracaldera volcanism caused resurgence of the west central part of the caldera floor. Extrusion of rhyolite, rhyodacitic and basaltic rocks occurred around the resurgent region between 0.6 and 0.5 my ago. Extrusion of rhyolite domes (Inyo domes) has occurred in the western third of the caldera intermittently to as recently as 500-600 years ago (Miller, 1984). In view of the large size of the caldera and its relatively young age, it is of great practical and theoretical importance to understand the nature of the fluid flow and geothermal systems in the caldera and the mechanisms of cooling of any large magma chamber which might underlie the caldera.

The Long Valley caldera has been extensively studied by the U. S. Geological Survey (see Muffler and Williams, 1976). The geology and the geologic history of the caldera as discussed above were described by Bailey et al. (1976). The geophysical studies of the area have been numerous and detailed. In particular, the geometry of the fill of the caldera was described by Kane et al. (1976) and evidence for a contemporary magma chamber was developed from seismic data by Hill (1976) and Steeples and Iyer (1976).

The regional thermal setting of the caldera was discussed by Lachenbruch et al. (1976b) and the convective and conductive heat flow associated with the shallow hydrologic regime was discussed by Lachenbruch et al. (1976a) and Lewis and Sorey (1976). Subsequent studies of the heat flow associated with the hydrothermal system of the caldera have been published by Sorey et al. (1978), Diment et al. (1980) and Sorey (1984). In particular, Lachenbruch et al. (1976a), Sorey et al. (1978) and Diment et al. (1980) discussed in detail data from numerous shallow (less than 30 m) and intermediate (50 to 300 m deep) depth holes drilled for temperature gradient and heat flow studies. Sorey et al. (1978) described the groundwater hydrologic regime in the caldera and discussed some hypothetical models of the geothermal systems within the caldera. Since 1980 there has been extensive seismic activity along the south side of, and south of the caldera (Ryall and Ryall, 1981, 1983; Sherburne, 1980) which may be related to magmatism (Savage, 1983). Hermance (1983) has summarized recent geophysical studies of the caldera.

The heat transport models discussed by Sorey and Lewis (1976) and Sorey et al (1978) are characterized by a magma chamber under the western half of the caldera, major fluid upflow in the system only in the vicinity of Hot Creek gorge, and deep recharge (1-3 km depth) from the east and the west sides of the caldera toward Hot Creek. No significant shallow flow is included in the model, and the activity near Casa Diablo hot springs is not modeled. The magma chamber is assumed to be steady-state, so that the rate of magma influx must match the rate of heat loss in the geothermal system. The consequences of such an assumption in terms of the amount of magma flux are discussed by Lachenbruch et al. (1976b).

At the time of the geothermal studies mentioned in the previous paragraph, no direct information on the deep system within the caldera was

available and interpretation of the geothermal system was based on the shallow data. Since these studies, thermal and lithological data from three deep holes in the caldera have become available (Smith and Rex, 1977; Petroleum Information Corporation, 1980; Gambill, 1981). These new data are not consistent with some major features of the models proposed previously.

During the same period of time, a better understanding of heat transfer in geothermal systems has developed. While the influence of lateral fluid flow on the thermal profiles and heat flow associated geothermal systems has long been realized, quantitative analysis has been lacking, in part because of lack of sufficient observations to constrain possible models. However, with the development of more sophisticated modeling techniques and with deep drilling in geothermal systems, a number of types of models have been developed. Several models have been discussed for the Imperial Valley geothermal systems (Goyal and Kassoy, 1980; Lau; 1980, Lippmann and Bodvarsson, 1983). However, the information for application of these numerical techniques usually does not exist until extensive deep drilling has occurred, and simple analytic approximations may be more useful in the early exploration stages of geothermal evaluation.

A very common phenomenon in Basin and Range geothermal systems, and indeed associated with many geothermal systems, is the intermittent injection of warm to hot water into the shallow cold water hydrologic system from a reservoir or circulating system deeper in the geothermal system. Flow patterns in many geothermal systems appear to change on the order of a few hundreds to a few thousands of years. Very often, the transient changes in the flow system result in temperature overturns. These temperature overturns were initially discussed by Bodvarsson (1969, 1973), who derived a one-dimensional temperature-time model for them. Ziagos and Blackwell (1981,

1984) developed a two-dimensional model for such flow systems (see also Bodvarsson et al., 1980, 1982). The object of this paper is to apply the model of Ziagos and Blackwell (1981, 1984) to the Long Valley system to demonstrate the usefulness of the solution, to elucidate the characteristics of the shallow geothermal system in the Long Valley Caldera, and to characterize the overall geothermal system and its history.

In the process of applying the flow model to the shallow geothermal system in Long Valley, three different hypotheses with respect to the deep geothermal system underlying the shallow system will be evaluated. These hypotheses are: 1) that in fact no deep system underlies the caldera and the high temperatures in the geothermal system are associated with warming of water in the west end of the caldera by dikes underlying the very young rhyolite domes; 2) a deep system exists in the central part of caldera with temperatures in excess, perhaps much in excess, of 180-200°C, which feeds the shallow system (this has been the model upon which most of the previous analyses have been based); 3) a deep system exists in the west or southwest end of the caldera with minimum temperatures between 180°C and 200°C, which feeds the shallow system.

TEMPERATURE AND HEAT FLOW PATTERN

The shallow heat flow characteristics of the Long Valley caldera have been discussed extensively by Lachenbruch et al. (1976a) and by Sorey et al. (1978). These data can be supplemented with information from the three subsequent deep drill holes and one shallow (200 m) drill hole which was not used in the previous discussions. The hole locations have been taken from Sorey et al. (1978, Plate I). Heat flow values for holes not discussed in that paper are based on thermal conductivities listed in Table 5 of Sorey et

al. (1978). The hydrologic properties of the caldera have been discussed in detail by Sorey et al. (1978). Particularly pertinent to this discussion is the shallow hydrology. The water table elevation drops approximately 350 m between the west edge of the caldera and the Owens River - Lake Crowley region. The strike of the water table contours is approximately north-south (Sorey et al., 1978).

Shallow Hole Results Temperature-depth data in shallow holes in the Long Valley caldera have been discussed by Diment et al. (1980). Temperature-depth curves for the southern part are shown in Figure 1. The locations of the holes are shown in Figure 2. Temperature gradients are extremely high near the surface; in some of the holes temperatures exceed 100°C at depths of less than 50 meters. However, most of the holes show a temperature maximum at shallow depths and temperature decreases below 50 to 100 m, so that temperatures at depths of 200-300 m are much lower than those at shallow depths. Temperatures in other holes in the caldera, particularly to the north of the holes shown in Figure 1 (see Figure 2), show little if any temperature increase to depths of at least 150-300 m.

Figure 2 shows a "shallow" heat flow map similar to that presented by Sorey et al. (1978), but modified by including data from Chance #1, Endogeneous #1, and Clay Pit #1 (see Table 1). Inclusion of these data changes the configuration of the very high heat flow values. Instead of being confined to the area west of Hot Creek (where there are extensive hot springs), the contours of high heat flow extend to the west, and the heat flow anomaly is depicted as a sausage-shaped feature at least 10 km long, 3 or 4 km wide, with heat flow values in excess of 1000 mWm^{-2} over the whole area. In most of the previous discussions and models, major significance has been attached to the Hilton Creek fault zone and to the hot springs in Hot Creek

(see Figure 2). It has been generally concluded that significant recharge of hot water into the shallow system is occurring at these positions (Lachenbruch et al., 1976a; Sorey and Lewis, 1976; Sorey et al., 1978). However, the argument for this recharge near Hot Creek is weakened by the presentation of the heat flow data in Figure 2. It is true that maximum heat flow values in the caldera occur in the vicinity of the Hilton Creek fault zone, but high heat flow values extend to the west up the hydrologic gradient. In view of the strong groundwater flow from west to east (see Sorey et al., 1978) it seems unlikely that the shallow geothermal leakage would move up the hydrologic gradient, and in fact, it seems much more likely that the fluid would move in the direction of the hydrologic flow (from west to east).

Deep Hole Results Temperature-depth curves from the three deep drill holes are shown on Figure 3 (P.I., 1980; Smith and Rex, 1977 Sorey, personal communication, 1983) and estimated heat flow values from these holes are shown in Table 1. The data from Union Geothermal Incorporated Clay Pit #1 and Republic Geothermal Incorporated 66-29 do not represent equilibrium temperatures while the data from the second logging of Union Geothermal Incorporated Mammoth #1 do represent equilibrium temperatures. The cooling effect of the drilling is clearly shown on the 8/29/79 log run shortly after completion of drilling. For the purposes of this discussion, however, the holes are probably close enough to equilibrium to constrain the interpretation.

The high temperatures anticipated on the basis of the fluid geochemistry do not occur in the wells (1.5-2.1 km deep) within the caldera fill, which might be expected to represent the porous units that would permit geothermal fluid circulation. In fact, well 66-29 has a sub-regional temperature of only 72°C at a depth of 2100 m (see Table 1).

Heat flow values based on the bottom hole temperature data from these three wells are shown in Table 1 as "deep" heat flow. The thermal conduc-

tivity values have been assumed based on measured values (Sorey et al., 1978, Table 5) with upper limit assumed in calculating heat flow. Nonetheless, the heat flow values are significantly lower than might have been anticipated (see Sorey et al., 1978, for example). The actual observed values range from a maximum of 130 mWm^{-2} at the Clay Pit #1 hole to approximately 40-120 mWm^{-2} (depending on the assumptions) for the 66-29 and Mammoth #1 wells. Heat flow values outside the caldera to the east and north are regional to subregional (see Table 2). The highest regional heat flow outside the caldera is observed to the west at Devil's Post Pile (159mWm^{-2}).

Thus the heat flow values for the deep holes, with the possible exception of Clay Pit #1, are less than or equal to regional background heat flow. If a major magma chamber has existed and remained uncooled in the western part of the caldera for a period of a 0.5-1 my, then heat flow values at a depth of 2 km could be expected to be 50 to 200% higher than those actually observed (Lachenbruch et al., 1976b; Sorey et al., 1978) unless the temperatures are held low by rapid cold fluid flow along a down or laterally flowing limb of a major convection system. Furthermore, the available drill holes do not locate any major high temperature geothermal system circulating within the caldera fill since the highest observed temperature below 330 m is 106°C (except for the narrow high temperature zone in Mammoth #1 at 700 m).

Based on the data, a conceptual model for the geothermal system is shown in Figure 4. Hot water is charged into a shallow aquifer at a depth of 50 to 100 m, and into a deep aquifer at about 700 m to the west or south of Casa Diablo hot springs. The fluid comes either from groundwater heated by dikes or from geothermal fluid recharge from depth. This model does not include significant thermal fluid input into the shallow system from Hilton Creek fault zone, which has previously been the focus of most of the attention. An

analytical model that can be applied to this area will be briefly discussed in the next section.

THE SHALLOW GEOTHERMAL SYSTEM

Description of Model The basic model is as follows: a geothermal circulation system exists with relatively great depths of circulation and relatively high temperatures (for large scale systems to exist, flow has to occur over periods of tens to hundreds of thousands of years). The lower parts of the circulation system are kept open by solution as the colder waters are drawn toward the heat source and raised in temperature. However, circulation paths in the upper parts of the systems are often sealed by deposition as the rising hot fluids cool and precipitate minerals. Thus the actual paths by which the system exhausts fluid to the surface may vary as a function of time depending on the details of the tectonic and volcanic activity associated with the geothermal system. For example, active faulting may fracture or refracture a conduit which then leaks fluid for a period of a few hundred to a few thousand years until it is resealed. At some later time, the process is repeated. When a fracture is opened, fluid with a positive hydrostatic pressure with respect to cold groundwater rises up the newly opened fracture system to the water table. The hot water then floats on top of or displaces the cold groundwater and flows down the regional hydrologic gradient. As a result, very high gradients exist in the air column above the groundwater, and depending on the age of initiation of the flow, large negative temperature gradients exist below the flow zone. The fluid may also be injected into confined permeable horizons with similar results. In the model used in this paper the effects of the upflow zone are not included and conductive heat transfer is assumed outside of a discrete horizontal aquifer.

Mathematical Modeling The temperature-depth curves shown in Figures 1 and 3 dramatically illustrate the temperature overturns observed in all of the holes along an east-west section from Casa Diablo to Lake Crowley. Ziagos and Blackwell (1981, 1984) discuss a model for temperature and heat flow in and above a geothermal system characterized by lateral fluid flow along a thin sub-horizontal aquifer. A similar model with a slightly different boundary condition was presented by Bodvarsson et al. (1982).

Of particular interest are the temperatures in the aquifer (assumed to be thin and at depth ℓ) and the conductive temperatures below the aquifer. If the aquifer has been flowing for a long enough period of time so that the temperatures in the aquifer can be considered steady-state, then the temperature in the aquifer as a function of lateral position (x) is given by:

$$T(x,\ell,t) = T_a \, e^{-\alpha x/\ell} \, \mathrm{erfc}\left[\frac{\alpha x}{\sqrt{4kt''}}\right] \qquad (1)$$

where the parameter α is given by $\alpha = K/VMC$. In this equation, K is the thermal conductivity of the rock, V is velocity of water flow through the aquifer, C is heat capacity of the water, and M is mass per unit area of water in contact with the rock. The parameter K is thermal diffusivity and $t'' = t - x/V - \alpha\ell x/3k$. At some time (based on the value of the argument of the complementary error function) after the front of the heat flow has passed a point, the aquifer temperature equation simplifies to:

$$T(x,\ell) = T_a \, e^{-\alpha x/\ell} \qquad (2)$$

The approximate solution for the temperature in the half-space below the aquifer ($z \geq \ell$), where x is the distance from the recharge point, z is the

depth below the aquifer and ℓ is the depth to the aquifer, is given by

$$T(x,z,t) = T_a e^{-\alpha x/v} \text{ erfc } \frac{\alpha x + v\ell - z}{4kt''} \qquad (3)$$

A similar equation applies in the layer over the aquifer ($z \leq \ell$), except that the solution is the sum of the differences of solutions like Equation (3). The major approximations are the assumption of no heat conduction in the x-direction, and conductive heat transfer outside the aquifer. Input data necessary to use this model include an estimate of the parameter α, the aquifer recharge temperature (T_a), the time (t), and the background gradient. Conversely, temperature-depth data may be inverted to estimate T_a, α and t (Ziagos and Blackwell, 1984).

Characteristics of Shallow Aquifer Sorey et al. (1978) have discussed in detail the hydraulic characteristics of the shallow geothermal system in Long Valley. The pertinent information from that discussion is summarized in Table 3. Sorey et al. (1978, p. 32-33) indicate the heat loss from this part of the system is about 2×10^8W. They estimate that this heat loss corresponds to a flow of approximately 250 kg/sec of thermal fluid at a temperature of approximately 210°C. They model the system assuming that most of the hot fluid upwells in the vicinity of Hot Creek, while a smaller amount rises above Casa Diablo Hot Springs. Several different models are assumed but they all have similar characteristics. Including all the possible sources, a total heat loss for the Long Valley caldera of 2.8×10^8 W was calculated. This value corresponds to an average heat flow for the caldera (an area of approximately 450 km^2) of 600 mWm^{-2}.

The total heat loss of the caldera is quite modest in comparison to some of the large caldera systems. The mean heat flow for the Taupo graben

(Elder, 1965) and the Yellowstone caldera (Fourier et al., 1976) is 2000 mWm^{-2} averaged over the area of the calderas. Because of the larger sizes of these two caldera features, the total heat losses are much greater than Long Valley, but average heat flow values are also much higher.

Heat loss values characteristic of Long Valley are similar to those found in different types of geothermal systems. For example, the Roosevelt Hot Springs system in Utah has a heat loss which is very analogous to Long Valley. The total heat loss at Roosevelt is occurring along a fracture zone approximately 4 km long by 2 km wide, and corresponds to a natural flow of approximately 200 kg/sec of water at a temperature of 260°C (Ward et al., 1978). Other hot spring systems such as Leach Hot Springs, Nevada, and so forth, have heat losses of 10^7-10^8 W. The point of this comparison is that the total heat loss for the Long Valley Caldera is not particularly high when compared to typical heat loss values associated with geothermal systems overlying large, shallow silicic magma chambers. Therefore, either the geothermal system may be in the waning stages, the magma chamber is more deeply buried under rocks less porous than the other caldera systems discussed, or the geothermal system in existence today is not directly related to geothermal systems which might have been associated with the cooling of the magma chamber associated with caldera formation and resurgence. Hence, rather than utilizing models that involve one or more widespread high-temperature convection system, the geothermal system in the Long Valley caldera may be characterized by a model involving a relatively small zone of upflow.

Application of Analytic Aquifer Temperature Model As illustrated in Figure 4, the data are consistent with recharge of fluid at the far western end of the caldera and lateral flow of the hot fluid down the hydrologic gradient toward Lake Crowley. The flow takes place in a shallow and a deep

aquifer. Utilizing the information discussed by Sorey et al. (1978), the parameters in the horizontal flow model discussed in the first paragraph of this section were estimated. These parameters are shown in Table 3. The aquifer is assumed to be 3.1 km wide, have a thickness of 32 m and an average porosity of 35%. Based on the discussion of Sorey et al. (1978), it is assumed that half of the geothermal fluid volume (130 ℓ/sec) is discharged by the springs in and above Hot Creek so that of the total mass flow, only 120 ℓ/sec actually reaches Lake Crowley. Of the total heat loss of 2.8×10^8 W, 1.2×10^8 W is lost by convective heat loss by spring flow (mostly in and above Hot Creek), 1.5×10^8 W is lost by conductive cooling of the hot aquifer, and only 0.1×10^8 W actually reaches Lake Crowley as convective loss at the downstream end of the aquifer. The actual fluid loss at the springs in Hot Creek Gorge is 247 ℓ/sec, so that some dilution by cold groundwater may have occurred either upstream or near the hot springs (up to a factor of about two).

In Table 3, two columns are shown for the groundwater aquifer above Hot Creek. Sorey et al. (1978) used a uniform thickness of 32 m for the aquifer below Hot Creek after noting that the thickness ranges from 20 to 46 m. The temperature data from Chance #1 and Endogeneous Δl suggest that the aquifer above Hot Creek may be somewhat thicker. Therefore for the purposes of this discussion, the calculations were made for aquifer thicknesses of 32 and 70 m. If the aquifer is 32 m thick, then the fluid flow rate is on the order of 228 m/yr, and if the aquifer is 70 m thick the velocity is 104 m/yr. In the thicker case the fluid velocity in the aquifer above and below Hot Creek is about the same, whereas if the thickness is constant the velocity is approximately half as fast below as above Hot Creek. In either case, the differences above and below Hot Creek would be accounted for by the loss of

fluid at the hot springs in Hot Creek gorge.

One of the important model parameters for discussion of the aquifer thermal conditions is α. Utilizing the data shown in Table 3, α was calculated for each different situation. For the two cases of flow above Hot Creek, α is 0.00310 and 0.00678. Below Hot Creek, the calculated value for α from the data presented by Sorey et al. (1978) is 0.00645.

Using these parameters, the theoretical change in temperature with distance along the aquifer can also be calculated. The short time approximation to aquifer temperature includes the complementary error function term (Equation 1). In the long time behavior, the error function term becomes 1 and the aquifer temperature is given by equation (2).

The magnitude of the error function term is estimated by assuming that the flow has been in existence for approximately 500-600 years and evaluating the term at a distance of 14 km from the input point. In this case the value of the complementary error function is 0.944 or within 5.6% of steady state. Thus the long time approximation can be used in this application.

The relation of temperature to distance in the aquifer is shown in Figure 5. The plotted temperature is the maximum temperature in the drill hole as a function of distance from Casa Diablo Hot Springs. The value plotted is obviously not the anomalous temperature, as no background has been subtracted. Of course a quantity of interest would be the background temperatures and gradients below the aquifer at each point. An argument can be made based on the data below Hot Creek, that the background temperature is approximately constant with distance and so would have no effect on the rate

of change of the temperature with distance. Above Hot Creek, the situation is more complicated, but because only two data points exist, not much can be said about that part of the flow system from the temperature distribution as a function of distance.

Using the data from the holes below Hot Creek, a exponential curve was fit to the data shown in Figure 5. The calculated value of α is 0.00582 for the aquifer below Hot Creek compared to the value derived from hydrologic reasoning of 0.00645. The difference is only 10% and since these two analyses are derived from completely different approaches the agreement is remarkable. The results demonstrate that the flow model can be used in other geothermal systems without such complete data if one or the other of the two sets of information were available. In many cases the hydrologic information may be easier to obtain without extensive drilling than the aquifer temperature. The great importance of determining hydrologic conditions for interpretation of the heat flow values, and vice versa, is clearly demonstrated.

The question of the input aquifer temperature (T_a) to be used is not significant below Hot Creek as the aquifer temperature is observed at Hot Creek. On the other hand the initial aquifer temperature (T_a) to be used for the portion of the aquifer above Hot Creek is not known directly. A conservative temperature to use would be just higher than that observed in the wells at Casa Diablo Hot Springs. A more realistic temperature to be used might be that derived from geochemistry (approximately 210°C). If T_a is 210°C, then the exponential curve shown (which was calculated by using the α values as shown in Table 5) can be extrapolated westward. In this case, the temperature of 210°C should occur at a distance of approximately 5 km from Casa Diablo Hot Springs. The most logical direction would be to the west,

although there are other possibilities as discussed below. This distance information could be used in a design of an exploration program to determine the upflow zone or deep reservoir for possible geothermal exploitation.

MODELING OF TEMPERATURE-DEPTH CURVES

Deep Holes Other characteristics of the flow involve the length of time of flow and the background temperatures on which the flow is superimposed. In order to evaluate these parameters, theoretical temperature-depth data can be compared to observed temperature-depth data. If temperature-depth data were available from only one position as is the case in some situations, then it would not be possible to unambiguously separate the background temperature effect from the temperature effect of the aquifer (Ziagos and Blackwell, 1984). In Long Valley temperature data are available in the aquifer as a function of distance so that α and T_a can be independently determined. In addition there are temperature data for several holes which penetrate through the aquifer so that a more complete discussion of the background temperature effects and time period of flow is possible. In this section, the long time approximation equation is fit to each of the temperature-depth curves suitable for modeling using flow parameters listed in Table 3. The deep holes are discussed first.

The most informative and interesting hole for this part of the discussion is the Mammoth #1 deep hole at Casa Diablo Hot Springs as it shows the effects of transient flow in two aquifers. Observed and calculated temperature-depth curves are shown in Figures 6 and 7 for two different assumed background temperature characteristics. The equilibrium log is plotted for comparison. The

model of background temperature shown in Figure 6 assumes that the background temperature in the caldera at the site of the drill hole is consistent with a heat flow value of 85 mWm^{-2}. Thus the gradient in the upper part of the hole is consistent with a conductivity of 1.05 $Wm^{-1}K^{-1}$, the gradient in the Bishop Tuff is consistent with a thermal conductivity of 1.7 $Wm^{-1}K^{-1}$, and the gradient in the bottom part of the hole is consistent with an assumed conductivity for quartzite of 4.2 $Wm^{-1}K^{-1}$.

At intermediate depths in the hole (between 200 and 500 m) the effects of the two aquifers interfere and so their effects cannot be independently determined. However, there is no interference in the bottom part of the hole so an estimate of the age of the deeper aquifer can be determined from that part of the hole. The effects of the aquifer superimposed on this background are shown in Figure 6. It can be seen from simple curve comparison that an age of flow for the deeper aquifer of about 4000 years is consistent with the data. If the effects of the deep aquifer are subtracted from the shallow part of the temperature-depth curve, a temperature effect and subsequently an age for the shallow aquifer can be determined. The superposition of the effects of the aquifers is shown in Figure 6. Using this background, an age for the upper aquifer on the order of about 1500 years is calculated. In this calculation the same assumed α and T_a have been used for the deeper aquifer as for the shallower aquifer, even though the characteristics of the deeper aquifer are unknown (since only one temperature-depth curve is available). Changes in these parameters would not change the calculated age significantly, however. With the assumed background, the age of both the aquifers would be on the order of thousands of years and both would be considerably older than the age inferred for the groundwater aquifer below Hot Creek (see following section).

Since the argument was made above that there is only one groundwater aquifer at shallow depths, another model of background temperatures was examined, which gave results for the shallow aquifer more consistent with the aquifer below Hot Creek. In this calculation (Figure 7), the background temperature was assumed to be approximately 84°C plus 11°C/km times the depth in km. The superposition of several calculated aquifer ages for both the deep and the shallow aquifer are shown in Figure 7. In this case, best ages for the deep aquifer and shallow aquifer of approximately 3,100 years and 700 years are calculated. A conductivity of 1.05 $Wm^{-1}K^{-1}$ was assumed for the upper aquifer calculation. A conductivity of 1.7 $Wm^{-1}K^{-1}$ was assumed for the lower aquifer calculation.

It might appear that the assumption of the background temperature in the calculation is arbitrary compared to the assumption of conductive heat flow in the first case. However, it is clear that temperatures are subnormal in the eastern part of the caldera, and temperatures in the Clay Pit #1 hole are not compatible with conductive heat flow in the caldera even if the effects of the transient aquifers are ignored.

The fit to the observed temperature-depth curve illustrated in Figure 7 is quite good and the effect of superposition is clearly shown. Comparison of the location of the aquifers to the geology suggests that the shallow aquifer is coincident with or just below the groundwater table aquifer and that the deeper aquifer occurs just below the top part of the Bishop Tuff.

Modeling of Shallow Holes Calculated effects of temperatures based on transient aquifer flow applied to the shallow holes east of Casa Diablo Hot Springs are shown in Figures 8 and 9. As in the case of the Mammoth #1 hole, two different backgrounds are investigated. The first of these consists of a background gradient of 110°C/km and a surface temperature of 10°C (shown in

Figure 8). This background gradient implies a conductive heat flow of 80-120 mWm^{-2} given a thermal conductivity of 1.05 $Wm^{-1}K^{-1}$. The difficulty with this model is that it implies successively older ages for the aquifer in drill holes further downslope along the aquifer because the temperatures are constrained to go through the bottom point of holes R-7 and C-5. Furthermore, extension of this gradient to depth is not consistent with the deep data in Republic #66-29. In fact the background temperature in that hole at 1500-2000 m is apparently about 50°C which would be reached at about 350 m using the assumed background gradient.

In the second model a constant background temperature in this part of the caldera of 40°C is assumed. In this case a more consistent set of ages for various holes are obtained. These ages are summarized in Table 4. The results from hole Mammoth #1, discussed above, are also included. In both cases the results obtained using the Model 2 background temperatures are preferred because of their general consistency as a function of distance east of Casa Diablo hot springs. In general the holes north of and including R7 (R7, R2, C7, C10, not including #66-29) have an apparent aquifer age on the order of 150 ± 100 years while the southern holes (R4, R6, and C5) have apparent aquifer ages on the order of 200-500 years.

In fitting calculated temperatures to observed temperatures in these holes, the assumption is made that the temperature in the aquifer is uniform. However, it is quite obvious from consideration of the temperature-depth curves that the temperatures are not exactly uniform and picking a point to match for the conductive effect below the aquifer is subjective. Thus it is possible to change the actual ages of match by a few tens of years depending on the precise point picked to start the comparison. In view of the other assumptions and interpretations, this variation does not significantly

affect the results.

The shape of the temperature-depth curve in hole #66-29 is not similar to the shallow holes. However, it is interesting that the maximum temperature observed in the upper part of #66-29 is consistent with its position in the groundwater flow system (see Figure 5). It is not clear whether the groundwater flow system is somewhat deeper at this point or whether it is blocked from the area around the hole site by permeability variations.

There is a significant variation in the calculated age of the aquifer in the different holes. The ages are most consistent for the holes in the northern half of the group. Two southern holes have significantly older ages. Two of the holes(R5 and CH 1) have curves which indicate either a very thick aquifer or vertical leakage (either upward from a deeper aquifer or downward from the groundwater aquifer). Because the temperatures in the holes reflect variations in aquifer characteristics (thickness, three-dimensional permeability, porosity, thermal conductivity, and variations in water table elevation, etc.) as well as the effects of the assumed flow,the agreement of ages may be as good as can be expected. The holes may not be completely grouted, so that intrahole water flow may occur and the holes C7 and C10 are not deep enough for a reliable determination of age.

The results are that an age of several hundred years for the aquifer is reasonable. At a velocity of flow of 100 m/year, it would take over 100 years for temperature changes in the aquifer to propagate from the western end to the eastern end. The older age of the aquifer at Casa Diablo hot springs is therefore consistent with the expected age progression.

If the background temperature in this part of the caldera is 40°C, the deeper aquifer (along the top of the Bishop Tuff--see Figure 4) observed in Mammoth #1 may also be present in hole #66-29, but considerably reduced in

amplitude. In this case the relative temperature amplitude in both aquifers is similar, suggesting similar flow velocities. It is possible that the effects of the aquifers have been considerably smeared by the drilling effect, and if the hole had been allowed to reach equilibrium, then the temperature-depth curve would resemble the one in Mammoth #1 more closely (see Figure 3). As noted by Diment et al. (1980, p. 38), the temperatures are not at equilibrium. In drilling geothermal wells, temperature-depth curves of this type will often be smoothed drastically by the drilling effect, even to the point that the aquifers are not recognized during the initial logging. An example of this particular phenomenon was clearly illustrated by Benoit et al. (1983) in the Desert Peak geothermal system in western Nevada. In such cases, the geothermal implications of the hole can be completely misinterpreted unless enough time is allowed for recovery to a more stable temperature configuration. This interpretation for hole #66-29 is speculative, however, in view of the fact that we do not know the equilibrium temperatures in the hole. The temperatures in the hole, though, are nonetheless consistent with the background temperature on the order of 40-50°C below 1000 m. This temperature is much below regional.

DISCUSSION AND CONCLUSIONS

One object of this paper is to investigate the characteristics of the shallow geothermal aquifer in Long Valley caldera in order to illustrate the application of the model developed by Ziagos and Blackwell (1981, 1984) and to use this model to determine some characteristics of the shallow flow system. It is concluded that transient thermal conditions are present in two major aquifers in the southern half of the Long Valley caldera. The first of these aquifers involves hot fluid flow along or just below the groundwater table,

and it is this system that is responsible for most of the geothermal manifestations presently observed in the southern half of the caldera. Hot water is recharged from some point west or south of Casa Diablo Hot Springs and flows down the regional hydrologic gradient to exit at Lake Crowley. Along the way approximately half the original volume of the hot fluid is lost in the geothermal manifestations such as those along Hot Creek, at Casa Diablo and between Hot Creek and Lake Crowley. Geothermal flow in the aquifer was initiated 500-700 years ago. This age is in remarkable agreement with the age of the last major activity along the Inyo Crater zone of 500-600 years (Miller, 1984). A second transient thermal aquifer occurs below the top of the Bishop Tuff. This aquifer has been in existence for a longer period of time (on the order of 3000 years).

Based on this discussion, the second objective of this paper can be discussed: the three hypotheses describing possible geothermal systems in the caldera. These hypotheses are: 1) that in fact no deep system underlies the caldera and the high temperatures in the geothermal system are associated with warming of water in the west end of the caldera by dikes underlying the very young rhyolite domes; 2) a deep system exists in the central part of the caldera with temperatures in excess, perhaps much in excess of 180-200°C, which feeds the shallow system (this has been the model upon which most of the previous analyses have been based); 3) a deep system exists in the west or southwest end of the caldera with temperatures above 180°C to 200°C which feeds the shallow system. The evidence from the temperatures in the deep holes, and the consistency of the interpretation based on transient aquifer flow with the temperature and hydrologic evidence indicate that hypothesis number 2 can be disregarded as the major controlling part of the geothermal system. Thus only hypotheses 1 and 3 remain possibilities.

If the shallow aquifers are charged from a deep source at a temperature near 210°C, as implied by the geochemistry, the input point would be 4-6 km from Casa Diablo hot springs. The distance uncertainty is quite large, however, as we know very little about the actual flow characteristics of the aquifer above Casa Diablo. The recharge might be from ring fractures along the southwest or northwest, or from faults or fractured intrusive conduits in the western third of the caldera. The deep recharge might be associated with fractures related to the zones along which seismic activity has recently occurred(which are the right distance from Casa Diablo hot springs). If so the first indications might be observed at Casa Diablo hot springs. Fumaroles exist on Mammoth Mountain (Sorey et al., 1978) and these manifestations might be related to the source of the hot fluid.

A further interesting speculation is that the shallow geothermal system might be associated with only shallow flow and in fact no deep flow is involved. If the ages of these aquifers correspond to the ages of a possible intrusive associated with the Inyo domes, the shallow systems may merely be groundwater heated by flow past a shallow silicic intrusive underlying these young domes. Thus the presence of the geothermal system would imply that a still hot silicic magma underlies the west side of the caldera at very shallow depths. The heat loss value for the geothermal system of 2.0×10^8 W could be supplied by complete cooling of about .003 km^3/year of liquid dacite. Thus, over a period of a 1000 years the shallow cooling of about 3 km^3 of intrusive material could supply the geothermal system with heat. Such a volume is not unreasonable given the amount of extrusive activity associated with the Inyo Domes.

A final objective is to remove effects of the shallow flow system so that the background characteristics of temperature in the Long Valley caldera can

be evaluated. The analytical model seems to be applicable to the shallow data, although some uncertainties are involved because of the many geologic and hydrologic complexities. Thus we conclude that the section shown in Figure 4 represents the present conditions in the southern half of the caldera.

If the transient effect of hot water flow in the two shallow aquifers is removed from the temperature-depth section shown in Figure 4, the temperatures in the caldera before recent changes in the aquifer flow are as shown in Figure 10. The background temperatures inferred from the analyses discussed with reference to Figures 7 and 9 were used to construct the isotherms shown in Figure 10. Previous to 3000 years ago, there was a large scale, low temperature geothermal flow system in the south half of the caldera having maximum temperatures on the order of 100-120°C. Along the section studied, major downflow is along the east side of the caldera, lateral circulation occurs in the lower parts of the caldera fill (Bishop Tuff), and major upflow occurs at the west side of the caldera. In addition mixing with cold groundwater at shallow depths may occur along the west side (see Table 3 footnote). The flow system is three-dimensional, and in the vicinity of the resurgent dome, either the flow system is being heated more effectively, or it is flowing less rapidly due to reduced permeability (as indicated by the high temperatures at depth in Clay Pit #1).

The correspondence of this inferred temperature-depth-distance distribution in the caldera to some of the calculated convective systems is rather remarkable. Because of the geometry, however, it is more like a regional flow system than a local geothermal system (the aspect ratio of the system may be as much as 10:1). This large-scale flow system was modeled using an approximate formulation of the fluid flow and heat transfer equations

discussed by Lau (1980). Flow patterns and temperatures were calculated for a heat source in the west side of the caldera, a fluid flow system approximately corresponding to the limits of the caldera, and a Rayleigh number of 200. Calculated results were very similar to those actually observed and/or postulated. Temperatures in the flow system were initially in excess of 200°C. However, after period of approximately 100,000 years, temperatures in the flow system decreased to about 100°C and remained at that temperature for an additional several hundred thousand years. The maximum calculated flow velocities were on the order of 1 m/yr.

Based on these observations and numerical results, the evolution of geothermal systems in Long Valley caldera can be discussed. During formation, the caldera was filled with almost a thousand meters of very hot Bishop Tuff. Extensive and very active geothermal systems developed associated with the cooling of the Bishop Tuff. This phase of the caldera geothermal system might have lasted for 100,000 to 200,000 years. Subsequently, long-term geothermal flow developed with the flow being driven by the presence of a rejuvenated magma system under the resurgent dome and/or west side of the caldera. Fluid recharge was from the east side of the caldera and discharge occurred along the west side of the caldera. This or a similar flow system has been in existence for several hundred thousand years and resulted in cooling of any magma on the west side of the caldera, the intrusive associated with the resurgent dome and shallow intrusive feeders for 0.1-0.6 MY volcanism. It is this geothermal system that is probably responsible for the extensive saline deposits observed near Crowley Lake and for which a long period flow is required (as discussed by Sorey et al., 1978). By 5000 years ago the activity of the fluid flow had diminished as the cooling had proceeded to the point that the flow was no longer effective and/or mineral deposition

had sealed off many of the channelways and fluid flow temperatures were quite low. Somewhere in the system, fluid with temperatures on the order of 210°C+ may still have been available, however. The previous flow system had homogenized temperatures over distances of kilometers and had a period of flow of several tens or hundreds of thousands of years. Within the last few thousand years, the hot fluid has been injected at least twice into shallow aquifers as a result of tectonic and/or intrusive/thermal events. As a consequence, shallow penetration of hot water with two orders of magnitude greater fluid flow velocities has been superimposed on the existing convection pattern. This aquifer flow represents circulation on a relatively small scale, however, compared to the much larger distributed flow system associated with the caldera at earlier times.

From the point of view of geothermal exploration, the major enigma of Long Valley is the location of the possible high temperatures in a geothermal system and the question of whether or not an exploitable geothermal system exists. Obviously production of geothermal fluid from the thin aquifers, even though temperatures are relatively high, would not be very effective. It is clear that the west side of the caldera holds the key to the understanding of the source of the hot fluid and to the potential location of geothermal systems of commercial exploitable temperatures. The remainder of the caldera is either too old, too well sealed or too cooled by convection flow to offer attractive targets for geothermal exploitation.

The research described in this paper was supported by DOE Basic Energy Sciences Grant #AC03-81ER10973 to Southern Methodist University. The development of these ideas is based on interaction with John Ziagos and Shari Kelley. Gene Sumenich pointed out to the author the existence in the public domain of the geothermal data from the Mammoth #1 and Clay Pit #1 geothermal wells, Donald Michaels helped the author obtain a copy of one of the references and Michael Sorey furnished details to the author of some temperature-depth data which were used in the interpretation, and made comments on an early version of the manuscript.

BIBLIOGRAPHY

Bailey, R. A., G.B. Dalrymple, and M.A. Lanphere, 1976. Volcanism, Structure, and Geochronology of Long Valley Caldera, Mono County, California. J. Geophys. Res., 81: 725-744.

Bodvarsson, Gunnar, 1969. On the temperature of water flowing through fractures. J. Geophys. Res., 74: 1987-1992.

Bodvarsson, Gunnar, 1973. Temperature inversions in geothermal systems. Geoexploration, 11: 141-149.

Bodvarsson, Gudmundur S., S. M. Benson, and R. A. Witherspoon, 1982. Theory of the development of geothermal systems changed by faults. J. Geophys. Res., 87: 9317-9328.

Diment, W. H., T. C. Urban, and M. Nathenson, 1980. Notes on the shallow regime of the Long Valley caldera, Mono County, California. Geothermal Resources Council Trans, 4: 37-40.

Elder, J. W., Physical processes in geothermal areas, in Terrestrial Heat Flow, Geophys. Mono. Ser. v.8, ed. W. H. K. Lee, pp 211-239, AGU, Washington D.C., 1965.

Fournier, R. O., D. E. White, and A. H. Truesdell, Connective heat flow in Yellowstone National Park, in Proceedings of the Second U.N. Symp. on Development and Use of Geothermal Energy, v.1, pp 731-740, U.S. Government Printing Office, Washington, D.C., 1976.

Gambill, D.T., 1981. Preliminary Hot Dry Rock Geothermal Evaluation of Long Valley Caldera, California, Rep. LA-8710-HDR, 22 pp., Los Alamos Nat. Lab., Los Alamos, N. Mex.

Goyal, K. P., and D. R. Kassoy, 1981. A plausible two-dimensional vertical model of the East Mesa geothermal field, California, U.S.A. J. Geophys. Res., 86: 10719-10733.

Hermance, J.F., 1983. The Long Valley/Mono Basin volcanic complex in Eastern California: Status of present knowledge and future research needs, Rev. Geophys. Space Phys., 21, 1545-1565.

Hill, D. P., 1976. Structure of Long Valley Caldera, California, from a Seismic Refraction Experiment. J. Geophys. Res., 81: 745-753.

Kane, M. F., 1976. A Gravity and Magnetic Investigation of the Long Valley Caldera, Mono County, California. J. Geophys. Res., 81: 754-762.

Kilbourne, R.T., C.W. Chesterman, S.H. Wood, 1980. Recent volcanism in the Mono Basin-Long Valley region of Mono County, California, Mammoth lakes, California, Earthquakes of May 1980, Spec. Rep., 150, edited by R.W. Sherburne, pp. 7-22, Cal. Div. Mines Geol., Sacramento, Calif.

Lachenbruch, A. H., M.L. Sorey, R.E. Lewis, and J.H. Sass, 1976a. The Near-Surface Hydrothermal Regime of Long Valley Caldera. J. Geophys. Res., 81: 763-768.

Lachenbruch, A. H., J.H. Sass, R.J. Munroe, and T.H. Moses, 1976b. Geothermal Setting and Simple Heat Conduction Models for the Long Valley Caldera. J. Geophys. Res., 81: 769-784.

Lau, K. H., 1980. Effect of permeability on cooling of a magmatic intrusion in a geothermal reservoir, Lawrence Livermore Natl. Lab. VCRL-52888, 37pp.

Lippmann, M.J., and G.S. Bodvarsson, 1983. Numerical studies of the heat and mass transport in the Cerro Prieto geothermal field, Mexico, Water Resources Res., 19, 753-767.

McNitt, J.R., 1963. Exploration and development of geothermal power in California, Calif. Div. Mines Geology Special Rept., 75.

Miller, C. D., Chronology of Holocene eruptions at the Inyo volcanic chain, central eastern California - Implications for possible eruptions, U.S. Geol. Surv. Redbook Conf. on Long Valley, 1984.

Muffler, L. J. P. and D. L. Williams, 1976. Geothermal Investigations of the U. S. Geological Survey in Long Valley, California, 1972-73. J. Geophys. Res., 81: 721-724.

Petroleum Information Corp., 1980. Completion of geothermal wells in Mono-Long Valley ale area reported, National Geothermal Service, June 20, 1980. Petroleum Information Corp., 2 (25), Denver, Colo., 2 p.

Ryall, F., and A. Ryall, 1981. Attenuation of P and S waves in a magma chamber in Long valley Caldera, California, Geophys. Res. Lett., 8, 557-560.

Ryall, A., and F. Ryall, 1983. Spasmodic tremor and possible magma injection in Long Valley Caldera, eastern California, Science, 219, 1432-1433.

Savage, J.C., and M.M. Clark, 1982. Magmatic resurgence in Long Valley Caldera, California: Possible cause of the 1980 Mammoth Lakes earthquakes, Science, 217, 531-533.

Sherburne, R.W., ed., 1980. Mammoth Lakes, California Earthquakes of May, 1980, Spec. Rep. 150, Calif. Div. Mines Geol., Sacramento, Calif.

Smith, J. L., and R. W. Rex, 1977. Drilling results from the eastern Long Valley Caldera. Amer. Nuclear Soc. Mtg. on Energy and Mineral Recovery Research, Golden, Colo., April 12, 1977, 529-540.

Sorey, M. L., Evolution and present state of the Hydrothermal system in Long Valley caldera, U.S. Geol. Surv. Redbook Conf. on Long Valley, 1984.

Sorey, M. L., and R. E. Lewis, 1976. Convective Heat Flow from Hot Springs in the Long Valley Caldera, Mono County, California. J. Geophys. Res., 81: 785-791.

Sorey, M. L., R. E. Lewis, and F. H. Olmsted, 1978. The Hydrothermal System of Long Valley Caldera, California. U. S. Geol. Surv. Prof. Paper 1044-A, p. A1-A60.

Steeples, D. W. and H. M. Iyer, 1976. Low-Velocity Zone Under Long Valley as Determined From Teleseismic Events. J. Geophys. Res., 81: 849-860.

Ward, S. H., W. T. Parry, W. P. Nash, W. R. Sill, K. C. Cook, R. B. Smith, D. S. Chapman, F. H. Brown, J. A. Whelan, and J. R. Bowman, 1978. A summary of the geology, geochemistry, and geophysics of the Roosevelt Hot Springs thermal area, Utah. Geophysics, 43: 1515-1542.

Ziagos, J. P., and D. D. Blackwell, 1980. A model for the effect of horizontal fluid flow in a thin aquifer on temperature-depth profiles. Geothermal Resources Council Trans., 5, 221-224.

Ziagos, J. P., and D. D. Blackwell, 1984. A model for the transient temperature effects of horizontal fluid flow in geothermal systems, in preparation.

Figure Captions

Figure 1. Shallow temperature-depth curves from the Long Valley, California. Data from Diment et al. (1980) and McNitt (1973) (Endogeneous #1). The locations of the holes are shown in Figure 2.

Figure 2. Location of holes and shallow heat flow map of the Long Valley caldera. The outline of the physiographic edge of the caldera is shown as a solid line. The dotted line represents the outline of the resurgent dome; dashed lines represent mapped normal faults (the Hilton Creek fault zone) and the ruled pattern indicates the young rhyolite domes of the Inyo domes complex. Locations and identifying numbers for each hole are shown. Locations of the major hot springs are also shown. Contours of heat loss from the shallow aquifer are in units of mWm^{-2} (1×10^{-6} cal/cm^2 sec = 41.84 mWm^{-2}).

Figure 3. Temperature-depth curves from deep and shallow holes in the Long Valley caldera (locations are given in Figure 2). The Clay Pit #1 and Long Valley 66-29 holes are probably not represented by equilibrium temperature measurements.

Figure 4. Conceptual model of the geothermal system in the southern half of the Long Valley caldera. The lithologic data are taken from published reports by Smith and Rex (1977), Petroleum Information, Inc. (1980) and Gambill (1981). Location and sense of displacement along the normal faults associated with the Hilton Creek

fault zone are shown. The presence of two temperature overturns associated with the groundwater aquifer and the "top of the Bishop" aquifer are shown. The presence of subnormal temperatures in the eastern part of the caldera is indicated by comparison with the regional isotherms (see extreme right hand side of figure) based on an assumed typical heat flow of 80 mWm^{-2}.

Figure 5. Plot of maximum temperature in the shallow groundwater aquifer as a function of distance from Casa Diablo hot springs. The Hot Creek hot springs are associated with the change in slope of the temperature vs. distance curve. The line shows a least squares fit to the temperature-distance data below Hot Creek. The calculated value of the flow parameter α from this fit (0.00582) can be compared to the independent calculation of the value of α from the hydrologic data in Table 3 (0.00645).

Figure 6. Comparison of observed and calculated temperatures in Mammoth #1 (and Endogenous #1) at Casa Diablo hot springs based on an assumed heat flow of 85 mWm^{-2} and a surface temperature of 10°C. Theoretical curves calculated for the two different aquifers for different flow periods are shown. Calculated shallow aquifer temperatures are indicated by the dashed lines and calculated deep aquifer temperatures are indicated by dot-dash lines.

Figure 7. Same as Figure 6, but with an assumed "surface" temperature of 84 C and a background gradient of 11°C/km.

Figure 8. Comparison of calculated and observed temperatures from shallow holes east of Hot Creek. The background temperature assumed for this model is 100°C/km with a surface temperature of 10°C. The numbers shown on each curve refer to the age of the flow at each point. Hole C-4 is actually east of the area in consideration.

Figure 9. Same as Figure 8, but with an assumed background temperature of 40°C below a depth of 30m (constant with position). All other parameters are the same.

Figure 10. Hypothetical temperature-depth-distance model for the southern half of the Long Valley caldera if the effect of shallow overflow in the transient aquifers is removed. The temperatures were reconstructed by interpolation from background temperatures for Mammoth #1 and the holes east of Hot Creek (Figures 7 and 9).

Table 1. Heat flow values calculated for holes drilled in Long Valley not discussed by Lachenbruch et al., (1976b) and Sorey et al., (1978). For calculation of the deep and shallow gradients the surface temperature was assumed to be 10°C. The assumed mean thermal conductivity for each deep hole is $1.7 Wm^{-1}K^{-1}$ (a maximum value). The shallow thermal conductivity was assumed to be $1.05 Wm^{-1}K^{-1}$.

Hole Name	Location	Depth m	Bottom Hole Temperature °C	Mean Gradient °C/km	Mean Heat Flow mWm^{-2}	Maximum Shallow Temp °C	Shallow Heat Flow mWm^{-2}
Long Valley * 66-29	3S/29E-29db	2130	72	28.2	$\leq$ 48	70	289
Mammoth * 1	3S/28E-32bdb	1585	102	58.0	$\leq$ 99	169	1368
Clay Pit * 1	3S/28E-15add	1808	147	75.8	$\leq$129	113	557
Endogeneous * 1	3S/28E-32b	200		-	-	172	1546
Chance * 1	3S/28E-35b	210	125	-	-	134	2170

Table 2. Measured heat flow outside of, but in the vicinity of, the Long Valley Caldera (data from Lachenbruch et al., 1976b)

	Elevation	Gradient	Heat Flow	Distance from Rim (Direction)
	m	°C/km	mWm^{-2}	km
Devils Postpile	2316	51.4	157	3 (WSW)
Aeolian Buttes	2240	31.2	91	13 (NNW)
Waterson Canyon	2133	30.0	93	0 (SE)
Waterson Trough	2316	78.1	88	1 (E)
Waterson Trough	2393	25.0	70	3 (E)
Round Mountain	2225	24.0	79	6 (E)
Johnny Meadow	2637	6.1	17	6 (N)
Sagehen Meadow	2560	9.3	30	11 (N)

Table 3. Parameters of the groundwater aquifer in the southern part of the Long Valley Caldera. Aquifer characteristics below Hot Creek are from Sorey et al. (1978). The flow rate was calculated from the amount of fluid at 210°C required to release 2×10^8W of heat upon cooling (Sorey et al., 1978).

	Above Hot Creek		Below Hot Creek
	Case 1	Case 2	
Aquifer Input Temperature (°C)	210	210	120
Heat Loss (cal/gm)	214	214	
Flow Rate (l/sec)	250*	250*	120**
Width of Aquifer (km)	3.1	3.1	3.1
Thickness of Aquifer (m)	32	70	32 (20-46)
Depth To Aquifer (m)	60	60	30
Porosity of top of Aquifer(%)	35	35	35
Velocity of Flow (m/yr)	228	104	109
Thermal Conductivity($Wm^{-1}K^{-1}$)	1.05	1.05	1.05
Flow Parameter, $\alpha = K/MVC$	0.00310	0.00678	0.00645

*Assuming no dilution of the input hot fluid. In fact dilution may occur as the measured flow rate at the Hot Creek hot springs is 247ℓ/sec (Sorey et al., 1978, p. 33).

**The difference in the two flow rates is the volume of hot fluid lost along and west of Hot Creek.

TABLE 4. Age of intiation of hot water flow in the groundwater table and Top-of-Bishop aquifers in the southern part of Long Valley. The Model 1 and Model 2 ages are based on different assumptions of the background temperatures (see text). The model 2 ages are preferred.

	Groundwater Table Aquifer			
	Model 1		Model 2 (best)	
	Age (years)	ΔT(°C)	Age (years)	ΔT (°C)
Mammoth #1	3000	150	700	82
Chance #1	"old"	55	"old"	
C 10	250	90	250	55
C 7	"young"		"young"	
R 7	200-300	57	50-200	35
R 5	"old"	55	"old"	33
C 5	300-500	52	200-300	30
R 2	350-450	40	50-200	15
R 4	600-700	40	400-500	15
	Top-of-Bishop Aquifer			
Mammoth #1	5000	92	3100	61
#66-29	-	-	-	18(?)

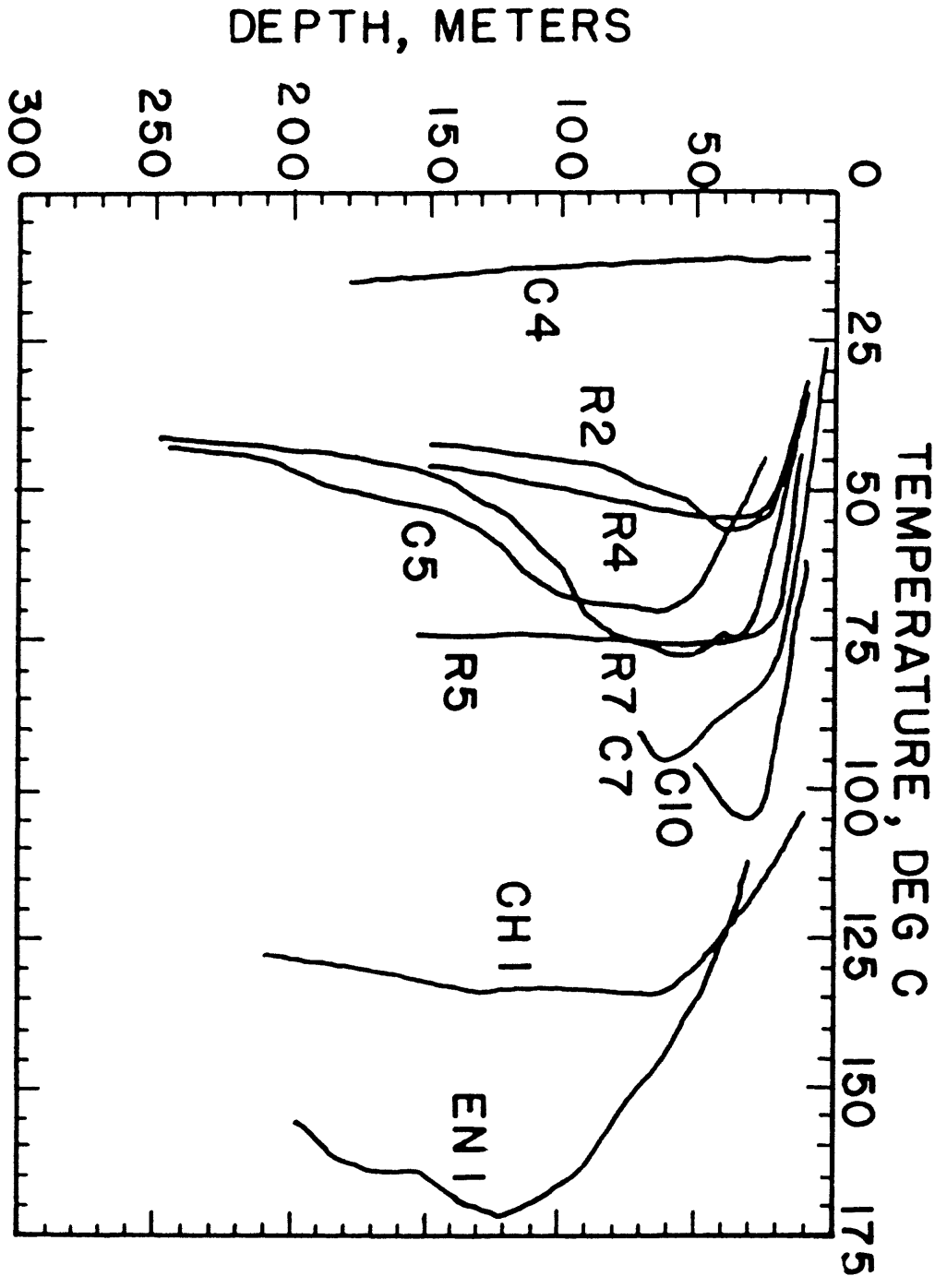
DEPTH, METERS
300
250
200
150
100
50
0
TEMPERATURE, DEG C
25
50
75
100
125
150
175
C4
R2
R4
C5
R5
R7
C7
C10
CH I
EN I

FIGURE 1

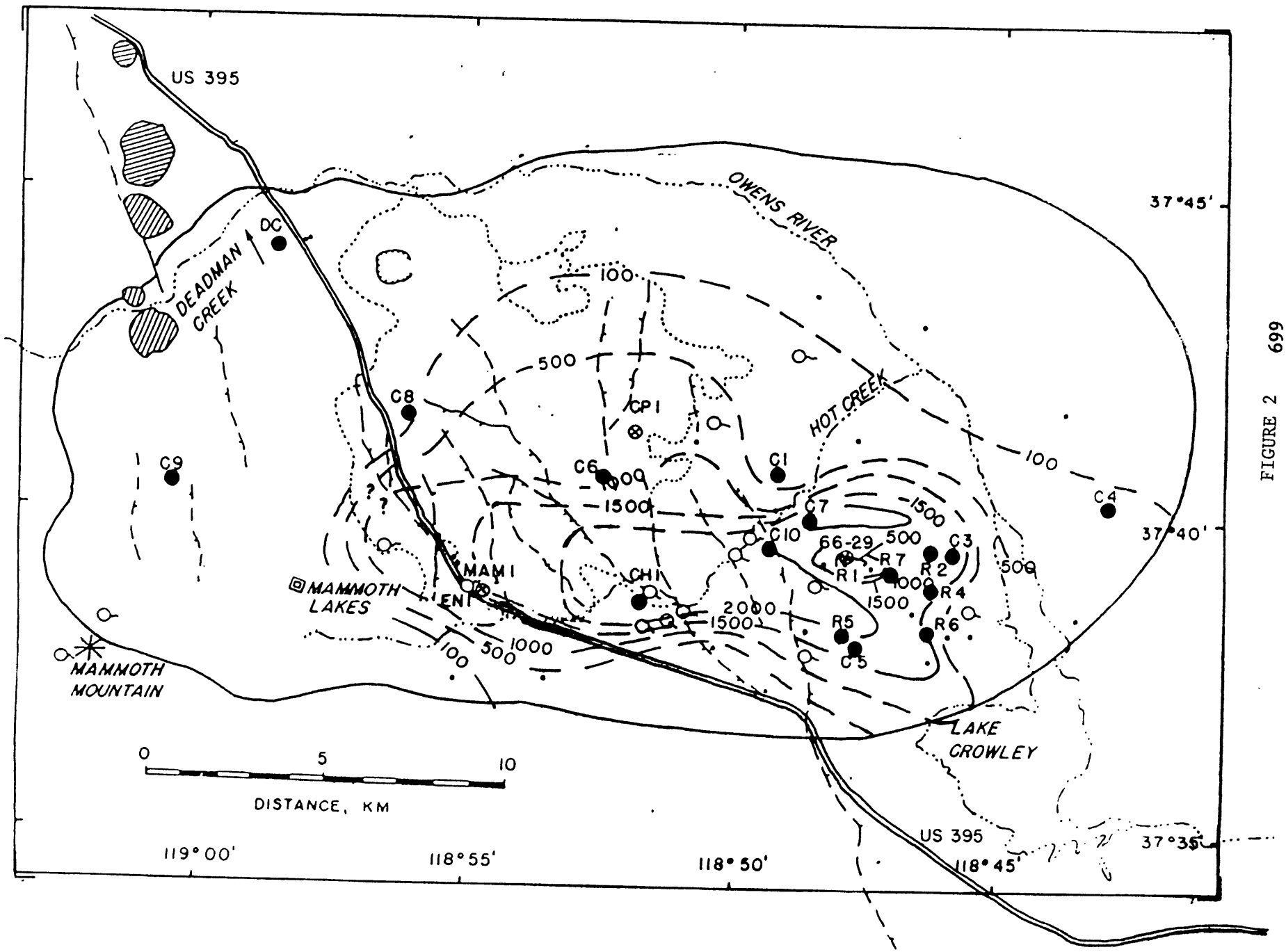
US 395
OWENS RIVER
37°45'
DEADMAN CREEK
DC
100
500
C8
CP1
HOT CREEK
C9
C6
1000
1500
C1
C7
C10
66-29
500
C3
C4
37°40'
R7
R2
R1
1000
R4
1500
2000
R5
R6
C5
MAMI
CH1
MAMMOTH LAKES
EN1
MAMMOTH MOUNTAIN
LAKE CROWLEY
0
5
10
DISTANCE, KM
119°00'
118°55'
118°50'
US 395
118°45'
37°35'

FIGURE 2 699

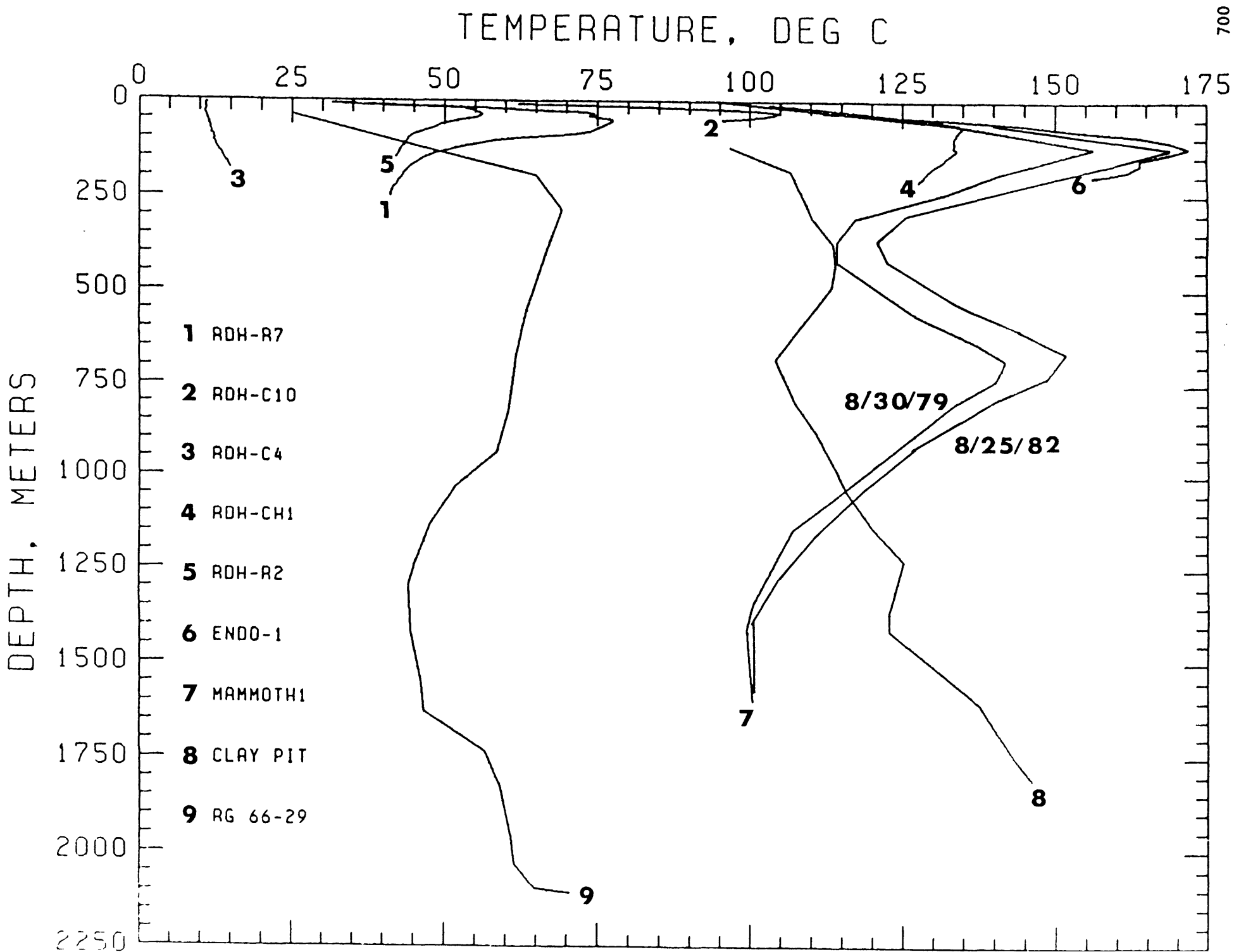
TEMPERATURE, DEG C
0
25
50
75
100
125
150
175
DEPTH, METERS
0
250
500
750
1000
1250
1500
1750
2000
2250
1 RDH-R7
2 RDH-C10
3 RDH-C4
4 RDH-CH1
5 RDH-R2
6 ENDO-1
7 MAMMOTH1
8 CLAY PIT
9 RG 66-29
8/30/79
8/25/82

FIGURE 3

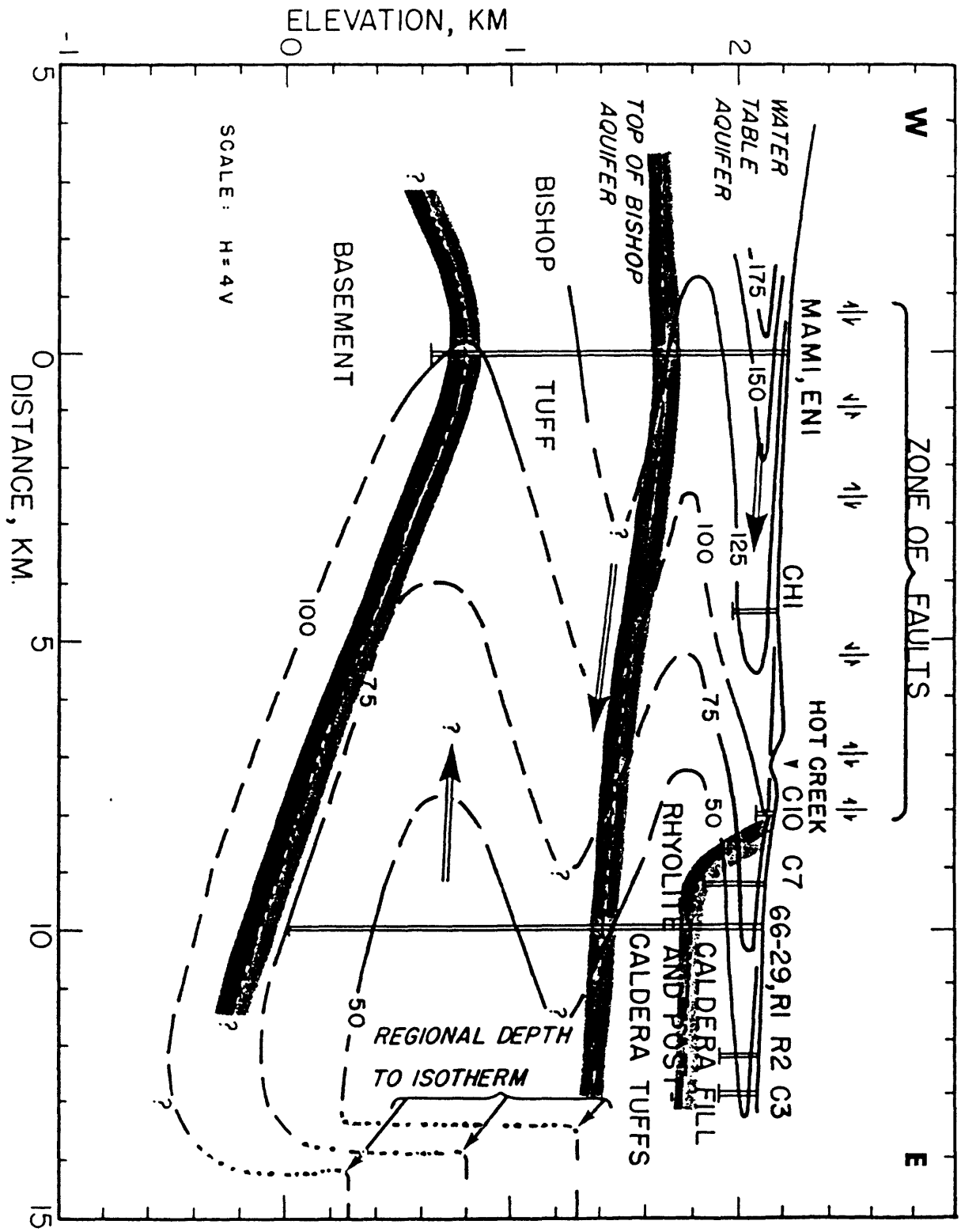
ELEVATION, KM
-1
0
1
2
W
E
ZONE OF FAULTS
WATER TABLE AQUIFER
TOP OF BISHOP AQUIFER
BISHOP TUFF
BASEMENT
MAMI, ENI
CHI
HOT CREEK
C10
C7
66-29, RI
R2
C3
RHYOLITE AND POST-CALDERA FILL
CALDERA TUFFS
REGIONAL DEPTH TO ISOTHERM
175
150
125
100
75
50
SCALE: H=4V
DISTANCE, KM.
5
0
5
10
15

FIGURE 4

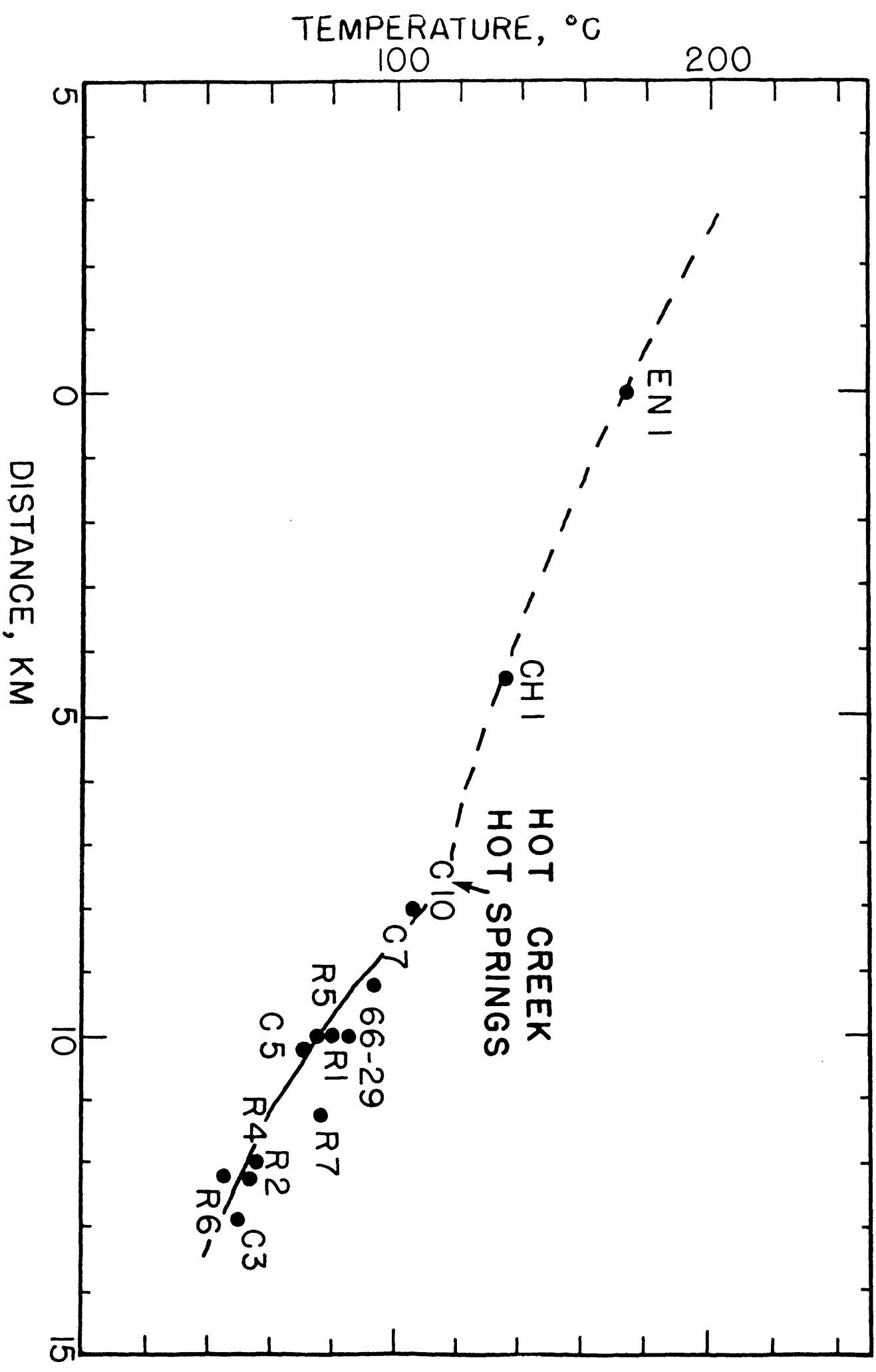
TEMPERATURE, °C
100
200
5
0
5
10
15
DISTANCE, KM
EN 1
CH 1
HOT CREEK
HOT SPRINGS
C10
C7
66-29
R5
R1
C5
R7
R4
R2
R6
C3

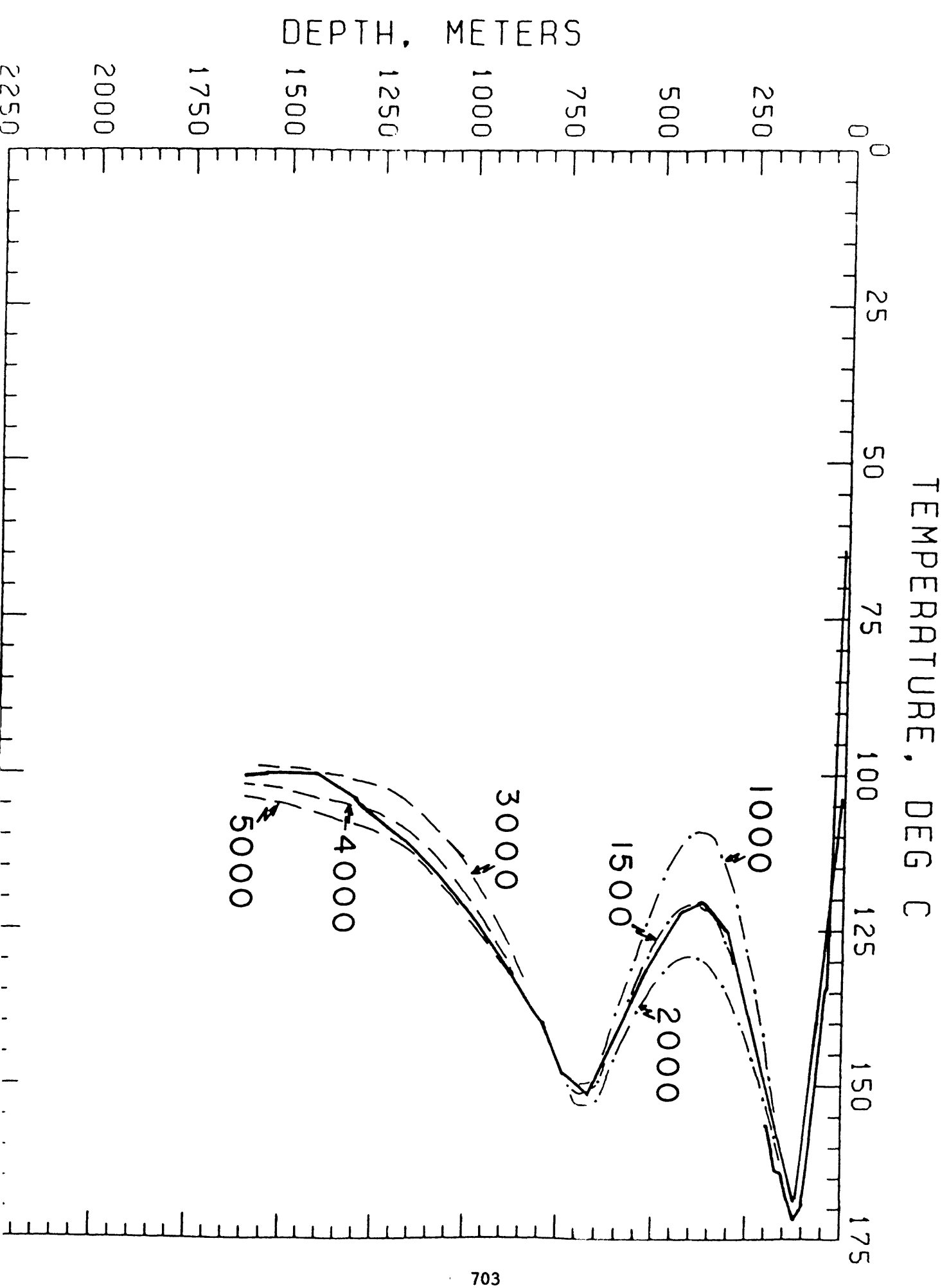
DEPTH, METERS
0
250
500
750
1000
1250
1500
1750
2000
2250
TEMPERATURE, DEG C
25
50
75
100
125
150
175
1000
1500
2000
3000
4000
5000

FIGURE 6

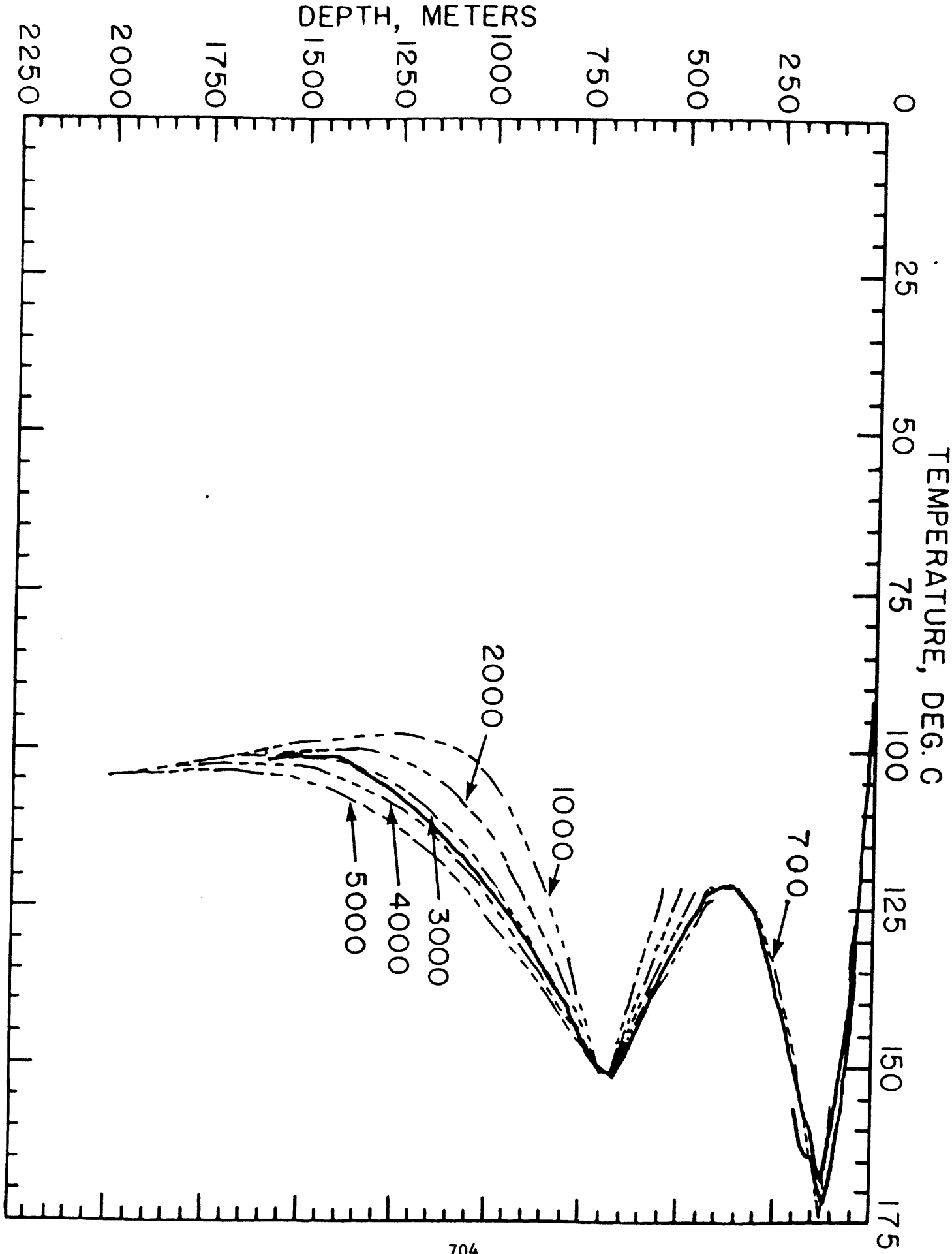
DEPTH, METERS
2250
2000
1750
1500
1250
1000
750
500
250
0
25
50
75
100
125
150
175
TEMPERATURE, DEG. C
2000
1000
700
5000
4000
3000

FIGURE 7

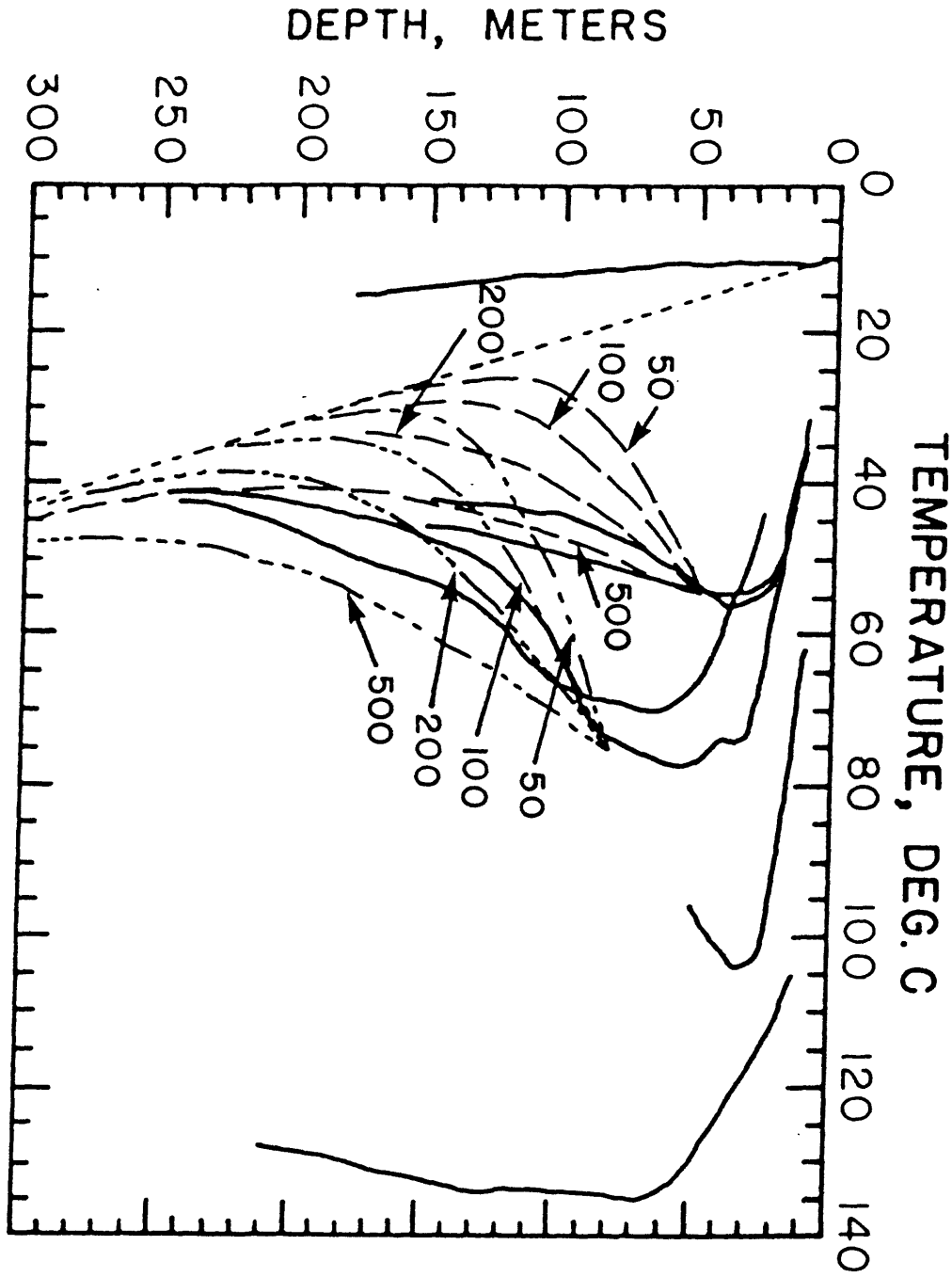
DEPTH, METERS
300
250
200
150
100
50
0
0
20
40
60
80
100
120
140
TEMPERATURE, DEG. C
200
100
50
500
500
200
100
50

FIGURE 8

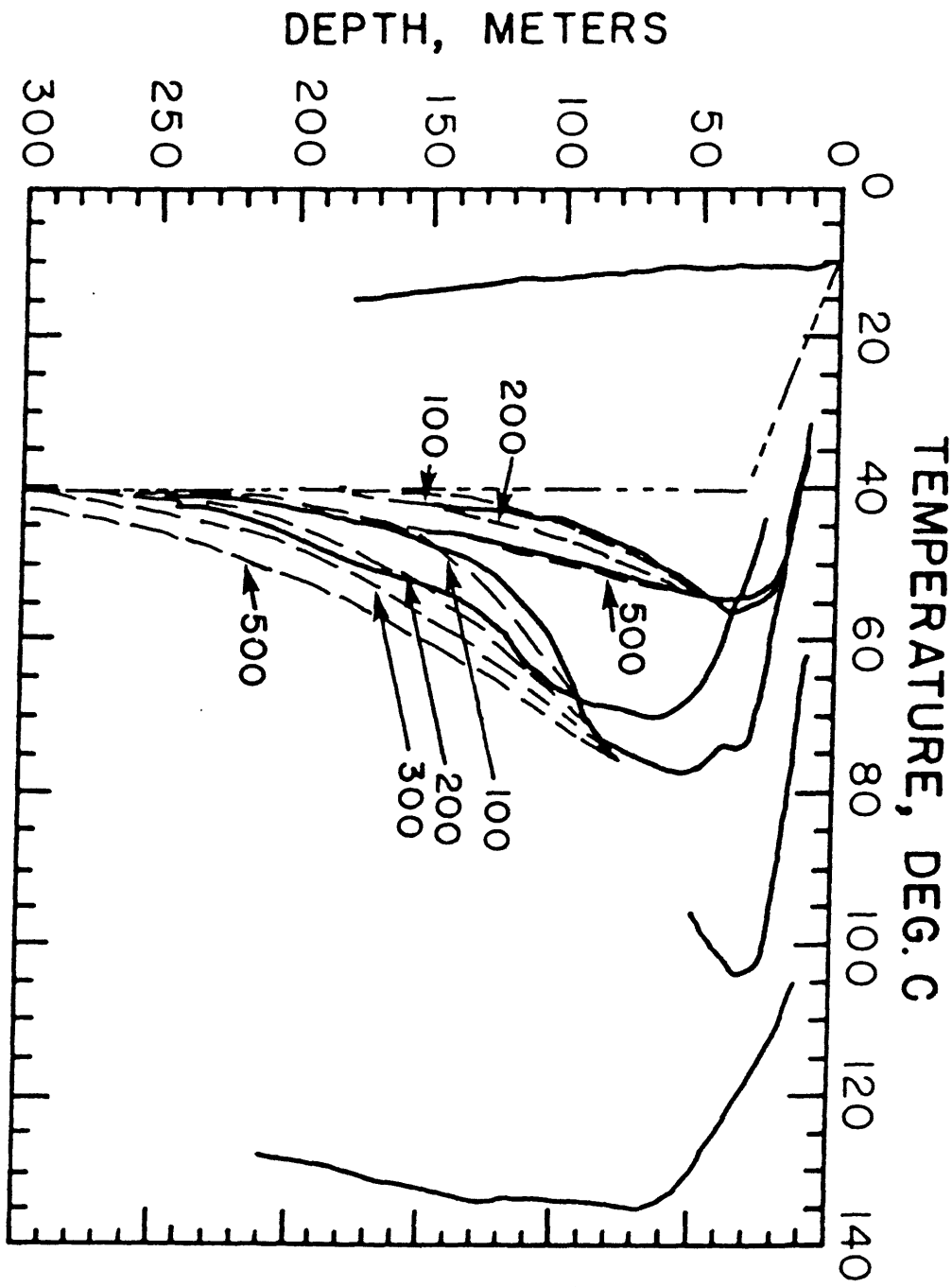
DEPTH, METERS
300
250
200
150
100
50
0
0
20
40
60
80
100
120
140
TEMPERATURE, DEG. C
100
200
500
500
300
200
100

FIGURE 9

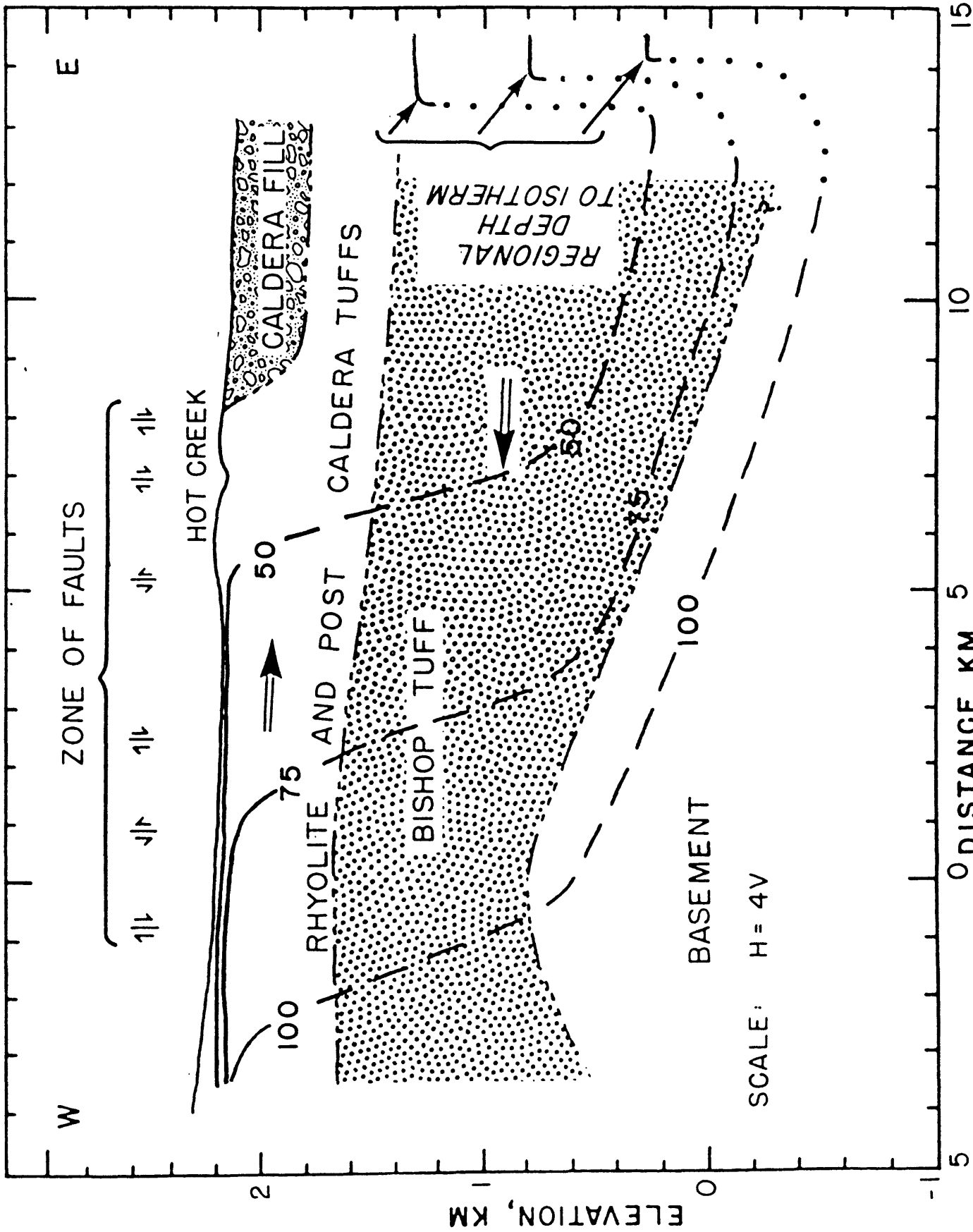
E
W
CALDERA FILL
HOT CREEK
ZONE OF FAULTS
CALDERA TUFFS
REGIONAL DEPTH TO ISOTHERM
RHYOLITE AND POST BISHOP TUFF
BASEMENT
50
75
100
SCALE: H = 4V
ELEVATION, KM
DISTANCE, KM
2
1
0
-1
5
10
15

FIGURE 10

Soil Hg° and Rn Distribution Pattern at Long Valley Caldera, Eastern California

Stanley N. Williams

Kenneth W. Hudnut

Department of Earth Sciences
Dartmouth College
Hanover, N.H. 03755 USA

A three-phase program to study the concentration of Hg° and Rn in soil gas was begun July, 1983 in Long Valley Caldera, eastern California. The first phase involved a survey of more than 600 sites in or adjacent to the caldera. Preliminary interpretation of that data is presented. The second phase involves monitoring of Rn concentration at 17 sites chosen on the basis of survey results and accessibility. The third, anticipated, phase will involve limited resampling for Hg° of selected areas during summer, 1984.

Rn was measured using commercially available "Track-Etch Detector Cups" placed in holes dug 40cm deep into the soil or surficial material. These cups are passive integrating devices which use an alpha particle-sensitive film to measure Rn concentration. The cups were collected after 30 days and processed by the Terradex Corporation (their manufacturer).

Soil samples were collected from the base of each of the holes for Hg° analysis. The air-dried < 80 mesh stainless steel- seived fractions were analyzed for Hg° using a Jerome Instrument Model 301

Gold Film Hg° detector. The lower limit of detection in routine use is 10 ppb and analytical precision is about 17% at the 100 ppb level (Varekamp and Buseck, in press).

Rn monitoring is conducted by placing the detector cups at the base of a section of PVC tubing, which extends to a depth of 40 cm below the surface and projects to a convenient height above the ground. The upper end of the tube is covered by a removeable cap and the cups are removed and replaced on a monthly basis.

Sampling strategy was planned to allow heavy coverage (200m spacing) of the areas of seismicity and uplift as well as major structures. Less detailed traverses (1 km spacing) were conducted over areas of no current activity and simple geology. This survey sampled nearly twice as many sites as had previous workers and the areas adjacent to the numerous dirt roads were necessarily used as sites for traverses for the sake of time.

The data show that about 45% of the samples sites had Hg° less than 10 ppb. The data below that level looks quite coherent but will not be further considered for the present. The data fall into three populations, which can be interpreted as background (geometric mean $\bar{X}$ = 12.5 ppb), aureole ($\bar{X}$ = 26 ppb) and peak ($\bar{X}$ = 520 ppb). A lower threshold for anomalous values is difficult to select because of population overlap, but using 40 ppb reveals that 45% of the data is anomalous (about the same as the 1982 results of Varekamp and Buseck, in press). Peak mean values in 1983 are, however, significantly higher than in 1982 (520 ppb was opposed to 140 ppb).

Rn data also falls into three different populations when plotted on logarithmic cumulative frequency paper. The lowest concentration group (geometric mean $\overline{X}$ = 47 T/mm^2/30 days) is quite small and represents only 2% of the data. The middle concentration group ($\overline{X}$ = 260 T/mm^2/30 days) represents 96% of the data. A peak group ($\overline{X}$ = 1450 T/mm^2/30 days) represents 2% of the >600 samples. From consideration of the areal distribution of the low concentration group, it appears to be some kind of Rn low and not a background group. Cox (1983) observed such anomalies at Kilauea caldera. No older public Rn data exist to use for comparison with our 1983 data.

Monitoring is taking place at 17 permanent sites (often at U.S.G.S. - maintained geodetic stations). Only two months' data are in hand so it is premature to report them.

A significant and widespread Hg° anomaly occurs within Long Valley Caldera. A much more restricted (areally) Rn peak occurs within the south central portion of the caldera and extends out of it, to the southeast (corresponding to the epicentral zone). Hg° seems to be concentrated in fumarolic zones and to follow structures (particularly the edges of grabens e.g. east side Inyo Graben, Long Canyon graben). Rn shows a similar tendency to be high in graben structures. Both Hg° and Rn are low in adjacent horst blocks.

Many of the low Rn population values fall in the north and northwest part of the Inyo Crater line. This corresponds with a Hg° low. A large Hg° high occurs over the east-central and southern

portion of the Inyo Crater line. A convection cell related to upwelling geothermal fluids might explain the pattern.

The major Rn peak does not follow geology or structure but does seem to be closely related to earthquake distribution. Hg° values in the area of highest Rn are actually much lower than those measured in 1975 (Matlick and Buseck, 1976) in the same area (Sherwin Creek). This may reflect recent flushing out of residual Hg° by greater heat flow or increased rate of ground gas flow.

In conclusion, our survey of soil Rn and Hg° shows distribution patterns which can be related to the geothermal system of Long Valley Caldera. Changes in the shapes and intensities of those distribution patterns seem to be related to magmatic resurgence which began in 1980. Rn peaks appear to be restricted to the immediate area of seismicity. Hg° peaks are much more widespread and apparently reflect the movement by convecting fluids of Hg° vapors.

References Cited

Cox, M.E., 1983, Summit outgassing as indicated by radon, mercury and pH mapping, Kilauea volcano, Hawaii: Jour. Volcanol. Geotherm. Res., v. 16, p. 131-151.

Matlick, J.S. and Buseck, P.R., 1976, Exploration for geothermal areas using mercury: a new geochemical technique: Proc. 2nd U.N. Symp. on Devel. and Use of Geotherm. Res., v. 1, p. 785-792.

Varekamp, J.C. and Buseck, P.R., in press, Possible site of future eruptions in the Long Valley (CA) area, based on Hg anomaly patterns: Geology.

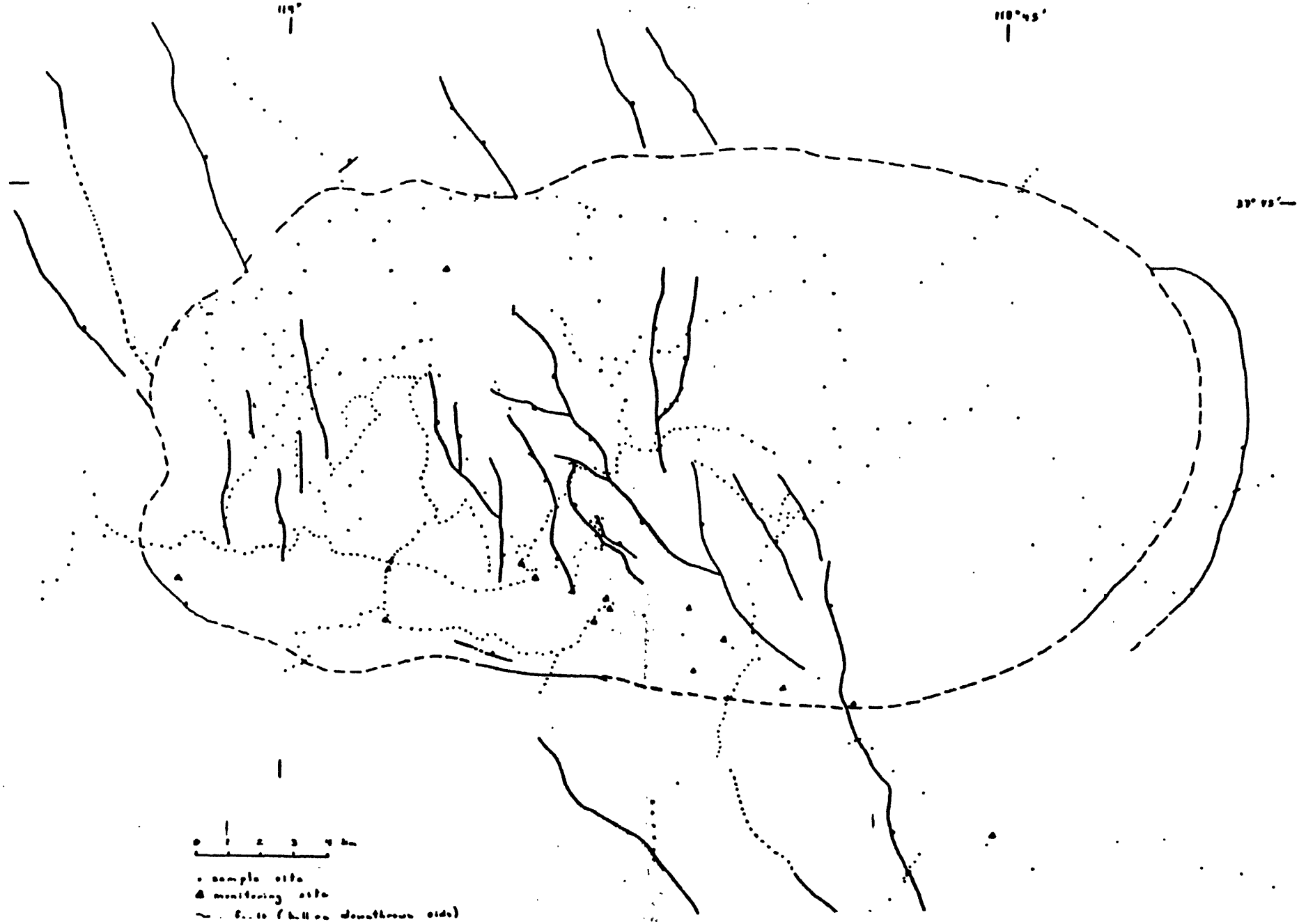

Figure 1: Sketch map of Long Valley Caldera, eastern California with sites of Hg^{o} and Rn soil gas survey indicated. Structure after Bailey and Koeppen, 1977.

HISTORICAL UNREST AT LARGE QUATERNARY CALDERAS OF THE WORLD, with special reference to Long Valley, California

C.G. Newhall[1], D. Dzurisin[1], and L.S. Mullineaux[2]

[1]U.S. Geological Survey, Cascades Volcano Observatory
Vancouver, Washington 98661
[2]Scripps Institute of Oceanography
La Jolla, California 92093

Red Book Conference on Long Valley
January 1984

ABSTRACT

Historical seismicity, ground deformation, thermal activity, and eruptions at large Quaternary calderas of the world are: (a) common, (b) typically long-lived, (c) complex in their spatial and temporal patterns, and (d) caused by combinations of tectonic, magmatic, and hydrothermal processes. Three fundamental causes of caldera unrest are regional tectonic strain, magmatic intrusion, and change in a hydrothermal system beneath a caldera. Other processes may occur in response to these three stimuli, and further contribute to unrest. Possible responses include expansion and deformation of a magma body, and expansion of (water-saturated) country rock above the magma reservoir. We do not attempt to prove the applicability of any single process or combination of processes at specific calderas. Instead, we demonstrate the general plausibility of each process, and argue that the complexity of caldera systems makes it likely that any given episode of unrest is caused by a combination of these processes.

Recent unrest at Long Valley caldera can be plausibly explained as a regional extension event, followed by slight in-situ expansion or deformation of the caldera's large silicic magma body. An intrusion of basaltic magma near the base of that silicic magma body, in 1980, is possible but not required by the data.

Large magma bodies beneath calderas are dynamic systems, in delicate balance between quiet and unrest. The stimuli for unrest need not be large; most often, the stimuli are common geological processes such as regional tectonic strain and small magmatic intrusions from depth.

----------A note from Rabaul----------

" Between four and five years ago, when the erection of a Quarantine Station was being considered, some Heads of Departments, including myself, inspected Vulcan Island with the object of seeing whether it was suitable or otherwise for such a purpose. I had been twice on the island previously to see whether it might not be made into an animal or plant Quarantine Station, but turned it down as there was evidence that it was subject to frequent rising and subsidence.

On my last visit a casuarina tree which had been well above high water mark was particularly noticeable as being about twelve inches below water level, and the shore line seemed to have tilted. For these reasons I stated that I did not consider the island suitable for a Quarantine Station on account of the danger of its possible sudden subsidence, a statement treated with some levity by my companions, but having had personal experience with volcanic eruptions in other parts of the world I know that it was no joke. My final remark was "it came up in a night and might go down in a night and I would suggest that life buoys be hung round the verandah rails of the buildings where they would at least be ornamental, but would not be required if the island went up instead of down." (George H. Murray, 1937, in a preface to unpublished remarks about the 1937 eruption of Vulcan, Rabaul Caldera)

INTRODUCTION

Recent unrest at Long Valley caldera--seismicity, ground deformation, and increased fumarolic activity--has stimulated much speculation but no clear consensus about the responsible processes (Ryall and Ryall, 1981a, 1983; Savage and Clark, 1982; Savage and Cockerham, 1984), or about implications for future volcanic and seismic hazards in the area (Miller and others, 1982; Ryall and Ryall, 1984).

In parallel with intensive monitoring and studies of the geologic history of the Long Valley area, we need to ask whether unrest like that at Long Valley has been observed elsewhere. This paper reviews geophysical and geochemical unrest at large calderas of the world. More fundamentally, it compares unrest in and above large magma reservoirs, of which calderas are a handy indicator. We examine the nature, frequency, duration, outcomes, and possible causes of caldera unrest, in much the same way as epidemiologists examine the general occurrence and possible causes and controls of a puzzling disease. This "epidemiological" approach cannot conclusively identify the cause of a disturbance at any specific caldera, but it does provide ideas that can be tested with monitoring data from specific calderas, including Long Valley.

Rather than consider a small number of apparently close analogues of Long Valley, (i.e., calderas of similar age, dimensions, magma, and unrest), we have chosen to consider a larger variety of calderas including some which differ significantly from Long Valley (e.g., summit calderas of basaltic shield volcanoes). Within this large set we distinguish between gross differences in magma composition and the nature of unrest, and less often between differences in caldera age, diameter, and hydrothermal activity. Our reasons for considering a large set are: (1) no single caldera is likely to be a perfect analogue of Long Valley; (2) even if an identical caldera with identical unrest could be found, the final outcome at Long Valley need not be the same as occurred at the analogue; and (3) we can learn more about general processes of unrest by comparing a variety of calderas and unrest. For example, Kilauea and Mauna Loa are certainly not close analogues of Long Valley, but we can learn more about the possible effects of magma composition, density, and viscosity on the nature of unrest if the sample includes both mafic and silicic magma bodies.

This report is based upon a much larger but as yet incomplete compilation of details about worldwide caldera unrest (C. Newhall and others, unpublished data). In the present report we have omitted evidence for some of our conclusions, and cited only a few details of unrest at specific calderas. A companion paper by Dzurisin and Newhall (1984) discusses recent events at Long Valley, Yellowstone, the Phlegraean Fields, and Rabaul in more detail. Our conclusions in both papers are ideas to be tested, rather than proven facts.

Terminology

The following terms have special definitions in this paper.

"Large caldera"--a volcanic depression with a diameter of at least 5 km, many times the diameter of vent(s) therein. The term "caldera" is further restricted here to depressions formed largely by collapse into a magma reservoir beneath. This restricted, genetic definition is adopted so that the diameter of a caldera can be used as a rough guide to the size of the underlying magma body. Calderas formed as a result of large

volcanic avalanches or erosion are excluded from this discussion. A few calderas less than 5 km in diameter, e.g., Oshima and Ontake, have been considered because they illustrate processes that probably act, but have not been documented, at larger calderas.

"Quaternary caldera"--a caldera listed in the Catalogue of Active Volcanoes of the World (IAVCEI, 1951-), in the Data Sheets on Post-Miocene Volcanoes of the World (IAVCEI, 1973-), or in various primary sources, unless there is positive evidence that the caldera formed more than 2 my ago.

"Unrest"--
We distinguish three non-overlapping types of unrest--eruption only, broadly-defined, and narrowly defined--according to the phenomena noted.

"Eruption only": an eruption, without reported precursory seismicity, uplift, or other anomalous geophysical or geochemical activity;

"Broadly-defined unrest": a significant change in seismicity, ground deformation, or fumarolic activity, sometimes culminating in an eruption;

"Narrowly-defined unrest": increased seismicity and uplift, sometimes culminating in an eruption.

Our distinctions are between three types of reports; in fact much of the unrest in the first two categories would properly belong in the third, narrowly-defined category if historical reports were more detailed.

"Episode of unrest"--a period of unrest of unspecified duration, preceded and followed by relatively quiet periods of equal or longer duration. Typically, episodes of unrest last several months or years, and are preceded and followed by several years or decades of quiet.

"Caldera-year of unrest" (c-y): a calendar year at one caldera, during which unrest is known to have occurred. The duration is not considered--one day counts the same as 365 days. The purpose of this definition is to normalize observational data to some common, reproducible basis that is not dependent on whether the observer chooses to report unrest as many discrete events or as a smaller number of episodes of closely related events. For example, we can refer to six caldera-years of increased seismicity at Long Valley, from 1978 to the present, without needing to decide whether or how to group seismic events. The same principle applies to ground deformation: using Long Valley again as an example, we can speak of approximately 5 caldera-years of ground deformation, rather than argue about whether one or many episodes of ground deformation occurred within that period.

Nature of available data

Historical reports are woefully incomplete. Anecdotal reports by early explorers, passing sea captains, and local villagers are usually short and describe only what was detectable and of interest to the observers. Commonplace events often go unreported, regardless of how interesting these might be to scientists. Precise timing of events is rarely given, and one is lucky in most cases to discover the relative order of events. Reporting has markedly improved in recent years, with

the result that small events seem to be more frequent now than in the past. Discussions of the absolute frequency of various events, and even the relative frequencies of large and small events, should consider an interval recent enough to ensure complete reporting, but long enough to include several recurrences of the events in question. For most purposes in this paper, we have restricted our attention to the past 100 years.

No two authors will report the same event in the same way, much less report different events at different locations in a consistent way. Most of the original reports that we have consulted contain brief, passing references to an eruption or some other form of unrest. At the other extreme, a few reports contain far more detail than we can possibly include here. Secondary sources, such as the Catalogue of Active Volcanoes of the World (IAVCEI, 1951-) or Volcanoes of the World (Simkin and others, 1981) are helpful guides to primary sources.

Reports from the volcanological literature are naturally biased toward unrest that led to eruptions. Only occasional mention is made of seismic or other unrest that did not lead to an eruption, even if that unrest occurred at a young volcanic center. Reports from the seismological literature are biased toward events of particular seismological interest, and do not always mention an association with a volcano or volcanic activity. Geothermal reports often examine a small part of a volcanic system in great detail, but seldom address relations to the broader volcanic and tectonic setting. Only rarely do reports integrate volcanological, seismological, and geothermal observations at a given site of unrest. We have tried to eliminate as much reporting bias as possible, but we recognize that the data included here may still reflect some bias from our volcanological background and our suspicion that much of the unrest at large calderas would either not occur or would be of a different character in non-volcanic settings.

DISCUSSION

We have counted approximately 200 large Quaternary calderas, among which we distinguish three groups according to the composition of the products of their caldera-forming eruptions--"mafic," with SiO_2 less than 57%, "silicic," with SiO_2 greater than or equal to 57%, and those for which the composition of the caldera-forming eruption is not known. In a series of questions, we will examine the prevalence and nature of historical unrest, likely precursors to eruptions, and likely causes and controls of unrest at these calderas.

The prevalance and nature of historical unrest at large calderas

1. What proportion of the world's large Quaternary calderas have exhibited unrest in the past 100 years?

At least half of our sample of 200 large Quaternary calderas have exhibited one form or another of unrest within the past 100 years, as indicated in Table 1.

Table 1

	Magma of caldera-forming eruption			
	"Mafic"	"Silicic"	Composition unknown	Total
Number of large calderas with:				
No historical unrest	7	46	45	98
Eruption only	2	12	6	20
Broadly defined unrest (w/ or w/o eruption)	9	36	15	60
Narrowly defined unrest (w/ or w/o eruption)	5	11	4	20
Total	23	105	70	198

2. How prevalent, in terms of caldera-years within the past 100 years, is unrest at large Quaternary calderas? Using the same categories as above, the data are:

Table 2

	Magma of caldera-forming eruption			
	"Mafic"	"Silicic"	Composition unknown	Total
Eruption only	135 c-y	353	99	587
Broadly-defined unrest	58	354	81	493
Narrowly-defined unrest	91	171	14	276
Total	284	878	194	1356

In a typical year, therefore, some form of unrest occurs at approximately 14 calderas (1356 c-y/100 yr), including narrowly-defined unrest at approximately 3 calderas (276 c-y/100 yr), and eruptions at 6 or more calderas (587 c-y/100 yr).

3. What, more precisely, is the nature of unrest at large Quaternary calderas?

Table 3 shows the average duration, maximum magnitude, and number of reported episodes of each type of unrest. Unrest that occurred during or after eruptions is not included, so that what is shown may be considered as precursory or potentially precursory to an eruption. Reporting of most geophysical and geochemical activity is so incomplete that the actual number of episodes of unrest is almost certainly several times greater than shown in Table 3.

In an effort to determine how often a particular geophysical or geochemical change demonstrably does not accompany another form of unrest, we counted reports that explicitly stated that a given change did not occur. The reports are so few that they do not warrant separate reporting by category. We suspect that most geophysical and geochemical parameters change during unrest at large calderas, and that the absence of any report of change means only that the changes are undetected or unreported. One change of particular interest at Long Valley--broad, subtle, caldera-wide uplift--is only noted where precise levelling, gravity surveys, a tide gauge, or a changing shoreline permits its recognition. It seems significant that broad, subtle, generally long-period uplift occurs within at least 9 out of 14 large calderas where adequate surveys have been made. Calderas that are known to show such uplift (alternating in most cases with subsidence) are: the Phlegraean Fields, Rabaul, Aira, Iwo-Jima, Long Valley, Yellowstone, Kilauea, Mauna Loa, and Krafla. Levelling surveys around the margin of Toya caldera several years before and after eruptions show only minor caldera-wide deformation, but broad uplift may have occurred immediately before an eruption in 1910. Surveys made over only a few years at Taupo, Kakuto, Chijiwa, and Askja show subsidence or irregular deformation.

Table 3

	Magma of caldera-forming eruption		
	"Mafic"	"Silicic"	Composition unknown
Local seismicity			
avg. duration	wks	wks-mo	mo
M maximum	7.2, at Kilauea	7.0, at Rabaul, Aira	6.0, at Chijiwa
Max cumulative seismic E release (ergs)	10^{22}, at Kilauea	10^{22}, at Rabaul, Aira	10^{20}, at Chijiwa
sample size (N)	78	104	17
Tremor			
avg. duration	hrs	days	hrs
sample size (N)	63	5	2
Uplift			
avg. duration	mo-yrs	yrs	yrs
max cumul. uplift	300m, at Oshima	290m, at Usu	9m, at Iwo-Jima
(or, excluding extreme values),	2m, at Krafla	5m, at Lou-Tuluman	9m, at Iwo-Jima
max rate(per day)	)0.5m/d, at Oshima	2m/d, at Rabaul	.003m/d, at Karkar
(or, excluding extreme values),	.01m/d, at Krafla	2m/d, at Rabaul	.003m/d, at Karkar
sample size (N)	67	23	9
Subsidence			
avg. duration	yrs	mo-yrs	decades
sample size (N)	30	18	1
Tilt			
avg. duration	mo	mo	mo
sample size (N)	34	16	3
Horizontal strain			
avg. duration	mo	mo-yrs	(decade)
sample size (N)	25	5	1
Ground fracturing			
avg. duration	hrs-days	wks	decades
sample size (N)	65	15	2
Magnetic changes			
avg. duration	-	wks-mo	-
sample size (N)	1	3	0
Gravity changes			
avg. duration	mo	yrs	(mo)
sample size (N)	4	4	1
Thermal changes			
avg. duration	-	mo	yrs
sample size (N)	5	39	10
Fumarole, gas changes			
avg. duration	mo-yrs	mo	mo-yrs
sample size (N)	12	58	24
Spring, lake changes			
avg. duration	mo	mo-yrs	yrs
sample size (N)	8	34	6

4. What portion of the unrest described in #3 was precursory to eruptions? How often have the same precursors occurred without an eruption?

Values for sample size (N) (Table 3) are subdivided below into two values "A:B," where A= the number of episodes of a specific change that culminated in an eruption, and B= the number of similar episodes that did not culminate in an eruption.

Table 4a

	Magma of caldera-forming eruption		
	"Mafic"	"Silicic"	Composition unknown
Local seismicity	77: 1	49: 55	9: 8
Tremor	63: 0	5: 0	2: 0
Uplift	67: 0	17: 6	9: 0
Subsidence	28: 2	5: 13	0: 1
Tilt	34: 0	7: 9	3: 0
Horizontal strain	25: 0	2: 3	0: 1
Ground fracturing	65: 0	12: 3	2: 0
Magnetic changes	1: 0	2: 1	0: 0
Gravity changes	4: 0	2: 2	1: 0
Thermal changes	3: 2	23: 16	8: 2
Fumarole, gas changes	5: 7	33: 25	19: 5
Spring, lake changes	4: 4	18: 16	5: 1

For example, "49: 55" in the first row of Table 4a indicates that at silicic calderas, 49 episodes of local seismicity culminated in eruptions while 55 other episodes did not.

The frequency with which entire episodes of unrest (combinations of symptoms) have been followed by eruptions cannot be derived from Table 4a, but is shown below. A:B are as in Table 4a.

Table 4b

	Magma of caldera-forming eruption			
	"mafic"	"silicic"	composition unknown	Total
Broadly-defined unrest	20:2	60:73	27:15	107:90
Narrowly-defined unrest	59:0	10:6	3:0	72:6
Total	79:2	70:79	30:15	179:96

The most obvious inference from Tables 4a and 4b is that unrest at large calderas often leads to eruptions. Two-thirds (179/275) of the reported episodes of unrest culminated in eruptions, with a particularly high incidence at mafic calderas.

However, lest these values be misinterpreted, we suggest three important cautions. First, unrest is much more likely to be reported if it culminates in an eruption than if it does not. This bias increases the apparent likelihood that unrest will culminate in an eruption. Second, the data for mafic calderas are dominated by Kilauea and Mauna Loa, and further biased by the fact that we have considered intrusions at those volcanoes to be precursors to ensuing eruptions (for consistency with other calderas where intrusions may go unnoticed). The implication in Tables 4a and 4b that unrest at mafic calderas almost always leads to eruptions is thus partly an artifact. Third, the data mix small-scale, local events with those affecting the caldera as a whole. If we consider only unrest that is strictly similar to that in Long Valley--repeated

seismic swarms and broad, caldera-wide uplift above a large silicic magma body--we can find 3 eruptions in 5 completed and 4 incomplete episodes of unrest. These are: with eruptions--Aira (1914, 1955 ff.), Rabaul (1937); without eruptions--Rabaul (1919-23), Phlegraean Fields (1969-74); without eruptions but still restless--Yellowstone (1959?-present), Rabaul (1971-present), Long Valley (1978-present), and the Phlegraean Fields (1982-present).

A few additional observations are pertinent to forecasting eruptions at large calderas, including Long Valley.

(a) Probably none of the eruptions in this compilation occurred entirely without precursors. Many occurred without reported precursors, and a few reportedly occurred without precursors, but such instances are probably attributable to inadequate monitoring or failure to recognize the significance of precursors in advance.

(b) Some eruptions, particularly phreatic eruptions, were probably preceded by no more precursory activity than has already occurred at Long Valley. This is not to say that we think a phreatic eruption is imminent at Long Valley, but rather to recall a lesson learned at Mount St. Helens in 1980: there are some circumstances in which an eruption can begin after a long series of precursory activity, without any further short-term escalation in activity. We know very little about the precursors to phreatic eruptions, and it is conceivable that a phreatic eruption could occur in any of several locations in Long Valley during another strong seismic swarm, without or very soon after a dramatic change in other indicators.

(c) It is especially difficult at large calderas to recognize the significance of seemingly unrelated activity--widely separated in space or time. The larger the magma system, the more complex and prolonged can be the precursors to an eruption.

(d) Eruption precursors at small volcanic centers tend to intensify as the eruption nears, culminating in an eruption within a period that is rarely longer than a few months. Unrest at large calderas, however, often proceeds in fits and starts and may continue for years or decades, making it very difficult to know whether any particular increase in activity will lead to an eruption in the near-term. If we are to give any assurance that an eruption at a large caldera will be successfully forecast, we and the public must also be prepared to accept a few false alarms.

(e) Most magmatic eruptions from new or long-inactive vents at calderas have been preceded by pronounced seismicity and ground deformation. In at least some instances, unrest accelerated remarkably within a few hours to a few days before the eruption (e.g., Phlegraean Fields, 1538; Rabaul, 1878, 1937). However, only a few hours of increased activity preceded the 1977 eruption of Usu, previously quiet since 1945 (Yokoyama and others, 1981).

(f) Rabaul, the caldera in this compilation that seems most likely to have an eruption in the near future, has exhibited systematic inflation and a systematic increase in the number of earthquakes (and probably in the energy release of each swarm) since 1971, including a marked recent acceleration of that activity (McKee and others, 1983). These systematic increases contrast with irregular patterns of unrest at most other calderas, and probably increase the likelihood that an eruption will eventually occur.

5. What is the nature and size of historical eruptions at large calderas? (past 100 years only)

Table 5a

Nature of eruptions	Magma of caldera-forming eruption: mafic	silicic	composition unknown	Total
phreatic explosions	5	55	17	77
"normal" explosions (includes all explosions that were not reported to be phreatic).	ca 67	175	73	315
lava flows	ca 115	54	18	187
lava lakes	10	0	3	13
domes (including cryptodomes)	0	14	4	18
submarine, subglacial	0	12	12	24
unknown	10	18	7	35

(Note: Two or more of these phenomena may occur during a single eruption.)

As expected, lava flow and lava lake activity is common during mafic eruptions at calderas; explosions, lava flows and dome growth are common during silicic eruptions.

Table 5b

Size of eruptions	Magma of caldera-forming eruption: Mafic	Silicic	Composition unknown	Total	
Maximum VEI* =6	0	0	0	0	(8)**
=5	0	1	1	2	(19)
=4	2	8	1	11	(102)
=3	6	36	14	56	(617)
=2	42	135	59	236	(2882)
=1	6	17	7	30	(338)
=0	19	14	4	37	(354)
=unknown	13	29	15	57	

*=Volcanic Explosivity Index (Newhall and Self, 1982); values may be equated roughly with the bulk volume of tephra erupted. VEI 0=less than 10^4 m^3; VEI 1=10^4-10^6 m^3; VEI 2=10^6-10^7 m^3; VEI 3=10^7-10^8 m^3; VEI 4=10^8-10^9 m^3; VEI 5=10^9-10^{10} m^3; VEI 6=10^{10}-10^{11} m^3.

**=Numbers in parentheses are totals for all historical eruptions, including those associated with calderas (from Simkin and others, 1981).

The relative proportions of various size eruptions in the worldwide sample (column at far right, Table 5b, in parentheses) include eruptions throughout historical time (much longer than just the past 100 years) and are therefore biased toward larger eruptions by poor early reporting of small eruptions. Despite that bias, the relative proportions of VEI's in the caldera sample for the past 100 years (column labeled "Total," Table 5b) are similar to the proportions for the worldwide historical sample. Although large calderas hold a greater potential for catastrophic eruptions than small centers, most eruptions at large calderas are relatively small.

The magma composition of post-caldera eruptions need not be that of the caldera-forming eruption. In fact, most post-caldera eruptions at "silicic calderas" are of more mafic magma than that of the caldera-forming eruption, as seen in Table 5c.

Table 5c

	Magma of caldera-forming eruption			
	Mafic	Silicic	Composition unknown	Total
Minimum SiO2 of latest eruption:				
less than 57:	120	169	69	358
greater than or equal to 57:	0	65	33	98
Total	120	234	102	456

Numbers are approximate because they include some eruptions for which the composition was known only in general terms, e.g., mafic or silicic.

These data are biased toward lower silica contents, because we have used the minimum of any range in reported silica values. However, we do not think the bias negates a general conclusion that mafic magmas prevail in post-caldera eruptions, even at silicic calderas.

Possible influences on the nature of unrest at large calderas

6. Are there special characteristics of unrest at large calderas, unlike those observed in other volcanic or tectonic settings, that might give some clue to the processes responsible for unrest?

Many aspects of unrest at large calderas differ from unrest in other settings. Three of the most pertinent differences are:

(a) Unrest at large calderas may last centuries, millenia, or longer, e.g., at the Phlegraean Fields and at Iwo-Jima. Uplift and subsidence at Aira Caldera has been occurring at least since measurements were begun in the 1890s. Other episodes of broad, caldera-wide unrest are known to have lasted for several years or several decades, e.g., several episodes of unrest at Rabaul Caldera within the past century and a half. Nearly all periods of unrest at large calderas last longer than similar unrest (seismic swarms, uplift, etc.) at smaller volcanic centers. Typically, unrest at small centers lasts from a few hours to a few months, rarely more than a year, before culminating in an eruption, intrusion, or a return to quiet.

(b) Seismicity, uplift, increased thermal activity, and eruptions at a given caldera do not always occur together in time and space; centers of each may shift location from one episode of unrest to the next, or even within single episodes of unrest. Uplift before the 1538 eruption of Monte Nuovo in the Phlegraean Fields was centered at Pozzuoli, 3 km from where the eruption ultimately occurred. Uplift in the Rabaul caldera bears only a crude spatial relation to eruption sites, which are structurally determined by the caldera's ring fractures. Seismic swarms preceding the 1979 eruption of Ontake Volcano were 7-15 km SE of Ontake--so far away that they were not considered to be related. Uplift at Long Valley has been centered on the resurgent dome, but most seismic swarms have occurred along the southern caldera ring fracture or south of the caldera. Uplift at Kilauea and Mauna Loa is centered on the

calderas, but eruptions may occur many kilometers down-rift from these calderas.

Some of this complexity probably reflects structural control, e.g., at Kakuto Caldera and Kirisima Volcano. A certain amount of complexity is predicted by theoretical models, e.g., parallel ridges of uplift on either side of a rising dike (Dieterich and Decker, 1975; Pollard and others, 1983). Some of the remaining complexity, we think, reflects the complex geometry and plumbing of large magma reservoirs. Geologic mapping of the dissected roots of ancient volcanoes has shown that magma reservoirs beneath large calderas commonly had irregular tops or cupolas. Seismic studies also suggest complexity in the structure of large magma reservoirs (Hill, 1976; Ryall and Ryall, 1981b; Sanders, 1983). We envision that large magma reservoirs are mushy zones that can expand or "fill" much like a sponge, inflating slightly when filled and deflating slightly when drained (Dzurisin and others, 1980). Assuming that some pods of molten material are interconnected, a disturbance in any one portion of a magma reservoir by shaking, squeezing, or injection of melt may eventually be distributed in complex ways throughout the magma reservoir. Judging from the long duration of unrest at silicic calderas, it may take years for a disturbance to propagate through a viscous silicic magma body.

(c) Unrest at large calderas may occur in multiple episodes, sometimes increasing and decreasing several times before culminating in an eruption, intrusion, or return to quiet. Seismicity may occur in repeated swarms rather than in a monotonic increase, and uplift may alternate with subsidence. The length of periods between "peaks" varies as greatly as the duration of unrest itself--from centuries or millenia in the case of the Phlegraean Fields uplifts, to days in the case of seismic swarms during particularly intense unrest.

7. Are there any correlations between characteristics of calderas in this compilation and the nature or frequency of their unrest to suggest factors that might influence unrest?

We have considered four characteristics of calderas that might exert an influence on the nature of unrest. The first is magma composition of the caldera-forming eruption, which in most cases approximates the composition of any large magma body presently beneath the caldera. Some differences in unrest can be attributed to the difference in viscosity (several orders-of-magnitude) between mafic and silicic magmas. Perhaps the most striking difference in unrest at mafic and silicic calderas is that unrest at mafic calderas leads to eruptions much more consistently than does unrest at silicic calderas (Tables 4a, 4b). An influx of mafic magma into the roots of a mafic caldera may rise to the surface or force an equivalent volume of magma from the top of the reservoir, but an influx of mafic magma into the roots of a silicic caldera may easily be trapped beneath or incorporated into the reservoir, and need not always cause an eruption from the top of the reservoir. Silicic magmas act as a density barrier to basaltic melt (Smith, 1979; Hildreth, 1981).

A second possible influence on unrest is magma reservoir size, as reflected by caldera diameter (Table 6).

Table 6

	Caldera diameter (km)					
	5-10	10-15	15-20	20-25	more than 25	unknown
Number of calderas in each size category, quiet for past 100 yrs	41	12	6	2	7	ca 30
Number of calderas in each size category, active in past 100 yrs	61	19	13	5	2	0
Average repose (between post-caldera eruptions) (N=number of repose periods)	20±34 yr (N=168)	16±27 (N=117)	14±25 (N=54)	23±89 (N=51)	no eruptions (N=0)	n.a.
Avg. duration of each episode of seismic unrest (regardless of whether it culminated in an eruption)	wks-mo (N=15)	mo-yrs (N=29)	wks-mo (N=13)	wks (N=12)	mo (N=7)	n.a.

We expected that large calderas would prove to be more restless than small calderas, because rates of basaltic magma supply from depth are probably higher at large magma bodies than at small ones (Shaw, this volume). Also, even without further magma supply, large magma bodies will remain molten longer than small ones. The proportion of restless to quiet calderas of similar diameter increases slightly with increasing caldera diameter (except for the largest calderas, which are too few for any generalization).

We did not know whether repose periods would increase or decrease with increasing caldera diameter. On the one hand, magma bodies beneath larger calderas might effectively buffer influxes of magma from depth, and cause repose periods to increase in duration with increasing caldera diameter. On the other hand, more frequent supply of basaltic magma, inferred above, might cause shorter repose periods with increasing caldera diameter. The available data are ambiguous, and may be meaningless because reposes between active periods at large calderas are often longer than historical records. Long reposes between active periods may represent periods between influxes of mafic magma from depth, and the "average" repose periods shown here may in some cases reflect only short periods of quiet between eruptions that are all related to a single influx of mafic melt.

Finally, we expected that because of the supposed buffering effect, the duration of seismic unrest would tend to increase with increasing caldera diameter. The available data do not support this idea.

A third possible influence on caldera unrest is age of the caldera. Intuitively, we might expect that older calderas would exhibit less frequent eruptions and more sluggish (prolonged) unrest than younger calderas. Our compilation shows:

Table 7

	Age($\times 10^3$yr)			
	0-10	10-50	50-100	100+
Avg. repose (yrs between post-caldera eruptions)	10+13 (N=102)	18+35 (N=49)	52+137 (N=23)	7+6 yr (N=11)
	Age($\times 10^3$yr)			
	0-10	10-50	50-100	100+
Avg. duration of each episode of seismic unrest (regardless of whether it culminated in an eruption)	wks (N=15)	wks-mo (N=30)	mo (N=8)	mo-yrs (N=8)

Repose periods in the first three age categories seem to increase with increasing age of the caldera, but this relation does not hold for ages greater than 100,000 yr. The data suffer from the same limitations noted with regard to caldera diameter, and can neither prove nor disprove a correlation between caldera age and repose periods. The correlation between duration of seismic unrest and age of the caldera is better, though still with regrettably few data points.

A fourth possible influence on unrest is the presence of an extensive hydrothermal system. Do earthquakes or uplift show any correlation with the extent of surficial hydrothermal manifestations in calderas? We distinguished three somewhat arbitrary degrees of surficial hydrothermal manifestation--minor, moderate, and extensive. Examples of these three classes are Krakatau (minor), Aso or Okmok (moderate), and Yellowstone (extensive).

Table 8

	Surface Hydrothermal Manifestations		
	Minor	Moderate	Extensive
Number of reported episodes of seismic unrest	10(9%)	52(24%)	71(48%)
Average duration of seismic unrest	days-wks	wks-mo	wks-mo
Number of reported episodes of uplift	12(6%)	18(8%)	16(11%)

Values in parentheses are the percentages of calderas in each group that have exhibited historical seismicity and uplift. There is a striking correlation of reported seismicity (and a tenuous correlation of reported uplift) with surface hydrothermal manifestations. On the basis of these numbers alone, however, we cannot be sure whether seismic activity is really more common where there is hydrothermal activity, or whether people like to live where there are hot springs and are therefore present to report seismicity. The apparent increase in the duration of seismic unrest with increasing hydrothermal activity suggests that there is a real correlation, but might also be explained by uneven reporting. Seismic swarms have been reported in a number of geothermal areas, and have been interpreted as focused release of regional strain in small increments, "lubricated" by higher pore pressures in geothermal areas (Minakami, 1960; Ward and Bjornsson, 1971; Hiraga, 1972; Hill and others, 1975; and others).

Likely causes and processes of caldera unrest

8. What causes have been proposed for unrest at large Quaternary calderas?

Three general stimuli have been suggested as causes of unrest at calderas: regional tectonic strain, magmatic intrusion, and changes in hydrothermal systems beneath calderas.

a. Regional tectonic strain. Unrest at calderas can reflect:
   (i) strain that is uninfluenced by the presence of a caldera i.e., that occurs only coincidentally at a caldera; or
   (ii) strain that is focused at a caldera because the caldera acts as a hole-in-a-plate.

b. Magma intrusion. Unrest at calderas can also occur when:
   (i) mafic magma intrudes into the base of a large mafic magma reservoir;
   (ii) mafic magma intrudes into the base of a large silicic magma reservoir;
   (iii) mafic magma intrudes through rocks overlying or alongside a large magma reservoir;
   (iv) silicic magma intrudes from a small or large silicic reservoir, into overlying rock.

c. Changes in a hydrothermal system. Changes in temperature, pore pressures, and circulation in a hydrothermal system beneath a caldera can occur as a result of tectonic strain or magmatic intrusion, or independently, as a result of climatic variation, self-sealing, or man's activities.

These three fundamental processes, a-c, can also trigger additional processes. Among the responses that have been suggested are:

d. Squeezing and deformation of a magma body, by regional tectonic strain;

e. Buoyant rebound of a magma body, upon release of tectonic or lithostatic confining stress;

f. In-situ expansion of a magma body, caused by
   (i) vesiculation,
   (ii) partial remelting of recently solidified magma, or
   (iii) thermal expansion,
   (processes that may in turn have been caused by tectonic strain, including earthquakes, or by magmatic intrusion)

g. Thermal expansion of country rock and groundwater above a large magma body and beneath a caldera, as could be triggered by a magmatic intrusion or a tectonically-induced influx of hot groundwater.

Let us examine each of these processes in more detail, together with arguments that each is a plausible cause of caldera unrest.

(a-i) Unrest caused by regional strain, uninfluenced by the presence of a caldera. Tectonic stresses can cause regional seismicity and ground deformation--hence efforts to monitor these parameters as possible precursors to large tectonic earthquakes. In some instances such seismicity and ground deformation may occur in the vicinity of calderas, coincidentally, and not be significantly influenced by the presence of the caldera or large underlying magma reservoir.

Two observations from this paper and from Newhall and others (unpublished data) support the plausibility of this process. First, seismicity and ground deformation similar to that which occurs at calderas can also occur in non-caldera, and even non-volcanic settings. For example, seismic swarms and uplift at Matsushiro, Japan in 1897, 1941-44, and 1965-68 are thought by most Japanese workers to be caused by regional tectonic strains and movements of groundwater (Ichikawa, 1969; Kasahara, 1970; Nakamura, 1971; Ohtake, 1976), without any clear involvement of the relatively small, old volcanic systems of the area. Similar unrest of probable tectonic origin has occurred on the Izu Peninsula, Japan in 1930 and 1974-80+ (Tsumura, 1977; Fujita and Tada, 1983), and the Kii Peninsula, Japan in the 1920's and in 1952-53 (Kanamori, 1972).

Second, many episodes of unrest do not culminate in eruptions, and some have patterns of seismicity and deformation that parallel regional patterns and cross-cut a caldera without obvious influence from the caldera. For example, occasional seismic swarms and regional tilting and faulting near Taupo Caldera (New Zealand) are thought to reflect regional extensional processes (Otway and others, 1984). Similar earthquake swarms and horizontal strains have been noted elsewhere in the Taupo Volcanic Zone, without any obvious relation to a caldera or large magma reservoir.

(a-ii) Unrest caused by regional strain, focused by the presence of a caldera. Stresses in the uppermost crust will be influenced locally by a caldera, much as stresses in a plate are influenced by a hole in the plate. The effects of a hole in a plate are well known to structural engineers, and the same type of analysis was applied to the Timber Mountain caldera in Nevada, to explain a bending of regional Basin and Range faults near the northern and southern margins of the caldera (Christiansen and others, 1965; Cummings, 1968). If, for example, extensional stress is applied in an E-W direction in the vicinity of a caldera, the extensional stress will be amplified at the northern and southern margins of the caldera, and minor N-S compression will result at the western and eastern margins of the caldera. We speculate that the amplified stresses in the northern and southern sectors will result in greater-than-average seismicity in those sectors, around the ring fracture of a caldera in an E-W extensional regime. Different stress regimes will lead to different influences of a caldera on local stress patterns.

Evidence that some caldera unrest is a result of focused regional strain release includes:

--as above, some episodes of caldera unrest show no obvious relation to magmatic or volcanic processes;

--the intersections of calderas and regional faults tend to be areas of high seismicity--e.g., the northwest margin of Aso caldera, the southern margin of Kakuto caldera, the eastern margin of Chijiwa caldera, the southern margin of Kutcharo caldera, the northern margin of Yellowstone caldera, and the southern margin of Long Valley caldera, among others; and

--some periods of caldera unrest are also periods of increased regional unrest, e.g., at and near Long Valley, from 1978 to the present.

These spatial and temporal correlations of caldera unrest and regional strain suggest that regional strain release might be focused at calderas, and hence cause caldera unrest. However, the correlation might also result from a more fundamental relation--that regional faults tend to localize the formation of calderas themselves, by focusing magma supply from depth and by creating a structural environment in which collapse can readily occur.

(b) Magmatic intrusions of mafic or silicic magma, into country rock or into a shallow magma reservoir. Various combinations of intruding magma and receiving "host" are possible, including (i) mafic magma intruding into a mafic magma reservoir (e.g., Kilauea, numerous instances); (ii) mafic magma intruding into a silicic magma reservoir (e.g., beneath Rabaul caldera, before and during 1937 and perhaps again in 1971-84); (iii) mafic magma intruding into country rock, above or alongside a large magma reservoir (e.g., during most rift eruptions of Kilauea, or at Tavurvur, Rabaul, in 1941); (iv) silicic magma intruding into overlying or adjacent country rock (e.g., Vulcan, Rabaul, in 1937).

All large shallow magma reservoirs presumably owe their existence to repeated supply of basaltic magma from depth. In the case of mafic intrusions into mafic reservoirs, the incoming magma will simply supplement the volume of similar magma already in the reservoir. Mafic intrusions into silicic reservoirs, however, may not be able rise through the less dense silicic magma, and will instead pond beneath the silicic reservoir. This ponding or underplating process provides the heat necessary to maintain many sub-caldera magma reservoirs in a molten, eruptible state. Occasionally, an influx of basaltic magma may trigger eruptions in a silicic magma reservoir, particularly if the larger silicic reservoir is otherwise ready to erupt.

Some observations consistent with magmatic intrusion as a cause of caldera unrest are:

--many cases of unrest culminate in eruptions;

--geophysical models of unrest are often consistent with a magmatic intrusion;

--some unrest is along linear chains of vents, or fissures, clearly situated above a dike;

--in a few instances influxes of magma can actually be traced, from their seismicity and changing patterns of ground deformation, up into (and through) a shallow magma reservoir (e.g., Kilauea, 1959).

(c) Changes in a hydrothermal system. Any mechanism that increases pore water pressure can be expected to cause subtle uplift above a hydrothermal system. Increases in pore water pressure also tend to reduce friction and permit regional strain release in small increments, as in earthquake swarms rather than mainshock-aftershock sequences.

Pore pressures in a hydrothermal system beneath a caldera can increase if tectonic strain restricts circulation, or if a magmatic intrusion raises the temperature of pore waters. Such responses to tectonic and magmatic stimuli are described below, in item (g). An increase in pore pressures might also occur as a result of self-sealing of pores by precipitation of silica and other minerals. Circulation becomes restricted and pore pressures increase, thereby causing uplift. Such changes probably occur over relatively long time periods--centuries or longer--but might occur faster if some other change were to cause rapid precipitation of silica.

Other possible controls on pore pressures include climatic variation and man's activities. Climatic variation can probably change the inflow of water over periods of centuries or longer, and thereby affect groundwater temperatures and pore pressures. Man can deplete hydrothermal systems by fluid withdrawal, stimulating subsidence and declining temperature. Fluid withdrawal has caused subsidence at Kakuto Caldera, among others, and has caused groundwater temperatures to decline at Hakone Caldera (Oki and others, 1978). Remarkable subsidence due to geothermal fluid withdrawal has occurred at Wairakei, New Zealand, near though not in the Taupo caldera; cumulative subsidence at Wairakei exceeded 8 m by 1982 (Allis and Barker, 1982). Partial re-inflation can be achieved by re-injection of fluids, but has not yet been attempted at Wairakei.

Even where pore waters are not confined, and therefore cannot build up pore water pressure, convective heating of country rock can cause that rock to thermally expand, in the same way as discussed in (d), above. Typical coefficients of thermal expansion for tuffs, sandstones, and other likely caldera-filling "country rock" are in the order of $10^{-5}/^{o}C$, so heating by 100°C could cause a 0.1 percent volume increase in the country rock. That percent increase in a slab of rock 5 km thick could cause uplift in excess of 5 m. Babbage (1847) concluded that thermal expansion and contraction of rock beneath the Pozzuoli area (Phlegraean Fields) was the cause of uplift and subsidence there, even though the existence of the Phlegraean Fields caldera was not known at the time. Changes due to thermal expansion and contraction will occur at rates limited in most cases by rates of groundwater diffusion and convective heat transfer. For this reason, thermal expansion is unlikely to explain short-term changes, over periods of less than a year.

Observations consistent with a hydrothermal contribution to caldera unrest include:

--numerous examples of an increase in the temperature of fumaroles and thermal waters, and a smaller but still significant number of instances of artesian hot springs that have developed during caldera unrest;

--seismicity and perhaps uplift are apparently more common where there are known hydrothermal systems (see question # 7);

--a detailed correspondence between seismicity and the higher-temperature portion of a hydrothermal system has been documented

at Hakone caldera (Hiraga, 1972; Oki and others, 1978);

--many eruptions at calderas begin as phreatic eruptions, and some never progress beyond phreatic activity.

The three primary stimuli of unrest--tectonic strain, magmatic intrusions, and hydrothermal changes, can induce other processes that also contribute to caldera unrest, as below.

(d) Squeezing and deformation of a magma body. Compression will squeeze two sides of a magma body, and most likely cause uplift of its roof. Extension could cause subsidence of the roof of the reservoir. If a conduit of relatively small diameter rises from a reservoir of much larger diameter, small horizontal strains at depth may cause large vertical movements in the conduit--just as slow squeezing of the sides of a milk carton causes milk to rise rapidly through a straw. If a large block of crust has collapsed into a magma reservoir, to form a caldera, that block may act as a piston of a diameter roughly equal to that of the magma reservoir. Horizontal strain may therefore cause a roughly equal vertical strain. A better analogy to the wide-conduit case is a water-filled balloon; squeezing in one direction will cause comparable distension in other directions.

Nakamura (1971, 1975) and Yamashina and Nakamura (1978) infer that a small-diameter conduit and crater floor of Mihara Volcano, within the Oshima caldera, act as a volumetric strain gauge for compression in the Sagami Bay area just south of Tokyo. More than 400 m of piston-like rise in the elevation of the crater floor, from 1933-1950, corresponded to approximately one microstrain of regional contraction.

Another observation suggests deformation of magma reservoirs during some caldera unrest: some episodes of uplift are followed by equal amounts of subsidence, without any eruption or other explanation for the reversal. For example, uplift at the Phlegraean Fields is matched by subsidence. Atitlan Caldera may exhibit similar behavior. The periods of such uplift are of the same order of magnitude as the periods of large tectonic earthquakes in these regions.

(e) Release of tectonic confining pressure. Magma is generally buoyant and will tend to rise through most crustal rock. It can be confined by the weight of overlying rock (lithostatic P), augmented or decreased by regional horizontal stresses. Compressive tectonic stresses will tend to trap magma before it reaches the surface. Conversely, tectonic extension will tend to reduce confining pressure, permitting a buoyant rebound even without a magmatic intrusion per se. The concept is similar to that of isostatic rebound, but the change in "load" is a change in horizontal stress, rather than vertical load.

(f) In-situ expansion of a magma reservoir. Magma is subject to volume changes by (i) vesiculation at shallow depths; (ii) partial remelting of recently solidified magma, by heating or addition of volatiles; or (iii) thermal expansion. (i) and (ii) involve phase changes; (iii) involves only thermal expansion of the existing phases of the magma. Depending on the volume of the magma reservoir, only a small percentage of expansion can account for commonly observed uplifts of the ground surface. For example, a 0.1 percent expansion of a magma

reservoir that is 1 km thick would cause about 1 m of uplift. Vesiculation is thought to be unlikely below depths of about 1 to 2 km, because inferred volatile contents are not high enough to cause saturation and exsolution at the pressures below that depth, but a small percent of expansion can be expected at shallower depths. Vesiculation could in turn be caused by an addition of volatiles from a magmatic intrusion, an increase in the temperature of magma (decreasing the solubility of gas in melt), from mechanical shaking, or from a decrease in confining pressure. A simple analogy to this process of volume increase by vesiculation is a bottle of soda pop--any of the four stimuli will cause vesiculation and a volume increase, whereas degassing, cooling, stilling, or re-pressurization will allow the volume to return to normal.

An increase in T or P_{H_2O}, or a decrease in confining P, can cause remelting of some hot, recently-solidified rock. Most igneous rocks are denser than their equivalent melt, by a factor of roughly 5 to 10 percent (Skinner, 1966), so remelting would cause a volume increase. Substantial heating would be required to overcome the heat of fusion of crystalline material.

A third mechanism for in-situ volume change in a magma reservoir is simple thermal expansion, without any phase change. Coefficients of volumetric thermal expansion for silicate melt(s) are in the order of 10^{-5} to $10^{-3}/^{o}C$, and in the order of 20-40 x $10^{-6}/^{o}C$ for typical minerals of crystallizing magma (Skinner, 1966).

Most of these mechanisms for in-situ volume change would act slowly, over decades to millenia, but phase changes in response to mechanical shaking could perhaps occur within years or less, depending on the viscosity, T, and gas content of the magma.

Observations consistent with in-situ expansion of magma include:

--some uplift is aseismic, e.g., that at Long Valley caldera (few epicenters on resurgent dome, where deformation is centered);

--some uplift is reversible, followed by equal amounts of subsidence;

--the center of uplift at a caldera is sometimes offset from the center of seismicity, or the point of eruption. The most common instance is broad uplift of the central part of a caldera floor, followed by an eruption along the rim of that caldera, as when an influx of mafic magma heats or otherwise causes an expansion of a large magma body, and then itself rises around the pre-existing magma and erupts. Examples include eruptions of Sakurajima, on the rim of Aira caldera, of Tavurvur on the rim of Rabaul caldera, and of Monte Nuovo, inside but not in the center of the Phlegraean Fields caldera.

(g) Expansion of (water-saturated) rock overlying the magma reservoir, in response to one or more of the three fundamental stimuli described above (a-c). At Yellowstone, the Hebgen Lake earthquake in 1959 severely disturbed the hydrothermal system, cracked self-sealed caps, and brought deep, hot water into shallow zones where it presumably heated the shallow country rock and might have increased pore pressures. Hydrothermal activity is also thought to have increased in response to tectonic strain, and then contributed significantly to unrest at Matsushiro (Ichikawa, 1969; Kasahara, 1970; Nakamura, 1971; Ohtake,

1976). Matsushiro is not a caldera, but is noted here to illustrate a general process.

A magmatic intrusion will heat groundwater and tend to cause uplift. Groundwater or fumarole temperatures increased shortly before volcanic eruptions at the Phlegraean Fields (1538), Rabaul (1941), Toya (1977), and numerous other calderas. Oliveri del Castillo and Quagliariello (1969) and Grindley (1976) inferred that pore pressures raised by magmatic intrusion also cause long-term uplift ("bradyseisms") at the Phlegraean Fields.

Unrest at Yellowstone, Matsushiro, and the other cited examples is probably not primarily a result of an expansion of water-saturated country rock beneath these areas, but hydrothermal changes probably have contributed to that unrest, as responses to one or more of the three fundamental stimuli (a-c). Depending on the details of hydrothermal circulation beneath a caldera, such effects could probably occur over a period of several months to decades.

How does the preceding discussion relate to Long Valley?

Ryall and Ryall (1981a, 1983) argued that current unrest at Long Valley began as part of a regional strain event starting in 1978, and that the May 1980 earthquakes were fundamentally part of the process of Basin and Range extension. Such extension is expectable, judging from geologically young Basin and Range faults in Long Valley, known fault displacements during the 1872 Lone Pine earthquake in nearby Owens Valley, and continuing slow regional extension documented by J.C. Savage and co-workers.

Julian (1983) suggested that at least 2 of 4 M=6+ earthquakes at Long Valley in May 1980 were caused or accompanied by dike intrusion. This too is expectable in an extensional tectonic setting, especially if that intrusion might have been from depth toward the level of the large silicic magma reservoir of Long Valley. Indeed, heatflow studies by Lachenbruch and others (1976, 1978) and thermal calculations by Smith and Shaw (1975) have shown that a magma body like that beneath Long Valley cannot be maintained without continuing heat input, probably in the form of episodic additions of basaltic magma to the base of the silicic body. An aspect of the May 1980 M=6+ earthquakes that has received little attention is their depth--the second, third and fourth of four were between 10 and 15 km deep (Cramer and Toppozada, 1980; Given and others, 1982; R.S. Cockerham, pers. commun., 1984). These depths are lower than the top and possibly lower than most of the large magma body inferred by Hill (1976), Steeples and Iyer (1976), and Sanders (this volume) to underlie the caldera. A few of the aftershocks occurred around 11 km depth (Archuleta and others, 1982). Three of the four large earthquakes were also located south of the caldera. If magma moved in May 1980, it probably rose to a depth of about 10 km, beneath or just south of the main Long Valley magma reservoir, and not upward from its top.

Given that the May 1980 earthquakes unquestionably occurred, and may have signalled an intrusion of basaltic melt into or just south of the Long Valley magma reservoir, we suggest a simple two-stage process in which (1) an initial regional extension event, with or without basaltic intrusion from depth, triggered (2) a prolonged set of readjustments within the main Long Valley magma body.

How might the large magma body respond to a mechanical and thermal disturbance? Savage and Clark (1982) demonstrated that broad, largely aseismic uplift and extension of the resurgent dome occurred sometime between July 1979 and September 1980, and that the magma reservoir beneath Long Valley had probably inflated. We have noted several mechanisms in the list of processes above that might cause inflation--possibly addition of new magma, or slight expansion of the existing magma. It would require less than a 0.1% increase in volume of the main body of magma to account for the observed uplift at Long Valley. Or it may be that the magma reservoir hasn't inflated at all but has simply rebounded following release of tectonic confining stress.

Support for the plausibility of such a two-step model is found in numerous instances in which large tectonic earthquakes have clearly disturbed magma beneath calderas. Strong tectonic earthquakes were followed within hours to months by unrest at Askja, 1875; Krakatau, 1880(?); Kakuto, 1913, 1961, 1966-67; Rabaul, 1910, 1916, 1919, 1971; Suoh, 1933; Akan, 1933, 1982; Kuttyaro, 1938, 1959(?); Karymsky, 1940, 1952, 1960-67; Maly Semiachik, 1952; Tao-Rusyr, 1952; Yellowstone, 1959; Cordillera Nevada, 1960(?); Batur, 1963; and Krafla, 1975. Eleven of these twenty-three instances have culminated in eruptions, and a twelfth, Rabaul 1971-present, is threatening to do the same. Some of the eruptions have followed an earthquake by only a few days (e.g., the Suoh eruption in 1933, the Kamchatka eruptions in 1952, and the Puyehue, Cordillera Nevada eruption of 1960); perhaps significantly, several of these were phreatic explosions. Other less certain examples could be added, e.g., renewed unrest in the Phlegraean Fields in 1982, less than two years after the 1980 "Naples" earthquake. Yet other episodes of caldera unrest may have been triggered by slow tectonic strain, e.g., Oshima in the early 1920s and in 1950-51, and Fernandina in 1968.

A simple correlation cannot prove that regional strain (with or without basaltic intrusion) actually causes unrest at these calderas, but we think that the circumstantial evidence for such a relation, just cited, is good. Extending this to Long Valley, we think that a two-stage model of an initial, relatively deep disturbance and subsequent inflation or deformation of the residual magmatic reservoir is also adequate to explain the general features of unrest at Long Valley since 1978.

Such processes could culminate in an eruption if the initial stimulus is large enough to set off a cascading series of responses in the large reservoir (e.g., accelerating vesiculation). Some lag time is inevitable before it becomes clear whether such a threshold has been exceeded. If the initial disturbance does not push the large reservoir beyond a threshold toward eruption, the response of the large system should decay with time. Consistent with such a model, the general level of seismicity at Long Valley appears to be declining irregularly.

SUMMARY AND CONCLUSIONS

Our review of unrest at calderas worldwide suggests that unrest like that at Long Valley is common, and that it could be caused by a simple two-stage model of tectonic disturbance and response of the residual magma body, with or without intrusion of basaltic magma from depth. Indeed, we think regional extension and four M=6 earthquakes should be expected to disturb a 17 x 32 km hole in a plate, underlain by hot, weak, and partly fluid material. Intrusion of mafic melt during that extensional event would only increase the likelihood of subsequent unrest. We are not convinced that dike intrusion has occurred during the current unrest anywhere above the level of the residual magma reservoir, nor do we know of any reason to suppose that such an intrusion is imminent.

Large residual magma bodies beneath calderas are more dynamic than we previously realized. Subtle ground deformation appears to be common, perhaps even the rule rather than the exception. Seismic swarms and thermal changes are also common. We are led to the conclusion that the stimuli for this frequent unrest need not be large, because large magma reservoirs are already in a delicate balance between quiet and unrest. Instead, the most likely stimuli are common geological processes such as regional tectonic strain or small magmatic intrusions from depth.

ACKNOWLEDGMENTS

We have received helpful reviews and tips about unrest, by region, from F. Barberi, G. Luongo, R. Scandone, M. Sato, J. Keller, G. Heiken, W. Duffield, J. Latter, I. Nairn, P. Otway, P. Lowenstein, P. de St. Ours, C. McKee, B. Talai, A.C. Effendi, S. Bronto, L. Aguila, K. Lajoie, D. Shimozuru, K. Ono, K. Nakamura, Y. Katsui, I. Yokoyama, J. Riehle, T. Miller, C. Gardner, D. Harlow, R. Wunderman, D. Sussmann, S. Williams, T. Simkin, P. Einarsson, P. Baker, L. Siebert, and L. McClelland. W.H.K. Lee kindly searched his extensive reference lists, bringing to light a number of important references. J. Johnston assisted with some programming to make the data manageable, and E. Klassen, J. Seeley, and M. Mosner translated papers that we might otherwise have overlooked.

REFERENCES

Archuleta, R.J., Cranswick, E., Mueller, C., and Spudich, P., 1982, Source parameters of the 1980 Mammoth Lakes, California, earthquake sequence: J. Geophys. Res., v. 87, p. 4595-4607.

Allis, R.G., and Barker, P., 1982, Update on subsidence at Wairakei: Proc. Pacific Geothermal Conference 1982, part 2, p. 365-370.

Babbage, C., 1847, Observations on the Temple of Serapis, at Pozzuoli, near Naples, with remarks on certain causes which may produce geological cycles of great extent: Quart. Jour. Geol. Soc. London, v. 3, p. 186-217.

Christiansen, R.L., Lipman, P.W., Orkild, P.P., and Byers, F.M., Jr., 1965, Structures of the Timber Mountain caldera, southern Nevada, and its relation to basin-range structure: U.S. Geol. Surv. Prof. Paper 535-B, p. B43-48.

Cramer, C.H. and Toppozada, T.R., 1980, A seismological study of the May 1980 and earlier earthquakes near Mammoth Lakes, California, in Sherburne, R.W., ed., Mammoth Lakes, California earthquakes of May 1980: Calif. Div. Mines Geol. Special Report 150, p. 91-130.

Cummings, D., 1968, Mechanical analysis of the effect of the Timber Mountain Caldera on Basin and Range Faults: J. Geophys. Res., v. 73, p. 2787-2794.

Dieterich, J.H. and Decker, R.W., 1975, Finite element modeling of surface deformation associated with volcanism. J. Geophys. Res., v. 80, p. 4094-4102.

Dzurisin, D., Anderson, L.A., Eaton, G.P., Koyanagi, R.Y., Lipman, P.W., Lockwood, J.P., Okamura, R.T., Puniwai, G.S., Sako, M.K., and Yamashita, K.M., 1980, Geophysical observations of Kilauea Volcano, Hawaii, 2. Constraints on the magma supply during November 1975-September 1977: Jour. Volcanol. Geotherm. Res., v. 7, p. 241-269.

Dzurisin, D. and Newhall, C.G., 1984, Recent seismicity and ground deformation at Long Valley (California), Yellowstone (Wyoming), the Phlegraean Fields (Italy), and Rabaul (Papua New Guinea), this volume.

Fujita, N. and Tada, T., 1983, Anomalous crustal uplift in the northeastern part of the Izu Peninsula, central Honshu, Japan, Tectonophysics, v. 97, p. 147-152.

Given, J.W., Wallace, T.C., and Kanamori, H., 1982, Teleseismic analysis of the 1980 Mammoth Lakes earthquake sequence: Bull. Seism. Soc. Am., v. 72, p. 1093-1109.

Grindley, G. W., 1976, Relation of volcanism to earth movements, Bay of Naples, Italy: in Gonzales-Ferran, O. (ed.), Andean and Antarctic Volcanology Problems, Rome, International Association of Volcanology and Chemistry of the Earth's Interior, p. 598-612.

Hildreth, W., 1981, Gradients in silicic magma chambers: Implications for lithospheric magmatism: J. Geophys. Res., v. 86, p. 10153-10192.

Hill, D. P., 1976, Structure of Long Valley caldera, California, from a seismic refraction experiment: J. Geophys. Res., v. 81, no. 5, p. 745-753.

Hill, D.P., Mowinckel, P., and Peake, L.G., 1975, Earthquakes, active faults, and geothermal areas in the Imperial Valley, California: Science, v. 188, p. 1306-1308.

Hiraga, S., 1972, Earthquake swarms of geothermal fields in Japan. J. Japan Geotherm. Res. Assn., v. 9:1, ser. 32, p. 30-39.

Ichikawa, M., 1969, Matsushiro earthquake swarm: Geophys. Mag., V. 34, p. 307-331.

International Association of Volcanology and Chemistry of the Earth's Interior (various authors), 1951-1984, Catalogue of Active Volcanoes of the World Including Solfatara Fields: Naples and Rome, IAVCEI, 22 volumes to date.

International Association of Volcanology and Chemistry of the Earth's Interior, Working Group on the World Volcanological Map, eds., 1973-1984, Data Sheets of the Post-Miocene Volcanoes of the World, with Index Maps: Rome, IAVCEI, unpaginated.

Julian, B. R., 1983, Mechanisms of earthquakes near Long Valley caldera, California: Evidence for dike injection: Nature, v. 303, p. 323-325.

Kanamori, H., 1972, Relation between tectonic stress, great earthquakes and earthquake swarms: Tectonophysics, v. 14, p. 1-12.

Kasahara, K., 1970, The source region of the Matsushiro earthquake swarm: Bull. Earthq. Res. Inst. v. 48, p. 581-602.

Lachenbruch, A.H., Sass, J.H., Munroe, R.J., and Moses, T.H., Jr., 1976, Geothermal setting and simple heat conduction models for the Long Valley Caldera: J. Geophys. Res., v. 81, p. 769-784.

Lachenbruch, A.H. and Sass, J.H., 1978, Models of an extending lithosphere and heat flow in the Basin and Range province, in Smith, R.B. and Eaton, G.P., 1978, Cenozoic Tectonics and Regional Geophysics of the Western Cordillera: Geol. Soc. Am. Memoir 152, p. 209-250.

McKee, C.O., Johnson, R.W., Lowenstein, P.L., Riley, S.J., Blong, R.J., de Saint Ours, P., and Talai, B., 1983, Rabaul caldera, Papua New Guinea: Volcanic hazards and eruption contingency planning: Geol. Surv. Papua New Guinea Report 83/17, 38 p., and updated reports to the Smithsonian's SEAN Bulletin.

Miller, C. D., Mullineaux, D. R., Crandell, D. R., and Bailey, R. A., 1982, Potential hazards from future volcanic eruptions in the Long Valley-Mono Lake area, east-central California and southwest Nevada - A preliminary assessment, U. S. Geological Survey Circ. 877, 10 p.

Minakami, T., 1960, Fundamental research for predicting volcanic eruptions Pt. I: Bull. Earthquake Res. Inst., v. 38, p. 497-544.

Nakamura, K., 1971, Volcano as a possible indicator of crustal strain: Bull. Volcanol. Soc. Japan, v. 16, p. 63-71.

Nakamura, K., 1975, Volcano structure and possible mechanical correlation between volcanic eruptions and earthquakes: Bull. Volcanol. Soc. Japan, v. 20, p. 229-240.

Newhall, C.G. and Self, S., 1982, The Volcanic Explosivity Index (VEI): An estimate of explosive magnitude for historical volcanism: J. Geophys. Res., v. 87, C2, p. 1231-1238.

Ohtake, 1976, The Matsushiro earthquakes after 10 years: Kagaku (Science), v. 46, p. 306-313. (J)

Oki, Y., Aramaki, S., Nakamura, K., 1978, Volcanoes of Hakone, Izu and Oshima: Hakone, Hakone Town Office, 88 p.

Oliveri del Castillo, A., and Quagliariello, 1969, Sulla genesi del bradisismo flegreo; Atti Assoc. Geof. It., XVIII Conv., Naples, p. 557-594.

Otway, P. M., Grindley, G. W., and Hull, A. G., 1984, Earthquakes, active fault displacement and associated vertical deformation near Lake Taupo, Taupo Volcanic Zone, New Zealand Geol. Surv. Rpt. N. Z. G. S. 110, 73 p.

Pollard, D.D., Delaney, P.T., Duffield, W.A., Endo, E.T., and Okamura, A.T., 1983, Surface deformation in volcanic rift zones, in Morgan, P. and Baker, B.H., eds., Processes of Continental Rifting, Tectonophysics, v. 94, p. 541-584.

Ryall, A., and Ryall, F., 1981a, Spatial-temporal variations in seismicity preceding the May 1980, Mammoth Lakes, California, Earthquakes, Bull. Seis. Soc. Am., v. 71, no. 3, p. 747-760.

Ryall, A., and Ryall, F., 1981b, Attenuation of P and S waves in a magma chamber in the Long Valley caldera, California, Geophys. Res. Lett., v. 8, no. 6, p. 557-560.

Ryall, A. and Ryall, F., 1983, Spasmodic tremor and possible magma injection in Long Valley Caldera, California: Science, v. 219, p. 1432-1433.

Ryall, A. S., and Ryall, F. D., 1984, Increased potential for a major earthquake in the White Mountains seismic gap, California and Nevada, Bull. Seis. Soc. Am., in press.

Sanders, C., 1983, Location and configuration of magma bodies beneath Long Valley, California, determined from anomalous earthquake signals (abstr.): Eos, v. 64, p. 890; full text in this volume.

Savage, J. C., and Clark, M. M., 1982, Magmatic resurgence in Long Valley caldera, California: Possible cause of the 1980 Mammoth Lakes earthquakes, Science, v. 217, p. 531-533.

Savage, J. C., and R. S. Cockerham, 1984, Earthquake swarm in Long Valley caldera, California, January 1983: Evidence for dike intrusion, submitted to J. Geophys. Res. (abstract: Cockerham and Savage, Eos, v. 64, p. 890).

Shaw, H.R., 1984, A note on links between magma-tectonic rate balances, plutonism and volcanism: this volume.

Simkin, T., Siebert, L., McClelland, L., Bridge, D., Newhall, C., and Latter, J.H., 1981, Volcanoes of the World: Stroudsburg, PA, Hutchinson Ross Publ. Co., 232 p.

Skinner, B.J., 1966, Thermal expansion, in Clark, S.P., Jr., ed., Handbook of Physical Constants, Geol. Soc. Am. Memoir 97, p. 78-96.

Smith, R.L., 1979, Ash-flow magmatism, in Chapin, C.E. and Elston, W.E., eds., Ash-Flow Tuffs, Geol. Soc. Am. Spec. Paper 180, p. 5-27.

Smith, R.L. and Shaw, H.R., 1975, Igneous-related geothermal systems, in White, D.E. and Williams, D.L., eds., Assessment of Geothermal Resources of the United States, U.S. Geol. Surv. Circular 726, p. 58-83.

Steeples, D.W. and Iyer, H.M., 1976, Low-velocity zone under Long Valley as determined from teleseismic events: Jour. Geophys. Res., v. 81, p. 849-859.

Tsumura, K., 1977, Anomalous crustal activity in the Izu Peninsula, Central Honshu: Jour. Phys. Earth, v. 25 Suppl., p. S51-S68.

Ward, P.L. and Bjornsson, S., 1971, Microearthquakes, swarms, and the geothermal areas of Iceland: J. Geophys. Res., v. 76, p. 3953-3982.

Yamashina, K. and Nakamura, K., 1978, Correlations between tectonic earthquakes and volcanic activity of Izu-Oshima Volcano, Japan: J. Volcanol. Geotherm. Res., v. 4, p. 233-250.

Yokoyama, I., Yamashita, H., Watanabe, H., and Okada, Hm., 1981, Geophysical characteristics of dacite volcanism--the 1977-78 eruption of Usu Volcano: Jour. Volcanol. Geotherm. Res., v. 9, p. 335-358.

POSTCALDERA EVOLUTION AND CURRENT ACTIVITY OF THE YELLOWSTONE CALDERA

By

Robert L. Christiansen

Abstract

Three large calderas of the Yellowstone Plateau volcanic field represent similar cycles of rhyolitic volcanism during the past 2 million years, with distinct precaldera, caldera-forming, and postcaldera stages. Postcollapse events in the Yellowstone caldera, youngest of three, demonstrate continued evolution of the Yellowstone magmatic system. Intermittent basaltic eruptions within and around the volcanic field are essentially independent of the rhyolitic cycles, but no basalts erupt within the calderas during their rhyolitic activity. Basaltic magmas provide the heat that has maintained voluminous rhyolitic magmas beneath the volcanic field for over 2 m.y.

The third volcanic cycle began about 1.2 m.y. ago and climaxed 630,000 years ago with eruption of the compositionally zoned 1,000-km^3 Lava Creek Tuff and formation of the Yellowstone caldera by collapse. The Lava Creek is a composite ash-flow sheet, related to two overlapping ring-fracture zones; early postcollapse uplift of each of the two cauldron blocks formed a pair of resurgent domes. Early postcaldera volcanism produced relatively undifferentiated lavas from the ring-fracture system. The climactic eruption, caldera formation, resurgent doming, and early intracaldera rhyolitic volcanism all occurred within less than 100,000 years.

Since about 155,000 years ago, more than 900 km^3 of highly differentiated rhyolitic lavas have erupted within the caldera. This renewed volcanism began with a flow that nearly covered the western resurgent dome, followed shortly by renewed uplift of the dome and the eruption of several

other rhyolitic flows. The younger intracaldera rhyolites erupted in three short episodes, about 155,000, 110,000, and 75,000 yr ago. Many of the flows are exceptionally large, some having volumes of more than 50 km^3. Some pyroclastic eruptions accompanied this activity, including two moderately vouminous ash flows, one of which produced a small caldera. Intracaldera eruptive vents of the past 155,000 years are along two linear zones extending across the caldera from tectonic fault zones outside. A few postcaldera rhyolites erupted outside the caldera, principally in a zone radial to its northern margin.

Yellowstone's volcanism occurs in a region of tectonic extension, where stress appears to be concentrated at the intersection of three regional trends. One trend, the downwarped northeast-trending eastern Snake River Plain, is a volcanic axis along which rhyolitic volcanism has propagated toward Yellowstone through late Cenozoic time. Fault blocks around the caldera area are of basin-range extensional type, trending southwards away from the south margin and northwestward to westward away from the north margin. Tectonic structures localize most aspects of the Yellowstone's volcanism and hydrothermal discharge, including the ring-fracture system itself, but the volcanic field in turn influences the local development of tectonic structures.

Mineralogical, chemical, and isotopic compositions of the Lava Creek Tuff and younger rhyolites reflect the evolution of a large magmatic system, including differentiation in a magma chamber, major interactions with crustal materials, and probable continued incremental additions of magma to the subvolcanic chamber from deeper parts of the system. The Lava Creek magma was compositionally and thermally zoned, with lower-temperature, volatile-enriched, differentiated magma above a larger volume of higher-temperature

less differentiated magma. The early intracaldera lavas represent magma chemically and thermally continuous with the dominant volume of Lava Creek magma, but large isotopic shifts record catastrophic effects during and immediately following caldera collapse. In particular, $\delta^{18}O$ was drastically lowered by more than 5 permil; Pb and Sr were shifted to more radiogenic compositions. Intracaldera rhyolites erupted since about 155,000 years ago are again more differentiated, approaching the most evolved Lava Creek compositions, and show partial recovery toward isotopic values characteristic of earlier magmatic stages.

Yellowstone's massive hydrothermal convection system reflects a long-lived magmatic heat source, discharging heat at an average rate of more than 1,700 mW/m^2, about 20 times the average for the northern Rocky Mountains. A continued shallow magmatic heat source, driven ultimately by basaltic magmas from the mantle, is further indicated by a high flux of ^3He from the thermal areas. Geologic evidence that magma still exists in the Yellowstone chamber includes the absence of basalts from the caldera and the episodic eruption of large volumes of rhyolite from extended tectonic faults across the caldera, possibly reflecting cyclic magmatic heating and hydrothermal cooling of the magma-chamber roof. Activity of the magmatic system is also suggested by high levels of seismicity in and near the caldera, generally shallow earthquake foci, small magnitudes, swarm seismicity, changes in principal stress directions, continued uplift at high rates along the caldera axis, low seismic velocities, high attenuations, low densities, high electrical conductivity, and a shallow Curie depth.

The Yellowstone caldera probably retains the capacity for future eruptive activity. It is even possible that in the last 155,000 years Yellowstone has entered a fourth volcanic cycle that could lead to another voluminous pyroclastic eruption.

Introduction

The Yellowstone caldera is the youngest major element of a 7,500 km^2 caldera complex at the focus of the Yellowstone Plateau volcanic field. This volcanic field, one of the most voluminous accumulations of erupted rhyolitic magma on Earth, has evolved during about the past 2 million years through three similar volcanic cycles, each of which included distinct precaldera, caldera-forming, and postcaldera stages. The evolutionary stages of the older two cycles, whose climactic caldera-forming events occurred 2.0 and 1.3 m.y. ago, left imperfectly preserved geologic records and are known partly by analogy to various aspects of the third cycle.

The precaldera and caldera-forming stages of the third volcanic cycle were complex. The third cycle began about 1.2 m.y. ago and climaxed with eruption of the 1,000-km^3 Lava Creek Tuff and formation of the 45x70 km Yellowstone caldera 630,000 years ago. The Lava Creek Tuff is a single cooling unit that shows no evidence for even slight erosion during its emplacement; it was erupted without significant cessation during a single event, probably lasting no more than a few hours or days. Nevertheless, the Lava Creek comprises two stratigraphically distinct members that center respectively in the western and eastern portions of the Yellowstone caldera. The caldera formed by collapse, perhaps largely during but at least partly just after eruption of the Lava Creek. It preserves evidence for two ring-fracture zones, each of which defines a segment of the caldera that probably produced the major portion of each of the two members of the Lava Creek Tuff. The Lava Creek was erupted from a compositionally and thermally zoned magma chamber but consists entirely of high-silica rhyolite (>75 % SiO_2).

Basalts have erupted intermittently around the margins of the volcanic system through all three cycles, essentially independently of the individual

rhyolitic cycles. No basalt, however, has erupted within the caldera of each cycle during its period of rhyolitic activity. Ultimately basalt has erupted through the caldera floors of the first and second cycles where they are not overlapped by rhyolitic activity of the third cycle. Basalts of the Snake River Plain province, west of the Yellowstone Plateau volcanic field, now encroach on the older parts of the volcanic field as they cool and gradually subside. Basaltic volcanism appears ultimately to represent the fundamental magmatism of the region and to provide the source of heat that produces and maintains rhyolitic magmas at higher levels over long periods, but the Yellowstone caldera itself has not yet erupted intracaldera basalts.

Documentation of the volcanic history just summarized and the evidence for it is included in an extensive treatment, not yet published (Christiansen, in press) but some of which was summarized in three recent papers (Christiansen, 1979, 1982, 1984). Emphasis here is on the postcaldera history of the Yellowstone Plateau, particularly its past 155,000 years, and on the current state of activity of the caldera region.

Early postcollapse geologic history

Postcollapse volcanism in the Yellowstone caldera records two distinct phases. The earliest postcollapse events included resurgent doming of each caldera segment and subsequent eruption of the chemically least-evolved rhyolites of the volcanic field (designated stratigraphically as the Upper Basin Member of the Plateau Rhyolite; Christiansen and Blank, 1972). Much of the evidence for the existence of two caldera segments is in the presence of the two resurgent domes, the Mallard Lake dome in the western caldera segment and the Sour Creek dome in the eastern segment (fig. 1). As noted in the next paragraph, early uplift of these domes is demonstrated by the ages of postdoming rhyolite flows on the flanks of each dome. This evidence is

straightforward for the Sour Creek dome, but early postcollapse uplift of the Mallard Lake dome must be inferred somewhat indirectly because, as noted later, the dome was subsequently uplifted again about 155,000 years ago. Nevertheless, a shallow research drill hole on the immediate northwest flank of the Mallard Lake dome (White and others, 1975, p. 48) encountered Lava Creek Tuff only 10 m below the surface at a location where it must have stood topographically above the lava flows that immediately postdate doming.

The oldest known intracaldera volcanic units are postdoming rhyolitic lava flows of the Upper Basin Member in both caldera segments (the Biscuit Basin flow in the Mallard Lake segment and the Canyon flow and related units in the Sour Creek segment). These oldest postcollapse rhyolites lack or contain only sparse sanidine phenocrysts; the Biscuit Basin flow yield suficient sanidine to give a K-Ar age of 542,000±42,000 years, and the Canyon flow yielded two plagioclase ages of 692,000±18,000 and 613,000±11,000 years (J. D. Obradovich, written communication, 1982). Thus, at the level at which such data can realistically resolve real geological distinctions, these flows probably are only slightly younger than the Lava Creek Tuff, which has an average sanidine K-Ar age of 630,000 years (Obradovich, written communication, 1982). These rhyolitic lava flows lap onto the flanks of the two domes but are not uplifted; thus, the flows postdate resurgent doming of the two caldera segments. It appears that eruption of the Lava Creek Tuff, collapse on two overlapping ring-fracture zones to form the Yellowstone caldera, resurgence of the floors of the two caldera segments, and early postcollapse rhyolitic volcanism in each segment all occurred in less--possibly much less--than 100,000 years.

Lavas of the Upper Basin Member are chemically and mineralogically distinct from most other rhyolites of the Yellowstone Plateau volcanic field.

These lavas range as low as 72% SiO_2 (water-free). Their predominant phenocryst mineral is notably sieved plagioclase of about An_{30} composition, compared to about An_{20} or less in most of the other rhyolites. Mafic minerals, particularly clinopyroxene, are more abundant than in any of the other Yellowstone rhyolites, and orthopyroxene is present as a minor phenocryst phase.

After resurgent doming and eruption of the oldest postcollapse rhyolites, the Yellowstone caldera continued to produce similar lavas, at least until about 275,000 years ago. Only one such flow is exposed within the caldera, but others could be covered by younger rhyolites. The 275,000-yr. flow, like the older postcollapse rhyolites, contains abundant plagioclase phenocrysts, but they are accompanied by more abundant sanidine than in most of the older rhyolites.

Caldera volcanism of the last 155,000 years

Beginning a little more than 150,000 years ago, the Yellowstone caldera appears to have entered a new phase in its evolution. Since that time, voluminous rhyolitic lava flows, poor or lacking in plagioclase phenocrysts have filled the caldera nearly to its rim and locally overflowed it. This period also has been marked by at least two periods of uplift within the caldera, one of which appears to continue today. Rhyolitic volcanism may yet recur as the Yellowstone magmatic system continues to evolve, as suggested by evidence to be summarized in later sections.

This youngest phase of Yellowstone volcanism began with the eruption of a large rhyolitic lava flow, the Mallard Lake flow (fig. 1), from the eastern part of the western ring-fracture zone. (This flow is designated stratigraphically as the Mallard Lake Member of the Plateau Rhyolite by Christiansen and Blank, 1972). At least part of this flow remains buried, but

the exposed part nearly covered the older resurgent dome of the Mallard Lake caldera segment. Compared to the older postcollapse rhyolites the Mallard Lake flow is more differentiated. Phenocrysts of quartz and sanidine are common, but plagioclase is sparse; mafic phenocrysts are sparse and include minor opaque-oxide, clinopyroxene, and orthophyroxene. The plagioclase typically is about An_{20}.

Shortly after eruption of the Mallard Lake flow, renewed uplift further domed the western cauldron block. The Mallard Lake flow was uplifted on the new dome, which is elliptical, about 11 by 19 km across, and has a complex axial northwest-trending graben system (fig. 1). The fault pattern clearly shows its origin by domical uplift. Minor grabens bifurcate from the axial faults. Faults at the northwestern end splay outward and decrease in displacement; the southeastern end is buried but shows the beginnings of a similar splayed pattern.

Uplift of the present Mallard Lake dome occurred about 155,000 years ago, as shown by K/Ar dating of related rhyolites (Obradovich, written communication, 1982). Sanidines from the domed Mallard Lake flow have a mean K-Ar age of 151,000±5,000 years; an undomed overlying flow north of the dome gives a sanidine K-Ar age of 153,000±2,000 years. In addition, several younger flows both east and west of the dome have nominal K-Ar ages ranging from 147,000 to 168,000 years. All of these dates average 157,000 years and probably indicate formation of the dome within a brief period about 155,000±10,000 years ago, not resolvable by K-Ar dating.

Intracaldera rhyolitic volcanism since uplift of the Mallard Lake dome has occurred in three short episodes about 155,000, 110,000, and 75,000 yr ago. These flows are designated stratigraphically as the Central Plateau Member of the Plateau Rhyolite (Christiansen and Blank, 1972). All are similar in

chemistry and petrography and occur within the basin of the Yellowstone caldera or locally spill over its rim. All have SiO_2 contents of 76% or more and have abundant phenocrysts of quartz and sanidine. A few have subordinate plagioclase, but most have only a single feldspar phenocryst phase. Mafic phenocrysts are sparse but include ferroaugite and titanomagnetite; the youngest flows also have minor fayalite.

The eruptions that produced the Central Plateau Member, although they varied in style at various times, were characterized mainly by voluminous extrusions of rhyolitic lava. The individual flows are exceptionally large and thick, the largest having maximum diameters as great as 32 km and thicknesses of more than 300 m. Some individual flows have volumes of more than 50 km^3. Mapping of these flows demonstrates that each of them is characterized by a similar pattern of internal zonation, much like that described by Christiansen and Lipman (1966). The interior of each flow (where sufficient exposures allow it to be seen) consists of distinctly flow-layered microcrystalline rhyolite. At the base and margins, this layering tends to parallel the contacts of the flow, but at higher internal levels the layering generally becomes steeper and more contorted. Each flow has an envelope of flow breccia that formed by the breakup of a continuously forming chilled crust while the lava flow grew and moved by internal expansion and creep of its viscous interior. Locally the brecciated margin contains bands of relatively unbroken lava that remained fluid within the zone of brecciation. Most of the breccia envelope is glassy--pumiceous on its outer carapace and vitrophyric within. The contact between crystalline interior and glassy margin, however, is transitional and can lie at different positions within the flow--either within the fluidally layered rhyolite or within the flow breccia--depending on local factors during cooling. The transition between

glassy and crystalline parts of the flow generally is marked by a zone of abundant spherulites and lithophysae.

Besides the large lava flows, significant pyroclastic eruptions occurred during emplacement of the Central Plateau Member. Deposits left by the pyroclastic precursors to extrusions of the individual flows are not generally exposed, probably both because the vent areas are covered by the large lava flows and because of generally poor exposure in the densely forested caldera. Pumiceous ash beds do, however, occur in late Pleistocene lake sediments at several places in the eastern part of the caldera (Richmond, 1974, 1977). K-Ar dating and stratigraphy of these beds indicate ages comparable to those of the Central Plateau flows; these probably are downwind ash layers related to vent-opening eruptions of the large lava flows.

In addition to these small pyroclastic eruptions, at least two larger pyroclastic eruptions were associated with eruption of the Central Plateau Member. One of them produced deposits preserved in the western part of the caldera, underlying the Pitchstone Plateau and Grants Pass flows (fig. 1). This pyroclastic unit has been mapped as the tuff of Cold Mountain Creek (Christiansen and Blank, 1974a, b) and is generally nonwelded or only slightly welded. It may date the opening of the Pitchstone Plateau-Grants Pass linear vent system (fig. 1) and be a direct precursor of the subsequent lavas. A rhyolitic ash-flow sheet east of Shoshone Lake and around West Thumb is older than the tuff of Cold Mountain Creek. This unit, the tuff of Bluff Point (Christiansen, 1974; Christiansen and Blank, 1975c), must have erupted in the general vicinity of West Thumb, part of Yellowstone Lake, for it is widely distributed around that area (although largely buried to the east) and is most densely welded, has the thickest zones of devitrification, and has generally larger and more abundant phenocrysts and xenoliths near there. Vitrophyric

rhyolite fragments are the most abundant inclusions in this tuff. The basin of West Thumb itself probably is a caldera within the much larger Yellowstone caldera that collapsed as a result of the Bluff Point eruption (Christiansen and Blank, 1972; Christiansen, 1974). Parts of the West Thumb caldera were subsequently buried by younger flows and sediments. Although small compared to the Yellowstone caldera, the basin of West Thumb is nearly 10 km in diameter and is nearly as large as the well-known caldera of Crater Lake, Oregon. A lava flow beneath the tuff of Bluff Point appears to have extruded from a vent now downdropped in the West Thumb caldera. The tuff of Bluff Point probably represents an explosive late-stage eruption from the same vent although some unusual factor must have been involved this inversion of the usual time sequence from pyroclastic eruption to lava extrusion from the same vent. One speculative possibility is that this sequence resulted from the introduction of lake water into the erupting system. A hydromagmatic phase might have initiated rapid unloading of the partly degassed magma, triggering degassing from a deeper part of the magma chamber and producing a sustained pyroclastic eruption that tore out fragments of the still glassy older flow and caused subsidence of the vent to form the caldera.

The eruptions of the Central Plateau Member between 155,000 and 75,000 years ago, following renewed uplift of the Mallard Lake dome, flooded the western segment of the Yellowstone caldera with more than 900 km^3 of rhyolitic lavas, burying the west rim of the caldera. The consistent chemical and mineralogical differences between the Mallard Lake and younger flows and the older postcollapse rhyolites, the apparent lack of intracaldera volcanism between about 275,000 and 155,000 years ago, the doming that accompanied or immediately succeeded the first extrusions of the younger age group, and the voluminous mineralogically similar rhyolites that erupted following this break

in continuity all suggest that the events since about 155,0000 years ago represent the rejuvenation of magma at shallow levels in the Yellowstone chamber (Christiansen, 1984). The absence of intracaldera eruptions for about the last 75,000 years cannot be interpreted unambiguously. The 75,000-year pulse may have exhausted the potentially eruptable magma, or alternatively the latest interval--longer than previous ones--could imply that the conditions for recurrence of eruption are enhanced.

Eruptive vent sources for all the Central Plateau flows are along two linear zones that extend across the caldera (fig. 1). These zones have, with few exceptions, vented rhyolitic magma only where they intersect the caldera ring-fracture system. A few younger postcollapse rhyolites did vent outside the caldera, particurly along a radial fault zone to the north--the Norris-Mammoth corridor--that lies along a northward extrapolation of the eastern of the two Central Plateau vent zones (compare figs. 1 and 2). Both rhyolites and basalts occur in this corridor, and their eruptions spanned much of the time of both early and late intracaldera activity. The only other postcaldera rhyolites outside the Yellowstone caldera also occur to the north, in a diffuse zone beyond the western linear zone of Central Plateau vents (fig. 1).

Several of the extracaldera rhyolites are either nonporphyritic or only sparsely porphyritic, suggesting that the magmas were quite hot, probably maintained at high temperatures by close association with basaltic magmas. Several complexes of mixed rhyolitic and basaltic lavas occur in the Norris-Mammoth corridor (Wilcox, 1944) along with the more abundant separate rhyolitic and basaltic lava flows.

Late Cenozoic tectonics

The Yellowstone Plateau volcanic field lies in a region of active tectonic

extension. Three regional late Cenozoic tectonic trends intersect at Yellowstone: the northeast-trending eastern Snake River Plain represents a great crustal downwarp or semigraben (Kirkham, 1931; Braile and others, 1982); approximately north-trending faults and a parallel zone of seismicity south of the Yellowstone Plateau are continuous with the eastern marginal zone of the northern Basin and Range region (Smith and Sbar, 1974; Doser and Smith, 1983); and east-west to northwest-trending faults are reflected in the topography, tectonics, and seismicity of the Rocky Mountains west of Yellowstone and north of the eastern Snake River Plain (Myers and Hamilton, 1964; Smith and Sbar, 1974). These three intersecting trends suggest a focus of extensional lithospheric stresses that localize the Yellowstone Plateau volcanism. These tectonic systems are still active, as shown by young faults and earthquakes in the northern and southern parts of the region (fig. 2) and by late Pleistocene and Holocene basaltic volcanism (Leeman, 1982) and high heat flow (Brott and others, 1981) in the eastern Snake River Plain. The eastern Snake River Plain, furthermore, defines an axis along which voluminous rhyolitic volcanism has propagated successively northeastward, toward Yellowstone, for the past 15 m.y. at a rate of about 3.5 cm/yr (Armstrong and others, 1975; Christiansen and McKee, 1978).

The bounding faults of the parallel linear ranges and valleys, where data are available, generally are normal although Ruppel (1972, 1982) has interpreted some as being vertical and considers the linear ranges of Idaho north of the Snake River Plain to be uplifted blocks bounded by monoclinal drape folds. Fault displacements are mainly dip-slip, but some may have relatively minor strike-slip components. Faults of late Quaternary age, postdating the Lava Creek Tuff, occur rather widely around the margins of the Yellowstone Plateau, mainly as parts of zones that bound the major blocks that

extend outward from the plateau.

Most of the major young faults south of the Yellowstone Plateau are downthrown to the east and bound the east sides of west-tilted blocks. Each major tilted block south of the plateau, proceding eastward from the Teton Range, is lower than that to the west. The Absaroka Mountains lie east of the easternmost fault zone of this system and have been only very gently deformed in late Cenozoic time (e.g., Fisher and Ketner, 1968). There was little or no late Cenozoic differential uplift between the Absaroka Range and the adjacent Big Horn Basin to the east but only broad uplift of the entire Absaroka-Big Horn region. Thus, each of the major east-dipping normal fault zones south of the Yellowstone Plateau has less aggregate displacement than the next zone to the west.

Normal faults north of the caldera form a less distinct series of linear zones and intervening tilted blocks. Ruppel (1972) discusses the late Cenozoic normal faults of this northern area and regards the Gallatin Range as a horst bounded by vertical faults. Ruppel (1972, p. A51) additionally suggests, on the basis of discontinuous topographic lineaments, that the Gallatin Range is a northward structural extension of the Teton Range, the intervening portion of the block being buried by the Yellowstone Plateau of the western caldera area. If so, this fault-block system may branch; the post-Lava Creek fault zone east of the Gallatin Range swings southeastward to merge with faults of the Norris-Mammoth corridor (fig. 2). The merged zone of faults and volcanic vents (figs. 1 and 2) extends beneath caldera-filling lavas, changing gradually from more northwest trends outside the caldera to nearly north within it. The pre-Lava Creek ancestry and continued post-Lava Creek control of volcanism by faults in the Norris-Mammoth corridor are demonstrated by partly buried fault blocks of pre-Quaternary rocks, a linear

zone of volcanic vents, and the Roaring Mountain hydrothermal area. This band extrapolates into the Yellowstone caldera as the eastern zone of Central Plateau vents. The continuity of these features suggests strongly that zones of faults east of the Gallatin Range are structural continuations of faults east of the Red Mountains block (fig. 2). The western line of vents for the Central Plateau Member (fig. 1) connects the trend of the Teton fault zone into the structurally depressed block of the Madison Valley near West Yellowstone and suggests at least a branching relation between the buried extensions of the Teton and Madison Ranges, as noted by Hamilton (1960).

Structural control of postcaldera volcanism and thermal discharge

Yellowstone is best known as a region of impressive hydrothermal features, particularly the numerous hot springs and geysers. The main factors that localize these features are major fractures, enabling deep circulation of meteoric waters, and local topographic controls of hydrologic upflow. Thus, the most active hot-spring systems lie in topographic basins within and immediately adjacent to the caldera ring-fracture zones (Christiansen, 1984, fig. 6.7). Both the Mallard Lake and Sour Creek caldera segments are encircled by hot springs and areas of active acid alteration that include all the principal areas of thermal discharge in Yellowstone National Park. Other areas of relatively weak or local activity occur in these same zones as well as in other isolated areas. This distribution implies structural control of the thermal activity. In the northeastern part of the caldera, part of the major thermal activity occurs along a tectonic fault zone that arcs around the east margin of the topographic caldera, functioning in effect as part of the ring-fracture zone. The only significant hydrothermal activity that extends far from the caldera is that of the Norris-Mammoth corridor, the locale of long-lived tectonic and volcanic activity, as noted earlier.

Because of incomplete exposure, the vents for early postcollapse Upper Basin Member lava flows in the Mallard Lake caldera segment cannot be pinpointed. They can, however, be inferred from outcrop distributions and the orientations of fragmentary flow-top structures to have been within a few kilometers of the western flank of the Mallard Lake dome (fig. 1). In the Grand Canyon-Broad Creek area, known vents for Upper Basin rhyolites all lie immediately adjacent to the Sour Creek dome. Thus, the early postcaldera eruptions were localized within the compound ring-fracture zone of the Yellowstone caldera.

Vents for many individual flows of the Central Plateau Member and extracaldera rhyolites are known directly, and the vent areas for most others can be inferred reasonably well from map relations. As noted earlier, all known and inferred eruptive vents of the Central Plateau Member lie in two linear zones. Each of these zones trends at both ends toward major tectonic fault zones outside the caldera. Central Plateau flows vented only within the compound ring-fracture zone of the Yellowstone caldera where it is intersected by these two major fault alignments. One of these eruptive zones essentially connects the Teton fault zone and its northern continuation (Love, 1961; Love and others, 1972; Love and Keefer, 1975; Doser and Smith, 1983) with faults of the the upper Madison Valley, as recognized by Hamilton (1960). The second fissure zone trends from near the Flat Mountain Arm of Yellowstone lake, through the West Thumb caldera, and along the axis of the Central Plateau. It connects recurrently active faults bounding the steep eastern scarp of the Red Mountains (Love and Keefer, 1975) with the Norris-Mammoth corridor and the fault systems bounding the east side of the Gallatin Range (Ruppel, 1972). Notably, many earthquakes within the Yellowstone caldera occur along this eastern zone (fig. 2). One sequence of such earthquakes included a

magnitude-6.1 earthquake and an associated swarm in June, 1975 (Pitt and others, 1979).

The cauldron blocks of both segments of the Yellowstone caldera, now uplifted as two resurgent domes, are elongated northwestward, parallel to other tectonic trends across the caldera, and lie directly athwart the extrapolated axis of the eastern Snake River Plain. Thus, the locations of the fundamental elements of the Yellowstone magmatic system, the two ring fracture zones, were themselves probably controlled by major tectonic intersections.

Not only did regional structures control volcanic structures, but the latter in turn locally influenced the development of tectonic structures. The largest fault zones, notably the Teton and Gallatin systems, decrease in displacement as they approach the Yellowstone caldera. Furthermore, there are more north-trending normal faults in a zone about 25-45 km wide around the Yellowstone Plateau than there are within the same longitudinal band farther north or south (fig. 2). These factors, together with the seismicity pattern, appear to show that the Yellowstone caldera and related older volcanic structures occur in a zone of concentrated crustal stress and have acted as a local boundary against which much displacement on the regional fault system is taken up. Apparently, broad uplift above the Yellowstone magmatic system is reflected in increased average elevations near its margins but results in decreased local relief on individual fault blocks as they enter the zone of uplift.

Postcaldera geochemical and isotopic evolution

The major events discussed in this paper conveniently group into the caldera-forming Lava Creek eruption, early intracaldera ring-fracture eruptions, the intracaldera linear-vent eruptions and localized uplifts of the

last 155,000 years, and contemporaneous extracaldera eruptions. Differences among the erupted magmas of these groups are distinct, chemically in terms of both major and trace elements and isotopically in O, Pb, and Sr.

The Lava Creek Tuff erupted from a compositionally and thermally zoned magma chamber, in which a zone of lower-temperature, volatile-enriched magma with increased concentrations of incompatible trace elements lay above a higher-temperature, less differentiated dominant volume (Hildreth, 1981, figs. 2, 3, 8; Christiansen, 1984, fig. 6.6). SiO_2 in the Lava Creek Tuff has a narrow range between 75 and 77 %, and magmatic quench temperatures ranged between 820 and 900°C. The earliest erupted postcollapse lavas represent a chemical and thermal continuum of the Lava Creek magma to less differentiated compositions and higher temperatures (Hildreth and others, 1984). The earliest Upper Basin Member units range from compositions similar to the less differentiated Lava Creek to compositions that are among the least evolved rhyolites erupted in the Yellowstone Plateau volcanic field; SiO_2 in these early postcollapse rhyolites ranges 72-76 % and magmatic quench temperatures 900-923°C.

It was noted earlier that the types and abundances of phenocrysts in the Upper Basin Member differ from those of other rhyolites. Sanidine is sparse or lacking, quartz is relatively sparse, plagioclase and clinopyroxene are abundant, and orthopyroxene occurs in place of the fayalite of the Lava Creek. Similarly, the elemental compositions of the phenocryst phases of the Upper Basin rhyolites vary systematically from those of the Lava Creek but demonstrate virtual continuity between their respective compositional ranges (Hildreth and others, 1984, fig. 8).

In contrast to this continuous variation in compositional trends, some of the isotopic systematics of the Upper Basin Member show drastic changes in the

Lava Creek magma during the brief time--less than 100,000 years--between the caldera-forming eruption and the earliest postcaldera rhyolites (fig. 3). Whereas Lava Creek Tuff ranges in $\delta^{18}O$ from 6.0 to 6.8 permil, these early Upper Basin units range from 0.6 to 1.9 permil (Hildreth and others, 1984). (It must be noted that the cited values were determined on quartz phenocrysts and were demonstrated by Hildreth and others to reflect isotopic equilibration with coexisting feldspar and titanomagnetite at magmatic temperatures; the values do not reflect subtle superimposed alteration effects). This depletion of ^{18}O by more than 5 permil affected a large magmatic volume, represented by flows in both segments of the Yellowstone caldera whose vents were separated by as much as 45 km. Probably hundreds of km^3 of magma were affected. Such a drastic depletion of the heavy isotope of oxygen (by far the most abundant element of the rhyolitic magma) is interpreted to reflect the ingestion of large amounts of meteoric water by the magma; chemical and petrographic data preclude massive contamination by altered wall rocks as the source of the ^{18}O depletion. The amount of water required to affect this depletion greatly exceeds the local solubility of water in the rhyolitic magma and thus may reflect both the effects of recurrent explosive volcanism in allowing access of water to the magma and opportunities for mixing and the effects of magmatic convection in preventing local saturation.

Not only was ^{18}O severely depleted in the Lava Creek magma chamber during the immediate postcaldera period, but Pb and Sr isotopes too were rapidly shifted to more radiogenic ratios (Doe and others, 1982). Tracking of the isotopic shifts among O, Pb, and Sr (fig. 3) indicates that all three elements were affected by significant contamination events during and immediately following foundering of the caldera. Ingestion of roof material, possibly including altered older rhyolites, probably is required to explain

the isotopic shifts of the trace elements Pb and Sr, but it should be emphasized that by far the major effect on the magma was its interaction with large amounts of meteoric water as reflected in the O isotopes.

Later eruptions of the Upper Basin Member, as represented by the 275,000-yr flow preserved south of the Mallard Lake dome, appear to represent partial recovery of the Yellowstone magma from the drastic effects of the immediate postcollapse period (fig. 3). Plagioclase in this flow still exceeds sanidine, and clinopyroxene is abundant. However, its mineralogical, chemical, and isotopic compositions all show trends back toward those of the Lava Creek Tuff.

An apparent hiatus in caldera eruptions ended with the events that began about 155,000 years ago and have nearly filled the Mallard Lake caldera segment with high-silica rhyolitic lavas. The more than 900 km^3 of lavas erupted since then all have SiO_2 contents >76 % and are enriched in incompatible trace elements (Christiansen, 1984, fig. 6.6). Chemically, these lavas probably reflect both the redifferentiation of magma in the Yellowstone chamber and the addition of new rhyolitic magma to the shallow subvolcanic chamber from deeper-crustal sources. Although these lavas are still very light in O-isotopic composition--ranging 4.4-5.3 permil $\delta^{18}O$--they represent a trend of magmatic O-isotopic values back toward precaldera levels. Pb and Sr too reflect this isotopic recovery (fig. 3), which probably indicates remixing in the Yellowstone magma chamber with increments of relatively undepleted and uncontaminated magma. Entry of this magma into the high-level Yellowstone chamber may have been reflected in the renewed uplift of the western resurgent dome.

The three groups of late postcaldera rhyolites, erupted at intervals of about 35,000-45,000 years, show small but discernable variations that suggest

increasing degrees of differentiation and continued recovery from the drastic caldera-related magmatic disturbances. Iron content of the ferroaugite phenocrysts increases in the younger flows, and only the youngest contain fayalite. Isotopic ratios of O, and probably of Pb and Sr, generally show trends between these groups that imply partial recovery from the disturbed early postcaldera ratios to values more like the Lava Creek Tuff (fig. 3). Additional trace-element data show this trend as well (W. Hildreth and R. L. Christiansen, 1984, unpublished data), and a few values for Rb/Sr, calculated for the liquids from elemental distribution coefficients, show a serial progression toward higher ratios for successively younger flows of the Central Plateau Member (Doe and others, 1982, table 3).

That the chemical and isotopic data just discussed reflect major events in the subcaldera magma chamber is strongly indicated by comparison to lavas of the same ages that were erupted outside the caldera, especially in the Norris-Mammoth corridor. The extracaldera lavas show a range of chemical and mineralogical compositions but most of them have relatively unaffected isotopic ratios. $\delta^{18}O$ remains in the range 6.4-7.8, and Pb isotopic values include the least radiogenic ratios of the volcanic field. These lavas probably represent partial melts that have risen in the crust as small, relatively independent bodies with only slight interaction with upper crustal rocks or meteoric waters. They represent something approximating a base level against which both short-term and long-term secular variations in isotopic ratios of the large Yellowstone magmatic system can be judged.

Thermal activity, seismicity, and surface deformation

Although the Yellowstone caldera has not erupted for about the past 75,000 years, the energy flux represented by its impressive hydrothermal activity provides a significant measure of the state Yellowstone's magmatic system.

The water circulated in the hot-spring systems of Yellowstone and similar regions is mainly of meteoric origin; more than 95 percent must be meteoric according to isotopic data reviewed by White (1969, p. 280). Truesdell and Fournier (1976) reviewed other data that indicate the various thermal areas at or near the surface in Yellowstone probably all discharge from a deeper, largely interconnected hydrothermal system with a reservoir temperature of 340-370°C. Using a method based on the chloride content of the waters, the total convective thermal output of the principal hydrothermal areas of the Firehole River drainage, west of the Mallard Lake resurgent dome, was estimated by Fournier and others (1976) as about 2,200 MW. The average heat flow over the area of the Firehole drainage basin is about 46,000 mW/m^2, over 700 times the world average. Thermal flux from all chloride-bearing springs in Yellowstone National Park northeast of the continental divide, an area containing most but not all of the major thermal features of the Yellowstone caldera, was estimated to be at a rate of about 5,100 MW; the total output from all springs and fumaroles in the rhyolite plateau is at least 5,300 MW. The average heat flow from the Yellowstone caldera and the Norris-Mammoth corridor, thus, is over 1,700 mW/m^2, about 27 times the global average and about 20 times the average for the northern Rocky Mountains (Blackwell, 1969). Furthermore, a marine-type survey of conductive heat flow through the bottom sediments of Yellowstone Lake (Morgan and others, 1977) showed that values of 100-300 mW/m^2 just outside the caldera, somewhat above the regional average, rise to 600-700 mW/m^2 at the edge of the caldera ring-fracture zone. Even higher values characterize areas of sublacustrine hydrothermal discharge. Geologic studies show that similar hydrothermal discharge has characterized the Yellowstone caldera at least through Holocene time and probably has done so for more than 100,000 years and possibly since

formation of the caldera.

The heat source for such sustained high thermal discharge can only reasonably be considered to be magmatic (White, 1957, p. 1641-1643). An exceptionally high flux of ^{3}He and related rare-gas isotopes from Yellowstone thermal areas, necessarily from deep sources, confirms this conclusion (Craig and others, 1978, 1979; Kennedy and others, in press). Such hydrothermal systems, developing as stages in the evolution of volcanic fields, are in effect deeply circulating convective heat-flow systems related to the cooling and crystallization of magma and driven by the density differences between cold and hot water (White, 1957; 1968). Even considering a magmatic heat source, however, White (1968, p. C102) noted that long-continued high heat flow from a system such as Yellowstone is impossible to explain merely by static cooling of a body of magma beneath the deeply circulating hot-water system. Convective circulation of magma in a chamber can help maintain high temperatures at the base of the deep hydrothermal system, but massive hydrothermal circulation will quickly cool the magma. Using the assumptions of White (1957, p. 1642; 1968, p. C102), the heat flow of about 5,300 MW estimated for the hydrothermal systems of the Yellowstone Plateau would require the crystallization and cooling from 900° to 500°C of about 0.10 km^3 of rhyolitic magma per year (Fournier and others, 1976). If the hydrothermal system were driven by static cooling of the Yellowstone magma chamber for the last 600,000 years, a total of 60,000 km^3 of rhyolitic magma would have had to crystallize and cool--a batholith more than 20 km thick under the rhyolite plateau. Geophysical data, enumerated later, are generally incompatible with wuch a conclusion, as is the necessity for continued magmatic convection to carry heat to the base of the hydrothermal system. Furthermore, the absence of basalts within the Yellowstone caldera and

voluminous rhyolitic volcanism younger than 155,000 years indicate that a magmatic heat source must have existed beneath the caldera until recently and probably still exists. The rhyolitic magma in the large crustal chamber beneath Yellowstone must be maintained at high temperature by the continued supply of thermal energy. The source of that energy can only be continued injection of basaltic magma into the base of the rhyolitic system from a source region in the upper mantle. This conclusion is reinforced by similar arguments for voluminous rhyolitic systems in general by Smith (1979) and Hildreth (1981). The high flux of ^{3}He also is specifically consistent with a continued mantle contribution to the Yellowstone magmatic system, especially in view of the high ^{4}He flux to be expected in this region of high U-Th Archean continental crust.

Other active geophysical processes of the Yellowstone caldera are also significant in evaluating the magmatic system. Regional seismicity north of the eastern Snake River Plain extends eastward to the Yellowstone caldera (fig. 2). Near the caldera rim, earthquakes are generally as deep as about 10 km, and the largest shocks have magnitudes greater than 6; seismicity continues southeastward across the caldera, where it becomes more episodic and swarmlike, magnitudes are generally smaller, and maximum focal depths are generally less than about 6 km (Smith and Braile, 1984). Just south of the caldera, there are generally fewer earthquakes than near the north rim but regional seismicity continues southward along the transition between the Middle Rocky Mountains and Great Basin (Doser and Smith, 1983). Fault trends and seismic focal mechanisms near the Yellowstone caldera have been interpreted as indicating changes in the directions of crustal stresses resulting from concentrated lithospheric extension near the caldera (Smith, 1978; Smith and Braile, 1984).

Repeated monitoring of surface deformation in the Yellowstone area has only recently been undertaken. A first-order levelling was made in 1975-1977 and compared to a survey of 1923. This levelling showed maximum uplift of more than 700 mm, relative to areas outside the caldera, along an axis extending between the two resurgent domes (Pelton and Smith, 1979, 1982; Smith and Braile 1984). Preliminary data from a partial relevelling done in the fall of 1983 indicates that this uplift continues, probably at a rate greater than than assumed by averaging the previous data over the enitre period of more than 50 years between surveys (D. Dzurisin and R. L. Christiansen, unpublished data, 1983). Such high uplift rates could reflect the movement of magma at relatively shallow levels in the Yellowstone system. The axis of uplift, as shown by the 1976 and 1983 surveys, coincides with the Elephant Back fault system, a complex graben having very young but only small displacements (fig. 1).

Current state of the Yellowstone magmatic system

The sustained thermal output of the Yellowstone system, a high level of shallow swarmlike seismicity, and rapid axial uplift of the Yellowstone caldera all suggest that magma exists in the Yellowstone chamber. Several geological observations accord with this possibility, including the absence of basalts from the floor of the caldera, in contrast to their presence all around the caldera and their abundance in parts of the volcanic field that have not erupted during the third volcanic cycle, such as the Island Park area west of Yellowstone (Christiansen, 1982). Basalts clearly are an integral part of the volcanic field. Basaltic magmas have existed within the magmatic system throughout its more than 2-m.y. lifetime and are necessary to maintain its thermal output, but they have not yet erupted within the Yellowstone caldera. In order for the Yellowstone magmatic system to have evolved

continuously for the past two million years, as its systematic isotopic evolution shows (Hildreth and others, 1984), a continued input of thermal energy is required to maintain the rhyolitic magmas; otherwise they would crystallize completely in a few hundred-thousand years (White, 1968). This suggests that a body of low-density rhyolitic magma prevents the denser basaltic magmas from rising through it and has not crystallized sufficiently to allow fractures to penetrate it deeply.

The patterns of chemical evolution, structural control, and age groupings among the intracaldera eruptions of the past 155,000 years provide further insight into the subsurface evolution of the Yellowstone magma chamber. As noted earlier, rhyolites of the Central Plateau Member have erupted from the the ring-fracture system only where it intersects two linear tectonic zones that trend across the caldera from beyond its margins. These eruptions occurred in three distinct episodes of uncertain, but relatively short duration about 155,000, 110,000, and 75,000 years ago, and successively erupted magmas appear to be successively more differentiated. Oxygen-isotopic values suggest that a major portion of the Central Plateau magma was present continuously in the Yellowstone magmatic system long before it appeared at the surface as rhyolitic lavas (Hildreth and others, 1984). An interpretation that accounts for these correlated observations is that magma in a chamber beneath the Yellowstone caldera has undergone considerable crystallization from its roof downward but continues to differentiate at lower levels where it remains largely liquid. Regional extension is concentrated in the caldera area, but when magma occupies a relatively high level in the chamber, the heated roof zone does not sustain brittle fracture and only small faults close to the surface can break. No accessible conduits are opened to levels where eruptions might be triggered. As the roof zone is cooled by hydrothermal

convection, however, magma crystallizes beneath that roof, which becomes successively more brittle. Eventually it can accumulate sufficient extensional stress to be broken by larger faults. Tectonic fault zones then extend into the roof zone and downward toward the partly solidified intrusion, allowing the episodic rise of magma from lower levels and providing access to shallower levels where degassing and eruption can be triggered. Meanwhile, the roof zone is reheated and brittle faulting is again retarded until hydrothermal cooling can again drive a repetition of the cycle.

Geological and geophysical evidence taken together show that magma probably is still at least partly molten beneath the Yellowstone Plateau (Eaton and others, 1975; Smith and Christiansen, 1980; Lehman and others, 1982; Smith and Braile, 1984). Seismic-refraction studies indicate that an upper-crustal body that produces significant attenuation of seismic waves and has a P-wave velocity of about 5.7 km/s lies beneath the the Yellowstone caldera in the place of a regional layer having a P-wave velocity of 6.0 km/s; areas of even lower seismic velocities and higher attenuation occur locally near the northeastern and southwestern sides of the caldera (Schilly and others, 1982; Lehman and others, 1982; Smith and others, 1982; Smith and Braile, 1984). Although the data are not fully conclusive, Pitt (in Eaton and others, 1975) suggested that a zone beneath the eastern part of the Yellowstone caldera produces a shadowing of seismic S waves. Iyer and others (1981) demonstrated anomalous teleseismic P-wave delays beneath the Yellowstone caldera, modelling the data by a 15% reduction in P-wave velocities within the crust and a 5% reduction in the upper mantle to depths of 250 km. Teleseismic P-delays similarly characterize older parts of the Yellowstone-Snake River Plain region farther west, but the anomalies are considerably smaller--being modelled as averaging about 3.5 % velocity

reduction--and probably represent analogous magmatic systems that have aged for several million years since the end of active rhyolitic volcanism (Evans, 1982). Daniel and Boore (1982) showed that S waves too are anomalously attenuated in the crust beneath the Yellowstone caldera and noted that a high average crustal Poisson's ratio probably indicates the presence of fluids. A large negative gravity anomaly of 60 mGal is mapped over the Yellowstone caldera and its margins (Blank and Gettings, 1974). The areal extent of this anomaly is such that it cannot be modelled solely by low-density fill in the caldera; much of it could reflect a shallow body of solidified or partially molten magma. Modelling of aeromagnetic data suggests depths to Curie temperatures of about 10 km beneath the Yellowstone Plateau in general and as shallow as 6 km beneath parts of the caldera (Bhattacharyya and Leu, 1975). Materials of high electrical conductivity at relatively shallow depths beneath the Yellowstone Plateau are indicated by magnetotelluric data (Stanley and others, 1977).

Thus, geophysical data delineate an anomalous crustal and upper-mantle structure beneath Yellowstone (Smith and Braile, 1984). Sustained high heat flow, rapid uplift, intense swarm seismicity, suggested S-wave shadowing, low seismic velocities, high attenuations, low densities, high electrical conductivity, and a shallow Curie depth all indicate high temperatures at shallow levels and suggest the presence of magma. The absence of basalts within the caldera and episodic eruption of voluminous highly differentiated rhyolitic lavas suggest an underlying magma body that may be nearly as far evolved as those that produced the three major ash-flow sheets about 2.0, 1.3, and 0.6 m.y. ago. The Yellowstone caldera area probably retains the capacity for future eruptive activity. The activity of the last 155,000 years suggests at least the possibility that the Yellowstone magmatic system is not merely

the residuum of the declining third volcanic cycle but could have begun a new cycle.

Further volcanism in some form is likely to occur in the Yellowstone region. Rhyolitic lavas could erupt in the Yellowstone caldera or the Norris-Mammoth corridor, even if the system remains in a decaying third volcanic cycle. Basaltic volcanism could occur in any of several zones of recurrent activity marginal to the caldera and eventually probably will invade the caldera itself. A major new magmatic insurgence could initiate a fourth volcanic cycle, or a fourth cycle might already have begun. Such a development could even lead to climactic ash-flow eruptions and collapse to form a new caldera.

Acknowledgments

My work in the Yellowstone region has been done over many years with the collaboration of several valued colleagues. I am especially indebted to H. R. Blank, Jr., who collaborated in most of the geologic mapping fundamental to the study, to Wes Hildreth, with whom I continue petrologic and geochemical studies, and to R. B. Smith, who has been generous and stimulating in sharing geophysical data and interpretations. My association with Don White, Bob Fournier, Al Truesdell, and Pat Muffler in their studies of Yellowstone's hydrothermal systems has been continuous for nearly 20 years. Recently, only through the enthusiastic participation of Dan Dzurisin has it become possible to begin a sustained program of monitoring surface deformation in Yellowstone.

References cited

Armstrong, R. L., Leeman, W. P., and Malde, H. E., 1975, K-Ar dating, Quaternary and Neogene volcanic rocks of the Snake River Plain, Idaho: American Journal of Sciences, v. 275, p. 225-251.

Bhattacharyya, B. K., and Leu, L. K., 1975, Analysis of magnetic anomalies over Yellowstone National Park: Mapping of Curie point isothermal surface for geothermal reconnaissance: J. Geophys. Res., v. 80, p. 4461-4465.

Blackwell, D. D., 1969, Heat-flow determinations in the northwestern United States: Jour. Geophys. Res., v. 74, p. 992-1007.

Blank, H. R., Jr., and Gettings, M. E., compilers, 1974, Complete Bouguer gravity map, Yellowstone-Island Park region, Idaho-Montana-Wyoming: U.S. Geol. Surv. Open-file Map 74-22.

Braile, L. W., Smith, R. B., Ansorge, J., Baker, M. R., Sparlin, M. A., Prodehl, C., Schilly, M. M., Healy, J. H., Mueller, S., and Olsen, K. H., 1982, The Yellowstone-Snake River Plain seismic profiling experiment: Crustal structure of the eastern Snake River Plain: J. Geophys. Res., v. 87, p. 2597-2610.

Brott, C. A., Blackwell, D. D., and Ziagos, J. P., 1981, Thermal and tectonic implications of heat flow in the eastern Snake River Plain: Jour. Geophys. Res., v. 86, p. 11709-11734.

Christiansen, R. L., 1974, Geologic map of the West Thumb quadrangle, Yellowstone National Park, Wyoming: U.S. Geological Survey Geologic Quadrangle Map GQ-1191.

Christiansen, R. L., 1979, Cooling units and composite sheets in relation to caldera structure, in Chapin, C. E., and Elston, W. E., eds., Ash-flow tuffs: Geol. Soc. Am. Spec. Pap. 180, p. 29-42.

Christiansen, R. L., 1982, Late Cenozoic volcanism of the Island Park area, eastern Idaho, in Bonnichsen, B., and Breckenridge, R. M., eds., Cenozoic Geology of Idaho: Idaho Bur. Mines and Geol. Bull. 26, in press.

Christiansen, R. L., 1984, Yellowstone magmatic evolution: Its bearing on understanding large-volume explosive volcanism, in Explosive volcanism: Inception, evolution, and hazards: Washington, National Academy of Sciences, p. 84-95.

Christiansen, R. L., in press, The Quaternary and Pliocene Yellowstone Plateau volcanic field of Wyoming, Idaho, and Montana: U.S. Geological Survey Professional Paper.

Christiansen, R. L., and Blank, H. R., Jr., 1972, Volcanic stratigraphy of the Quaternary rhyolite plateau in Yellowstone National Park: U.S. Geol. Surv. Prof. Pap. 729-B, p.B1-B18.

Christiansen, R. L., and Blank, H. R., Jr., 1974a, Geologic map of the Old Faithful quadrangle, Yellowstone National Park, Wyoming: U. S. Geol. Survey Geol. Quad. Map GQ-1189.

Christiansen, R. L., and Blank, H. R., Jr., 1974b, Geologic map of the Madison Junction quadrangle, Yellowstone National Park, Wyoming: U. S. Geol. Survey Geol. Quad. Map GQ-1190.

Christiansen, R. L., and Blank, H. R., Jr., 1974c, Geologic map of the Norris Junction quadrangle, Yellowstone National Park, Wyoming: U. S. Geol. Survey Geol. Quad. Map GQ-1193.

Christiansen, R. L., and Lipman, P. W., 1966, Emplacement and thermal history of a rhyolite lava flow near Fortymile Canyon, southern Nevada: Geol. Soc. America Bull., v. 77, p. 671-684.

Christiansen, R. L., and McKee, E. H., 1978, Late Cenozoic volcanic and tectonic evolution of the Great Basin and Columbia Intermontane regions, in Smith, R. B., and Eaton, G. P., eds., Cenozoic tectonics and regional geophysics of the western Cordillera: Geol. Soc. Am. Mem. 152, p. 283-311.

Craig, H., Lupton, J. E., Welhan, J. A., and Poreda, R., 1978, Helium isotope ratios in Yellowstone and Lassen Park volcanic gases: Geophys. Res. Letters, v. 5, p. 897-900.

Craig., J., Welhan, J. A., Poreda, R., and Lupton, J. E., 1979, Helium isotope variations in the Yellowstone-Snake River Plain region and the western U.S. [abstract]: Am. Geophys. Union Trans. (EOS), v. 60, p. 945.

Daniel, R. G., and Boore, D. M., 1982, Anomalous shear wave delays and surface wave velocities at Yellowstone caldera, Wyoming: Jour. Geophys. Res., v. 87, p. 2731-2744.

Doe, B. R., Leeman, W. P., Christiansen, R. L., and Hedge, C. E., 1982, Lead and strontium isotopes and related trace elements as genetic tracers in the upper Cenozoic rhyolite-basalt association of the Yellowstone Plateau volcanic field, U.S.A.: J. Geophys. Res., v. 87, 4785-4806..

Doser, D. I., and Smith, R. B., 1983, Seismicity of the Teton-southern Yellowstone region, Wyoming: Seism. Soc. Am. Bull., v. 73, p. 1369-1394.

Eaton, G. P., Christiansen, R. L., Iyer, H. M., Pitt, A. M., Blank,H. R., Jr., Zietz, I., Mabey, D. R., and Gettings, M. E., 1975, Magma beneath Yellowstone National Park: Science, v. 188, p. 787-796.

Evans, J. R., 1982, Compressional wave velocity structure of the upper 350 km under the eastern Snake River Plain near Rexburg, Idaho: Jour. Geopys. Res., v. 87, p. 2654-2670.

Fisher, F. V., and Ketner, K. B., 1968, Late Tertiary syncline in the southern Absaroka Mountains, Wyoming, in Geological Survey Research, 1968: U.S. Geological Survey Prof. Paper 600-B, p. B144-B147.

Fournier, R. O., White, D. E., and Truesdell, A. H., 1976, Convective heat flow in Yellowstone National Park: Second United Nations Symposium on the Development and Use of Geothermal Resources, Proceedings, p. 731-739.

Hamilton, W., 1960, Late Cenozoic tectonics and volcanism of the Yellowstone region, Wyoming, Montana, and Idaho: Billings Geol. Soc. Guidebook 11, p. 92-105.

Hildreth, W., 1981, Gradients in silicic magma chambers: Implications for lithospheric magmatism: J. Geophys. Res., v. 86, p. 10153-10192.

Hildreth, W., Christiansen, R. L., and O'Neil, J. R., 1984, Catastrophic isotopic modification of rhyolitic magma at times of caldera subsidence, Yellowstone Plateau volcanic field: Jour. Geohys. Res., in press.

Iyer, H. M., Evans, J. R., Zandt, G., Stewart, R. M., Coakley, J. M., and Roloff, J. N., 1981, A deep low-velocity body under the Yellowstone caldera, Wyoming: Delineation using teleseismic P-wave residuals and tectonic interpretation: Geol. Soc. Am. Bull., v. 92, pt. II, p. 1471-1646.

Kennedy, B. M., Lynch, M. A., Reynolds, J. H., and Smith, S. P., in press, Intensive sampling of noble gases in fluids at Yellowstone: I. Early overview of the data; regional patterns: Geochim. Cosmochim. Acta

Kirkham, V. R. D., 1931, Snake River downwarp: J. Geol. v. 39, p. 456-483.

Leeman, W. P., 1982, Olivine tholeiitic basalts of the Snake River Plain, Idaho, in Bonnichsen, B., and Breckenridge, R. M., eds., Cenozoic Geology of Idaho: Idaho Bur. Mines and Geol. Bull. 26, in press.

Lehman, J. A., Smith, R. B., Schilly, M. M., and Braile, L. W., 1982, Upper-crustal structure of the Yellowstone caldera from seismic delay time analyses and gravity correlations: J. Geophys. Res., v. 87, p. 2713-2730.

Love, J. D., 1961, Reconnaissance study of Quaternary faults in and south of Yellowstone National Park, Wyoming: Geol. Soc. America Bull., v. 72, p. 1749-1764.

Love, J. D., and Keefer, W. R., 1975, Geology of sedimentary rocks in southern Yellowstone National Park, Wyoming: U.S. Geological Survey Prof. Paper 729-D, 60 p.

Love, J. D., Reed, J. C., Jr., Christiansen, R. L., and Stacy, J. R., 1972, Geologic block diagram and tectonic history of the Teton region: U.S. Geological Survey Misc. Geol. Invest. Map I-730.

Morgan, P., Blackwell, D. D., Spafford, R. E., and Smith, R. B., 1977, Heat flow measurements in Yellowstone Lake and the thermal structure of the Yellowstone caldera: Jour. Geopys. Res., v. 82, p. 3719-3732.

Myers, W. B., and Hamilton, W., 1964, Deformation accompanying the Hebgen Lake, Montana, earthquake of August 17, 1959: U.S. Geol. Surv. Prof. Pap. 435, 55-98.

Pelton, J. R., and Smith, R. B., 1979, Recent crustal uplift in Yellowstone National Park: Science, v. 206, p. 1179-1182.

Pelton, J. R., and Smith, R. B., 1982, Contemporary vertical surface displacements in Yellowstone National Park: Jour. Geophys. Res., v. 87, p. 2745-2761.

Pitt, A. M., 1979, Preliminary map of earthquake epicenters in Yellowstone National Park and vicinity, 1973-1978: U. S. Geological Survey Open-file Map 79-717.

Pitt, A. M., Weaver, C. S., and Spence, W., 1979, The Yellowstone Park earthquake of June 30, 1975: Seismol. Soc. America Bull., v. 69, p. 187-205.

Richmond, G. R., 1974, Surficial geologic map of the Frank Island quadrangle, Yellowstone National Park, Wyoming: U.S. Geological Survey Misc. Geol Invest. Map I-642, 1:62,500.

Richmond, G. R., 1977, Surficial geologic map of the Canyon Village quadrangle, Yellowstone National Park, Wyoming: U.S. Geological Survey Misc. Geol Invest. Map I-652, 1:62,500.

Ruppel, E. T., 1972, Geology of pre-Tertiary rocks in the northern part of Yellowstone National Park, Wyoming: U.S. Geological Survey Prof. Paper 729-A, 66 p.

Ruppel, E. T., 1982, Cenozoic block uplifts in east-central Idaho and southwest Montana: U.S. Geological Survey Prof. Paper 1224, 24 p.

Schilly, M. M., Smith, R. B., Braile, L. W., and Ansorge, J., 1982, The 1978 Yellowstone-eastern Snake River Plain seismic profiling experiment: Data and upper crustal structure of the Yellowstone region: Jour. Geophys. Res., v. 87, p. 2693-2704.

Smith, R. B., 1978, Seismicity, crustal structure, and intraplate tectonics of the interior of the western Cordillera, in Smith, R. B., and Eaton, G. P., eds., Cenozoic tectonics and regional geophysics of the western Cordillera: Geol. Soc. Am. Mem. 152, p. 111-144.

Smith, R. B., and Braile, L. W., 1984, Crustal structure and evolution of an explosive silicic volcanic system at Yellowstone, in Explosive volcanism: Inception, evolution, and hazards: Washington, National Academy of Sciences, p. 96-109.

Smith, R. B., and Christiansen, R. L., 1980, Yellowstone Park as a window on the earth's interior: Scientific American, v. 242, no. 2, p. 84-95.

Smith, R. B., and Sbar, M. L., 1974, Contemporary tectonics and seismicity of the Western United States, with emphasis on the Intermountain Seismic Belt: Geol. Soc. Am. Bull., v. 85, p. 1205-1218.

Smith, R. B., Schilly, M. M., Braile, L. W., Ansorge, J., Lehman, J. L., Baker, M. R., Prodehl, C., Healy, J., Mueller, S., and Greensfelder, R. W., 1982, The 1978 Yellowstone-eastern Snake River Plain seismic profiling experiment: Crustal structure of the Yellowstone region and experiment design: J. Geophys. Res., v. 87, p.2583-2596.

Smith, R. L., 1979, Ash-flow magmatism, in Chapin, C. E., and Elston, W. E., eds., Ash-flow tuffs: Geol. Soc. Am. Spec. Pap. 180, p. 5-27.

Stanley, W. D., Boehl, J. E., Bostick, F. X., and Smith, H. W., 1977, Geothermal significance of magnetotelluric sounding in the eastern Snake River Plain-Yellowstone region: J. Geophys. Res., v. 82, p. 2501-2514.

Truesdell, A. H., and Fournier, R. O., 1976, Conditions in the deeper parts of the hot spring systems of Yellowstone National Park, Wyoming: U.S. Geological Survey Open-file Report 76-428, 22 p.

White, D. E., 1957, Thermal waters of volcanic origin: Geol. Soc. America Bull., v. 68, p. 1637-1658.

White, D. E., 1968, Hydrology, activity, and heat flow of the Steamboat Springs thermal system, Washoe County, Nevada: U.S. Geological Survey Prof. Paper 458-C, 109 p.

White, D. E., 1969, Thermal and mineral waters of the United States--Brief review of possible origins: Int. Geol. Congress (23rd), Prague (1968), v. 19, p. 269-286.

Wilcox, R. E., 1944, Rhyolite-basalt complex on Gardiner River, Yellowstone Park, Wyoming: Geol. Soc. Am. Bull., v. 55, p. 1047-1080.

Figure captions

Figure 1. Map of Yellowstone National Park showing the Yellowstone caldera, the Mallard Lake and Sour Creek resurgent domes, postcaldera rhyolite flows, and volcanic vents. Boundary of Yellowstone National Park shown for reference. Heavily stippled areas, ring-fracture rhyolites of the Upper Basin Member of the Plateau Rhyolite; lightly stippled area, Mallard Lake Member of the Plateau Rhyolite; hatch-bordered areas, flows of the Central Plateau Member of the Plateau Rhyolite, controlled by linear fractures (hachures on younger side of contact). Also indicated are axial grabens of the two resurgent domes and the Elephant Back fault zone, axial to younger northeast-trending uplift of the whole caldera. PP, Pitchstone Plateau flow; GP, Grants Pass flow, both of the Central Plateau Member.

Figure 2. Map of the Yellowstone National Park region showing earthquake epicenters (from Pitt, 1979; Smith and Christiansen, 1980; Doser and Smith, 1983) and important tectonic faults. Boundary of Yellowstone National Park shown for reference. Also indicated are locations of major mountain ranges and fault zones, Yellowstone caldera, Island Park, and the eastern Snake River Plain.

Figure 3. Diagram of variation in isotopic ratios of rhyolites with time, for caldera-forming and postcaldera eruptions from the Yellowstone caldera and its margins. Blocks indicate ranges of analyzed values; numbers in parentheses indicate number of samples analyzed; arrows indicate direction of isotopic evolution of subcaldera rhyolitic magma. A, O-isotopic ratios ($\delta^{18}O$) from Hildreth and others (1984). B, Pb-isotopic ratios from Doe and others (1982). C, Sr-isotopic ratios from Doe and others (1982) and Hildreth and others (1984). Note that ordinate values in B and C decrease upward to facilitate comparison with A.

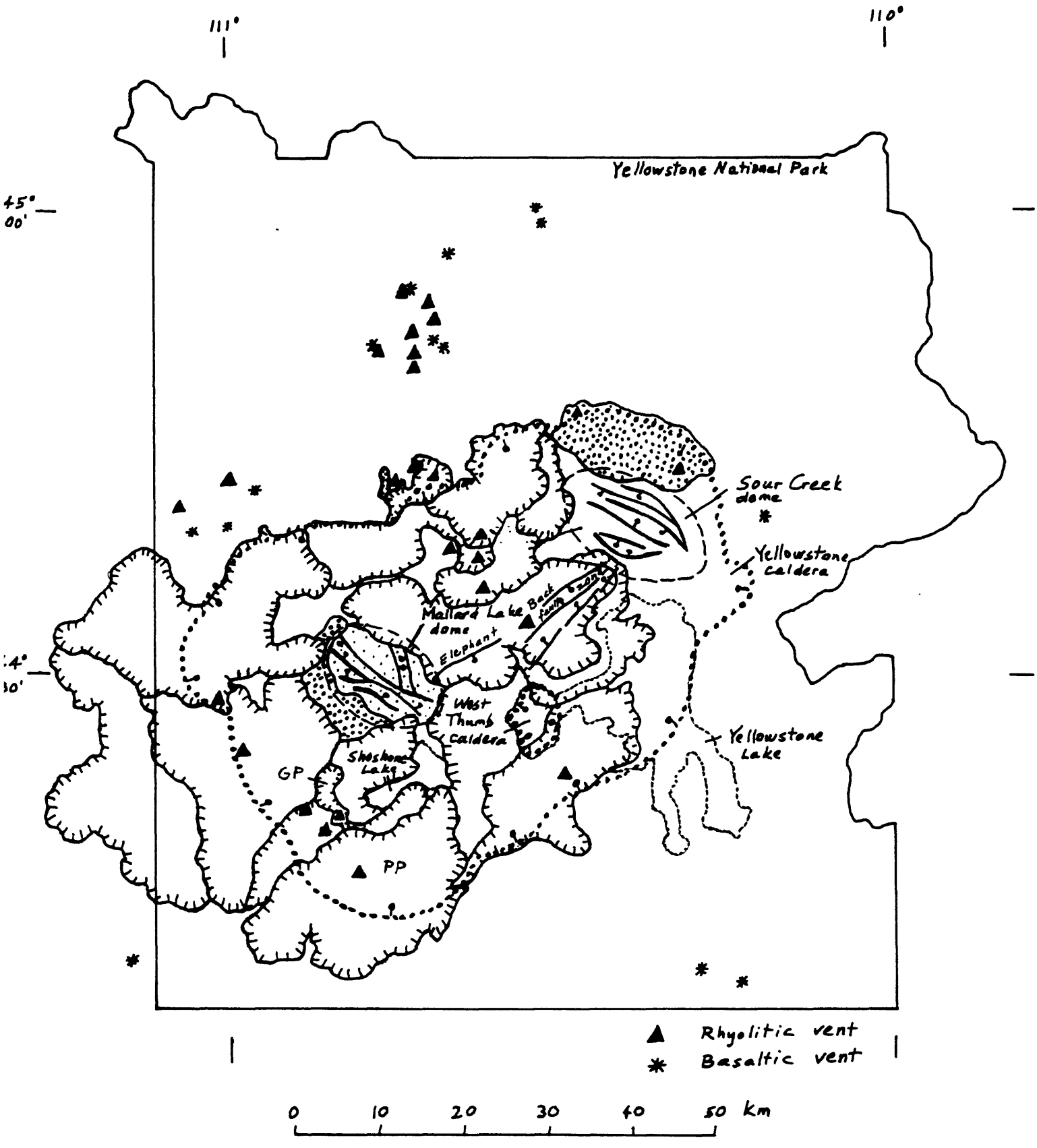
111°
110°
Yellowstone National Park
45° 00'
Sour Creek dome
Yellowstone caldera
Mallard Lake dome
Elephant Back fault
West Thumb caldera
Yellowstone Lake
Shoshone Lake
GP
PP
Rhyolitic vent
Basaltic vent
0 10 20 30 40 50 km

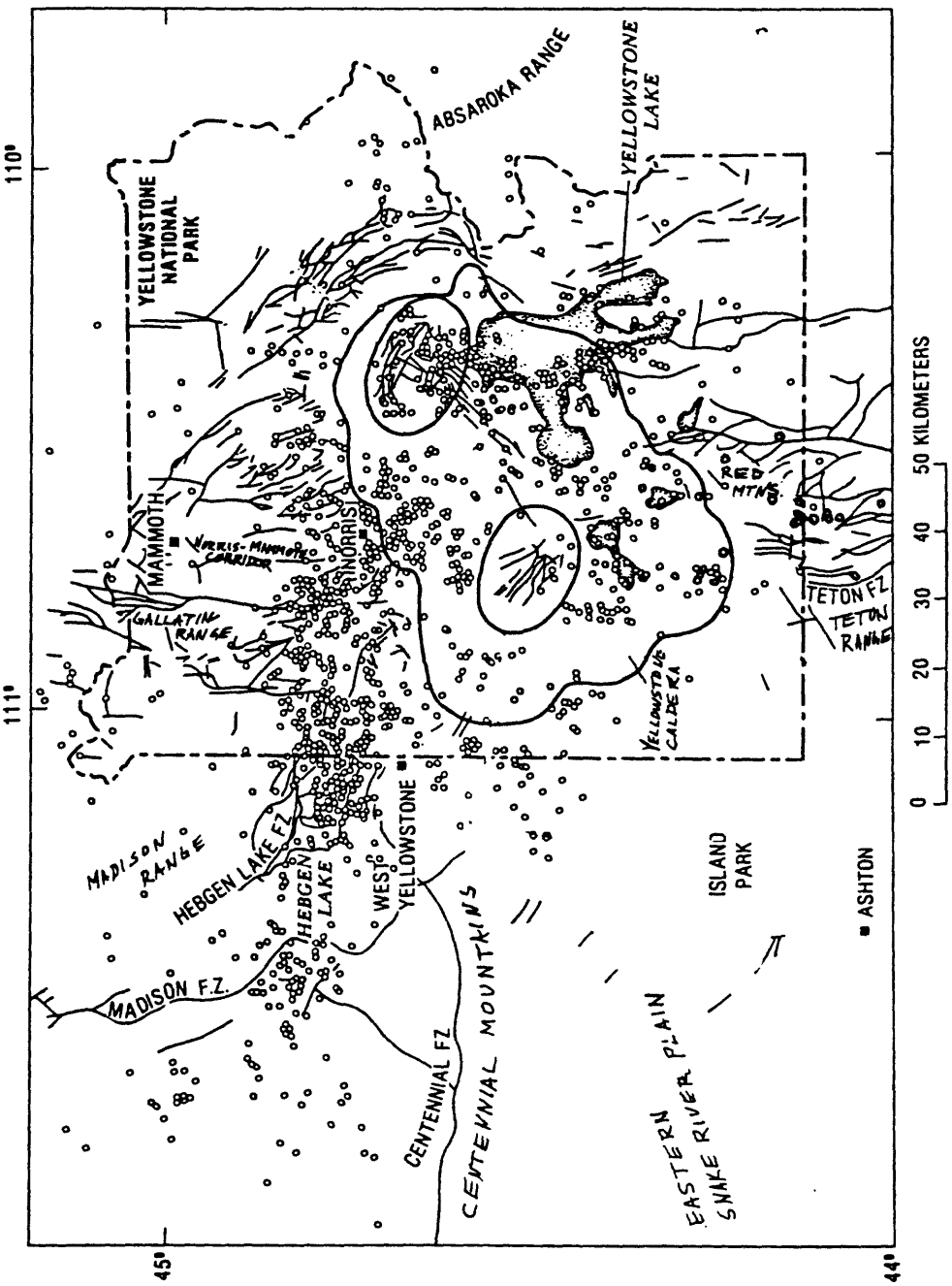
YELLOWSTONE NATIONAL PARK
ABSAROKA RANGE
YELLOWSTONE LAKE
MAMMOTH
NORRIS
GALLATIN RANGE
YELLOWSTONE CALDERA
RED MTNS.
TETON FZ
TETON RANGE
MADISON RANGE
HEBGEN LAKE FZ
HEBGEN LAKE
WEST YELLOWSTONE
MADISON F.Z.
CENTENNIAL FZ
CENTENNIAL MOUNTAINS
EASTERN SNAKE RIVER PLAIN
ISLAND PARK
ASHTON
110°
111°
45°
44°
0 10 20 30 40 50 KILOMETERS

Fig. 2

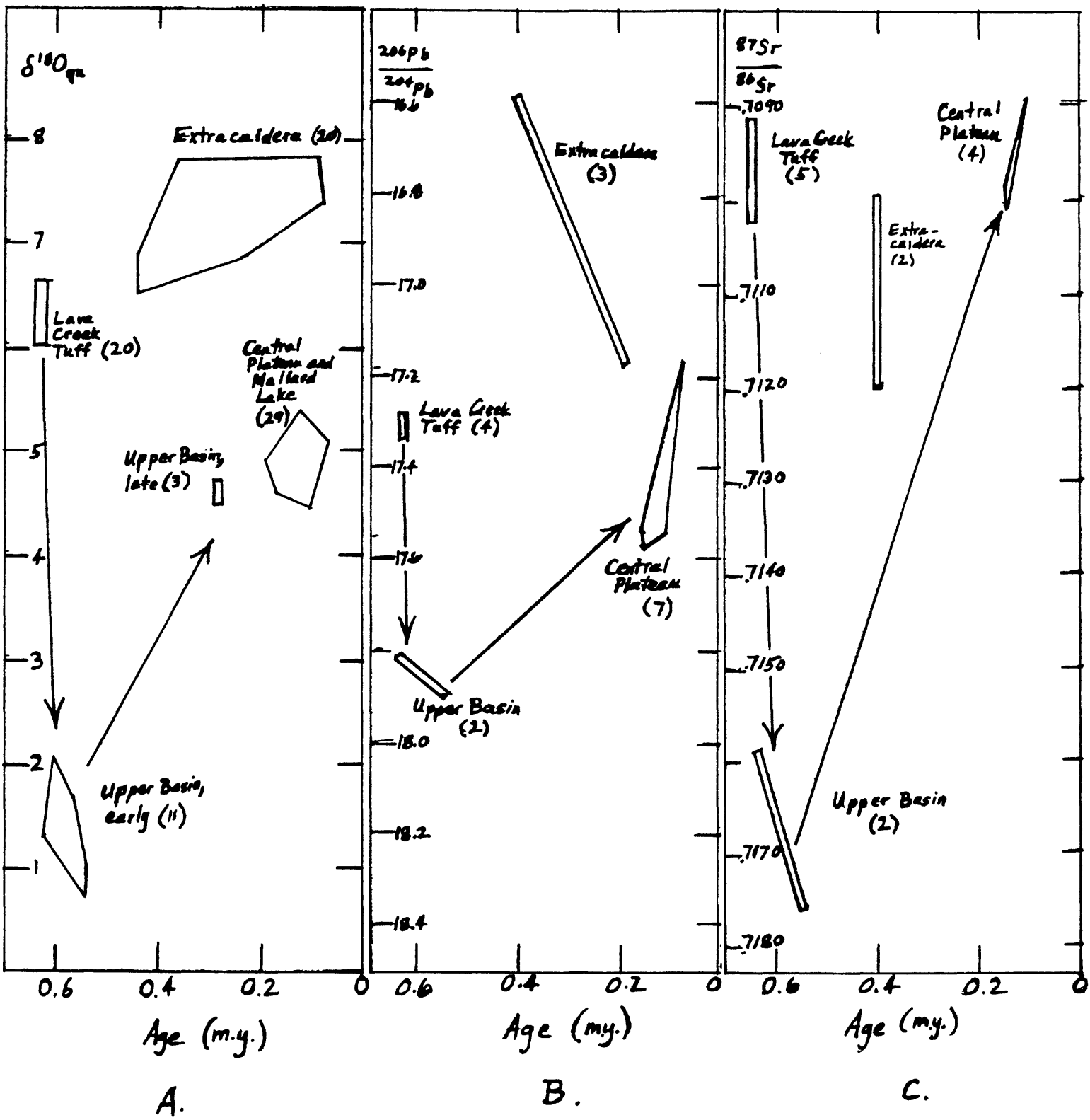
δ18Oqz
8
7
6
5
4
3
2
1
Extra caldera (20)
Lava Creek Tuff (20)
Central Plateau and Mallard Lake (29)
Upper Basin, late (3)
Upper Basin, early (11)
0.6
0.4
0.2
0
Age (m.y.)
A.
206Pb/204Pb
16.6
16.8
17.0
17.2
17.4
17.6
18.0
18.2
18.4
Extra caldera (3)
Lava Creek Tuff (4)
Central Plateau (7)
Upper Basin (2)
0.6
0.4
0.2
0
Age (m.y.)
B.
87Sr/86Sr
.7090
.7110
.7120
.7130
.7140
.7150
.7170
.7180
Lava Creek Tuff (5)
Extra-caldera (2)
Central Plateau (4)
Upper Basin (2)
0.6
0.4
0.2
0
Age (m.y.)
C.

FIG. 3

RECENT GROUND DEFORMATION AND SEISMICITY AT LONG VALLEY (CALIFORNIA), YELLOWSTONE (WYOMING), THE PHLEGRAEAN FIELDS (ITALY), AND RABAUL (PAPUA NEW GUINEA)

Daniel Dzurisin and Christopher G. Newhall

United States Geological Survey
David A. Johnston Cascades Volcano Observatory
5400 MacArthur Blvd.
Vancouver, Washington 98661

Submitted to Red Book on:
Active Tectonic and Volcanic Processes at Long Valley Caldera

April 1984

RECENT GROUND DEFORMATION AND SEISMICITY AT LONG VALLEY (CALIFORNIA), YELLOWSTONE (WYOMING), THE PHLEGRAEAN FIELDS (ITALY), AND RABAUL (PAPUA NEW GUINEA)

ABSTRACT

This review summarizes geologic histories and selected monitoring results through March 1984 at Long Valley, Yellowstone, the Phlegraean Fields, and Rabaul calderas. At Long Valley, increasing seismicity in the eastern Sierran block adjacent to the caldera starting in October 1978 culminated with 4 M=6+ earthquakes in May 1980, followed by numerous smaller earthquake swarms through early 1984. Ground deformation since 1979 includes at least 40 cm of uplift and 50 cm of horizontal extension centered on the resurgent dome, and local extension plus right-lateral shear in the caldera's south moat.

Yellowstone caldera and the adjacent Hebgen Lake region have experienced 7 M=6+ earthquakes, 1 M=7.1 earthquake, and numerous swarms of smaller earthquakes during the past century. First-order level surveys revealed as much as 72 cm of uplift during 1923-76, centered over a low-velocity body interpreted as the remnants of a silicic magma reservoir responsible for 3 caldera-forming eruptions in the past 2 million years. In October 1983, leveling along a line that spans the deforming area indicated that an additional 17 cm of uplift occurred during 1976-83.

The Phlegraean Fields caldera near Naples, Italy has been the site of remarkable ground deformation during the past 2,000 years; Roman ruins record vertical movements relative to sea level by as much as 12 m. Ground subsidence of about 1.5 cm/yr since 2,000 yrs B. P. reversed to uplift 1,000 yrs B. P., and accelerated dramatically before the Monte Nuovo eruption of 1538 A. D. Subsidence averaging 1.5 cm/yr followed the eruption until 1969-72, when 170 cm of uplift and a small increase in microseismicity were noted. After about 30 cm of subsidence during 1973-74, uplift resumed in June 1982; net uplift during 1969-March 1984 was about 2.8 m. Uplift reached 5 mm/day and earthquakes (M_{max}=4.0) damaged numerous buildings in Pozzuoli in October 1983; on October 11, authorities advised the evacuation of 70,000 residents. Uplift of 2-4 mm/day and sporadic seismic swarms were continuing as of March 1984; seismic energy release during January-March 1984 was almost as large as the cumulative energy release during all of 1983.

Relative calm prevailed at Rabaul caldera following eruptions in 1937 (507 dead) and 1941-43, until a series of large tectonic earthquakes occurred beneath the Solomon Sea in mid-1971. Seismicity beneath the caldera began to increase in late 1971, accompanied by uplift that now exceeds 100 cm. Seismicity and ground deformation accelerated markedly starting in September 1983, and a stage 2 eruption alert (eruption possible within months; voluntary evacuation) for the city of Rabaul and nearby villages was declared on 29 October 1983. An inferred magmatic intrusion beneath the caldera on 15 January 1984 was accompanied by an intense earthquake swarm (M_{max}=4.9) and 5 cm of rapid uplift. The largest swarm (M_{max}=5.1) to date occurred on 3 March 1984 beneath the

eastern rim of the caldera, accompanied by tilt changes of up to 50 microradians near the center of uplift.

Unusual activity at Long Valley since 1979 is comparable in many respects to that which preceded (by months or years) historic eruptions at Rabaul and the Phlegraean Fields, and a Long Valley eruption in the foreseeable future is therefore plausible. However, the prevalence of unrest at other young calderas suggests that some processes responsible for that unrest do not always culminate in eruptions.

INTRODUCTION

In order to place recent activity at Long Valley caldera in a broader context, Newhall, Dzurisin, and Mullineaux (1984) compiled information on historical unrest at about 100 large Quaternary calderas worldwide. In this related review, we describe in more detail the geologic histories and recent activity at 4 selected calderas: Long Valley (California), Yellowstone (Wyoming), the Phlegraean Fields (Italy), and Rabaul (Papua New Guinea). These examples were chosen because recent unrest has been severe (Phlegraean Fields and Rabaul) and because the authors are familiar with recent monitoring results at each caldera. Eyewitness accounts of historical eruptions at the Phlegraean Fields and Rabaul are included as examples of possible eruption scenarios at Long Valley.

Material presented here is almost entirely from the work of others; it was selected not for completeness at any one caldera, but for uniformity from one caldera to the next. A short DISCUSSION section outlines similarities and differences between Long Valley and the other calderas, as a basis for assessing the relative likelihood of eruptions in the foreseeable future.

LONG VALLEY

The geologic history and recent activity at Long Valley caldera are addressed in detail elsewhere in this volume. A skeletal outline is included here for comparison with more complete descriptions of the other calderas.

Geologic History

The geologic history of Long Valley caldera was described by Bailey, Dalrymple, and Lanphere (1976); the following summary is based on that framework and may not include more recent results or interpretations. Long Valley caldera in east-central California (Figure 1) is a 17 x 32 km elliptical depression that formed by collapse in response to the eruption of about 600 km^3 of rhyolitic magma (Bishop Tuff) 0.7 m. y. ago. Almost immediately after the caldera-forming eruption, rhyolite tuffs, domes, and flows accumulated within the caldera to a thickness of at least 500 m. Uplift began in the western part of the caldera soon thereafter, forming a resurgent dome by 0.6 m. y. B. P. Subsequent eruptions occurred from vents on the caldera floor 0.5, 0.3, and 0.1 m. y. ago, and from the outer ring fracture 0.2 m. y. to 50,000 yrs. ago.

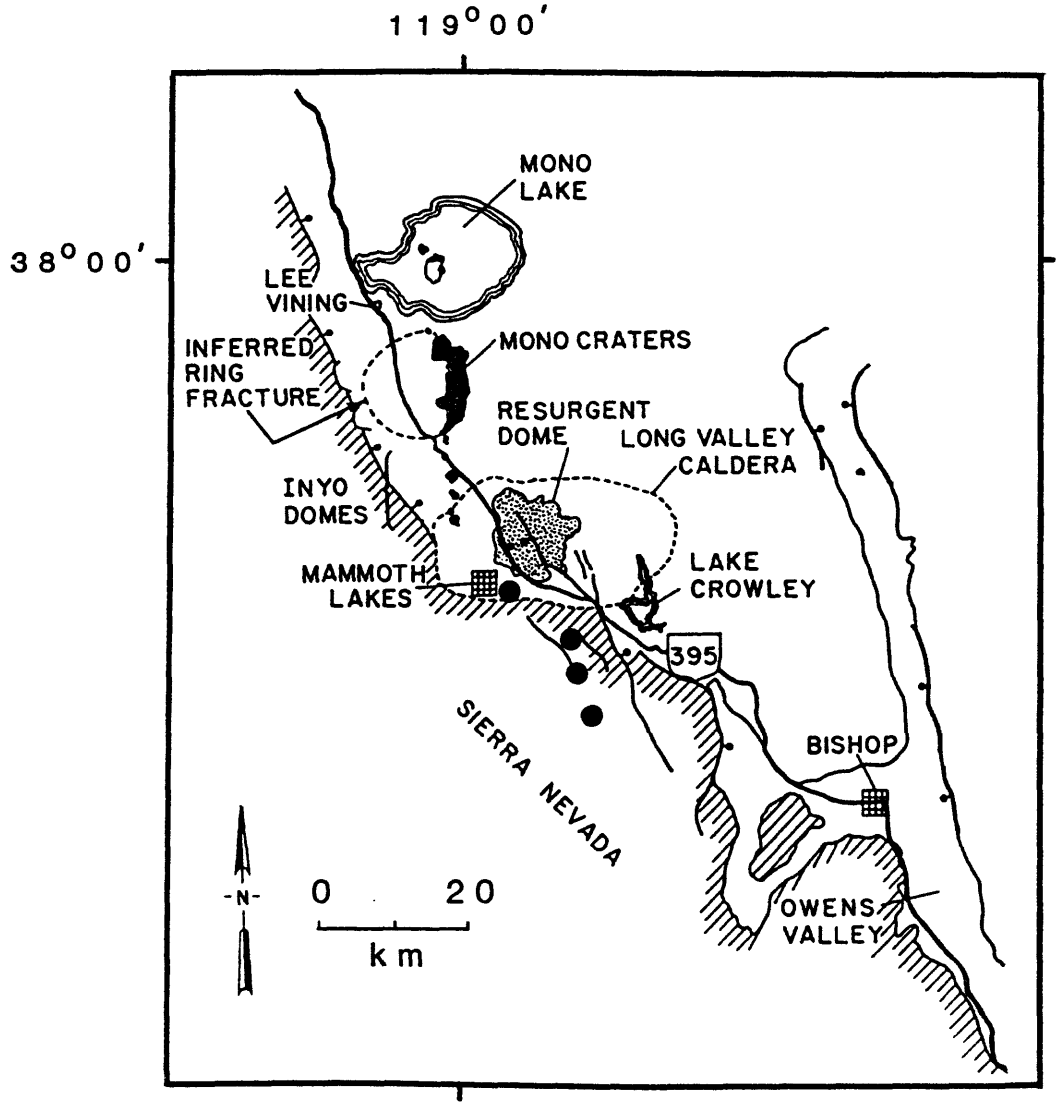

Figure 1. Generalized map of the Long Valley/Mono Basin area after Hermance (1983). The darkly shaded portions of the map represent Holocene eruptive centers. Also shown are the epicenters of 4 M=6+ earthquakes which struck the area during 25-27 May 1980 (black dots).

As the magma body remnant from the Bishop Tuff eruption was depleted by subsequent eruptions and by crystallization, magma from two other sources invaded the Long Valley system. Basaltic lava flows and cinder cones in the caldera's west moat are part of a chain of mafic rocks extending from southwest of Mammoth Mountain 45 km northward into Mono basin. The intracaldera basalt flows range in age from 150,000 to 60,000 yrs B. P.

The Inyo and Mono vents north of and within Long Valley caldera have been active for at least 40,000 yrs; during the past 1,500 years, they have erupted rhyolitic domes and/or pyroclastic deposits every few centuries. Miller (1983) has shown that the most recent eruptive activity within Long Valley caldera occurred about 550 years ago from the southern part of the Inyo volcanic chain. Explosive eruptions from South Deadman, Obsidian dome, and Glass Creek vents produced rhyolitic tephra, pyroclastic flows, and lava flows; shortly thereafter, phreatic explosions formed the nearby Inyo Craters. The potential for future eruptions from the Inyo or Long Valley systems is underlined by the presence of a substantial volume of magma starting about 8 km beneath Long Valley caldera, which has been identified by seismic refraction (Hill, 1976), teleseismic studies (Steeples and Iyer, 1976), and attenuation of locally generated S and P waves (Ryall and Ryall, 1981a).

Current Activity

The onset of current unrest at Long Valley caldera cannot be precisely established. Ryall and Ryall (1981b, 1983) noted a general decrease in seismicity in the southern part of the Sierra Nevada-Great Basin boundary zone from January 1977 to September 1978, followed by a burst of M=3+ earthquakes that began on 4 October 1978 with a M=5.7 shock 15 km southeast of the caldera. During the next 18 months, the epicentral zone grew to the northwest toward the caldera and activity gradually concentrated near the south part of the caldera rim (Figure 2). Intense swarms began in mid-May 1980, about 10 days before the sequence culminated with four M=6+ earthquakes on May 25-27 (including one inside the caldera beneath its southern moat; see Figure 1). Julian (1983) and Julian and Sipkin (1984) suggest that nodal plane solutions for at least 2 of the largest shocks are consistent with dike intrusion (compensated-linear-vector-dipole mechanism) rather than slip faulting (double-couple mechanism), but Wallace (1984) argues for oblique, dip-slip faulting on moderately dipping planes.

Savage and Clark (1982) reported that leveling along U. S. Highway 395 in 1975 and October 1980 documented uplift of as much as 25 cm centered on the resurgent dome (Figure 3). Precise trilateration surveys spanning the caldera indicated marginally significant east-northeast extension during 1972-79, but later indicated large horizontal displacements directed radially outward from the caldera during July 1979-September 1980 (Figure 4). It therefore seems likely that uplift began sometime after July 1979, perhaps coincident with the seismic increase that started in October 1979.

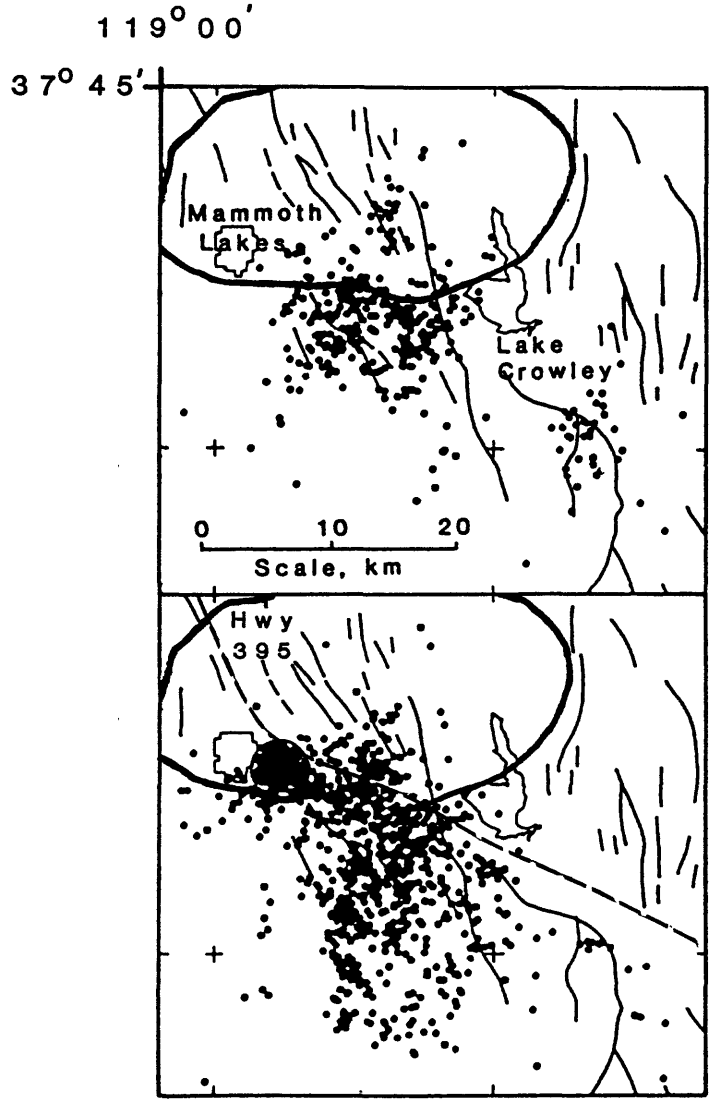

Figure 2. Seismicity near Long Valley caldera (heavy line) before and after the large 25-27 May 1980 swarm, from Ryall and Ryall (1983). Top panel shows the locations of 386 earthquakes that occurred from 4 October 1978 to 24 May 1980; bottom shows 1,088 quakes for the period 25 May 1980 to 1 October 1982. Intense swarms, some with the appearance of spasmodic tremor, occurred in the circled area immediately east of Mammoth Lakes in the lower panel; this swarm area extended to the southeast during the January 1983 swarm. Mapped faults shown by light lines; U. S. Highway 395 by dashed line in lower panel.

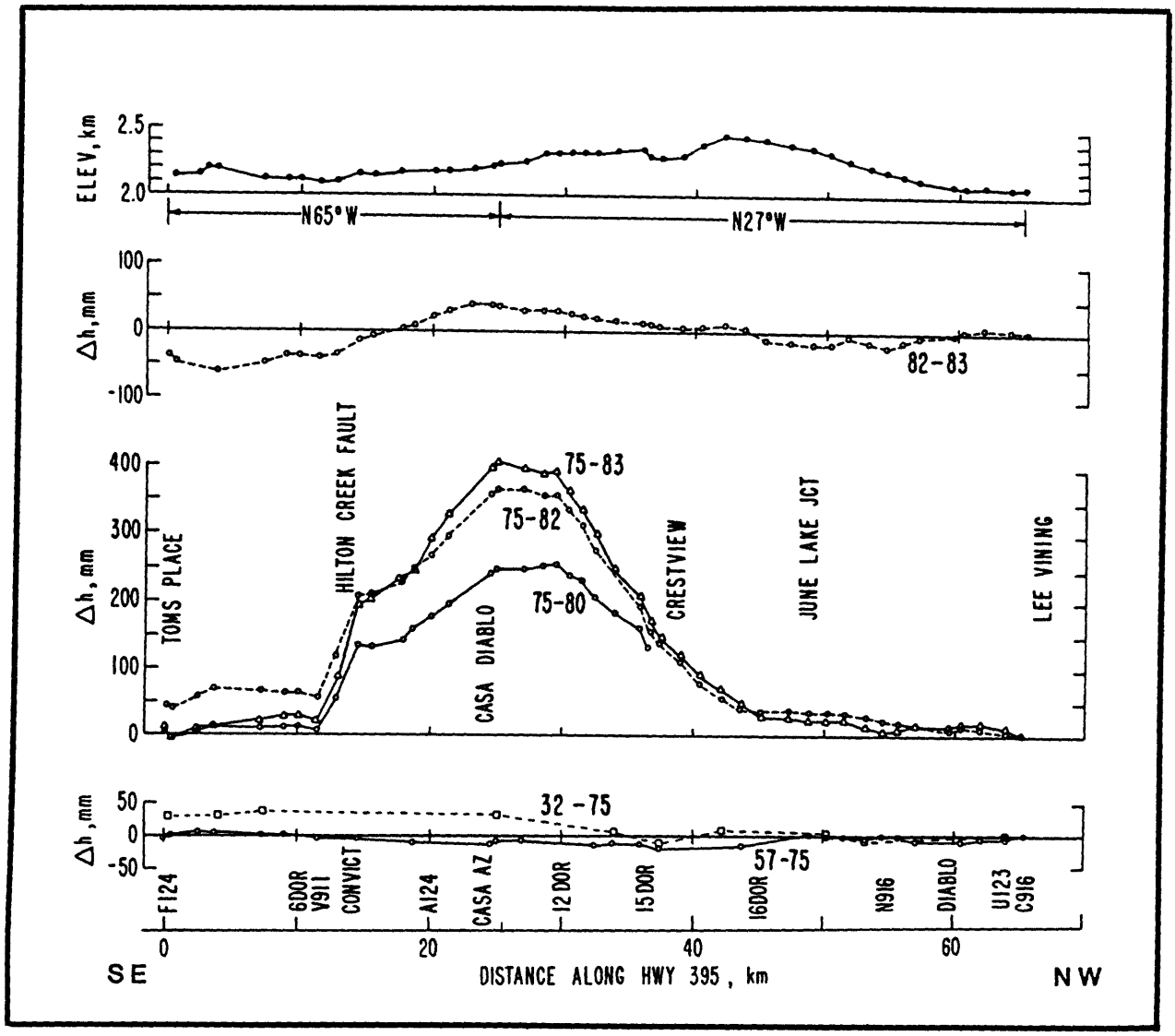

Figure 3. Elevation changes along U. S. Highway 395 across Long Valley caldera (see Figure 2) from leveling surveys in 1932, 1957, 1975, 1980, 1982, and 1983. Note the lack of appreciable deformation prior to 1975, and the progressive uplift since 1980. Figure is from Savage, Estrem, and Castle (1983).

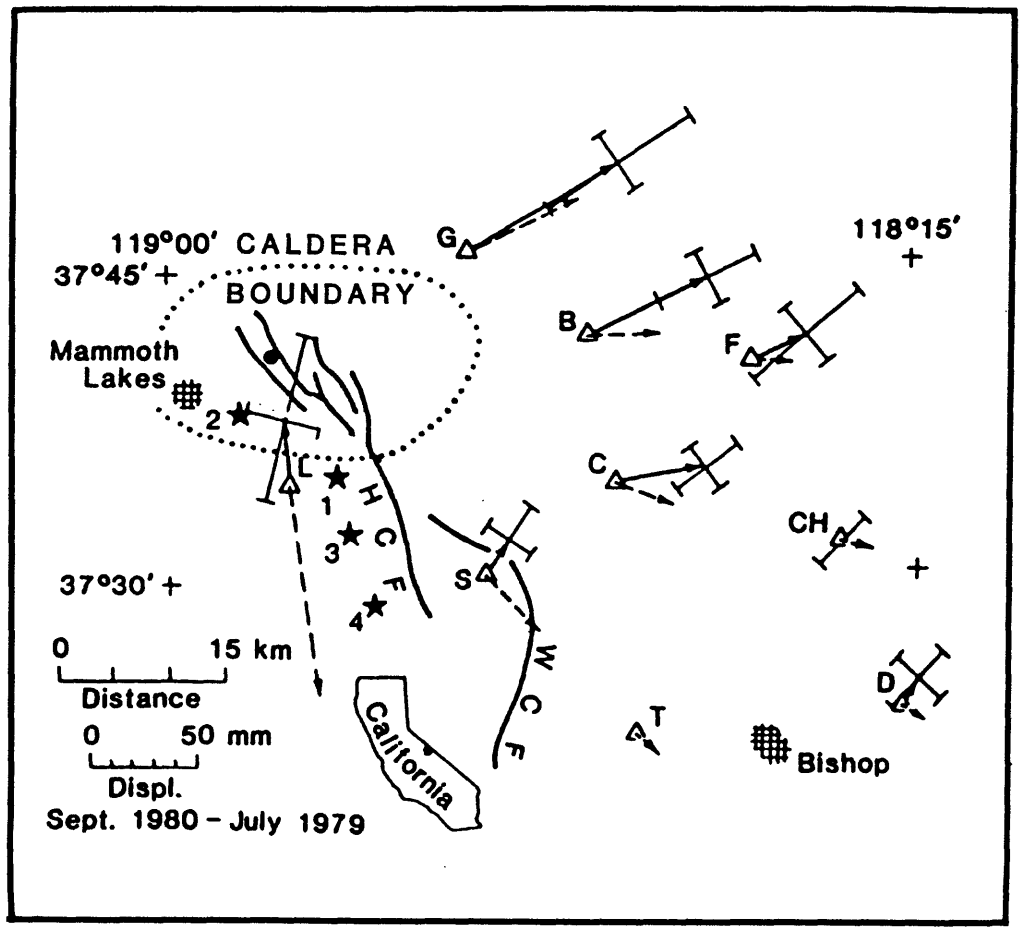

Figure 4. Horizontal displacements near Long Valley caldera from precise trilateration surveys in July 1979 and September 1980; figure from Savage and Clark (1982). Solid arrows show observed displacements, dashed arrows show displacements expected from expansion of a spherical magma chamber at 11 km depth. Stars indicate epicenters of 4 M=6+ earthquakes during 25-27 May 1980, in order of occurrence. Solid dot = center of resurgent dome; HCF = Hilton Creek Fault; WCF = Wheeler Crest Fault.

Relatively rapid deformation continued through at least January 1983. Maximum uplift along U. S. Highway 395 during 1975-83 was about 40 cm; results from an intracaldera trilateration network indicated about 50 cm maximum extension during 1978-82 (Denlinger and Riley, 1983).

Generally elevated seismicity punctuated by earthquake swarms, some having the character of spasmodic tremor, also continued through 1983 (Ryall and Ryall, 1983; Figure 5). Most of the swarms since May 1980 have occurred in a relatively small area of the caldera's south moat, hereafter called the swarm area. The largest shock in 1981 was a M=5.7 event in the Sierran block south of the caldera on September 30. Unfortunately, no leveling or trilateration surveys were conducted in 1981.

A moderate earthquake swarm occurred in the caldera's south moat during 7-8 May 1982, followed by 4 events of M=3.0-3.4 in a 10 day period starting on July 30. Smaller swarms occurred beneath the Hot Creek thermal area on 19 September and 3-4 November 1982, and in the swarm area on 14 December and 21 December.

The most intense and prolonged earthquake swarm at Long Valley caldera since May 1980 began on 6 January 1983, when a sequence of small earthquakes in the swarm area rapidly accelerated and assumed the appearance of spasmodic tremor (i. e., a sequence of small earthquakes, with few or no intervening quiet periods). Within two hours, 2 M=5+ quakes and hundreds of smaller shocks had occurred; activity began to wane later that day and returned to pre-swarm levels by the end of the month. Hypocenters from the January 1983 swarm define a near-vertical plane sub-parallel to the adjacent part of the caldera rim, extending about 8 km laterally and from 0-10 km in depth (Savage and Cockerham, 1983; Figure 6). Fault plane solutions and trilateration results suggest right lateral slip on a fault defined by the hypocentral distribution, and east-northeast extension, interpreted by Savage and Cockerham (1983) as evidence for dike intrusion into the caldera's ring fracture system.

Seismicity in the swarm area and adjacent Sierra Nevada block to the south has continued, but at a generally low level, since the January 1983 earthquake swarm (R. Cockerham, oral communication). The first of a series of minor flurries that usually included a few dozen quakes in the swarm area in a few hours occurred on 9 March 1983. Similar events continued through early 1984, but at a declining rate. The largest, on 22 May 1983, included at least 120 quakes (largest M=2.8) in a 4-hour interval. A flurry of activity on 3-4 July 1983 near Mt. Aggie, 5 km south of Convict Lake, included one M=5.0 and one M=4.0 quake, followed by numerous aftershocks. A small swarm near Mammoth Mountain on 24 September 1983 included about 50 quakes in one hour; another on November 14-15 at the southeast end of the January 1983 epicentral zone included two M=3+ quakes in a flurry of about 40 events.

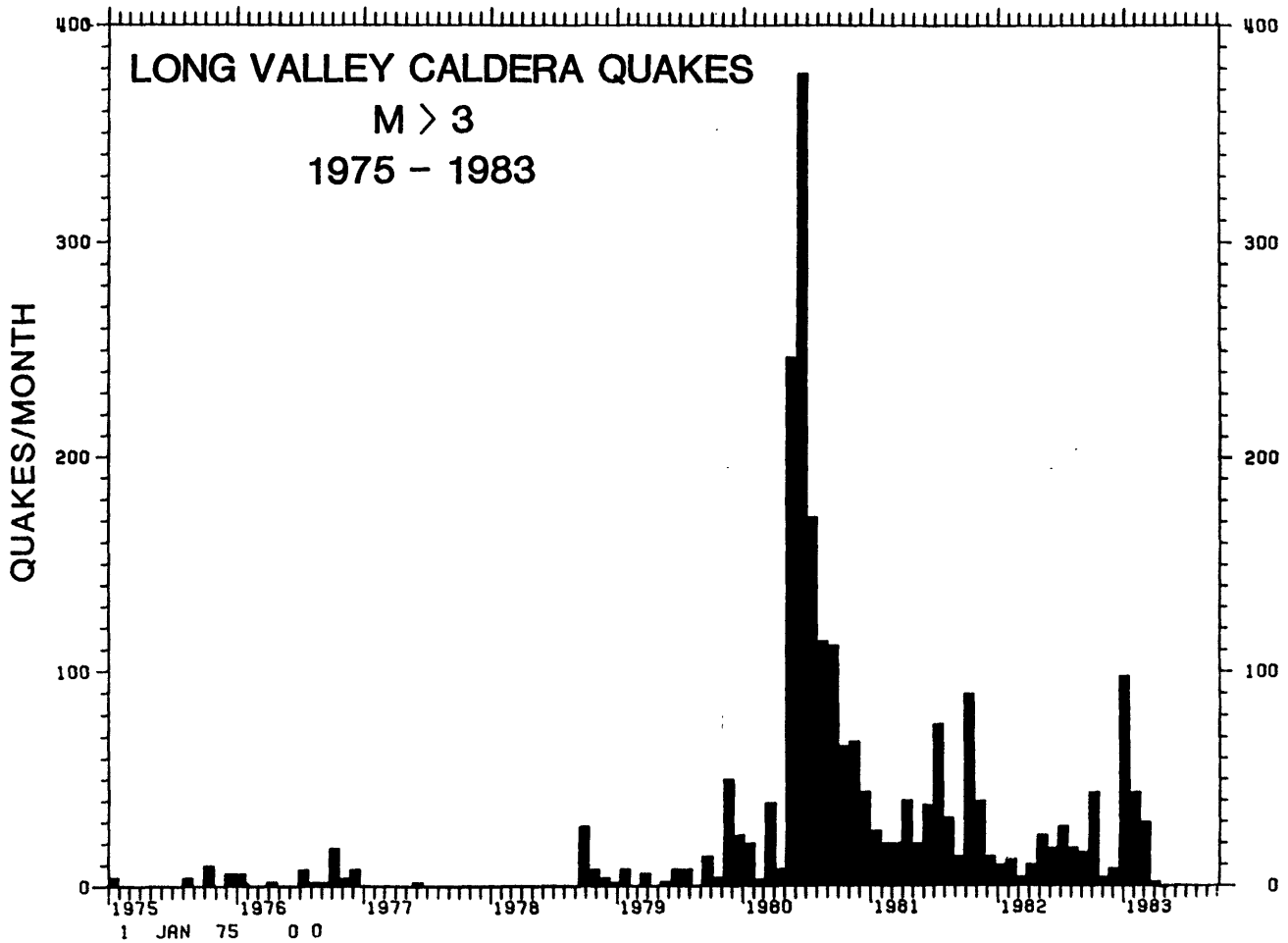

Figure 5. Histogram of the monthly number of earthquakes larger than magnitude 3 beneath Long Valley caldera and the adjacent Sierran block during 1975-83. Note the increase in late 1978 reported by Ryall and Ryall (1981b, 1983), and the continued high level of seismicity following the large May 1980 swarm. Data provided by R. Cockerham.

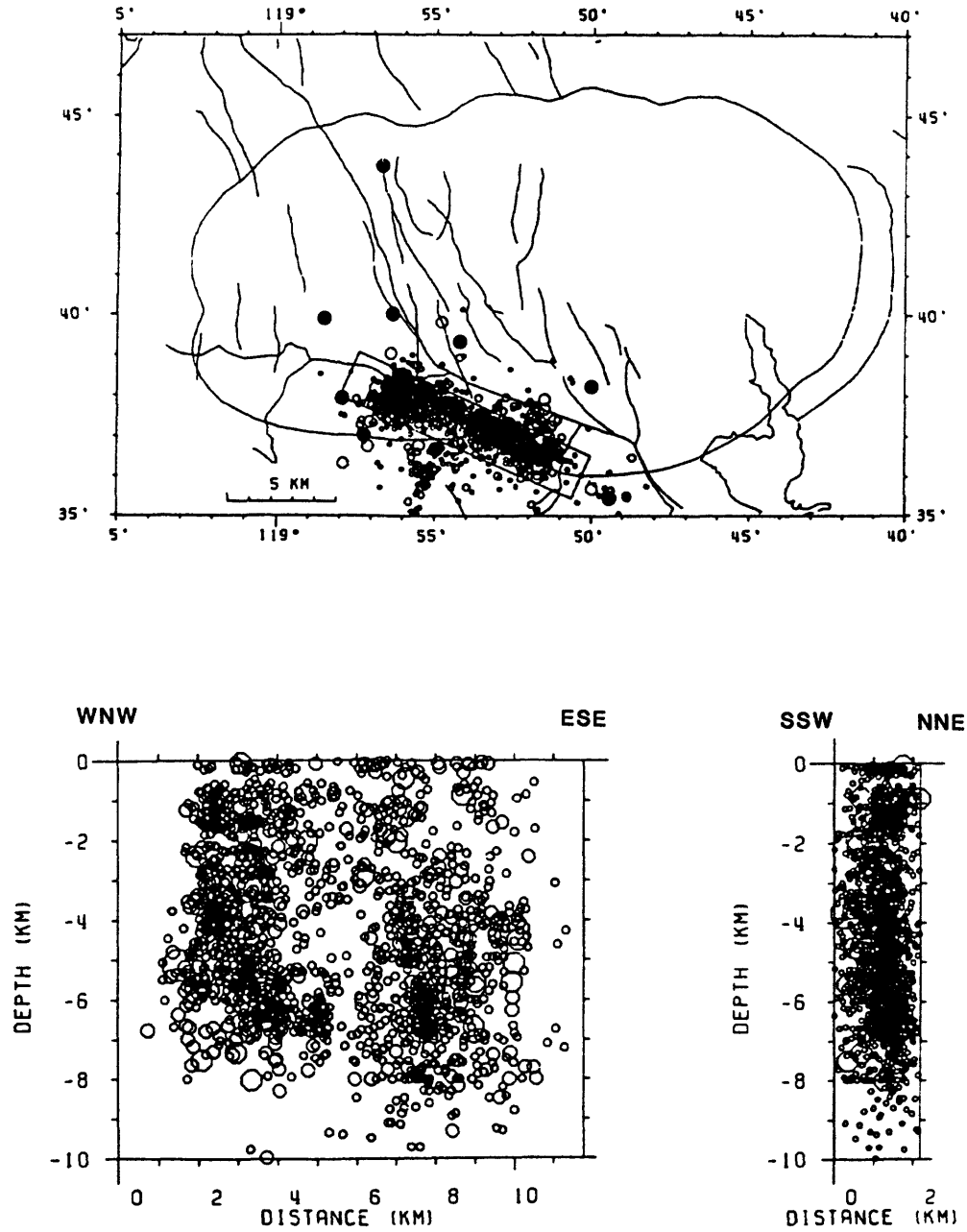

Figure 6. (Top) Epicentral distribution of earthquakes during the January 1983 swarm, from Savage and Cockerham (1983). (Bottom) Projections of the swarm hypocenters onto vertical planes trending parallel (left) and perpendicular (right) to the trend of the epicenters. Solid dots represent seismometers; size of earthquake symbols proportional to magnitude of earthquake.

YELLOWSTONE

Geologic History

Christiansen (1983, 1984) has written extensively on the geology and evolution of the Yellowstone Plateau volcanic field; this brief review is based largely on his work. It is included here mainly for comparison with Long Valley, the Phlegraean Fields, and Rabaul.

During the past 2 million years, the Yellowstone Plateau volcanic field has experienced three cycles of rhyolitic volcanism, each climaxed by eruption of voluminous ash flows accompanied by caldera collapse. The first cycle climaxed about 2.0 m. y. ago, forming a caldera that extended more than 75 km from Island Park to central Yellowstone. This gigantic eruption, among the largest yet known, produced roughly 2,500 km^3 of rhyolitic ash flows that formed the Huckleberry Ridge Tuff.

The second volcanic cycle was the smallest of the three; it was confined to the Island Park area and climaxed about 1.3 m. y. ago with the eruption of about 300 km^3 of Mesa Falls Tuff. The resulting caldera was about 16 km across, nested within the west part of the much larger first-cycle caldera.

The center of rhyolitic activity then shifted eastward to the present Yellowstone Plateau, where the third volcanic cycle began about 1.2 m. y. ago. For about 0.6 m. y., rhyolitic lavas erupted sporadically on the Yellowstone Plateau above an evolving shallow crustal magma chamber. Following the development of an extensive ring fracture system, a climactic eruption 0.6 m. y. ago emplaced more than 1,000 km^3 of the Lava Creek Tuff and formed a composite caldera about 85 km long and 45 km wide. Resurgence soon thereafter formed the Sour Creek and Mallard Lake structural domes (Figure 7). Doming resumed in the western caldera about 150,000 years ago, accompanied by extrusion of 1,000 km^3 of rhyolitic lava flows that fill most of the present caldera.

Trimble and Smith (1975) pointed out that earthquake focal depths in the Hebgen Lake area since 1959 range from near the surface to about 15 km, but within Yellowstone caldera the maximum depth has been only about 5 km. They suggest that the decrease in focal depths beneath the caldera may reflect increased temperatures and pore pressures related to the hydrothermal system and, ultimately, to a magmatic heat source at depth. Eaton et al. (1975) argued from a variety of geophysical evidence that a large, partially molten body exists beneath Yellowstone caldera at depths below a few kilometers. Although the last known eruption at Yellowstone occurred 75,000 years ago, Christiansen (1983, p. 8) concluded that: "Further volcanism almost certainly will occur in the Yellowstone National Park region" and Smith and Braile (1982, p. 234) agreed that: "...the geologic record and the new geophysical models suggest future volcanic activity in the Yellowstone Plateau". These conclusions are reinforced by Yellowstone's spectacular hydrothermal features and by contemporary seismicity and intracaldera uplift.

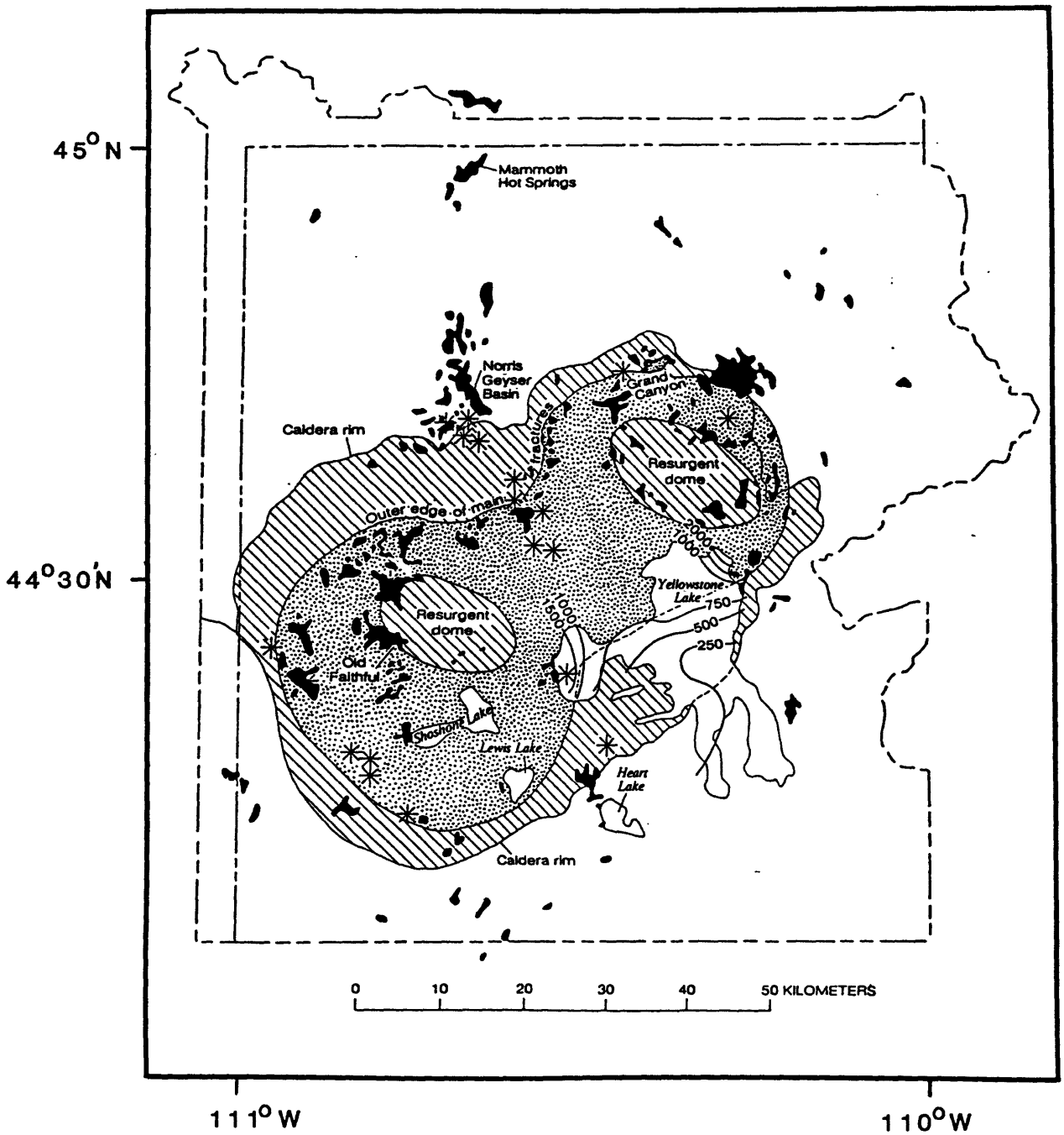

Figure 7. Third cycle Yellowstone caldera (dot pattern) after Christiansen (1983), showing locations of Sour Creek dome (upper right), Mallard Lake dome (lower left), ring-fracture system (line pattern), postcollapse intracaldera rhyolitic vents (stars), active and recently active hydrothermal features (black areas), and contours of heat flow in Yellowstone Lake (in mW/m^2). Outline of Yellowstone National Park shown for reference.

Current Activity

Trimble and Smith (1975) noted that the first information on earthquakes in the Yellowstone region was from F. V. Hayden, leader of the first scientific expedition in the area, who reported that severe shocks were felt northeast of Yellowstone Lake in 1871. From that date until 1959, at least 76 earthquakes strong enough to be felt were reported in the Yellowstone Park-Hebgen Lake region; Smith and Braile (1982) report that 7 of these exceeded magnitude 6.

A M=7.1 earthquake struck the Hebgen Lake area, 50 km northwest of the center of Yellowstone caldera, on 17 August 1959. The earthquake killed 28 people, caused over 11 million dollars damage, produced subsidence by as much as 6.7 m in the West Yellowstone basin, and triggered spectacular hydrothermal changes in Yellowstone National Park (Trimble and Smith, 1975).

The Hebgen Lake area and to a lesser degree Yellowstone caldera have continued to be seismically active since 1959 (Figure 8). Eaton et al. (1975) pointed out that earthquakes commonly occur in swarms of up to several hundred events within a few hours to a few days, in a region only a few kilometers across. In August 1972, a pronounced change in the thermal activity at Norris geyser basin was followed shortly by a small earthquake swarm, and in 1973 a major swarm occurred near the south end of Yellowstone Lake (Trimble and Smith, 1975).

Leveling surveys in Yellowstone National Park during 1923 and 1975-77 indicated uplift by as much as 72.6 cm, roughly symmetric about an axis connecting the Mallard Lake and Sour Creek domes in the central caldera (Figure 9). Pelton and Smith (1979, 1982) argued that this rapid uplift (average = 1.4 cm/yr) could not have been sustained for more than a few centuries without producing notable effects, and concluded that it was caused by recent influx of molten material into the upper crust beneath the caldera.

Motivated by the large historic uplift at Yellowstone and by recent events at Long Valley caldera, a crew from the Cascades and Hawaiian Volcano Observatories in October 1983 re-leveled to first order standards a 20-km line spanning the known uplift at Yellowstone. The 1983 route (Figure 9) followed the National Park highways from Trout Creek (10 km south of Canyon Junction) to Indian Pond (4.5 km east of Fishing Bridge) via Lake Junction.

The 1983 survey was not tied to a stable datum outside the caldera, but extrapolation based on the shape of the 1923-76 profile indicates about 17 cm of additional uplift during 1976-83. That result increases the total uplift since 1923 to about 90 cm (Figure 10). The uplift rate at benchmark B11 near the deformation axis increased from an average of 1.4 cm/yr during 1923-76 to 2.1 cm/yr during 1976-83, and the shape of the more complete 1976-83 profile suggests that the maximum uplift rate at the axis increased from about 1.6 cm/yr during 1923-76 to about 2.4 cm/yr during 1976-83 (Figure 11).

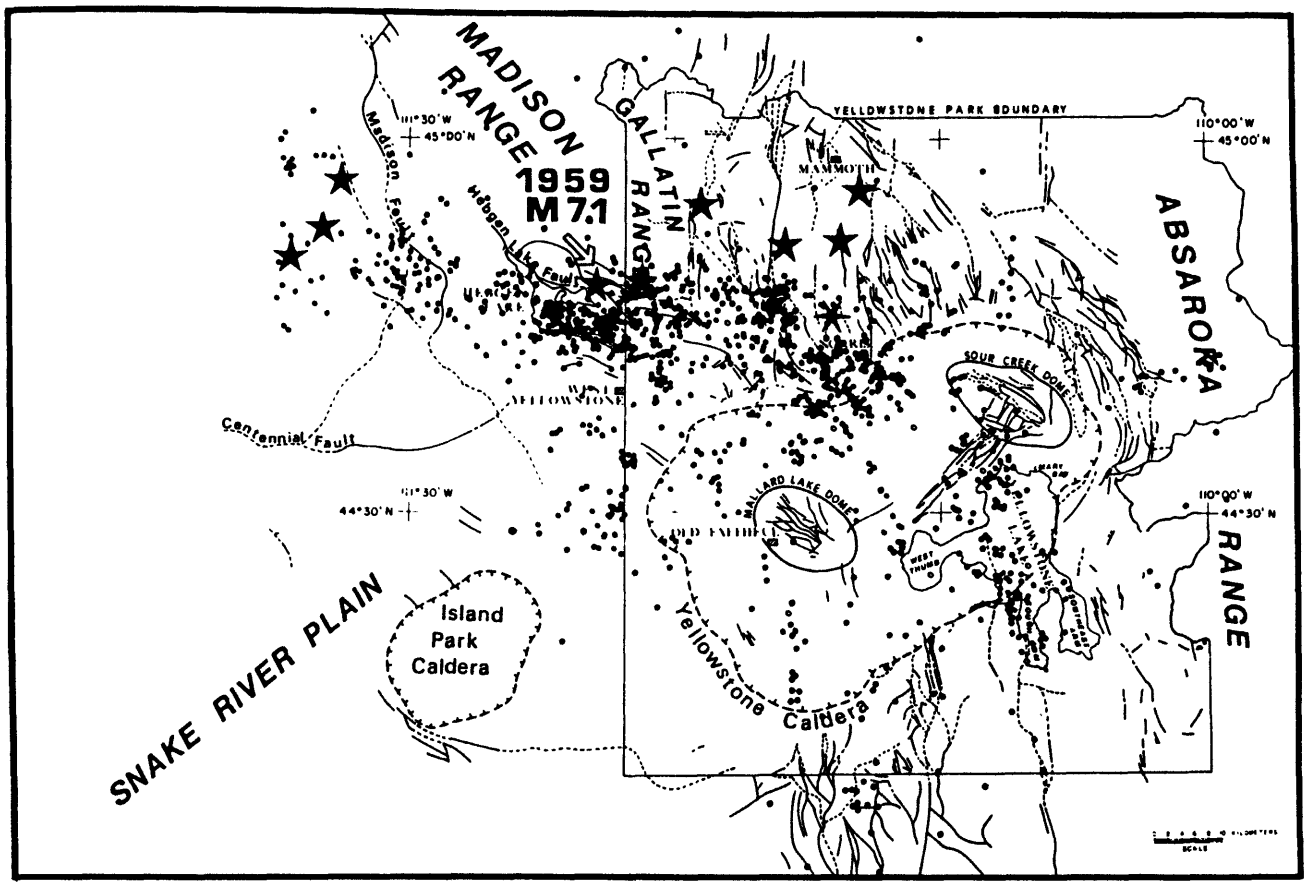

Figure 8. Earthquake and fault distribution in the Yellowstone-Hebgen Lake region during 1971-79 from Smith and Braile (1982). Large stars correspond to the epicenters of historical magnitude 6-7 earthquakes.

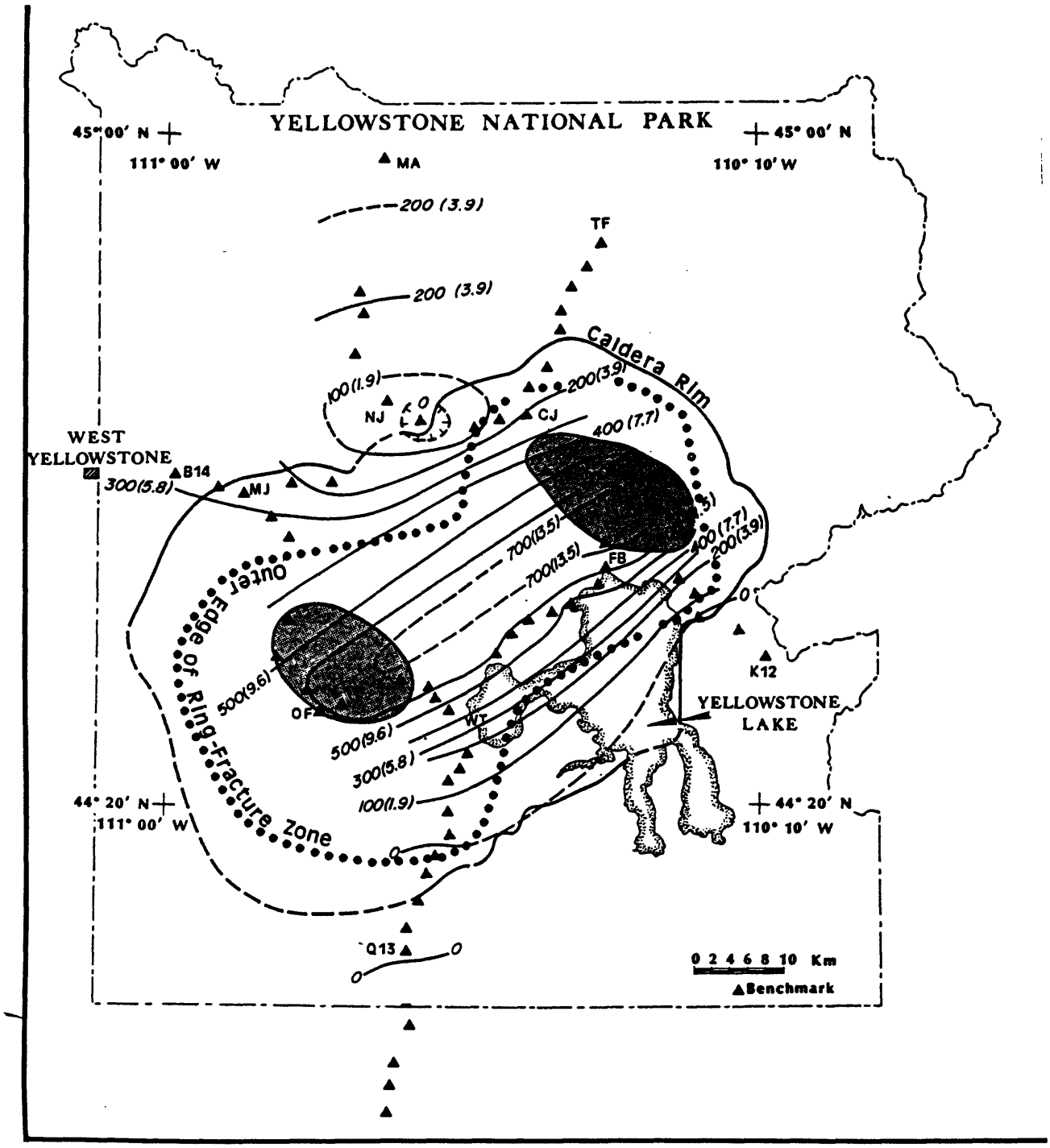

Figure 9. Contour map of elevation changes at Yellowstone caldera during 1923-75, from Pelton and Smith (1982). Benchmarks are shown as black triangles; contour interval is 100 mm, with corresponding uplift rates (mm/yr) in parentheses. The segment from Canyon Junction (CJ) to Lake Butte (10.5 km southeast of Fishing Bridge, FB), part of which was re-leveled in October 1983, crosses the axis of the uplift near the Sour Creek dome (upper right shaded area).

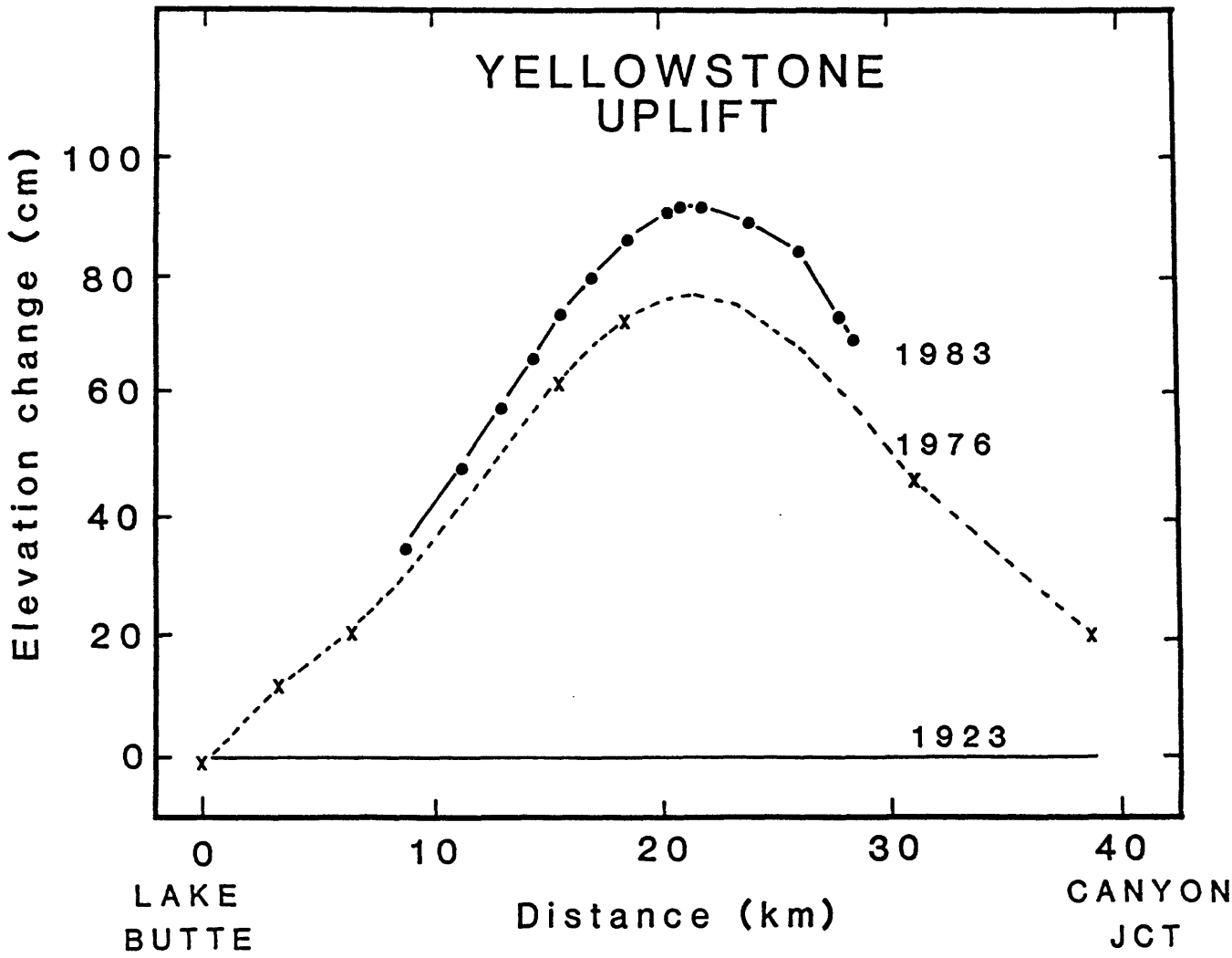

Figure 10. Net uplift between Canyon Junction and Lake Butte since 1923. The 1923 and 1976 surveys were tied to an assumed stable base at Sylvan Lake, 10 km SE of Yellowstone caldera; the 1983 survey is a floating one. To estimate net uplift during 1976-83, we first fit a smooth curve to the 1923-76 data, then added changes measured during 1976-83. About 9 mm of relative subsidence near the crest of the 1976-83 profile is not apparent here owing to the coarse vertical scale and the large spacing between benchmarks prior to 1976.

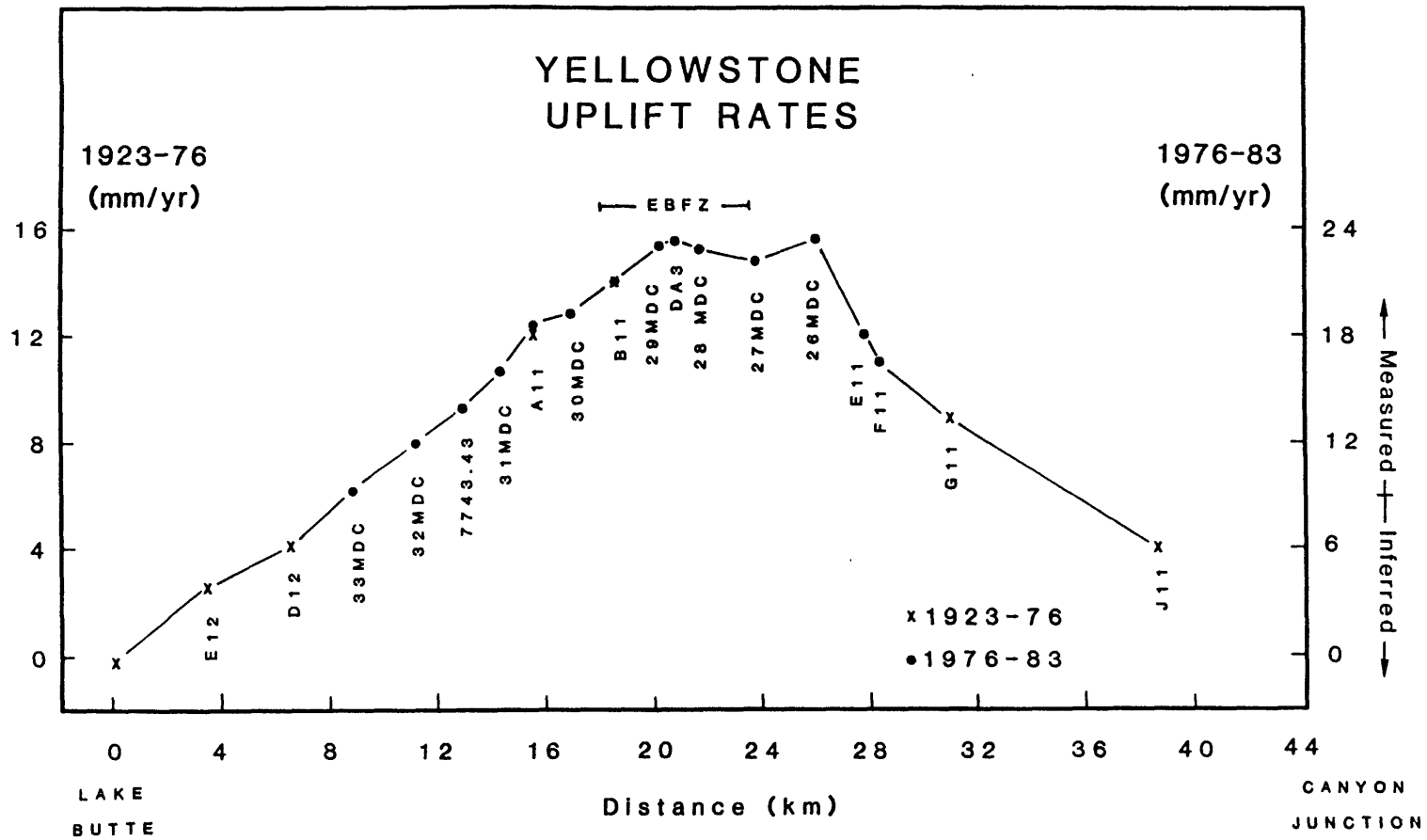

Figure 11. Uplift rates between Canyon Junction and Lake Butte during 1923-76 (x's) and 1976-83 (dots). Note that the profiles are very similar in shape, but the 1976-83 rates are about 50% higher than those for 1923-76. A small zone of relative subsidence occurs near the Elephant Back fault zone (EBFZ) in the 1976-83 data; uplift may be causing differential movement across this complex horst-and-graben structure.

With only 3 first-order level surveys at Yellowstone since 1923, it cannot be known whether the uplift rate is currently increasing, decreasing, or remaining constant. Possible scenarios include, but are not limited to, the following: 1) uplift began before 1923 and has slowly accelerated; 2) uplift began in about 1940 and has continued at a constant rate; or 3) uplift began after 1940 (just prior to 1959 Hebgen Lake earthquake?), peaked at a rate greater than 2.4 cm/yr, and has since declined.

There is a suggestion in the 1976-83 profile that about 9 mm of relative subsidence occurred during that interval between the Mud Volcano area (BM 26MDC) and Lee Hardy Rapids (BM DA3; Figure 11); a similar pattern could not have been detected earlier owing to a lack of benchmarks at key locations. The area of apparent subsidence lies partly within the Elephant Back fault zone, a complex system of horsts and graben probably formed by regional extension during resurgence about 150,000 yrs ago. Contemporary uplift may have re-activated this system of normal faults, and episodic uplift in the past may have played a role in the development of the fault zone. However, the case for recent subsidence relies heavily on a single benchmark (26MDC), and additional measurements of more closely-spaced benchmarks are therefore required to confirm this intriguing result.

PHLEGRAEAN FIELDS

The next 2 sections draw heavily on material made available to D. Dzurisin and D. P. Hill during a two week visit to the Phlegraean Fields in October 1983. We are indebted to the United States Office of Naval Research for their financial support, and to staff of the University of Naples, University of Pisa, and Vesuvius Volcano Observatory, particulary G. Luongo and F. Barberi, for their cordiality and willingness to share data and ideas.

Geologic History

Rosi et al. (1983) recently summarized the structural evolution, volcanic history, and eruptive mechanisms of the Phlegraean Fields caldera and associated vents. Pre-caldera deposits include trachytic and latitic lavas and tuffs erupted from mostly submarine vents beginning at least 50,000 years ago. The submarine sequence is overlain by subaerial products from several vents, some of which are still recognizable outside the caldera. The recent history of large elevation changes associated with volcanic activity in the Phlegraean Fields suggests that the transition from submarine to subaerial activity may partly reflect regional uplift caused by shallow magmatic intrusions.

Activity culminated about 35,000 years ago with the eruption of 80 km^3 (dense rock equivalent) of trachytic magma (62% SiO_2) to form the Breccia Museo and Campanian Ignimbrite, followed by collapse of the 11 km x 13 km Phlegraean Fields caldera (Figure 12). Armienti et al. (1983) offer petrologic evidence that the volume of the Phlegraean Fields magma chamber at the time of caldera collapse was at least 240 km^3; they infer from the presence of contact metamorphic rocks recovered from deep

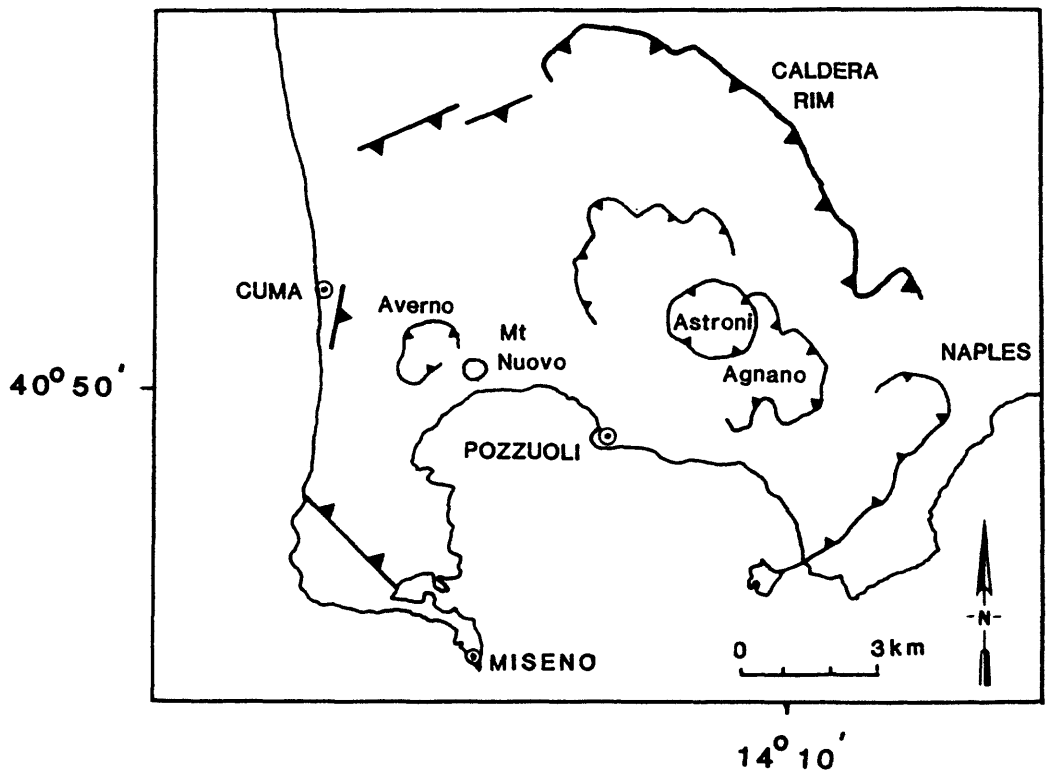

Figure 12. Sketch map of the Phlegraean Fields caldera after Rosi et al. (1983) showing recognizable parts of the caldera rim, selected post-caldera vents, and population centers.

geothermal wells that the top of the chamber was within 5 km of the surface.

Post-caldera volcanic activity in the Phlegraean Fields was divided by Rosi et al. (1983) into 3 main phases (Figure 13): 1) ancient submarine volcanism (35,000 to 10,500 yrs B. P.); 2) early subaerial volcanism (10,500 to 8,000 yrs B. P.); and 3) recent subaerial volcanism (4,500 yrs B. P. to 1538 A. D.). After collapse, the caldera was invaded by the sea and progressively filled by a series of latitic to trachytic tuffs (55-57% SiO_2) from submarine vents. By 10,500 years ago, infilling (and structural doming?) had progressed to the point that subsequent vents were mostly subaerial. Activity from 10,500 to 8,000 years ago was concentrated in the western and east-central sectors of the caldera, and generally migrated inward toward the caldera's center. Products from these central vents were mostly trachytic, but during the same interval scattered vents along the caldera rim produced trachybasalts and latites. Eruptions from the central caldera included highly explosive Plinian and hydromagmatic activity, were accompanied by collapse of craters up to 3 km in diameter, and deposited up to 1 m of ash over the current site of Naples.

A thick soil layer marks an apparent hiatus in eruptive activity in the Phlegraean Fields from 8,000 yrs B. P. to 4,500 yrs B. P., but dramatic uplift of the central caldera began about 5,400 yrs B. P., lifting a marine terrace 40 m above current sea level. Eruptions from numerous vents in the uplifted area began about 4,500 yrs B. P., leading Rosi et al. (1983) to attribute the uplift and ensuing eruptions to a period of shallow magmatic intrusion. Vents continued to migrate toward the center of the caldera during this period and erupted volumes decreased, as the magma body beneath the caldera was depleted by eruptions and by cooling. Armienti et al. (1983) used these patterns and petrologic arguments to suggest that the Phlegraean Fields magma chamber has been mostly a closed system for the past 10,000 years, and that only about 4 km^3 of molten material remains beneath Pozzuoli.

The most recent eruption in the Phlegraean Fields produced Monte Nuovo, a low trachyte cone about 1 km in diameter, in 1538 A. D. Sea level data from the Roman marketplace Serapeo in Pozzuoli, near the center of the caldera, indicate subsidence at a steady rate of 1.5 cm/yr from 2,000 to 1,000 yrs B. P., followed by roughly 500 years of progressive uplift (Figure 14). In 1501, King Ferdinand ceded to Pozzuoli a strip of land which had earlier emerged along the coast near the city (Caputo, 1979). The Pozzuoli charter of 1511 tells of many felt earthquakes per year for many years, and other documents suggest that frequent strong earthquakes shook the city in 1534. In 1536 virtually every house in Pozzuoli was damaged by earthquakes; experience since 1982 suggests that this implies numerous magnitude 3-4 shocks, but probably none greater than magnitude 5.

Many quakes were felt in Naples (implies magnitude 4-5) and Pozzuoli starting in May 1538; these continued until 26-27 September 1538, when the earth was continuously shaken and the sea at the Bay of Pozzuoli withdrew 400 m owing to rapid uplift of the shoreline (Caputo, 1979). On

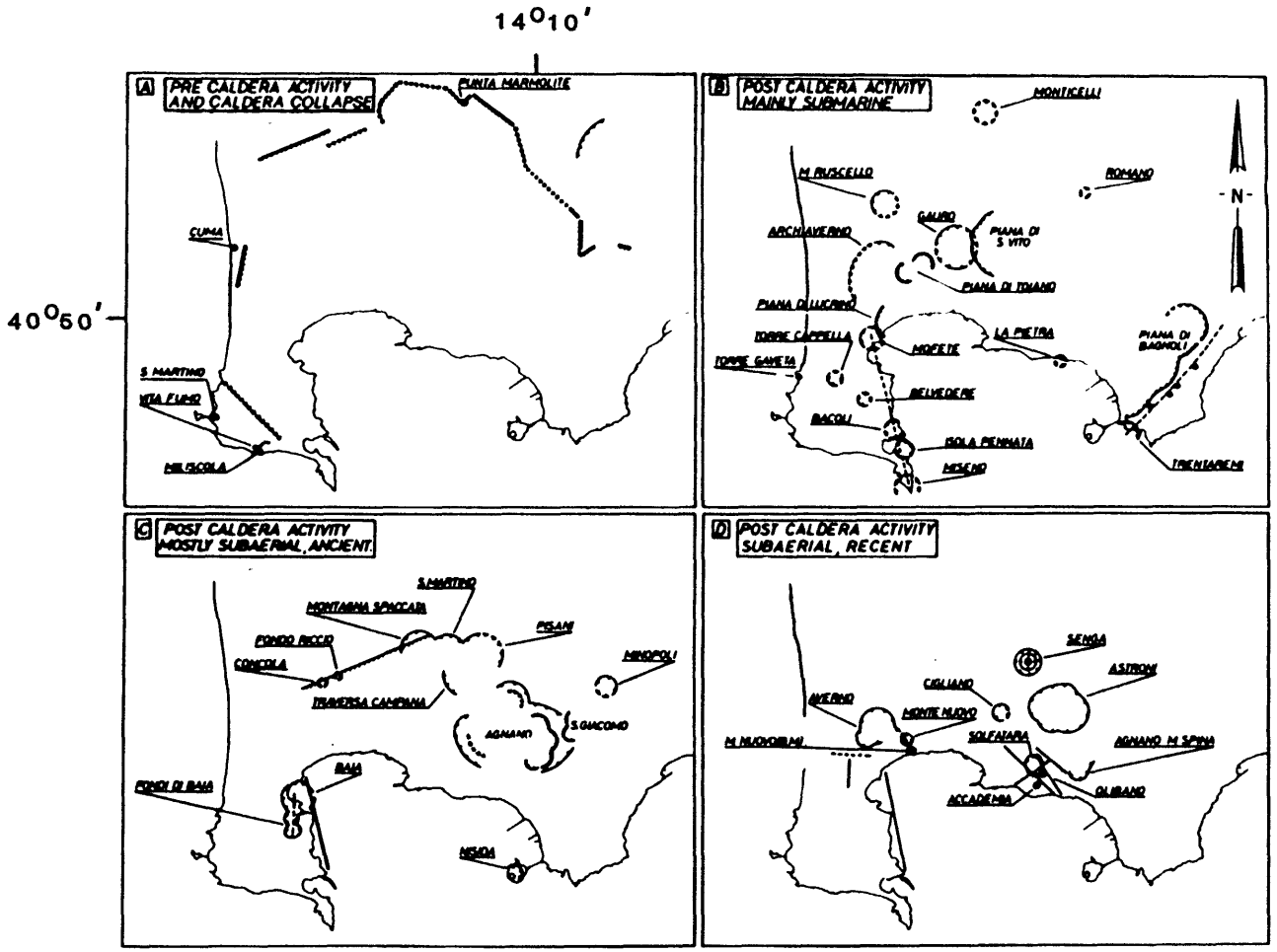

Figure 13. Four phases of Phlegraean Fields evolution identified by Rosi et al. (1983): A. pre-caldera activity and caldera collapse (≥35,000 yrs B. P.), B. post-caldera submarine activity (35,000-10,500 yrs B. P.), C. ancient post-caldera subaerial activity (10,500-8,000 yrs B. P.), and D. recent post-caldera subaerial activity (4,500 yrs B. P. to 1538 A. D.)

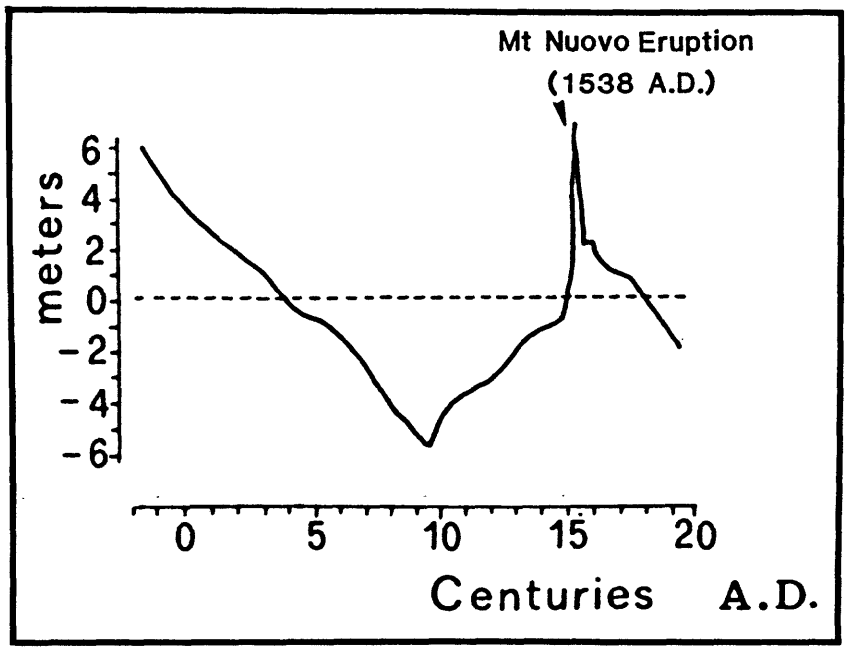

Figure 14. Vertical ground movements at the Phlegraean Fields since 0 A. D. inferred from sea level records at the Roman market place Serapeo (Yokoyama, 1971).

September 28, hot and cold water gushed from fissures along the newly-exposed shoreline, which began to subside on September 29 several hours before the eruption began. Violent explosions starting that evening accompanied the growth of Monte Nuovo scoria cone to a height of 100 m and diameter of 1000 m in 24 hours; earthquakes and volcanic explosions continued at least until October 6.

Caputo (1979) estimated that 4-5 m of uplift occurred in Pozzuoli during the 48 hours preceding the start of the Monte Nuovo eruption. The eruption was primarily Strombolian in character, producing about 0.03 km^3 of locally welded scoria, but eyewitness accounts also testify to heavy rains of mud and repeated "horizontally-directed base-surge explosions" (Rosi, et al., 1983, p. 281) that may have uprooted large trees in Pozzuoli, about 5 km from the vent. Twenty-four people were reported killed near the vent. Rosi et al. (1983) noted that Phlegraean Fields eruptions are usually more explosive than would be expected from the relatively mafic composition of their products (49-62% SiO_2), and cited evidence for strong magma/water interaction during most eruptions.

Current Activity

Steady subsidence of the caldera floor at 1.5 cm/yr resumed shortly after the Monte Nuovo eruption and continued at least until 1968 (Figure 15). In March 1969, a leveling survey along the coastal road of the Bay of Pozzuoli detected a broad uplift centered at Pozzuoli Harbor; the subsequent history of the uplift was tracked by 37(!) additional surveys through August 1974. Initially, uplift averaged about 5 mm/day, but the rate gradually slowed until September 1972, when the onset of subsidence was first noted. The maximum uplift measured from 1953 to December 1972 was 154 cm; adjustment for subsidence during 1953-68 (from tide gauge records) suggests that the true maximum uplift during 1969-72 was about 171 cm (Corrado et al., 1976).

The number of microearthquakes beneath Pozzuoli increased slightly during 1970-72, then decreased with the onset of subsidence (Figures 16 and 17). The energy release from these quakes was remarkably low for an active volcanic area; Corrado et al. (1976) reported that only a few shocks were felt in a limited area during 1970-71, and that no Phlegraean Fields earthquakes were recorded by low-gain seismometers 9-12 km from the epicenters.

The area subsided by about 30 cm during September 1972-August 1974, then remained relatively stable until uplift resumed abruptly in July 1982 (Figure 18). By mid-October 1983, the rate of uplift had increased to about 5 mm/day, and seismicity had increased to its highest level since the seismic network was installed in 1970 (Figure 19). The largest quake through December 1983 was a magnitude 4.0 event on September 9, 1983; the largest swarm so far included about 170 instrumentally recorded quakes on October 13, 1983. Even this mild seismic energy release has caused substantial damage to the pervasive "tuffa stone" construction in the area, and a mostly voluntary evacuation of about 70,000 Pozzuoli residents began on 11 October 1983.

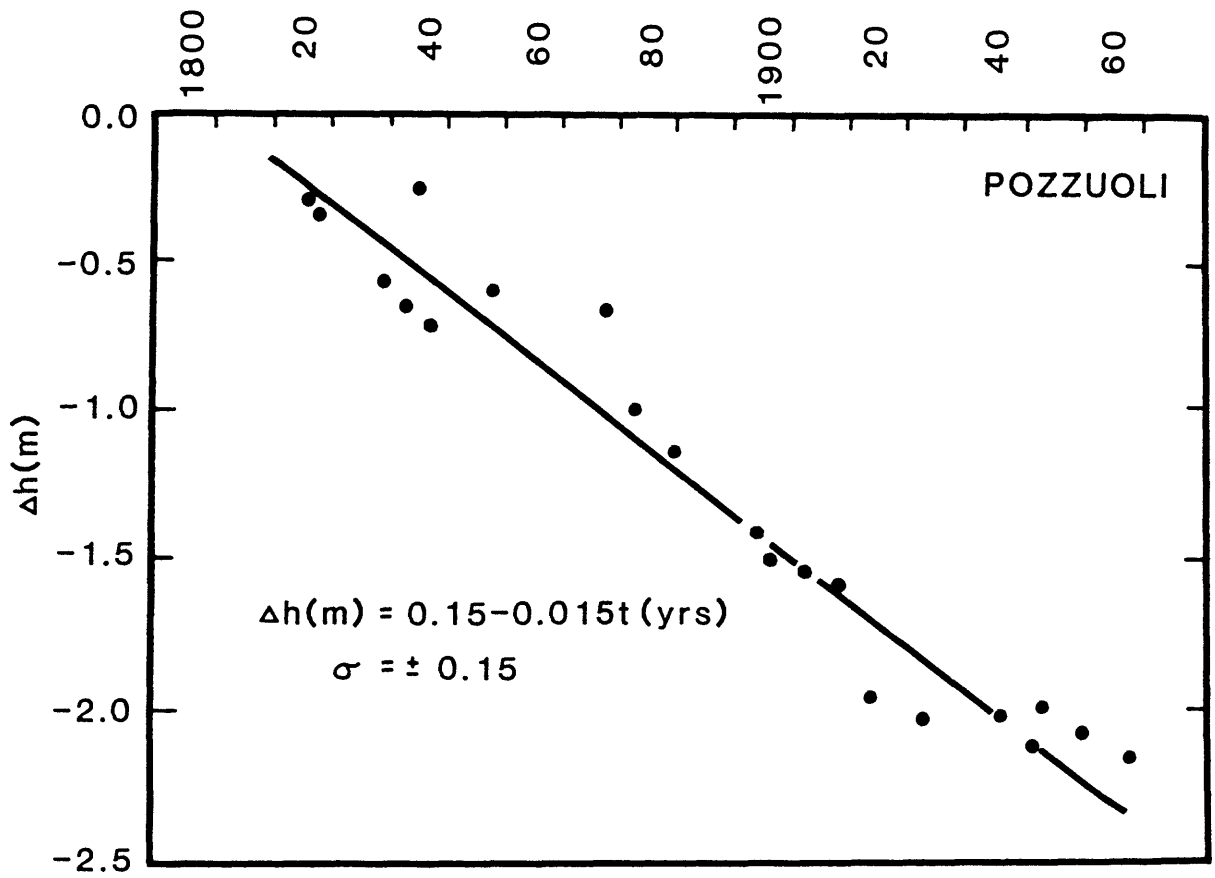

Figure 15. Record of Phlegraean Fields subsidence during 1800-1968 A. D., relative to mean sea level at the Serapeo. Unpublished data from G. Luongo and F. Barberi.

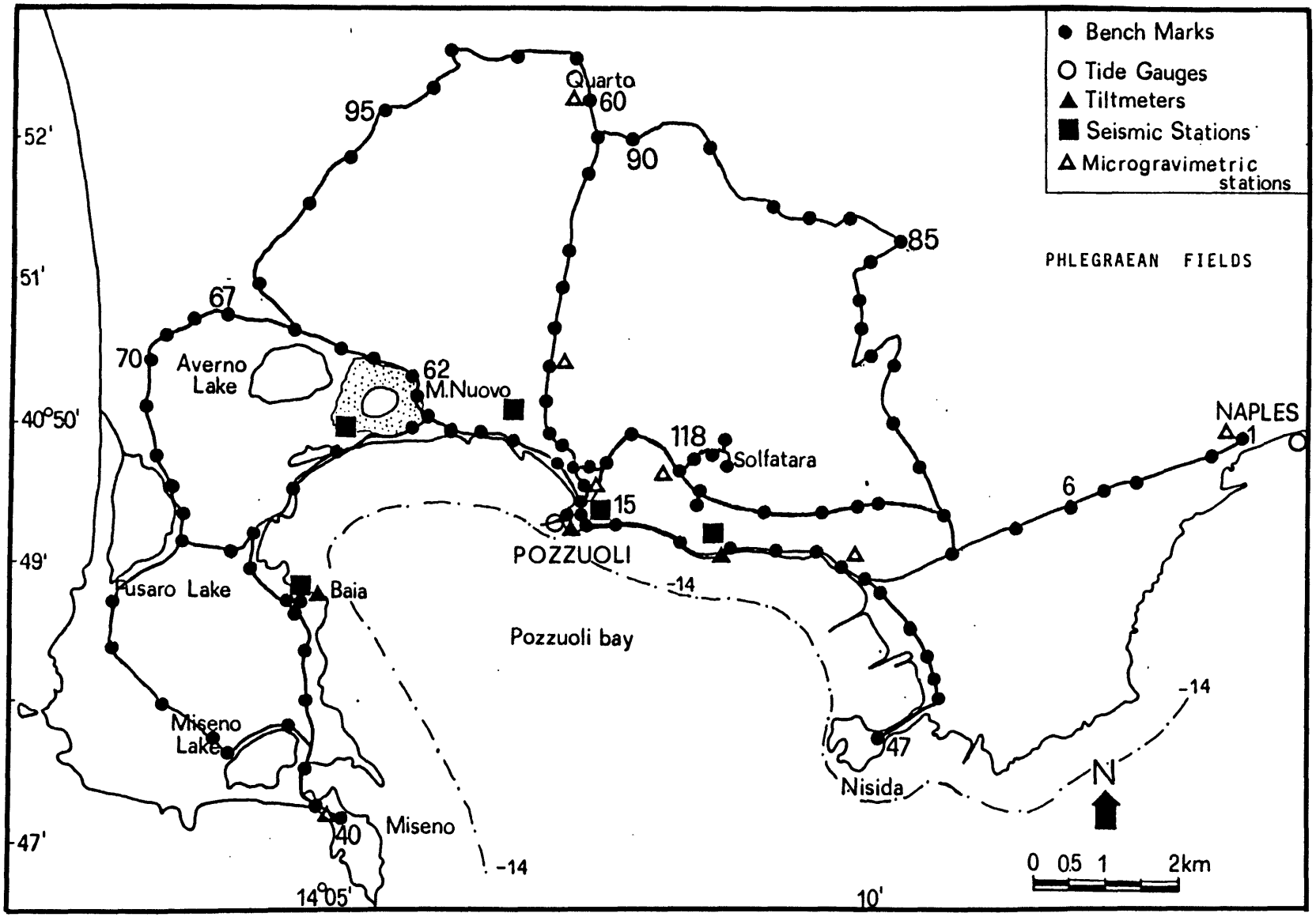

Figure 16. Monitoring network at the Phlegraean Fields, showing the locations of leveling routes, tide gauges (Bay of Pozzuoli and Bay of Naples), tiltmeters, seismometers, and gravity stations. Unpublished data from G. Luongo and F. Barberi.

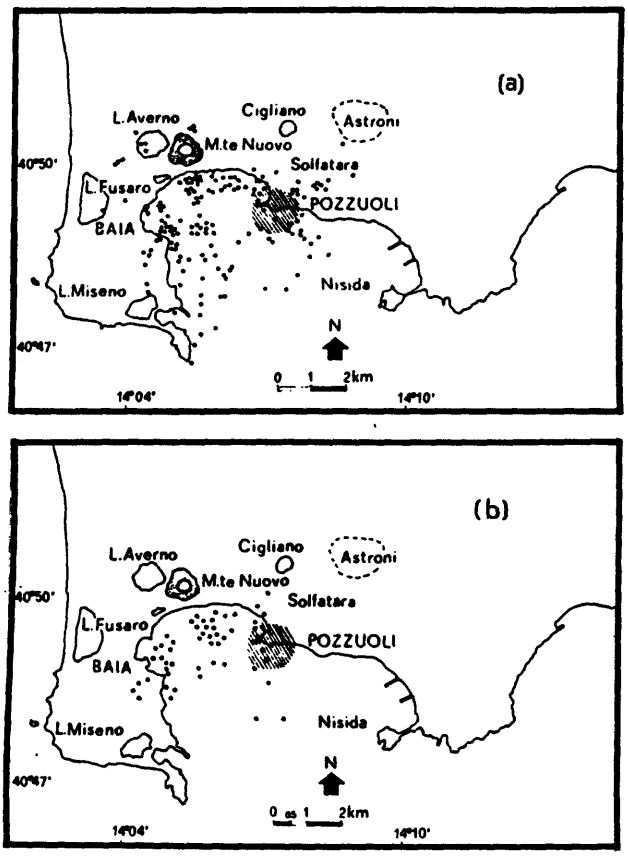

Figure 17. Earthquakes (dots) in the Phlegraean Fields during (a) 1970-October 1972 and (b) October 1972-1974, from Corrado et al. (1976). Most epicenters were located beneath the Bay of Pozzuoli, near the center of the caldera (see Figure 12 for location of caldera rim). Stippling indicates the approximate center of uplift during 1969-72.

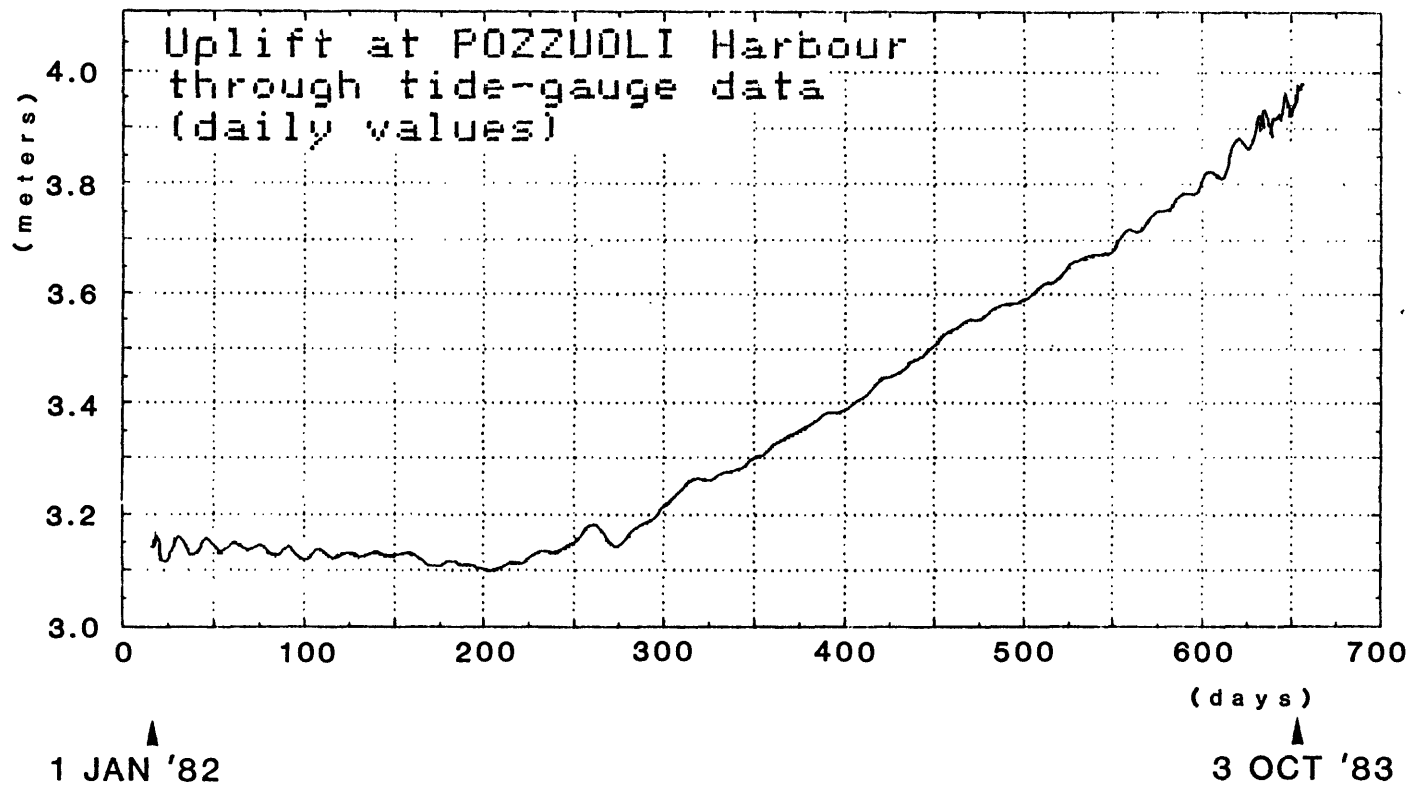

Figure 18. Tide gauge record from Pozzuoli harbor showing the rapid resumption of uplift in July 1982. Unpublished data from G. Luongo and F. Barberi.

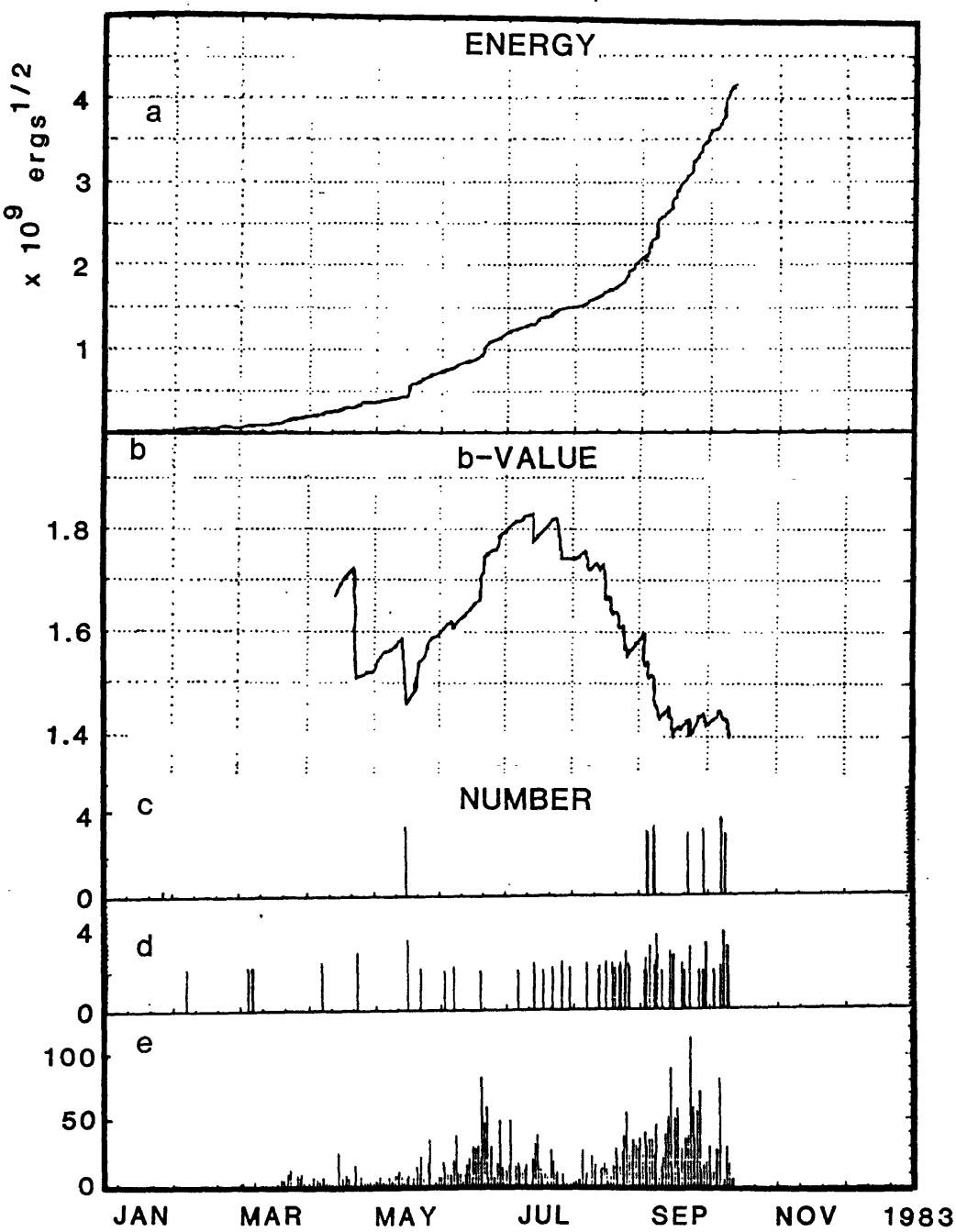

Figure 19. Earthquake activity at the Phlegraean Fields during January-September 1983: a) energy release; b) b-value; c) number of quakes larger than magnitude 3.0; d) number of quakes larger than magnitude 2.0; e) total number of recorded quakes. Unpublished data from G. Luongo and F. Barberi.

Uplift at Pozzuoli during January 1982-March 1984 totalled 140 cm, increasing the net uplift since 1969 to about 280 cm (G. Luongo and F. Barberi, written communication). Sporadic earthquake swarms and uplift of 2-4 mm/day were continuing as of March 1984. Seismic energy release during January-March 1984 was nearly as great as the cumulative energy release during 1983, although the increase did not begin until March 1983.

Leveling data fit to the Mogi (1958) model of elastic crustal deformation suggest that the source of the 1969-72 and 1982-present uplift lies about 3 km beneath Pozzuoli (Figure 20); hypocenters of associated earthquakes are scattered throughout the caldera, but are all less than 3 km deep. There has been no discernible migration of earthquakes either vertically or horizontally, and microgravity changes associated with the current uplift can be explained by observed elevation changes without invoking variations in subsurface mass distribution (G. Luongo and F. Barberi, written communication).

RABAUL

Much of the information presented in this section was provided by Peter Lowenstein and Chris McKee of the Rabaul Volcanological Observatory; their written and oral material was supplemented by Norm Banks and Tom Murray, who installed electronic tiltmeters and trilateration stations at Rabaul during November-December 1983.

Geologic History

Ancestral Rabaul volcano was a low shield with satellitic cones on its north, east, south, and northwestern flanks. Early basaltic volcanism produced lava flows and scoriae, but subsequent explosive activity deposited widespread andesitic, dacitic, and minor rhyolitic tephra (McKee et al., 1983).

Rabaul caldera at the east end of New Britain island (Figure 21) is a 9 km x 14 km elliptical depression breached on the southeast by Blanche Bay and flooded by the Bismarck Sea. Its walls rise 100 to 400 m above sea level, and its floor is a maximum of 295 m below sea level. At least 2 (possibly 3) stages of caldera formation were recognized by McKee (1981): 1) eruption of 20+ km^3 of dacite and collapse of an outer caldera about 3,500 yrs B. P.; 2) eruption of 11 km^3 of dacite and collapse of an inner caldera 1,400 yrs B. P.; and 3?) eruption of 1+ km^3 of dacite from the central caldera between 3,500 and 1,400 yrs B. P.

Eruptions continued at Rabaul following the 1,400 yrs B. P. caldera collapse, forming the volcanoes Rabalanakaia, Tavurvur, Sulfur Creek, Vulcan Island, and Vulcan (Figure 22). Dates of historic eruptions include 1767 (source vent unknown), 1791 (Tavurvur), 1850 (Sulfur Creek), 1878 (Vulcan Island, Tavurvur), 1937 (Vulcan, Tavurvur), and 1941-43 (Tavurvur). Each of these eruptions was relatively small; the largest was probably the 1937 Vulcan event which involved only about 0.3 km^3 of tephra but killed 507 people (Fisher, 1939; McKee, 1981; McKee et al., 1983; Lowenstein, 1982).

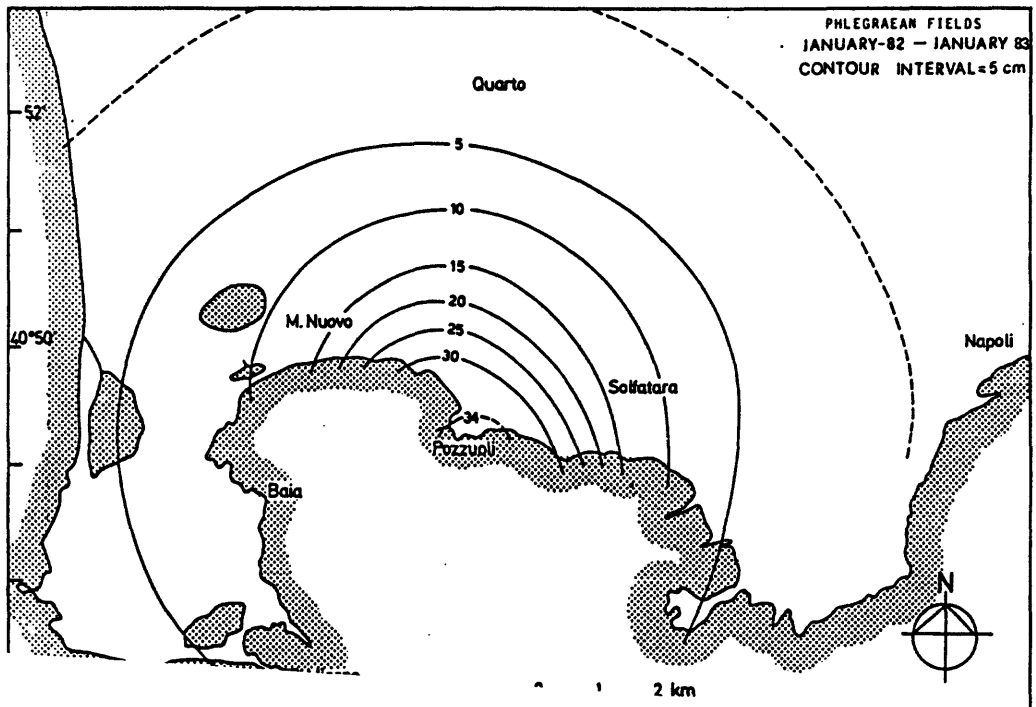

Figure 20a. Contour map of Phlegraean Fields uplift during 1982 repeated leveling surveys. Contour interval = 5 cm. Unpublishe[d] from G. Luongo and F. Barberi.

repeated leveling
from G. Luongo and F. Barberi.

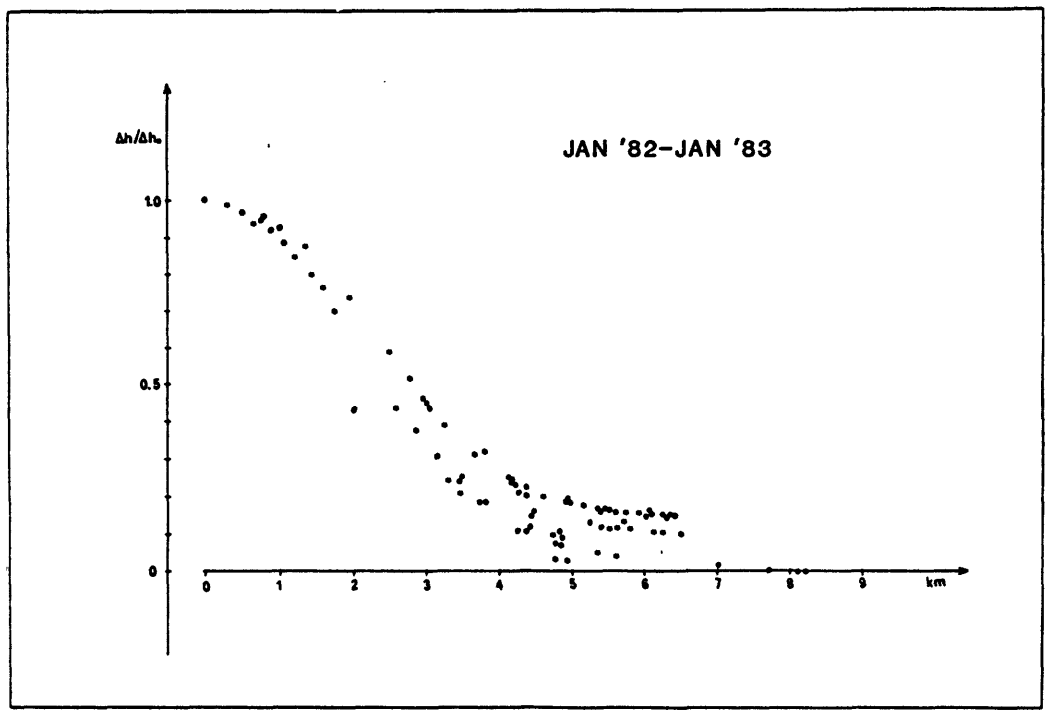

Figure 20b. Plot of normalized uplift versus lateral distance from the deformation center. The point-source elastic model of Mogi (1958) fit to these data suggests that the deformation source lies at about 3 km depth.

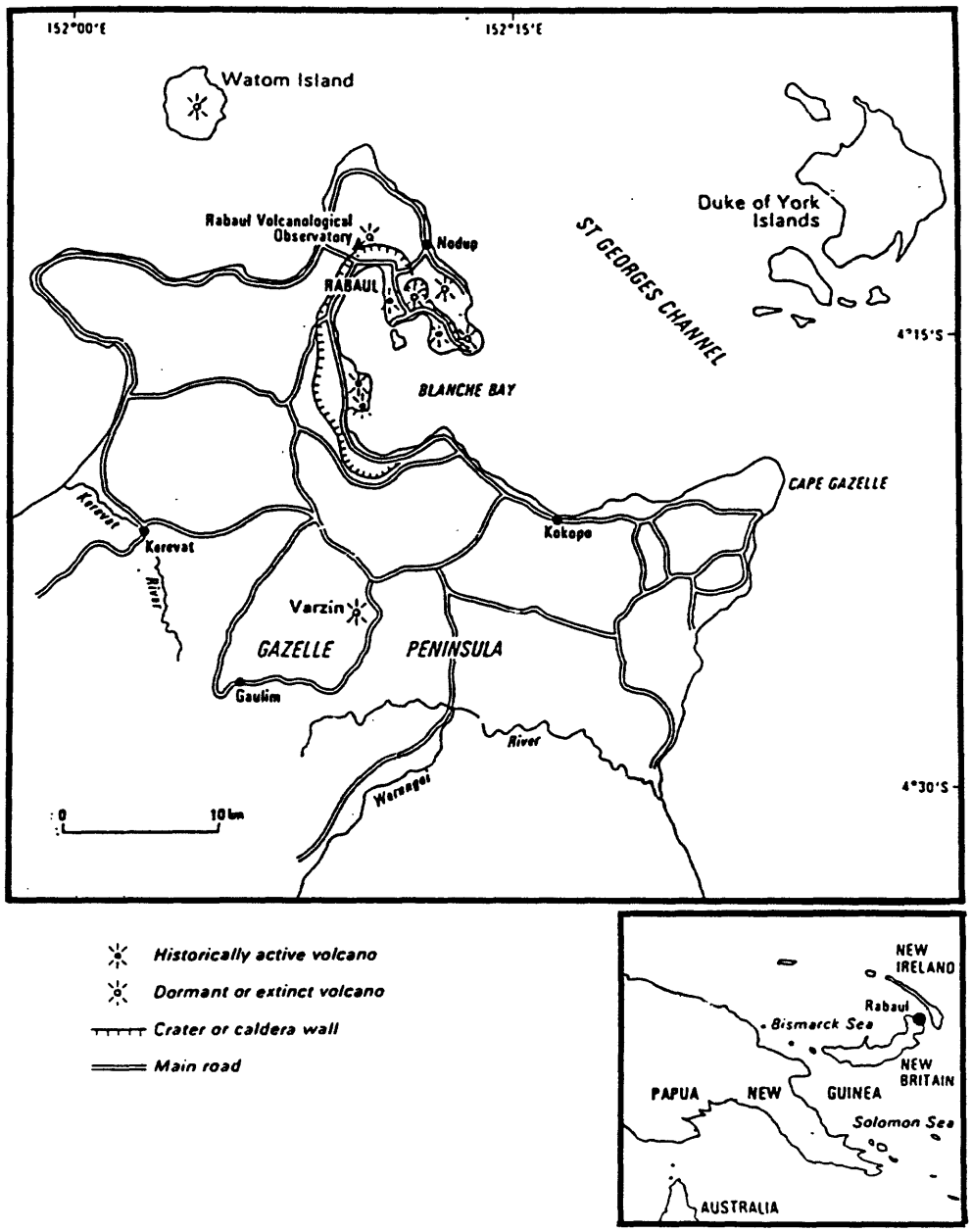

Figure 21. Northeast tip of New Britain island, showing Rabaul caldera breached by Blanche Bay (McKee et al., 1983). Note also the Rabaul Volcanological Observatory adjacent to the north part of the caldera rim.

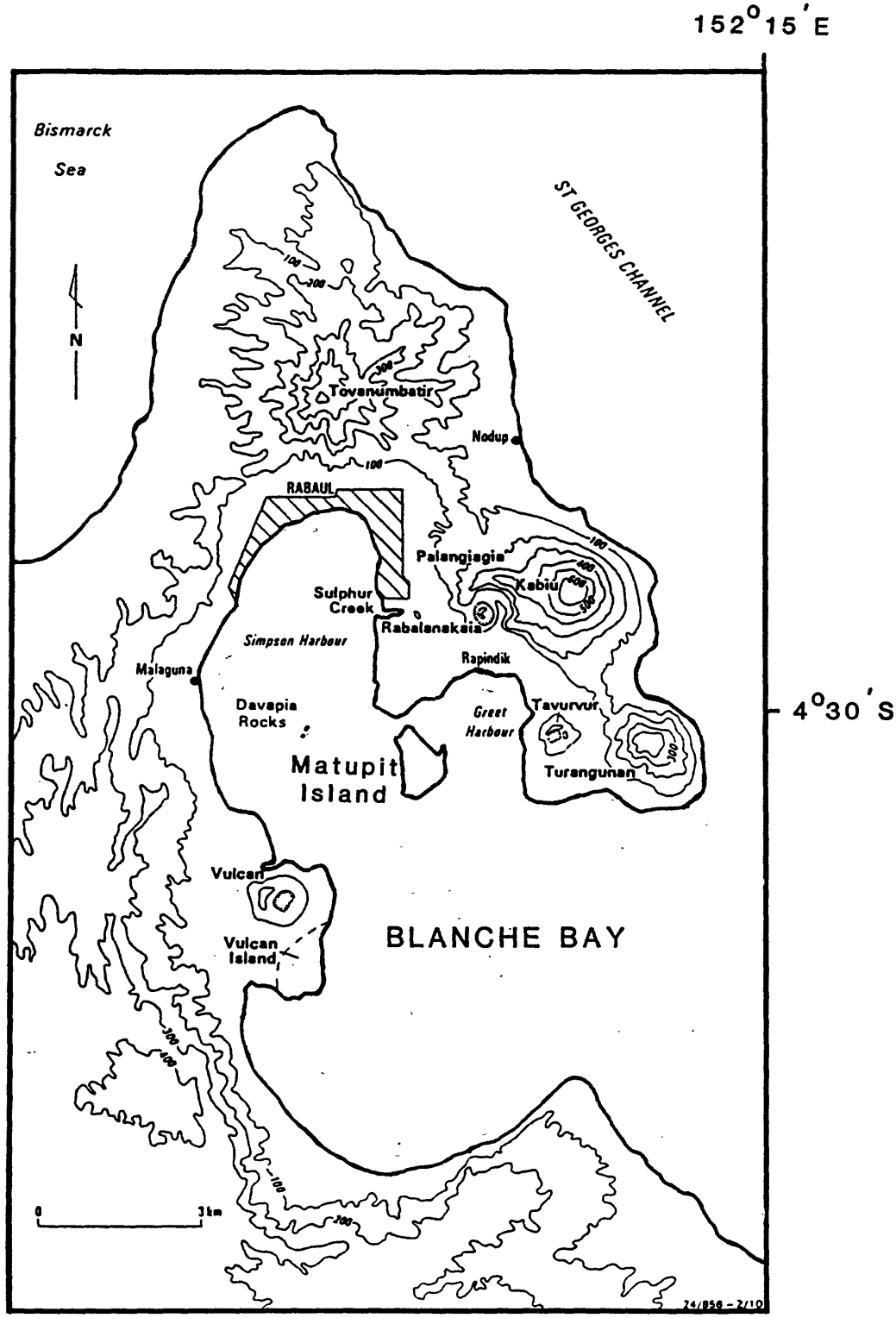

Figure 22. Topography and geography of Rabaul caldera, including intra-caldera and satellite volcanoes (McKee et al., 1983). Contours in meters.

The following report on the 1937 eruption at Rabaul is from Lowenstein (1982, pp. 13-15):

> "The only [recognized] precursors to the 1937 eruption were a swarm of earthquakes felt locally for a day or two before the start, and visible uplift of islets and reefs by up to 2 m 6-8 hrs before, in the vicinity of the subsequent Vulcan eruptive center...
>
> A ragged-edged column of black liquid-like ejecta about 10 m in diameter first rose about 12 m into the air, then eruption followed eruption, increasing in intensity until the column reached a height of about 7,500 m. There were continual noisy explosions and spectacular lightning effects. About 500 people were killed during this early activity. Some hours later, brief lulls in the eruption preceded the appearance of the crater rim above sea surface. For the rest of the night and all the next day the violence of the eruption was undiminished, and strong earth tremors continued. Before midnight on 29 May, the cone was estimated to be about 30 m high and by the following morning, about 180 m high. Dull red glows above the main crater and red incandescent ejecta were observed at night during this peak of activity and ash fell 240 km downwind from Rabaul.
>
> The intensity declined from 31 May and the eruption ceased by late 2 June, leaving a new cone standing about 230 m above sea level. Several subsidiary craters had apparently been active. The actual volume of pumice and ash produced was estimated to be about 0.3 km^3. Rabaul harbor was almost completely choked by pumice [it was possible to walk across], which took more than four months to drift away completely.
>
> Tavurvur volcano, situated on the opposite side of the harbor, also erupted vigorously during the Vulcan eruption... This activity lasted less than one day, and created a linear group of four vents trending northeast across the summit. No new magmatic material was ejected."

The early part of the 1937 Vulcan eruption was submarine and phreatomagmatic, but activity became subaerial within hours and a Plinian column developed which at times produced Peleean activity. Relatively minor phreatic activity at Tavurvur from June 1941 to December 1943 is the most recent eruptive activity at Rabaul; repose periods since 1767 have ranged from less than 1 year to 59 years.

A striking and worrisome aspect of the historic record at Rabaul is virtually simultaneous activity from vents on opposite sides of the caldera rim in 1878 and 1937. Clouds of vapor were seen rising from Blanche Bay during the 1878 eruption in a line between Vulcan Island and Tavurvur; in 1937 a series of about 5 explosions occurred near the northern end of Vulcan in a line extending towards Tavurvur (McKee et al., 1983). In 1878, simultaneous eruptions produced basalt at Tavurvur

and dacite at Vulcan Island; in 1937, a dacitic eruption at Vulcan was accompanied by phreatic explosions at Tavurvur.

These observations suggest that Rabaul caldera is underlain by a residual dacitic magma chamber that is episodically intruded by basalt from a deeper source, sometimes triggering dacitic eruptions at one site along the ring fracture and basaltic eruptions at another. Combined with the distribution of recent epicenters along most of the caldera rim (see below), this model suggests that the Rabaul ring fracture system may still be susceptible to high volume dacitic eruptions and additional caldera collapse.

Current Activity

Seismic surveillance at Rabaul began in 1940, but the record is relatively complete and uniform only since 1967. Most local earthquakes since 1967 have been short-period, volcano-tectonic events at depths of 0-6 km; much deeper earthquakes of unknown significance were first recognized in 1982. The level of seismicity beneath the caldera was relatively constant during 1967-71, with 20-100+ earthquakes typically recorded each month (Lowenstein and McKee, 1982).

Since late 1971, however, seismicity has progressively increased, as evidenced by numerous swarms of quakes at shallow depths beneath the caldera (Figure 23a). "These swarms typically last from about 10 minutes to several hours, and individual earthquakes may take place at such short intervals that their resolution on seismograms is prevented" (McKee et al., 1983, p. 23). The strongest earthquakes so far occurred during swarms in September-October 1980 (M_{max}=5.2), January-March 1982 (M_{max}=5.1), and March 1984 (M_{max}=5.1).

Seismicity increased dramatically in September 1983, when the number of recorded caldera quakes exceeded 2,000, more than twice the previous monthly high in March 1982 (Figure 24). The exponential increase that began in late August was punctuated by intense swarms near Tavurvur on September 13 and 19, 1983; the latter swarm included more than 600 instrumentally recorded earthquakes, with M_{max} =4.2. Background seismicity remained high following the September swarms, until additional swarms occurred in Rabaul Harbor on October 15 and 29, 1983. Each consisted of a few felt and several hundred instrumentally detected quakes; following the October 29 swarm, a stage 2 eruption alert was declared. According to a pre-determined alert sequence, stage 2 implies the possibility of an eruption within weeks to months, but does not require evacuation.

Additional swarms occurred on November 5 and 27, 1983, as background seismicity increased from 10 to 15 times the pre-August level. The November 27 swarm was the first since September 1983 to occur on the west side of the caldera, near Vulcan/Vulcan Island, and was tentatively interpreted as a readjustment to earlier swarms on the east side, near Tavurvur (P. Lowenstein, written communication).

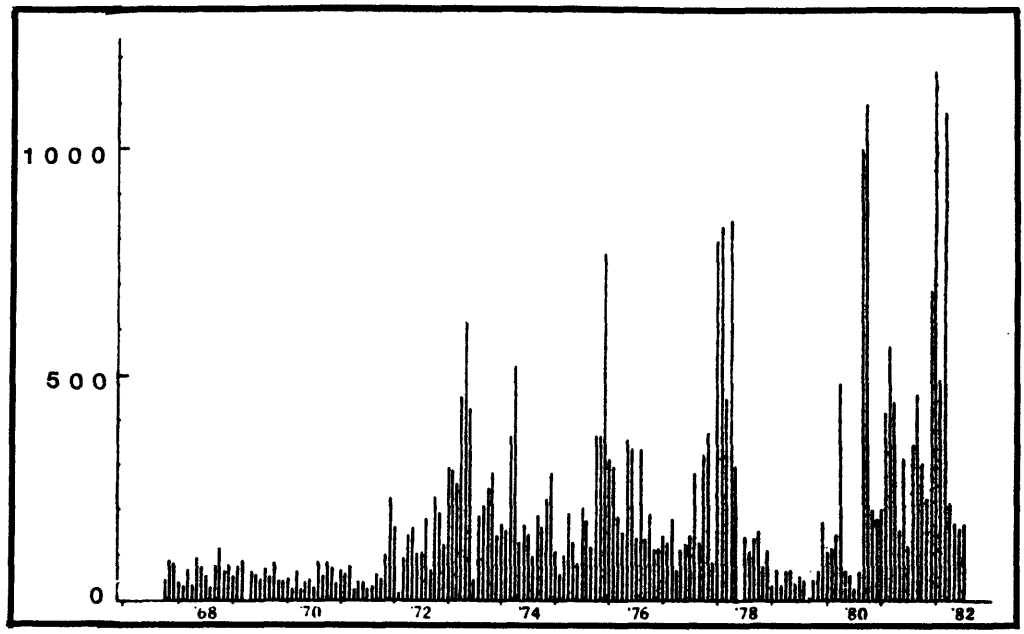

Figure 23a. Monthly number of earthquakes recorded at Rabaul caldera during 1967-82 from McKee (1982).

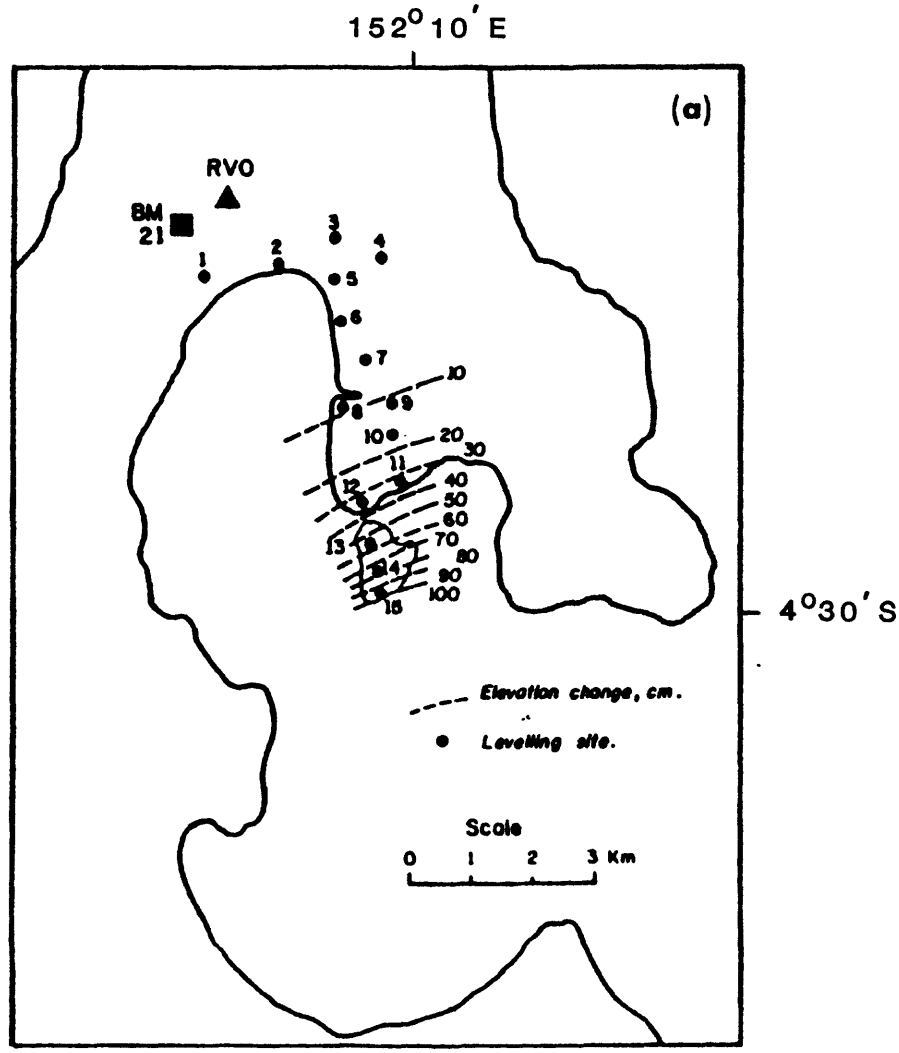

Figure 23b. Contours of uplift at Rabaul caldera during 1973-82 from McKee (1982); changes shown relative to stable BM 21 near the Rabaul Volcanological Observatory.

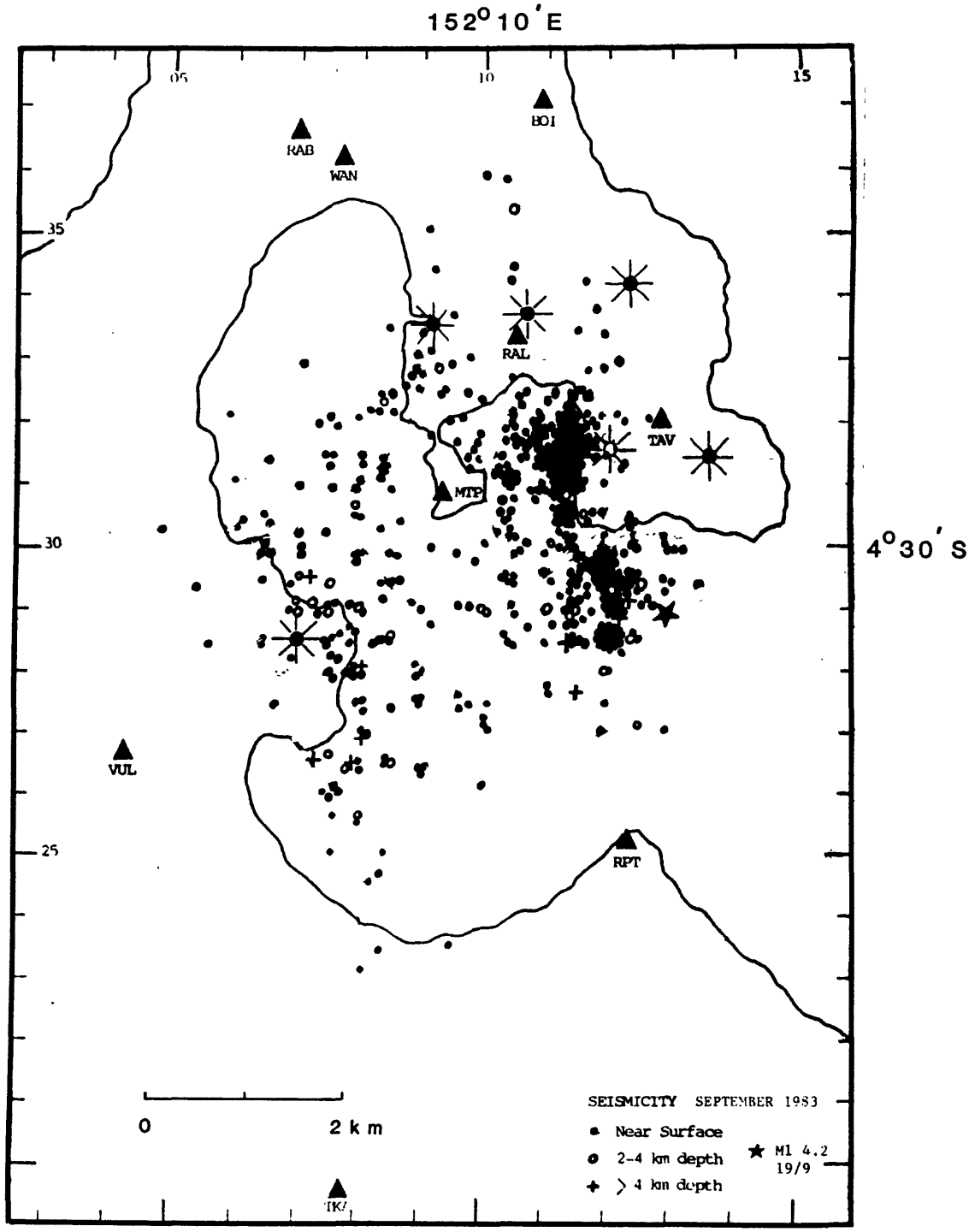

Figure 24. Distribution of earthquakes at Rabaul caldera during September 1983. Most events occurred during intense swarms on September 13 and 19. Triangles indicate seismic stations, sunbursts show post-collapse eruption centers near the caldera rim. Plot from Rabaul Volcanological Observatory Monthly Report, September 1983.

A flurry of volcanic earthquakes at Rabaul was apparently triggered by 2 M=6+ regional tectonic earthquakes on 20-21 December 1983. Monthly caldera earthquake counts during August-December 1983 were 330, 2130, 5200, 5700, and more than 7000, respectively. A large earthquake swarm on 15 January 1984 (M_{max}=4.9) was accompanied by 3 cm of uplift on the NE coast of Greet Harbor and 5 cm of uplift at the southern tip of Matupit Island*. Additional swarms occurred on 12 February, 17 February, 26 February, and 3 March 1984; the largest earthquake was a M=5.1 shock on March 3 (N. Banks, written communication).

The spatial distribution of earthquakes near Rabaul caldera during 1977-82 is shown in Figure 25; only about 10% of all earthquakes are sufficiently well-recorded (5 or more stations) to be accurately located. Most of the located events occurred within 2 km of the surface in two arcuate, inward-facing zones - one near the entrance to Blanche Bay, the other in the western part of the caldera. This distribution led McKee et al. (1983) to suggest that stress release was occurring along faults that define the rim of an inner caldera formed 1400 yrs. ago. Seismicity during 1983-early 1984 occurred in a 30 km^2 area within and between the arcuate zones shown in Figure 25 (N. Banks, written communication).

McKee et al. (1983) noted a close relationship between contemporary seismicity and recently active volcanoes along the caldera rim. The most notable of these is in the Vulcan Island/Vulcan area, and the same is true to a lesser degree at Tavurvur and Davapia Rocks. The zone of strongest seismicity is centered on a submerged conical edifice at the mouth of Blanche Bay. Caldera-wide distributions of historical eruptions and recent seismicity at Rabaul suggest that most of the caldera's ring fracture system is susceptible to failure; recent ground deformation has been more localized and helps to constrain likely eruption sites.

Techniques and instruments used to monitor ground deformation at Rabaul for the past decade include wet and dry tilt, leveling, gravimetry, and sea-level monitoring; electronic tiltmeters and a horizontal strain network were installed in November 1983. Leveling and microgravity surveys since 1973 from a stable benchmark near the Rabaul Volcanological Observatory to Matupit Island in the central caldera record progressive uplift of the island's southern shore by more than 100 cm (Figure 23b).

Dry tilt surveys since 1981 and data from a bubble tiltmeter near Tavurvur since 1972 confirm a center of uplift south of Matupit Island (Figure 26). Tilting has been most rapid near the southern shore of Matupit Island (4-8 μrad/month); application of the elastic Mogi (1958) model suggests a deformation source only 1-2 km beneath the caldera floor.

*Now connected to the mainland Gazelle Peninsula by a causeway.

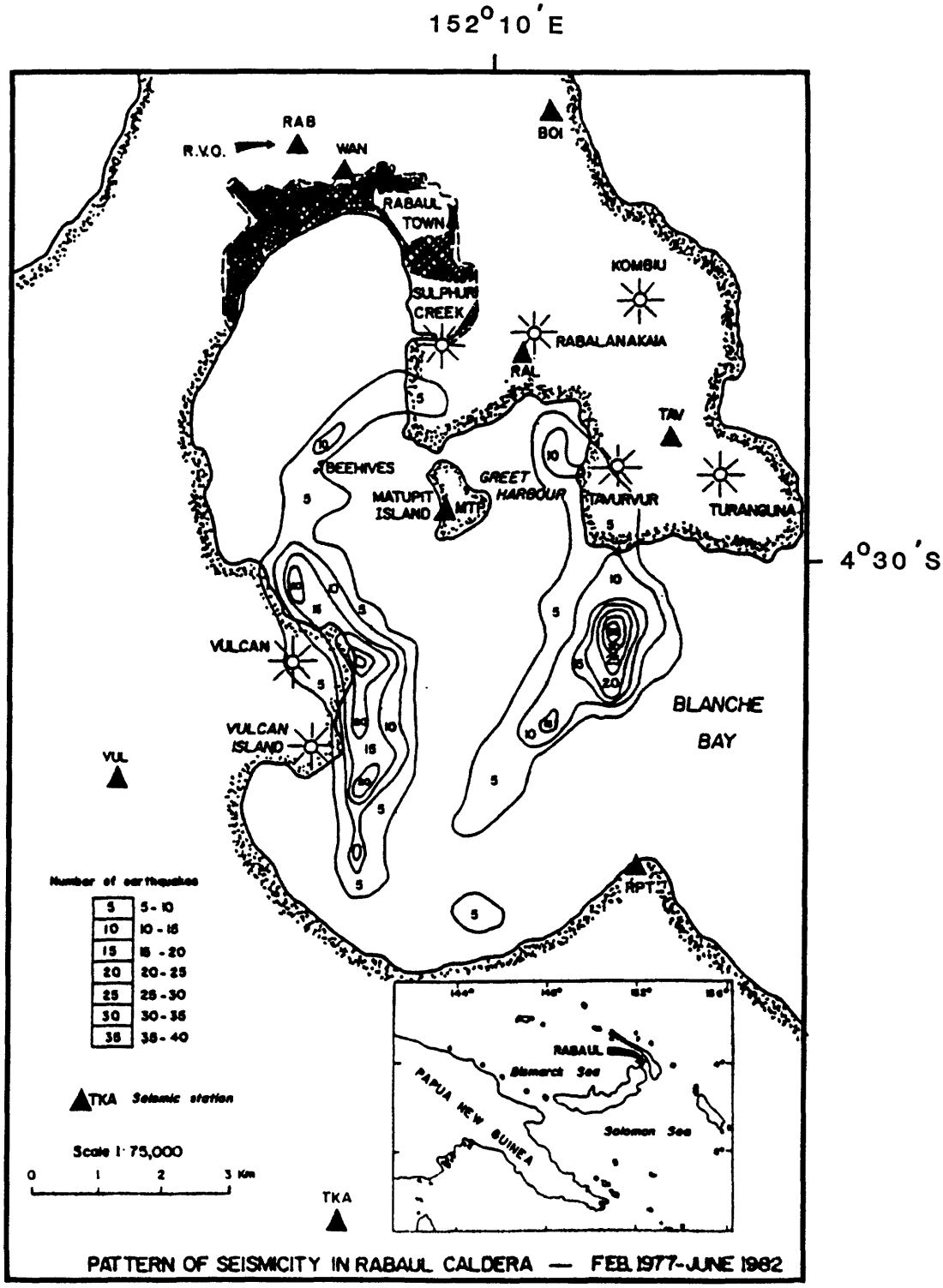

Figure 25. Distribution of seismicity in Rabaul caldera during February 1977-June 1982 from McKee (1982). Seismic stations are represented by triangles; volcanic centers by sunbursts.

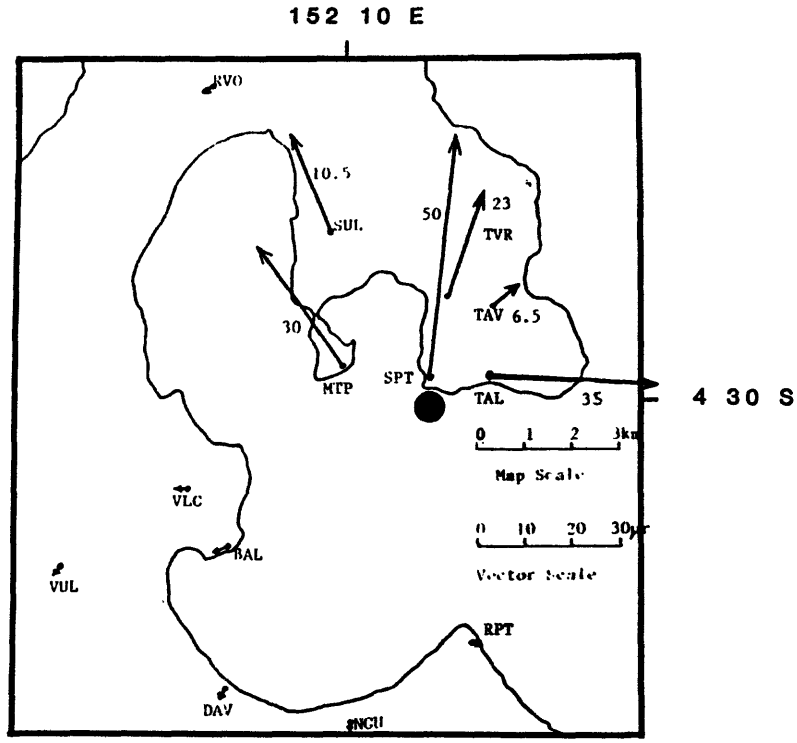

Figure 26a. Dry tilt changes at Rabaul caldera during September 1983, showing an inflation center (dot) southeast of Matupit Island (MTP).

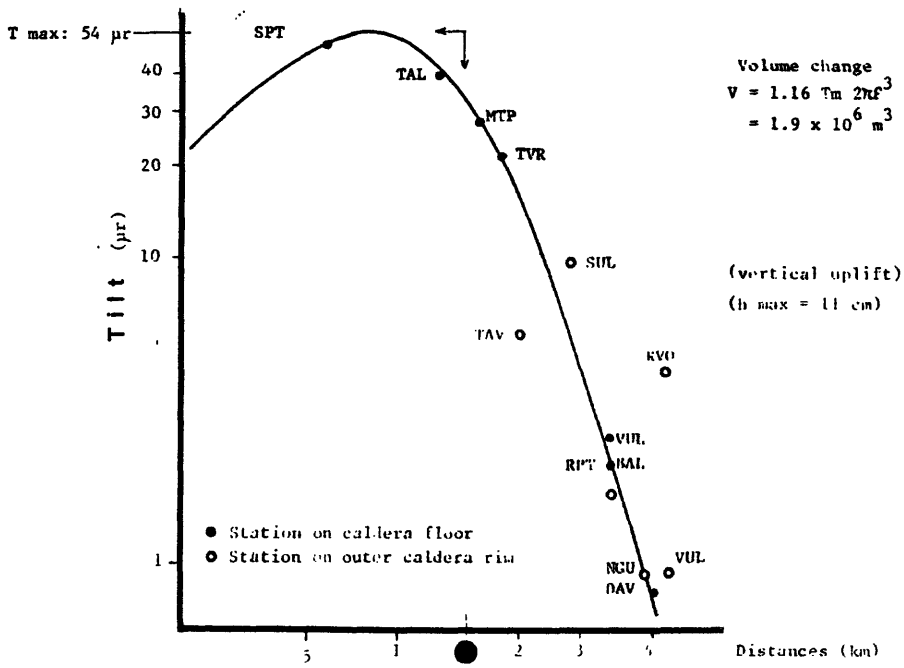

Figure 26b. Plot of tilt change versus distance from the deformation center, with solid line showing the result expected from intrusion of 2 x 10^6 m^3 of magma at 1.7 km depth beneath the dot in Figure 26a. Plots from Rabaul Volcanological Observatory Monthly Report, September 1983.

Accelerated uplift centered about 1.5 km south of Tavurvur was first detected by dry tilt measurements in early September 1983, soon after the onset of increasing seismicity in late August. A sharp tilt change of 49 μrad accompanied the September 19 earthquake swarm, and tilts of up to 20 μrad accumulated gradually before the October 29 swarm. The latter was accompanied by tilt changes of up to 40 μrad, and followed by an increase in the background tilt rate by about a factor of two. Ground cracks were first noted on the west flank of Tavurvur following the October 29 swarm. Inflationary tilt changes of 30 and 50 μrad accompanied the 15 January and 3 March 1984 earthquake swarms, respectively. Between earthquake swarms in early 1984, separate deformation centers near Vulcan and beneath Greet Harbor were inflating at 1-2 μrad/day.

McKee et al. (1983, p. 27) concluded that: "The cause of the apparent changes at Rabaul caldera is uncertain, but possibly the series of large tectonic earthquakes in the Solomon Sea in mid-1971 affected the roots of the volcano by acting as a trigger for the mobilization of deep-seated magma. The climax of this evolutionary trend may be an eruption." Subsequent events at Rabaul have served to underscore that possibility, as evidenced by the current stage 2 eruption alert.

DISCUSSION

A complete discussion of current unrest and its implications at any of the four calderas described here is beyond the scope of this paper. Instead, we highlight some of the similarities and differences among the calderas, draw some inferences about the processes responsible for unrest, and comment briefly on the relative likelihood of near-term eruptions.

Comparative Statistics

Of the calderas studied, Yellowstone is the largest (85 km x 45 km, 1,000 km^3 erupted during collapse) followed by Long Valley (32 km x 17 km, 600 km^3), the Phlegraean Fields (13 km x 11 km, 80 km^3) and Rabaul (14 km x 9 km, several tens of km^3). Ranked by age, the order reverses: Rabaul (caldera formation 3,500 yrs B. P., most recent eruption 41 yrs B. P.), Phlegraean Fields (35,000 yrs B. P., 445 yrs B. P.), Long Valley (700,000 yrs B. P., 550 yrs B. P.), and Yellowstone (600,000 yrs B. P., 75,000 yrs B. P.). Small calderas form more often and evolve more quickly than large calderas (Smith, 1979); the 4 calderas described here span a large range in size and age, and are probably not anomalous in either respect.

Statistics concerning the calderas' residual magma reservoirs are less precise, but there is ample geophysical evidence at each caldera for the existence of at least some partial melt. At Yellowstone and Long Valley, geophysically anomalous zones tens of kilometers wide and 5-10 km deep probably contain residual rhyolite (72-76% SiO_2); the inferred sources of contemporary uplift lie within these residual magma reservoirs at about 10 km depth. The magma reservoirs at the Phlegraean Fields and

Rabaul are much smaller (less than 10 km wide), shallower (1-3 km deep), and less silicic (62-66% SiO_2); ground deformation has accordingly been more localized at these calderas than at Yellowstone or Long Valley.

The Phlegraean Fields reservoir is probably the shallowest and most mafic (SiO_2 = 62%) of the group, which may partly account for that caldera's long history of dramatic ground movements. However, some other circumstance may contribute to long-term subsidence at the Phlegraean Fields, or perhaps subsidence at comparable calderas such as Rabaul has gone unnoticed owing to the relative shortness of historic records.

Processes of Unrest

Recent rates of ground deformation at the Phlegraean Fields and Rabaul are significantly greater than at Long Valley or Yellowstone, but seismic energy release has been greater at Yellowstone/Hebgen Lake and Long Valley. In fact, a surprising aspect of recent unrest at the Phlegraean Fields is the modest seismic energy release that has accompanied 2.5 m of uplift in little more than a decade. A possible explanation is that smaller, less viscous systems can erupt with less seismic disruption to the surrounding crust than larger, more viscous systems.

It is interesting to note that most large earthquakes at Yellowstone and Long Valley have occurred outside those calderas, whereas most earthquakes at Rabaul and the Phlegraean Fields have occurred inside the calderas. Rabual and the Phlegraean Fields have shallower magma chambers, have erupted more recently, and have experienced more rapid uplift than Yellowstone or Long Valley. The contribution of magmatic processes to recent unrest is therefore less ambiguous at Rabaul and the Phlegraean Fields than at Long Valley or Yellowstone. High rates of seismic energy release in tectonically active areas outside Yellowstone and Long Valley suggests that recent unrest at those calderas may involve a magmatic response to regional tectonic processes (Newhall, Dzurisin, and Mullineaux, 1984). Relative to the Phlegraean Fields and Rabaul, Yellowstone and Long Valley are much larger, older, and presumably more complex systems where magmatism is more closely linked to regional tectonism. For this reason, total seismic energy release alone is not a reliable indicator of near-term eruptive potential at large calderas.

Eruptive Potential

The facts and inferences listed above lead us to believe that the Phlegraean Fields and Rabaul are currently the world's most dangerous calderas. Activity has intensified at both calderas recently, and both pose a significant threat to heavily populated areas. The Phlegraean Fields caldera threatens a larger human population and may pose a more serious evacuation problem. However, Rabaul is of equal or greater concern for the following reasons: 1) activity there has progressively intensified for more than a decade, whereas Phlegraean Fields activity has been episodic; 2) Tavurvur last erupted 41 years ago, Monte Nuovo 445 yrs ago; 3) the 1937 Vulcan eruption involved 0.3 km^3 of juvenile material, the Monte Nuovo eruption produced an order of magnitude less;

and 4) at Rabaul, multiple caldera collapses in the recent past and simultaneous historic eruptions from widely separated parts of the ring fracture system raise the possibility of additional caldera collapse in the foreseeable future.

Long Valley has experienced less uplift but more seismic energy release than Rabaul or the Phlegraean Fields. The Inyo system produced eruptions within Long Valley caldera only 550 years ago, but the Long Valley magma chamber has not been tapped for about 50,000 years. These facts combined with the current low rates of ground deformation and seismic energy release at Long Valley suggest to us that the near-term eruption probability there is significantly less than at Rabaul or the Phlegraean Fields. Yellowstone caldera last erupted 75,000 years ago and uplift there has been steady and slower than at Long Valley, implying a correspondingly lower probability of eruption in the near term.

A critical element of the Long Valley situation which is difficult to assess by analogy with other calderas is the potential role of the Inyo magmatic system in future eruptions within or near Long Valley caldera. The Inyo system has fed eruptions inside Long Valley caldera as recently as 550 years ago, and future interactions between the Inyo and Long Valley magmatic systems cannot be discounted. The residual Bishop chamber was last tapped about 50,000 yrs ago, roughly 100 times the interval since the last Inyo eruptions. The apparent cause of recent uplift at Long Valley is expansion of the residual Bishop magma chamber, but the presence of recent Inyo vents inside the caldera is also an important factor to be consisdered in volcanic hazards assessments for the Long Valley area (Miller et al., 1982).

We conclude that Rabaul and the Phlegraean Fields are each more likely to erupt in the foreseeable future than is Long Valley; an eruption at Yellowstone is much less likely. Thus, Rabaul and the Phlegraean Fields currently provide the best opportunities in the world to study processes in large silicic magma systems that could plausibly lead to eruptions in our lifetimes. Yellowstone provides an excellent opportunity to study unrest that will probably not lead to an eruption in the near term. In summary, unrest at Long Valley remains a legitimate concern that can be addressed in part by a comparative study of similar volcanic centers, in conjunction with a comprehensive monitoring program.

ACKNOWLEDGEMENTS

The authors are grateful for helpful reviews by W. A. Duffield and C. D. Miller, and for permission to use unpublished data from G. Luongo, F. Barberi, P. Lowenstein, and C. McKee.

REFERENCES

Armienti, P., Barberi, F., Bizouard, H., Clocchiatti, R., Innocenti, F., Metrich, N., Rosi, M., and Sbrana, A., 1983. The Phlegraean Fields: magma evolution within a shallow chamber, J. Volc. and Geotherm. Res., v. 17, no. 1/4, p. 289-312.

Bailey, R. A., Dalrymple, G. B., and Lanphere, M. A., 1976. Volcanism, structure, and geochonology of Long Valley caldera, Mono county, California, J. Geophys. Res., v. 81, no. 5, p. 725-744.

Caputo, M., 1979. Two thousand years of geodetic and geophysical observation in the Phlegraean Fields near Naples, Geophys. J. R. Astr. Soc., v. 56, p. 319-328.

Christiansen, R. L., 1983. The Quaternary and Pliocene Yellowstone Plateau Volcanic Field of Wyoming, Idaho, and Montana, U. S. Geol. Surv. Prof. Paper 729- , in press.

Christiansen, R. L., 1984. Postcaldera evolution and current activity of the Yellowstone caldera, this volume.

Corrado, G., Guerra, I., Lo Bascio, A., Luongo, G., and Rampoldi, R., 1976. Inflation and microearthquake activity of Phlegraean Fields, Italy, Bull. Volcanol., v. 40-3, p. 1-20.

Denlinger, R. P., and Riley, F., 1983. Deformation of Long Valley caldera, Mono County, California between 1975 and 1982, J. Geophys. Res., in press.

Eaton, G. P., Christiansen, R. L., Iyer, H. M., Pitt, A. M., Mabey, D. R., Blank, H. R. Jr., Zietz, I., and Gettings, M. E., 1975. Magma beneath Yellowstone National Park, Science, v. 188, p. 787-796.

Fisher, N. H., 1939. Geology and volcanology of Blanche Bay and the surrounding area, New Britain, Territory of New Guinea Geological Bull. 1, 68 pp.

Hermance, J. F., 1983. The Long Valley/Mono Basin volcanic complex in eastern California: Status of present knowledge and future research needs, Rev. Geophys. and Space Phys., v. 21, no. 7, p. 1545-1565.

Hill, D. P., 1976. Structure of Long Valley caldera, California, from a seismic refraction experiment, J. Geophys. Res., v. 81, no. 5, p. 745-753.

Julian, B. R., 1983. Mechanisms of earthquakes near Long Valley caldera, California: Evidence for dike injection, Nature, in press.

Julian, B. R., and Sipkin, S. A., 1983. Earthquake processes in the Long Valley caldera area, California, EOS Trans. Am. Geophys. Union, v. 64, no. 45, p. 890.

Lowenstein, P. L., 1982. Problems of volcanic hazards in Papua New Guinea, Geological Survey of Papua New Guinea Report 82/7, 61 pp.

Lowenstein, P. L. and McKee, C. O., 1982. Rabaul caldera, SEAN Bulletin, v. 7, no. 8, p. 9-13.

McKee, C. O., Johnson, R. W., Lowenstein, P. L., Riley, S. J., Blong, R. J., de Saint Ours, P., and Talai, B., 1983. Rabaul caldera, Papua New Guinea: Volcanic hazards and eruption contingency planning, Geological Survey of Papua New Guinea Report 83/17, 38 pp. (submitted to J. Volcanology and Geotherm. Res.)

McKee, C. O., 1981. Recent eruptive history of the Rabaul volcanoes, present volcanic conditions, and potential hazards from future eruptions, Geological Survey of Papua New Guinea Report 81/5, 16 pp.

Miller, C. D., 1983. Chronology of Holocene eruptions at the Inyo volcanic chain, California, EOS Trans. Am. Geophys. Union, v. 64, no. 5, p. 900.

Miller, C. D., Mullineaux, D. R., Crandell, D. R., and Bailey, R. A., 1982. Potential hazards from future volcanic eruptions in the Long Valley-Mono Lake area, east-central California and southwest Nevada - A preliminary assessment, U. S. Geological Survey Circ. 877, 10 p.

Mogi, K., 1958. Relation of the eruptions of various volcanoes and the deformations of the ground surfaces around them, Bull. Earthquake Res. Inst., Tokyo Univ., v. 36, p. 99-134.

Newhall, C. G., Dzurisin, D., and Mullineaux, L. S., 1984. Historical unrest at large Quaternary calderas, this volume.

Pelton, J. R., and Smith, R. B., 1982. Contemporary vertical surface displacements in Yellowstone National Park, J. Geophys. Res., v. 87, no. B4, p. 2745-2761.

Pelton, J. R., and Smith, R. B., 1979. Recent crustal uplift in Yellowstone National Park, Science, v. 206, p. 1179-1182.

Rosi, M., Sbrana, A., and Principe, C., 1983. The Phlegraean Fields: structural evolution, volcanic history, and eruptive mechanisms, J. Volc. and Geotherm. Res., v. 17, no. 1/4, p. 273-288.

Ryall, A., and Ryall, F., 1981a. Attenuation of P and S waves in a magma chamber in the Long Valley caldera, California, Geophys. Res. Lett., v. 8, no. 6, p. 557-560.

Ryall, A., and Ryall, F., 1981b. Spatial-temporal variations in seismicity preceding the May 1980, Mammoth Lakes, California, Earthquakes, Bull. Seis. Soc. Am., v. 71, no. 3, p. 747-760.

Ryall, A. S., and Ryall, F. D., 1983. Increased potential for a major earthquake in the White Mountains seismic gap, California and Nevada, Bull. Seis. Soc. Am., in press.

Savage, J. C., and Clark, M. M., 1982. Magmatic resurgence in Long Valley cladera, California: Possible cause of the 1980 Mammoth Lakes earthquakes, Science, v. 217, p. 531-533.

Savage, J. C., Estrem, J. E., and Castle, R. O., 1983. Uplift across Long Valley caldera, California, 1975-1983, in press.

Savage, J. C., and R. S. Cockerham, 1983. Earthquake swarm in Long Valley caldera, California, January 1983: Evidence for dike intrusion, submitted to J. Geophys. Res.

Smith, R. L., 1979. Ash-flow magmatism, in Chapin, C. E. and Elston, W. E., eds., Geol. Soc. Am. Special Paper 180, Ash-Flow Tuffs, p. 5-27.

Smith, R. B., and Braile, L. W., 1982. Crustal structure and evolution of an explosive silicic volcanic system at Yellowstone National Park, Wyoming Geological Association 33rd Annual Field Conference Guidebook, Geology of Yellowstone Park area, Mammoth Hot Springs, Wyoming, September 15-18, 1982, p. 233-250.

Steeples, D. W., and Iyer, H. M., 1976. Low-velocity zone under Long Valley as determined from teleseismic events, J. Geophys. Res., v. 81, no. 5, p. 849-859.

Trimble, A. B., and Smith, R. B., 1975. Seismicity and contemporary tectonics of the Hebgen Lake-Yellowstone Park region, J. Geophys. Res., v. 80, no. 5, p. 733-741.

Wallace, T., 1984. A re-examination of the moment tensor solutions of the 1980 Mammoth Lakes earthquakes, this volume.

Yokoyama, I., 1971. Pozzuoli event in 1970, Nature, v. 229, p. 532-533.

IMPLICATIONS OF SILICIC VENT PATTERNS FOR THE PRESENCE OF LARGE CRUSTAL MAGMA CHAMBERS

Charles R. Bacon
U. S. Geological Survey
345 Middlefield Road
Menlo Park, California 94025

for Long Valley Red Book

Abstract. On the basis of the distribution of silicic vents, many volcanic fields can be grouped with (1) igneous systems that may be small and whose eruptions are controlled by regional tectonics, (2) those that probably include sizable crustal magma bodies, or (3) relatively small-volume systems that are transitional between 1 and 2. Linear vent patterns that are aligned normal to the regional least principal stress (σ_3) commonly are associated with absence of evidence for large shallow magma bodies. The Coso volcanic field and the Inyo-Mono domes in California and the South Sister area in Oregon are examples of such systems. The 1960 dacitic fissure eruption at Cordón Caulle in southern Chile evidently is linked to stress relaxation associated with the great earthquake that occurred 48 hours before the eruption began. Large shallow magma chambers are thought to perturb the local stress field so that areal patterns of silicic vents are diffuse, radial, or arcuate. Such systems may erupt great volumes of pyroclastic material catastrophically and produce large calderas. Well preserved examples of late precaldera leaks of silicic magma occur at Long Valley, California, and Mount Mazama (Crater Lake), Oregon. Other possible examples are noted. Some of these, those which formed calderas smaller than Crater Lake, apparently were preceded by silicic eruptions from aligned vents. Bearing in mind that there exists a transitional group between tectonically-controlled small systems and very large magma chambers, vent distributions can be useful in evaluating potential volcanic hazards for silicic volcanic fields.

INTRODUCTION

The distribution of silicic vents in volcanic fields reflects the areal extent of subjacent magma reservoirs and the stress field in roof rocks at the time of eruption. Interpretation of vent patterns is based on the relation between stress and dike orientation [Anderson, 1936; Nakamura, 1977; Pollard, et al., 1984] and on observations of zonation of large crustal igneous systems and their evolution [Smith and Shaw, 1975; Smith, 1979; Hildreth, 1981]: (1) dikes that feed volcanic eruptions tend to be oriented normal to the least principal compressive stress (σ_3), parallel to the maximum horizontal compressive stress; (2) large volume silicic eruptions occur where igneous activity has been focused for long periods; (3) virtually all differentiated magmas capable of eruption are ultimately underlain by basaltic magma, which provides the heat source to maintain crustal magma reservoirs; (4) in such systems, basaltic magma is unlikely to reach the surface within the area of ongoing silicic volcanism; and (5) large silicic systems have long histories, on the order of 10^4-10^7 yr., and may experience multiple cycles of differentiation, eruption, waxing, and waning. In the present interpretation, vent distribution is used to distinguish between silicic volcanic fields which probably are underlain by large shallow chambers and those which may be fed by deep and(or) small reservoirs. A transitional group of moderate-volume systems (e.g., Krakatau) is characterized by linear arrays of precaldera silicic vents, followed by comparatively small, but catastrophic, caldera-forming eruptions. Examples of each of the three groups are presented, many of which were recognized with the help of the compilation of Newhall, et al. [1984].

VENT PATTERNS

Linear arrays of coeval volcanic vents are fed by dikes whose orientation in an homogeneous medium is perpendicular to the least principal compressive stress. Dikes locally may follow preexisting fractures, particularly in the near-surface environment, if orientations are appropriate [Pollard, et al., 1984]. Some eruptions may initiate from pipe-like fingers of dikes at sites of structural weakness; this effect should not be confused with the growth of cylindrical conduits from dikes owing to local perturbations in the magma flow regime, as described by Delaney and Pollard [1981]. The degree to which coeval vents tend to be aligned in a particular volcanic field is related to the difference between horizontal principal stresses. Vent alignments commonly define the orientation of maximum horizontal compressive stress in tectonically active regions [Nakamura, 1977]. A large shallow magma body beneath a volcanic field perturbs the tectonic stress field and promotes radial, arcuate, or diffuse vent patterns. The existence of such patterns thus can be used to infer the presence of crustal magma bodies, although linear vent patterns may not necessarily rule out sizable magma chambers.

SILICIC VOLCANIC FIELDS WITH LINEAR ARRAYS OF VENTS

Linear vent patterns are characteristic of many silicic volcanic fields, few of which have been studied geophysically. Evidence for large or shallow magma chambers generally is absent.

Tectonic control of eruptions near Puyehue volcano

Dacitic fissure eruptions northwest of Puyehue volcano at Cordón Caulle in southern Chile appear to be closely linked with major tectonic events. Beginning 48 hours after the main shock of the great 1960 Chilean earthquake

(M_S = 8.5) and about 300 km southeast of the epicenter, lava was erupted from 28 crater pits aligned WNW along more than 14 km of new fissures [Katsui and Katz, 1967]. Plafker [1972] showed that most of the tectonic deformation accompanying the earthquake occurred between the trench and the volcanic chain: Vertical movements were characterized by a broad asymmetric downwarp elongate parallel to the volcanic chain, with flanking zones of marked uplift on the seaward side and minor, possibly local, uplift on the landward side; horizontal displacements involved shifts in a generally seaward direction and transverse tensile strains aross the zone of subsidence. These observations are consistent with the general model of Nakamura and Uyeda [1980], in which σ_3 changes from vertical orientation near a convergent plate boundary to horizontal near the volcanic front. Although Plafker [1972] indicates that horizontal extension accompanying the 1960 earthquake was in a WNW direction at the latitude of the eruption (parallel to the trend of vent alignment) the pattern of deformation suggests that the eruption took place because coseismic extension and subsidence west of the volcanic chain relieved accumulated strain, causing a decrease in horizontal compressive stress sufficient to allow a dike to propagate upward from a silicic magma reservoir. Apparently the dike took 48 hours to reach the surface.

The WNW azimuth of the main fissures of the 1960 eruption is approximately parallel to nearby fissures that fed a similar eruption in 1921-22 [Katsui and Katz, 1967]. Perhaps coincidentally, the 1921 eruption started 32 days after a great earthquake (M 8.4), whose epicenter was nearly 1400 km north of Puyehue. West-northwest to NW and ENE are common vent alignment directions in the Andes of southern Chile [Moreno Roa, 1976]. The direction of convergence between the Nazca and South American plates is known to be approximately ENE [Minster and Jordan, 1978], but the orientation of principal stress axes in the upper crust in this part of South America does not appear to be well constrained [Richardson, et al., 1979]. Nevertheless, it seems clear that the Cordón Caulle dacitic eruptions have been tectonically controlled. Whether a large silicic magma chamber is present is unknown.

Coso volcanic field

The Coso volcanic field, in eastern California, is an example of a young, probably active, silicic system for which there is no geologic or geophysical evidence for a large, shallow magma chamber [Duffield, et al., 1980; Bacon, 1982]. Basalts, many of which have mixed with silicic magma, erupted repeatedly around the southern half of the 8x16 km field of 38 Pleistocene high-silica rhyolite lava flows and domes (Fig. 1). Basaltic vents of specific eruptive episodes tend to be aligned NNE, perpendicular to σ_3 inferred from surface faulting and earthquake focal mechanisms. Throughout the last 230,000 yr., however, basaltic volcanism has been concentrated along a major structural discontinuity that trends WNW. Rhyolite was erupted in seven episodes, each consisting of chemically homogeneous magma. Rhyolitic vents occur in a general NNE-trending array, but vents of as many as three ages are aligned along preexisting fracture zones as though these were sites where dike-fed conduits found the least resistance in breaking through to the surface. Eruptions have occurred near the center of the field throughout its history, suggesting a magmatic focus in the central region; outlying domes rarely interfere with one another. A steep gradient in heat flow around a zone of very high values [Combs, 1980] approximately outlines the central area, lending further support to the magmatic focus hypothesis. The composition of the rhyolites does not vary in a monotonic way [Bacon, et al.,

1981], but a general trend towards more widespread venting of greater volumes of aphyric rhyolitic magma suggests that the system has been growing.

Eruptions from the Coso system are thought to be tectonically controlled. Bacon et al. [1981] suggested that extension of the crust allows strain to build until magma pressure overcomes the sum of rock strength and σ_3, and a magma-filled fracture forms; dike emplacement relieves some strain and the system goes into repose until stress conditions are again favorable for additional leaking of the reservoir. Inclusions of hybrid andesitic magma in some domes suggest that there has not been a large volume of silicic magma in the reservoir, which is thought to be zoned from rhyolite downward to basalt [Bacon and Metz, 1984]. The last rhyolitic eruption probably was about 60,000 yr. ago. If extension continues at a long-term constant rate, the next eruption could be expected to be similar to previous ones. If the system continues to build, a shallow chamber eventually may develop and a catastrophic eruption might occur in the future.

South Sister

The Three Sisters area in the central Oregon Cascades [E. M. Taylor and N. S. Macleod, written commun., 1981] is another example of a late Quaternary silicic system whose vent pattern appears to be tectonically controlled (Fig. 2A). Several rhyodacite domes about 2,500 yr. old on the south flank of South Sister form an approximately N-S linear array [Fig. 2B; Scott, 1983]. Close to South Sister, the distribution of vents suggests radial trends. Vents for the Holocene rhyodacites suggest that the silicic system is smaller than 4x6 km.

Hundreds of Quaternary basaltic vents dot the region. Holocene basaltic vents form six left-stepping echelon N-S arrays, each 4-10 km long, that define a 75-km-long NNW-trending zone. The South Sister silicic system lies at a thermal focus where this zone intersects the axis of the chain of High Cascade polygenetic volcanoes. A less well developed 25-km-long NNE-trending zone of right-stepping echelon N-S alignments of Holocene basaltic vents continues south from the south end of the NNW-trending zone, roughly at the west end of the Newberry Volcano--Brothers Fault Zone complex (not shown in Fig. 2). Since alignments of coeval vents commonly are parallel to local normal faults and because the Oregon Cascades are known currently to be under N-S maximum horizontal compressive stress [Zoback and Zoback, 1980], the N-S vent alignments are reflecting the tectonic stress field. The zones of echelon vent patterns may overlie major lithospheric flaws along which some strike-slip motion may occur at depth. The rhyodacitic domes probably were fed by dikes emanating from a rather small, comparatively deep reservoir beneath the south side of South Sister; dikes may have migrated laterally to feed outlying domes. Tectonic control of vent patterns thus is evident for the entire region and on a local scale as well. Elapsed time since the last eruption may have been insufficient for a large shallow chamber to develop (see Crater Lake example). A moderate-volume pyroclastic eruption might very well take place in the near future, but a caldera-forming event seems unlikely.

Inyo--Mono domes

The Inyo--Mono domes evidently comprise an igneous system whose vent pattern is tectonically-controlled, and which apparently has not grown to a shallow-chamber stage. The volume and frequency of eruptions suggest that the system is growing and vigorous. Vents define a 37-km-long N-S array from the

islands in Mono Lake to the west moat of Long Valley caldera (Fig. 3). Locally, segments of the chain deviate from the overall N-S trend where they apparently follow older structures in the shallow subsurface. The domes are underlain by dikes, as evidenced by narrow grabens between coeval domes [Miller, 1984; Sieh, et al., 1983]. The overall trend of the chain is parallel to normal faults and reflects the regional tectonic stress regime. Basaltic vents occur 2-5 km west of the axis and surround its south end within the western quarter of Long Valley caldera [Bailey, et al., 1976]. The most evolved magmas, high-silica rhyolite, have been erupted near the center of the chain at Mono Craters, coincidentally astride the east side of an ancient (Cretaceous?) fracture zone inferred to be circular [Kistler, 1966, fig. 32]. The Mono Craters vents, however, can be broken into NW, N-S, and NE alignments, although this is not essential to the argument that these vents are genetically unrelated to the postulated older "ring structure". Rhyolitic domes containing mafic magmatic inclusions, presumably hybrid magma from the interface between a rhyolitic reservoir and underlying basalt by analogy with the Coso volcanic field [Bacon and Metz, 1984], occur only in the center of the Mono Craters field and were emplaced early in its history [Wood, 1977].

Results of a teleseismic P-delay study suggest that comparatively low-velocity material is confined to a vertical tabular zone elongated in a N-S sense beneath the Mono Domes [H. M. Iyer, oral commun., 1983]. Other geophysical techniques have failed to detect a large shallow magma chamber or any thermal anomaly associated with such an a body. The youngest Mono Craters magmas are aphyric and eruptions have occurred along the entire chain in what would be historic time in many parts of the world. Further eruptions clearly are likely in the near future, but the tectonically-controlled vent pattern suggests that a caldera-forming event may be a long way off.

SILICIC SYSTEMS WITH DIFFUSE VENT PATTERNS

Distributions of silicic vents that are diffuse, arcuate, or radial and lack contemporary or younger mafic vents within the silicic field are thought to reflect the presence of large crustal magma chambers. Most examples of such silicic volcanic fields are poorly preserved, having been partially engulfed by subsequent caldera-forming eruptions. The calderas themselves provide compelling evidence for shallow magma bodies.

Long Valley Glass Mountain

In contrast to the systems just described, Glass Mountain, on the NE edge of Long Valley caldera [Bailey, et al., 1976; Metz, 1984], is an example of a pile of high-silica rhyolitic lavas and tuffs that leaked intermittently for over 1,000,000 yr. from the same reservoir that ultimately produced the Bishop Tuff. The castastrophic eruption of the Bishop Tuff and formation of Long Valley caldera 700,000 yr. ago took place about 100,000 yr. after the youngest dated Glass Mountain eruption. Because older vents are covered by younger lavas and because much of Glass Mountain disappeared into Long Valley caldera, it is difficult to constrain the entire pattern of vents. The distribution of the Tuff of Taylor Canyon [Krauskopf and Bateman, 1977], a series of thin ash flows and widespread air falls erupted from the Glass Mountain center, suggests that the field of rhyolitic vents was probably at least 11x12 km (Fig. 4). The rhyolites do not appear to have been emplaced in any particular geographic progression [Metz, 1984] or along any obvious trends that could be related to tectonic stress regimes. The silicic field appparently was small relative to the area that eventually collapsed to form the caldera and was

eccentric to Long Valley. Chemical changes with time are not monotonic, but there is an overall trend toward less-evolved high-silica rhyolite [Metz, 1984]. The Bishop Tuff evidently was slightly less-differentiated than most of the preserved Glass Mountain rhyolites. Indications of the potential for a caldera-forming eruption that one might have found 800,000 yr. ago would have been the diffuse pattern of vents and the very long history of eruption of highly differentiated silicic magma.

Third volcanic cycle, Yellowstone

During the last 2 m.y. the Yellowstone Plateau volcanic field has evolved through three cycles consisting of eruption of rhyolitic lava flows followed by pyroclastic eruptions accompanied by large-scale caldera collapse [Christiansen, 1984a]. Because its products are best preserved, the youngest cycle is most thoroughly known [Christiansen, 1984b]. Voluminous rhyolitic lava flows leaked intermittently for 600,000 yr. from fracture zones that are thought to have outlined the area that later collapsed to form the third-cycle caldera. The inferred vent pattern [Christiansen, 1984a, fig. 6.5] approximately delineated the extent of a subjacent rhyolitic magma chamber. The local stress field probably was strongly influenced by bouyant rise of low-density silicic magma, causing a departure from the regional extensional regime to one of diminished horizontal deviatoric stress.

Formation of the 45 x 75 km caldera was associated with eruption of 1000 km^3 of rhyolitic magma 630,000 yr. ago. More than 1000 km^3 of rhyolitic magma have been erupted as lava flows since the caldera collapsed, mostly within the last 150,000 yr. Vents for these youngest eruptions concentrate in two zones that extend across the caldera from outlying fault zones [Christiansen, 1984a, fig. 6.7] to form roughly NNW-trending arrays. Most of these vents occur within ring fracture zones of the caldera. Christiansen [1984a, p. 90] suggests that increased rigidity, brought about by crystallization of magma at the top of the chamber during this interval, has allowed tectonic fracturing of the roof zone and tapping of deeper rhyolitic magma sources. Seismic velocity structure summarized by Smith and Braile [1984] appears to be consistent with absence of extensive bodies of silicic magma in the upper crust beneath the zones of young postcaldera vents. However, Smith and Braile [1984] also note that maximum focal depths of earthquakes systematically decrease from about 20 km outside to about 5 km within the caldera, a pattern that would be compatible with a shallow magma chamber. Ongoing uplift within the caldera [Smith and Braile, 1984, fig. 7.5] may be related to migration of magma. Interpretation of vent distribution should be made in light of the vast scale of the Yellowstone system. Although vents are concentrated in grossly linear zones, which apparently correspond to old structural discontinuities in the shallow crust, the area affected by venting of chemically similar rhyolite is on the order of 40x40 km. This observation can be considered evidence for a large crustal magma body, despite the ambiguity of interpretation of the seismic information.

La Primavera

The Sierra La Primavera, near Guadalajara Mexico, is a field of rhyolitic lava flows and domes superimposed on a circular caldera [Mahood, 1981]. The caldera formed 95,000 yr. ago during eruption of about 40 km^3 of magma [Mahood, written commun., 1984] to form the Tala Tuff. Arcuate and short linear (subradial?) patterns of postcaldera rhyolitic vents, without intervening more mafic vents, imply the presence of a shallow silicic chamber

(Fig. 5). All of the lavas of the two youngest groups are eccentric to the caldera and some lie within the area between the southern precaldera rhyolitic lavas and the caldera itself. Although the area is one of mild extension, the pattern of postcaldera vents appears to be non-tectonic. This suggests that the shallow magma body did not die with the moderate-volume caldera-forming eruption and, in fact, may be growing. The potential for a second catastrophic event appears to be high.

Ilopango

The caldera of Ilopango in El Salvador [Williams and Meyer-Abich, 1955] has several dacitic domes on its north wall that evidently predate caldera formation. Some domes on the south side of the caldera also may be late, precaldera features. The dacitic domes of Ilopango appear to be the remains of a diffuse cluster, slightly eccentric to the caldera. Impressive alignments of mafic vents NW of Boqueron volcano, about 30 km WNW of Ilopango caldera, define a NNW azimuth [Williams and Meyer-Abich, 1955, fig. 4]. Because of their wide distribution that suggests a diffuse pattern, the Ilopango dacitic domes may have indicated the presence of a large shallow magma chamber before the caldera-forming eruption.

Crater Lake

Mount Mazama, the volcanic complex that erupted approximately 50 km^3 of rhyodacitic magma and formed Crater Lake caldera about 6,800 yr. ago, had a history that might have forewarned of its climactic eruption [Bacon, 1983]. Mount Mazama consisted of a stack of overlapping andesitic shields and stratovolcanoes, built on an earlier silicic volcanic field in many eruptive pulses over at least 400,000 yr. Around this andesitic pile, monogenetic cones erupted basalt from time to time along tectonic trends. About 70,000 yr. ago several vents produced a few km^3 of homogeneous dacite, some of which erupted explosively (Fig. 6). The area affected by dacitic vents was at least 30 km^2 and their pattern was diffuse, suggesting that a silicic chamber may have been present. Only minor andesitic eruptions took place after this time, and dacite continued to erupt locally until about 40,000 yr. ago (Fig. 7). The first indication that a rhyodacitic magma body was developing was the eruption of a dozen small domes (Sharp Peak, Fig. 8) on NE trends radial to the area that later collapsed to form the caldera. The age of these domes is poorly constrained, but is probably between 20,000 and 40,000 yr. A compositionally similar dome vented near the north rim of the caldera (hill 7352') about 30,000 yr. ago [D. E. Champion, written commun., 1984]. About the same time, Williams Crater (formerly known as Forgotten Crater) and a vent about 1 km to the west erupted basalt and caused the emplacement of an extensive lava flow and several domes of commingled andesite and dacite; Williams Crater marks the west margin of the silicic magma reservoir at that time. These few volcanic events were the only ones to leave a recognizable record between c. 50,000 yr. and 7,000 yr. B.P. During this time, the entire volume of rhyodacitic magma that erupted in the climactic event must have evolved.

About 7,000 yr. B.P. the shallow chamber began to leak significant volumes of rhyodacitic magma. These leaks took the form of three lava flows: Redcloud Cliff, Llao, and Grouse Hill (Fig. 8). Other rhyodacitic flows may have been present within the area that collapsed to form the caldera. About 140 yr. later a fourth lava flow, the Cleetwood flow, was erupted. The composition of this lava is identical with the first pumice of the climactic eruption, except

that the lava had a much lower water content upon eruption. The four flows continued the non-tectonic pattern of vents. Surprisingly, the climactic eruption began before the Cleetwood flow had cooled. Although each of the four precursory lava eruptions began with an explosive phase, flow of magma to the surface apparently was sufficiently sluggish to allow the magma to de-gas during ascent so that conduits eventually were plugged with viscous rhyodacite. Only the Llao flow was preceded by a voluminous pyroclastic phase, but this spread tephra over parts of several western states. Loss of several km^3 of magma from the top of the chamber over a comparatively short period to form the lava flows may have depressurized the system, without accompanying loss of volatile pressure, so that vapor saturation occurred at greater depth than before and the climactic eruption could be sustained.

The lessons from Crater Lake are two-fold. First, for some 20,000 to perhaps 30,000 yr. rhyodacitic magma leaked infrequently from a generally diffuse pattern of vents; this much time evidently was needed to brew at least 50 km^3 of differentiated magma. Second, at least four comparatively degassed lava flows leaked during approximately two centuries before the catastrophic eruption and the climactic event followed emplacement of the youngest lava flow very closely in time.

SMALL CALDERAS WITH PRECALDERA SILICIC VENTS

Three relatively small caldera-forming systems with late, precaldera silicic lava flows or domes are described. In the cases cited here, there is compositional similarity between the precaldera lava and the pumice of the caldera-forming eruption and(or) stratigraphic relations suggest that the interval between the two types of eruptions was short. Information on the distribution of vents is sketchy, but is consistent with linear arrays or small clusters of vents within the area of caldera formation. These systems form a category that is transitional between tectonically-controlled systems and large shallow chambers. Magma reservoirs apparently were too small to greatly affect the stress regime in the roof rocks. Calderas of this group are smaller than Crater Lake caldera and eruption volumes appear to have been substantially less than the approximately 50-km^3 of magma ejected by the climactic eruption of Mount Mazama.

Krakatau

Krakatau is the only example other than Mount Mazama for which precise dating of a precaldera lava eruption is available. The former volcano of Perboewatan, which was located in what is now the northern part of the 7-km-diameter Krakatau caldera, was the site of a rhyodacitic eruption in 1680-81 [Verbeek, 1885, in Simkin and Fiske, 1983]. This eruption produced pumice and lava; the composition of the lava was virtually identical to that of the most differentiated pumice of the 1883 caldera-forming eruption [Westerveld, 1952, tables 8 and 9]. Both Perboewatan and the adjacent volcano of Danan were composed of similar lava [Verbeek, 1885, in Simkin and Fiske, 1983, fig. 57a]. Vents for these were located within an older depression approximately coincident with the caldera formed in 1883. Vents active on August 11, 1883 [Simkin and Fiske, 1983, fig. 11], two weeks before the catastrophic eruption, suggest a NNW trend that seems to mimick the general trend of earlier silicic vents. The approximately NE direction of plate convergence, derived from Minster and Jordan [1978], is roughly perpendicular to the elongated vent distribution, but it is unclear whether this indicates absence of tectonic control of precaldera vents.

The 200 yr. interval between the last precaldera rhyodacite and the culminating eruption of Krakatau is reminiscent of Mount Mazama. The caldera-forming eruption of Krakatau produced about 10 km^3 of magma [Self and Rampino, 1981], however, and the caldera is significantly smaller than Mazama's. Smith [1979, fig. 2] shows a general proportionality between caldera area and ash-flow eruption volume that implies systematic behavior of caldera-forming systems. It is reasonable, therefore, to expect that Krakatau and Crater Lake fall on opposite sides of a gradational boundary between relatively small-volume magma chambers that leak along linear trends and moderate- to large-volume chambers that affect the local stress field to the extent that precaldera leaks take place in non-tectonic patterns.

Nisyros

On the southeast quadrant of the island of Nisyros, Greece, are several rhyodacitic lava flows similar in composition to the pumice of the caldera-forming eruption [DiPaola, 1975]. Two of the vent areas for the lavas are preserved and an unknown number of related vents was engulfed during formation of the approximately 3-km-diameter caldera. Although their age is not precisely known, the rhyodacite flows are the youngest precaldera lavas. They are noted here to draw attention to the possibility that eruption of these lavas may have occurred only a short time before the caldera-forming event. Nisyros clearly was a small system and the distribution of precaldera silicic vents was focused, if not linear.

Cape Riva eruption, Santorini

Santorini, the next volcano of the Aegean arc west of Nisyros, also produced silicic domes prior to a major pyroclastic eruption [Druitt, 1983; T. H. Druitt, written commun., 1984]. This event, the Cape Riva eruption of 18,500 yr. B.P., probably accounted for several km^3 of dacitic magma and very likely was accompanied by caldera formation. The Skaros-Therasia dacitic domes are exposed in the wall of the present caldera, which formed during the Minoan eruption about 3500 yr. B.P. The domes are the youngest rocks below the Cape Riva pyroclastic deposits and may predate the Cape Riva eruption by only a short interval of time. Dacite of the Skaros-Therasia domes is compositionally similar to the pumice of the Cape Riva eruption. Exposures are inadequate to precisely define the distribution of vents for the domes, but most vents are thought to have been located on a structural discontinuity that is one of two NE-trending linear arrays of vents of various ages that cross the present caldera. Like Krakatau, the Cape Riva stage of Santorini apparently falls into the category of relatively small-volume systems transitional between large chambers and tectonically-controlled systems.

LONG VALLEY TODAY

The postcaldera history of Long Valley [Bailey, et al., 1976] suggests that this system may have the potential for further voluminous pyroclastic eruptions. Unlike the Inyo--Mono Domes, Long Valley caldera shows geophysical evidence of being underlain, in part, by silicic magma at perhaps 8 km depth [e.g. Steeples and Iyer, 1976; Hill, 1976; Hill, et al., 1984; Sanders, 1984]. Postcaldera silicic vents circumscribe the resurgent dome within the caldera (Fig. 9), as is typical of shallow magma chambers which have experienced caldera formation [Smith and Bailey, 1968]. The youngest (100,000 yr.) rhyolite erupted in the western caldera moat from a NNW-trending chain of vents which adjoins the south end of the Inyo Domes. Bailey [1984] indicates

that these flows are chemically more evolved than earlier moat rhyolites and their composition implies a return the style of trace-element fractionation shown by the Bishop Tuff.

The local pattern of the 0.1-m.y.-old vents could be tectonically-controlled. The overall pattern of postcaldera rhyolite vents, however, suggests the presence of a large silicic chamber, or remnants of such, long after the caldera-forming eruption. Recent deformation of the Long Valley area [Savage, et al., in press; Castle, et al., submitted] can be interpreted as being caused by readjustment of a crustal magmatic system to tectonic movements. Conceivably, the Long Valley magma chamber might be capable of another catastrophic eruption. Because precursory effects for such events are poorly understood, it is not known whether such an eruption would take place with little warning or on the heels of the eruption of one or more lava flows, such as at Crater Lake.

CONCLUSION

Because of the long, open-system evolution of well-studied volcanic systems, specific volcanic fields cannot be trusted to behave as they have in the past. Forecasts of future activity must be based on models developed through detailed study of the petrologic and eruptive histories of a variety of young volcanic systems. Although the record is fragmentary and models speculative, the distribution of vents in silicic volcanic fields can provide useful information concerning the likelihood of catastrophic pyroclastic eruptions by suggesting whether or not a large, shallow magma chamber is present. Diffuse, radial, or acruate patterns of silicic vents, without intervening coeval or younger mafic vents, can outline the dimensions of large crustal magma chambers that may produce pyroclastic eruptions of on the order of at least 50 km^3 of magma. In such cases, eruption of silicic lava may be an immediate precursor to a caldera-forming event, as was the case at Mount Mazama. Linear arrays of coeval silicic vents that reflect the regional tectonic stress regime of the upper crust may be fed from small or deep reservoirs incapable of catastrophic eruption. Silicic vents that form linear arrays in areas of focused silicic volcanism, however, may forewarn of relatively small caldera-forming events that eject less than a few tens of km^3 of magma, such as the 1883 eruption of Krakatau. These general principles are intended to applied in concert with detailed geologic and geophysical studies of specific volcanic fields, for only with a multidisciplinary approach can we begin to understand the evolution and to predict the future behavior of silicic volcanic systems.

Acknowledgments. I thank C. J. Michelsen and C. G. Newhall for aid in searching the literature for examples of precaldera silicic domes. Jenny Metz kindly gave me access to her data on Long Valley Glass Mountain prior to publication. T. H. Druitt provided unpublished information on Santorini. E. M. Taylor, N. S. MacLeod, and W. E. Scott shared information on the ages and locations of volcanic vents in the Three Sisters region. Reviews by Druitt, Wes Hildreth, and Julie Donnelly-Nolan are greatly appreciated. Ideas presented in this paper developed over a period of several years, during which time I have benefited from discussions with R. L. Christiansen, Donnelly-Nolan, W. A. Duffield, Hildreth, Kazuaki Nakamura, and R. L. Smith. I take sole responsibility, however, for any errors in fact or unlabeled speculations that may appear in this work.

REFERENCES

Anderson, E. M., The dynamics of the formation of cone-sheets, ring-dykes, and cauldron-subsidences: Roy. Soc. Edinburgh Proc., v. 56, p. 128-163, 1936.

Bacon, C. R., Time-predictable bimodal volcanism in the Coso Range, California: Geology, v. 10, p. 65-69, 1982.

Bacon, C. R., Eruptive history of Mount Mazama and Crater Lake caldera, Cascade Range, U. S. A.: J. Volcanol. Geotherm. Res., v. 18, p. 57-115, 1983.

Bacon, C. R., and J. Metz, Magmatic inclusions in rhyolites, contaminated basalts, and compositinal zonation beneath the Coso volcanic field, California: Contrib. Mineral. Petrol., in press, 1984.

Bacon, C. R., R. Macdonald, R. L. Smith, and P. A. Baedecker, Pleistocene high-silica rhyolites of the Coso volcanic field, Inyo County, California: J. Geophys. Res., v. 86, p. 10223-10241, 1981.

Bailey, R. A., Chemical evolution and current state of the Long Valley magma chamber: Long Valley Red Book, 1984.

Bailey, R. A., and R. P. Koeppen, Preliminary geologic map of Long Valley caldera, Mono County, California: U. S. Geol. Surv. open-file map 77-468, scale 1:62,500, 1977.

Bailey, R. A., G. B. Dalrymple, and M. A. Lanphere, Volcanism, structure, and geochronology of Long Valley Caldera, Mono County, California: J. Geophys. Res., v. 81, p. 725-744, 1976.

Castle, R. O., J. E. Estrum, and J. C. Savage, Uplift across Long Valley caldera, California: J. Geophys. Res. (submitted), 1984.

Christiansen, R. L., Yellowstone magmatic evolution: Its bearing on understanding large-volume explosive volcanism: in Explosive volcanism: Inception, evolution, and hazards: National Academy Press, Washington, D. C., p. 96-109, 1984a.

Christiansen, R. L., Postcaldera evolution and current activity of the Yellowstone caldera: Long Valley Red Book, 1984b.

Combs, J., Heat flow in the Coso geothermal area, Inyo County, California: J. Geophys. Res., v. 85, p. 2411-2424, 1980.

Delaney, P. T., and D. D. Pollard, Deformation of host rocks and flow of magma during growth of minette dikes and breccia-bearing intrusions near Ship Rock, New Mexico: U. S. Geol. Surv. Prof. Paper 1202, 61 p., 1981.

DiPaola, G. M., Volcanology and petrology of Nisyros Island (Dodecanese, Greece): Bull. Volcan., v. 38, p. 944-987, 1975.

Druitt, T. H., Explosive volcanism on Santorini, Greece: Ph.D. Thesis, Cambridge Univ., 269 p., 1983.

Duffield, W. A., C. R. Bacon, and G. B. Dalrymple, Late Cenozoic volcanism, geochronology, and structure of the Coso Range, Inyo County, California: J. Geophys. Res., v. 85, p. 2381-2404, 1980.

Hildreth, W., Gradients in silicic magma chambers: Implications for lithospheric magmatism: J. Geophys. Res., v. 86, p. 10153-10192, 1981.

Hill, D. P., Structure of Long Valley Caldera, California, from a seismic refraction experiment: J. Geophys. Res., v. 81, p. 745-753, 1976.

Hill, D. P., E. Kissling, J. H. Luetgert, and W. D. Mooney, Constraints on magma chamber geometry from reflected P waves: Long Valley Red Book, 1984.

Katsui, Y., and H. R. Katz, Lateral fissure eruptions in the southern Andes of Chile: J. Fac. Sci. Hokkaido Univ., ser. IV, v. 13, p. 433-448, 1967.

Kistler, R. W., Structure and metamorphism in the Mono Craters quadrangle, Sierra Nevada, California: U. S. Geol. Surv. Bull. 1221-E, 53 p., 1966.

Krauskopf, K. B., and P. C. Bateman, Geologic map of the Glass Mountain quadrangle, Mono County, California, and Mineral County, Nevada: U. S. Geol. Surv. map GQ-1099, scale 1:62,500, 1977.
Mahood, G. A., A summary of the geology and petrology of the Sierra La Primavera, Jalisco, Mexico: J. Geophys. Res., v. 86, p. 10137-10152, 1981.
Metz, J., Chemical evolution of the precaldera Long Valley magma chamber: Long Valley Red Book, 1984.
Miller, C. D., Holocene eruptions at the Inyo volcanic chain, California--Implications for possible eruptions in Long Valley caldera: Geology, in press, 1984.
Minster, J. B., and T. H. Jordan, Present-day plate motions: J. Geophys. Res., v. 83, p. 5331-5354, 1978.
Moreno Roa, H., The Upper Cenozoic volcanism in the Andes of southern Chile (from 40°00' to 41°30' S. L.): in O. Gonzales-Ferran, ed., Andean and Antarctic volcanology problems: Naples, IAVCEI, p. 143-171, 1976.
Nakamura, K., Volcanoes as possible indicators of tectonic stress orientation: J. Volcanol. Geotherm. Res., v. 2, p. 1-16, 1977.
Nakamura, K., and S. Uyeda, Stress gradient in arc-back arc regions and plate subduction: J. Geophys. Res., v. 85, p. 6419-6428, 1980.
Newhall, C. G., D. Dzurisin, and L. S. Mullineaux, Historical unrest at large Quaternary calderas of the world: Long Valley Red Book, 359 p, 1984..
Plafker, G., Alaskan earthquake of 1964 and Chilean earthquake of 1960: Implications for arc tectonics: J. Geophys. Res., v. 77, p. 901-925, 1972.
Pollard, D. D., P. T. Delaney, and J. H. Fink, Igneous dikes: Propagation mechanics and associated geologic structures: Long Valley Red Book, 1984.
Richardson, R. M., S. C. Solomon, and N. H. Sleep, Tectonic stress in the plates: Rev. Geophys. Space Phys., v. 17, p. 981-1019, 1979.
Sanders, C. O., Location and configuration of magma bodies beneath Long Valley, California, determined from anomalous earthquake signals: Long Valley Red Book, 1984.
Savage, J. C., W. H. Prescott, M. Lisowski, and N. E. King, Deformation in the White Mountain seismic gap, California-Nevada: J. Geophys. Res., in press, 1984.
Scott, W. E., Character and age of Holocene rhyodacite eruptions at South Sister volcano, Oregon: Trans., Am. Geophys. Un., v. 64, no. 45, p. 899-900, 1983.
Self, S., and M. R. Rampino, The 1883 eruption of Krakatau: Nature, v. 292, p. 699-704, 1981.
Sieh, K., S. H. Wood, and S. Stine, Most recent eruption of the Mono Craters, eastern central California: Trans., Am. Geophys. Un., v. 64, no. 45, p. 889, 1983.
Simkin, T., and R. S. Fiske, Krakatau 1883, the volcanic eruption and its effects: Washington, D. C., Smithsonian Inst. Press, 464 p., 1983
Smith, R. B., and L. W. Braile, Crustal structure and evolution of an explosive silicic volcanic system at Yellowstone National Park: in Explosive volcanism: Inception, evolution, and hazards: National Academy Press, Washington, D. C., p. 96-109, 1984.
Smith, R. L., Ash-flow magmatism, in C. E. Chapin, and W. E. Elston, eds., Ash-flow tuffs: Geol. Soc. Am. Spec. Paper 180, p. 5-27, 1979.
Smith, R. L., and R. A. Bailey, Resurgent cauldrons: in R. R. Coats, R. L. Hay, and C. A. Anderson, eds., Studies in volcanology: Geol. Soc. Am. Mem. 116, p. 613-662, 1968.

Smith, R. L., and H. R. Shaw, Igneous-related geothermal systems, in D. E. White, and D. L. Williams, eds., Assessment of geothermal resources of the United States--1975: U. S. Geol. Surv. Circ. 726, p. 58-83, 1975.
Steeples, D. W., and H. M. Iyer, Low-velocity zone under Long Valley as determined from teleseismic events: J. Geophys. Res., v. 81, p. 849- 860, 1976.
Westerveld, J., Quaternary volcanism on Sumatra: Geol. Soc. Am. Bull., v. 63, p. 561-594, 1952.
Wood, S. H., Distribution, correlation, and radiocarbon dating of late Holocene tephra, Mono and Inyo craters, eastern California: Geol. Soc. Am. Bull., v. 88, p. 89-95, 1977.
Zoback, M. L., and Mark Zoback, State of stress in the conterminous United States: J. Geophys. Res., v. 85, p. 6113-6156, 1980.

FIGURE CAPTIONS

Fig. 1. Map of the Pleistocene part of the Coso volcanic field, California, showing rhyolite lava flows and domes, basalt vents, and heat-flow contours [after Bacon, 1982].

Fig. 2. (A) Pleistocene vents in the Three Sisters region, Oregon [modified after E. M. Taylor and N. S. Macleod, written commun., 1981]. W = Mount Washington, SS = South Sister, BB = Bachelor Butte. (B) South flank of South Sister, showing Holocene rhyodacites of Devils Hill and Rock Mesa eruptive episodes [modified after Scott, 1983].

Fig. 3. Map of Inyo--Mono Domes, Quaternary basalt and andesite vents, and silicic lavas of Long Valley system less than about 200,000 yr. old [modified after Bailey, et al., 1976, and Wood, 1977].

Fig. 4. Map showing minimum extent of rhyolitic tuffs related to the Glass Mountain volcanic center, high-silica rhyolites of Glass Mountain, and recognized vents [modified after Bailey and Koeppen, 1977, Krauskopf and Bateman, 1977, and J. Metz, written commun., 1983]. Distribution of tuffs suggests Glass Mountain silicic center extended farther south and much was engulfed by Long Valley caldera.

Fig. 5. Map of rhyolitic lava flows and domes of the Sierra la Primavera complex, Jalisco, Mexico [modified after Mahood, 1981].

Fig. 6. Map showing approximately 70,000-yr.-old andesite and dacite flows and vents at Mount Mazama. Present caldera rim shown for reference.

Fig. 7. Map showing approximately 40,000- to 50,000-yr.-old andesite flows, dacite flows and vents, and basalt vents at Mount Mazama. D = dacitic dome(s) southwest of summit of Mount Mazama inferred from distribution of pyroclastic-flow deposits. Present caldera rim shown for reference.

Fig. 8. Map showing late Quaternary rhyodacite flows and vents and basalt vents at Mount Mazama. Rim of Crater Lake caldera shown for reference. C = approximate location of vent for initial phase of caldera-forming eruption [single-vent phase of Bacon, 1983]; outer limit of ring-fracture zone marks probable locus of vents for ensuing caldera-collapse phase [ring-vent phase of Bacon, 1983]. Numbers 1-4 on Holocene rhyodacite flows indicate order of eruption.

Fig. 9. Map showing postcaldera volcanic rocks, vents for moat rhyolites, and Quaternary basalt and andesite vents in Long Valley region [modified after Bailey, et al., 1976].

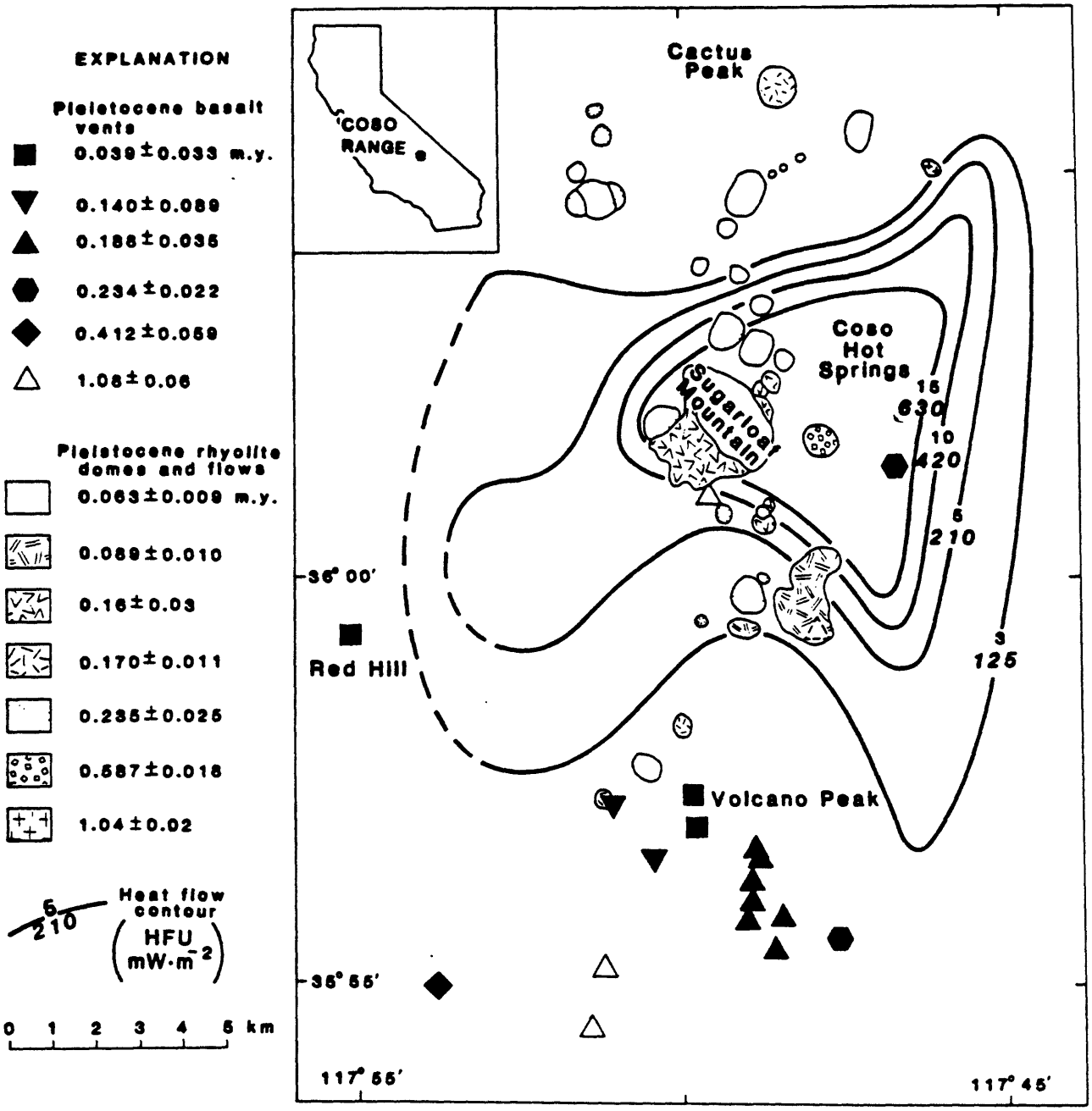
EXPLANATION
Pleistocene basalt vents
0.039±0.033 m.y.
0.140±0.089
0.188±0.035
0.234±0.022
0.412±0.059
1.08±0.06
Pleistocene rhyolite domes and flows
0.063±0.009 m.y.
0.089±0.010
0.16±0.03
0.170±0.011
0.235±0.025
0.587±0.018
1.04±0.02
5
210
Heat flow contour
(HFU mW·m⁻²)
0 1 2 3 4 5 km
COSO RANGE
Cactus Peak
Coso Hot Springs
Sugarloaf Mountain
15
630
10
420
5
210
3
125
Red Hill
Volcano Peak
36° 00'
35° 55'
117° 55'
117° 45'

FIGURE 1

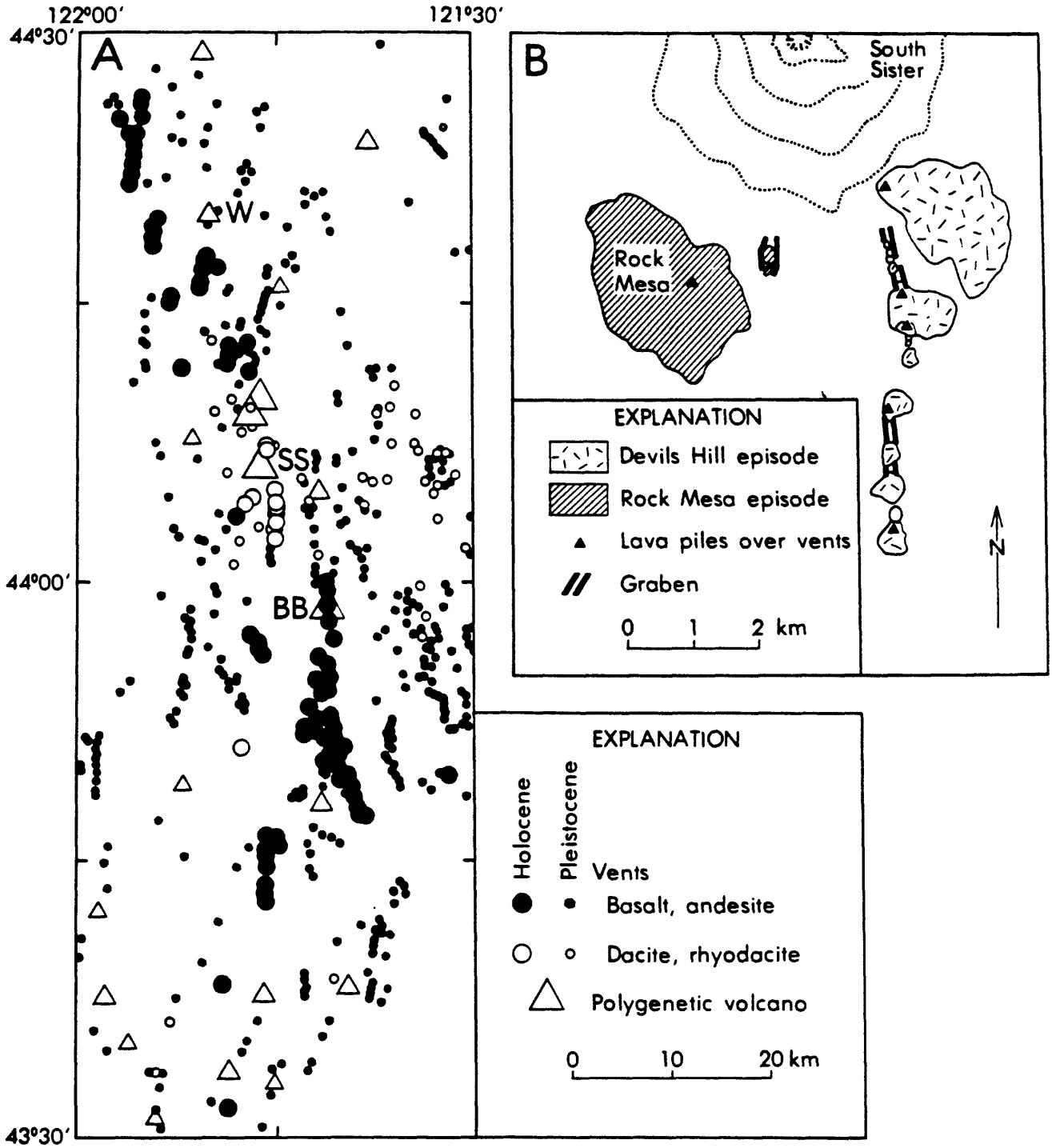
122°00'
121°30'
44°30'
44°00'
43°30'
A
W
SS
BB
B
South Sister
Rock Mesa
EXPLANATION
Devils Hill episode
Rock Mesa episode
Lava piles over vents
Graben
0 1 2 km
N
EXPLANATION
Holocene
Pleistocene
Vents
Basalt, andesite
Dacite, rhyodacite
Polygenetic volcano
0 10 20 km

FIGURE 2

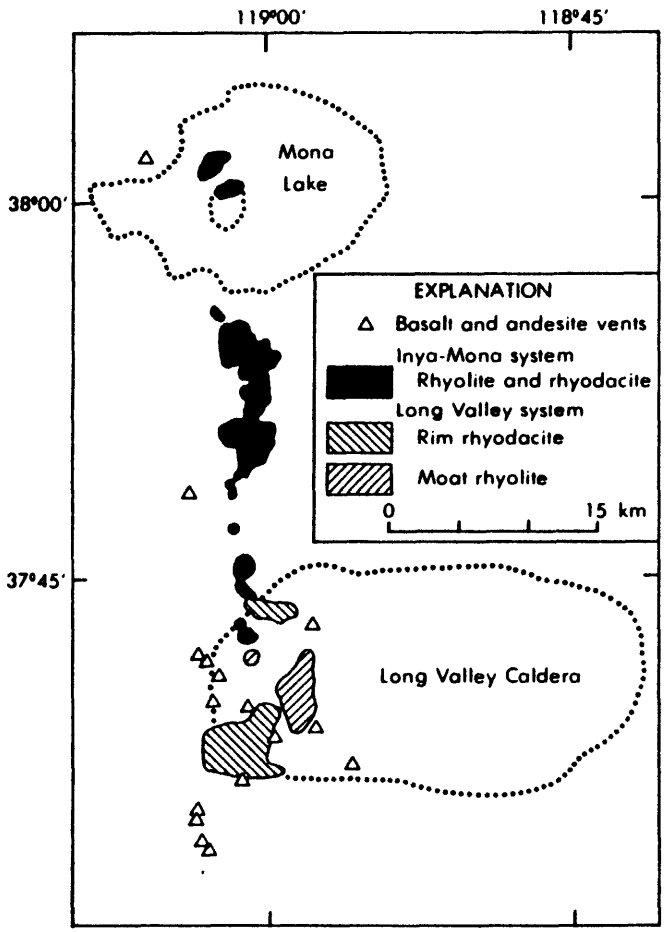

FIGURE 3

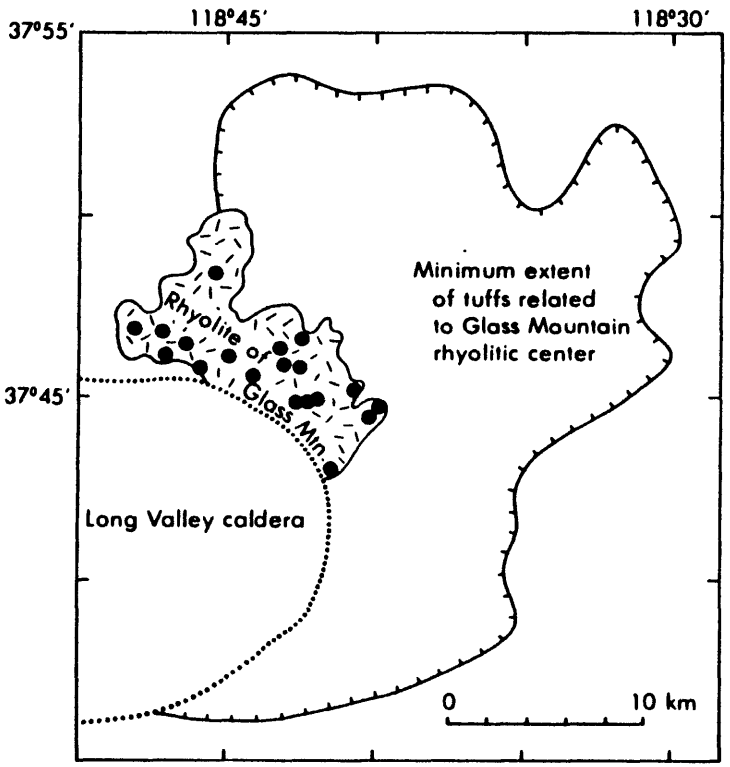

FIGURE 4

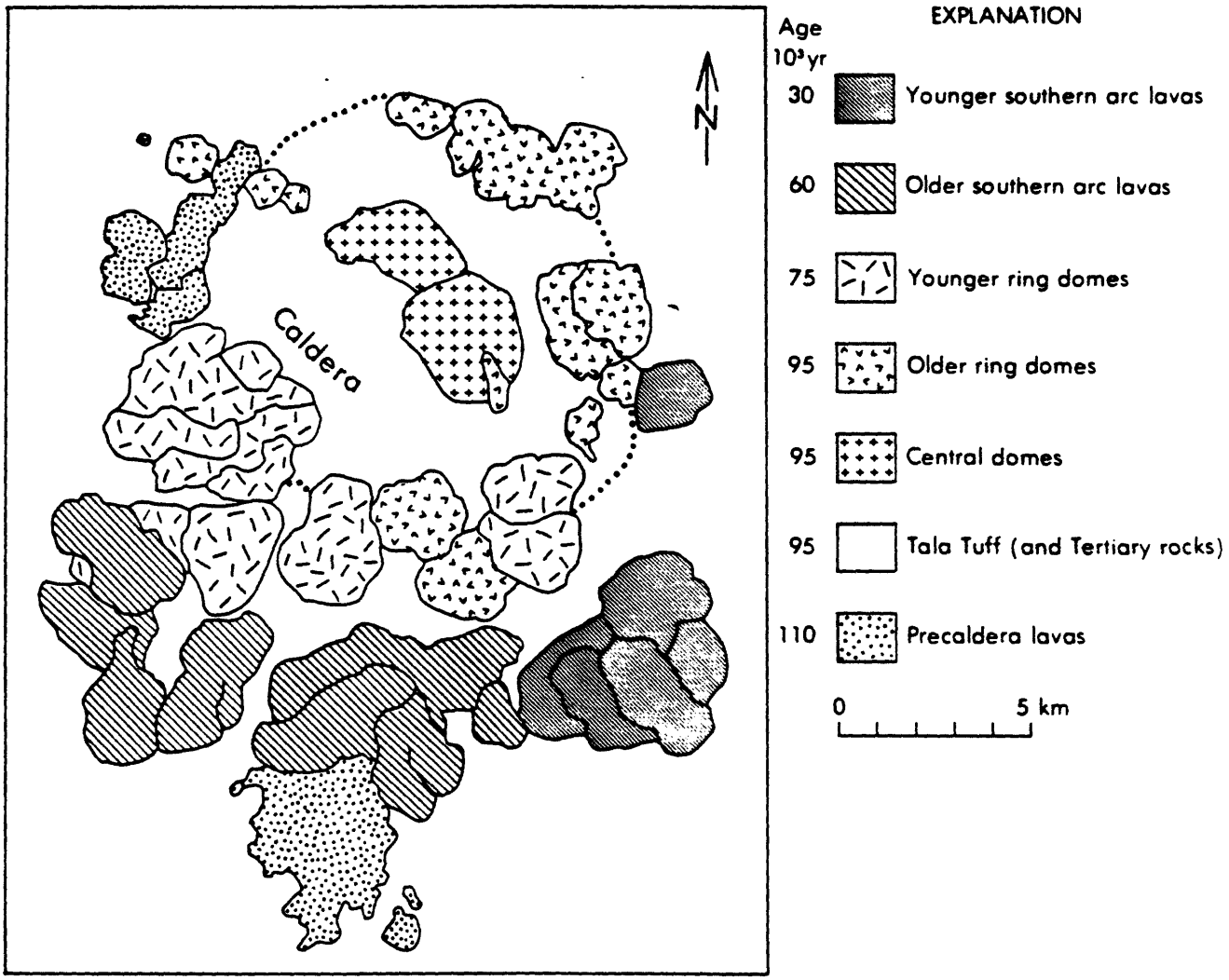
Caldera
N
EXPLANATION
Age
10³yr
30
Younger southern arc lavas
60
Older southern arc lavas
75
Younger ring domes
95
Older ring domes
95
Central domes
95
Tala Tuff (and Tertiary rocks)
110
Precaldera lavas
0
5 km

FIGURE 5

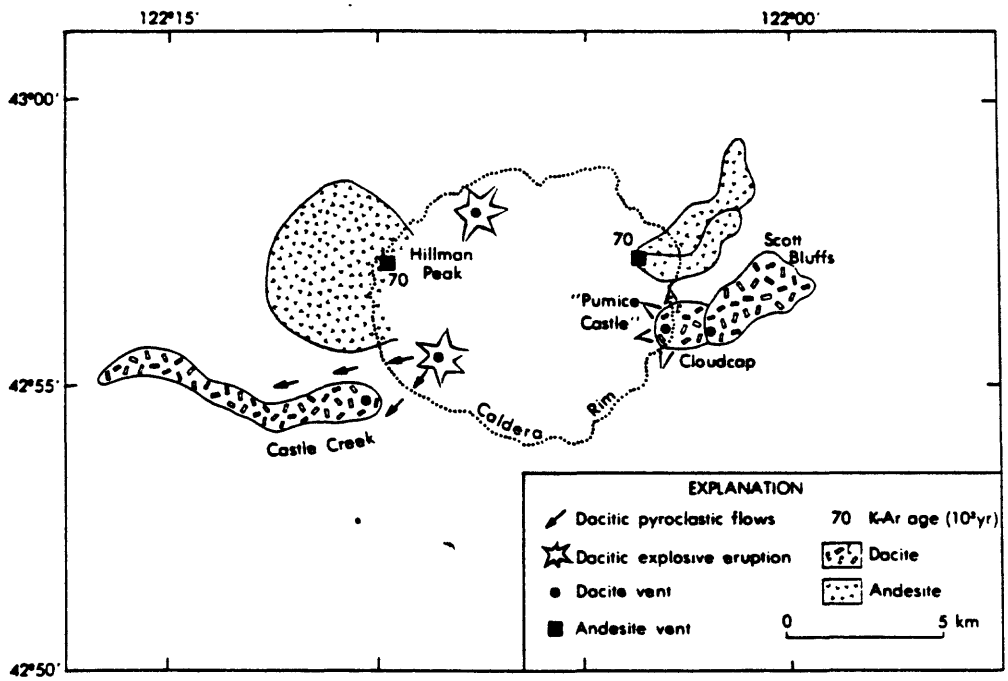

FIGURE 6

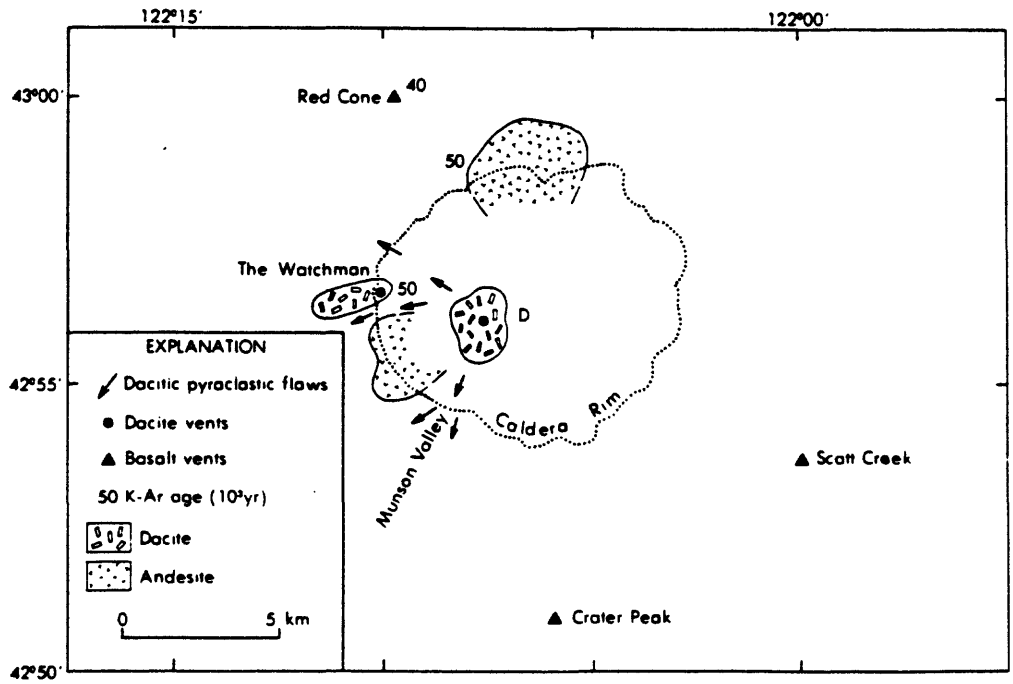

FIGURE 7

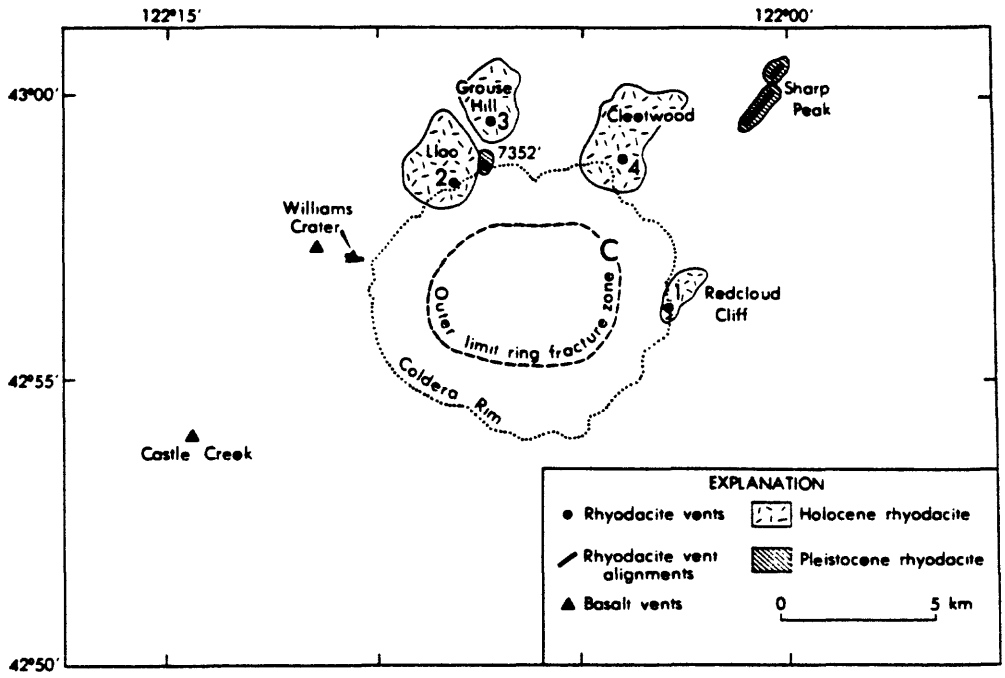

FIGURE 8

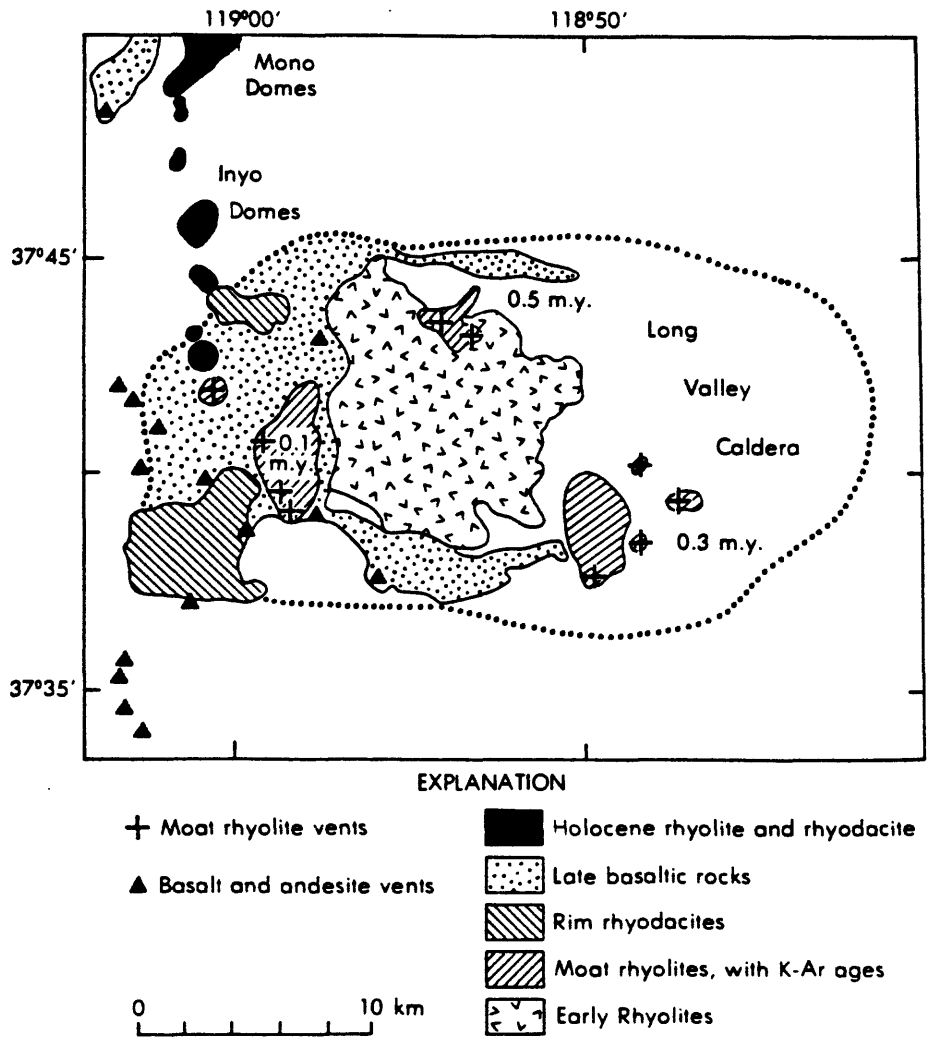

FIGURE 9

lipman2,long,4/24/84

STRUCTURE OF THE TERTIARY QUESTA CALDERA, NEW MEXICO--AN ERODED ANALOG FOR CURRENT ACTIVITY AT LONG VALLEY

Peter W. Lipman

U. S. Geological Survey, Denver, CO 80225

ABSTRACT

The late Oligocene Questa caldera in northern New Mexico, eroded to levels where deep caldera structures and cogenetic batholithic intrusions are exposed, displays structures that may be analogous to features associated with current unrest at Long Valley caldera, eastern California. Features common to both calderas include: (1) regional extensional tectonic structures that have interacted with the more local caldera-related stress field; (2) orientation and distribution of mapped or inferred caldera-related dikes that are strongly influenced by regional structural trends, (3) complex deformation along segments of the caldera boundary that truncate regional structural trends; (4) structurally highest portions of the postcollapse magma chamber underlie the apical graben on the resurgent dome, and (5) postcollapse magmatic activity has been sustained by addition of new magma to the high-level system, in the case of Questa for 3-4 m.y. after collapse.

INTRODUCTION

Increased seismic activity and associated ground deformation that began in the late 1970's in the Long Valley caldera area, eastern California, has prompted concern about potential hazards associated with possible renewed volcanism in this area (Miller et al., 1982). As a result, understanding of the Long Valley magmatic system, already well studied as a result of geothermal-related investigations (Muffler and Williams, 1976), has been augmented in the last few years by intense study by geologic, geophysical, and geochemical techniques (this volume). Because limited erosional dissection of the Long Valley area precludes direct observation of many potentially critical volcanic, intrusive, and regional tectonic features that bear on interpretation of the magmatic history and future potential hazards, interpretations of features at Long Valley can be enhanced by comparisons with possibly similar volcanic and tectonic analogs elsewhere.

This paper summarizes features of the late Oligocene Questa caldera in northern New Mexico, that are possible analogs with inferred concealed features at Long Valley. Both caldera systems have evolved within major rift environments, and they show complex interactions between the regional extensional stress field and divergent local stresses related to development of a large shallow magma chamber. At Questa, upper levels of the consolidated magma chamber, as well as deep structures of the associated caldera, have been exposed by structural disruption and deep erosion along the east margin of the Rio Grande rift

(Lipman, 1981, 1983). After summarizing the geologic setting and nature of recent seismicity and deformation at Long Valley, I describe structures of the Questa caldera area that may represent the results of similar processes in the past. Significant comparisons include: (1) relations between regional extensional tectonics and caldera-related magmatic stress fields, (2) nature of deformation along structural boundaries of calderas, (3) geometry of subcaldera magma chambers, (4) geometry and structural control of dike intrusion, and (5) longevity and replenishment of silicic magmatic systems.

LONG VALLEY AREA

The Long Valley caldera, along with Mono and Inyo Craters and Mono Basin to the north, are young volcanic centers alined along the west margin of the Great Basin adjacent to the east front of the Sierra Nevada (Bailey et al., 1976; Hermance, 1983). Seismicicity, high heat flow, and recent faulting indicate that this margin of the Basin Range province has been the locus of by relatively rapid east-west crustal extension.

Geologic setting

Long Valley caldera is a 20x35 km elliptical depression in east central California, that collapsed following eruption of about 600 km^3 of rhyolitic Bishop Tuff about 0.7 Ma (Bailey et al., 1976). The caldera lies along the east front of the Sierra Nevada and is elongate east-west, roughly perpendicular to regional extensional faults of Owens Valley and the Sierran front (Fig. 1).

Figure 1--NEAR HERE

Bishop Tuff spread widely as a regional ash-flow sheet, filling local topographic depressions, but mostly only a few tens of meters thick. Collapse of the Long Valley caldera concurrent with eruption permitted Bishop Tuff to pond within the collapsing caldera to a thickness of nearly 2 km, as indicated by drill data. Renewed eruption of rhyolitic tuffs, domes, and lava flows began within the caldera almost immediately after the caldera-

forming eruption. Uplift of the western caldera floor produced essentially the present resurgent dome by about 0.6 Ma. Subsequent eruptions from vents on the caldera floor and along western ring fractures 0.5 to 0.05 Ma attest to continued evolution and probable replenishment of the subcaldera magma body (Bailey, 1983). Eruptions along the Inyo and Mono Craters, extending north from Long Valley, have occurred as recently as 500-600 years ago (Miller, 1983), and provide evidence that silicic magma has reached shallow crustal levels recently in the Long Valley area. Thermal modelling of heat flow in the Long Valley caldera area suggests that the shallow subcaldera magmatic system could not have survived more than a few hundred thousand years without replenishment by additional magma (Lachenbruch et al., 1976).

Current activity

Current unrest at Long Valley caldera seemingly began with a flurry of earthquakes 15 km southeast of the caldera in October 1978, followed by a gradual increase in activity near the south caldera margin (Ryall and Ryall, 1983). Intense earthquake swarms in May 1980 culminated with four earthquakes of M=6+ on May 25-27, including one with an epicenter in the south caldera moat. The associated large earthquakes well south of the caldera have been interpreted as related either to regional tectonic unrest or to dike intrusion (Julian and Cockerham, 1983). Continued seismic activity since 1980 in the south moat, including an especially intense and prolonged swarm in January

1983 (Savage and Cockerham, 1984), defines a near-vertical plane parallel to the south caldera rim extending about 8 km laterally and as much as 10 km deep (Fig. 2). Fault-plane solutions and

---

Figure 2--NEAR HERE

---

deformation data suggest right-lateral slip and east-northeast extension along a fault defined by the hypocenters; this zone of seismic activity is interpreted by Savage and Cockerham as evidence for dike intrusion into the caldera ring-fracture zone. Apparent "spasmodic tremor" and an anomalous zone of seismic shear-wave attenuation indicative of shallow magma beneath the southern part of the resurgent dome are seismic evidence for a role of magma in the current unrest at Long Valley (Ryall and Ryall, 1983; Sanders, 1984).

Leveling and trilateration surveys during the period of increased seismicity have documented as much as 40 cm of uplift centered on the resurgent dome and large horizontal displacments extending radially outward from the caldera (Savage and Clark, 1982; Denlinger and Riley, 1984). The uplift is asymmetric, with steepest gradients on the south flank of the resurgent dome adjacent to the seismically active zone; horizontal displacements also indicate a component of east-northeast extension. Thus, the deformation and seismic data together indicate complex interactions between renewed magmatic uplift of the resurgent dome, structural effects of the south caldera margin, and regional tectonics.

A major concern is the possibility that the seismic and deformation data may be recording the rise of magma that could lead to a volcanic eruption in the south moat (Miller et al., 1982). Previous geologically recent postcaldera volcanism has been mostly along the Inyo and Mono Craters to the north, but even a small eruption in the south moat could cause major volcanic hazards because it is near the resort town of Mammoth Lakes.

QUESTA AREA

The 26-Ma Questa caldera and cogenetic volcanic and plutonic rocks of the Latir volcanic field (Fig. 3) are exposed in cross section in the Sangre de Cristo Mountains of northern New Mexico, as a result of structural and topographic relief along the Rio

---

Figure 3--NEAR HERE

Grande rift (Lipman, 1981, 1983; Reed et al., 1983). The volcanic sequence of the Latir field is generally similar to that of other Tertiary igneous accumulations in the southern Rocky Mountains: initial dominantly intermediate-composition lavas and breccias erupted from clustered central volcanoes were followed by voluminous outpouring of silicic ash-flow tuff associated with caldera collapse and emplacement of granitic rocks in the vent region. Scattered erosional remnants of the the caldera-related ash-flow sheet (the Amalia Tuff, a distinctive weakly peralkaline rhyolite) and associated precaldera andesite-quartz latite lavas are preserved as far as 45 km from the source caldera. After caldera formation, Miocene sedimentary rocks of the Santa Fe Group and local intebedded basaltic flows accumulated within the region of the Latir field in growing fault-block basins of the Rio Grande rift (Table 1).

Table 1--NEAR HERE

Questa caldera structure

Like Long Valley caldera, the Questa caldera is elliptical in plan, elongate in an east-west direction perpendicular to regional extensional structures of the Rio Grande rift (although the western margin of the Questa caldera is truncated by the rift and buried by rift fill). The related ash-flow sheet, the Amalia Tuff, is typically only a few tens of meters thick outside the caldera, but the tuff and associated slump breccias ponded to a thickness of 2-3 km within the caldera, indicating eruption concurrent with collapse. Postcollapse rhyolitic lava flows are preserved locally outside the caldera, but the record of postcollapse activity within the caldera is largely missing due to erosion, and only indirect evidence can be obtained from intracaldera intrusions and from volcaniclastic rocks in adjacent areas.

The structure of the Questa caldera is complex, due in large part to interaction with faulting along the Rio Grande rift, which was actively extending during the caldera cycle (Fig. 4).

Figure 4--NEAR HERE

The general style of early rift-related faulting in the Questa area was to tilt strata to the east and drop blocks to the west, repeating and attenuating the upper crustal section. Tilting locally approaches 90^0, especially within the Questa caldera.

The main bounding ring fault of the caldera is nowhere exposed, even at the deepest erosional levels, apparently because

the structural boundary has widely localized shallow granitic intrusions. Granitic intrusions, that are cogenetic with the Questa caldera as indicated by compositions and radiometric ages similar to the Latir volcanic rocks, include discontinuously exposed batholithic granitic rocks and a compositionally and texturally diverse assemblage of dikes, sills, and irregular laccoliths.

Batholithic granitic rocks

Granitic rocks, interpreted as cogenetic with the Latir volcanic field, are exposed discontinuously over an area of 20x35 km and range from mesozonal quartz monzonite to epizonal porphyritic granite and aplite (Reed et al., 1983). The rocks generally become more silicic, finer-grained, and more epizonal in character to the north. These changes accord with stratigraphic evidence indicating shallower depths of erosion north of the Questa caldera than to the south since Miocene time (Fig. 5). Although the granitic rocks are exposed as discrete

---

Figure 5--NEAR HERE

---

compositionally and texturally distinct plutons at present exposure levels, petrologic gradations within some plutons and regional gravity data (Cordell, 1978) suggest that the entire Questa caldera and a contiguous area of about 10x20 km to the south are underlain by cogenetic granitic rocks at shallow depth (Figs. 5, 6). The granitic rocks are most readily discussed

---

Figure 6--NEAR HERE

---

in three groups: dominantly mesozonal plutons south of the caldera, mineralized plutons along the south caldera margin, and epizonal plutons within central and northern parts of the caldera. Tertiary intrusions other than a few porphyro-aphanitic dikes and sills are absent north of the caldera.

Southern plutons. The largest exposed Tertiary intrusive bodies are areas of porphyritic quartz monzonite as much as 9 km across, best exposed along the Rio Hondo south of the caldera (Fig. 6). The quartz monzonite of Rio Hondo is characterized on its northeast side by a steep linear contact that appears localized along a major northwest-trending regional normal fault (Figs. 4, 6). Elsewhere, contacts are variable in dip but gentle over large areas that represent roof zones of the intrusion. Most of the Precambrian country rock between bodies of Tertiary quartz monzonite occurs along ridge crests above gently dipping contacts with quartz monzonite that clearly connect at similar altitudes. Irregularly along this roof zone, the quartz monzonite grades into silicic granite. The roof zone of the Rio Hondo pluton is also cut by hundreds to thousands of northwest-trending rhyolitic dikes and lesser number of more mafic dikes, interpreted as representing intrusion of liquid interior portions of the batholith into the consolidated margins (Fig. 7).

Figure 7--NEAR HERE

Available K-Ar and fission-track ages of the Rio Hondo rocks are interpreted as representing emplacement ages of 25-26 Ma, variably reset by slightly younger adjacent plutons.

A second major Tertiary granitic pluton in the southern area, exposed on Lucero Peak south of Rio Hondo, is relatively coarse light-colored equigranular granite that is everywhere separated from the Rio Hondo pluton by a septum of Precambrian rocks (Reed et al., 1983). Contacts of the granite of Lucero Peak dip gently to steeply outward. Similar to the Rio Hondo pluton, a subhorizonal roof zone, veined by aplite and pegmatite is preserved along high ridges. The main Lucero Peak pluton has yielded concordant K-Ar and fission-track dates of about 22 Ma. In contrast to the Rio Hondo pluton, the main mass of the Lucero Peak lacks cross-cutting dikes, suggesting a younger emplacement age, in agreement with the radiometric data. However, an eastern Lucero body is cut by dikes, locally altered, and contains pyrite and molybdenite. These dikes probably represent the youngest intrusive activity in the southern area of Tertiary intrusions.

Plutons along the southern caldera margin. Three pyritized and hydrothermally altered plutons containing molybdenum deposits are alined east-west along the Red River, following the south margin of the caldera (Fig. 6). These plutons postdate caldera collapse and intrude both Precambrian rocks of the caldera wall and Tertiary volcanic units of the caldera floor and fill, including the Amalia Tuff. Their roof zones extend highest within upthrown blocks bounded by north- or northwest-trending

regional fault systems that cross the caldera margin. These plutons are thought to represent fault-localized cupolas along an intrusive mass that is interconnected at shallow depth, constituting a partial ring intrusion along the south caldera margin. Associated with the Red River intrusions is a major east-west swarm of rhyolitic dikes that cuts Precambrian rocks just south of the caldera wall (Fig. 7; Reed et al., 1983). Available ages indicate that these intrusions are about 23 Ma.

Central and northern intracaldera plutons. Plutons within central and northern parts of the caldera are compositionally and texturally diverse, and detailed relations among them and with the Red River intrusions are uncertain. These plutons mainly intrude Precambrian rocks of the caldera floor where it is structurally most elevated. They are interpreted as related to postcollapse resurgence of the caldera and contain only minor associated altered or mineralized rocks at exposed levels.

The largest intrusive masses are exposed low along the mountain front, presumably because these are the deepest structural and erosional levels. The main masses, exposed along Rito del Medio and Cañada Pinabete (Fig. 6), consist of similar fine- to medium-grained equigranular granite. Rito del Medio pluton is characterized by miarolitic cavities as much as 1 cm across.

An eastern structurally higher body, best exposed in Virgin Canyon (a major tributary to Rito del Medio), ranges from equigranular granite, similar to those just described, to distinctive marginal acmite-arfvedsonite granite and rhyolite

porphyry of weakly peralkaline composition. This border phase of the Virgin Canyon pluton is chemically identical to late-erupted parts of the Amalia Tuff and is interpreted as a quenched portion of the magma that was largely erupted to form the tuff. The Rio del Medio and Virgin Canyon bodies have yielded fairly concordant radiometric ages of 25-27 Ma, interpreted as the time of emplacment.

Large discontinuous dike-like masses of similar peralkaline granite porphyry are also traceable for 4 km along the northern caldera margin, defining an incomplete ring dike as much as 100 m thick dipping steeply to the south. These are the northernmost granitic intrusions in the Latir field. Compositionally similar smaller dikes and irregular intrusions of peralkaline rhyolite porphyry also occur widely within the caldera, as described in the next section.

Between Rito del Medio and the Red River intrusions, roof-zone exposures of medium-grained granite of the Cabresto Lake pluton are low-silica granite, transitional between Rio Hondo quartz monzonite and the more silicic granites along the Red River and farther north within the caldera. These are the least differentiated granitic rocks within the caldera. The Cabresto Lake pluton contains more silicic granite porphyry along its southern margin, within about 2 km of the Moly Mine intrusion, suggesting interconnection at shallow depth. The Cabresto Lake pluton has yielded somewhat discordant radiometric ages (22-25 Ma), interpreted as recording partial resetting of an earlier emplacement age by younger Red River intrusions.

Hypabyssal intrusive rocks

Porphyro-aphanitic dikes, sills, laccoliths, and small irregular intrusions commonly cut volcanic rocks of the Latir field and adjacent Precambrian rocks (Fig. 7). Compositions range from basalt to silicic rhyolite, with rhyolitic and quartz latitic intrusions most numerous.

Rhyolitic rocks range from aphanitic to coarsely porphyrytic; porphyritic rhyolites contain phenocrysts of quartz and K-feldspar. Biotite-bearing metaluminous rhyolites occur throughout the region; weakly peralkaline rhyolites lacking biotite are confined to the caldera area. The peralkaline rhyolites within the caldera form scattered small dikes and irregular intrusions without a strong directional orientation; these rocks document the continued availablilty of peralkaline magma during and after caldera collapse.

A major northwest-trending dike swarm, consisting of hundreds of individual dikes, cuts the Rio Hondo pluton and adjacent Precambrian rocks south of the Questa caldera (Fig. 7; Reed et al., 1983). Dikes range from basalt to rhyolite; rhyolite is dominant in the center of the swarm, and quartz latite is most common in peripheral areas. Dikes are most numerous over the flat-lying roof zone of the Rio Hondo pluton, where locally for distances of 1 km or more, only a few percent of country rock is preserved as screens between rhyolite dikes. Cross-cutting relations are locally so complex that individual dikes cannot be mapped. Development of the major swarm is interpreted to have

resulted from regional rift-related extension concurrent with emplacement of the batholithic granitic rocks.

Rhyolitic dikes trending east-west dominate along the south margin of the caldera; to the south, trends of dikes shift to merge irregulary with the northwest-trending dike swarm just described (Fig. 7; Reed et al., 1983) Some east-west rhyolite dikes along the caldera margin are as much as 15 m thick, forming massive cliffs and fins.

Quartz latite forms dikes 1-10 m wide throughout the map area, and constitutes the dominant dike type away from the intense swarms of rhyolite dikes. Large irregular areas of intrusive quartz latite near the southeast caldera margin are interpreted as irregular laccoliths and sills emplaced in the Tertiary sedimentary and volcanic sequence. Quartz latite also forms irregular intrusive bodies emplaced locally along major Tertiary normal faults. Andesitic and basaltic dikes are smaller and less numerous than the more silicic intrusions.

DISCUSSION

Structures of the eroded Questa caldera offer insights into possible features of the Long Valley caldera that may be responsible for the current episode of magmatic unrest there. Key features include relations between regional extensional tectonism and the caldera magmatic system, geometry and longevity of the the subcaldera magma body, and style of deformation along caldera- bounding faults in an extensional tectonic regime.

Both Questa and Long Valley magmatic systems have evolved during periods of intense regional extension, respectively associated with opening of the Rio Grande rift and with extension along the western margin of the Basin and Range province. At Questa, structural relations between the Tertiary igneous rocks and regional faults demonstrate that extensional deformation was intense during volcanism, although movement continued on many faults after the culmination of volcanism. The major northwest-trending dike swarm south of the Questa caldera demonstrates regional extension during consolidation of the Rio Hondo pluton. Paleomagnetic data show that the cogenetic granitic underpinnings of the Questa caldera, which yield radiometric ages little different from the volcanic rocks they intrude, cooled through their Curie temperatures (about 500^{0} C.) after most tectonic tilting of intracaldera caldera rocks was complete (Hagstrum et al, 1982, and written commun., 1984). These relations indicate that maximum deformation in the Latir field was nearly concurrent with caldera formation.

Both Questa and Long Valley have semi-rectilinear outlines,

with linear segments of the walls oriented approximately parallel and perpendicular to concurrently active regional faults. In addition, these calderas are both elongate perpendicular to regional normal faults. Collapse occured preferentially in directions where regional normal faults converge with the ring faults and was inhibited in directions where the regional and caldera structures intersect at a high angle.

If regional extension is concurrent with caldera evolution, complex structures can be expected along segments of the caldera wall and bounding faults that are transverse to regional structural trends. At Questa, east-west segments of the caldera ring-fault zone, that were transverse to regional extensional structures, acted as transform or tear faults to accomodate contrasting degrees of extension and tilting within and outside the caldera, during resurgence as well as during subsidence. Analogous deformation currently seems associated with seismicity in the south moat of Long Valley, where a component of strike-slip motion would be required along the southern caldera boundary to accomodate east-west extension of the block-faulted terrain north and south of the caldera. The striking change in dike direction from regional to caldera-related trends along the south margin of the Questa caldera (Fig. 7) documents the large scale on which caldera structures can perturb the regional stress field. Similar reorientations at Long Valley are recorded by seismic, geodetic, and magnetotelluric observations (Hermance, 1983).

The great east-west dike swarm along the south margin of the

Questa caldera may have been the product of repeated events such as those responsible for the linear seismic zone in the south moat of Long Valley. Although hundreds of dikes are present in this setting at Questa, it is likely that only a small fraction were associated with surface volcanism. Similarly, many dikes may have been inturded into the ring-fracture system at Long Valley without associated eruptions. Postcollapse volcanic events are relatively sparse along margins of well preserved silicic caldera systems: only a few to several tens seem typical (Lipman, 1984).

The linear trends of vents for the Inyo and Mono volcanic chains, north of Long Valley, suggest eruption from north-trending dikes emplaced along extensional faults associated with the east front of the Sierra Nevada (Miller, 1983). The dike system beneath these vents may thus be analogous to the dike swarm south of the Questa caldera, associated with the roof zone of the Rio Hondo pluton. The widespread exposures of granitic rocks south of the Questa caldera and their close correlation with gravity anomalies show that caldera-related magma chambers need not be precisely centered below the caldera, although cross-section interpretations for Questa suggest caldera formation above the originally shallowest portion of the overall magma chamber (Fig. 5). Similarly to interpretation of the east-west zone at Questa, only a small proportion of the hundreds to thousands of northwest-trending dikes south of the caldera could have been associated with surface volcanism. Analogously, many dike injection events may take place along the Mono-Inyo trend

without magma reaching the surface.

Features of dikes at Questa also provide possible analogues for the inferred dike injection into regional faults south of the Long Valley caldera (Julian and Cockerham, 1983). No geophysical or other evidence suggests presence of a large silicic magma body south of Long Valley caldera, but magma could have migrated southward along regional structures from the caldera area. Southeast of the Questa caldera, exceptional exposures of grooves and mullions on the walls of several large rhyolite dikes, that follow a major regional extensional fault zone, show that they were emplaced laterally rather than vertically. Such lateral movement of magma, localized by the regional stress field, has been well documented for dikes associated with many volcanic shields and cones (Nakamura, 1978). Nevertheless, a better comparison with the block-faulted region south of Long Valley may be the area north of the Questa caldera, where no dikes have been found, even though major regional extensional faults disrupted the Latir volcanic field at about the time of caldera formation. This part of the Latir field is beyond the north limit of the cogenetic batholith, as indicated both by absence of exposed intrusive rocks and by termination of the gravity anomaly associated with the intrusions (Fig. 6).

Finally, the geometries and ages of intrusions within and adjacent to the Questa caldera offer insights into geophysical models of the magma chamber beneath Long Valley. Interpretation of shear-wave attenuation suggests that magma is present at depths as shallow as 4.5 km, forming several interconnected

cupolas below the medial graben faults of the resurgent dome (Sanders, 1984). At Questa, high points on the composite batholith also are within the caldera along the crest of the resurgent dome; highest structural levels of other plutons are within upthrown portions of regional extensional fault blocks. Although roof zones of some plutons dip gently over large areas, steep sides of several plutons follow regional faults, and the faults cannot be shown to offset the plutons. Probably, most plutons were still liquid during major regional faulting, as is also suggested by the paleomagnetic data (Hagstrum et al., 1982). Radiometric data also indicate that sequential intrusion and magmatic replenishment continued for 3-4 m.a. after caldera formation, accompanied by active hydrothermal systems and associated mineralization. Similarly, in the Long Valley area recurrent silicic volcanism over the past 2 m.y. could not have been sustained without repeated replenishment by additional magma (Lachenbruch et al., 1976).

In summary, the eruptive history, structural features, and petrologic development of geologically young ash-flow calderas can provide data on early stages in the evolution of silicic magmatic systems; study of eroded older analogues, where cogenetic intrusions are exposed, provides a record of the deeper structures of calderas and the late stages of evolution of silicic magmas.

REFERENCES

Bailey, R. A., Postcaldera evolution of the Long Valley magma chamber, eastern California (abs.), EOS, 64, 889, 1983.

Bailey, R. A., G. B. Dalrymple, and M. A. Lanphere, Volcanism, structure, and geochronology of Long Valley caldera, Mono County, California, J. Geophys. Res., 81, 725-744, 1976.

Cordell, L., Complete Bouguer anomaly map of the Taos Basin section of the Rio Grande rift, New Mexico, U.S. Geol. Surv. Open-File Map 78-317, 1978.

Denlinger, R. P., and F. Riley, Deformation of the Long Valley caldera, Mono County, California between 1975 and 1982, J. Geophys. Res., 89, in press, 1984.

Hagstrum, J. T., P. W. Lipman, and D. P. Elston, Paleomagnetic evidence bearing on the structrual development of the Latir volcanic field near Questa, New Mexico, J. Geophys. Res., 87, 7833-7842, 1982.

Hermance, J. F., The Long Valley/Mono Basin volcanic complex in eastern California: Status of preseent knowledge and future research needs, Rev. Geophys. and Space Phys., 21, 1545-1565, 1983.

Julian, B. R., and R. S. Cockerham, Evidence for dike-intrusion earthquake mechanisms near Long Valley caldera, California, Nature, 303, 323-325, 1983.

Lipman, P. W., Volcano-tectonic setting of Tertiary ore deposits, southern Rocky Mountains, in Dickinson, W. R., and Payne, W. D., eds., Relation of tectonics to ore deposits in the southern cordillera, Arizona Geol. Soc. Digest, 14, 199-

213, 1981.

Lachenbruch, A. H., M. I. Sorey, Re. E. Leis, and J. H. Sass, The near-surface hydrothermal regime of Long Valley caldera, J. Geophys. Res, 81, 763-784, 1976.

Lipman, P. W., The Miocene Questa caldera, northern New Mexico: relation to batholith emplacement and associated molybdenum mineralization, in The genesis of Rocky Mountain ore deposits, Proceedings Denver Region Exploration Geologists Society Symposium, 133-148, 1983.

Lipman, P. W., The roots of ash-flow calderas in western North America, J. Geophys. Res., 89, in press, 1984.

Miller, C. D., Chronology of Holocene eruptions at the Inyo volcanic chain, California, EOS, 64, 900, 1983.

Miller, C. D., D. R. Mullineaux, D. R. Crandell, and R. A. Bailey, Potential hazards from future volcanic eruptions in the Long Valley - Mono Lake area, east-central California and southwest Nevada, a preliminary assessment, U.S. Geol. Surv. Circ. 877, 10 pp., 1982.

Muffler, L. J. P., and D. L. Williams, Geothermal investigations of the U. S. Geological Survey in Long Valley, California, 1972-1973, J. Geophys. Res., 81, 721-724, 1976.

Nakamura, K., Volcanoes as possible indicators of tectonic stress orientation, J. Volcan. Geotherm. Res., 2, 1-16, 1977.

Reed, J. C. Jr., P. W. Lipman, and J. M., Robertson, Geologic map of the Latir Peak and Wheeler Peak Wildernesses and Columbine-Hondo Wilderness Study Area, Taos County, New Mexico, U.S. Geol. Surv. Misc. Field Studies Map MF-1570B,

1983.

Ryall, A., and F. Ryall, Spasmodic tremor and possible magma injection in Long Valley caldera, eastern California, Science, 219, 1432-1433, 1983.

Sanders,, C. O., Location and configuration of magma bodies beneath Long Valley, California, determined from anomalous earthquake signals, J. Geophys. Res., 89, in press, 1984.

Savage, J. C. and M. M. Clark, Magmatic resurgence in the Long Valley caldera, California--possible cause of the 1980 Mammoth Lakes earthquakes, Science, 217, 531, 1982.

Savage, J. C., and R. S. Cockerham, Earthquake swarm in Long Valley caldera, California, January 1983: evidence for dike intrusion, J. Geophys. Res., 88, submitted, 1984.

FIGURES

Figure 1. Generalized map of the Long Valley/Mono Basin area, showing its position relative to the Sierra Nevada to the west and the Basin and Range province to the east (after Hermance, 1983). Darkly shaded portions of the map represent Holocene eruptive centers. Shown by black circles are the epicenters of four M=6+ earthakes of 25-27 May 1980.

Figure 2. Epicentral distribution (top) of earthquakes during the January 1983 swarm at Long Valley (Savage and Cockerham, 1984). The box encloses earthquake epicenters plotted in cross-section (bottom). Solid dots (top) represent locations of seismometers.

Figure 3. Structural map of the southern Rocky Mountains, showing location of Latir volcanic field and associated Questa caldera (from Lipman, 1981).

Figure 4. Miocene and younger normal faults, in relation to the Questa caldera (diagonal-line pattern). Faults are dashed where approximately located, dotted where concealed; bar and ball indicates downdropped side. Dashed line indicates margins of mountainous areas (light stipple). Solid triangles, locations of major mountain peaks. From Lipman (1983).

Figure 5. North-south cross section through the Questa

caldera and associated subvolcanic batholith. Section drawn at 106° 30′ (see Fig. 6), parallel to trend of Rio Grande rift to reduce effects of these structures. Basal Tertiary surface rises to south, probably due to uplift over batholith, and deepest exposed batholithic rocks to south are interpreted to have been about 5 km below Tertiary land surface. From Lipman (1983).

A. Geologic section: units:

Ts, rift sedimentary rocks of the Santa Fe Group

Tgy, Younger granitic intrusions related to Mo mineralization

Tgp, Peralkaline granite at crest of resurgent intrusion within caldera; chemically identical to Amalia Tuff

Tg, low-silica granite within caldera and granitic cap overlying quartz monzonite (Tqm) outside caldera

Tqm, Quartz monzonite at deeper levels of batholith

Tt, Amalia Tuff (ash-flow deposits of Questa caldera)

Tq, Precaldera lava-dome complex on caldera floor

Ta, Precaldera andesite

pC, Precambrian metamorphic and granitic rocks

B. Bouguer gravity profile; data from Cordell (1978).

Figure 6. Bouguer gravity field in relation to Tertiary granitic intrusions associated with the Latir volcanic field. Contour interval, 4 milligals; hachures point toward gravity lows. Gravity data from Cordell (1978). Granitic intrusions (diagonal-line pattern). from north to south: RM, Rito del Medio, VC, Virgin Canyon; CB, Canãda Pinabete; CL, Cabresto Lake;

RR, Red River, MM, Moly Mine; BC, Bear Canyon; RH, Rio Hondo; LP, Lucero Peak. Dashed lines indicate margins of mountainous areas (light stipple); heavy hachured line, topographic wall of the Questa caldera (dotted, where concealed in Rio Grande rift). From Lipman (1983).

Figure 7. Generalized distribution of Tertiary intermediate and silicic intrusions associated with the Latir volcanic field. Heavy-stipple pattern, granitic intrusions; diagonal-line pattern, large masses of porphyritic quartz latite; coarse-stipple pattern, large rhyolitic intrusions. Thin lines, dikes of rhyolite and quartz latite. Dashed lines indicate margins of mountainous areas (fine stipple); hachured line, topographic wall of the Questa caldera (dotted, where concealed in Rio Grande rift). From Lipman (1983).

TABLE 1. Generalized Tertiary igneous and stratigraphic sequence of the Latir volcanic field

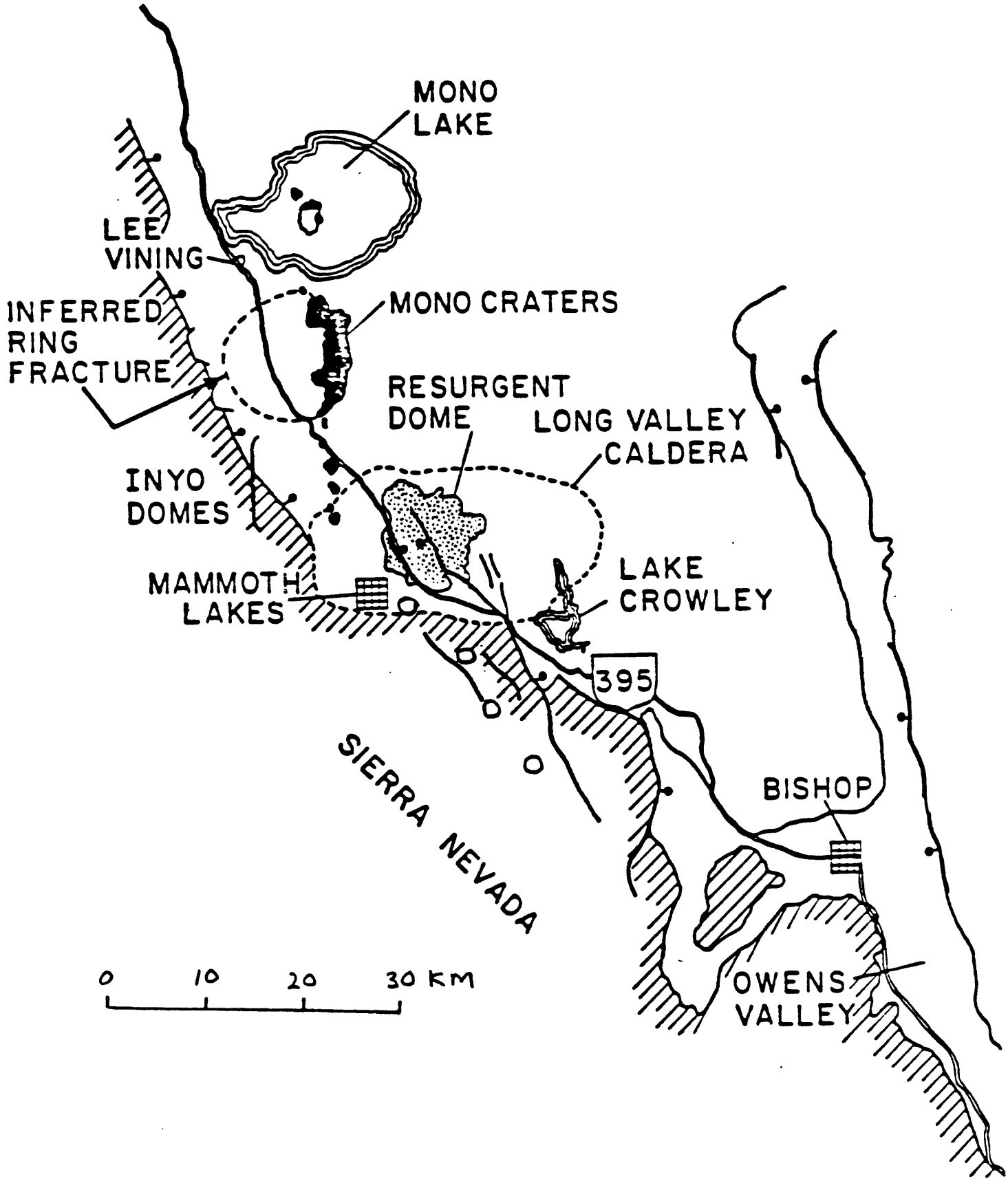
MONO
LAKE
LEE
VINING
INFERRED
RING
FRACTURE
MONO CRATERS
RESURGENT
DOME
LONG VALLEY
CALDERA
INYO
DOMES
MAMMOTH
LAKES
LAKE
CROWLEY
395
SIERRA NEVADA
BISHOP
OWENS
VALLEY
0 10 20 30 KM

Figure 1.

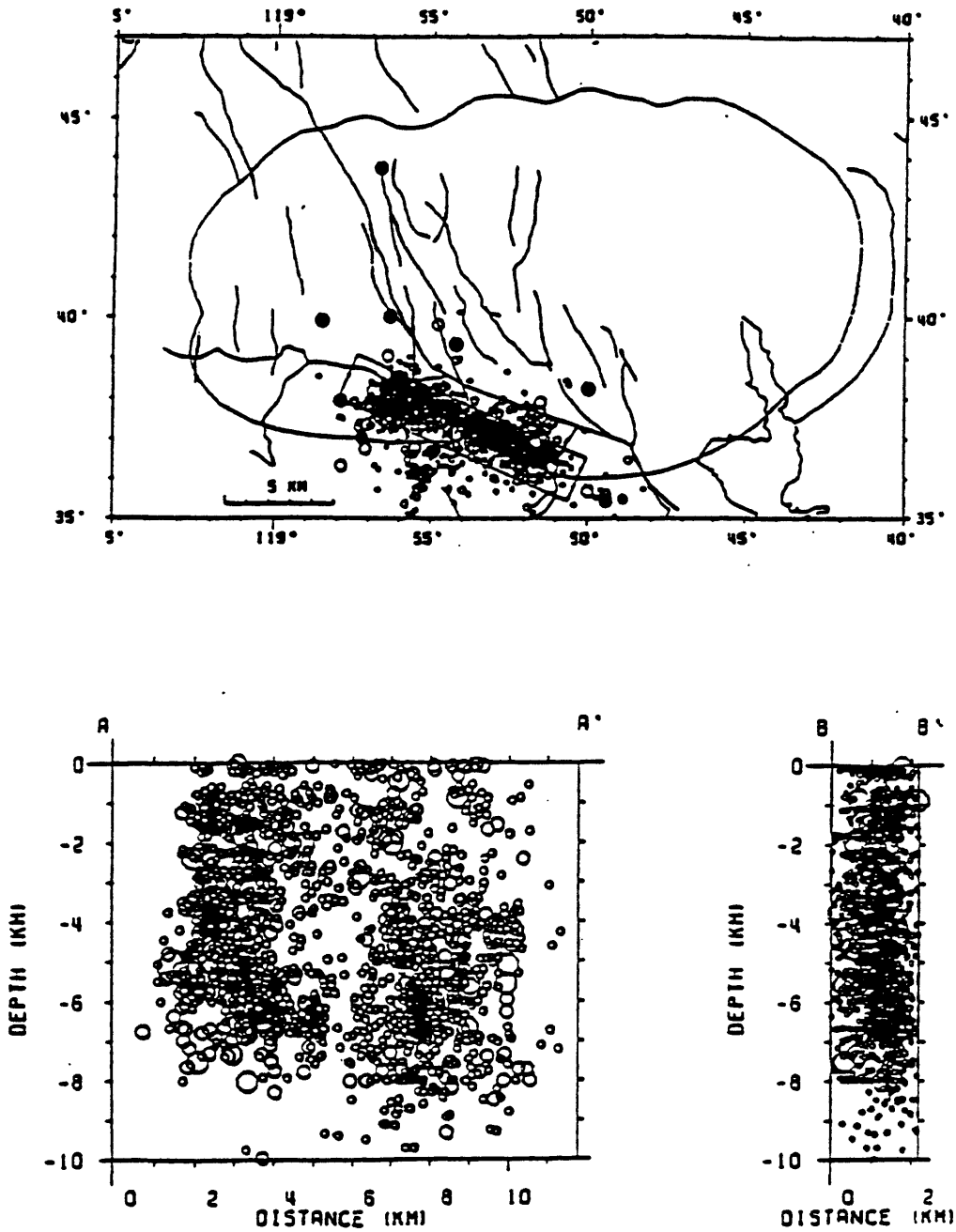
5°
119°
55°
50°
45°
40°
45°
40°
35°
5 KM
A
A'
B
B'
0
-2
-4
-6
-8
-10
DEPTH (KM)
0
2
4
6
8
10
DISTANCE (KM)

FIGURE 2

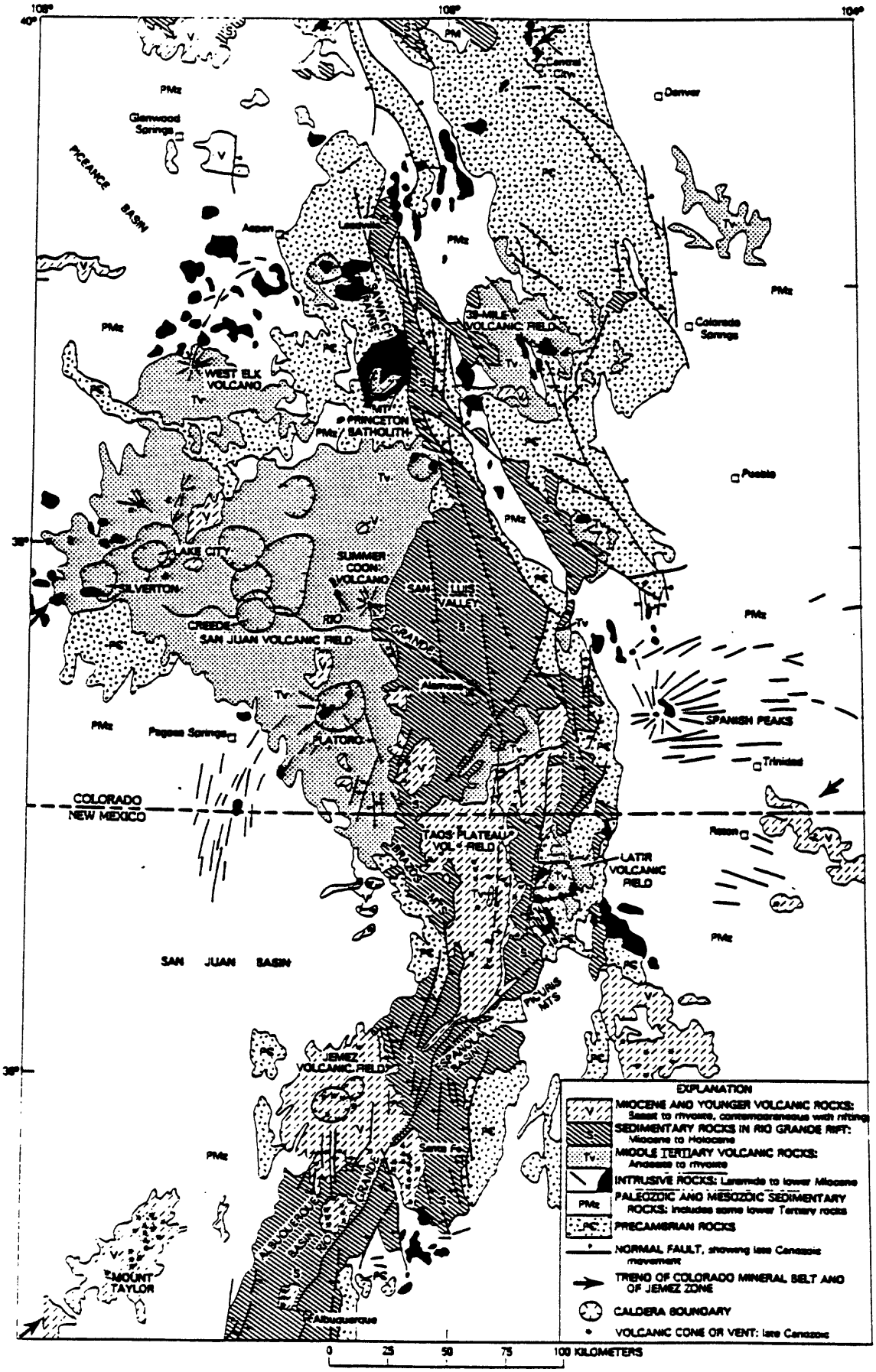
108°
106°
104°
40°
38°
PICEANCE BASIN
Glenwood Springs
Aspen
Leadville
Central City
Denver
Colorado Springs
Pueblo
Trinidad
Raton
WEST ELK VOLCANO
PRINCETON BATHOLITH
MT. SAWATCH RANGE
39-MILE VOLCANIC FIELD
LAKE CITY
SILVERTON
CREEDE
SAN JUAN VOLCANIC FIELD
SUMMER COON VOLCANO
SAN LUIS VALLEY
RIO GRANDE RIFT
Alamosa
La Jara
Pagosa Springs
Platoro
SPANISH PEAKS
COLORADO
NEW MEXICO
TAOS PLATEAU VOLCANIC FIELD
LATIR VOLCANIC FIELD
SAN JUAN BASIN
JEMEZ VOLCANIC FIELD
SANGRE DE CRISTO MTS
ESPAÑOLA BASIN
ALBUQUERQUE BASIN
RIO GRANDE
Albuquerque
MOUNT TAYLOR
EXPLANATION
MIOCENE AND YOUNGER VOLCANIC ROCKS: Basalt to rhyolite, commonly associated with rifting
SEDIMENTARY ROCKS IN RIO GRANDE RIFT: Miocene to Holocene
MIDDLE TERTIARY VOLCANIC ROCKS: Andesite to rhyolite
INTRUSIVE ROCKS: Laramide to lower Miocene
PALEOZOIC AND MESOZOIC SEDIMENTARY ROCKS: Includes some lower Tertiary rocks
PRECAMBRIAN ROCKS
NORMAL FAULT, showing late Cenozoic movement
TREND OF COLORADO MINERAL BELT AND OF JEMEZ ZONE
CALDERA BOUNDARY
VOLCANIC CONE OR VENT: late Cenozoic
0 25 50 75 100 KILOMETERS

FIGURE 3

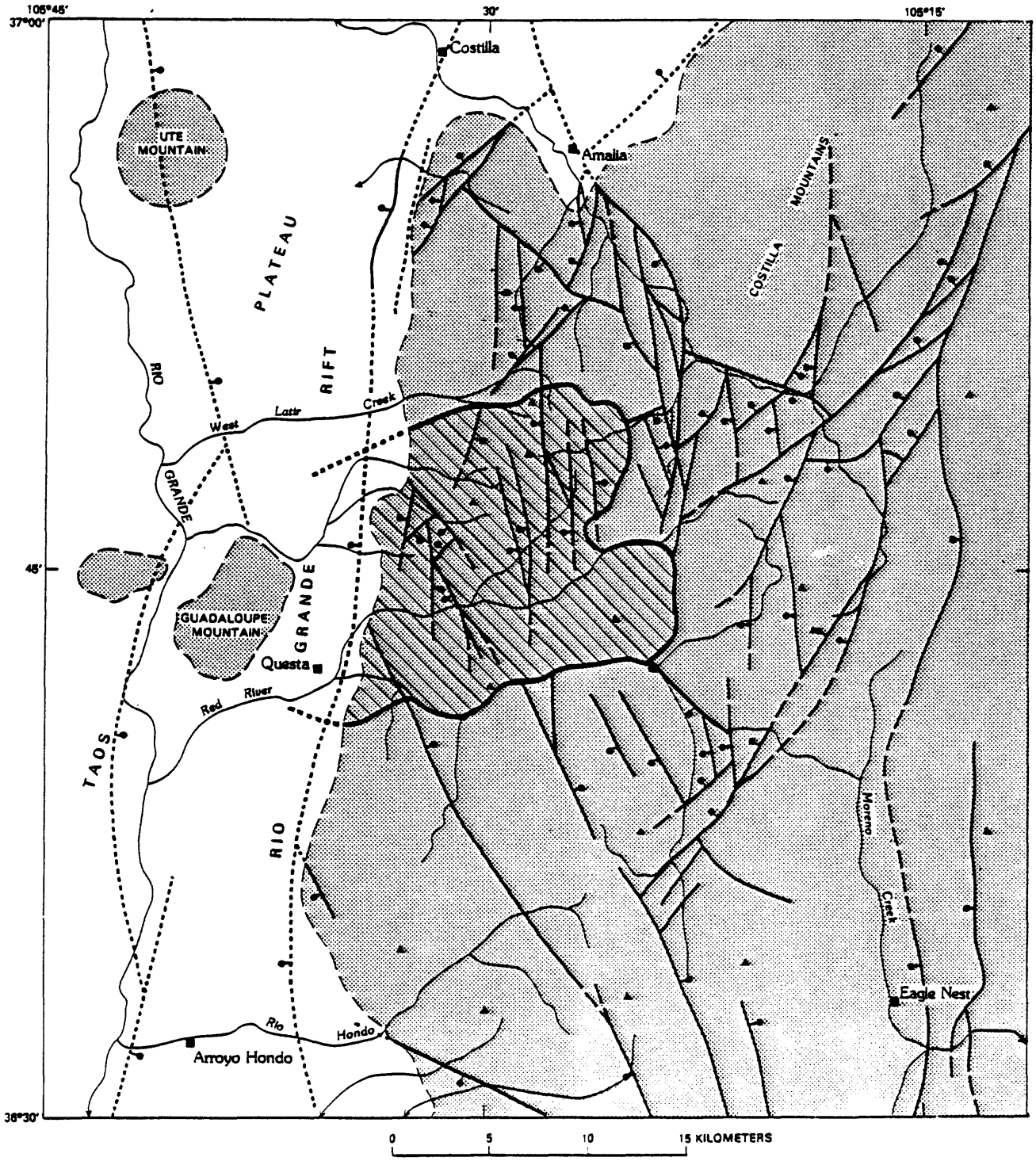
106°45'
30'
105°15'
37°00'
Costilla
Amalia
UTE MOUNTAIN
PLATEAU
COSTILLA MOUNTAINS
RIO GRANDE RIFT
West Latir Creek
RIO GRANDE
GUADALOUPE MOUNTAIN
Questa
Red River
TAOS
RIO
Moreno Creek
Eagle Nest
Rio Hondo
Arroyo Hondo
36°30'
0 5 10 15 KILOMETERS

FIGURE 4

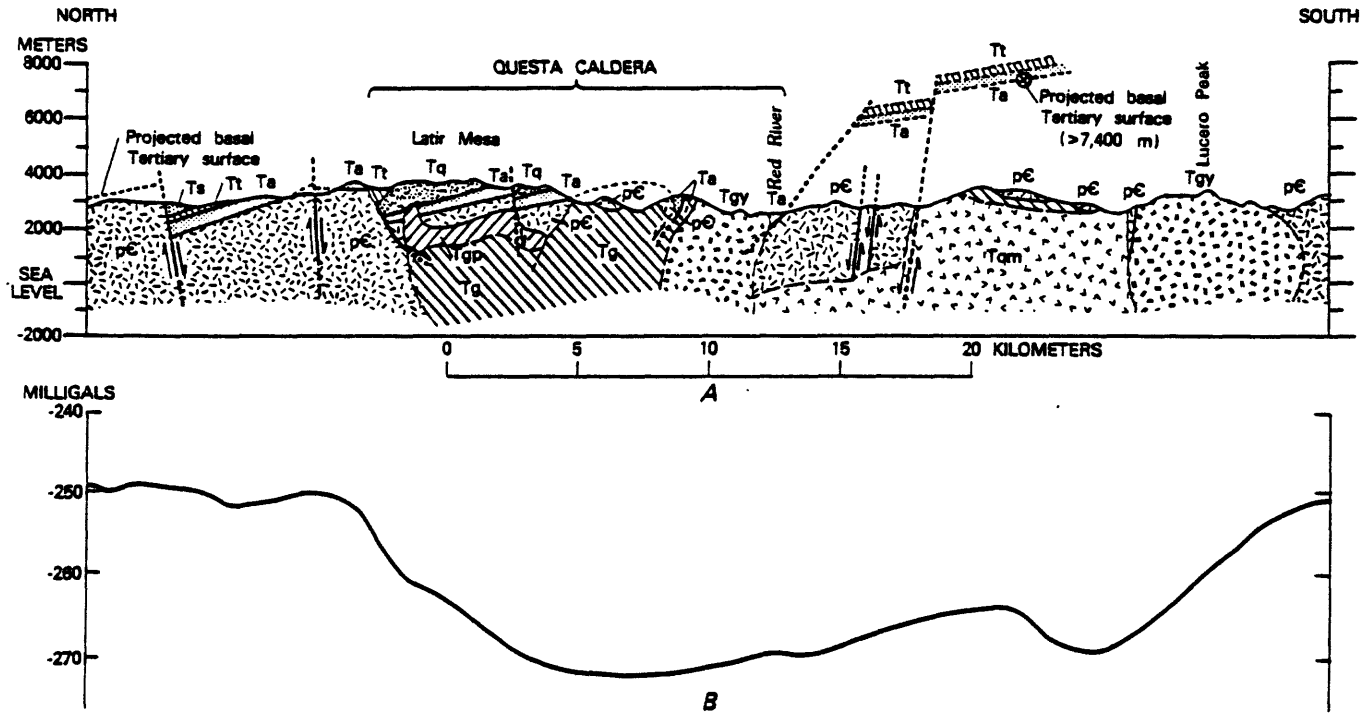
NORTH
SOUTH
METERS
8000
6000
4000
2000
SEA LEVEL
-2000
QUESTA CALDERA
Projected basal Tertiary surface
Latir Mesa
Red River
Lucero Peak
Projected basal Tertiary surface (>7,400 m)
Tt
Ta
Ts
Tq
Tgy
Tgp
Tqm
pC
0
5
10
15
20 KILOMETERS
A
MILLIGALS
-240
-250
-260
-270
B

FIGURE 5

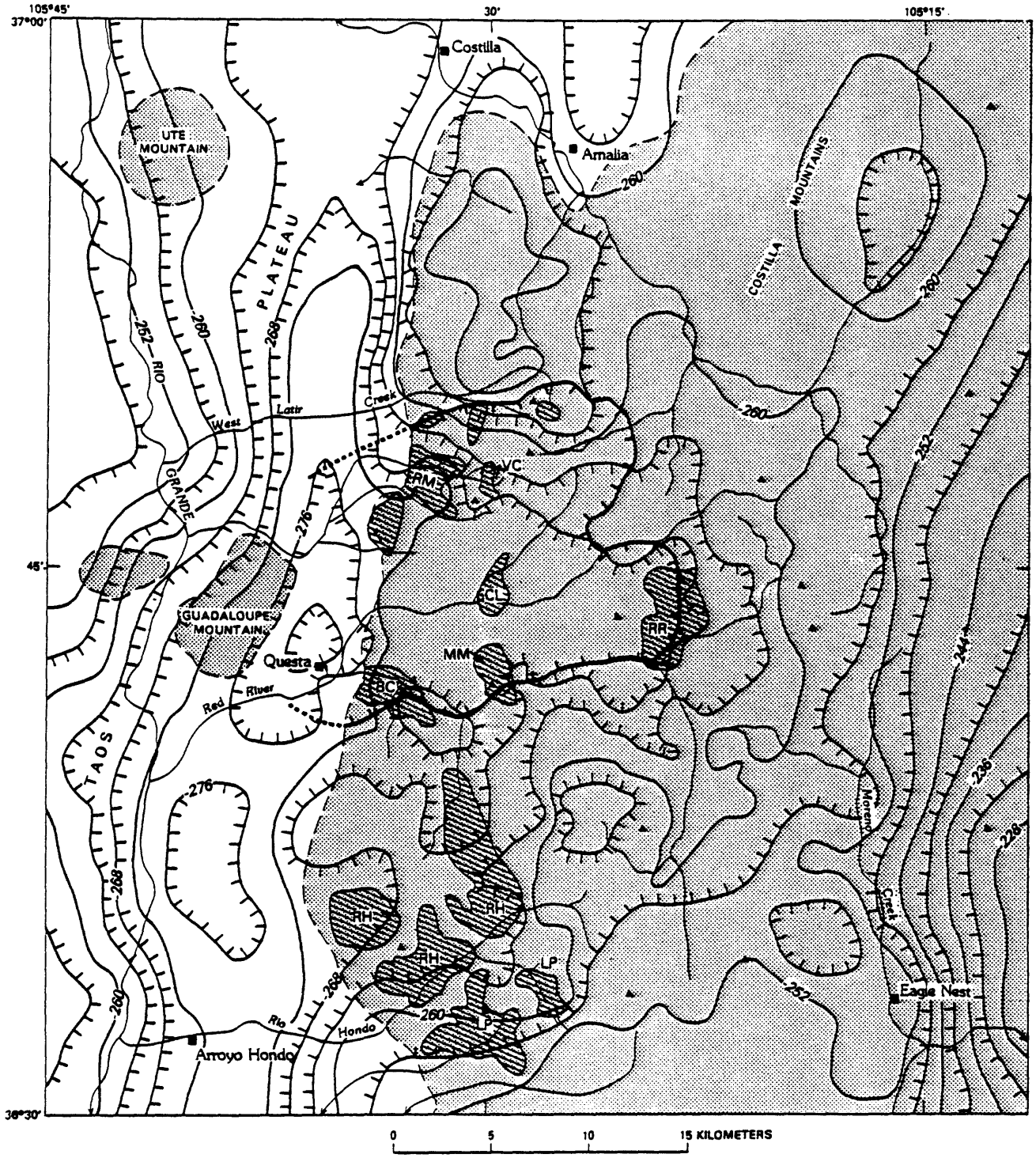
105°45'
30'
105°15'
37°00'
Costilla
Amalia
UTE MOUNTAIN
PLATEAU
COSTILLA MOUNTAINS
RIO GRANDE
West Latir Creek
VC
RM
CL
RR
MM
GUADALOUPE MOUNTAIN
Questa
Red River
BC
TAOS
Morena Creek
RH
LP
Eagle Nest
Rio Hondo
Arroyo Hondo
45'
36°30'
0 5 10 15 KILOMETERS

FIGURE 6

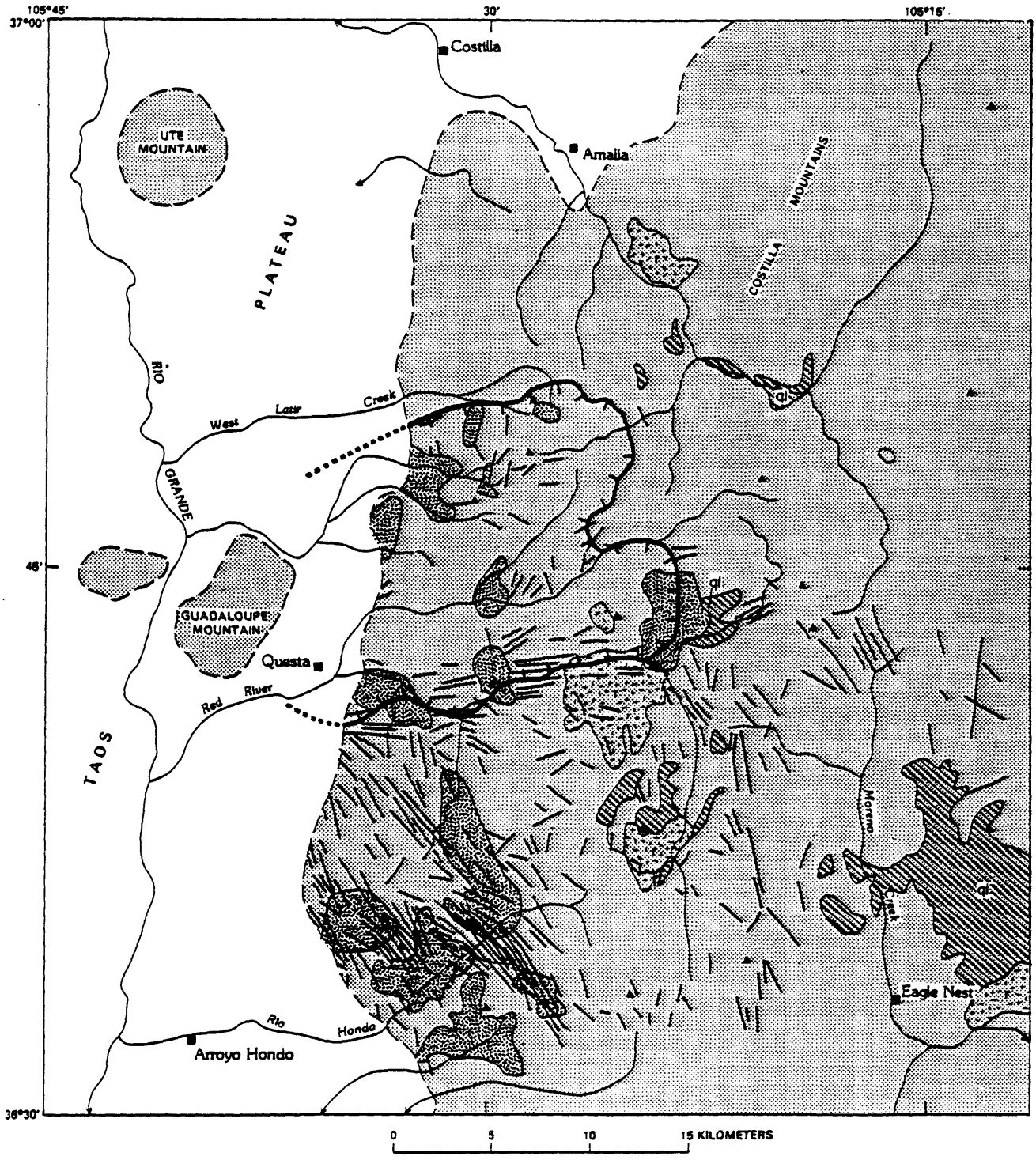
105°45'
30'
105°15'
37°00'
Costilla
UTE MOUNTAIN
Amalia
PLATEAU
COSTILLA MOUNTAINS
RIO GRANDE
West Latir Creek
45'
GUADALOUPE MOUNTAIN
Questa
Red River
TAOS
Moreno Creek
Eagle Nest
Rio Hondo
Arroyo Hondo
36°30'
0 5 10 15 KILOMETERS

FIGURE 7

TABLE 1. Generalized Tertiary igneous and stratigraphic sequence of the Latir volcanic field

[Ages estimated from unpublished K-Ar and fission-track determinations by H. H. Mehnert and C. W. Naeser (written commun., 1981, 1982)]

Unit	*Age (m.y.)*	*SiO_2 content*	*Composition and distinctive features*
Rift-related sedimentary and volcanic rocks			
Santa Fe Group			
Sediments from Precambrian sources	5-15		Silt to fanglomerate
Sediments from volcanic sources	16-22		Mostly conglomerate
Basaltic lava flows	15-16	44-51	Basanite to silicic alkalic basalt
Intrusive rocks of the Questa magmatic system			
Late mineralized plutons			
Intrusions along the Red River	22-23	76-77	Aplite and granite porphyry
Lucero pluton	22	76	Medium grained granite
Evolved intracaldera plutons			
Rito del Medio pluton	26	76	Medium grained granite
Canada Pinabete pluton	26	76	Medium- to fine-grained granite
Virgin Canyon intrusion and related rocks	26	76	Acmite-arfvedsonite granite and rhyolite porphyry
Cabresto Lake pluton	25-26*	72	Biotite-hornblende granite
Southern batholithic rocks			
Rio Hondo plutons	25-26*	64-76	Porphyritic quartz monzonite, locally grading into granite near roof
Amalia Tuff and cogenetic lava flows	26*	77-80	Rhyolitic ash-flow tuff and lava flows; phenocrysts of quartz, chatoyant sanidine
Precaldera volcanic rocks			
Comendite of Ortiz Peak	about 26	72	Forms thick flows and domes; large blocky K-feldspar phenocrysts
Latir Peak Quartz Latite	26-27	65-66	Forms thick flows and domes; phenocrysts of plagioclase, biotite, and hornblende
Andesitic and rhyodacitic flows	26-35	57-64	Variable in composition and texture; from many clustered central volcanos
Volcaniclastic sedimentary rocks	26-35		Mainly mudflow deposits, forming alluvial aprons around andesitic volcanoes
Tuff of Tetilla Peak	27	72	Weakly welded lithic-rich ash-flow tuff; highly variable in thickness
Early Tertiary sedimentary rocks (Vallejo Fm.)	Eocene(?)		Discontinuous post-Laramide sediments; weakly indurated; locally characterized by greenish cobbles of quartzite in reddish matrix

*Estimated age; discordant radiometric ages interpreted as variably reset by later igneous events.

A note on links between magma-tectonic rate balances. plutonism and volcanism

By

Herbert R. Shaw

U.S. Geological Survey

Menlo Park, CA 94025

Paper presented at Long Valley
"Redbook" Conference Napa CA, Jan.,84.
Submitted to JGR July 24, 1984

ABSTRACT

With R. L. Smith's model of ash-flow magmatism as the point of departure, quantitative regimes of crustal magmatic evolution are outlined. The average extrusive regime of ash-flow magmatism operates at a rate of about 0.001 km^3/yr; progressively larger episodes of increasing repose times characterize the evolution of caldera-forming eruptions. The intrusive regime operates at an inferred average rate of about 0.01 km^3/yr expressed in terms of the volumetric influx of mafic magma from the mantle, based on the record of silicic rates of extrusion. This rate is almost identical with the mean cumulative rate for the Hawaiian-Emperor system of basaltic volcanism, which is determined to be 0.015 km^3/yr. Fluctuations about a mean rate of 10^{-2} km^3/yr lead to a threefold classification of magmatic regimes, in terms of source power, depending on whether they are persistently greater than (HHER regime), about equal to (MHER regime), or lower than (LHER regime) the mean Hawaiian-Emperor rate. Ash-flow magmatism correlates with the MHER regime, averaged over a sufficiently long time. Thus, the conditions of Hawaiian-Emperor magmatism are identified with a characteristic balance of magma transfer rates that optimize mechanisms for creation of high-level chambers of derivative and fractionated silicic magma in the terminology of Smith's model. These conditions represent a balance point, and a bifurcation, in dynamic paths of magmatic evolution leading to widely divergent types of plutonic-volcanic associations. Categorical examples of the principal types of igneous path are discussed relative to

continental basalt, silicic ash-flow, batholithic granite and intrusive porphyry systems. The Henry Mountains, UT, are thought to represent an example of an intrusive porphyry generated in the LHER regime of a mafic source system lacking sufficient power for volcanic expression or significant mineralization. Long Valley, CA, (and possibly other systems along the eastern front of the Sierra Nevada), is an example operating at the mean rate with transient excursions to higher and lower rates. In regions of extension, these regimes give rise to basaltic eruptions ranging from isolated cinder cones to flood basalts.

INTRODUCTION

In his paper Ash-Flow Magmatism, Robert L. Smith (1979) described for the first time the quantitative history of magmatism necessary to sustain ash-flow eruptions from high-level magma chambers in the earth's crust. These relations are shown in Figure 1a taken from that paper (Smith, 1979, Figure 12). The conditons thus identified represent a special set of average magma transport rates in the crust that precisely balance the generalized eruptive mechanism for a broad class of volcanoes involving periodic accumulation and discharge of the most fractionated portion of derivative magma, using "most fractionated" and "derivative" in the specific sense defined by Smith (1979, Figure 12). Figure 1b compares tne open-system age-volume relation of Figure 1a with age-volume relations for closed-system solidification of magma chambers according to the calculations of Smith and Shaw (1975, 1979).

A major point of the present paper is that the conditions that support periodic ash-flow volcanism represent a characteristic regime among a spectrum of magma-transport paths and transport rates from sources in the earth's mantle into the crust. Synoptic examples of magma-transport rates and the consequent thermal anomalies produced at high levels in the crust are shown in Figure 2 (from Shaw, 1980, Figure 19). The purpose of tnis particular spectrum of injection and heating rates is to reveal the necessary, if not sufficient, conditions for tne development of thermal anomalies in whicn high-level magma chambers can exist, and to illustrate the magma-transport rates required for periodic storage, fractionation and climactic ash-flow eruptions; flow-through or piecemeal intrusion without

significant volcanism also depend on such rate balances, within the constraints of tectonically controlled paths of injection (Shaw, 1980). Figure 1b presents information that bridges the relations for open-system models of Figure 1a and Figure 2 with consideration of volumes and longevities of closed-system models, as discussed below.

The present paper attempts to summarize these relations in a way that relates the Smith (1979) model of volcanic evolution to the simplified Shaw (1980) model of magma transport. As a starting point, I refer to Smitn (1979) as the framework within which the Shaw model of transport is assumed to operate. I then discuss tne effects of departure from the Smith model of volcanism and extrapolate these variations to suggest the quantitative volumetric conditions characteristic of certain families of igneous intrusions that may or may not have had volcanic relatives. The Henry Mountains, Utah, is an example of a system that never achieved the conditions of tne Smith model, either in the sense that the spectrum of transport rates necessary to produce tne intrusions was insufficient to support high-level chambers capable of periodic volcanism, or in the sense that the intrusions represent the chambers of a volcanic evolution aborted before the Smith conditions of climactic eruption were reached. Otner examples of departures from the evolutionary conditions of ash-flow magmatism are pointed out on both larger and smaller scales.

THE SMITH MODEL OF VOLCANISM

Figure 12 of Smith (1979), represented here as Figure 1a, is a landmark in the history of quantitative studies in volcanology. It encompasses in a two-dimensional diagram the physical-chemical balances among the dynamic, thermal and rneological parameters of volcanic evolution. Simplistically, it traces a special dynamical balance among variables affecting the rates of change of temperature, chemical and phase composition, depth, magma viscosity, rock strength, stress and strain in a complex system of great lithologic diversity. The balance is special because, for whatever reasons, if any one variable were substantially modified in its time dependence, the result would be an entirely different type of igneous product. On the one nand, the result of one form of deviation is to permit more or less continuous extrusions of lava at the earth's surface without any buildup of nigh-level chambers that can lead to fractionation and climactic ash-flow eruption. On the other hand, the diametrically opposed form of deviation leads to conditions in which there may be little extrusion of lava in any form and insufficient accumulation of magma in chambers to permit fractionation and climactic eruption.

I can't say which of the physical-chemical rate variables is changed to cause one or the other deviation, because the resultant evolution is a product of the net changes in a complex set of variables without any necessary identities in any one or several variables. For example, the conditions of eruptibility are bracketed by Smith (1979) in terms of what he calls minimum and maximum viscosity barriers. This concept of "viscosity barrier" involves changes in the physical parameters that

define viscosity in the strict sense of classical fluid dynamics, but it also implies composite conditions at least of phase states, chemical composition, temperatures, strain rates and longevities of flow that defy definition in terms of any known rheological equations of state. Empirically, and descriptively, the concept indicates the extremal types of magmatic flow conditions that are identified with ash-flows eruptions.

Detailed description of the eruptive processes implied by Smith's model is left to his own words. Admittedly, Figure 1a is difficult to visualize without considerable study and experience. One aspect of Figure 1a (Smith, 1979, Figure 12), however, is simple, and it identifies the balances I wish to emphasize. This is the relationship between time (periodicity) and magma volume (ash-flow eruption volume). If each of the systems continued to operate repetitively in the same mode for indefinitely long times, points along the eruptive curve would represent a steady-state average eruption rate. This average rate, as identified by Smith's graph, is 0.001 cubic kilometers per year of ash volume for all systems regardless of size, within the framework of such a graphical simplication; actual rates for any single system undoubtedly deviate somewhat from such an overall correlation designed to represent all systems. According to estimates made by Smith and Shaw (1973, 1975, 1979), the magma chamber that supports the generation of the eruptive silicic fraction is about an order of magnitude larger in volume. Hence, the overall magma supply rate required to generate such a series of chambers is about 0.01 km^3/yr.

Although these open-system rates (0.001 km^3/yr, eruptive; 0.01 km^3/yr, intrusive) represent a key to the present discussion, I also use Figure 1a, despite its difficulties, to emphasize another point. An intrinsic part of Smith's (1979) model is the existence of a root system that supplies primitive magma to sustain the growth and eruptive potential of the more silicic portions of the system. In fact, Smith and Shaw (1975, 1979) viewed this supply rate as crucial to the ultimate thermal potential of igneous-related geothermal systems (including the related hydrothermal systems). The line marked "penetration limit" in Figure 1a signifies the injection potential for mafic magma into the upper parts of the system. The Snaw (1980) model of transport views the supply of mafic magma as a plexus of injection pulses controlled by conditions of extensional fracture of the lithosphere-crust section. The two models come together with regard to the crustal levels and rates at which the injection pulses create and sustain high-level silicic derivations, however these derivatives have evolved chemically. Figures 1 and 2 symbolize this connection.

I find it helpful to view Figure 1a as a mosaic of time-lapse sections through the volcanic plumbing system on many different volume and depth scales. The fact that the relevant data for the construction of Figure 1a were not specifically discussed by Smith (1979)--because of the sheer quantities of descriptive data--the basis for its construction requires additional comment. Basically, the reasoning depends on data for the relation between caldera areas and ash-flow volumes (Smith, 1979, Figure 2) relative to concepts of composition gradients within the magma chambers (Smith, 1979, Figures 9 and 10), combined with the varieties of evidence

for the characteristic times required to produce the ash-flow volume (recurrence times for multiple systems, etc). The latter are not documented in Smith (1979), but the general spectrum of time scales representing the active lifespans of systems of different sizes are indicated categorically by the catalogs of Smith and Shaw (1975, 1979) and Smith et al. (1978). For example, the well-studied Valles I and II ash-flow sheets each have volumes of about 300 km^3 and were separated in time by about 300,000 years (Figure 1a); the best estimate of chamber volume is about 3000 km^3 (see Smith and Shaw, 1975, Table 7, Column 9; ages are given in Column 6). These data yield the volume:time ratios cited, respectively, of 10^{-3} km^3/yr (extrusive ratio) and 10^{-2} km^3/yr (intrusive ratio). Other systems of diverse sizes and compositions yield similar ratios.

The above ratios can be qualitatively understood by reference to Figure 1b, which is based on the longevity of instantaneously emplaced magma volumes without subsequent additions. The median ratio in the stippled region, which is nearly the centroid of the time-volume range in Figure 2 as well as (except for the systems that are currently active) the centroid of the time-volume range in the systems evaluated by Smith and Shaw (1975, 1979), is about 10^{-2} km^3/yr; the latter time-volume range is represented by the hachured area in Figure 1b . Because this rate is the chamber volume divided by its solidification time, a similar volume would have to be introduced repetitively to sustain a chamber in the molten state over longer times. This reasoning is crude, because it does not consider the heating effects of the subsolidus history. For example, the smaller volumes in Figure 1b have smaller volume:time ratios than the

larger volumes (cf., crosses and dotted lines at log V = 0 and log V = 4, respectively). However, higher rates (or shorter recurrence times) at the smaller volumes, and smaller rates (or longer recurrence times) at the larger volumes would be required to produce an equivalent influence on crustal conductive thermal states in terms of conditions permitting persistence of magma chambers in a molten state. That is, the larger systems have more pervasive thermal influences, while the smaller systems have more localized influences. Hence, the supply rate is larger than the solidification ratio in small systems and smaller than the solidification ratio in large systems for the same overall rate of magmatic evolution toward the ash-flow stage.

Such models of repetitive closed system emplacement and cooling times can be refined to some extent in terms of calculations of thermal states in the crust that would balance given constant rates of magma emplacement (rather than intermittent instantaneous emplacements). The results of some calculations of this type are given in Figure 2 and compared with the instantaneous emplacement models in the stippled region of Figure 1b. On an order-of-magnitude basis the results are similar for calculations within the range of caldera-forming ash-flow systems. The reason for this resemblance is that it takes roughly the same amounts of magma (for systems within a given size range) to produce similar thermal effects in the crust over a prolonged time whether tne emplacement is intermittently instantaneous or is incrementally progressive.

Thus, there is reasonable temporal and dimensional consistency between the different modes of portraying rates in Figure 1a, Figure 1b, and Figure 2. 'In any detailed comparisons, however, the relationship between chamber shape, area and longevity must be taken into account specifically. Figure 2 is based on a constant area of 100 km^2 and thicknesses (rows of profiles) of 1, 5 and 10 km, whereas the lines of solidification times were calculated for chambers of constant shape and varying volume (see Smith and Shaw, 1975, 1979; Smith and others, 1978).

The above constancy of average steady state rates implies a unique characteristic of the evolution of caldera-forming systems. Because the larger systems documented by Smith (1979), such as the Valles, Timber Mountain, Yellowstone, and Fish Canyon systems, consist of ash-flow eruptions involving many stages of smaller-type systems, the same rough constancy of average long-term eruption rates is characteristic of the expanding growth of a volcanic province capable of producing the same relationships among caldera size, ash-flow volumes and periodicity portrayed by Smith. This is because the chamber system grows roughly an order of magnitude faster than the time-averaged eruption rates. The implication is, therefore, that systems satisfying the Smith conditions are also areally and volumetrically growing systems so long as the supply rate of primitive magma keeps pace.

THE SHAW MODEL OF MAGMA TRANSPORT RATES

Figure 2 (Shaw, 1980, Figure 19) was derived while working on numerical estimates of igneous-related geothermal energy (Smith and Shaw, 1973, 1975, 1979, and unpublished data), based on the spectrum of episodic extrusion rates determined from volumetric and age data for the Hawaiian-Emperor chain; see Figure 3 taken from Shaw and others (1980, Figure 10). The thermal anomalies depicted in Figure 2 were calculated by allowing magma to accumulate within a reference area of 100 km^2 at the indicated depth intervals in the crust for the time intervals shown on the graphs. This reference area happens to correspond to a value near the lower limit of the epicontinental caldera areas shown by the plot of caldera areas versus ash-flow volumes given by Smith (1979, Figure 2); it is roughly comparable to the areal extent of the Mount Mazama chamber (Crater Lake, Oregon). For systems with larger areas, the time scales shown in Figure 2 here would be increased roughly in proportion to the increased volume.

The primary import of Figure 2, for the purposes of the present discussion, is represented by the general balances between the amplitude of the thermal anomaly (modeled to a maximum temperature of 1200°C for basaltic primitive magma) and the volumetric rate of introduction of magma into a fixed interval at high crustal levels; the interval is filled by magma in a time given by the product of area times thickness divided by the rate (e.g., 100x1/0.3 = 333 years). After that time there is eitner flow-through, or the interval grows in thickness. At rates of the order 0.001 km^3/yr the anomalies created during the emplacement time are just

approaching temperatures in the silicic to intermediate range of magma temperatures (roughly 800°-1000°C) in the 100 km^2 reference area. At rates of the order 0.01 km^3/yr temperatures approach 1200°C, characteristic of the more mafic magmas. Combining these observations with an average rate of about 0.01 km^3/yr deduced from Figure 1 for the evolution of magma chambers capable of producing ash-flow eruptions, a general relationship is indicated concerning ash-flow systems in the available spectrum of transport rates for basaltic systems. That is, the higher temperatures of the mafic magma, and the profiles of Figure 2 symbolize the more primitive parts of the systems in Figure 1a.

As a general rule-of-thumb, high-level magma chambers capable of supporting ash-flow eruptions of types consistent with the Smith model are sustained by mafic feeder systems derived from mantle sources and operating in the same locus at an average rate of tne order 0.01 km^3/yr for a period of time sufficient to produce a chamber system roughly ten times the ash-flow volume (see Smith and Shaw, 1973, 1975, 1979). The overall period of time, however, is not given directly by either Figure 1 or Figure 2 which indicate the longevities of magmatic states without taking into account pauses or periods of very low rates. Generally, the evolution of a large volcanic province (such as the Jemez Mts, New Mexico vis-a-vis the culminating stages of the Valles caldera) takes place over a much longer time in an episodic fashion (ca. 10 m.y. for the Jemez system).

On the one hand, the periodicity scale of Figure 1a identifies only the time necessary to establish or re-establish the necessary volumes of most fractionated magma capable of eruption from a system already having

established the appropriate mechanisms for optimal evolution of primitive and derivative magma types. This implies prior stages of eruptions from smaller ash-flow systems or prior stages of volcanism lacking caldera-type eruptions. Figure 2, on the other hand, identifies the minimum times for magma emplacement consistent with the indicated thermal regimes; the profiles show relations between magma input rates and the times required to allow molten chambers to exist at high crustal levels at temperatures appropriate to derivative and primitive magma (roughly 800° to 1200°C). By inference, from Figure 1a, when the input rate is too low, there is insufficient thermal energy to produce a silicic fraction in adequate volumes to sustain caldera-forming eruptions. When the input rate is too high, however, the thermal states favor more mafic compositions throughout the chamber and basaltic rather than rhyolitic volcanism. A rate of about 10^{-2} km^3/yr represents a balance that seems to favor accumulation of eruptible, usually more silicic, magma in volumes sufficient to produce caldera-forming eruptions.

The minimum time scale for caldera-forming eruptions applies only when an optimum type of magmatic focus has already been established capable of containing the requisite eruptible fractionated volume. Geologically, many factors exist to prolong the buildup of the fractionated volume. One of these factors is the lag time required to build the thermal anomaly in the first place and to establish the thermal regime in which efficient fractionation can proceed. The shortest possible buildup time (for a given area) would be at least twice the solidification time, and, by inference, at least twice the recurrence time for silicic fractionation in a repetitive system (see Valles I and II in Figure 1a, and compare with

Figure 1b). This minimum estimate is based on the idea that about the same total amount of thermal energy is needed to produce the derivative and fractionated stage of a chamber as is needed to produce a precursive sequence of more mafic magma. Generally, buildup takes a much longer time, implying episodes of relatively low supply rates from the mafic source and/or migration. Some migration usually occurs even in nested caldera complexes, so the greater areal distribution also implies a stretching out of the total time scales of silicic evolution prior to climactic ash-flow eruption stages. Once a "derivative" chamber has been achieved, however, the time for silicic fractionation is consistent with the times estimated from consideration of either emplacement rates (Figure 2) or of averaged repetitive solidification times (Figure 1b). Variations about the mean rate must occur, however, and therefore relative increases and decreases of silicic fractionation rates are also implied (see Figure 3).

CONTINUITY AND PERIODICITY OF BASALTIC SUPPLY RATES

Considerations of time scales raise questions concerning mechanisms influencing the distribution and longevity of magma transfer from the mantle. The overall average rates derived from Figures 1 and 2 effectively treat the magma transfer as a constant supply rate into a single geographic locus of specified areal extent, whereas, in detail, the timing and localization is typically episodic. The spectrum of variable basaltic supply rates shown in Figure 3 for the Hawaiian-Emperor system spans a duration of about 75 million years and spans a linear geographic swath about 6000 km in length and several hundred kilometers in width. The aggregate volume is 10^6 km^3, comparable to Olympus Mons on Mars and large batholithic complexes on Earth (see Figure 4). The duration of this source in a fixed geographic locality such as one of the Hawaiian Islands, however, may be less than a million years.

The Hawaiian-Emperor volcanic chain is probably one of the most rapidly and systematically propagating magmatic sources in the world. Peak supply rates are also among the largest documented for volcanic systems, and the volumetric rates are proportional to the propagation rates (Swanson, 1972; Shaw, 1973; Shaw and others, 1980). Variable supply rates lower than peak Hawaiian rates operating in one geographic locus are envisioned as the mafic feeder systems for continental magmatism over durations measured in millions of years in that the average thermal power is approximately the same as that of the epicontinental types of ash-flow systems operating at peak efficiency (compare Figures 1 through 5). The Snake River-Yellowstone trend is commonly viewed as a comparable system in

theories of Plate Tectonics; note again, however, the proportionality of mean supply rate (Figure 4) to mean ash-flow volume rate (Figure 1a) of 10:1 during the culminating stages of the silicic evolution. Silicic eruption rates equaling the basaltic supply rates would suggest possibilities of extreme rejuvenation and/or transient flushing of fractionated magma from the system.

The distribution of the Hawaiian-Emperor basaltic volcanoes provides quantitative constraints for the scale of melting anomalies in the mantle, as demonstrated by Jackson and others (1972), Snaw (1973), Jackson (1976) and Shaw and others (1980). Data in Shaw and others (1980, Figure 8) show that wnen activity on subparallel and overlapping loci is studied closely, basaltic foci may be shortlived or may persist in time for several million years in the same general position along the chain. Also, and contrary to popular belief, activity has existed synchronously over several hundred kilometers along the lengtn of the chain from time to time during its evolution.

Melting anomalies in the mantle resembling tne H-E system are viewed as sources of injection paths into continental crust in a manner resembling the funneling effect described by Shaw (1980, Figure 5); i.e., propagating basaltic systems are envisioned as the mafic support systems for high-level silicic magma chambers. The general characteristics of such systems, as stated by Shaw and others (1980, p. 690-691), describes the general areal and temporal variability of subcrustal heat sources for cratonic silicic systems:

> If a melting anomaly were defined on the basis of relatively synchronous ages (~1 m.y. differences) of mature volcanoes, it would vary in size and shape along tne length of the chain: its long-chain dimension would vary from as much as 400 km to zero,

and its cross-chain width would vary from about 300 km to zero. For most of the chain the melting anomaly would be ovoid, with its down-chain length exceeding its cross-chain width. Thus, we think of the melting anomaly as an ovoid volume of the asthenosphere, ranging up to a few hundreds of kilometers in length and width, which oscillates in size and shape with time, and which is capable of producing magma at any time that may or may not reach the surface. Thus viewed, the melting anomaly has progressed the length of the Hawaiian-Emperor chain and has delivered volcanic material to the surface in a very episodic manner.

Figure 4 shows the cumulative volume of basalt versus age along the Hawaiian-Emperor chain. The episodic nature of this evolution is evident; plateau-like periods of low extrusion rates persist as long as 15 million years or so, then they are offset by abrupt and accelerative increases in volume rates. In general, the average rate over the latest 22 million years or so exceeds the average rate over the preceding 50 million years or so, although in either age interval rates even exceeding 0.1 km^3/yr are possible at any time, as shown by Figure 3. The overall average is about 0.015 km^3/yr, which is the average growth rate (approximately 10^{-2} km^3/yr) of periodically evolving ash-flow systems as inferred from Smith (1979); see Figure 1.

Figure 5 shows the age distribution of first-order rate variations about the mean value for the Hawaiian-Emperor system obtained from the smoothed cumulative curve in Figure 4; that is, Figure 5 is based on average slopes, while Figure 3 represents more "instantaneous" variations. Evidently, numerous time intervals existed in which net rates oscillated about an average of 0.01 km^3/yr for millions of years. Other intervals existed where net rates were much lower for periods exceeding 10 million years, and yet others existed where they greatly exceeded 0.01 km^3/yr for millions of years. Such time series of variable rates for

basaltic volcanism offer a basis for a general classification of continental magmatic regimes when the supply rates are viewed in the light of Smith's model of ash-flow magmatism.

For the purposes of the present discussion I tentatively identify three source-rate regimes delineated on the basis of comparisons of Figures 1 and 2 with Figures 3 through 5; they are designated as follows: LHER (low Hawaiian-Emperor rate), MHER (mean Hawaiian-Emperor rate), and HHER (high Hawaiian-Emperor rate). LHER refers to net rates lower than the overall mean value of 0.015 km^3/yr, MHER refers to net rates oscillating about the mean rate, and HHER refers to net rates exceeding the mean, each for durations lasting at least a few million years. Any one of these regimes may be transitional to another depending on factors influencing mantle propagation and/or disconnection of crustal pathways from the mantle source. Assuming that the source persists longer than the duration of continental volcanic systems, the regime MHER is identified as the general regime compatible with sustained ash-flow magmatism over long times. These regimes are roughly outlined in terms of time intervals in Figure 5.

CONTINENTAL INTRUSIVE REGIMES SUGGESTED BY BASALTIC SOURCE RATE REGIMES

Any of the regimes for magma supply rates may result in transient intrusive events of limited volume if the continuity with the source is truncated by the vagaries of Plate Tectonic motions. The intrusive character then will depend on the volumetric pulse, possibly ranging from isolated dikes and sills, to basaltic cinder fields or even to localized but voluminous basalt flow fields of relatively short duration. For example, an isolated pulse of injection at the highest rates for a period of 100,000 years could produce a basaltic lava field with a volume exceeding 10^4 km^3. This is a large lava field by standards of continental basaltic volcanism, yet it does not necessarily represent a significant thermal anomaly in the crust (e.g., in terms of geothermal potential) if a high-level derivative system had no chance to evolve. Incidentally, this possibility emphasizes the importance of combined geologic mapping and saturation dating of continental volcanic provinces of all types if we are ever to be in a position to classify their dynamical characteristics in ways that identify either economic or hazards potentials.

The more interesting intrusive regimes are those that persist over millions of years. The highest rate regime, HHER, may produce extensive deep crustal layered intrusions, which in turn may become the sources of extensive basaltic flow-through under appropriate continental stress conditions. Such an intrusive regime is thought to give rise to flood basalt provinces such as the Columbia River, Deccan, Keeweenawan, and similar basalt systems. In this regime, there is little opportunity for

high-level ash-flow systems to develop, because the conditions permitting evolution of derivative and fractionated magma volumes are overpowered, so to speak, and have no chance to operate. If there are high-level injections, flow-through is so rapid that residence times for individual magma batches are quite brief, perhaps only weeks to years (see Shaw and Swanson, 1970; Shaw, 1980).

Figure 5 identifies time intervals that would be candidates for periods of potential flood basalt volcanism if a comparable source were concentrated in a fixed continental locality. For example, between about 22 and 12 m.y. B.P., the net rates were consistently greater than 10^{-2} km^3/yr. Prior to 27 m.y. B.P., rates were predominantly less than 10^{-2} km^3/yr, but relatively high rates occur in three closely spaced episodes between about 61 and 54 m.y. B.P. In the event of rough global synchroneity of some magmatic episodes (McBirney et al., 1974; Shaw, 1980; Shaw, et al., 1980) similarly high rates might also be expected elsewhere. The Miocene Columbia River basalts and Cretaceous-Tertiary Deccan basalts correlate approximately with the age intervals of relatively high rates.

During times for which rates oscillate both above and below the mean rate (MHER), conditions are ripe for oscillatory evolution of silicic cratonic systems if the durations exceed a few million years. In Figure 5, the latest 8 m.y. B.P. conspicuously represents such a time interval. Coincidentally, this is also the time during which our largest, and ultimately most dangerous, active or potentially active silicic systems have evolved in the western U.S. (Yellowstone, WY; Long Valley, CA; Valles, NM, and their environs), not to mention the numerous silicic

systems of lesser but major hazard potentials (see catalog of silicic systems and their sizes in Smith and Shaw, 1975, 1979; Smith et al., 1978). The time interval 24 m.y. B.P. to about 17 m.y. B.P. also represents an oscillatory interval, analogous to the presumed source power for a cratonic system such as the San Juan volcanic field of about the same age.

Obviously, other temporal correlations can be sought among the age distribution of silicic ash-flow volcanism and voluminous plutonism in the western U.S., but they need to be examined in terms of more explicit rate data for both short-term and long-term histories of magmatic injection into continental crust. Our present substantial progress in this direction, stimulated by the geothermal energy program, needs to be intensified in the interests of hazards assessment programs.

The LHER regime involves injection rates that are too low to support magma chambers in which derivative and fractionated magma can evolve. As shown by Figure 2, if the rate is of the order 0.001 km^3/yr or less, the high-level thermal anomaly has too low an amplitude to form extensive regions above the liquidus even if the injection rate persists for millions of years. The total volumetric scale of this regime of piecemeal plutonic evolution, however, could be large. For example, a rate of 0.001 km^3/yr operating for 10 million years would produce an intrusive complex with a volume of 10^4 km^3 (note that this also suggests an expansion of the reference area according to consistency with crustal depths). This is a volume resembling the batholithic scale of isolated plutons. But, I do not imply that batholithic plutons in general evolve according to this regime. In fact, the largest batholithic systems are thought to involve long periods of higher oscillatory rates. Referring again to Figure 5,

the time between about 40 m.y. B.P. and 27 m.y. B.P. exemplifies a period when low-rate plutonic complexes lacking volcanic fractions would have evolved if similar rates operated in a continental setting; the Henry Mountains, Utah, are thought to have been emplaced about this time (early to middle Tertiary) according to Hunt et al. (1953).

ASH-FLOW MAGMATISM AS A DYNAMIC DIVIDE FOR THE ENERGETICS OF CONTINENTAL IGNEOUS EVOLUTION

In a crude way, the average conditions required for ash-flow magmatism separate two distinctly different types of magmatic evolution. In the one (HHER) there is little opportunity for major fractionation except in terms of residual crystal accumulations in isolated magma batches. In the other (LHER) there is great opportunity for piecemeal crystal-liquid separation processes, but the energy is too low to allow phenomena such as extensive crustal melting, liquid-state diffusion, double-diffusive fractionation, diffusive assimilation, vapor phase transport, and so on. The ash-flow regime (MHER) is the one that nappens to be uniquely capable of the richest diversity of processes that can give rise to derivative and fractionated magma types in high-level chambers.

In short, this simple twofold (or threefold) scheme clarifies some of the puzzling questions of magma types and types of continental intrusions in a way that is, to a first approximation, independent of geochemical arguments concerning provenance. To be sure, in each of these regimes based on energetic balances there is also a classification, not addressed here, based on chemistry (Smith, 1979, unpublisned data). Whether an igneous system relates to one or another type of genetic regime from the standpoint of ore deposits must also be related to its type of magmatic rate regime, both in terms of chemistry and the thermal energy required to sustain hydrothermal systems (Smith and Shaw, 1979).

It has long been wondered why among granitic plutons of otherwise similar bulk composition, one may be associated with a porphyry copper deposit, another with metasomatic deposits, another with extensive hydrothermal deposits while a fourth may be devoid of association with significant mineral deposits of any kind. Discussion of the varieties of mineralization regimes is beyond the scope of this paper, but I suggest that a major influence on the products is the overall path of genetic rate regimes relative to the balances I have outlined. The Smith model, besides classifying ash-flow systems, identifies an optimal evolutionary path for certain classes of mineralization and also represents an energetic bifurcation that dynamically separates other broad classes of igneous and igneous-related geothermal and mineralization products. (Note added: This subject was specifically discussed by R. L. Smith in his address to the S.E.G. during the Indianapolis GSA Meeting, Nov. 3, 1983).

THE HENRY MOUNTAINS, UTAH

These intrusions were made famous by G. K. Gilbert as the type locality for features he described as laccolites, a term later modified to laccoliths, apparently at the suggestion of J. D. Dana (Gilbert, 1877; Dana, 1880; Hunt, 1953). Other than the reports cited, and the analysis of the mechanics of laccolithic intrusion by Pollard and Johnson (1973), tnere is little information on the geochronology and evolution of the Henry Mountains in relation to other types of igneous systems. This system, however, appears to depart dramatically from the style of intrusive features associated with basaltic fields and also from the styles of intrusive features associated with ash-flow volcanism, although there are some resemblances to deformations associated with endogenous rhyolite domes. The intrusive features suggest a form of relatively sluggish plastic flow of porphyritic magma of intermediate compositions containing ubiquitous phenocryst concentrations ranging from roughly 30 to 50 percent. Although tne structural features are impressive, the intrusive volumes do not exceed some tens of cubic kilometers and apparently were emplaced at rates that would not support the existence of aphyric magma chambers. Hunt (1953) gives chemical, modal and volume data consistent with these impressions.

The emplacement of the Henry Mountains intrusions is thought to nave occurred in the early to middle Tertiary over a geologically short period

of time. Except for rare occurrences of basaltic and aplitic dike rocks reported by Hunt (1953), the greatest proportion of the intrusions consists of similar porphyritic diorite of relatively restricted chemical and modal compositions. If there had been volcanic equivalents, apparently they would have been latitic. As Hunt pointed out, the Henry Mountains intrusions chemically resemble other intrusive and extrusive centers in and around the Colorado Plateau. He also observed that the fine-grained matrix of the porphyritic diorite was chemically of rhyolitic affinities.

These characteristics fit a general description of derivative magma in Figure 1a, but apparently there was little opportunity to form fractionated magma, and, even if there had been, the resulting silicic system would have been among the smallest volumes listed in the catalogs of Smith and Shaw (1975; 1979) and Smith and others (1978). It is also interesting that the inferred early to mid-Tertiary age falls within the long interval of low H-E rates in Figure 5 (i.e., the interval from 40 to 27 m.y. B.P.).

Aside from the question of whether these intrusions are entirely of laccolithic character as described by Gilbert (1877) or have central cores of stock-like affinities as deduced by Hunt (1953), the Henry Mountains may be an example of a system operating in the LHER regime for a duration insufficient to sustain formation of high-level chambers capable of producing fractionated magmas or to support the evolution of any extensive volcanic equivalents. The intrusions themselves, accordingly, would represent the bouyant rise of incipient chambers aborted during the derivative stage.

The accuracy of these impressions awaits detailed analysis of the chemistry, geochronology and volumetric history of emplacement, but the Henry Mountains symbolize the importance of intrusive styles relative to the lower magma transport rates and may eventually be established as one of the calibration points in a classification of intrusive rate regimes.

COMMENTS ON THE VARIETY OF INTRUSIVE RATE REGIMES

Inspection of a catalog of igneous systems, such as the one outlined by Smith and Shaw (1975, 1979) for high-level silicic systems, compared with the geographic and temporal rate variations in basaltic source systems derived from the mantle (Figs. 3, 4 and 5), reveals a rich diversity of potential composite effects. The simplistic rate classification introduced here is a preliminary breakdown of characteristic types of igneous systems based on dynamic criteria as adjuncts to their chemistry and rock types. As the discussions of Smith (1979) illustrate, rock type and major element chemistry are important but insufficient criteria for the classification of igneous systems. Dynamic classifications are required to distinguish and document the great disparities of crustal paths and evolutionary histories of igneous rocks that in hand specimen, or even in surface outcrop, might look identical.

Daly's (1933) concept of "clans" is an important approach to the familial relations of igneous systems. An accurate descriptive terminology, however, will have to be one that identifies the appropriate dynamic states and the multiplicity of possible plutonic-volcanic products which, even in one system, may vary in composition, mineralogy and textures over virtually the entire igneous range of rock types. Something like an igneous power spectrum, in terms of amplitudes and frequencies of basaltic rate regimes, will be required to characterize the vital signs of each uniquely different igneous system. Smith's (1979) approach to volume- and time-dependent parameters represents a major step toward a dynamic basis for classification of igneous systems.

INTRUSIVE RATE REGIMES AND CONCEPTS OF RESIDENCE TIMES

Discussion of a complete dynamic classification of igneous systems is not attempted in this paper. I suggest, however, that there is a hierarchy of dominant factors to be considered, the most conspicuous of which, based on the correlations discussed above, are the mantle source-rate and intrusive-rate regimes. Other factors that characterize different igneous regions of the globe depend on tectonic stress regions related to plate tectonics (and smaller scale stress domains within these regions) and to the varieties of lithologies within such regions.

As discussed by Shaw (1980), the interaction of magma generation rates, stress domains and injection rates leads to a spectrum of residence times which effectively determine the types of intrusive and volcanic suites seen at high crustal levels and at the surface. Specific geochemical signatures of these suites, of course, are influenced by the chemical path incurred in transit from the melting source to the surface. In this general model, the entire sequence of evolutionary processes is self-regulatory; that is, in the broadest sense it represents a cyclical feedback loop.

A key factor in the genetic circuit is the dynamics of magma generation in the mantle relative to the dynamics of tectonic deformation of the continental crust. To the extent that these dynamic regimes become decoupled, the magma generation rates in the mantle are independently imposed on the crustal tectonic regimes. Eventually, however, if a given intrusive rate regime persists, crustal tectonics will be influenced by

that regime. For example, if the HHER regime were superimposed on a crustal region dominated by horizontal compression, the intrusive style might be reflected in stratiform ultramafic and gabbroic intrusions, as mentioned earlier. At some stage in this process, however, the crustal stress states probably will become reoriented or may degenerate to a condition that permits horizontal extension accompanied by comparatively unimpeded flow-through of basaltic magma. In such a case the system may experience a transition from long residence times at high injection rates to short residence times at high injection rates.

Thus, a more refined dynamic classification than is attempted here must take into account not only the dominant intrusive rate regimes but the evolution of tectonic stress states and the subsequent chemical interactions implied by the residence times and magma injection paths. An example of this approach is given by Bacon (1983b) relative to the evolution of the Coso volcanic field, California. In terms of the present classification of intrusive rate regimes, the Coso system has been operating at a power possibly somewhat less than the MHER regime for a duration of about 0.5 m.y. The intrusive rate has been sufficient to generate silicic magma, but so far it has been insufficient to generate the ash-flow stage of magmatism; see Bacon (1982, 1983b). Documentation of the at present less energetic systems, such as the Henry Mountains intrusions and the Coso volcanic field, is highly important to the development of a dynamic classification of the igneous rocks. In a sense, this importance is even greater than that of the more emphasized ash-flow systems, because the lower rate systems document processes during the approach to the climactic ash-flow stages of eruption.

TERMINAL STAGES OF INTRUSIVE REGIMES

Apparently, there must be evolutionary affinities of plutonic associations analogous to the characteristic affinities of ash-flow systems. Before mentioning some of the types of plutonic or plutonic-volcanic associations that come to mind, I take some liberties with Smith's diagram (Figure 1a) which are intended to show, by comparison with the basaltic rate regimes of Figure 5, some of the possible directions of deviation from conditions of ash-flow magmatism.

Figure 6 portrays one way in which the Smith diagram of Figure 1a might terminate in the subsolidus. That is, the scale of ash-flow systems has a size limit, and there must be regimes that permit large-scale plutonic systems without evolution to stages of ash-flow volcanism. The maximum size and time span for Figure 6 are crudely scaled to the magnitude of the Sierra Nevada batholith; that is, the maximum volume is of the order 10^6 km^3, and the maximum time span is of the order 10^8 years.

Figure 6 identifies a "magmatic reversal" in the earth's geothermal gradient and a depth interval progressively approaching and intersecting the solidus and possibly the liquidus temperatures characteristic of a range of magmatic systems._/ Like the Smith diagram, the curves in Figure 6 represent a composite, or time-lapse view, of different stages in an evolutionary sequence. Judging from the maximum sizes of distinct

_/ By "magmatic reversal" I am referring to the existence of a molten interval of the crust that is anomalous relative to normal crustal sections. Usually, this will also be associated with a reversal, or reversals, in the thermal gradient. During certain late stages of zoned chambers, however, actual temperature gradients are not necessarily reversed, depending on the gradients of melting points with composition in derivative and fractionated magma.

igneous plutons, however, this example may include stages near the limit of magmatic regimes capable of sustaining a quasisteady balance between injection rates and maintenance of an at least partially molten high-level magma chamber (cf, Figure 2).

For example, a vertical section at the right-hand margin of Figure 6 (section B) would have a thermal gradient approaching but not quite intersecting the solidus. This thermal gradient resembles the upper portions of the right-hand profiles in the middle and bottom rows of thermal anomalies in Figure 2 relative to the 100 km^2 reference area; the lower portions would depend on the total area of influence and the overall time scale. Such a system would correspond to a condition of progressive regional metamorphism without magma generation. Like the scale ranges for magmatic systems, there must also be analogous classifications for regional metamorphic systems associated with magmatic injections that did not produce high-level chambers.

A vertical section at the position of the heavy dashed vertical line in Figure 6 (section A) has a thermal profile something like the middle profile in the second row of profiles in Figure 2, although the time scale would be longer. Such a system is capable of producing derivative and fractionated magma and to erupt in the manner discussed by Smith (1979). The distribution of residual magma and solid rock types for this case is indicated schematically at the left. At the termination of the life of the mafic support system, the solidified products would be zoned from silicic at the top to mafic at the bottom. Between the conditions of vertical sections A and B, however, a series of pluton types with complex

internal chemical gradients and less sharply defined vertical gradients of rock types would be produced.

Considering the variety of basaltic source signatures available from the rate spectrum of either Figure 3 or Figure 5, many distributions other than the simple vertical zonations of Figure 6 are both possible and expected. On the one hand, if a given high-level magmatic evolution is governed by the net time variations, it can be reactivated at any stage of the solidification process, and a renewed regime of derivative and fractionated magma can be superimposed on the previous evolution. This is roughly the situation involved in the history of multiple caldera systems of otherwise simple form; the Valles and Yellowstone systems are of this type, and by inference it would be suspected for a system the size of the Long Valley, California, chamber. On the other hand, if in addition to the net temporal fluctuations there are also spatial variations analogous to the ones implicit in Figure 3, there is great potential diversity in the rates of evolution of geographically related clusters of high-level magmatic systems. Some of the complexities shown by large fields relate to analogous temporal-spatial rate variations (e.g., the Snake River-Yellowstone trend, the San Juans, and so on).

In some situations, there may be little evidence in the solidified sections of derivative magma types to distinguisn between a system that never achieved tne eruptive stage of ash-flow magmatism and a waning system that had no evidence of its fractionated and erupted fractions through factors involving posteruptive tectonics and/or denudation. The overall regional signatures of effects in the two cases, however, should

be quite different. The evolution in each case will have to be pieced together on the basis of the composite evidence of plutonic, volcanic, and mineralization histories.

Residual plutonic associations that represent the roots of caldera-forming high-level magma chambers have had a different history of minor and trace element concentrations than other systems that never achieved that status. That may explain why some plutonic associations of large scale have different mineralization histories than other plutons of similar size and major element composition. Examples of productive plutons could be nested within a batholithic complex of relatively barren plutons because of the temporal-spatial variations of mafic sources discussed above.

In other situations, some of the isolated granitic plutons of diapiric or of syntectonic characteristics are formed within the LHER magmatic regime. Examples such as the Colville batholith described by Waters and Krauskopf (1941) could represent an example of this regime, or it may be residual within a more extensive regional regime of higher generation rates. Many examples of intrusive porphyries may also be generated in the LHER regime, either in isolation or superimposed on residual plutons of a previous or associated MHER regime. Some porphyry copper deposits might be found as products of subsystems representing part of a caldera-forming system, or they might evolve independently at the same characteristic rates, whatever those may be. Possibly there is an evolutionary branch of the rate spectrum for ash-flow systems that is characteristic of the porphyry copper type of intrusive history.

The overall signature of mafic source systems in the mantle should be evident in the record of well-documented volcanic-plutonic continental igneous associations. Reconstructions based on the Smith model and the volumetric proportionalities indicated by Smith and Shaw (1973, 1975, 1979) provide data that make it possible to infer the magmatic power (in terms of volume rates) of the mantle source relative to some volcanic and/or plutonic provinces. However, a chronologic catalog of volumetric data for mafic systems analogous to the catalog of silicic systems is essential to documentation of the quantitative igneous history of the subcontinental mantle.

In this regard, a suggestive comparison on the largest scale is indicated by the cumulative volume shown in Figure 4 for tne Hawaiian-Emperor system. The total volume extruded over the 75-million-year history is about 10^6 km^3 relative to an area of the order $10^6 km^2$. By comparison, the total volume of the Sierra Nevada plutons to a depth of 10 km is also about 10^6 km^3 relative to an area of about 10^5 km^2, and the duration of batholithic emplacement was of the order 10^8 years (Kistler and others, 1971; Shaw and others, 1971), giving a rate of about 10^{-2} km^3/yr. It appears, therefore, that on this basis much of the Sierran evolution operated in the oscillatory MHER regime in which episodically extensive ash-flow systems would be expected, although in a syncopated fashion relative to the chronological variations of pluton ages. Offsets in the timing of volcanic and plutonic ages are artifacts of the complexities shown by the composite histories and tne fact that the residual pluton histories are much prolonged relative to the

maxima of ash-flow extrusion rates. Furthermore, some of the Sierran plutons probably formed in the LHER regime, making the composite history locally difficult to decipher.

It is also difficult to identify specific plutons with specific volcanic products because of the subsequent plutonic histories. However, a key to the puzzle is the relation between local volume rates of growth, depth intervals, durations, and total areas of influence. For example, the evolution of root systems in the Hawaiian-Emperor system itself can be considered by reference to Figure 2 and the total area of influence. In these terms, there are about 10^6 km^2 divided by 10^2 km^2 (reference area in Figure 2) = 10^4 reference systems in the H-E system. In order for each root system to achieve liquidus temperature at crustal depths, an average time of at least 30,000 years is required (depending on the depth range considered). Thus, the minimum total time required for such a propagating system to produce a pervasive zone of plutons at crustal depths is at least 3×10^8 years ($30{,}000 \times 10^4$), which is several times the total lifetime of the Hawaiian-Emperor system. That is, the type of crustal anomaly, as indicated earlier, depends not only on the source power but its areal focus and rates of migration.

If the Sierra Nevada batholith is considered in the same terms as the Hawaiian-Emperor system, the number of reference areas relative to Figure 2 (100 km^2) is about 10^3. Assuming a depth interval of the order 10 km (i.e., crustal thickness as the limit), Figure 2 indicates that times of 30,000 to 300,000 years are required to achieve persistent

magmatic conditions at a supply rate of the order 10^{-2} km^3/yr. Thus, the total time for the evolution of the system as a whole is between 3×10^7 and 3×10^8 years. This fits well with the emplacement duration of about 10^8 years, and suggests that the Sierra Nevada evolution represents an areally migrating source that was intermittently sufficiently focused and powerful to satisfy conditions for ash-flow magmatism. The volcanic effectiveness, then, depended on the duration of areal focusing at a mean rate oscillating about the MHER.

The above generalizations can be reduced to the following rule-of-thumb: ash-flow magmatism can occur if the magmatic source flux is of the order 10^{-2} km^3/yr divided by the active area, and lasts for a time given by the "Dominant Volume" divided by the mean rate after the liquidus temperature is achieved in a crustal anomaly, if the "active area" and the "chamber area" are the same. Thus, the ratios of time (years), chamber volume (κm^3) and ash-flow volume (km^3) are in the approximate proportions 1000:10:1. Near climactic stages of chemical evolution, eruptive evolution may be greatly accelerated relative to these rates or may be accelerated at some time after the appropriate silicic compositions have been achieved.

CONCLUDING REMARKS ON RELATIONS BETWEEN RATE REGIMES, SEISMIC SIGNATURES AND VOLCANIC HAZARDS

Shaw (1980) proposed that there are systematic relations between magma injection rates, seismic energy release, recurrence times and maximum earthquakes. The resemblance to models presently being proposed for magmatic activity at Long Valley, CA, is evident (see, S.S.A. Abstracts, Salt Lake City Meeting, May 1983), although evaluation of specific models is not attempted here. In combination with the magmatic source rate spectra discussed in the present paper, it is also evident that the volumetric history of continental volcanism offers a basis for delineation of magma-tectonic seismic regions. In view of the cyclical feedback relations between magma-tectonic rate processes and Plate Tectonic processes, a knowledge of magma-related seismic processes and provinces should also contribute importantly to our general knowledge of continental earthquake processes--besides its relevance to Volcanic Hazards programs. In both respects, precise and comprehensive data are needed for volumes and ages of volcanic-plutonic associations in the U.S. In this regard, all rate regimes are important. As a conjecture, I suggest that a comprehensive catalog of seismomagmatic regions, together with their prior rates of evolution, will contribute to the general knowledge of potential seismic moment distributions in other continental regions.

A final comment concerns the possible maximum rates at which an already evolved silicic magma chamber may approach an eruptive stage.

This presupposes either the rejuvenation of a prior eruptive history, or the culminating stages of an evolving system without prior caldera-forming eruptions. Reference to the graphs of Figures 3 and 5 shows that rates of the order 0.1 km^3/yr can be sustained for times long compared to the repose times between silicic eruptions identified by Smith (1979). Such rates are an order of magnitude larger than the mean evolutionary rate. Consequently, a system that has already developed the fractionated volume in Figure 1a can be brought rapidly to the climactic stage by a higher supply rate. Conceivably, even a few years at a rate of 10^{-1} km^3/yr (and transiently even higher rates) could activate or reactivate a major ash-flow eruption in a system already sufficiently advanced in its chemical evolution. For example, a hundred years at 10^{-1} km^3 represents an inflation of the order 10 km^3, which approximates the volumetric magnitude of a Mazama-like eruption and is roughly an order of magnitude larger than the Mt. St. Helens eruption. In this context, studies by C. R. Bacon (1983a) at Crater Lake, Oregon, demonstrate the potentiality of a rapid sequence of multiple climactic eruptions on a time scale of the order 200 years.

Although the general implications are dramatic relative to potential eruptions from a large caldera-forming system such as Long Valley, highly specific information is necessary to assess the proximity of a climactic stage. In this regard, the critical data represent a combination of the chemical rate of fractionation and the volumetric rate of influx to the root system of primitive magma (Figure 1a). Current studies should emphasize evaluation of both factors insofar as possible over the latest

stages of the magma-tectonic history, including evaluation of neighboring systems; attempts to determine the present volumetric rates of chemical evolution are of critical importance. Even if it is considered unlikely, the possibility of a large-scale eruption from the Long Valley caldera, or from a neighboring system of the eastern Sierra Nevada region, should be given sufficient credence to maintain current studies at the highest levels of priority. Needless to say, similar conclusions apply to the Yellowstone region and many other systems of smaller scale in the western U.S.

Acknowledgements

I thank Wes Hildreth, Susan Russell-Robinson, John Stormer, and Patrick Muffler for constructive criticisms. I also thank Anne Gartner for all computer data processing, and Fidelia Portillo for her implementation of the drafting of figures. My thanks also go to R. L. Smith for the years of patient dialogue concerning ash-flow magmatism, and to Marie Jackson for discussions of the Henry Mountains intrusions.

References

Bacon, C. R., Time-predictable bimodal volcanism in the Coso Range, California, Geology, 10, 65-69, 1982.

Bacon, C. R., Eruptive history of Mount Mazama and Crater Lake caldera, Cascade Range, U.S.A., J. Volc. Geoth. Res., 18, 57-115, 1983a.

Bacon, C. R., Possible relations between magmatism, extension rates, and the state of stress in the crust, Geol. Soc. Am. Abstracts with Program, 15, no. 5, 288, 1983b.

Daly, R. A., Igneous rocks and the depths of the eartn, New York, McGraw-Hill Book Co., Inc., 1933.

Dana, J. D., Gilbert's report on the geology of the Henry Mountains, Am. Jour. Sci., 19, 17-25, 1880.

Gilbert, G. K., Report on the geology of the Henry Mountains, U.S. Geographical and Geological Survey, Rocky Mountain Region, 160 pp., 1877.

Hunt, C. B., P. Averitt, and R. L. Miller, Geology and geography of the Henry Mountains region, UT, U.S. Geol. Sur. Prof. Pap., 228, 1953.

Jackson, E. D., Linear volcanic chains on the Pacific plate, in Geophysics of the Pacific basin, Am. Geophys. Union Monogr., 19, 319-335, 1976.

Jackson, E. D., E. A. Silver, and G. B. Dalrymple, Hawaiian-Emperor chain and its relation to Cenozoic circumpacific tectonics, Geol. Soc. Am. Bull., 83, 601-617, 1972.

Kistler, R. W., J. F. Evernden, and H. R. Shaw, The Sierra Nevada plutonic cycle, Part I. The origin of composite granitic batholiths, Geol. Soc. Am. Bull., 82, 853-868, 1971.

McBirney, A. R., J. F. Sutter, H. R. Naslund, K. G. Sutton, and C. M. White, Episodic volcanism in the central Oregon Cascade range, Geology, 2, 585-589, 1974.

Pollard, D. D., and A. M. Johnson, Mechanics of growth of some laccolithic intrusions in the Henry Mountains, UT, Tectonophysics, 18, 311-354, 1973.

Shaw, H. R., Mantle convection and volcanic periodicity in the Pacific; Evidence from Hawaii, Geol. Soc. Am. Bull., 84, 1505-1526, 1973.

Shaw, H. R., The fracture mechanisms of magma transport from the mantle to the surface, in Physics of magmatic processes, edited by R. B. Hargraves, pp. 201-264, Princeton University Press, Princeton, N.J., 1980.

Shaw, H. R., E. D. Jackson, and K. E. Bargar, Volcanic periodicity along the Hawaiian-Emperor chain, Am. J. Sci., 280-A, 667-708, 1980.

Shaw, H. R., Kistler, R. W., and Evernden, J. F., Sierra Nevada plutonic cycle: Part II, Tidal energy and a hypothesis for orogenic-epeirogenic periodicities, Geol. Soc. Am. Bull., 82, 869-896, 1971.

Shaw, H. R., and D. A. Swanson, Eruption and flow rates of flood basalts, in Columbia River basalt symposium, 2nd Proceedings, edited by E. H. Gilmour, and D. Stradling, pp. 271-299, Eastern Washington State College Press, Cheney, Wash., 1970.

Smith, R. L., Ash-flow magmatism, Geol. Soc. Am. Special Paper 180, 5-26, 1979.

Smith, R. L., and R. A. Bailey, The Bandelier Tuff: A study of ash-flow eruption cycles from zoned magma chambers, Bull. Volc., 29, 83-104, 1966.

Smith, R. L., and H. R. Shaw, Volcanic rocks as geologic guides to geothermal exploration and evaluation: EOS [American Geophysical Union Trans.], 54, 1213, 1973.

Smith, R. L., and H. R. Shaw, Igneous-related geothermal systems, in Assessment of geothermal resources of the United States--1975, edited by D. E. White and D. L. Williams, U.S. Geol. Sur. Circ. 726, pp. 58-83, 1975.

Smith, R. L., and H. R. Shaw, Igneous-related geothermal systems, in Assessment of geothermal resources of the United States--1978, edited by L. J. P. Muffler, U.S. Geol. Sur. Circ. 790, p. 12-17, 1979.

Smith, R. L., H. R. Shaw, R. G. Luedke, and S. L. Russell, Comprehensive tables giving physical data and energy estimates for young igneous systems of the United States: U.S. Geol. Sur. Open-File Rept. 78-925, 1978.

Swanson, D. A., Magma supply rate at Kilauea volcano, 1952-1971, Science, 175, 169-170, 1972.

Waters, A. C., and K. Krauskopf, Protoclastic border of the Colville batholith, Geol. Soc. Am. Bull., 52, 1355-1418, 1941.

FIGURE CAPTIONS

Figure 1a. The volume-periodicity relation for ash-flow eruptions from high-level magma chambers; simplified, and embellished, from Smith (1979, Figure 12, p. 19). The curve labeled Max. Eruption Level is Smith's estimate of the deepest average level tapped, as measured from the top of the molten chamber; this level is usually within the zone of "Derivative" magma but may reach "Primitive" magma in the smaller systems capable of eruptions of a few cubic kilometers or less. The curve labeled Primitive Magma is Smith's Primitive Magma A. The dashed line is the highest level in the chamber to which any new pulse of primitive magma is thought to be capable of penetrating; therefore its intersection with the zero depth coordinate gives the largest chamber (order of 10 km^3) for which primitive magma might be seen in the eruptive product. The lines marked 50 percent and 100 percent represent depth-volume relations for systems with progressively greater crystal contents (see Smith, 1979, for discussion, and Figure 6). The lens-like symbols in the zone of primitive magma indicate my interpretation of the pulsatory nature of magma percolation from the mantle according to mechanisms of extensional fracture and "failure cascades" (Shaw, 1980); Figure 2 represents the potential thermal states of such intervals as the "packing" of intrusive pulses increases to 100 percent of the interval.

Figure 1b. Solidification times for magma chambers spanning the size scales of caldera-forming systems. Solidification refers to crystallization for a liquidus-solidus interval from 850°C to 650°C and a depth of cover of 4 km. The convective slab is the "reasonable" limit of most rapid solidification; it assumes "ideal stirring" (contact maintained at magma temperature) during the first 50 percent crystallization, and conduction thereafter. The conductive cube (or sphere) is the longest-lived at constant volume. This is because the calculated curves are for constant shape; volume increases as the cube of a characteristic length, and cooling time increases roughly as the square of that length, hence time is roughly proportional to the two-thirds power of volume at constant shape. The stippled area corresponds to the volume range of Figure 2, and roughly to the emplacement time span of the middle column of emplacement rates in Figure 2. The hachured area is the approximate bounds of systems evaluated by Smith and Shaw (1979, Figure 3; incidentally, curve 3 of that figure should read "conduction m=n=10Z slab" instead of "convection"). The crosses and vertical dotted lines are examples discussed in the text relative to average volume rates inferred from this diagram for repetitive intrusion. This ratio is roughly 10^{-2} km^3/yr in the centroid of the stippled area. Such ratios, and the rule-of-thumb of Smith and Shaw (1975) that the silicic extrusive volume is roughly one-tenth of the total supporting magma chamber volume, represent one aspect of the rationale for the time-volume scale of Figure 1a; the same argument represents the theme of the present paper that such rates are characteristic of magma chambers

supporting evolving caldera-forming systems. Systems older than the solidification times have subsolidus thermal states (and geothermal potentials) related to the size scale of the residual thermal anomaly, unless there has been recent resupply to the root system of primitive magma in Figure 1a. Systems that are about the same age as the solidification times can be suspected of still containing magma and of being susceptible to rejuvenation by basaltic inputs; younger systems, of course, should contain significant amounts of molten magma and may be volcanically active unless there have been unusual quenching effects (see discussion of hydrothermal quenching effects in Smith and Shaw, 1979).

Figure 2. Thermal anomalies in the crust generated by given rates of influx of basaltic magma (after Shaw, 1980, Figure 19, p. 256); see text for discussion, and Smith and Shaw (1975, 1979). The rows indicate depth intervals for storage of primitive magma at high levels in the crust; the depth intervals are 5 to 6 km (top row), 5 to 10 km (middle row) and 5 to 15 km (bottom row). The columns represent rates (numbers in parentheses in km^3/yr) of influx of primitive magma into these intervals to sustain a magma chamber at (a) the liquidus of tholeiitic basalt (left column), (b) the approximate liquidus of intermediate to silicic derivative magma (middle column), or (c) the approximate solidification state (greater than 50 percent crystals) of intermediate to silicic derivative magma (right column). These column regimes correspond in a very crude way to a progression from the high Hawaiian rate (HHER) in the upper left frame, to the lowest of

(nonzero) Hawaiian rate regimes (LHER) in the lower right frame; the oscillatory MHER regime is likely in the middle column of this sequence. The calculations of thermal profiles are based on standard source models for layered media with conductive boundary conditions. The temperatures are fairly accurate as to maxima and the surface gradients; otherwise they are sketched in to merge with a reference geothermal gradient of 30°C/km. Each calculation is based on a standard area of 100 km^2, corresponding to maximum magma volumes of 100, 500 and 1000 km^3, respectively, for the three rows; extrapolation to composite systems or to systems of larger areal extent is proportional to the greater area and to any shifts in assumed starting times. Persistence of the source beyond the maximum time implies either flow-through, and increasing local temperatures, or to an increasing interval thickness. Therefore, profiles of increasing thickness and the same rates also indicate the effects of prolonging the duration of the heat source.

Figure 3. Episodic variation of basaltic extrusion rates along loci of the Hawaiian-Emperor chain (after Shaw and others, 1980, Figure 10, p. 696). These are "instantaneous" rates determined from calculated volumes and durations of individual volcanoes of the chain, as contrasted with Figure 5 which represents smoothed values derived from least square regressions on line intervals of Figure 4.

Figure 4. Cumulative volumes of basaltic lava to form the Hawaiian-Emperor chain based on data in Shaw and others (1980, Table 2, p. 686). Slopes of different episodic curve segments give smoothed net variations in extrusion rates as contrasted with Figure 3 which shows details of the temporal variations along loci.

Figure 5. Slopes of curve segments in the net cumulative record of Figure 4 relative to the mean linear rate. On this graph the mean linear rate of 0.0147 km^3/yr has a slope of zero, and zero rate is a slope of -14.7 ($X10^{-3}$) km^3/yr; zero rate corresponds to horizontal curve segments in Figure 4, and 100 on the ordinate rate would correspond to 0.1 km^3/yr. The reason the rate on this graph at age zero is only about 0.07 km^3/yr rather than the present observed value of 0.1 km^3 (or the projected instantaneous value of 0.3 km^3/yr in Figure 3), is because of averaging over the latest 3 m.y.

Figure 6. Elaboration of the terminal stages of Figure 1 in terms of possible crystal-liquid distributions, volume and time; see text for discussion of sections A and B. This diagram is a schematic enlargement of the right side of Figure 1a. The zoned interval at the left margin represents the inferred solidification states for temperatures implied by the crystallization contours (the dashed curves labeled 50, 75, 100 percent) where they intersect the vertical section A (an age somewhat greater than 10^7 years, and a volume somewhat larger than 10^4 km^3). Residual, still-molten

derivative magma exists in an upper zone separated by solid derivative from a lower hybrid zone that may or may not grade down into molten primitive magma. This zoning may persist until solidification is complete, or it may be rejuvenated by superposition of some new rate regime of primitive magma according to the rate curves of Figure 5 and the thermal effects of Figure 2. Beyond a certain size and age, however, there is some limit of depth, volume rate and duration of supply that is not capable of sustaining a high-level molten silicic system. This limit corresponds to conditions of piecemeal composite intrusions merging with conditions of migmatite zones and regional thermal metamorphism.

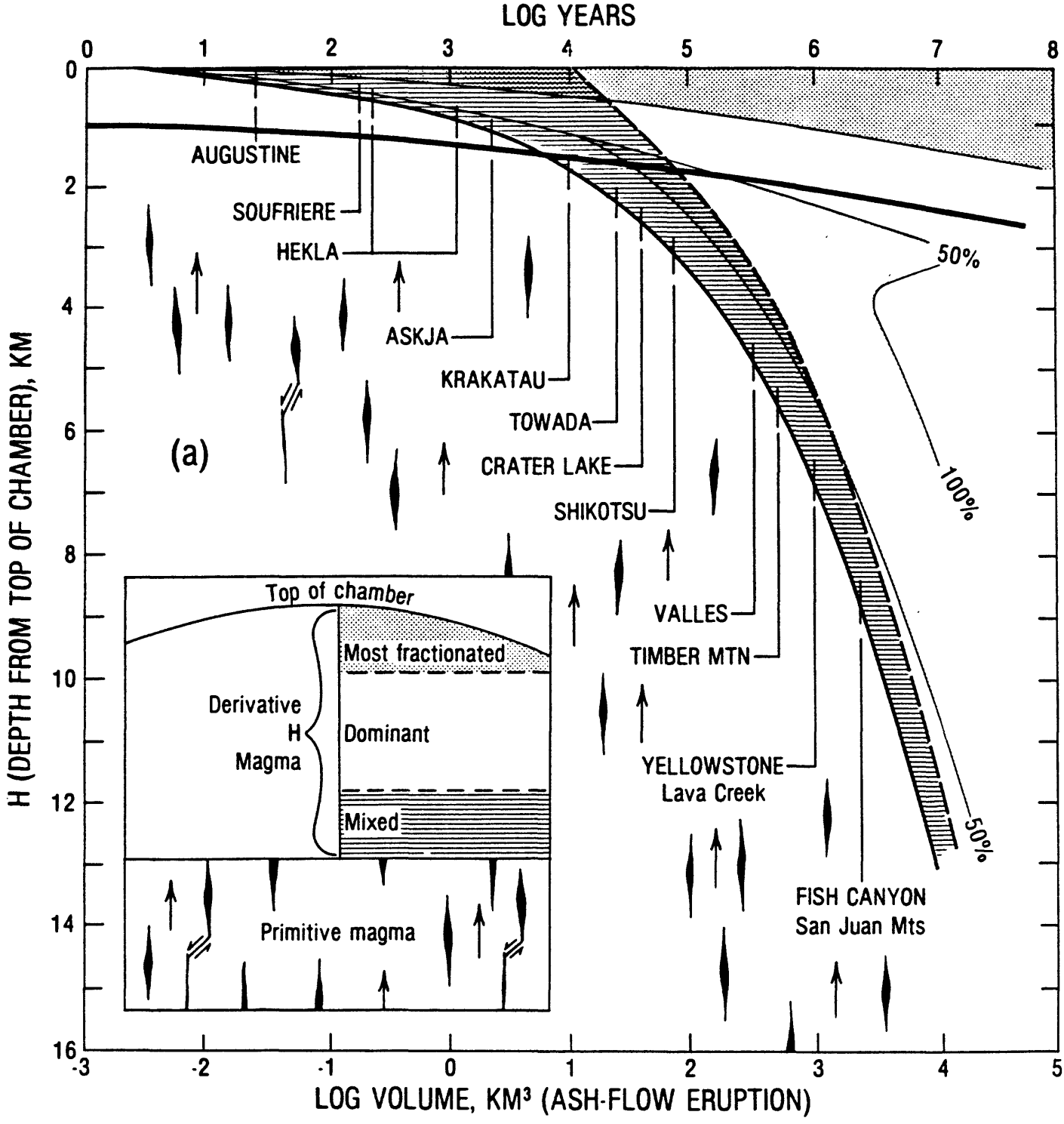

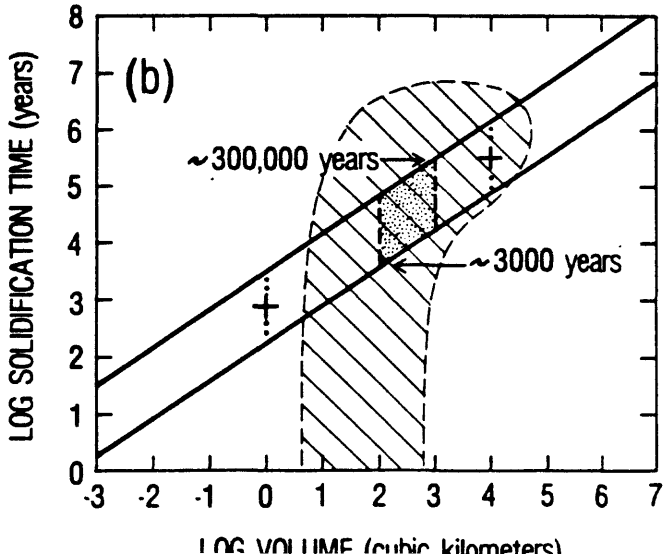

EXPLANATION FOR (a)

- Maximum eruption level
- Primitive magma (below curve; transiently to the penetration limit)
- Penetration limit
- Potential mixed magma
- Zone of solidification (within derivative magma)
- Most fractionated

Fig. 1.

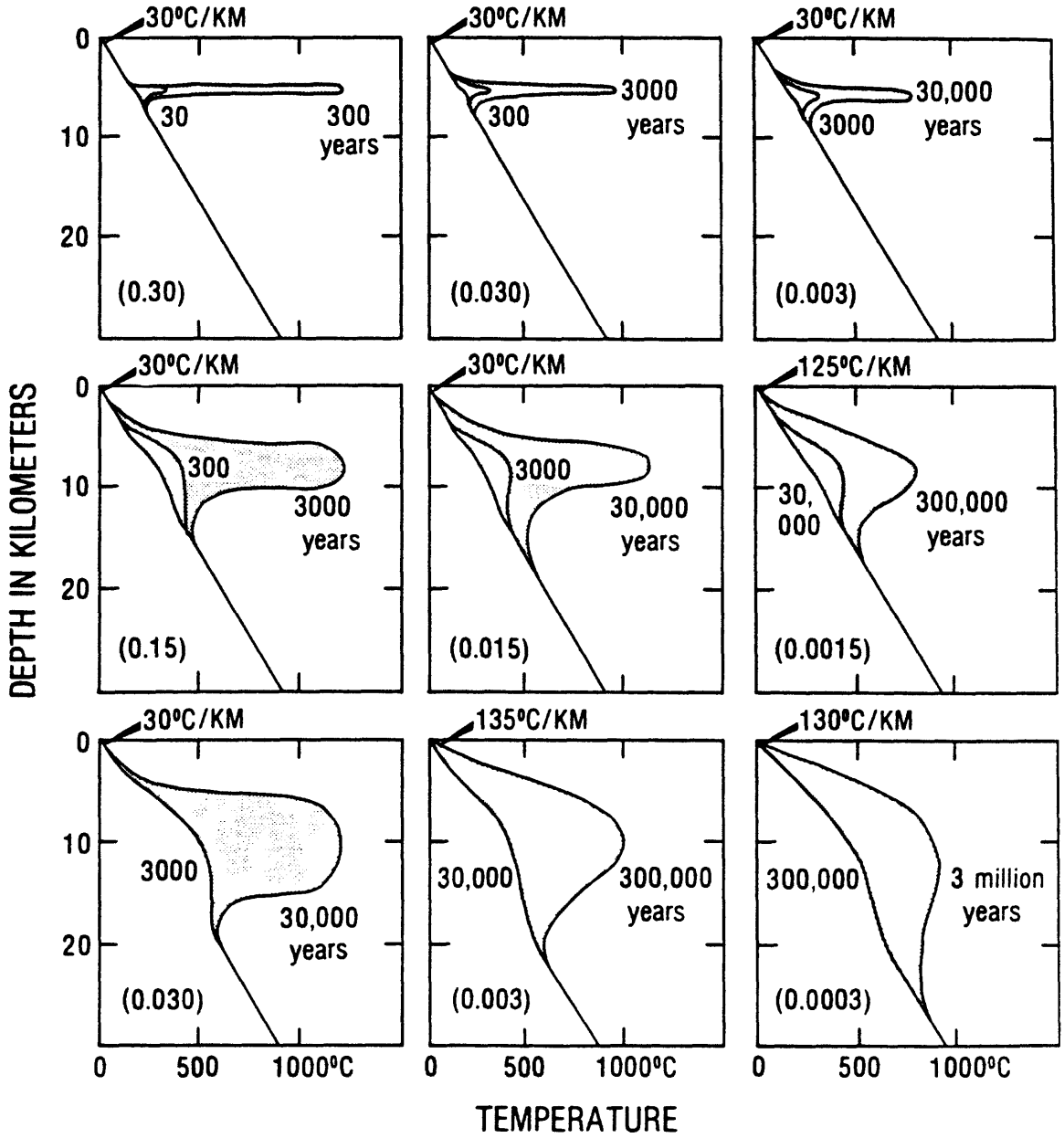
30°C/KM
30
300
years
(0.30)
30°C/KM
300
3000
years
(0.030)
30°C/KM
3000
30,000
years
(0.003)
30°C/KM
300
3000
years
(0.15)
30°C/KM
3000
30,000
years
(0.015)
125°C/KM
30,
000
300,000
years
(0.0015)
30°C/KM
3000
30,000
years
(0.030)
135°C/KM
30,000
300,000
years
(0.003)
130°C/KM
300,000
3 million
years
(0.0003)
0
10
20
0
500
1000°C
DEPTH IN KILOMETERS
TEMPERATURE

Fig. 2.

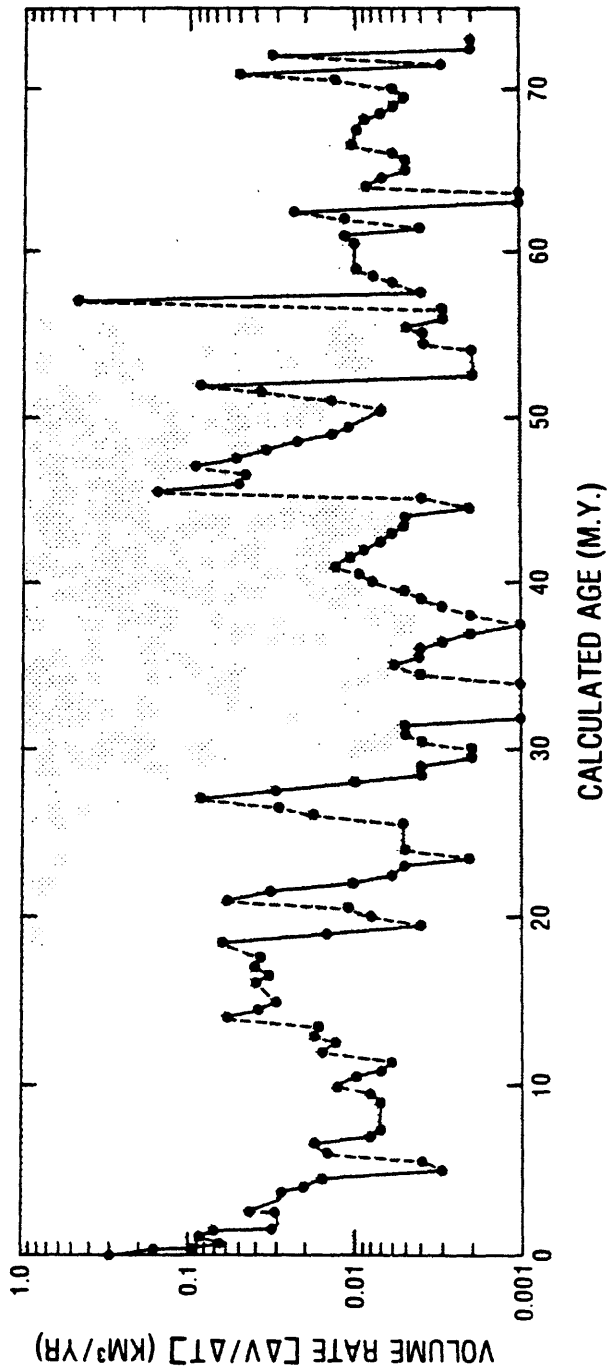
VOLUME RATE [ΔV/ΔT] (KM³/YR)
1.0
0.1
0.01
0.001
0
10
20
30
40
50
60
70
CALCULATED AGE (M.Y.)

Fig.3.

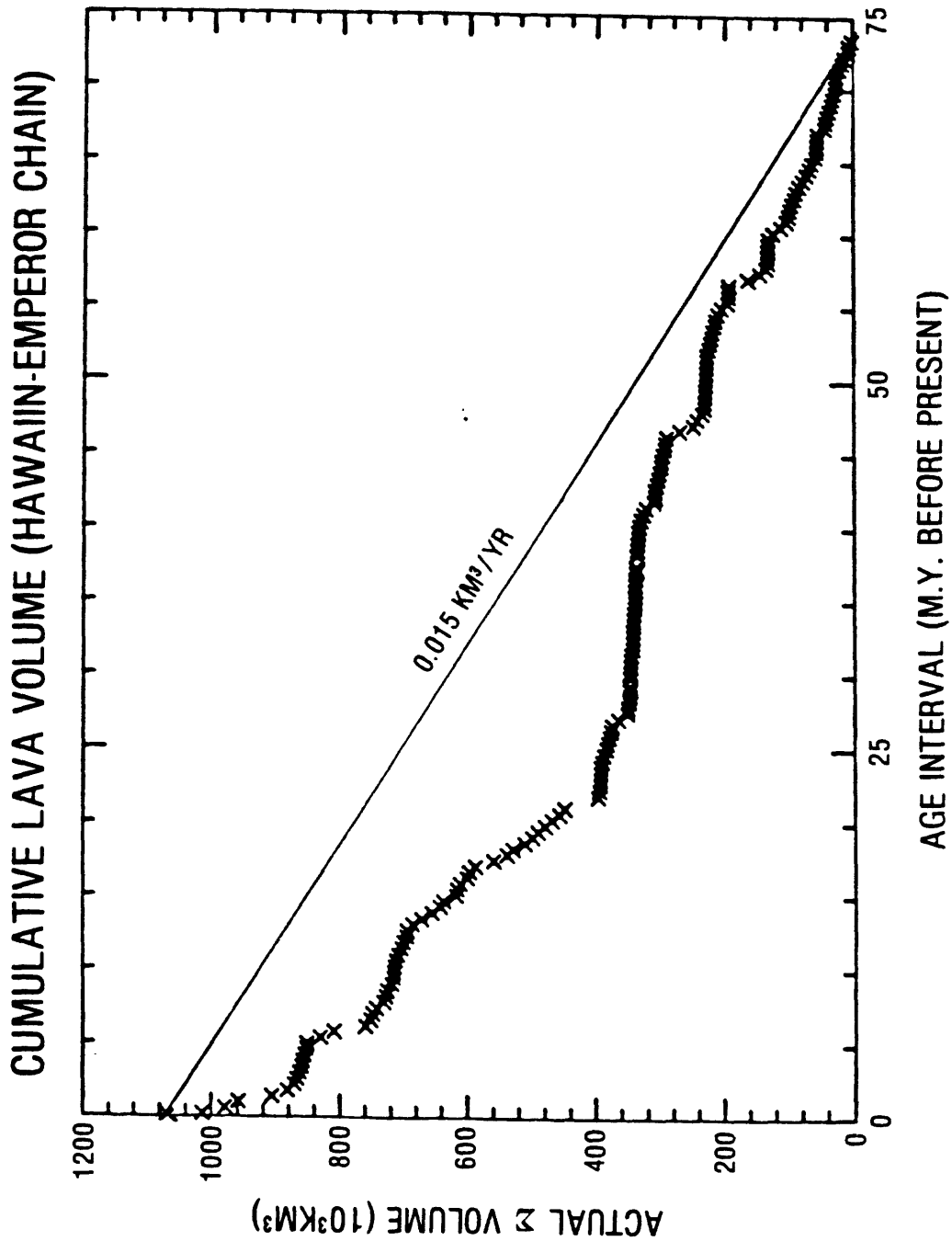
CUMULATIVE LAVA VOLUME (HAWAIIN-EMPEROR CHAIN)
ACTUAL Σ VOLUME (10³KM³)
AGE INTERVAL (M.Y. BEFORE PRESENT)
0.015 KM³/YR
0
200
400
600
800
1000
1200
0
25
50
75

Fig. 4.

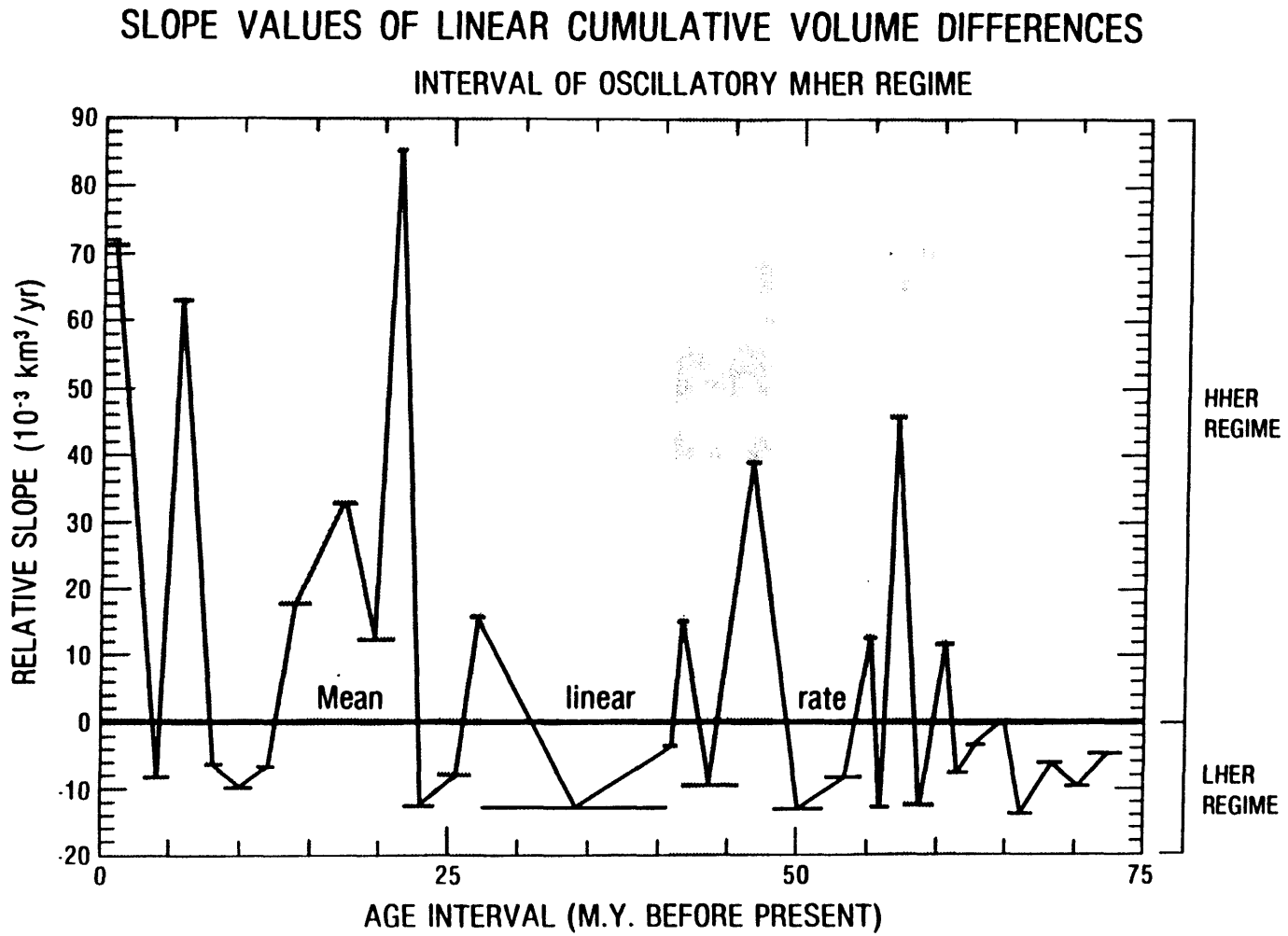
SLOPE VALUES OF LINEAR CUMULATIVE VOLUME DIFFERENCES
INTERVAL OF OSCILLATORY MHER REGIME
RELATIVE SLOPE (10⁻³ km³/yr)
90
80
70
60
50
40
30
20
10
0
-10
-20
0
25
50
75
AGE INTERVAL (M.Y. BEFORE PRESENT)
Mean
linear
rate
HHER REGIME
LHER REGIME

Fig. 5.

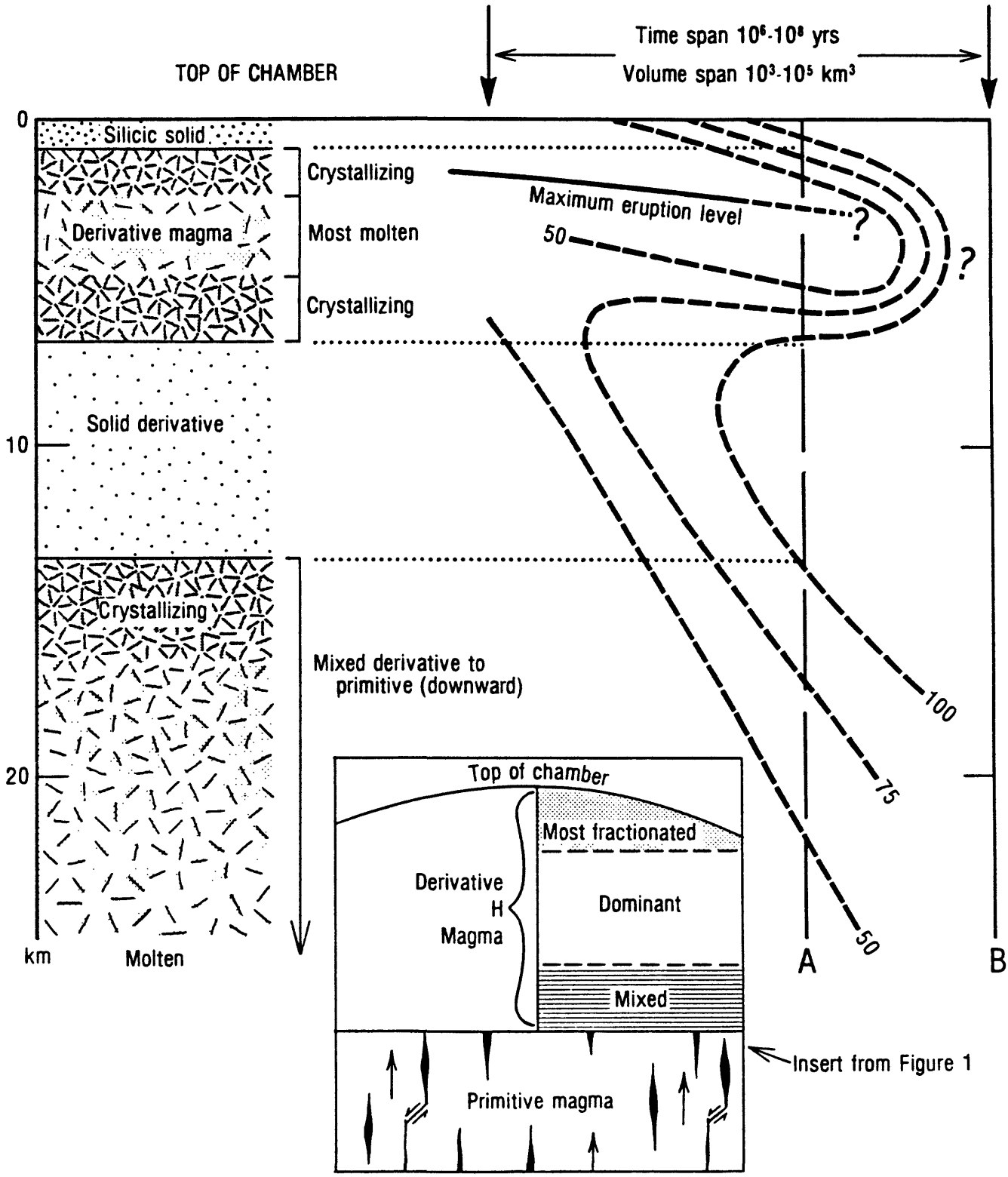

SCHEMATIC OF VOLCANIC-PLUTONIC TRANSITION

Fig. 6.